AFRL-ML-WP-TR-2005-4102

ADVANCED HIGH CYCLE FATIGUE (HCF) LIFE ASSURANCE METHODOLOGIES

J. Gallagher, T. Nicholas, A. Gunderson, J. Ruschau,
P. Miedlar, A. Hutson, G. Hardy, D. Walls, C. Annis,
R. deLaneuville, P. Gravett, E. Hindle, M. Szolwinski, R. Naik, B. Cowles, J. Adamson,
R. Pettit, K. Kersey, M. Marotta, D. Corbly, R. VanStone, D. Slavik, M. Hartle,
R. McClain, K. Wright, H. Merrick, D. Cameron, Y. Lenets, J. Hartman, K. Cornet,
D. Wildman, C. Weeks, P. Bastnagel, T. Cook, A. Chaterjee, S. Hudak, K. Chan,
C. McClung, D. Davidson, G. Chell, Y. Der Lee, T. Farris, A. Grandt, P. Golden,
H. Murthy, B. Bartha, J. Matlik, D. Garcia, E. Perez-Ruberté, P. Rajeev, A. Kallmeyer,
P. Kurath, G. Glinka, and B. Lawless

University of Dayton
Research Institute
300 College Park
Dayton, OH   45469-0120

JULY 2004

Final Report for 01 April 1999 – 01 July 2004

STINFO FINAL REPORT

MATERIALS AND MANUFACTURING DIRECTORATE
AIR FORCE RESEARCH LABORATORY
AIR FORCE MATERIEL COMMAND
WRIGHT-PATTERSON AIR FORCE BASE, OH 45433-7750

NOTICE

Using Government drawings, specifications, or other data included in this document for any purpose other than Government procurement does not in any way obligate the U.S. Government. The fact that the Government formulated or supplied the drawings, specifications, or other data does not license the holder or any other person or corporation; or convey any rights or permission to manufacture, use, or sell any patented invention that may relate to them.

This report was cleared for public release by the Air Force Research Laboratory Wright Site Public Affairs Office (AFRL/WS) and is releasable to the National Technical Information Service (NTIS). It will be available to the general public, including foreign nationals.

THIS TECHNICAL REPORT IS APPROVED FOR PUBLICATION.

/s/_____   /s/_____
RYAN J. MORRISSEY, Project Engineer   ROLLIE E. DUTTON, Chief
Metals Branch   Metals Branch
Metals, Ceramics & NDE Division   Metals, Ceramics & NDE Division

/s/_____
GERALD J. PETRAK, Assistant Chief
Metals, Ceramics & NDE Division
Materials & Manufacturing Directorate

This report is published in the interest of scientific and technical information exchange and its publication does not constitute the Government's approval or disapproval of its ideas or findings.

REPORT DOCUMENTATION PAGE

Form Approved
OMB No. 0704-0188

The public reporting burden for this collection of information is estimated to average 1 hour per response, including the time for reviewing instructions, searching existing data sources, searching existing data sources, gathering and maintaining the data needed, and completing and reviewing the collection of information. Send comments regarding this burden estimate or any other aspect of this collection of information, including suggestions for reducing this burden, to Department of Defense, Washington Headquarters Services, Directorate for Information Operations and Reports (0704-0188), 1215 Jefferson Davis Highway, Suite 1204, Arlington, VA 22202-4302. Respondents should be aware that notwithstanding any other provision of law, no person shall be subject to any penalty for failing to comply with a collection of information if it does not display a currently valid OMB control number. **PLEASE DO NOT RETURN YOUR FORM TO THE ABOVE ADDRESS.**

1. REPORT DATE *(DD-MM-YY)*	2. REPORT TYPE	3. DATES COVERED *(From - To)*
July 2004	Final	04/01/1999 – 07/01/2004

4. TITLE AND SUBTITLE	5a. CONTRACT NUMBER
ADVANCED HIGH CYCLE FATIGUE (HCF) LIFE ASSURANCE METHODOLOGIES	F49620-99-C-0007
	5b. GRANT NUMBER
	5c. PROGRAM ELEMENT NUMBER 61102F

6. AUTHOR(S)	
J. Gallagher, T. Nicholas, A. Gunderson, J. Ruschau, P. Miedlar, A. Hutson, G. Hardy, D. Walls, C. Annis, R. deLaneuville, P. Gravett, E. Hindle, M. Szolwinski, R. Naik, B. Cowles, J. Adamson, R. Pettit, K. Kersey, M. Marotta, D. Corbly, R. VanStone, D. Slavik, M. Hartle, R. McClain, K. Wright, H. Merrick, D. Cameron, Y. Lenets, J. Hartman, K. Cornet, D. Wildman, C. Weeks, P. Bastnagel, T. Cook, A. Chaterjee, S. Hudak, K. Chan, C. McClung, D. Davidson, G. Chell, Y. Der Lee, T. Farris, A. Grandt, P. Golden, H. Murthy, B. Bartha, J. Matlik, D. Garcia, E. Perez-Ruberté, P. Rajeev, A. Kallmeyer, P. Kurath, G. Glinka, and B. Lawless	**5d. PROJECT NUMBER** 2306D
	5e. TASK NUMBER X
	5f. WORK UNIT NUMBER FQ8671-0200194P0

7. PERFORMING ORGANIZATION NAME(S) AND ADDRESS(ES)	8. PERFORMING ORGANIZATION REPORT NUMBER
University of Dayton Research Institute 300 College Park Dayton, OH 45469-0120	UDR-TR-2003-00115

9. SPONSORING/MONITORING AGENCY NAME(S) AND ADDRESS(ES)	10. SPONSORING/MONITORING AGENCY ACRONYM(S)
Materials and Manufacturing Directorate Air Force Research Laboratory Air Force Materiel Command Wright-Patterson AFB, OH 45433-7750	AFRL/MLLMN
	11. SPONSORING/MONITORING AGENCY REPORT NUMBER(S) AFRL-ML-WP-TR-2005-4102

12. DISTRIBUTION/AVAILABILITY STATEMENT
Approved for public release; distribution is unlimited.

13. SUPPLEMENTARY NOTES
Report contains color.

14. ABSTRACT

This program was a follow-on effort to a program on Improved High Cycle Fatigue (HCF) Life Prediction, USAF Contract F33615-96-C-5269, the results of which are documented in the final report on that PRDA program [1]. This program continued work on addressing key issues associated with developing, verifying, & implementing a material damage tolerant design methodology capable of predicting HCF limits & material thresholds for Ti-6Al-4V. The methodology development was extended to another titanium alloy, Ti-17, and to a nickel-base single crystal alloy, PWA 1484.

15. SUBJECT TERMS
High Cycle Fatigue, Low Cycle Fatigue, fretting damage, foreign object damage (FOD), intrinsic material capability (stress threshold), crack nucleation, and propagation behavior, single crystal alloys, titanium alloys

16. SECURITY CLASSIFICATION OF:			17. LIMITATION OF ABSTRACT:	18. NUMBER OF PAGES	19a. NAME OF RESPONSIBLE PERSON (Monitor)
a. REPORT Unclassified	**b. ABSTRACT** Unclassified	**c. THIS PAGE** Unclassified	SAR	1,166	Ryan J. Morrissey
					19b. TELEPHONE NUMBER *(Include Area Code)* (937) 255-9830

Standard Form 298 (Rev. 8-98)
Prescribed by ANSI Std. Z39-18

i

TABLE OF CONTENTS

TABLE OF CONTENTS (Continued)

TABLE OF CONTENTS (Continued)

APPENDICES (Continued)

APPENDICES (Continued)

APPENDICES (Continued)

APPENDICES (Continued)

APPENDICES (Continued)

APPENDICES (Continued)

APPENDICES (Continued)

LIST OF FIGURES

LIST OF FIGURES (Continued)

LIST OF FIGURES (Continued)

LIST OF FIGURES (Continued)

LIST OF FIGURES (Continued)

LIST OF FIGURES (Continued)

LIST OF FIGURES (Continued)

LIST OF FIGURES (Continued)

LIST OF FIGURES (Continued)

LIST OF FIGURES (Continued)

LIST OF FIGURES (Continued)

LIST OF FIGURES (Continued)

LIST OF TABLES

LIST OF TABLES (Concluded)

Foreword

This program was a follow-on effort to a program on Improved High Cycle Fatigue (HCF) Life Prediction, USAF Contract F33615-96-C-5269, the results of which are documented in the final report on that PRDA program [1]. This program continued work on addressing key issues associated with developing, verifying, and implementing a material damage tolerant design methodology capable of predicting HCF limits and material thresholds for Ti-6Al-4V. The methodology development was extended to another titanium alloy, Ti-17, and to a nickel-base single crystal alloy, PWA 1484. These developments are necessary to prevent failures due to HCF loading in existing aircraft, to allow the introduction of more robust design procedures for engines being developed for next-generation aircraft such as the Joint Strike Fighter (F-35), and to guide updates to the damage tolerant specifications for HCF in the ENSIP document. The focus in this program was on the development of both fracture mechanics and total life methods to control HCF in a range of materials for fan, compressor, and turbine components in the engine using threshold and endurance limit concepts.

The Air Force Office of Scientific Research (AFOSR) sponsored this program entitled "Advanced High Cycle Fatigue (HCF) Life Assurance Methodologies" under Contract F49620-99-C-0007; Dr. Craig Hartley (AFOSR/NA) acted as the Air Force's contract monitor. Dr's. Jeffrey Calcaterra and Ryan Morrissey of the Air Force Research Laboratory Materials and Manufacturing Directorate (AFRL/ML) acted as the technical monitors for the program. The University of Dayton Research Institute (UDRI) managed this damage tolerant design technology development and verification contract for the Air Force. Organizations that supported this UDRI contract were Pratt & Whitney Aircraft (P&W), General Electric Aircraft Engines (GEAE), Honeywell Engines (previously, Allied Signal Engines), Allison Advanced Development Corporation (AADC), Southwest Research Institute (SwRI), Purdue University, United Technologies Research Center (UTRC), University of Illinois, North Dakota State University (NDSU) and University of Waterloo.

The management structure of the program focused on addressing the type of damage that could occur in-service within a damage-state team structure. There were three damage-state teams that each addressed the effects of a specific type of in-service damage that could reduce the HCF resistance of engine hardware. In addition to the three damage states (HCF/LCF, FOD, and attachments), major efforts on total life and fracture mechanics methods, including small cracks, as well as notches and multiaxial behavior were addressed. These teams were comprised of both engine company representatives, to ensure that the efforts would address engine hardware design needs, as well as other members who brought technical expertise to the problems. It would be hard to find a team of experts more qualified to solve the problems addressed in this program anywhere in the country or throughout the world from a combined application and technology point of view. The program managers (PM) and other key contributors involved in the program were as follows:

- For UDRI: Joseph Gallagher/Ted Nicholas (PM), Allan Gunderson, John Ruschau, Peggy Miedlar, Alicia Hutson, Gloria Hardy.
- For P&W: David Walls (PM), Charles Annis, Robert deLaneuville, Phillip Gravett, Edward Hindle, Matt Szolwinski, Rajiv Naik, Brad Cowles, Johnny Adamson, Richard Pettit, Keith Kersey, Michael Marotta.
- For GEAE: Dennis Corbly (PM), Robert VanStone, Donald Slavik, Michael Hartle, Robert McClain, Ken Wright.
- For Honeywell: Howard Merrick (PM), Dave Cameron, Youri Lenets, James Hartman.
- For AADC: Kenneth Cornet/Durell Wildman (PM), Craig Weeks, Phillip Bastnagel, Thomas Cook, Amit Chaterjee.
- For SwRI: Stephen Hudak (PM), Kwai Chan, Craig McClung, David Davidson, Graham Chell, Yi-Der Lee.
- For Purdue: Thomas Farris (PM), Alten Grandt, Patrick Golden, Haradanahalli Murthy, Bence Bartha, John Matlik, Dan Garcia, Eddie Perez-Ruberté, Pakalapati Rajeev.
- For NDSU: Alan Kallmeyer.
- For University of Illinois: Peter Kurath.
- For University of Waterloo: Greg Glinka.

This report covers work conducted over the time period from April 1999 to July 2004.

Executive Summary

High Cycle Fatigue (HCF) is still a subject of great concern within the U.S. Air Force. While progress has been made in understanding and evaluating causes of HCF related failures in a prior program (Contract F33615-96-C-5269)[1], additional work has been conducted under this follow-on program (Contract Number F49620-99-C-0007).

While pure HCF is a relatively straightforward problem from a materials point of view, HCF in conjunction with other damage mechanisms is not only more complex, but is the cause of most HCF related materials problems. Pure HCF can be addressed by material testing to establish fatigue strength limits under typical stress ratios, frequency, and cycle counts. The addition of statistics and factors of safety produce a robust design if material processing, surface conditions, and size effects are accounted for properly. On the other hand, HCF in conjunction with other damage mechanisms such as low cycle fatigue (LCF), fretting at attachment regions, and foreign object damage (FOD) is extremely difficult to model and predict, partly because of the unlimited number of combinations of loading that must be addressed. Further, the mechanisms are complex and do not lend themselves to simple analyses such as linear damage summation concepts. While pure HCF failures only occur after millions of repeated load (stress) applications, HCF combined with other damage mechanisms may occur at low cycle counts if the fatigue limit strength or crack propagation threshold is reduced from that obtained under pure HCF with no damage. Methods that have been successful in controlling LCF failures can be ineffective when dealing with HCF failures since the ability to describe the threshold behavior of a crack or the fatigue limit strength may not be adequately characterized. To ensure durability of a component it is imperative that the applied vibratory stress levels are kept sufficiently low (below an intrinsic material capability, or stress threshold) such that cracks would not be expected to initiate for these levels under given damage conditions. High cycle fatigue capability, altered by LCF, attachment distress, foreign object damage (FOD), inherent material heterogeneities, and other damage types, has been identified as a significant parameter

whose knowledge is essential to HCF damage tolerance. Further, there are impending requirements to incorporate damage tolerant specifications for HCF into the ENSIP document.

In response to the Air Force's concerns about loss of operational readiness, maintenance costs, and the adequacy of the HCF design systems used by the aircraft engine companies, the National Turbine Engine High Cycle Fatigue Science and Technology Program was begun. The Materials Damage Tolerance Action Team of this program placed major emphasis on the development of a new damage tolerance life prediction and design methodology for turbine engine rotating structures subjected to HCF loadings. This report chronicles the progress of Phase 2 of this methodology development, funded under USAF Contract Number F49620-99-C-0007, which is a follow-on to the work described in the final report of Phase 1 (AFRL-ML-WP-TR-2001-4159-Ref.1). While the work in Phase 1 was aimed primarily at titanium fan and compressor airfoil components because of the historical importance of HCF in these components, the focus of this effort was to extend the development of improved HCF methods for titanium Ti-6-Al-4V to another alloy, Ti-17, at both room and elevated temperatures. In addition, the methodologies were evaluated for their applicability to a single crystal alloy, PWA 1484, where temperature and orientation effects both have to be taken into account. Both fracture mechanics and fatigue life methods were applied in setting design thresholds that accounted for in-service damage. As in Phase 1, the emphasis on damage was concentrated on LCF, attachment distress, and FOD. In order to accomplish this, notch geometries and multiaxial stress states had to be considered.

The work on this contract was performed by a team of engine manufacturers and research organizations that had the wherewithal to (a) define the requirements, (b) contribute to material understanding necessary to establishing HCF threshold methods, (c) develop enhanced methods for accounting for in-service damage, and (d) verify these methods. The UDRI led team included Pratt & Whitney, General Electric Aircraft Engines, Honeywell, Allison Advanced Development Corporation, Southwest Research Institute, Purdue University, North Dakota State University, University of Waterloo, and the University of Illinois. This phase of the program was performed in parallel with an Air Force-sponsored Multidisciplinary University Research Initiative (MURI) program that was conducted and managed by the University of California (Berkeley). The focus of the MURI program

(High-Cycle Fatigue and Time-Dependent Failure in Metallic Alloys for Propulsion Systems, grant number F49620-96-1-0478) was to establish advanced analytical and materials understanding of the crack nucleation and propagation behavior under HCF loading conditions. Joint meetings were periodically held to share findings and define future requirements. Results of this and the prior program are being transitioned into design practices by the engine industry and form the basis of many of the updates to the ENSIP guide specification to address high cycle fatigue.

Chapter 1
Background of the HCF Program

1.1   INTRODUCTION

Around 1995, a number of high cycle fatigue (HCF) incidents took place within the US Air Force fighter fleet which resulted in engine failures and, at times, grounding of the fleet. Since operational readiness was affected by some of these events, a team was put together to rapidly determine the root causes and to suggest solutions. The root causes, which were all related to HCF, highlighted HCF as a major cause of concern to the Air Force. While the issue of HCF involves both vibratory response of engine components as well as material capability, one major portion of a program was put together to solve these problems dealing with material capability under HCF loading conditions. In particular, the findings of the investigating team pointed to the degradation of HCF material response due to initial manufacturing deficiencies or in-service operation. Under the latter category, low cycle fatigue (LCF) usage, foreign object damage (FOD), and fretting fatigue were all found to contribute to the loss of HCF material capability during operation. In the mid 1990's, accounting for such degradation was limited to either highly empirical approaches such as a universal knockdown factor, or neglecting such material debit in some aspects of the design procedure. Experience to date had not clearly identified HCF as a design problem. To overcome some of these shortcomings, a major program was put together by the Materials Directorate of AFRL to address these issues over approximately a six-year period. A major part of that program was a contract with the University of Dayton Research Institute involving the participation of the major engine manufacturers as well as universities and research institutes. The participants in this program constituted a unique team having capability ranging from the very fundamental aspects of materials and mechanics to the direct application of technology to engine design. Further, many of the participants had extensive familiarity with existing and past field problems involving HCF. The results of the first phase of this program were reported in the final report of a PRDA contract program [1]. The present report summarizes progress made on the second phase of the program, administered

through AFOSR (herein referred to as the BAA program) with technical oversight from AFRL/ML.

1.2 OBJECTIVES AND APPROACH

The objectives of the program were the development of technologies for assessing the HCF capability of typical materials subjected to HCF in the field and to implement them into design procedures. One of the first issues addressed in the program was the choice of material. There was a desire to have a model material representative of a wide material class that was used extensively in the engine industry and for which there was a broad database. After much deliberation, two materials were chosen. The first, which was studied extensively in the first phase of the program [1], was alpha-beta processed Ti-6Al-4V, which is commonly used throughout the industry in fan and compressor components. A group of 200 forgings were produced from a single lot following carefully prepared specifications and quality control. All participants in the HCF program; the ML in-house researchers, the contactors and sub-contractors on the AFOSR MURI program, individual contractors and grantees working on related HCF problems, and all the participants in this contractual program, made use of this material to minimize material variability. The material was evaluated mostly at room temperature where material behavior is primarily elastic in the HCF regime.

For comparison evaluation of behavior of a titanium alloy having a different microstructure, and to assess behavior at elevated temperature, a limited effort was conducted on a beta forged titanium alloy, Ti-17. This alloy is also commonly used in industry, particularly at elevated temperature.

The second part of the program explored a material that showed some degree of inelastic or creep behavior including frequency and time dependent effects, as well as a degree of anisotropy. The main considerations in choosing such a material were producibility and availability, experience in using the material, the existence of a database, and applicability to turbine engine design. The material chosen was a single-crystal nickel-base superalloy, PWA 1484, from Pratt and Whitney. Castings were obtained and specimens machined with primary axis orientations in several crystal directions.

2

The approach taken in both the titanium and single-crystal portions of the program focused primarily on the tolerance of a material to damage. Total life approaches, based on damage initiation, and fracture mechanics approaches were used to assess the damage tolerance of a material. In addition to smooth bars, component geometries included notched components where steep stress gradients can occur. Multiaxial loading was addressed because of the nature of stresses encountered at stress concentrators, in the contact region, and in complex geometries in general. Foreign object damage (FOD), which includes combinations of residual stresses, cracking, stress concentrations, and microstructural damage, was also addressed. In all of these studies, the underlying theme associated with HCF loading was the necessity to define go-no go loading conditions, necessitating the use of threshold and endurance limit concepts. This was done because the high frequencies encountered under HCF rendered the application of conventional damage tolerance methods involving inspecting for cracks impractical for HCF.

The approaches taken for both parts of the program, dealing with titanium and single-crystal nickel, involved both total life methods and fracture mechanics approaches, the latter dealing primarily with thresholds for the onset of HCF. The program addressed damage development and its effect on HCF behavior in the form of LCF and LCF/HCF interactions, FOD, and contact fatigue. Multiaxial behavior, where most of the work was done in titanium, was studied in order to handle complex geometries and complex stress states, especially those encountered in contact regions. Notch fatigue was studied in order to be able to better handle steep stress gradients such as those encountered in FOD and in contact fatigue, but under conditions where the stress field is better defined. An integral part of such analyses required tools dealing with small cracks, where long crack fracture mechanics is not applicable, and shakedown, where elastic-plastic behavior is encountered in the initial load cycles and eventually becomes purely elastic. A final issue addressed, necessitated by the anisotropic nature of single-crystal materials, was the comparison of isotropic analyses with anisotropic analyses for stress distributions and fracture mechanics parameters.

In conducting the studies mentioned above, a considerable amount of data was generated dealing with mechanical behavior of the two titanium alloys, Ti-6Al-4V and Ti-17, as well as the S/C alloy PWA 1484. All of the data generated under this program, as well as the prior PRDA program [1] were delivered to the prime contractor, UDRI, who, in turn,

established a data base that was accessible to all of the participants in the program. At the conclusion of the program, the data base was to be delivered to the Air Force. This data base will be released together with this report as public information and will be accessible through AFRL/MLL, Attn: Dr. Jeffrey Calcaterra, Wright-Patterson AFB, OH 45433.

1.3   REPORT ORGANIZATION

This final report on the BAA program describes the progress made in characterizing the HCF behavior of titanium and single-crystal nickel alloys. The titanium work and the nickel work are described in Chapters 3 and 4. Chapter 3 deals primarily with titanium alloy Ti-6Al-4V at room temperature with a limited study of high temperature behavior. The other alloy studied was Ti-17 at both room and elevated temperature. The technology developments are broken down into five sections:

1. Baseline behavior and HCF/LCF interactions
2. Multiaxial behavior
3. Notch effects
4. Foreign object damage (FOD)
5. Attachment fatigue

Chapter 4 deals with the behavior of PWA 1484, a nickel-base single-crystal alloy, and the models for use in other high-temperature anisotropic materials. The volume is divided into six sections:

1. Material
2. Fracture mechanics based modeling
3. Endurance limit modeling
4. Notch effects
5. Attachment fatigue
6. Implementation into design

Most of the sections and subsections were not prepared by a single author or company; rather they represent a team effort involving more than one company in general. The entire report was put together and edited by UDRI as the prime contractor for this entire effort.

Chapter 2
Accomplishments and Recommendations

2.1   OVERALL PROGRAM ACCOMPLISHMENTS

The accomplishments of this program are detailed in this voluminous report and its Appendices. A few are highlighted below to give an idea of the type of developments that took place under this program. They are presented in no particular order, but those dealing primarily with HCF in titanium are presented first before those that are more pertinent to anisotropic, high temperature materials.

(a) A methodology was developed to characterize the worst-case notch under FOD. As notch sharpness increases, the effective stress concentration factor reaches a limit. In the presence of the very steep gradients present near sharp notches, cracks can be shown to initiate, but not propagate. The worst-case notch methodology enables one to compute an effective HCF fatigue limit stress based on the propagation and arrest of cracks in steep stress gradients. The model was demonstrated to predict HCF threshold stresses as a function of notch geometry within the exit criteria established by the HCF team. The model is directly applicable to FOD and extendable to attachment fatigue. To accomplish this effort, a notched-fatigue database was developed covering a wide range of notch depths and acuities representative of those encountered in service-induced FOD.

(b) Two approaches for shakedown for notch geometries and other cases of concentrated stresses for proportional and non-proportional loading were developed and validated. The methodologies deal with both isotropic and anisotropic materials and are validated for some specific test geometries. The shakedown procedures are incorporated into computer codes to address this very complex mathematical procedure.

(c) An extensive investigation evaluated a number of multiaxial fatigue models, both critical plane and equivalent stress types. Several new models, primarily modifications of existing approaches, were postulated and evaluated. Depending on the database used, whether uniaxial or multiaxial, different models were shown to be the most robust under the particular

conditions. The ability of the various models to consolidate data, and the strengths and weaknesses of each model were documented for a very large database going from the HCF regime down to lower lives nearer to LCF. Test results obtained at different stress ratios as well as different fatigue lives were used. Among the models evaluated were the Smith Watson Topper, Findley, Equivalent stress, and Modified Manson-McKnight.

(d) Methods for determining statistically significant minimum properties for fatigue limit stress were evaluated using step and staircase approaches. Use was made of a random fatigue limit (RFL) model with its associated statistical behavior for the evaluation. Step loading was found to be generally effective, but not to provide significant time savings over conventional test methods. The applicability of step testing was found to be somewhat questionable for some tests in Ti-17 for unexplained reasons.

(e) Efficient methodologies for contact stress analysis were developed and refined for both similar and dissimilar materials. The procedures, based on numerical solutions of singular integral equations, were put into computer codes for ease of use. Procedures for applying the methods for complex load histories were demonstrated.

(f) Analytical procedures for predicting fatigue life and fatigue limit stresses at notches and under stress gradients were developed. Approaches using effective notch fatigue factors, k_f, and equivalent stressed areas, Fs, were applied to problems involving FOD. The use of a critical depth for stress analysis was found to be necessary in certain cases.

(g) A methodology was developed for a simplified test procedure to determine the equivalent small crack behavior from a long crack threshold test. Results confirmed the applicability of the K_{max} = constant test method as an effective alternative to the direct study of naturally initiated small cracks. Actual small crack behavior of Ti-6Al-4V was successfully measured at R = 0.1 and R = 0.5, using the replication technique. The crack nucleation mechanism was observed to be affected by the choice of stress ratio. However, small crack propagation behavior appears to be stress ratio insensitive. For single crystal materials, the following accomplishments are noted:

(h) K analyses for various combinations of loading and crystal orientations were obtained using anisotropic elasticity. Comparison of the anisotropic solutions with existing isotropic solutions showed that the errors involved using isotropic theory were generally

6

small. Specific examples were used to demonstrate the accuracy of existing isotropic solutions.

(i) Mixed mode thresholds for fatigue crack propagation were obtained experimentally and predicted analytically for several different crack directions and material orientations.

(j) Notch fatigue analysis methods were evaluated for anisotropic material properties including the incorporation of time-dependent material behavior. Results at 1900°F demonstrate that stress ratio or mean stress is an important consideration for modeling notch behavior from smooth bar data. For non-zero mean stresses, creep becomes a factor in the shakedown of the stress field at the notch. Common approaches such as use of q or Fs required extensive fitting of data at different values of R, thereby minimizing the truly predictive capability of such models.

(k) Constitutive modeling was refined and applied to critical plane models.

(l) Anisotropic shakedown methods were developed through extension of isotropic methods and incorporated into computer codes.

In achieving all of these accomplishments and addressing all of the other topics in this program, a considerable amount of mechanical testing had to be conducted. The results of the testing are summarized, where appropriate, throughout the report and the accompanying appendices. In addition, a comprehensive data base was generated which contains all of the raw data that can be sorted by material, testing organization, and objective of the test. The data have been assembled into a Microsoft Access data base. Information on gaining access to the data base is contained in Chapter 1, Section 1.2.

2.2   IMPLEMENTATION

(a) Both PWA and GE have implemented the use of advanced analytical methods for determining stresses in the contact region at a dovetail and are using those results for evaluating fatigue life. In particular, the code CAPRI developed under this program, and modifications of this code, are being used for efficient stress analysis.

(b) An approach for predicting notch behavior from smooth bar fatigue data is being used for evaluating fatigue life of notched components and has been successfully applied to extend the life of an existing piece of hardware. The approach is based on a statistical analysis of smooth bar fatigue data along with a method for evaluating the contribution of equivalent surface areas based on the local stress at that area. This so-called Fs approach is very similar to Weibull statistics and has been shown to be able to predict fatigue lives of materials having a broad range of stress concentrations and geometric features although many of the predictions were non-conservative.

(c) Although models for addressing multiaxial stress states have been in existence for some time and are used regularly in design, this program provided for the first time, a thorough assessment of existing models. This, in turn, led to modifications being implemented and new models being added to the inventory of existing analytical tools in industry, particularly for analysis in the HCF regime.

(d) Methods for FOD analysis, developed, modified, or evaluated under this program, are now part of design for FOD tolerance within the engine industry. These methods are now able to take into account the severity of FOD which includes the effect of the damage (notch) geometry including effective values of k_t, residual stress fields developed under FOD impacts, and microstructural damage including microcracking. In addition to incorporation of effective notch sensitivity, new capabilities for evaluating fatigue limit stresses have been adopted.

Perhaps the biggest breakthrough on this program is the demonstration that analytical methods now exist for predicting the response of any leading edge geometry to a given hard body impact and the methodology to predict subsequent fatigue resistance using models developed here.

(e) Methods for computing threshold stress intensities for anisotropic materials have been developed and verified and are now being used for design and analysis. In particular, the applicability of existing isotropic K analysis has been demonstrated for specific geometries and material orientations.

2.3   RECOMMENDATIONS

While tremendous progress has been made in the development of HCF technologies and their implementation into the design processes of the major engine manufacturers, a number of weaknesses in the existing technology base have been uncovered during the process. Methods now exist to better predict the HCF behavior of components that are subject to prior LCF, to FOD, and to fretting in contact regions. In getting to this point, several aspects of material behavior have been identified where the ability to understand and predict the response is still less than complete. Some of the areas where further research and development is recommended are outlined below:

(a) Contact fatigue - The ability to determine stresses in the contact region has been greatly advanced, but the development of predictive models for both fatigue initiation and the threshold for propagation of fatigue cracks is still required. It is still unknown whether fatigue failures in the contact region are due to pure HCF, pure LCF, or a combination of the two. The highly nonlinear nature of the damage accumulation in the contact region, and the potential interaction of LCF cycles during startup and shut down of an engine with the in-flight vibratory loading, still remains mostly unknown. The modeling concepts developed under this program should be extended to address the interaction problem as well as to address damage under pure LCF loading. Included in these studies should be an in-depth look at the role of environment in the degradation of the contact region, primarily at elevated temperatures for both titanium and nickel-base alloys.

(b) FOD - There are two aspects of the FOD problem that still provide a stumbling block for the implementation of the technology developed for assessing the severity of damage from foreign objects. The first deals with the variability of material response under nominally identical impact conditions. Both analyses and tests have shown that objects impacting on leading edge geometries cause damage in the form of reduction of fatigue limit stress that are extremely sensitive to the exact location of the impact with respect to the center of the leading edge configuration. Only a more complete series of tests can provide enough information with which to quantify the extent and variability of the damage produced. The second major problem is to identify the specific object that a leading edge may be subjected to in service. Although the nature of the damage that occurs in the field has been quantified, the

specific object causing this damage has not been adequately identified. It is highly recommended that a standard impacting object or series of objects, e.g. sand particle, stone, workman's tool, be identified with which to assess the damage that may be imparted to a blade or vane. Parameters such as impact velocity and impact angle can be estimated from the operational usage (take-off and landing speed) of an engine as well as the geometry and orientation of the component. From this information, the damage of a given object can be determined through analysis and test, once the impacting object is defined. Rather than identify the severity of damage in terms of a given k_t or k_f, where a robust design shows no improvement over a fragile design, it is recommended that the object potentially causing the damage be identified in terms of a standard, similar to what is done for evaluation of vulnerability of components to bird strike where "standard" birds are used as impacting objects. Another aspect of this program that is unfinished is the application of the FOD methodologies including the worst case (sharp) notch approach to the experiments performed early in this program and in the proceeding PRDA program [1].

     (c) HCF/LCF interactions and cumulative damage modeling - While empirical data on both crack growth and total life under combined HCF and LCF have been obtained, the modeling that has been developed has been largely empirical and uses linear damage summation concepts in most cases. Enough data are available which show that linear damage summation is generally inadequate and better modeling needs to consider the actual damage mechanisms. In particular, the question of cycle counting must be addressed as stress levels in the HCF regime are encountered. The general concepts of cycle counting for high stress LCF, and a threshold or endurance limit for HCF, appear to be generally accepted. For cycle counts in the intermediate region of cyclic life, say 10^4 to 10^6 cycles, it is not clear how damage should be summed. Numbers of cycles are high, yet the stresses are above the fatigue limit so that a threshold concept cannot be applied readily. This problem is particularly applicable to transient loading which is above the fatigue limit stress while the baseline vibratory loading is below that limit. It appears that both crack or damage initiation as well as propagation should have to be considered in such a problem. The applicability of such modeling concepts eventually has to be extended to highly nonlinear problems such as stresses in contact regions where the stress analysis, itself, is extremely complex.

(d) Palliatives for FOD - Although not developed directly under this program, the use of residual compressive stresses produced by conventional shot peening or laser shock processing (LSP) has provided a high level of FOD tolerance in some applications. The application of LSP, and another surface treatment called low plasticity burnishing (LPB), is not based much on analysis but rather on empirical data. Methods do not exist yet to predict the complete residual stress profile in a complex geometry such as a blade or vane that is subjected to LSP or LPB to a small area, typically along a leading edge. In addition to being able to predict the residual stress profile, models are needed to predict crack initiation and crack propagation under combined states of applied and residual stresses, where the latter involve stress gradients in the material. While advances have been made in dealing with stress gradients under certain conditions, the available models are not sufficiently robust to apply to a general stress field with arbitrary gradients in multiple directions.

(e) Palliatives for contact fatigue - In addition to having inadequate methods to design surface treatments to produce residual stresses, the science behind the use of coatings to mitigate fretting fatigue damage is quite elementary. Coating technology, and stress analysis and modeling of coated materials was not addressed under the present program. Much remains to be learned about how coatings work and how to analyze the mechanical behavior of a coated material in terms of crack initiation under complex stress fields present at contact regions, and crack propagation under those very same stress fields with steep gradients. Other aspects of this problem that warrant further investigation are the role of residual stresses from surface treatments in mitigating both crack nucleation as well as crack propagation (thresholds) and the role of friction in determining the stress states arising from contact fatigue. In the latter case, knowledge of the role of friction in the resulting stress fields is critical in the development of coatings for improving the resistance of contact areas to fretting or galling.

(f) Notch methods – Notch methods provide input for two classes of problems: the treatment of actual notch or stress concentration geometries, and the treatment of gradient stress fields such as those encountered under contact stress conditions. In particular, the approximation of damage from FOD as being equivalent to a very sharp notch should be further investigated to develop a continuous approach to the development of crack growth threshold modeling including small crack effects. This type of information will be of

11

particular use in the development of advanced models for the initiation and propagation of cracks under contact fatigue stress states. Additional work in notch methods requires the consideration of multiaxial stress fields in the uniaxial models already developed and the extension of gradient methods such as the Fs approach to gradients into the depth of the material in addition to gradients along the surface. This latter consideration is important in considering stress gradients due to residual stresses from surface treatments where the stresses are uniform along the surface but decay into the depth.

(g) Shakedown methods – Stress redistribution due to local plasticity in the form of a stress concentration such as a notch is referred to as shakedown because it occurs incrementally with cycles of loading. Shakedown methods still need to be developed for both titanium and S/X materials (isotropic and isotropic materials) for more general material behavior including time-dependent effects and more general cyclic loading. Extension of some of the present methods that are limited to rectangular geometries needs to be accomplished for more general geometries.

(h) Extension to elevated temperatures and other materials - It is almost obvious, but the developments needed to produce more robust design tools for HCF prevention have to be extended to all applications and materials. The extension of total life and crack growth models to materials at high temperatures involves the additional considerations of time-dependent material behavior as well as environmental effects, which degrade material properties. In particular, at the highest temperatures, S/X materials appear to demonstrate frequency effects on fatigue life. Both data and an understanding of this behavior are lacking at the present time. Of particular interest is the characterization and understanding of the three-dimensional threshold for crack growth in S/X materials at elevated temperature. Further characterization of S/C materials is needed in the areas of constitutive model development, only a small amount of which was developed under this program, and crack growth modeling involving considerations of both creep and environmental effects. An additional consideration involving the use of other materials, specifically in the area of contact fatigue, is the use of dissimilar materials in the contact region and how existing analyses and models can be extended to such situations.

(i) Validations – While many of the models and technical approaches developed under this program have been validated in the laboratory under specimen sample tests, little has been done to validate approaches on actual component geometries or on subcomponent or feature specimens. It is well known that scale-up from lab specimen to component is not straightforward, and aspects such as size effects or defect distributions are not readily scalable. In addition, scale-up may involve extension of concepts from specimens where behavior is primarily elastic to components where local behavior may be non linear. Aspects such as stress or strain control in experiments must be considered when extending modeling concepts to actual components. Validation under realistic conditions is considered to be an important aspect in the future transition of HCF technologies to robust design practices.

(j) Correlations with non-destructive inspection - A final area for future work, one where little or no effort was devoted to in this program, is the relationship between damage which may lead to HCF failure and the use of nondestructive inspection to detect and quantify the extent of such damage. This issue is particularly important in assessing the fatigue capability in regions of contact where extent of damage in terms of geometry measurements on the surface does not appear to be directly related to fatigue capability. The relationship between observable damage and fatigue capability is also important in FOD where residual stresses and subsurface microstructural damage may contribute to loss of structural integrity but may not be readily detectable. It is important to establish the effects of detectable damage on HCF capability as well as to identify damage that may occur which is not detectable. In this case, the prediction of damage evolution and growth is important.

In this, and most of the other areas needing additional work, the use of statistics cannot be understated. In fact, probabilistic design methodologies may hold the greatest possibilities of benefit in future design and analysis approaches for the HCF problem.

Chapter 3
Titanium Alloys

3.1   HCF/LCF

3.1.1   Introduction

Two titanium alloys were used in this investigation: an alpha-beta alloy, Ti-6Al-4V, in a forged plate condition and a beta-processed alloy, Ti-17, in the form of a hollow pancake forging.

3.1.1.1   Ti-6Al-4V

The Ti-6-4 alloy used in this study was received as plate in the solution-treated and over aged (STOA) condition. The forging stock material was a double VAR melted Ti-6-4, 2.5 inches (6.35 cm) diameter bar stock from Teledyne Titanium, produced in accordance with AMS 4928. It was supplied in random lengths of 12 to 14 feet (305 to 427 cm), in mill annealed condition: 1300°F (704°C)/2 Hr/AC. The billet was then sectioned into forging multiples, 16 inches (40.7 cm) in length, which were preheated to 1720°F (938°C) for up to one hour prior to being pressed into their final forging dimensions of 16 x 6 x 0.8 inches (40.7 x 15.3 x 2.0 cm). Forging was done on a National 8,000 ton mechanical press with dies initially heated to 300°F (149°C). Glass-lubricant coated bars were preheated to 1720°F ± 20°F (938°C ± 11°C) for 30 minutes in a continuous furnace and rapidly transferred to the press. After a one stroke forging, the pieces were simply air-cooled.

Solution heat treatment was done in a Lindberg air furnace at 1710°F (±25°F) [932°C (±14°C)] for one hour. The rack of forgings, heat-treated on edge, was rolled out of the furnace after heating at temperature and fan air-cooled at a cooling rate, from 1700°F to 1000°F (927° to 538°C), of 360°F/min (200°C/min). The solution-treated forgings were cleaned of glass lubricant, oxide and alpha case using caustic and acid baths as well as grit blasting. The cleaned forgings were vacuum annealed at 1300°F (704°C) for two hours at temperature and fan cooled in argon. This processing resulted in a microstructure consisting

14

of 60-vol% of equiaxed primary alpha with an average 20μm grain-size with the remainder transformed beta (Figure 3.1) and is identical to the alloy used in the earlier HCF program [1]. The room temperature mechanical properties of the Ti-6-4 plate as processed and heat-treated are σ_y = 134.8 ksi (930 MPa) and σ_{UTS} = 141.8 ksi (978 MPa).
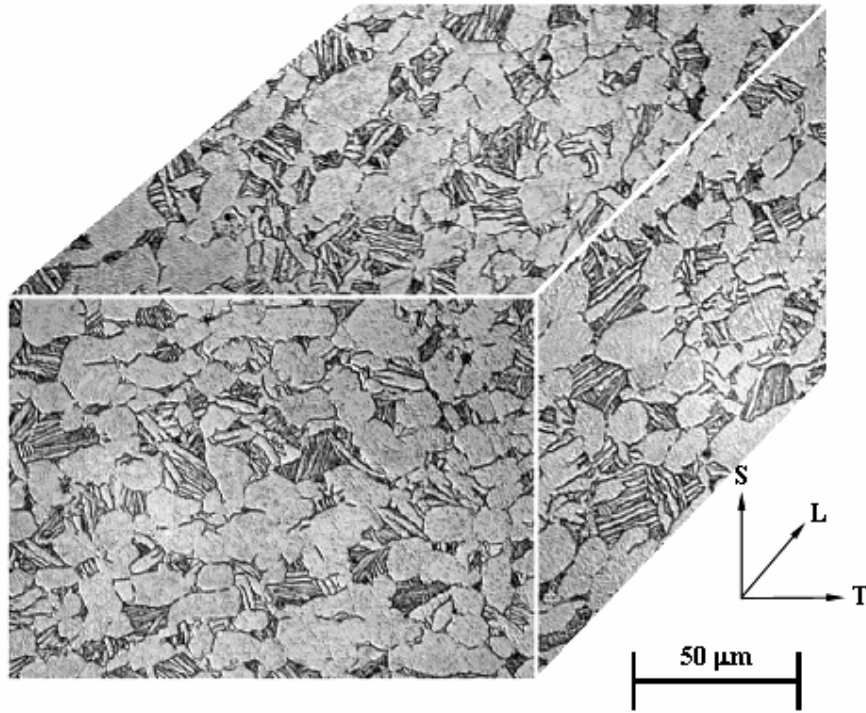
Figure 3.1. Mill-annealed microstructure of Ti-6Al-4V plate forging.

3.1.1.2   Ti-17

Ti-17 was selected for the program as a representative beta forged titanium alloy to compare with the results obtained on Ti-6Al-4V in the previous PRDA program and the current contract. The Ti-17 material used in this study was taken from two companion forgings. Each measured approximately 27.6" O.D. x 9.3" I.D. x 5.6" thick. One of the forgings was machined into a blisk configuration and was used for bench testing and validation of FOD methods and all other specimens were taken from the second forging. Titanium Metals Corp. supplied the forging stock as 10" round billet. The Houston Operations of Wyman-Gordon, Inc, performed the forging.

The chemistry from the top and bottom of the ingot (see Table 3.1) was within the acceptable ranges of GEAE Spec C50TF57. The beta transus, as determined by sequential metallographic analysis, ranged from 1635° to 1645°F. The billet stock was ultrasonically inspected in accordance with P3TF15-S13 and found to be acceptable.

Table 3.1. Chemistry of the Ti-17 Ingot used in the Program

	Ti	Al	Sn	Zr	Mo	Cr
Ingot Top	bal.	5.22	2.07	1.94	3.94	4.18
Ingot Bottom	bal.	5.10	2.05	2.01	3.84	4.08
C50TF57	bal.	4.50-5.50	1.5-2.5	1.50-2.50	3.50-4.50	3.50-4.50

All other trace and residual elements were within specification. The forgings were heat-treated at 1475°F for four hours, followed by a water quench. Final heat-treatment was performed at 1150°F for eight hours followed by air-cooling. The resulting microstructure is compared with Ti-6-4 forgings from the PRDA program in Figure 3.2. The 0.2% yield and ultimate tensile strengths at room temperature in these Ti-17 forgings in the tangential direction were determined to be 151 ksi and 168 ksi, respectively.

(a)   (b)
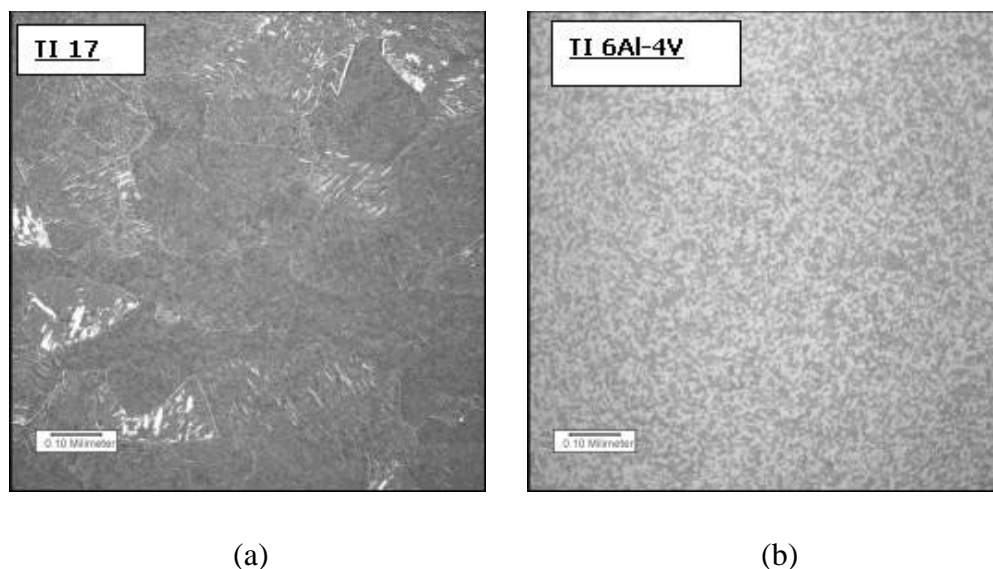
Figure 3.2. Microstructures of the (a) Ti-17 and (b) Ti-6-4 forgings.

Specimens were excised from the blisk forgings. FOD and crack growth specimens were low stress ground as the final machining step. LCF and HCF specimen preparation included low stress grinding, a longitudinal polish, and stress relief for eight hours at 1130°F in a vacuum.

3.1.2   Fatigue Crack Growth Behavior and Models

The application of linear elastic fracture mechanics (LEFM) and the stress intensity factor, K, to characterize crack growth behavior, has been described in the final report for Phase 1. Methods for representing crack growth data, fitting data to different growth laws, and test methods for obtaining data are all described there. In this section, the applicability of LEFM to small cracks, the extension of crack growth modeling to a second material, and the use of other crack geometries is described.

3.1.2.1   Ti-6Al-4V at 500°F

Two surface flaw specimens were used to generate 500°F threshold data at R = -1 as shown in Figure 3.3. Three compact tension specimens (h=.6, w=1.0, b=.375 inches) were used to generate 500°F threshold crack growth data in Figure 3.4. Multiple sets of region 1 data were generated on a single sample.

The data were reduced to obtain the 3.94E-9 inches/cycle (1E-10 m/cycle) threshold per the ASTM E647 method (fitting a straight line in log-log coordinates through the lowest 5 or more points with positive da/dN's, and extrapolating to 1E-10 in cycle), and also by taking the minimum delta K at which growth was observed. As shown in Table 3.2, the two methods gave comparable results.

The threshold data derived by the ASTM method is described by the curve in Figure 3.5. The data scatter is fairly tight in the region tested. As R→1, the curve cannot be correct, because finite ΔK results in infinite K_{max} as one approaches this limit. To illustrate this, a fracture toughness cutoff is also plotted, based on a K_{IC} value of 57-ksi in$^{1/2}$, a room temperature value given in MIL-HDBK-5 for Ti 6-4. The actual fracture toughness, and the resulting cutoff would be expected to vary with temperature and thickness, and is beyond the scope of this investigation.
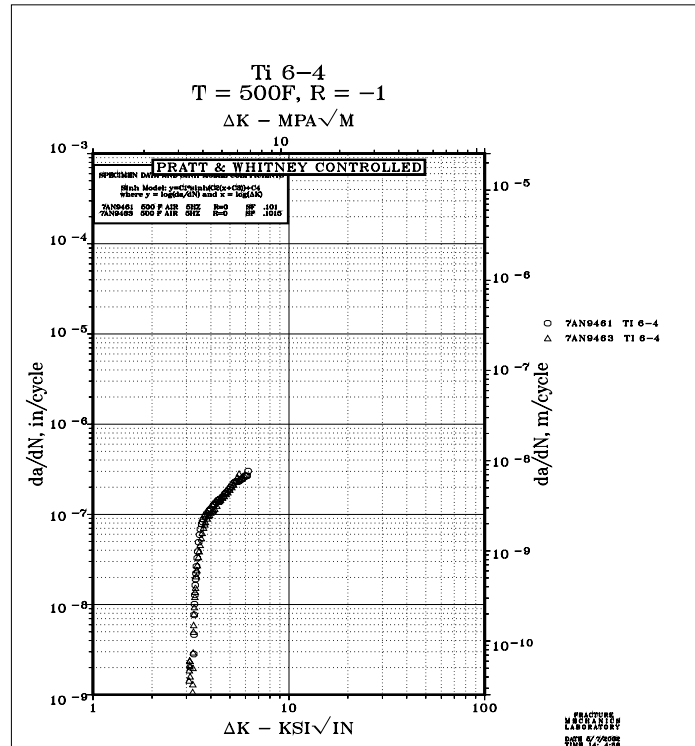
Figure 3.3.   Crack growth rate data for Ti 6-4, at 500°F under R= -1
conditions (ΔK = calculated based on R=0).
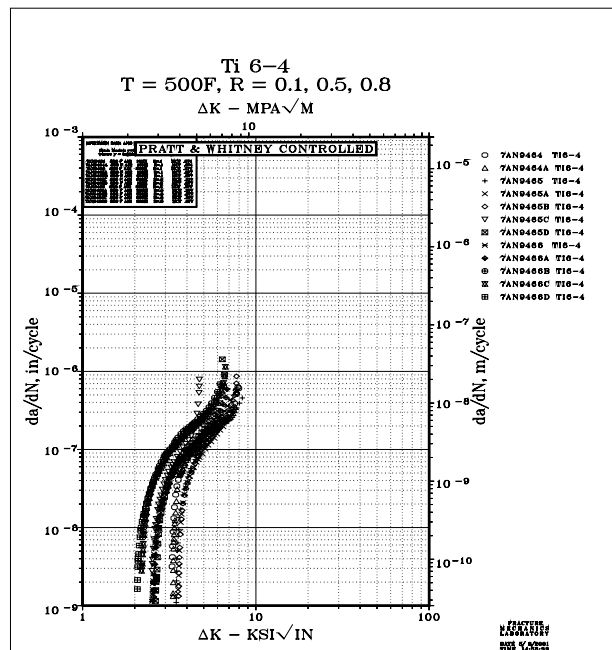
Figure 3.4. Region I crack growth rate data for Ti-6-4, R = .1, .5, .8.

18

Table 3.2. Crack Growth Threshold Data for Ti-6-4 at 500°F

Specimen	R	Frequency (Hz)	$K_{threshold}$ ASTM E647 (3.94e-9 in/cycle)	$K_{threshold}$ Minimum value for which growth was observed
9461	-1	5	6.55	6.49
9463	-1	5	6.25	6.15
9464	0.1	10	3.30	3.27
9464A	0.1	10	3.34	3.32
9465	0.1	20	3.46	3.41
9465A	0.1	10	3.51	3.53
9465B	0.1	20	3.60	3.57
9465C	0.5	20	2.54	2.50
9465D	0.5	10	2.67	2.63
9466	0.5	20	2.56	2.49
9466A	0.5	20	2.60	2.56
9466B	0.8	20	2.21	2.18
9466C	0.8	20	2.21	2.17
9466D	0.8	20	2.09	2.04
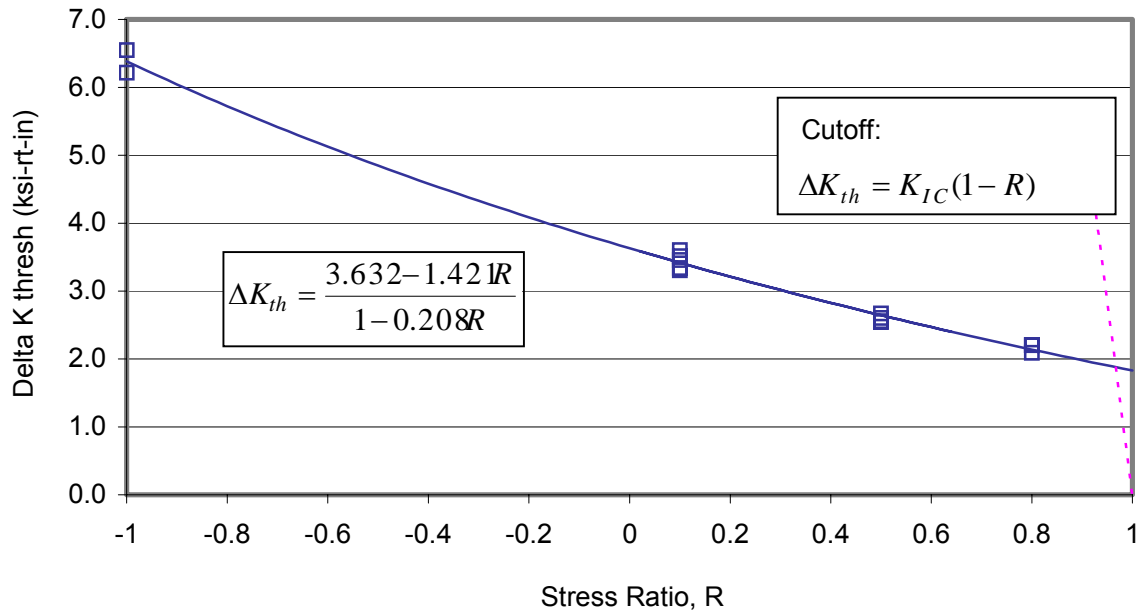
Figure 3.5. Crack growth threshold model for Ti-6-4 at 500°F.

3.1.2.2   Ti-17 at 75°

Fatigue crack growth rate (FCGR) testing for Ti-17 was obtained with Kb surface flaw geometries. The specimen-loading axis was oriented along the blisk radial direction. The crack depth direction was oriented along the blisk axial direction. An EDM semicircular pre-flaw 0.005-inch deep in the center of the width dimension was used to obtain the Kb surface flaw. Specimens are loaded through button head ends fixed into the load frame grips. Crack growth was monitored with potential drop techniques. Crack growth is reported after 0.002 inch of pre-crack growth at low K. Increasing K tests were performed at constant load ranges at selected R. Threshold fatigue tests were performed at decreasing K-gradients of

-30 in^{-1}. The K-gradient describes the rate at which load is reduced to determine ΔK_{th}. Though this value is well below the ASTM E649 recommended value, GEAE has found good results with these shed rates for surface flaws in aircraft engine materials.

All crack growth rate data were analyzed with the Raju-Newman surface flaw K-solution at the crack depth (a) and surface positions (2c). The final analysis includes minor corrections to the crack size and shape with post-test crack size measurements. Fatigue crack

length measurements were converted to growth rates as a function of ΔK as shown in Figures 3.6 and 3.7.

These data include results from shed tests as well as constant load (increasing K) tests at $R \approx -1$, 0.1, and 0.5. These data are fit with the sigmoidal crack growth Equation (3.1) adjusted for mean stresses with the Walker Equation (3.2).

$$da/dN = \exp(B)\,(K_{eff}/K_{th})^{P}\,[\ln(K_{eff}/K_{th})]^{Q}[\ln(K_{ic}/K_{eff})]^{d} \qquad (3.1)$$

where, K_{th}, B, P, Q, D, and K_{ic} are material constants and where

$$K_{eff} = K_{max}\,(1\text{-}R)^{m} = \Delta K\,(1\text{-}R)^{m\text{-}1} \qquad (3.2)$$

m = m+ for positive R and m= m- for negative R.
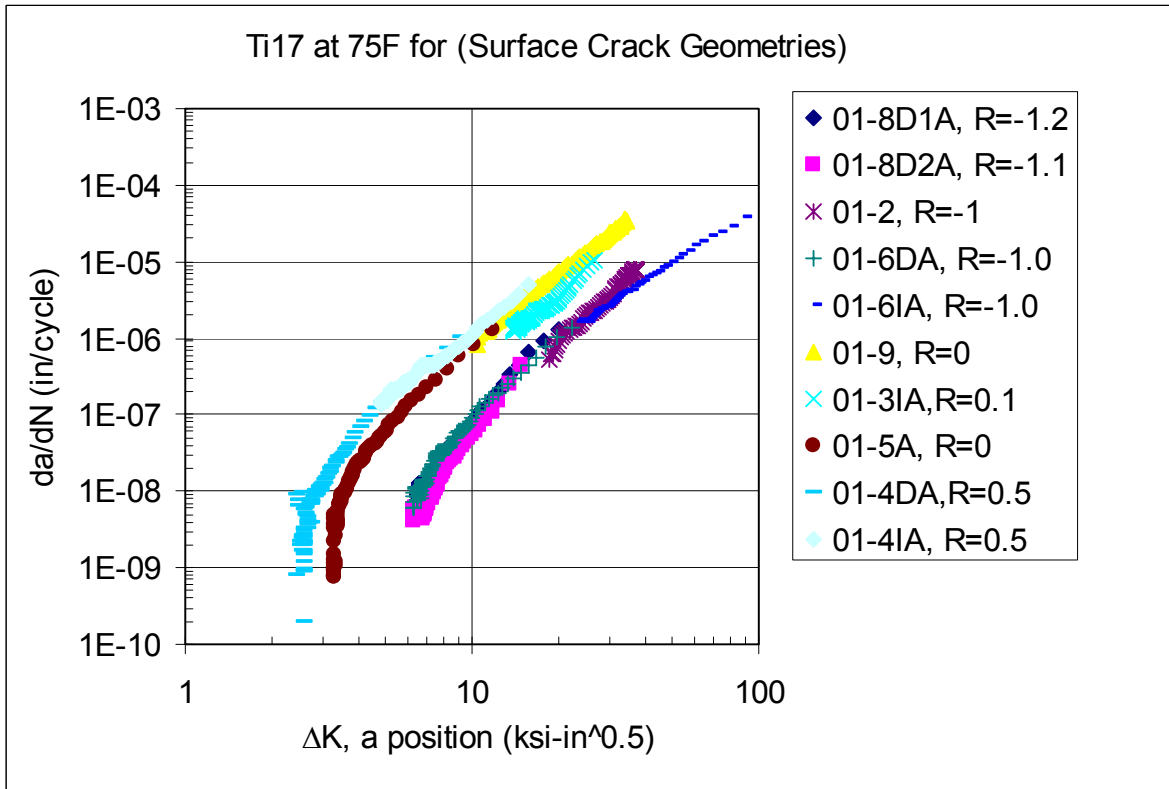
Figure 3.6. Ti-17 crack growth rates at the crack depth position for 75°F.

21
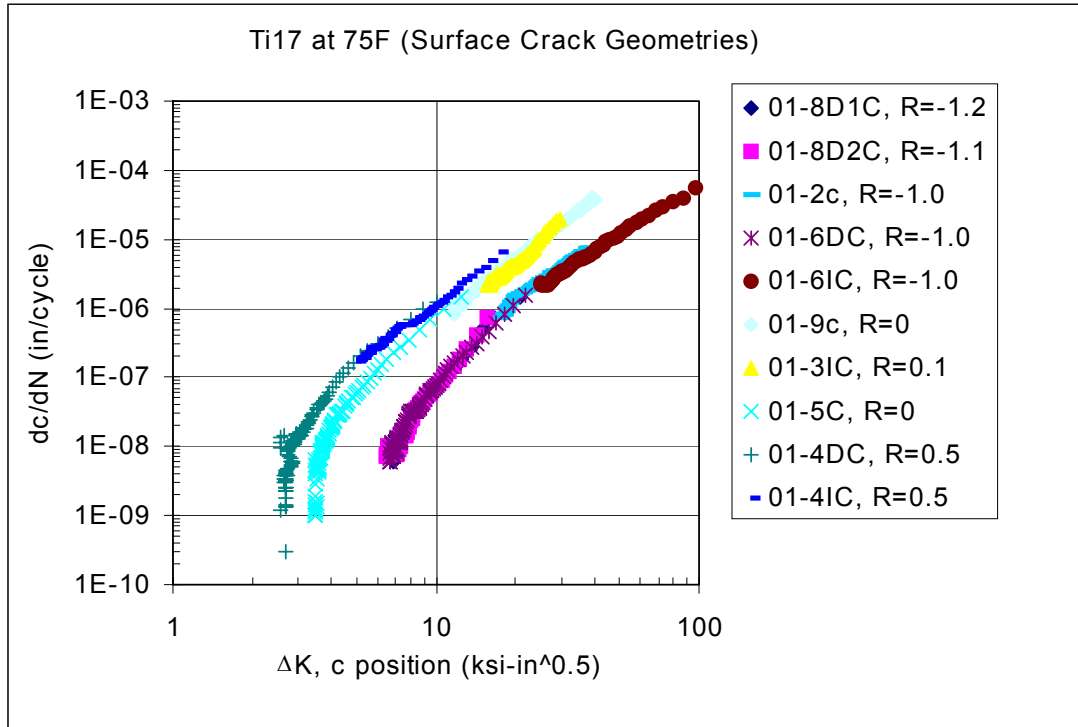
Figure 3.7. Ti-17 crack growth rates at the crack surface position for 75°F.

The data and the K_{eff} correlation for the Ka (crack depth position) and Kc (surface position) are shown in Figures 3.8 and 3.9. The resulting material constants for Ti-17 at 75°F are given in Table 3.3. The dual Walker exponent and the sigmoidal relationship accurately model the influence of R and ΔK on crack growth rates. No additional constraint loss model adjustments were required to obtain the correlation at the surface position. These material constants were subsequently utilized to assess HCF/LCF methods.

Table 3.3. Ti-17 Sigmoidal Curve Constants at 75°F

K_{th}	3.277
B	-15.921
P	1.8774
Q	0.73692
D	-0.93565
K_{ic}	60
m+	0.647
m-	0.158
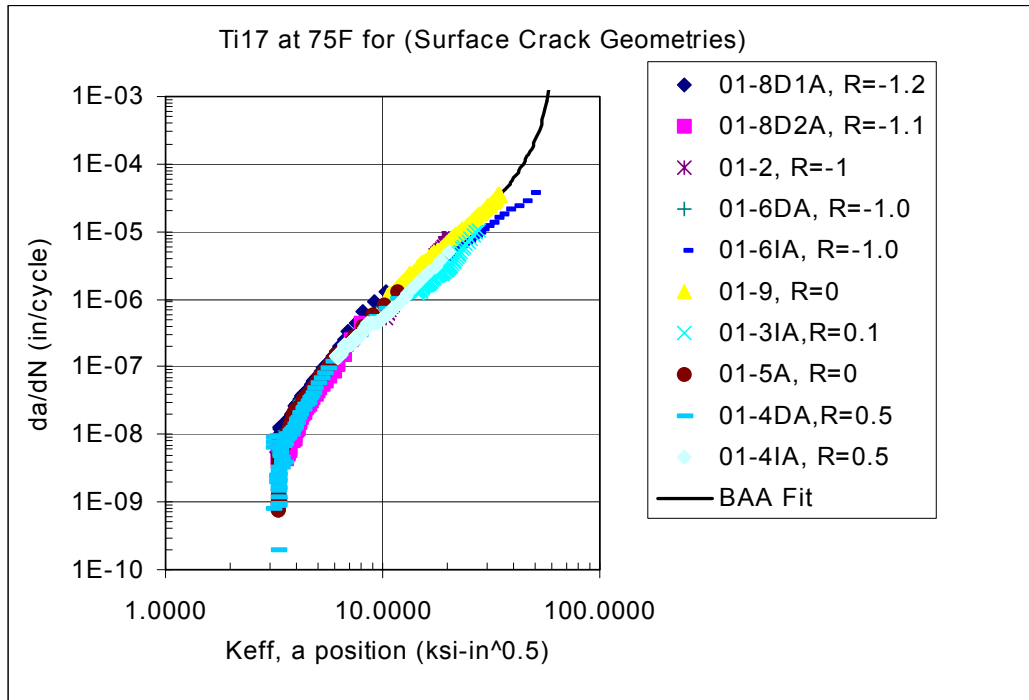
Figure 3.8. Ti-17 crack growth rate results at the crack depth position
for 75°F with the sigmoidal and Walker models.
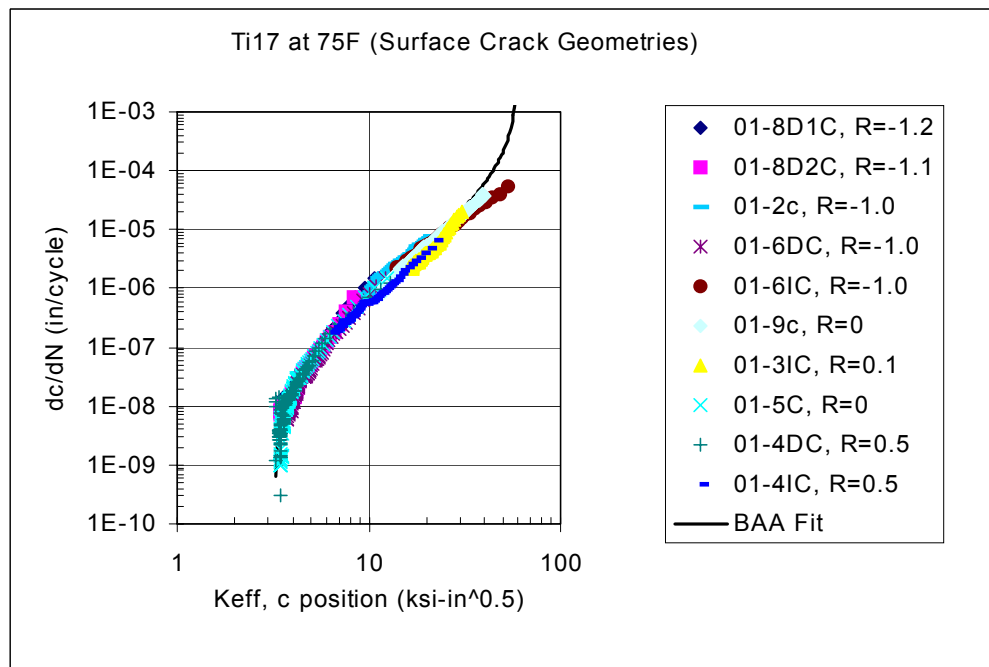
Figure 3.9. Ti-17 crack growth rate results at the crack surface position
for 75°F with the sigmoidal and Walker models.

3.1.2.3   Ti-6-Al-4V Small Crack Behavior

A recent study [2] has shown that the predictions based on long fatigue crack propagation data greatly overestimated the actual crack propagation life in a forged Ti-6-Al-4V titanium alloy representative of a turbine engine fan blade material. Recognizing the importance of the da/dN – ΔK input used for crack propagation life prediction, an additional effort [3] was initiated within the USAF Improved High Cycle Fatigue (HCF) Life Prediction Program to monitor and characterize the development of the HCF-induced cracks in Ti-6Al-4V alloy from an initially undamaged state.

The data reported [3] would be invaluable for developing the crack propagation-based life prediction approach. At the same time, the direct observation of the naturally initiated cracks is extremely difficult to apply without having a) prior knowledge about the fatigue behavior of the material, b) skilled personnel and c) sophisticated equipment. It is prohibitively time-consuming and considerably more expensive than conducting conventional fatigue crack propagation testing. Besides, direct observation (via surface replication technique) of naturally initiated small cracks might be difficult or even impossible to apply to the tests simulating actual service conditions such as high/low temperatures or liquid environments.

Within the same USAF Improved High Cycle Fatigue (HCF) Life Prediction Program, fatigue crack propagation behavior of the same titanium alloy and microstructure [3] was studied under both constant-R and constant-K_{max} conditions [4]. Comparison of the results from both studies [5] shows very good agreement between actual small crack data and long crack data obtained from constant-K_{max} test. Since the equipment, specimen design, level of complexity and cost associated with the constant-K_{max} testing are essentially the same as for conventional (constant-R) fatigue crack growth testing, this method may represent an effective alternative to the direct study of the naturally initiated small cracks.

In the present study, the propagation behavior of naturally initiated small cracks was studied at stress ratios of R = 0.1 and R = 0.5. No significant difference was observed between small crack propagation behavior at R = 0.1 and R = 0.5 when the replication test results were presented in the form of "da/dN – a'" or "da/dN – ΔK" form. At both stress ratios tested,

small cracks were shown to propagate much faster than the long cracks under identical conditions. These results further support the applicability of the K_{max} = constant test method as an effective alternative to the direct study of the naturally initiated small cracks.

In Figure 3.10, the fatigue crack propagation rate plotted as a function of the crack size for R = 0.5 (points) is compared to the earlier data for R = 0.1 (lines). No significant difference can be seen between small crack propagation behavior at R = 0.1 and R = 0.5. Similarly, reasonable agreement exists between the small crack data for both R = 0.1 and R = 0.5 when plotted in a "da/dN – ΔK" format. At the same time, both sets of small crack data appear to be shifted to the left in respect to the available long crack data for the same material and microstructure.

The results obtained further confirm the applicability of the K_{max} = const test method as an effective alternative to the direct study of the naturally initiated small cracks. The detailed description of the test program is given in Appendix A.
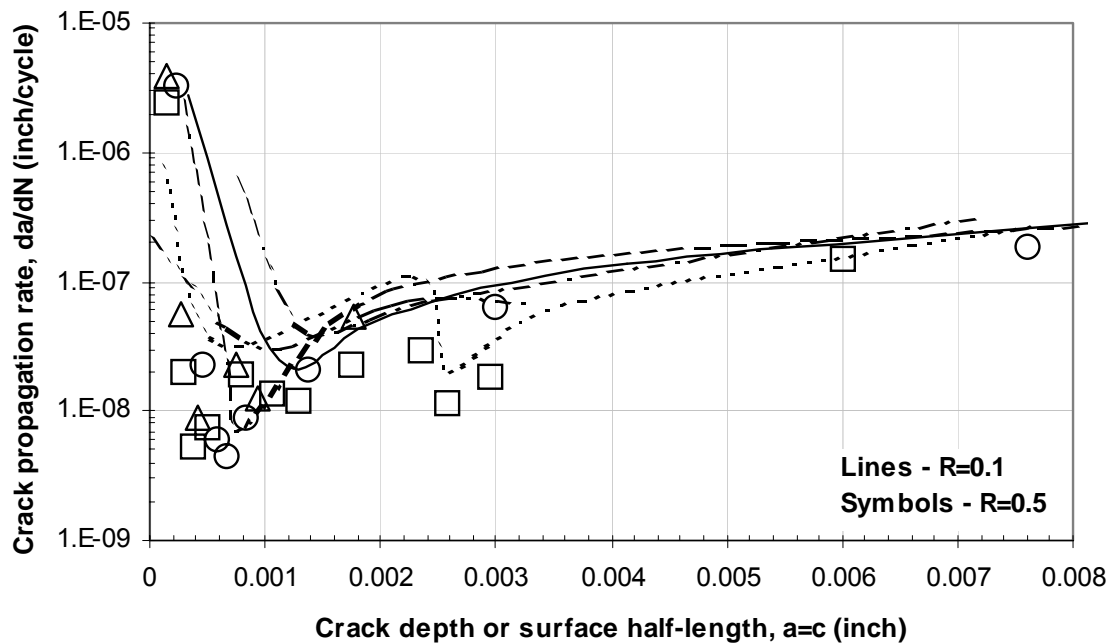
(a)

Figure 3.10(a & b). Crack propagation rate as a function of crack size (a) and ΔK (b).
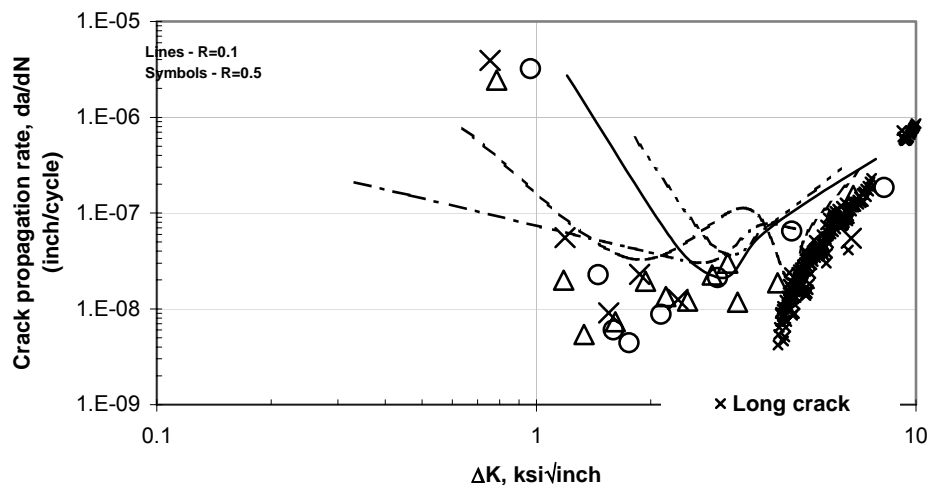
(b)

Figure 3.10(a & b). Crack propagation rate as a function of crack size (a) and ΔK (b).

3.1.3   Total Life Methods for Smooth Specimens

Total life is determined for specimens under either constant load or constant strain conditions. While the propagation life from some arbitrary (small) crack size is finite in the LCF regime, the propagation life for very high numbers of cycles to failure becomes small. In the HCF regime, this approach is often referred to as initiation or crack nucleation. In the first phase of this program, total life methods concentrated on consolidation of data obtained at different stress ratios (R). For HCF, the constant life Haigh diagram (often referred to as a Goodman diagram) was used to represent data at different values of R. In this section, statistical approaches for representing S-N data and different methods for experimentally determining the fatigue limit strength are described.

3.1.3.1   Ti-6-4 at 75°F -Step and Staircase for Minimum HCF Capability in Ti-6Al-4V

The majority of Ti-6Al-4V tests and methods with Ti-6Al-4V specimens at 75°F are presented in the PRDA V final report. Additional tests were run to establish the best way to obtain HCF minimum properties using step and staircase approaches. Step tests are subjected to multiple load levels on each specimen to establish the specimens fatigue capability. The specimen is initially subjected to a constant stress range for a set number of cycles. If failure

does not occur within the block, the maximum stress on the specimen is increased until failure. The constant life endurance stress range is calculated by Equation 3.3 as:

$$\Delta\sigma_{ES} = \Delta\sigma_{PS} + (\Delta\sigma_F - \Delta\sigma_{PS})(N_f / N_{RO}) \tag{3.3}$$

where, $\Delta\sigma_{ES}$ is the constant life endurance stress range (or endurance strength), $\Delta\sigma_{PS}$ is the stress range from the prior unfailed block, $\Delta\sigma_F$ is the stress range from final block, N_f is the cycles to failure in the final block, and N_{RO} is the number of cycles in each block prior to failure. Step tests will result in a failure point for each specimen tested. This can be an advantage when material is costly and test failures are required for needed assessments. A summary of the step test matrix in this evaluation is provided in Table 3.4.

The tests were run for Ti-6Al-4V at 75°F, R=0.1, and 900 Hz. Tests were run with 10^7 fatigue blocks and 4 ksi maximum stress steps. The average number of cycles/specimen was ~5.2×10^7 cycles for a total of 260×10^6 cycles for the step test program. Tests at 1000 Hz were not used for the assessment given the potential issues with the GEAE kHz machine at 1000 Hz.

Table 3.4. Ti-6Al-4V Step Test Matrix at 900 Hz, R=0.1, and 75°F

Spec ID	frequency (Hz)	Starting Smax* (ksi)	Final Smax at failure (ksi)	# Steps	Last Step Nf	Interpolated Smax (ksi)
121-2	900	61.5	77.5	4	8202785	76.78
124-4	900	61.5	89.5	7	1125814	85.95
47-10	900	61.5 (**)	81.5	5	5617819	79.75
173-2	900	65.5	77.5	3	5627646	75.75
47-9	900	65.5	81.5	4	8252952	80.80

*step evaluation procedure (4 ksi Smax steps if no failure after 1e7 cycle blocks)
        if # steps =0, drop the starting Smax on the next specimen
        if # steps =1-4, repeat the same starting Smax on the on the next specim
        if # steps >4, increase the starting Smax on the next specimen
** specimen 47-10 begun at initial Smax of 61.5 ksi.

Alternatively, a single load level on each specimen is used for the staircase approach. A summary of the staircase matrix is provided in Table 3.5. The first staircase test was run at Smax=67 ksi without failure. Stresses were increased on additional specimens until failure occurred within 10^7 cycles. Stresses on subsequent tests were continually increased or decreased based on Nf of the last tests vs. 10^7 target life. Roughly ½ of the specimens failed within the targeted life regime. Six of the staircase tests were long life failures that continued overnight or through the weekend awaiting setup of the next test specimen. Given over-night or weekend test time was run without additional costs, the staircase matrix (Table 3.5) was similar in cost to the step matrix (Table 3.4). More staircase tests can be run at similar costs to step tests with multiple steps/specimens.

Table 3.5. Ti-6Al-4V Staircase Test Matrix at 900 Hz, R=0.1, and 75°F

Spec ID	Specimen Smax*	Nf if failure before 10^7	Nf runout	Nf if failure after > 10^7
124-7	67.0		1.00E+07	
78-6	71.0		1.00E+07	
171-17	75.0			112048815
78-8	79.0	6436100		
173-4	75.0	6809400		
124-5	71.0		1.00E+07	
171-16	75.0			22303000
121-14	79.0		1.00E+07	
121-9	83.0	993941		
171-12	79.0	963730		
171-14	75.0			25831000
171-8	79.0			43796000
171-18	83.0		1.00E+07	
171-6	87.0	8255264		
171-3	83.0		1.00E+07	
124-12	87.0	404495		
121-11	83.0	4216400		
121-10	79.0	3253398		
121-2	75.0			31539755
171-5	79.0			21505004
78-7	83.0	631424		
121-5	79.0	4793082		
47-17	75.0	6996302		
171-13	71.0	767559		
121-18	67.0		1.00E+07	
47-3	71.0		1.00E+07	

*staircase evaluation procedure
  - if failure prior to 10^7, drop Smax by 4.0 ksi on the next specime
   - if no failure by 10^7, remove specimen and increase Smax by 4

The step and staircase results are plotted in Figure 3.11. The results are qualitatively very similar. A quantitative assessment of the step tests was done with probability plots (Figure 3.12). Here, 50 corresponds to the average (50%) fatigue capability of the step test. The slope on probability plots corresponds to the scatter for 10^7 fatigue capability. This can be compared with the fatigue capability of staircase tests analyzed in Figures 3.13 and 3.14. A 1D scatter in the stress direction is assumed in Figure 3.13. The 1D stress scatter assumption is similar to analysis of the step tests. A 1D life scatter is assumed in Figure 3.14. The scatter assumption in life is similar to the approach typically used in analyzing low cycle fatigue results.

Predictions with the step and staircase tests with baseline tests from the PRDA program ($Nf<10^6$ cycles) were also analyzed with the random fatigue limit (RFL) model. The RFL model is described in detail in Appendix B.
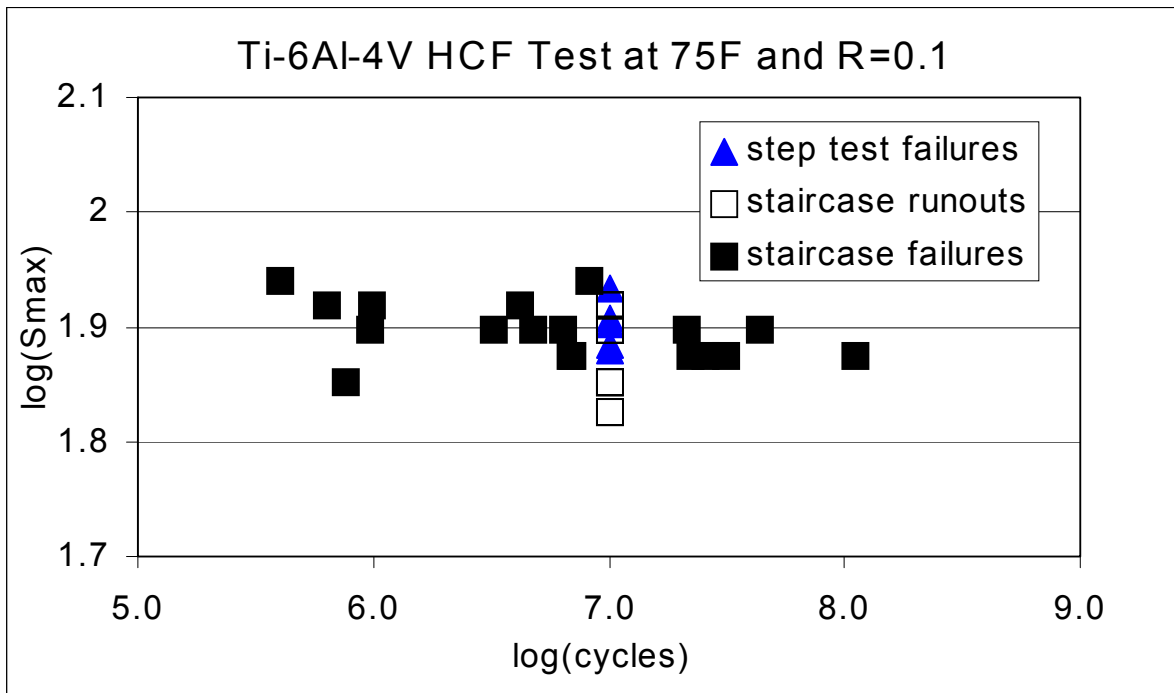
Figure 3.11. Step and staircase test results for Ti-6Al-4V at 75°F and R=0.1 (step at interpolated S_{max} using the step interpolation approach).
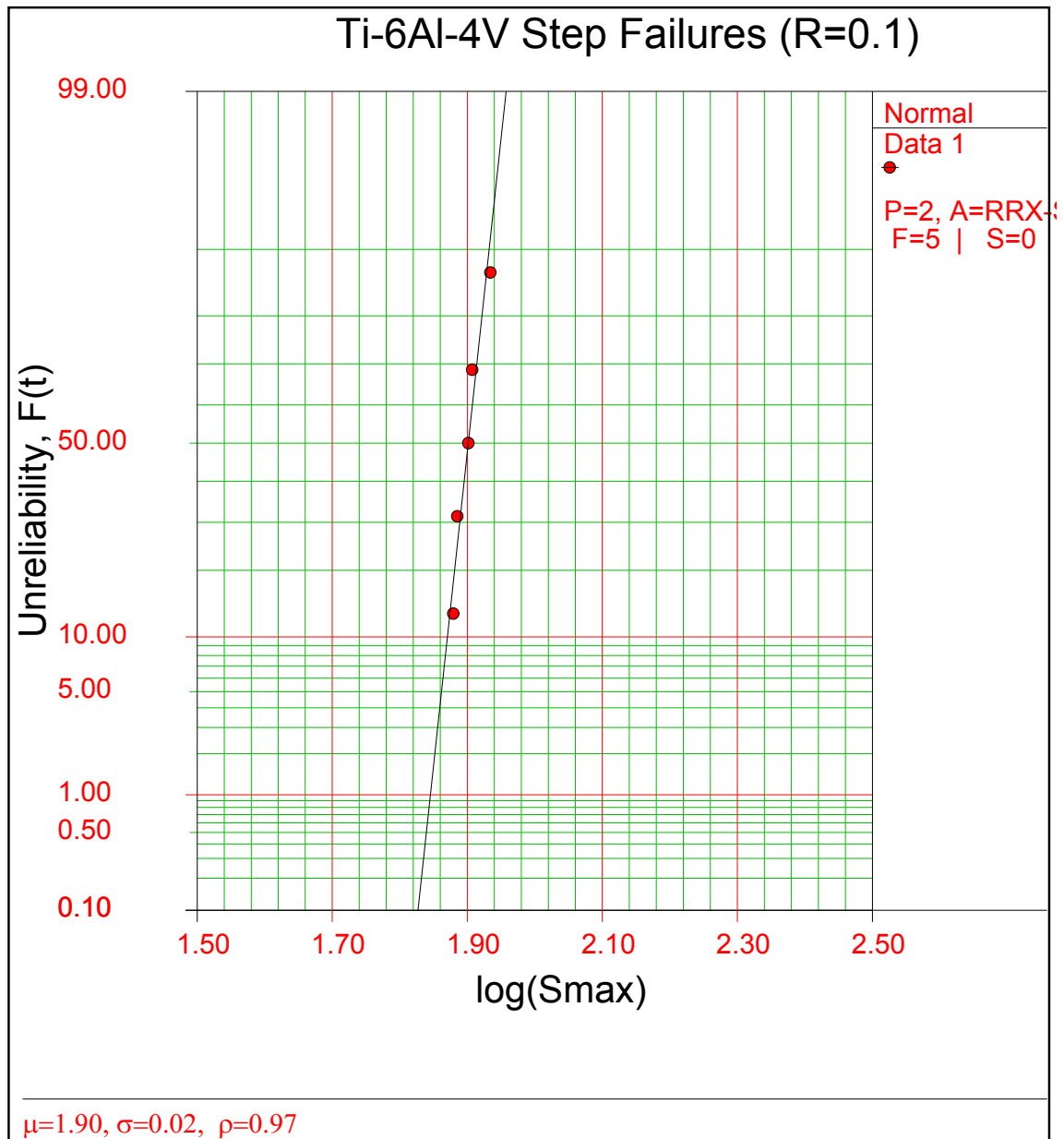
Figure 3.12. Step test results for Ti-6Al-4V at 75°F and R=0.1 shown on a probability plot.

30
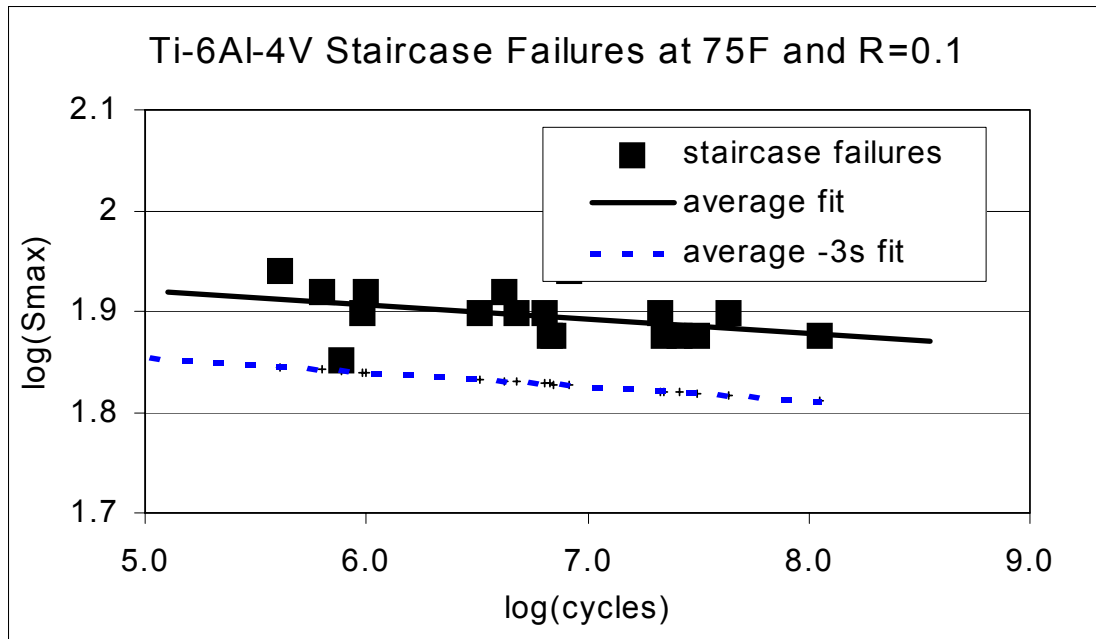
Figure 3.13. Staircase failures for Ti-6Al-4V at 75°F and R=0.1 with average and–3s predictions assuming a 1D stress scatter.
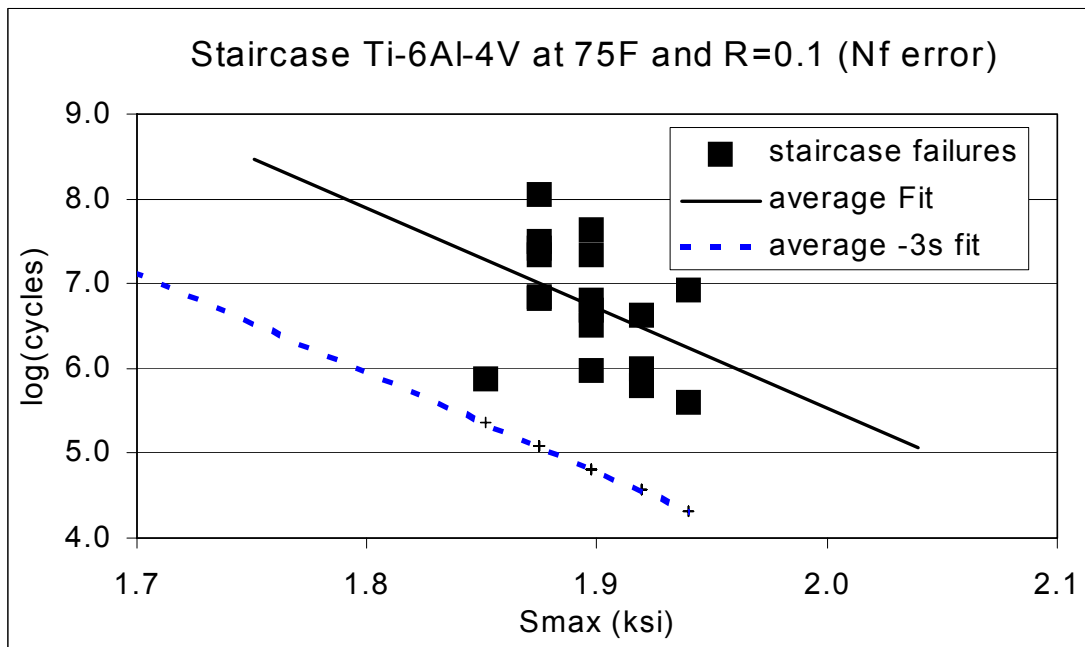
Figure 3.14. Staircase failures for Ti-6Al-4V at 75°F and R=0.1 with average and –3s predictions assuming 1D life scatter.

The baseline tests with $Nf<10^6$ cycles were selected as LCF tests that would typically be available from test programs in addition to HCF properties. The model treats runout and failure tests with 2D scatter in both life (LCF regime) and the endurance stress (HCF regime). An advantage of the RFL model is that the 1D scatter assumptions are not required. The RFL model predictions with the baseline + step or staircase results are given in Figure 3.15.

| (a) | (b) |
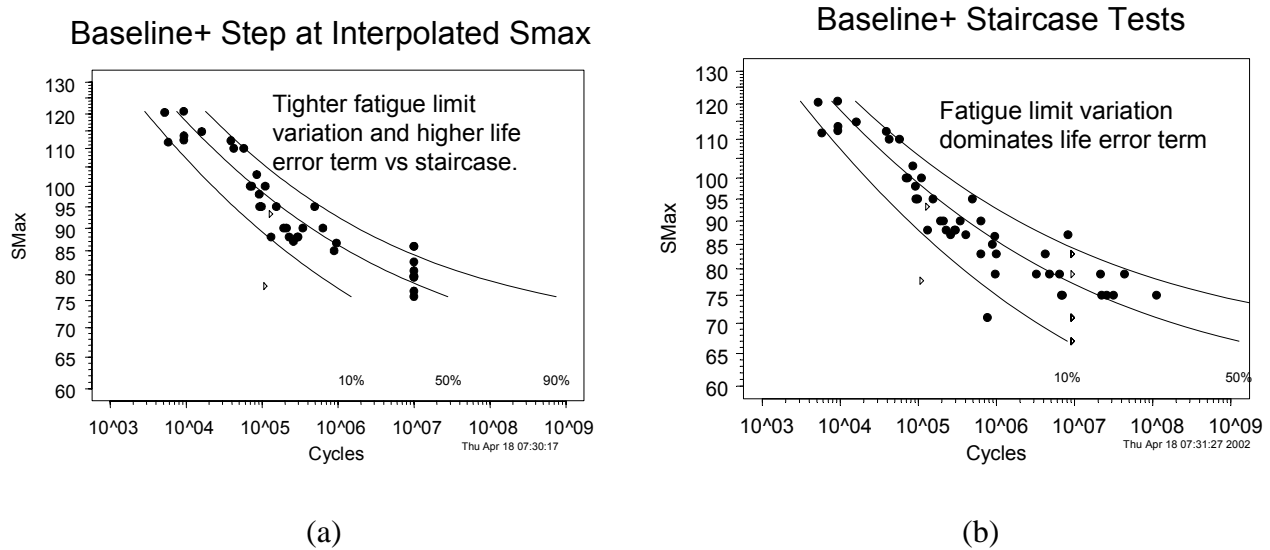
Figure 3.15 (a & b). Random Fatigue Limit Model predictions using baseline tests ($Nf<10^6$ cycles) + step or staircase approaches.

In Figure 3.16, the average and lower bound HCF limits for all approaches are summarized. Average HCF limits are relatively insensitive to the assumptions. Predicted lower bound limits are highly dependent on the assumed scatter direction for the 1D scatter approaches (stress vs life scatter). Lower bound limits are also highly dependent on the assumed scatter type (1D vs 2D scatter). The best approach needs to be assessed within the current design systems. Additional work establishing confidence limits for the RFL model also is needed for use in design.

The RFL assessment for all single load Ti-6Al-4V tests is also included as a final assessment. Load control tests with maximum stresses above the material yield stress were not used in the final analysis. HCF tests on the GEAE test machine at 1000Hz were excluded given possible control problems with these tests (PRDA report).
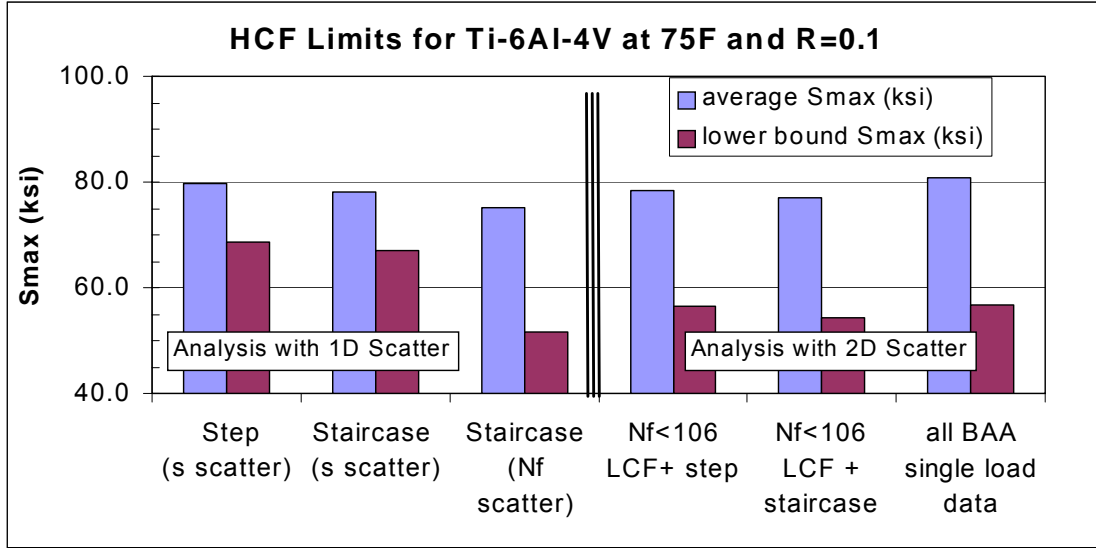
Figure 3.16. Summary of predicted average and lower bound HCF limits for Ti-6Al-4V
at 75°F and R=0.1. (Note: similar predictions for step and staircase approaches
with the 1D stress (s) scatter assumption; similar lower bound prediction with
step or staircase with 2D scatter assumption; different lower bound predictions
for 1D stress vs. life scatter; different lower bound prediction with 1D Vs 2D
scatter assumptions).

The model was fit with strain and load control tests at different R with the σ_{equiv} damage
parameter defined as:

$$\sigma_{equiv} = 0.5 \left(E\Delta\varepsilon\right)^w \left(\sigma_{max}\right)^{1-w} \tag{3.4}$$

where σ_{equiv} is the alternating Walker equivalent stress, E is the average elastic modulus for
the material (E=16840 ksi for Ti-6Al-4V at 75°F), $\Delta\varepsilon$ is the total strain range, σ_{max} is the
maximum stress as measured on test specimens or calculated with elastic-plastic analyses, and
w is a material constant. Strain control tests were used to establish the baseline half-life stress-
strain properties. The values of maximum stresses and strain are taken from strain control
measurements near the specimen half-life. The test results and Ramberg-Osgood fit are given
in Figure 3.17. The constant w=0.42 was obtained with a non-linear regression of the strain
and load control tests. The average and -3s RFL fits are given in Figure 3.18.
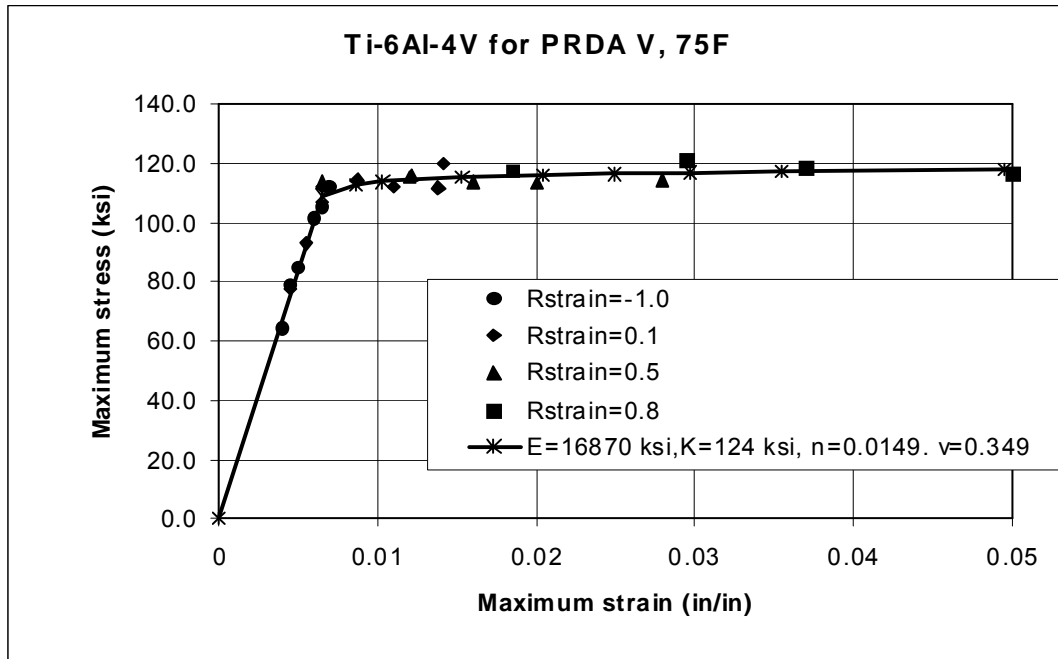
Figure 3.17. Maximum stress-strain results and fit for Ti-6Al-4V at 75°F elastic-plastic analyses.
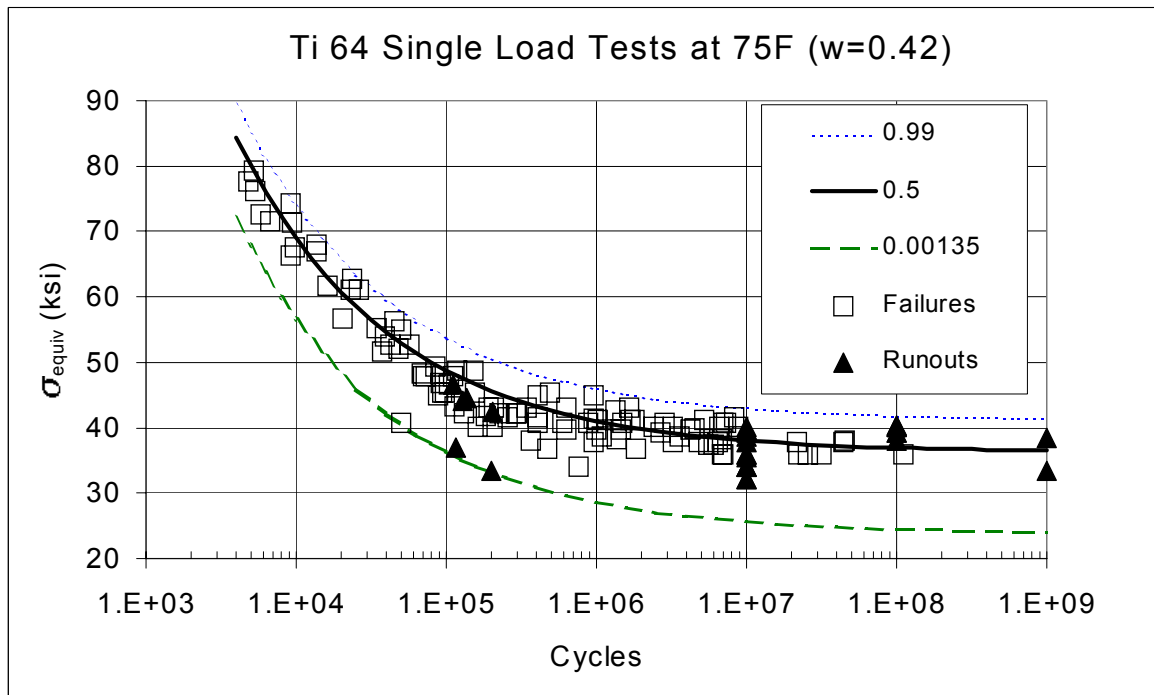
Figure 3.18. Single load test results and random fatigue limit fits for Ti-6Al-4V tests at 75°F.

The average and –3s RFL fits are given below in Equations 3.5 and 3.6 for Ti-6Al-4V at 75°F.

$$\text{Ti-6Al-4V average fit: } \log (N_f) = -2.39472 \log (\sigma_{equiv} - 36.199) + 7.629937 \tag{3.5}$$

$$\text{Ti-6Al-4V -3s fit: } \log (N_f) = -2.39472 \log (\sigma_{equiv} - 23.758) + 7.629937 \tag{3.6}$$

Step tests at the interpolated failure stresses were not used in the final baseline fits. Though step and single load tests produce equivalent results for R=0.1 (Figure 3.19a), step tests potentially produced unrealistically high allowable HCF limits at R=-1 (Figure 3.19b). Possible issues with step tests at negative R should be assessed in future work.

(a)   (b)
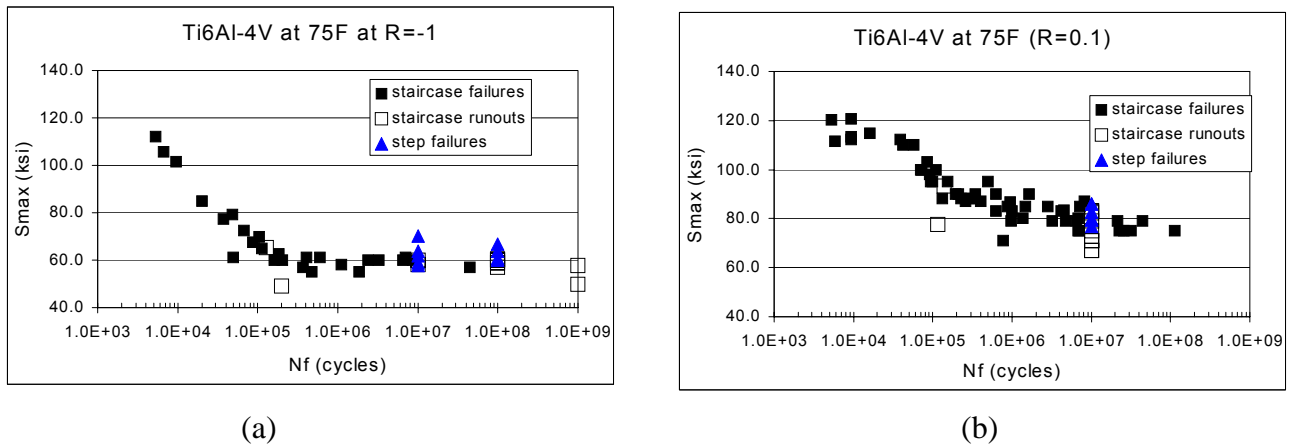
Figure 3.19. (a & b)   Step and staircase results for Ti-6Al-4V at 75°F. Note similar behavior at R=0.1 but increased allowable HCF limits for step tests at R=-1.0.

3.1.3.2   Ti-17 Smooth Specimen Testing and Methods at 75°F

Smooth specimen tests in load or strain control were used to establish baseline Ti-17 fatigue properties. The specimen load axis was oriented along the blisk radial direction. Prior to testing, smooth specimens were low stress ground and polished with a stress relief in a vacuum furnace for eight hours at 1130°F. Strain control LCF tests at 30 cycles/minute were used to obtain baseline LCF and stress-strain properties. Maximum stresses-strain values near Nf/2 for each specimen and the Ramberg-Osgood correlation for Ti-17 at 75°F are given in

Figure 3.20. High cycle fatigue properties were obtained at 360 Hz from tests at UDRI. The smooth specimen geometry for HCF testing is shown in Figure 3.21.
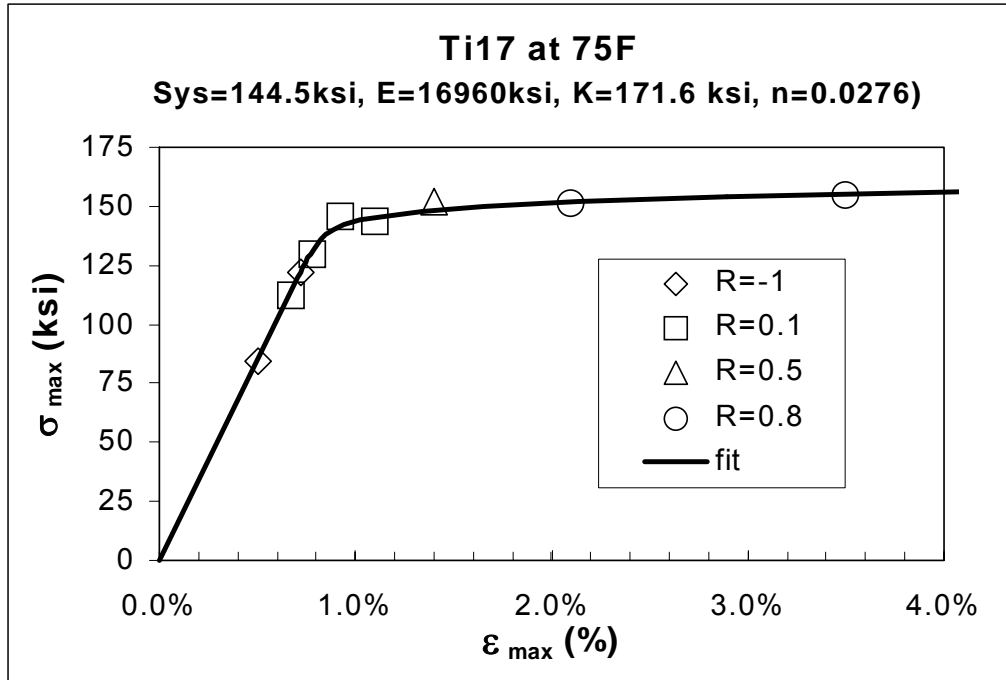
Figure 3.20. Half-life stress-strain behavior and fit for Ti-17 at 75°F.
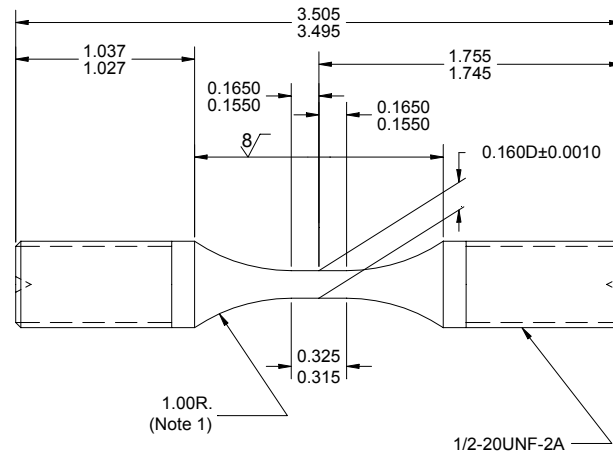
Figure 3.21. Smooth specimen geometry for baseline Ti-17 HCF tests.

Two issues were uncovered as the smooth specimen HCF tests results were analyzed. First, it was found that smooth specimens machined as lot 1 had a higher endurance stress than specimens machined in lot 2 (Figure 3.22). Secondly, it was found that endurance stresses for step tests were significantly higher than those found with single load tests (Figure 3.23).
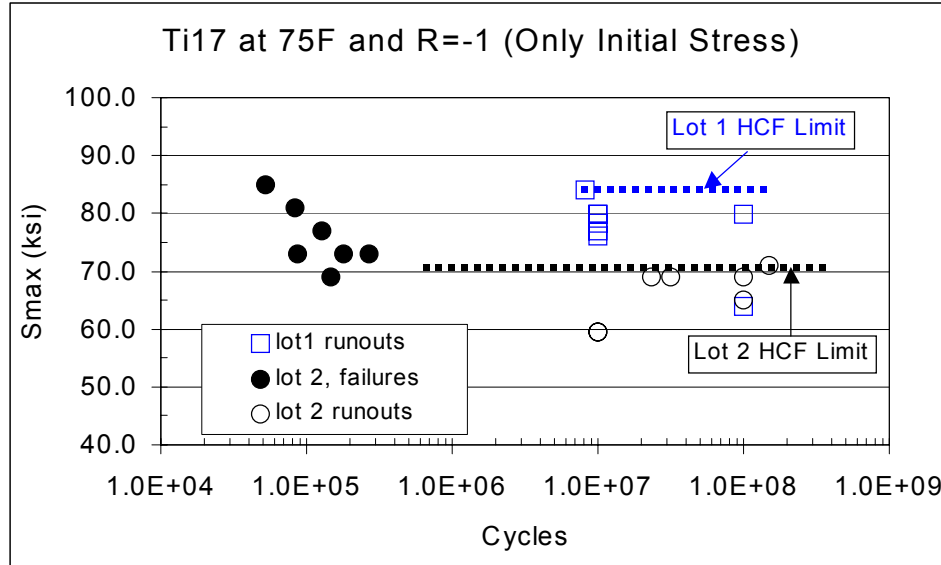
Figure 3.22. HCF limits for lot 1 and lot 2 specimens with initial stresses at R=-1.0. (Note the higher apparent HCF threshold for specimens machined in Lot 1).
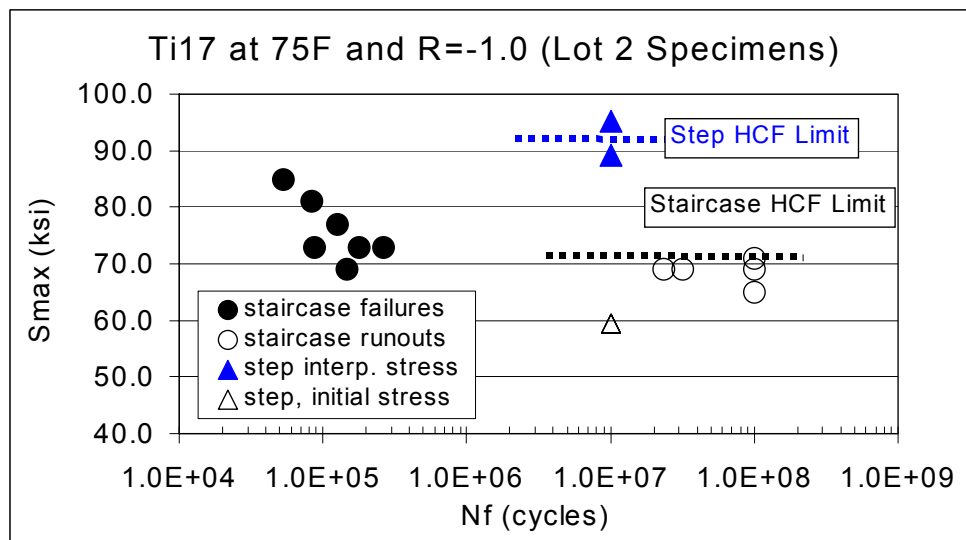
Figure 3.23. HCF limits for single load staircase tests and step tests at the interpolated fatigue stress at R=-1.0. (Note the higher apparent HCF threshold for specimens tested with the step test procedure).

Unfortunately, specimens were not available in sufficient quantity to understand these issues. The most consistent data set included strain control and single load staircase tests from both machining lots. This data and the average RFL fits through the tests are shown in Figure 3.24.
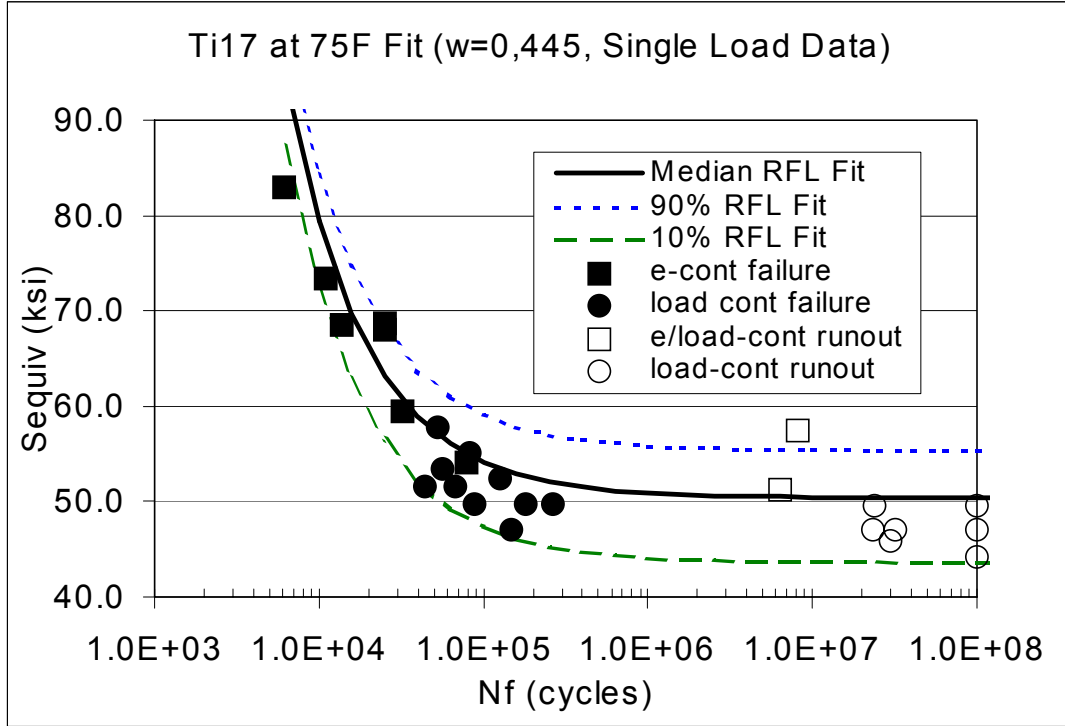
Figure 3.24. Ti-17 fatigue tests average fatigue curve at 75°F.

The average RFL fits for Ti-17 at 75°F are given in Equation 3.7.

Ti-17 average fit: $\log (Nf) = -1.12613 \log (\sigma_{equiv} - 50.414) + 5.647592$ (3.7)

σ_{equiv} is defined in Equation 3.4. The constant w=0.445 produced the best fit correlating theTi-17 results at 75°F. The baseline Ti-17 stress-strain response and average life fit is used to assess HCF for notches and airfoil geometries with simulated foreign object damage as discussed in Sections 3.3 and 3.4.

3.1.3.3   Critical Plane Modeling of Ti-6Al-4V at 500°F

HCF testing for the smooth Ti-6Al-4V (AMS 4928) material at 500°F, was completed and the data is shown in Figure 3.25. The tests were conducted at R = -1, 0.1, 0.5, and 0.8. Also included were step tests at R = 0.5. The R = 0.8 and 0.5 specimens were tested at maximum cyclic stress levels above 100 ksi. Since the cyclic yield strength at 500°F is ~100 ksi, it is believed that these data may have been influenced by the effects of cyclic plasticity and creep. The R = 0.8 data were not included in the critical plane analysis below. The data in Figure 3.25 was analyzed using the Smith-Watson-Topper (SWT) and the Findley critical plane models.

Ti-6Al-4V, Smooth HCF Data, 500 F
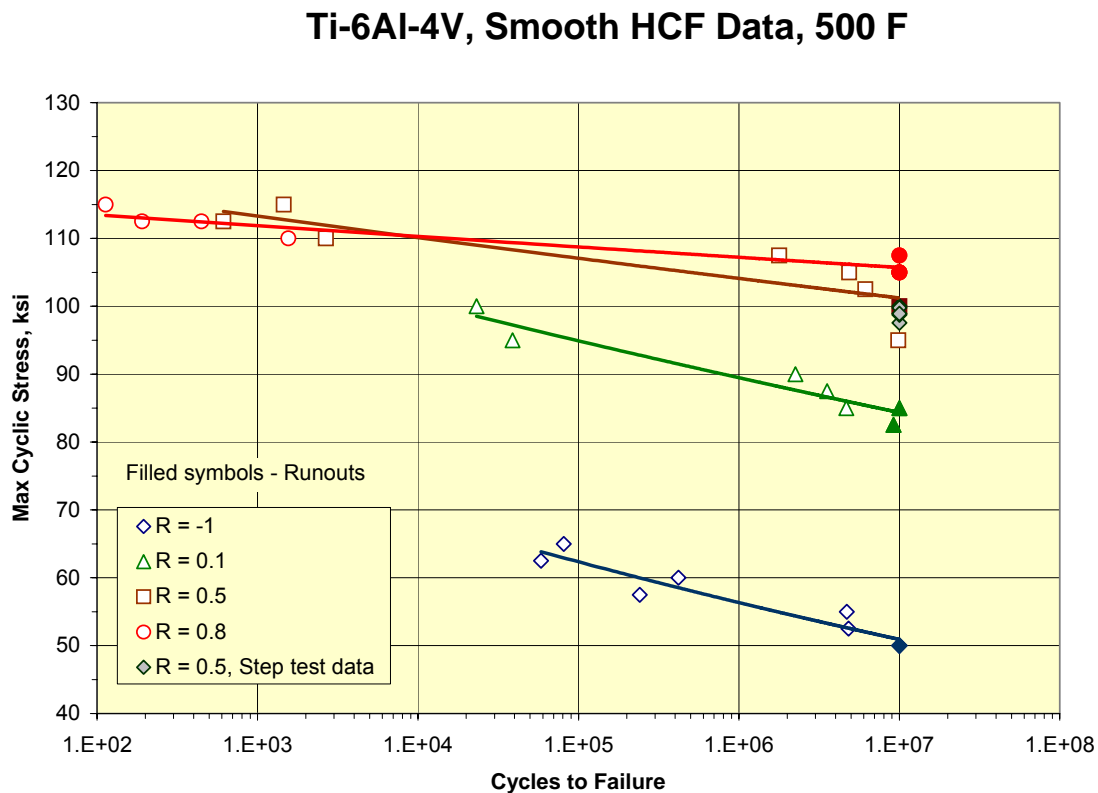
Figure 3.25. Max cyclic stress versus life curves for Ti-6A1-4V tested at 500°F.

The SWT parameter was calculated as the product of the maximum normal strain amplitude, ε_a, on a 'critical plane' and the maximum normal stress, σ_{max}, on the critical plane:

$$SWT = \sqrt{\sigma_{max}\varepsilon_a E} \tag{3.8}$$

The 'critical plane' for any given multiaxial loading cycle is determined by computing the SWT parameter (for all time steps in the fatigue cycle) along planes with orientation angles ranging from 0 – 180 degrees with respect to the axial loading direction. Along each plane the max normal ε_a and the max normal σ_{max} are computed over the entire fatigue cycle, using appropriate transformation equations for stress and strain. The plane on which the SWT parameter is the maximum (for all time steps of the loading cycle) is then the 'critical plane' for the given loading cycle. In mathematical form this procedure can be expressed as:

$$SWT = \max_{\theta=0\text{-}180}\left[\max_{\substack{\text{fatigue}\\ \text{cycle}}}\left\{\sqrt{\sigma_{x,max}\varepsilon_{x,a}E},\sqrt{\sigma_{y,max}\varepsilon_{y,a}E}\right\}\right] \tag{3.9}$$

where, $\varepsilon_{x,a}$ and $\varepsilon_{y,a}$ are the max normal strain amplitudes in the x- and y-directions and $\sigma_{x,max}$ and $\sigma_{y,max}$ are the max normal x- and y-stresses over all time steps at a given orientation angle, θ. The results for the SWT parameter are shown in Figure 3.26. The correlation of the different stress ratios using the SWT parameter does not seem to be very good. A least-squares curve-fit obtained using the linear SWT parameter and the log of the life is shown in Figure 3.26. The SWT curve-fit for the RT data is also shown in Figure 3.26. For life cycles greater than 5×10^5, there is no difference between the RT and the 500 F SWT curve-fits suggesting that the 500 F condition does not influence the RT HCF strength, where, k is a fitting parameter. For the present study, k = 0.31 was used. This optimized value of k was obtained as that value which minimized the square of the difference between the FIN data value (for all the different R-ratios) and the curve-fit. This value of k was similar to the value obtained for the RT smooth data.

The FIN parameter is calculated using the maximum shear stress amplitude, τ_a, on a 'critical plane' and the maximum normal stress, σ_{max}, on the critical plane:

$$FIN = \tau_a + k\sigma_{max} \tag{3.10}$$

Ti-6Al-4V, SWT Damage Parameter, 500 F, Smooth
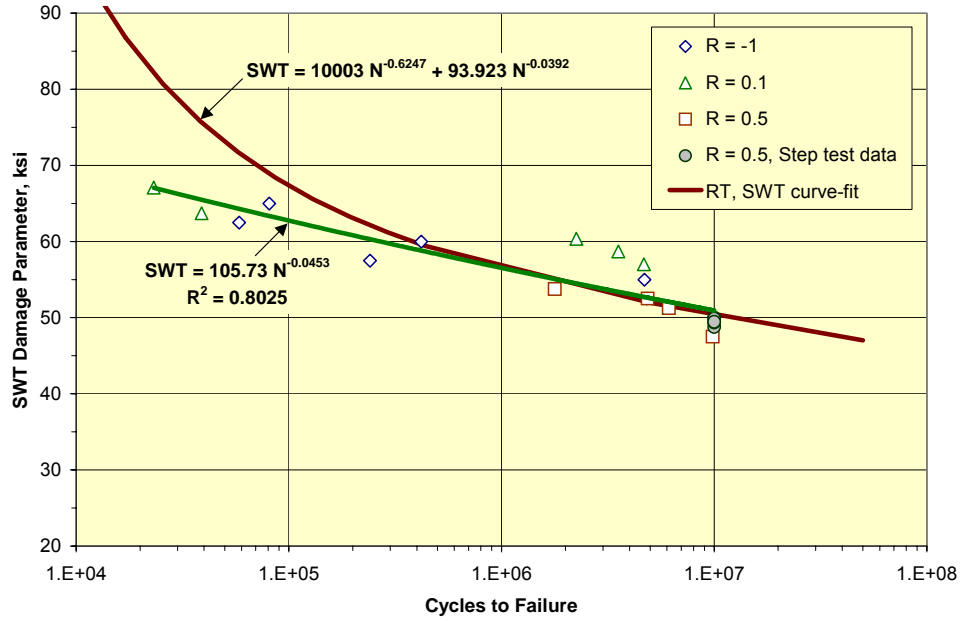
Figure 3.26. SWT parameter versus life curve for Ti-6Al-4V tested at 500°F.

The 'critical plane' for any given multiaxial loading cycle is determined by computing the FIN parameter (for all time steps in the fatigue cycle) along planes with orientation angles ranging from 0 – 180 degrees with respect to the axial loading direction. Along each plane the max τ_a and the max normal σ_{max} are computed over the entire fatigue cycle, using appropriate transformation equations for stress and strain. The plane on which the FIN parameter is the maximum (for all time steps of the loading cycle) is then the 'critical plane' for the given loading cycle. In mathematical form this procedure can be expressed as:

$$FIN = \max_{\theta=0\text{-}180} \left[\max_{\substack{\text{fatigue} \\ \text{cycle}}} \left\{ \tau_a + k_2 \sigma_{x,max}, \tau_a + k_2 \sigma_{y,max} \right\} \right]$$ (3.11)

where, τ_a is the max shear stress amplitude and $\sigma_{x,max}$ and $\sigma_{y,max}$ are the max normal x- and y-stresses over all time steps at a given orientation angle, θ. The results for the Findley damage parameter are shown in Figure 3.27. The correlation of the different stress ratios using the Findley parameter is quite good. A least squares curve-fit obtained using the linear FIN

41

parameter and the log of the life is shown in Figure 3.27. The Findley parameter curve-fit for the RT data is also shown in Figure 3.27. For fatigue cycles greater than 250,000, the 500°F Findley curve-fit is above the RT curve-fit suggesting that the 500°F condition does not degrade the RT HCF strength.

Ti-6Al-4V, Findley Damage Parameter, 500 F, Smooth
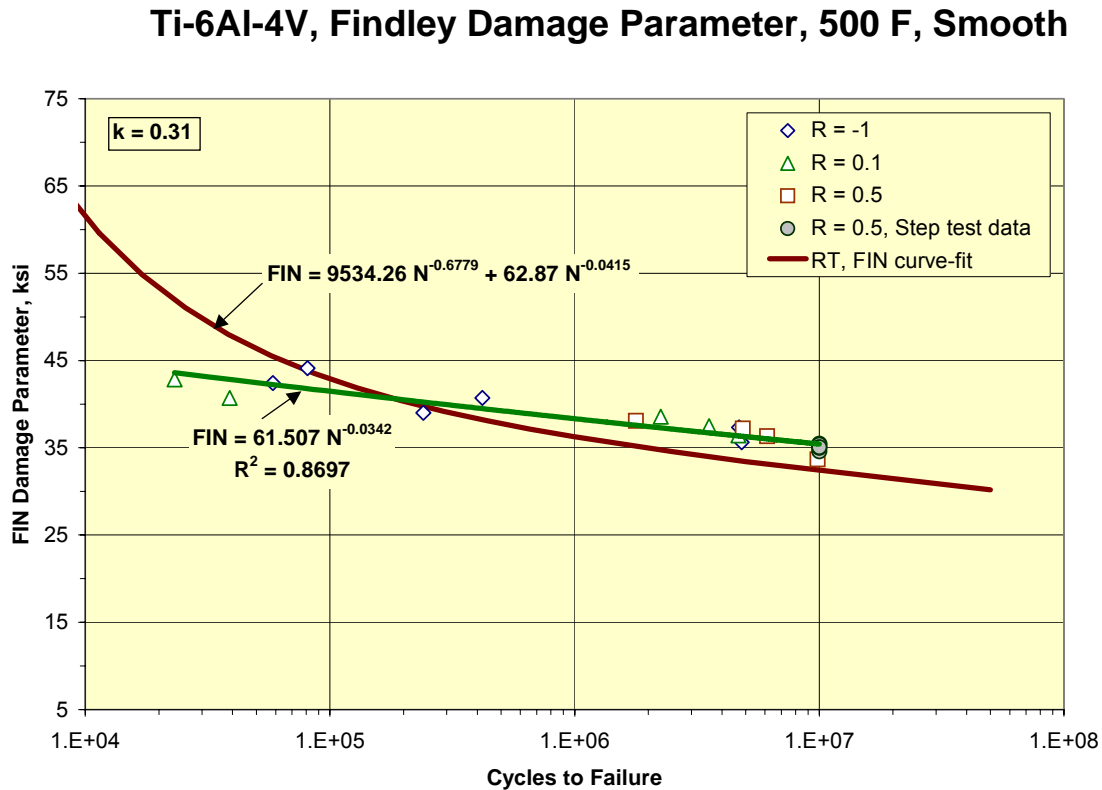
Figure 3.27. Findley parameter versus life curve for Ti-6Al-4V tested at 500°F.

3.1.4   HCF/LCF Interactions for Ti-6Al-4V at 75°F

HCF and LCF tests are used to establish baseline material properties. Mission tests can be used to assess additional failure modes that may exist if HCF/LCF interactions are important. This was explored with mission tests at 75°F with Ti-6Al-4V material from the PRDA program. The criteria used to select relevant mission tests includes: a) tests that avoid specimen ratcheting failure modes that are not representative of component failures, (b) LCF stresses that are in the main regime of design interest (average Nf~10,000 cycles),

(c) HCF stresses that are in the regime of design interest (R>0.5 and HCF $\geq 10^7$ cycles),
(d) mission histories that include LCF + periodic HCF cycles until mission failure, and e) tests
that can be run economically in the lab. A double edge V-notch specimen geometry used in
the PRDA program was used to avoid ratcheting for load control testing. Loads were selected
to keep the fatigue lives in the regime of design interest. Baseline notch R=0.1 LCF tests
were run to identify stresses for an LCF failure of ~10,000 cycles. Baseline notch HCF tests
were used to identify the R-ratio for an average HCF failures of ~10^7 cycles. All interaction
tests were missions that were repeated until failure. Missions include an LCF load-up (R=0.1)
+ 10,000 to 100,000 repeated HCF cycles (R=0.7 to 0.9) + an LCF unload reversal (R=0.1)
for each mission. The baseline and mission test conditions for the notch geometry are given
in Table 3.6.

Table 3.6. Baseline and HCF/LCF Mission Tests

SP ID	LCF Smin	LCF Smax	HCF Smax	HCF Smin	HCF/mission	Freq (Hz)	exper HCF cycles	experimental missions	Pred Mission Life with Fs
36-13	9	90	NA	NA	LCF	0.5	NA	9,963	11,365
36-2	8	80	NA	NA	LCF	0.5	NA	10,766	16,489
48-7	8	80	NA	NA	LCF	0.5	NA	10,821	16,489
36-14	NA	NA	80	56	HCF	1K	234,894,301	234,894,301	6,370,632
48-2	NA	NA	80	56	HCF	1K	11,694,364	11,694,364	6,370,632
36-10	NA	NA	80	56	HCF	1K	2,613,654	2,613,654	6,370,632
36-9	8	80	80	56	10,000	0.5/1K	16,400,000	1,640	613
48-5	8	80	80	56	10,000	0.5/1K	71,682,975	7,168	613
36-8	8	80	80	56	100,000	0.5/1K	14,298,296	143	63
36-4	8	80	80	56	100,000	0.5/1K	9,312,872	93	63
48-4	8	80	80	56	100,000	0.5/1K	405,933,382	4,059	63
36-12	8	80	80	72	10,000	0.5/1K	142,814,527	14,281	16,222
36-11	8	80	80	65	10,000	0.5/1K	94,130,587	9,413	16,222
note: predicted life obtained with initiation code (average fatigue curve, Miner's rule, 1e10 cutoff on Nf)									

The first group of mission tests was used to assess the HCF capability when minimal
LCF damage is present. This was evaluated with 10,000 to 100,000 HCF cycles/mission with
a HCF cycle from 56 to 80 ksi (R=0.7). These conditions were intentionally selected to avoid
significant predicted LCF damage. The number of HCF cycles to failure for these mission
tests is compared to the number of cycles to failure for HCF alone with probability plots as
shown in Figure 3.28. Given the similarity of these distributions for the small set of data

presented, a significant HCF/LCF interaction does not seem to be present for cases when HCF damage dominates.
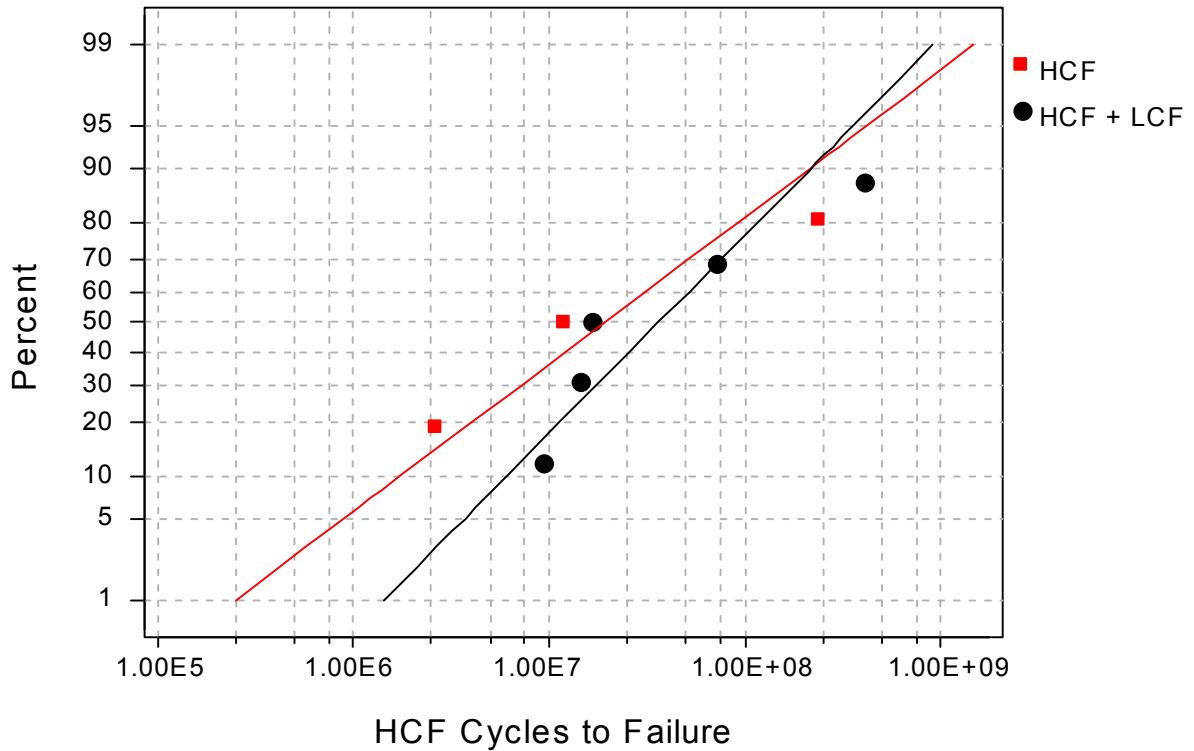
Figure 3.28. Capability of notched HCF tests compared to the HCF capability of HCF/LCF mission tests when HCF damage dominates.

The second group of tests was run to assess if LCF failure modes are influenced when minimal predicted HCF damage exists. Minimal HCF damage was evaluated with mission tests that included an LCF load-up reversal (R=0.1) + 10,000 repeated HCF cycles [Smax=80 ksi; Smin=72 for R=0.9 or 65 ksi for R=0.82].   The HCF parameters were selected near the minimum allowable stress for a 10^7 HCF limit. Ideally, a designer can ignore HCF when the HCF stresses are at or below the minimum material capability. The number of LCF cycles to failure for the notch mission tests as compared to Nf for the notch specimens with LCF alone is shown in Figure 3.29 Predicted Nf uses the average smooth specimen Sequiv fatigue curve from the PRDA program with the modified Manson-McKnight fatigue parameter. The local stresses from the notch are obtained from elastic-plastic analysis. Notch life is predicted with the local notch stresses and notch gradients with the Fs approach. These

44

tests are predicted well within the 2X scatter bands that are representative of a reasonably accurate LCF life method. Low predicted HCF damage assuming no HCF/LCF interaction works well for these mission tests where the HCF damage is minimal. This is probably the area of most interest to design - one can select a HCF limit based on minimum properties such that HCF can be ignored as a failure mode in a mission that contains HCF and LCF conditions.
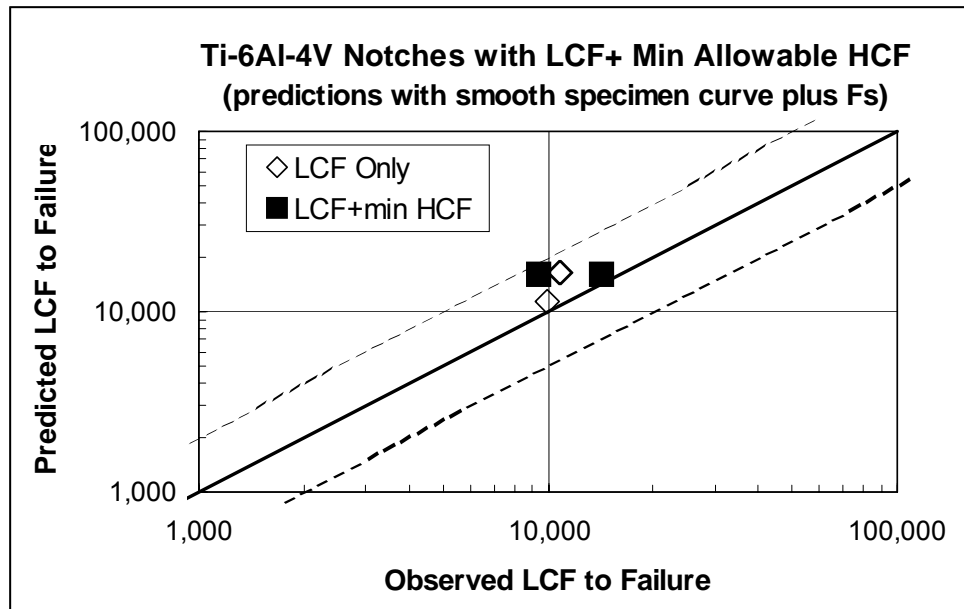
Figure 3.29. Notched LCF tests compared to the LCF of HCF/LCF
mission tests with minimal HCF damage.

3.2   MULTIAXIAL MODELING

Over 20 multiaxial fatigue models were evaluated based on their ability to correlate uniaxial and biaxial smooth specimen fatigue data. The data used for comparison purposes included uniaxial data at various stress ratios, and proportional and non-proportional biaxial data that included multiaxial mean stresses. Test data from Ti-6Al-4V at room temperature (RT) and 500°F and Ti-17 at RT were considered; however, the primary model evaluations were performed using only the Ti-6Al-4V RT data set as this included the greatest number of data points. A small number of simulated biaxial mission history tests were also conducted to

evaluate the ability of the models to predict fatigue damage accumulation under more complex load histories.

The fatigue models evaluated in this program included both "equivalent-stress" (stress-invariant) methods and "critical-plane" approaches. The equivalent-stress models utilize a scalar parameter, typically consisting of an equivalent stress range and a mean or maximum equivalent stress term, to represent the multiaxial cyclic stress state. The critical-plane models are based on the assumption that fatigue cracks will initiate on "critical planes" in the material, defined as planes that experience the greatest accumulation of fatigue damage as generated by a combination of cyclic normal and/or shear stresses or strains. The equivalent-stress models have the advantage of ease of implementation, whereas the critical-plane models are often considered to be more closely associated with phenomenological observations regarding fatigue crack development.

The following subsections describe the multiaxial fatigue data used in the evaluation process and the results of the model evaluations for the two titanium alloys at the different temperatures. A discussion of the mission history results is included at the end of the section. Further details of the multiaxial tests and model evaluations can be found in Appendices C, D, and E.

3.2.1 Smooth Specimen Multiaxial Test Data

Over 30 biaxial tests were conducted by the University of Illinois on solid round specimens of Ti-6Al-4V and Ti-17. All specimens were stress relieved and chem milled. These tests encompassed a variety of stress states, including torsion at various stress ratios (R = −1, 0.1, and 0.5), proportional tension-torsion (R = −1 and 0.1), and non-proportional tension-torsion load paths with various mean stress levels. The test conditions were selected to provide a rigorous examination of the multiaxial models, and in particular to evaluate the models for load paths designed to simulate portions of actual service events.

The non-proportional load paths are illustrated in Figure 3.30. The circle path (90° out-of-phase) is often considered to provide a critical examination of deformation and fatigue damage. The triangle, box, and check paths are designed to simulate portions of actual service events. The box path, in particular, is representative of the stress state produced near

46

the edge-of-contact region in fretting fatigue simulations. Additional details regarding the experimental procedures and results are contained in Appendix C.
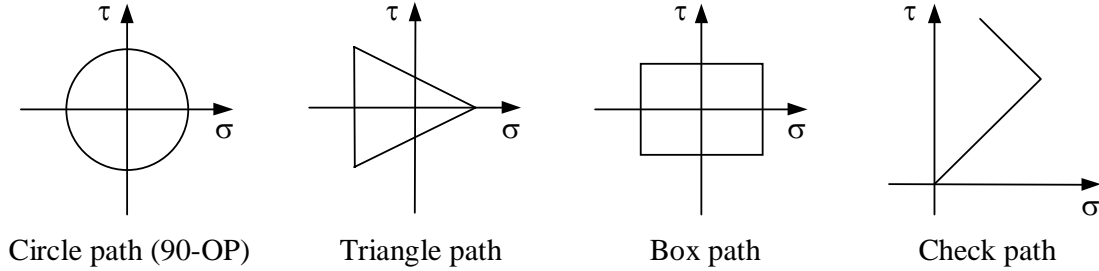
Figure 3.30. Non-proportional biaxial load paths.

Although the majority of the multiaxial tests were conducted in the elastic range, a few tests experienced small-scale plasticity on the first reversal. For these tests, the surface stresses were determined from the measured surface strains using an elastic-plastic finite element analysis conducted in ANSYS. This analysis utilized the half-life cyclic stress-strain curve generated from the uniaxial strain-controlled LCF database.

3.2.2   Multiaxial Modeling of Ti-6Al-4V at Room Temperature

Based on the preliminary evaluations of all the multiaxial models considered in this program (see Appendix D), four models were selected for detailed study: the modified Manson-McKnight (MMM) model, the Smith-Watson-Topper (SWT) parameter, the Findley model, and the Fatemi-Socie-Kurath (FSK) model.

The MMM model was the only equivalent-stress model found to provide good agreement with the experimental results. For a multiaxial stress state, the damage parameter (DP) for this model is defined in terms of a Walker equivalent stress as

$$DP_{MMM} = \sigma_{eqv} = 0.5(\Delta\sigma_{psu})^{w}(\sigma_{max})^{1-w} \tag{3.12}$$

where, $\Delta\sigma_{psu}$ is a "pseudo stress range" defined as

$$\Delta\sigma_{psu} = \frac{1}{\sqrt{2}}\sqrt{(\Delta\sigma_{xx} - \Delta\sigma_{yy})^2 + (\Delta\sigma_{yy} - \Delta\sigma_{zz})^2 + (\Delta\sigma_{zz} - \Delta\sigma_{xx})^2 + 6(\Delta\sigma_{xy}^2 + \Delta\sigma_{yz}^2 + \Delta\sigma_{zx}^2)}$$

$$\tag{3.13}$$

and σ_{max} is calculated as $\sigma_{max} = \sigma_{mean} + 0.5\Delta\sigma_{psu}$, where

$$\sigma_{mean} = \frac{\beta}{2\sqrt{2}}\sqrt{(\Sigma\sigma_{xx} - \Sigma\sigma_{yy})^2 + (\Sigma\sigma_{yy} - \Sigma\sigma_{zz})^2 + (\Sigma\sigma_{zz} - \Sigma\sigma_{xx})^2 + 6(\Sigma\sigma_{xy}^2 + \Sigma\sigma_{yz}^2 + \Sigma\sigma_{zx}^2)}$$

(3.14)

In these equations, $\Delta\sigma_{ij}$ and $\Sigma\sigma_{ij}$ define the stress range and summed stress, respectively, for each stress component based on the maximum and minimum points in the fatigue cycle, and β is

$$\beta = \frac{(\Sigma\sigma_1 + \Sigma\sigma_3)}{(\Sigma\sigma_1 - \Sigma\sigma_3)}$$

(3.15)

where, $\Sigma\sigma_1$ and $\Sigma\sigma_3$ are the sums of the first and third principal stresses, respectively, at the maximum and minimum stress points in the fatigue cycle. The exponent w is a material and temperature-dependent constant that collapses variable mean stress data into a single curve.

Several critical plane models were found to provide fair to good correlation of the uniaxial data, with varying levels of success in correlating the biaxial data. Results are shown here for three critical plane models, selected to represent both normal (tensile) and shear-based parameters.

The SWT parameter is a normal stress/strain based model, with the damage parameter defined as

$$DP_{SWT} = (\varepsilon_a)(\sigma_{max})$$

(3.16)

where, ε_a is the normal strain amplitude and σ_{max} is the maximum normal stress in the cycle on the critical plane. This model is included because it is a well-known parameter that is representative of all the tensile-based critical plane models. The SWT parameter shown in Equation 3.16 is sometimes reformulated for ease of comparison to other models; for example, the term $(\sigma_{max}\varepsilon_a E)^{1/2}$ produces a similarity to the MMM model (Equation 3.12) with $w = 0.5$, and retains the same units as the original parameter. In using this variation, however, it must be recognized that the square-root operation tends to artificially enhance the accuracy of the model by minimizing differences between values.

The Findley and FSK models are formulated based on the assumption that the cyclic shear stress or strain is the primary damage-causing component on the critical plane, but the normal stress on that plane plays a secondary role. The Findley damage parameter is defined exclusively in terms of stress:

$$DP_{FIN} = \tau_a + k\sigma_{max} \tag{3.17}$$

where, τ_a and σ_{max} are the shear stress amplitude and maximum normal stress in the cycle, respectively, on the critical plane, and k is a material and temperature dependent parameter that collapses variable mean stress data into a single curve. The FSK model makes use of the shear strain amplitude, and is defined as

$$DP_{FSK} = \gamma_a \left(1 + k\frac{\sigma_{max}}{\sigma_y}\right) \tag{3.18}$$

where, γ_a is the shear strain amplitude on the critical plane, σ_y is the yield strength of the material, and k is again a material and temperature dependent parameter that collapses variable mean stress data into a single curve.

In this analysis, the critical plane was defined as the plane experiencing the maximum value of the damage parameter, rather than the plane experiencing the maximum shear or normal stress or strain amplitude. Under general multiaxial loading conditions, the critical plane must be determined by an incremental search algorithm, in which the damage parameter is computed on all planes (in specified increments) from 0 to 180°. When implemented in conjunction with finite element codes or for large load histories, this procedure can be computationally expensive. However, under certain conditions (e.g., proportional, in-phase biaxial loading), the critical plane orientation and associated damage parameter can be analytically determined. Closed-form expressions for the SWT and Findley models are included in Appendix E.

The predictions from the four multiaxial models for the uniaxial Ti-6Al-4V data at RT are shown in Figures 3.31 through 3.34. None of the step-test data were used in these evaluations. The predictions are presented in two formats for each model. The DP vs. N curves show the experimental damage parameter, calculated from the measured stress or

strain values, vs. experimental life. The curves shown in these plots were generated from a least squares fit to the data, assuming an equation of the form

$$DP = AN^b + CN^d \tag{3.19}$$

where, A, b, C, and d are curve-fitting constants. A sound model will collapse all the variable mean stress data into a single curve that can be adequately represented by Equation 3.19. However, direct comparison of the models using these plots is difficult due to the widely differing definitions of the damage parameter for each model. Consequently, a second approach was employed to provide a direct comparison of the models for the uniaxial data. In this approach, the maximum uniaxial cyclic stress level for a given stress ratio (R) was calculated from the predicted value of the damage parameter at a given fatigue life (N). This value was then plotted against the actual (measured) value of the maximum cyclic stress at that life. These results are shown in the form of plots of predicted σ_{max} vs. actual σ_{max}. For some of the models, this latter approach required the assumption of elastic conditions for stress-strain calculations; consequently, only the HCF (load-control) data were used for these comparisons.

As is evident from Figures 3.31 through 3.34, all four models provided reasonable correlations for the uniaxial data. A quantitative comparison between the models is included in Table 3.7. For each model, the ratio of actual to predicted σ_{max} was calculated for every uniaxial data point. The average and standard deviation of the group of data are shown in the table for each model. As would be expected, the average value is very near unity for each model, since the predicted values were generated from a least-squares curve fit to the data. The standard deviation values are more useful for comparison, as they represent the degree of scatter in the data about the predicted curve. Note that the MMM, SWT, and FSK models all have similar standard deviations, while the Findley model displays a slightly higher value. This is primarily due to the fact that the Findley model under-predicted the allowable stress levels for the R = 0.5 data, as can be seen in Figure. 3.33. The MMM model also displayed the same tendency, although to a lesser degree (Figure 3.31).
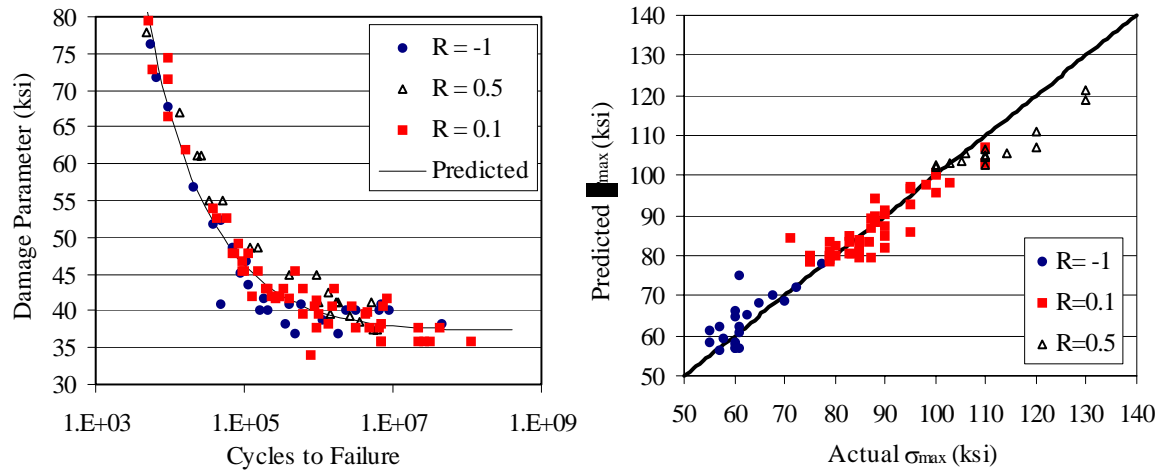
Figure 3.31.   Modified Manson-McKnight (MMM) model applied to uniaxial Ti-6Al-4V RT data.
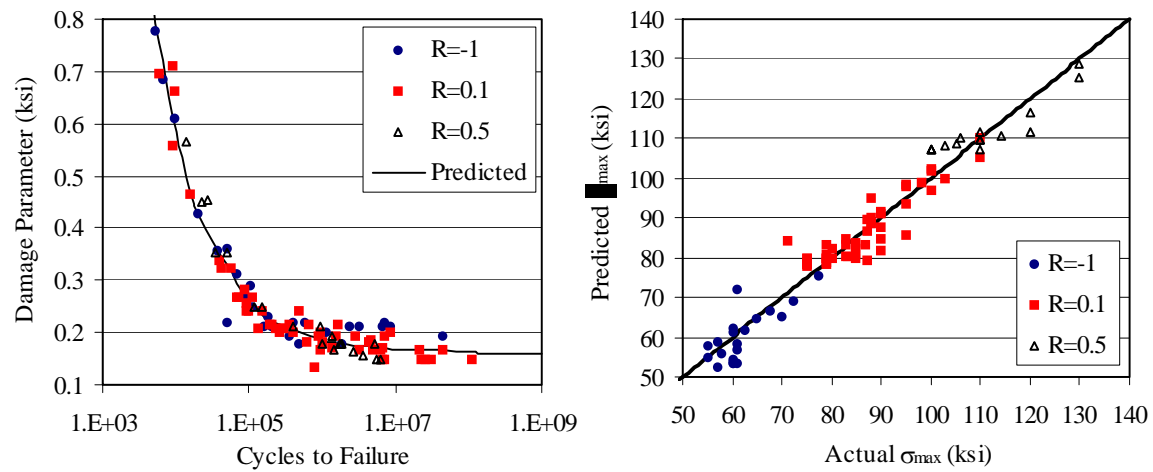
Figure 3.32. Smith-Watson-Topper (SWT) model applied to uniaxial Ti-6Al-4V RT data.
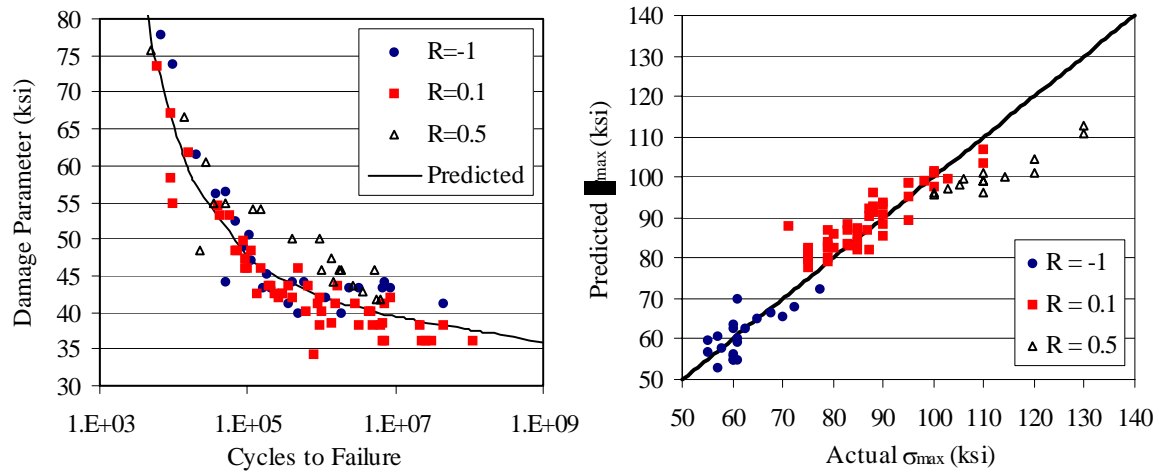
Figure 3.33. Findley model applied to uniaxial Ti-6Al-4V RT data.
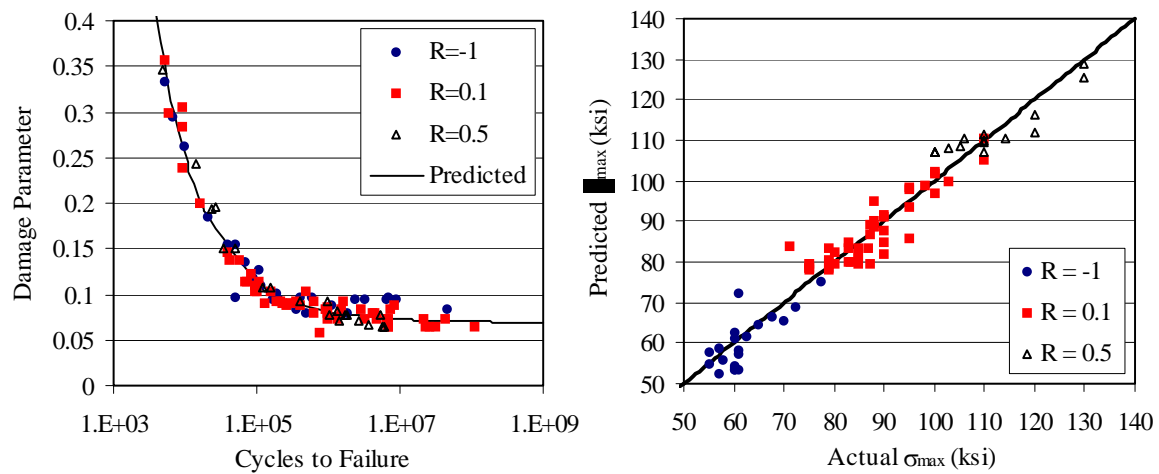
Figure 3.34. Fatemi-Socie-Kurath (FSK) model applied to uniaxial Ti-6Al-4V RT data.

Table 3.7. Comparison of Models for Uniaxial Ti-6Al-4V RT Data: Actual/Predicted σ_{max}

Model	MMM	SWT	Findley	FSK
A/P σ_{max} (average)	1.002	1.008	1.008	1.009
A/P σ_{max} (stand. dev.)	0.056	0.056	0.072	0.058

The predictions of the four models for the biaxial Ti-6Al-4V RT data are shown in Figures 3.35 through 3.38, where the curve in each figure represents the fit to the uniaxial data. The differences between the models are more pronounced when comparing the biaxial predictions. With the exception of the SWT model, the biaxial data are reasonably centered about the uniaxial baseline curves. The SWT model is noticeably non-conservative, in that the biaxial tests were more damaging than predicted by the uniaxial curve. The MMM model had difficulty correlating the torsion data, and was highly non-conservative in its damage prediction of the circle (90–OP) path. The Findley model produced fairly good predictions for most of the load paths, with the notable exception of the box path, in which the damage estimates were highly conservative. However, by changing the definition of the σ_{max} term in the Findley parameter from the maximum-normal-stress in the cycle to the maximum-normal-stress at the shear reversal points, the Findley predictions for the box path are substantially improved. Similar to the Findley model, the FSK model was also found to be conservative in its damage predictions for the box path.
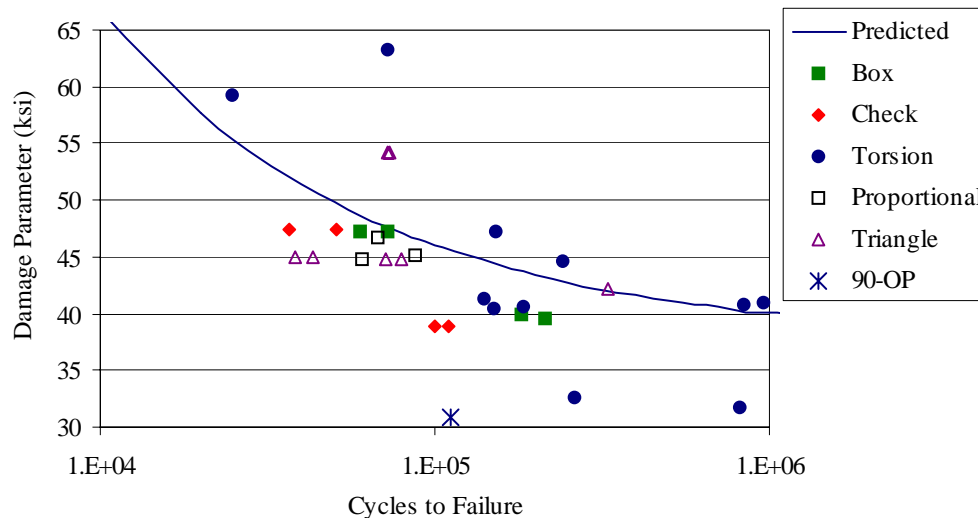
Figure 3.35. MMM model applied to biaxial Ti-6Al-4V RT data.

53
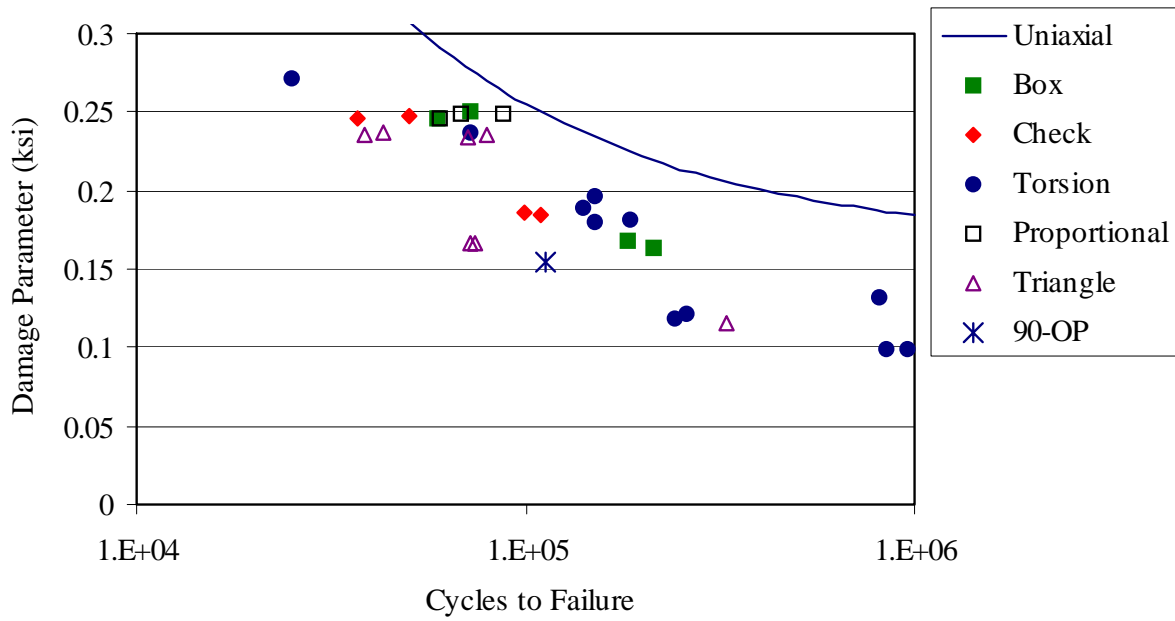
Figure 3.36. SWT model applied to biaxial Ti-6Al-4V RT data.
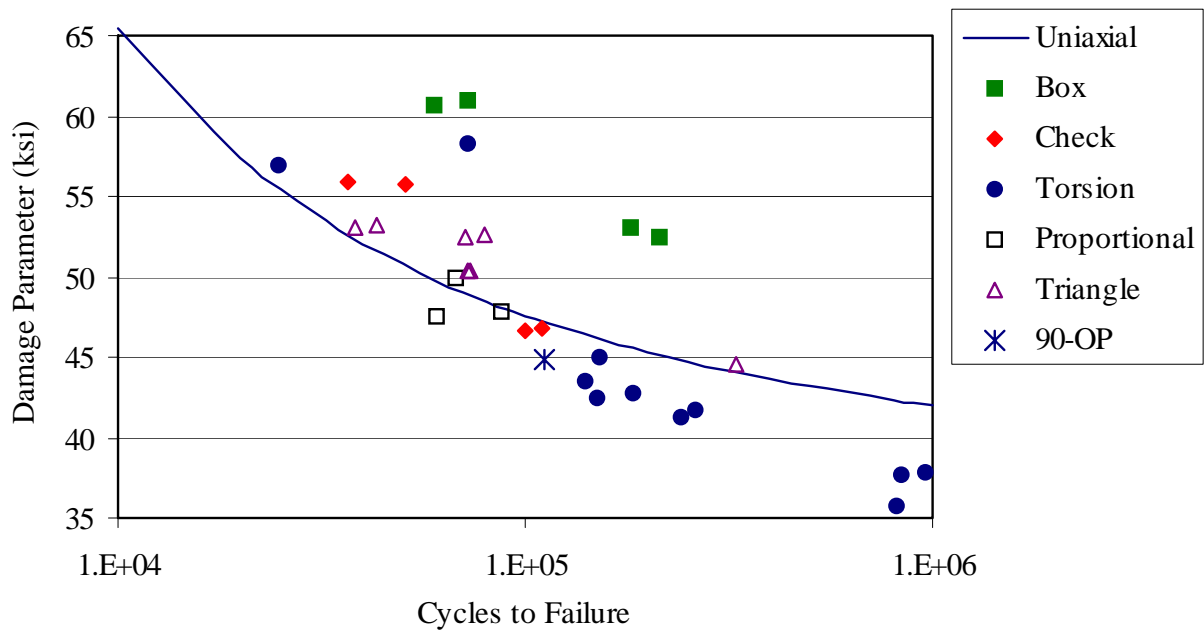
Figure 3.37. Findley model applied to biaxial Ti-6Al-4V RT data.
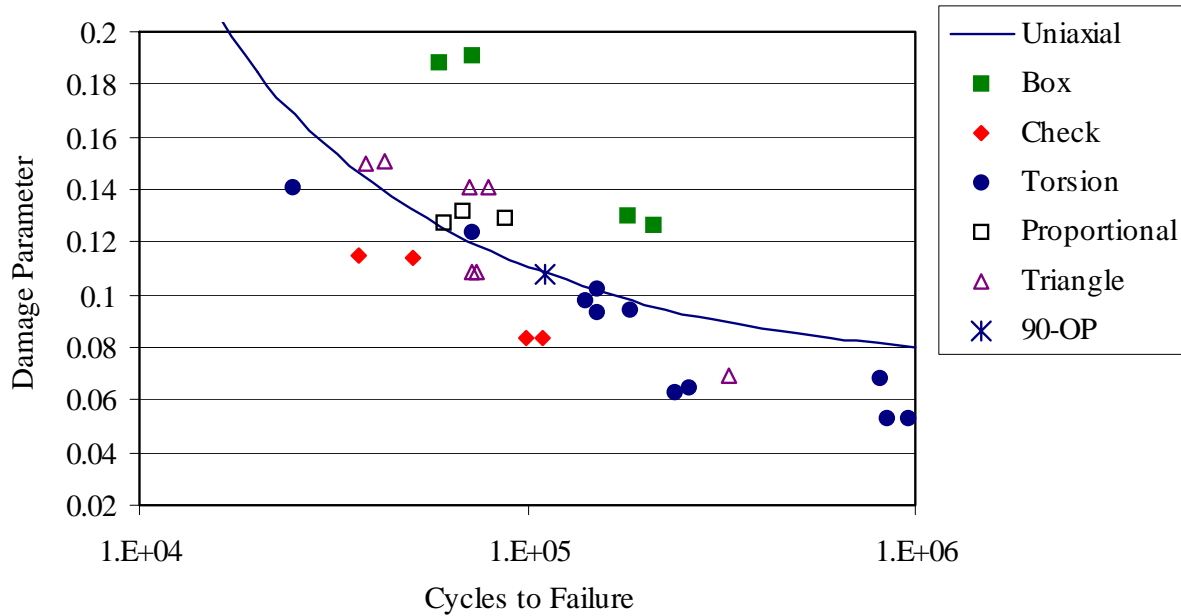
Figure 3.38. FSK model applied to biaxial Ti-6Al-4V RT data.

Due to the complexity of the biaxial load paths and the differing definitions of damage parameter for each model, direct quantitative comparisons cannot be made between the models as was done for the uniaxial data. Indirect comparisons can be made, however, by considering the average value and standard deviation of the set of actual/predicted damage parameter ratios from each model for the biaxial data. These values are shown in Table 3.8, along with the curve-fit parameters for each model. These results show that the Findley model produced the lowest overall scatter in the data (lowest standard deviation in the actual/predicted DP values). The MMM and SWT models also produced reasonably low scatter, but the SWT model had a very low average value, indicating the model is non-conservative when used to predict biaxial fatigue damage. Due to the fact that the tensile-based critical plane model (SWT) produced very poor predictions of the biaxial damage, while the shear-based models (Findley and FSK) were reasonably accurate, it can be concluded that the initiation of fatigue cracks in Ti-6Al-4V is driven primarily by shear stresses.

Table 3.8.   Curve-Fit Parameters and Model Comparisons for Biaxial Ti-6Al-4V RT Data: Actual/Predicted Damage Parameter

Model	k	A	b	C	d	A/P DP (Avg.)	A/P DP (St. Dev.)
MMM	--	3501.8	-0.5164	36.74	0.00068	0.953	0.122
SWT	--	223.46	-0.6840	0.1861	-0.00783	0.737	0.121
Findley	0.379	7190.8	-0.6347	52.896	-0.0186	1.020	0.101
FSK	54.3	91.074	-0.6783	0.0795	-0.00695	1.025	0.229

In addition to the constant-amplitude biaxial tests, six biaxial "mission-history" tests were also conducted on Ti-6Al-4V. These tests were designed to simulate actual mission histories, in which a small number of highly damaging LCF cycles are coupled with a larger number of low-damage HCF cycles. The purpose of these tests was to experimentally assess HCF/LCF interactions within a multiaxial stress state, and to evaluate the ability of the models to predict fatigue damage accumulation under more complex load histories. In this program, the mission histories were derived from the box and check paths, which made up the LCF cycles. The HCF cycles were defined from a small segment of the corresponding LCF cycle, as shown in Fig. 3.39. The stress levels for each cycle were selected to provide a substantial difference in fatigue lives between the HCF and LCF cycles. Specifically, stress levels for the LCF cycles corresponded to the previous tests that resulted in fatigue lives in the range of 40,000 to 60,000 cycles. Stress levels for the HCF cycles were selected based on model predictions to result in fatigue lives on the order of 10^8 cycles.

Two sets of box mission tests and one set of check mission tests were run. Box missions 1 and 2 consisted of 1 LCF cycle coupled with 50 HCF cycles and 5 HCF cycles, respectively; the check mission consisted of 1 LCF cycle with 50 HCF cycles. Two tests were run at each condition. The experimental results are shown in Table 3.9.
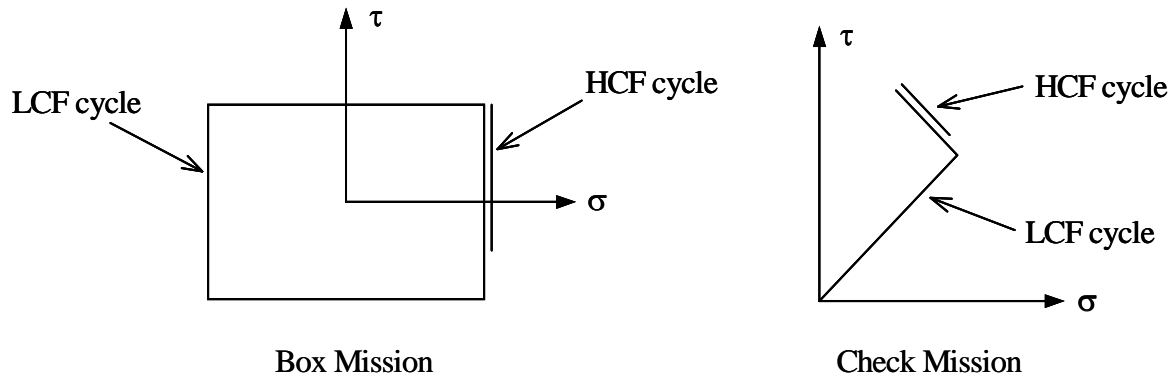
Figure 3.39. Biaxial mission histories.

Table 3.9. Experimental Mission History Results

Cycle/Mission	Box Mission 1 1 LCF/50 HCF	Box Mission 2 1 LCF/5 HCF	Check Mission 1 LCF/50 HCF
Average LCF Life	65,900	65,900	43,700
Average Mission Life	20,400	44,100	47,200

It is evident from Table 3.9 that there is a strong interaction effect between LCF and HCF cycles in the box mission histories, but not in the check mission. None of the multiaxial models were successful at predicting the interaction effects in the box mission using a linear cumulative damage rule. However, this is more likely a problem with the linear damage assumption rather than the models themselves. A linear damage assumption predicts essentially no difference between the LCF and mission lives for all three missions. Experimentally, a factor of three reduction in fatigue life was found in the box history when 50 HCF cycles were included, and a noticeable decrease in life was observed when just 5 HCF cycles were added. This indicates a highly nonlinear rate of damage accumulation in Ti-6Al-4V when LCF and HCF cycles are combined. However, the rate of damage accumulation is dependent on load path, as the check mission did exhibit results consistent with a linear damage assumption. More details on the multiaxial modeling of the mission histories are included in Appendix D.

57

3.2.3 Multiaxial Modeling of Ti-6Al-4V at 500°F

A limited number of uniaxial and biaxial fatigue data points for Ti-6Al-4V at 500°F were also generated for model evaluations. As with the RT evaluations, no uniaxial step-test data were included in this analysis due to the uncertainty associated with those results. Excluding the step-test data, 16 uniaxial data points at R = −1, 0.1, and 0.5 were available. In addition, four biaxial tests were conducted: two proportional tests at R = 0.1 and two non-proportional box-path tests.

Model correlations for both the uniaxial and biaxial 500F data from the SWT, Findley, and FSK critical plane models are shown in Figures 3.40 through 3.42. The solid curve in each figure represents the best fit to the uniaxial data assuming an equation of the form shown in Equation 3.19. In all cases, the model predictions were quite poor for this set of data. The uniaxial data appear to exhibit an increasing slope with increasing life, which is not well accounted for by any of the models. A complication with this data set was the lack of measured strain values from the uniaxial tests. As a result, all strains were estimated from elastic relations, which likely introduced significant errors in the analysis.
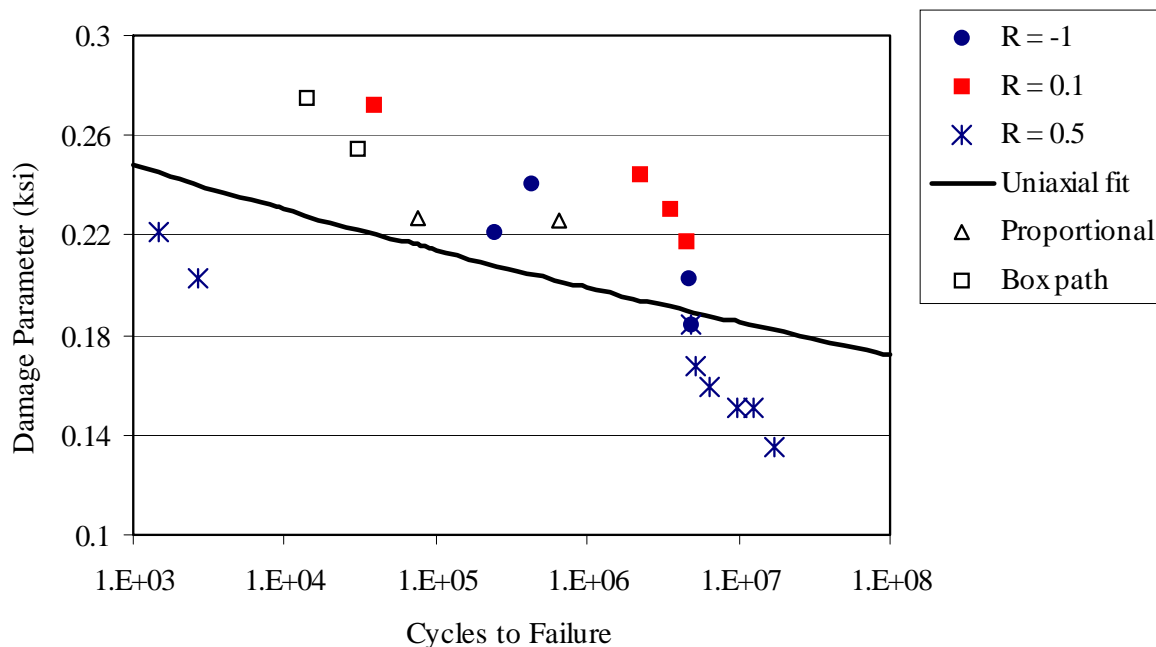
Figure 3.40. SWT model applied to uniaxial and biaxial Ti-6Al-4V 500°F data.
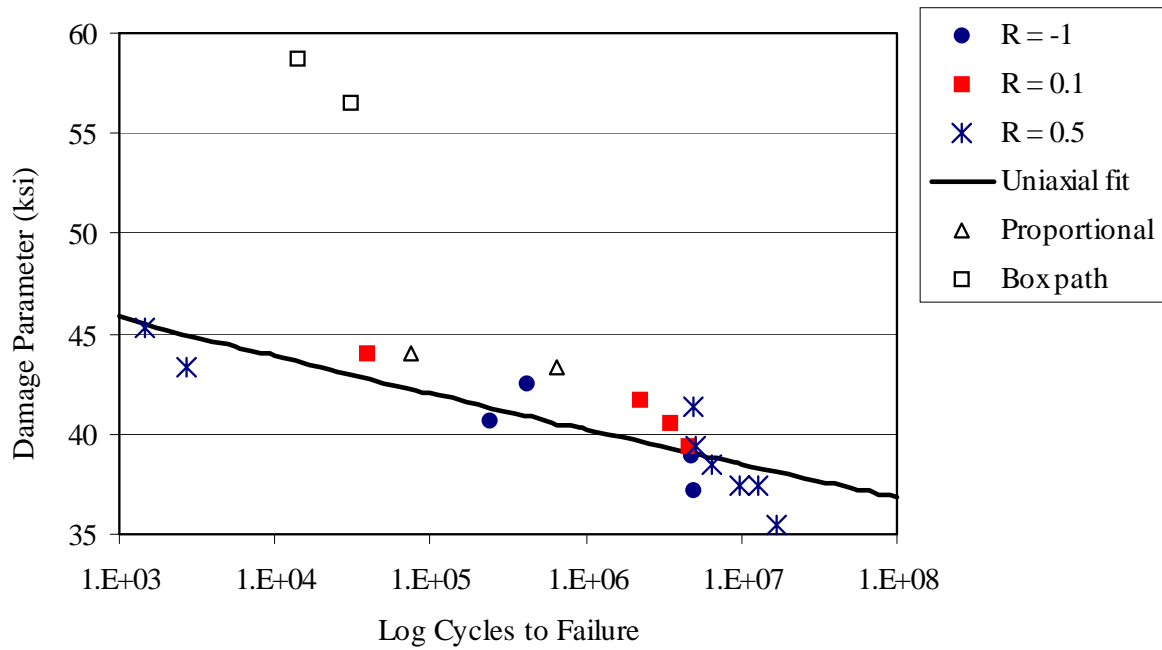
Figure 3.41. Findley model applied to uniaxial and biaxial Ti-6Al-4V 500°F data.
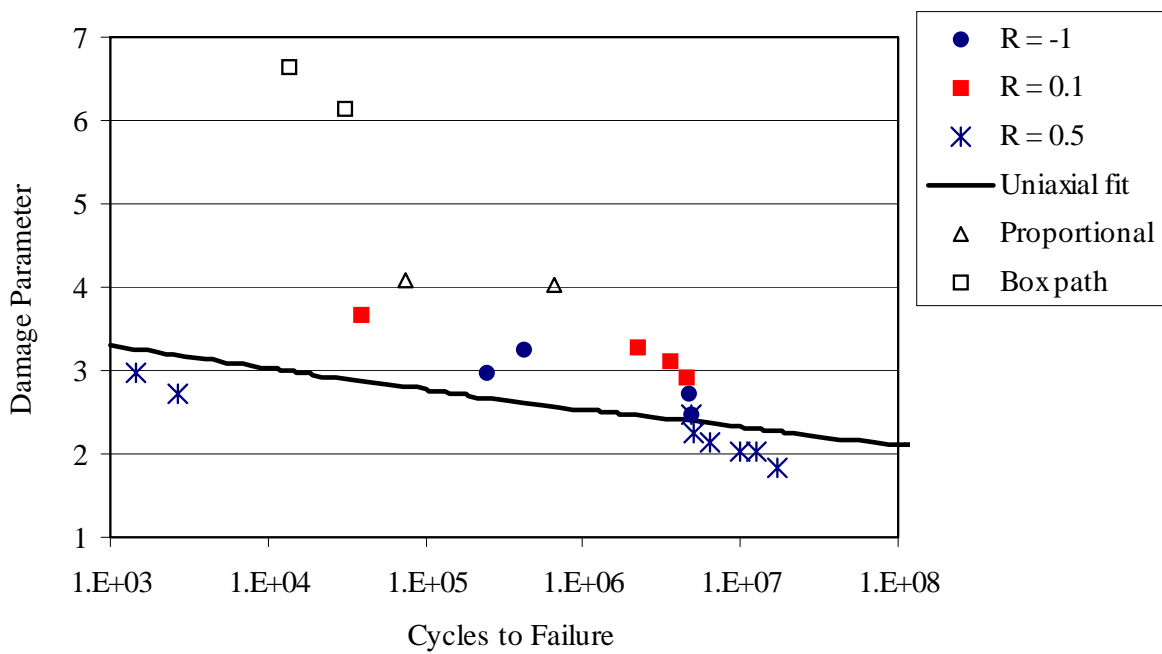
Figure 3.42. FSK model applied to uniaxial and biaxial Ti-6Al-4V 500°F data.

59

Despite the reduced confidence in the model predictions for the 500°F data, it is still worthwhile to note that the Findley and FSK models were again highly conservative in their damage predictions for the box path. In this case, the SWT model provided better predictions for the biaxial data. However, more accurate strain calculations would be required before greater confidence could be placed in these analyses.

3.2.4   Multiaxial Modeling of Ti-17 at Room Temperature

The three critical-plane fatigue models were also evaluated using a set of uniaxial and biaxial fatigue data for Ti-17 at room temperature. As before, no step data were included in the evaluations. The uniaxial set consisted of strain-control (LCF) and stress-control (HCF) data at stress ratios of R = −1, 0.1, 0.5, and 0.8. The biaxial set included torsion data (R = −1, 0.1), proportional tension-torsion data (R = 0), and non-proportional check path data. The results of the model correlations are shown in Figures 3.43 through 3.45. The curves shown in each plot represent a best fit to the uniaxial data, assuming an equation of the form shown in Equation 3.19.
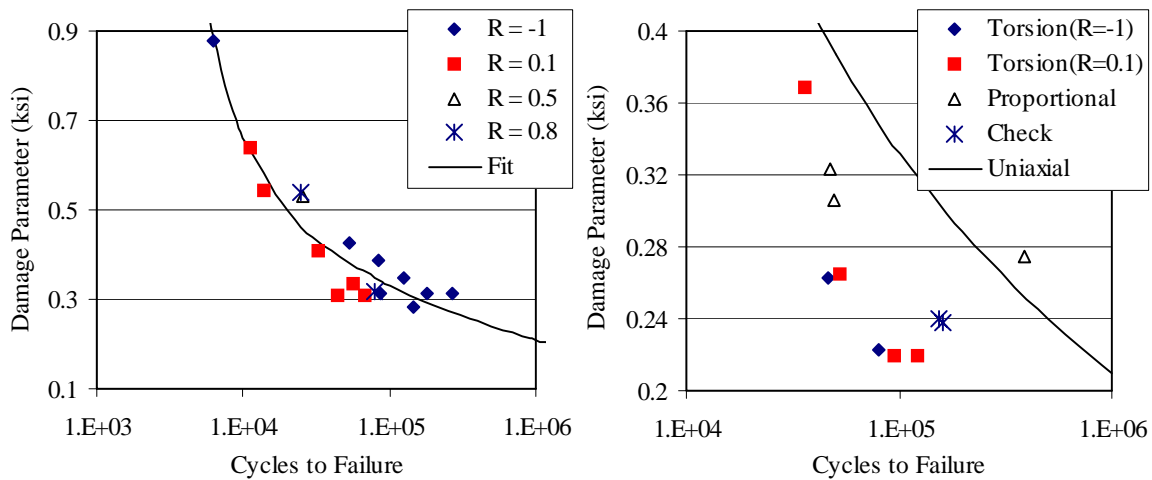
Figure 3.43. SWT model applied to uniaxial and biaxial Ti-17 RT data.
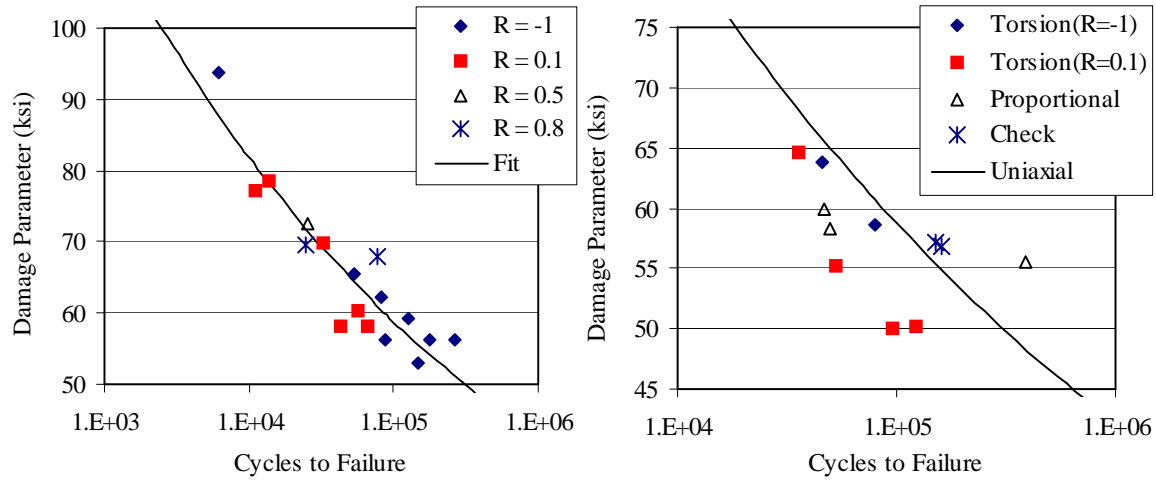
Figure 3.44. Findley model applied to uniaxial and biaxial Ti-17 RT data.
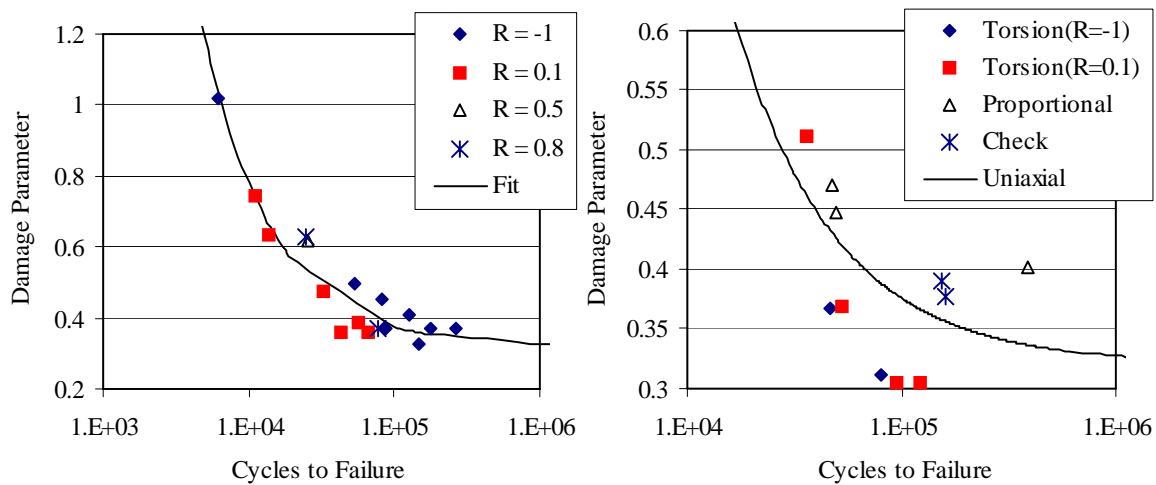
Figure 3.45. FSK model applied to uniaxial and biaxial Ti-17 RT data.

As with the Ti-6Al-4V RT data, all three models adequately collapsed the variable mean stress uniaxial data, although there appears to be a little more separation of the data by stress ratio, most noticeably between R = −1 and R = 0.1 data at higher lives. When applied to the biaxial data, the SWT critical plane model was again generally non-conservative, indicating that fatigue crack initiation may be driven primarily by shear stresses in Ti-17. The Findley and FSK models produced better overall damage predictions for the biaxial data, although both models tended to underestimate the fatigue damage caused by the torsion tests.

61

3.2.5   Summary and Conclusions

The majority of the multiaxial fatigue models considered in this study were reasonably successful at predicting mean stress effects in Ti-6Al-4V and Ti-17 under uniaxial loading conditions. However, significant differences were noted between models in their ability to predict multiaxial fatigue lives or damage. Of the equivalent-stress models, only the modified Manson-McKnight model provided reasonably good multiaxial predictions. The Findley critical-plane model provided the best overall correlations with experimental data for multiaxial loadings; however, the definition of the maximum normal stress in the cycle for this model is ambiguous and may be dependent on the load path. Since the normal (tensile) stress based critical plane models were all highly non-conservative in their multiaxial predictions, it appears that fatigue crack development in these titanium alloys is driven primarily by cyclic shear stresses.

The limited data pertaining to LCF/HCF interactions in Ti-6Al-4V indicate that small (HCF) cycles can cause significantly more damage than predicted by a linear cumulative damage rule, but the effect of the HCF cycles on the LCF mission life is dependent on the load path. When used in conjunction with a linear damage rule, none of the multiaxial models were successful at predicting the observed experimental behavior. However, this is likely due in large part to the assumption of linear damage accumulation, and may be improved with a nonlinear damage model. In any case, it is clear that multiaxial mission-life prediction must take into account the nuances of the load path and the relationships between the LCF and HCF cycles. This poses severe challenges with the use of equivalent-stress models, in which the multiaxiality of the stress state is washed out in the calculation of an equivalent scalar parameter. With critical plane models, however, the comparison of LCF and HCF damage on specific planes may provide better insight and flexibility in modeling the load-path dependence of LCF/HCF interactions.

3.3   NOTCH EFFECTS

3.3.1   Notched Specimen Behavior and Modeling

The occurrence of foreign object damage (FOD) in fan and compressor blades, as well as fretting-fatigue at blade-to-disc attachments, can significantly reduce the high cycle

fatigue (HCF) resistance of advanced turbine engines. In both cases, the reduction in fatigue resistance is due to highly concentrated stresses near the surface of the component. The steep stress gradients that are often associated with such stress concentrations represent technical challenges for predicting HCF resistance. Moreover, the extent of the stress concentration is strongly dependent on the geometry of the notch, or contact condition, and these can vary significantly in service.

The prediction of the fatigue life under given loading conditions or the fatigue limit loading that will last forever (equivalent to an endurance stress) in a specimen or component which contains a notch or stress concentration requires a number of steps and obtaining information on the behavior and fatigue characteristics of the material. To be able to describe the behavior of a notched specimen or component, the first thing that is needed is a stress analysis capability that considers both elastic and elastic-plastic behavior where applicable. It has been demonstrated over the years that the maximum or hot spot stress at a notch is insufficient to predict the fatigue life or fatigue limit stress from smooth bar data. The difference is usually associated with the existence of a stress gradient, which, in turn, results in a smaller area subjected to high stresses than in a smooth bar. In addition, if the local peak stresses are beyond yield, stresses will be redistributed with cycling, referred to a shakedown, and local stress ratios may vary from the applied stress ratio.

Once the stresses in the vicinity of a notch are known, both crack initiation and subsequent propagation have to be addressed. Crack initiation models can be either scalar in nature or orientation dependent as in what are described as critical plane models. Both types are described in this report. The presence of severe stress gradients require modifications to conventional stress or strain based models that rely on maximum values at a point. The uses of such models are referred to as total life methods.

Models based on crack growth, specifically addressing whether stress intensities are and remain above the threshold stress intensity, are another approach to determining the integrity of the contact region. These are referred to as fracture mechanics methods. In both the fracture mechanics and total life approaches, the crack length to which a crack initiates as well as the initial crack length from which propagation begins are critical aspects of the life prediction methodology.

This section describes experimental and analytical efforts for overcoming the challenges associated with notch fatigue, including 1) critical fatigue experiments to define the functional dependence of notch threshold stresses on notch depth, notch root radii, and applied stress ratio; 2) development and validation of efficient engineering methods for estimating the relaxation and redistribution of stresses (shakedown) due to plastic deformation at notches; and 3) development and validation of engineering methods based on both crack initiation and crack growth/arrest concepts for predicting the fatigue threshold stresses at notches of varying acuity under both axial loading and bending. Procedures for consolidation of data at different values of R while accounting for stress gradients are developed. Results are obtained for both the Ti-6Al-4V and Ti-17 materials at room and elevated temperatures.

3.3.1.1 Fatigue of Notched Specimens

A. *Notched Specimen Behavior*

Notch specimens were used to establish fatigue behavior for stress concentrations. The specimen load axis was oriented along the blisk radial direction. Notch specimens were low stress ground and polished with a vacuum anneal for eight hours at 1130°F. The dimensions for the double edge V-notch specimen geometry is shown schematically in Figure 3.46.

The dimensions for the double edge U-notch specimen geometry are shown schematically in Figure 3.47. The specimen simulative of airfoil leading edge geometries is shown in Figure 3.48. The specimen was tested under 4-point bending to simulate airfoil leading edge stress gradients. The loading fixture and specimen alignment was checked with strain gages for an un-notched blunt tip specimen. The strain gage locations, neutral axis, and moment of inertia are given in Figure 3.49. The strain gage results at the peak stress locations (gages 1,2,4,6) compare very favorably to finite element predictions (Figure 3.50).

The blunt tip leading edge geometry was used to assess the fatigue capability of small notches. The machined notches were ~0.010 inches deep with a 0.0044 inch root radii. A representative small-machined notch geometry in the bend specimen is shown in Figure 3.51. Stresses were obtained for each notch test with 3D elastic and elastic-plastic finite element analysis using ANSYS at the interpolated failure loads for each specimen. Step tests

64

V-Notch Double Edge Notch Specimen

IANGLE
(90º)

NOTCH
(0.047 in.)

WIDTH
(0.236 in.)

THICK (Thickness)
(0.142 in.)

RADROOT
(0.021 in.)

LENGTH = 3.0 *WIDTH
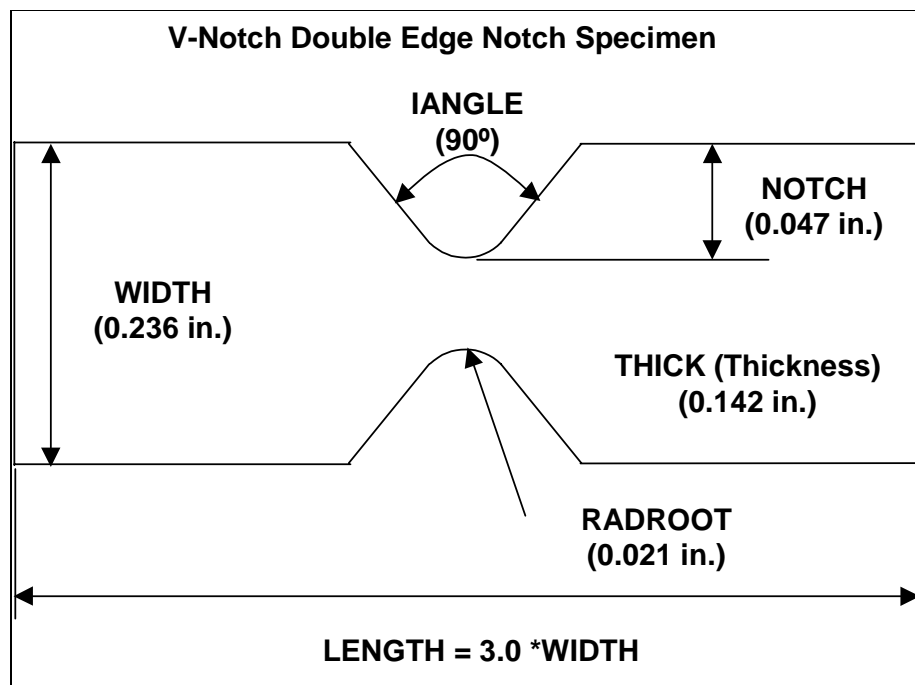
Figure 3.46 Double edge V-notch geometry.

Circular Double Edge Notch Specimen

RADIUS
(0.047 in.)

WIDTH
(0.236 in.)

THICK (Thickness)
(0.142 in.)

LENGTH = 3.0 *WIDTH
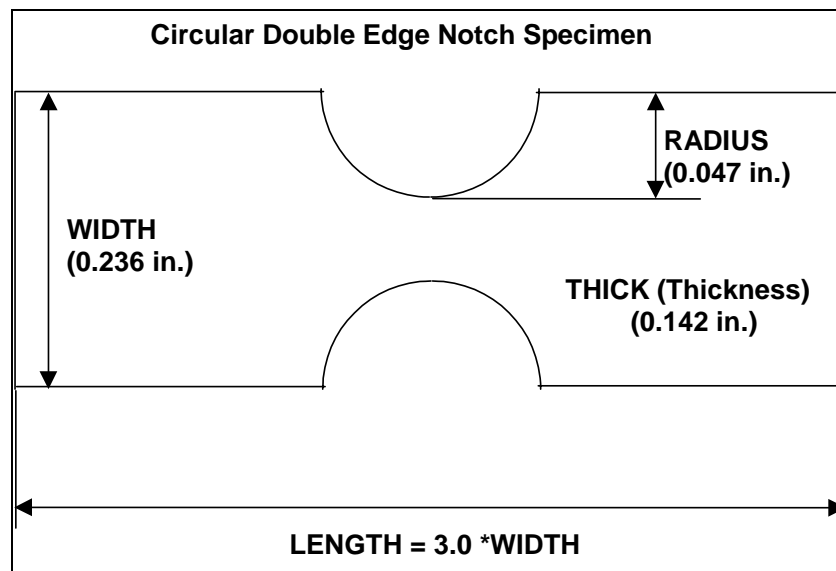
Figure 3.47. Double edge U-notch geometry.

FOUR POINT BENDING SPECIMEN

LENGTH
(6.00 in.)

L1
(1.0 in.)

HEIGHT
(0.2 in.)

WIDTH
(0.6 in.)

L2
(2.0 in.)

SHARP TIP DETAIL

TIPLENG
(0.25 in.)

RAD
0.014 (IN.)

THKROOT
(0.032 in.)

RADTIP
0.007 (IN.)

BLUNT TIP DETAIL

TIPLENG
(0.25 in.)

RAD
0.014 (IN.)

THKROOT
(0.090 in.)

RADTIP
0.014 (IN.)
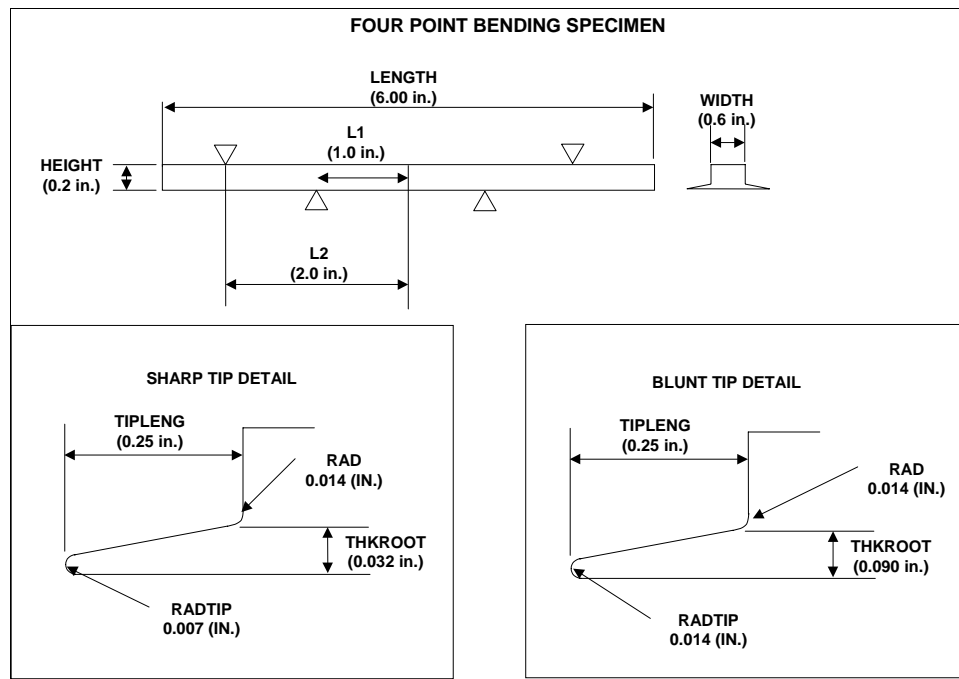
Figure 3.48. Bend bar simulating sharp and blunt airfoil leading edge geometries.

Bending Specimen Geometric Values		
	Sharp Tip	**Blunt Tip**
Area (in^2)	0.1317	0.1497
Moment of Inertia (in^4)	0.4821E-3	0.5205E-3
CBOT (in.)	0.0923	0.0868
CTOP (in.)	0.1077	0.1132

gage 1

CTOP

Centroid

Bending Axis

gage 5

gage 3

CBOT

gage 6

gage 2

gage 4
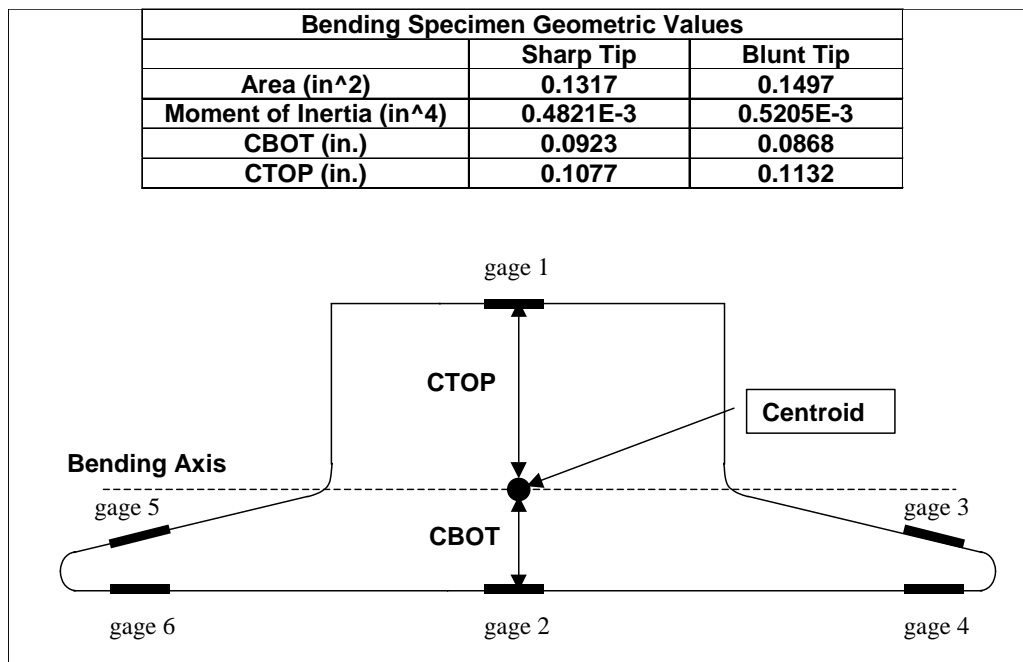
Figure 3.49. Ti17 bend specimen parameters and strain gage locations.
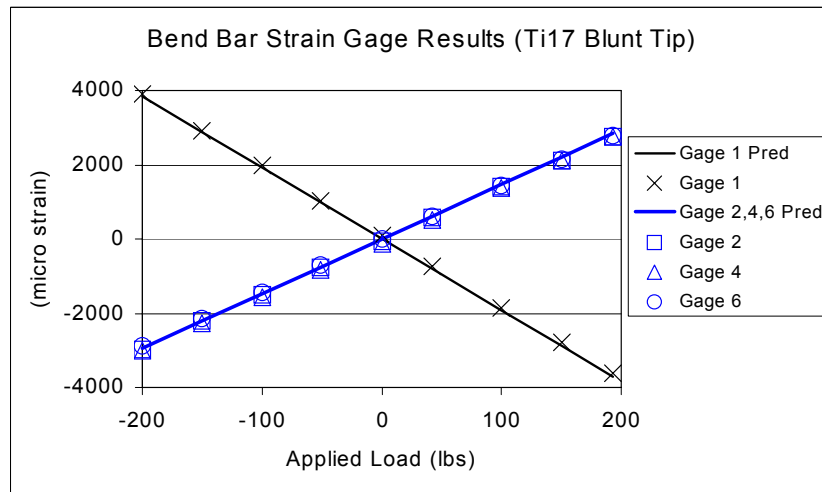
Figure 3.50. Strain gage results and predictions for the bend bar geometry.

were used for the notch methods given few single load notch tests were available in the program. Nominal dimensions were used for the double edge V-notch and U-notch geometries. Nominal specimen dimensions with actual measured notch depths were used for the small-machined notches in the bend bar geometries.
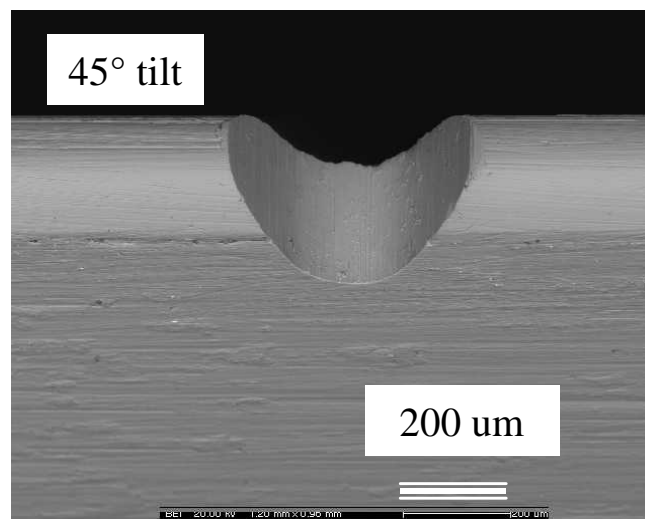
Figure 3.51. Small-machined notches in the Ti-17 sharp tip bend bar geometry

The critical specimen location was selected from the ANSYS model. σequiv with the modified Manson-McKnight parameter is calculated for the critical node stresses from the maximum and minimum load. The modified Manson-McKnight parameter is defined in the PRDA program final report [1]. The notch tests with σequiv at the peak stress

67

locations and the baseline fatigue curve for Ti-17 is shown in Figure 3.52. The notch benefit is small for the conventional notch geometries (double edge V-notch and U-notch geometries). The peak local stress approach with the smooth specimen curve is conservative for the small notch tests (notch test results above the smooth specimen curve). The small notches are of the size most relevant to FOD applications. Notch methods will be based on the small-machined notch tests.
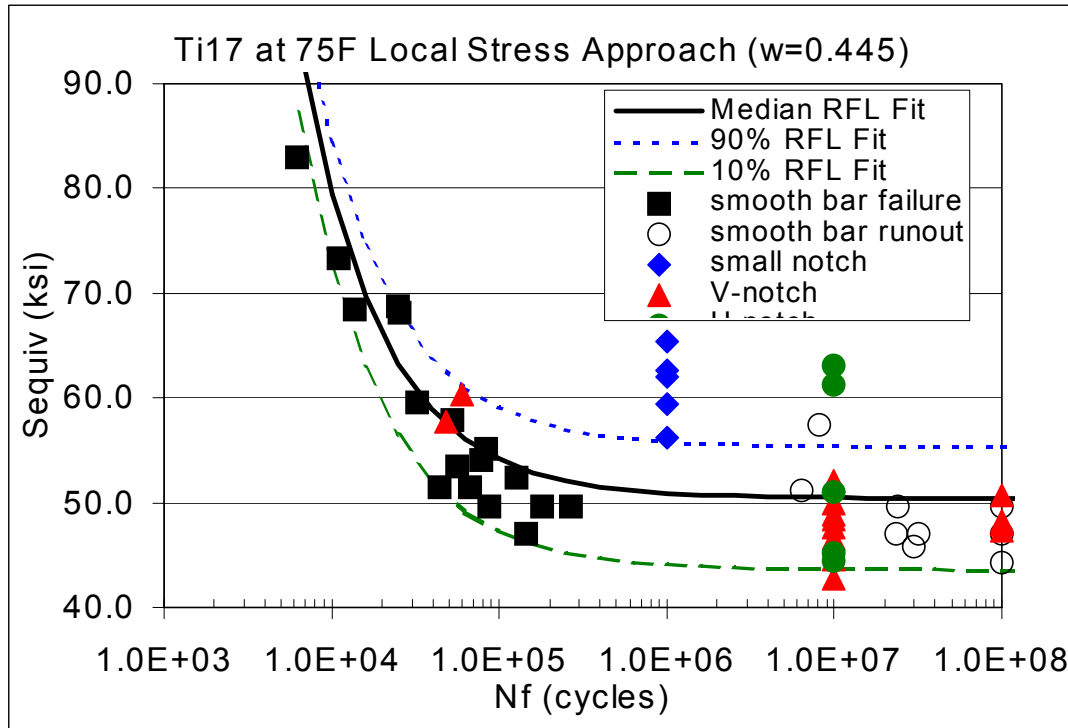
Figure 3.52. Smooth and notched bar fatigue results with the peak local stress approach.

B.   *Notch Life Methods*

A feature stress (Fs) and a q-k_f approach were evaluated to correlate the small notch behavior. Both approaches address the conservative nature of the local stress life models with smooth specimen fatigue curves for notch life prediction. The Fs approach has been outlined in the PRDA program. This approach uses the surface stress weighting term given as:

$$Fs = \sum_{i=1}^{n} \left[-\left(\frac{\sigma_i}{\sigma_{max}} \right)^{\alpha} \Delta A_i \right]$$ (3.20)

where, Fs is the stressed area weighting term, σ_{max} is the maximum principal stress on the surface for the maximum load case, σ_i is the first principal stress of all elemental faces on the surface, ΔA_i is the area of all elemental faces on the surface, and α is a material constant. The local notch stress is adjusted with Fs as shown in Equation 3.21 prior to using the smooth specimen life curve.

$$\sigma_{equiv,\, Fs\, adj} = \sigma_{equiv,\, peak} \left(\frac{Fs_{notch}}{Fs_{ref}} \right)^{1/\alpha}$$ (3.21)

where, $\sigma_{equiv,peak}$ is the local concentrated elastic-plastic notch stress, Fs_{notch} is the feature stress parameter for the notch of interest, Fs_{ref} is the feature stress parameter for the baseline smooth bar geometry (0.161 in^2 for the HCF smooth specimen geometry in Figure 3.52), and $\sigma_{equiv,Fsadj}$ is the peak notch stress adjusted for Fs for use with smooth bar fatigue curves. The material constant alpha is selected that correlates notch and smooth specimen behavior.

The second notch method evaluated is a q-k_f approach. This approach is taken from the Peterson handbook as given with Equations 3.22 through 3.24.

$$\sigma_{equiv,\, q\, adj} = Kf \left(\sigma_{equiv,\, unnotched} \right)$$ (3.22)

$$Kf = 1 + q(Kt - 1)$$ (3.23)

$$q = \frac{1}{\left(1 + \dfrac{a}{\rho} \right)}$$ (3.24)

where, $\sigma_{equiv,unnotched}$ is calculated at the critical location without the notch present, k_t=notch concentrated stress/unnotched stress, ρ is the notch root radius, and 'a' is a material constant. k_t can be difficult to define for 3D component geometries, but the approach is well suited to

small FOD or machined notches where the local stress can be referenced to the stresses in the unnotched geometry.

The correlation of small notch fatigue tests with the Fs and q approaches are shown in Figure 3.53. The correlation was produced with α=60 for the Fs approach and a=1.8 mils for the q-k_f approach. The correlation is similar for both approaches. The ability of these approaches to predict the HCF capability of specimens with simulated foreign object damage will be explored in later sections.
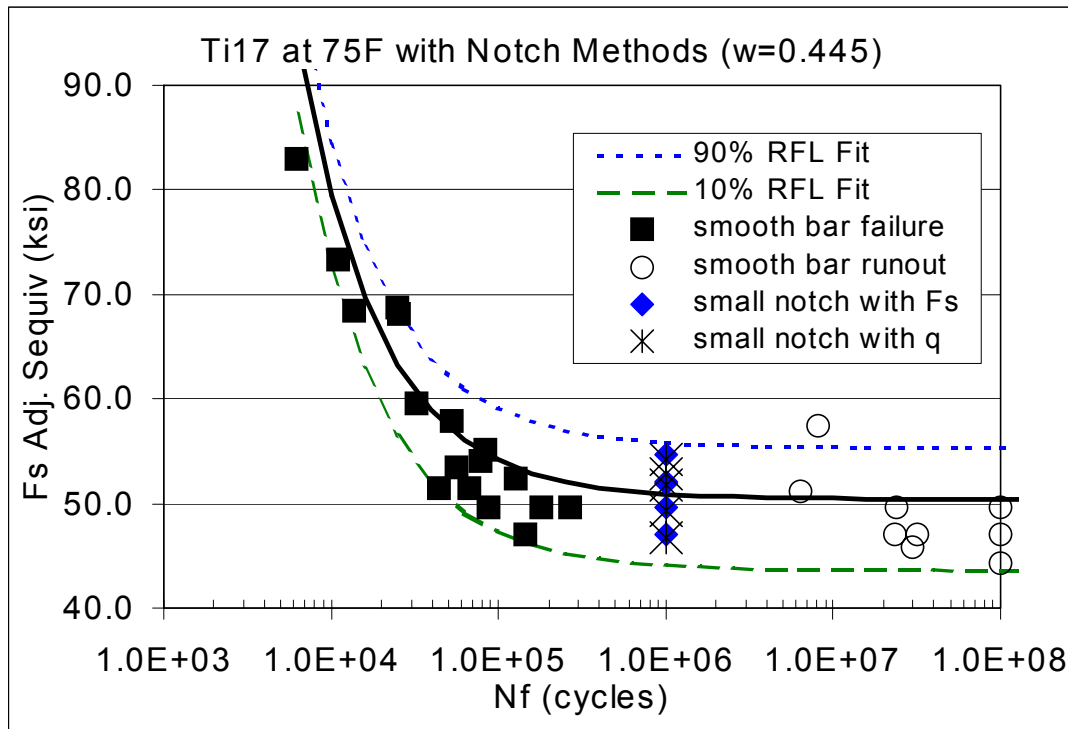
Figure 3.53. Small notch correlation with Fs and q-k_f approaches as compared to smooth specimen fatigue curves.

3.3.2   Fatigue of Small Sharp Notches

This section summarizes experiments designed to assess the HCF resistance of small, sharp notches typical of those encountered in service-induced FOD [1,6]. The primary objective of generating these results was to provide data to assess the viability of various fatigue models for predicting HCF notch behavior. Consequently, care was taken to produce these notches without residual machining stresses, and where possible with surface finishes

identical to those on smooth specimens used to characterize the materials' basic fatigue resistance [1]. In this way, the predictive models can be assessed with minimal confounding effects. The critical issue for the models to address is how to properly account for the steep stress gradients that exist at these sharp notches. The magnitude of the local notch stresses, and the steepness of the stress gradient were varied by employing test specimens with a wide range of notch depths and notch root radii, respectively. In addition to their relevance to FOD, the experimental data and model verification are also relevant to attachment fatigue where steep stress gradients can occur at the high stresses generated at the edge-of-contact region.

3.3.2.1 Specimen and Notch Preparation

All tests were performed using the double edge notched (DEN) specimens shown in Figure 3.54. This specimen was optimized for use with SwRI's kHz fatigue test machines. A variety of notch configurations were used to facilitate the production of notches having varying notch depths (b) and notch root radii (ρ), as shown in Figure 3.55. Notch Type 1 was used to produce sharper and shallower notches, while Notch Types 2 and 3 were used to produce deeper and blunter notches. Although the notch flank angle varied for these different types of notches, this factor had no significant influence on the test results, in part due to the fact that when producing the deep, sharp notches the dimension b_1 was always maintained greater than ρ_2.

One of the primary challenges in preparing these specimens was to machine the sharp notches in a reproducible, residual stress-free manner, with the desired surface finish. To achieve these conditions, the following three-step procedure was developed: 1) wire electro-discharge machining (EDM) to reliably produce small, sharp notches; 2) stress relieve at 1300°F for one hour to eliminate both bulk and notch residual stresses; 3) chem mil to remove possible EDM recast layer and associated embrittlement, as well as to produce a surface finish matching that previously used to generate the smooth bar S-N data that are used as input to the predictive models [1].
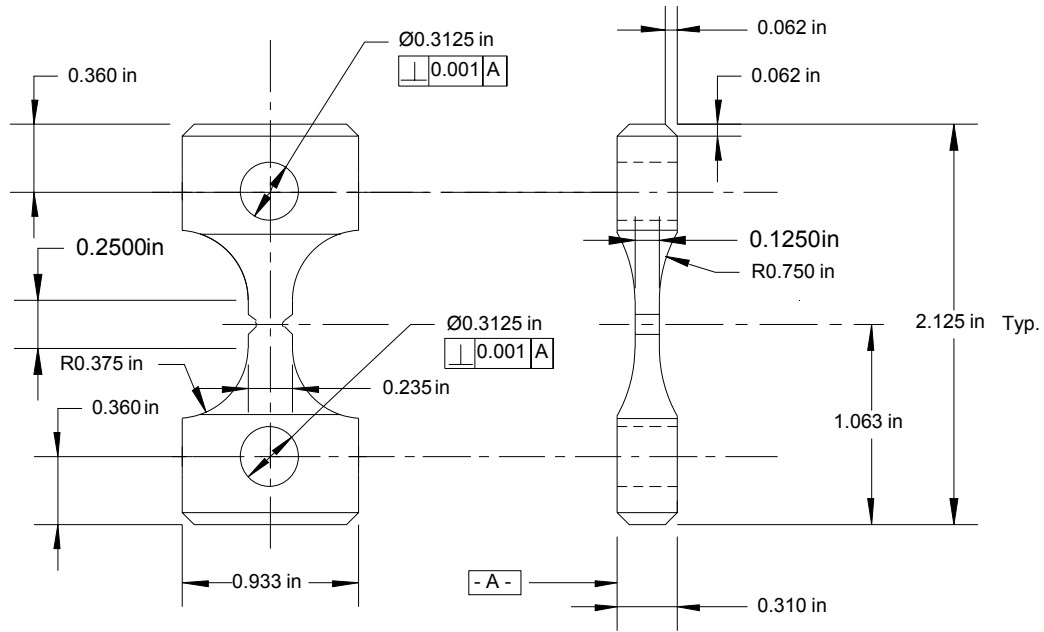
Figure 3.54. Double-edge-notch fatigue specimen used for small, sharp notch testing at 1000 Hz.

Notch Type 1: $b_2 = 0$
Notch Type 2: $b_1 = > 2\rho_2$
Notch Type 3: $b_1 = 0$
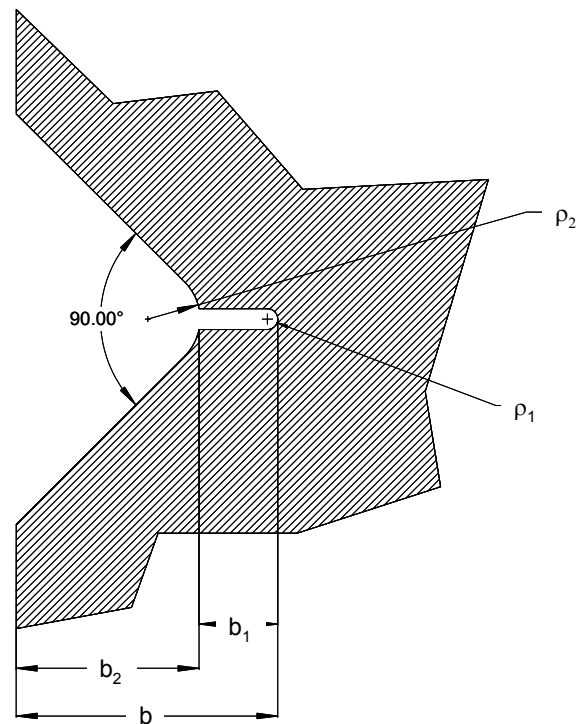
Figure 3.55. Different notch types employed to facilitate machining of notches with a wide range of depths and radii.

Cross sectional views of typical notches produced by this three-step process are shown in Figure 3.56. Further metallographic sections of the notches indicate that the chem milling, which typically removed 0.0015 in. to 0.002 in. of material, was sufficient to eliminate the EDM recast layer as shown in Figure 3.57.

Figure 3.58 shows several SEM images of the EDM and chem milled notch surfaces. The top two micrographs illustrate the typical surface produced by EDM in Step 1 of the above notch preparation for root radii of 4 and 15 mils; note the irregular protrusions characteristic of melting and solidification in the recast layer. This surface condition was subsequently removed by chem milling so as to preclude premature crack initiation under HCF loading. The bottom two micrographs represent nominally similar notches as in the top two micrographs, but after chem milling. The characteristic alpha/beta microstructure of Ti-6Al-4V confirms that the recast layer has been eliminated by removal of 1.0-1.5 mils of material from the original notch surface using chem milling in Step 3 of notch preparation.
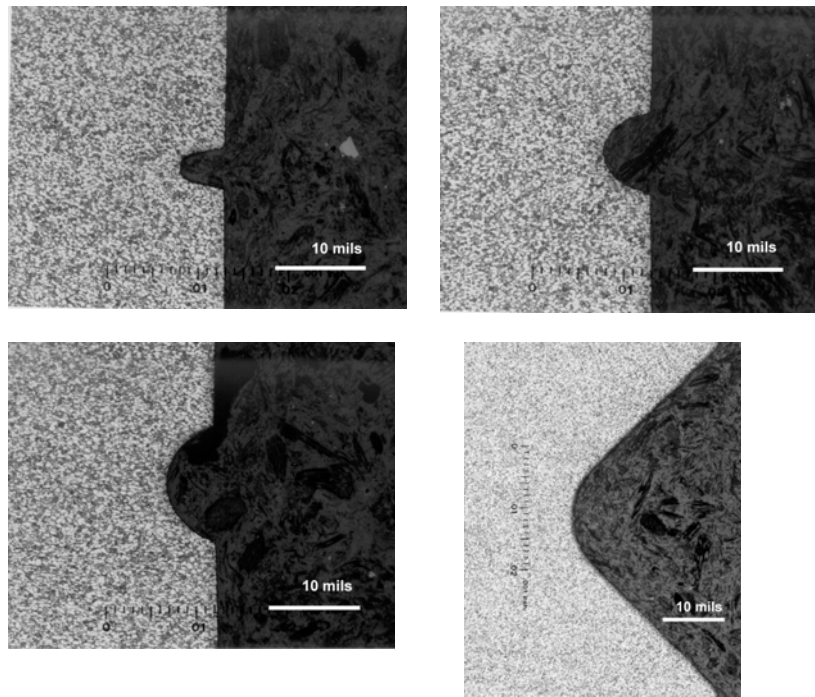
Figure 3.56. Etched cross-sections of typical notches showing root radii of 2.5, 4, 6, and 21 mils that were machined using EDM plus chem milling.

73
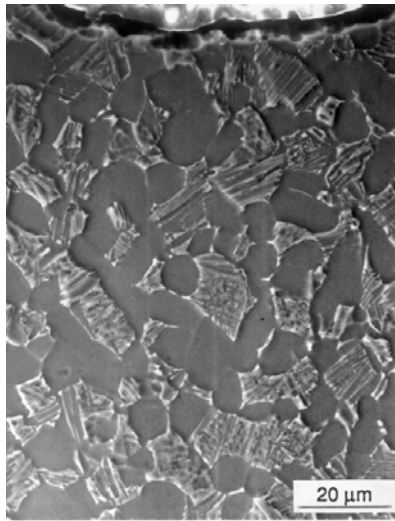
After EDM

After EDM + Chem Mill
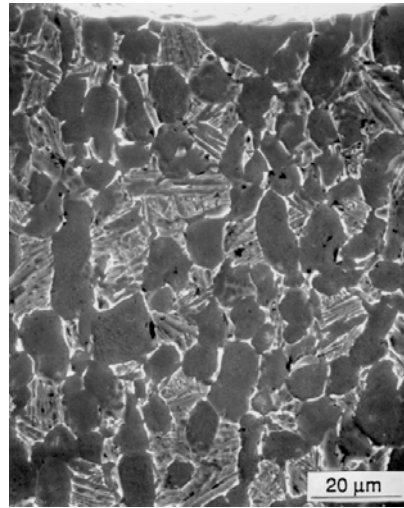
Figure 3.57. SEM micrographs of sectioned and etched surfaces below
notches after EDM versus after EDM plus chem milling; note
lack of recast layer at the notch surfaces near top of photo on right.
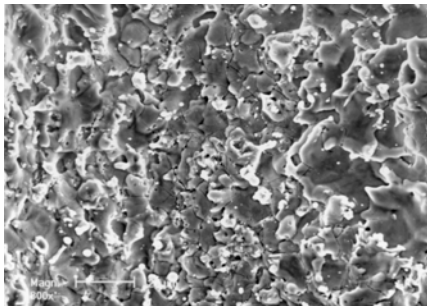
Unnotched
Fatigue

$\rho = 0.004$ in.
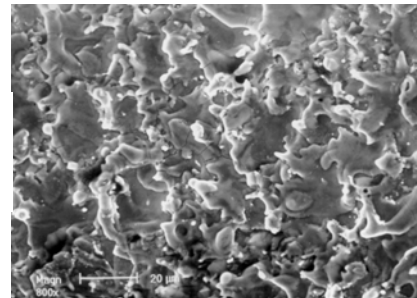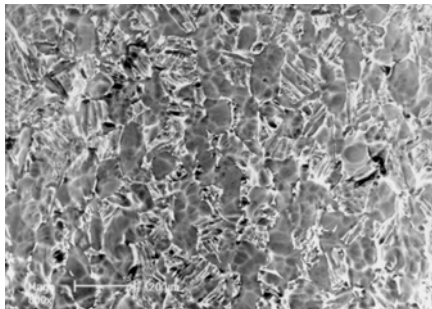
$\rho = 0.015$ in.

After
Chem
Milling

$\rho = 0.0065$ in.
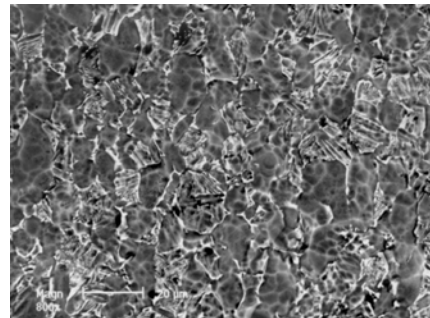
$\rho = 0.015$ in.

Figure 3.58. Comparison of typical surface morphology of notch surfaces after EDM and
chem milling.

The use of chem milling limited the sharpness of the notches to 3.8 mils or larger. Since notches sharper than this were crucial to test various aspects of the notch models, as well as to accurately represent the geometry of service–induced FOD, selected specimens were prepared and tested without the final chem milling step; these specimens had root radii of 1.98 mils, the sharpest used in the current test program.

3.3.2.2 Notch Test Procedure

For maximum testing efficiency, all notch testing was conducted using a step-loading procedure that involved 5% increases in applied stress after each 10^7 cycles until specimen failure occurred. Since Ti-alloys do not appear to exhibit coaxing, this test procedure has been demonstrated to give results that agree with those from testing multiple specimens to failure at a fixed stress range [7]. All experiments were conducted in SwRI's 1000 Hz resonance test machine. As will be demonstrated below, these results were in good agreement with previously generated data on these same materials obtained at 60 Hz [1].

Fracture mechanics based model predictions in Section 3.3.8 indicate the potential importance of both notch radii and notch depth on the threshold stress. Thus, experiments were designed to cover a wide range of notch geometries with radii ranging from nominally 0.002 inches to 0.021 inches and depths ranging from 0.009 inches to 0.050 inches. These notch dimensions are representative of those observed in several previous surveys of service-induced FOD [1,6].

3.3.2.3 Small Notch Test Results

Because of the three-step machining process described above, actual notch dimensions differed somewhat from the target dimensions. Table 3.10 summarizes the actual notch dimensions achieved, as well as the corresponding elastic stress concentration factors, k_t, computed from Peterson [8].

Table 3.10.   Ti-6Al-4V Small Sharp Notched Fatigue Test Results

Test Series	Spec. ID	b in.	in.	kt*	Test Steps	Total Cycles to Failure	Threshold Stress, ksi*	Notch Preparation	Notch Type
1	138-4	0.0470	0.0210	4.16	3	27,725,956	14.7	EDM+CM	3
1	138-6	0.0470	0.0210	4.16	3	23,813,460	14.5	EDM+CM	3
1	138-7	0.0470	0.0210	4.16	3	20,390,221	14.2	EDM+CM	3
1	153-2	0.0470	0.0210	4.16	4	30,275,938	14.8	LSG+CM	3
1	153-3	0.0470	0.0210	4.16	5	41,132,047	15.5	LSG+CM	3
1	153-4	0.0470	0.0210	4.16	4	37,882,602	15.4	LSG+CM	3
2	153-13	0.0469	0.00197	11.8	9	82,843,655	4.9	EDM	2
2	153-33	0.0500	0.0038	9.00	7	68,634,405	5.9	EDM+CM	2
2	153-14	0.0475	0.0047	7.95	4	31,927,301	5.6	EDM+CM	2
2	153-43	0.0495	0.0064	7.08	3	29,236,240	6.0	EDM+CM	1
2	153-44	0.0484	0.0064	6.99	9	90,519,234	7.9	EDM+CM	1
2	153-9	0.0240	0.00197	8.61	10	91,688,391	7.3	EDM	2
2	153-31	0.0244	0.0038	6.46	10	95,274,059	9.8	EDM+CM	2
2	153-42	0.0236	0.0060	5.23	9	81,216,268	11.1	EDM+CM	1
2	153-39	0.0089	0.0064	3.43	8	70,904,954	16.3	EDM+CM	1

*Threshold values expressed as nominal applied (gross cross sectional) stress ranges.

The notch threshold stress ranges, ΔS_{th}, (at 10^7 cycles) measured in the step tests are also given along with the total number of steps and total cycles to failure for each specimen. For consistency with the fracture mechanics calculations of Section 3.3.8, the threshold stress ranges and k_t values are expressed in terms of gross-section stress. As indicated in the first column of Table 3.10, two series of experiments were performed. Series 1 experiments were designed to assess the influence of the three-step notch preparation procedure on the measured threshold stress, while the Series 2 experiments were designed to assess the influence of notch depth (b) and notch root radii (ρ) on the measured threshold stress.

The Series 1 experiments used the same relatively mild (Type 3) notch geometry tested at Metcut at 60 Hz earlier in the HCF Program [1]. Since low stress grinding can be used to prepare these mild notches, a comparison of notch preparation procedures involving low stress grinding versus chem milling was possible. Comparison of the present results at 1000 Hz, with those previously generated at 60 Hz also enabled an evaluation of the potential influence of test frequency on the measured results. Results expressed in terms of threshold stress ranges are summarized in Figure 3.59 where three sets of data are compared: 1) 60 Hz

Metcut data on notches prepared by Low Stress Grinding plus Chem Milling (LSG + CM); 2) 1000 Hz SwRI data on notches prepared by LSG + CM; and 3) 1000 Hz SwRI data on notches prepared by Electro-discharge Machining plus Chem Milling (EDM + CM). Good agreement was found among data from the above three cases. On average, the threshold stress range at failure was 14.8 ksi with a standard deviation of ±0.5 (±3.4%). These results confirmed that the EDM step in the three-step notch preparation procedure did not measurably influence the notched fatigue endurance, and that data obtained at 60 Hz and 1000 Hz are not significantly different.

The measured threshold stress ranges from the Series 2 experiments on small, sharp notches of varying geometry are summarized in the bottom portion of Table 3.10. It should be noted that two or three of the small, sharp notch tests just got to monotonic yielding based on the fact that the max stress given by k_t x $\Delta S/(1-R)$ was greater than the assumed yield strength of 124 ksi. However, this small bit of plasticity did not make a significant influence on the WCN predictions.
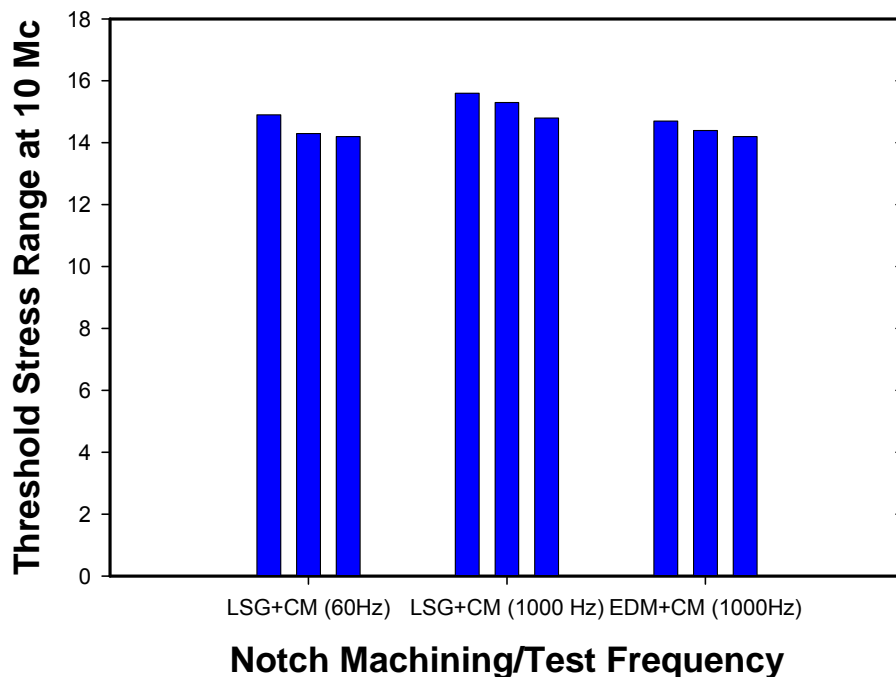
Figure 3.59. Comparison of threshold stress ranges for various notch machining procedures and test frequencies. (All data acquired with notches of depth = 47 mils and radius = 21 mils at 10 million cycles and R=0.5).

These data are also plotted in Figure 3.60, where they are differentiated by the three different notch depths and plotted as a function of k_t, corresponding to the different notch radii. For comparison, the solid curve in this figure corresponds to $\Delta S_{th} = \Delta\sigma_e/ k_t$, where $\Delta\sigma_e$ is the smooth-bar endurance limit at $R = 0.5$ and 10^7 cycles (48.0 ksi). As can be seen the data tend to follow the general shape of curve defined by $\Delta S_{th} = \Delta\sigma_e/ k_t$, although they tend to lie above this curve, particularly for the milder notches ($k_t < 6.5$). Further discussion of the possible reasons for this trend is provided in Section 3.3.7, where measured results are compared to predictions from the worst-case notch model.
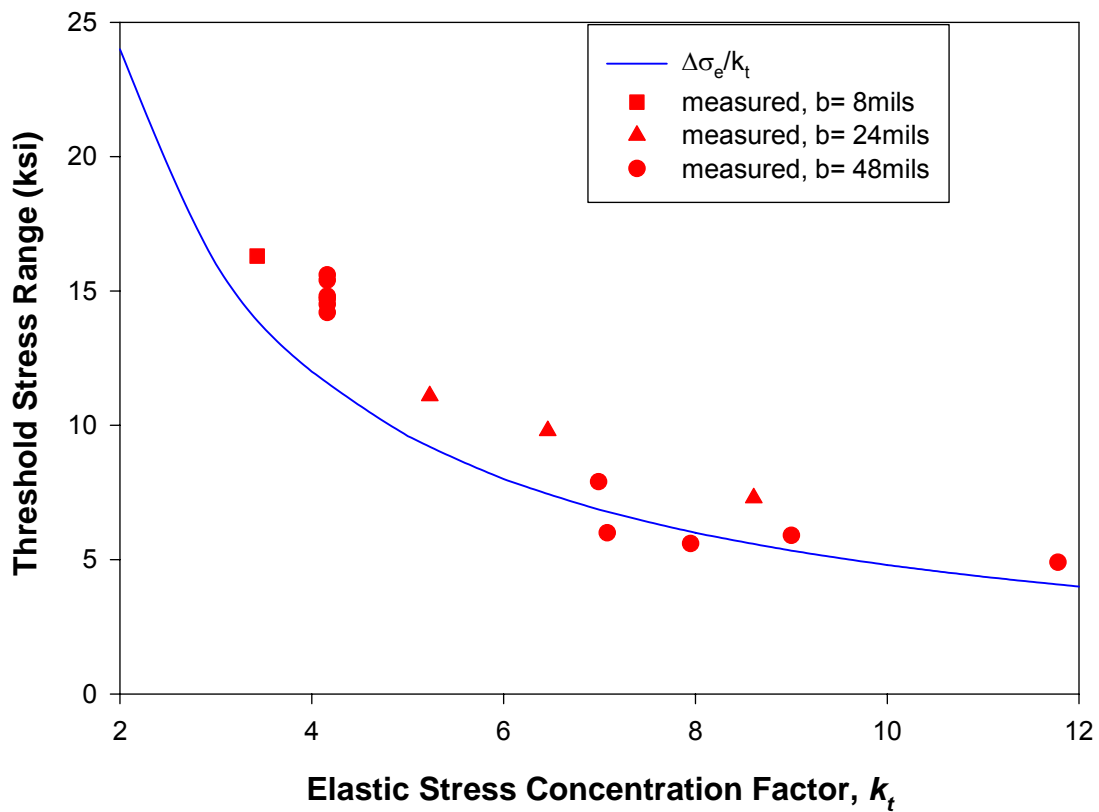
Figure 3.60. Threshold stress ranges for small, sharp notch specimens with varying notch radii and notch depths compared to simple crack initiation criterion given by $\Delta\sigma_e/k_t$. (All data obtained at 10 million cycles and R=0.1, and are expressed as gross stress ranges.)

3.3.2.4   Conclusions

Small, sharp notches can be reliably machined using: EDM + Stress Relief + Chem Mill. Both metallography and fatigue testing confirmed that the EDM recast layer is removed at these notches by the final Chem Mill. The above critical experiments are relevant to both FOD and attachment fatigue where steep stress gradients can occur.

3.3.3   Finite Element Analysis of Notched Components

The ability to assess the effect of a notch or other stress concentration on the fatigue resistance of components is largely dependent on the ability to accurately determine the stress/strain distributions or gradients in the vicinity of the notch. Although elastic stress and strain distributions can be efficiently generated using finite element techniques, localized plastic deformation often occurs in the vicinity of sharp notches and discontinuities. The inclusion of nonlinear elastic-plastic material behavior into finite element models requires significantly greater computational resources (i.e., memory and time), particularly in cases in which cyclic plasticity must be accounted for. Furthermore, the models often require greater attention to details such as mesh refinement, element shape, and nonlinear solution procedures. Due to the added complexities and computational requirements involved in elastic-plastic finite element analysis, approximate methods that can efficiently and accurately model the stress redistribution resulting from plastic deformation near notches are highly desirable. However, such methods must be validated using proven and reliable techniques.

As part of the effort to develop efficient prediction techniques for the HCF resistance of notched components, several elastic-plastic finite element models were generated and solved for a variety of notched components under various loadings. There were two primary objectives in performing these analyses: (1) to provide reliable elastic-plastic stress-strain distributions in notched components subjected to uniaxial and multiaxial loadings, for the purposes of assessing the capabilities and accuracy of the approximate notch analysis methods developed in this program, and (2) to provide the notch stress information required by the crack initiation models for predicting HCF threshold stresses at sharp notches.

All finite element analyses of notched components were conducted using the commercial software ANSYS. A multilinear kinematic hardening rule was used in conjunction with the cyclic stress-strain curve for Ti-6Al-4V at room temperature obtained

from half-life LCF data generated in this program. Applying a Ramberg-Osgood fit to the data, the cyclic stress-strain curve for Ti-6Al-4V can be expressed as

$$\varepsilon = \frac{\sigma}{E} + \left(\frac{\sigma}{K}\right)^{\frac{1}{n}} = \frac{\sigma}{16870} + \left(\frac{\sigma}{124}\right)^{\frac{1}{0.0149}} \tag{3.25}$$

where, σ has units of ksi, and the cyclic yield strength was taken as $\sigma_y = 109.2$ ksi. From this equation, cyclic stress-strain values were calculated and used as input for the models. The stress-strain values are shown in Table 3.11.

Table 3.11. Stress/Strain Values Used in ANSYS Elastic-Plastic Analyses (Kinematic Hardening)

Stress (ksi)	109.22	113.0	114.0	115.5	116.3	116.8	117.2	117.6	118.3	119.7	121.0
Strain (in/in)	.006474	.008659	.01030	.01536	.02043	.02497	.02965	.03551	.04951	.1007	.2004

All models were constructed using 8-node, three-dimensional structural solid elements with extra displacement shapes included for better accuracy. A mesh refinement study was performed on each model to verify that the discretization error was sufficiently small. For each of the elastic-plastic analyses in which cyclic plasticity was anticipated, 10 to 20 cycles were run to ensure the local (notch-root) plastic strains reached a cyclically stable state. This was verified by examining the equivalent plastic strain and the largest principal plastic strain at the root of the notch at the end of each load cycle. In most cases, it was found that negligible changes in these values occurred after the fifth cycle, and the analysis was subsequently terminated after 10 cycles. In a few cases involving large-scale, nonproportional plastic straining, 20 cycles were completed to ensure a stable state had been reached.

For the models being used as validation measures to the approximate notch analysis methods, both elastic and elastic-plastic finite element analyses were conducted. The elastic stress and strain distributions across the notch section were used as inputs to the approximation models, and the resulting elastic-plastic approximate solutions were compared to the elastic-plastic finite element results for accuracy. The specific notch geometries considered in this study and the resulting comparisons and threshold stress estimates are

included in Sections 3.3.7 and 3.3.8. Further details of the finite element notch analyses are included in Appendices F and G.

3.3.4   Approximate Notch Analysis

Notches in structural components subjected to high cycle fatigue can cause significant stress concentrations that often result in localized plastic deformation, leading to premature initiation of fatigue cracks. Therefore, the fatigue strength and durability estimations of notched components require detailed knowledge of the stresses and strains in such regions.

The stress state in the notch tip region is multiaxial in most cases and often involves complex loading such as out of phase torsion and bending loads. Although modern Finite Element commercial software packages make it possible to determine notch tip stresses in elastic and elastic plastic bodies with a high accuracy for short loading histories, such methods are still impractical in the case of long loading histories experienced by turbine engine components subjected to combined LCF and HCF, for example. A representative cyclic loading history may contain from a few thousands to a few millions of cycles. Therefore incremental elastic-plastic finite element analysis of such a history would require prohibitively long computing time. For this reason more efficient methods of cyclic elastic-plastic stress analysis are necessary. One such a method, suitable for calculating multiaxial elastic-plastic stresses and strains in notched bodies subjected to proportional and non-proportional loading histories, is the equivalent strain energy density method. In this method, use is made, analogous to the original Neuber rule, of the equivalence of increments of the total distortional strain energy density contributed by each pair of associated stress and strain components.

The equalities of strain energy increments for each set of corresponding hypothetical elastic and actual elastic-plastic strains and stress increments at the notch tip can be shown graphically (Figure 3.61) as the equality of surface areas of the two pairs of rectangular elements representing the increments of strain energy density. The area of dotted rectangles represents the total strain energy increment of the hypothetical elastic notch tip input stress while the area of the hatched rectangles represents the total strain energy density of the actual elastic-plastic material response at the notch tip.
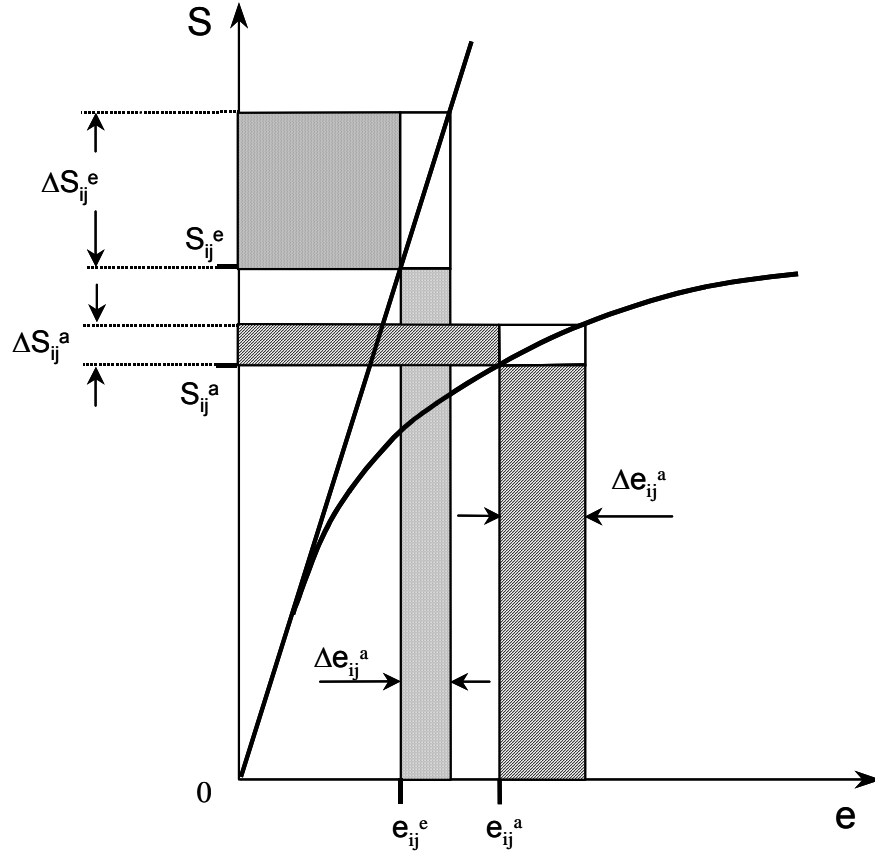
Figure 3.61. Graphical representation of the incremental Neuber rule.

The method developed uses the ratios of strain energy density contributed by each pair of corresponding stress and strain components. In order to analyze non-proportional loading paths the energy equations are written in an incremental form. Because the ratios of strain energy density increments seem to be less dependent on the geometry and constraint conditions at the notch tip than the ratios of stresses or strains, the analyst is not forced to make any arbitrary decisions about the constraint while using these equations. Because plastic yielding is dependent mainly on deviatoric stresses the entire formulation is written in deviatoric stress space.

In the case of a monotonic (no unloading) non-proportional stress path the qualitative correctness and accuracy of the method was demonstrated by comparing the calculated notch tip stress-strain histories to those obtained from the finite element method. The elastic-plastic finite element stress results were obtained using the ABAQUS finite

element package. The isotropic strain-hardening plasticity model was used for calculations. The geometry of the notched element was that of the circumferentially notched bar shown in Figure 3.62. The loads applied to the bar were monotonically increasing torsion in the first phase and then increasing tension in the second phase with the torsion load being kept constant. The maximum applied load levels were chosen to be 50% higher than it would be required to induce yielding at the notch tip if each load was applied separately.
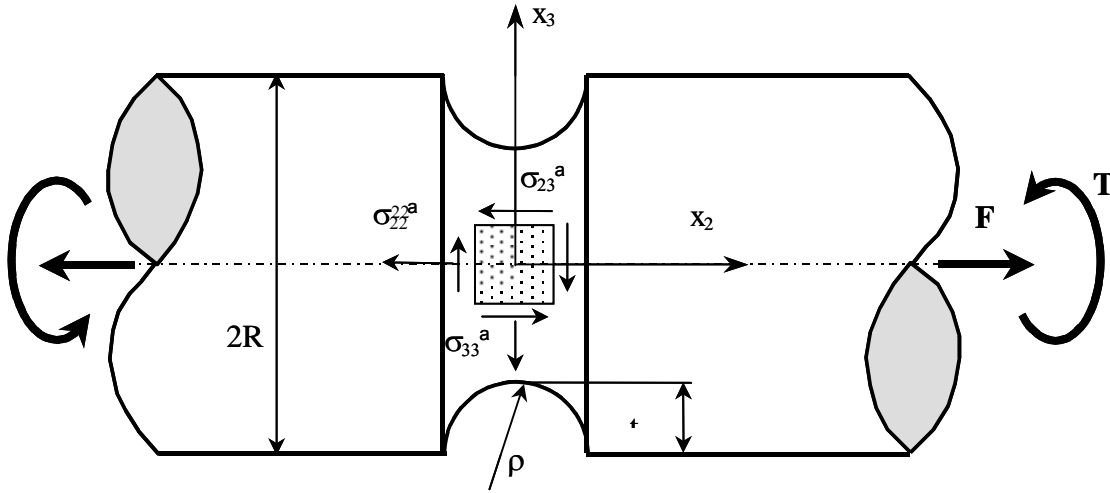
Figure 3.62. Stress-strain coordinates and geometry of torsion-tension notched bar.

The calculated and the FEM determined strain components, $\varepsilon_{22}{}^a$ and $\varepsilon_{23}{}^a$, and the stress components, $\sigma_{22}{}^a$ and $\sigma_{23}{}^a$, are shown in Figures 3.63 and 3.64. Note that the calculated stresses and strains and the results of the finite element analysis are identical in the elastic range. This is expected since the model converges to the elastic solution in the elastic range. Just beyond the onset of yielding at the notch tip, the strain results that were predicted using the proposed model and the finite element data begin gradually to diverge. It can be concluded that the method based on the equivalence of the total strain energy increments overestimates the actual notch tip strains but the predicted strains are reasonably close to the numerical FEM data. Details on the methodology for two and three-dimensional notch analysis and validation are provided in Appendix H.
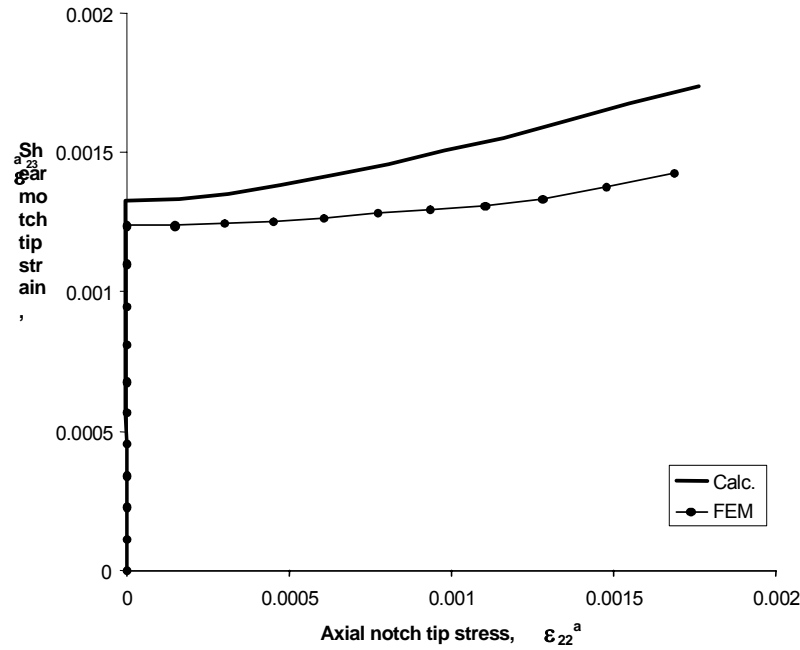
Figure 3.63. Comparison of the calculated and FEM determined strain paths for the monotonic non-proportional torsion-tension input stress history.
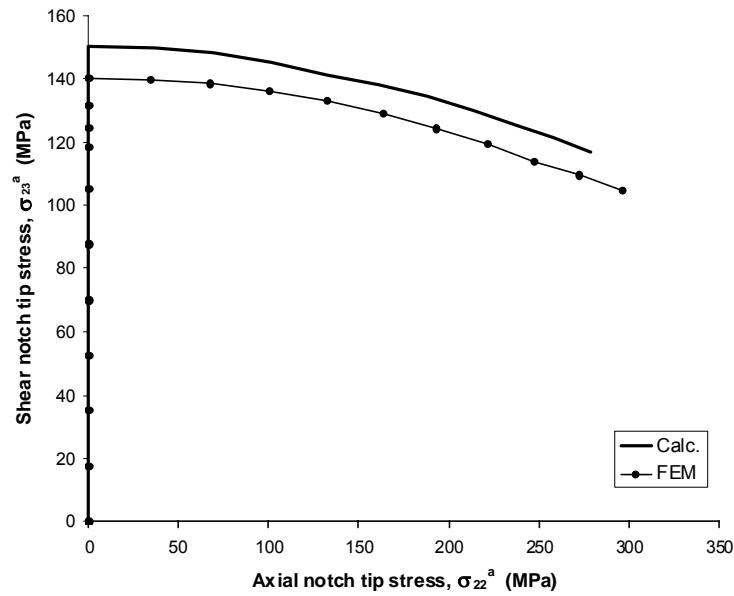
Figure 3.64. Comparison of the calculated and FEM determined stress paths for the monotonic non-proportional torsion-tension input stress history.

84

3.3.5 Shakedown Analysis Method For Isotropic and Anisotropic Materials

Shakedown occurs due to stress relaxation and redistribution arising from non-linear strains generated during loading. Plastic deformation can occur in regions of high stress, such as notches and underneath contact surfaces. A compressive residual stress is left in the structure after elastic unloading as a consequence of stress relaxation. This static compressive stress is beneficial in inhibiting both crack initiation and crack propagation by lowering the local stress ratio, R, and in helping to increase the critical crack size by reducing the maximum crack-tip driving force. After the formation of the compressive residual stress, the structure is said to have undergone shakedown. Following shakedown in typical turbine engine components, further load excursions will result only in linear-elastic behavior as non-linear behavior has been "shaken out".

Stress analyses for determining the relaxed and residual stress states due to shakedown for use in design and reliability assessments generally rely on time-consuming and costly procedures such as non-linear finite element analysis (FEA). To more readily obtain shakedown stresses, a simplified shakedown methodology was developed that utilizes linear elastic stress solutions which, in general, do not require as much FEA computing resources to generate as do non-linear solutions. The details of the developed shakedown methodology are given in Appendix I: Isotropic Shakedown Methodology for Bivariant Stress Field.

In two previous projects separately funded by the FAA and P&W, SwRI developed and delivered two shakedown stress analysis modules for isotropic materials. The module developed for the FAA performs a shakedown stress analysis based on a univariant stress field and has been incorporated into the DARWIN^{TM} computer program [9]. The module developed for P&W enables shakedown analyses to be performed for bivariant stress fields. These modules are appropriate for isotropic materials under proportional loading conditions, and account for load shedding and re-distribution while maintaining force and moment balance. These existing modules were used together with shakedown software developed by Professor Glinka at the University of Waterloo for isotropic materials, to provide a starting point for the current work, which is designed to extend the capability of the existing methodology in a number of areas critical to high cycle fatigue.

85

The present task involved integrating and extending the shakedown methodology for bivariant stressing developed for P&W to non-proportional loading for isotropic and anisotropic materials. The extension to non-proportional loading is necessary to properly treat contact stresses at attachments. The methodology for estimating nonlinear stresses from linear elastic solutions for isotropic materials developed by Glinka was utilized as the starting point in the development of a point relaxation module for both isotropic and anisotropic materials. Since there were no analytical shakedown methodologies for anisotropic materials available to help guide the development of the current work, a new approach had to be formulated and implemented.

Verification of the developed isotropic shakedown module was accomplished by comparing the analytical results with the finite element solutions SwRI obtained employing the ABAQUS computer program. Only a summary of this verification is given herein; more details are presented in Appendix I.

The major accomplishment of the isotropic shakedown project was the development of the isotropic shakedown module for bivariant stressing employing Fortran 77. The module implements a shakedown methodology that has been enhanced by SwRI to include a modified Neuber approach, and a load shedding and re-distribution scheme. The module has been verified against three-dimensional elastic-plastic finite element results for a notched plate subjected to various combinations of remote tension and bending for materials displaying a wide range of strain hardening capacities.

3.3.5.1 Development of Isotropic Shakedown Module for Non-Proportional Loading

The isotropic shakedown methodology was initially based on Glinka's delivered point relaxation module, and an extended module that he also delivered that attempted to take account of load re-distribution. However, under some circumstances the predictions of Glinka's extended modules had unacceptable inaccuracies, and it was agreed by the HCF Team that SwRI would improve the accuracy of this module by integrating Glinka's point relaxation module with the isotropic shakedown module developed previously by SwRI for DARWIN^{TM} and Pratt & Whitney. The improved module enables a more accurate determination of load shedding and load re-distribution under bivariant stressing conditions than does Glinka's extended shakedown module.

It turned out, that this new shakedown module could still not capture the high levels of triaxiality at the notch predicted by finite element computations. It was, therefore, necessary to significantly modify some of the methodology incorporated in Glinka's point relaxation module. These major modifications included a change to the way Neuber's rule was implemented, basing the new approach on equivalent stresses and strains rather than the individual stress components. Glinka's approach resulted in excessive constraint, leading to much lower peak stress values at the notch for the primary principal stress (the stress component normal to the load bearing section) when compared with the stress levels determined by FEA. In addition, Glinka's approach tended to predict an out-of-plane stress (the secondary principal stress) that differed little from the linear elastic solution because of the constraint imposed on the distribution of incremental strain energy density. SwRI modified this approach based on a parameter derived from the linear elastic solution to account for stress triaxiality. This parameter is a measure of the degree of plane stress/plane strain conditions at each nodal position.

This enhanced shakedown module has been validated against FEA results and found to be in excellent agreement with them. It is emphasized that the new improved shakedown module is not at present applicable to reverse loading conditions. The extension of the module to these situations is beyond the scope of the present task.

To account for the non-proportional loading, an incremental approach is utilized based on Glinka's point relaxation module for non-proportional loading. The introduction of the incremental approach to account for the non-proportionality in the loading path requires revising the scheme used in the P&W's shakedown module. To do this, a "pseudo" stress normal to the load bearing section is defined to "store" the elastic-plastic results at the current step. This pseudo stress is also used to estimate the elastic-plastic increment for the next step during the course of non-proportional loading. The implementation of the "pseudo" stress required revision of the schemes used for evaluating load shedding and for maintaining force and moment balance over the load bearing section.

The point relaxation program provided by Professor Glinka at Waterloo University was modified and linked with the SwRI's isotropic shakedown routine. During the shakedown computation, which involves stress relaxation, load shedding and load

87

redistribution, the SwRI isotropic shakedown routine calls the point relaxation module for each node of a refined mesh that represents the load bearing section. The program structure is shown as a flowchart in Figure 3.65.
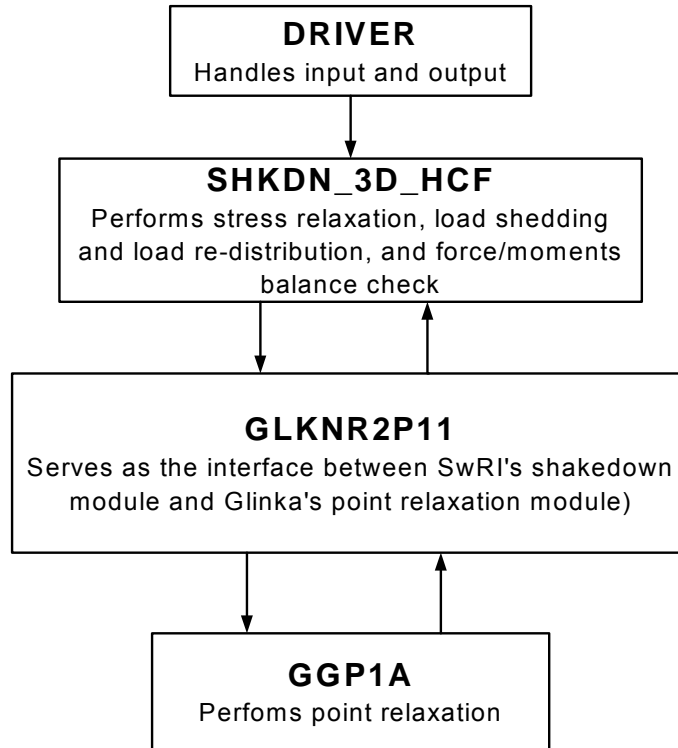
Figure 3.65. Flow diagram for SwRI's isotropic shakedown module.

3.3.5.2   Validation of Isotropic Shakedown Module for Non-Proportional Loading

Extensive validation of the enhanced isotropic shakedown module developed by SwRI has been performed. The validation is based on the FEA results previously generated by SwRI for notched 3-D plates subjected to various combinations of tensile stresses and bending moments, as illustrated in Figure 3.66.
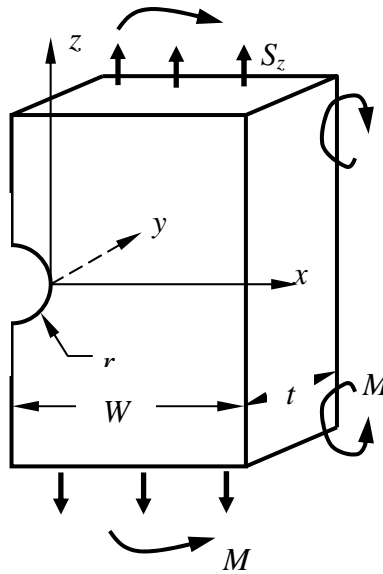
Figure 3.66. Geometry and loading conditions for finite element analysis used to verify SwRI's isotropic shakedown module. Various combinations of tensile stresses and moments were applied to the notched plate.

Table 3.12 summarizes the loading combinations applied to the notched plates. The dimensions of the plate are 10 inches for the width (W), 5 inches for the thickness (t), and 20 inches for the height (h). The radius (r) of the notch is equal to 1 inch. The hypothetical materials used in the validation display a wide range of strain, hardening capacity, including a case with low hardening that was representative of Ti-6Al-4Ti. The constitutive relationship between stress and strain was represented by a Ramberg-Osgood equation.

Table 3.12. **Load Combinations used in the Verification of the Isotropic Shakedown Model for Bivariant Stressing for a Material with Strain Hardening Capacity Typical of Ti-6Al-4V**

Loading Cases	Applied Loads		
	S_z (ksi)	M_x (ksi-in)	M_y(kip-in)
A	50	0	0
B	25	0	2500
C	25	1600	0
D	20	1800	1800
E	55	0	0
F	30	0	3500
G	30	2500	0
H	25	2400	2400

Only part of the validation is provided in this section. (Full results are presented in Appendix I.) The hypothetical material constitutive relationship used to generate the results reported here had a strain hardening capacity typical of Ti-6Al-4V. A plot of the Ramberg-Osgood equation representing the stress-strain curve is shown in Figure 3.67.

The plot shows Stress σ, ksi (y-axis, 0 to 100) versus Strain ε, in/in (x-axis, 0.00 to 0.20), with the equation:

$$\varepsilon/(\sigma_o/E)=\sigma/\sigma_o+\alpha(\sigma/\sigma_o)^\beta$$

where $\alpha=0.43$, $E=27700$ksi
$\sigma_o=62.52$ ksi, $\beta=31.5$
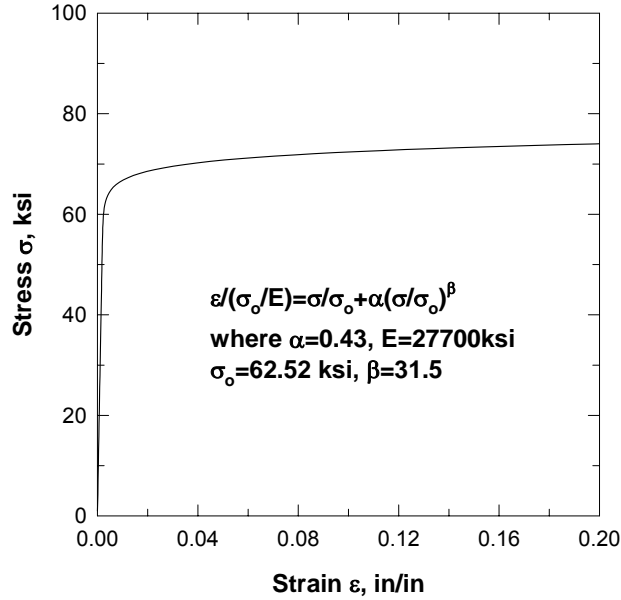
Figure 3.67. The stress-strain curve used for validation showing the Ramberg-Osgood equation and the values of the parameters used.

Comparisons between the developed shakedown model results and the FEA results are shown in Figures 3.68 and 3.69 for Loading Cases A and B in Table 3.12, respectively. Loading Case A applies a remote tension to the notched plate which leads to a stress magnification factor equal to 3.28, while Loading Case B has an additional in-plane bending moment applied. The results predicted by the as-received Glinka's point relaxation module are also included in the figures to demonstrate the importance of the modifications made by SwRI to capture the triaxial stress state at the notches, and the need to maintain force and moment balance. As can be seen, the results obtained by the SwRI's shakedown module (open symbols) are in very good agreement with the results obtained from FEA (gray solid symbols). The variation of the out-of- plane stress predicted by the point relaxation method (symbols with a cross inside) tends to follow the linear elastic solution and predicts much lower stress values than the FEA results.

To get good agreement between the isotropic shakedown model and FEA results, it was necessary to modify the isotropic shakedown module received from Professor Glinka to capture the stress triaxiality at the notch tip arising from out-of-plane constraint and to take account of force and moment balance during the load redistribution process. The detailed procedure is summarized in [Appendix I]. The newly developed enhanced isotropic shakedown module that incorporates the modifications described above can achieve solution accuracy comparable with FEA results, especially for materials such as Ti-6Al-4V, which display low strain hardening capacity.

3.3.6   Comparison of Approximate Notch Analysis Methods

Several notched component geometries were selected to provide validation measures and comparisons for the elastic-plastic approximation methods developed by Glinka and SwRI. These geometries were selected with the intent of providing a variety of loading conditions to thoroughly evaluate the accuracy and limitations of the approximation methods. Loading combinations and levels were chosen to produce an array of cyclic elastic-plastic stress/strain states, ranging from small scale, first-reversal proportional plasticity to large scale, non-proportional cyclic plasticity.

Of the two codes evaluated in this program, the Glinka code is more versatile in its present form, as it is not restricted by notch or component geometry or type of loading; i.e., it can be used to analyze proportional or non-proportional cyclic loading applied to any notched component. While the SwRI methodology is not restricted on its theoretical basis to certain notched component geometries or loadings, the delivered code was limited to the analysis of a rectangular cross-section under monotonic loading (not cyclic). Consequently, the validation of the SwRI code was more limited than that of the Glinka code.

3.3.6.1   Validation of the Glinka Code

The three component geometries used in the validation of the Glinka code are shown in Figures 3.70 through 3.72. Geometry 1 (Figure 3.70) was intended to provide a baseline validation test for the approximation methods.

91
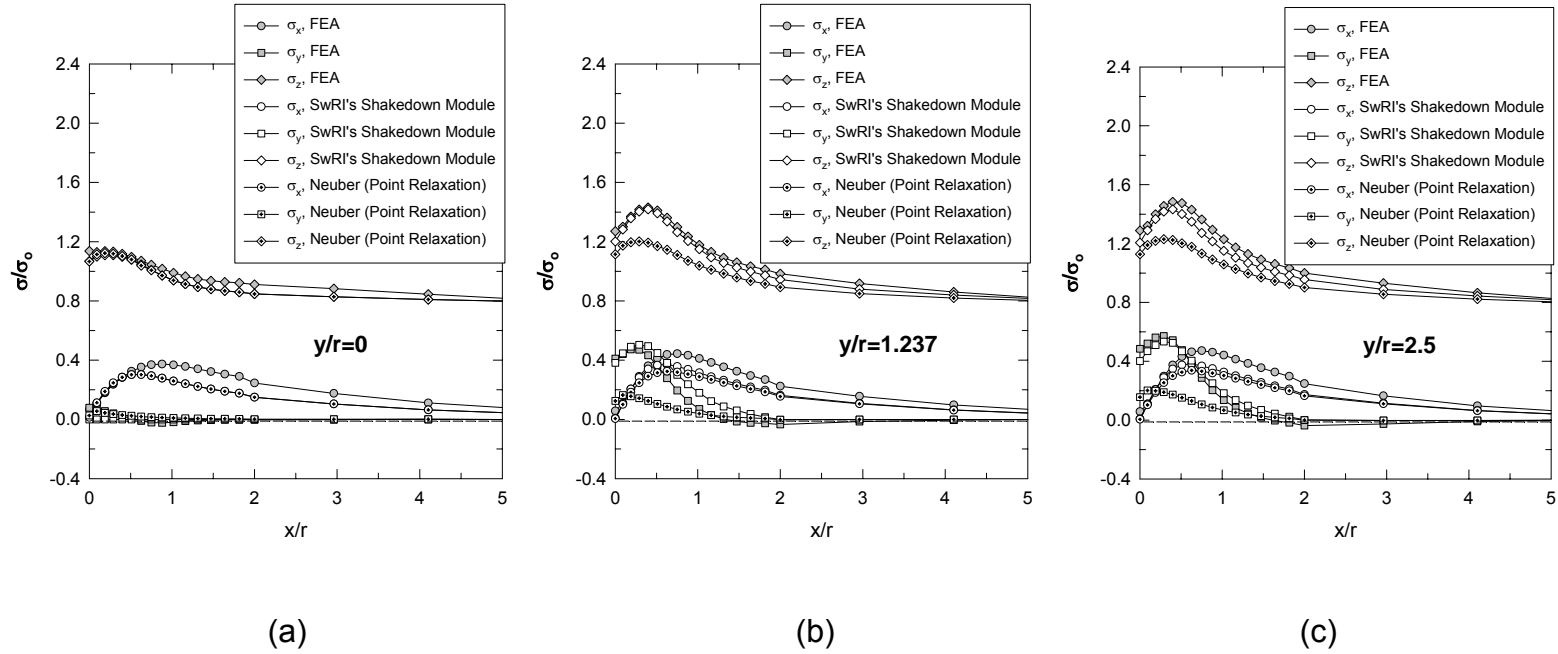
Figure 3.68.   Comparison of stress components predicted by SwRI's isotropic shakedown module with the results obtained from FEA for Loading Case A (Table 3.12). The results computed from Glinka's point relaxation module are also included. Results in (a) are for $y/r=0$ (the free surface at the side of the plate), (b) are for $y/r=1.237$ (a plane one quarter of the way through the plate), and (c) are for $y/r=2.5$ (at the mid-plane). The results in (a) predicted by SwRI's isotropic shakedown module cannot be visually differentiated from the point relaxation results.
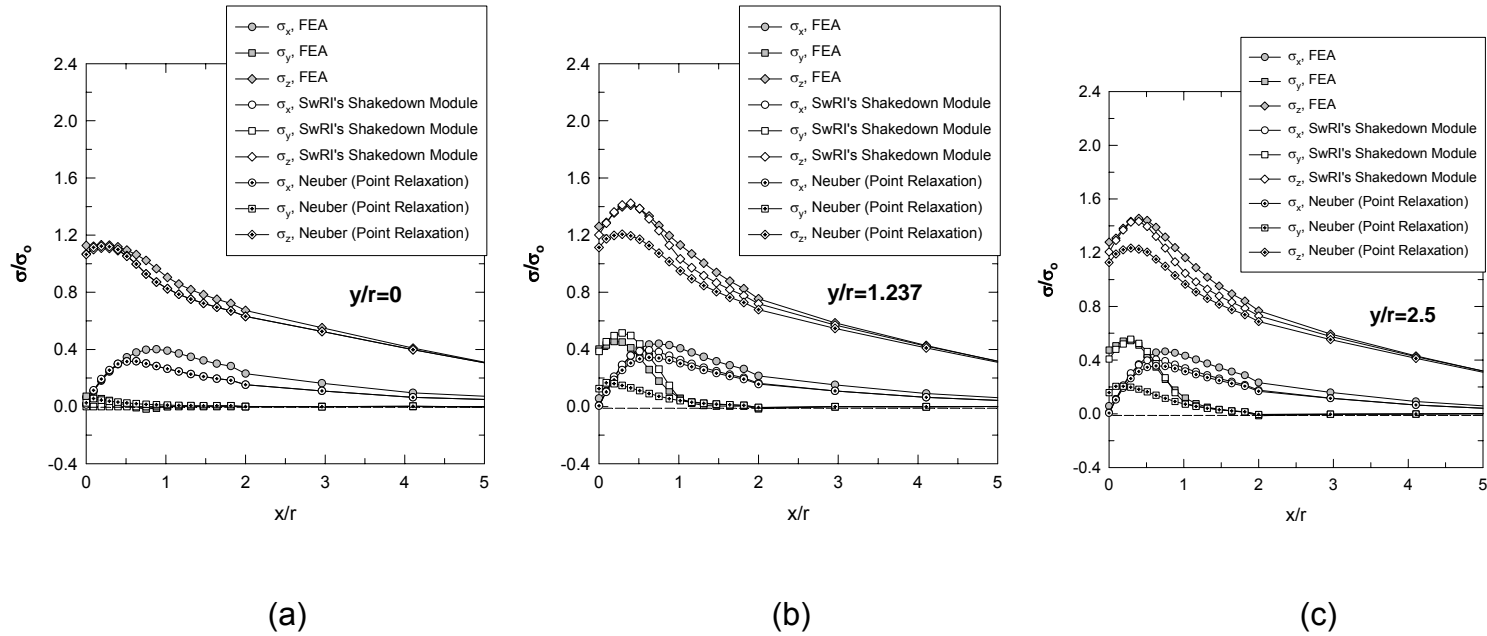
Figure 3.69. Comparison of stress components predicted by SwRI's isotropic shakedown module with the results obtained from FEA for Loading Condition B (Table 3.12). The results computed from Glinka's point relaxation are also included. Results in (a) are for y/r=0 (the free surface at the side of the plate), (b) are for y/r=1.237 (a plane one quarter of the way through the plate), and (c) are for y/r=2.5 (at the mid-plane). The results in (a) predicted by SwRI's isotropic shakedown module cannot be visually differentiated from the point relaxation results.
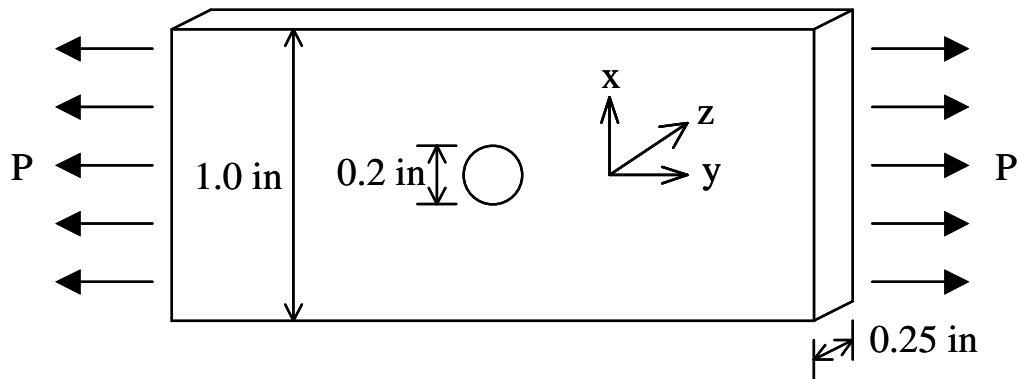
Figure 3.70. Geometry 1 for Glinka code validation: flat plate with center hole in tension.

The stress gradients around the notch are not too severe, and typical of those found in many service components. The notch plasticity levels were varied by applying a range of load magnitudes. In all cases, the loading was applied cyclically at R = 0 (R = P_{min}/P_{max}), with nominal stress levels (P_{max}/A, with A defined on the gross cross-section) varying from 40 ksi to 100 ksi in 20 ksi increments. An elastic analysis was also performed to provide the input required by the approximation code. For this geometry, the elastic-plastic stress gradients were compared along a line through the notch section at both the midplane and outer surface of the component.

Geometry 2 (Figure 3.71) represents the notched tension/torsion specimen tested by the University of Illinois as part of the HCF program.
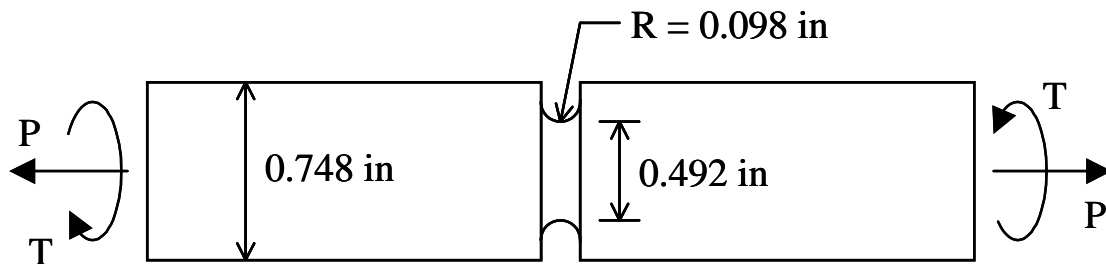
Figure 3.71. Geometry 2 for Glinka code validation: round bar with large circumferential notch in tension/torsion.

This component provides a more thorough validation of the multiaxial capabilities of the approximation methods. A variety of multiaxial stress/strain gradients were produced in the notch section by varying the relative axial and torsion load levels. Four cyclic loading cases were considered for this geometry: (1) axial loading only (R = 0), (2) torsion loading only (R = 0), (3) proportional loading (R = 0, with $\sigma_{max} \approx \tau_{max}$ at notch root), and (4) non-proportional loading (box path with R = −1). The box path consists of a four-point cycle, with load levels ordered as follows: (1) P_{max}, T_{max}, (2) $-P_{max}$, T_{max}, (3) $-P_{max}$, $-T_{max}$, (4) P_{max}, $-T_{max}$. For each load case, one elastic analysis and three elastic-plastic analyses were performed. The elastic-plastic stress gradients were compared along a radial line through the notch section.

Geometry 3 (Figure 3.72) is similar to Geometry 2, except the circumferential notch is smaller and sharper. This geometry was designed to produce stress gradients similar to those experienced near edge-of-contact (EOC) fretting locations. This component geometry, loaded in tension/torsion, is intended to provide a more critical validation of the approximation module under loading conditions commonly experienced in aircraft turbine engines. Two cyclic loading cases were considered for this geometry: (1) proportional loading (R = 0, with elastic $\tau_{max} \approx 0.6\sigma_{max}$ at notch root), and (2) non-proportional loading (box path with R = −1). For each load case, one elastic analysis and three elastic-plastic analyses were performed. The elastic-plastic stress gradients were compared along a radial line through the notch section.
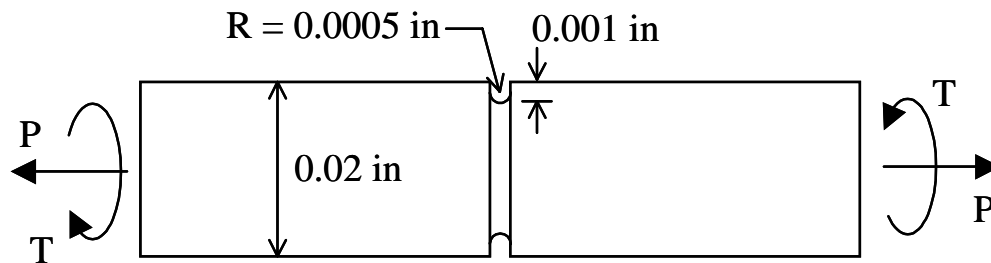
Figure 3.72. Geometry 3 for Glinka code validation: round bar with small circumferential notch in tension/torsion.

Sample comparisons between the elastic-plastic stresses obtained from the finite element analyses and the Glinka code for the three geometries are shown in Figures 3.73 through 3.75. Complete results are included in Appendix F.

Surprisingly, the greatest discrepancies between the FEA and Glinka results were found in Geometry 1 (e.g., Figure 3.73).
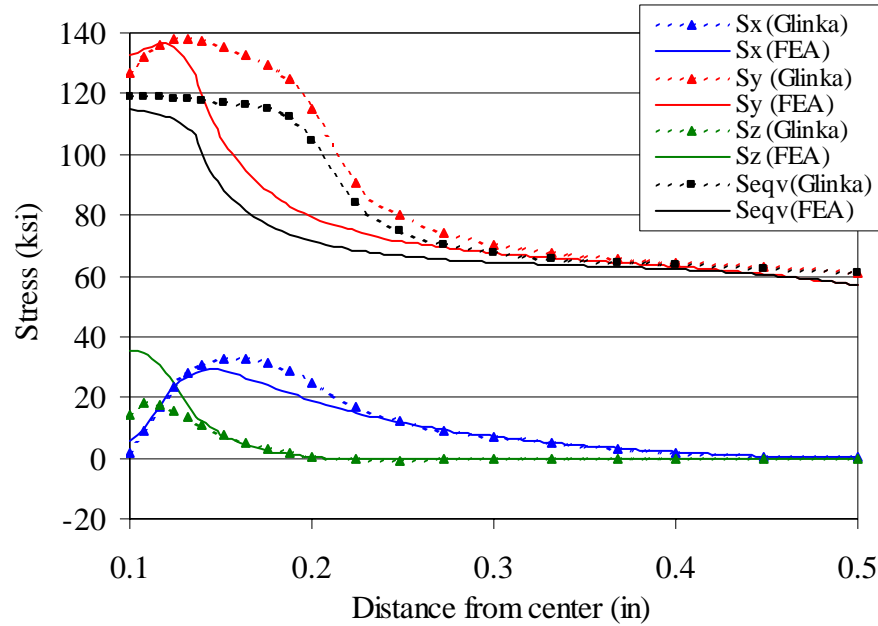
Figure 3.73. Comparisons between FEA and Glinka stresses for Geometry 1, P/A = 60 ksi, center of notch section at maximum load.

At maximum load, the Glinka code overestimated the magnitude of the equivalent stress in the yield zone, as well as the depth of the yield zone, along both the edge and centerline of the component. Corresponding discrepancies were found in σ_y. At minimum load (unloading), σ_{eqv} and σ_y from FEA and Glinka were in agreement at the notch surface, although the Glinka code predicted much higher residual stresses below the notch root. This is a result of the larger plastic zone size calculated by the Glinka code at peak load.

The results from the Glinka code were generally found to be in better agreement for Geometries 2 and 3. Figure 3.74 shows a typical comparison for Geometry 2 at one of the four corner points of the box path.

96
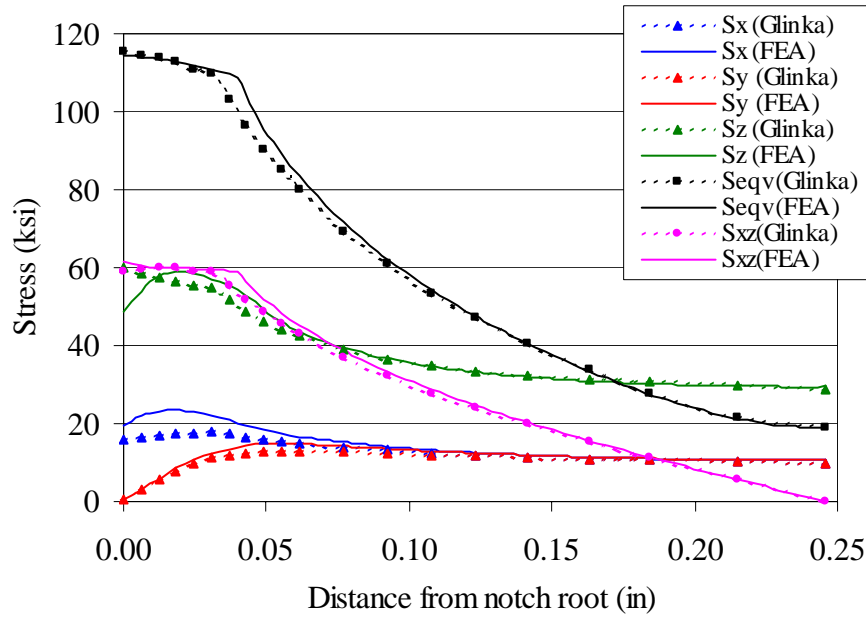
Figure 3.74. Comparisons between FEA and Glinka stresses for Geometry 2, box path (non-proportional loading), P = 8200 lb, T = 1435 in-lb, point 1.

Figure 3.75 shows the comparison for Geometry 3 under proportional loading, at maximum load. In most cases, as illustrated in Appendix F, the equivalent stress distributions through the notch section from FEA and Glinka were quite similar, although there were some discrepancies in the individual stress components. For example, there was a significant error in the Glinka axial stress (σ_z) at point 3 of the box path for Geometry 2; however, the error was reduced at point 4. In addition, there were discrepancies in some of the stress components just below the notch surface in Geometry 3 at maximum load, although the stresses at the notch root were reasonably accurate.

The superior performance of the Glinka code for Geometries 2 and 3, relative to Geometry 1, likely results from the method by which the Glinka code redistributes the stresses across the notch section. Specifically, the Glinka code utilizes the elastic equivalent stress distribution along a single line through the notch section, rather than considering the elastic stress distribution over the entire cross-section. This method presents no problems for Geometries 2 and 3 since the stress distributions on any cross section are axisymmetric;

97
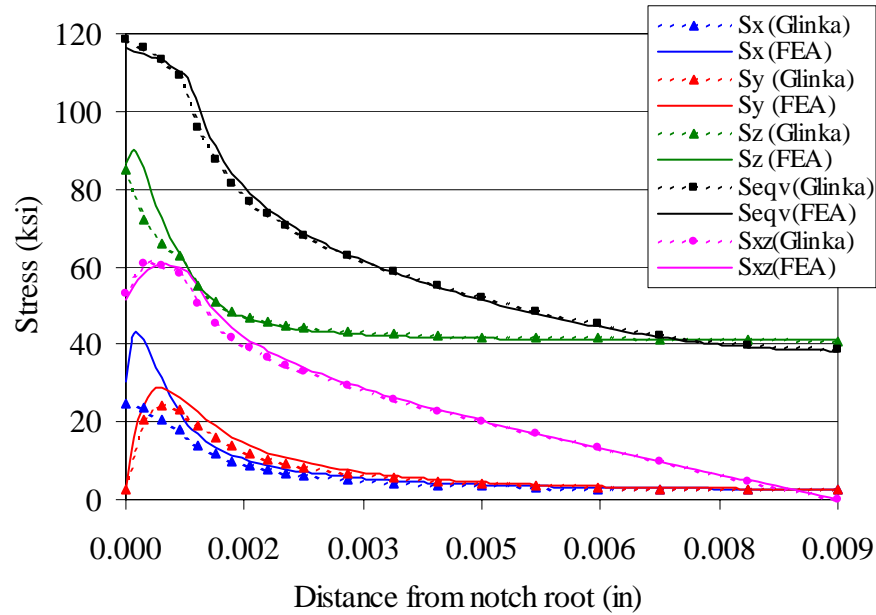
Figure 3.75. Comparisons between FEA and Glinka stresses for Geometry 3, proportional loading, P/A = 40 ksi, T = 0.06 in-lb, maximum load.

i.e., the stress distributions are identical along any radial line. Thus, using the elastic equivalent stress gradient along a single radial line to account for redistribution of elastic-plastic stresses is sufficient. In contrast, for Geometry 1, the stress distribution varies through the thickness of the component due to the constraint near the notch. In this case, the stress redistribution due to yielding must take into account the gradients in two directions. The Glinka code, in the current form, cannot fully account for bi-directional stress gradients.

3.3.6.2   Validation of SwRI Code

Due to the geometric restrictions of the SwRI code, only two component geometries were used to validate the results from this program. The first geometry was the same Geometry 1 used in the validation of the Glinka code, shown in Figure 3.70, subjected to the same loading levels (although only the results at maximum load were considered, as the code was not set up for cyclic loading). The second geometry is shown in Figure 3.76, identified as Geometry 4.
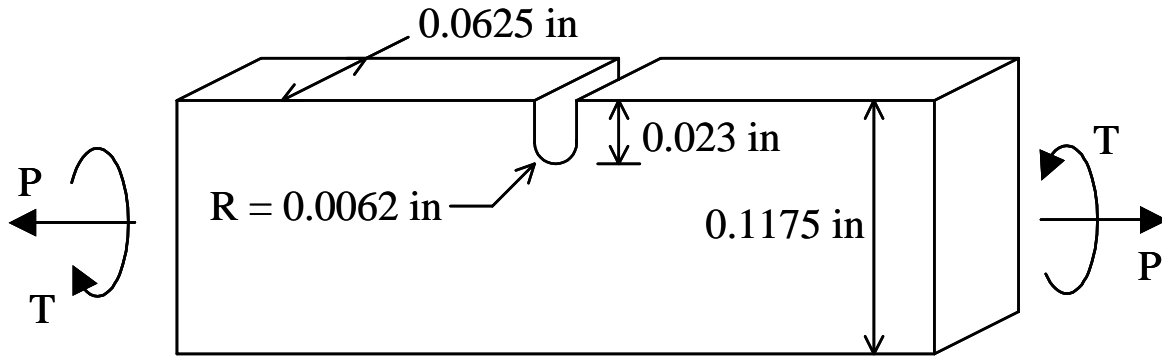
Figure 3.76. Geometry 4 for SwRI code validation: rectangular bar with edge notch in tension/torsion.

This geometry consisted of a rectangular component containing a small edge notch in one side only. This notch was intended to produce much steeper stress gradients than those encountered in Geometry 1. This geometry was subjected to two loading conditions: axial loading and combined axial/torsion loading. In each case, one elastic analysis and three elastic-plastic analyses were performed. The elastic-plastic stress gradients were compared along a line through the notch section at both the midplane and outer surface of the specimen, for both geometries.

Sample comparisons between the elastic-plastic stresses obtained from the finite element analyses and the SwRI code are shown in Figures 3.77 and 3.78. In these plots, all stresses have been normalized with respect to the yield strength. Complete results are included in Appendix F. Note that in the SwRI comparison for Geometry 1, the y and z axes have been interchanged relative to the Glinka comparisons.

In comparing the elastic-plastic results obtained from the Glinka and SwRI codes for Geometry 1 (Figures 3.73 and 3.77), it is clear the SwRI code was in much closer agreement with the FEA results than the Glinka code. Although there were small discrepancies in σ_y and σ_z at the notch root along the specimen centerline (Figure 3.77), the depth of the plastic zone was accurately approximated, and the stress magnitudes just below the surface were in close agreement. Along the edge of the component, the stress results were in very close agreement with FEA calculations (see Appendix F).
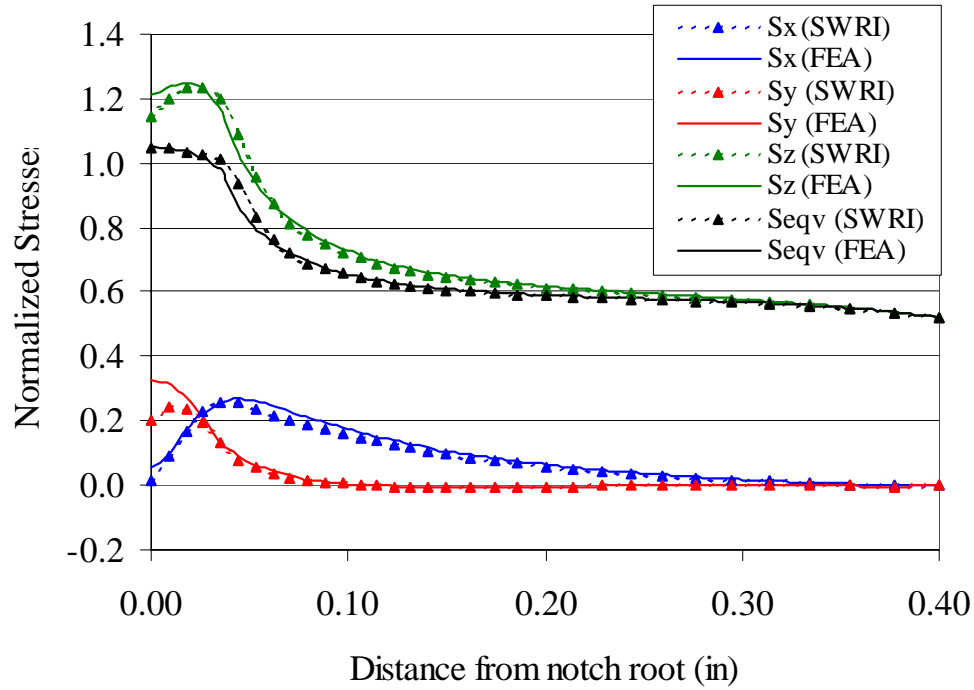
Figure 3.77. Comparisons between FEA and SwRI stresses for Geometry 1,
P/A = 60 ksi, center of notch section at maximum load.
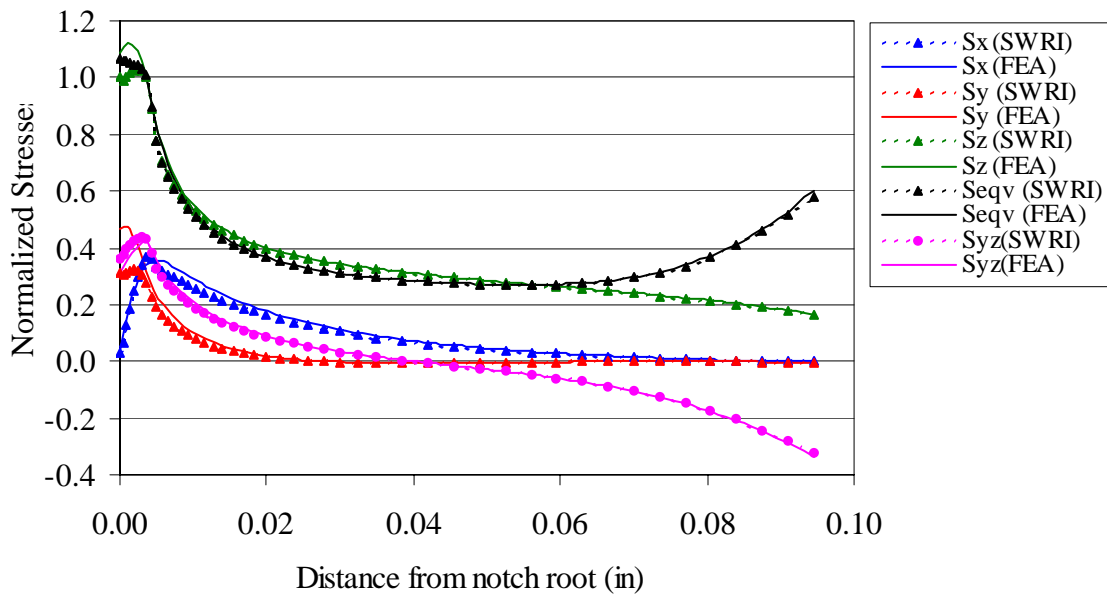
Figure 3.78. Comparisons between FEA and SwRI stresses for Geometry 4
proportional loading, P/A = 30 ksi, T = 4.5 in-lb, center of
notch section at maximum load.

In approximating the elastic-plastic stresses from the elastic solution, the SwRI code takes into account the full stress distribution on the entire component cross-section, rather than along a single line as the Glinka code does. Thus, full equilibrium is maintained as the stresses are redistributed across the section due to yielding. As a result, the stress gradient through the thickness of the part (from the centerline to the edge), which affects the magnitudes of the stress components and the depth of the plastic zone, is better accounted for by the SwRI code, leading to more accurate elastic-plastic stress estimates in components with a rectangular cross-section. For axisymmetric components, in which a stress gradient occurs in only one direction (radial), the differences between the two codes would likely be much less. This could not be verified, however, as the SwRI code was not formulated to analyze such components.

A sample elastic-plastic approximation from the SwRI code for Geometry 4 is shown in Figure 3.78. This component consisted of a rectangular cross-section with a sharp edge notch subjected to combined axial and torsional loads, producing a more complex stress state with steeper gradients than found in Geometry 1. Along the component centerline (Figure 3.78), there were some notable differences between the SwRI and FEA computed magnitudes of σ_z and σ_y at the notch root, although the size of the plastic zone and the σ_{eqv} distribution were in very close agreement. Along the edge of the component, the agreement between the SwRI and FEA results was very good (see Appendix F).

3.3.6.3 Summary

The two approximate elastic-plastic notch analysis methods considered here both displayed promising results under certain conditions. The Glinka code provided reasonable stress estimates for axisymmetric components (such as circumferentially notched round bars), in which the stress gradients are limited to one direction. However, for non-axisymmetric components, in which the stress gradients may be bi-directional, the Glinka approximations were much less accurate. The SwRI code provided better overall stress approximations for components with a rectangular cross-section. However, in the current form, the SwRI program is more limited in its versatility, as it has not been coded to analyze non-rectangular sections or handle loading conditions that result in cyclic plasticity. In addition, some problems were encountered in running the SwRI code under loading

conditions that produced very large-scale plasticity. This should not be considered a serious drawback, however, as the primary intent of the approximation code is to analyze notched components under conditions of fairly localized yielding.

3.3.7   Threshold Stress Estimates Using Fracture Mechanics

The fracture mechanics approach employed herein to predict the HCF threshold stress, ΔS_{th}, assumes that microcracks can initiate relatively early in the life of a notched component due to the damage imparted by the initial FOD impact, the highly concentrated HCF stresses associated with either the FOD notch or the edge-of-contact zone, or the intermittent occurrence of low cycle fatigue (LCF). Moreover, since the stress gradients at sharp notches and edge-of-contact zones are steep and die out at relatively short distances from the notch surface, it is necessary to consider the unique behavior of small fatigue cracks [10,11,12] when performing a fracture mechanics analysis. Based on the notch analysis of Topper et al [13], methods to predict the threshold stresses for FOD [14,15,16] and fretting fatigue [17,18] have been developed. Comparisons of model predictions with results of simulated FOD and machined notch experiments [15,16,1], as well as fretting fatigue experiments [16,17,1], have been encouraging.

The method used, termed the "Worst Case Notch" (WCN) model, enables the boundaries between crack initiation, crack growth followed by arrest, and crack growth to failure to be delineated, as illustrated in Figure 3.79 [13,14,15]. As shown, "true" crack initiation, indicated by the lower curve in Figure 3.79 (a), is assumed to actually occur as predicted by the classical S-N approach when the applied stress range is equal to the endurance limit divided by the elastic stress concentration factor $(\Delta\sigma_e/k_t)$. However, for sharper notches, the initiated cracks can subsequently arrest due to the unique behavior of small cracks, which cause ΔS_{th} to initially increase, achieve a maximum, and finally decrease as crack size increases, as shown in Figure 3.79 (b). The growth/arrest boundary in Figure 3.79 (a) is determined by equating the applied stress intensity factor (SIF) range to the threshold SIF for fatigue crack propagation. The unique behavior of small fatigue cracks is modeled in the WCN approach by a crack-size-dependent threshold SIF [17,18,19] that is consistent with experimental data on a variety of engineering materials [19] including Ti-6Al-4V [20].

102
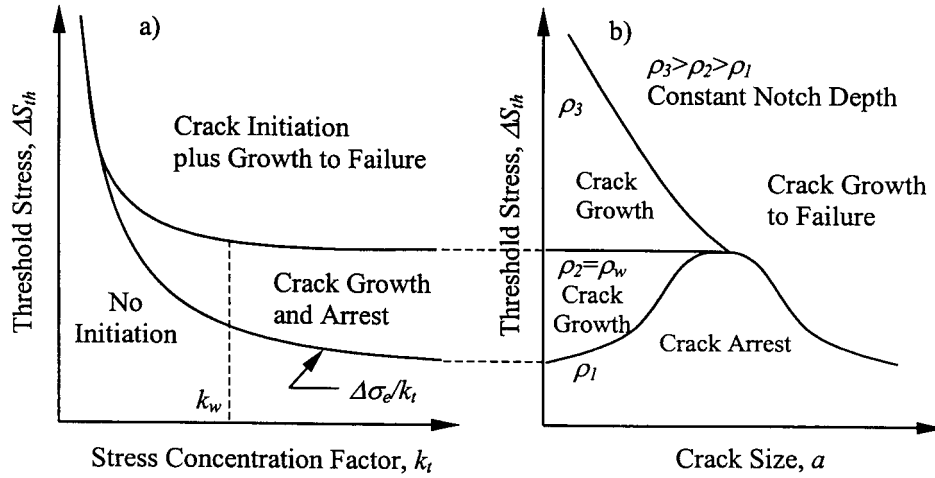
Figure 3.79. Schematic representation of the Worst Case Notch (WCN) model.

The remainder of this section summarizes several enhancements to the WCN model, and compares the model predictions with the small, sharp notch experimental results described in Section 3.3.1. Additional details on the development of the enhanced WCN model are provided in Appendix K.

3.3.7.1 Incorporation of Notch Plasticity and Surface Cracks in the WCN Model

The WCN model was originally developed for through-thickness cracks and surface cracks with one degree of freedom (DOF) emanating from notches [14,15,16,1]. Consequently, in analyses involving thumbnail cracks, these cracks were restricted in shape so that they remained semi-circular, and crack growth was characterized only by the SIF at the deepest point on the flaw. These restrictions resulted in certain predicted crack growth behaviors that were not entirely consistent with observations. To overcome these limitations, the WCN model has been extended to semi-elliptical surface cracks whose growth is characterized by two DOF, namely, the SIFs at both the surface and deepest points on the crack front. In these cases, crack growth and arrest is determined by the manner in which crack shapes evolve from the initially specified shapes, and this evolution is governed by the stress gradient ahead of a notch and the crack growth rate equation. Therefore, implementation of the WCN model for two DOF cracks requires HCF crack growth calculations to be performed. To facilitate these calculations the crack growth rate behavior was described using the Walker crack growth rate equation based on an effective stress

intensity factor, ΔK_{eff} [1, see Section 3.2.2.2)]. This general equation describes crack growth rate behavior from initiation at threshold through to failure from the onset of static failure modes.

To incorporate notch plasticity and associated shakedown of the mean stresses at the notch, an approximate elastic-plastic stress analysis was used to determine the local notch-tip stress state. The methodology used here was based on the isotropic shakedown module for univariant stressing developed for the computer code, DARWIN[TM] [21]. This univariant shakedown method is a simpler version of the bivariant shakedown method described in Sections 3.3.5. The shakedown module requires as input the elastic stress field ahead of a notch, which was obtained using a modification of the method of Amstutz and Seeger [22], as described in [1].

Figure 3.80 compares predictions of the WCN model for a 2-D through-thickness crack both with and without plastic shakedown for a notch of 0.025 inch depth and varying notch radii to give the range of k_t values shown. In this figure, the threshold stress is normalized by the limiting threshold value obtained for a notch with a high k_t. As indicated, the threshold values determined with and without shakedown differ significantly at the initiation of cracking, but the two sets of values differ only slightly at the threshold stress corresponding to failure. The reason for this can be seen from the plot of the local stress ratio (R) that is also presented in Figure 3.80. At the higher cyclic stresses needed to initiate and propagate cracks to failure, shakedown has occurred at the notch tip and changed the local stress ratio at initiation so that it is no longer simply related to the remote stress ratio, specified as being 0.5 in this example. Indeed, at high k_t values, the local stress ratio becomes negative. Although these negative stress ratios will increase the cyclic threshold stress needed to initiate cracking, they clearly do not significantly influence the threshold needed to cause propagation to failure. This is a consequence of the fact that the residual stress field due to shakedown is very localized at the notch tip, and cracks can readily propagate to depths where the localized stress has little influence on the applied SIF. Threshold stresses that fall between the initiation and failure envelopes shown in Figure 3.80 will initiate cracks either on the initiation envelope, or at cyclic stress values above this envelope if shakedown occurs, but these cracks are predicted to eventually arrest.

104
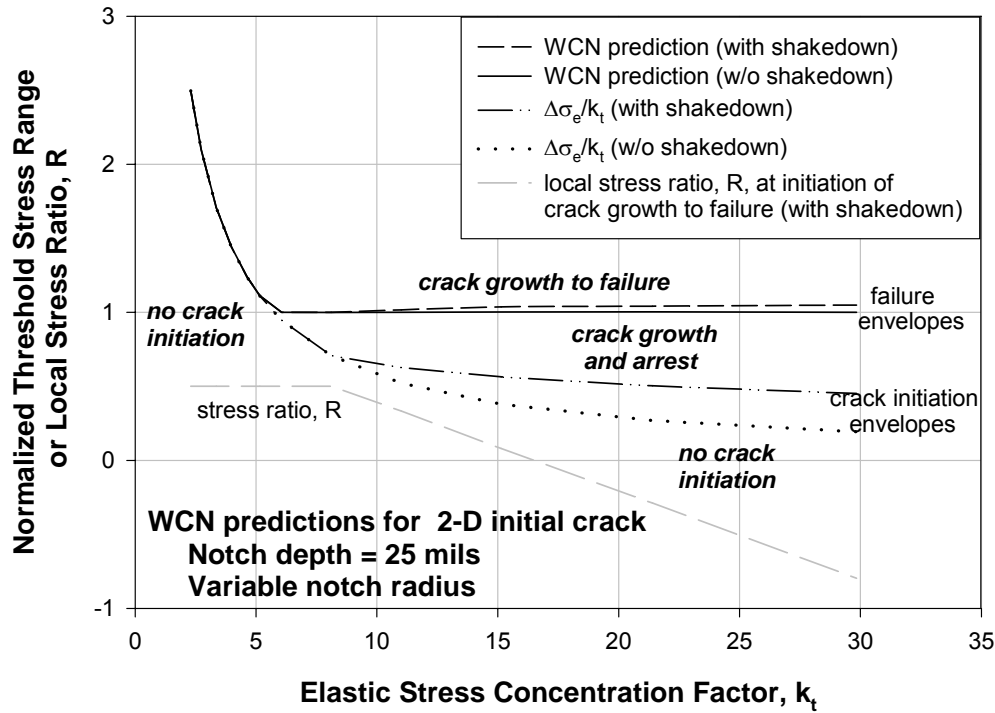
Figure 3.80. Comparison of WCN model predictions with and without plastic shakedown of notch-tip stresses. The local R-value is also shown to decrease with increasing notch severity as the result of plastic shakedown.

Figure 3.81 compares WCN model predictions for 2-D and 3-D surface cracks. Although the trends in threshold behaviors for the two cases are similar, the 3-D crack model for notches with high k_t values predicts that failure will occur at threshold stresses less than those predicted for the 2-D crack. It should be noted that in the fatigue crack growth calculations the 3-D crack was allowed to grow at both the deepest and surface locations of the crack front, so that situations could occur during growth where one location was propagating when the other crack tip location was not, and vice versa. This is the reason why the crack with the additional DOF associated with the 3-D crack gives lower threshold stresses.

It should be pointed out that the small, sharp notch experiments described in Section 3.3.1 were designed based on calculations using the 2D model, since the 3D model was not available at that time. Based on the results of the more accurate 3D model, experimental

discrimination between the predicted threshold stress for initiation and for failure will be more challenging to demonstrate since these two curves lie closer together than they do for predictions based on the approximate 2D model.
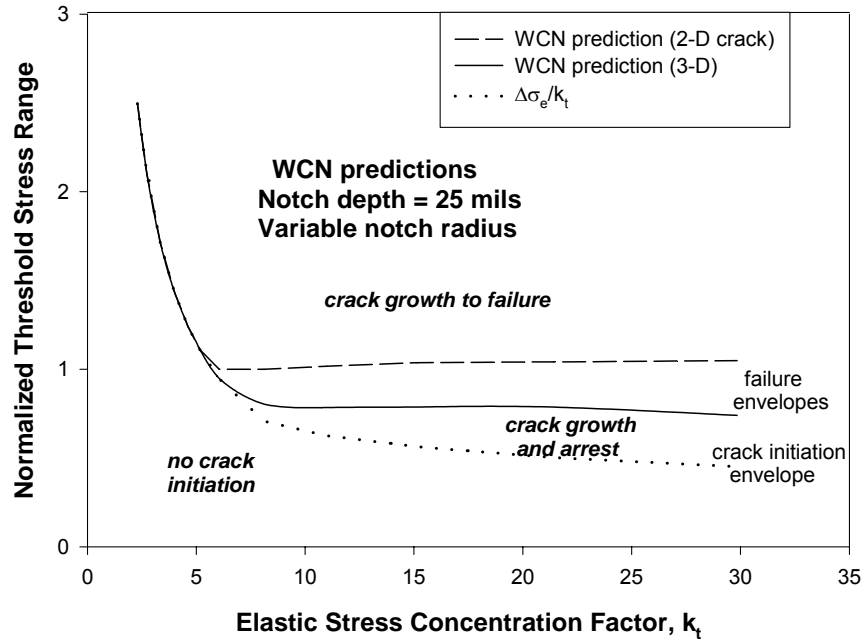
Figure 3.81. Comparison of WCN model predictions for 2-D versus 3-D cracks. All results include the effects of plastic shakedown of notch mean stresses.

3.3.7.2 Comparison of WCN Predictions with Experimental Results

Results from the small, sharp notch tests are summarized in Figure 3.82, where they are compared to predictions of the 3D WCN model. In discussing these results, it is useful to separately consider blunt ($k_t < 6.5$) and sharp ($k_t > 6.5$) notches. For the case of blunt notches, the data tend to lie above the curve defined by the assumed initiation curve ($\Delta\sigma_e/k_t$), regardless of notch depth. However, for the sharp notches, the data tend to be layered with respect to notch depth as predicted by the WCN model. This is most clearly illustrated for the case of the notch depth of 24 mils where the data point is considerably above the initiation curve but in excellent agreement with the WCN prediction for $b = 24$ mils. A similar trend can be seen for the case of $b = 48$ mils, however in this case the

106

distinction between the predicted initiation and failure curves is less distinct because the two curves are relatively close together.

Ideally, one would like to generate additional small sharp notch data at higher k_t values for all notch depths to verify the predicted limiting values for the various notch depths. However, generating such data is limited by the sharpest notches that can be machined. In fact recall that the sharpest notch radii in the present experiments ($\rho = 2$ mils) could only be produced by EDM, since the final chem milling used for all other notches significantly reduced the notch sharpness to about $\rho = 4$ mils. Initially there were reservations about machining sharp notches by using EDM (without subsequent chem milling) because of the possibility of producing notches that would initiate cracks prematurely. However, this does not appear to have been the case since the threshold stresses for small sharp EDM notches were significantly above the initiation curve, as well as above data on blunter notches produced by EDM plus chem milling. Moreover, this trend is consistent with the WCN theory that predicts a limiting threshold stress that depends on notch depth and corresponds to the growth and arrest of microcracks in the steep stress gradient ahead of the sharp notches.

The fact that blunt notches ($k_t < 6.5$) also resulted in measured threshold stresses that were above the initiation curve, corresponding to $\Delta\sigma_e / k_t$, could be due to a number of factors. First, this simple initiation criterion may be inaccurate for the biaxial stresses that exist at the notch surface. Thus, it may be necessary to include a more accurate multiaxial crack initiation criterion such as that employed in the Fs approach described in Section 3.3.8. To assess this hypothesis, the Fs predictions of Section 3.3.8 are included in Figure 3.82 for comparison. These predictions, which use the multiaxial criterion, shift the predictions in the correct direction—i.e., they predict higher threshold stresses than those given by $\Delta\sigma_e / k_t$. However, the predicted results are now greater than the measured results. This is an undesirable prediction for use in HCF design since the predictions are non-conservative with respect to the measured results. It may be that the multiaxial initiation criterion is accurate for blunt notches, but the surface area correction term in Fs is overcompensating for notch size effects.
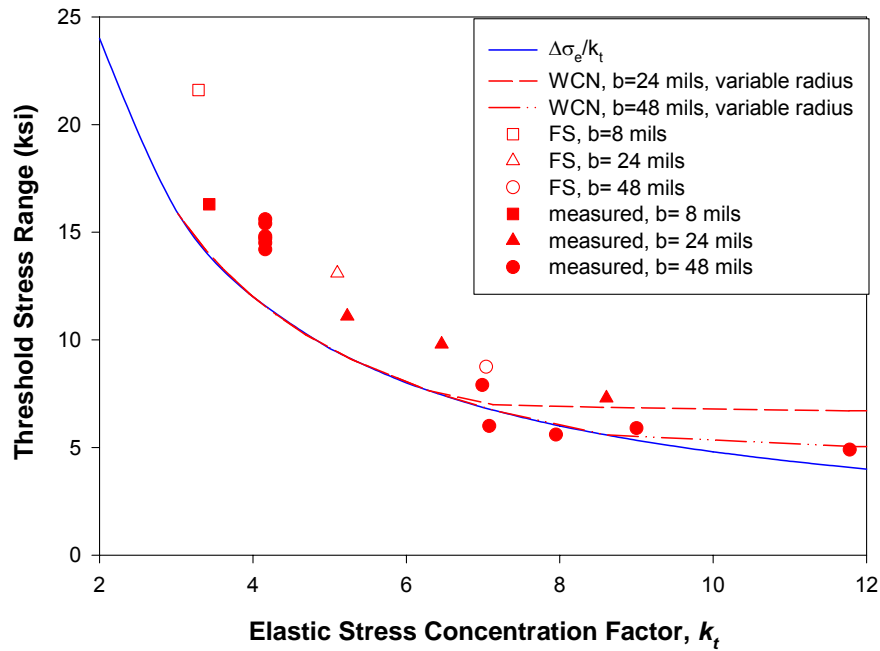
Figure 3.82. Comparison of WCN and Fs model predictions with small, sharp notch data for varying notch depths.

An alternative explanation for the deviation between the measured blunt notch data in Figure 3.82 and the simple initiation prediction given by $\Delta\sigma_e/ k_t$ is that crack growth is contributing to the specimens life, which would effectively increase the threshold stress in the step test. It may be possible to differentiate between the above two interpretations by carefully monitoring experiments for the presence of crack initiation, crack growth or arrest. This could be achieved either by interrupting multiple specimens and performing metallographic sectioning, or by obtaining crack size measurements on a single specimen using either crack replication, or direct observation in a cyclic loading stage of a scanning electron microscope.

3.3.7.3   Exit Criteria Assessment for Fatigue Notch Predictions

The initial phase of the HCF program established exit criteria for both FOD and attachment fatigue model predictions [1]. Since the objective of the notch models

summarized in this section was to provide a predictive capability that could be applied to FOD and attachment fatigue, it is appropriate to use these FOD and attachment fatigue exit criteria to gage the success of the notch models. These exit criteria are expressed in terms of two statistical parameters—a mean ratio (A/P) of actual measured (A) to predicted (P) values, and a relative coefficient of variation (RCOV). The RCOV is the ratio of the coefficient of variation (COV) of the predicted results to the COV of baseline results, which consist of key materials' property data input needed to perform the predictions. For example, in the case of the WCN model, the baseline was the threshold stress intensity factor values (ΔK_{th}) as a function of load ratio (R); in the case of the Fs model the baseline was the multiaxial fatigue initiation data versus R and stress state. The COV values for both of the above baseline cases were found to be equal (COV = 0.100) [1] thereby simplifying the comparison of the two notch models. The ideal case of perfect agreement between A and P values is characterized by a mean ration (A/P) = 1 and a RCOV = 1. Values of the above statistical parameters for the WCN and Fs model predictions are summarized in Table 3.13, where they are compared to the Exit Criteria for FOD and attachment fatigue.

Table 3.13. Comparison of FOD and Contact Fatigue Exit Criteria Against Notch Model Predictions

FOD and Attachment Fatigue Exit Criteria		WCN Predictions	Fs Predictions
Mean ratio (A/P):	1 ± 0.15	1.11	0.80
RCOV:	< 2.5	1.32 [1]	1.19 [2]
COV:	---	0.132	0.119

[1] – The baseline COV for the WCN predictions is given by $\Delta K_{th}(R)$ with a COV = 0.100

[2] – The baseline COV for the Fs predictions is given by the multiaxial initiation parameter with COV = 0.100

The statistics for the WCN and Fs model predictions in Table 3.13 were determined by fitting the results to Weibull cumulative distribution functions as shown in Figure 3.83. For comparison, the baseline results for the case of $\Delta K_{th}(R)$ are also shown. (Results for the multiaxial initiation parameter are not shown but would have a similar slope to that of the $\Delta K_{th}(R)$ data since both baseline data sets have a COV = 0.100.)
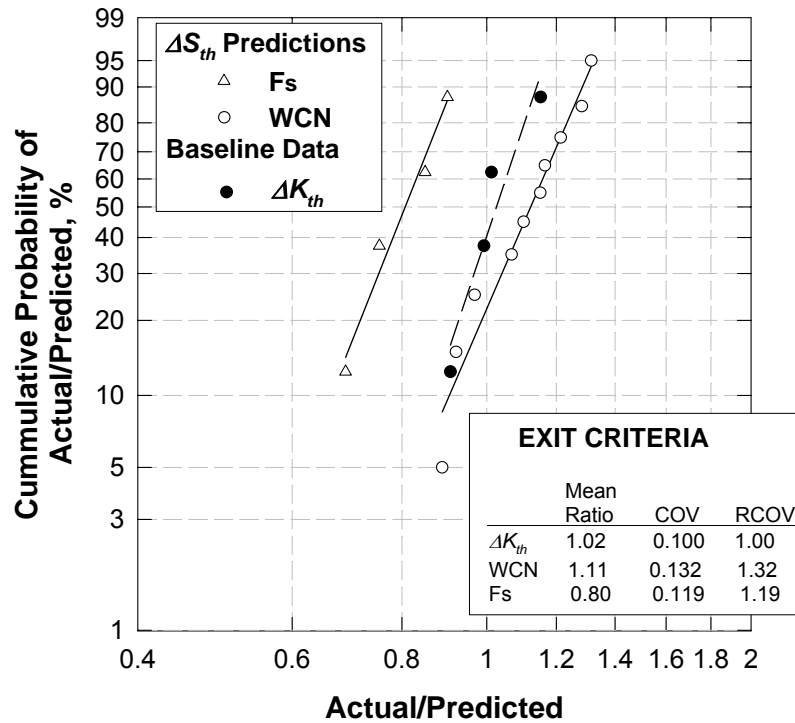
Figure 3.83. Comparison of Weibull plots for WCN and Fs model predictions. Baseline plot ΔK_{th} vs R data is also shown for comparison. The WCN model predictions meet the exit criteria, while the Fs model fails to meet the exit criteria due to its non-conservative predictions (A/P = 0.80).

In Figure 3.83, the decreased slopes of the notch model predictions relative to that of the baseline curve reflect the expected higher COV of the predictions versus the input baseline materials property data. The mean ratio (A/P) for each of the predictive models is given by the respective (A/P) value at 50% cumulative probability of occurrence. The fact that the curve for the WCN predictions falls to the right of the baseline curve and exhibits a mean ration (A/P) = 1.11 indicates that the WCN predictions are conservative with respect to the actual measured results by about 10%. In contrast, the curve for the Fs predictions is

110

to the left of the baseline curve and exhibits a mean ration (A/P) = 0.80 indicating that the Fs predictions are non-conservative with respect to the actual measured results by about 20%. Based on results in Table 3.13 and Figure 3.83 it can be concluded both the WCN and Fs predictions meet the RCOV exit criterion, however the mean ratio (A/P) criterion is only met by the WCN predictions and not met by the Fs predictions.

3.3.8   Threshold Stress Estimates using the Stressed-Surface-Area (Fs) Approach

It is well known that the use of the peak notch root stress, as calculated from the theoretical stress concentration factor, k_t, results in overly-conservative fatigue life predictions for notched components. Although there are likely numerous contributing factors, evidence suggests that the stress gradients near the notch play a significant role; i.e., the steeper the stress gradient, the more non-conservative the prediction using K_t. To account for this phenomenon, a common design methodology employs a fatigue notch factor, k_f, which corrects k_t as a function of the notch root radius for use in fatigue calculations.

An alternative technique for analyzing the fatigue characteristics of notched components makes use of the amount of highly stressed surface area in the vicinity of a notch. The stressed-surface-area, or Fs approach, accounts for the stress gradient effect through consideration of the stress distribution on the surface of a component in the vicinity of the notch. In applying this method, a factor is calculated that provides a correction to the peak notch root stress as determined by theoretical, numerical (e.g., FEA) or experimental techniques. The corrected notch root stress may then be used in conjunction with conventional fatigue life/strength prediction methods employed for unnotched components.

To evaluate the capabilities of the Fs method in predicting allowable long-life stress levels for simulated FOD specimens, the method was used to estimate the threshold (long-life) stress levels for the small-notch specimens tested by SwRI. An elastic finite element analysis was first performed for each specimen to obtain the peak notch root stress and the surface stress distribution across the specimen.

A geometry dependent factor, Fs_{notch}, was then calculated for each specimen as

$$Fs_{notch} = \sum_{i=1}^{n} \left(\frac{\sigma_{1,i}}{\sigma_{max}} \right)^{\alpha} A_i \tag{3.26}$$

where, the summation is performed over the elements in the model adjacent to a free surface of the specimen, $\sigma_{1,i}$ is the first principle stress on the free surface of element i (averaged at the nodes), A_i is the free-surface area of element i, σ_{max} is the maximum notch root stress, and α is a material constant obtained by correlating smooth and notched test data. Since Fs_{notch} is calculated from a ratio of stresses, it does not change appreciably with load level provided notch root yielding is small; thus, it was calculated from an elastic FEA solution. This factor was then used to determine the adjusted notch root stress,

$$\sigma_{notch}^{Fs,adjusted} = \left(\frac{Fs_{notch}}{Fs_{ref}} \right)^{1/\alpha} \sigma_{notch}^{peak} \tag{3.27}$$

where, Fs_{ref} is the value of Fs for a baseline axial specimen and σ_{notch}^{peak} is the peak notch root stress at a particular load level. The peak stress in Equation 3.27 must take into account localized yielding, and must therefore be calculated from an elastic-plastic finite element analysis. The adjusted notch root stress can then be used in conjunction with conventional stress-life data to estimate the corresponding fatigue life or fatigue limit load for a particular notched specimen.

In this analysis, the peak and adjusted notch root stresses were calculated in terms of the modified Manson-McKnight (MMM) equivalent stress for the cyclic loading condition, with $\alpha = 35$ and $Fs_{ref} = 0.161$. The following function was used to relate the MMM parameter to the fatigue life of Ti-6Al-4V:

$$0.5(\Delta\sigma_{psu})^w (\sigma_{max})^{1-w} = 3501.8N^{-0.5164} + 36.74N^{0.00068} \tag{3.28}$$

Equations 3.26 through 3.28 were used to estimate the nominal threshold stress levels for the notched specimens corresponding to a fatigue life of 10^7 cycles, assuming a stress ratio of R = 0.5.

The small-notch specimens tested by SwRI and modeled in this analysis consisted of a double-edge notched specimen with rectangular cross-section, with gross-section dimensions of 0.235 inch × 0.125 inch. The notch geometry is illustrated in Figure 3.84. For this analysis, notch dimensions (ρ and b) were chosen to correspond to the average measured notch dimensions of the specimens tested by SwRI. It should be noted that in many cases, the measured notch dimensions deviated substantially from the target values, and there were substantial deviations from the average for certain specimens within a group. Thus, direct comparison between the experimental and predicted threshold stress levels must be done with caution.
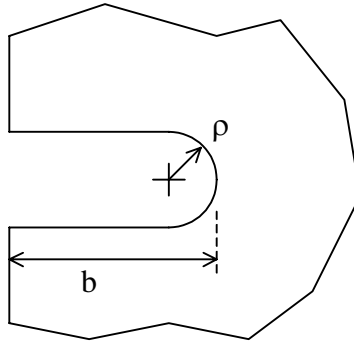
Figure 3.84. Small notch details.

The notch dimensions and associated elastic stress concentration factors for the notched specimens considered in this study are shown in Table 3.14. These notch dimensions correspond to the eleven configurations of notch-type 1 originally identified for testing by SwRI. The stress concentration factors were calculated from the elastic FEA solution. Two values of k_t are included in the table for each specimen, one based on the net-section area through the notch (the traditional definition of k_t), and the other based on the gross-section area (0.235 inch × 0.125 inch). The net-section k_t values range from approximately 2.7 to 5.

Threshold stress estimates were generated using the Fs approach for the eleven notched specimens listed in Table 3.14. Due to experimental difficulties, not all notch configurations were ultimately tested. The predicted threshold stress levels, based on the gross cross-section dimensions, are shown in Table 3.15. Also included in this table, where applicable, are the experimentally determined values obtained by SwRI, for notches of

113

similar dimensions. The experimental values represent the 10^7-cycle notch fatigue strength at R = 0.5 obtained using a step-test approach.

Table 3.14. Small Notch Dimensions and Elastic Stress Concentration Factors

Notch ID	ρ (in)	b (in)	k_t (net section)	k_t (gross section)
1	0.0047	0.0041	2.94	3.04
2	0.0049	0.0080	3.59	3.86
3	0.0035	0.0023	2.70	2.76
4	0.0038	0.0085	4.07	4.39
5	0.0054	0.0040	2.77	2.87
6	0.0064	0.0080	3.24	3.48
7	0.0062	0.0230	4.56	5.67
8	0.0064	0.0490	4.99	8.55
9	0.0090	0.0090	2.96	3.21
10	0.0090	0.0240	3.94	4.95
11	0.0090	0.0500	4.27	7.43

Table 3.15. Threshold Stress Estimates for Small Notched Specimens Using the Fs Approach

	Predicted				Experimental			
No.	ρ (in)	b (in)	σ_{max} (ksi)	$\Delta\sigma$ (ksi)	$\Delta\sigma$ (ksi)	Spec. ID	ρ (in)	b (in)
1	0.0047	0.0041	51.0	25.5				
2	0.0049	0.0080	39.6	19.8				
3	0.0035	0.0023	57.4	28.7				
4	0.0038	0.0085	35.0	17.5				
5	0.0054	0.0040	53.0	26.5				
6	0.0064	0.0080	43.2	21.6	16.3	153-39	0.0064	0.0089
7	0.0062	0.0230	26.2	13.1	11.1	153-42	0.0060	0.0236
8	0.0064	0.0490	17.5	8.75	6.0	153-43	0.0064	0.0495
					7.9	153-44	0.0064	0.0484
9	0.0090	0.0090	45.4	22.7				
10	0.0090	0.0240	29.5	14.75				
11	0.0090	0.0500	19.9	9.95				

Although limited in number, the comparisons between experimental and predicted threshold stress levels provide some useful information concerning the capabilities and accuracy of the Fs approach. In all cases, the predicted threshold stress levels exceeded the experimental values. However, the differences between the actual and modeled notch dimensions may have contributed to the discrepancies to some degree. For example, in case

#6, the actual notch depth was approximately 10% greater than the modeled value. This would increase the effective stress concentration factor, thereby reducing the nominal threshold stress level. The differences in notch dimensions were less severe in the other cases.

Despite being slightly non-conservative, the predicted threshold stress levels obtained using the Fs approach for the small-notched components can be considered to be reasonably accurate. This indicates that the stressed-surface area (Fs) method has the capability to account for the steep stress gradients encountered in the vicinity of small notches, such as may result from foreign object damage to fan and compressor blades. More details on the implementation of the Fs approach may be found in Appendix G.

3.3.9   Critical Plane Modeling of Notched Ti-6Al-4V HCF Data at 500°F

HCF testing for the notched (k_t = 2.5) Ti-6Al-4V (AMS 4928) material was conducted at 500°F, and the data are shown in Figure 3.85. The tests were conducted at R = 0.1, 0.5, and 0.8. Some of the R = 0.8 and 0.5 specimens were fatigued to 10^7 cycles at a lower stress level and then further cycled at a higher stress until failure. The step-test formula was used for these specimens to account for the damage accumulation during the initial cycling and also to determine the stress level at which specimen failure would occur after 10^7 cycles.

The data in Figure 3.85 was analyzed using the Smith-Watson-Topper (SWT) and the Findley critical plane models. The effect of plasticity at the notch was accounted for by using the cyclic stress-strain curve for Ti-6Al-4V at 500°F (from the Pratt & Whitney database) along with the Glinka notch shakedown code GG3. The results for the SWT parameter calculated at the notch tip are shown in Figure 3.86. The correlation of the different R-ratios using the SWT parameter is reasonably good. However when compared to the SWT curve-fit for the 500°F smooth data, there seems to be a shift between the smooth and notch curves. Using the concept of the a_o parameter, it was shown for the Ti-6Al-4V RT data that the smooth and notched curves correlated better when the damage parameter was calculated at a distance a_o from the notch tip. For the 500°F data, it was decided to use a_o = 0.0033 inch based on earlier studies at RT.

115

S-N Curves for Ti-6-4, K_t = 2.5, 500 F
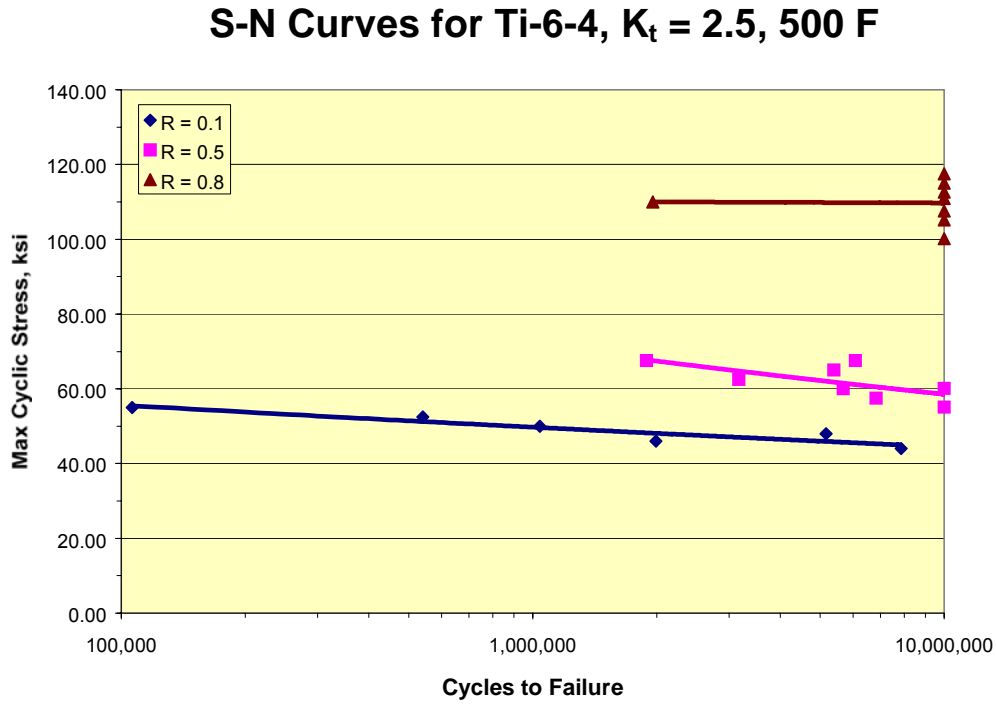
Figure 3.85. Max cyclic stress versus life curves for notched Ti-6Al-4V tested at 500°F.

Notch Tip SWT Damage Parameter
K_t = 2.5, 500 F
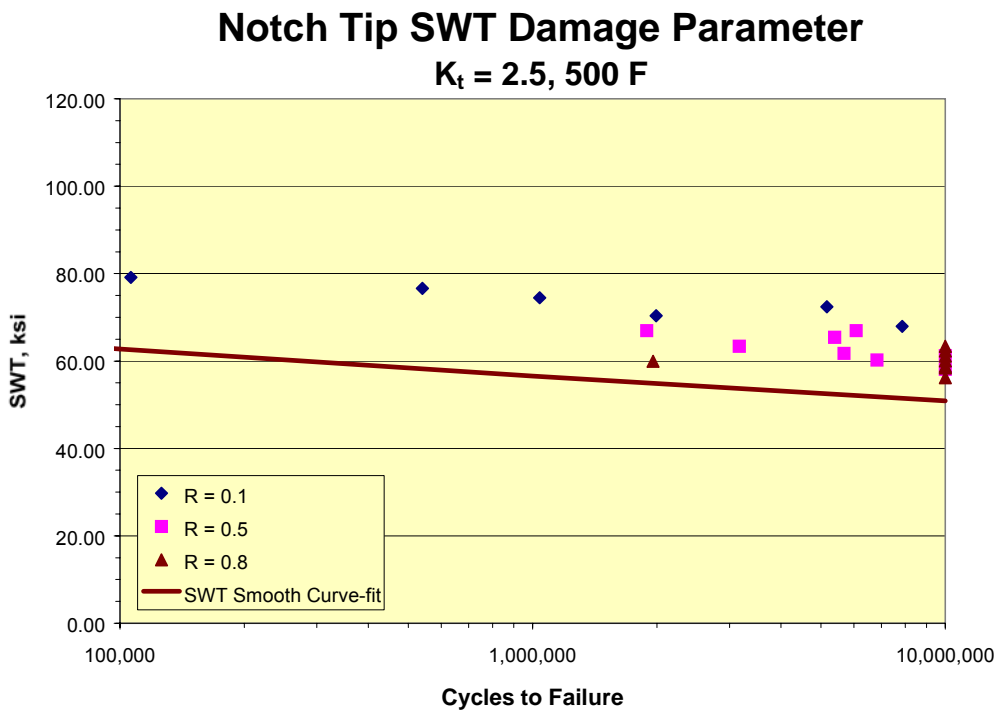
Figure 3.86. SWT parameter calculated at notch tip for Ti-6Al-4V.

Figure 3.87 shows the SWT parameter calculated at this value of a_o. The correlation between the smooth and the notched data is much better by using notch stresses and strains at $a_o = 0.0033$ inch to calculate the SWT damage parameter.

SWT Parameter at 0.0033" from Notch Tip
K_t = 2.5, 500 F
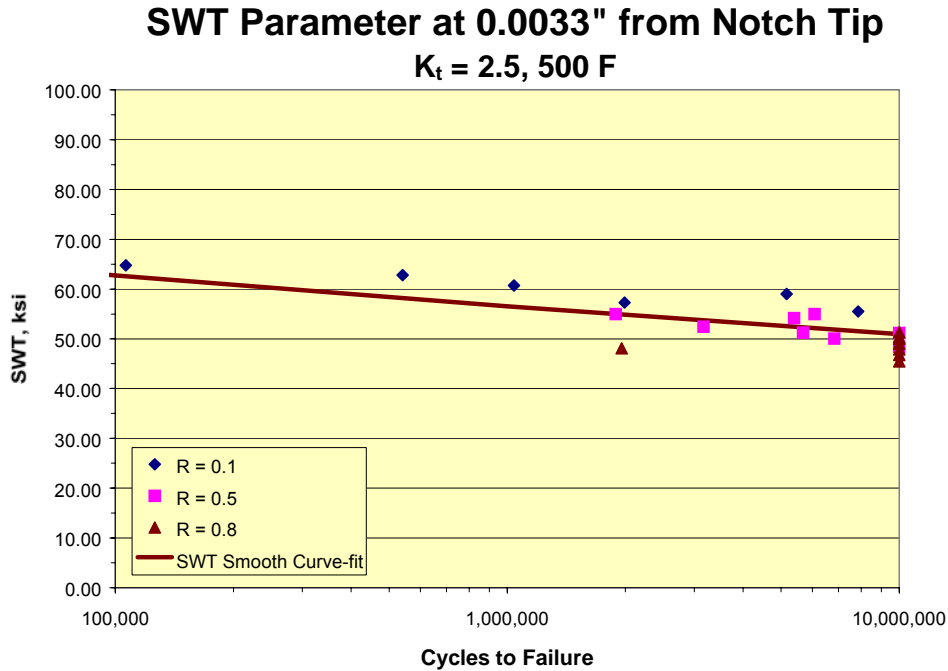
Figure 3.87. SWT parameter calculated at 0.0033" from notch tip for Ti-6Al-4V.

The results for the FIN parameter ($k = 0.26$) calculated at the notch tip are shown in Figure 3.88. This optimized value of k was obtained as that value which minimized the square of the difference between the FIN data value (for all the different R-ratios) and the curve-fit. The correlation of the different R-ratios using the FIN parameter is reasonably good. However when compared to the FIN curve-fit for the 500°F smooth data, there seems to be a slight shift between the smooth and notch curves. Figure 3.89 shows the FIN parameter calculated at the same value of $a_o = 0.0033$ inch.

The correlation between the smooth and the notched data is slightly better using notch stresses and strains at $a_o = 0.0033$ inch to calculate the FIN damage parameter. However, this correlation could be improved by using a slightly lower value for a_o

Notch Tip FIN Damage Parameter
K$_t$ = 2.5, 500 F
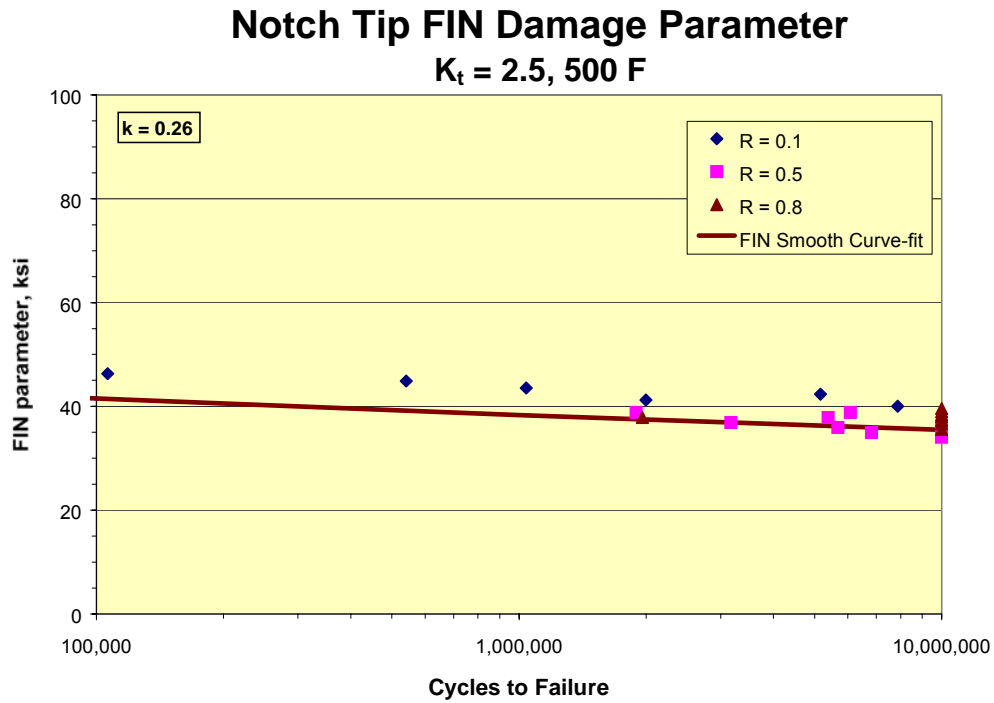
Figure 3.88. FIN parameter calculated at notch tip for Ti-6Al-4V.

FIN Parameter at 0.0033" from Notch Tip
K$_t$ = 2.5, 500 F
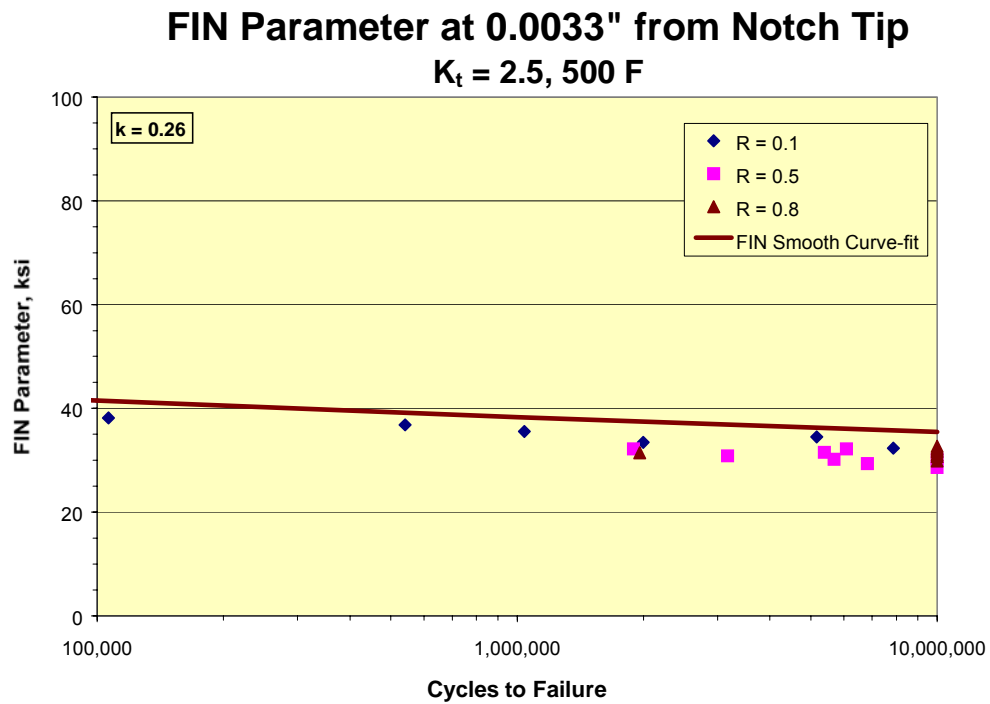
Figure 3.89. FIN parameter calculated at 0.0033" from notch tip for Ti-6Al-4V.

3.4   FOREIGN OBJECT DAMAGE (FOD)

3.4.1   Introduction to Foreign Object Damage (FOD)

Foreign object damage (FOD) occurs when objects such as sand, stones, workman's tools, or other debris are ingested into an engine. These events take place typically upon takeoff and landing. In the earlier program, assessments were made of the nature of the damage found in some typical airfoil components. The damage is typically in the form of a notch covering a wide range of notch depths, radii, and possible cracking at the root of the notch. In addition to characterizing the notch geometry, residual stresses were calculated for several different impact conditions and were found to vary with the angle of impact. In parallel studies, microstructural damage was found to occur below the surface of severe impacts. The severity of a notch, from a geometric point of view, is characterized by a stress concentration factor, which, under FOD, can vary significantly in service. This is clearly illustrated for the case of service-induced FOD, shown in Figure 3.90, where damage can range from dents, to sharp tears, to rounded and v-shaped notches of varying depths.
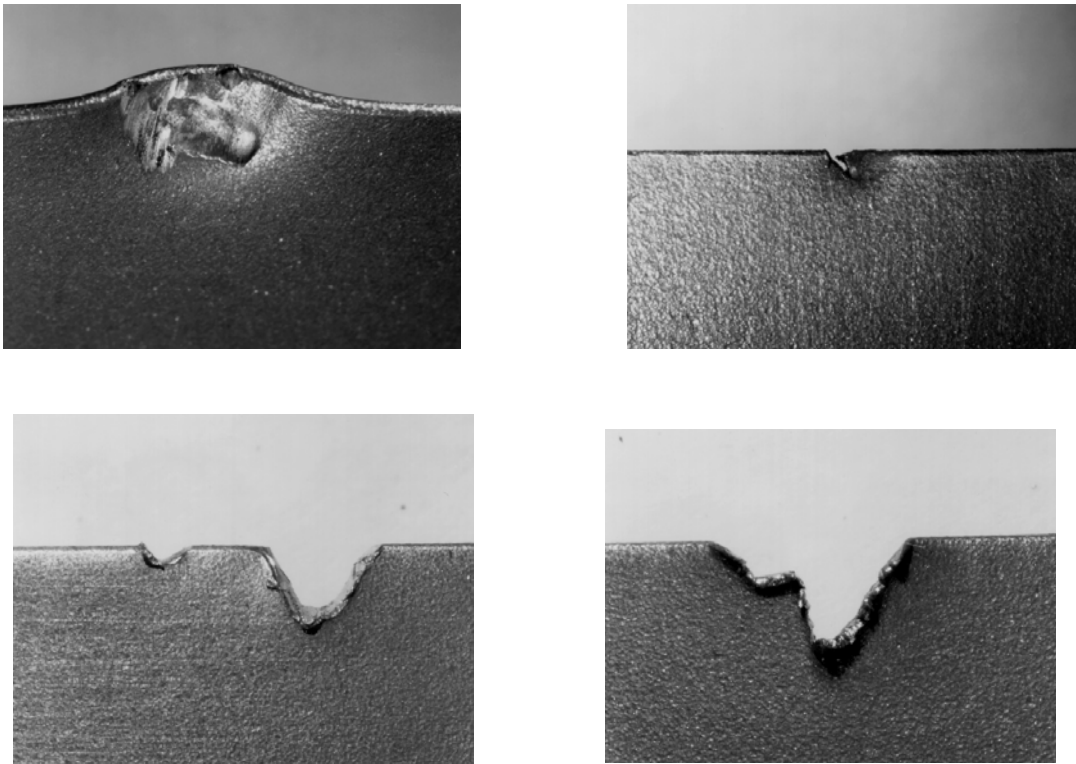
Figure 3.90.   Examples of dents, gouges, and notches produced by FOD at leading edge of a fan blade (10X Mag.).

As shown in Figure 3.91, surveys of service-induced FOD have confirmed the wide variation in FOD depth [6,19].
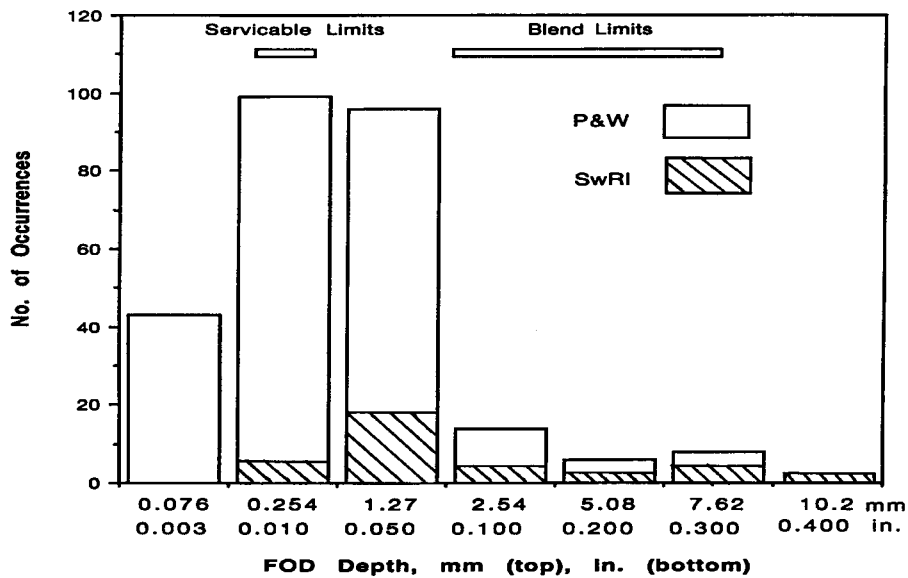
Figure 3.91. Distribution of service-induced FOD depth from several surveys.

These variations in overall FOD geometry result in a wide range of elastic stress concentration factors (k_t) as shown in Figure 3.92 [19].
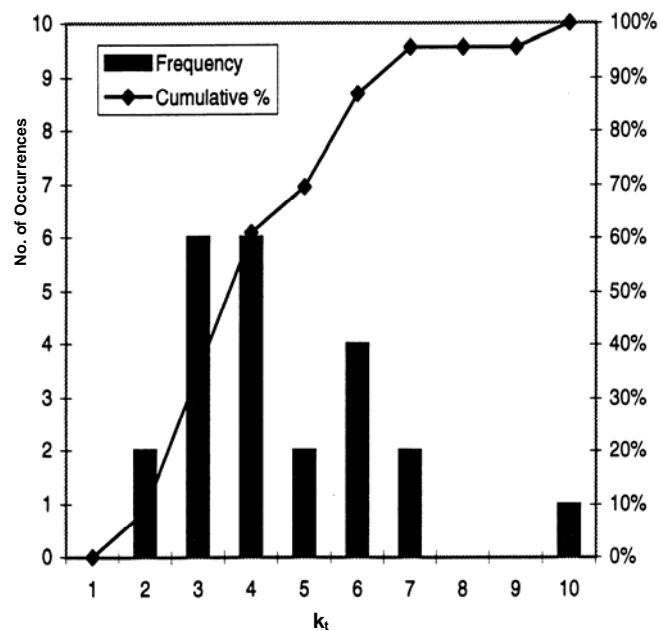
Figure 3.92. Distribution of elastic stress concentration values for service-induced FOD from the SwRI survey.

Thus, robust engineering methods are needed to predict the influence of these geometric variables on HCF threshold stresses. In this section, analytical and experimental investigations are described where the fatigue limit strength of a material subjected to real or simulated FOD is characterized. In addition to the experiments and modeling, a perturbation study is carried out analytically to assess the fatigue strength under a range of geometric variables associated with the FOD event.

3.4.2   Foreign Object Damage Methods

3.4.2.1   Test Specimen Geometries to Simulate FOD

Different test specimen geometries were used to simulate leading edge airfoil geometries. The axial specimen geometry is shown in Figure 3.93. This specimen was tested under axial applied loads. The edges of the specimen were machined with a 12-mil root radius that is simulative of a blunt tip airfoil leading edge geometry. The bending specimen geometry is shown in Figure 3.94. This specimen is tested under 4-point bending to simulate the stress gradients in an airfoil. The edge of this specimen was machined with 7- mil or 14-mil root radii to simulate a sharp and blunt tip airfoil geometry.
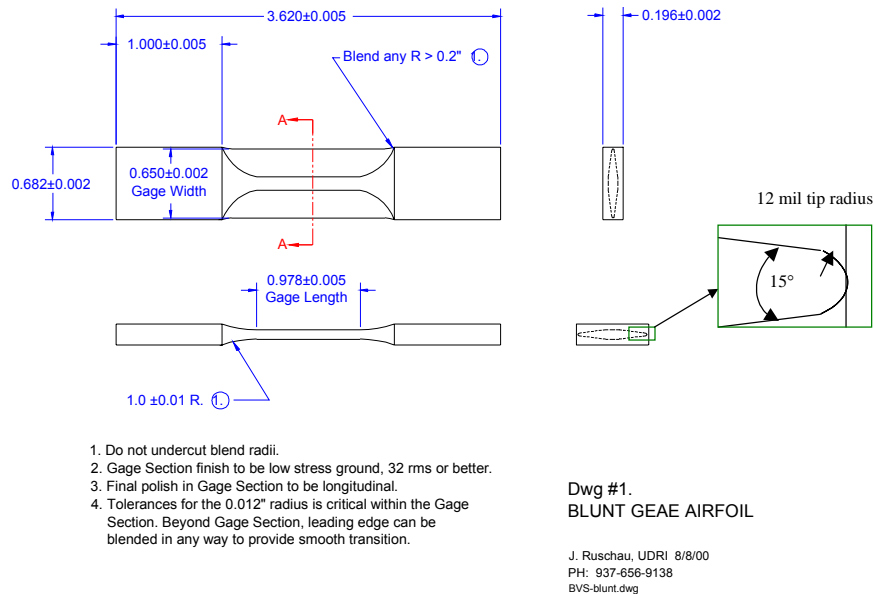
Figure 3.93. Axial loaded specimen to simulate a blunt tip airfoil leading edge.

FOUR POINT BENDING SPECIMEN

LENGTH (6.00 in.)
WIDTH (0.6 in.)
L1 (1.0 in.)
HEIGHT (0.2 in.)
L2 (2.0 in.)

SHARP TIP DETAIL

TIPLENG (0.25 in.)
RAD 0.014 (IN.)
THKROOT (0.032 in.)
RADTIP 0.007 (IN.)

BLUNT TIP DETAIL

TIPLENG (0.25 in.)
RAD 0.014 (IN.)
THKROOT (0.090 in.)
RADTIP 0.014 (IN.)
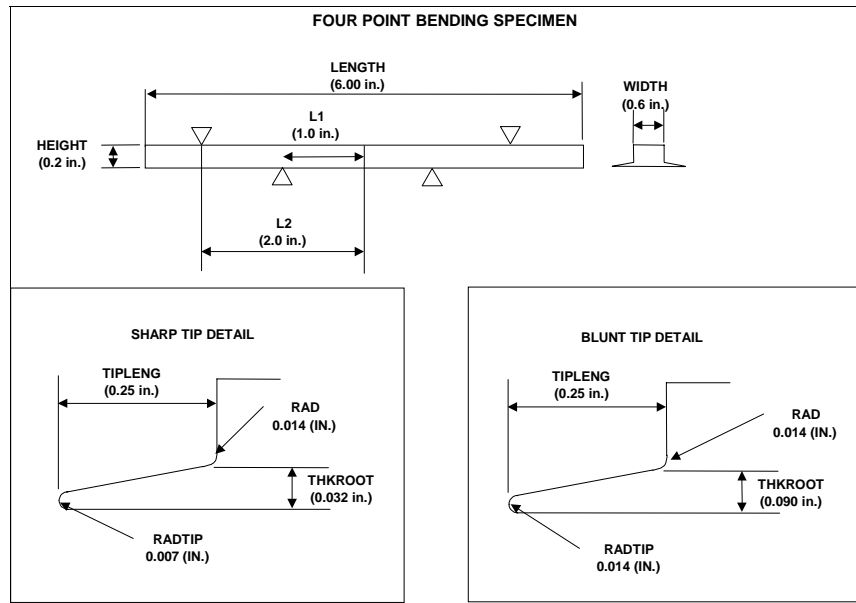
Figure 3.94. Bend bar simulating sharp and blunt airfoil leading edge.

3.4.2.2   Simulated FOD Characterization

Airfoil FOD was simulated at the edge of the axial and bending specimens with a steel chisel indenture fired from a solenoid gun. The solenoid gun provides a relative high velocity impact compared to techniques like a pendulum with much better control and repeatability than ballistic impact methods. The FOD indenture had a nominal root radius of 5 mils with a 60° included angle. FOD at ~10 mils deep with a 30° impact angle is shown with different views in Figure 3.95. Note in Figure 3.95(b) the onset of shear cracks in the material being extruded during the FOD introduction process. FOD at ~20 mils deep is shown with different views in Figure 3.96. Numerous shear cracks were observed on the flanks of the FOD damage in the extruded material, but no tears or cracks were observed at the root of the FOD notches. Fatigue tests were run for specimens with simulated FOD to establish the HCF capability of specimens with FOD.

(a)   (b)
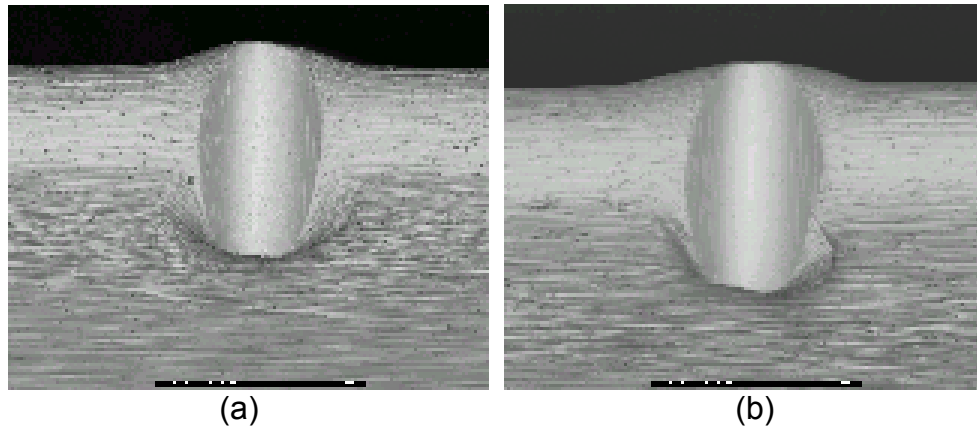
Figure 3.95. SEM micrographs of FOD damage with a nominal depth of 10 mils
              introduced at 20 degrees into a blunt tip Ti-17 axial FOD specimen.

(a)   (b)
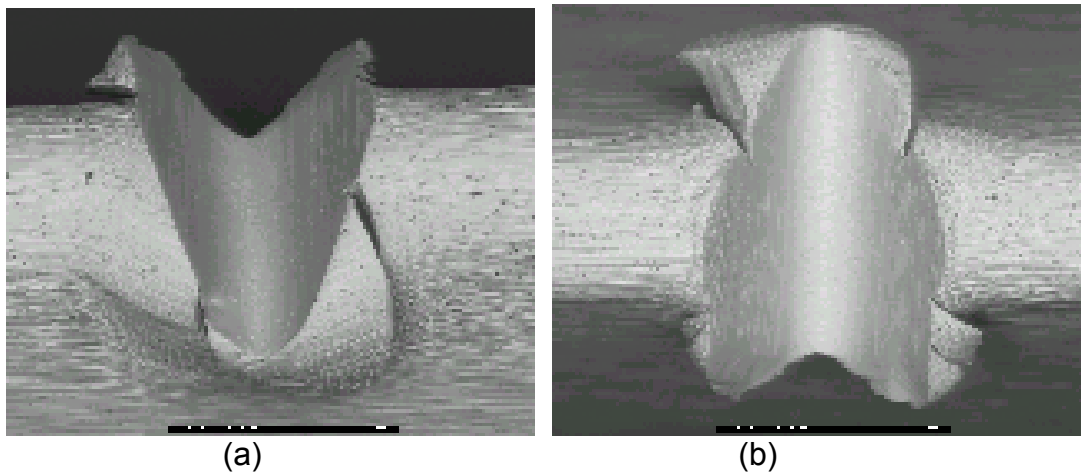
Figure 3.96. SEM micrographs of FOD damage with a nominal depth of 20 mils
              introduced at 20 degrees into a blunt tip Ti-17 axial FOD specimen.

Post-test fractography was used to measure the FOD depth and impact angle as schematically shown in Figure 3.97. The FOD depth was determined with a line normal to the FOD as a notch depth profile. The FOD impact angle was determined from a line normal to the FOD impact with respect to a line tangent to the specimen leading edge face. An example of deep FOD in a sharp tip bend specimen is given in Figure 3.98. Lines to obtain the FOD impact angle and depth are shown schematically. An example of shallow FOD in the blunt tip bend specimen is given in Figure 3.99. FOD depths and angles have been obtained with fractography for all failed specimens for FOD modeling. Pre-test FOD dimensions were used for modeling when failure was not at the FOD impact.
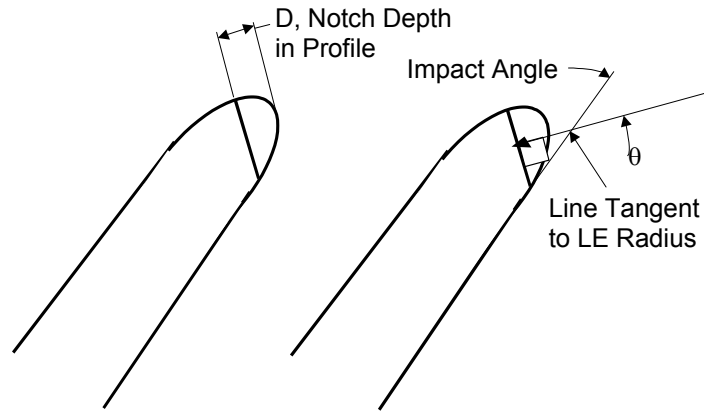
Figure 3.97. Schematic view of FOD depth (D) and impact angle (θ) as measured on fracture planes.

01-13

D: FOD depth

θ: FOD angle
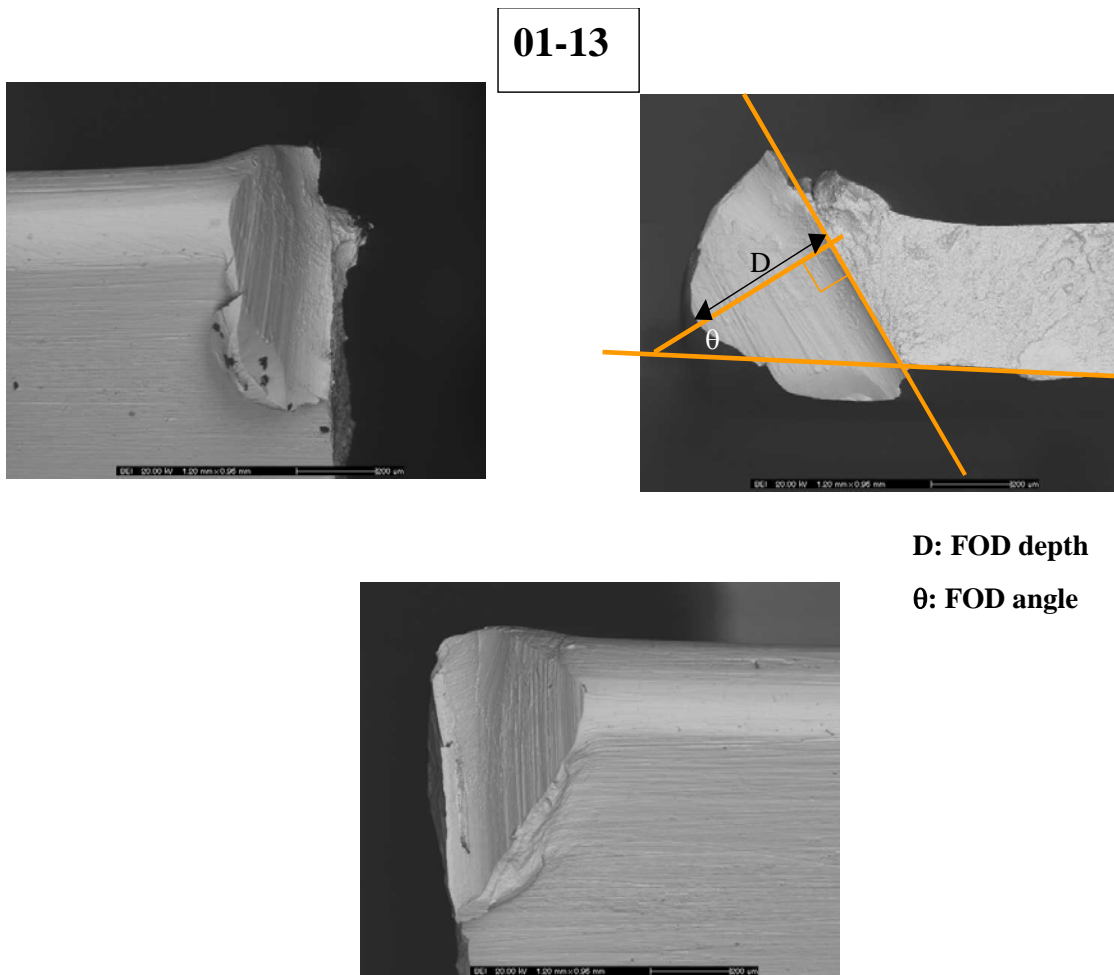
Figure 3.98. Fractography for deep FOD in the sharp tip geometry for specimen 1-13S. D is the FOD depth and θ represents the FOD orientation.

01-45
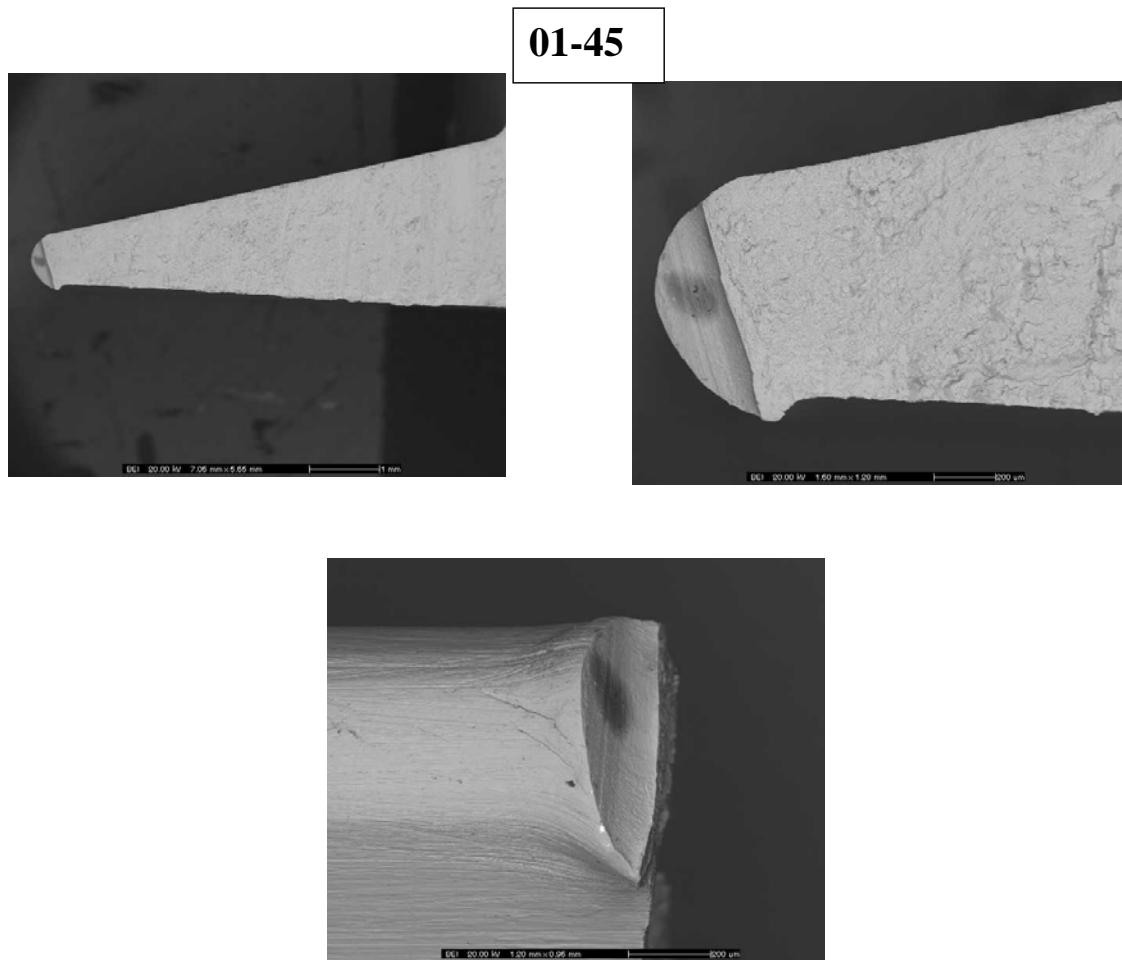
Figure 3.99. Fractography for shallow FOD in the blunt tip geometry for specimen 1-45B.

3.4.2.3   Test Matrix and the HCF Capability of Specimens with Simulated FOD

The Ti-17 axial FOD tests were run at UDRI. The axial specimen test matrix is summarized in Table 3.16.

Table 3.16. Summary of the Axial FOD Test Matrix

Axial FOD Specimens	R= -1.0, As-FODed	R= -1.0, FODed+SR	R= 0.5, As-FODed
10 deg FOD impact	6	4	
30 deg FOD impact	6	6	3
50 deg FOD impact	6	4	

Fatigue tests were predominately run at R= -1 to match HCF validation test conditions (Ti-17 FOD validation testing). Each of these tests was designed to be 10^7 cycle step tests.

Three different FOD impact angles were evaluated for the axial tests in the as-FODed and FODed+stress relief (SR) condition. The as-FODed case is most relevant for engine applications. Tests with FOD+SR were used for methods assessment for cases where residual stresses were minimized with a stress relief in a vacuum furnace for eight hours at 1130°F after the FOD impact. The Ti-17 bending tests were run at Cincinnati Test Lab on Sontag machines under the direction of GEAE. The bending specimen test matrix is summarized in Table 3.17. Each of these tests was designed to be a 10^6 cycle step test. Bending tests were run at one nominal impact angle for sharp and blunt tip leading edge geometries. Tests were run for the geometries in the as-FODed and FODed+SR conditions.

Table 3.17. Summary of the Bending FOD Test Matrix

Bending FOD Specimens	R= -1.0, As-FODed	R= -1.0, As-FODed
Sharp Tip, 30 deg FOD impact	6	4
Blunt Tip, 30 deg FOD impact	5	4

The HCF results are given as k_f as a function of geometry, impact angle, stress relief, and the FOD depth. k_f is defined as Sequiv with the smooth specimen curve (Figure 3.100) for the test life normalized by Sequiv at the specimen failure stress calculated for the unnotched condition.
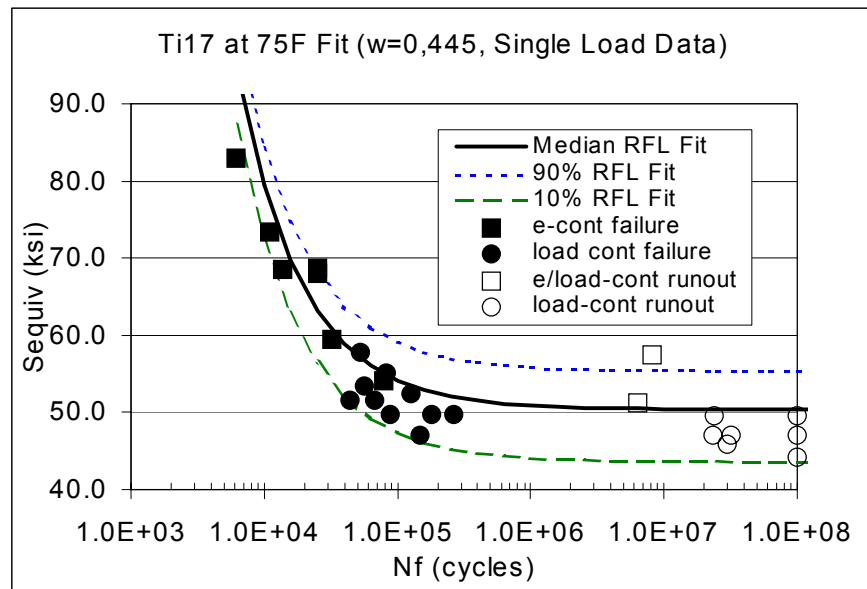
Figure 3.100. Ti-17 fatigue tests average fatigue curve at 75°F.

Calculated k_f for axial and bending tests are given in Figures 3.101 through 3.102. These results indicate significant scatter, but clearly show several trends. Increasing FOD depth and increasing impact angles increases k_f, thus reduces FOD tolerance to HCF. The blunt tip generally produced lower k_f or more HCF capability for FOD in the bend geometry. This data will be used to assess k_f predictions for specimens with FOD.
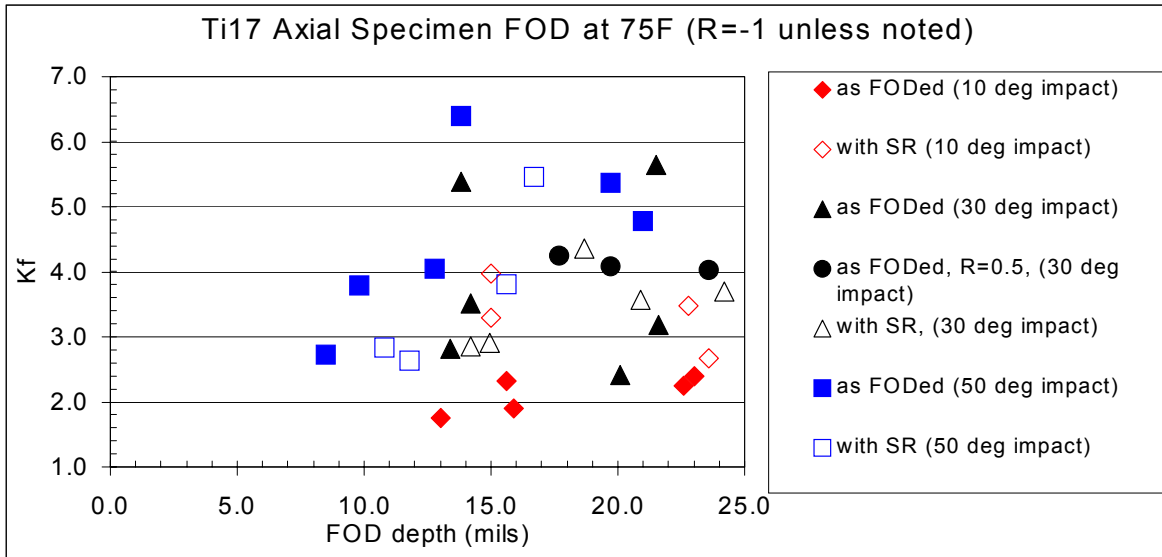
Figure 3.101. Variation in k_f with FOD depth for room temperature Ti-17 axial FOD step tests that were successfully completed.
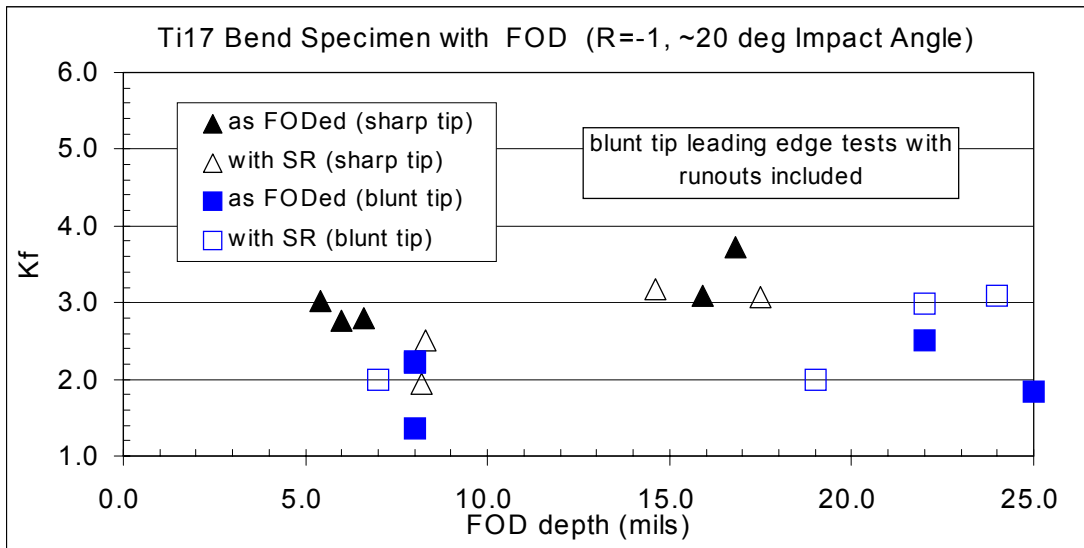
Figure 3.102. S max as a function of the estimated FOD depth for pizza hut specimens.

3.4.2.4   Stress Analysis

        3D elastic and elastic-plastic stress analysis was performed with ANSYS for each FOD test. The FOD notch was modeled by subtracting an indenture volume from the base model (Figure 3.103). The average FOD notch root radius (4.4 mils) and flank angle (81°) are taken from FOD measurements prior to failure (Figure 3.104). The FOD depth and impact angle was measured from SEM micrographs of failed specimens (examples given in Figures 3.99 and 3.100). A 3D elastic-plastic stress analysis with ANSYS was performed for each specimen at the average interpolated failure loads. This analysis incorporates the skewed notch front, the notch V-shape, and the notch root radius.
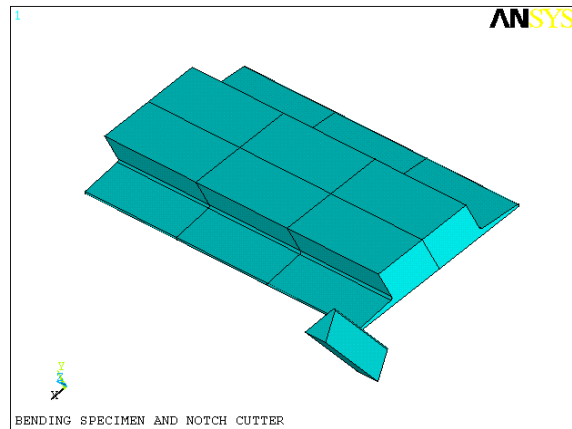
Figure 3.103. Example of the wedge impacting the specimen edge for FOD modeling.
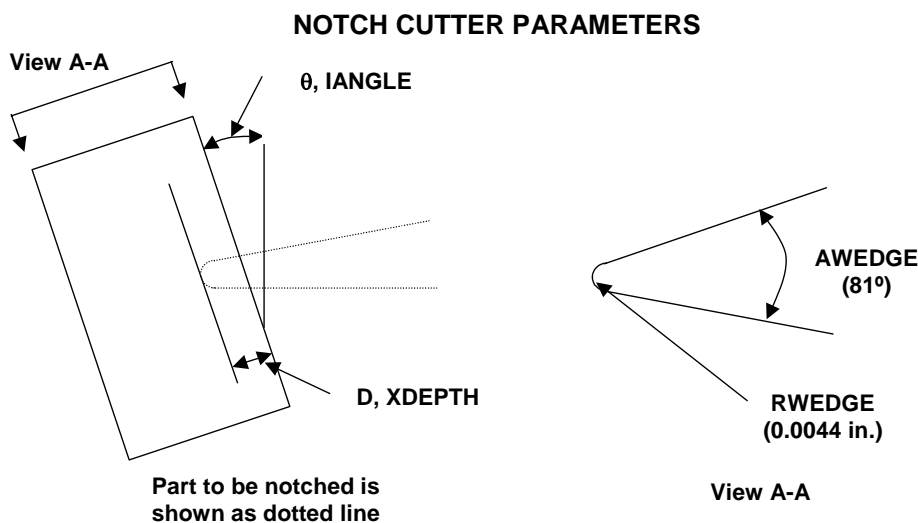
Figure 3.104. Cutting tool dimensions for FOD geometry modeling with ANSYS.

Elastic stresses in the axial FOD specimen for an intermediate FOD depth and a range of impact angles are shown in Figures 3.105 through 3.107. Elastic stresses in a blunt tip-bending specimen for a low and high impact depth are given in Figures 3.108 and 3.109. Elastic stresses in a sharp tip bending specimen for low and high impact depths are given in Figures 3.110 and 3.111. Elastic calculated k_ts as a function of FOD impact angle and depth of notch for the axial geometry are summarized in Figure 3.112. Elastic calculated k_ts as a function of FOD depth for the sharp and blunt tip geometries in bending are shown in Figure 3.113. The k_t correlation is also provided for life method assessments for FOD.
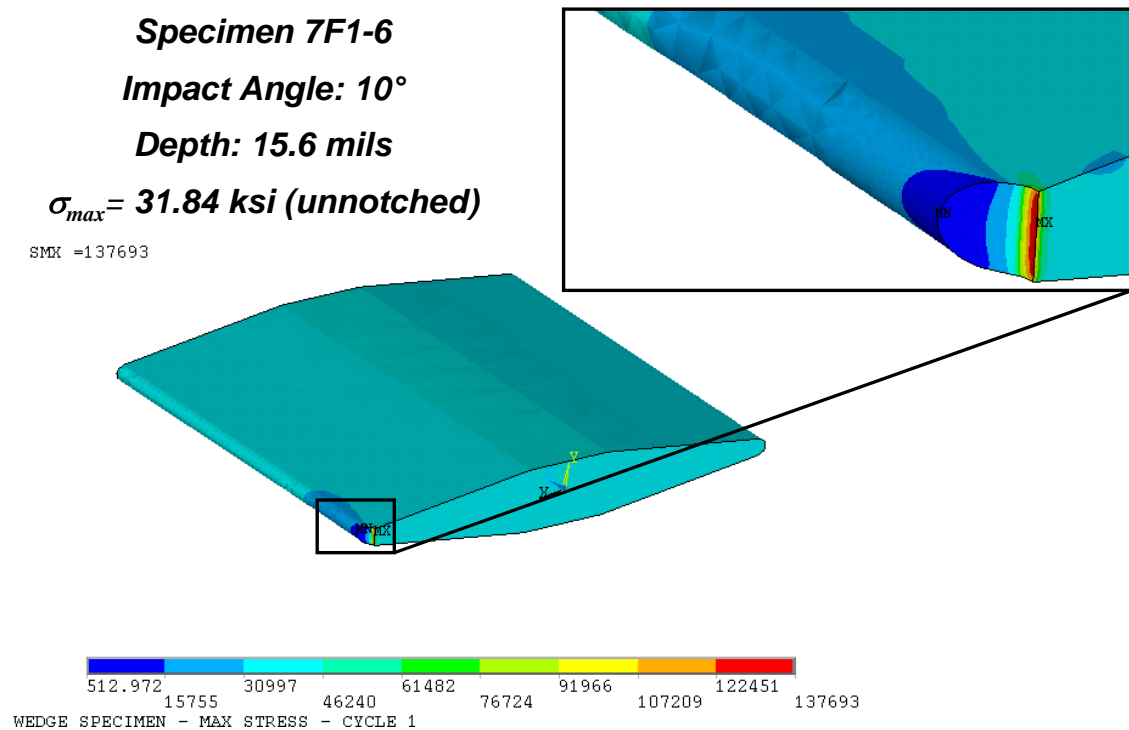
Figure 3.105. Stress analysis for axial FOD for a low FOD impact angle (Specimen 7F1-6).

129

Specimen 7F1N-55

Impact Angle: 30°

Depth: 14.2 mils

σ_{max}= **21.10 ksi (unnotched)**

SMX =90941

```
347.47        20479           40611           60743           80875
       10413          30545           50677           70809           90941
WEDGE SPECIMEN - MAX STRESS - CYCLE 1
```
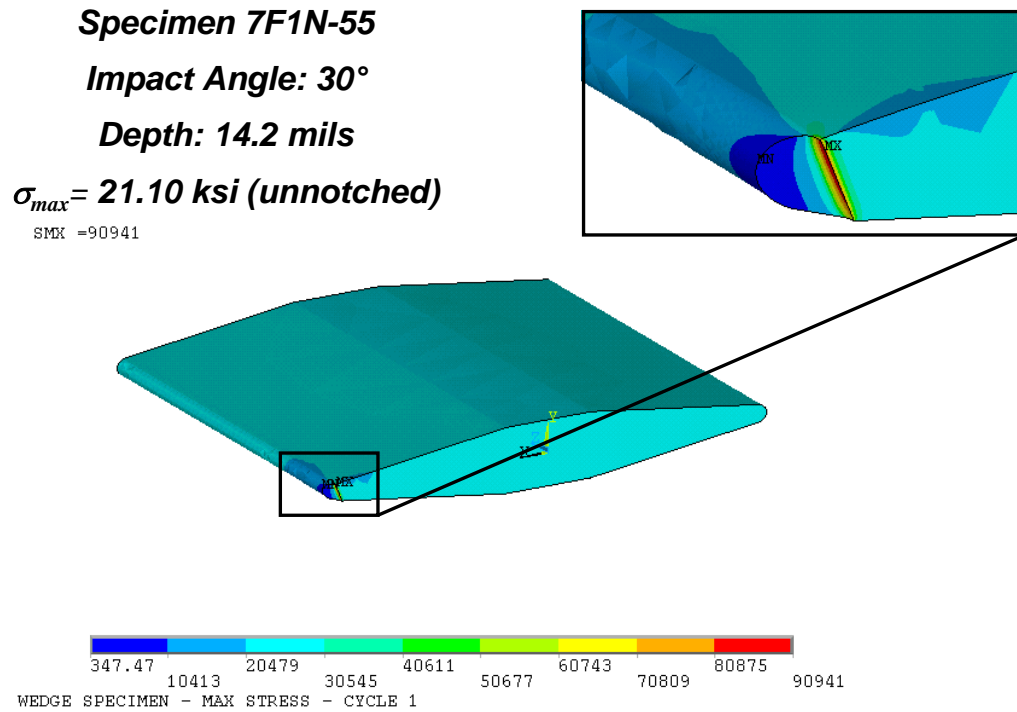
Figure 3.106. Stress analysis for axial FOD for an intermediate FOD impact angle (Specimen 7F1N-55).

Specimen 7F16-22

Impact Angle: 50°

Depth: 13.8 mils

σ_{max}= **11.16 ksi (unnotched)**

SMN =143.982
SMX =49538

```
143.982       11121           22097           33074           44050
       5632           16609           27585           38562           49538
WEDGE SPECIMEN - MAX STRESS - CYCLE 1
```
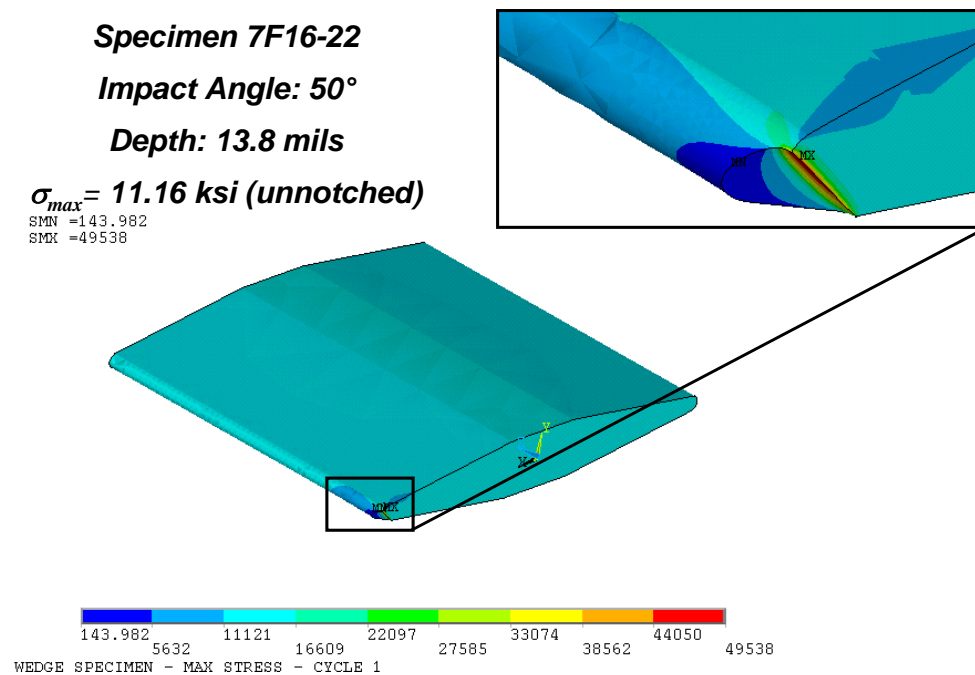
Figure 3.107. Stress analysis for axial FOD for a high FOD impact angle (Specimen 7F16-22).

130

Specimen 01-22S
Impact Angle: 28°
Depth: 5.4 mils
M_{max}= 129.57 in-lbs

ANSYS 6.0
APR 19 2002
14:32:40
.330212
7572
15143
22715
30286
37858
45429
53001
60572
68144
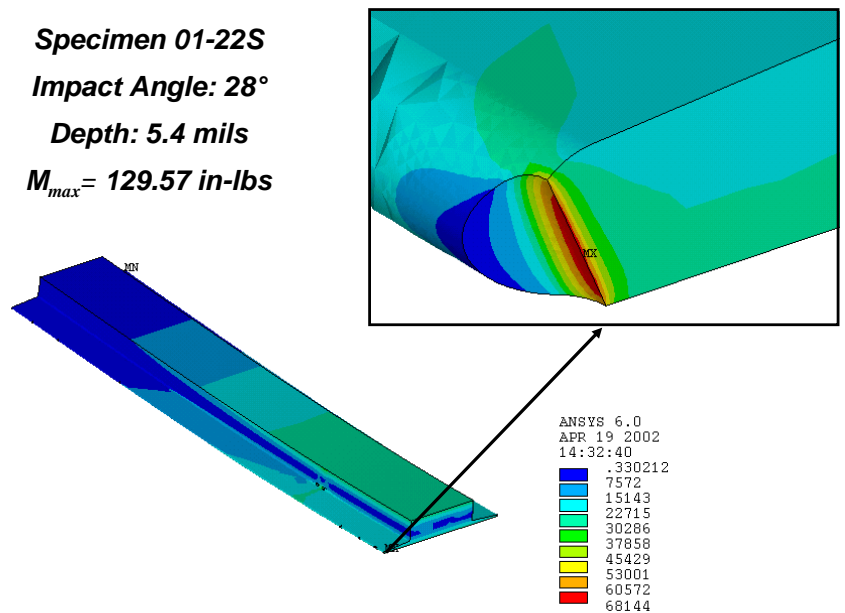
Figure 3.108. Stress analysis for bending-low FOD depth in a sharp tip geometry (Specimen 01-22S).

Specimen 01-20S
Impact Angle: 35°
Depth: 17.5 mils
M_{max}= 127.50 in-lbs

.322172
14232
28464
42696
56927
71159
85391
99623
113854
128086
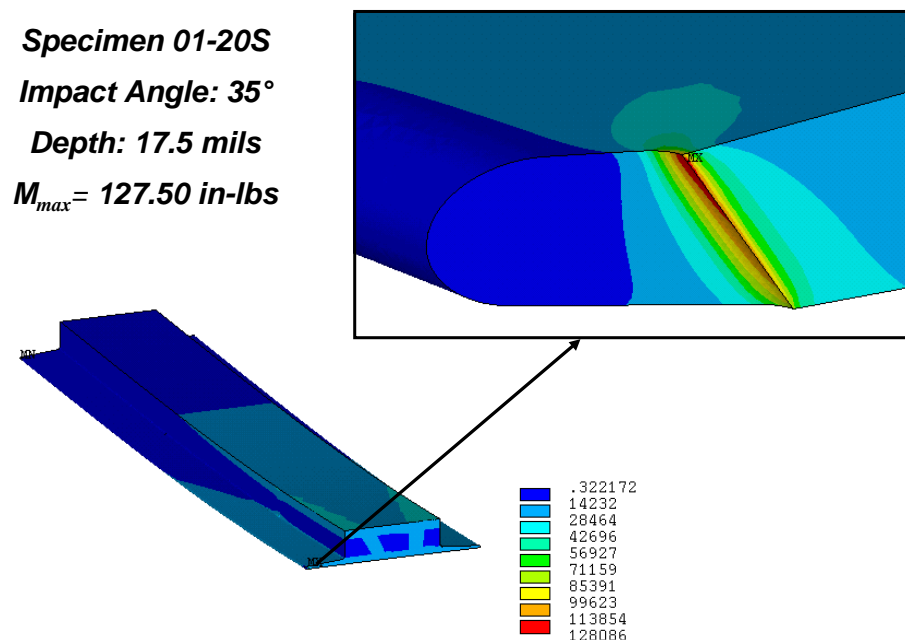
Figure 3.109. Stress analysis for bending-high FOD depth in a sharp tip geometry (Specimen 01-20S).

131

Specimen 01-45B
Impact Angle: 20°
Depth: 7.0 mils
M_{max} = **225.20 in-lbs**

	.780474
	11371
	22742
	34113
	45483
	56854
	68225
	79595
	90966
	102337
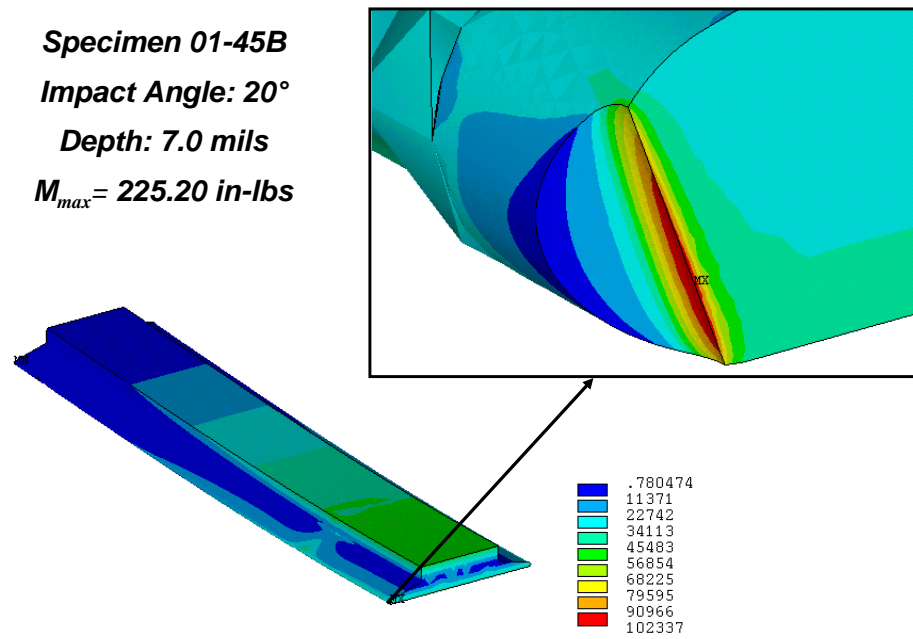
Figure 3.110. Stress analysis for bending-low FOD depth in a blunt tip geometry (specimen 01-45B).

Specimen 01-26B
Impact Angle: 22°
Depth: 22.0 mils
M_{max} = **106.69 in-lbs**

	.704596
	12054
	24106
	36159
	48212
	60265
	72318
	84371
	96424
	108476
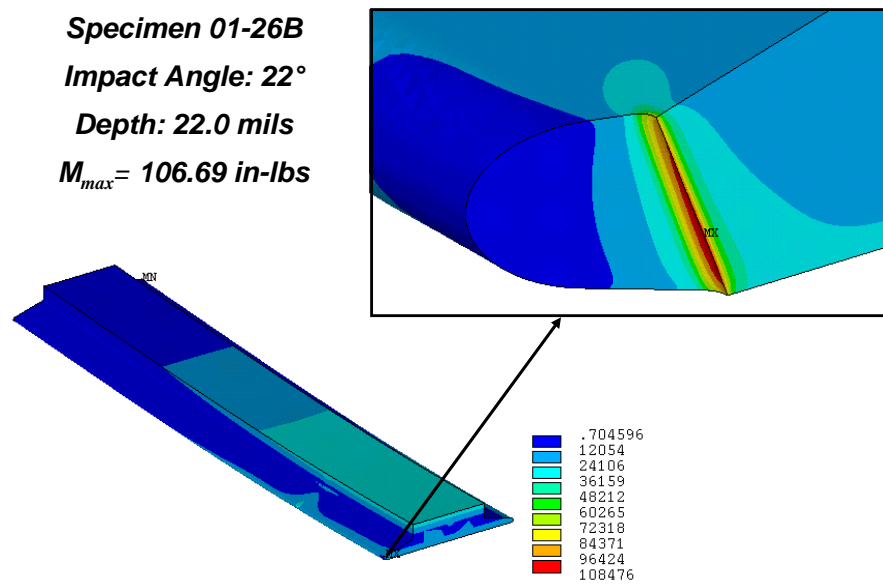
Figure 3.111. Stress analysis for bending for a high FOD depth in a blunt tip geometry (specimen 01-26B)
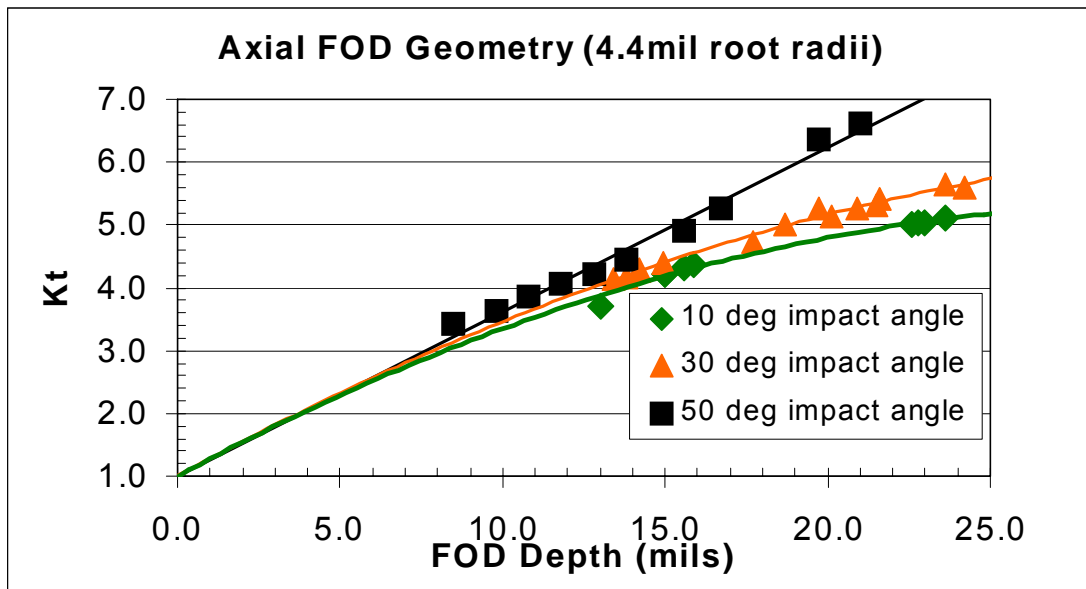
Figure 3.112.   Elastic calculated k_ts for measured FOD depths and
impact angles in the axial specimen geometry.
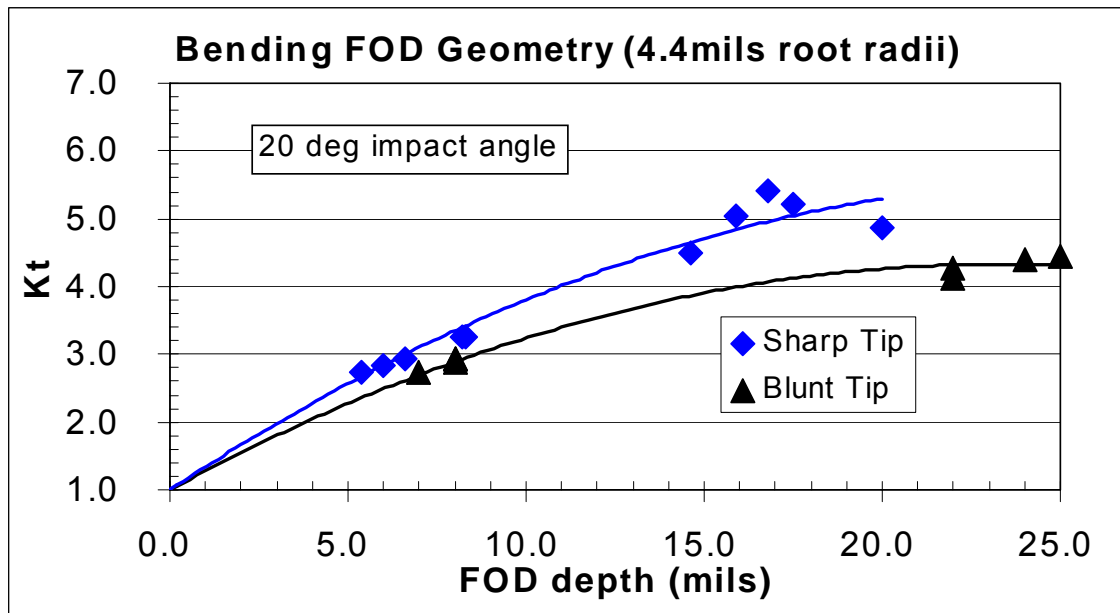
Figure 3.113.   Elastic calculated k_ts for measured FOD depths and impact
angles in the bend specimen geometry.

3.4.2.5 Predictions of Allowable HCF Limits for Specimens with FOD

　　　　Crack initiation methods were used to predict allowable HCF limits for FOD. The
baseline HCF capability for Ti-17 is taken from the smooth specimen correlation (Figure
3.100). The first prediction ignored the FOD stress concentration and damage. This
approach is easy to implement, but is inaccurate for FOD tests (Figure 3.114). This result is
generally non-conservative as expected. FOD decreases the fatigue capability of airfoil
geometries and needs to be accounted for with a FOD tolerant design system.

　　　　The next approach utilizes the calculated local peak stresses with the smooth
specimen fatigue curve. For this approach, stress components are obtained from the notch
geometry with maximum and minimum load cases at the interpolated loads with 3D elastic-
plastic stress analysis. This approach is generally conservative (Figure 3.115) as expected.
The local stress approach with smooth specimen fatigue curves under-predicts the HCF
capability of specimens for small notches (Figure 3.116).
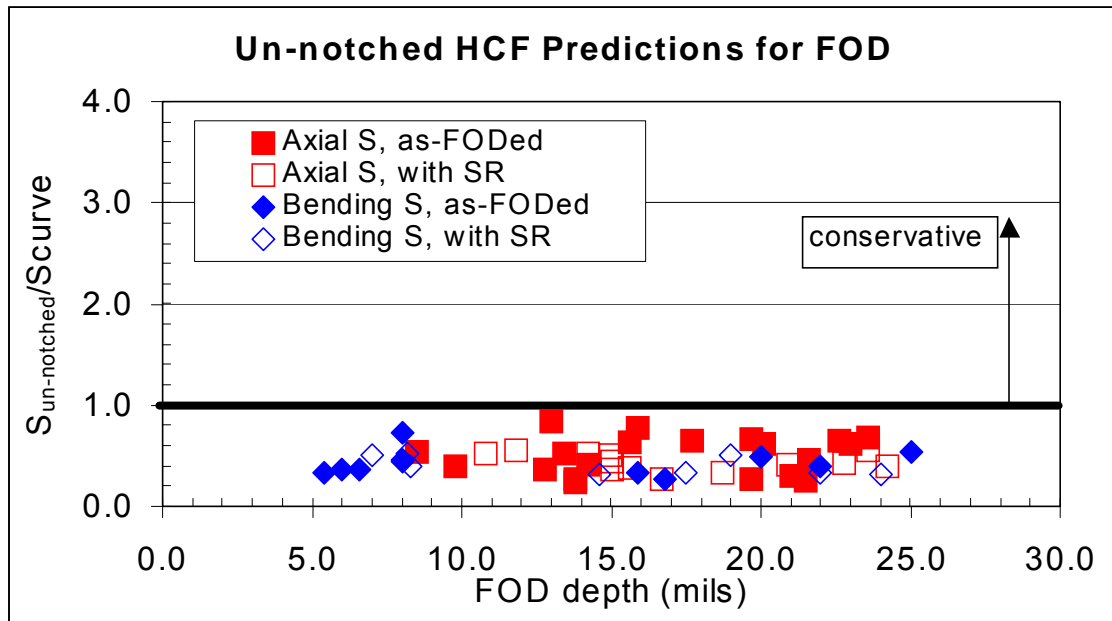
Figure 3.114. Prediction of the HCF capability of specimens with FOD
　　　　　　　　using the unnotched stresses.
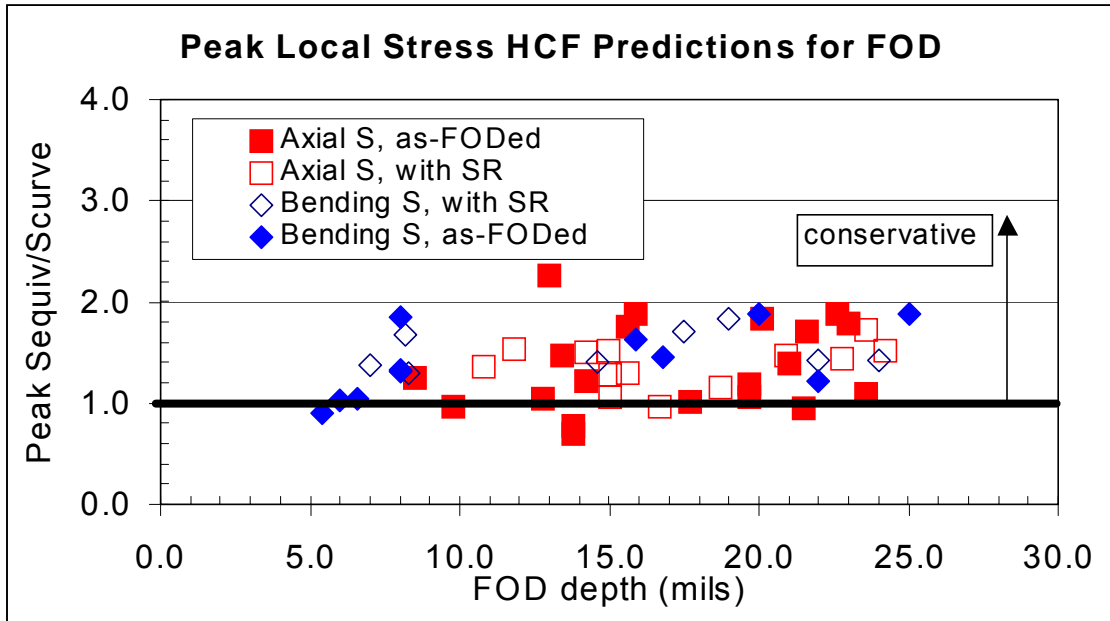
Figure 3.115. Prediction of the HCF capability of specimens with FOD from the peak concentrated stress.
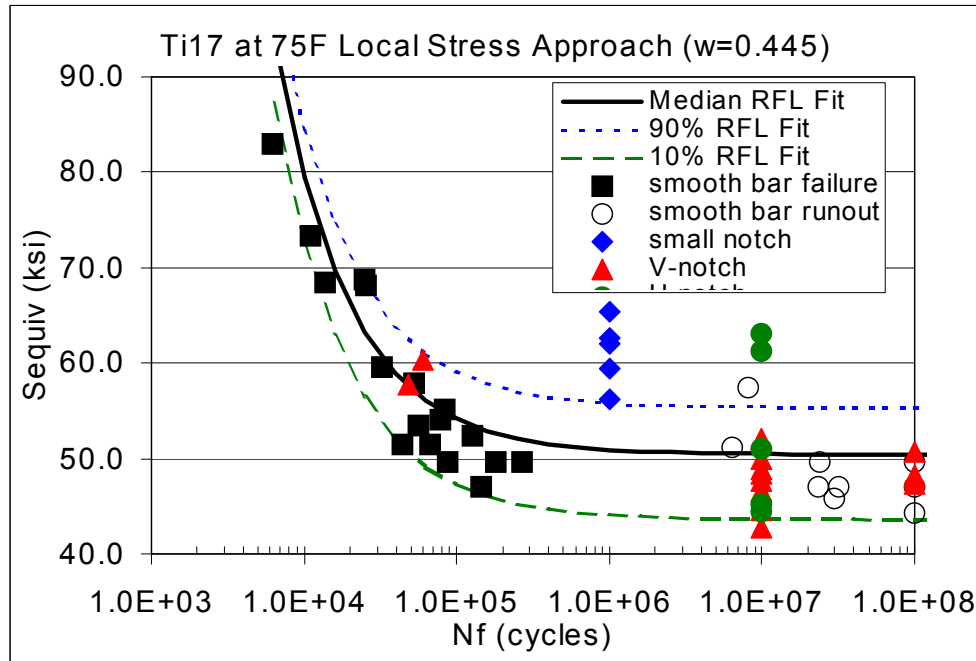
Figure 3.116. Smooth and notched bar fatigue results with the peak local stress approach.

Local stress approaches were modified with notch fatigue stress concentration (k_f-q) and feature stress (Fs) approaches. The constant a=1.8 mils was found to correlate small Ti-17 machined notch tests at 75°F (Figure 3.117). This approach is used to predict FOD capability from k_t and q.
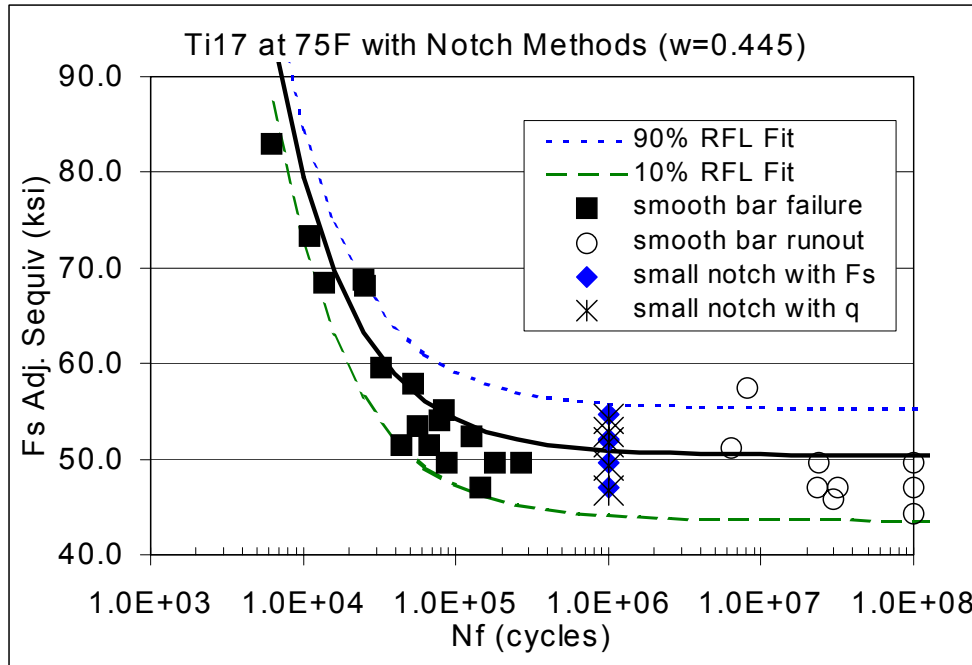
Figure 3.117. Small notch correlation with Fs and q-k_f approaches as compared to smooth specimen fatigue curves.

These predictions are represented with solid black lines for different geometries and impact angles in Figures 3.118 through 3.122. Significant scatter exists in FOD tests results, but calculated k_f with the q approach generally provides a reasonable prediction of the mean HCF behavior of specimens with FOD for different impact angles and FOD depths. The results are summarized for tests in the as-FODed and as-FODed + stress relief (SR) conditions in Figures 3.123 and 3.124. The predictions are best with a reduction in test scatter when the stress relief cycle is employed after FOD to reduce residual stresses (Figure 3.124). Results with q and Fs approaches are similar as summarized in Figures 3.125 and 3.126. Additional work should include: a) assessment of q and Fs approaches for notch and FOD tests over a range of notch root geometries, b) evaluation of the q and Fs approaches with airfoil test results, and c) implementation of the approaches for design applications.
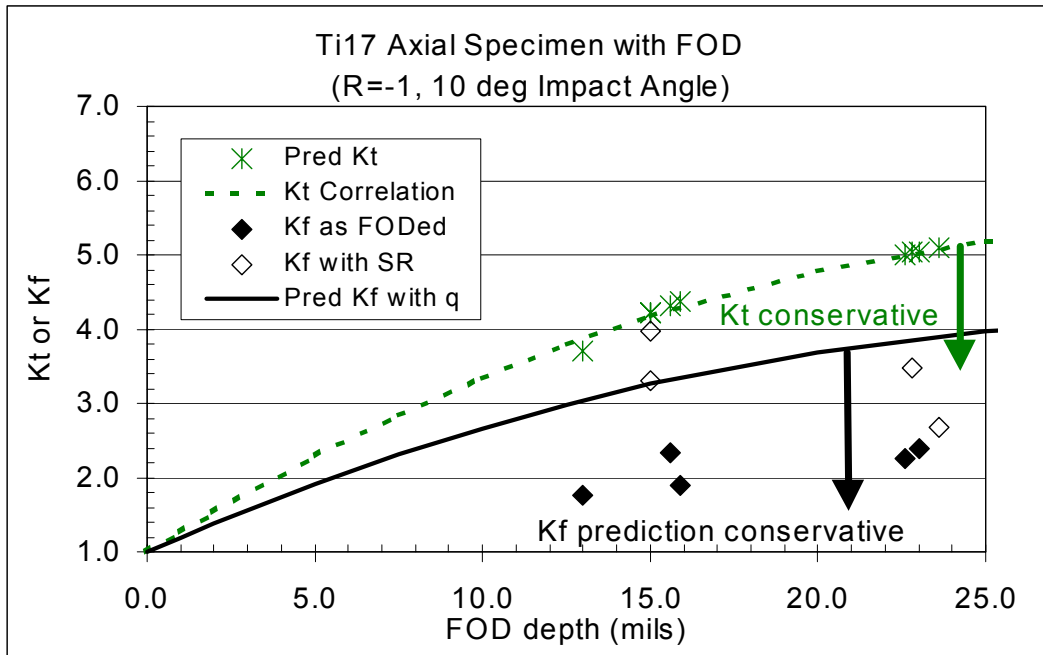
Figure 3.118. Predicted and experimental k_f for FOD tests in the axial specimen geometry with a 10-degree impact angle.
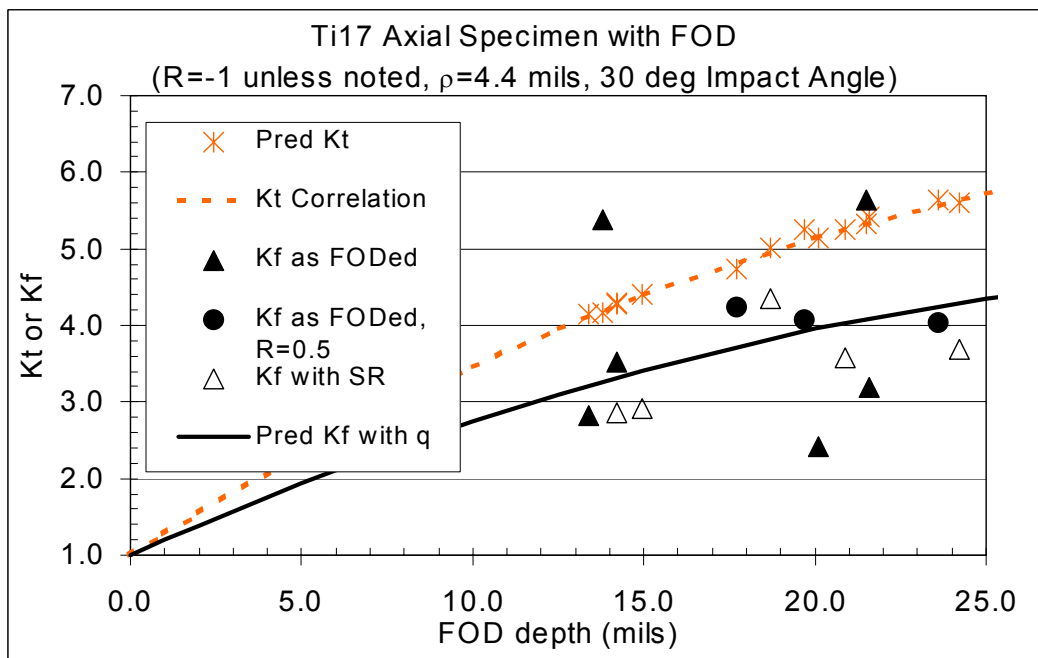
Figure 3.119. Predicted and experimental k_f for FOD tests in the axial specimen geometry with a 30-degree impact angle.
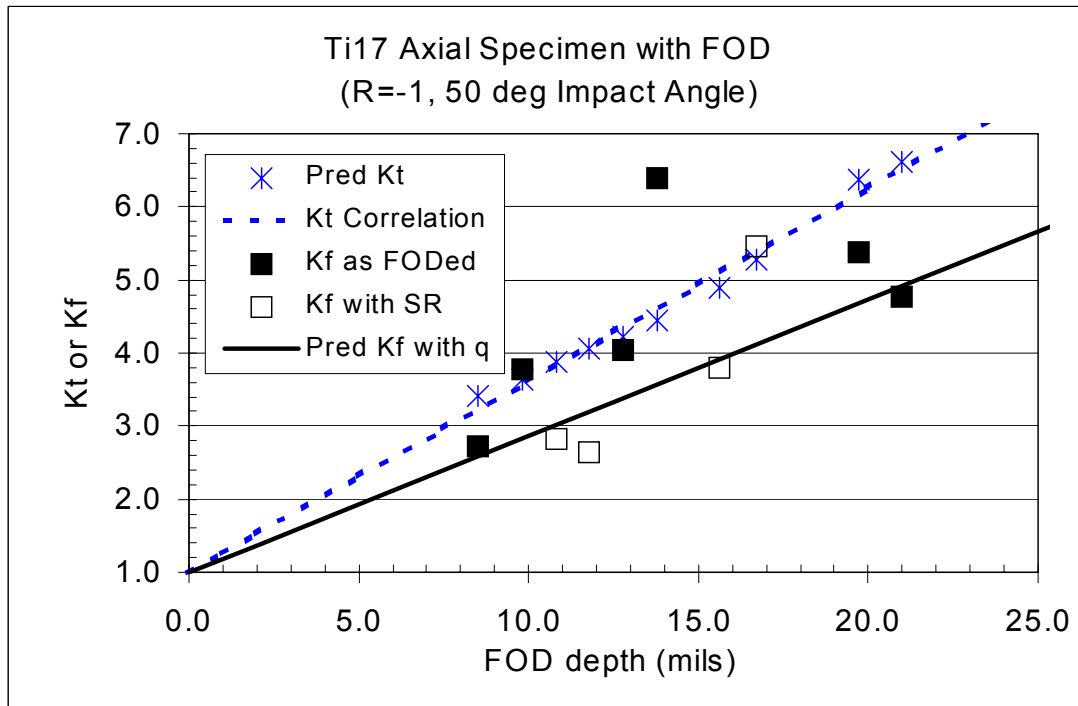
Figure 3.120. Predicted and experimental k_f for FOD tests in the axial specimen geometry with a 50-degree impact angle.
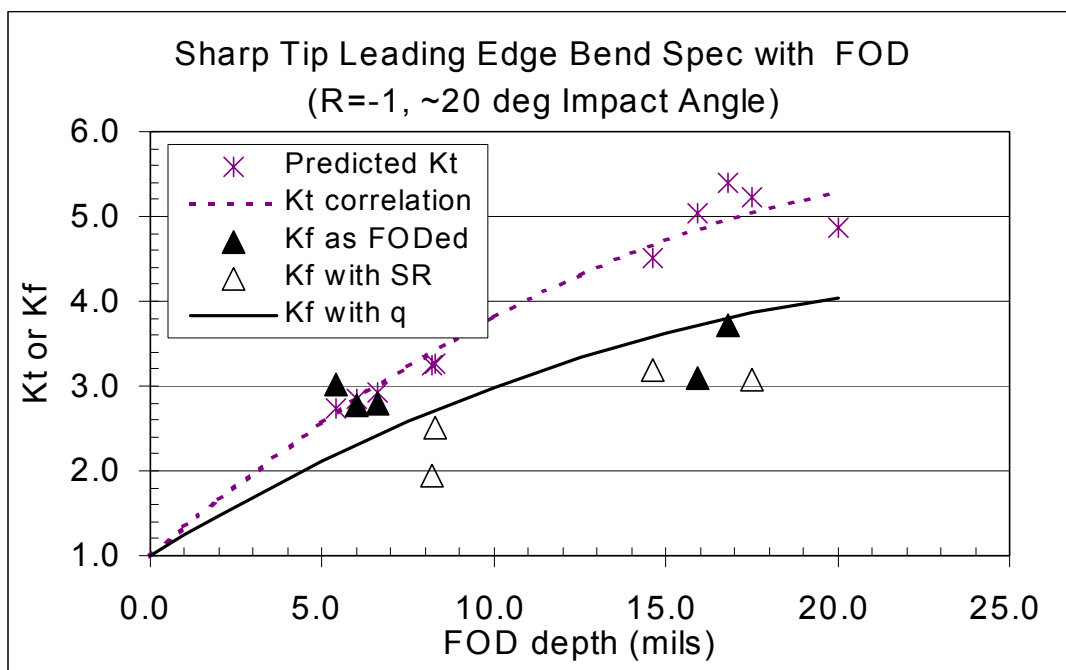
Figure 3.121. Predicted and experimental k_f for FOD tests for a bending specimen with the sharp tip geometry.
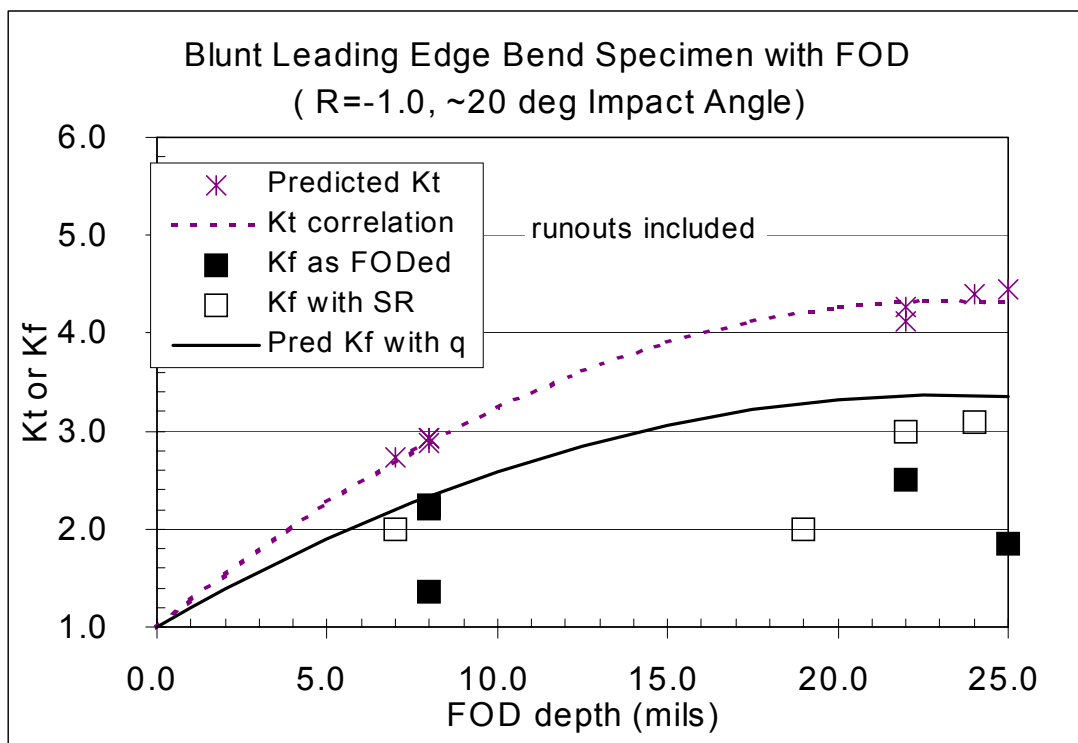
Figure 3.122. Predicted and experimental k_f for FOD tests for a bending specimen with the blunt tip geometry.
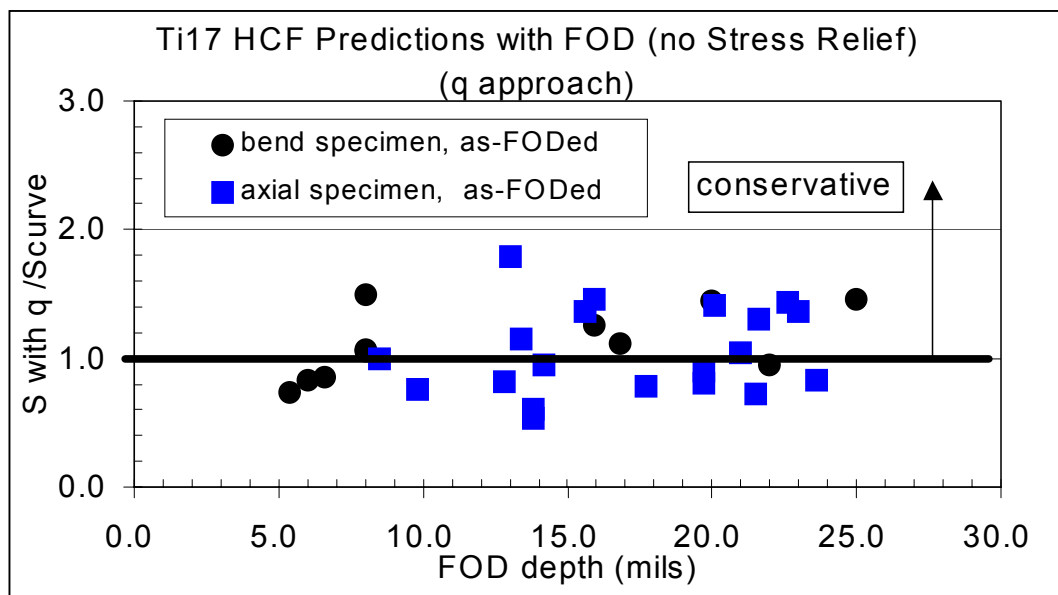
Figure 3.123. Predicted HCF capability vs. the baseline fatigue behavior for as-FODed tests.
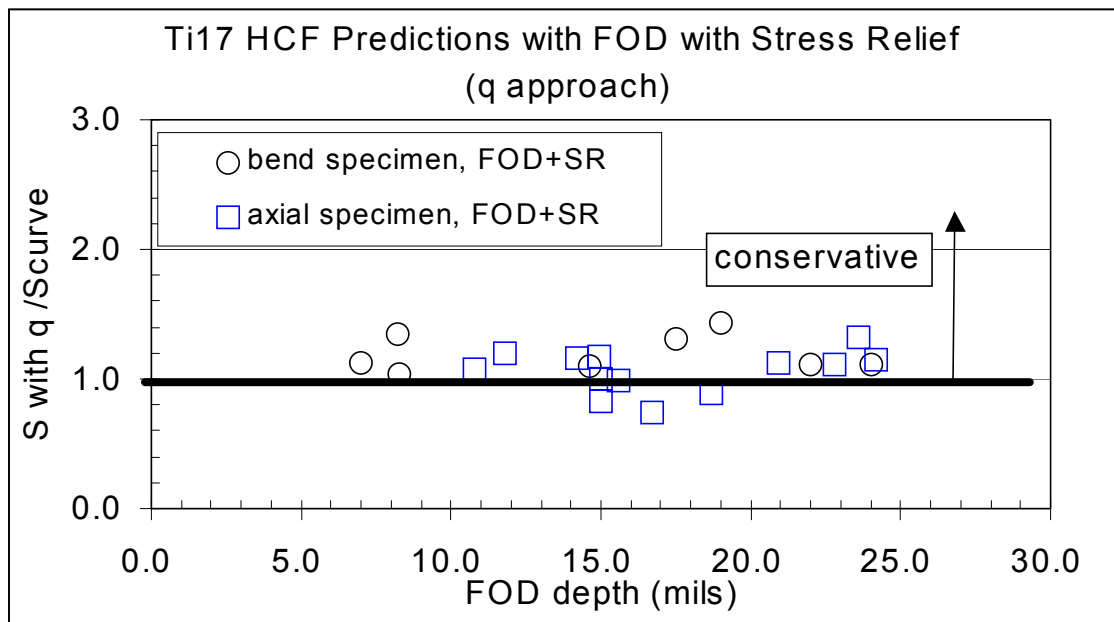
Figure 3.124. Predicted HCF capability vs. the baseline fatigue behavior
for as-FODed tests with a stress relief cycle to minimize
residual stresses.
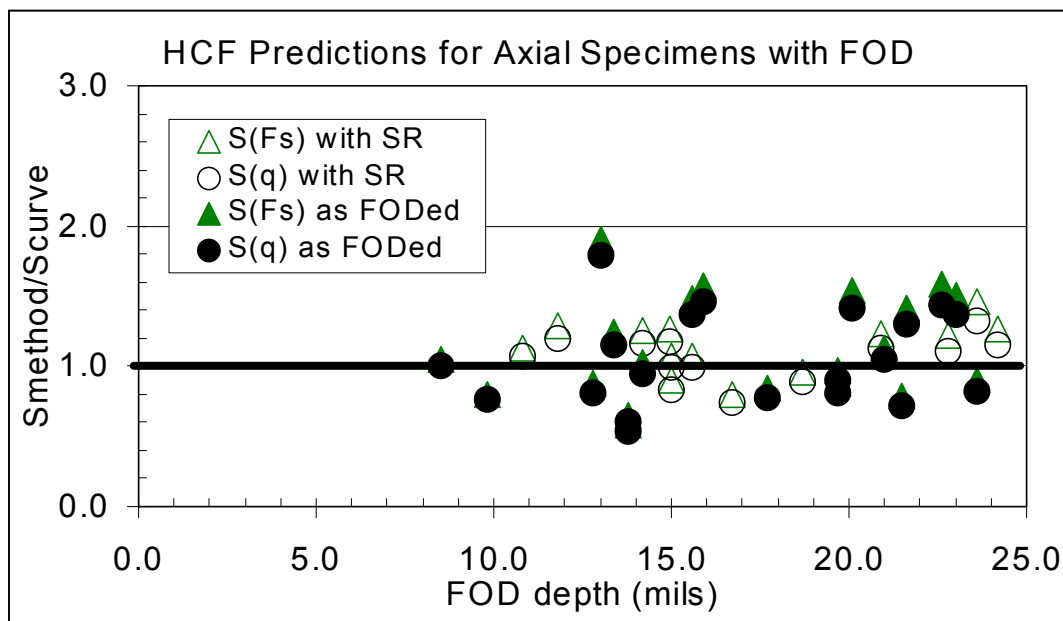
Figure 3.125. Similar predicted HCF capability with q and Fs approaches
for axial specimens with FOD.
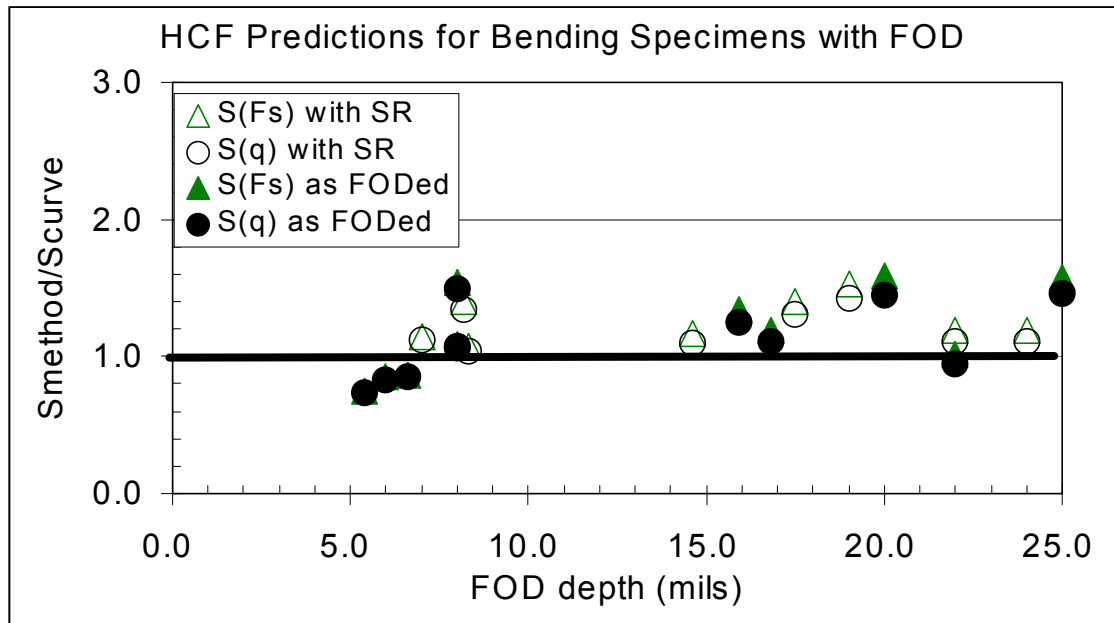
Figure 3.126. Similar predicted HCF capability with q and Fs approaches
for bending specimens with FOD.

3.4.3   New Analytical Results for Ti-6-4

3.4.3.1   Overview of FOD Analytical Studies

Analytical modeling studies of leading edge FOD impact events were conducted to determine the effects of various parameters on leading edge damage, residual stress distribution, and predicted high cycle fatigue capability. The parameters investigated were impact velocity, impact angle, blade centrifugal loads, projectile geometry, and imperfect impact. This work is a follow on effort to the previously documented work (in Chapter 5 and Appendix 5B of the HCF PRDA Final Report) [1]. More in-depth documentation of this current analysis is included in Appendix L of this report. MSC/DYTRAN was used for analysis of the high speed, impact events. Existing DYTRAN finite element models of the AF/UDRI specimen were utilized for the analysis. Figure 3.127 shows the AF/UDRI specimen finite element model geometry and a close up of a steel ball projectile.
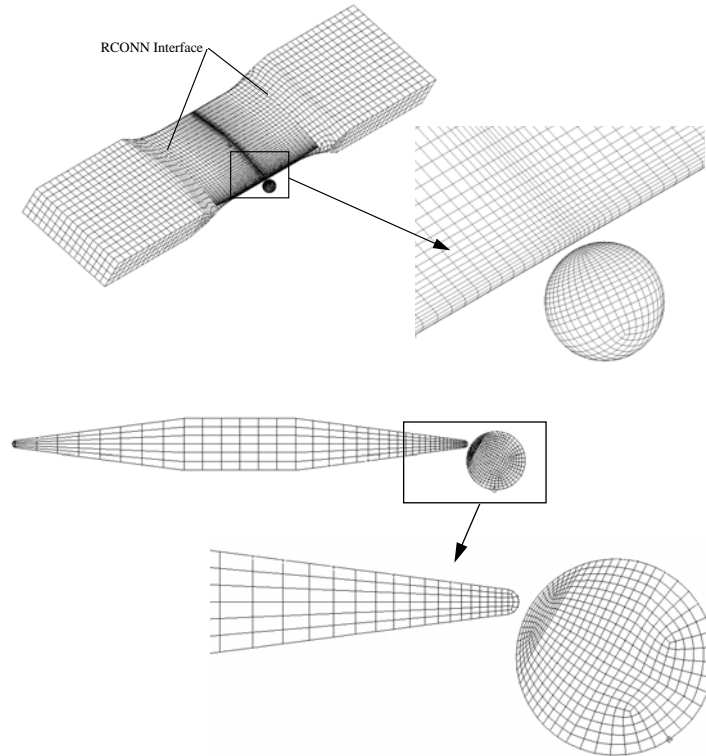
Figure 3.127. Finite element model of sharp edge specimen impacted at 30°.

The dynamic analysis modeling included rate dependent material properties and material failure. The material failure model is based on the Von Mises yield function. Material strain rate dependency is included. The chosen material failure model allows for failure of the element by definition of an effective plastic strain at failure. The high strain rate effective plastic strain at failure utilized in this analysis is 35%. The selection of 35% was based on a combination of literature surveys and finite element correlation with impact specimens exhibiting failure. The single effective plastic strain variable utilized does not distinguish between different material failure modes such as tension, compression, shear, and mixed modes. Incorporating a material failure model that predicts different failure modes should be addressed in future work. A more accurate failure model will provide a better residual stress state and deformation of the FOD site location. Mesh density and material model sensitivity studies were performed previously and documented in the HCF PRDA Final Report. The current work has developed a HCF-LCF fatigue cycles to failure model based upon a Walker methodology. This fatigue model is used to investigate parameter influences on predicted fatigue life to failure.

142

Three analytical studies were performed in this effort. The first analytical study is an investigation of blade preload (due to centrifugal load) effects on the residual stress distribution around the FOD site. The second study looks at projectile geometry effects by comparing a steel ball impact to an equal mass steel cube impacting along an edge of the cube. The third study looks at the effect of imperfect FOD impact by perturbing the location of the impact site. For these three studies residual stress distributions, and predicted cycles to failure are investigated and compared.

3.4.3.2   FOD Analytical Findings

The centrifugal loading study indicated that as blade preload increased higher compressive and tensile residual stresses would be produced at the FOD site. Figures 3.128 and 3.129 illustrate the higher local stress levels due to the 20-ksi blade preload. Figures 3.128 and 3.129 show the residual stress field chord wise through the specimen blade cross-section. The blade in Figure 3.128 was impacted at a 0 ksi preload stress before being loaded to the 40-ksi nominal section stress shown. Figure 3.129 has the blade impacted at a 20-ksi preload stress prior to being loaded to the 40-ksi nominal section stress shown.

0° Impact 40 ksi Nominal Stress   **30° Impact 40 ksi Nominal Stress**

S33	VALUE
	-1.31E+05
	-7.50E+04
	-5.00E+04
	-2.50E+04
	-1.38E-10
	+2.50E+04
	+5.00E+04
	+7.50E+04
	+1.16E+05
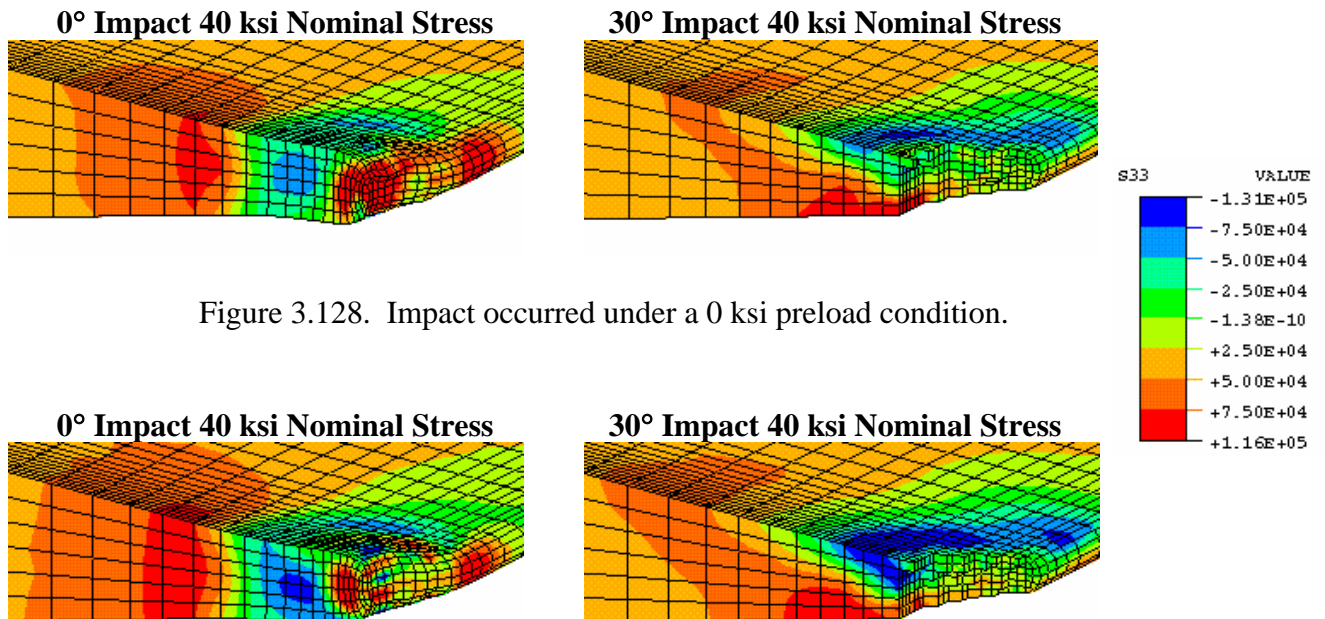
Figure 3.128. Impact occurred under a 0 ksi preload condition.

0° Impact 40 ksi Nominal Stress   **30° Impact 40 ksi Nominal Stress**

Figure 3.129. Impact occurred under a 20 ksi preload condition.

The influence of preload on predicted fatigue life was not clearly observed, and might be attributed to a relative coarse mesh density, and the use of a simple material failure model. It was observed that including residual stress does reduce the predicted fatigue life to failure by more than a few orders of magnitude as indicated in Figure 3.130, which also shows that increasing the impact angle reduces the predicted fatigue life. More variance exists in the "without residual stress" predicted fatigue life results. Model mesh density might affect the variance. After impact, the finite element model is faceted at the local FOD. Local facets produce sharp angles that are stress risers. Including the residual stress reduces the predicted fatigue life and smoothes out the curves.
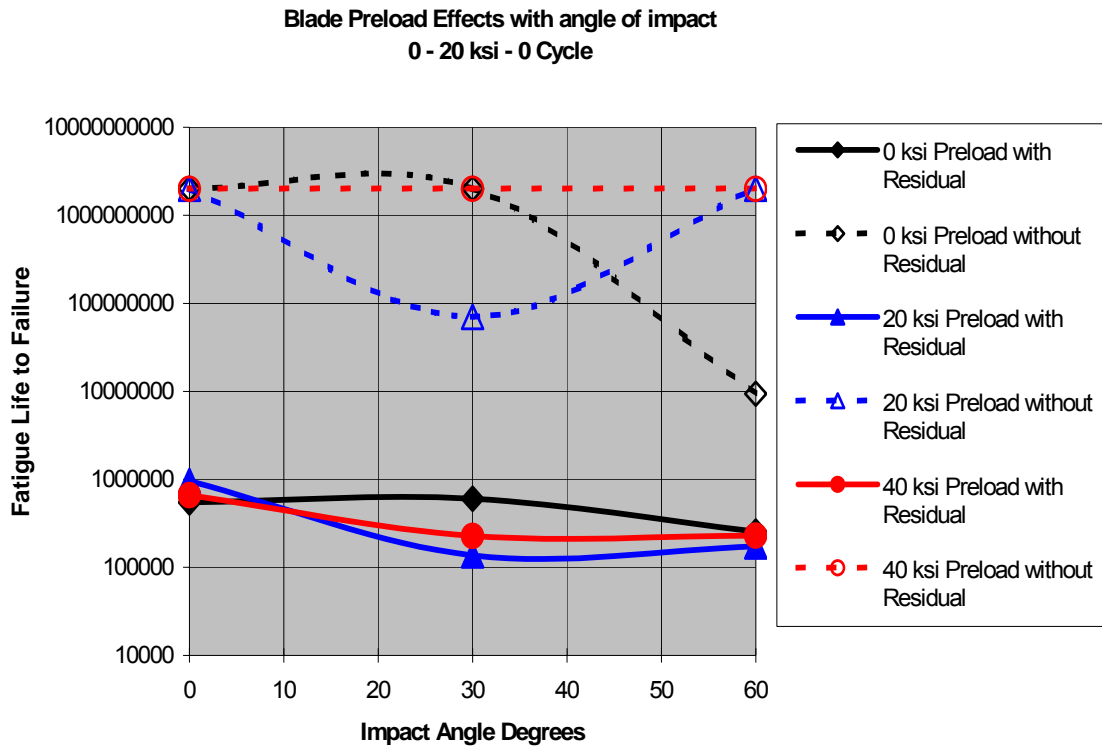
Figure 3.130. Predicted fatigue life of preloaded blade cycled to 20-ksi nominal stress.

The steel ball versus cube analytical study also showed that including residual stress reduced the predicted fatigue life. The equal mass steel cube proved to be more damaging to predicted life than the ball. In this study a velocity effect was observed for the 45-degree impact. Predicted fatigue life decreased as velocity increased but the curves were also converging with the increasing velocity. This suggested a possible upper limit on

velocity for a minimum predicted fatigue life point. The impact site perturbation study used the blunt edge specimen to investigate the effect of imperfect 0 degree and 30-degree impacts. A perfect impact would occur on the centerline tip of the specimen leading edge radius. As the velocity vector was perturbed away from the perfect impact, significant variation in predicted fatigue life to failure was observed. Predicted fatigue life was seen to vary by a factor of 2.9 for the 0 degree impact perturbation study and by a factor of 4.9 for the 30 degree perturbation study. Overall, it was found that residual stress, projectile geometry, impact velocity, and impact angle affect predicted fatigue life. This study has shown that the capability now exists to predict fatigue life given the characteristic impact of a foreign object. Further methodology development and calibration to test specimens will have to be done to accurately predict life, but this effort is not seen as significant. Additional analysis information may be found in Appendix L.

3.4.4 FOD Validation

Current airfoil leading edge high-pressure compressor (HPC) damage tolerance design evaluation methods rely heavily on empirical data, which inevitably lag behind new airfoil design technology and materials. Extrapolation of the empirical data to new designs is tenuous. Obtaining bench data for new design evaluations is costly and does not provide the information in time for impact during the design phase.

Therefore, this program endeavors to develop a reliable analytical tool to evaluate leading edge damage tolerance. This tool needs to be easily implemented into the current design system and be fast enough to be a useful design tool. Development and validation of this tool requires a complete and well-controlled set of experimental data. This section describes how this experimental dataset was obtained, and used to evaluate/validate the analytical models proposed.

3.4.4.1 Experimental Approach

An advanced front stage HPC blisk design, shown in Figure 3.131, was chosen as the test vehicle for the airfoil FOD fatigue tests. The blisk was conventionally machined out of a Ti-17 forging. The airfoil surfaces were tested in the as bench finished condition; i.e., not shot-peened. The blades were wire-EDM'ed from the blisk to provide the individual specimens, as seen in Figure 3.132.
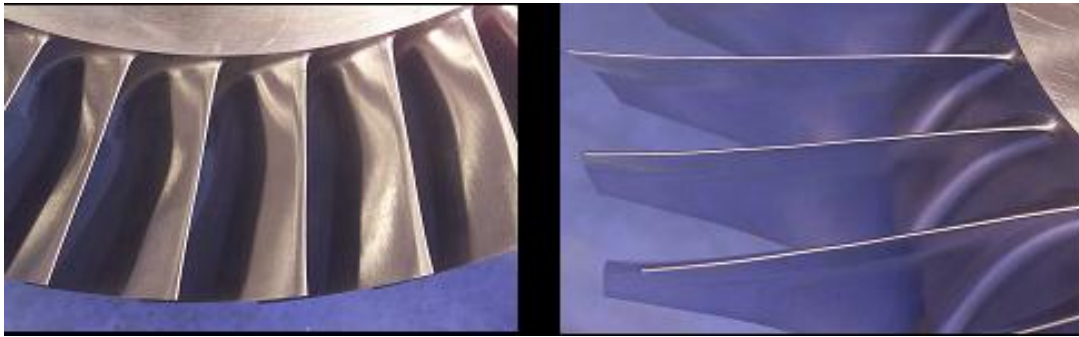
Figure 3.131. Blisk prior to wire EDM removal of blade specimen.
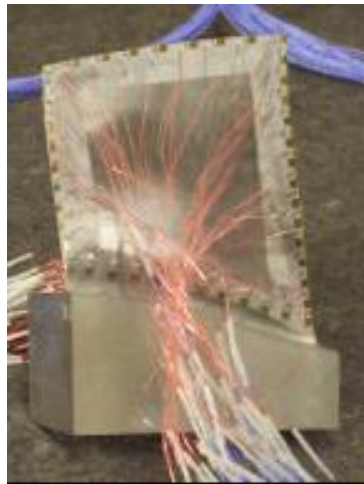
Figure 3.132. Individual blade specimen instrumented for bench vibe stress distribution testing.

Careful definition of the FOD characteristics was essential for the analytical modeling. Although real field FOD is irregular and difficult to define with a few parameters, the simple notches defined in Figure 3.133 are considered typical and representative. All the notches have a 60 degree included wedge angle, and a defined notch root radius. The notch depth was defined as a true profile depth as shown. The impact angle was taken from the concave surface leading edge tangent line as shown. The leading edge thickness was defined 0.015 inches aft of the leading edge.
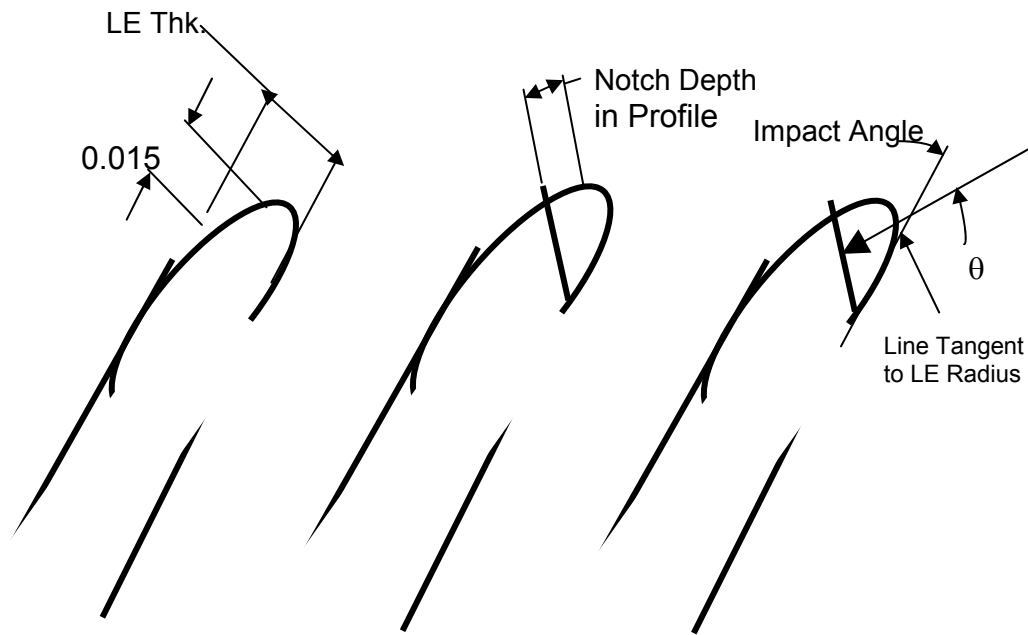
Figure 3.133. FOD notch geometry definition.

The following parameters were experimentally investigated in DOE fashion as shown in Table 3.18: mode shape, notch depth, impact angle, and notch root radius. The different mode shapes represent a change in leading edge thickness and unnotched stress field. The second flex critical vibratory location is further out in span than the first flex, and therefore, is at a thinner leading edge location. The second flex through-the-thickness stress gradient is approximately twice that of the first flex mode.

Table 3.18. FOD Test Matrix

Run No.	Mode	Notch Depth (in.)	Impact Angle	Notch Rad. (in.)
1	1F	Unnotched	0	N/A
2	1F	.008 - .012	20	0.003-0.004
3	1F	.018 - .022	20	0.003-0.004
4	1F	.008 - .012	40	0.003-0.004
5	1F	.018 - .022	40	0.003-0.004
7	2F	.008 - .012	20	0.003-0.004
8	2F	.018 - .022	20	0.003-0.004
9	2F	.008 - .012	40	0.003-0.004
10	2F	.018 - .022	40	0.003-0.004
11	1F	.018 - .022	40	Sharp (~ 0.001)
12	2F	.018 - .022	40	Sharp (~ 0.001)
3-4 specimens per run no.				LE Thk (in.)
			1F	0.024
			2F	0.020

147

The range of notch depths extends from just large enough to be easily detected to the most severe notch that would not produce a tear (initial crack).   The range of impact angles covers those experienced by front stage compressors due to particle velocity and blade stagger.   The notch root radii ranged from 0.0035 to as sharp as could be reliably produced (~0.001). All but two conditions had at least three test specimens, and one had four.

The notches were produced by a relatively low impact velocity method. A solenoid gun and tool bit were used to accurately produce the desired notches. The fatigue tests were conducted as step-tests run to 10^7 cycles using siren excitation. The excitation level was controlled with a strain gage remote from the notch location and the leading edge tip deflection was also recorded.

Scanning Electron Microscope photographs in Figure 3.134 show representative FOD notches for the test matrix conditions. The blunt root radius notch shows a little more out-of-plane material flow than the sharp notch.
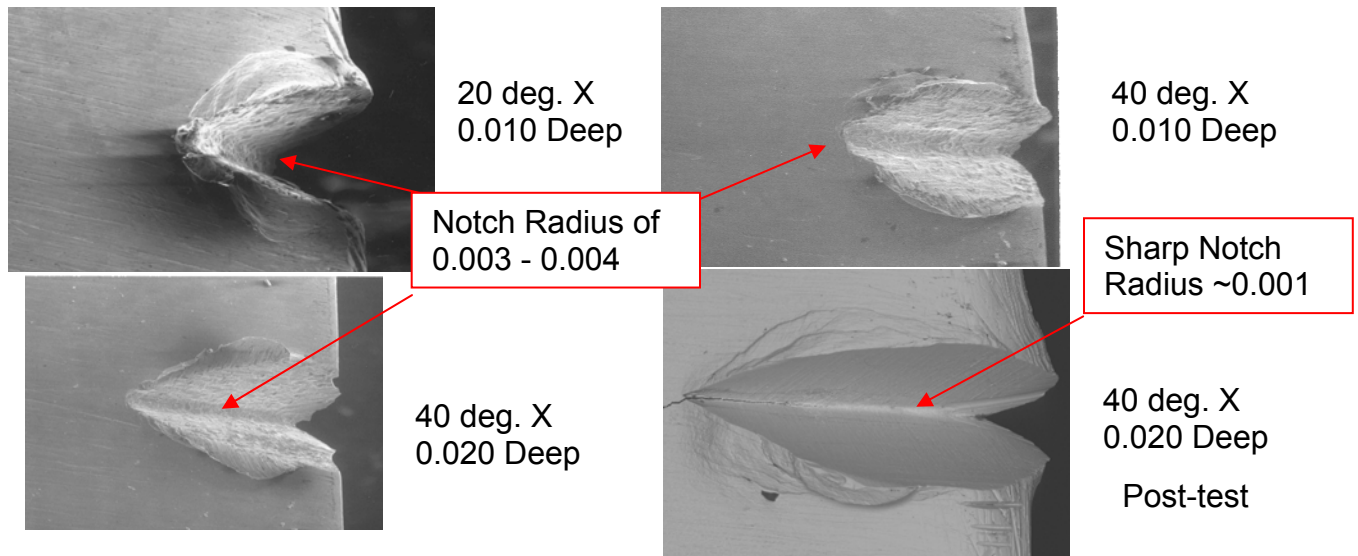
Figure 3.134. SEM photographs of representative FOD notches.

3.4.4.2   Analytical Approach

Two analytical methods for predicting leading edge HCF damage tolerance were evaluated. The first method is the fatigue notch sensitivity (q) conversion of the theoretical stress concentration factor (k_t) to fatigue notch factor (k_f) given by Equation 3.29. The fatigue notch factor is defined as the unnotched fatigue limit over the notched fatigue limit, which is taken to be equivalent to the notched stress over the unnotched stress. The fatigue notch sensitivity (q) was experimentally determined to be 0.71 for Ti-17 smooth and small notch specimens with notch root radii of 0.0044 inch. The material constant (*a*) was then calculated to be 1.8 mils for this Ti-17 material.

The second method attempts to take into account the fact that the stressed area for a notch is much smaller than that of a typical axial fatigue test specimen used to generate Goodman fatigue data. The Fs factor is calculated by Equation 3.30 for both the notched geometry and the axial fatigue test specimen. The ratio of these Fs factors taken to the exponent $1/\alpha$ provides a reduction factor for the concentrated notch stress. The material constant (α) was determined to be 60 from smooth and small notch Ti-17 specimens.

$$k_f = 1 + q(k_t - 1) = \sigma_{notched} \Big/ \sigma_{unnotched} \tag{3.29}$$

where: $\quad q = 1 \Big/ \left(1 + \dfrac{a}{\rho}\right)$

k_t is defined as the notch concentrated stress/ unnotched stress
ρ is the FOD root radius
 a is a material constant

$$Fs = \sum_{i=1}^{n} \left[\left(\frac{\sigma_{i,notch}}{\sigma_{max,notch}} \right)^{\alpha} \right] \Delta A_i \tag{3.30}$$

where: $\quad k_f = 1 + q(k_t - 1) = \sigma_{notched} \Big/ \sigma_{unnotched}$

Fs$_{Ref}$ is the surface area for the axial baseline test specimen.
α is a material constant

Both analytical methods obtain the notch concentrated stress from a finite element sub-model solution of the notched blade leading edge as described in the following section.

Finite element sub-modeling was used to estimate the FOD notch concentrated stress. The following outlines the sub-modeling procedure used. A solid model section of the actual blade leading edge, extending 0.25 inch in each direction from the notch location as shown in Figure 3.135, was imported into ANSYS. A solid model of the 60-degree wedge impact tool was created with the desired tip radius for the notch root. The tool was then intersected with the leading edge at the vibratory critical location, to the desired depth and at the correct impact angle, to generate the notch of interest using Boolean subtraction. The region immediately surrounding the notch (0.10 inch x 0.10inch), was segregated into a separate volume for meshing with ten-node-tetrahedral elements, see Figure 3.136. The mesh size in the notch root radius was limited to ten percent of the notch radius. The remainder of the sub-model was meshed with eight-node-brick elements. The modal displacements from the full model solution were then scaled and mapped onto the sub-model cut boundaries. A static stress solution was then generated to obtain the notch concentrated stress.
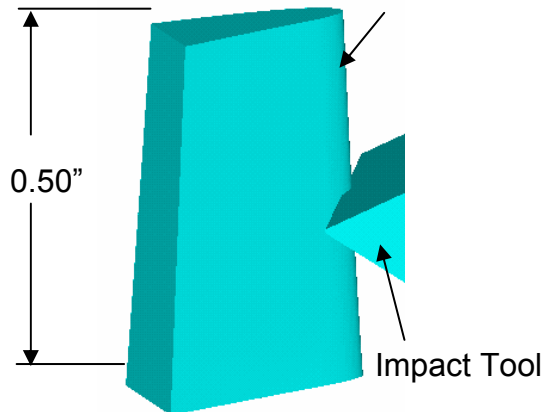
Figure 3.135.   Solid model of blade leading edge
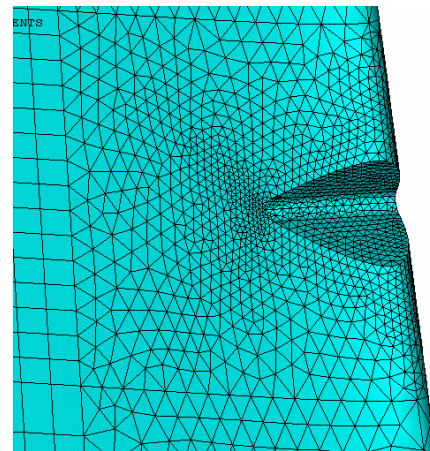
Figure 3.136.   FE mesh of notched leading edge.

This sub-model approach only provided an element size reduction of 20% from a full model approach (40,000 Vs 50,000), and is therefore unnecessary from a computational standpoint. Future analysis will be done with a full model using modal analysis.

The full finite element model of the blade specimen was validated using bench test frequency and strain distribution data. The FEM frequencies for the first 11 modes were all within 3% of the bench frequencies as shown in Figure 3.137, which is excellent agreement considering that blade-to-blade variation can be more than 3% for some modes.
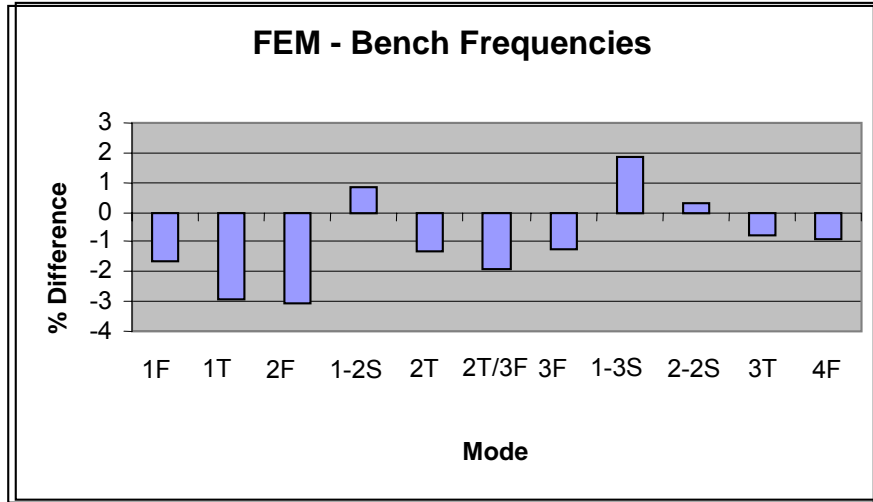
Figure 3.137. FEM frequency predictions compared to bench data.

Figure 3.132 showed a photo of the bench test specimen with strain gages. The leading edge strain gage data is compared with the FEM predictions for the first two flex modes in Figure 3.138. There is excellent agreement between the FEM and bench data in terms of % max. radial strain. These comparisons provided good validation for the FEM.
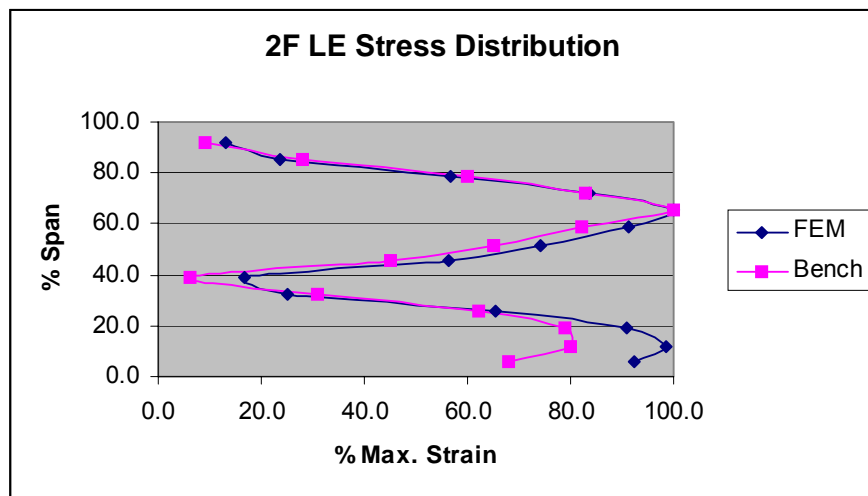
Figure 3.138. FEM leading edge strain predictions compared to bench data.

The unnotched FEM sub-model static stress results were compared with the full FEM modal results for first flex validation. Figure 3.139 shows the radial stress (SX) normalized by the max. equivalent stress (SEQV) at the notch section. These are plotted against the airfoil axial and tangential coordinate locations to help visualize the stress gradients. The agreement between the models is excellent everywhere except near the sub-model boundary.
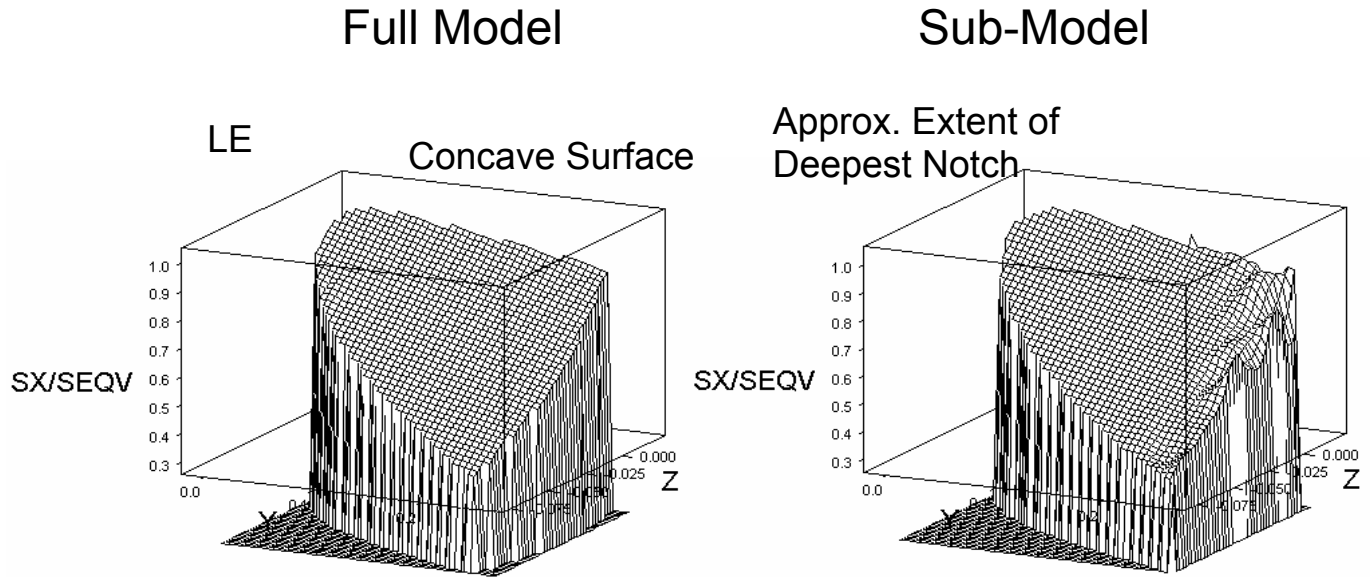
Figure 3.139. Comparison of 1F leading edge radial stress/max. equ. stress.

The boundary-affected area of the sub-model is substantially removed from the notch area as shown. Therefore the first flex sub-model was considered validated.

3.4.4.3   Results

The notch fatigue test results are presented in terms of fatigue notch factor (k_f) versus notch depth for both first flex (Figure 3.140) and second flex (Figure 3.141) modes. The different impact angles and notch root radii are plotted as different symbols. A regression analysis of these DOE results was conducted for each mode and the resulting correlation fits are shown as the solid lines.
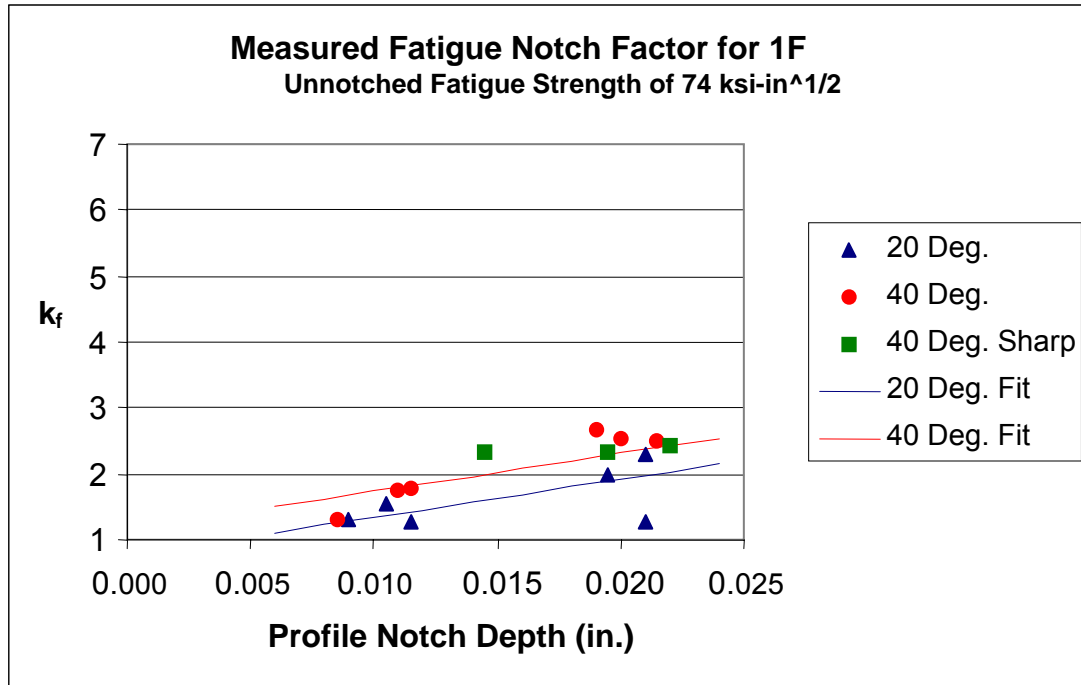
Figure 3.140. Measured fatigue notch factor for first flex.
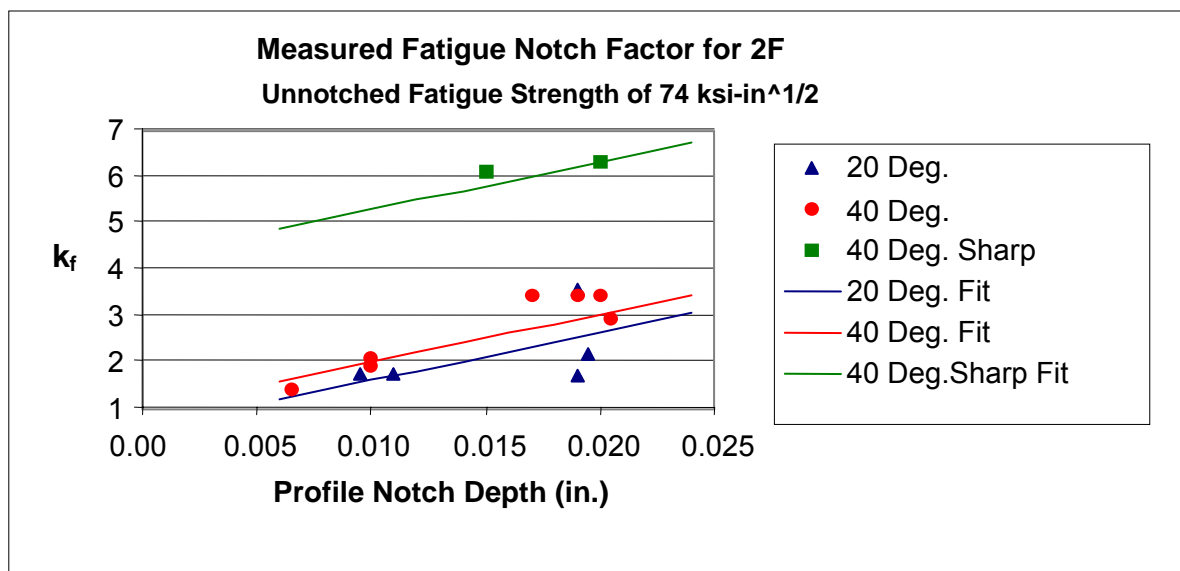
Figure 3.141. Measured fatigue notch factor for second flex (2F).

For the first flex results, the notch depth and impact angle were both found to be statistically significant parameters ($p < 0.05$). The notch root radius influence was insignificant. For the second flex mode, both the notch depth and notch root radius were statistically significant parameters. However, the impact angle still accounted for a significant amount of the variation and was again included in the correlation.

The cause of the difference in the notch root radius effect between modes is unresolved. Fractographic analyses of the failed second flex sharp and 0.0035 root radius specimens may be performed to try to determine what difference there may be in the crack initiation. Scanning electron microscope photos of the unopened cracked specimen were inconclusive.

The results, for the first flex mode, from both the q-k_f (Figure 3.142) and Fs (Figure 3.143) analysis methods are shown along with the corresponding experimental results. The results are again plotted in terms of k_f versus notch depth for the two different impact angles. Each method's sensitivity to notch root radius was investigated by analyzing a second slightly larger 0.0045 radius.
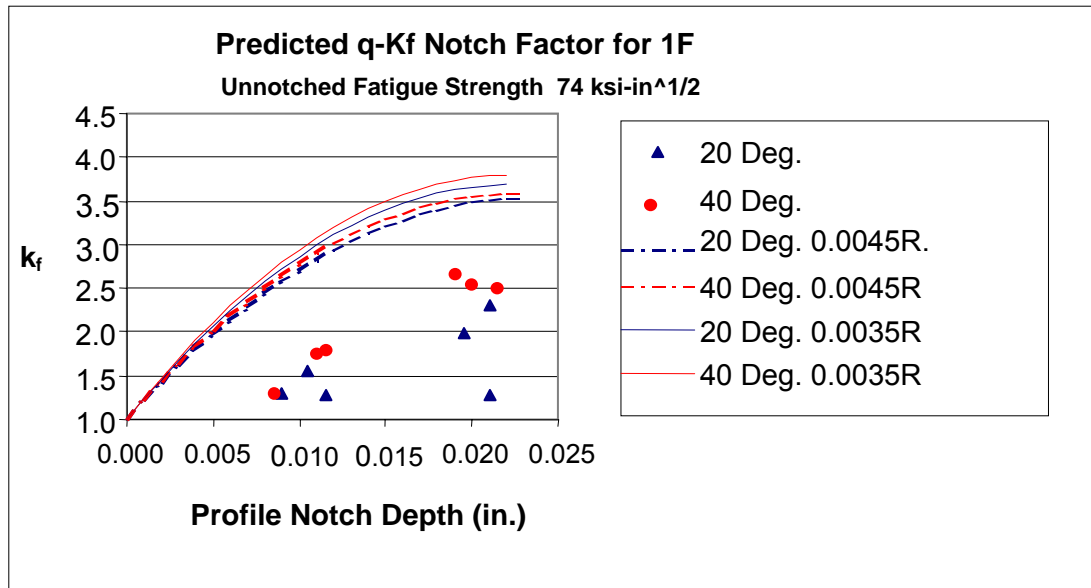
Figure 3.142. Predicted q-k_f notch factor for first flex compared to measurement.

Predicted Fs Notch Factor for 1F
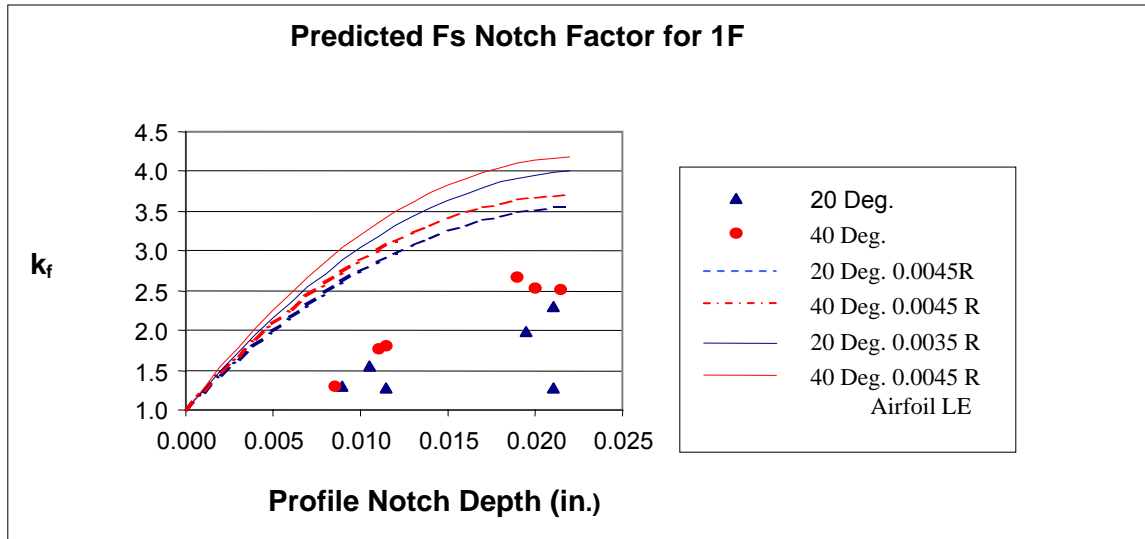
Figure 3.143. Predicted Fs notch factor for first flex compared to measurement.

Both analysis methods are conservative compared to the data and give very similar results for the 20-degree, 4.5 mil notch radius case. Both methods over predict the notch depth sensitivity and slightly under predict the impact angle sensitivity. However, the Fs method's impact angle dependence better matches the data trend. Finally, the Fs method appears to be more sensitive to the notch root radius. Recall that for this first flex mode, there was no notch root radius dependence in the data.

3.4.4.4   Conclusions

Definitive conclusions are difficult to draw from this one airfoil data set and the corresponding analysis predictions for only one of the modes. For the geometry tested, the data does indicate a moderate dependence on the FOD notch depth and a weak dependence on the impact angle. The notch root radius dependence is yet to be understood.

The prediction methods are similar and conservative for the geometry tested. However, these same methods applied to laboratory test specimens are able to predict the mean FOD HCF damage tolerance.

Although it is too early to down select to either analysis method, these results favor the q-k_f method, which has slightly better agreement with the data. Another advantage of the q-k_f method is that it is easier to implement than the Fs method. However, additional

155

evaluation of both methods is required using the second flex data and the sharp notch data. Additional airfoil data sets will also be required to validate/calibrate either method.

3.5 ATTACHMENT FATIGUE IN Ti-6A1-4V

3.5.1 Introduction

The prediction of the fatigue life under given loading conditions or the fatigue limit loading that will last forever (equivalent to an endurance stress) in an attachment region requires a number of steps and obtaining information on the behavior and fatigue characteristics of the materials in contact. For the purposes of this program, it is assumed that the behavior is governed solely by the contact stress field, independent of any material degradation (or strengthening) in the contact region due to the contact conditions. Thus, wear is not considered as a possible mechanism in the analyses described in this section. The only tribological factor considered is the coefficient of friction, which, it is recognized, may evolve with number of cycles as does wear.

To be able to describe the behavior of an attachment region, the first thing that is needed is a stress analysis capability, which considers sliding (slip) where applicable, and full contact (stick) where applicable. The general case where both slip and stick are present, generally referred to as fretting fatigue, is a non-linear problem because the stick and slip regions do not remain fixed. The general analysis of this problem has to track the evolution of the stick/slip boundary and account for the moving stress field. Numerical and analytical methods are described for obtaining the stress fields in the attachment region in this section.

Once the stresses are known, both crack initiation and subsequent propagation have to be addressed. Crack initiation models can be either scalar in nature or orientation dependent as in what are described as critical plane models. Both types are described in this report. The presence of severe stress gradients require modifications to conventional stress or strain based models that rely on maximum values at a point. The uses of such models are referred to as total life methods.

Models based on crack growth, specifically addressing whether stress intensities are and remain above the threshold stress intensity, are another approach to determining the

156

integrity of the contact region. These are referred to as fracture mechanics methods. In both the fracture mechanics and total life approaches, the crack length to which a crack initiates as well as the initial crack length from which propagation begins are critical aspects of the life prediction methodology.

Finally, models are developed and tested for several different contact geometries under a range of loading conditions where data obtained at different values of stress ratio have to be consolidated. Specimens range from flat uniaxial under constant normal loading to a single tooth fir tree geometry. Consolidation of data at different values of R and accounting for stress gradients are based on procedures developed under this program and are described in the earlier chapters that deal with initiation methods, total life methods, multiaxial stress methods, and notches.

This section begins with a description of the contact stress analysis CAPRI that was developed at Purdue under the previous contract and transitioned to the engine companies and the Air Force. Next follows a brief description of extensions to the code required for dissimilar material contacts and arbitrary load histories resulting in CAFDEM that has also been transitioned to the engine companies. This leads to application of stresses calculated by CAFDEM and CAPRI to total life prediction of experiments conducted under controlled laboratory conditions. As mentioned above, total life prediction requires information about fretting crack sizes and experiments aimed at assessing these cracks are described next. The chapter concludes with description of the use at the engine companies of the attachment fatigue life prediction capability developed under the BAA program.

3.5.2   Contact Stress Analysis

Efforts of the PRDA program showed that stresses at the edge-of-contact in gas turbines contain large gradients. Typical gradients are illustrated in Figure 3.144. It is costly and difficult to quantify these gradients using the finite element methods embedded in existing engine company design systems. Purdue researchers developed software based on FFT solution to the singular integral equations that govern contact between two similar materials, CAPRI. Figure 3.144 illustrates comparison between CAPRI, or quasi-analytic, results and those obtained using conventional finite element method (FEM) calculations. Note the large gradients. CAPRI performs these calculations much faster than does FEM.

CAPRI was transitioned to the engine companies and the Air Force at the conclusion of the PRDA program. Engine company personnel requested that the capability to analyze dissimilar material contacts as well as arbitrary load histories be added to the code. These efforts led to the development of CAFDEM described in Appendix M.
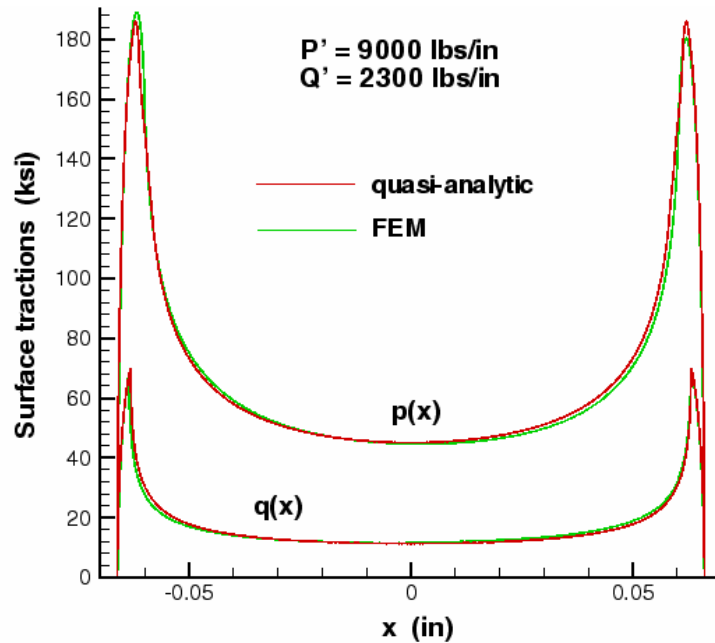
Figure 3.144. Typical stress distributions associated with fretting fatigue of nominally flat contacts [20].

3.5.3   Experimental Results

3.5.3.1   Fretting Fatigue Experimental Rig

The blade/disk contact is equivalent to a nominally flat profile in contact with a flat surface. The forces acting on the contact can be resolved into a normal component and a tangential component over the contact region. Nominally flat fretting pads, with rounded edges, and flat *dog-bone* specimens are used to duplicate the local geometry at the blade/disk attachments in engine hardware. To simulate the loading conditions, the nominally flat pad and the flat specimen are clamped together to generate a normal load and then subjected to an oscillatory tangential load. Such a configuration was achieved in the laboratory using a fretting chassis attached to a standard uniaxial servo-hydraulic testing machine. In addition to the contact loading, the laboratory experiments apply a bulk load to

the specimen. The bulk load applied plays a significant role in growth of cracks initiated due to high stress gradients generated by the contact.

The fretting chassis, used for the standard fretting fatigue tests at room temperatures, is a superstructure built on the fatigue machine that allows the generation of tangential loads that are in phase with the bulk load while applying a nominally constant normal load. Figure 3.145 shows the components of the fretting chassis schematically. The stiff beam provides the bulk of the stiffness of the chassis. The pads rest on the top platform that also provides the means of application of the normal load. The normal load is applied via a pair of hydraulic actuators that transmit the load onto the top platform. Note that the two pressure rods ensure that pressure is applied symmetrically to the pads. The thin steel diaphragms offer little resistance to the pressure loading, but offer a large resistance that carries the portion of the tangential load transmitted to the chassis. This ensures that almost all of the pressure is transmitted to the specimen through the pads, while maintaining the required stiffness to produce a large tangential force. A finite element analysis has shown that more than 98% of the pressure is transmitted to the specimen. The pad-tops fix the pads to the chassis. The tangential force produced was about 50% of the bulk load applied, subject to a maximum of the force required to produce gross sliding. This load is monitored throughout the fatigue experiments, by recording the difference of the upper and lower load cell readings.

Figure 3.145 shows a schematic of the various loads. The crush load (normal load) per unit depth is P, Q is the tangential load per unit depth, F_o is the force applied at the bottom of the specimen (measured by the actuator load cell). The reaction force as measured by the cross-head load cell (top grip) is referred to as F. Note that the difference between F_o and F gives the tangential force, $2Q$. The bulk stress, σ_o, is F_o divided by the cross-sectional area of the specimen.
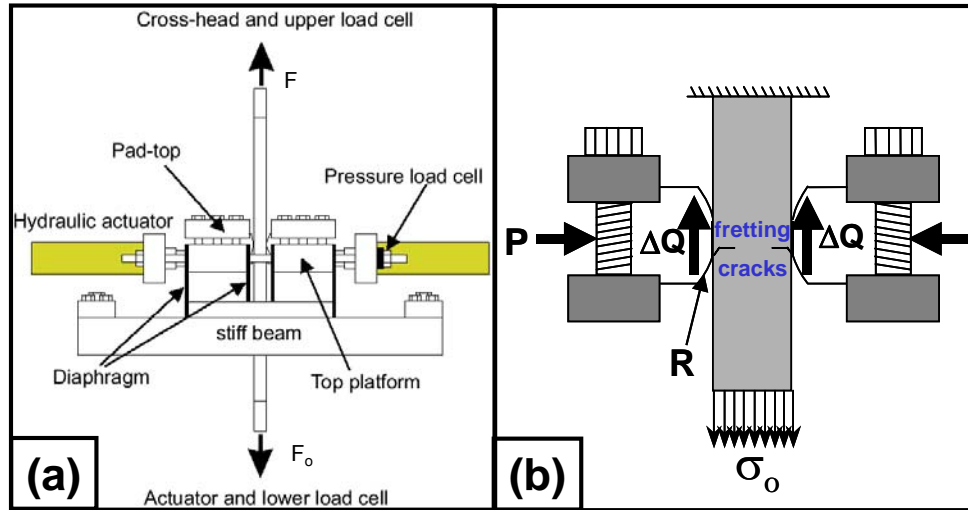
Figure 3.145. Components of the fretting chassis with a schematic detailing the definition of forces applied to the rig [23].

3.5.3.2 Fretting Fatigue Lives of Ti-6Al-4V on Ti-6Al-4V Contacts

Results for fretting fatigue experiments at Purdue conducted with Ti-6Al-4V/Ti-6Al-4V experiments are given in Table 3.19. The experimental parameters were chosen with guidance from the engine companies to develop edge-of-contact stresses similar to those that occur in hardware. The desired ratio between normal and tangential loads was greater than the initial coefficient of friction. Thus sliding occurred during the first few fretting cycles. The friction (coefficient of friction) increased due to sliding so that the fretting contact transitioned to partial slip. This common phenomena is called mixed-mode fretting in the literature [21]. It is illustrated by results for contact between Inco718 and Ti-6Al-4V shown in Figure 3.146. The results in Table 3.19 are for the steady-state stick zone conditions. The friction coefficient used in the calculation of equivalent stress is 0.5. Figure 3.146 also illustrates that the stick-zone is not symmetric within the contact due to the effect of the bulk stress. The stress calculations include this effect as well [22].

160

Table 3.19. Experimental Data for Ti-6Al-4V/Ti-6Al-4V Fretting Contacts*

	Inputs			Measured			Calculated		
Exp.	P (lbs/in)	σ_{max} (ksi)	R_σ	Q_{max} (lbs/in)	Q_{min} (lbs/in)	N_f	σ_{eq} (ksi)	N_i	N_{prop}
PR02	9176	39.7	-0.07	3916	-3337	54,744	67.1	4847	40,957
PR03	9080	32.0	-0.06	3129	-2580	160,628	63.6	6268	197,952
PR04	9104	35.2	-0.02	3220	-2636	144,242	67.1	4847	146,177
PR05	9451	42.7	-0.01	3868	-3204	39,947	68.2	4504	41,327
PR06	9525	40.5	-0.03	3739	-3283	69,279	68.6	4388	54,778
PR07	9099	38.1	-0.05	3479	-3260	93,930	66.1	5197	85,586
PR09	9995	48.1	-0.01	4607	-3775	26,391	71.1	3762	19,146
PR10	9432	48.4	-0.02	3309	-1893	386,049	65.0	5630	232,404
PR11	6669	41.9	0.49	2337	-1425	337,578	56.4	12,427	157,986
PR12	6709	49.8	0.50	2389	-2029	161,986	59.2	9229	68,385
PR16	6677	50.1	0.49	3080	-1461	168,637	58.2	10,208	37,282
PR22	6763	42.1	0.50	2293	-1464	1,285,642	57.4	11,112	135,940
PR23	6787	46.0	0.50	2719	-1369	245,311	57.6	10,875	65,229
PR13	6792	34.8	0.49	1978	-1122	1,728,051	54.8	15,086	471,084
PR14	6768	39.0	0.49	1978	-1524	1,000,038	58.7	9700	595,004
PR17	6717	41.9	0.49	2304	-1472	1,000,863	54.6	15,479	129,113
PR20	6755	39.0	0.49	2436	-1079	1,502,266	57.7	10,749	210,079

*Loads are illustrated in Figure 3.149. N_f is total number of experimental cycles; σ_{eq} is the equivalent stress for the loading parameter; N_i is the initiation life associated with the equivalent stress; and N_{prop} is the propagation life.
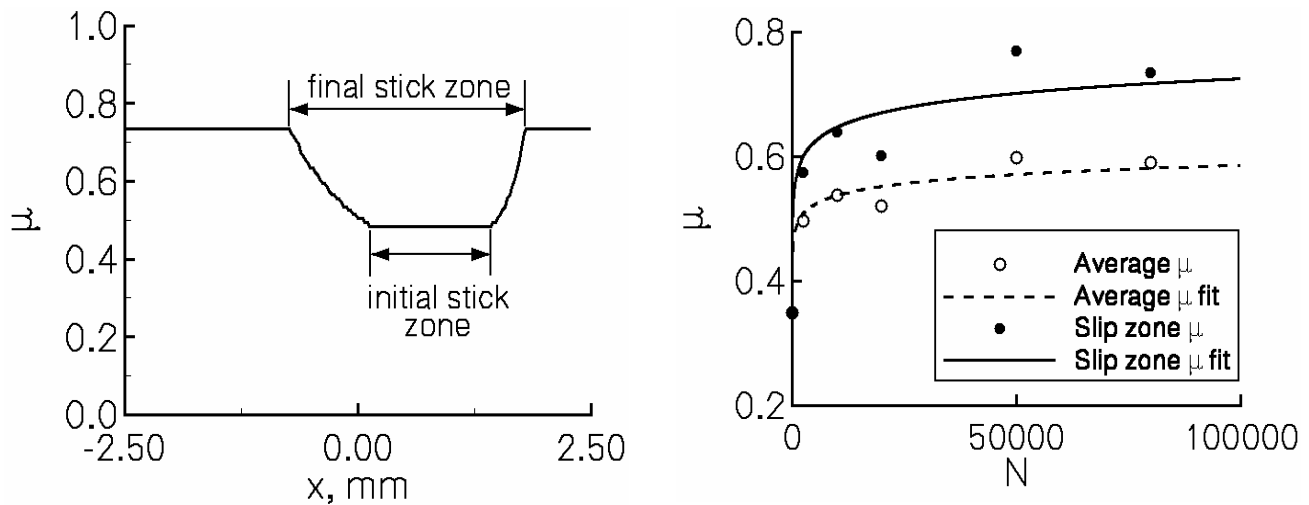
Figure 3.146. Illustration of transition of friction coefficient and growth of
stick zone during mixed-mode fretting fatigue experiment.

161

3.5.4   Fatigue Life Prediction

As illustrated previously, the fretting contact problem has been solved very efficiently using a set of singular integral equations (SIE) that relate the relative slip and the initial gap function to the contact tractions. An FFT based approach is used to obtain the sub-surface stress distributions for similar material contacts and a discrete Fourier transform technique has been successfully implemented for solving sub-surface stresses associated with dissimilar material contact. This approach can also be used for any arbitrarily specified profile and hence is more flexible than finite elements and is computationally efficient.

The complexity of fretting adds another level to the already intricate phenomenon of fatigue crack nucleation. While many theories for fretting crack nucleation have been proposed, most of them fall short of quantitative prediction of the cycles to crack nucleation [25-26]. From the stress analysis, it is clear that the fretting fatigue stress state is highly complex and multiaxial. Therefore, a model for a quantitative prediction of nucleation life has to take into account the multiaxial stress state in the specimen.

Stress invariant life parameters offer an approach for life calculation that is independent of the coordinate system and without the need to calculate a critical plane orientation and hence are obtainable very fast from the given stress field. The parameter σ_{eq} is defined as [27]

$$\sigma_{eq} = 0.5(\Delta \sigma_{psu})^w (\sigma_{max})^{(1-w)} \tag{3.31}$$

The stress invariant effective stress range is defined as

$$\Delta \sigma_{psu} = \frac{1}{\sqrt{2}} \sqrt{(\Delta \sigma_{xx} - \Delta \sigma_{yy})^2 + (\Delta \sigma_{yy} - \Delta \sigma_{zz})^2 + (\Delta \sigma_{zz} - \Delta \sigma_{xx})^2 + 6(\Delta \sigma_{xy}^2 + \Delta \sigma_{yz}^2 + \Delta \sigma_{zx}^2)}$$

$$\tag{3.32}$$

where, $\Delta \sigma_{psu}$ is the alternating pseudo stress range, and $\Delta \sigma_{ij}$ defines the pseudo-stress range for each stress component based on maximum and minimum points in the fatigue cycle. The Manson-McKnight mean stress term used to establish σ_{mean} and σ_{max} is given as:

$$\sigma_{mean} = \frac{\beta}{2\sqrt{2}} \sqrt{(\Sigma\sigma_{xx} - \Sigma\sigma_{yy})^2 + (\Sigma\sigma_{yy} - \Sigma\sigma_{zz})^2 + (\Sigma\sigma_{zz} - \Sigma\sigma_{xx})^2 + 6(\Sigma\sigma_{xy}^2 + \Sigma\sigma_{yz}^2 + \Sigma\sigma_{zx}^2)}$$

(3.33)

where σ_{mean} is the mean stress, and $\Sigma\sigma_{ij}$ represents the summed stress for each stress component based on maximum and minimum points in the fatigue cycle. The Manson-McKnight coefficient ($\beta = \beta_{MM}$) is defined as $\beta_{MM} = \frac{\Sigma\sigma_1 + \Sigma\sigma_3}{\Sigma\sigma_1 - \Sigma\sigma_3}$ where $\Sigma\sigma_1$ is the sum of the first principal stresses at the maximum and minimum stress points in the fatigue cycle and $\Sigma\sigma_3$ is the sum of the third principal stress at the maximum and minimum stress points in the fatigue cycle.

As is described elsewhere in this report, the large stress gradients at the edge-of-contact require special treatment. Here the approach taken is to modify the local stress by a stressed area term that recognizes the peak stress with the stress gradients on the surface are important. This approach is based on the probability of finding a weak grain on the surface where the stress is high and has been adapted from weak link approaches. Further background on the stressed area approach (Fs) and its use with the present data is in given in Reference [23]. The application of the Fs approach to notch fatigue can be found in Appendix G. (See also section 3.3.8.)

Two sets of experiments were analyzed, using the equivalent stress and the stressed area approach, to obtain an estimate of the life of Ti-6Al-4V specimens used in the experiments. The first set of experiments is for contact of similar isotropic materials (Ti-6Al-4V) detailed in Table 3.19 [28], whereas the second set involved fretting contact of dissimilar isotropic materials (Inco718 pads and Ti-6Al-4V specimens, detailed in Table 3.20).

The value of μ used was 0.5 for the first set and 0.74 for the second. The equation governing the crack nucleation from the baseline uniaxial testing data was reduced to

$$\sigma_{eq} = 52476 \, (N_i)^{-0.6471} + 450.85 \, (N_i)^{-0.03582}$$

(3.34)

Table 3.20. Experimental Conditions for Fretting Fatigue Experiments with Ti-6Al-4V Specimens and IN718 Pads*

Expt. No.	Controllable Loads			Measured/Calculated Loads				σ_{eq} (ksi) no residual σ	σ_{eq} (ksi) with residual σ	Life
	P (lb/in)	Top σ_{max} (ksi)	Top σ_{min} (ksi)	Bot. σ_{max} (ksi)	Bot. σ_{min} (ksi)	Q_{max} (lb/in)	Q_{min} (lb/in)			
Fret01	8251	23.1	7.7	35.5	0.5	3716	-2145	74.1	52.6	686600
Fret02	8160	24.1	8.2	35.6	0.3	3463	-2369	76.8	48.5	1000000
Fret03	8568	27.8	9.7	40.6	0.3	3837	-2811	76.9	43.1	394218
Fret04	8137	28.2	9.9	39.8	0.2	3484	-2887	81.5	52.2	114266
Fret05	8129	30.9	11.7	45.0	0.2	4234	-3468	80.5	62.6	119400
Fret06	8292	31.5	12.3	45.0	0.2	4059	-3643	81.6	54.6	116022
Fret07	8221	34.7	12.1	50.6	0.3	4779	-3560	80.9	64.0	127343
Fret08	8184	34.8	13.2	49.9	0.3	4526	-3866	81.4	57.4	32435
Fret09	8371	39.1	13.5	56.0	0.1	5065	-4031	82.8	65.5	51304
Fret10	8068	37.9	14.3	54.8	0.2	5066	-4213	85.3	64.1	25402
Fret11	8620	34.9	23.1	50.7	10.1	4746	-3895	85.0	63.2	64130

*Nucleation lives were predicted using σ_{eq} in Equation 3.34. σ_{eq} is calculated with and without the residual stress effect. Fret02 is a runout test. Propagation lives were predicted by fracture mechanics calculations [29].

The elastic contact stresses representative of the experiments indicated that the material near the contact edge yields plastically. This effect was treated approximately by capping σ_{max} at 110 ksi. Comparison between the predicted nucleation lives and experimental lives in Table 3.19 illustrates that propagation must be included in a total life approach.

3.5.5   Verification of Stress Analysis Through Crack Prediction Analysis in Pads

As indicated in Table 3.19, the measured fatigue lives (N_f) were much longer than those calculated (N_i) by the equivalent stress analysis given in Equation 3.34.   The problem is that this "initiation" life model does not account for the possibility of fatigue crack growth during the fatigue process. In conventional fatigue loading, this may not be an issue, as cracks quickly propagate to failure once they have formed, so that the total fatigue life is predominantly a period of crack nucleation as predicted by the equivalent stress model. One unique feature of the fretting fatigue process, however, is that the large contact stresses are confined to a small area, and rapidly decrease in magnitude outside that region. Thus, it is possible for fretting induced cracks to slow down, and possibly arrest, before coming under the influence of the cyclic stress fields associated with remote loading outside the contact zone.

A "total life" analysis was conducted to include both crack formation by the equivalent stress model and a fatigue crack growth period obtained by mode I fracture mechanics predictions. Stress intensity factors were computed by weight function procedures in this latter case for small cracks that developed in the contact stress gradients predicted by the fretting analysis [29], and used with the fatigue crack growth properties of the test material to predict the fatigue crack portion of life. The total fatigue life, defined as the sum of the equivalent stress "initiation life" prediction and the "crack growth" life, is shown in Figure 3.147 for the titanium/titanium fretting experiments.
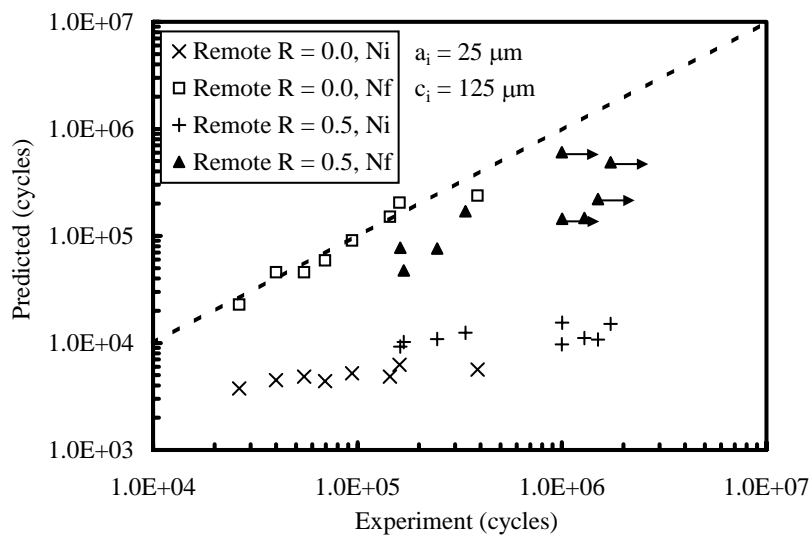
Figure 3.147. Comparison of predicted to experimental lives for Ti-6Al-4V on Ti-6Al-4V fretting fatigue tests. The predictions are plotted for initiation only (N_i = plus and x symbols) and initiation plus propagation (N_f = square and triangles) [29].

Similar results for Icon718 fretting pads in contact with Ti-6-4 specimens are shown Figure 3.148. Note that incorporating a fatigue crack growth period in the total life calculation gives much better predictions for the fretting fatigue life in both material combinations, and that these calculations required the dissimilar contacting material capabilities of CAFDEM.

165
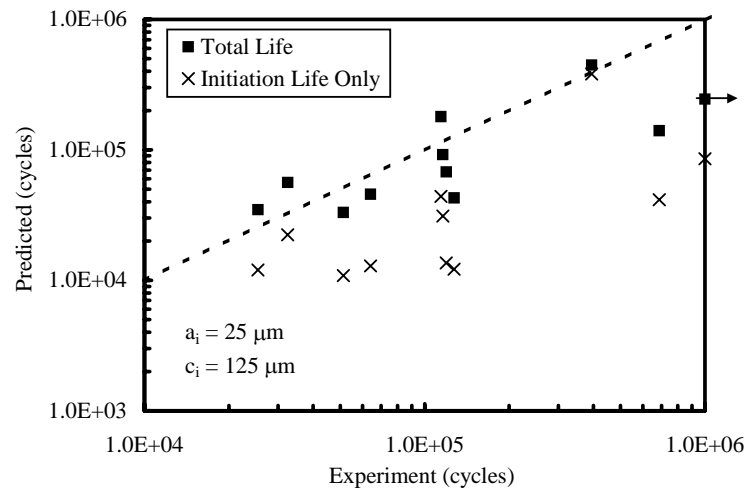
Figure 3.148. Predicted and experimental life comparison for Inco718 on Ti-6Al-4V fretting fatigue tests [29].

3.5.6 Coupling Capri/CAFDEM with FEM

3.5.6.1 Background

General Electric Aircraft Engines (GEAE) and Purdue University have developed a computationally efficient method for analyzing three-dimensional partial slip contact problems. The approach is to combine the advantages of the finite element method (FEM) with that of the singular integral equation (SIE) methods developed at Purdue University. FEM is used to model the influence of the blade and disk geometry along with the engine operating conditions (speed, gas loads, and blade loads) to (1) determine the pressure and shear load inputs to the SIE method and (2) to determine the "bulk" stress distribution resulting from the remote (non-edge of contact) loading. The superposition of the edge of contact and bulk gradients are important for determination of stress gradients necessary for fracture mechanics evaluations of cracks initiating at or near the edge of contact location.

The 3D FEM model allows for stress analysis of complicated 3D geometry where 2D analytical models fail, and the 2D SIE model allows for computationally efficient, high resolution contact stress evaluation where 3D models fail. The loads are obvious input requirements for the SIE method. In addition to the stresses due to contact, the engine

166

operational loads generate a significant bulk stress in the subsurface material. The SIE does not incorporate the bulk stress into the contact stress solution; therefore, the hybrid model includes the effects of both contact and bulk stresses by superposing the 2D SIE contact stress solution with the 3D bulk stress obtained from the same coarse 3D FEM model that supplies the contact loads. The contribution of the contact stresses in the coarse model FEM solution is assumed to be negligible. In conjunction with the edge of contact stresses, the SIE method calculates the expanded contact length. This contact length indicates the location in the FEM model from which the bulk stresses should be obtained. A bulk stress gradient is extracted from the FEM model along a straight path perpendicular to the surface at the edge of contact into the subsurface depth. The stresses of interest are those that would open a crack, namely stresses perpendicular to the projected crack plane. The final contact stress solution is then reported as the SIE tangential stress superposed with the FEM calculated bulk stress.

This approach also results in a significant reduction in time to determine the localized stresses at the edge of contact. For a simple case, FEM modeling using the Cormier, et al. [30] submodeling approach can take over a week of engineering time as compared to hours for the hybrid FEM-SIE method. This detailed submodeling requires an extremely fine mesh size often on the order of 0.00005 inch for a fully converged solution. Such fine mesh models are not typically generated for disk-blade dovetail attachments.

This hybrid method is demonstrated for a typical airfoil geometry and then is validated based on a comparison of the hybrid and a pure FEM analysis. Examples are also given for engine components that have been analyzed using the hybrid method.

This numerical/analytical hybrid method uses a "coarse" FEM model (Figure 3.149) to obtain the component bulk stresses, loads, and moments. Although referred to as "coarse" for purposes of resolving contact stresses, these meshes are typical of models used for LCF calculations with element sizes on the order of .05 inch (three orders of magnitude coarser than that required for a converged edge of contact FEM solution).
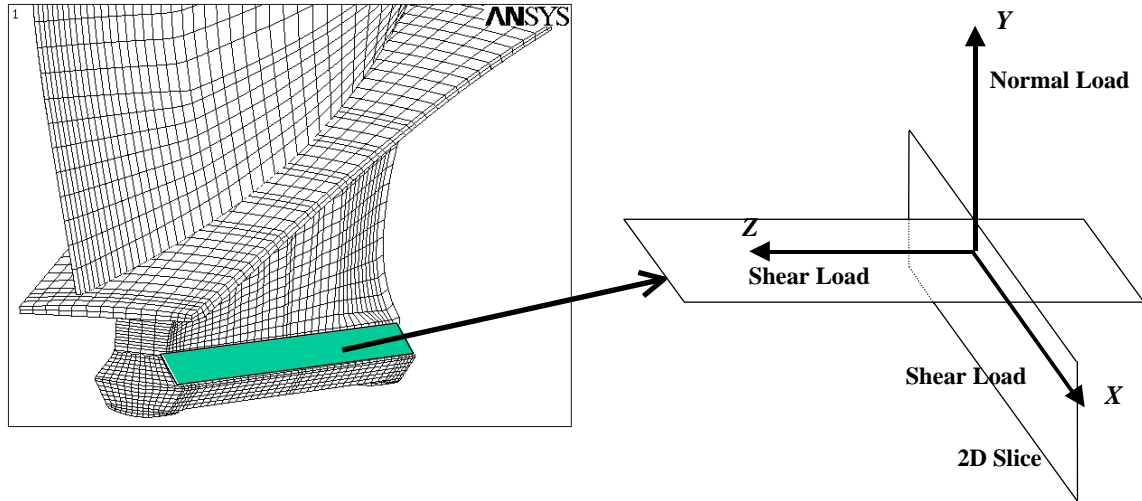
Figure 3.149. 3D FEM model of dovetail notch illustrating 2D slice taken for
SIE contact stress evaluation.

The results of these FEM analyses can provide the necessary inputs for the hybrid
method, so that no additional FEM analyses are required to perform a hybrid contact
analysis. Equivalent 2D contact loads are then calculated at parallel x-y plane slices for
several z-locations into the depth of the contact by taking the "coarse" mesh FEM result and
dividing by the distance between nodal slices. These 2D loads can then be used by the SIE
to evaluate the associated contact stresses at each nodal slice. Experience has shown that
this mesh size is adequate to obtain converged values of the contact loads (and is also coarse
enough to avoid including any significant level of stress concentration from the edge of
contact loading). The final hybrid solution is obtained by superposing the SIE calculated
edge of contact stress gradient with the bulk stress gradient obtained by FEM.

3.5.6.2   Validation of Hybrid FEM-SIE Method

The results of a very fine mesh FEM analysis were compared with those from the
hybrid method. The case used for comparison is a titanium disk dovetail attachment with
the axis of the dovetail skewed relative to the axis of rotation of the disk. The coarse FEM
model used in the hybrid process had element sizes on the order of 0.070 inches in the
contact region, while the fine FEM model element sizes are on the order of 0.0005 inches.
The detailed FEM analysis was not performed using the very structured submodeling

168

approach of Cormier, et.al. [30] and based on the mesh size is probably not a fully converged edge of contact FEM stress analysis. Needless to say, the fine FEM model took weeks to prepare and run, while the coarse model is a relatively routine stress analysis conducted in a much shorter time interval.

Figure 3.150 compares a stress gradient obtained using the hybrid process described with a stress gradient extracted from a finely discretized FEM model. These are the stresses perpendicular to the projected crack plane (parallel to the pressure face and are plotted along a vector perpendicular to the pressure face). The stresses in Figure 3.150 are normalized relative to the peak surface stress determined from the fine FEM mesh. The result from the hybrid method results in a local surface stress 14% higher than the FEM results. It is anticipated that if the FEM analysis had used a more refined mesh that the local stress would be somewhat higher. In any case, the stress gradients for both methods were very similar.
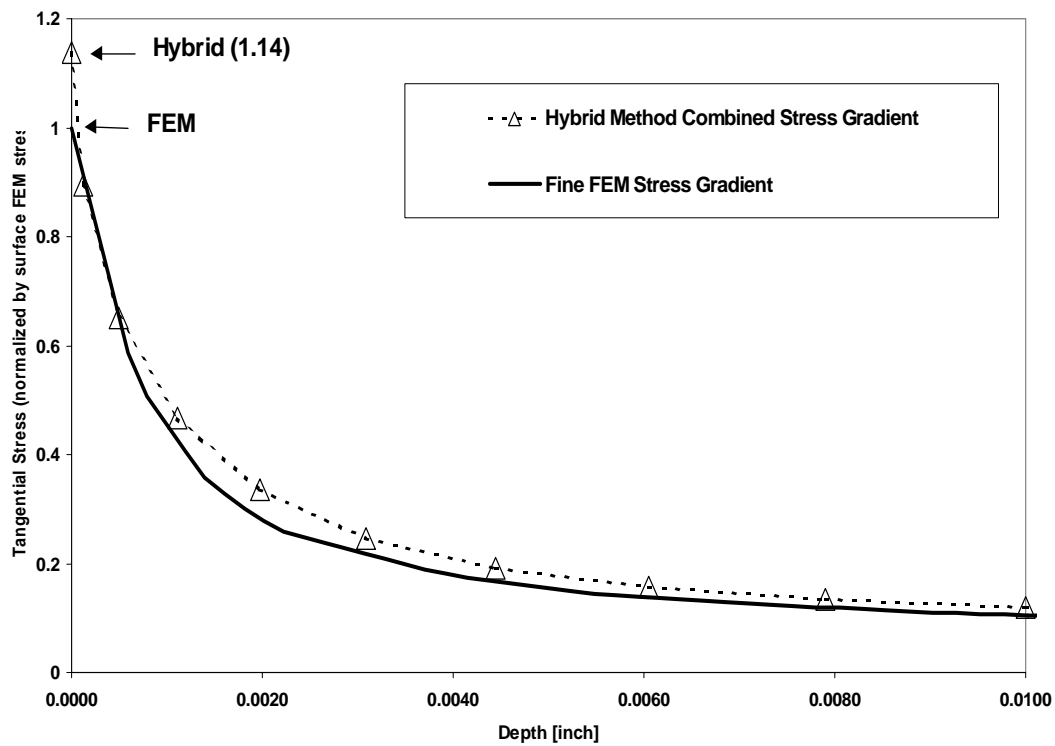
Figure 3.150. Comparison of hybrid approach stress gradient to fine FEM.

3.5.6.3   Use of Hybrid Method for Component Evaluation

The hybrid method has been successfully used to perform stress analyses for more than 15 different GEAE engine applications. These evaluations were performed and funded by GEAE engine programs and projects. The majority of these applications are dovetail attachments, although analysis of interrupted rabbet joints has also been performed. These analyses have been used to examine field events, provide insights to design and modifications of attachment regions, to evaluate the effects of non-conforming hardware, to confirm and reinforce FEM analyses, and to examine the sensitivities of various parameters on the local edge of contact stresses. The hybrid method, and the SIE analysis in particular, has been invaluable for the timely examination of the relative performance of various design geometries and loadings.

For most of these cases, the results of the hybrid stress analysis were used as input for fracture mechanics evaluations. These evaluations utilized standard fracture mechanics methods in use at GEAE and are utilized to determine the growth of typical edge of contact cracks. Due to the generally large stress magnitudes that occur at the surface of edge of contact problems, a method based on the work of Neuber [31] was used to estimate stress redistribution due to material plastic behavior. The gradients for mission points with stresses less than the peak stress were determined by permitting elastic unloading from the elastic-plastic gradient. All fracture mechanics analyses were performed using GEAE's state of the art fracture mechanics code. The features of this code include temperature dependent material properties as well as the influence of cyclic crack growth, time dependent crack growth, and shot peening. The appropriate options were used for the evaluation of the components.

For the cases where there was significant field experience, there was an excellent correlation between the fracture mechanics analysis and the field experience. The population of components evaluated included cases where both field cracks had and had not

been experienced. This positive correlation strongly suggests that the hybrid FEM-SIE method is an accurate stress analysis method.[1]

3.5.6.4   Future Development Needs

In the process of evaluating GEAE operating components, several issues were raised as to either the accuracy or process for determining the inputs to the hybrid FEM-SIE stress analysis methods. The potential benefits of including this method in the GEAE design and stress analysis toolbox have generated significant interest; however, there have been several features of this method that will require further development if they are to be included in our standard best practices. Some of these areas of interest are elaborated upon below.

A typical military mission, including the different types of missions experienced by a single aircraft (also known as mission mix) often consists of over 10,000 mission points. For life critical features such as bolt holes, local stresses can be accurately predicted through use of mission simulation programs and limited use of FEM analysis based on linear response. This same approach cannot be applied to contact regions due to the non-linear or path-dependent nature of friction in the contact region. Analysis of these complex missions using SIE analysis would require the definition of P, Q, and M for each mission point. At the current time, the absence of such technology limits the use of the hybrid FEM-SIE method.

---

[1]Subsequent to the completion of the work described herein, several other numerical exercises have been carried out using a hybrid FEM/SIE method. In the cases studied, the dovetail configurations were such that the forces developed were dependent upon the compliance of the specific dovetail as well as the local contact (pad) geometry. This makes these configurations statically indeterminate. It was found that the force obtained from a "crude" finite element analysis was not a converged value, that is, a finer mesh provided a different value. This issue is exacerbated by the nonlinear effect that friction plays in mission calculations. Thus, putting the force from a crude FEM analysis into the SIE code CAPRI did not provide an accurate local stress analysis. Only the use of a very fine mesh provided a nearly convergent solution, which tended to negate the benefits of using CAPRI for an accurate and time-efficient solution for local stresses. The degree of accuracy of the hybrid method described in this report, and the degree of inaccuracy of the hybrid method applied to statically indeterminate problems is dependent on the specific geometry involved and, thus, no general conclusions can be drawn at this point.

It should also be noted that after this report was written, modifications have been made to the computer code CAPRI so that it now considers bulk loads in the solution.

Many applications, especially for turbine components, involve dovetail attachments between blades of one material type and a disk of a different type of material. Much of the experience at GEAE has involved the use of CAPRI, the similar material version of SIE. The recent development at Purdue of CAFDEM, the dissimilar material version of SIE, allows the effects of these dissimilar material attachments to be analyzed. Initial uses of CAFDEM at GEAE have been met with issues pertaining to robustness and difficulties obtaining solution convergence. Although in general solutions are ultimately obtained by manipulation of various convergence parameters, such manipulations make the automated implementation of CAFDEM difficult. Enhancement of the robustness of the numerical solution of the SIE for dissimilar materials would accelerate the use of this method in the GEAE analysis toolbox.

In addition to the history effects inherent in a mission, the variation of both the normal and tangential loads is a reality between time points of a mission. The implementation of the SIE solution in CAFDEM allows for the variation of both of these load parameters, while the similar material version, CAPRI, assumes a constant normal load while accounting for the variation of the tangential load. Development of a version of CAPRI that allows the variation of both loads would permit a more wide spread use of this technology.

3.5.6.5   Summary Comments Regarding GEAE Experience

The significant developments made to edge of contact stress analysis in this program have made a great difference in the way in which gas turbine disk-airfoil attachments are analyzed. This has led to a much better understanding of the localized loading and material capability at these critical locations. The highly collaborative interaction between Purdue University and the engine companies has led to practical ways to implement basic knowledge of the physics of contacts into engineering analyses of operating components. Application of the hybrid FEM-SIE method combined with the positive correlation with field experience has accelerated the introduction of this technology into the tools used by GEAE designers. A few technological barriers still need to be breached before this technology can be fully implemented as a standard process, but the progress made

during this program has made a very significant contribution to the analysis and life prediction of disk-blade attachments.

3.5.7   Conclusion

The summary accomplishment of the attachment fatigue team is the notion that fretting fatigue can be treated with conventional mechanics-based life prediction tools. The favorable agreement between prediction and experiment supports the case that fretting fatigue can be modeled using conventional fatigue life prediction approaches provided that the analysis is capable of correctly obtaining the local contact stress field. Mechanics and materials research conducted by many members of the HCF materials team, as well as the USAF sponsored MURI on HCF, have gone into supporting the idea that fretting can be treated using conventional fatigue and fracture tools. This is a substantial accomplishment in the fretting fatigue basic research community. Much of the data presented above and in the substantial set of publications resulting from this program substantiates this conclusion.

As is detailed in Section 3.5.6.3, the above conclusion led GEAE to use life prediction tools developed as part of the program to analyze 15 different GEAE engine applications. Pratt & Whitney used this notion to develop a comprehensive set of tools that it is using in attachment fatigue life prediction as summarized in Appendix N. Figure N4 of that Appendix illustrates clearly that attachment fatigue life prediction meets the program exit criteria. Such rapid technology transition is a major accomplishment.

It is recommended that work continue to validate the life prediction tools for complicated load histories in controlled laboratory settings as well as further developing the life prediction tools for coated and shot-peened surfaces. Such development requires a combination of fretting fatigue experiments to assess the effect of surface treatment on tribology, detailed fractography of the fretting specimens and pads and embedding the effect of surface treatment in the modeling capability.

Chapter 4
Nickel Based Single Crystal Alloys

4.1   MATERIAL

PWA 1484 is a second-generation single crystal alloy containing nominally 3% Re and developed by P&W for advanced turbine airfoil applications. The alloy is bill of materials for the Joint Strike Fighter (JSF) and was selected by the HCF Consortium as the material of choice for this program. PWA 1484 is a precipitation strengthened cast mono grain nickel superalloy based on the Ni-Cr-Al system. The macrostructure of this material is characterized by parallel continuous primary dendrites spanning the casting, without interruption, in the direction of solidification. Secondary dendrite arms (perpendicular to solidification) define the interdendritic spacing. Solidification for both primary and secondary dendrite arms proceeds in <001> family directions. Carbides, undissolved eutectic pools and associated microporosity are concentrated in the interdendritic regions. These features represent microstructural discontinuities, and often exert a controlling influence on the fatigue crack initiation behavior of the alloy.

4.1.1   Microstructure

The microstructure consists of approximately 60% by volume of γ' precipitants in a Γ matrix. In both alloys the cuboidal precipitate ranges from 0.35 to 0.6 m. The γ' precipitate, based on the intermetallic compound Ni3Al, is the strengthening phase in nickel based superalloys. The high volume fraction of γ' precludes dislocation bypass at low and intermediate temperatures forcing precipitate shearing. Long-range dislocation motion via precipitate shearing is favored because the ordered precipitate is coherent with the matrix. The atomic lattices of each are coplanar with only a slight lattice spacing mismatch. The precipitates resist this shearing to a varying degree due to temperature and environment, depending on dislocation dynamics within the ordered γ' structure.

4.1.2   Coatings

The original plan for this program was to test all except a few specimens in the uncoated condition. However, initial work on uncoated specimens at 1900°F ([Appendix O](#)) showed that there was a significant effect of oxidation on the uncoated surface on the failure mode and HCF capability. Since all production single crystal turbine blades are fabricated with some type of environmental coating to eliminate such oxidation effects, continuing to test uncoated material created the risk that the HCF models produced by this program would not be valid for single crystal turbine blades in an engine. Therefore, the decision was made in December 2000, to apply a commercially available PtAl diffusion coating to all Task S.2 specimens to be tested later at 1900°F. (Specimens tested early in the program at 1900°F were uncoated since the crack growth behavior being determined was for the base alloy in the presence of air. All specimens tested at 1100°F were also uncoated.) PtAl coatings are in relatively wide use on single crystal turbine blades from many engine manufacturers, so this coating type represented a point of common ground.

Howmet Thermatec Division was selected as the coating supplier and a purchase order was placed to coat the gage sections of specimens with their single phase MDC150L PtAl coating. The ends of the specimens were masked to prevent coating that might interfere with the threads that provided load introduction and alignment. A coating cycle was selected to produce a coating approximately 2-mils thick. Because the coating process was at high temperature and the specimens were already fully heat treated, after coating the specimens were re-heat treated using standard PWA 1484 parameters at and below the coating temperature (i.e., specimens were not re-solutioned or primary aged).

The coating microstructure as received from Howmet is shown in Figure 4.1. This figure shows a coating of overall thickness of 0.0021 inches. The coating is divided into two layers, as is typically seen in diffusion aluminide coatings on superalloys: an outer, Al-rich additive layer of single-phase β-Ni (Pt) Al, and an inner inter-diffusion layer consisting of a mixture of β, γ', and refractory metal TCP's and carbides. While such coatings are brittle at low temperatures, they are known to be ductile at the 1900°F test temperature selected for the higher temperature tests.
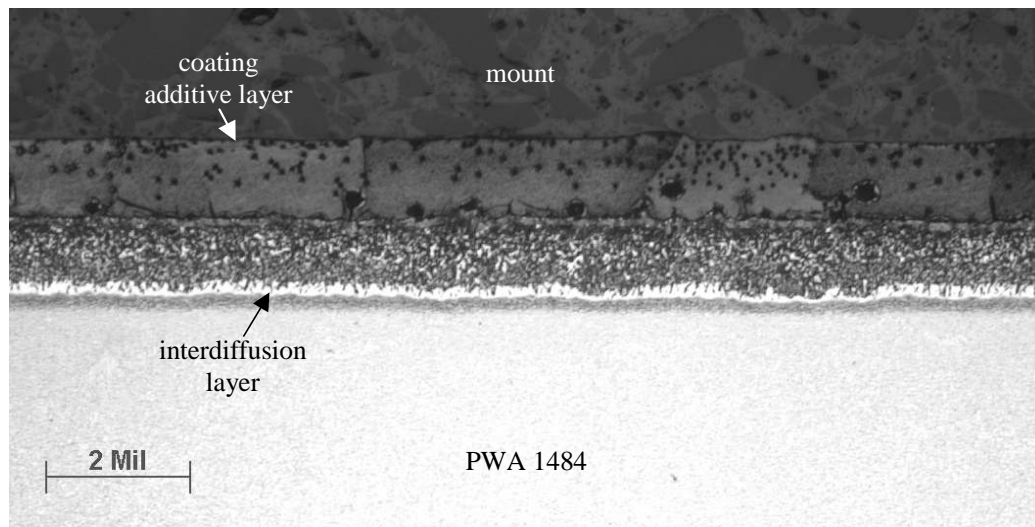
Figure 4.1. Typical microstructure of MDC150L PtAl coating applied
on 1900°F PWA1484 specimens.

4.1.3   Fabrication

4.1.3.1   Procurement

Precision Cast Components (PCC) Airfoils Inc., a current production source for
PWA 1484 castings, was selected to provide cast material for the program after a review of
all possible potential suppliers.

Master alloy was obtained from a single heat that conformed to the specification
chemistry of PWA 1484. Master heat chemistry certifications were supplied by PCC. The
master heat chemistry, major elements, is given below:

C	Cr	Co	Mo	W	Al	Ta	Re	Hf	Ni
0.026	4.97	9.92	1.92	5.9	5.69	8.57	2.89	0.09	Bal

All bar and plate castings made from the master heat were serialized so that they
could be traced to the master heat. All castings were etched and inspected metallographically
to ascertain the presence of non-conforming defects. Defects would include recrystallized
and equiaxed grains, low and high angle boundaries, slivers, and striations. These were

carefully mapped for each casting and their location documented (1,2,3). Three types of round bar castings were made:

1.) 0.625" diameter by 6" long with a primary orientation of <001>,

2.) 0.625" diameter by 6" long with a primary orientation of <011>

3.) 1.0 " diameter by 8" long with a primary orientation of <001>.

Additionally, single crystal slabs were cast as follows:

1.) Short slabs: 3" tall by 6" wide by 0.625" thick having the primary <001> orientation in the 6" direction, The secondary orientations of the short slabs was intentionally varied. Some were cast to provide <001>, some with <110> and some with a <120> orientation.

2.) Tall slabs: 6" tall by 3"" wide by 0.625" thick having the primary <001> orientation in the 6" direction

3.) Thick slabs: 6" tall by 3" wide by 1.75" thick having the primary <001> orientation in the 6" direction.

All bar and slab castings were Hot Isostatically Pressed (HIP) per the recommended PWA 1484 requirement such that non-surface connected porosity would be less than 1%. Heat treatment was performed by PCC and conformed to the PWA 1484 specification. Foundry certifications were supplied by PCC Airfoils Inc. and these covered the master heat detailed chemistry, master heat stress rupture qualification test, and metallographic reports documenting any residual non-surface connected porosity and solution requirements for each type of casting.

A. *Grain Maps*

Grain maps were used to identify the location of secondary grain imperfections and any defects. The following types of secondary grain defects were mapped: High Angle Boundaries (HAB): These boundaries are visible grain boundaries of secondary grains that grow in the same direction as the main crystal. For the round bars, an HAB was defined as a deviation of 8 degrees or more of the secondary grain from the main crystal. Low angle boundaries (LAB) occurred when the deviation of the secondary grain was less than 8 degrees. These boundaries were considered acceptable defects and were not identified on the grain maps.

- *Slivers*: Slivers are narrow, secondary grains that are aligned with the primary orientation and are usually too fine for a determination of the misorientation.

- *Freckle Chain*: During crystal growth secondary dendrites often break off. These broken dendrite tips then become nuclei for chains of secondary equiaxed grains usually aligned in the crystal growth direction. The occurrence of the freckle chains was recorded in the Grain Maps.

- *Equiaxed Cluster*: An equiaxed cluster is a collection of several misoriented secondary grains with a low aspect ratio. These growth defects were also recorded in the Grain Maps.

4.1.3.2 Orientation

Laue x-ray diffraction measurements were performed and reported by PCC Airfoils Inc. The Laue results showed that the primary orientation of all bars was within the required 10 degrees of <001>. In addition, the degree of misorientation between the required secondary and primary orientation and a casting's serial number was also provided. The orientation data for each casting was carefully documented in detail referencing the serial number of the casting.

4.2 FRACTURE MECHANICS MODELING AND TESTING

4.2.1 Background

4.2.1.1 Objectives and Approach

The objective of this work was to develop analytical and experimental approaches for addressing the effects of frequency, stress ratio, crystal orientation, and temperature on the threshold and near-threshold fatigue crack growth behavior of PWA 1484 single crystal alloy under HCF conditions. In addition to the above, mode mixity (K_{II}/K_I) was also included as one of the potentially significant parameters influencing crack growth behavior. Thus, part of the analytical effort involved computation of the stress intensity factor for mixed-mode cracks. Companion experiments involved the determination of the fatigue crack growth threshold as a function of stress state and crystal orientation, using an asymmetric four point bend (AFPB) test technique. The influence of mode-mixity on the FCG threshold was determined at 1100°F as a function of stress state ranging from pure Mode I to pure

Mode II. The results were used to develop a fracture mechanics approach for treating high-cycle, mixed-mode fatigue crack growth in single crystal blades.

The applicability of isotropic solutions to stress intensity analysis of anisotropic materials was investigated using finite element methods. For various crack and material orientations, the FEM results indicated that errors in using isotropic solutions were generally small and, as a consequence, isotropic solutions were used throughout the analyses in this section for Mode I calculations.

While fracture testing was performed primarily on smooth specimens, a fracture study from blunt notches was also conducted to simulate the notched behavior typical of the edge of contact region of the blade attachment. The objective of this particular effort was to determine the methods necessary for analyzing the growth or arrest of HCF cracks in a notch stress field at 1900°F. Since stress concentrations are one of the more common sites for crack initiation, it was deemed important to be able to model the growth of cracks from notches, particularly under HCF excitation where cracking is expected to proceed very rapidly once the driving force for growth exceeds the threshold. One of the additional complicating factors at 1900°F, in addition to the usual complexities of notch analysis, is the occurrence of time-dependent stress relaxation around the notch due to creep. While notched specimens were fabricated for testing, experimental verification of the pre-test predictions was never performed.

The possibility of interaction between HCF and LCF loading was also explored to a limited extent.

4.2.1.2   Scope

A comment that applies to both isotropic and anisotropic materials is that of the definition of a mixed-mode threshold. This is particularly relevant to anisotropic single crystal alloys where the extension of a crack depends not only on the loading conditions (the mode mixity), but also on the crystal orientation with respect to the crack. If a crack extends in a non-self similar manner (it kinks, for example), then it cannot be considered to be a true mixed mode crack growth threshold. For engineering purposes, however, we consider this to be the mixed mode threshold. This threshold, however, may not be an inherent material property and may depend on crack length.

179

In this section, the threshold for crack propagation is determined for PWA 1484 alloy using different specimen geometries, analyses, and test methods as used by GEAE and PWA. The application of linear elastic fracture mechanics (LEFM) and the stress intensity factor, K, to characterize crack growth behavior, has been described in the final report for Phase [1]. Methods for representing crack growth data, fitting data to different growth laws, and test methods for obtaining data are all described there. The applicability of LEFM to small cracks, the extension of crack growth modeling to a second material, and the use of other crack geometries was subsequently investigated and is reported in the titanium section of this final report. In particular, the prediction of threshold stress under HCF to notched components, including those subjected to FOD, was investigated and is documented in this report. Notch analysis was used to develop a method to predict the threshold stresses for FOD and fretting fatigue where steep stress gradients are encountered. Comparisons of model predictions with results of simulated FOD and machined notch experiments as well as fretting fatigue experiments were encouraging. The method used, termed the "Worst Case Notch" (WCN) model, enables the boundaries between crack initiation, crack growth followed by arrest, and crack growth to failure to be delineated.

The parameters particularly relevant to single crystal alloys were examined to some degree in the program, but only two temperatures were evaluated—1100°F, representing a typical operating temperature in the blade attachment region, and 1900°F, representing a typical operating temperature on the blade surface. Models were developed for each temperature, with no interpolation between them. Most of the lower temperature work was performed at Pratt & Whitney, with the higher temperature work taking place predominantly at GEAE. Mixed mode testing was performed at Southwest Research Institute. HCF/LCF interaction testing was performed at Pratt & Whitney.

4.2.2   Mode I; Smooth

4.2.2.1   <u>K-Calculations</u>

Single crystal superalloys possess elastic anisotropy, which, in principle, can affect the computation of the stress intensity factor for cracks. In order to determine the extent of the effect of anisotropy, and whether it was satisfactory to use existing isotropic K-solutions in this program, an investigation of the effect of the anisotropy of PWA 1484 was

undertaken. Two-dimensional, plane stress analyses were conducted by both PWA and GEAE using slightly different methods on different illustrative problems. PWA used FRANK2D and the associated J-integral calculations. GEAE used the ANSYS code with COD and stresses approaching the crack tip for their calculations.

A. Review of Anisotropic Elasticity

The K solutions for a single crystal (anisotropic) alloy require an understanding of anisotropic elasticity for their development and application. Details and a background tutorial in anisotropic elasticity are presented in Appendix P for completeness in this report.

B. Calculation of the Stress Intensity Factor in Anisotropic Media

For a crack in an infinite anisotropic plate subject to a far field stress, Sih et al [32] showed that the stress intensity solution is identical to the isotropic case

$$\begin{Bmatrix} K_I \\ K_{II} \end{Bmatrix} = \begin{Bmatrix} \sigma_y^\infty \\ \tau_{xy}^\infty \end{Bmatrix} \sqrt{\pi a} \tag{4.1}$$

Chan and Cruse [33] demonstrated that in many situations, isotropic stress intensity solutions for test specimen geometries adequately approximate the anisotropic solutions for single crystal materials. In structural analyses, however, it is not clear that this will generally be true. Often, it may be desirable to calculate stress intensity factors directly from strain energy release rates, g_I and g_{II}, obtained from finite-element solutions. For mixed mode loading involving Modes I and II (excluding Mode III for now), Sih gave the following relationships for g_I and g_{II}

$$g_I = -\frac{K_I^2}{2} A_{22} \operatorname{Im}\left[\frac{\mu_1 + \mu_2 + K_{II}/K_I}{\mu_1 \mu_2}\right] \tag{4.2}$$

$$g_{II} = \frac{K_{II}^2}{2} A_{11} \operatorname{Im}\left[\mu_1 + \mu_2 + (K_I/K_{II})(\mu_1 \mu_2)\right] \tag{4.3}$$

Equations (4.2) and (4.3) can be solved in terms of the stress intensity factors K_I and K_{II} as

$$K_I = \sqrt{\frac{g_I}{A + B K_{II}/K_I}} \tag{4.4}$$

181

$$K_{II} = K_I \frac{K_{II}}{K_I} \tag{4.5}$$

where,

$$\frac{K_{II}}{K_I} = \frac{-D}{2C} + \frac{g_{II}}{g_I}\frac{B}{2C} \pm \sqrt{\left(\frac{g_{II}}{g_I}\right)^2\left(\frac{B}{2C}\right)^2 + \frac{g_{II}}{g_I}\left(\frac{A}{C} - \frac{BD}{2C^2}\right) + \left(\frac{D}{2C}\right)^2}$$

$$A = -\frac{A_{22}}{2}\mathrm{Im}\left[\frac{\mu_1 + \mu_2}{\mu_1\mu_2}\right]$$

$$B = -\frac{A_{22}}{2}\mathrm{Im}\left[\frac{1}{\mu_1\mu_2}\right]$$

$$C = \frac{A_{11}}{2}\mathrm{Im}\left[\mu_1 + \mu_2\right] \tag{4.6}$$

$$D = \frac{A_{11}}{2}\mathrm{Im}\left[\mu_1\mu_2\right]$$

The sign of the Mode II stress intensity must be determined from the sign of the displacements, as illustrated in Figure 4.2.

K_I   K_II
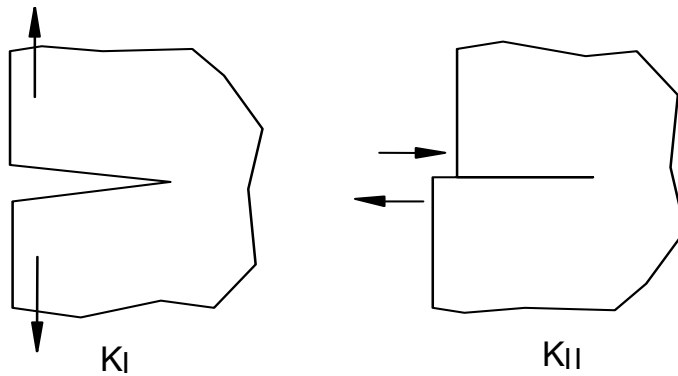
Figure 4.2.   Illustration of crack tip loading modes
(shown with positive sense).

While the above Equations (4.2- 4.6) are true for 2D cracks propagating in a principal plane (the crack faces normal to the principal plane), cracks of more general orientation involve interaction between Modes I, II, and III. The involvement of Mode III is treated in [34], but is beyond the scope of the current investigation.

For the more restricted case of single crystal materials for which $E_1=E_2$ (crack propagating within principal 1-2 plane[1]), we have $A_{11}=A_{22}$ and $\text{Im}(\mu_1\mu_2)^{\pm1}$ vanishes, eliminating the coupling terms in (4.4) and (4.5). Furthermore, the remaining terms in the Im[ ] operator become equal in magnitude, but opposite in sign, leaving

$$K_i = \sqrt{\frac{2g_i E_1}{\text{Im}[\mu_1 + \mu_2]}} \qquad (4.7)$$

and the mode mixity relation

$$\frac{K_{II}}{K_I} = \sqrt{\frac{G_{II}}{G_I}} \qquad (4.8)$$

C. Single Edge Notched (SEN) Specimen Analysis (Pin-Loaded PW Specimen)

A pin-loaded, single edged notched specimen of aspect ratio h/w=6 was analyzed using the FRANC2D fracture code (see www.cfg.cornell.edu) with specially orthotropic properties representative of PWA 1484 material at 1100°F and 1900°F. The stress intensity factors were determined based on plane stress assumptions, using J-integral calculations provided by FRANC2D[2]. The values are believed to be well within 1 percent accuracy, based on comparable studies with isotropic solutions. As illustrated in Figure 4.3, the effect of orthotropy on the stress intensity factors of <001/010> crack orientation is within six percent of the isotropic solution up to a/w=0.8.

---

[1] Note that the anisotropic formulation is singular when $E_1=E_2$. To obtain numerical results it is suggested that in this case E_1 and E_2 be specified as slightly different.

[2] A special purpose version of FRANC2D was used that has the calculation of strain energy release rates enabled for anisotropic materials by way of the J-integral.
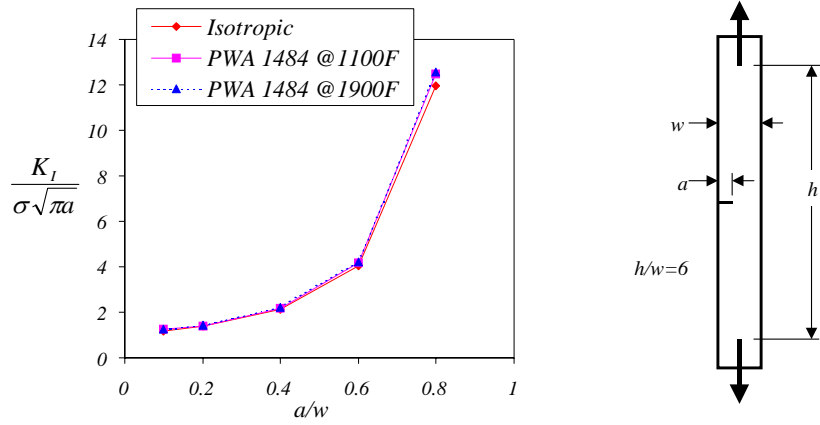
Figure 4.3. FRANC2D analysis of single-crystal SEN specimen.

The deviation from the equation used to calculate mode I SIFs for isotropic SEN specimens was developed for various orientations (all of which exhibit the symmetry implied by Equation P2 of Appendix P), and is summarized in Figure 4.4 as a smoothed fit of correction factors to account for anisotropy. (Note that the isotropic analysis showed the isotropic SIF equation to be within about 0.5 percent accuracy over the range studied). The deviations due to anisotropy were not very large, but might not always be considered negligible.
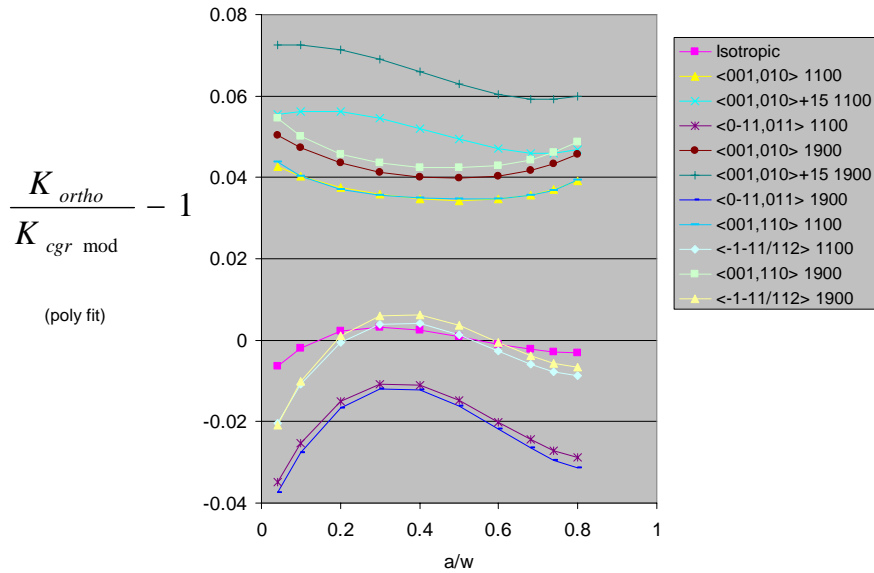
Figure 4.4.   2D anisotropic correction factors for pin-loaded SEN specimens at 1100°F and 1900°F.

184

The SEN specimens used were nominally 0.05 inches thick, and 0.5 inches wide in the gage section, with pin loaded ends three inches apart center to center. Threshold crack growth data was taken at a/w values ranging from about 0.27 to 0.62. Thus, the correction factor at a/w = 0.45 was used for all specimens, resulting in corrected stress intensity factor error estimated at 0.5 percent or less. The correction factors obtained in this manner are tabulated in Table 4.1, and were used to correct the threshold data for anisotropy for creation of the PW threshold model, as will be explained in a later section.

Table 4.1. Anisotropic Correction Factors $K_{I\,ortho}/K_{I\,iso}$ for Pin-Loaded SEN Specimen with a/w = 0.45

Temperature (F)	Orientation	$K_{I\,ortho}/K_{I\,iso}$
1100	<001/010>	1.0345
1100	<001/010>+15°	1.0507
1100	<0-11/011>	0.9874
1100	<001/110>	1.0348
1100	<-1-11/112>	1.0030
1900	<001/010>	1.0398
1900	<001/010>+15°	1.0645
1900	<0-11/011>	0.9861
1900	<001/110>	1.0423
1900	<-1-11/112>	1.0052

D. Four Point Bend Specimen Analysis (SwRI Specimen)

A similar analysis was performed for the SwRI 4-Point Bend Specimen to obtain anisotropic corrections to the isotopic solution, but was only evaluated for the symmetric loading scenario, with a/w=0.45. The results are given in Table 4.2.

E. Single Edge Notched (SEN) Specimen Analysis (Fixed End GEAE Specimen)

Pratt & Whitney also performed an anisotropic solution for a fixed end SEN specimen in the <001/010> orientation only, at a/w=0.45, with the results given in Table 4.3. Comparisons can be made with the results of calculations provided by GEAE in Section 4.2.2.1.F.

Table 4.2. Anisotropic Correction Factors $K_{I\,ortho}/K_{I\,iso}$ for Symmetrically Loaded 4-Point Bend Specimens with a/w = 0.45

Temperature (F)	Orientation	$K_{I\,ortho}/K_{I\,iso}$
1100	<001/010>	1.0363
1100	<001/010>+15°	1.0481
1100	<0-11/011>	0.9814
1100	<001/110>	.8860
1100	<-1-11/112>	1.093
1900	<001/010>	1.0426
1900	<001/010>+15°	1.0616
1900	<0-11/011>	0.9799
1900	<001/110>	.8749
1900	<-1-11/112>	1.118

Table 4.3. Anisotropic Correction Factors $K_{I\,ortho}/K_{I\,iso}$ for GEAE Fixed End SEN Specimen

Temperature (F)	Orientation	$K_{I\,ortho}/K_{I\,iso}$
1100	<001/010>	1.062
1900	<001/010>	1.070

F.   *K – Calculations for Edge Crack Specimen by GEAE*

A 2D plane stress finite element analysis (using ANSYS) of an edge crack (Figure 4.5) was conducted by GEAE for four different material orientations rotated with respect to the stress axis (0, 20, 30, and 45 degrees) and four values of a/t (0.125, 0.250, 0.375, 0.5). Anisotropic elastic properties for PWA 1484 were used as supplied by Pratt & Whitney. The elastic properties have cubic symmetry, so three independent constants were needed, effectively, a Young's modulus, E, a Poisson's Ratio, ν, and a shear modulus, G, all in the material coordinate system. Figure 4.5 shows the definition of material orientation and a/t for the edge crack model. In these analyses, highly refined models were used to calculate stress intensity values for an edge crack subjected to a 1-ksi remote stress. The stress intensity calculations were performed using both the crack opening displacements and the stresses approaching the crack tip.
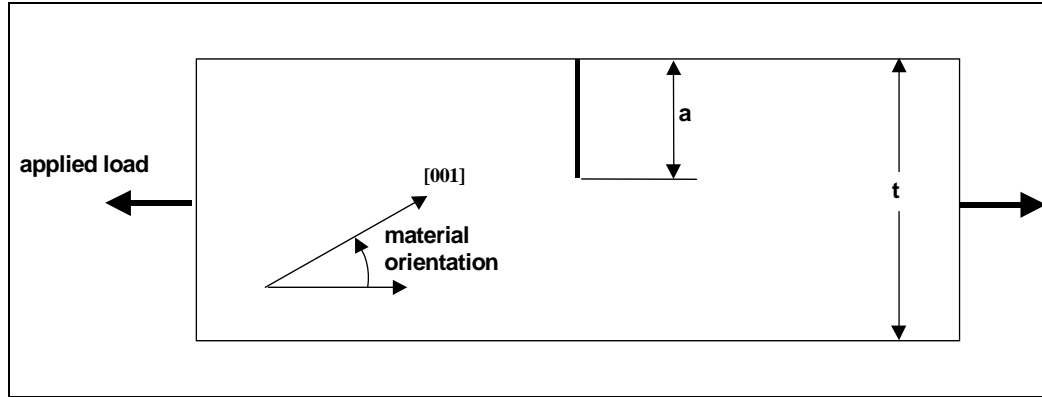
Figure 4.5. Edge crack geometry for single crystal stress intensity calculations.

For all cases, the two methods gave results that were in close agreement with each other and with the isotropic handbook solution by Tada [35]. Figure 4.6 shows the effect of misorientation from the specimen axis on the K_I value obtained, at fixed values of a/t. The deviation of isotropic K_I from the ANSYS anisotropic solution was relatively small, in all cases less than or equal to 3%. The Tada isotropic solution gave values about 3% lower than the anisotropic solution for a 0° misorientation. As the misorientation angle increased to about 25°, the difference dropped to near zero; with further increase in misorientation to 45° the isotropic Tada solution overestimated the anisotropic one by about 3%.

Figure 4.7 shows the K solution for a range of a/t at a material orientation of 30 degrees. The deviations between anisotropic and isotropic solutions were negligible and essentially independent of a/t ratio.

A second study was undertaken to examine the effect of rotation of the material about a common stress axis on the anisotropic K. A 3D edge crack model was created as shown in Figure 4.8. The figure also shows a close up of the crack tip region. In this particular problem, the model was fixed to simulate a plane strain condition and stress intensities were calculated from the stresses approaching the crack tip. One material axis was assumed to be in the direction of load. The other material axes were rotated through a range of angles (θ) as shown in Figure 4.8. Figure 4.9 shows the orthotropic stress intensity values as a function of angle. The isotropic edge crack solution from Tada is also plotted in Figure 4.9. The largest difference between the two solutions is less than 3%.

187

Anisotropic vs Isotropic K-Solution (Edge Crack)
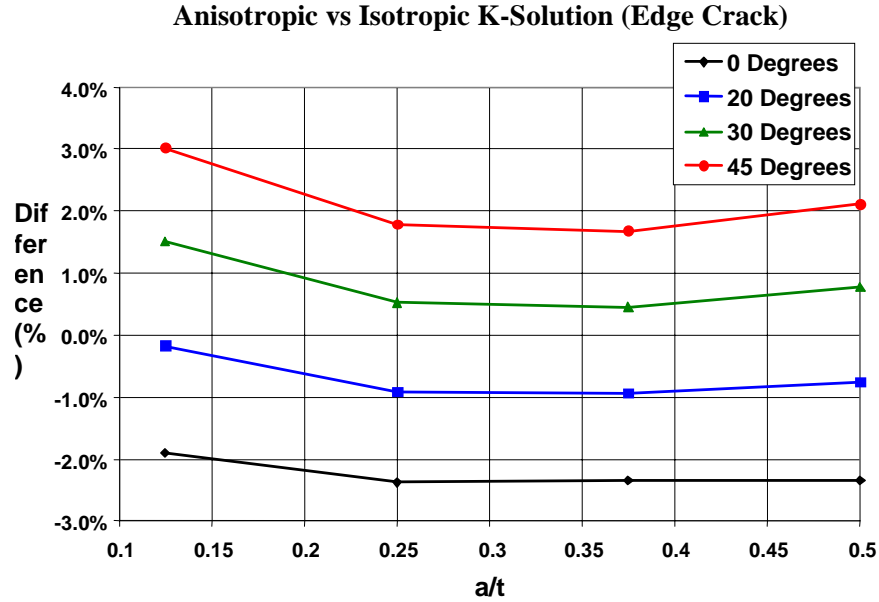
Figure 4.6. Dependence of anisotropic K (using stress) on rotation of PWA1484 material about an axis perpendicular to the plane of Figure 4.5, compared with Tada [35].

Orthotropic PW1484 Stress Intensity (30 Deg)
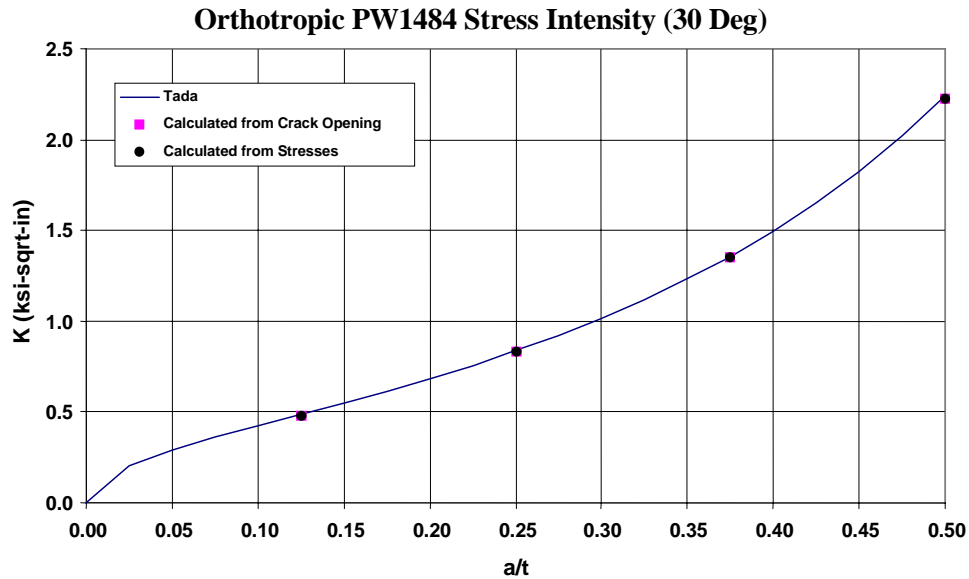
Figure 4.7. Comparison of stress intensities calculated by anisotropic finite element mModel (using crack opening and stress) and Tada's [35] isotropic solution at a material orientation of 30°.
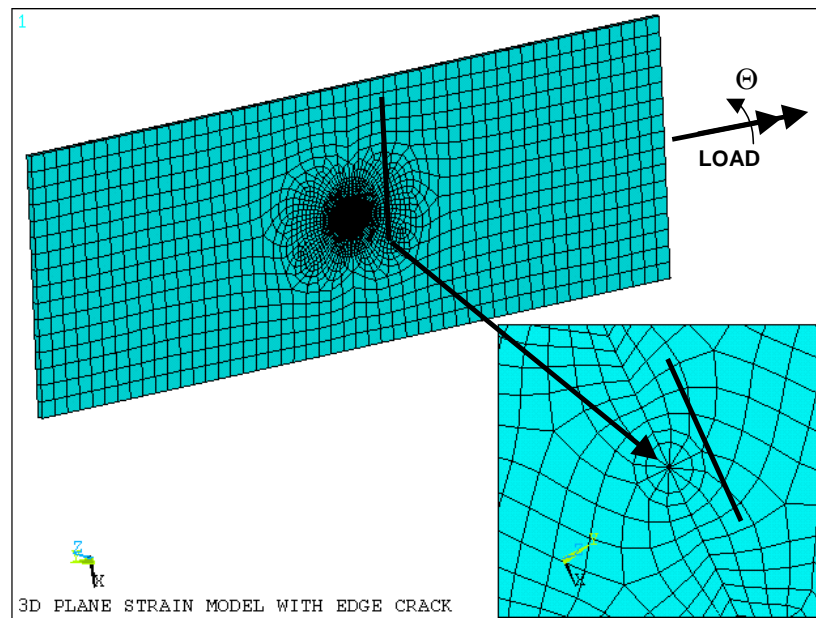
Figure 4.8. Model used to investigate effect of material orientation about loading <001> axis.

K vs. Rotation About Load Direction
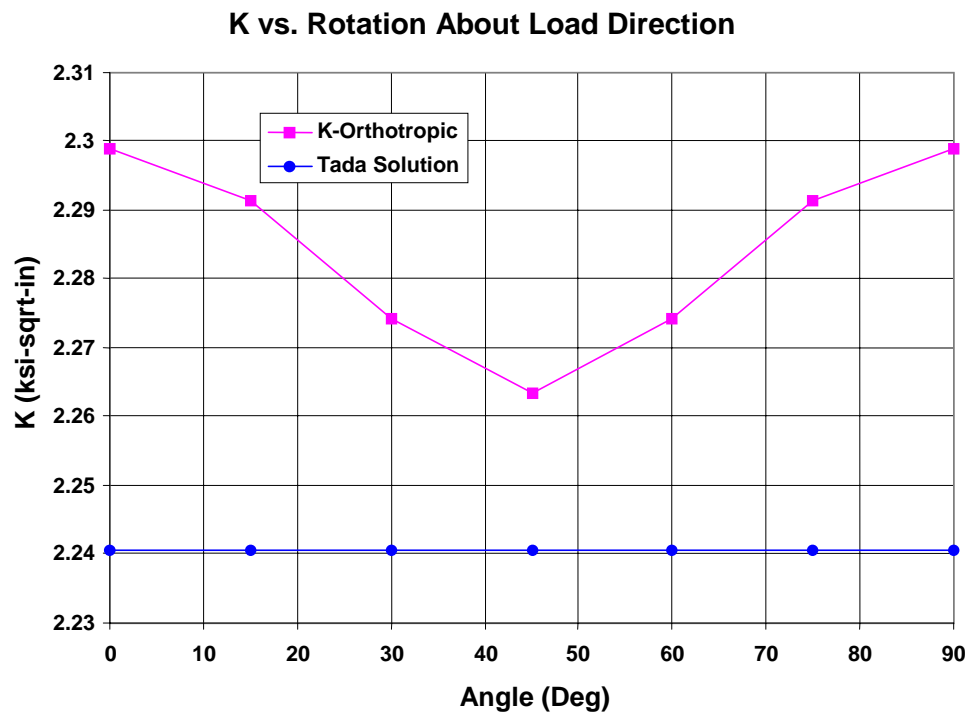
Figure 4.9. Stress intensity as a function of angle of rotation about the <001>axis.

Based on these analyses, it was judged that the effect of anisotropy on the K-value was not significant, and all K values reported in this document by GEAE were obtained from isotropic solutions.

4.2.2.2 Threshold Testing: Fracture Mechanics Test Method & Specimen Geometry

A pin loaded single edge notch specimen with dimensions of width of 0.50 inches and a thickness of 0.050 inches was chosen for the majority of the crack growth testing described in this report. The sample geometry is shown in Figure 4.10.

This specimen design was selected because it permits the analysis of a through thickness crack in thin sections and is efficient from a material availability standpoint. The gripping scheme for this geometry allowed for maximum freedom of rotation. Initial testing incorporated knurled bushings clamped to either side of the sample with a threaded bolt. The bushings were attached to the load train with a clevis, which allowed the bushing to rotate but not the sample.
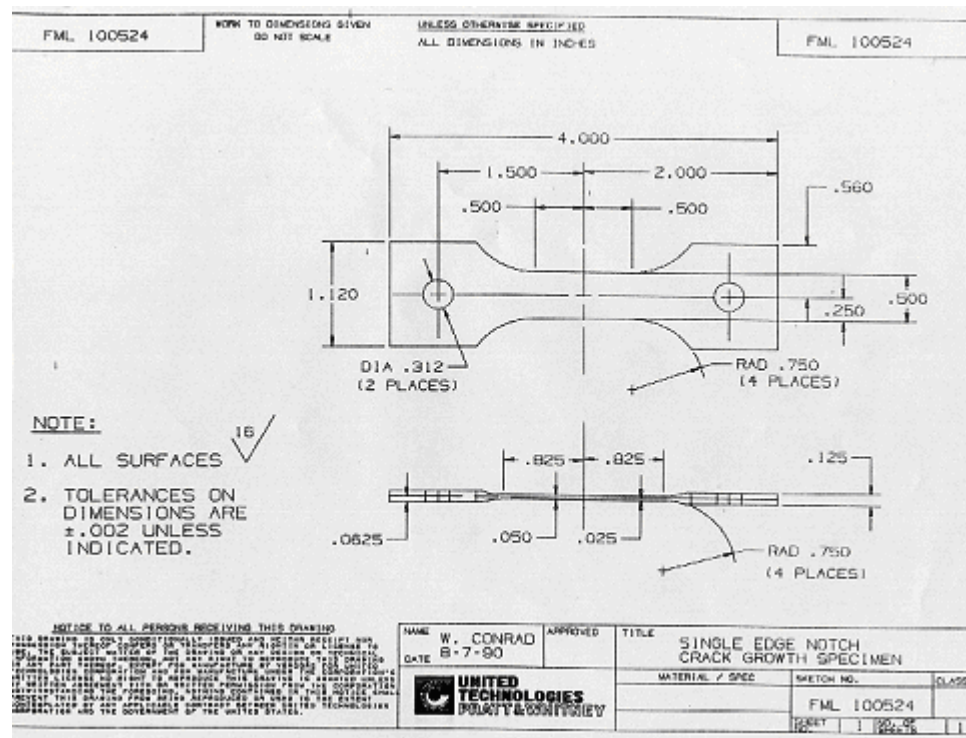
Figure 4.10. PW pin-loaded single edge notched fatigue crack growth.

This created a situation that resulted in out of plane global octahedral crack growth. The gripping scheme was changed to a strictly pin loaded arrangement where the pin diameter was 75% of the specimen loading hole. This dramatically reduced the friction between the loading pin and the sample pinhole and changed the fracture mode to a macroscopically planer crack. This also produced better confidence that the stress intensity solution for a pin loaded SEN specimen would be valid, since it assumes free rotation at the loading pins. Figure 4.11 shows the difference in crack path as a result of the adjustment in gripping schemes.

The stress intensity for a Single Edge Notch specimen also assumes the material is isotropic and that the crack is progressing though five or more randomly oriented crystals. Single crystal materials do not fit this constraint of the K solution. A 2 dimensional orthotropic analysis of K_I was determined from a FRANC2D J-integral, for the <001/010> orientation.

Figure 4.11.   Photographs of the result from the gripping scheme adjustments and sharper EDM starter notch. Left-hand side is global octahedral mixed mode fracture. The right hand side in mono-planer mode I fracture.

The results show that β, the geometry factor in the stress intensity solution, remains equivalent through a normalized crack length (a/w crack length divided by specimen width) of a/W 0.6, then begins to deviate slightly. The results of the analysis are shown in Figure 4.12.

$$\beta = \frac{K_I}{\sigma\sqrt{\pi a}}$$
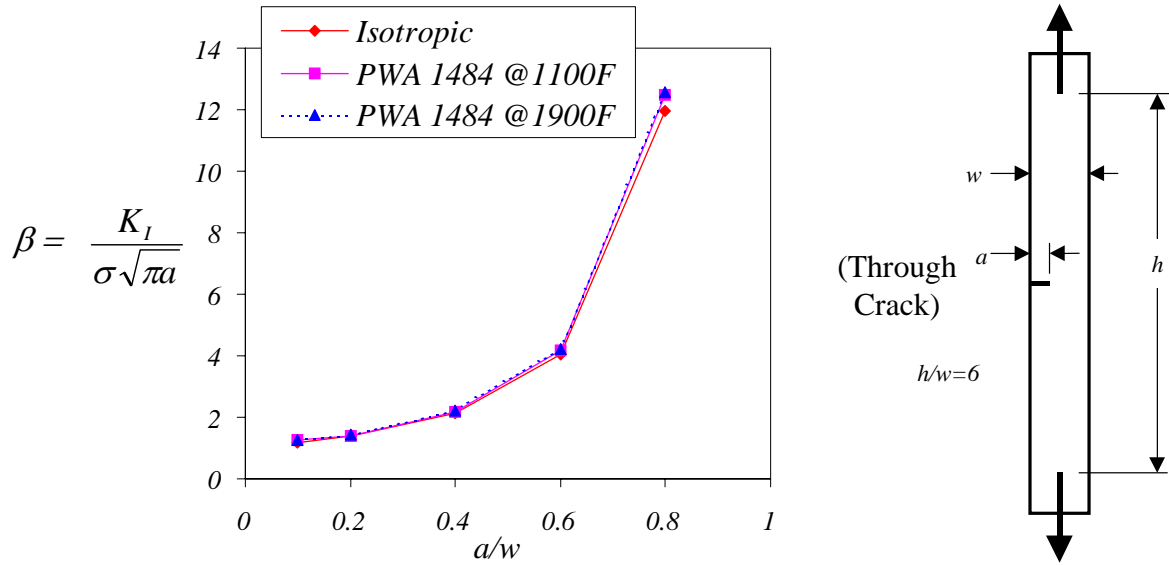
Figure 4.12. Anisotropic versus isotropic stress intensity geometry factor analysis.

A computerized system developed by Fracture Technology Associate (FTA) was used to monitor the crack growth and control an MTS servo-hydraulic test frame. The crack length was monitored continuously using the reversing Direct Current Electrical Potential Drop (DCEPD) measurement technique, enabling stress intensity to be controlled as a function of crack length. A single analytical relation converted the normalized electrical potential drop into the corresponding crack length, namely Johnson's equation [36]. The computer continuously recorded the test data, and in real time calculated the crack length, the stress intensity factor, and the linear regression analysis of crack growth rate. The test mode could then be automatically changed when the crack reached a predetermined value. Computer monitoring and control is an intricate part of threshold testing.

A. K-Gradient Determination

Fatigue crack growth threshold data generation is typically begun by cycling at a ΔK level, which is at, or slightly above the precrack level. Subsequent loading is then decreased incrementally as the crack propagates. This process is repeated throughout the test until crack arrest is achieved. Threshold testing done in this study, was generally started at growth rates at or below 1×10^{-6} in / cycle to avoid influencing the threshold result from prior loading history of the precrack procedure.

The $K_{gradient}$ or rate of load shedding is another important factor in generating fatigue crack growth rate threshold values. The normalized K-gradient is defined as $C = (1/K)*(dK/da)$. ASTM recommends values of (-2 in^{-1}) or less but states that higher values of C for certain materials have been found to be acceptable. The purpose of this experiment is to find the highest value of C that would allow threshold material property data generation without the undesirable effect of loading history on PWA 1484 at 1100°F at three different stress ratios (R = 0.1, 0.5 and 0.8). Experiments were performed at C = -6, -10, -20 and –30. All but two of the near threshold tests were conducted at a cyclic frequency of 10-20 Hz. Comparison of this data was aided by generating two or more threshold tests on a single sample, which eliminated specimen-to-specimen variations from the comparison of different values of C. This was made possible because the higher shed rates utilized less specimen ligament for each data set. Typically three to four threshold tests were performed on each sample; Table 4.4 summarizes the results. The data clearly shows that shed rates as high as 30 in^{-1} could be used without compromising the test results.

It is also noteworthy to mention the abruptness at which ΔK threshold occurs in this material. Crack arrest takes place, at or below 2E-7 in/cycle independent of stress ratio and shed rate, suggesting a well-defined crack growth limit. This behavior was also noted by Cunningham, *et al,* [37] and was given the demarcation ΔK_{lim} to describe this phenomenon.

B. Methods

Methods and capability to perform threshold crack growth testing on single crystal superalloys have been demonstrated for some time, at least since the 1980's [38,39]. The method demonstrated followed ASTM E647 for the most part, although specific test specimens and K-shed rates, C (C = 1/K [dK/da]), have deviated from the ASTM recommendations. In these early efforts, temperatures as high as 2000°F and K-shed rates up to 20 in^{-1} were used, and the applicability of electrical potential drop (PD) methods for crack monitoring and test control were demonstrated. More recently, similar procedures were demonstrated in [40,41]. These test methods were for the most part used in the present investigation. Some testing was performed at each test temperature to confirm that the shed rates selected were low enough to not influence the threshold results.

Table 4.4. Summary of Test Conditions for Single Crystal Alloy Shed Rate Study
Frequency =20Hz Orientation=001/010 (A2LR7, A2LKR, A2LLK, A2LRN)

Test ID	Stress Ratio	Temperature (deg F)	K-Gradient (1/in)	Frequency Hz	ΔK_{th} (ksi√in)
9301A (A2LR7-5)	0.50	1,100	-20.0	10 Hz	3.87
9301B (A2LR7-5)	0.50	1,100	-20.0	10 Hz	3.86
9302A (A2LR7-6)	0.80	1,100	-20.0	10 Hz	2.80
9302B (A2LR7-6)	0.80	1,100	-20.0	10 Hz	2.86
9336A (A2LKR-9)	0.80	1,100	-10.0	20 Hz	2.84
9336B (A2LKR-9)	0.80	1,100	-20.0	20 Hz	2.81
9336C (A2LKR-9)	0.80	1,100	-30.0	20 Hz	2.93
9336D (A2LKR-9)	0.80	1,100	-30.0	20 Hz	3.08
9337A (A2LLK-1)	0.80	1,100	-6.0	20 Hz	2.98
9337B (A2LLK-1)	0.80	1,100	-30.0	20 Hz	3.32*
9337C (A2LLK-1)	0.80	1,100	-30.0	20 Hz	2.96
9337D (A2LLK-1)	0.80	1,100	-30.0	20 Hz	3.08
9338A (A2LRN-1)	0.10	1,100	-6.0	20 Hz	5.67
9338B (A2LRN-1)	0.10	1,100	-30.0	20 Hz	5.59
9338C (A2LRN-1)	0.10	1,100	-30.0	20 Hz	5.49
9339A (A2LRN-2)	0.10	1,100	-10.0	20 Hz	6.09
9339B (A2LRN-2)	0.10	1,100	-20.0	20 Hz	6.15
9339C (A2LRN-2)	0.10	1,100	-30.0	20 Hz	6.36
9340A (A2LRN-3)	0.10	1,100	-6.0	20 Hz	5.65
9340B (A2LRN-3)	0.10	1,100	-30.0	20 Hz	6.19
9340C (A2LRN-3)	0.10	1,100	-30.0	20 Hz	6.21
9341A (A2LRN-4)	0.10	1,100	-10.0	20 Hz	5.61
9341B (A2LRN-4)	0.10	1,100	-20.0	20 Hz	5.51
9341C (A2LRN-4)	0.10	1,100	-30.0	20 Hz	5.75
9342A (A2LRN-5)	0.10	1,100	-20.0	1 Hz	7.30
9342B (A2LRN-5)	0.10	1,100	-20.0	10 CPM	7.01
9343A (A2LRN-6)	0.76(12.0)	1,100	-20.0	20 Hz	2.89
9343B (A2LRN-6)	0.80(18.0)	1,100	-20.0	20 Hz	2.48
9343C (A2LRN-6)	0.80(27.0)	1,100	-20.0	20 Hz	2.69**

* False threshold due to test interruption.
** Not a true threshold since crack continued to grow at 2-3 x 10^{-9} inches/cycle.

In the current program, several specimen geometries were used according to the purpose required. The bulk of the testing was performed on pin-loaded single edge notched specimens. The PW version of this specimen is shown in Figure 4.10 and the GEAE version in Figure 4.13.
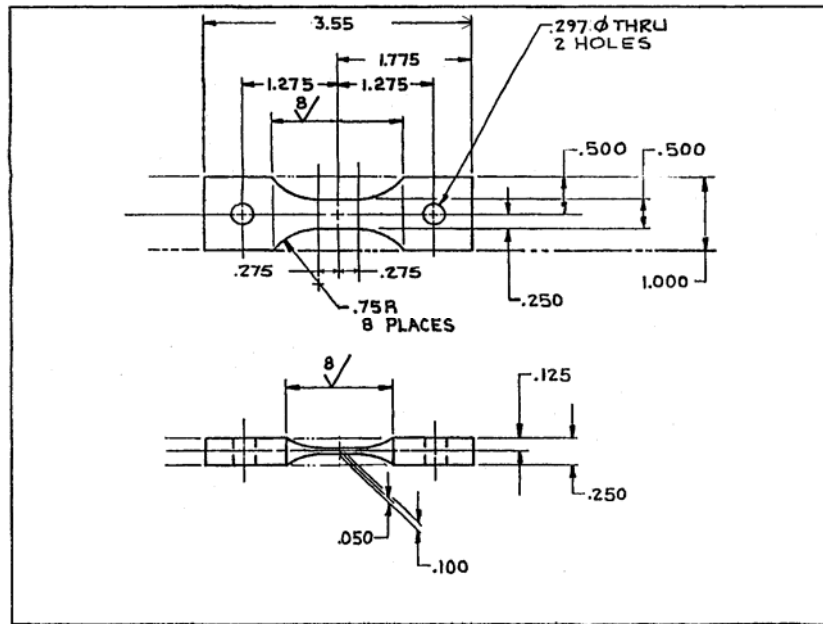
Figure 4.13. GEAE pin-loaded single edge notched fatigue crack growth specimen.
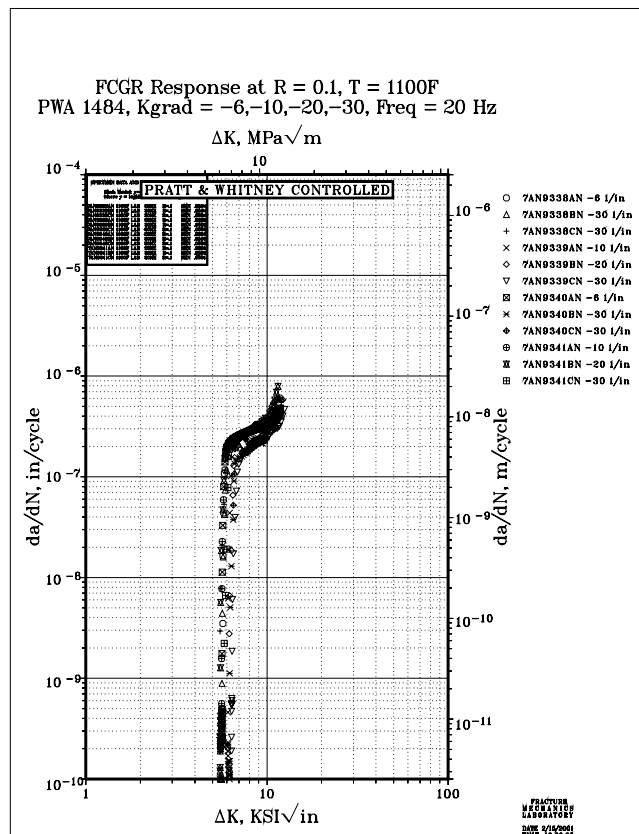
Figure 4.14. Shed rate effects in PWA1484 at 1100°F, R = 0.1.

195

At 1100°F a K-shed rate investigation was performed using the pin-loaded SEN specimen of Figure 4.13. Stress-ratios of both 0.1 and 0.8 were examined, using material with <001>/<010> crack orientation. Shed rates, C, of -6, -10, -20, and -30 in^{-1} were examined, and as shown in Figures 4.14 and 4.15 and Table 4.5, all thresholds were similar. To be slightly conservative, all subsequent shed rates were performed at a rate of C = -20 in^{-1}.

Table 4.5. Threshold Measurements in PWA1484 as a Function of Stress Ratio and Shed Rate at 1100°F. Orientation = <001>/<010>

Test ID	Stress Ratio	Temperature (deg F)	K-Gradient (1/in)	Frequency (Hz)	ΔK_{th} (ksi$\sqrt{in}$)
9301A (A2LR7-5)	0.50	1100	-20.0	10	3.87
9301B (A2LR7-5)	0.50	1100	-20.0	10	3.86
9302A (A2LR7-6)	0.80	1100	20.0	10	2.80
9302B (A2LR7-6)	0.80	1100	-20.0	10	2.86
336A (A2LKR-9)	0.80	1100	-10.0	20	2.84
9336B (A2LKR-9)	0.80	1100	20.0	20	2.81
9336C (A2LKR-9)	0.80	1100	-30.0	20	2.93
9336D (A2LKR-9)	0.80	1100	-30.0	20	3.08
9337A (A2LLK-1)	0.80	1100	-6.0	20	2.98
9337B (A2LLK-1)	0.80	1100	-30.0	20	3.32*
9337C (A2LLK-1)	0.80	1100	-30.0	20	2.96
9337D (A2LLK-1)	0.80	1100	-30.0	20	3.08
9338A (A2LRN-1)	0.10	1100	-6.0	20	5.67
9338B (A2LRN-1)	0.10	1100	-30.0	20	5.59
9338C (A2LRN-1)	0.10	1100	-30.0	20	5.49
9339A (A2LRN-2)	0.10	1100	-10.0	20	6.09
9339B (A2LRN-2)	0.10	1100	-20.0	20	6.15
9339C (A2LRN-2)	0.10	1100	-30.0	20	6.36
9340A (A2LRN-3)	0.10	1100	-6.0	20	5.65
9340B (A2LRN-3)	0.10	1100	-30.0	20	6.19
9340C (A2LRN-3)	0.10	1100	-30.0	20	6.21
9341A (A2LRN-4)	0.10	1100	-10.0	20	5.61
9341B (A2LRN-4)	0.10	1100	-20.0	20	5.51
9341C (A2LRN-4)	0.10	1100	-30.0	20	5.75
9342A (A2LRN-5)	0.10	1100	-20.0	1	7.30
9342B (A2LRN-5)	0.10	1100	-20.0	0.17	7.01
	(K_{max})				
9343A (A2LRN-6)	0.76(12.0)	1100	-20.0	20	2.89
9343B (A2LRN-6)	0.80(18.0)	1100	-20.0	20	2.48
9343C (A2LRN-6)	0.80(27.0)	1100	-20.0	20	2.69**

* False threshold due to test interruption.
** Not a true threshold since crack continued to grow at 2-3 x 10^{-9} inches/cycle.
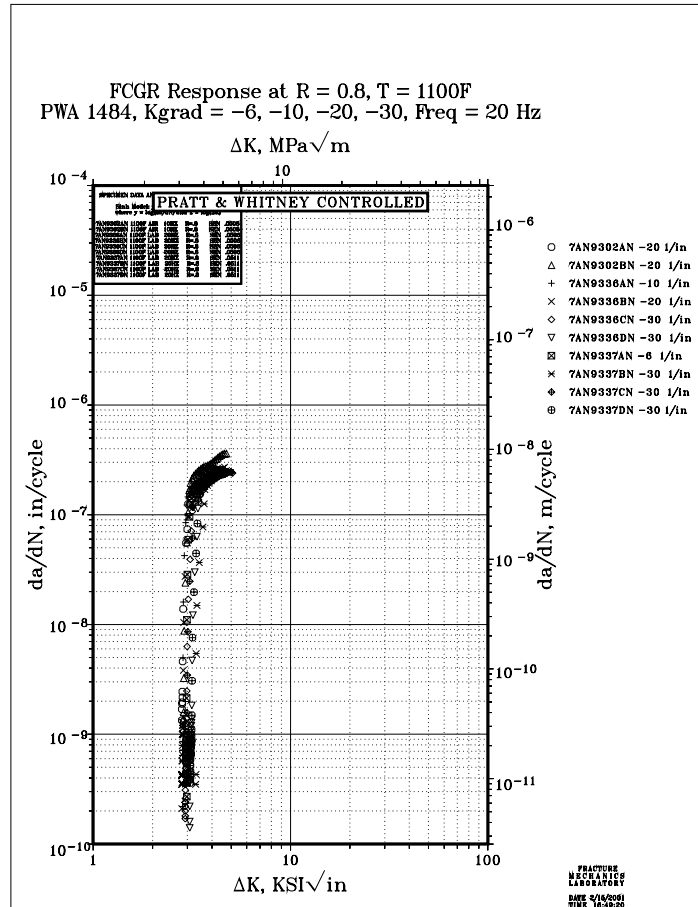
Figure 4.15. Shed rate effects in PWA 1484 at 1100°F, R = 0.8.

At 1900°F, the yield strength of PWA 1484 is significantly lower than at 1100°F, and there was some concern that the high shed rates possible at 1100°F might lead to artificial elevation of the threshold when used at 1900°F. In addition, there was concern that creep during testing might increase the inelastic zone and thus contribute to threshold elevation. Early in the program, before PWA 1484 material was received, shed tests with C = -10 and -20 in[-1] were performed at 1900°F on a similar single crystal alloy, Rene N5. These tests showed similar da/dN behavior between the sheds with different C's. To evaluate this on PWA 1484, several tests were performed at 1900°F with C = -20, -30, and -60 in[-1]. The results, shown in Figure 4.16, indicate that the threshold behavior is independent of C up to and including C = -30 in[-1]. At C = -60 there was a noticeable elevation of threshold. For the remainder of the shed testing, C = -20 in[-1] was used at 1900°F.

197
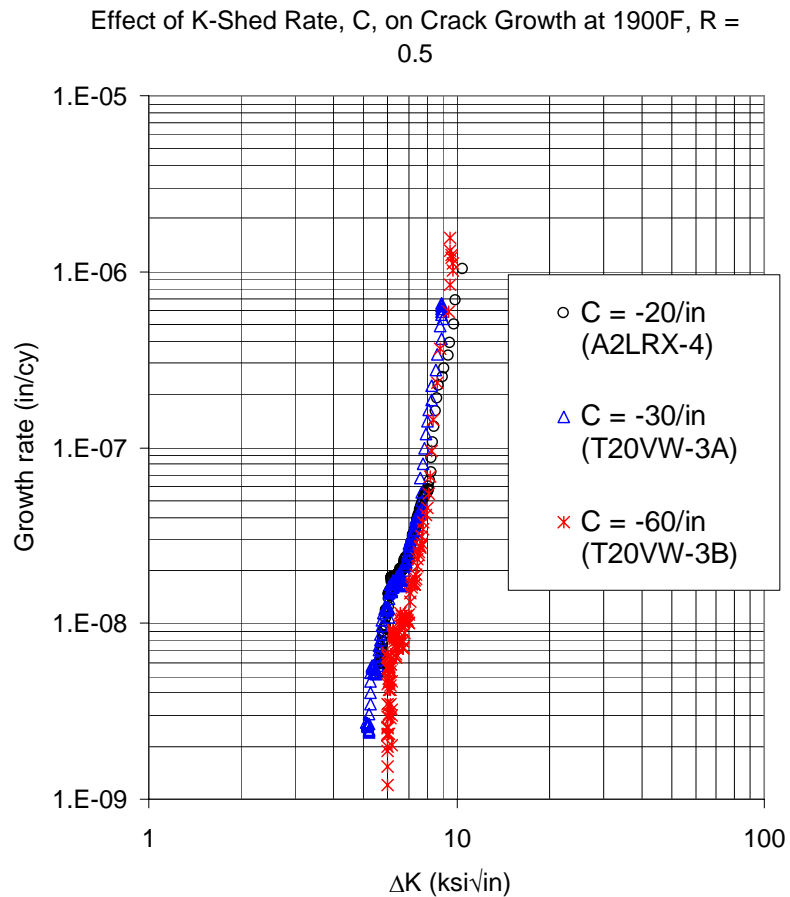
Figure 4.16. Shed rate effects in PWA 1484 at 1900°F, R = 0.5.

At 1900°F, several other threshold test methods were investigated during the effort to determine the effect of high frequency on threshold at 1900°F. These will be described in Section 4.2.2.2.*C,* in association with the high frequency tests.

The crack growth rate and threshold response of several different types of specimens used at GEAE was compared to demonstrate confidence in the test method and analysis. In addition to the pin end SEN geometry shown in Figure 4.13, GEAE investigated a fixed end SEN specimen, Figure 4.17, and a surface flawed specimen, Figure 4.18. These were examined for three reasons: first, it is quite possible for some portions of a turbine blade airfoil (the region represented by the 1900°F efforts) to sustain compressive stresses created by thermal gradients. In order to be able to test cycles with compression a specimen with greater compression stability than a pin-loaded SEN is required. Both the fixed end SEN

specimen and the surface flaw specimen provide significant compressive stability. Second, based on limited experience at lower temperatures, there was a concern for the introduction of loading pin sticking due to its oxidation and seizing against the mating surface. This might have the effect of diminishing the ability of the pin to rotate freely in the specimen or fixture, and thus change the loading boundary conditions and hence the stress intensity. In the limit a fully seized pin would act like a fixed end specimen. Finally, the ability to compare data from different crack geometries and loading types would provide a good test of the validity of our experimental and analytical methods at 1900°F.
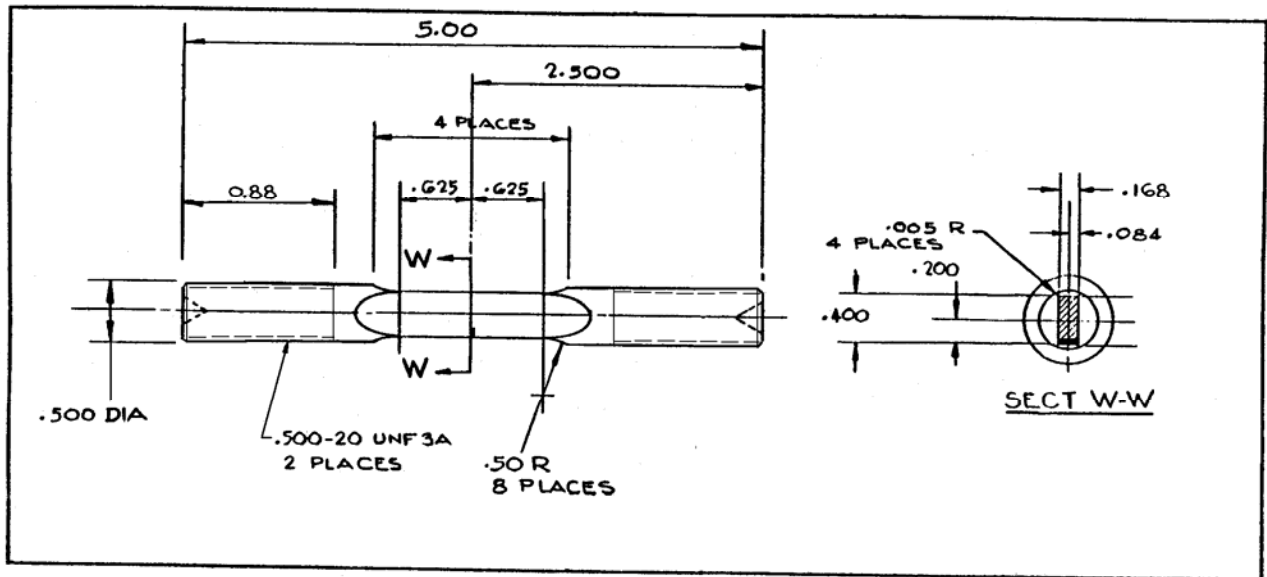
Figure 4.17. GEAE fixed end SEN crack growth specimen.

The fixed end SEN specimen design shown in Figure 4.17 was chosen as meeting the requirement of sustaining compressive loads during cycling based on GEAE experience with similar specimens. Since the K-solution for such a fixed end specimen depends on its geometry (the fixed end allows a bending moment which resists the crack opening to a variable extent), an analytical study was performed to develop the K-solution for this specimen, and to check it experimentally.

The initial step before using this specimen was to calculate the stress intensity (K) vs. crack size for an edge crack. This calculation was performed for both fixed and pinned end conditions using room temperature isotropic (Inconel 718) material properties.

199
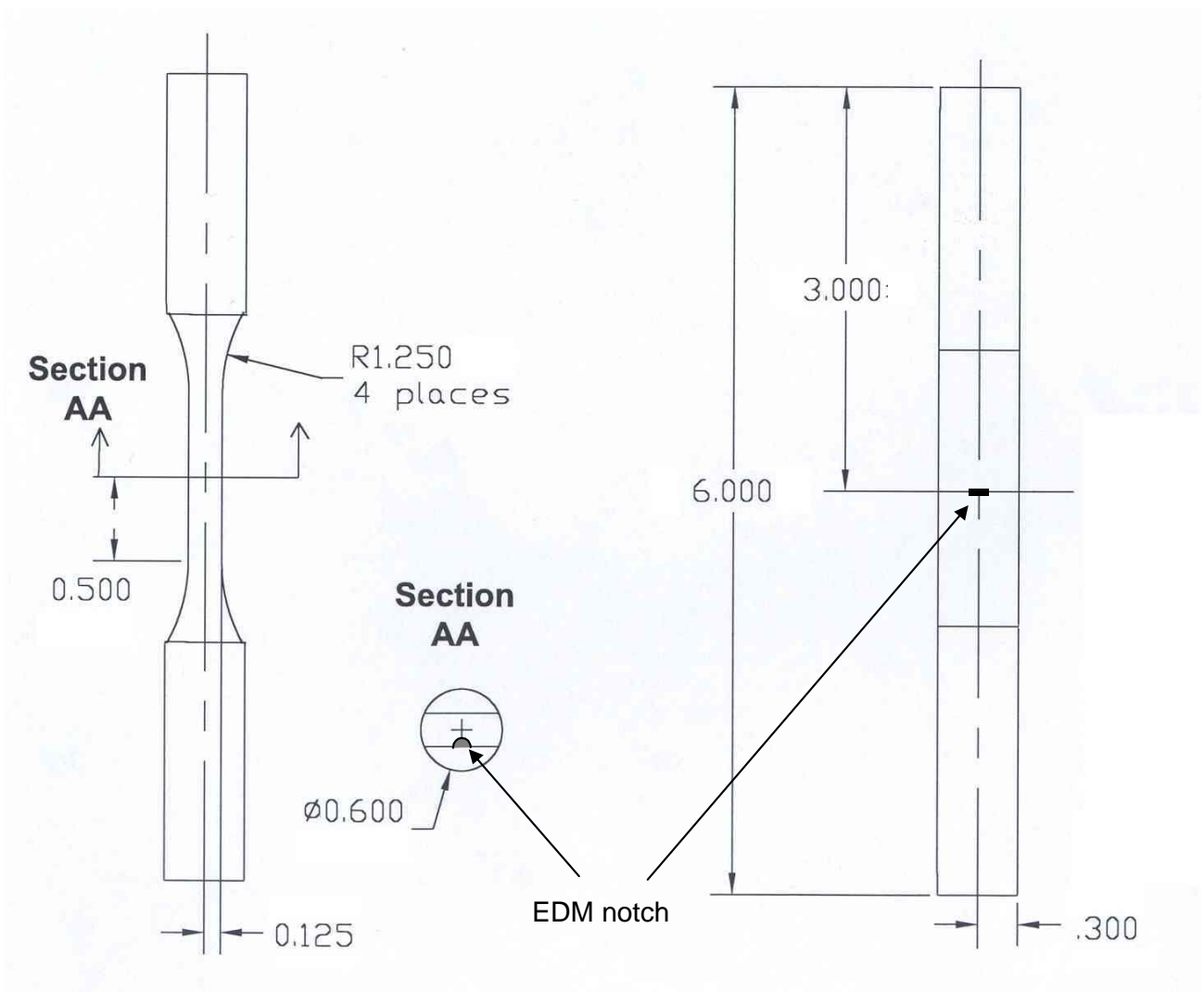
Figure 4.18. Surface flaw crack growth specimen.

Figure 4.19 shows a typical ANSYS finite element model used to calculate stress intensity. The crack tip was modeled with parabolic quarter-point elements. The K values were calculated from the crack opening displacements using the KCALC command in the ANSYS program. Details of this procedure are available in *ANSYS Structural Analysis Guide* [42]. Figure 4.20 shows the results of the stress intensity calculations. These results are normalized to a 1000 lb. axial load in the specimen.
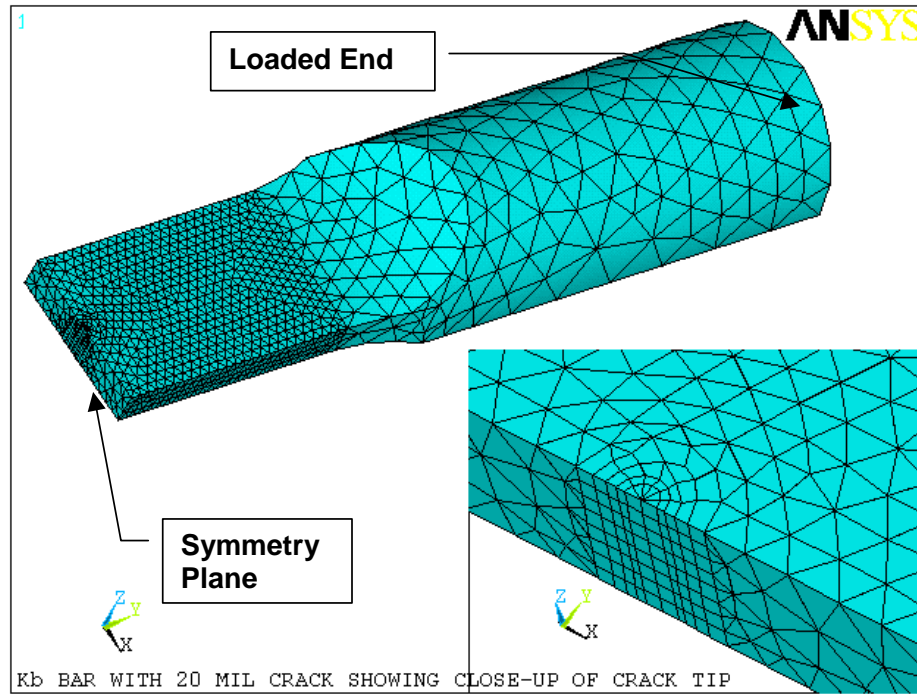
Figure 4.19. FEM model of fixed end crack growth specimen.

Since any test machine will have some degree of load train compliance that could cause deviation from the fully fixed end solution shown in Figure 4.20, calibration experiments were conducted to determine how closely the actual test machines at GEAE simulated a fixed end condition. Isotropic IN718 specimens were fabricated to the design of Figure 4.17 and a sharp EDM notch was machined across the edge to simulate an edge crack. A 0.5" gage length extensometer was placed across the EDM notch to measure the opening displacement during loading. The measured displacements were then compared with analytically predicted deflections produced during the previously discussed K calculations.

Figure 4.21 shows the results of this experiment, normalized to a 1000 lb. applied load. The curves labeled "Fixed" and "Pinned" are the analytical predictions. Since the finite element model used a plane of symmetry at the center of the specimen the predicted deflections (and the values shown in Figure 4.21) are half of the total crack opening deflections. The goal of this experiment was to match the analytical predictions within 5% of the fixed condition. The "95% Fixed – 5% Pinned" curve represents this goal. The "best

201

Edge Crack Test Specimen (1000 lb. Load)
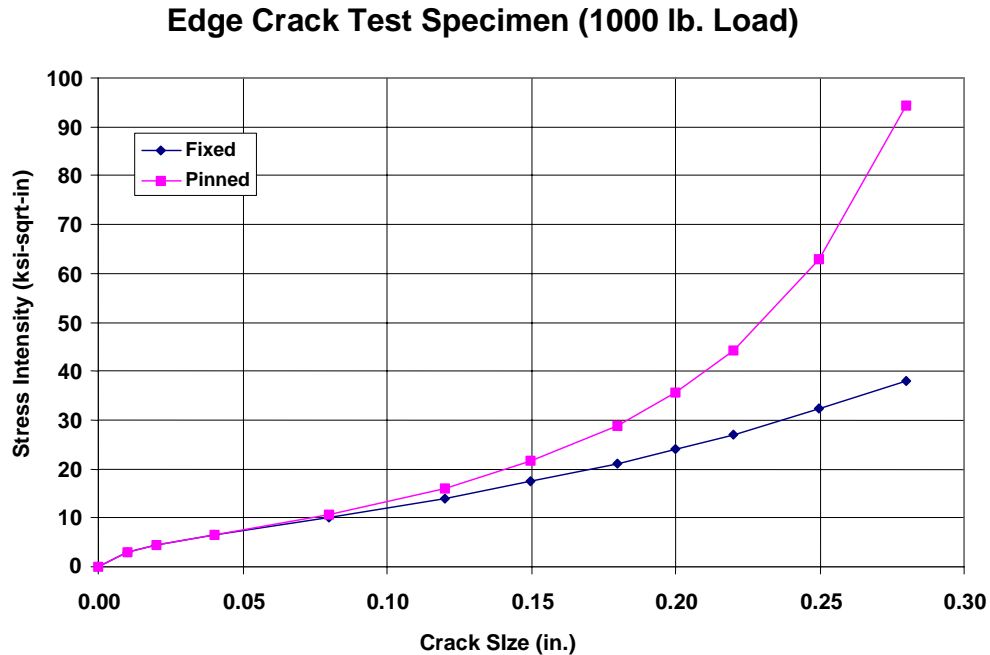
Figure 4.20. Stress intensity factor (isotropic) for fixed end specimen of Figure 4.18 under 1000 lb. axial load. Pinned-end solution is given for comparison.

case" measurement resolution for the extensometer is about ±.0001" for the total crack opening displacement, or ±.00005" for the half displacement. This measurement uncertainty is shown on Figure 4.21 as "Fixed + .05 mil". At a crack depth of about 0.22" the "95% Fixed – 5% Pinned" curve crosses the "Fixed + .05 mil" curve. This means that at this crack size and above it should be experimentally possible to distinguish differences in crack opening displacement of 5% or more above the fully fixed case with a 1000 lb. applied load. Therefore, an EDM notch of 0.250" was introduced and the specimen was loaded to 1000 lb. A second experimental case was also considered, this time with a 0.150" deep EDM notch and a 2500 lb. load. Those deflections were then scaled by the load ratio 1000/2500 and plotted on Figure 4.21. At the 0.250" crack size, both the GEAE and GE CRD measurements were close to the target value. For the 0.150" crack size, the CRD deflection was slightly high, but could still be a measurement accuracy issue. Based on this data, it was concluded that the fixed end solution was valid for the test setup used.

Crack Face Half-Deflections at 1000 lb
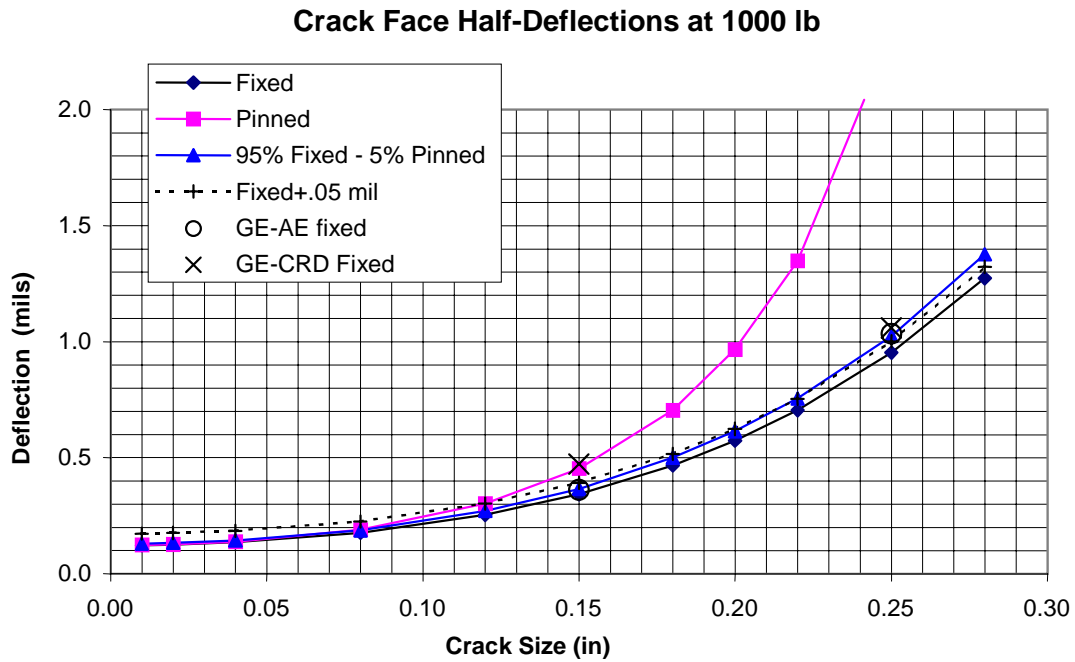
Figure 4.21. Dependence of edge crack mouth half-opening displacement on crack
depth, a, and end constraint for (isotropic) IN718.

Unfortunately, it was erroneously assumed that the K-solution for the present fixed end SEN specimen (Figure 4.17) was the same as the K-solution imbedded in existing fatigue crack growth data reduction programs at GEAE, and all K calculations were performed using that procedure. It was not until the end of the program, after comparison of GEAE and PW generated FCG data showed a difference between the two, that it was finally discovered that the K-solution for the specimen of Figure 4.17 was significantly different than that of the standard GEAE fixed end SEN specimen. Specifically, the K's for present specimen were higher than for the standard GEAE specimen, with the difference increasing as the crack length increased. This was due to the greater gage length of the specimen used in the present program. The original ANSYS K-solutions for the specimen of Figure 4.17 were compared to the GEAE in-house K-solution and a crack length-dependent polynomial expression was developed to correct the K-solution used to the actual (ANSYS) one. Based on fitting the ANSYS analysis points with a polynomial, the actual K-solution for this specimen can be approximated to within 1% (up to a/W = 0.7) by:

$$K = F\sigma\sqrt{\pi a}, \ \ \text{where: } F = 13.889a^2 + 1.8378a + 1.1176 \quad\quad (4.9)$$

As stated, the error in the K values for the fixed end specimen were not discovered until the end of the program, so the K's for the data shown in the quarterly and annual reports are incorrect. They have been corrected here.

The K-solution used for the pin-end SEN specimen was based on the Tada solution [35] and that for the surface flaw specimen was based on Newman-Raju. The large surface flaw specimen shown in Figure 4.18 was specially designed for this program to allow load shedding to threshold for a surface flaw while keeping the stress below 25 ksi to reduce potential creep effects.

When the corrected da/dN-ΔK data for the three different GEAE specimens were compared for a given test condition, no significant difference in behavior could be seen. Figure 4.22 shows a comparison of the fixed end SEN, the surface flaw, and the pin end SEN specimens (all tested at GEAE) at 1900°F, R = 0.05. The threshold K's for each specimen are listed in Table 4.6 and show a consistent average with small scatter. This, along with further comparisons shown below, show that crack growth behavior was specimen-geometry independent, even though the number of tests was not sufficient to perform statistical tests for differences.

Table 4.6. Thresholds for Different Geometry Specimens at 1900°F, R = 0.05

Test ID	Type	Orientation	Stress Ratio	Freq. (hz)	K-Grad (in^{-1})	ΔK_{th} (ksi$\sqrt{}$ in)
A2LPF-10	pin SEN	<001>/<010>	0.05	10	-20	7.65
A2LPF-1	fixed SEN	<001>/<010>	0.05	10	-20	7.54
A2LPE-1	fixed SEN	<001>/<010>	0.05	10	-20	7.17
T20W4-1	surface flaw	<001>/<010>	0.05	10	-20	7.03
T20W4-2	surface flaw	<001>/<010>	0.05	10	-20	7.27

Effect of Specimen Type on Crack Growth
at 1900F, R = .05
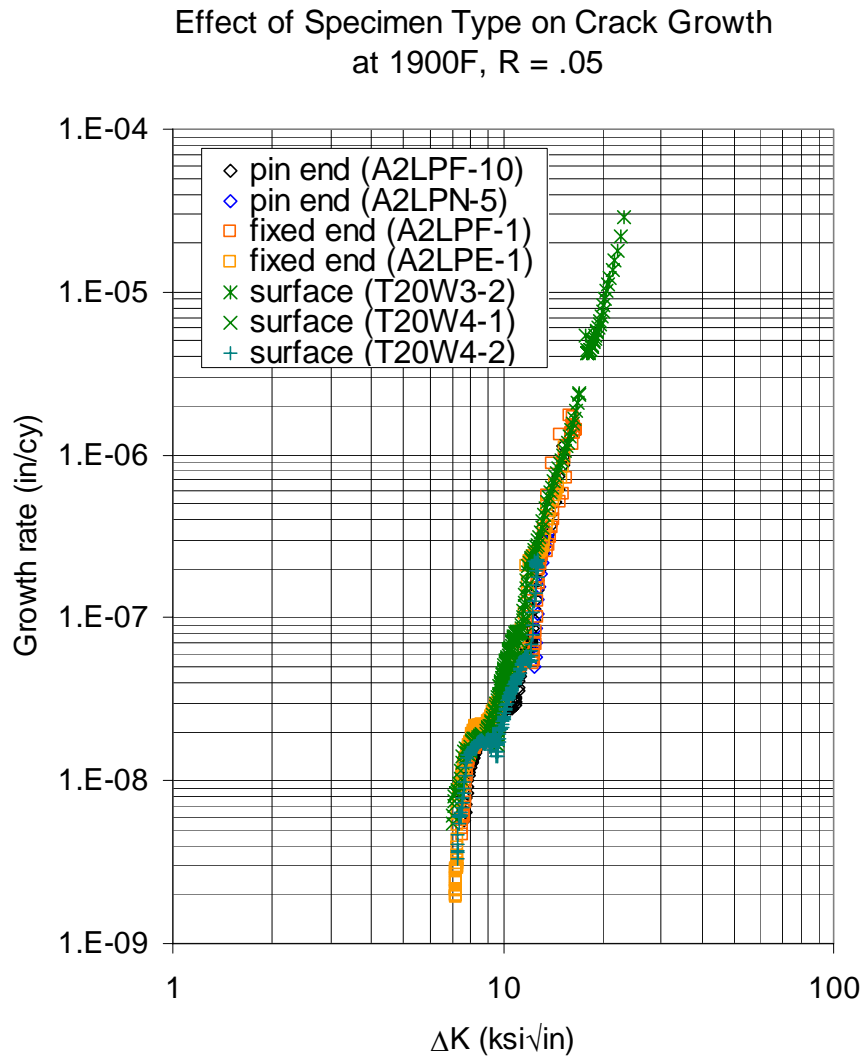
Figure 4.22. Comparison of fixed end SEN, surface flaw, and pin end SEN
(all tested at GEAE) at 1900°F, R = 0.05.

Inter-laboratory comparisons of fatigue crack growth and threshold were also performed. Comparisons between P&W and GEAE results at 1100°F, R = 0.1 and 1900°F, R = 0.5 were obtained. Data at 1100°F from both laboratories for the <001>/<100> crack orientation0[*] are shown in Figure 4.23. Here PW data using the specimen of Figure 4.10 at R = 0.1, 20 Hz, is compared with GEAE data using the specimen of Figure 4.13 at R = 0.1, 10 Hz. Both laboratories used PD to monitor crack growth and control the rate of K-shedding at -20 in[-1]. Both P&W and GEAE specimens were taken from the 6 inch x 3 inch x 5/8 inch.

---

[*] the first orientation is the crack plane normal, the second orientation is the crack growth direction

The results were quite similar within the scatter usually observed for cast materials. The average GEAE ΔKth value was 5.28 ksi√in with a standard deviation of 0.29, while the average PW ΔKth was 5.90 ksi√in with a standard deviation of 0.36. A t-test comparison of these two data sets suggests that although the difference is small (0.6 ksi√in), it is statistically different. In addition, the GEAE results show faster growth rates (about 2X) once the crack is above threshold.
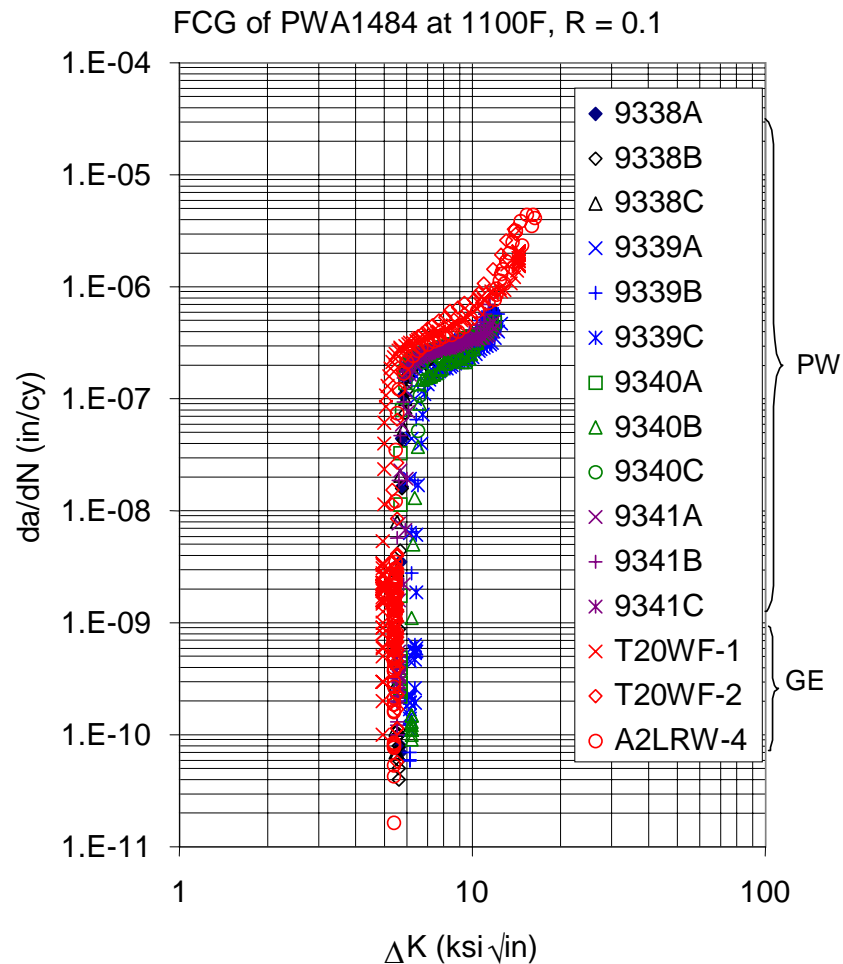
Figure 4.23. Comparison of P&W and GEAE measurements of crack growth and threshold of PWA 1484 <001>/<100> at 1100°F, R = 0.1.

A similar comparison of test laboratory differences was undertaken at 1900°F. At 1900°F, R = 0.5, Figure 4.24 shows pin end SEN data from P&W and pin end and fixed end SEN data from GEAE.

Effect of Test Laboratory on Crack Growth at
1900F, R = .5
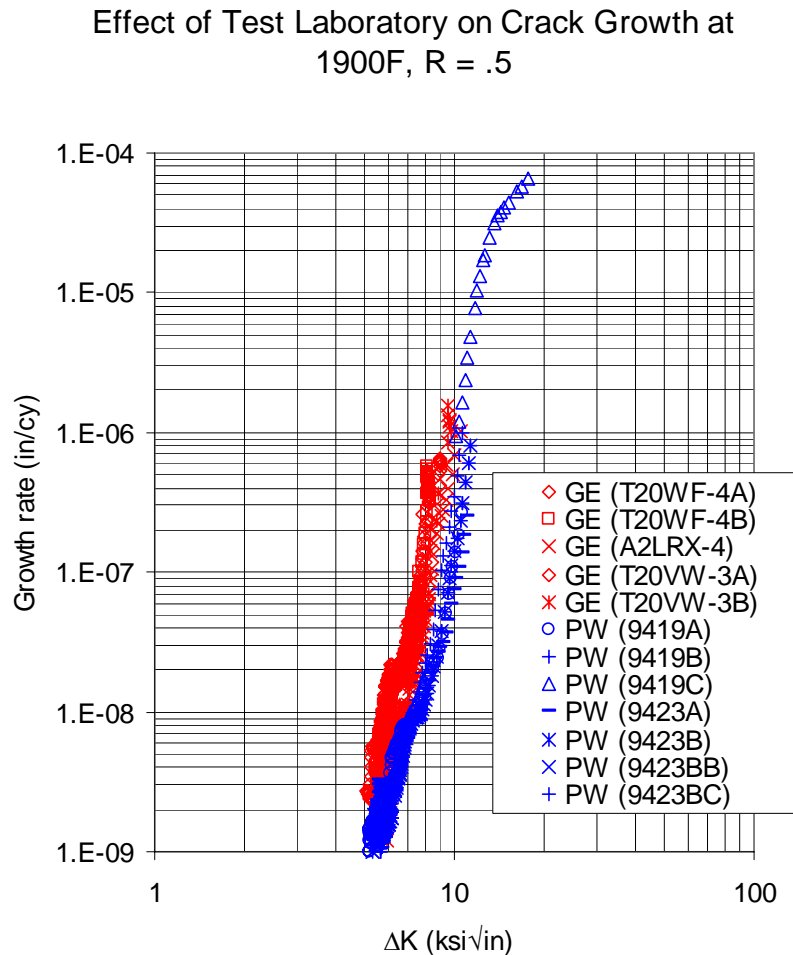
Figure 4.24. Pin end SEN data from PW and pin end and fixed end
SEN data from GEAE at 1900°F, R = 0.5.

Here there appears to be a tendency for the P&W data to lie below the GEAE data, by a factor of about 3 to 10. There is a frequency difference between the two laboratories (GEAE used 10 Hz, P&W used 20 Hz), which may contribute to this difference. Frequency effects will be discussed further in Section 4.2.2.2.C. The ΔK_{th} results for the two laboratories were also slightly different, as shown in Table 4.7. The P&W values were about 0.4 ksi√in higher on average than the GEAE values. A t-test comparison of these data showed that the difference was probably statistically significant, even though quite small.

Unlike the sharp crack arrest behavior seen at 1100°F or at 1900°F, R = 0.05, there was no distinct crack arrest seen in the 1900°F, R = 0.5 data (Figure 4.24). Therefore the threshold was taken as the K at which a crack growth rate of approximately 2 to 6 x 10^{-9} in/cy was obtained. The specific threshold growth rates for all specimens are listed in Table 4.7.

Table 4.7. Fatigue Crack Growth Thresholds for PWA 1484 at 1900°F, R = 0.5

Test ID	Type	Orientation	Freq. (hz)	K-Grad (in^{-1})	ΔK_{th} (ksi$\sqrt{}$ in)	da/dN at ΔKth (in/cy)
9419A	pin end SEN	<001+15°>/<010>	20	-20	5.49	2 x10^{-9}
9419B	pin end SEN	<001+15°>/<010>	20	-20	6.10	2 x10^{-9}
9423A	pin end SEN	<001>/<110>	20	-20	6.00	2 x10^{-9}
9423B	pin end SEN	<001>/<110>	20	-20	6.08	2 x10^{-9}
9423BB	pin end SEN	<001>/<110>	20	-20	5.53	2 x10^{-9}
9423BC	pin end SEN	<001>/<110>	20	-20	6.17	2 x10^{-9}
PW combined = 5.97 ± 0.27						
T20WF-4A	pin end SEN	<001>/<010>	10	-20	5.56	6 x10^{-9}
T20WF-4B	pin end SEN	<001>/<010>	10	-20	5.50	4 x10^{-9}
A2LRX-4	fixed end SEN	<001>/<010>	10	-20	5.64	6 x10^{-9}
T20VW-3A	fixed end SEN	<001>/<010>	10	-30	5.11	3 x10^{-9}
T20VW-3B	fixed end SEN	<001>/<010>	10	-60	5.97	6 x10^{-9}
GEAE combined = 5.56 ± 0.31						Overall = 5.76 ± 0.35

The error in K for the fixed end SEN specimen mentioned above also caused us to investigate the differences (when using the incorrect K-solution) between the pin-end specimen and the fixed end specimen as possibly due to a difference in response to creep at 1900°F. This effort was stimulated by approximate calculations of the amount of creep possible in either test specimen at 1900°F. The general practice used was to keep the gross section stress (ignoring the notch) below 25 ksi. This kept the expected time to rupture well beyond the anticipated test time. Because of the presence of the EDM notch, net section stresses at the start of a test were often greater than 25 ksi. Due to load shedding, the net

section stresses during most of the test, however, were lower, typically about 15 ksi. However, constitutive data at 1900°F suggested that approximately 0.1% creep could occur in the test times at the net section stresses in the gage section of these specimens. This level of creep, while not large, could alter the macroscopic stress distribution in the specimen, and hence its stress intensity. One test each on a fixed end and pin end SEN were performed at 1900°F under a steady maximum load of 25 ksi, with unloading every hour to monitor the elastic response. Both these tests showed measurable creep deformation (from an extensometer mounted on the gage section) during the test, and the pin end SEN specimen fractured.

In summary, the test specimens and methods used gave consistent results. Within each laboratory (GEAE or P&W) the results appeared to be highly consistent and repeatable as illustrated by the good agreement of different specimen types and the small variation in ΔK_{th} in, for example, Figures 4.14 and 4.22. Inter-laboratory differences, shown in Figures 4.23 and 4.24 were greater, but not large. At 1100°F, PW and GEAE results were statistically different, but similar from an engineering point of view. Various K-shed rates were used and results were found to be comparable up to and including $C = -20$ in^{-1}. At 1900°F, PW crack growth rates were slower than GEAE's at the same condition ($R = 0.5$) but the crack growth thresholds measured were identical. Threshold values were found to be independent of shed rates up to $C = -30$ in^{-1}.

The K-solutions determined for the various specimen geometries appeared to be appropriate even at 1900°F. While it is still a concern, no meaningful conclusions about the role of creep on the fatigue crack growth behavior could be made. In view of the good agreement of the different specimen types at 1900°F, it seems likely that creep does not have a strong effect on the applicability of K as a crack driving parameter, at least for the cycles investigated, at this temperature.

C. Frequency Effects (1900°F)

Since single crystal superalloys show time dependent mechanical behavior at 1900°F (as evidenced by the creep behavior described in Section 4.3.1.6, and the oxidation seen on the surfaces of specimens tested throughout this program) it was thought that it was likely that the fatigue crack growth threshold would depend on cycle time or frequency at

1900°F. The effort described in this section was undertaken to try to define to what extent the threshold and HCF crack growth behavior was frequency dependent.

The major hurdle to be overcome in this effort was the limited frequency capability of EPD systems. Most EPD systems require a finite amount of time to acquire and process the electrical signals, and as the test frequency is increased, the number of cycles that elapse during that time increase, allowing more crack growth to occur while the signal is being processed. Thus the system becomes less and less stable, since the feedback to shed the load as the crack advances arrives later and after larger increments of crack advance. Eventually, at high enough frequency, the crack can grow all the way across the specimen before the feedback signal can reduce the load. It is not known precisely at what frequency this effect would take over, but from the speed of our EPD systems, it was felt that it would be unlikely that we could control a test at 1000 Hz. Therefore, we adopted two alternate approaches:

1) Acquire conventional EPD K-shed data as a function of frequency at lower frequencies up to where we felt the test would remain under control. Most of these tests were performed at R = 0.05 at 10 and 30 Hz. Similar tests were also performed at R = 0.5 at 0.33, 10 and 20 Hz.

2) Explore alternate methods of measuring threshold. These involved a variety of uploading methods that did not require EPD.

Use of alternate specimens that might have a decreasing K with increasing crack length was also considered, but most of these required constant displacement control of the load points, and it was not possible to do that confidently on the high frequency MTS (1000 Hz) machine.

The results from Method 1, conventional EPD controlled K-shedding (C = -20 in^{-1}), are shown in Figure 4.25 and Table 8. The specimens were a mixture of pin-loaded and fixed end SEN specimens, as described in Section 4.2.2.2.*B*. All specimen orientations were <001>/<010>. The 10 Hz tests were performed in GEAE's Evendale, OH laboratory and the 30 Hz tests were performed at GEAE's Global Research Laboratory in Schenectady. At 10 Hz, a threshold of 7.46 ± 0.24 was obtained; at 30 Hz the threshold averaged 8.12 ± 1.35 or

9% higher. A t-test comparison of these groups suggested the difference was not statistically significant (the scatter at 30 Hz was quite large).
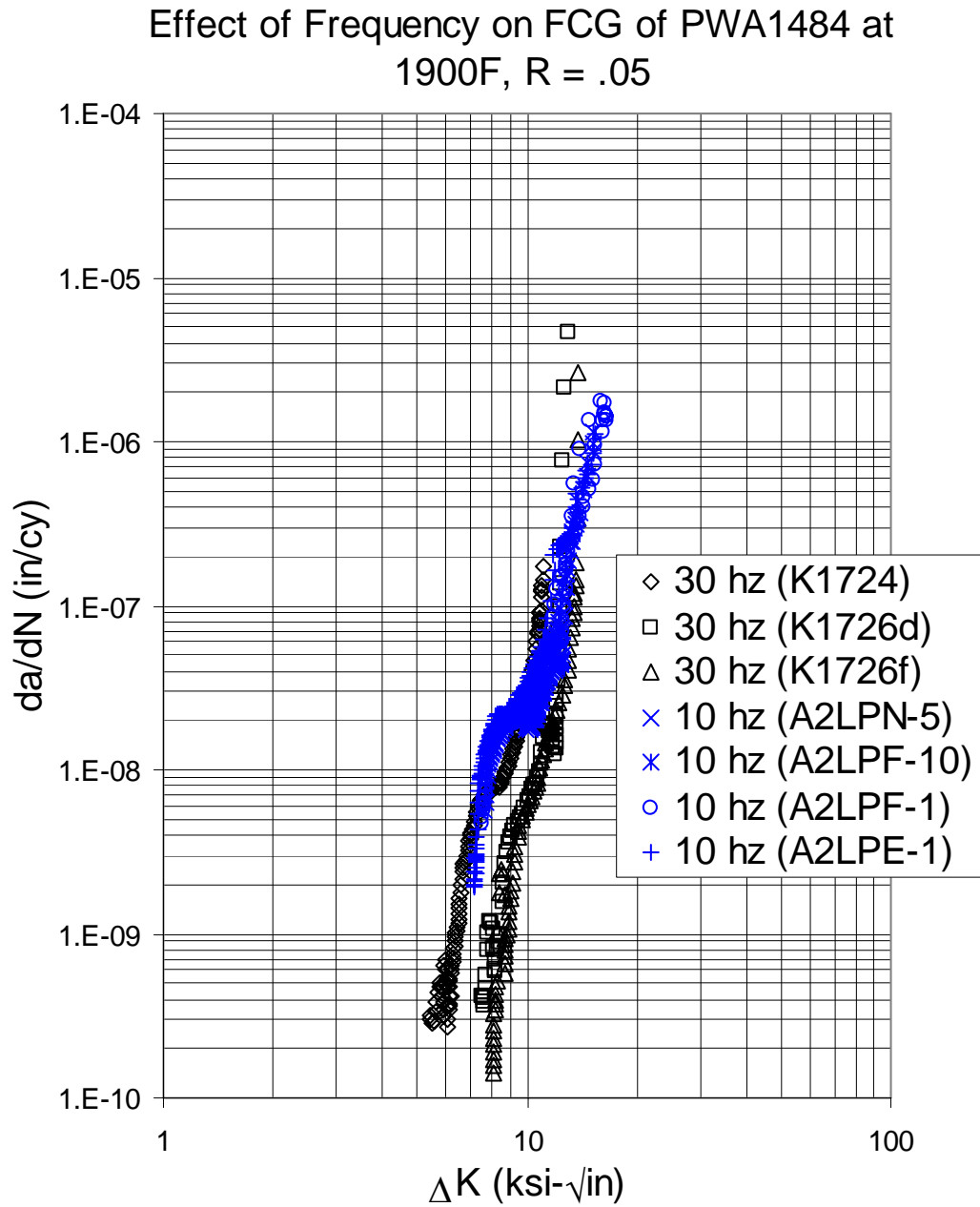
Figure 4.25. Comparison of 10 Hz and 30 Hz tests conducted with EPD controlled K-shedding at 1900°F, R = 0.05.

Table 4.8. Test Conditions and Results for the Effect of Frequency on Threshold at 1900°F

S/N	Type	Method	R-ratio	Frequency (hz)	Kth* (ksi√in)
K1724	pin end SEN	EPD Kshed	0.05	30	6.59
K1726d	fixed SEN	EPD Kshed	0.05	30	8.64
K1726f	fixed SEN	EPD Kshed	0.05	30	9.14
Average = 8.12					
A2LPN-5	pin end SEN	EPD Kshed	0.05	10	
A2LPF-10	pin end SEN	EPD Kshed	0.05	10	7.65
A2LPF-1	fixed SEN	EPD Kshed	0.05	10	7.54
A2LPE-1	fixed SEN	EPD Kshed	0.05	10	7.19
Average = 7.46					
A2LRW-1	fixed SEN	step load w EDP	0.05	10	8.96
A2LRW-2	fixed SEN	step load w EDP	0.05	10	7.90
Average = 8.43					
A2LRY-3	fixed SEN	step load w replicas	0.05	870	9.2
A2LYH-1	fixed SEN	step load w replicas	0.05	900	8.2
Average = 8.70					
A2LYH-2	fixed SEN	step load w replicas	0.05	10	5.4
T20WS-1	fixed SEN	step load w replicas	0.05	10	4.5
Average = 4.97					
A2LRY-4	fixed SEN	EPD Kshed	0.5	0.33	5.00
Average = 5.00					
T20WF-4A	fixed SEN	EPD Kshed	0.5	10	5.56
T20WF-4B	fixed SEN	EPD Kshed	0.5	10	5.5
A2LRX-4	fixed SEN	EPD Kshed	0.5	10	5.64
T20VW-3A	fixed SEN	EPD Kshed	0.5	10	5.97
T20VW-3B	fixed SEN	EPD Kshed	0.5	10	5.11
Average = 5.56 ± 0.31					
9419A	pinned SEN	EPD Kshed	0.5	20	5.49
9419B	pinned SEN	EPD Kshed	0.5	20	6.10
9423A	pinned SEN	EPD Kshed	0.5	20	6.00
9423B	pinned SEN	EPD Kshed	0.5	20	6.08
9423BB	pinned SEN	EPD Kshed	0.5	20	5.53
9423BC	pinned SEN	EPD Kshed	0.5	20	6.17
Average = 5.90 ± 0.30					

*K at a growth rate of $1 - 2 \times 10^{-9}$ in/cy

For Method 2, three methods variations were employed; two with EPD crack monitoring and one without. The first method, used on specimen A2LRW-1, involved pre-cracking at 1900°F, unloading and heating at 1900°F for 24 hours, and then performing a

series of constant load steps starting at 3 ksi√in and increasing in 1 ksi√in steps every 10^6 cycles if no crack advance was detected. The purpose of the 24 hr heat treatment at 1900°F was to try to relieve out any crack tip residual stresses induced by the precracking, thus hopefully eliminating crack growth retardation effects that might artificially raise the threshold. The process was only partially successful, since as can be seen in Table 4.8 and Figure 4.26, the threshold of this test was somewhat elevated (8.96 ksi√in) compared to the standard 10 Hz K-shed.
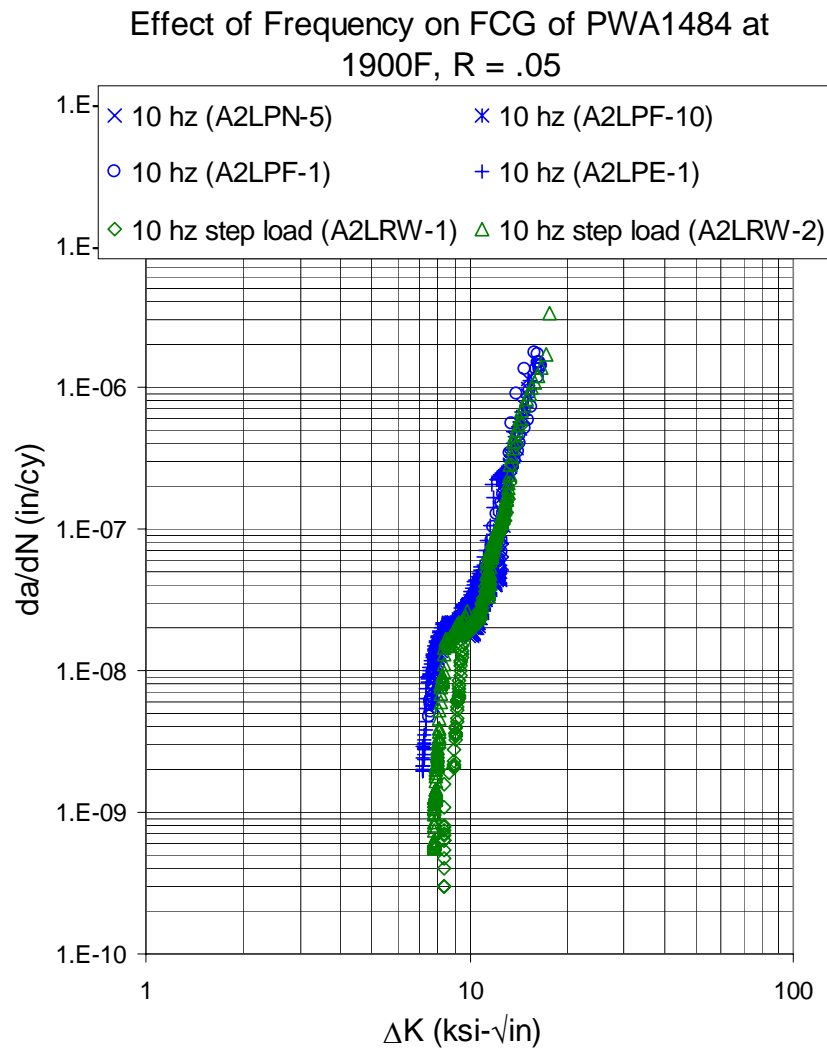
Figure 4.26. Fatigue crack growth behavior of EPD monitored specimens with step loading compared to K-shedding at 1900°F, R = 0.05.

The second variation attempted, specimen A2LRW-2, was similar to the first, except that after the precracking and 24 hour 1900°F heat treatment, a one hour hold was conducted at 1900°F at approximately 10 ksi compression. Then the sequence of 10^6 cycles constant load steps was performed. Between each load step, the 1900°F 1-hour hold at 10-ksi compression was repeated. The step loading sequence was begun at 5 ksi√in and continued in 0.5 ksi√in steps. As can be seen in Table 4.8 and Figure 4.26, the threshold by this procedure (7.90 ksi√in) was less than that of method one, but still somewhat elevated over that obtained by K-shedding with EPD control.

The final method used was to step load without any intervening heat treatments. Since the EPD monitoring would not be useful at 900 Hz, the crack advance was monitored by cooling the specimen to room temperature after each step and making an acetate tape replica of both sides of the specimen at the EDM notch root under a modest tensile load. An example of the cracking seen is shown in Figure 4.27. When it was clear that a crack was present and growing the specimen was fractured in tension at room temperature and the beachmarks that accompanied the end of each load step were used as the actual measure of crack advance. As seen in Figure 4.28, these beachmarks were quite evident and could be related to the load increments by counting back from the final fracture.
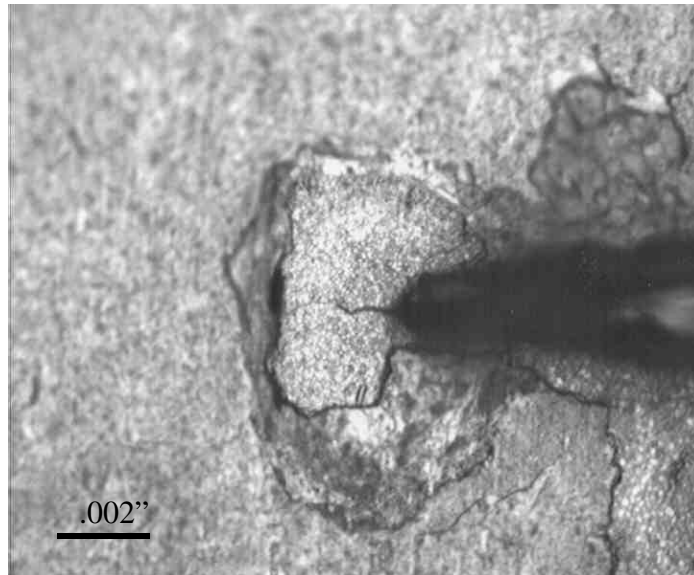
Figure.4.27. Cracking detected by acetate tape replication at
1900°F.S/N A2LYH-2, 1900°F, R = 0.05, 10 Hz.

214
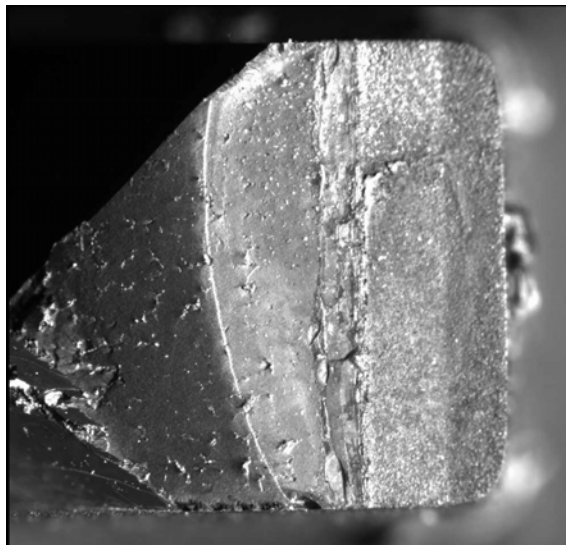
Figure 4.28.   Beachmarks on the fracture surface of a step loaded
              specimen. S/N:A2LRY-3 1900°F, R = 0.05, 900 Hz.

As shown in Table 4.8, two specimens were tested in this fashion at 10 Hz, and two others at 900 Hz. The threshold reported in the table is the lowest K for which measurable growth (usually about 1 - 2 x 10^{-9} in/cy) was obtained. The crack growth rates were determined by taking the average crack advance in the loading interval divided by the number of cycles (10^6 at 10 Hz and 10^7 at 900 Hz). The K's were calculated using the stress and the average crack length in the interval. The fixed end SEN bar K solution, described in Section 4.2.2.2.*B,* was used. The resolution of this method was significantly poorer than that obtained by using EPD, but it did permit a back-to-back comparison of 10 and 900 Hz.

The results are shown in Table 4.8 and Figure 4.29. Taking the K's for growth rates in the $1 - 2$ x 10^{-9} in/cy range as threshold shows that at 900hz the threshold is significantly higher (average of 8.7 ksi√in) than at 10 Hz. It is also noteworthy, and surprising, that the 10 Hz threshold obtained in this way (average of 5.0 ksi√in) was significantly lower than that obtained by step loading under EPD monitoring (average of 8.4 ksi√in). This difference seems larger than the likely error in measurement of crack growth rate. The reason for this is unknown; perhaps there are resistivity changes due to cyclic plasticity at the notch root masking the resistance change due to crack advance in the EPD method.
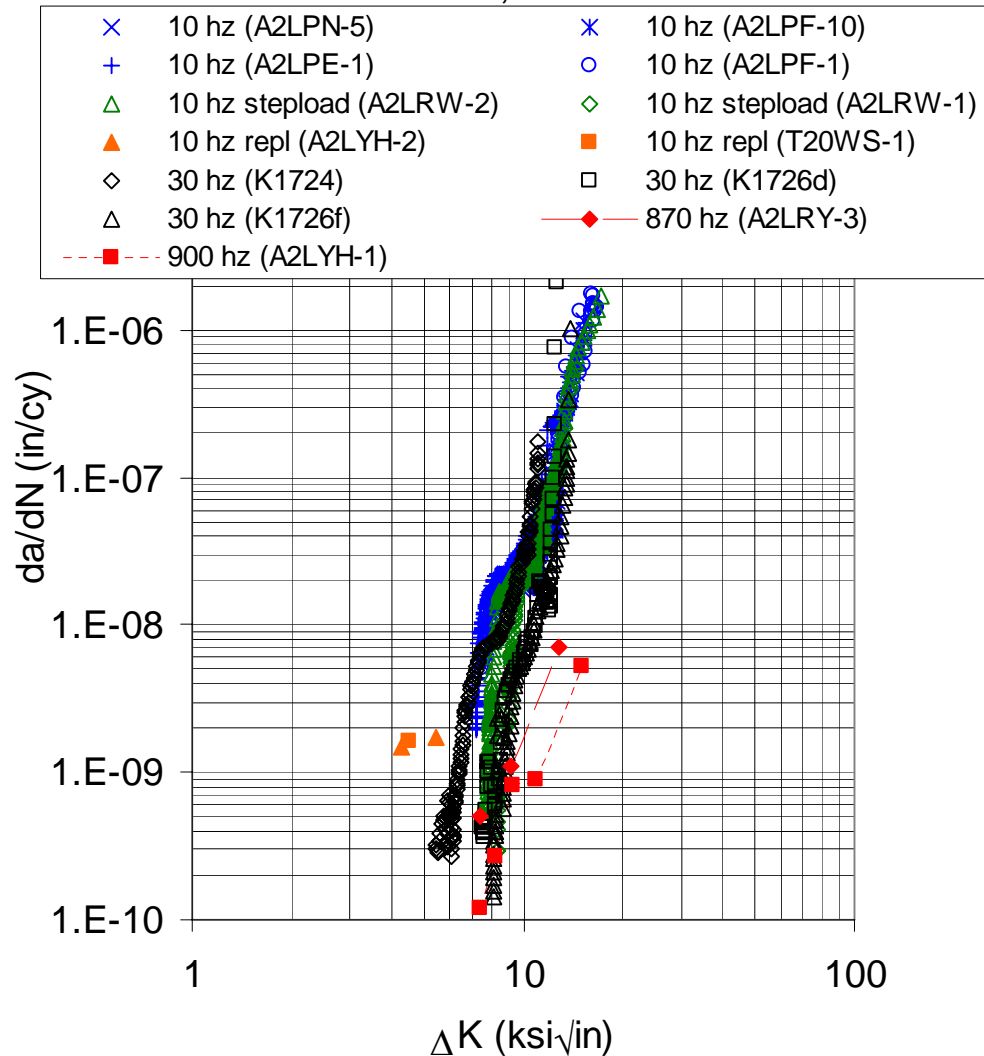
Figure 4.29. The frequency dependence of crack growth rate for all methods at 1900°F, R = 0.05.

The frequency dependence of threshold for all methods at R = 0.05 is presented in Figure 4.30. The two different methods of measurement, K-shedding with EPD and step loading with beachmark measurement, give different values of Kth, but both trends with frequency are quite similar. Expressed as a function of log(frequency), the best fit equations for these two methods are:

216

$$\text{K-shed with EPD: Kth (ksi}\sqrt{\text{in}}) = 0.606 \ln(f) + 6.06 \qquad (4.10)$$

$$\text{Step loading with beachmark measurement: Kth (ksi}\sqrt{\text{in}})$$
$$= 0.803 \ln(f) + 3.05 \qquad (4.11)$$

where, f is the frequency in Hz. The slopes of the two equations are similar, with an average of 0.705, or about 1.6 ksi$\sqrt{\text{in}}$ per decade of frequency change. Using this average slope and extrapolating the K-shed with EPD line gives a projected Kth at 900 Hz of 10.9 ksi$\sqrt{\text{in}}$.
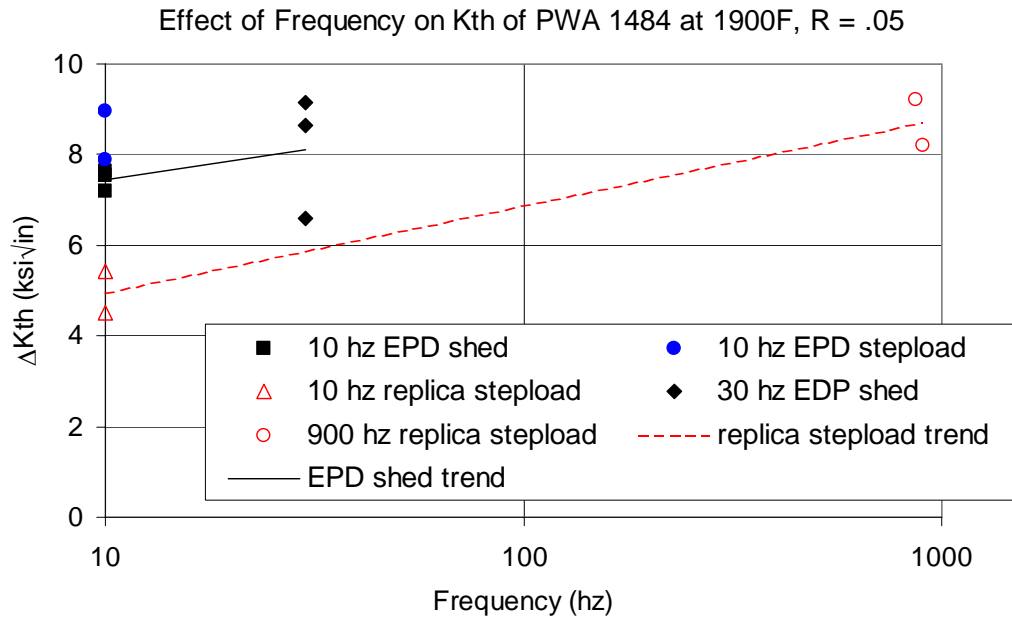
Figure 4.30. The frequency dependence of threshold for all methods at 1900°F, R = 0.05.

Test data with different frequencies were also available at 1900°F, R = 0.5, all using K-shedding with EPD control. Results from tests at 0.33, 10, and 20 Hz are shown in Table 4.8 and Figure 4.31, and show a similar trend of increasing threshold with increasing frequency. However, the dependence of K_{th} on frequency, shown in Figure 4.32 is significantly less than observed at R= 0.05. At R = 0.5, the frequency dependence can be represented by:

$$\text{Kth} = 0.222 \ln(f) + 5.15 \qquad (4.12)$$

so the change in Kth per decade in frequency is about 0.5 ksi$\sqrt{\text{in}}$ or 30% of that seen at R = 0.5.

217
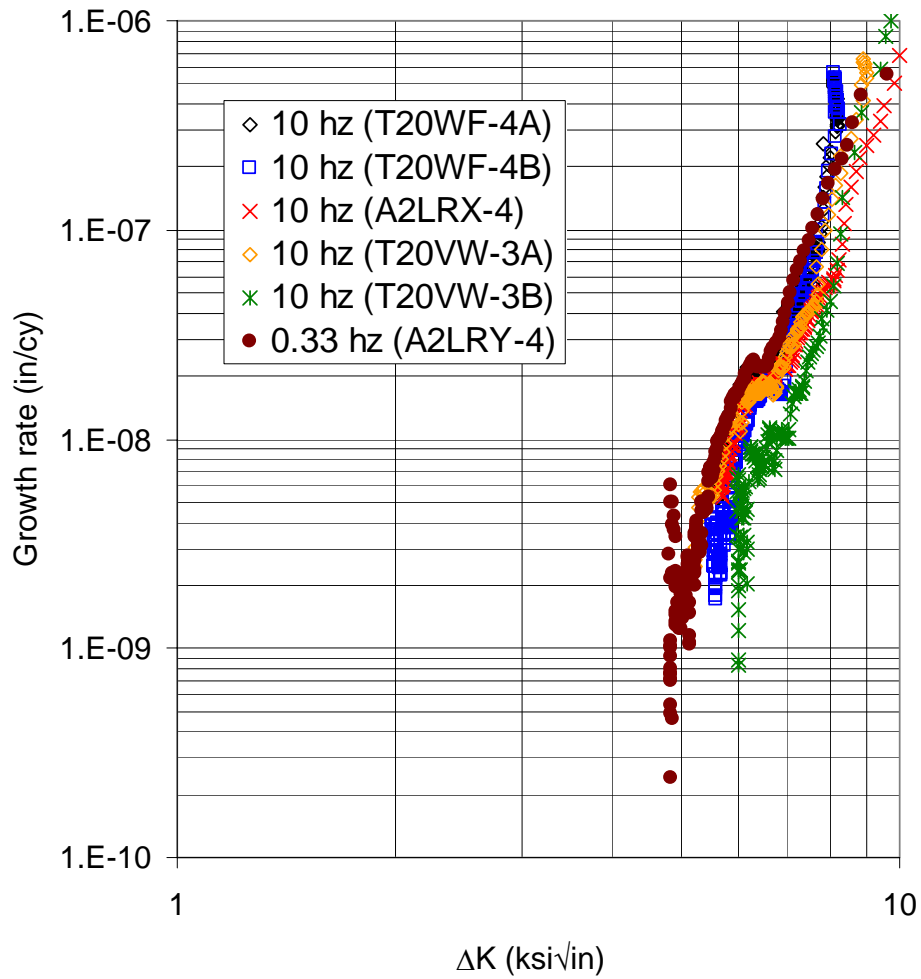
Figure 4.31. Dependence of fatigue crack with rate on frequency at 1900°F, R = 0.5.
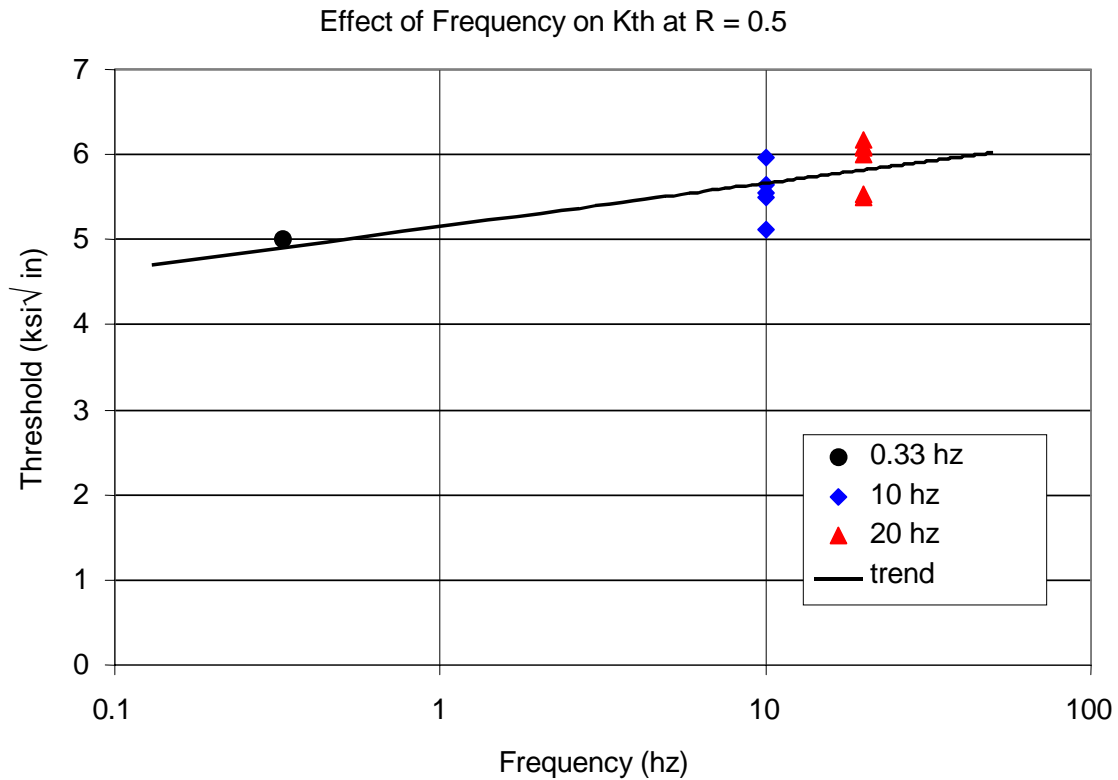
Figure 4.32. Dependence of crack growth threshold on frequency at 1900°F, R = 0.5.

In summary, this subtask demonstrated that single crystal superalloys, as exemplified by PWA 1484, show a frequency-dependent threshold and crack growth rate behavior at 1900°F. While the dependence of K_{th} is not large (0.5 to 0.8 ksi√in increase per factor of ten increase in frequency) it is consistent and is statistically significant. This behavior is similar to that seen at lower temperatures in fine-grained wrought superalloys, where increasing frequency decreases crack growth rate. The source of the frequency effect is unknown; it could be from either changes in inelastic deformation related to strain rate or to changes in environmental contributions or both.

D. Orientation Effects

Having established an acceptable $K_{gradient}$ for this material, crack growth rates as a function of crystallographic orientation could then be studied. Fatigue crack growth rate threshold testing was performed on the following orientations, <001/010>, <001+15/010>, <001/110> and <011/0-11>. The results of this testing are shown below in Figure 4.33.

Orientation Effect FCGR Response
PWA 1484, T = 1100F, R = 0.8, Freq = 20 Hz

Legend:
- 7AN9302A 1100F 10HZ R=.8 SEN .0508 <001/010>
- 7AN9302B 1100F 10HZ R=.8 SEN .0508 <001/010>
- 7AN9336A 1100F 20HZ R=.8 SEN .0506 <001/010>
- 7AN9337A 1100F 20HZ R=.8 SEN .0511 <001/010>
- 7AN11129A 1100F 20HZ R=.8 SEN .0514 <011/0-11>
- 7AN11129B 1100F 20HZ R=.8 SEN .0514 <011/0-11>
- 7AN11129C 1100F 20HZ R=.8 SEN .0514 <011/0-11>

Axes: da/dN (in/cycle) vs ΔK (ksi(in^.5))

Figure 4.33. Results of fatigue crack testing.

E. Stress Ratio

At 1900°F, threshold tests were performed at several different stress-ratios: R = -1, 0.05, 0.5, 0.7, and 0.8, using a combination of fixed end SEN (GE) and pin end SEN (PW and GEAE) specimens. GEAE testing was performed at 10 Hz and P&W testing at 20 Hz. Both laboratories used a K-shed rate, C = -20 in⁻¹. The crystallographic orientations of the specimens used by GEAE and P&W were different as noted in Table 4.9, but the orientation

study, reported in Section 4.2.2.2.*D,* showed that there was not a significant effect of orientation on fatigue crack growth and threshold at 1900°F, so this variable was ignored for the mean stress modeling. The test matrix and the thresholds measured are shown in Table 4.9. The fatigue crack growth behavior at three of the stress-ratios studied (R = 0.05 and R = 0.5 data have been shown in Section 4.2.2.2.*B* and are shown separately in Figures 4.34 through 4.36). The complete set of results for all R-ratios is shown in Figure 4.37.
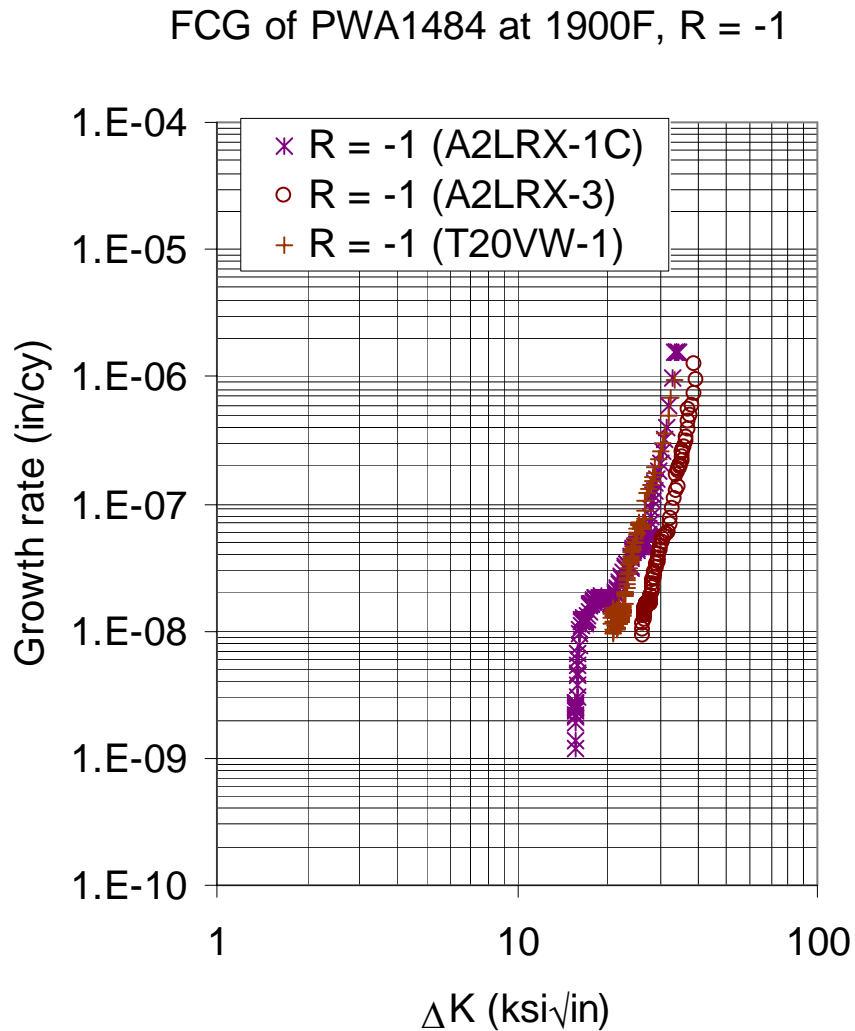
Figure 4.34. Fatigue crack growth rate behavior at 1900°F at R = -1.

Table 4.9. 1900°F Stress Ratio Effect Test Matrix and Results

Test ID	Type	Orientation	Stress Ratio	Freq. (Hz)	C (in^{-1})	ΔK_{th} (ksi$\sqrt{\text{in}}$)	K_{eq}* (ksi$\sqrt{\text{in}}$)
A2LRX-1C	fixed end SEN	<001>/<010>	-1	10	-20	15.6	7.80
A2LRX-3	fixed end SEN	<001>/<010>	-1	10	-20	-	-
T20VW-1	fixed end SEN	<001>/<010>	-1	10	-20	-	-
						R = -1 average ΔKth = 7.80	
A2LPF-10	pin SEN	<001>/<010>	0.05	10	-20	7.65	7.90
A2LPF-1	fixed SEN	<001>/<010>	0.05	10	-20	7.54	7.79
A2LPE-1	fixed SEN	<001>/<010>	0.05	10	-20	7.17	7.40
T20W4-1	surface flaw	<001>/<010>	0.05	10	-20	7.03	7.26
T20W4-2	surface flaw	<001>/<010>	0.05	10	-20	7.27	7.51
						R = 0.05 average ΔKth = 7.33 ± .26	
9419A	pin end SEN	<001+15°>/<010>	0.5	20	-20	5.49	8.50
9419B	pin end SEN	<001+15°>/<010>	0.5	20	-20	6.10	9.44
9423A	pin end SEN	<001>/<110>	0.5	20	-20	6.00	9.28
9423B	pin end SEN	<001>/<110>	0.5	20	-20	6.08	9.41
9423BB	pin end SEN	<001>/<110>	0.5	20	-20	5.53	8.56
9423BC	pin end SEN	<001>/<110>	0.5	20	-20	6.17	9.55
T20WF-4A	pin end SEN	<001>/<010>	0.5	10	-20	5.56	8.60
T20WF-4B	pin end SEN	<001>/<010>	0.5	10	-20	5.50	8.51
A2LRX-4	fixed end SEN	<001>/<010>	0.5	10	-20	5.64	8.73
T20VW-3A	fixed end SEN	<001>/<010>	0.5	10	-30	5.11	7.91
T20VW-3B	fixed end SEN	<001>/<010>	0.5	10	-60	5.97	9.24
						R = 0.5 average ΔKth = 5.76 ± 0.35	
9432A	pin end SEN	<001>/<110>	0.7	20	-20	3.87	8.27
9432B	pin end SEN	<001>/<110>	0.7	20	-20	4.24	9.06
9432C	pin end SEN	<001>/<110>	0.7	20	-20	-	-
9428A	pin end SEN	<001+15>/<010>	0.7	20	-20	3.52	7.52
9428B	pin end SEN	<001+15>/<010>	0.7	20	-20	3.93	8.39
9428B	pin end SEN	<001+15>/<010>	0.7	20	-20	-	-
T20VW-2	fixed end SEN	<001>/<010>	0.7	10	-20	-	-
						R = 0.7 average ΔKth = 3.75 ± 0.38	
9431A	pin end SEN	<001>/<110>	0.8	20	-20	2.68	7.39
9431B	pin end SEN	<001>/<110>	0.8	20	-20	2.89	7.97
9431C	pin end SEN	<001>/<110>	0.8	20	-20	-	-
9427A	pin end SEN	<001+15>/<010>	0.8	20	-20	2.66	7.34
9427B	pin end SEN	<001+15>/<010>	0.8	20	-20	2.86	7.89
9427C	pin end SEN	<001+15>/<010>	0.8	20	-20	-	-
A2LRX-2	fixed end SEN	<001>/<010>	0.8	10	-20	-	-
						R = 0.8 average ΔKth = 2.77 ± 0.12	

FCG of PWA1484 at 1900F, R = 0.7
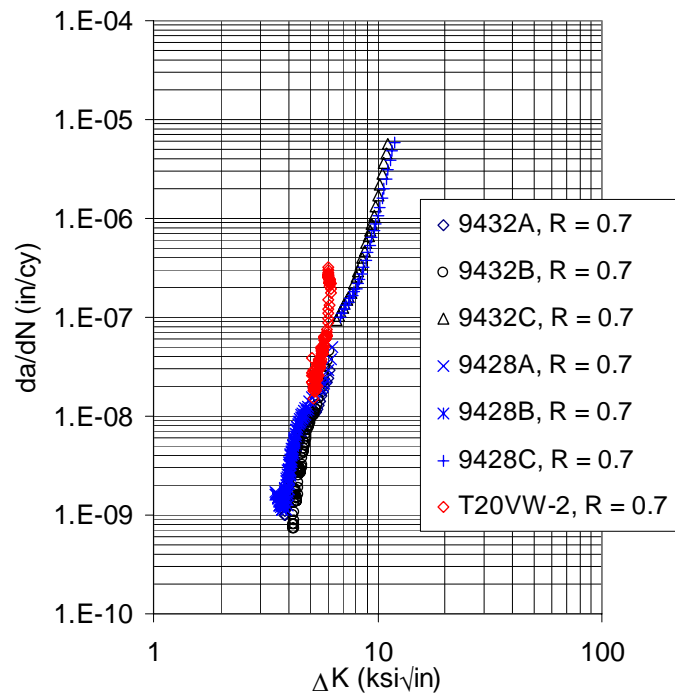
Figure 4.35. Fatigue crack growth rate behavior at 1900°F at R = 0.7.

FCG of PWA1484 at 1900F, R = 0.8
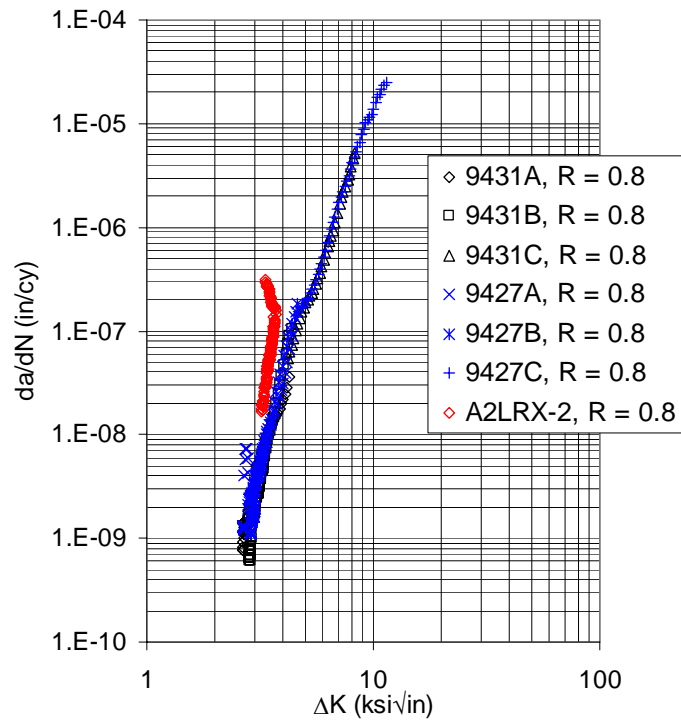
Figure 4.36. Fatigue crack growth rate behavior at 1900°F at R = 0.8.

As seen in Table 4.9 and Figure 4.37, the crack growth rate increases and the threshold decreases with increasing R-ratio. In addition to that trend, there are a few other items of note. At R = -1, test A2LRX-3 clearly appears to be out of line with the other two tests at this stress-ratio. No defect in the specimen or testing was noted, but this test was omitted from further modeling. At R = 0.7 and 0.8, the GEAE tests (T20VW-2 and A2LRX-2) tend to have higher growth rate, particularly at the beginning of the sheds. This is probably associated with the details of the test method, although specific reasons could not be determined. Both tests tended to merge into or close to the P&W data at the same stress-ratio as the shed proceeded. Finally, in contrast to the behavior at lower mean stress (R = 0.05 and below) no crack arrest was seen for the higher stress-ratio's tested, 0.5, 0.7 and 0.8.
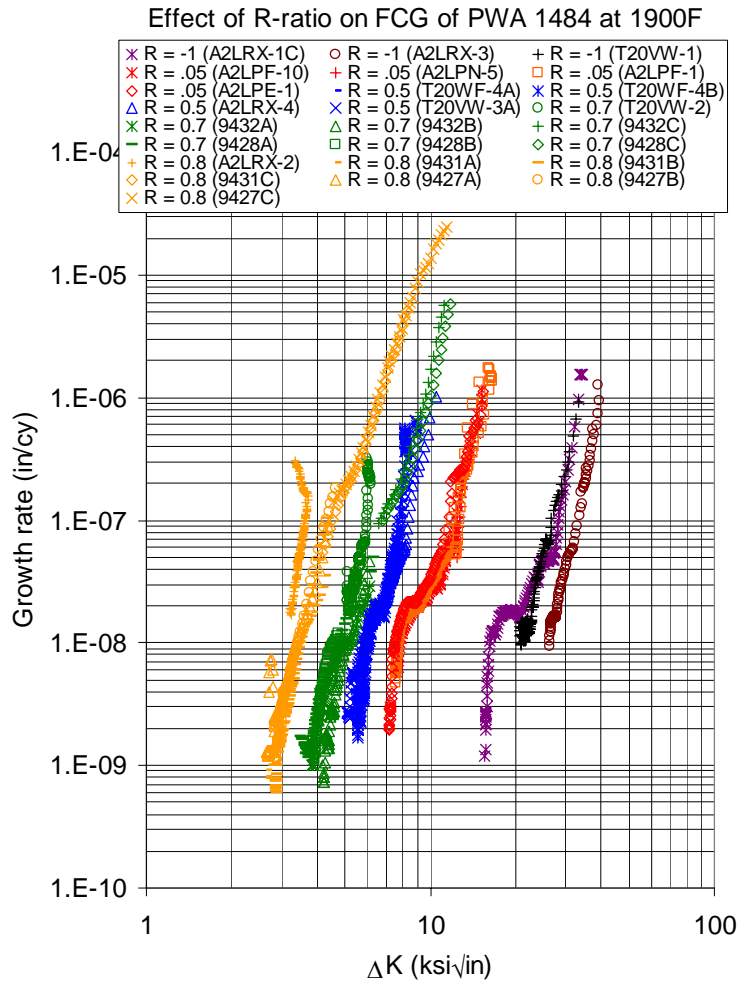
Figure 4.37. Fatigue crack growth rate behavior at 1900°F as a function of stress ratio, plotted using ΔK.
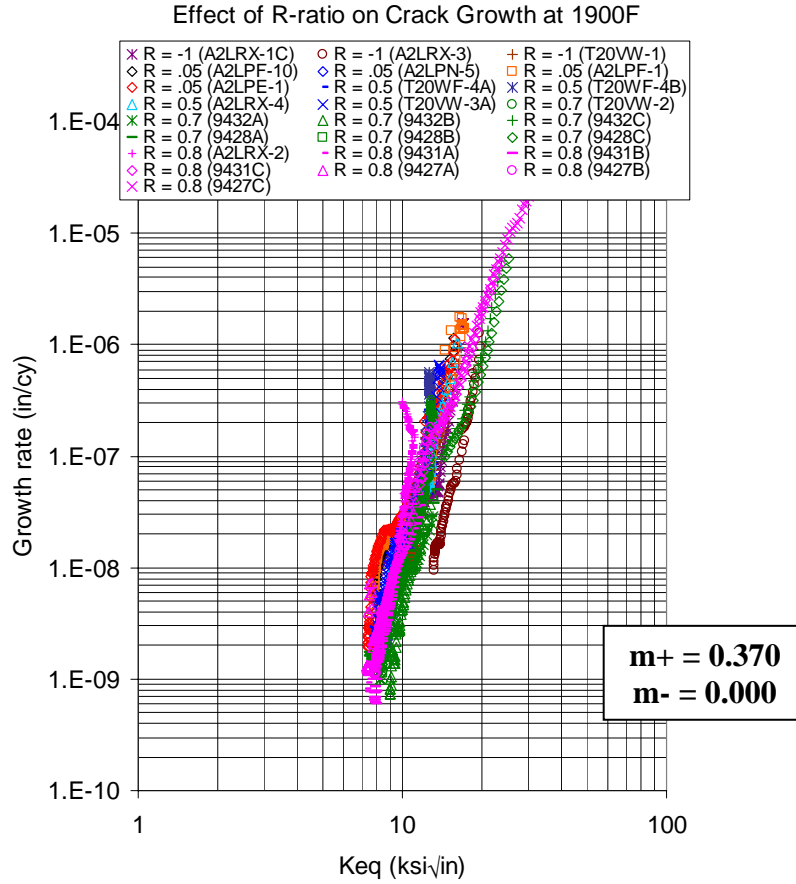
Figure 4.38. Fatigue crack growth rate behavior at 1900°F plotted using
Keq and the two-parameter Walker model.

At these stress-ratios the crack growth rate continuously decreased with decreasing
ΔK without ever ceasing growth altogether. Whether this is due to creep or environmental
effects isn't clear, although the presence of an arrest at the lower stress-ratios where the same
environment is present suggests that is more likely due to creep.

To put these data into a more convenient form from which K_{th} can be determined for
any stress-ratio, the data shown above were modeled using the Walker equivalent stress
intensity model:

$$K_{eq} = \Delta K(1-R)^{(m-1)} \tag{4.13}$$

where m is an empirical parameter fit from the data. Using all the data from specimens listed
in Table 4.9, the best-fit m value is 0.366. When the ΔK of Figure 4.34 is adjusted to K_{eq}
using Equation 4.13 and m = 0.366, the data group closer together. However, the R = -1 data

still tend to lie to the right of rest of the data. A further refinement of the model was made to assume that a different m applied for conditions with $R < 0$ than with $R > 0$. Using this approach, the best-fit m for $R \geq 0$ is m+ = 0.370 and the best-fit m for $R \leq 0$ is m- = 0.000. (m = 0 implies that the crack growth behavior is controlled by the maximum stress intensity in the cycle.) The crack growth results plotted using this two-parameter mean stress model are shown in Figure 4.36. Most of the results are collapsed onto one master da/dN-K_{eq} curve using this approach. The average K_{eq} threshold for this model is 8.20 ksi√in with a standard deviation of 0.59 ksi√in.

(a) Fractography

The fracture surfaces of representative specimens tested at 1900°F at $R = -1$, 0.05, 0.5, and 0.8 were examined to determine if any trends in fracture appearance could be discerned. The fracture surfaces for the four values of R are shown in Figures 4.39 through 4.42. In each of these specimens, the test sequence was: Pre-crack, K-shed to threshold, and fracture at room temperature. The photographs are oriented so that the crack growth direction is right-to-left, so that the threshold growth region is on the right of the crack arrest marking, with the room temperature fracture on the left of the marking. An optical photograph of each specimen is included because the fracture surface beachmarks (oxide colors) are much more visible than on SEM images. Three SEM images are shown for each specimen, in ascending order of magnification, centering on the crack arrest or threshold area at the middle of the specimen.

All of the 1900°F crack growth fracture surfaces examined had similar appearances, regardless of stress-ratio. In general, the fracture surfaces were highly oxidized, with a combination of gray and silvery oxides either separated into bands or co-existing in the same band. There was a tendency for silvery oxides to be more prevalent on the slower growth rate surfaces and the gray ones to be on the higher growth rate surfaces, but this trend was not always followed. On all fracture surfaces there were thicker and thin regions of oxide, evidence of oxide scale spalling during testing.

All fracture surfaces were quite flat and perpendicular to the stress axis, i.e., pure Mode I. This is in contrast to HCF specimens without precracks. Note that nearly all

the crack growth specimens were tested in a shed mode, so that K's (and growth rates) tended to be low, thus avoiding a transition to crystallographic cracking.

Two unusual features were seen at the crack arrest region.

1.) On some samples, ahead of the main crack front there were small, very smooth, semicircular crack segments, which appear not to be fully connected with the main crack. Examples can be seen in Figures 4.40 and 4.41. Since these segments are oxidized, it is clear that they were at least partially connected to the main crack prior to final fracture, possibly on a different plane than the final fracture plane. Since some crack growth tests showed fluctuating voltage signals near threshold (the crack would appear to arrest, then restart, then re-arrest), it may be that the intermittent initiation of this crack segments ahead the main crack and subsequent link up caused this phenomenon. Similar features were seen near the origins of unprecracked HCF specimens tested at 1900°F.

2) On the side of the arrest mark where the room temperature fracture begins, on most specimens there are regions of an unusual "feathery" structure that can extend as far as .008" (more typically .002") from the arrest point. Good examples are shown in Figures 4.39 and 4.41. They consist of regularly spaced bands about .001" wide perpendicular to the main crack front, and each consisting of a chevron-like pattern with the "V" pointing back to the arrest mark. These could be either features associated with the crack tip plastic deformation at room temperature involved in starting the fracture process, or they could be from the effect of thermal exposure at the crack tip (oxidation and stress) on the room temperature fracture process.

4.2.2.3 Threshold Model Development

A. Fracture Resistance Orthotropy

New developments in the characterization of fracture resistance as a function of crack orientation in two and three dimensions are described in some detail in Appendix Q. While the emphasis is on single crystal PWA 1484 alloy because of the pronounced directionality observed in the fracture resistance of this material, the concepts are also applicable to other symmetrically processed materials where the processing results in
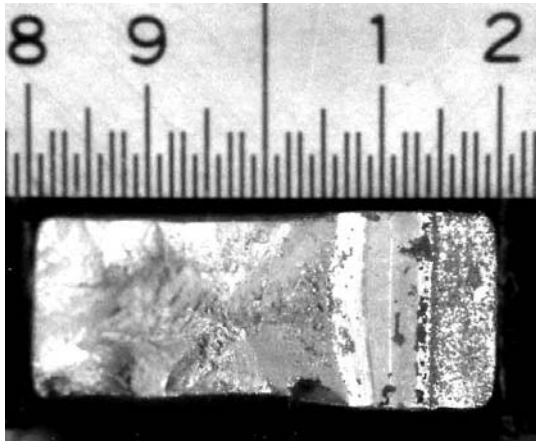
a) Optical
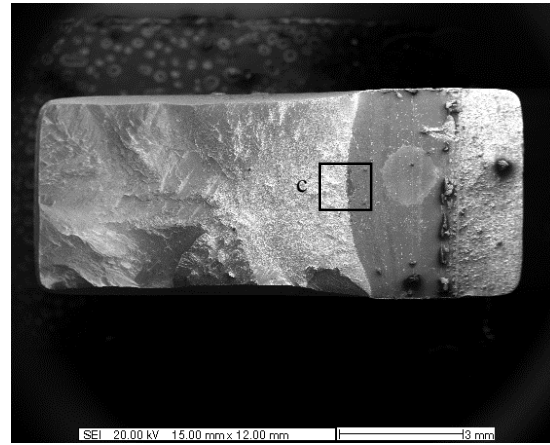
b) Low magnification SEM
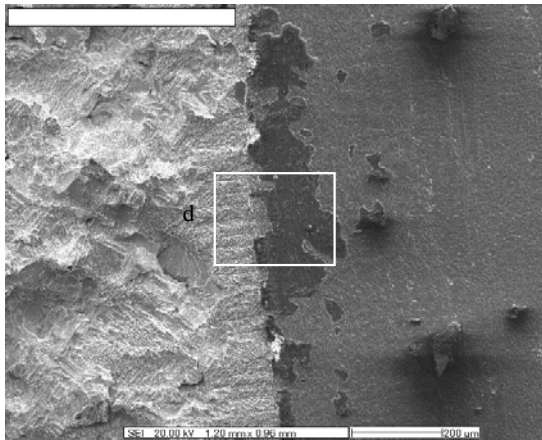
c) Magnification of crack arrest area in b)
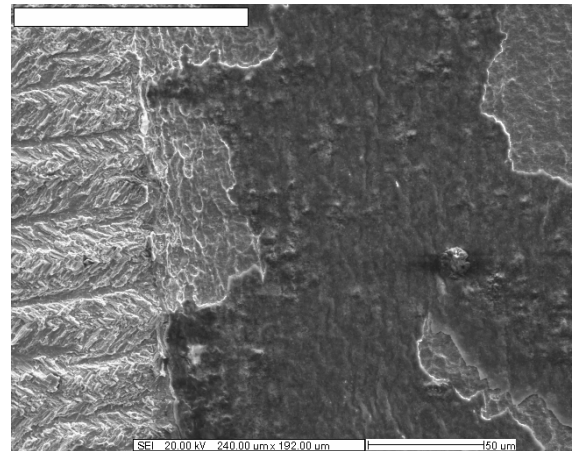
d) Magnification of crack arrest area in c)

Figure 4.39. Fracture morphology of PWA 1484 crack growth S/N A2LRX-1:
1900°F, R = -1, 10 Hz.
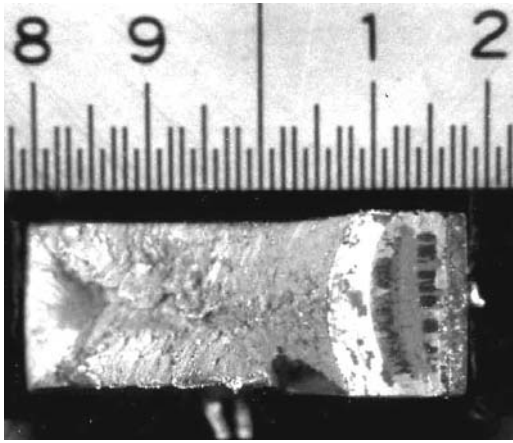
a) Optical
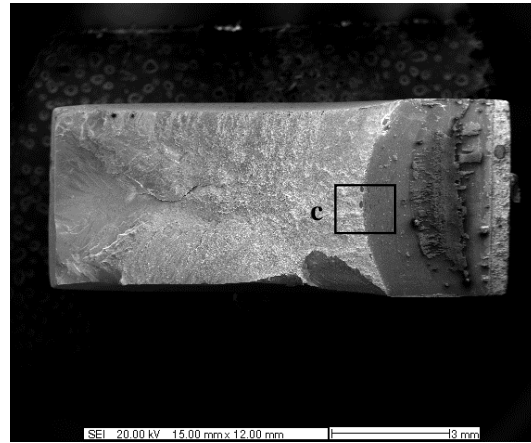
b) Low magnification SEM
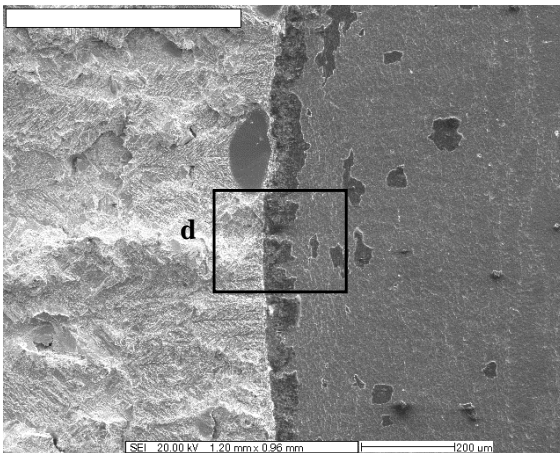
c) Magnification of crack arrest area in b)
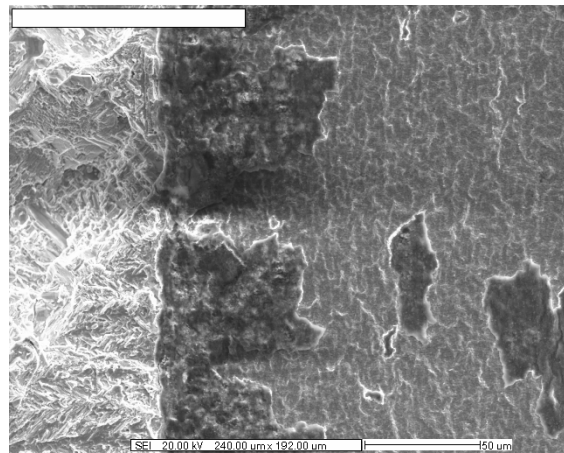
d) Magnification of crack arrest area in c)

Figure 4.40. Fracture morphology of PWA 1484 crack growth S/N A2LPE-1:
1900°F, R = 0.05, 10 Hz.
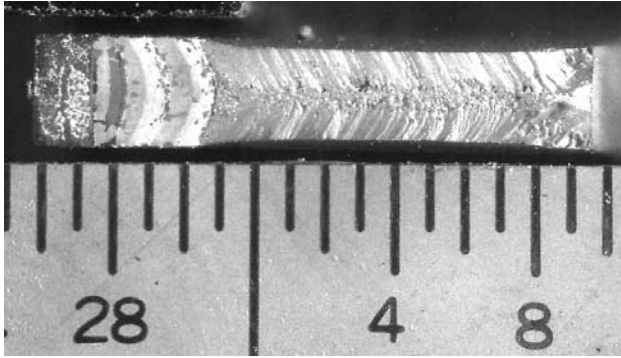
a) Optical
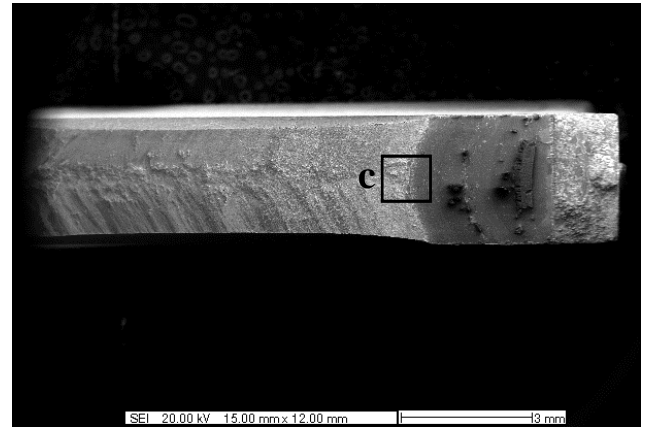
b) Low magnification SEM
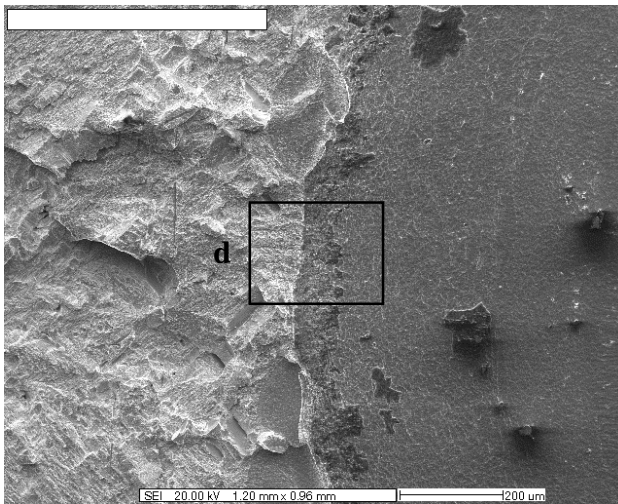
c) Magnification of crack arrest area in b)
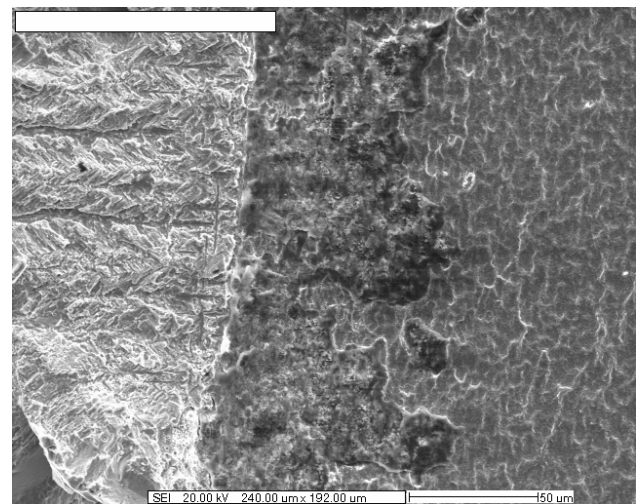
d) Magnification of crack arrest area in c)

Figure 4.41.   Fracture morphology of PWA 1484 crack growth S/N T20WF-4:
1900°F, R = 0.5, 10 Hz.
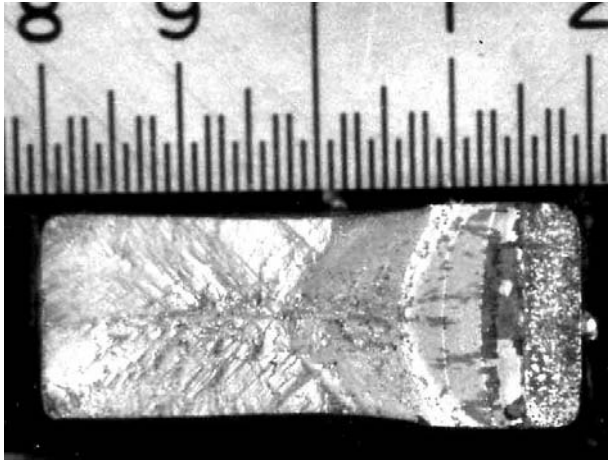
a) Optical
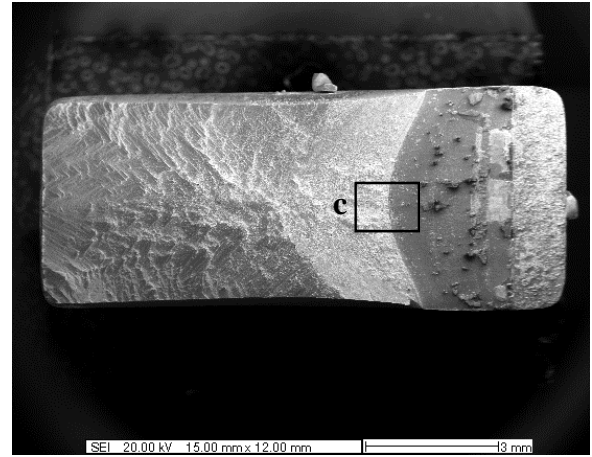
b) Low magnification SEM
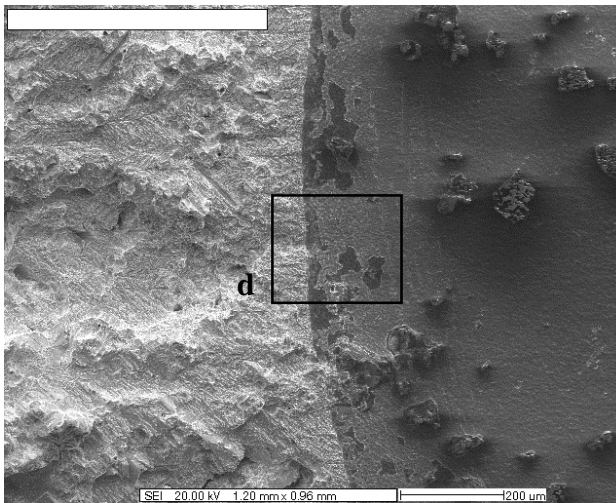
c) Magnification of crack arrest area in b)
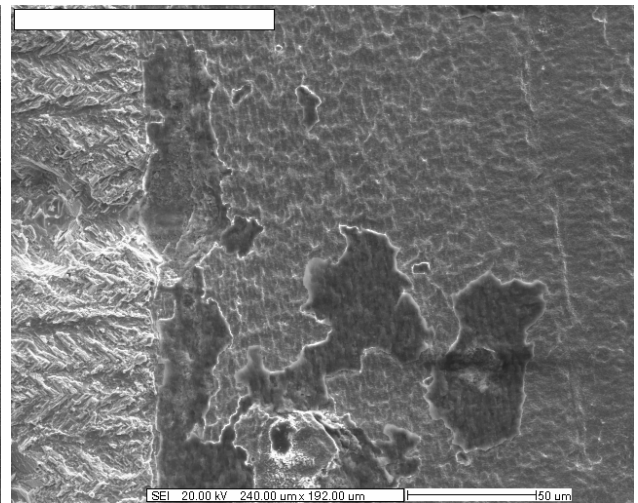
d) Magnification of crack arrest area in c)

Figure 4.42. Fracture morphology of PWA 1484 crack growth S/N A2LRX-2:
1900°F, R = 0.8, 10 Hz.

directional fracture properties. A threshold model is then developed based on experimental data obtained in this program.

B.   *Fitting of Test Results for Threshold Crack Growth in Single-Crystal PWA 1484 Nickel Alloy at 1100°F*

Single crystal data was gathered from P&W, GEAE, and SwRI efforts under this program to develop a PWA 1484 threshold model at 1100°F. At this temperature, it was observed that frequency, load ratio, and crack orientation were all significant parameters with regard to the crack growth threshold, thus all of these parameters were taken into account in the threshold model. For modeling purposes, the lowest *ΔK* at which crack growth was observed was used as the threshold. Optimization of the curve fit was accomplished using the *Solver* tool in Microsoft Excel spreadsheet application to minimize the square of the error in the fit by iterating the model coefficients. Stress intensity factors were corrected for crystalline anisotropy for the orientations for which solutions have been given previously. Threshold data for other orientations were not corrected for anisotropy.

The frequency effect was accomplished using a nonlinear fit of data taken at different frequencies in the <001/010> orientation at R=0.1, and R=0.8. The data was normalized to the threshold at 20 Hz, and is plotted against the fit in Figure 4.43.

$$\frac{K_{th}}{K_{th\,20Hz}} = 0.9973 + 0.2822\,\exp(0.2323 f) \tag{4.14}$$

where, *f* is the frequency in Hertz. It was assumed that the effect of higher frequencies than 20 Hz was negligible.   Clearly, additional data would be beneficial to give more credibility to the model.

A separate fit was then created to model the 20 Hz threshold as a function of load ratio and orientation. In the absence of test data from a sufficient variety of orientations to distinguish the three unique principal fracture threshold values described in Equation Q13, (Appendix Q), these values were all presumed equal in the model, reducing Equations Q11 and Q12 (Appendix Q) to:
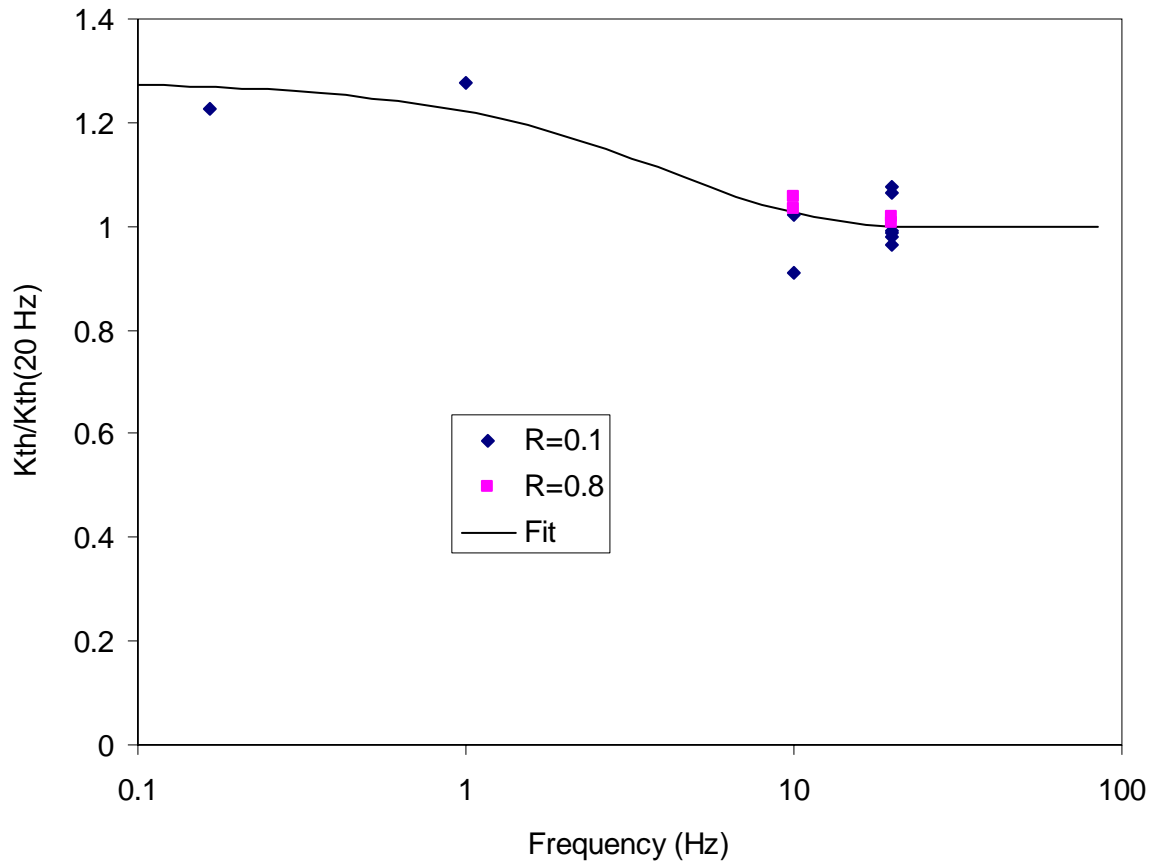
Figure 4.43. Frequency effect model.

$$
\frac{K_{th\,20Hz}(\mathbf{n},\mathbf{a})}{K_{principal}} = \left[\left(\frac{n_1^{\,2}\left[\left(a_2^{\,2}\right)^m + \left(a_3^{\,2}\right)^m\right]^{\frac{1}{m}}}{1-a_1^{\,2}} \right)^n + \left(\frac{n_2^{\,2}\left[\left(a_3^{\,2}\right)^m + \left(a_1^{\,2}\right)^m\right]^{\frac{1}{m}}}{1-a_2^{\,2}} \right)^n + \left(\frac{n_3^{\,2}\left[\left(a_1^{\,2}\right)^m + \left(a_2^{\,2}\right)^m\right]^{\frac{1}{m}}}{1-a_3^{\,2}} \right)^n \right] 2n
$$

(4.15)

The principal value of the threshold, and the fitting exponents m and n were obtained from the curve fit as functions of the load ratio $R=K_{min}/K_{max}$.

$$
K_{principal} = \frac{3.456}{0.5 + 0.862\,R}
$$

(4.16)

$$
m = 1.926 - 1.491\,R
$$

(4.17)

233

$$n = 0.8687 + 0.0431\,R \hspace{5cm} (4.18)$$

A correlation plot of actual vs. predicted values of the 1100°F threshold for the orientations available, load-ratios of 0.1, 0.5, and 0.8, and frequencies ranging from 10 CPM (cycles per minute) to 20 Hz is presented in Figure 4.44.
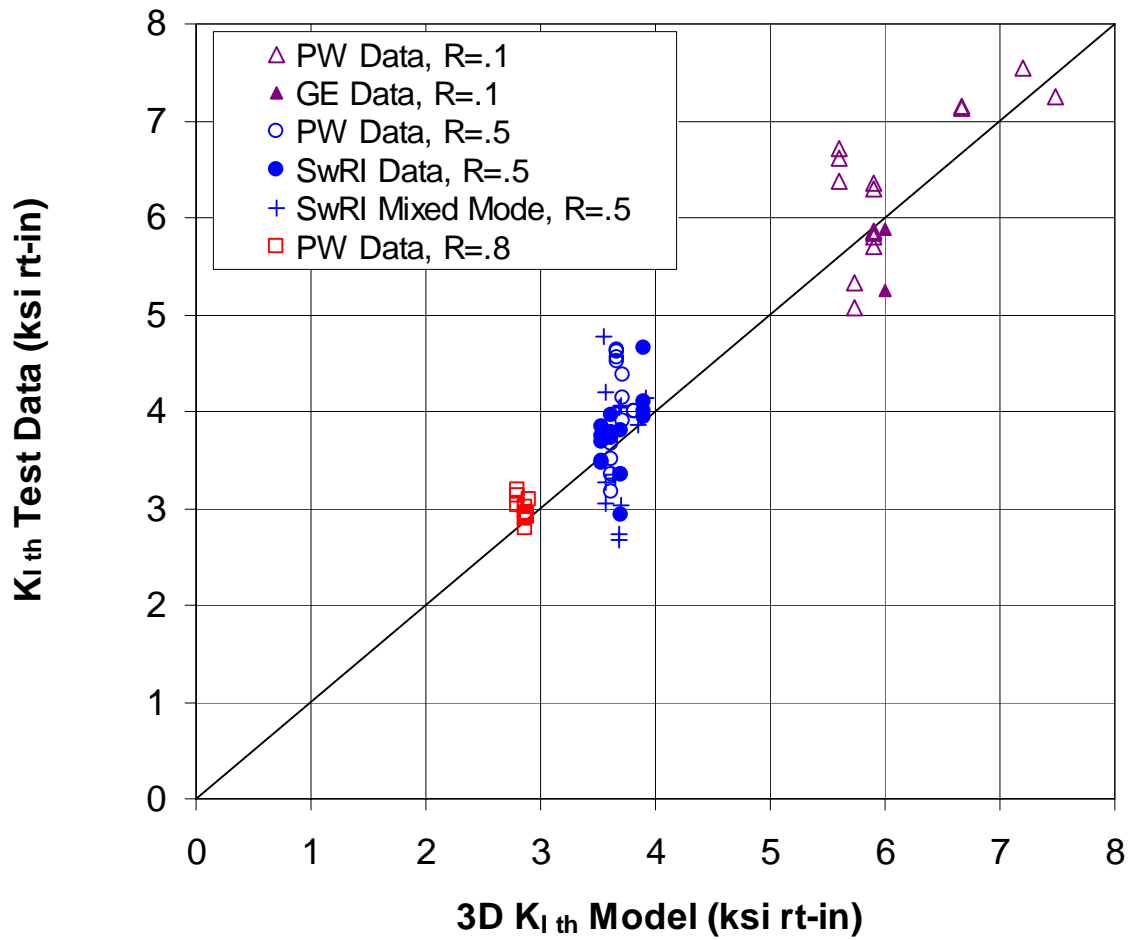
Figure 4.44. Correlation plot for 1100°F threshold model.

Unfortunately, the fracture resistance relationships for crack orientation are scalar functions of two vectors in 3D, and there is no way to plot the function over the entire domain, showing fit to test data. However, plots can be produced for severely restricted domains, such as the range of fracture resistance values as one rotates from one crack orientation to another orientation orthogonal to the first.

Selected data are plotted against the model prediction in Figure 4.45. Each data point shown is an average of available test data in the (nominal) orientations indicated. Only 10 and 20 Hz data is shown, the 10 Hz data being (very slightly) adjusted to a 20 Hz basis by way of Equation (4.45). Not all the data available are on the plots, because only some of the data are oriented conveniently for representation in the graphical manner shown. The SwRI mixed mode data in particular are excluded, and will be discussed in a separate section.

It was proposed that additional specimens be planned to improve confidence in the three-dimensional fit, as described in Table 4.10, along with orientations completed under the Pratt & Whitney effort. The table also gives source material casting numbers for the specimens tested, as well as proposed samples. Sample cutout diagrams are presented in Figures 4.47 and 4.48 for illustration purposes (not intended to represent a specimen-by-specimen cutout record). The proposed test orientations were not completed under the program, but are left as a recommendation for follow-on work.

4.2.3   Mode I; Notch Effects

The objective of this effort was to determine the methods necessary for analyzing the growth or arrest of HCF cracks in a notch stress field at 1900°F. Turbine airfoils at elevated temperatures (e.g., 1900°F) have many geometric complexities such as cooling holes and transitions from the airfoil skin to the internal ribs or blade platform that lead to stress concentrations. Since stress concentrations are one of the more common sites for crack initiation, it is important to be able to model the growth of cracks from notches, particularly under HCF excitation where once the driving force for growth exceeds the threshold, cracking is expected to proceed very rapidly. One of the additional complicating factors at 1900°F, in addition to the usual complexities of notch analysis, is the occurrence of time-dependent stress relaxation around the notch due to creep. The inclusion of such creep or stress relaxation effects was intended to be a significant part of the study, but the full study was not accomplished. A pre-test analytical study was performed, as will be described below, and notched specimens were fabricated for testing, but experimental verification (or not) of the pre-test predictions was never performed. Calculations were performed by GEAE for an assumed 2D edge notch geometry and by PWA for a 3D geometry.
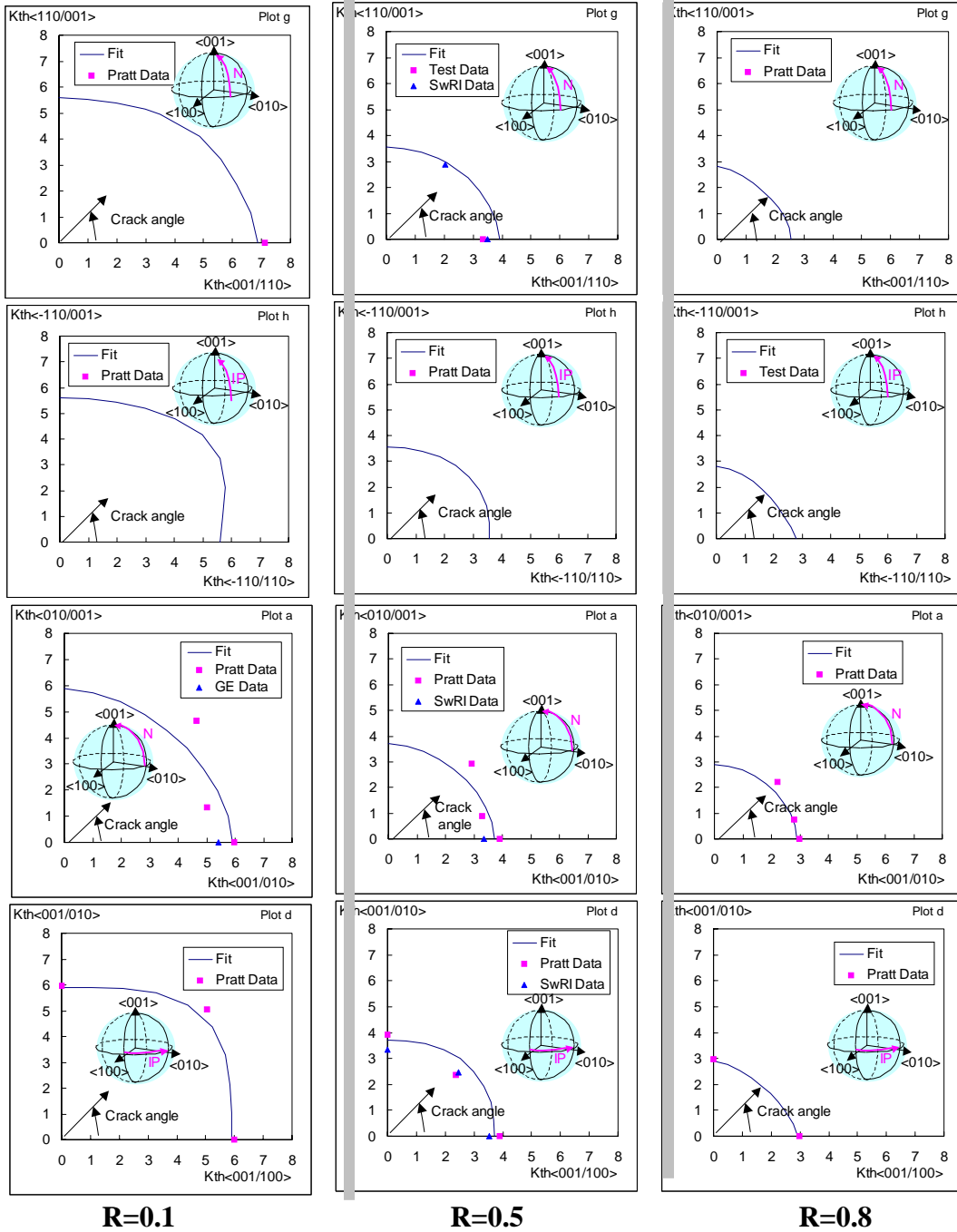
Figure 4.45. Fracture threshold model compared with test data, various crack orientations, 1100°F, 20 Hz Basis. Note: "N" in schematic refers to crack planes and direction passing through the origin and normal to curve indicated. "IP" refers to crack planes in plane with the curve indicated, and direction normal to the curve indicated. Some data points shown were corrected from 10 Hz to 20 Hz based on Equation (4.14).

236

Table 4.10. Summary of Current and Proposed Test Orientations for PWA 1484 SEN Threshold Testing at 1100°F

Config.	Crack Orient.	Casting Type	Casting Serial No.	C = completed P = proposed R Value		
				.1	.5	.8
1	<001/010>	PAP601225-A	A2LR7, A2LKR, A2LLK, A2LRN	C	C	C
2	<001/010>+15°	PAP601225-A	A2LPK	C	C	-
3	<011/0-11>	PAP601225-A	A2LRM	C	C	C
4a	<001/110>	PAP601225-B	T20VY	C	C	
4b		PAP601227-A	A2V12			P
5	<010/001>	PAP601225-A*	T20XJ	P	P	P
6	<010/100>	PAP601227-A*	A2V12	P	P	P
7	<110/001>	PAP601225-B*	T20XC	-	-	P
8	<-1-11/112>	PAP601225-B*	T20VY	-	-	P
9	<011/100>	Slanted-B	Z1LBN	-	-	P
10	<010/101>	Slanted-B*	Z1LBN	-	-	P
11	<-110/110>	Not Available	N/A	(Shown for reference)		
12	<-110/112>	Not Available	N/A	(Shown for reference)		

*Specimen longer than casting in orientation specified, requires weld extension on end grips.
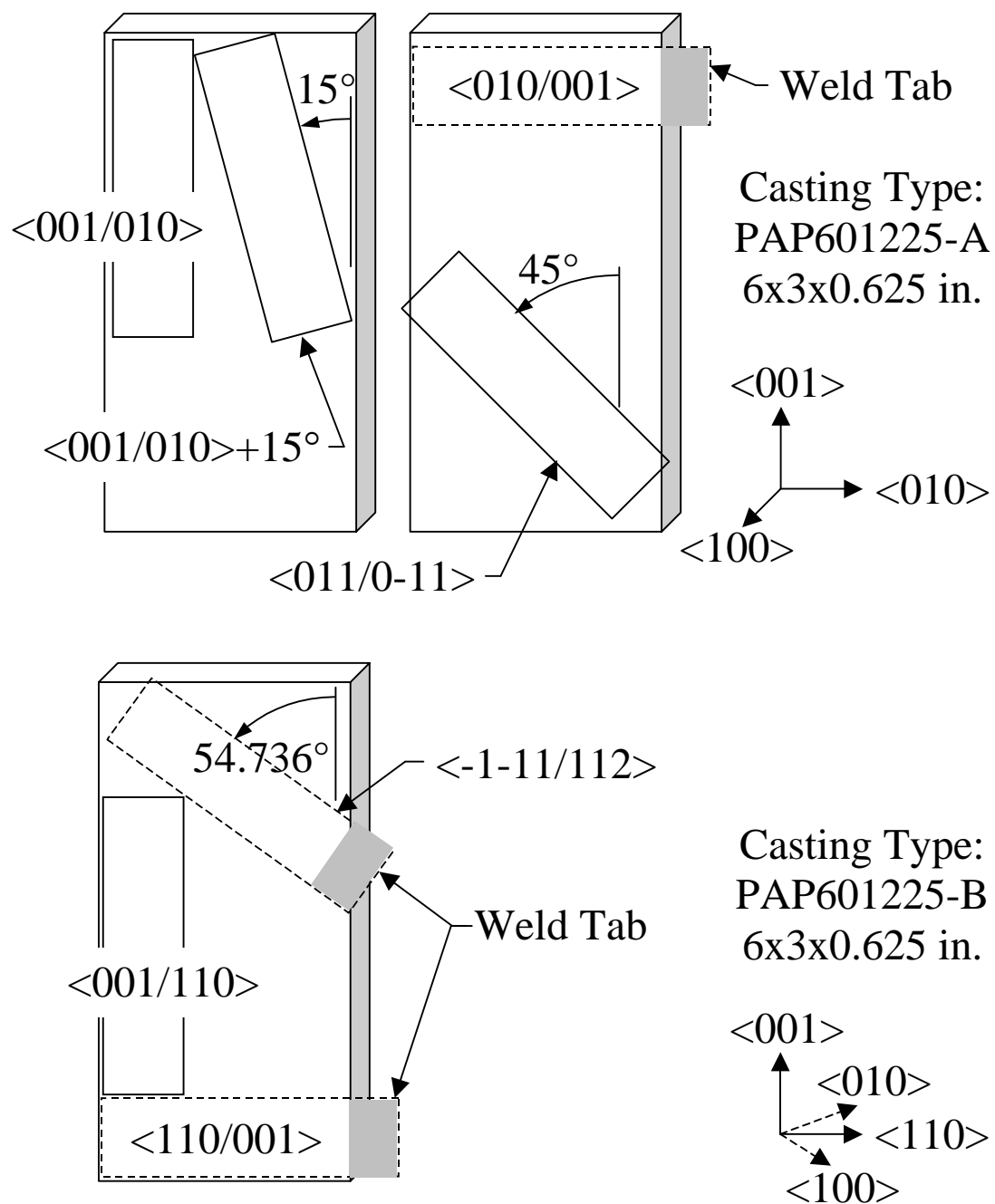
Figure 4.46. Sample cutout diagrams for various specimen configurations
(proposed specimen configurations shown in dashed lines).
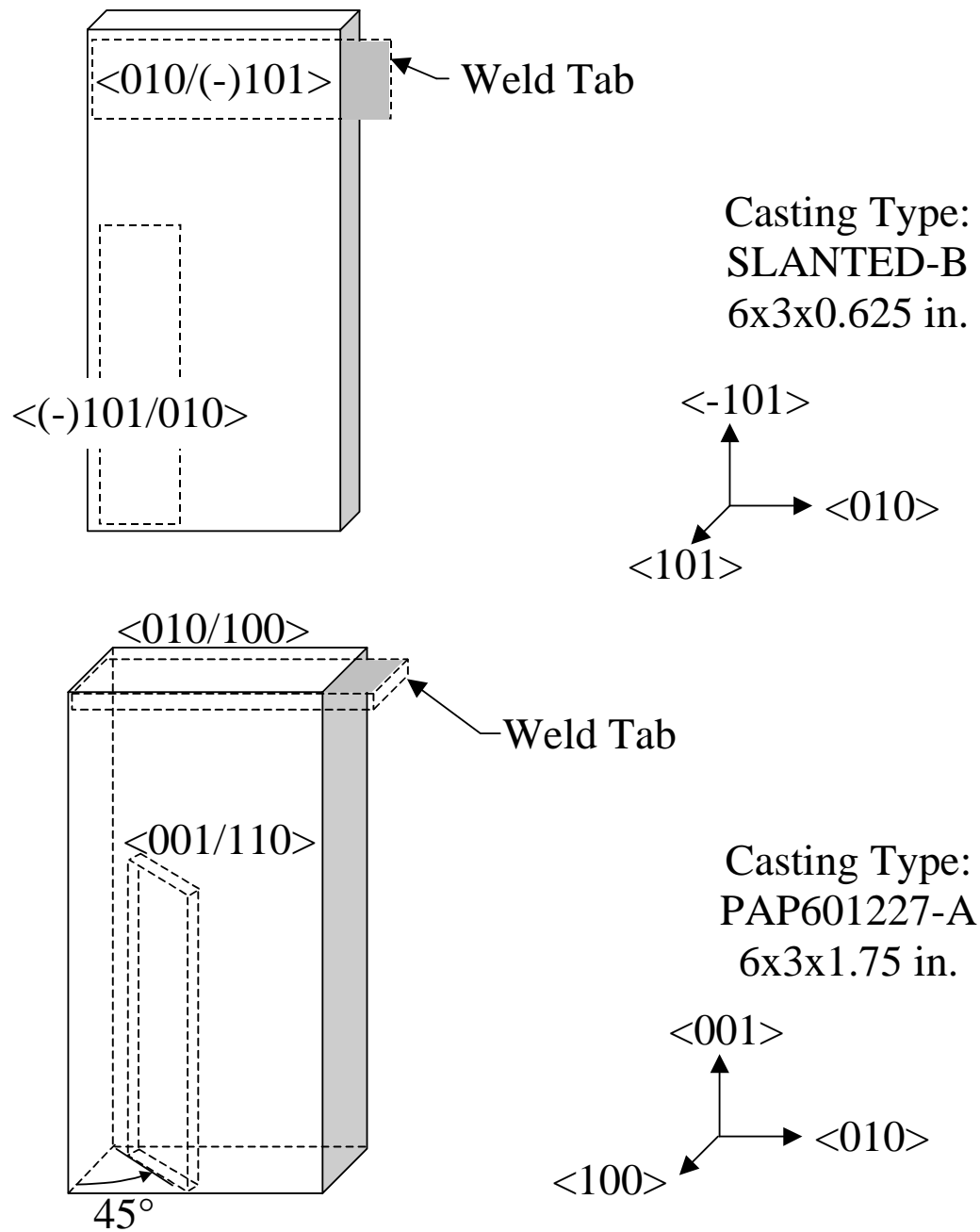
Figure 4.47. Sample cutout diagrams for various specimen configurations
(continued, new specimen configurations shown in dashed lines).

239

4.2.3.1   2D Analysis of Crack Growth Specimen by GEAE

The notch geometry selected for study by GEAE is shown in Figure 4.48. This specimen was a modification of the fixed-end SEN crack growth specimen with the addition of two opposing semi-circular edge notches 0.065 inch in radius in the center of the gage section. While this notch is larger in size than many (but not all) turbine blade notches, it represented a compromise choice in that smaller notches would have been more difficult to reproducibly machine and to obtain crack growth measurements from. Developing precracks in a small notch would be particularly difficult, since a small amount of excess growth could take the crack beyond the main part of the notch stress field. With a 0.065-inch radius notch we felt we could introduce 0.015 inch to 0.030-inch precracks and still keep the crack within a significant fraction of the notch gradient. The location selected for the starter notch was at the root of one of the notches, as indicated in Figure 4.48. In all cases a 2D or through-crack geometry was assumed.

Using ANSYS and GEAE's internal crack propagation code, PROPLIFE, an analytical study of the possible behavior of a through crack in this notched specimen at1900°F was performed, with the intent of identifying useful test conditions with
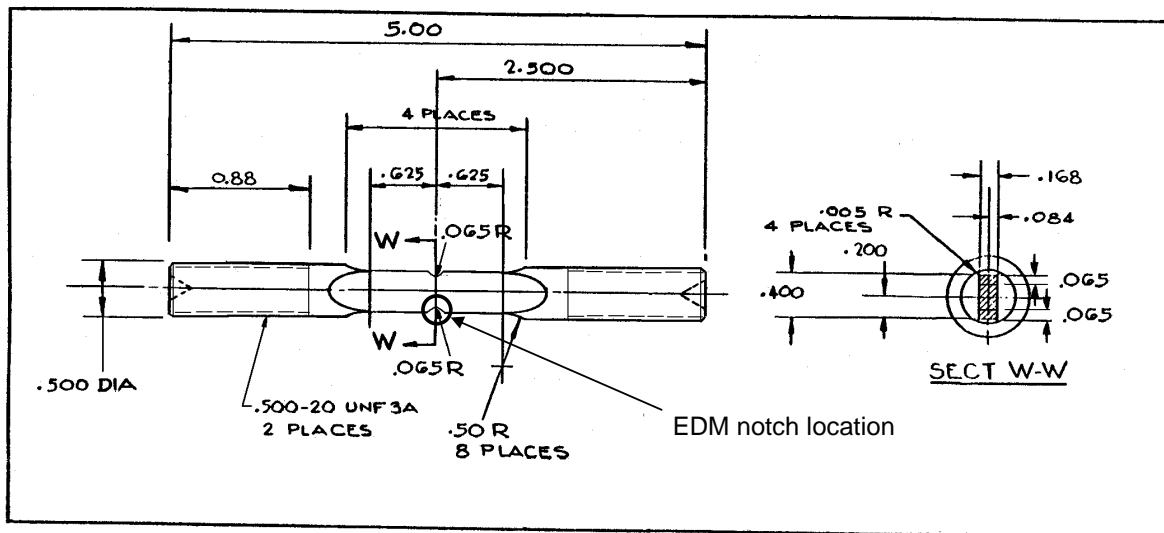
Figure 4.48. Double edge notched specimen selected for notch effects crack growth study.

which to test our capability to model the crack behavior. The first step was to perform an anisotropic elastic stress analysis of the specimen to extract the stress gradient away from the notch. This gradient is shown in Figure 4.49, for an applied average net section stress of 27.32 ksi (concentrated notch root stress of 50 ksi). The notch stress field extends approximately 0.05 inches in from the notch root on both sides. The minimum stress for an $R = 0.05$ cycle is also shown for comparison. This stress gradient was used in the prediction of crack growth for all cases in which creep was assumed to be absent. To approximate the effects of creep relaxation in the specimen at 1900°F, the maximum stress in the cycle was assumed to have relaxed to a value equal to the average net section stress (27.32 ksi). This represents a fully relaxed condition; in reality as time proceeds the stress gradient will gradually shift from the fully elastic one to the relaxed one. However, for the purposes of pre-test analysis, taking the fully relaxed gradient seemed useful for bounding the expected results. Notice in Figure 4.49 that the minimum cyclic stress for the fully relaxed condition
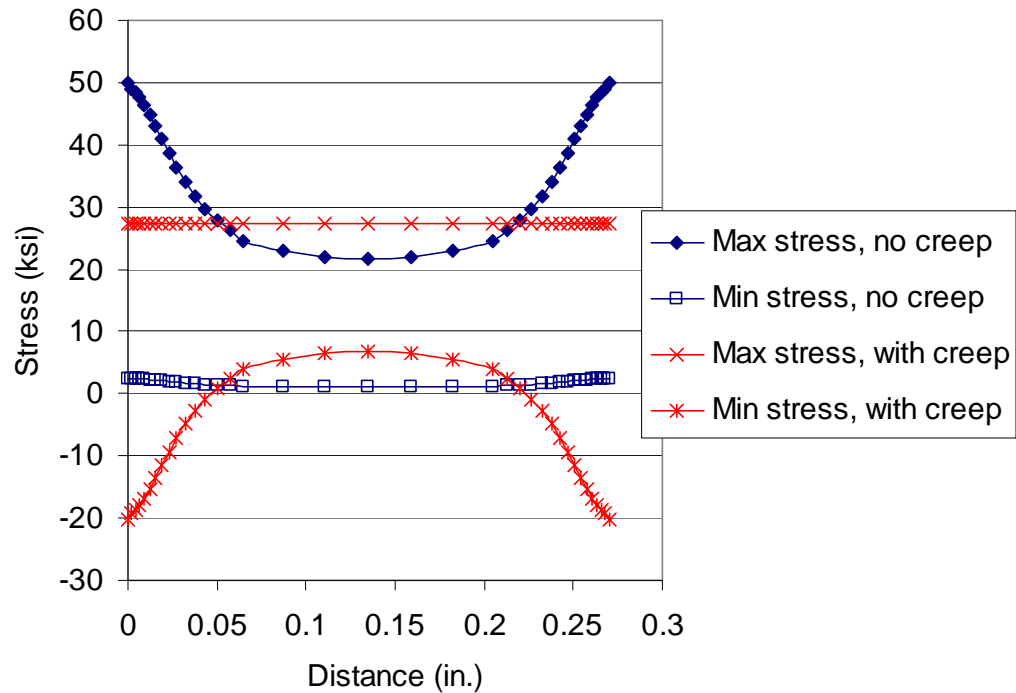
Figure 4.49. Notch stress gradients in specimen of Figure 4.48 for applied net-section stress of 27.32 ksi, $R = 0.05$, without and with full creep relaxation.

is now highly compressive at the notches, instead of simply near zero. Thus the mean stress has changed, and this was reflected in the crack growth analyses through the use of the Walker mean stress model described in Section 4.2.2.2.*E* (see Equation 4.13).

Crack propagation analyses of various cases were evaluated using PROPLIFE and the crack growth parameters for PWA1484 developed in Section 4.2.2.2.*E*. A Paris Law model for crack growth was used:

$$da/dN = CK_{eq}^n \tag{4.19}$$

where, $C = 9.88 \times 10^{-13}$ in/cy and $n = 4.847$ with m+ = 0.267 and m- = 0.000 (see Section 4.2.2.2.*E,* Equation 4.13). These values are slightly different than those reported in Sections 4.2.2.2.*B* and 4. 2.2.2.*E* because these studies were performed before the K-solution error discussed in Section 4.2.2.2.*B* was discovered. Although the absolute lives predicted would change, the trends reported here would be unaffected by these differences. Calculations were performed for both pinned (free) and fixed end conditions, but for the present specimen the fixed end condition is the relevant one.

Figure 4.50 shows the predicted crack size vs. cycles for a 0.015 inch pre-crack at a nominal net section maximum stress of 27.32 ksi (R = 0.05). The effect of creep, as modeled, is very significant. For the fixed end condition the predicted residual life jumps from 146,600 to 869,800 cycles when the notch stress gradient is assumed to be fully relaxed. The amount of relaxation that would be expected to occur would be a function of the time at maximum stress, so experimentally, it was planned to perform notched crack growth tests with and without a dwell at peak stress. The dwell would accelerate the stress relaxation relative to the crack growth rate and drive the test condition nearer to the fully relaxed condition modeled. However, the crack growth rate itself is likely to accelerate due to the dwell, so an analytical variation was performed assuming that the dwell crack growth rate was four times as fast as without a dwell. (There was no data to base this on, simply an assumption.) As shown in Figure 4.51, adding the dwell acceleration to the crack growth rate can almost entirely negate the life benefit resulting from the stress relaxation. The crack size vs. cycles for a case with creep relaxation and a 4x dwell growth rate acceleration is quite similar to that for no creep relaxation and no dwell acceleration!
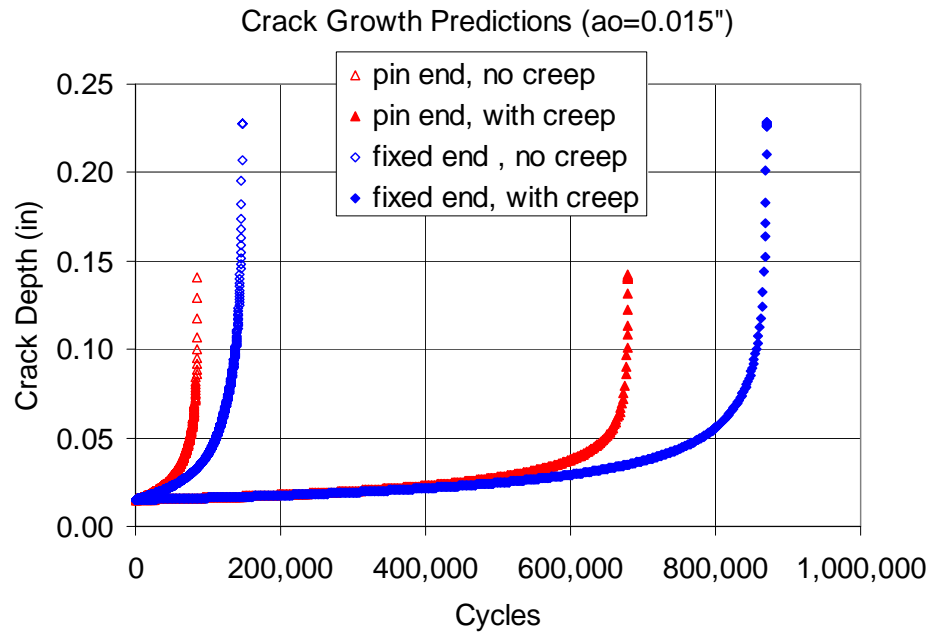
Figure 4.50. Predicted 1900°F notch crack growth from a .015 inch pre-crack at a nominal net section maximum stress of 27.32 ksi (R = 0.05).
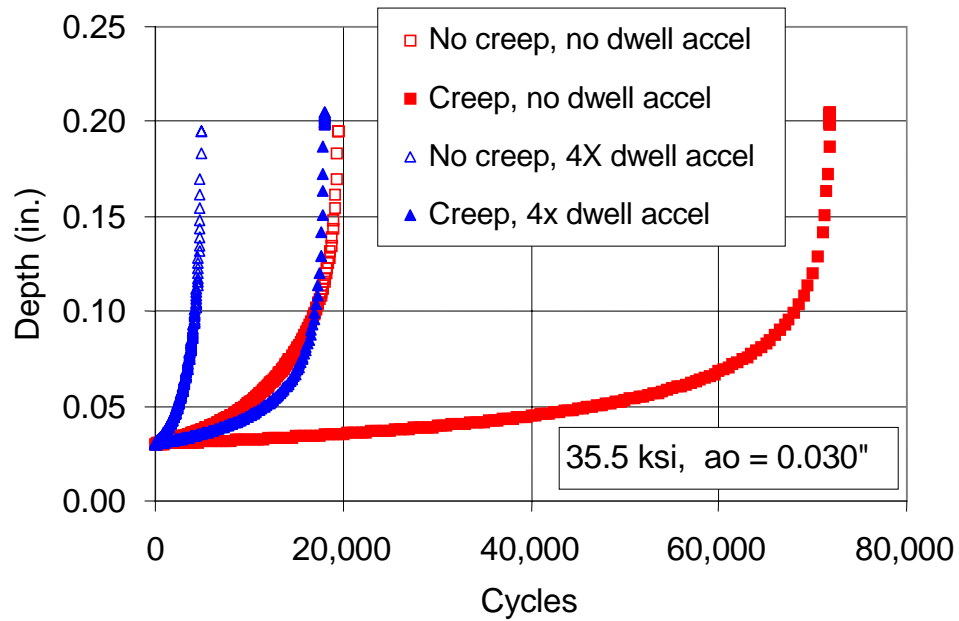
Figure 4.51. Effect of assumed 4X dwell crack growth rate acceleration on residual notch life.

Crack arrest was not predicted to occur as the crack grew out of the notch stress field in any of the cases examined. The nature of the stress gradient and specimen constraint studied here was such that the stress intensities always increased with increasing crack size. If notch crack arrest can occur, it probably will be seen only in much smaller notches of higher K_t.

The proposed test matrix (Table 4.11) included the following tests intending to examine the effect of the notch stress gradient and its relaxation with time due to creep at 1900°F.

Table 4.11. Proposed Test Matrix for Notched Crack Growth at 1900°F
(Notch R = 0.065", Precrack = 0.015")

Test No.	Cycle Type	Nominal Stress (ksi)	Expected Life (cy)	Expected life (hr)
1	10 hz	27.3	146,000	4.1
2	10 hz	21.8	432,000	12
3	10 hz	16.4	1,800,000	51
4	Creep + 10 hz	27.3	870,000	24
5	dwell (unnotched)	-	-	-
6	dwell (notched)	27.3	85,000 – 870,000	70+

The strategy would be to start with 10 Hz cyclic conditions (Tests 1 – 3) and lower the stress for each successive test. This would prolong the test and increase the time available for creep relaxation to occur, presumably slowing down the crack growth rate even more than expected from the simple reduction in stress (ΔK) level alone. Test 4 would take a different approach, applying a static creep exposure prior to HCF cycling. The creep exposure would be for 24 to 48 hr at a nominal stress at which about 0.5% creep is expected in that time. Tests 5 and 6 are intended to examine the effect of a dwell during fatigue cycling. Test 5 would be performed on a standard, unnotched crack growth specimen to obtain the crack growth rate in the presence of a short dwell. The dwell should be kept as short as possible so as to keep the test time for Test 6 to a reasonable length. A dwell of 1-2 seconds is suggested. Test 6 would then be performed using that same dwell cycle and the effect of the combined fatigue and stress relaxation during the dwell cycle would be

evaluated. Multiple tests of each type would need to be performed to determine their repeatability.

In summary, a pre-test analytical study was performed on the crack growth behavior in a notched specimen of PWA 1484, including the potential effects of creep relaxation. It appears likely that creep relaxation will significantly slow, but not arrest, crack growth out of notches. The amount of the slow down will be governed by the balance between the relaxation rate of the stresses and the rate of crack advance. A test matrix was planned but not executed to evaluate these effects.

4.2.3.2   3D Notch K Calculations by PWA

As part of the analytical study of crack growth behavior from a notch, it was hoped to specify a stress concentration high enough that the (elastic) stress intensity factor would reach a local minimum as the crack began to grow, potentially resulting in a situation where the crack might initiate, but then arrest at some small length.

To this end, an analysis of a Double Edge Notched (DEN) specimen geometry was performed. The DEN specimen (PW FML 102520) is initiated from a surface flaw emanating from one of the side notches, as illustrated in Figure 4.52. A three-dimensional analysis is thus required to obtain the stress intensity solution. The results are based on an isotropic FRANC3D/BES analysis, and are presented in Figure 4.53.

The polynomial fit describing the isotropic solution is

$$K_I = \sigma\sqrt{\pi a}\left[1.428 - 6.386\left(\frac{a}{w}\right) + 12.30\left(\frac{a}{w}\right)^2 + 76.38\left(\frac{a}{w}\right)^3 - 213.9\left(\frac{a}{w}\right)^4 + 99.20\left(\frac{a}{w}\right)^5 + 72.44\left(\frac{a}{w}\right)^6\right]$$

(4.20)

The formula is valid in the range 0.016<*a/w*<0.6.

While the normalized curve shown in Figure 4.53 does pass through a minimum, Equation 4.20, which provides the absolute value of K, has no minimum. Thus, a crack that initiates would be expected to continue growing under constant amplitude loading. No testing of this specimen geometry was performed under the present program.
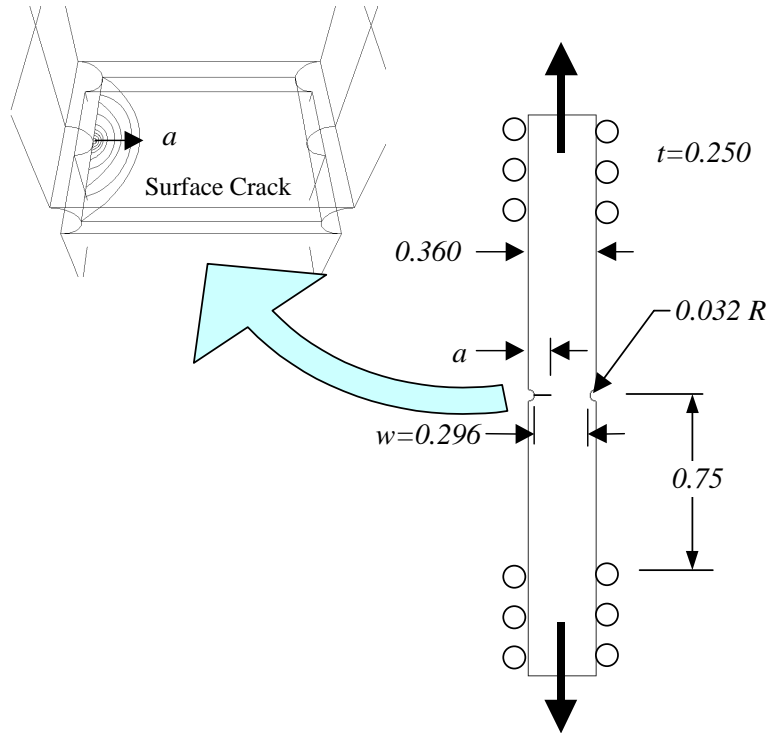
Figure 4.52. Geometry of FRANC3D model of double edge notched (DEN) fracture specimen.
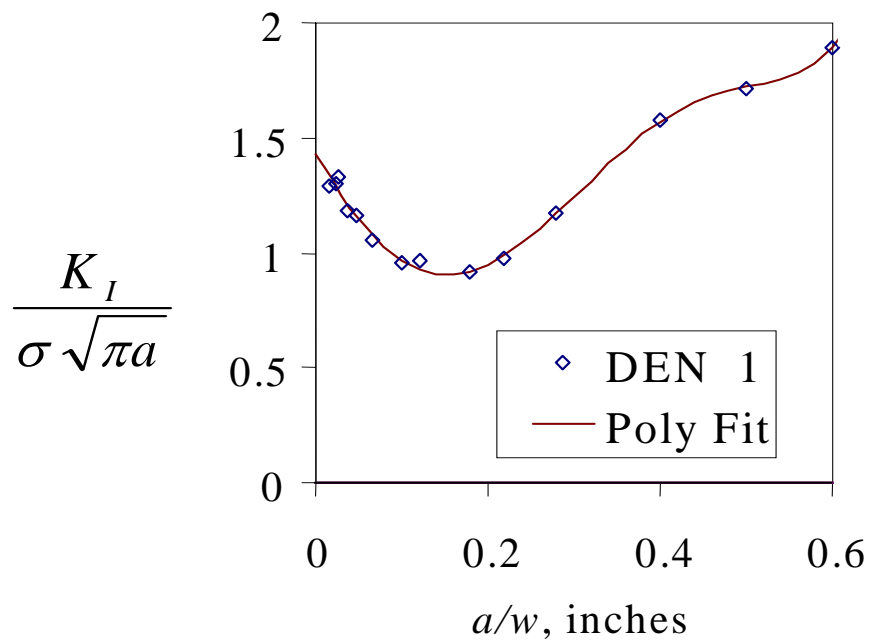
Figure 4.53. Results of isotropic FRANC3D analysis of double edge notched (DEN) fracture specimen.

4.2.4   Mixed-Mode Fatigue Crack Growth Thresholds

The objective of this work was to develop a methodology for treating the effects of stress state, frequency, crystal orientation, and temperature on the threshold and near-threshold fatigue crack growth (FCG) response of PWA 1484 single crystals subjected to high cycle fatigue. An integrated analytical and experimental approach was used to achieve this objective. The analytical efforts included stress intensity factor computation for mixed-mode cracks in single crystal alloy PWA 1484, mapping of fracture transition conditions, and model development. The analytical efforts were linked to an experimental study to determine the fatigue crack growth threshold of PWA 1484 as a function of stress state and crystal orientation, using an asymmetric four-point bend (AFPB) test technique. The influence of mode-mixity on the FCG threshold was determined at 1100°F as a function of stress state ranging from pure Mode I to pure Mode II. Both the analytical and experimental results were used to develop a fracture mechanics approach for treating high-cycle, mixed-mode fatigue crack growth in single crystal blades.

4.2.4.1   Crack Paths of Mixed-Mode Fatigue Cracks

It is well known that fatigue cracks in single crystal Ni-based Superalloys can proceed on crystallographic or non-crystallographic planes, depending on temperature, frequency, stress states, and environment [40,41,43-48]. Mixed-mode fatigue cracks in PWA 1484 propagated either as self-similar cracks on a (111) plane or as a deflected crack on a transprecipitate noncrystallographic (TPNC) plane at 1100°F. The former was observed in the <111> oriented crystals, while the latter was observed in <001> oriented crystals. The crack path in the $<111>/<01\bar{1}>$ crystal orientation is illustrated in Figure 4.54. In this <hkj>/<uvw> notation, <hkj> indicates the crack plane normal, while <uvw> shows the crack growth direction. The crack was fairly straight under Mode I fatigue. Under mixed Mode I and II loading, the crack continued to propagate in a self-similar manner initially, but then kinked and deflected to propagate along a curvilinear path, Figure 4.54. In contrast, mixed-mode cracks in the <001> orientation deflected immediately without exhibiting self-similar crack growth at 1100°F. The complex crack path dictated that individual crack specimens had to be analyzed to obtain the appropriate stress intensity factor ranges along the actual crack path.
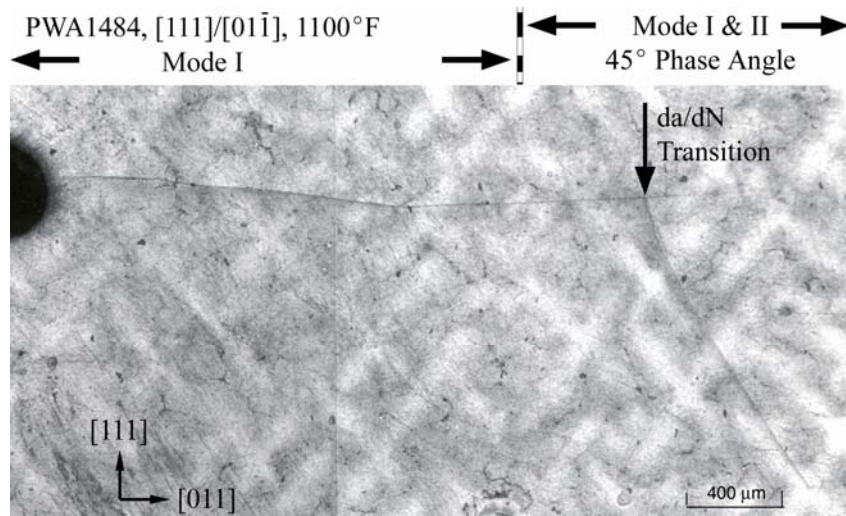
Figure 4.54. Fatigue crack path of [111]/[01$\bar{1}$] oriented PWA 1484 during Mode I loading and mixed Mode I and II loading at a 45° phase angle. At 1100°F, Mode I fatigue occurred on the (111) plane. The mixed-mode crack propagate self-similarly on (111) under mixed Mode I and II initially, but it subsequently deflected on a TPNC plane (Specimen SC-13).

4.2.4.2   Stress Intensity Factor Computation

Two different procedures were used to compute the stress intensity factors of mixed-mode cracks in PWA 1484: (1) for straight self-similar cracks, and (2) for deflected or kinked cracks. The first procedure was based on the K solutions generated for anisotropic materials using an anisotropic fracture mechanics code (BIECRX [49]). The anisotropic K solutions, which are summarized in Appendix R, are in agreement with He and Hutchison's analytical solutions for isotropic materials [50]. Thus, isotropic K solutions are adequate for single crystal Ni-alloys exhibiting self-similar crack growth. The second procedure was applied to deflected cracks in post-test data analysis after the crack deflection angle had been determined. This procedure was based on K solutions of deflected cracks computed using the FRANC2D/L finite-element code [51].

The stress intensity factors of individual deflected cracks in PWA 1484 mixed-mode specimens were computed using FRANC2D/L and assuming a crack path normal to the maximum principal tensile stress, which corresponds to the local Mode I direction [52]. A comparison of calculated and experimental crack paths indicated that the

248

observed crack path did not precisely follow the maximum tensile stress path. The largest deviation was observed in a single-crystal crack specimen (SC-16) that was tested under pure Mode II loading. The crack deflection angle was 48°, compared to a theoretical angle of 70.5° for deflection of a pure Mode II crack to the local Mode I path [52]. Consequently, in selected cases, K calculations along the actual crack path were also performed.

The K solutions for the actual crack path showed predominantly K_I with a small K_{II} at the tip of the deflected crack. The normalized K_I and K_{II} are plotted as a function of the actual crack length in Figure 4.55, which also compares the K solutions for the actual path against those for the maximum tensile stress (MTS) path. The comparison indicates that the deflected crack was essentially a local Mode I crack despite the deviation from the MTS direction. Detailed descriptions of the K solutions for self-similar and deflected cracks in PWA 1484 are presented in Appendix R.
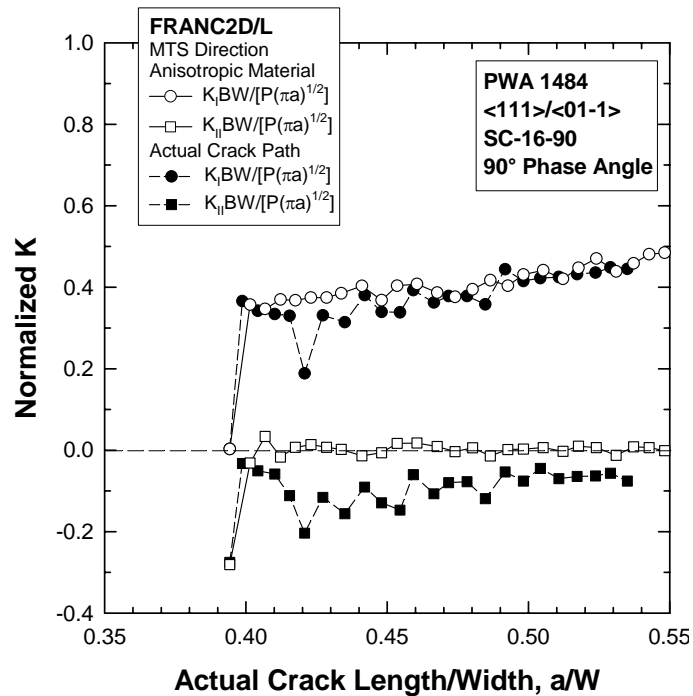
Figure 4.55. FRAN2D/L K_I and K_{II} solutions obtained using the actual deflected crack path for Specimen SC-16-90 tested under pure Mode II loading (K normalized as shown in the insert).

4.2.4.3   Fatigue Crack Growth Threshold Testing

The fatigue crack growth thresholds of PWA 1484 were determined at 1100°F, R= 0.5, and 20 Hz as a function of mode-mixity ranging from pure Mode I to pure Mode II using the decreasing-K approach, with a shed rate of -20 in^{-1}. Mode I threshold was determined during fatigue pre-cracking using symmetric four-point bending. After the Mode I threshold was obtained, mixed-mode thresholds were determined by asymmetric four-point bending by varying the mode-mixity phase angle, defined as ϕ = arctan ($\Delta K_{II}/\Delta K_I$), through the placement of the loading pins and the offset distance of the crack from the symmetry line of the load fixture. Fatigue crack growth rate data in the near-threshold regime were generated for mode-mixity phase angles that include 0° (pure Mode I), 22.5°, 45°, 60°, 80°, and 90° (pure Mode II). Stress intensity factors were then computed from the load and actual crack length data using appropriate K solutions. For deflected cracks, the K solutions generated by FRANC2D/L were used. The da/dN data were then used to assess the effects of mode-mixity and crystallographic orientation on the FCG threshold response of PWA 1484. Table 4.12 presents a summary of the crack orientation, thresholds, crack deflection angle, crack growth plane and direction in individual PWA 1484 specimens.

The FCG threshold obtained under Mode I loading generally differs from those obtained under mixed-mode loading. Figure 4.56 shows a comparison of the Mode I and the mixed-mode FCG threshold data for the <001>/<110> orientation. Both the da/dN and the ΔK_I values have been corrected for crack deflection and they are the actual values at the crack tip of the deflected crack. For comparison purposes, the K results computed based on the projected crack length without a correction for crack deflection are also presented. A lower value (2.07 ksi√in) of the FCG threshold was obtained when crack deflection was not taken into account in the K computation. The actual value of the threshold was increased to 2.74 ksi√in after the actual length of the deflected crack was used to compute the stress intensity factor ranges at the crack tip. Despite correction for the deflected crack path, the local Mode I threshold obtained under mixed-mode loading was still lower than the FCG threshold (4.51 ksi√in) determined under pure Mode I loading. A two-surface fracture plane analysis revealed that the deflected crack had the $<\bar{2}11>+4$ /<111>+4 orientation, which is different from the <001>/<010> orientation for the Mode I crack. Thus, the discrepancy in

250

the FCG thresholds can be attributed to a difference in the crystallographic orientation encountered by the Mode I and the deflected cracks.

There is good agreement between the Mode I threshold and the thresholds of deflected mixed-mode cracks when the crystallographic orientations at the crack tip are equivalent. A detailed examination of the initial and final crack orientations shown for all PWA 1484 test specimens indicated that the crack orientations for Specimens SC-5, SC-6, SC-7, and SC-8 under pure Mode I are <001>/<110>, which are close to (within 6°) those for the deflected cracks in SC-9 and SC-11.

Figure 4.57 compares the da/dN curves for <001>/<110> obtained under pure Mode I against those of deflected cracks that propagated under local Mode I. There is reasonably good agreement between the da/dN curves for the deflected (local Mode I) cracks and the pure Mode I cracks. Similarly, the crack orientations for SC-9, SC-10, and SC-11 are $<111>/<11\overline{2}>$ under pure Mode I. These crack orientations are comparable to the self-similar crack in SC-11 and to the deflected (local Mode I) cracks observed in SC-5, SC-6, SC-7, and SC-8. A comparison of the da/dN data of these specimens is shown in Figure 4.58. The negative slope exhibited by several specimens at $\Delta K_I = 5\text{-}7$ ksi√in is believed to be due to the fact that the transition from the initial to final crack planes was gradual, as opposed to the abrupt transition assumed in the FRANC2D/L analysis. Eliminating these data results in a scatter band on rates of 2X to 3X that is typical of most da/dN (ΔK) behavior. The corresponding values of ΔK_{th} are also reasonably consistent (within ±17%) for similar crystallographic orientations.

4.2.4.4 Fatigue Crack Growth Threshold Model Development

Analytical efforts in this task included modeling the: (1) dependence of FCG threshold on crystallographic orientation, (2) crack deflection path, and (3) transition of fracture morphologies from crystallographic to noncrystallographic cracking.

Table 4.12. Summary of Mode I & Mixed Mode Thresholds for PWA 1484 Single Crystals Tested at 1100°F, R = 0.5, & 20Hz.

Specimen	Initial Orientation	Precracking Mode I Threshold $\Delta K_{I,th}$, ksi√in	Mixed Mode Thresholds + corrected for crack deflection				Crack Deflection Angle, (ave)	Remarks	Final Orientation	
			Phase Angle, $\phi°$	$\Delta K_{eq,th}$ (ksi√in)	$\Delta K_{I,th}^{+}$ (ksi√in)	$\Delta K_{II,th}^{+}$ (ksi,√in)			Fatigue Crack Plane	Fatigue Crack Directions
SC-1	<001>/<010>	2.83	32	4.19	4.19	0	40	TPNC crack	5° off ($\bar{1}$10)	5° off [100]
SC-2	<001>/<010>	3.66	46	3.05	3.05	0	40, 62 (51)	TPNC crack	5° off ($\bar{2}$30)	5° off [320]
SC-3	<001>/<010>	3.23	90	5.94	0	5.94	No growth	TPNC crack	—	—
			80	3.26	3.26	0	50, 58 (54)	TPNC crack	($\bar{2}$30)	[320]
SC-4	<001>/<010>	3.22	34	4.77	4.77	0	45	TPNC crack	($\bar{1}$10)	[110]
			60	3.74	3.74	0	60	TPNC crack	3° off ($\bar{1}$20)	3° off [210]
SC-5	<001>/<110>	4.51	45	2.74	2.74	0	44, 36 (40)	TPNC crack	4° off ($\bar{2}1\bar{1}$)	4° off [11$\bar{1}$]
SC-6	<001>/<110>	5.25	48	3.02	3.02	0	30, 45 (37.5)	TPNC crack	($\bar{1}1\bar{1}$)	[21$\bar{1}$]
SC-7	<001>/<110>	4.63	80	3.30	3.30	0	48, 50	TPNC crack	6° off ($\bar{1}1\bar{1}$)	6° off [21$\bar{1}$]
			90	7.6	—	—	—	No growth	—	—
SC-8	<001>/<110>	4.45	60	3.35	3.35	0	58	TPNC crack	5° off ($\bar{1}1\bar{1}$)	5° off [21$\bar{1}$]
SC-9	<111>/<11$\bar{2}$>	3.63	45	3.87	3.87	0	43	TPNC crack	6° off (100)	6° off [011]
SC-10	<111>/<11$\bar{2}$>	3.46	60	5.72	2.81	4.99	0	(111) self-similar crack	(111)	[11$\bar{2}$]
SC-11	<111>/<11$\bar{2}$>	3.40	90	3.41	0	3.41	0	(111) self-similar crack	(111)	[11$\bar{2}$]
			90	4.14	4.14	0	53	TPNC crack	(100)	[011]
SC-13	<111>/<$\bar{1}$10>	3.46	45	5.13	3.63	3.63	0	(111) self-similar crack	(111)	[01$\bar{1}$]
			45	4.03	4.03	0	40, 66 (53)	TPNC crack	4° off (1$\bar{2}$0)	7° off [$\bar{1}$02]
SC-14	<111>/<$\bar{1}$10>	3.48	80	5.51	0.96	5.43	0	(111) self-similar crack	(111)	[01$\bar{1}$]
			22.5	4.05	4.05	0	20, 40 (30)	TPNC crack	7° off (2$\bar{3}\bar{1}$)	[$\bar{1}\bar{1}$3]
SC-15	<111>/<$\bar{1}$10>	3.68	—	—	—	—	—	Test specimen overloaded during cool-down	—	—
SC-16	<111>/<$\bar{1}$10>	3.84	90	4.55	0	4.55	0	(111) self-similar crack	(111)	[01$\bar{1}$]
			90	2.67	2.67	0	47, 48 (48)	TPNC crack	10° off (1$\bar{2}$0)	[$\bar{1}$02]
SC-17	<111>/<$\bar{1}$10>	3.74	22.5	9.10	8.41	3.48	0	(111) self-similar crack, high starting ΔK_{eq} (11 ksi√in)	(111)	[01$\bar{1}$]
SC-19	10° off <001>/ 10° off <110>	3.99	45	—	—	—	—	Test specimen initiated a second crack	—	—
SC-20	10° off <001>/ 10° off <110>	3.69	60	5.50	2.71	4.79	0	Self-similar crack	8° off (100)	8° off [01$\bar{1}$]

Figure 4.56. A summary of da/dN data vs. ΔK_I or ΔK_{eq} for <001>/<011> oriented PWA 1484 (SC-5) tested under Mode I or mixed Mode I and II loading at ϕ=45°.
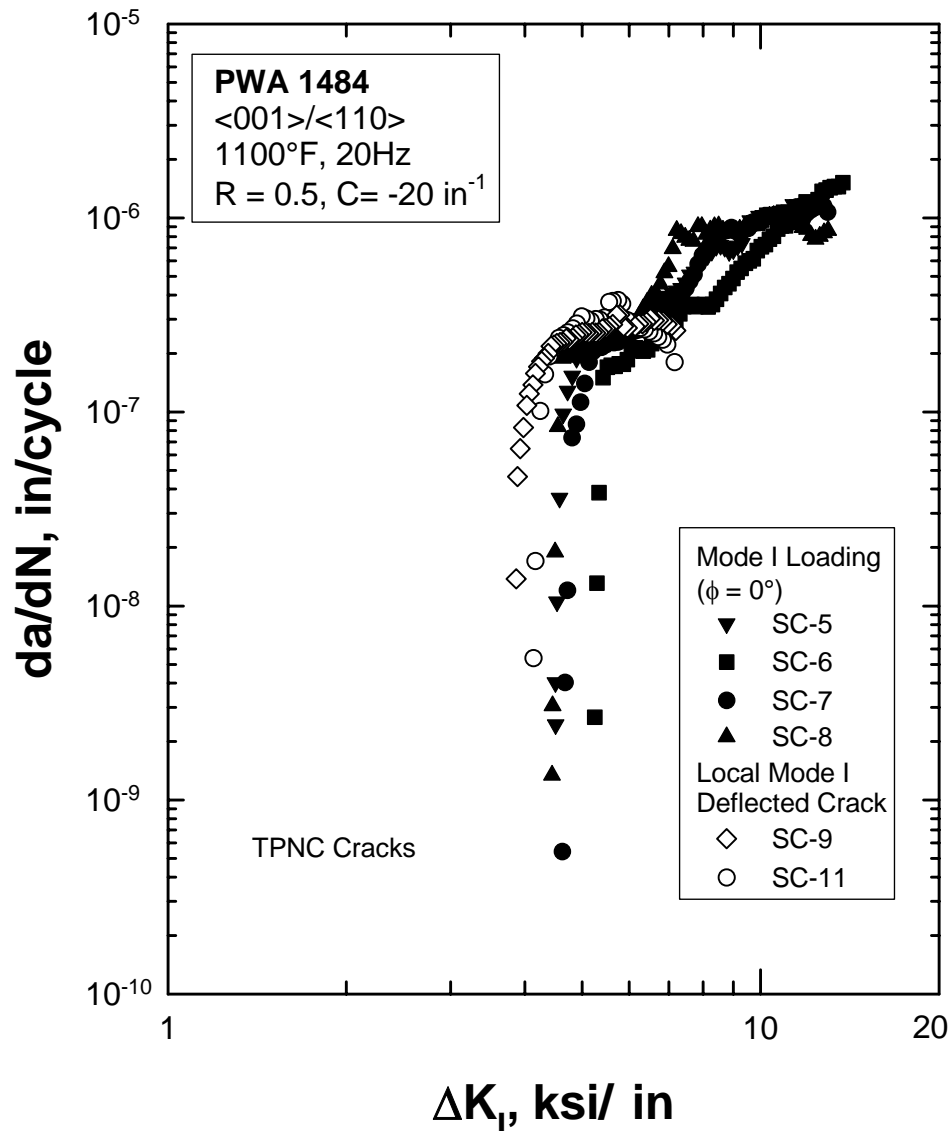
Figure 4.57.   A comparison of da/dN curves for pure Mode I cracks (SC-5, SC-6, SC-7, and SC-8) against local Mode I deflection cracks (SC-9 and SC-11) with the same <001>/<110> crack orientation.
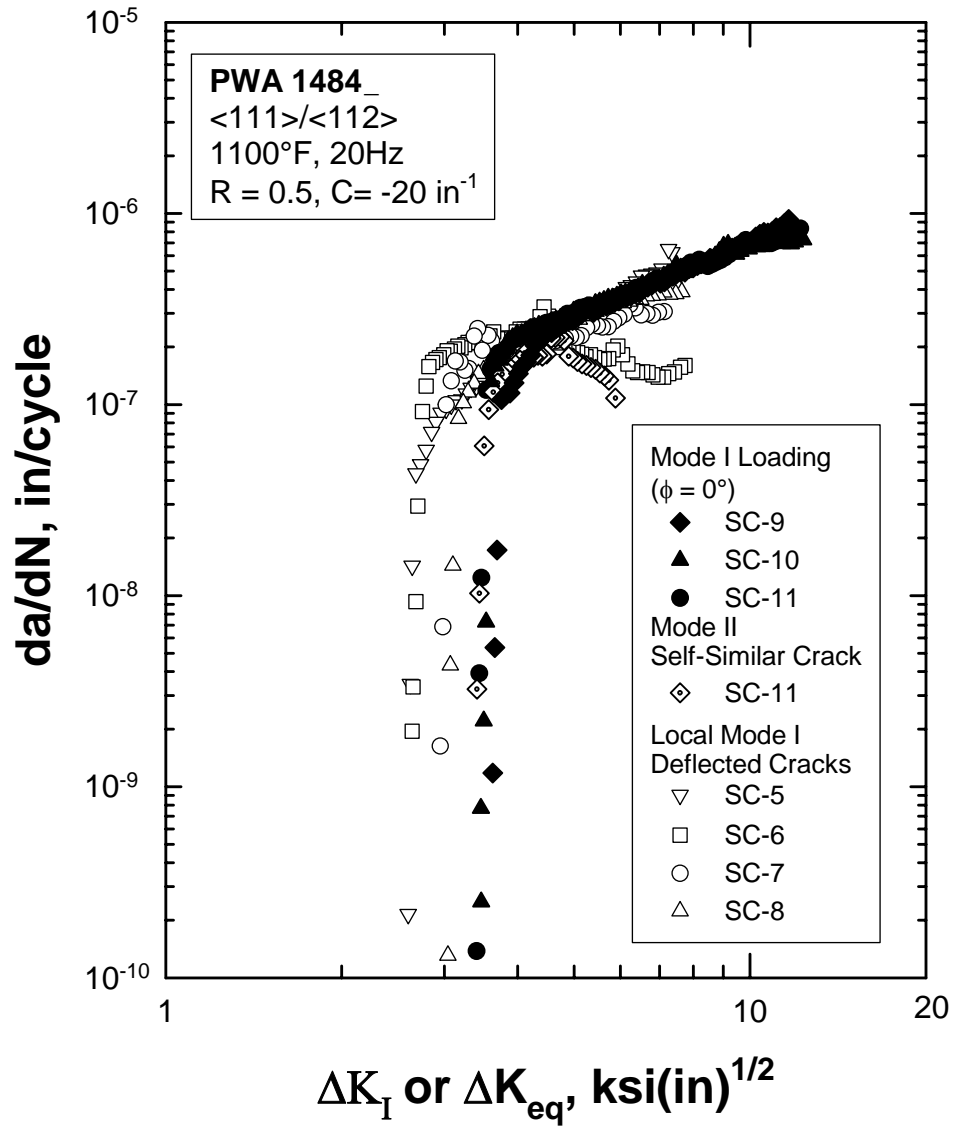
Figure 4.58. A comparison of da/dN curves for pure Mode I cracks, a Mode II self-similar crack, and local Mode I deflected cracks with the approximately same $<111>/<11\bar{2}>$ crack orientation.

A. Modeling Threshold Anisotropy

Threshold anisotropy in PWA 1484 is illustrated in Figures 4.59 and 4.60, which present the Mode I thresholds of PWA 1484 as a function of the angle β between the crack plane normal and a reference crystallographic axis for the initial <001>/<010> and <001>/<110> orientations, respectively. Both the angle β and the reference crystallographic orientation are defined in the figure inserts. In these figures, the values of the Mode I threshold, $\Delta K_{I,th}$, at $\beta = 0$ correspond to those measured under Mode I conditions, while those for $\beta > 0$ were the local $\Delta K_{I,th}$ values determined from deflected cracks during the remote mixed-mode loading. The highest Mode I threshold occurs in the <001>/<110> orientation, Figure 4.61. Lower values of $\Delta K_{I,th}$ occur in off-axis orientations that are about 40-60° from the <001> plane in the <001>/<110> system. These orientations are located near the central region of a standard stereographic triangle for cubic materials.

The anisotropic threshold model [53] developed at P&W was used to correlate the Mode I threshold data obtained under remote mixed-mode loading and pure Mode I loading conditions. According to this model [53], the fracture resistance, $K_p(\boldsymbol{n},\boldsymbol{a})$, at an arbitrary location ($\boldsymbol{n},\boldsymbol{a}$) of the crack front, where **n** and **a** are unit vectors representing the crack plane normal and crack growth direction, can be obtained by projecting the principal values onto the current crack orientation through a transformation process. The P&W model, which contains two fitting parameters, *n* and *m*, was applied to treat the Mode I fatigue thresholds of PWA 1484. The empirical constants *n* and *m* were evaluated by fitting the model to the Mode I threshold data of <100>/<010> and <100>/<110> oriented single crystal specimens. The former set of data was used to obtain a value of 5 for *m*, as shown in Figure 4.59. The latter set of threshold data was used to obtain an *n* value of 0.6-0.8, as shown in Figure 4.60. Note that in Figure 4.59, both the solid line (*n* = 0.6) and the dashed line (*n* = 0.8) lie on top of each other. Although the agreement is not perfect, the model, nonetheless, demonstrates that it is capable of capturing the general characteristics of the anisotropy of the fatigue crack growth thresholds exhibited by PWA 1484.
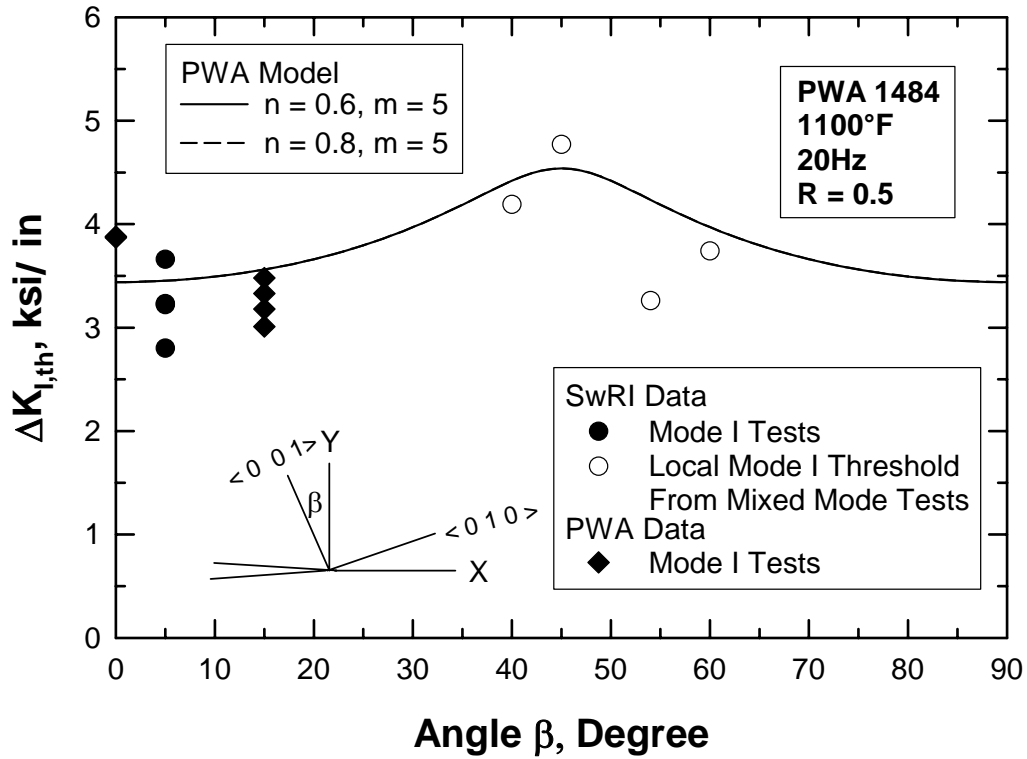
Figure 4.59. Fitting of P&W threshold model to FCG threshold data of PWA 1484 for the <001>/<010> orientation. The angle β corresponds to the crack deflection angle or the secondary orientation.
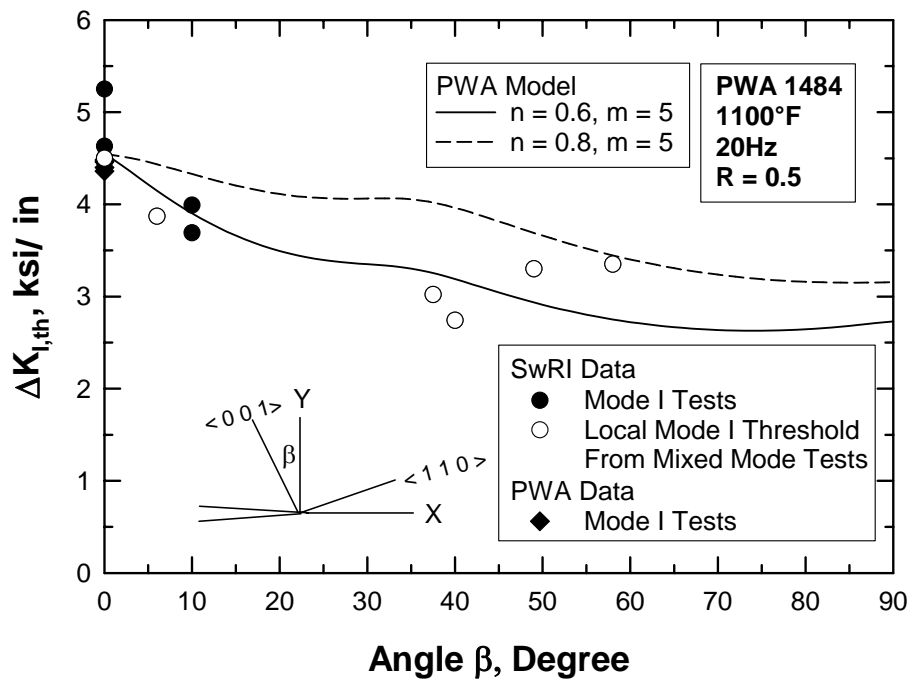
Figure 4.60. Fitting of the P&W threshold model to FCG threshold data of PWA 1484 for the <001>/<110> orientation.

B. *Modeling of Crack Deflection Path*

Fatigue crack growth in PWA 1484 can proceed on either (111) or TPNC planes. The FCG curve for continuum crack growth on the TPNC plane is compared against that for crystallographic crack growth on the (111) plane in Figure 4.61. For the TPNC crack, the Mode I threshold is lower and the slope of the da/dN curve is lower than comparable properties for crystallographic growth on the (111) plane. The two da/dN curves intersect at ΔK_t. Above ΔK_t, da/dN is higher for the (111) crack, but the TPNC crack grows faster at a given ΔK_{eq} ($= \left[\Delta K_I^2 + \Delta K_{II}^2\right]^{1/2}$) at $\Delta K < \Delta K_t$. The transition point, ΔK_t, depends on frequency, temperature, and environment and its values can be represented in terms of a map
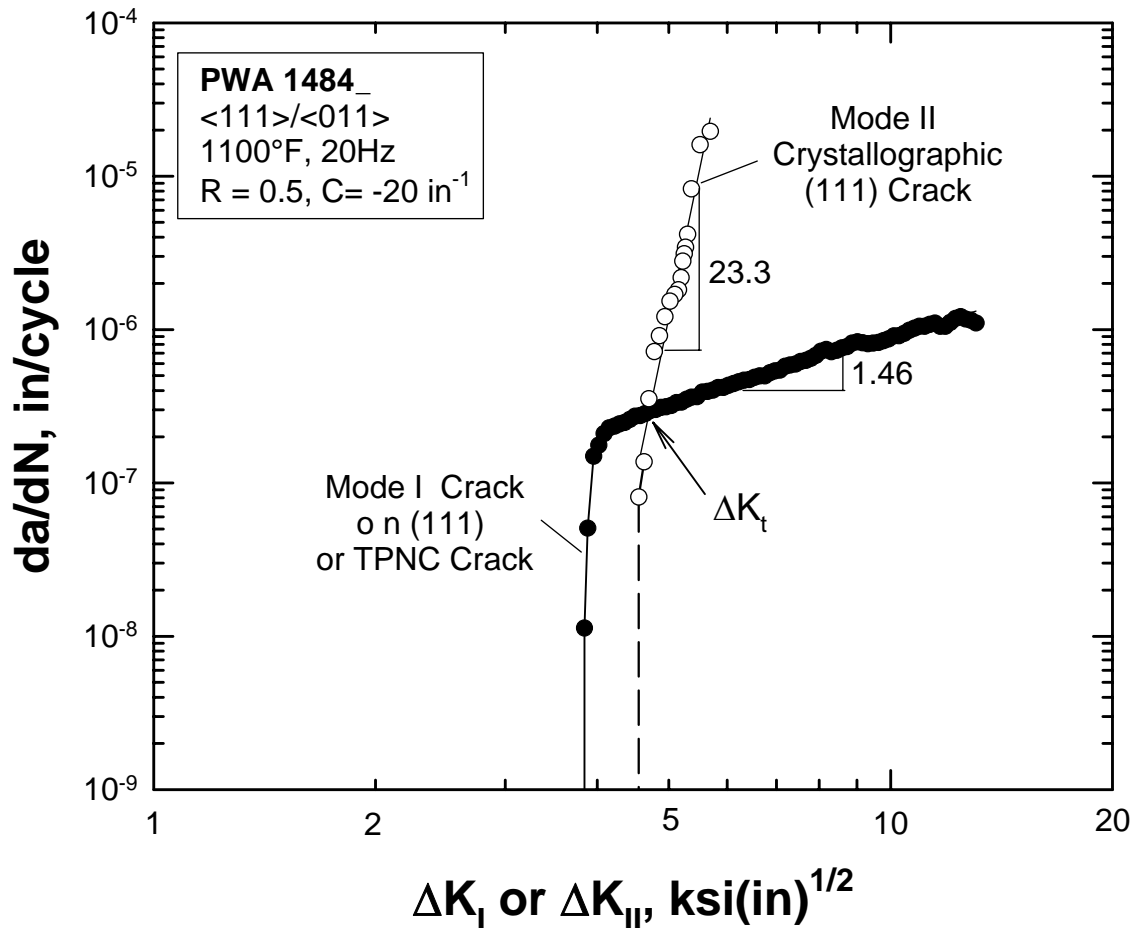
Figure 4.61. FCG data of a TPNC crack compared against that of crystallographic (111) crack in $<111>/<01\bar{1}>$ oriented PWA 1484. At $\Delta K_I > \Delta K_t$, the crystallographic (111) crack propagates at a high FCG rate than a TPNC crack at identical ΔK_{eq} values. The reverse is true for $\Delta K_I < \Delta K_t$. $\Delta K_{eq} = \left[\Delta K_I^2 + \Delta K_{II}^2\right]^{1/2}$.

depicting the various fracture morphologies. During load shedding, a crystallographic (111) crack would arrest when ΔK_{eq} drops below the threshold value, $\Delta K_{eq,th}$. Since ΔK_{eq} for the crystallographic (111) crack is still higher than $\Delta K_{I,th}$ for a Mode I crack on a TPNC plane, a driving force exists for the (111) crack to kink and deflect to a TPNC crack plane with a lower Mode I threshold, $\Delta K_{I,th}$. It should be noted that the crossover of the FCG curves for (111) and (001) cracks has also been observed in PWA 1480 at ambient temperature [54]. In addition, self-similar mixed-mode (111) crack growth has been reported to occur at significantly higher rates than a Mode I, TPNC crack in PWA 1422 at $\Delta K > \Delta K_t$ [55].

The influence of an orientation-dependent $\Delta K_{I,th}$ on the deflection of a generalized mixed-mode crack in PWA 1484 was modeled on the basis of a maximum crack growth rate criterion. The fatigue crack growth (FCG) response can be represented as

$$\frac{da}{dN} = A\left(\Delta K_{eq} - \Delta K_{eq,th}\right)^{\eta} \tag{4.21}$$

with

$$\Delta K_{eq} = \left[\Delta K_I^2 + \Delta K_{II}^2\right]^{1/2} \tag{4.22}$$

where, da/dN is the crack growth rate; ΔK_{eq} is the equivalent stress intensity range, and $\Delta K_{eq,th}$ is the corresponding equivalent mixed-mode threshold; A and η are empirical constants. Both ΔK_{eq} and $\Delta K_{eq,th}$ are taken to be a function of the crack deflection angle, θ. For simplicity, A and η are taken to be independent of θ. According to this analysis, a mixed-mode crack deflects in the direction of the maximum crack growth rate when the inequality given by

$$\frac{\partial}{\partial \theta}\left[\Delta K_{eq} - \Delta K_{eq,th}\right] \geq 0 \tag{4.23}$$

is satisfied. Equation (4.23) becomes

$$\frac{\partial}{\partial \theta}\left[\Delta K_I - \Delta K_{I,th}\right] \geq 0 \tag{4.24}$$

when crack growth occurs under Mode I conditions. Equations (4.23) and (4.24) indicate that crack deflection occurs in the direction where the difference between the crack driving force (ΔK_{eq} or ΔK_I) and the crack resistance ($\Delta K_{eq,th}$ or $\Delta K_{I,th}$) is maximum. For isotropic

materials, $\partial \Delta K_{I,th} / \partial \theta = 0$ and Equation (4.24) is reduced to the classical maximum tensile stress (MTS) criterion [52]. Furthermore, Equation (4.24) indicates that deviation from the MTS criterion is expected when $\partial \Delta K_{I,th} / \partial \theta \neq 0$. The amount of deviation would depend on the threshold anisotropy. According to this model, crack deflection is expected to occur when a change in the crack path increases the difference between the crack driving force and the fatigue crack growth threshold. Conversely, no crack deflection is predicted when Equation (4.23) and (4.24) are not met.

Equation (4.24) has been further developed into a model for computing the crack deflection angle in PWA 1484. Details of the model are described in Appendix R. The calculated and measured crack deflection angles are compared in Figure 4.62, which also shows the calculations based on the MTS (local Mode I) [52], the maximum energy
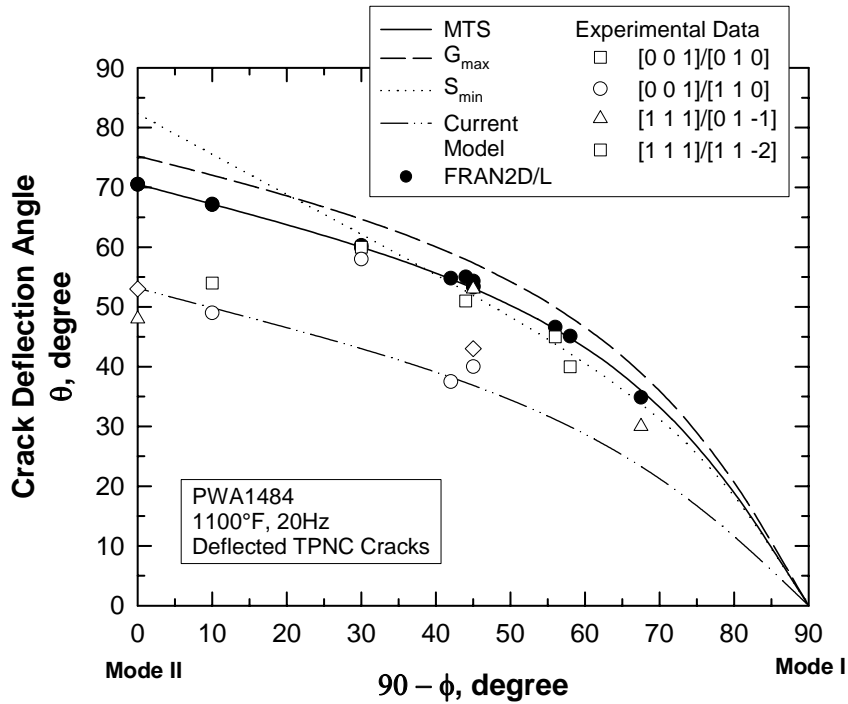
Figure 4.62. Calculated and measured crack deflection angles as a function of 90-ϕ, where ϕ = arctan ($\Delta K_{II}/\Delta K_{I}$) is the mode-mixity phase angle. Deviation of experimental data from the MTS criterion is caused by an orientation dependence of the Mode I threshold. The current model treats threshold anisotropy and shows how a small threshold anisotropy can cause a relatively large deviation in the crack deflection angle.

release rate (G_{max}) [56], and the minimum strain density (S_{min}) [57] criteria, as well as the FRANC2D/L results. For a given mode-mixity angle of ϕ, where $\phi = \arctan(\Delta K_{II}/\Delta K_{I})$, the predicted crack deflection angles are similar for the MTS, G_{max}, and S_{min} criteria. The FRANC2D/L results are in agreement with those of the MTS criterion since it was the crack growth direction criterion chosen in the computations. About 1/3 of the experimental data agreed with the MTS criterion and the FRANC2D/L criterion results, while the remaining 2/3 showed negative deviation (smaller crack deflection angles) from the MTS criterion. These deviations of the crack deflection angle are accounted for in the current model, which incorporates threshold anisotropy into a local Mode I crack growth criterion.

C. Modeling of Fracture Morphology Transition

A fatigue crack transition model was developed based on thermally activated slip in the crack-tip cyclic process zone that correlates fatigue crack growth morphologies to test parameters such as temperature, frequency, and stress intensity range. Derivation of the model is presented in Appendix R. The model predicts that the transition of macroscopic (111) mixed-mode fracture to TPNC (i.e., TPNC and ancillary (TPNC) Mode I fracture can be described by the relation

$$f\Delta K = A' \exp\left(\frac{-Q}{RT}\right) \tag{4.25}$$

where f is the cyclic frequency, ΔK is the stress intensity factor range, Q is the apparent activation energy, T is the absolute temperature, R is the universal gas constant, and A' is a pre-exponent coefficient. Equation (4.25) provides the basis for the construction of the fatigue crack growth mode map shown in Figure 4.63, which shows a plot of $f\Delta K$ versus T. The solid line is the macroscopic (111) to TPNC fracture transition boundary predicted by Equation (4.25). Macroscopic (111) fracture is prevalent at high $f\Delta K$ values and low temperature, while TPNC fracture is dominant at lower $f\Delta K$ values and high temperature. The PWA 1484 data from the literature [40,41,46] are divided into two fracture regimes, Macroscopic (111) and TPNC, separated by the calculated transition boundary. Two of the data points generated in this study fall on the wrong side of the transition boundary. This

suggests that the transition boundary may be improved by refitting to the experimental data. A recalibration of the model, however, requires additional experimental data since there are gaps in the fatigue crack growth mode map at high frequency and high temperatures that make a precise determination of the transition boundary uncertain at this time.
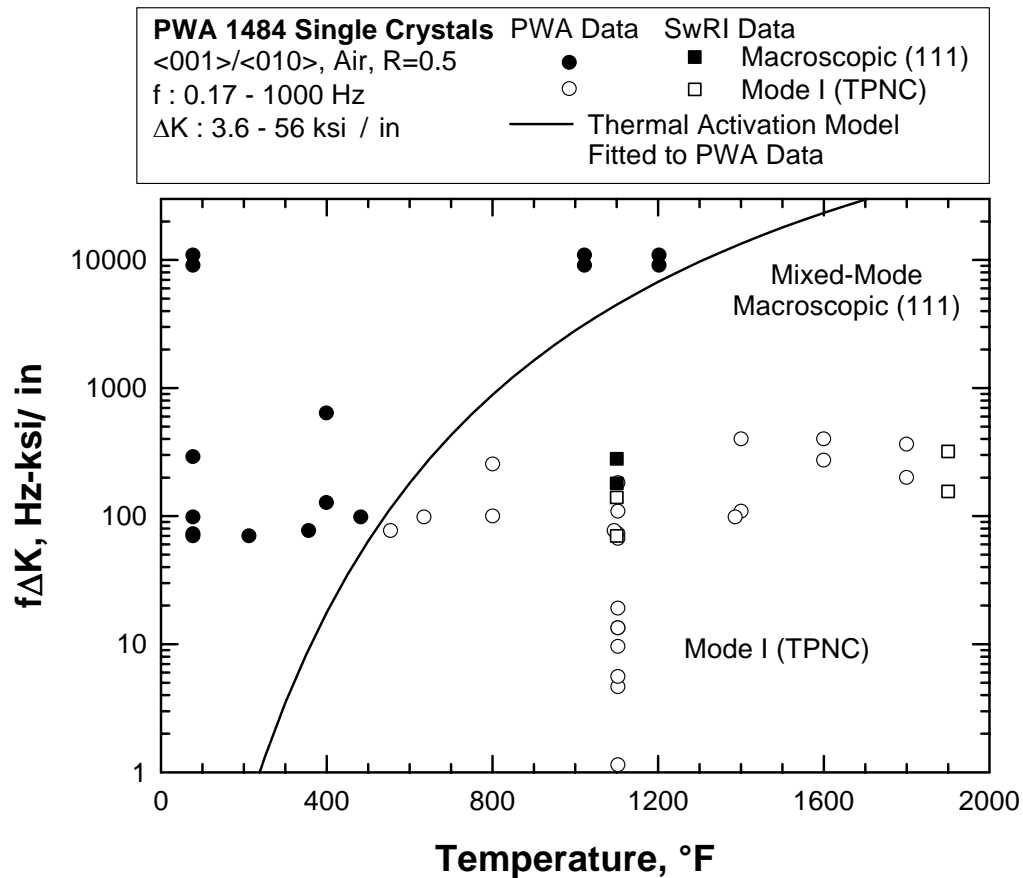
Figure 4.63. A fatigue crack growth morphology map for <001>/<010> PWA 1484 single crystals in air shows two fracture regimes: (1) mixed-mode macroscopic (111) fracture, and (2) Mode I transprecipitate non-crystallographic (TPNC) fracture. The solid line is the fatigue crack growth morphology transition boundary calculated based on the proposed thermal activation model. Experimental data are from Cunningham et al., [40, 41], and Milligan [58], as well as the present study. Mixed-mode macroscopic (111) fracture is favored at high frequency, high ΔK and low temperature, while TPNC fracture is favored at low frequency, low ΔK, and high temperature.

The transition of the fracture morphology appears to be influenced by the deformation shearing and by-pass of the γN precipitates by (111) slip, as well as by the activation of cube slip. Figure 4.64 shows the deformation mechanism map based on experimental data in the literature for PWA 1480 [59]. The transition boundaries were calculated on the basis of the experimentally determined activated energies and the appropriate Arrhenius equations for cube cross slip and γN by-pass. For PWA 1480, the activation energies are 12 and 120 kcal/mol [59] for cross slip on the cube plane and γ' by-pass, respectively. The activation energy for fatigue crack growth mode transition is 11.7 for PWA 1484, which is expected to be similar to that for PWA 1480. This comparison of apparent activation energies suggests that fatigue crack growth mode transition in PWA 1484 may be controlled by the activation of cross slip on the cube plane.
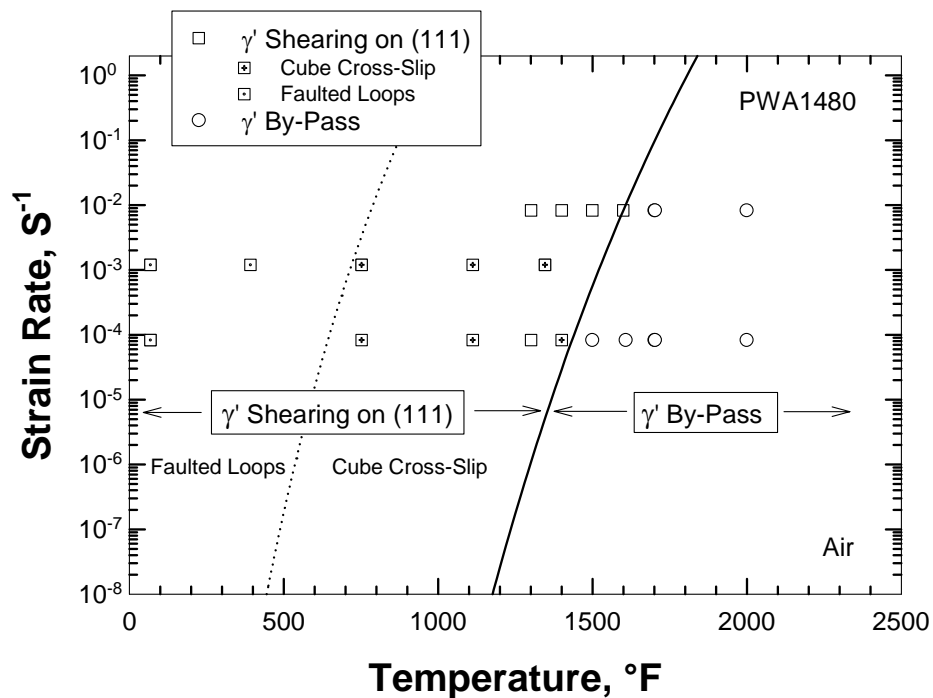
Figure 4.64. Deformation mechanism map for PWA 1480 shows three distinct regimes: (1) the formation of faulted dislocation loops in γN, (2) activation of cube slip in γN, and (3) γN by-pass by the Orowan mechanism. Experimental data are from Milligan and Antolovich [59].

263

4.2.4.5   Conclusions and Recommendations

(1) During mixed-mode decreasing-K crack growth threshold testing, (111) cracks in PWA 1484 initially propagated in a straight, self-similar manner but tended to deflect out of plane as transprecipitate non-crystallographic (TPNC) cracks. For TPNC cracks, the transition occurred immediately on changing the loading from the Mode I precracking to mixed-mode testing.

(2) The threshold stress intensities for (111) cracks under mixed Mode I and II and pure Mode II are higher than those for Mode I (111), as well as for TPNC cracks. Because of this, initially crystallographic (111) cracks can propagate below their threshold stress intensities by deflecting to TPNC cracks. Consequently, it is recommended that Mode I threshold stress intensity factors for TPNC cracks be employed in HCF assessments.

(3) Following deflection, mixed-mode TPNC cracks in PWA 1484 propagate on or near the maximum principal stress plane where $\Delta K_{II} = 0$. Thus, for engineering purposes, TPNC cracks subjected to mixed-mode loading can be treated as local Mode I cracks governed by a Mode I threshold. In so doing, crack deflection needs to be accounted for in computing the local stress intensity factors for deflected cracks.

(4) The Mode I threshold in PWA 1484 is a function of crystallographic orientation, and thus depends on the orientation of the crack plane (n) and the crack growth direction (a). The orientation dependence of $\Delta K_{I,th}$ (n, a) can be predicted reasonably well on the basis of the threshold values for the principal (<001>) axes through a transformation procedure using the 3-D model developed by P&W.

(5) Current data indicate that the minimum value of $\Delta K_{I,th}$ at R=0.5 is 2.67 ksi√in and occurs for a local Mode I deflected TPNC crack with a $<1\overline{2}0> + 10 /<\overline{1}02>$ orientation. The use of a minimum $\Delta K_{I,th}$ appears to be a tractable approach for HCF assessments of single crystal material. However, additional testing is warranted to verify that this minimum $\Delta K_{I,th}(n, a)$ value is valid for all orientations, as well as to define the dependence of the minimum $\Delta K_{I,th}(n, a)$ on load ratio (R).

(6) Mode I TPNC crack growth and crystallographic (111) crack growth are competing processes that exhibit different da/dN characteristics including different

264

thresholds and Paris slopes. The dominance of one crack growth morphology over another is dictated by the da/dN response of individual crack morphologies at a given ΔK and the local ΔK when the crack alters its path.

(7) The transition boundary between crystallographic (111) and TPNC fatigue crack growth depends on temperature, cyclic frequency, and applied stress intensity factor. An engineering model to describe this transition has been developed (Equation 4.56) on the basis of thermal activation of (111) and cube slip in the cyclic plastic zone of the crack tip.

(8) The asymmetric-four-point-bend (AFPB) test technique is a viable technique for studying fatigue crack growth mode transition and determining the mixed-mode fatigue crack growth thresholds of PWA 1484 at elevated temperatures.

4.2.5   HCF/LCF Interaction

This section focuses on fracture mechanics of a nickel based single crystal alloy, and the effect of high cycle fatigue HCF (high stress ratio) high frequency cycles, combined with low cycle fatigue LCF (low stress ratio) low frequency based cycle interaction loading.

4.2.5.1   HCF / LCF Interaction Testing Approach

The HCF / LCF test approach was based on the previous threshold data generated at 1100° F, for R=0.1 and 0.8 in the <001/010> orientation. The HCF / LCF testing started by precracking the sample from the starter notch to a specified crack length a_o. From the precrack the specimen was run at a stress ratio of 0.1 at a frequency of 10 CPM until a crack length of a_i is achieved. The target for a_i was selected to be well below the K_{max} threshold value for the R=0.8 test data. A block of 1000 cycles of R=0.8 at 60 Hz was then performed between each R = 0.1 LCF cycle. This block loading was continued until the calculated value for R = 0.8 threshold was superseded at crack length a_f. After growing beyond the calculated value of the R = 0.8 threshold, the loading was returned LFC loading only at R = 0.1. The test scheme was designed so that all loading blocks could be performed on a single sample so that specimen-to-specimen variation differences would not be included in the results. A schematic of the test approach is shown in Figure 4.65.
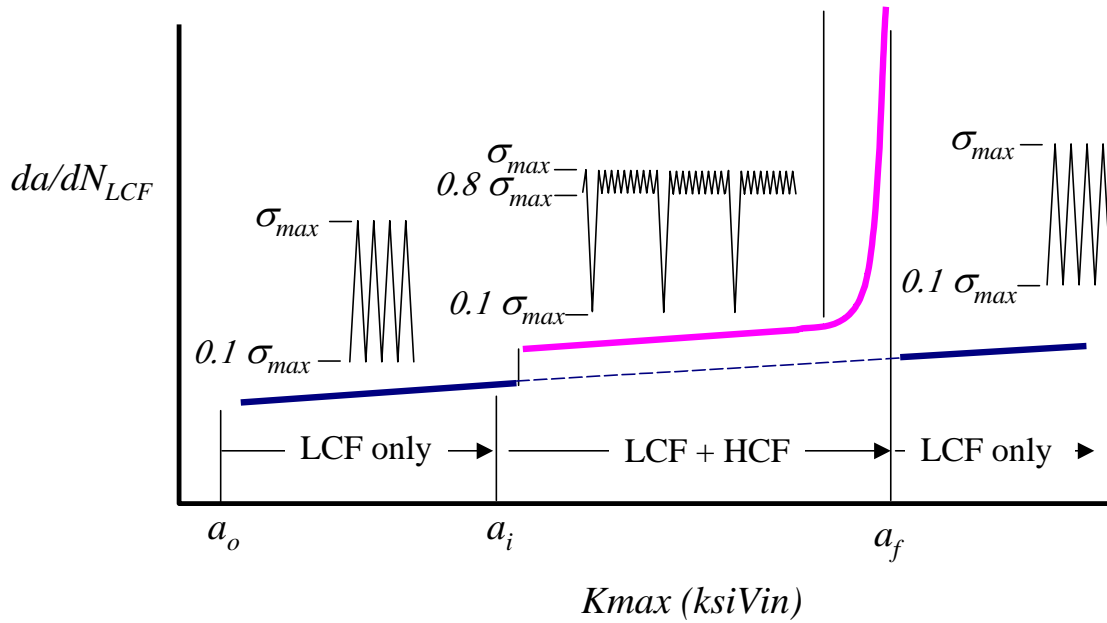
Figure 4.65. HCF / LCF testing approach and prediction.

A. HCF / LCF Testing

Specimen numbers 8906 and 8908 were tested under constant amplitude load control maintaining a σmax = 12.15 ksi nominal net section stress to allow stress intensity K to increase with increasing crack length to detect the onset of region II behavior of the R = 0.8 cycles. For the HCF portion of the combined 10 CPM and 60 Hz cycles, the 60 Hz test frequency could not be obtained instantaneously after the slower cycle LCF. Instead, the frequency was gradually raised from 10 Hz to 60 Hz over 50 cycles. The reverse of this practice was repeated on completion of the HCF block leading into the LCF cycle.

B. Initial HCF / LCF Test Results

The test results were dramatic. A sharp increase in crack growth rate occurred at crack length a_i corresponding to the change in waveform from LCF to LCF+HCF indicating that the R = 0.8 cycles did affect the crack growth rate. This was in direct contradiction to the anticipated response based on the earlier R = 0.8 threshold result. A return to pure LCF loading resulted in the anticipated return to the R = 0.1 region II trend. A second specimen was then run to confirm that the data were repeatable and the same result was achieved. The results are shown in Figure 4.66.
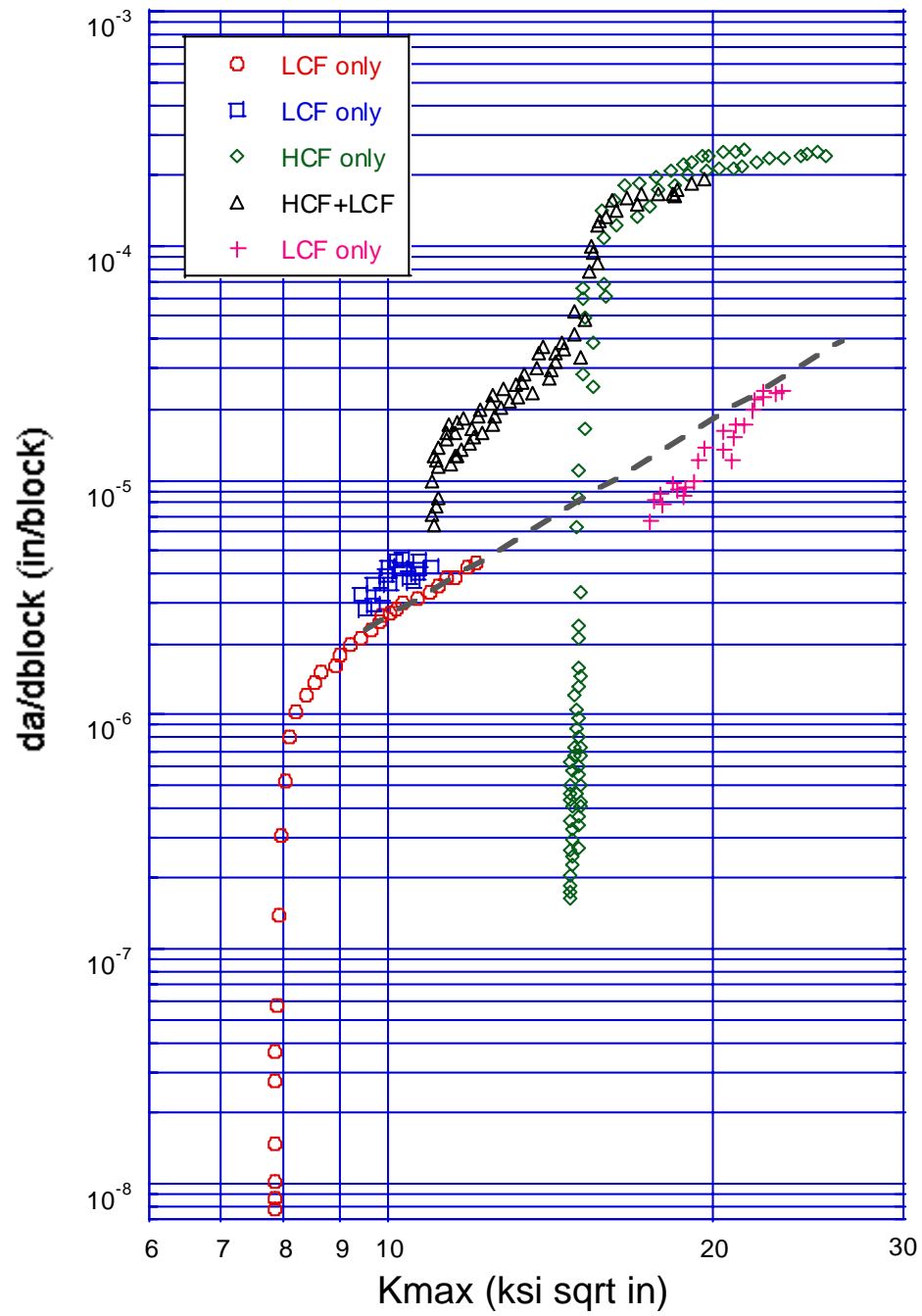
Figure 4.66. HCF/LCF interaction test results.

C.   HCF / LCF Test Plan 2

A new test plan was developed to explore the possible cause of the unexpected crack growth rate acceleration. Five loading schemes were devised and performed at a constant ΔK_{LCF} of 10 ksi$\sqrt{}$ in. The frequency for the LCF portion of each case was 10 CPM, and 60 Hz for the HCF portion. The loading schemes are shown in Figure 4.67 as Case (a) through Case (f). A single SEN sample was again used to perform all six cases in succession with each case consuming 0.015 – 0.020 inches of specimen ligament before proceeding to the next case.
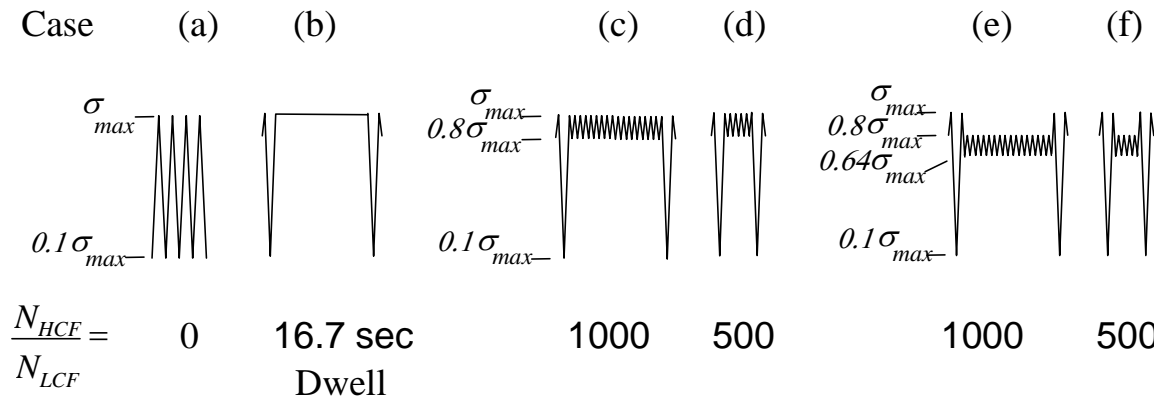
Figure 4.67.   Test plan 2, constant K testing to identify crack growth rate
                     acceleration drivers.

Comparison of the various case loading blocks suggest the higher mean stress or dwell is the significant contributor to the accelerated crack growth behavior as opposed to the quantity of HCF cycles. As shown in Figure 4.68, the application of dwell (Case (b)) resulted in nearly the same acceleration as adding 1000 R = 0.8 cycles or Case (c). The similarity between case (c) and (d) (1000 vs. 500 HCF cycles) suggests that the sensitivity to time dependant behavior is inclusive of very small differences in hold times and or cyclic frequency. In fact threshold testing done previously in this program shows clearly a pronounced frequency effect between 20 Hz, 1Hz and 10 CPM.

D. Conclusions

An initial plan was designed such that the ΔK for the LCF loading was well into region II. After a specific amount of crack growth, the loading scheme was to be changed so that 1000 HCF cycles were imposed in between single LCF cycles. For both cases the maximum stress (σ_{max}) was held constant. It was predicted that the LCF portion of the HCF / LCF interaction cycle would dominate thereby following the LCF region II crack growth rate trend until the ΔK for the R = 0.8 threshold had been superseded. Once this occurs the prediction was a steady but quick crack growth rate increase. The final portion the test plan was to return to pure LCF loading and verify that it returned to the LCF, R = 0.1 region II trend. The data generated from this experiment showed a dramatic crack growth rate increase at the onset of the HCF cyclic loading contrary to the prediction. A second sample confirmed the results of the initial testing.

A second test plan was devised which held another variable constant. This second test plan investigated the effects of several loading blocks by holding K-max constant. By holding K-max constant and plotting da/dN as a function of crack length (a) a direct comparison of the different waveform spectrum could be achieved. This method confirmed that the higher mean stress caused the acceleration in crack growth rate and not the HCF / LCF interaction effects. In fact, the results indicate that there is a dwell effect present in a temperature regime well below what has typically been called the creep regime. The significance of this finding is that very small decreases in frequency i.e. 10 CPM and 10 CPM with as little as an 8 second dwell at maximum load, cause up to a 2X to 3X acceleration in crack growth rate.

4.2.5.2   Fractographic Analysis

A fractographic analysis of the fracture features specific to the locations of each of the different loading blocks showed that they were mono-planer TPNC to varying amounts of ancillary TPNC fractures. This was consistent with Cunningham et al. findings for these temperature and frequency sets. What was evident however was that the LCF only fracture features were significantly more mono-planer than the complex waveform fracture features. Another observation is that even though ancillary cracking requires more energy to generate the secondary fracture surfaces it does not necessarily translate to faster crack growth rates.

One final observation in this experiment is the apparent frequency dependence in region I crack growth rate. The limited data produced under this program seem to indicate that different thresholds can be obtained based entirely on frequency changes. It has previously been assumed that frequency dependence diminishes with decreasing growth rate and is typically modeled this way. One possible explanation for both the HCF / LCF interaction effects and the region I frequency effects could be oxidation at the crack tip. This was also presented by Telesman as a possible cause stating that da/dN for the environmental mode to be in effect it is the requirement that the depth of oxygen penetration has to be on the same magnitude, or greater, than the crack growth increment per cycle. One possible method to explore this possibility would be to run the same experiments in an inert atmosphere.
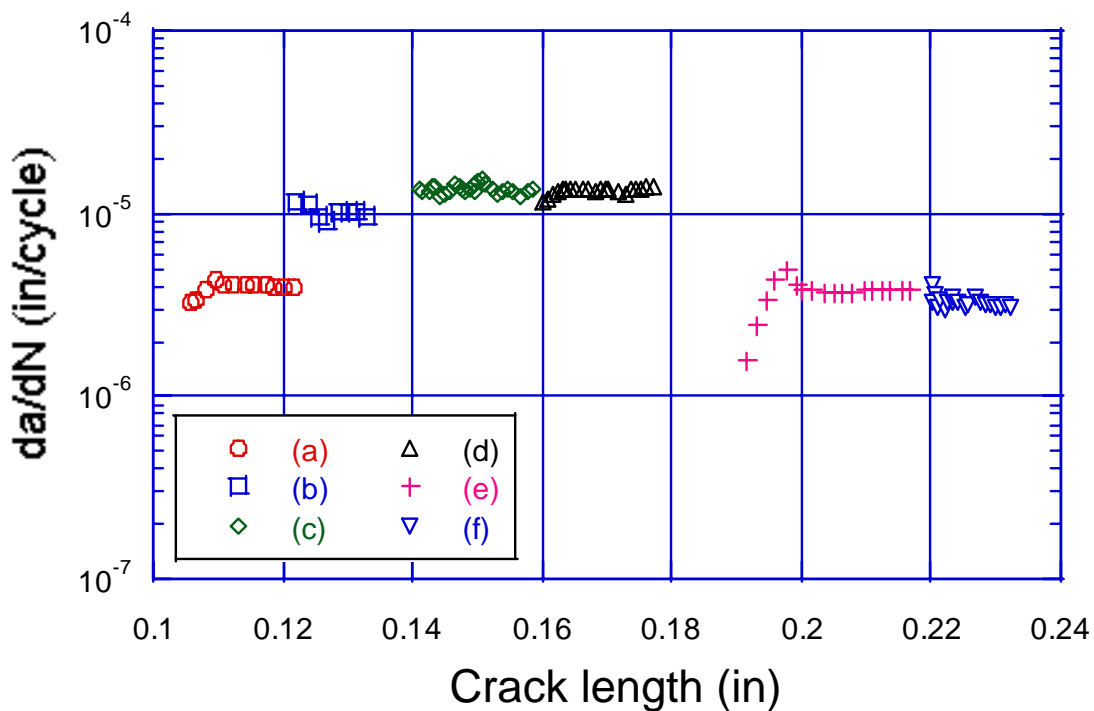
Figure 4.68 Test plan 2 results. Legend refers to loading blocks shown in Fig. 4.67.

4.3 HCF BASELINE ENDURANCE LIMIT MODELING

4.3.1 Testing

4.3.1.1 Test Methods (Data Comparison)

Eleven specimens were consumed to produce 24 data points using the step-test method. For the sake of clarity, step testing (in this report) is defined as fatiguing a sample until 1E7 cycles, then uploading 5% to 10% after each run-out until the specimen fails. Figure 4.69 shows the data plotted as σ_{max} verses cycles to failure. The blue squares represent non-step test data and the red triangles represent specimens that have run-out at least once then uploaded 5% – 10%. This process is repeated until the sample fails.

PWA 1484 HCF Step Test Fatigue Results
1100 F, R = 0.1, 30 Hz
<001>
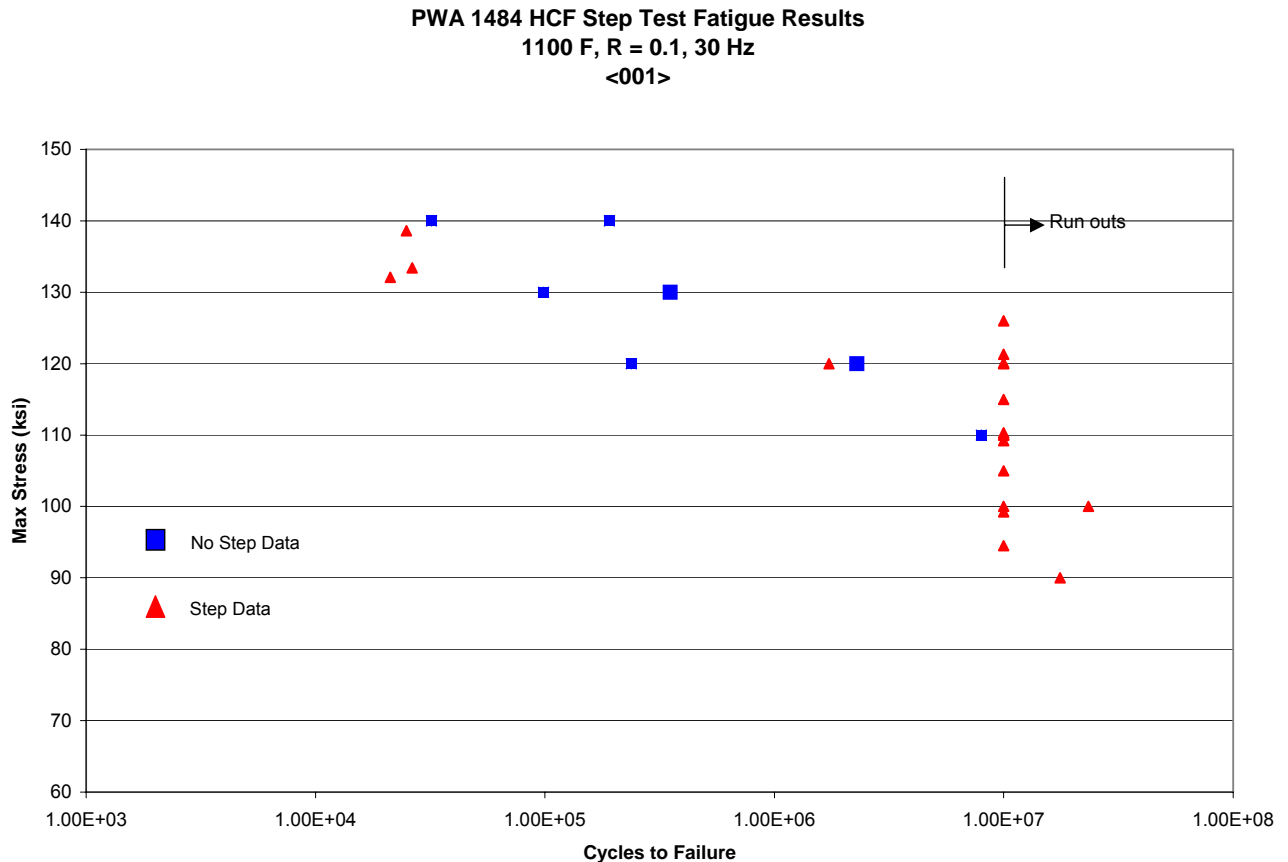
Figure 4.69. Step testing results.

Fractography was completed on five of the samples (Figures 4.70-4.74) in an effort to locate the failure mechanisms for both step-tested samples and non-step-tested samples.

271

The fractographic examination captured several failure mechanisms at the individual fatigue locations.
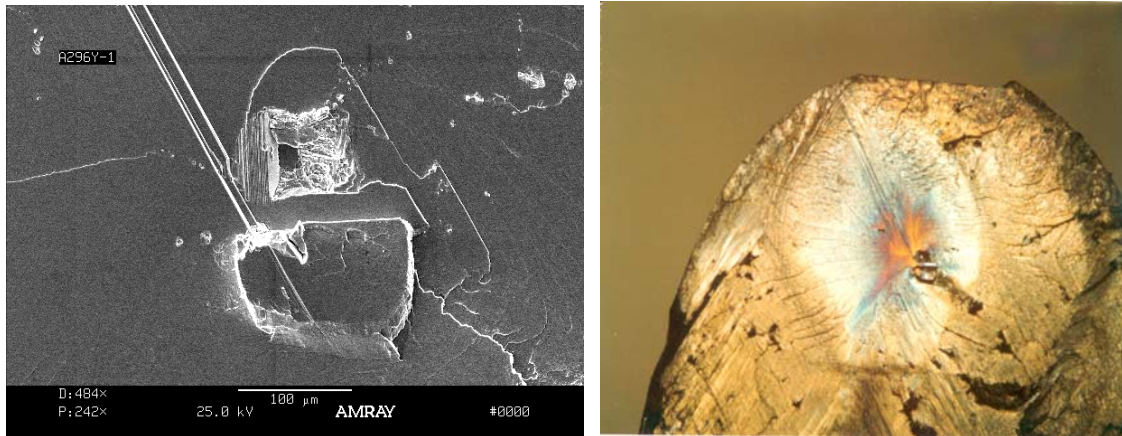
Figure 4.70. Specimen A296Y-1 Step test, σ_{max} at failure = 133.4 ksi, R = 0.1, 1100° F, N_f = 2.64E4. Failure origin is at a sub-surface carbide. Subsequent propagation exhibits crystallographic crack propagation in the (111) plane, accelerated in the <110> direction.
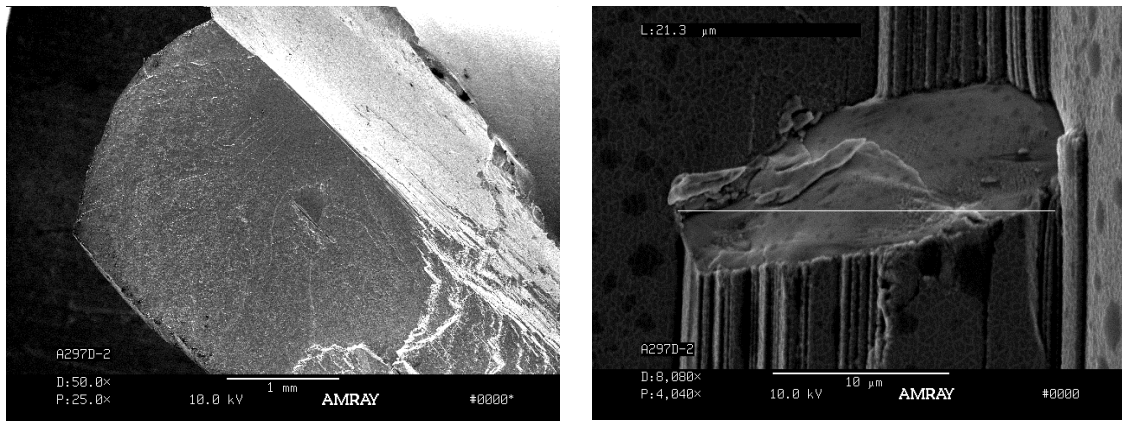
Figure 4.71. Specimen A297D-2 Non-step test, σ_{max} at failure = 140 ksi, R = 0.1, 1100° F, N_f = 1.91E5. Failure is very near the surface, originating at a carbide.
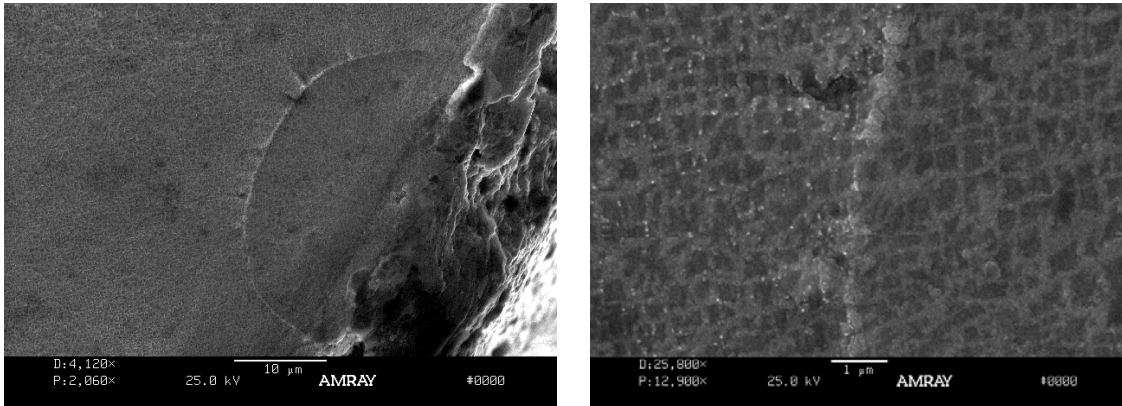
Figure 4.72. Specimen A297D-1 Step test, σ_{max} at failure = 138.6 ksi, R = 0.1, 1100° F, N_f = 2.49E4. Failure is from a non-crystallographic surface initiation.
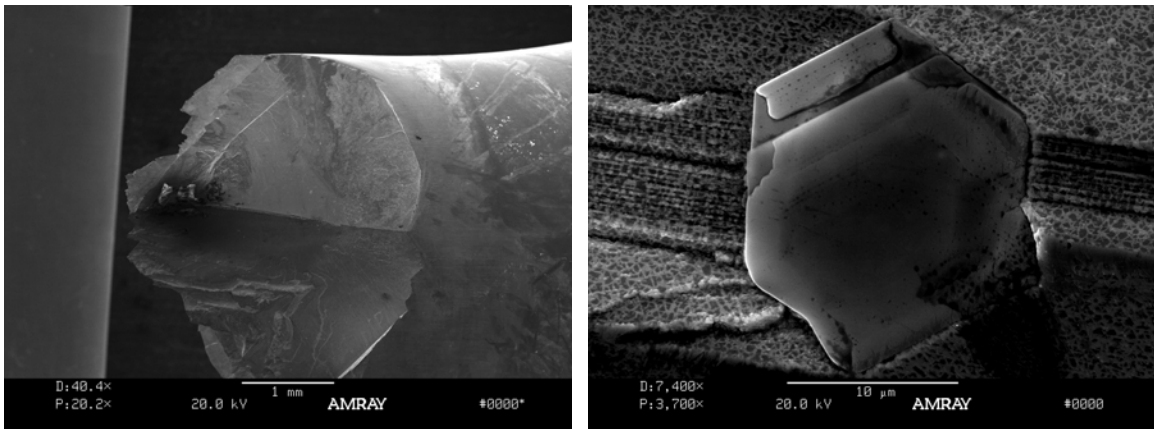
Figure 4.73. Specimen K1L1H-1 Non-step test, σ_{max} at failure = 130 ksi, R = 0.1, 1100° F, N_f = 9.86E4. Failure origin initiated at a carbide.
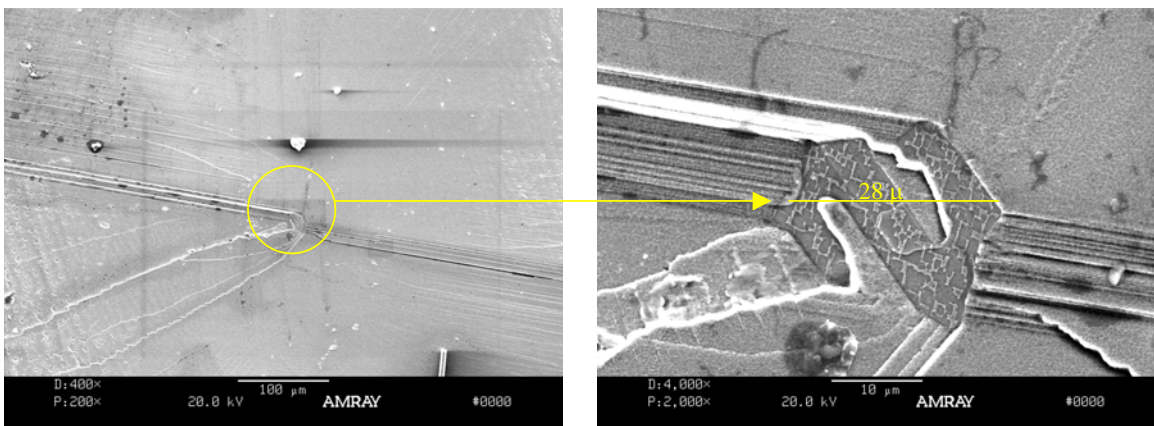
Figure 4.74. Specimen A297E-1 Non-step test, σ_{max} at failure = 120 ksi, R = 0.1, 1100° F, N_f = 2.29E6. Failure origin initiated at a $\gamma - \gamma$' eutectic.

A. 1100°F

GEAE, P&W, and Honeywell all performed HCF tests in their own laboratories at 1100°F, R = 0.1, 60 Hz to establish a basis of comparison between the laboratories. Metcut Research was also used for 1100°F testing by both P&W and Honeywell. A comparison of these results is shown in Figure 4.75. As can be seen, there is considerable variation among the data sets, with GEAE producing the highest results and Honeywell the lowest. To help compare results, both P&W and Honeywell sent specimens to Metcut Research for additional testing. Results at Metcut from the two participants, while closer, were still not identical. Some possible reasons for the difference in results obtained are:

1.   Differences in material from using different casting types. Microstructure and defect state could both vary somewhat with casting size or geometry.

2.   Specimen geometry and size differences. Smaller sizes or stressed volumes should lead to increased HCF strength, since the probability of finding a defect is less.

3.   Differences in machining of specimens. Surface residual stress or cold work is known to affect fatigue capability in superalloys. Unfortunately, the standard X-ray diffraction techniques for characterizing residual stress and cold work are not applicable to single crystal superalloys, so these differences could not be checked.

4.   Differences in test methods, such as temperature measurement and control, specimen alignment, or loading method.

It is interesting to note that the differences between test sources with the same participant (e.g., P&W specimens tested at P&W vs. P&W specimens tested at Metcut) tend to be less than the differences between participants at one test source (Metcut). This suggests that test methods are not the primary contributor to the differences seen.

One further experiment is suggested that could help evaluate whether specimen machining was a major factor. Existing specimens from different participants (machined at different sources) could be re-heat-treated to relieve most of the residual stress induced by the machining process.

274
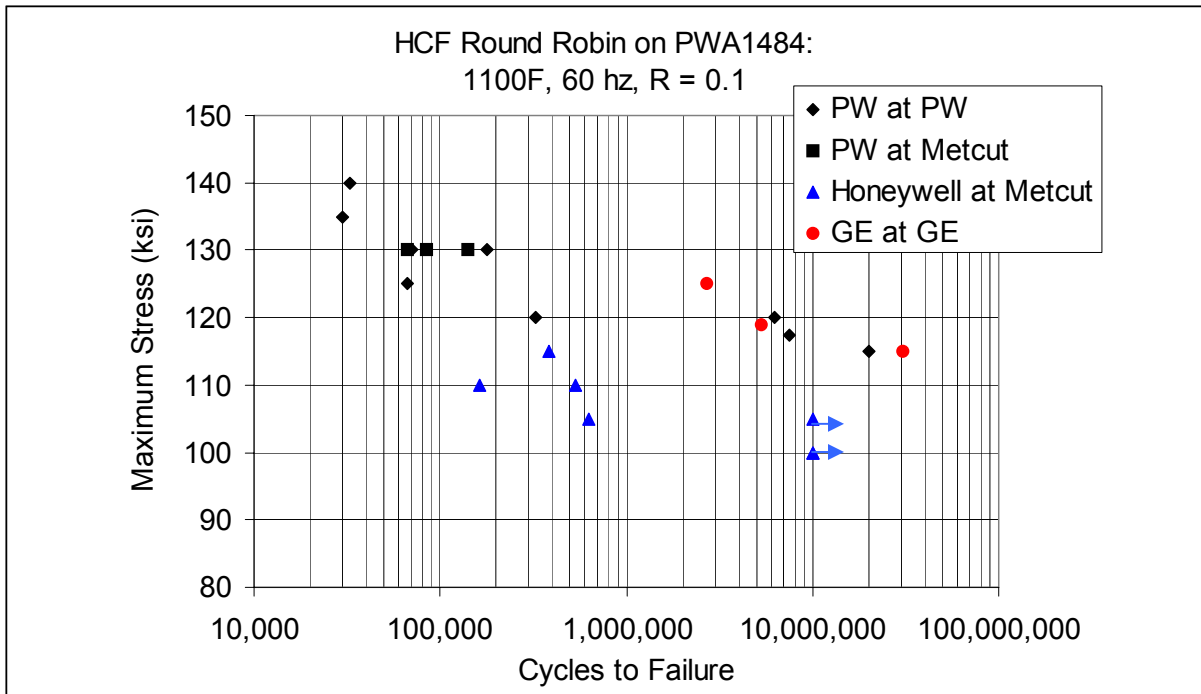
Figure 4.75. Comparison of PWA 1484 HCF data from different sources, 1100°F, R = 0.1, 60 Hz. (Honeywell data points at 10^7 cycles are runouts.)

Testing of these specimens should then eliminate much of the machining variability and would demonstrate the effect of the machining process by comparison with the data obtained on specimens machined after heat treatment. The similarity in results at 1900°F between GEAE tests at GEAE and Honeywell tests at Metcut as reported in Section 4.3.1.1.*B* supports the idea that the differences seen at 1100°F are related to specimen preparation and not testing. All 1900°F specimens were coated after machining, so the combination of the coating and the thermal cycle could have removed any differences in surface condition set up by machining.

B. 1900°F

Specimens for 1900°F total life testing were machined by Low Stress Grind of Cincinnati, from 6 inch x 3 inch x 5/8 inch cast slabs (GEAE), or from 6 inch long x 5/8 inch diameter cast bars (Honeywell) using conventional low stress grinding methods for superalloy materials. All castings were in the fully heat treated condition prior to machining.

Several different specimen geometries were used at 1900°F:

a) A 0.2-inch diameter cylindrical specimen with threaded ends, Figure 4.76. This specimen was used by GEAE primarily at 60 Hz (at Metcut) and at frequencies up to 200 Hz (at GEAE).

b) A 0.16-inch diameter cylindrical specimen with threaded ends, Figure 4.77. This specimen was used by GEAE at 900 Hz (at GEAE), since the larger specimen of Figure 4.76 could not be driven at this high a frequency. It was also used occasionally at lower frequencies.

c) A shorter 0.2-inch diameter cylindrical specimen with threaded ends, Figure 4.78, tested by Honeywell at Metcut.

Notched specimen geometries will be presented later, in Section 4.4.2.

As described in Section 4.1.2, all specimens (except for a few as noted) for 1900°F testing were coated with Howmet Thermatec's MDC150L, a commercial PtAl diffusion coating. These specimens were re-heat treated with the final two steps of the PWA 1484 heat treatment process after coating. 1900°F HCF testing was performed in two laboratories: GEAE and Metcut Research of Cincinnati. (Both GEAE and Honeywell used Metcut as a 1900°F testing source.) Most tests were performed using furnace heating of the specimen. Because of concern about history effects at high temperature, no step load testing was performed. All tests were conducted to failure and run-outs were not re-tested except for special multi-step tests described in Section 4.3.1.6.
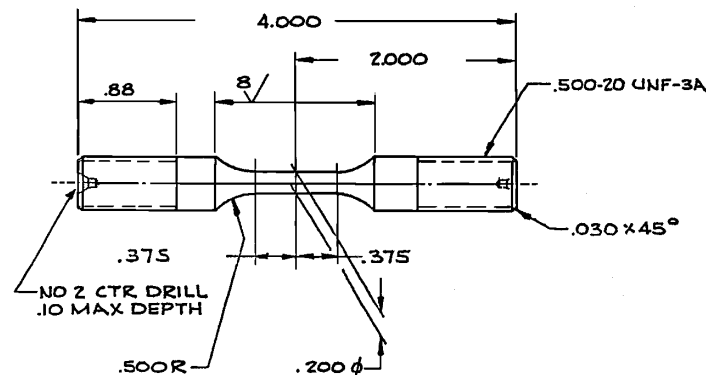
Figure 4.76. 0.2-inch diameter cylindrical GEAE HCF specimen with threaded ends.
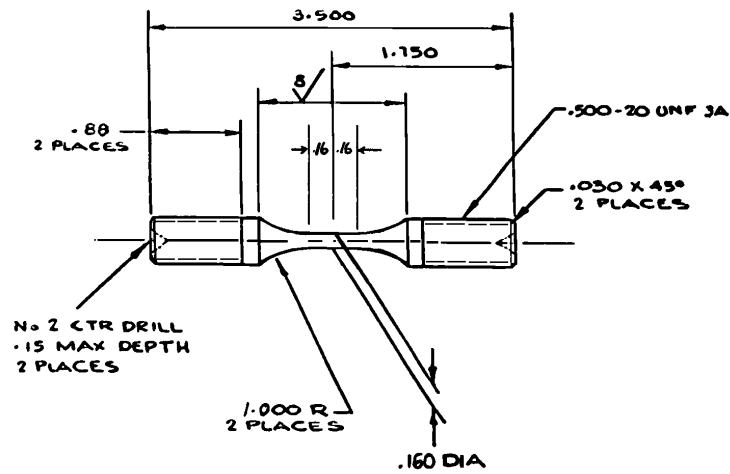
Figure 4.77. 0.16-inch diameter cylindrical GEAE HCF specimen with threaded ends.
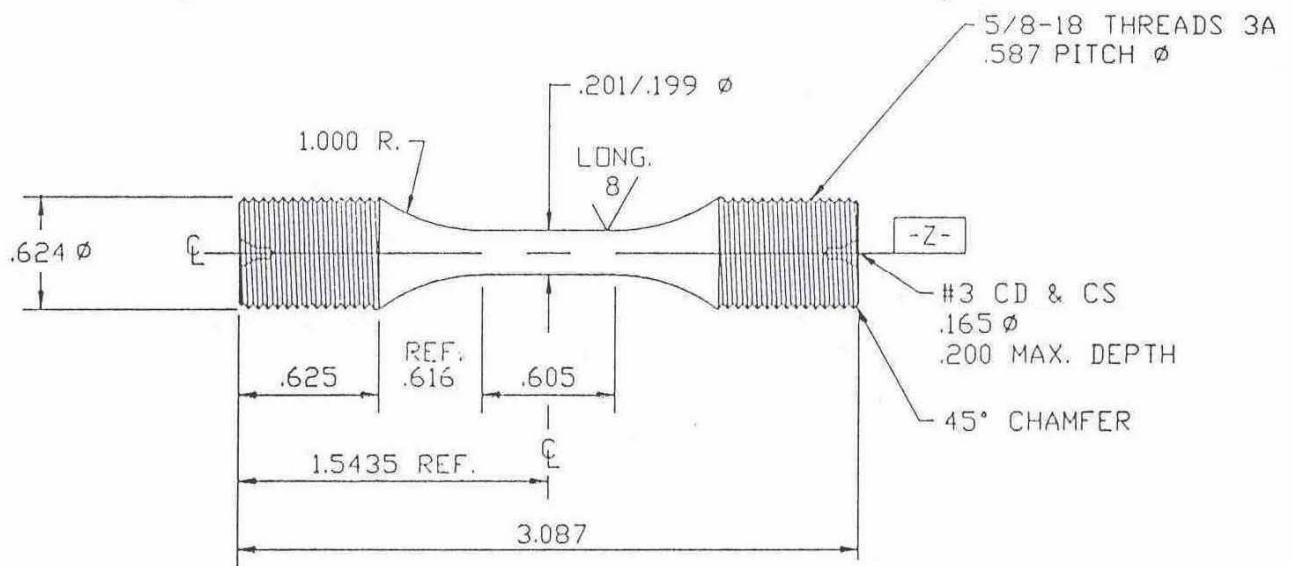
Figure 4.78. 0.2-inch diameter Honeywell HCF specimen.

A comparison between the GEAE and Metcut laboratories was performed at 1900°F, R = -1, 60 Hz with the results shown in Table 4.13.

Table 4.13.   Comparison of Test Laboratories at 1900°F, R = -1, 60 Hz on PtAl Coated PWA 1484

S/N	Specimen source	Test Lab	Alternating stress (ksi)	Cycles	Result
A2LLT-4	GEAE	GEAE	45.0	7,928,152	failed
A2LLT-5	GEAE	GEAE	48.0	3,353,378	failed
A2KLU-1	GEAE	Metcut	40.0	16,314,137	failed
A2KLU-3	GEAE	Metcut	42.5	12,688,845	failed
KIL56B	Honeywell	Metcut	54.0	205,482	failed
KIL3WB	Honeywell	Metcut	50.0	4,245,370	failed
KIL6VB	Honeywell	Metcut	46.0	8,941,513	failed
KIL2BT	Honeywell	Metcut	42.0	10,009,524	no failure
KIL7WT	Honeywell	Metcut	46.0	5,679,517	failed
KIL5LB	Honeywell	Metcut	42.0	10,187,190	no failure
KIL9FT	Honeywell	Metcut	50.0	1,264,133	failed

As can be seen in Figure 4.79, the results from the two organizations and laboratories were quite comparable, giving confidence to the interchangeable use of data from both sources.

278
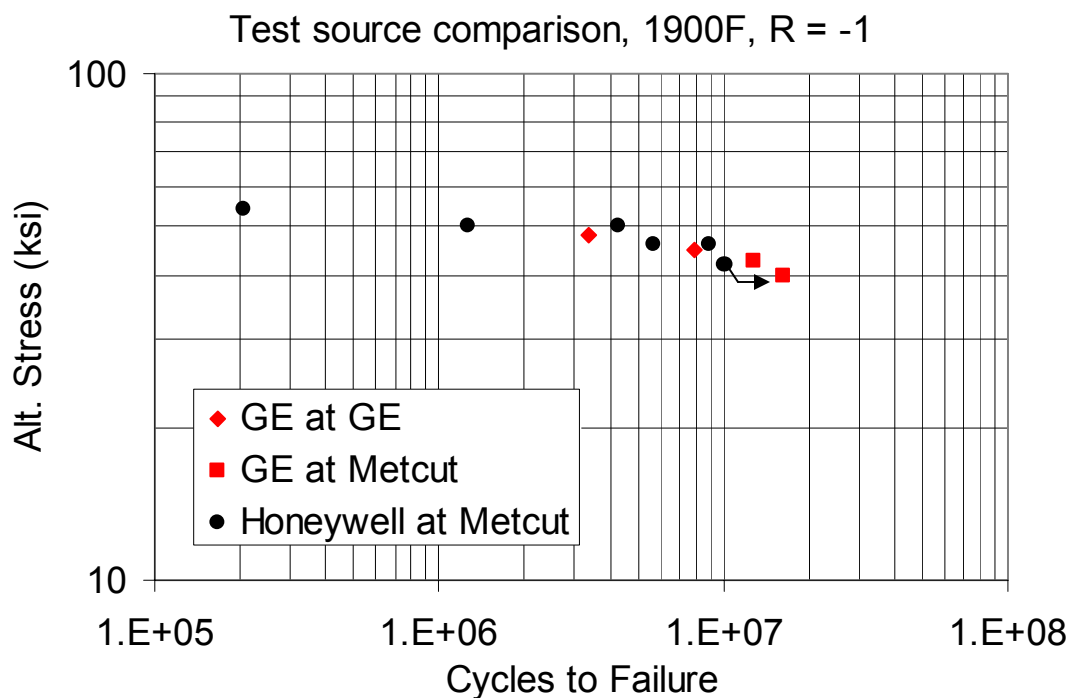
Figure 4.79. Comparison of 1900°F HCF results from different sources. R = -1, 60 Hz.

4.3.1.2   Frequency

   A. 1100°F Results

Limited testing was performed at two different frequencies at 1100°F to identify frequency effects and determine the applicability of standard low frequency test results to higher frequency turbine blade shank HCF conditions. All specimens were <001> oriented, uncoated PWA 1484, tested at R = 0.1. Tests were performed at 60 and 900 Hz in GEAE's high frequency MTS machine using 0.16-inch diameter cylindrical specimens (Figure 4.77).

The results are shown in Table 4.14 and Figure 4.80. There is clearly not a big effect of frequency at 1100°F. There may be a slight (1-2 ksi) decrease in the HCF capability at 900 Hz, but given the small number of samples tested and the level of scatter in the data, any difference is not statistically significant. Recall that in Section 4.3.1.1.*A*, the baseline 60

Hz results from several sources had much more variation than seen here between the 60 and 900 Hz tests.

Table 4.14. Effect of Frequency on 1100°F HCF of PWA 1484. R = 0.1, Uncoated

S/N	Frequency (Hz)	Alt. Stress (ksi)	Cycles to fail	Comment
T20VM	60	56.25	2.72E+06	failed
T20W3	60	51.75	3.06E+07	run out
T20W4	60	49.50	5.32E+06	run out
A2LPZ-1	885	48.4	4.38E+07	failed
A2LPZ-2	890	49.5	2.63E+06	failed
A2LPZ-4	890	47.3	5.14E+08	run out
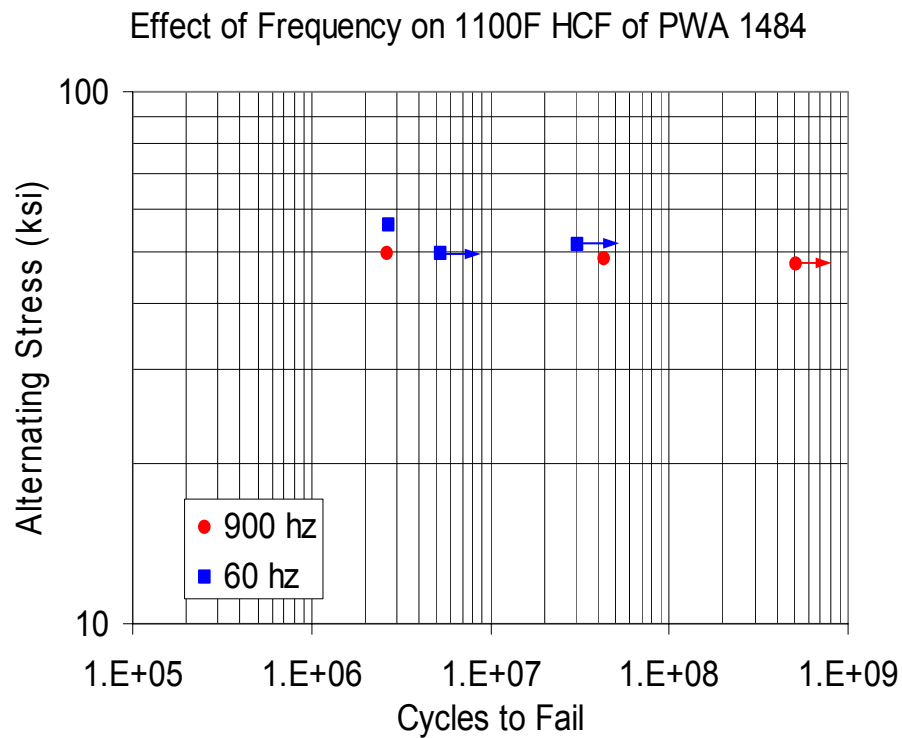
Figure 4.80. Effect of frequency on HCF of uncoated PWA 1484 at 1100°F, R = 0.1.

Fracture surfaces of specimens were highly crystallographic at both frequencies. Failures typically initiated internally and grew on one or more intersecting (111) type planes.

In summary, it appears from limited testing that frequency effects do not need to be considered at 1100°F for applying relatively low frequency laboratory results to higher frequencies seen in turbine blades.

B. 1900°F Results

Testing was performed at several different frequencies at 1900°F to identify frequency effects and determine the applicability of standard low frequency test results to higher frequency turbine blade airfoil HCF conditions. All specimens were <001> oriented PWA 1484, using a combination of 0.2 inch and 0.16 inch diameter cylindrical specimens, Figures 4.76 and 4.77. Tests were performed at 60, 200, and 900 Hz in GEAE's high frequency MTS machine and at 0.6 and 60 Hz in standard fatigue machines at Metcut. Behavior at several stress ratios was examined.

At 1900°F, both PtAl coated (MDC150) and uncoated specimens were tested at a variety of frequencies and stress ratios. For the uncoated results, see Appendix O. Only the coated behavior will be discussed here. The coated test matrix and results are shown in Table 4.15.

At R = -1, there was no detectable effect of frequency on HCF capability. Specimens tested at 60, 180, and 870 Hz all fell along a single S-N curve, as shown in Figure 4.81. One specimen tested at 0.6 Hz failed in significantly fewer cycles, suggesting a possible transition to frequency-dependent behavior at very low frequencies. The frequency independent behavior was surprising in view of the expectation that properties of PWA 1484 would be time or rate sensitive at 1900°F. Apparently HCF is purely cycle-dependent in this case of low mean stress fatigue.

Note also, in Figure 4.81 that there is no evidence of an endurance limit at 1900°F, R = -1 out to the highest number of cycles investigated (8×10^7). Thus at higher numbers of cycles the alternating stress capability should be expected to decrease further.

Table 4.15.   Test Matrix for the Effect of Frequency on HCF of Coated <001> PWA 1484 at 1900°F

S/N	Stress ratio	Frequency (Hz)	Alternating stress (ksi)	Cycles to Failure	Comment
A2LLU-5	-1	0.6	50	5,235	failed
A2LLT-5	-1	60	48	3,353,378	failed
A2LLT-4	-1	60	45	7,928,152	failed
A2KLU-3	-1	59	42.5	12,688,845	failed
A2KLU-1	-1	59	40.0	*16,314,137*	runout
A2LLU-1	-1	180	45	1,938,011	failed
A2LLU-2	-1	180	40	77,067,219	failed
A2LR1-5	-1	870	50	1,348,353	failed
A2LRB-2	-1	870	45	26,205,076	failed
A2LR1-3	-1	870	40	22,605,443	failed
A2LR2-1	-1	870	39	38,531,462	failed
A2LKV-1	0.1	0.6	23.4	67,667	failed
A2LLU-4	0.1	0.6	23.4	59,308	failed
A2LLF-2	0.1	0.6	22.5	91,820	failed
A2KLU-4	0.1	59	23.4	5,519,911	failed
A2LLG-1	0.1	250	23.4	13,858,078	failed
A2LLP-1	0.1	250	23.4	15,135,243	failed
A2LLP-5	0.1	370	30.5	4,155,470	failed
A2LLS-1	0.1	370	26.5	6,014,518	failed
A2LLF-5	0.1	400	23.4	21,191,046	failed
A2LLG-5	0.1	400	23.4	12,264,178	failed
A2LLH-5	0.1	400	20.5	55,686,529	failed
A2LR2-4	0.1	870	42.1	63,572	failed
A2LR2-5	0.1	870	23.4	41,399,374	failed
T20WC-1	0.5	370	12.0	6,987,858	failed
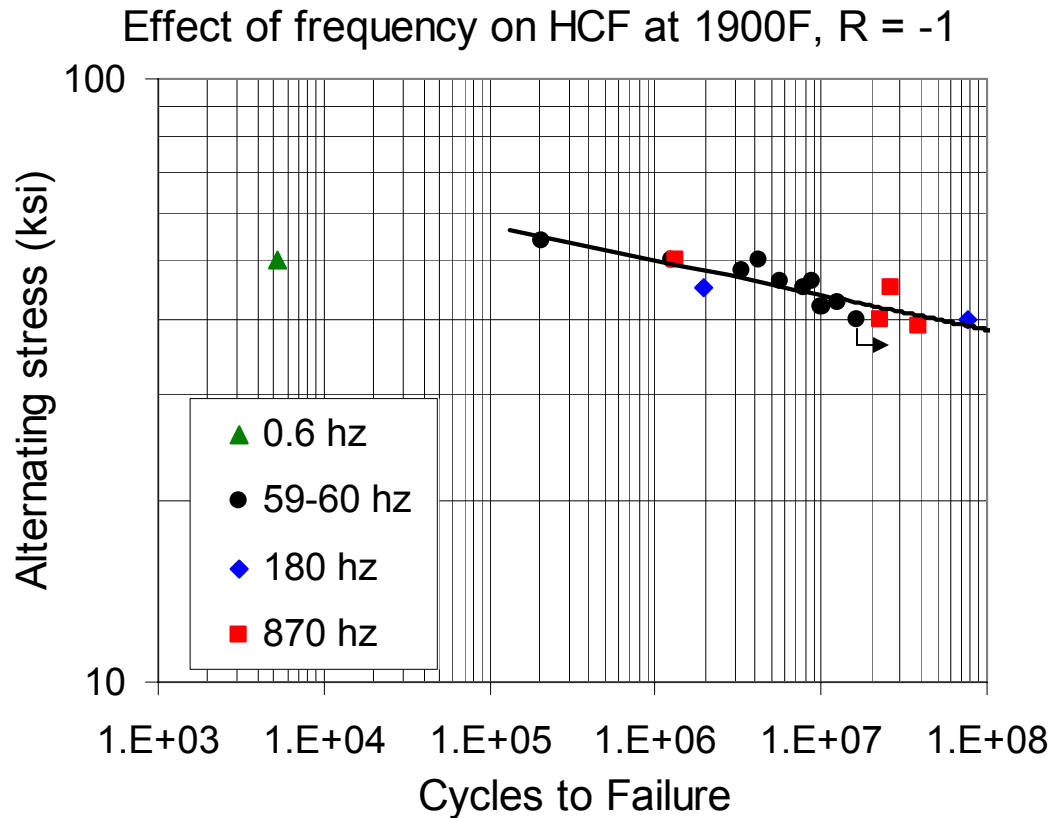
Figure 4.81. Effect of frequency on HCF capability of coated PWA
1484 <001> at 1900°F, R = -1.

The fracture appearance of selected specimens tested at different frequencies is
shown in Figures 4.82 and.4.83. Both internal and surface initiated failures were seen,
sometimes on the same specimen. There was a trend of internal initiation at higher stress and
frequency (shorter times) and for surface initiation at lower stress and frequency (longer
times) but there were exceptions to this trend in many cases. At longer times, cracking
developed in the PtAl coating, primarily at the grain boundaries. An example of this is seen
in Figure 4.84, which shows a longitudinal section through A2LKU-1, which did not fail in
over 16 x 10^6 cycles (Table 4.15) at 59 Hz. Multiple cracks can be seen in the outer layer of
the PtAl coating, many of which follow an angular path along the coating grain boundaries.
Some of these crack have penetrated to the substrate, where dark gray oxides have been
generated. A large number of cracks have continued or reinitiated into the substrate, and
show no evidence of arrest. The deepest crack seen was about .006 inch deep. These

observations support the notion that if an endurance limit exists, it is well beyond the conditions examined in this program.
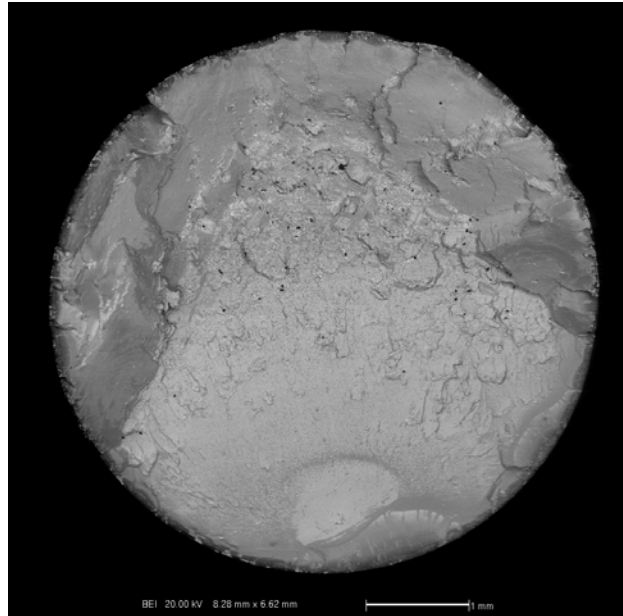
Figure 4.82. Fracture appearance of A2LLT-5, tested at 1900°F,
R = -1, 60 Hz, 48 ksi alternating stress (Nf = 3,353,378).
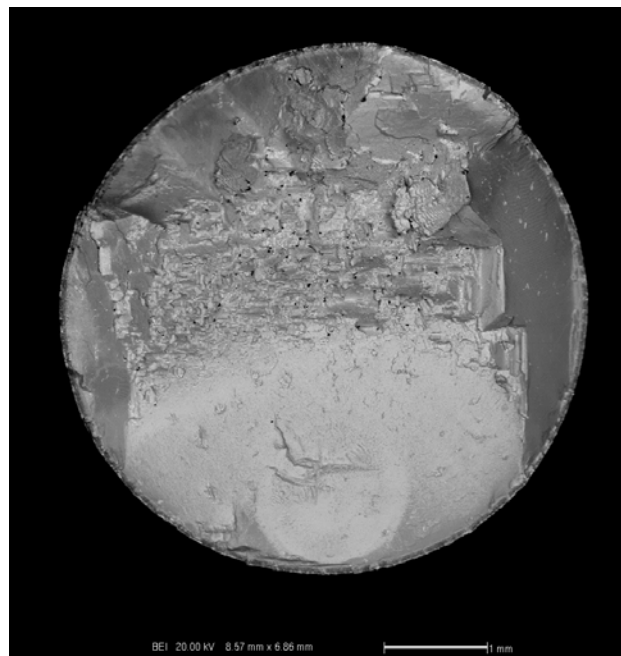
Figure 4.83. Fracture appearance of A2LLU-1, tested at 1900°F, R =
-1, 180 Hz, 45 ksi alternating stress (Nf = 1,938,011).
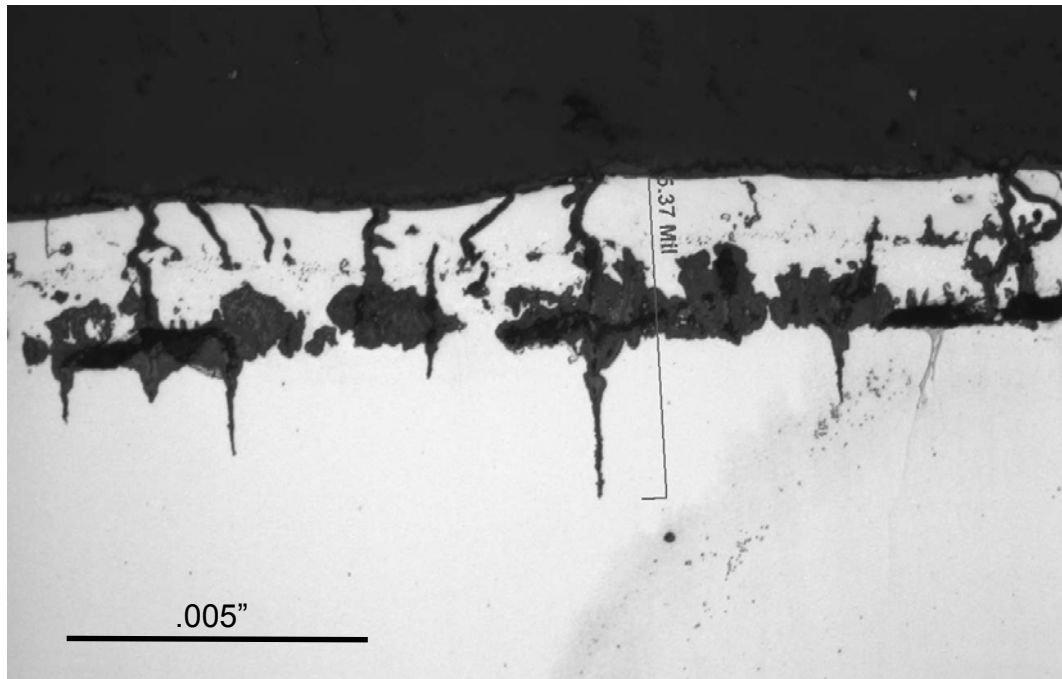
Figure 4.84.   Longitudinal section through A2LKU-1 (1900°F, R = -1, 59 Hz)
showing coating and substrate cracking and oxidation.

At R = 0.1, the dependence of HCF on frequency was quite different. Figure 4.85 shows S-N response for frequencies of 0.6, 59-60, 250, 370-400, and 870 Hz. At this stress ratio, there is a distinct layering of the data, with higher frequencies giving more cycles to failure. Viewed another way, Figure 4.86 shows these results at a constant alternating stress level of 23.4 ksi. As frequency increased the cycles to failure increased nearly proportionately, as indicated by the 45° dashed line. This dashed line represents a line of constant time to failure (27.8 hr). That this is true can be seen by replotting the time to failure vs. frequency as shown in Figure 4.87. Now the fatigue capability as measured by time to failure is nearly independent of frequency. There is a slight decrease in HCF capability as the frequency exceeds 60 Hz. This suggests that the behavior may be gradually transitioning toward cycle-dependent behavior at frequencies higher than 900 Hz.

Thus the behaviors at R = -1 and R = 0.1 may be all part of a single continuum with transition between cycle-dependent and time-dependent behavior, being a strong function of stress ratio. At low mean stress the transition frequency is low, and for practical

purposes the behavior is cycle dependent. As mean stress increases the transition frequency increases, so that at R = 0.1, it is greater than 870 Hz and now the behavior is predominantly time dependent.

These aspects of frequency-dependent behavior at 1900°F may require re-thinking how we apply conventional (30 to 60 Hz) HCF data to blades. For example, if a blade vibratory frequency is significantly above the frequency from which the data were obtained, then the blade HCF capability (alternating stress) would either be the same as (if considered on the basis of the total number of cycles) or less than the lab data (if considered on the basis of total time). If one is interested in protecting the blade against HCF for a given mission time, then at a higher cyclic frequency more cycles will occur in the same time, so the fatigue capability for those greater number of cycles will be less. This would be true unless an endurance limit behavior was observed, where the HCF capability does not decrease with further life increase. At 1900°F, such an endurance limit has not been observed to this point. More work is required to rationalize this behavior with generally successful blade HCF experience observed in the field.
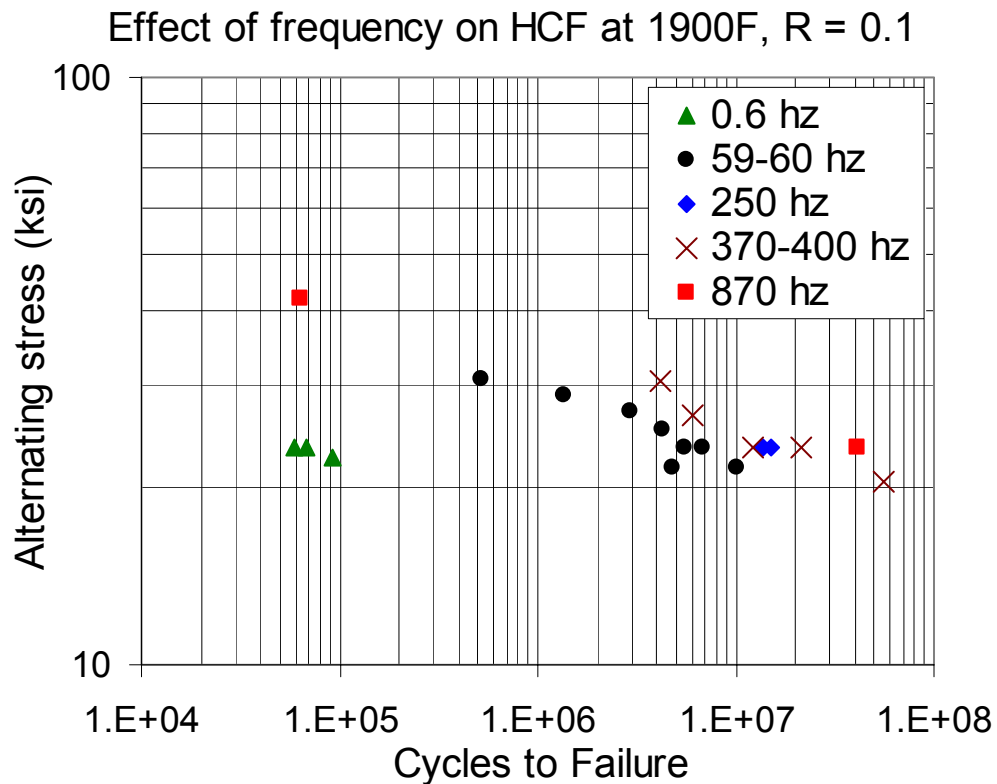
Figure 4.85. Effect of frequency on HCF of coated PWA 1484 <001> at 1900°F, R = 0.1.
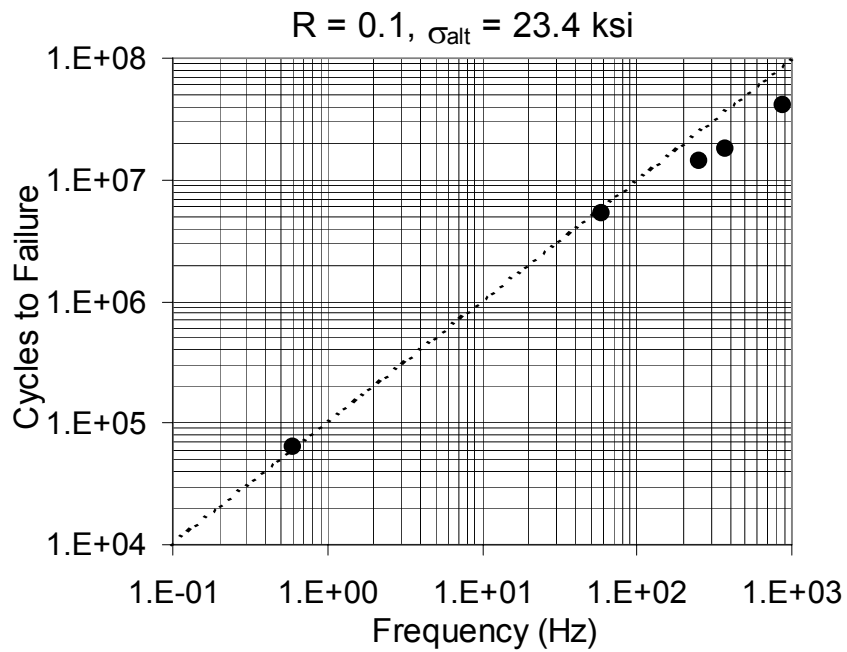
Figure 4.86. Frequency dependence of cycles to failure at alternating stress level of 23.4 ksi; 1900°F, R = 0.1
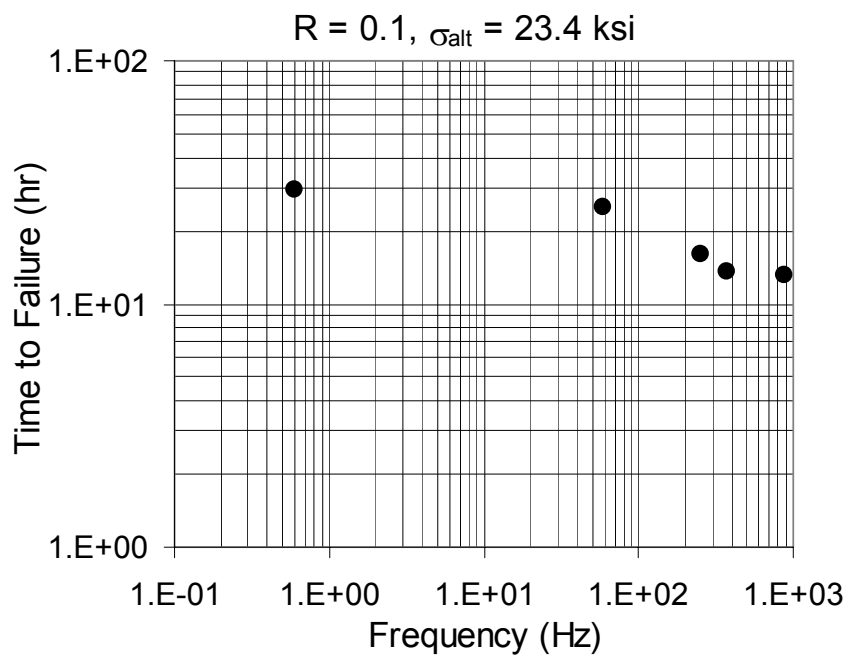
Figure 4.87. Frequency dependence of time to failure at alternating stress level of 23.4 ksi; 1900°F, R = 0.1.

Fractures at 1900°F, R = 0.1 appeared to be mostly surface initiated, with multiple coating cracks seen below the fracture surface. There were often indications of multiple surface initiations on a single fracture surface. Fractures were non-crystallographic, except for a very small overload region representing the final fracture, and in the early stages the fracture surface was quite smooth and featureless. Illustrations of these features are given in Figures 4.88 through 4.90.
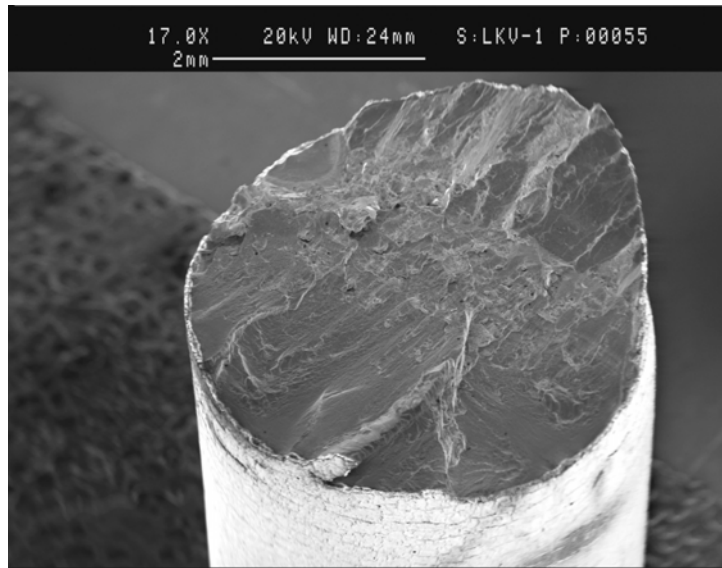
Figure 4.88.   Fracture appearance of A2LKV-1 tested at 1900°F, R = 0.1, 0.6 Hz, 23.4 ksi, alternating stress (Nf = 67,667).
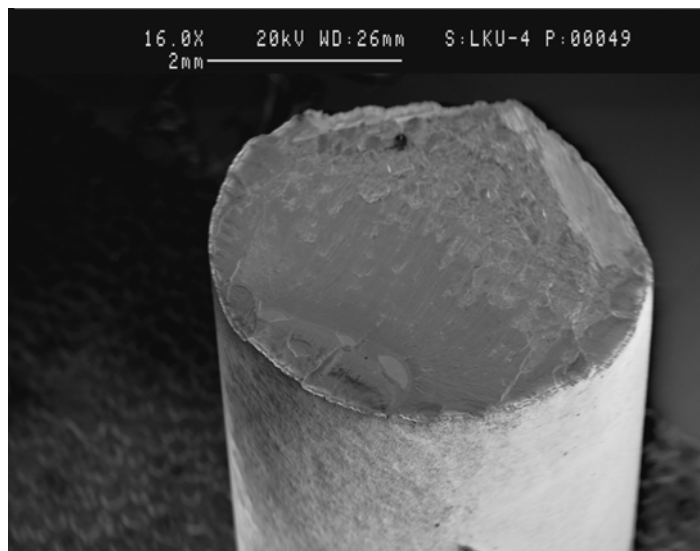
Figure 4.89.   Fracture appearance of A2LKU-4 tested at 1900°F, R = 0.1, 59 Hz, 23.4 ksi alternating stress (Nf = 5,519,911).
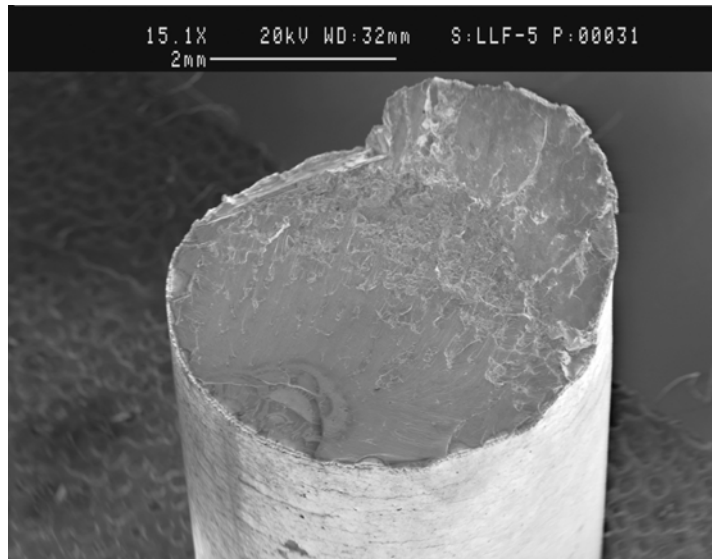
Figures 4.90. Fracture appearance of A2LLF-5 tested at 1900°F, R = 0.1,
400 Hz, 23.4 ksi alternating stress (Nf = 21,191,046).

One high frequency test was performed at R = 0.5, at f = 370 Hz. As shown in
Figure 4.91, the cyclic life of this test was nearly identical to those obtained at 59 Hz
(baseline Stress ratio tests from Section 4.3.1.5).   This is surprising in light of the large body
of results at R = 0.1 that show increasing cycles to failure with increasing frequency.
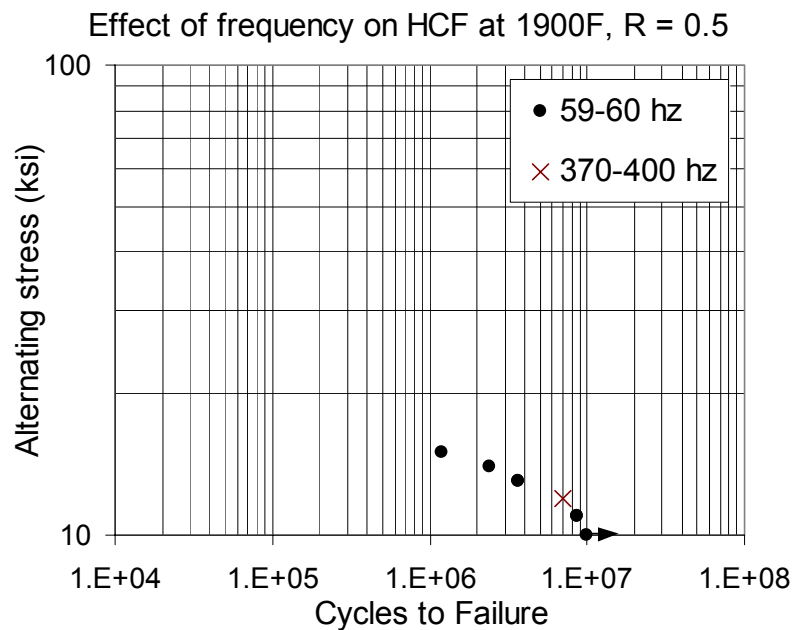
Figure 4.91. Effect of frequency on HCF of coated PWA 1484 <001> at 1900°F, R = 0.5.

It seems unlikely that the behavior would be reverting back to frequency independence, particularly in light of the model of 1900°F HCF behavior presented in Section 4.3.4. Additional testing is warranted at this condition to understand the role of frequency at high R.

4.3.1.3 HCF Orientation Effects testing

High cycle fatigue testing was performed on 4 crystallographic orientations. All crystallographic orientations are coincident with the loading axis. Two temperatures were investigated: 1100°F and 1900°F. The two temperatures were chosen to represent two areas of a turbine airfoil in service, the root or attachment location and the blade tip. The blade root location is typically exposed to lower temperatures and is loaded predominantly at lower stress ratios. The blade tip is exposed to higher temperatures and high mean stress loading. Test conditions were selected to mimic these two conditions and compare fatigue lives of the following orientations, <001>, <001+15>, <010> and <011>. A stress ratio of 0.1 was used for the 1100°F testing and a stress ratio of 0.8 was used for the 1900°F testing. The specimen geometry used in this investigation was a GEAE design and is shown in Figure 4.92. The table below lists the specimen number and orientation. Test results are shown in Figures 4.93 and 4.94.

Table 4.16. Test Specimen Orientation and Fabrication Description

orientation effects	smooth	<001+15>, <011>, <010>	32	32	100	**Tall Slab <001+15>** Round Bar <011> Tall Slab <010>	T20WX A2LLL A295W <011> A2964 <011> A296H <011> A295U <011> A2LKP <010>	1000H 160MO
orientation effects	smooth	<001+15>, <011>, <010>	24	24	100	Tall Slab <001+15> Round Bar <011> Tall Slab <010>	**T20VX <001+15>** A2LLL <001+15> A2960 <011> A295Z <011> A2965 <011> A296B <011> A2LL6 <010>	1000H 160MO
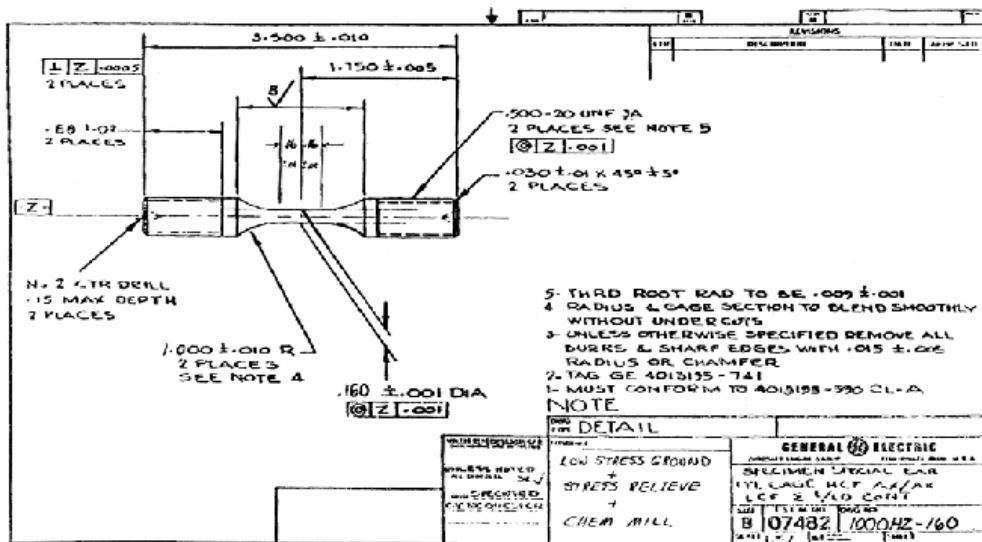
Figure 4.92. GEAE HCF specimen design.
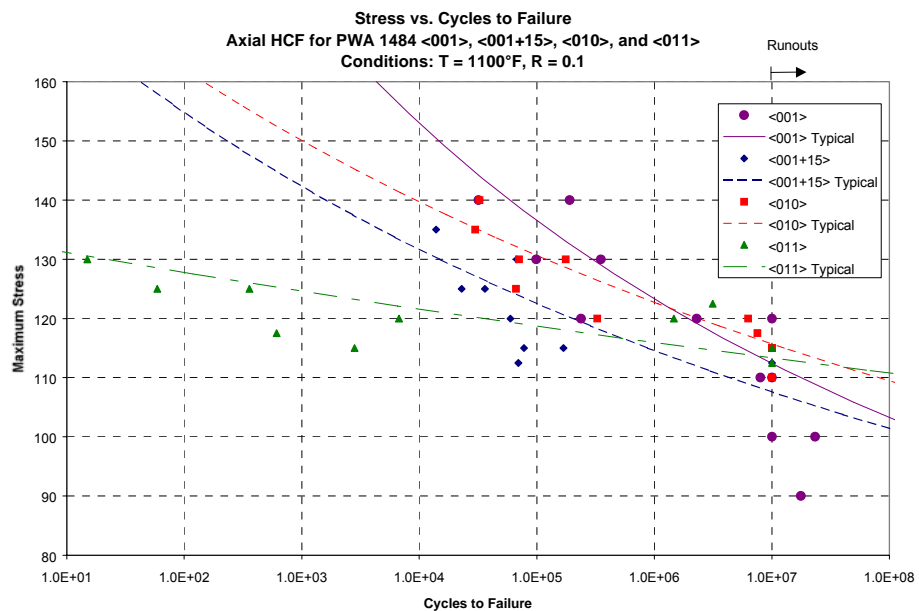
Figure 4.93. High cycle fatigue orientation effect testing, 1100°F and R=0.1.

Stress vs. Cycles to Failure
Axial HCF for PWA 1484 <001>, <001+15>, <010> and <011>
Conditions: T = 1900 F, R = 0.8
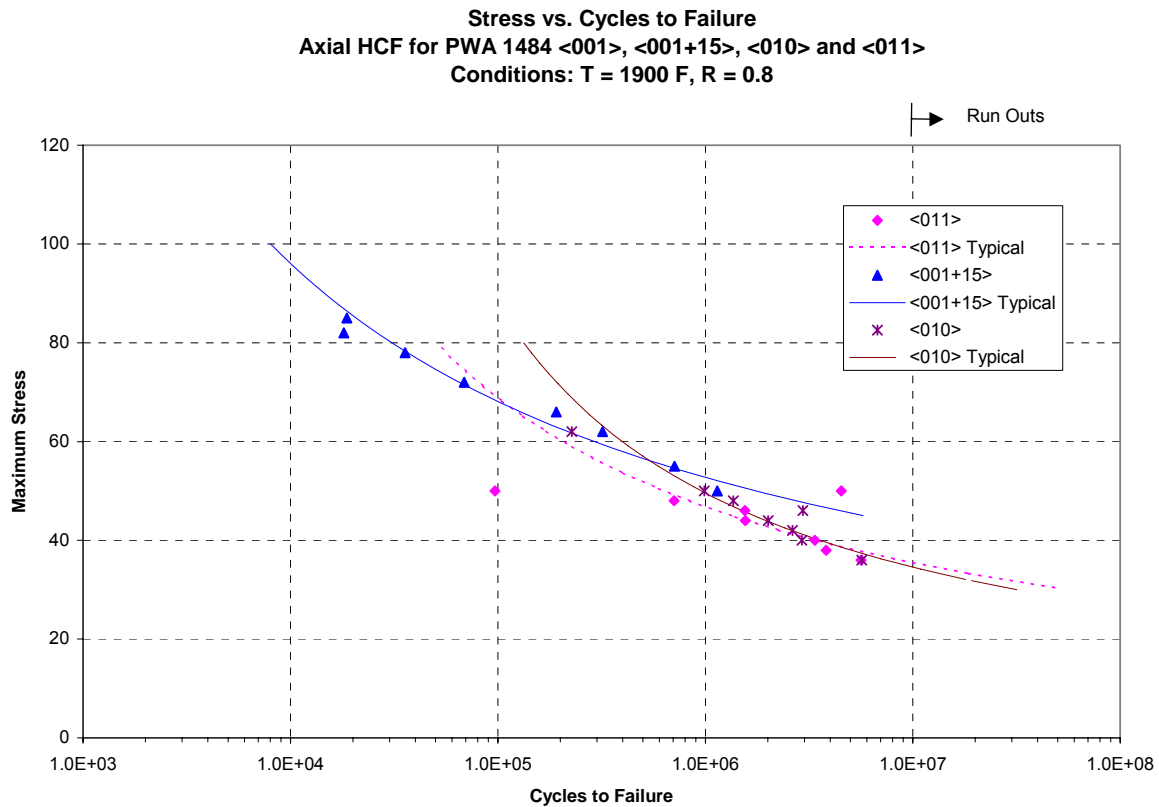
Figure 4.94. High cycle fatigue orientation effect testing, 1900°F and R=0.8.

4.3.1.4 Multiaxial

The intents of this portion of the program were to provide multiaxial test results under loading scenarios expressly selected to complement the modeling effort. Accordingly, several test conditions were originally in conjunction with the other participants and specified to be done using uncoated samples at 1100°F. Some of the tests that were part of the overall multiaxial effort were simple torsional tests. These latter results are documented in Section 4.3.1.7.*A* and this testing eventually included some coated samples at 1900°F.

There were a variety of experimental uncertainties associated with this testing and the first vendor could not produce repeatable alignment of his system. Metcut succeeded in getting alignment and had a grip system that met the requirements for repeatability. The other experimental unknown was the frequency of loading that might be achieved for this

mulitaxial HCF testing. Metcut's work with their system produced a frequency of approximately 2 Hz for this work. Based on this frequency it was decided to define a runout at 1 million cycles as opposed to the 10 million cycles used for the conventional axial HCF work.

All data are shown in the most straightforward, direct reporting of results, essentially as raw test information consistent with Honeywell's role in this effort. Any utilizations of the data are covered in the respective sections of this report dealing with modeling, etc.

A. *Multiaxial Results at 1100°F*

The conditions examined were in-phase axial-torsion at a shared stress ratio of 0.1 and one out-of-phase axial-torsion at R = -1. The in-phase data gathered are presented in Table 4.17 and Figure 4.95, while the single out-of-phase data point is provided in Table 4.18.

Table 4.17. Multiaxial Results at 1100°F, In-Phase Axial-Torsion, R = 0.1

Test Number	Specimen Number	Diameter (in)	Axial Stress Max (ksi)	Shear Stress Max (ksi)	Cycles	Results
9-02	ZOK-JC	0.3623	75.0	75.0	1,052,972	Removal
11-02	ZOK-FH	0.3625	85.0	85.0	889,921	Removal(1)
12-02	ZOR-XG	0.3625	95.0	95.0	748	Torsional Yield
13-02	ZOK-FH	0.3625	90.0	90.0	80,630	Fracture, GS
14-02	ZOK-JE	0.3620	90.0	90.0	153,338	Fracture, GS
15-02	ZOK-GJ	0.3629	88.0	88.0	118,743	Fracture, AR
16-02	ZOK-G3	0.3625	88.0	88.0	287,942	Fracture, GS
17-02	ZOK-JC	0.3623	85.0	85.0	381,870	Fracture, GS
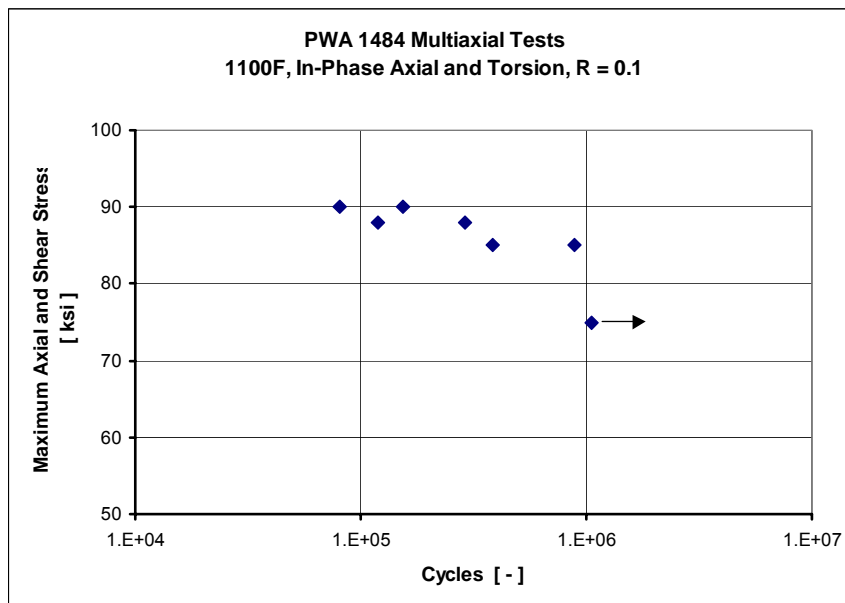
Figure 4.95. Plot of multiaxial results, 1100°F, in-phase axial-torsion, R = 0.1.

Table 4.18. Multiaxial Results at 1100°F, Out-of-Phase Axial-Torsion, R = -1

Test Number	Specimen Number	Diameter (in)	Axial Stress Max (ksi)	Shear Stress Max (ksi)	Cycles	Results
10-02	ZOK-EZ	0.3624	50.0	50.0	1,094,280	Removal

As this work progressed the modeling members of the consortium, particularly GEAE and PWA, were monitoring the data. They did not find good agreement with their efforts and this multiaxial work, as well as the related 1100°F torsional work reported in Section 4.3.1.7. Hence, this work was discontinued after evaluating the conditions specified. GEAE was interested in conducting some additional tests at 1900°F and those are shown in the latter part of Section 4.3.1.7.

With the difficulty the modeling participants were having in rationalizing the multiaxial data, there was some concern about whether the test apparatus was operating

correctly. To examine the fidelity of the apparatus, three tests were run in a strictly axial mode at the 1100°F temperature. The results of these tests are seen in Table 4.19.

Table 4.19. Multiaxial Results at 1100°F. Axial Load Only, R = 0.1

Test Number	Specimen Number	Diameter (in)	Axial Stress Max (ksi)	Shear Stress Max (ksi)	Cycles	Results
18-02	ZOK-LN	0.3625	110.0	0.0	1,323,201	Removal
19-02	ZOK-KJ	0.3625	115.0	0.0	1,032,041	Removal*
19-02A*	ZOR-KJ	0.3625	125.0	0.0	963,851	Fracture, GS

* This bar was up-loaded to Smax = 125 ksi level and the test continued.

The axial-only test results that were produced in the multiaxial frame displayed superior fatigue strength characteristics to those samples tested in the standard axial portion of the program (Section 4.3.1.5, Stress Ratio Effects). This suggests that there were no apparatus-induced difficulties that lead to the multiaxial test results that were of concern to the other participants.

The remainder of the work performed under the general umbrella of the 1100°F multiaxial effort was torsion tests reported Section 4.3.1.7, Torsion.

4.3.1.5   Stress Ratio Effects

The intent of this portion of the program was to provide uniaxial test results under varying stress ratios and to characterize the influence of this variable on the HCF strength at 1100°F and 1900°F. All testing was done using uncoated samples at 1100°F, while the 1900°F testing employed test coupons prepared with an appropriate platinum aluminide coating and re-aged accordingly. A minimum of four stress ratios were explored, R = -1, 0.1, 0.5, and 0.8 as had been agreed upon with the other team members. At 1100°F, testing at an additional stress ratio of -0.333 was done.

While initially begun at Honeywell, the results shown here are only those of the testing vendor, Metcut. All tests were axial, with a testing frequency of 59 Hz. All data are shown in the most straightforward, direct reporting of results, essentially as raw test

information consistent with Honeywell's role in this effort. Any utilizations of the data are covered in the respective sections of this report dealing with modeling, etc.

A. *Uniaxial Stress Ratio Effect Results at 1100°F*

The stress ratios examined for the 1100°F work were R = -1, 0.1, 0.5 and 0.8. The data from the tests are presented in Table 4.20. These data are also presented graphically in Figure 4.96 and Figure 4.97, showing Smax vs.N and Sa vs. N response, respectively.

Table 4.20. Axial Results at 1100°F, 59 Hz, All R's

Test Number	Specimen Number	R ratio	Diameter (in)	Axial Stress Max (ksi)	Cycles	Results
7-01	K1L67B	-1	0.2005	130.0	11,589	Frac/Gage
8-01	K1LA4T	-1	0.1999	115.0	31,778	Frac/Radius
9-01	K1L21B	-1	0.2000	80.0	165,210	Frac/Gage
10-01	K1L5KT	-1	0.2003	65.0	13,283,000	Removal
12-01	K1L1DB	-1	0.2004	75.0	1,612,914	Frac/Gage
13-01	K1L94T	-1	0.2001	70.0	10,374,280	Removal
14-01	KIL5WT	-1	0.1997	70.0	10,000,012	Removal
15-01	KIL2NT	-1	0.2004	75.0	1,384,473	Frac/Gage
16-01	KIL2AB	-1	0.2004	80.0	168,973	Frac/Radius
2-01	K1L5LT	0.1	0.2002	100.0	10,014,803	Removal
3-01	K1L2LB	0.1	0.1998	115.0	380,601	Frac/Gage
4-01	K1L9TB	0.1	0.2005	110.0	161,997	Frac/Gage
5-01	K1L1MT	0.1	0.2005	105.0	10,047,545	Removal
6-01	K1L7WB	0.1	0.2003	110.0	531,229	Frac/Radius
11-01	K1L6JT	0.1	0.2002	105.0	623,075	Frac/Gage
17-01	KIL3XB	0.1	0.2002	100.0	10,126,244	Removal
1-03	KIL95-B	0.5	0.2002	128.0	13,239,989	Removal
3-03	KIL20-B	0.5	0.2003	136.0	20,934	Frac/Gage
4-03	KILIC-T	0.5	0.2002	132.0	6,707,251	Frac/Gage
7-03	KIL65-T	0.5	0.2000	128.0	10,000,089	Removal
8-03	KIL6U-B	0.5	0.2002	132.0	840,234	Frac/Gage
9-03	KILIN-B	0.5	0.2001	136.0	923,849	Frac/Gage
10-03	KIL49-T	0.5	0.2001	132.0	940,573	Frac/Gage
1-01	K1L6TB	0.82	0.2001	100.0	10,074,206	Removal
2-03	KIL6U-T	0.8	0.2000	140.0	10,809,475	Removal
5-03	KILIN-T	0.8	0.2002	145.0	10,717,378	Removal
6-03	KIL49-B	0.8	0.2000	150.0	148.1 ksi max.	Failed on Loading
11-03	KIL20-T	0.8	0.2001	145.0	2,562	Frac/Gage
12-03	KILIC-B	0.8	0.2003	140.0	10,008,556	Removal
13-03	KIL95-T	0.8	0.2001	145.0	11,954,025	Removal
14-03	KIL65-B	0.8	-	147.0	10,353,146	Removal
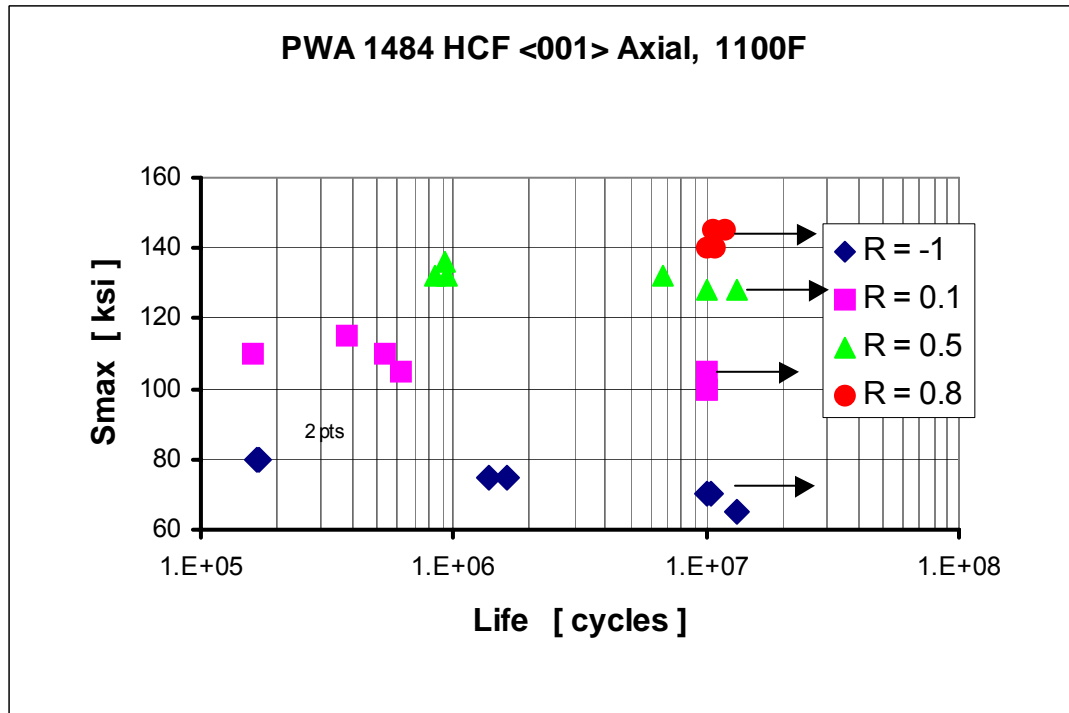
Figure 4.96. Plot of S_{max} versus N at 1100°F, axial, all R's.
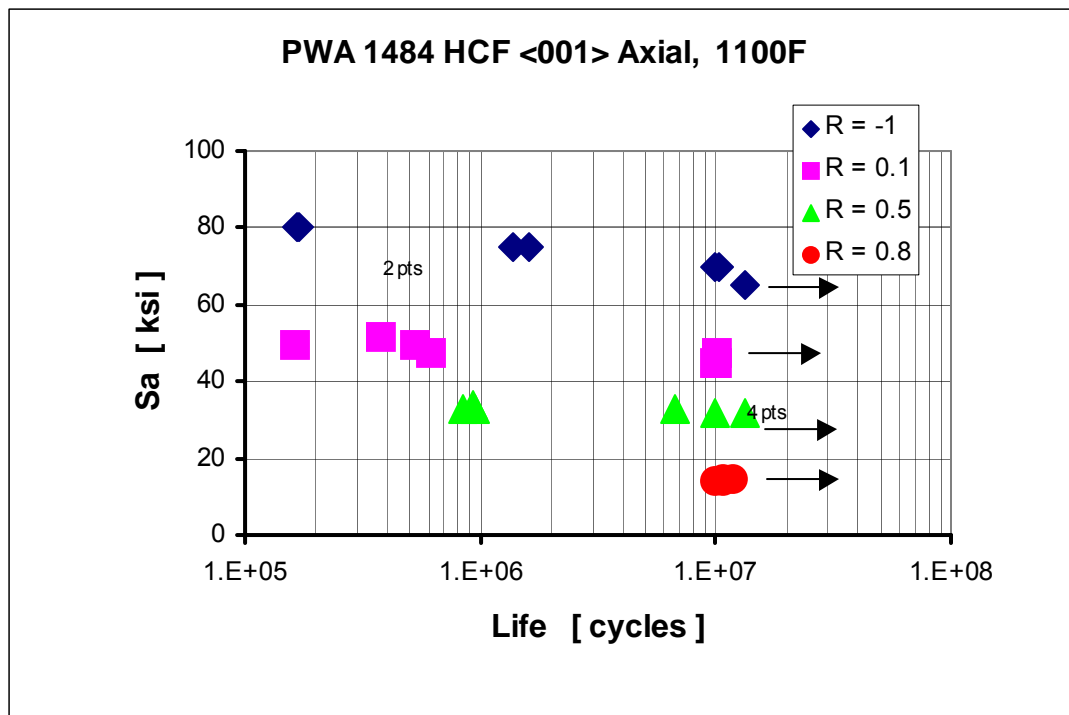
Figure 4.97. Plot of S_a versus N at 1100°F, axial, all R's.

Fractography was performed on some of the samples. In general, crack initiation was observed to be largely of sub-surface origin. Inclusions, apparently carbides, were featured at the crack initiation site. Crack propagation was crystallographic along what one can surmise to be the {111} type slip planes.

Examples of the fracture surfaces for different values of R are shown in Figures 4.98 through 4.101.
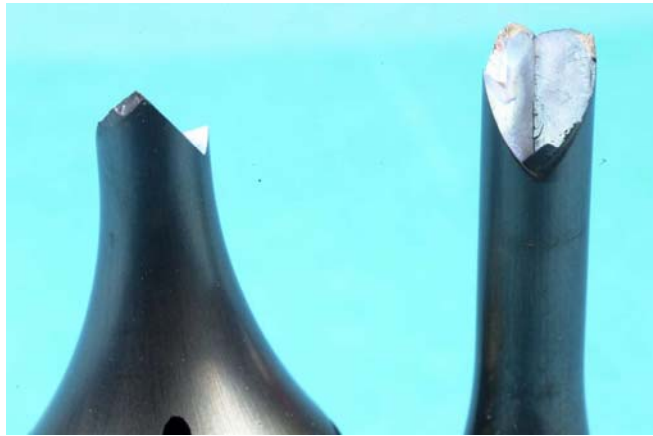
Figure 4.98. Fracture surface for R = -1; 1100°F; 1,612,914 cycles.
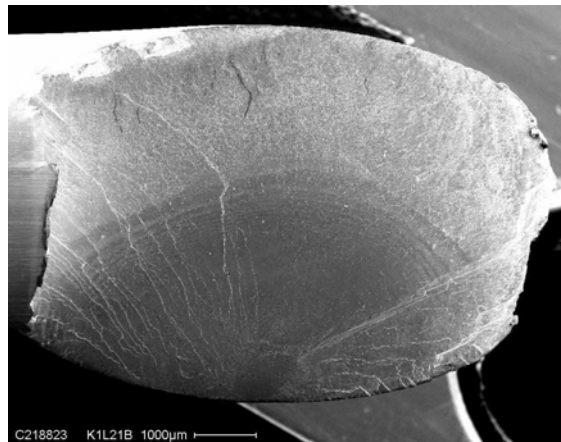
Figure 4.99. SEM of fracture surface for R = -1; 1100°F; 165,210 cycles.

Figure 4.100. Fracture surface for R = 0.1; 1100°F; 623,075 cycles.

Figure 4.101. Fracture surface for R = 0.5; 1100°F; 923,849 cycles.

B.   *Uniaxial Stress Ratio Effect Results at 1900°F*

The stress ratios examined for the 1900°F work were R = -1, -0.333, 0.1, 0.5 and 0.8. The data from the tests are presented in Table 4.21 and Table 4.22. These data are also presented graphically in Figure 4.102 and Figure 4.103, showing S_{max} vs. N and S_a vs. N response, respectively.

299

Table 4.21. Axial results at 1900°F. 59 Hz. R = - 1 and - 0.333.

Test Number	Specimen Number	R ratio	Diameter (in)	Stress Max (ksi)	Cycles	Results
2-02	KIL56B	-1	0.2005	54.0	205,482	Frac/Gage
3-02	KIL3WB	-1	0.2000	50.0	4,245,370	Frac/Gage
4-02	KIL6VB	-1	0.1998	46.0	8,941,513	Frac/Radius
8-02	K1L2BT	-1	0.2002	42.0	10,009,524	Removal
9-02	K1L7WT	-1	0.2003	46.0	5,679,517	Frac/Gage
12-02	K1L5LB	-1	0.1999	42.0	10,187,190	Removal
18-02	K1L9FT	-1	0.1998	50.0	1,264,133	Frac/Gage
32-02	KIL9GB	-0.333	0.2003	50.0	8,448,421	Frac/Gage
33-02	KILIYT	-0.333	0.2001	46.0	4,094,538	Frac/Radius
34-02	KIL2IT	-0.333	0.1997	46.0	4,911,837	Frac/Gage
35-02	KIL9GT	-0.333	0.1998	42.0	10,181,009	Removal
36-02	KILIPT	-0.333	0.2002	42.0	10,092,267	Removal
37-02	KIL66T	-0.333	0.2003	50.0	4,406,742	Frac/Gage

Table 4.22. Axial Results at 1900°F. 59 Hz. R = 0.1, 0.5 and 0.8.

Test Number	Specimen Number	R ratio	Diameter (in)	Stress Max (ksi)	Cycles	Results
1-02	KIL6GT	0.1	0.1998	64.0	1,348,227	Frac/Gage
6-02	KIL5VT	0.1	0.1997	60.0	2,948,910	Frac/Gage
5-02	KIL1BT	0.1	0.2005	68.0	523,034	Frac/Gage
7-02	K1L9TT	0.1	0.2004	56.0	4,269,687	Frac/Gage
10-02	K1L6JB	0.1	0.2004	52.0	6,879,073	Frac/Gage
11-02	K1L2CB	0.1	0.1999	48.0	10,073,210	Removal
13-02	K1L94B	0.1	0.2000	48.0	4,834,222	Frac/Radius
14-02	K1L4JT	0.1	0.2003	44.0	10,142,760	Removal
19-02	K1L5HT	0.1	0.2004	44.0	10,026,092	Removal
15-02	K1L59B	0.5	0.2005	56.0	2,418,868	Frac/Gage
16-02	K1L6TT	0.5	0.1998	52.0	3,670,069	Frac/Gage
20-02	K1L3XT	0.5	0.2004	44.0	8,633,021	Frac/Gage
23-02	K1L96T	0.5	0.2001	40.0	10,026,375	Removal
24-02	K1L9UT	0.5	0.2002	40.0	10,032,311	Removal

Table 4.22. Axial Results at 1900°F. 59 Hz. R = 0.1, 0.5 and 0.8 (continued)

Test Number	Specimen Number	R ratio	Diameter (in)	Stress Max (ksi)	Cycles	Results
25-02	K1L5XB	0.5	0.2001	44.0	8,618,224	Frac/Gage
30-02	KIL2NB	0.5	0.1998	60.0	1,194,767	Frac/Gage
31-02	KILA4B	0.5	0.2003	52.0	3,655,399	Frac/Gage
17-02	K1LA3T	0.8	0.1999	35.0	10,095,230	Removal
21-02	K1L7JB	0.8	0.2002	50.0	1,944,928	Frac/Gage
22-02	K1LA2B	0.8	0.2005	45.0	3,462,244	Frac/Gage
26-02	K1L1MB	0.8	0.2001	40.0	6,322,443	Frac/Gage
27-02	K1L67T	0.8	0.1998	35.0	10,328,912	Removal
28-02	KIL5WB	0.8	0.1997	40.0	5,876,726	Frac/Gage
29-02	KIL57B	0.8	0.2001	45.0	3,422,990	Frac/Gage
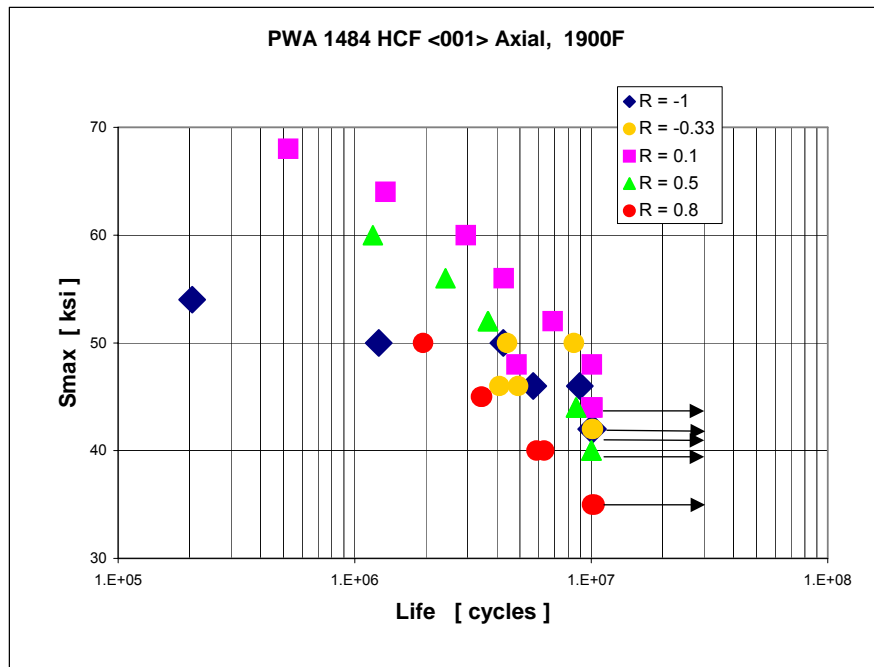
Figure 4.102. Plot of results of S_{max} versus N at 1900°F, Axial, all R's.
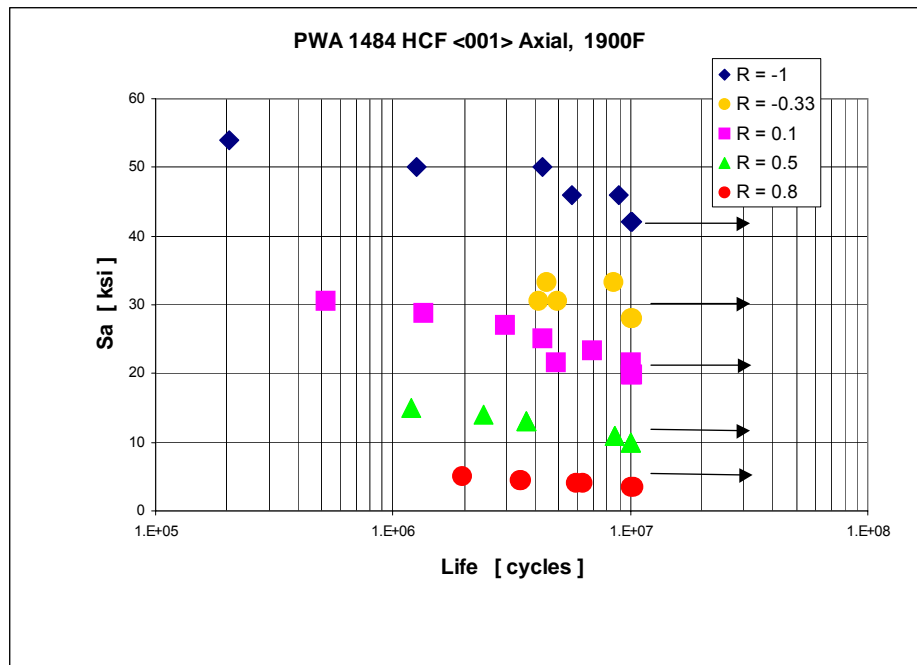
Figure 4.103. Plot of results of S_a versus N at 1900°F, Axial, all R's.

Fractographic work showed fatigue crack initiation originated at both sub-surface and surface locations with surface locations being more prevalent for the higher R-values. Typically, the sub-surface crack initiation sites were inclusion related. Figures 4.104 through 4.108, which are micrographs illustrating the fracture features for the 1900°F axial tests, demonstrate this trend. For the lower R-values, the fatigue induced cracks tend to be a significant portion of the overall specimen diameter. As the R-value is increased the classical fatigue crack zone decreases. At the highest R-value, 0.8, the fracture appearance is more indicative of creep rupture than fatigue. Clearly, at the higher R-values there is a strong fatigue-creep interaction taking place during testing.

Figure 4.104. Fracture surface for R = -1; 1900°F; 8,941,513 cycles.

Figure 4.105. Fracture surface for R = -0.33; 1900°F; 4,094,538 cycles.
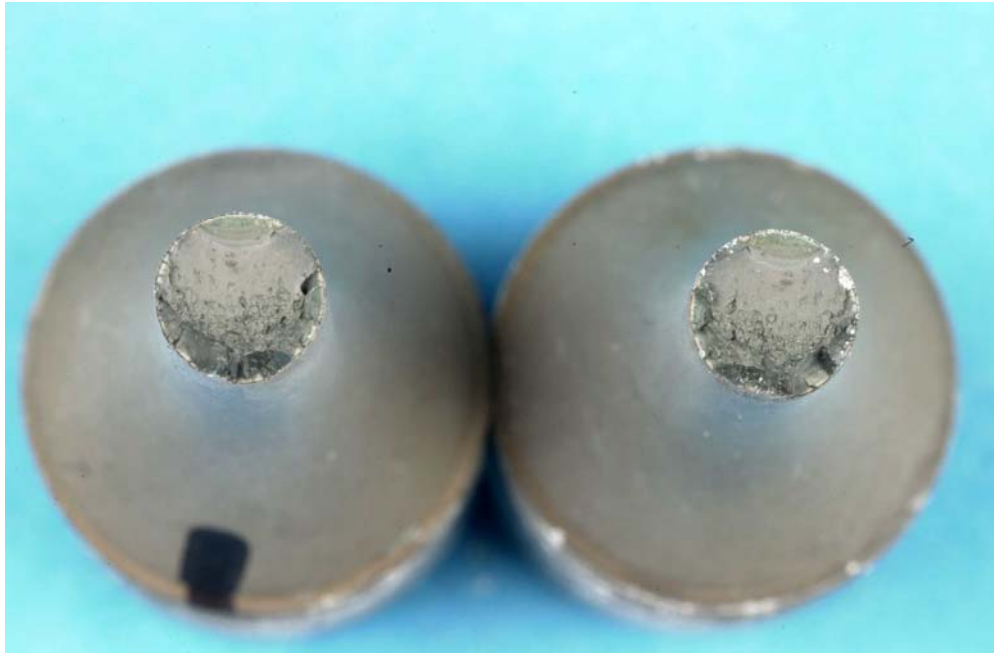
Figure 4.106. Fracture surface for R = 0.1; 1900°F; 6,879,073 cycles.

Figure 4.107. Fracture surface for R = 0.5; 1900°F; 3,670,069 cycles.

Figure 4.108. Fracture surface for R = 0.8; 1900°F; 3,462,244 cycles.

In addition to the 1100°F and 1900°F axial tests reported here, some axial-only tests were conducted in the tension-torsion rig. These tests, performed at 1100°F and R = 0.1 are documented in Table 4.19.

4.3.1.6 Creep Rupture

Because single crystal superalloys are subject to creep rupture damage and failure at high temperatures, creep rupture testing was performed on PWA 1484 specimens at 1900°F. A mixture of uncoated and coated specimens were tested, all of them of the type shown in Figure 4.76, that is, with 0.2 inch diameter cylindrical gage sections. Two methods were used; 1) conventional lever arm dead weight loaded creep stands and extensometry; 2) closed loop hydraulic fatigue test frames and side mounted extensometers. The latter were used because high quality creep data were also desired for constitutive modeling purposes. Several laboratories performed creep rupture testing: GEAE, Metcut, UDRI, and CTL.

Tests were performed at constant load at a range of stresses covering those expected to give failure in 10 to 200 hr. The discussion here will be focused on the <001> oriented

specimens; other orientations were also tested but these will be covered in the constitutive modeling Section 4.3.2.2. The rupture lives obtained are reported in Table 4.23 and are plotted against applied stress in Figure 4.109. The results showed a surprising amount of variation between sources, since it is generally considered that stress rupture behavior is less sensitive to test method than is fatigue, and that surface condition (coated or bare) is also usually less important in rupture. The most consistent set of results was obtained on coated specimens tested in closed loop machines at Metcut, and since this is the same specimen condition and test source as used for much of the HCF testing, it was considered to be the most likely to give results comparable to the HCF results. The coated Metcut rupture data were not significantly different than the bare Metcut data, lending support to the notion that stress rupture is not sensitive to coating. The coated Metcut data showed a power law dependence of time to failure on stress:

$$t_r = k_r \sigma^m \tag{4.26}$$

where, t_r is time to failure in hours, σ is stress in ksi, and k_r and m are fitted constants: $k_r = 2.19 \times 10^9$; m = -5.07 for PWA 1484 at 1900°F.

Table 4.23. Stress Rupture Lives of <001> PWA 1484 at 1900°

S/N	Surface	Source	Stress (ksi)	Rupture Time (hr)
A2LKW-1	Bare	CTL	35	19.3
TF1105	Bare	GE	35	11.6
TF1106	Bare	GE	30	50.1
TF1107	Bare	GE	25	91.7
A2LLG-2	Bare	Metcut	35	31.1
A2LLG-3	Bare	Metcut	35	33.7
A2LLG-4	Bare	Metcut	35	25.6
A2LLU-3	Coated	Metcut	35	34.4
A2LL9-2	Coated	Metcut	30	70.7
A2LLE-4	Coated	Metcut	33	42.4
A2LKV-4	Coated	Metcut	40	16.2
A2LKW-4	Bare	UDRI	35	17.6
A2LR3-4	Bare	UDRI	23	82.4
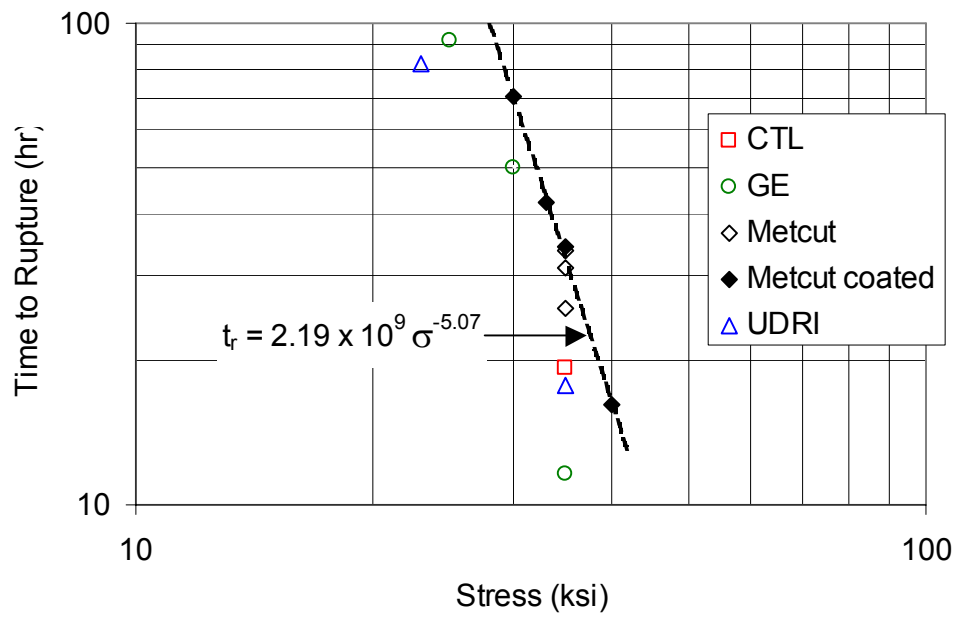
Figure 4.109. Dependence of stress rupture life of PWA 1484 on stress at 1900°F.

The typical fracture appearance of the stress rupture tested specimens is shown in Figure 4.110. The fractures were accompanied by extensive local deformation and necking, generating multiple surface connected cracks in the coating.

Figure 4.110(a) side view

Figure 4.110(a & b). Typical fracture surface of 1900°F stress rupture specimen showing necking and rough, dimpled surface.
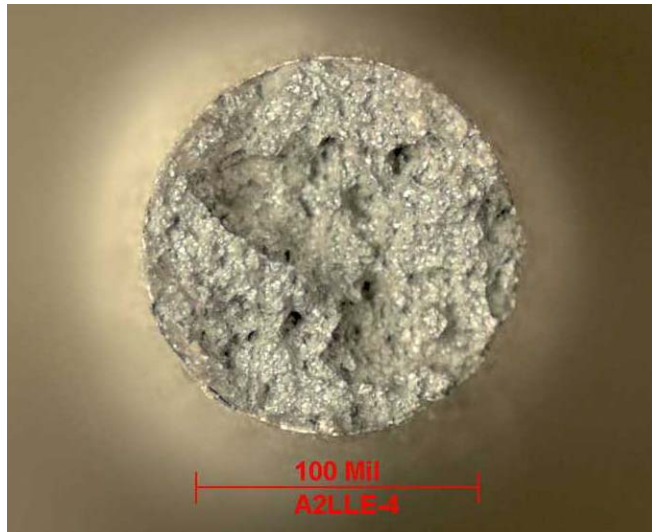
Figure 4.110(b) fracture surface

Figure 4.110(a & b).   Typical fracture surface of 1900°F stress rupture specimen
showing necking and rough, dimpled surface.

However, metallographic sectioning through the fracture, Figure 4.111, gave the
distinct impression that fracture initiated internally from multiple deformation-induced voids,
rather than from the coating cracks. The growth and link-up of such internal voids is a
classic ductile fracture process, and evidence of multiple void sites can also be seen on the
fracture surface, Figure 4.110.
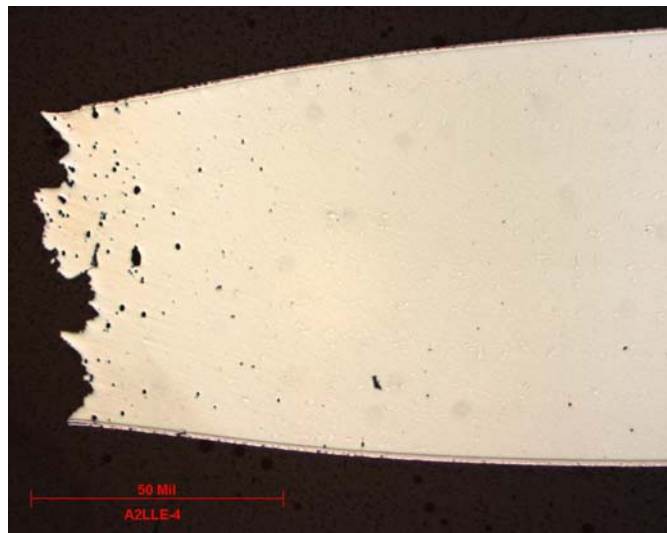
Figure 4.111.   Metallographic cross section of stress rupture
specimen showing necking and internal voids.

4.3.1.7   Torsional

        The intent of this portion of the program was to provide multiaxial results under select scenarios and to complement the modeling effort. The torsion-only tests were the first coupons tested using the Metcut equipment as documented in Section 4.3.1.4. Torsional test conditions were originally specified in conjunction with the other team members as part of the multiaxial activity to be done using uncoated samples at 1100°F. Eventually, the torsion testing evolved to include some work on coated samples at 1900°F per GEAE's request.

        Metcut's system produced a frequency of approximately 2 Hz for this work. Again for these tests runout was considered to be at 1 million cycles as opposed to the 10 million cycles used for the axial HCF work.

        All data are shown in the most straightforward, direct reporting of results, essentially as raw test information consistent with Honeywell's role in this effort.   Any utilization of the data is covered in the respective sections of this report dealing with modeling, etc.

      A. Torsional Results at 1100°F

        The conditions examined were fully reversed torsion (i.e. R = -1). The data gathered are presented in Table 4.24 and Figure 4.112.

Table 4.24. Torsional Results at 1100°F, Fully-Reversed Torsion

Test Number	Specimen Number	Diameter (in)	Axial Stress Max (ksi)	Shear Stress Max (ksi)	Cycles	Results
1-02	ZOK-HS	0.3631	0.0	60.0	505,419	Removal
2-02	ZOK-LY	0.3620	0.0	80.0	93,545	Fracture, GS
3-02	ZOK-FV	0.3628	0.0	78.0	248,084	Fracture, GS
4-02	ZOK-LM	0.3627	0.0	76.0	300,105	Fracture, GS
5-02	ZOK-HS	0.3631	0.0	90.0	63,192	Fracture, GS
6-02	ZOK-G5	0.3619	0.0	72.0	183,080	Fracture, GS
7-02	ZOK-H5	0.3632	0.0	72.0	207,009	Fracture, GS
8-02	ZOK-JZ	0.3620	0.0	68.0	1,011,198	Removal
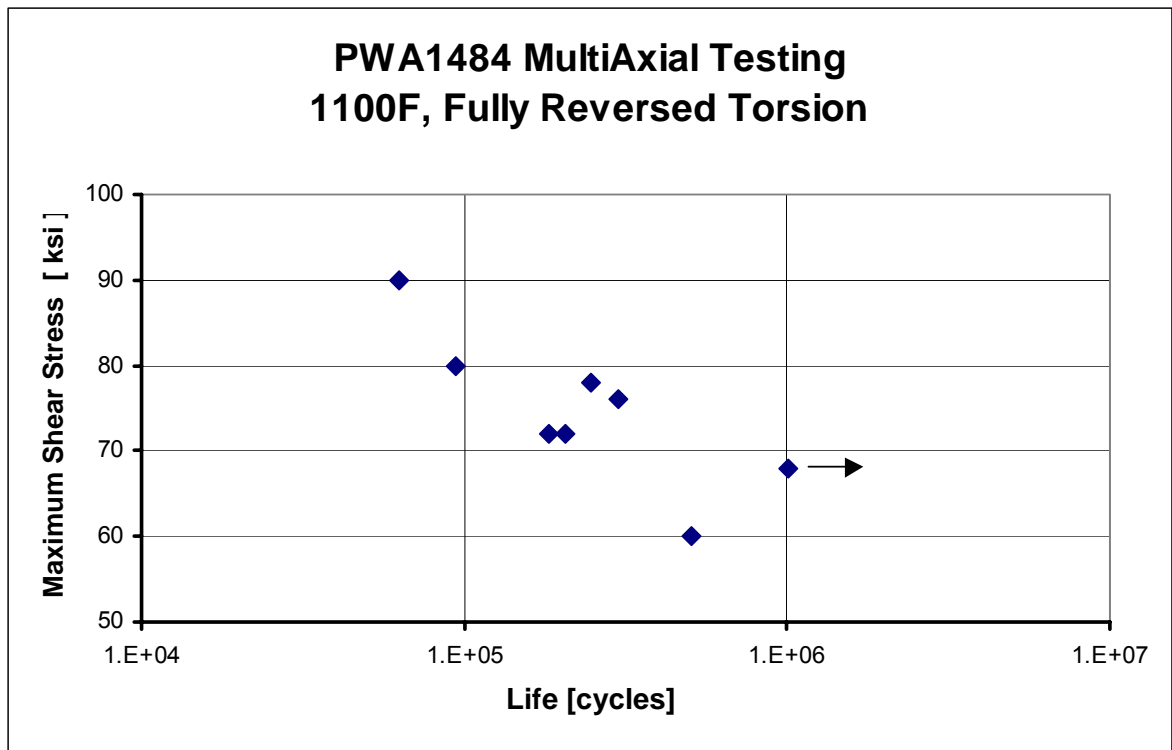
Figure 4.112. Plot of torsional fatigue results at 1100°F; fully reversed torsion.

As noted previously, as this work progressed, the modeling members of the consortium (particularly GEAE and PWA) were monitoring the data. They did not find good agreement with their efforts and the work was terminated. GEAE was interested in conducting some additional torsional fatigue tests at a higher temperature and those are shown in the following section.

B. *Torsional Results at 1900°F*

Tests at this temperature were conducted at the request of GEAE. To accomplish the test it was recognized that the test bars needed to be coated, so this was done using a compatible platinum aluminide and the bars re-aged appropriately. The load conditions examined for this part of the testing were only fully reversed torsion. The results of this testing are shown in Table 4.25 and Figure 4.113. Photographs of the broken specimens are shown in Figure 4.114.

Table 4.25. Torsional Results at 1900°F, Fully-Reversed Torsion

Test Number	Specimen Number	Diameter (in)	Axial Stress Max (ksi)	Shear Stress Max (ksi)	Cycles	Results
20-02	ZOK-FJ	0.3620	0.0	48.0	1,521	Yielded
21-02	ZOK-GG	0.3627	0.0	35.0	9,538	Fractured
22-02	ZOK-FU	0.3630	0.0	25.0	497,773	Fractured
23-02	ZOK-JN	0.3630	0.0	30.0	297,877	Fractured
				25.0	1,118,101	
	ZOK-J3	0.3630	0.0	30.0	206,106	Fractured
26-02	ZOK-H4	0.3620	0.0	35.0	89,512	Fractured
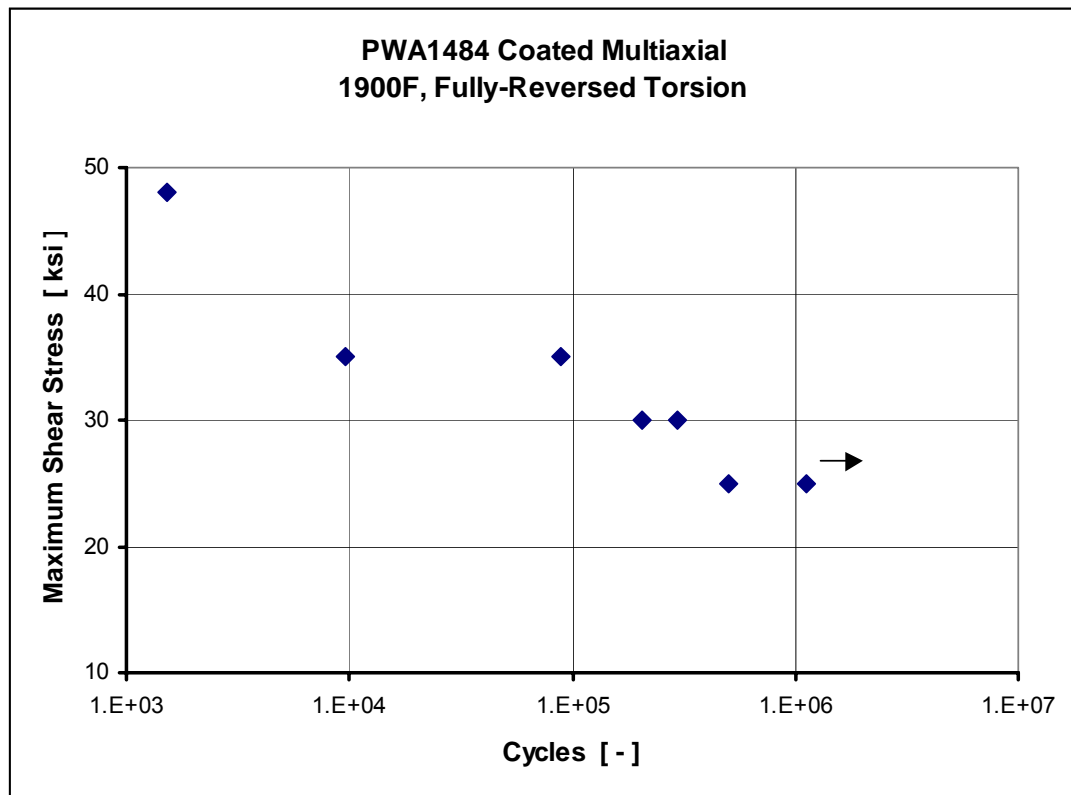
Figure 4.113. Plot of torsional fatigue results at 1900°F; fully reversed torsion.

In addition to the 1100°F and 1900°F torsional fatigue tests results, other related work was performed as part of the multiaxial effort including in-phase and out-of-phase axial-torsion tests. Those results were reported in Section 4.3.1.4, Multiaxial.

Figure 4.114. Photos of specimens fatigued in torsion.

4.3.2   Constitutive Modeling

4.3.2.1   Walker Model

Based on previous experience with modeling single crystal deformation, two existing constitutive approaches were selected for the prediction of PWA 1484 deformation, macromechanistic and micromechanistic. The macromechanistic approach is a phenomenological model which uses a fourth order tensor to invoke material anisotropy through the global stress-strain tensors. The micromechanistic approach is based on the

face-centered cubic microscopic slip theory developed by Dr. Walker for the NASA HOST program [60].

A. Constitutive Model Selection

Initially the macroscopic approach was favored because of its inherent computational speed advantage over the micromechanistic approach. The micromechanistic approach requires stress and strain transformation onto the twelve octahedral and six cube slip systems whereas the macroscopic approach works in the global system. As a result, the macroscopic approach is roughly three times faster computationally than the microscopic approach. However, further investigation of the macromechanistic approach indicated a significant shortfall in it applicability for combined normal and shear loadings such as occur in blade attachments. The available degrees of freedom afforded by the existing macromechanistic approach do not capture the correct anisotropic displacement field for all single orientations under shear loadings. Consultation with Dr. Walker subsequently indicated the macroscopic model would require a higher order displacement field capability (i.e., require up to a 6th order tensor transformation matrix) to predict the proper shear displacements for all single crystal orientations. This proposed correction to the existing macroscopic approach essentially negated its computational benefit over the microscopic approach and was considered risky relative to using the existing microscopic approach. The micromechanistic approach was therefore selected as the going-forward method for the single crystal constitutive modeling effort.

B. Constitutive Model Enhancement

The existing micromechanistic approach was available as a research software version, which relied upon multiple matrix manipulations and computations. By re-writing the matrix computations as explicit terms, the computational efficiency was significantly enhanced (it roughly doubled the computational speed).

The form of the constitutive model is based on the Walker Viscoplastic formulation, shown below. It is a power law relationship relating inelastic strain rate, $d\varepsilon^{in}$, to three state variables: deviatoric stress (σ), equilibrium (or back) stress (Ω), and drag stress (K). Written incrementally in one dimension,

313

$$d\varepsilon^{in} = \left(\frac{\sigma - \Omega}{K}\right)^{n} dt \,.$$

(4.27)

Evolutionary equations for Ω and K describe the change in state with inelastic deformation.

$$d\Omega = n_2 d\varepsilon^{in} - n_3 \Omega \left| d\varepsilon^{in} \right|$$

(4.28)

$$K = K_1 + K_2 e^{-n_7 |R|}$$

(4.29)

Ω governs the plastic deformation behavior including kinematic effects (evolution of the mean stress), and K defines the yield surface and isotropic characteristics, including hardening and softening.

The model details shown above are generic for one dimension. It must be pointed out that for single crystal modeling, state variable response is specific to each of the twelve octahedral and six cubic slip planes. Specific details on the application of this model to the PWA 1484 octahedral and cubic slip planes can be seen in [60], Figures 56-61.

C. Constitutive Model Constant Regression

The conventional means to obtain slip theory constitutive model constants for single crystal materials requires obtaining stress-strain behavior of <001> and <111> primary orientation test samples. Unfortunately, obtaining <111> test samples was not successful for the PWA 1484 material lot available. As such, an alternate constant determination method was developed to enable constant determination without obtaining <111> data. The alternate constant determination method uses an existing finite element (FE) code embedded within a nonlinear least squares constant regression routine to drive the constitutive model. By embedding the FE into the regression scheme, an alternate combination of two single crystal orientations can be used to determine model constants. The selected single crystal orientations should separate octahedral slip from cube slip to enable constant regression. One of the orientations should be <001> because a perfectly aligned <001> sample loads the octahedral slip systems, but not the cube slip systems. The second orientation should provide significant loading on the cube slip systems, such as <011>. The small deviations from perfectly aligned

314

crystal orientations are accommodated by the FE solution within the regression routine by inputting the actual test sample orientation.

Before attempting to regress constants for PWA 1484 using <001> and <011> data, a plan was in place to validate the regression method using existing PWA 1480 data. PWA 1480 constants derived from <001> and <011> data were in process when this effort was terminated. The validation strategy involved deriving PWA 1480 constants from <001> and <011> data to check the model prediction of <111> data. This was necessary since no PWA 1484 <111> data was forthcoming in this program. The validated method could then be applied to the <001> and <011> PWA 1484 data with some level of confidence in the model predictive capability for other orientations.

D. Experimental Data

The Experimental Mechanics group at the United Technologies Research Center performed monotonic and cyclic testing of PWA 1484. The table of completed and untested specimens is shown below.

Table 4.26. Completed and Untested PWA 1484 Specimens

Purpose	Primary Orientation	Degrees from Primary Orientation	Loading	#	Specimen
Calibration	<001>	2.7	Monotonic tension	1	001K1LAO
Calibration	<001>	6.7	Monotonic compression	1	001A2973
Calibration	<011>	8.6	Monotonic tension	1	011A296F
Calibration	<011>	5.8	Monotonic compression	1	011A295M
Calibration	<111>		Monotonic tension	1	(None)
Calibration	<111>		Monotonic compression	1	(None)
Calibration	<001> <001> <001> <001> <001>	0.5 0.7 2.7 not available not available	Complex cyclic	5	001A297A 001K1L5R 001K1L6D 001K1L9C 001K1L2U
Calibration	<011>	not available	Complex cyclic	1	011A296K
Calibration	<111>		Complex cyclic	1	(None)
Validation	<213>		Monotonic tension	1	(None)
Validation	<001>		Complex cyclic	1	(None)
Validation	<011>		Complex cyclic	1	(None)
Validation	<111>		Complex cyclic	1	(None)
Validation	<213>		Complex cyclic	1	(None)
Remaining	<001>	not available	Untested	1	001A2972
	<011> <011> <011>	not available not available not available		3	011A295Y 011A296D 011A296N

315

Buckling and compressive slip seen in the multiple strain end level cyclic test 001A297A prompted a redesign of the current MT-3 type specimen initially selected for data generation. The new specimen has a shorter gauge length in order to avoid buckling, but otherwise retains the same characteristics of the original specimen.

The data generated for this program is in Appendix S. In the <001> and <011> orientation, elastic-plastic behavior can be observed, with little monotonic hardening in either tension or compression (Figures S2 and S3 of Appendix S). Kinematic and isotropic hardening as well as an increased monotonic hardening slope is observed in the <001> complex cyclic tests (Figure S9 of Appendix S). Little difference is seen between monotonic and cyclic deformation behavior.

As of this date, monotonic testing for the <001> and <011> orientations is complete. In addition, the complex cyclic testing for these orientations is complete after multiple verification testing at the <001> orientation as seen above. Tensile and compressive tests for <111> and <213> were cancelled because available castings did not produce sufficient volume of consistently oriented material and other program priorities did not permit acquisition of replacement material.

4.3.2.2 1900°F Stouffer Model

A. Objective and Approach

PWA 1484 is a single crystal material with cubic symmetry for elastic response. The inelastic response of single crystal material can show considerable orientation dependence as well as tension/compression asymmetry [61]. The initial approach considered for constitutive modeling of PWA 1484 was to use the Stouffer-Dame-Sheh model [62]. The material test matrix was defined to provide the necessary input information to determine the parameters for model (primarily constant strain rate tests in tension and compression at several crystallographic orientations). Initial attempts to fit the parameters for the crystallographic unified model gave unsatisfactory results. A review of the available data indicated that the inelastic behavior for PWA 1484 at 1900°F was close to isotropic, so a simpler classical (separate plasticity and creep) approach was adopted.

B. Test Methods

Testing was performed at 1900°F on specimens cut from the three major crystallographic orientations: <001>, <110>, and <111>. Most of this testing was performed at UDRI, but the <111> tests were conducted at Cincinnati Testing Laboratory. The specimen geometry used for the UDRI test is shown in Figure 4.115. The long gage length provided high strain resolution, but did limit compressive strain levels to avoid plastic buckling. All specimens were tested in the uncoated condition. The absence of a coating was not expected to influence the constitutive response of PWA 1484.
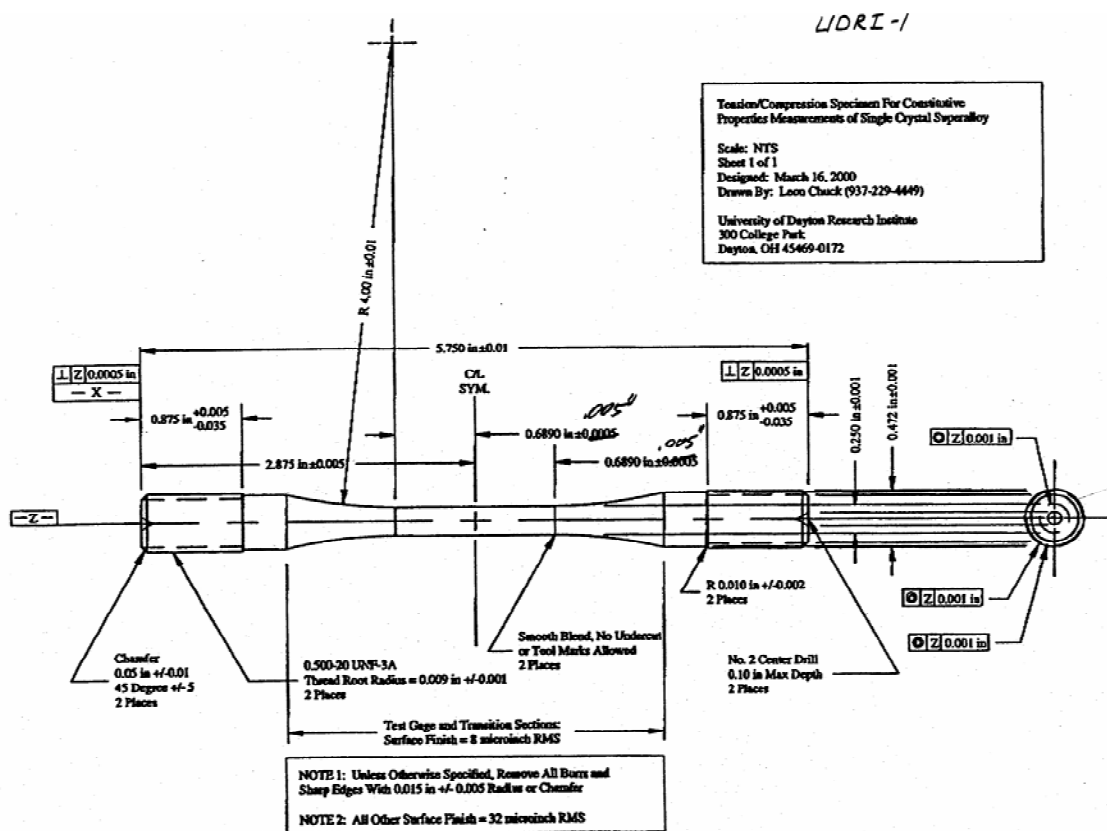
Figure 4.115. Large PWA 1484 specimen for 1900°F tension and creep testing at UDRI.

To prepare the test specimen for testing, two distinct points were identified at either end of the gage section. These markers are used as identifiers so any change in specimen length between them can be measured after testing is completed. The gage section

markers were made using a Rockwell Hardness Tester (Buehler, Model Macromet 3, S/N SUDX3266) set to the "C" scale. Two indents were made at the outside ends of the gage section ~ 2 inches apart. The specimen was supported using a small V anvil while being indented. After the indents were made, the distance between them was measured to the nearest 0.001-inch using a dial caliper (Brown & Sharp, Model 599-579-4, S/N 6P1750). A stereo microscope (Nikon, Model SMA-2T, S/N 314144) was used to check the alignment of the caliper jaws to the indents made in the specimen. The final preparation step was to coat the threaded portion of the specimen with boron nitride to ensure separation of the specimen and grip adapters after testing.

Preparation of the extensometer for testing required that the Instron strain controller and capacitive extensometer be calibrated. The Instron strain controller was calibrated by correlating the extensometer output voltages to the full range of the instrument. An extensometer extension of 0.0000 and 0.03937 inches (1 mm) was set to 0 V and 10 V, respectively. The extensometer signal conditioner was used to generate the 0 to 10 V signal. After the strain controller was calibrated, the extensometer calibration was checked and adjusted as needed. The extensometer calibration check was performed by displacing the extensometer, using a calibrating micrometer (Boeckeler Instruments, Model 4-MBR, S/N 19538), over the strain range of the test and comparing the extension to the strain controller output. The extension was checked every 9.84×10^{-6}-inches (0.25 mm). If the difference between the calibrating micrometer and strain controller readout was less than 0.5%, the extensometer was considered calibrated. If more than 0.5% error was noted, the extensometer signal conditioner was recalibrated. The extensometer readings were recorded in Excel.

The Instron Universal Tester (Model 8562, S/N H1004), fitted with Instron Corporation's reverse stress grips, also required pre-test preparation. The grips must be aligned with one another, and the load weighing system must be calibrated. This calibration was done automatically using the load controller. The grips must be aligned differently for tension and compression tests, and these two alignment procedures are described in the paragraphs that follow. In both tests, however, the bottom grip was aligned to the top grip.

Specimen A2LKK-1 was instrumented with eight strain gages for use during alignment. Four gages were oriented 90° apart around the center of the gage section. Two gages were oriented 180° apart above the gages at the center. The last two gages were oriented below the center gages 180° apart and 90° from the top gages. This configuration allowed the grips to be aligned both concentrically and angularly.

For tensile testing, the instrumented specimen was used to align the grips. The instrumented specimen was installed in the grip adapters, mounted in the top grip using three-piece copper collets, and allowed to come to thermal equilibrium. The load weighing system on the Instron was calibrated, and the eight strain gages were balanced to 0 με. The instrumented specimen was then installed in the lower grip using three-piece copper collets. The grips were first aligned angularly by pulling a small tensile load and balancing the center gages. The load was slowly increased to 1,750 lbs while keeping the four center gages balanced. The grips were then aligned concentrically by balancing the top and bottom sets of gages. When alignment was complete, the bottom grip was locked in position. The instrumented specimen was unloaded and then reloaded to 1,750 lbs (three times) to ensure there was no drifting of the grip alignment. Bending was kept under 0.5% during this procedure. When complete, the strain gage readings were recorded in Excel and the bending was calculated.

The test system was now ready for tensile testing. The instrumented specimen was removed from the test frame and the grip adapters were removed. The actual specimen to be tested was then installed in the grip adapters and mounted in the top grip using three-piece copper collets. The collets were kept in the same orientation they were in during the grip alignment procedure with the instrumented specimen. The Instron was calibrated and the test specimen was installed in the lower grip. The test specimen was loaded to a tensile load of 100 lbs. A pre-loading procedure, whereby the specimen was loaded from 100 to 800 lbs at a rate of 100 lbs/min, was completed to ensure the copper collets were seated in the radius of the grip adapters. The specimen was held at 800 lbs for 5 min and unloaded to 100 lbs at 7,000 lbs/min. The load was reduced to 10 lbs and the specimen was ready for testing. A photograph of the test setup is shown in Figure 4.116.
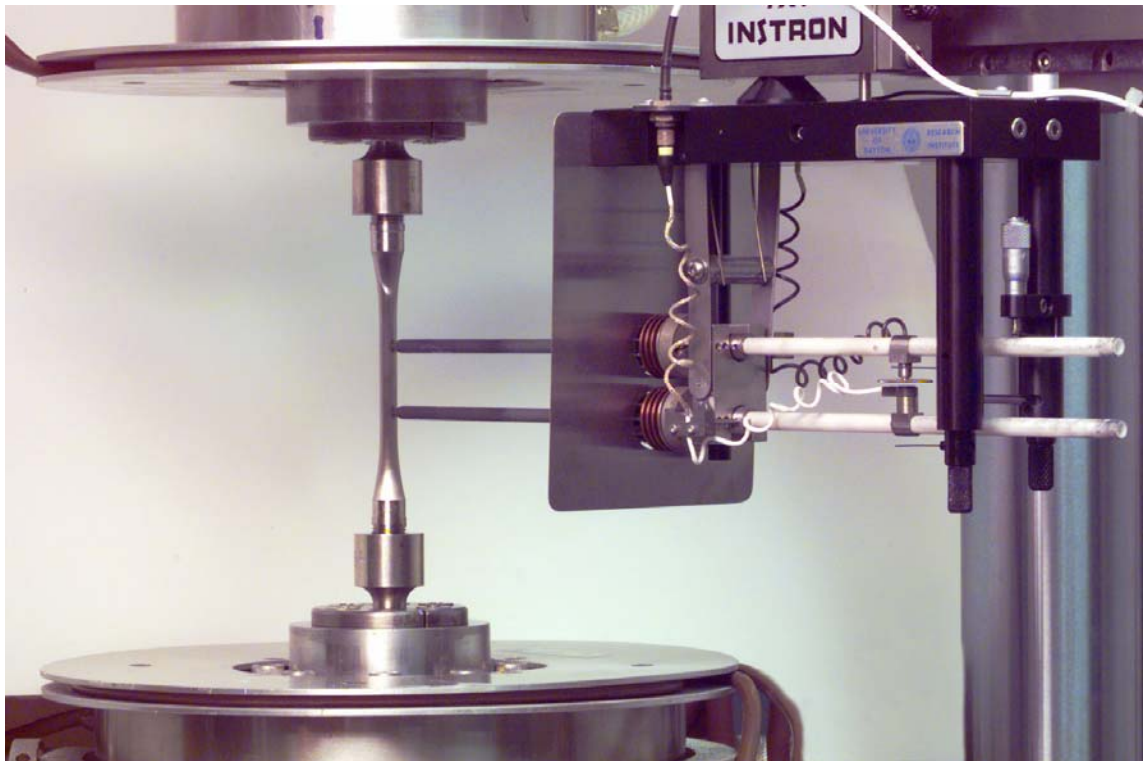
Figure 4.116. Set-up at UDRI for constitutive tests at 1900°F.

A slightly different method was used to align the test specimens for compression testing. The test specimen was put into the adapters and the orientation of the two adapters in relation to each other is marked. The instrumented specimen was then installed in the top grip with the two adapters in the same orientation to each other as marked using the actual test specimen. When the instrumented specimen reached thermal equilibrium, the strain gages were balanced and the load weighing system on the Instron was calibrated. The compression pistons in grips were actuated, and the specimen was aligned as described for tension. Alignment in tension set the angularity between the two grips. The instrumented specimen was then removed from the grips. Concentricity was aligned in compression using the Applied Test Systems (ATS) alignment fixture and the actual test specimen. The specimen was carefully screwed into the grip adapters and installed in the top grip so that all pieces were oriented in the same way as the original set up. The alignment fixture was then installed on the specimen and allowed to reach equilibrium. The four LVDTs were balanced

to 0 using the signal conditioner. The specimen was then installed in the lower grip. The compression pistons were actuated and the specimen was slowly loaded in compression to 250 lbs. The concentricity was adjusted, and the specimen was slowly loaded until further adjustment was needed. This process was continued to a load of 1,750 lbs for specimen A2LR3-2 and 2,500 lbs for the other three specimens. The adapters were changed between the first compression test and the three additional compression tests. The shaft length of the adapters was shortened to reduce the chance of buckling. When the specimen was at peak alignment load, the concentricity was adjusted to give 1% or less bending and the grip was locked in position. The specimen was unloaded and reloaded three times without further adjustment to check for 1% bending or better. If no further adjustment was necessary, the system was considered aligned. The specimen was then unloaded to 10 lbs (compression) and was ready for testing.

After preparing the specimen, extensometer, and test frame for testing, the furnace was turned on. A two-zone furnace was used with both zones set to 1900°F (1038°C). Once the furnace reached this temperature, it was left to soak for at least 30 min. The furnace was then opened, pulled around the specimen, and closed. Insulation was packed at both ends of the furnace to keep convection currents to a minimum. The specimen was held at 10 lbs during placement in the furnace and heating. As soon as the furnace was closed, the extensometer was inserted into the furnace, brought into contact with the specimen, and then backed off 1 to 2 mm. After the furnace recovered to 1900°F, it was held at temperature for 30 min before testing was initiated.

After the 30-min soak, the extensometer was set to the correct starting extension, brought into contact with the specimen, and the arms were released. The initial loading of the constant strain rate tests was controlled using Instron Corporation's Series IX software. The constant load tests were controlled using the function generator on the test frame load controller. All specimens tested in load control were loaded at 3,440 lbs/min (~70 ksi/min) to the test stress. Testing done with the Series IX software had the data collected in the software and used the data acquisition system. All testing that did not use Series IX had the data collected using the data acquisition system only. Strain control tests that went beyond the range of the extensometer were stopped and continued in position control. All testing in position control was executed using Series IX software.

After the test was completed, the furnace was opened and pushed back from the test specimen. The specimen was cooled to room temperature. The front of the test specimen shanks (top and bottom) were marked using a felt tipped marker. The specimen's front was defined as the point where the extensometer made contact with the test specimen. The test specimen was then removed from the grips and the grip adapters were removed. To preserve the fracture surfaces, the test specimen was returned to the original shipping sleeve with the threaded ends in contact with each other.

For <111> oriented specimens, no castings with <111> axes aligned parallel to the slab long axis were available. However, there were rectangular castings available with <001> long axes and <110> transverse in-plane axes. Blanks were cut from these at 54.7° to the <001> axis, giving a specimen axis of <111>. However, the 3-inch width of the castings kept the overall specimen length at about 3.5 inch. This was too small to make specimens of the type in Figure 4.115, but it was possible to fabricate slightly shortened cylindrical specimens of the type shown in Figure 4.76. These specimens could not be tested in UDRI's equipment, but were sent to CTL for testing. A <001> oriented specimen of the same geometry was creep tested at CTL and the creep response matched that of UDRI very closely, so the CTL results were judged to be comparable to those from UDRI.

The matrix of tests performed is shown in Table 4.27. It consisted of constant strain rate and constant load (creep) tests in the three major crystallographic directions. The constant strain rate tests were performed both in tension and in compression to check for the tension-compression anisotropy seen at lower temperatures. The constant strain rate tests were performed over a range of rates from 1×10^{-3} to 1×10^{-6} sec^{-1}. Most of these tests were performed out to a strain level of about 2% and then stopped and held at constant strain to generate stress relaxation information. The creep tests were usually performed at one stress, although in some cases where creep rates were low, the stress was increased after a period of time. Most creep tests were continued to failure.

Table 4.27. Matrix of Constitutive Property Tests Performed on PWA 1484 at 1900°F								
Test No.	**Specimen Axis**	Mode	**Direction**	**S/N**	**Strain rate (sec^{-1})**	**Max. stress (ksi)**	**Source**	**Comments**
1	[001]	const e-rate	tension	A2LKW-3	1.0E-03	54	UDRI	pulled to failure, total time = 0.062 hr.
2	[001]	const e-rate	tension	A2LKK-4	1.0E-04	63	UDRI	pulled to 2% strain and held at 2% for 9.9 hr. Re-zero'd and reloaded at 1x10-4 to failure. Extens. maxed out at 5.1%, time to failure = 0.72 hr.
3	[001]	const e-rate	tension	A2LR3-1	1.0E-05	55	UDRI	pulled to failure. Extens. maxed at 5.6% strain. Total time = 2.4 hr
4	[001]	const e-rate	tension	A2LKW-2	1.0E-06	42	UDRI	pulled to 2% strain in 5.56 hr and held for 1.1 hr. Total test time = 6.6 hr.
5	[001]	const e-rate	compression	A2LR3-2	1.0E-04	60	UDRI	strained to 2% in 2000 sec and stopped.
6	[001]	const e-rate	compression	A2LLK-2	1.0E-06	48	UDRI	strained to 2% in 20,000 sec, held at 2% for 11.7 hr. Total test time = 17.3 hr.
7	[110]	const e-rate	tension	Z1LBL-5	1.0E-04	71	UDRI	strained to failure with interruptions. No dwell at 2%. Total test time = .4 hr.
8	[110]	const e-rate	tension	Z1LBL-4	1.0E-06	49	UDRI	strained to 2%, then held at 2% strain for 12.5 hr. Total test time = 18.1 hr.
9	[110]	const e-rate	compression	Z1LBP-2	1.0E-04	72	UDRI	strained to 2%, then held for 10 hr. and unloaded.
10	[110]	const e-rate	compression	Z1LBL-3	1.0E-06	53	UDRI	stopped at 1.51% after 4.2 hr. No strain dwell.
11	[111]	const e-rate	tension	T20WT-5	1.0E-04	68	UDRI	strained to 4.3% in 449 sec. Slipped out of grip. Test stopped after 502 sec.
12	[111]	const e-rate	tension	A2LPR-1	1.0E-06	39	CTL	Tensile test to failure.
13	[001]	const load	tension	A2LKW-4	1.1E-07	35	UDRI	Ramped to 35 ksi in 30 sec. Crept at 35 ksi. Extensometer reached max travel at 15.8 hr. Specimen fractured at 17.6 hr.

Table 4.27. Matrix of Constitutive Property Tests Performed on PWA 1484 at 1900°F (Continued)								
Test No.	Specimen Axis	Mode	Direction	S/N	Strain rate (sec⁻¹)	Max. stress (ksi)	Source	Comments
14	[001]	const load	tension	A2LR3-3	4.8E-08	30, 23	UDRI	Ramped to 30 ksi in 27 sec. Crept at 30 ksi to 3.9% at 40.5 hr. Unloaded at 40.7 hr. Rezero'd time and strain scales. Reloaded at 23 ksi in 50 sec., Held at 23 ksi (extens. maxed out at 7.0% strain at 107.8 hr). Test continued at 23 ksi to failure at 117.4 hr.
15	[001]	const load	tension	A2LR3-4	2.1E-08	23	UDRI	Ramped to 23 ksi in 20 sec. Crept at 23 ksi (Extens max'd out at 7.5% at 81.5 hr). Specimen fractured at 82.4 hr
19	[110]	const load	tension	Z1LBP-3	6.9E-09	30, 35	UDRI	Ramped to 30 ksi in 26 sec. Held at 30 ksi for 26.7 hr, unloaded after .24% strain. Re-zero'd and reloaded to 35 ksi in 30 sec. Extens max'd out at 7.0% in 17.1 hr. Specimen fractured at 17.5 hr.
20	[110]	const load	tension	Z1LBP-1	1.2E-06	23, 30	UDRI	Ramped to 23 ksi in 20 sec. Held at 23 ksi. Reached 0.86% strain in 308.7 hr. Unloaded and re-zero'd. Reloaded to 30 ksi in 25 sec. Held at 30 ksi 5.3 hr, then unloaded, held at temperature until 17.0 hr. Re-zero'd and reloaded to 30 ksi in 30 sec. Extens. max'd out at 7.6% in 3.1 hr. Specimen fractured in 3.4 hr.
21	[111]	const load	tension	A2LPR-2	6.0E-06	35	CTL	Constant load creep test at 35 ksi. Failed in 28.4 hr.
22	[111]	const load	tension	A2LPR-3	4.8E-08	30	CTL	Constant load creep test at 30 ksi. Stopped after 39.9 hr.
23	[111]	const load	tension	A2LPR-4	1.8E-09	23	CTL	Constant load creep test. Stopped after 23 hr

C. Experimental Observations

The stress response obtained from all the tests is summarized in Figure 4.117. This figure shows the maximum stress obtained in each test as a function of the strain rate for that test. For the creep tests, the strain rate used was the minimum creep rate. Figure 4.117 suggests that the inelastic anisotropy of PWA 1484 is quite modest at 1900°F, since the data for all the orientations and stress directions (tension vs. compression) fall close to a single line. There is a slight tendency for the <110> orientations (blue, diamonds) to lie above the average trend line, and a slight tendency for the <111> orientations (red, triangles) to lie below it, indicating a small amount of anisotropy, but these differences are within the overall scatter of the population. The observation that the <110> direction tends to be the strongest is unusual; in nearly all other studies of strength anisotropy in single crystals, it is the weakest orientation.
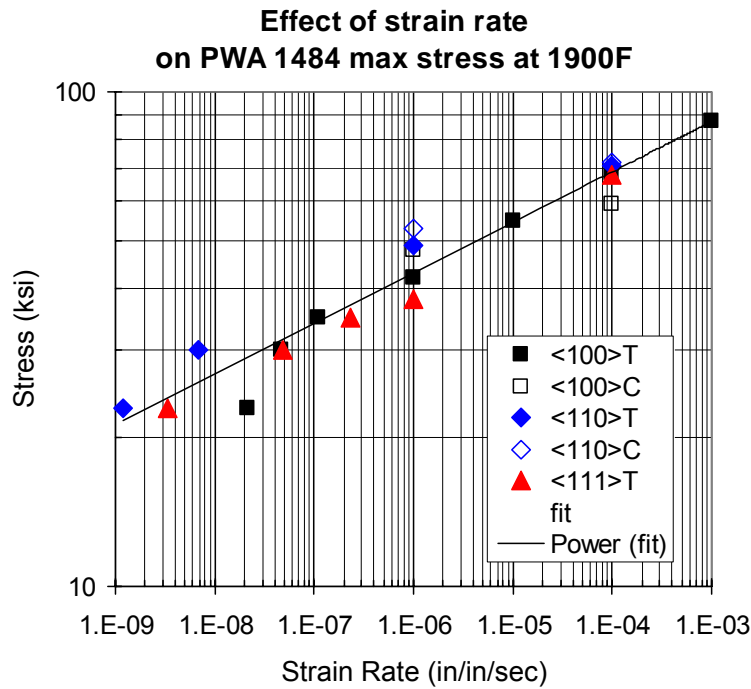
Figure 4.117. Effect of strain rate on maximum stress in PWA 1484 creep and tensile tests at 1900°F showing different orientations and loading directions (T= tension, C = compression).

D. Constitutive Model Comparison to Experimental Results

A comparison of the constitutive model predictions and strain control test data is included on the plots on the next several pages. Figures 4.118 and 4.119 show experimental data and constitutive model predictions for PWA 1484 at 1900°F for strain control tensile testing in the <100> and <110> orientations. Figures 4.120 and 4.121 shows similar comparisons for compressive testing. Figure 4.122 shows load control creep predictions and typical test data. In general the comparison is very good for the range of loadings (compressive and tensile at various strain rates) and the different orientations (<100> and <110>) for which test data was available. The most significant error was for the <100> compression test at a strain rate of 1E-4 inches/inch/sec. Note that the experimental results for <100> compression testing at a lower strain rate of 1E-6 inches/inch/sec matched fairly well with the model predictions, so the source of the error does not appear to be a general problem for predicting <100> compression behavior (test may be an outlier).
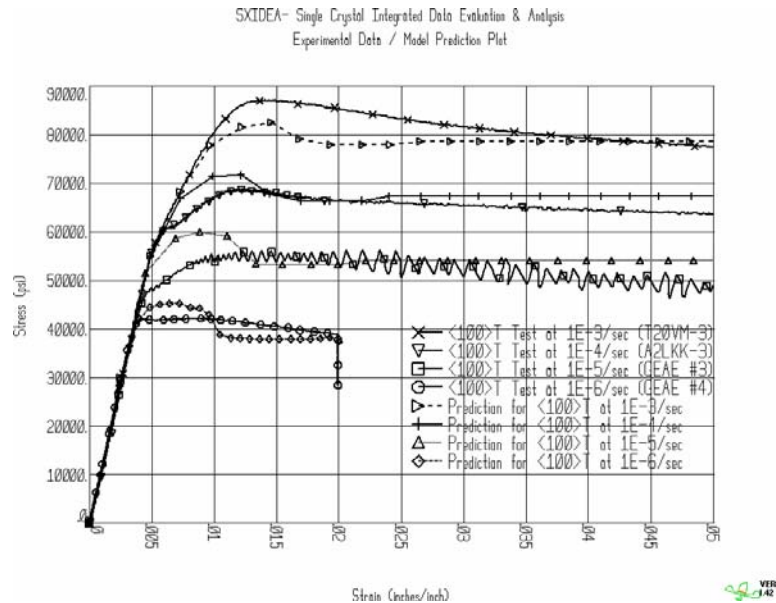
Figure 4.118. Experimental data and constitutive model predictions for <100> tensile tests at 1900°F for PWA 1484.
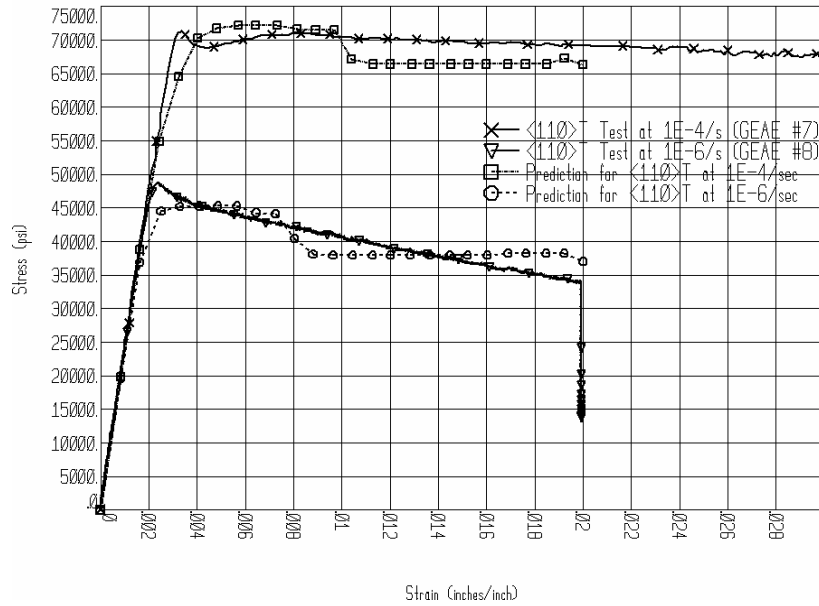
Figure 4.119.   Experimental data and constitutive model predictions for
                <110> tensile tests at 1900°F for PWA 1484.
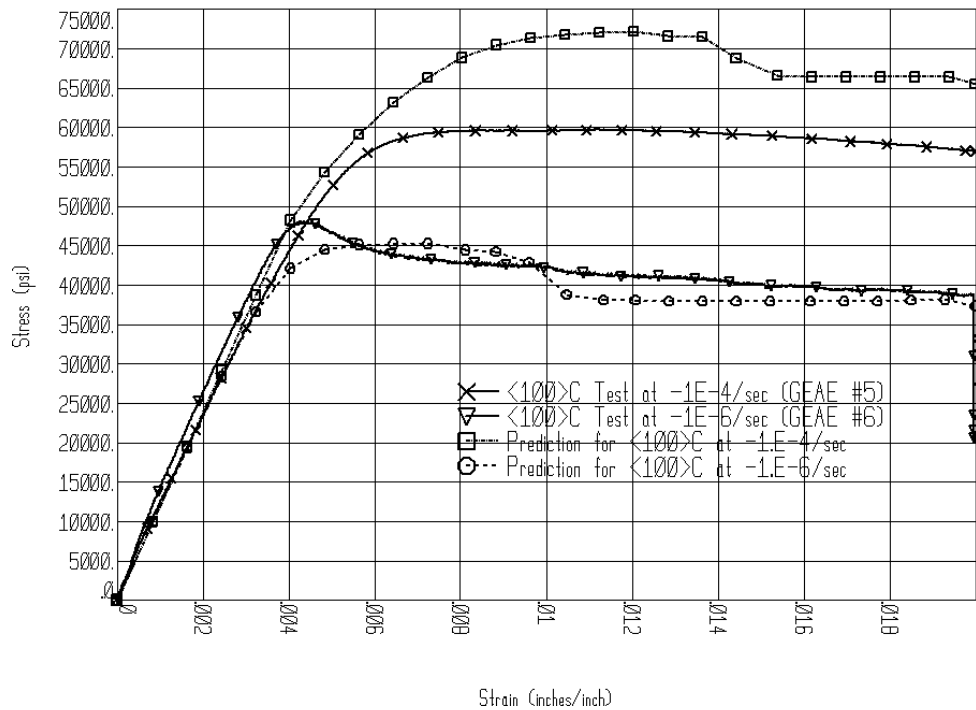
Figure 4.120.   Experimental data and constitutive model predictions for
                <100> compression tests at 1900°F for PWA 1484.

327
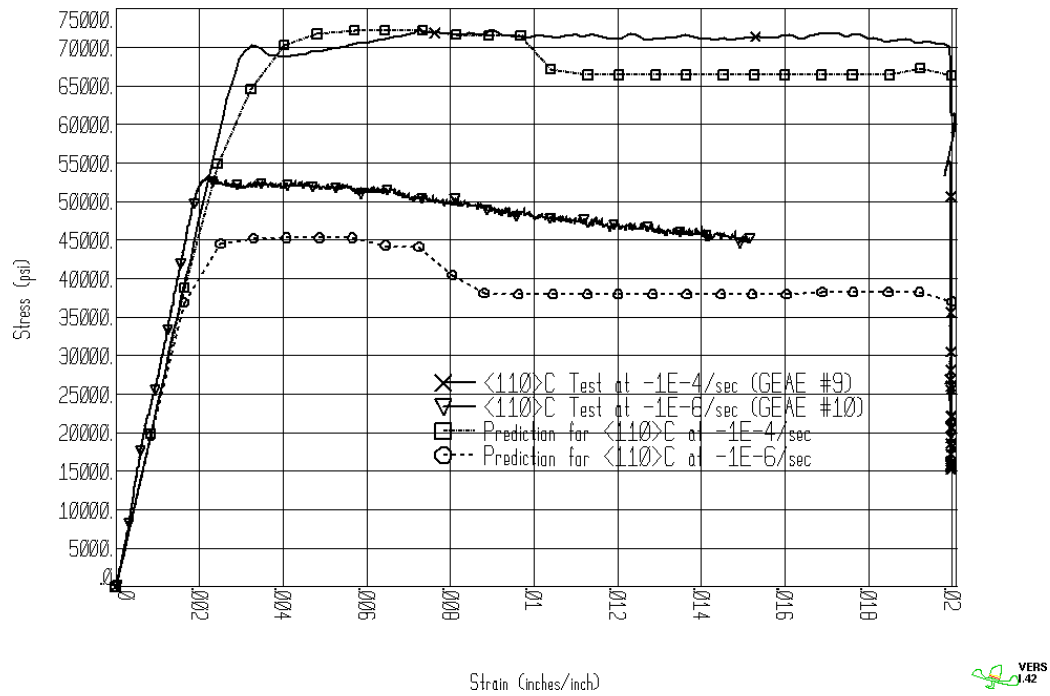
Figure 4.121. Experimental data and constitutive model predictions for
<110> compression tests at 1900°F for PWA 1484.
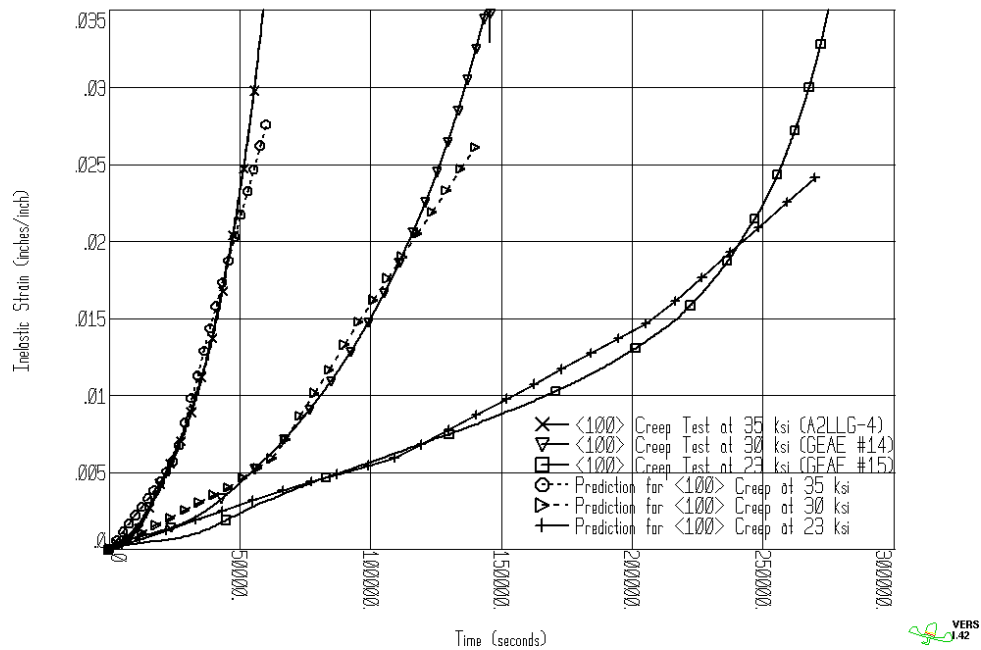
Figure 4.122. Experimental data and constitutive model predictions for
typical <100> creep tests at 1900°F for PWA 1484.

328

As a further demonstration of the capability of the constitutive model to describe the deformation at 1900°F, the fixed end fatigue crack growth test (T20VS-2) described in Section 4.2.2.2.*B* was analyzed. This test was performed as part of an effort to determine whether specimen creep was significantly affecting the stress intensity at the crack tip in the fixed end SEN geometry. The specimen geometry is shown in Figure 4.17. A 0.15-inch deep EDM notch was machined into one side of the gage section to simulate a fatigue crack. For this test a ½ inch gage length extensometer was placed across the EDM notch to monitor crack opening during the test. The specimen was loaded to a gross (unnotched) section stress of 15 ksi and held at constant load. At approximately 1-hour intervals the specimen was unloaded and reloaded to the same sress to check the elastic compliance to see if static crack growth occurred. No change in the slope of the unloading-loading stiffness curve was observed, but during the constant load dwells there was a significant amount of creep observed in the gage section.

Comparisons of the constitutive model predictions and measured deformation of the fatigue crack growth specimen are shown in Figure 4.123. This plot shows the baseline (1900°F) analysis slightly over-predicting the extensometer measurements. For this experiment, the temperature distribution in the gage was not perfectly uniform since an induction coil was used to allow the extensometer probes to access the specimen. Additional analysis assuming a uniform temperature of 1875°F matched the experimental measurements very closely. Measurement of the distortion of the fixed-end bar was also done after testing. In the notch plane it moved laterally about .005 inch. It also lengthened in the direction of load by about .0025 inch over a gage length of 0.389 inch along the bar centerline spanning the notch. Both of these post-test measurements are bounded by the analyses done at 1900°F and 1875°F. The correlation between the specimen analysis using the constitutive model and the experimental measurements appears to match within the expected data scatter, validating the constitutive model and analysis approach.
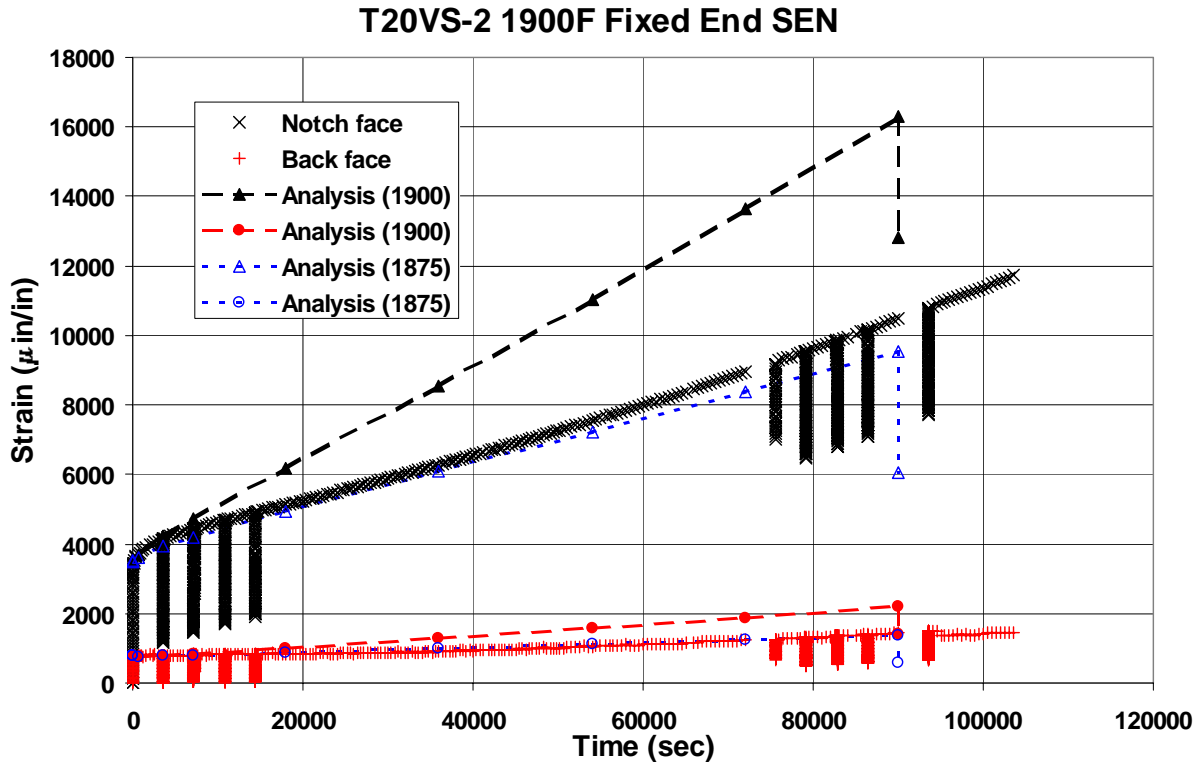
Figure 4.123. Experimental results and predictions for 1900°F fixed end SEN specimen.

4.3.3 Critical Plane Modeling

The objective of the critical plane modeling effort was to develop a failure mechanism-based approach, which also accounted for the micromechanics of the crystallographic slip deformation mechanism in a single crystal alloy. Several multiaxial critical plane fatigue damage parameters were calculated and evaluated based on how well they predicted the observed critical planes and also on how well they correlated the data for the different orientations.

4.3.3.1 Single Crystal HCF Failure Characterization

The fracture surfaces of all the smooth HCF specimens were studied using optical and scanning electron microscopy (SEM) to determine the failure mechanism. In all cases, octahedral slip was identified as the mode of failure based on the faceted appearance of the failure surface. The fatigue initiation site and the facet on which it

330

occurred was identified and marked for each specimen using a laser location technique together with X-ray diffraction measurements (see Appendix T). Table 4.28 summarizes the specimens, their orientations, the maximum cyclic stress levels, and the fatigue lives (Nf). Only the specimens that failed were considered in the present study.

Table 4.28. Summary of Specimens, Cyclic Stresses, Fatigue Lives, and Laue Angles

Orientation	Specimen ID	Max. Stress	Nf	Laue Angles, deg		
		(ksi)	(cycles)	δ	γ	β
<001+15>	T20WX-1	125	2.29E+04	-21.1	-13.2	29.2
<001+15>	T20WX-2	130	6.72E+04	26.4	2.1	-19.4
<001+15>	T20WX-3	120	5.94E+04	25.5	-3.1	-24.7
<001+15>	T20WX-4	115	1.69E+05	-22.3	-5.5	27.6
<001+15>	T20WX-5	135	1.39E+04	23.8	-9.4	-25.9
<001+15>	T20WX-6	125	3.62E+04	-23.1	-4.3	25.6
<001+15>	A2LLL-1	115	7.80E+04	11.1	-11.2	-38.5
<001+15>	A2LLL-2	112.5	6.97E+04	-9.9	-9.3	39.0
<010>	A2LKP-1	140	3.27E+04	0.9	1.8	44.3
<010>	A2LKP-2	130	1.77E+05	1.2	-0.6	-43.3
<010>	A2LKP-3	120	3.27E+05	-1.6	-1.5	45.4
<010>	A2LKP-4	125	6.66E+04	-1.6	-1.5	44.0
<010>	A2LKP-5	130	7.05E+04	1.5	1.1	-41.2
<010>	A2LKP-6	135	2.99E+04	0.5	2.4	41.4
<010>	A2LKP-7	120	6.26E+06	-0.1	-1.3	-36.4
<010>	A2LKP-8	117.5	7.54E+06	-1.9	0.1	-43.6
<001>	K1L1U-1	140	3.20E+04	1.3	6.3	42.6
<001>	K1L16-2	120	2.38E+05	1.6	-0.6	-42.6
<001>	K1L1H-1	130	9.86E+04	-2.4	-2.8	41.5
<001>	K1L1H-2	110	7.98E+06	2.3	-2.3	-40.7
<001>	K1L1V-1	120	1.73E+06	-2.9	6.2	-44.6

4.3.3.2   Critical Plane Analysis

The three Laue angles δ, γ, and β, measured in the failure characterization of each specimen formed the basis of the present analysis. These three angles provided the relationship between the loading axis (Z-axis or specimen axis) and the orientation of the single crystal axes in 3-D space. Using the applied fatigue stresses along the Z-axis, the stresses and strains in the crystal coordinate system were determined using 3-D transformation equations, which were based on the direction cosines derived from the three Laue angles. The stresses and strains in the crystal coordinate system were then

331

resolved along the octahedral planes and the 12 slip directions using a second set of transformation equations. These transformation equations and the direction cosines used in these equations are presented in Appendix U.

4.3.3.3   Critical Plane Models

Using these computed stresses and strains in the crystal coordinate system, it is possible to calculate multiaxial critical plane parameters to determine the amount of fatigue damage under a given set of applied cyclic stresses and strains. Six different critical plane models were evaluated in the present study. These were the Findley (FIN), Walls, Fatemi-Socie-Kurath (FSK), Shear stress range (SSR), Chu-Conle-Bonnen (CCB), and McDiarmid (McD) parameters. The Walls and SSR parameters had shown good correlation with single crystal LCF data in earlier studies. Details of the critical plane models and the critical plane search algorithms are given in Appendix V.

4.3.3.4   Results and Discussion

The critical planes determined by the different critical plane parameters are given in Table 4.29 along with the octahedral plane IDs on which fatigue initiation was actually observed. The four different octahedral planes are identified using the convention indicated in Figure 4.124. Some specimens exhibited fatigue initiations along the ridge formed by adjacent octahedral planes (Figure 4.125). Two or more octahedral initiation planes were reported for such specimens.

The specimens for which the predicted critical plane correlated with the observed plane have been highlighted for each different damage parameter in Table 4.30. Depending on the resolved stress and strain states on the octahedral planes, sometimes the parameters were found to be critical along more than one plane. The SSR and McD parameters had a greater tendency to become critical on multiple planes. The percent correlation for each parameter is indicated at the bottom of the table. All parameters had a correlation of at least 50% with the observed critical planes. The highest correlation was obtained using the CCB parameter, which uses an energy based formulation, followed by the Walls parameter, which tries to capture the mode mixity of the normal and shear strains on the octahedral planes. Both the SSR and McD parameters, which rely on the shear stress range along the slip directions were equally successful in

332

predicting the critical planes. Note that the McD parameter calculated using k = 0.1 was numerically very similar to the SSR parameter. The FIN and the FSK parameters, which use a combination of the shear stress range or shear strain range and the normal stress to determine the critical plane were only 50% successful in correlating with the observed critical planes.

The degree of correlation of the 'predicted' and the 'actual' critical planes is also a function of the statistical distribution of defects and their propensity to initiate fatigue damage on a certain octahedral plane. In the above correlation it is assumed that only defects along the 'predicted' critical planes lead to fatigue damage initiation. However, this approach neglects the statistical nature of the defect distributions. In Table 4.30, for example, the observed critical planes for three specimens (A2LKP-1, A2LKP-6, and K1L1U-1) were not predicted by any of the models. A combined statistical and micromechanical approach might be able to better capture the 'actual' phenomenon that leads to fatigue initiation in a single crystal material.

Table 4.29. Observed and Predicted Critical Octahedral Planes

Orientation	Specimen ID	Observed and Predicted Critical Octahedral Planes						
		Observed	FIN	WALLS	FSK	SSR	CCB	McD
<001+15>	T20WX-1	3	3	3	3	2	3	2
<001+15>	T20WX-2	1	1	1	1	4	1	4
<001+15>	T20WX-3	1	4	1	4	1	1	1
<001+15>	T20WX-4	3	3	3	3	2	3	2
<001+15>	T20WX-5	1	4	1	4	1	1	1
<001+15>	T20WX-6	3	3	3	3	2	3	2
<001+15>	A2LLL-1	1, 2	4	4	4	1, 3	1, 4	1, 3
<001+15>	A2LLL-2	3	3	3	3	2	3	2
<010>	A2LKP-1	4	1	1, 2	1	1, 2	2	1, 2
<010>	A2LKP-2	1, 2	4	1, 4	4	1, 4	1	1, 4
<010>	A2LKP-3	3, 4	3	3	3	2, 3, 4	3	2, 3, 4
<010>	A2LKP-4	3	3	3	3	2, 3, 4	3	2, 3, 4
<010>	A2LKP-5	1, 2	1	1	1	1, 2, 4	1	1, 2, 4
<010>	A2LKP-6	3, 4	1	1, 2	1, 2	1, 2	2	1, 2
<010>	A2LKP-7	1	3, 4	3, 4	3, 4	3, 4	4	3, 4
<010>	A2LKP-8	1, 2, 3	2, 3	3	2, 3	2, 3	3	2, 3
<001>	K1L1U-1	4	1	2	1	1, 2	2	1, 2
<001>	K1L16-2	1	4	1, 4	4	1, 4	1	1, 4
<001>	K1L1H-1	3, 4	3	3	3	2, 3, 4	3, 4	2, 3, 4
<001>	K1L1H-2	1	4	4	4	1, 3, 4	4	1, 3, 4
<001>	K1L1V-1	2	2	2	2	1, 2	2	1, 2
		% Correlation:	50.0	68.2	50.0	54.5	68.2	54.6
		Curve-fit, R^2	0.53	0.52	0.60	0.67	0.48	0.54
		Product	26.50	35.45	30.00	36.55	32.73	29.46

333

Octahedron viewed from Positive 3 -axis, <001>

Octahedral plane #3
<-1,-1,1>

Slip directions

Octahedral plane #2
<-1,1,1>

7

5

8

6

9

4

2 - axis, <010>

10

3

12

2

11

1

Octahedral plane #4
<1,-1,1>

Octahedral plane #1
<1,1,1>

1 - axis, <100>
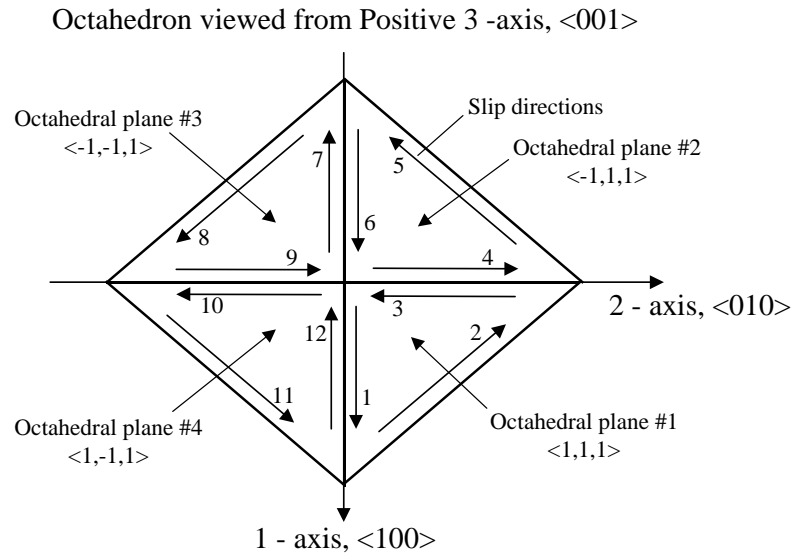
Figure 4.124. Plan view of octahedral <111> planes and <110> family of slip directions.

ORIGIN→

D:200×
P:100×   20.0 kV   100 μm   #0000*
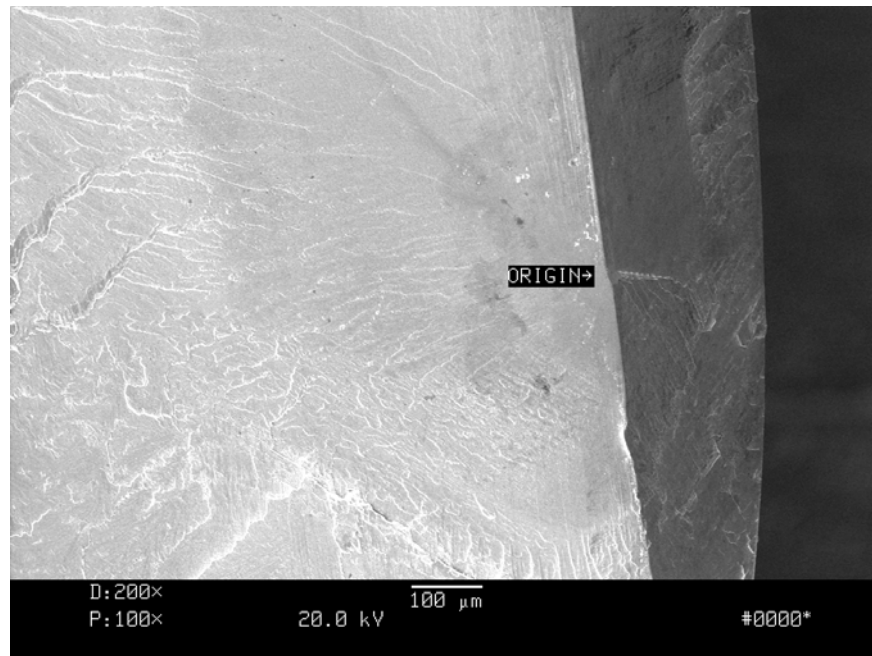
Figure 4.125. SEM photo showing fatigue initiation along ridge between
adjacent octahedral planes.

334

The different parameters were also evaluated by determining how well they were able to correlate the fatigue data for the different specimen orientations. Figure 4.126 graphically shows the HCF data in Table 4.28 as an S-N plot. Figure 4.126 clearly indicates that the traditional S-N approach cannot be used to correlate the fatigue data for the different specimen and loading orientations. It underscores the need for a new paradigm for the fatigue analysis of single crystal materials.

PWA 1484, Max Cyclic Stress versus Life, 1100 F, R = 0.1
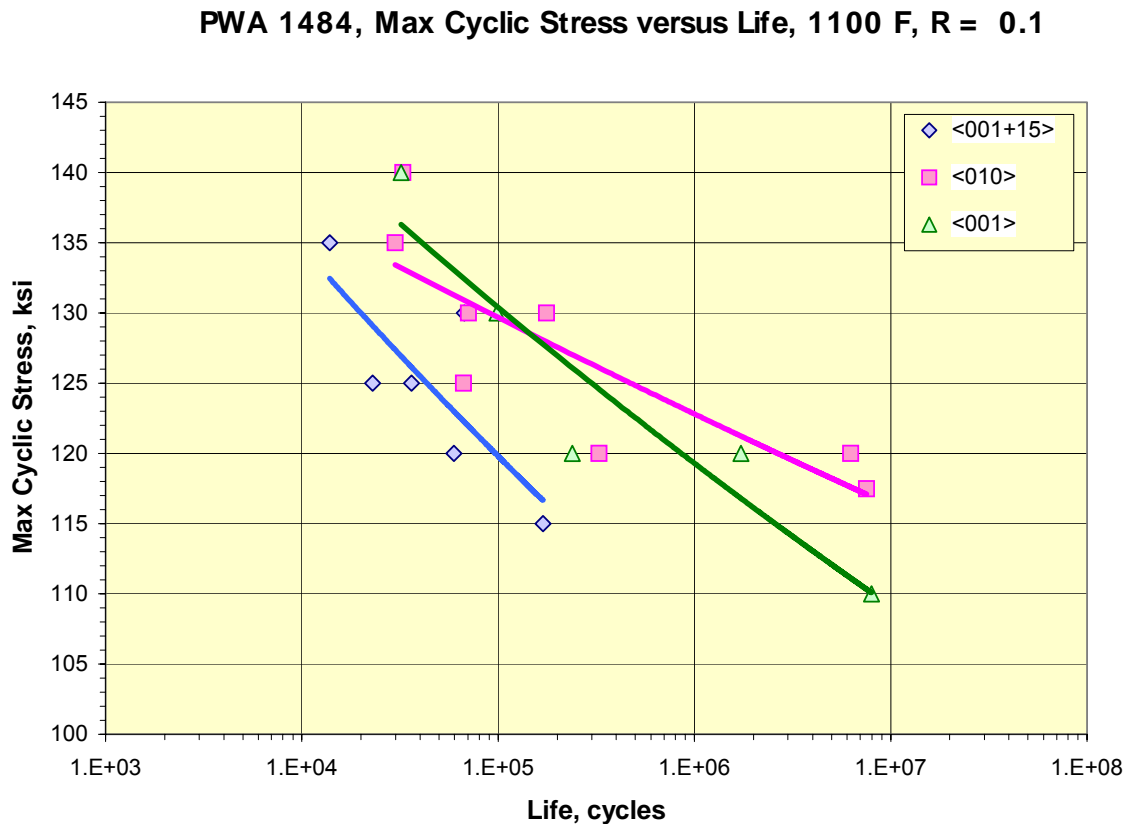
Figure 4.126. Max cyclic stress versus life for PWA 1484 at 1100^oF and R = 0.1.

Figure 4.127 shows a plot of the Walls damage parameter versus life for all the specimens using the applied cyclic stresses (from Table 4.28) and the measured crystal orientations (Table 4.28) for each specimen. The details of the analysis are given in Appendix W, along with the plots for the other damage parameters.

From an inspection of the results in Figure 4.127 (and Figures W1 through W5 of Appendix W), it appears that the SSR, CCB, McD, FSK and the Walls parameters were quite successful in correlating the fatigue data for the different specimen

335

orientations. The product of the correlation coefficient between the calculated and observed critical planes and the R^2 value of the damage parameter curve-fit to the fatigue data (see Table 4.29 and Appendix W) was used as a measure of how well the damage parameters performed. This evaluation indicated that the Walls, SSR, and CCB parameters were well suited for the HCF analysis of single crystal materials.

PWA 1484, Walls Damage Parameter versus Life, 1100 F, R = 0.1
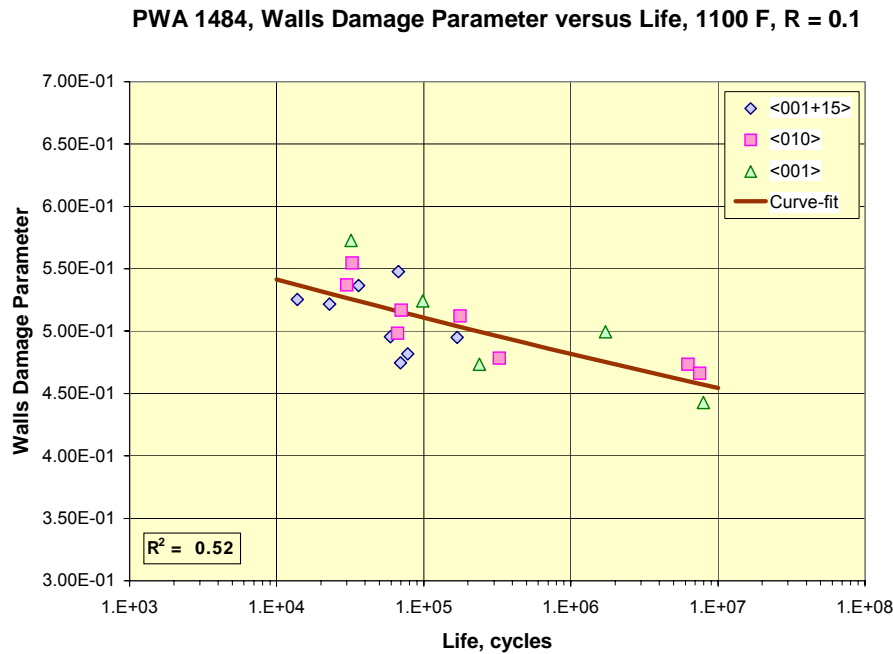
Fig. 4.127. Walls damage parameter versus life for PWA 1484 at 1100^oF and R = 0.1.

4.3.4   Stress Invariant Modeling

Because single crystal superalloys have anisotropic elastic and inelastic properties, their HCF behavior under complex loading conditions such as may exist in turbine blades bears examination. This section will examine one class of models for complex conditions, namely, stress invariant models. These models rely on the application of a single scalar quantity to represent the damage state of the material for an arbitrary loading, such as a multiaxial state of stress at a given orientation to the symmetry axes of the material, or even a uniaxial load applied at some orientation to the symmetry axes. One of the virtues of such models is their relative simplicity, and they are widely used for isotropic materials. However, their application to anisotropic

336

materials such as single crystal superalloys is less well established and will be examined here in view of the data generated in this program. The first section, 4.3.4.1, will examine the application of stress invariant models to complex stress states at 1100°F. The second section, 4.3.4.2, will be devoted to the application of these models at 1900°F and to the development of models for incorporating time dependent behavior into HCF at this high temperature.

4.3.4.1   1100°F

The most common evaluation of stress invariant models is done using data obtained from different stress states. Data from torsion, axial, and torsion + axial HCF tests on PWA 1484 were presented in Sections 4.3.1.7, 4.3.1.5, and 4.3.1.4, respectively. These results can be used to evaluate two simple models: effective stress, and maximum principal stress. The effective stress model assumes that at an equal level of effective stress the lives are the same, independent of the stress components that produced the effective stress. The effective stress is given by:

$$\sigma_{eff} = \frac{\sqrt{2}}{2}\left[\left(\sigma_x - \sigma_y\right)^2 + \left(\sigma_y - \sigma_z\right)^2 + \left(\sigma_z - \sigma_x\right)^2 + 6\left(\tau_{xy}^2 + \tau_{xy}^2 + \tau_{xy}^2\right)\right]^{1/2} \tag{4.30}$$

where, the normal stresses σ and shear stresses τ are in the specimen coordinate system (may be non-principal values). This is the most widely used model for isotropic materials. An alternate model is the maximum principal stress:

$$\sigma_{max} = \text{Maximum } (\sigma_1, \sigma_2, \sigma_3) \tag{4.31}$$

where, $\sigma_1, \sigma_2,$ and σ_3 are the three principal stresses derived from the stress state existing at the point of interest.

The stress states examined in Sections 4.3.1.4 and 4.3.1.7 include pure tension, pure torsion, in-phase torsion plus tension, and 90° out of phase torsion plus tension. The stress invariant models are evaluated for these as shown in Table 4.30. The first three loading states are straightforward; the last one requires attention because the shear and axial stresses are not proportional, but vary differently. Thus each point in the cycle needs to be checked to arrive at the maximum value of each of the models.

337

Table 4.30. Effective and Maximum Stress Models for Torsion and Axial Loading Conditions

Stress State	σ_z	τ_{yz}	Effective stress	Maximum stress
pure axial	$= \sigma_{axial}$	$= 0$	$= \sigma_{axial}$	$= \sigma_{axial}$
pure torsion	$= 0$	$= \tau_{torsion}$	$= \sqrt{3}\tau_{torsion}$	$= \tau_{torsion}$
torsion + axial, (in-phase)	$= \sigma_{axial}$	$= \tau_{torsion} = \sigma_{axial}$	$= 2\,\sigma_{axial}$ $=$ $2\tau_{torsion}$	$= (1 + \sqrt{5})/2\,\sigma_{axial}$ $= (1 + \sqrt{5})/2\,\tau_{torsion}$
torsion + axial, (90° out of phase)	$= \sigma_{axial}$	$= \tau_{torsion}$	$= \sqrt{3}\,\tau_{torsion}$	$= \sigma_{axial}$

For the cycle with equal torsion and axial stress applied 90° out of phase, the maximum effective stress occurs when the torsion is maximum, but the maximum principal stress occurs when the either the torsion or axial loading is maximum. Also, the effective stress never goes to zero in this cycle, since some component of load, axial or torsion, is always present, and the effective stress is not sensitive to the sign of the stress. However, since there is only one result for this cycle, and that one is a runout, it did not seem worthwhile to go into this cycle in great detail. Therefore only the maximum values in this cycle were used for comparison.

One further complication exists: some of the tests were performed at R = -1, while others were at R = 0.1. The pure axial results presented in Section 4.3.1.5 clearly show a stress ratio dependence of HCF at 1100°F.   Therefore the results were segregated by stress ratio and compared only within a given R.

The comparisons of different stress states are shown in Figures 4.128 through 4.131. At R = -1, three conditions were available for comparison: axial (at 59 Hz), torsional (at 2 Hz), and axial + torsional at 90° out of phase (2 Hz). When compared on the basis of effective stress, Figure 4.128, there is a distinct difference between the axial and torsional results, with the torsional loading showing greater capability than the axial loading. The axial + torsional 90° out of phase loading was also above the axial capability by an indeterminate amount. When these same results are compared on the

338

basis of maximum principal stress, Figure 4.129, the grouping is much tighter and if the runouts are ignored, the axial and torsional results fall on top of each other, suggesting that maximum principal stress governs HCF at this temperature.
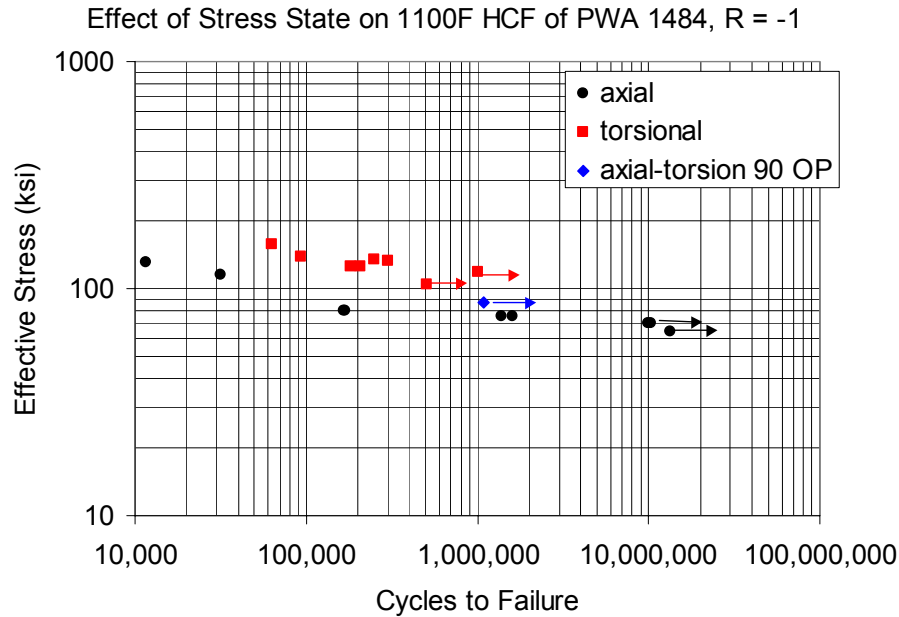
Figure 4.128.   Effect of stress state on 1100°F, R = -1 HCF of PWA 1484 using effective stress.
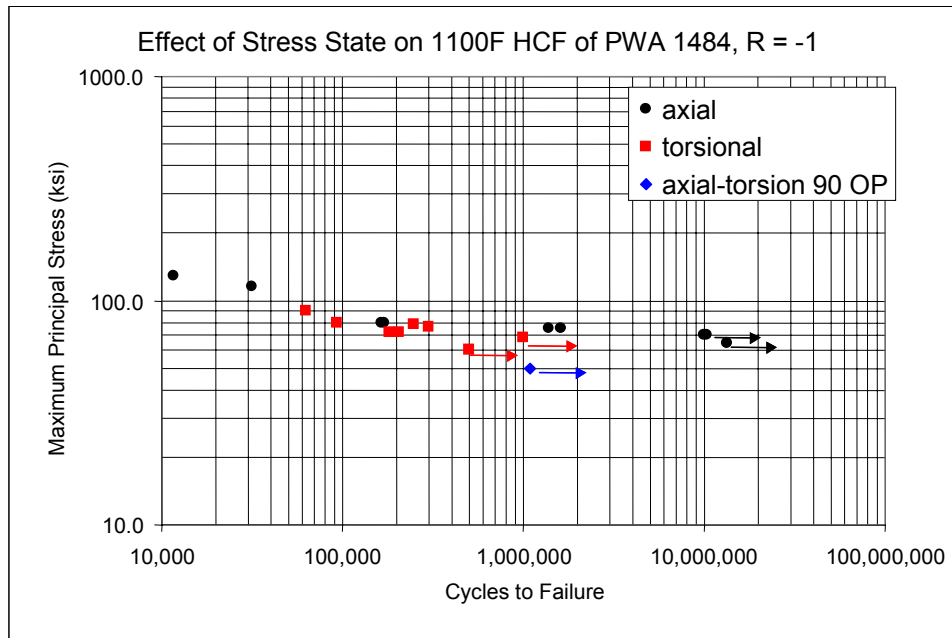
Figure 4.129.   Effect of stress state on 1100°F, R = -1 HCF of PWA 1484 using maximum principal stress.

The R = 0.1 results are similarly compared in Figures 4.130 and 4.131. While here neither model fully collapses the data as well as seen at R = -1, again the maximum principal stress model does noticeably better. Evidently the difference in frequency (2 vs. 59 Hz) between the axial and torsion results is not significant, since axial tests performed at 2 Hz on torsional specimens showed similar capability to the baseline 59 Hz results at R = 0.1. Therefore, it appears that maximum principal stress, and not effective stress, is the most suitable stress invariant model for evaluating stress state effects at 1100°F.

Effect of Stress State on 1100F HCF of PWA 1484, R = 0.1
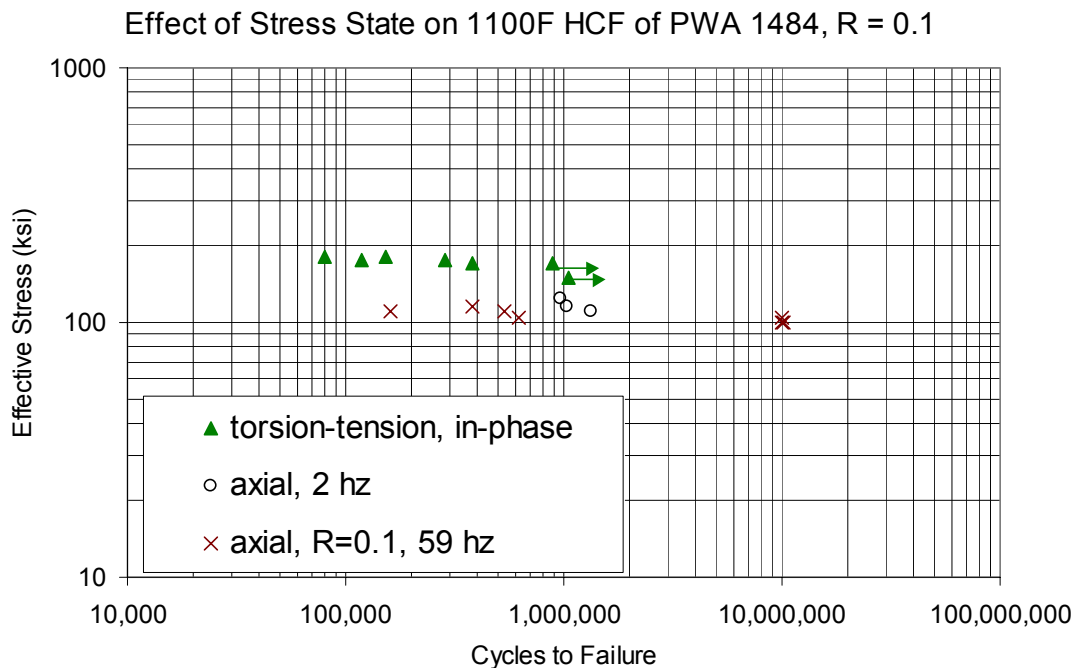
Figure 4.130. Effect of stress state on 1100°F, R = 0.1 HCF of PWA 1484 using effective stress.

4.3.4.2   1900°F

A less extensive study of the effect of stress state was performed at 1900F, as described in Section 4.3.1.7.*B*. Using these torsional and axial data, the effective stress and maximum principal stress models were compared as was done at 1100°F. Figure 4.132 shows the torsional and axial results compared on an effective stress basis and Figure 4.133 shows them on a maximum principal stress basis. At 1900°F the trend is

340
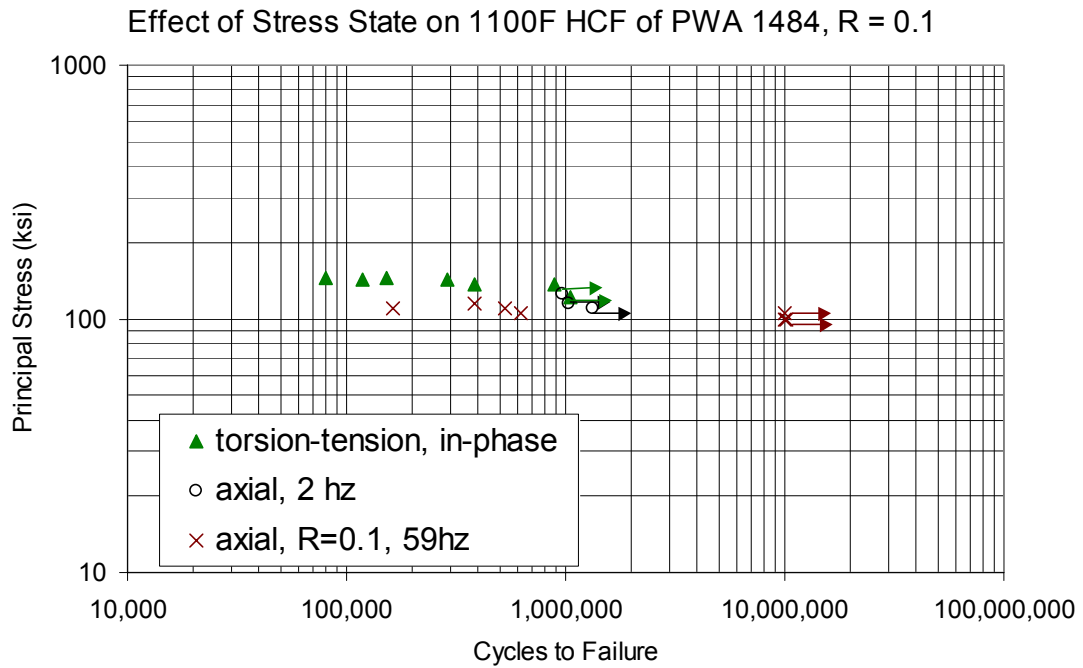
Figure 4.131. Effect of stress state on 1100°F, R = 0.1 HCF of PWA 1484 using maximum principal stress.
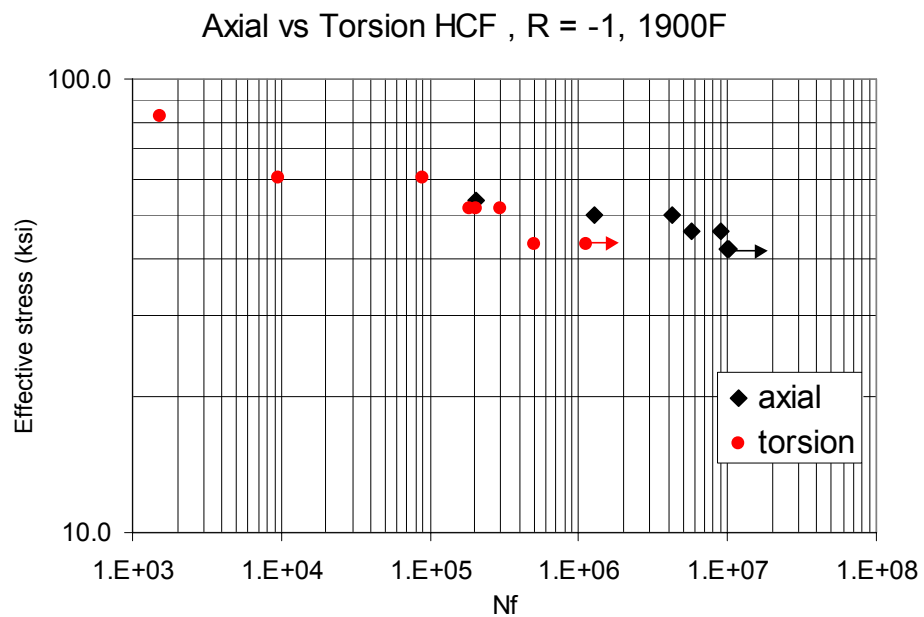
Figure 4.132. Effect of stress state on 1900°F, R = -1 HCF of PWA 1484 using effective stress.
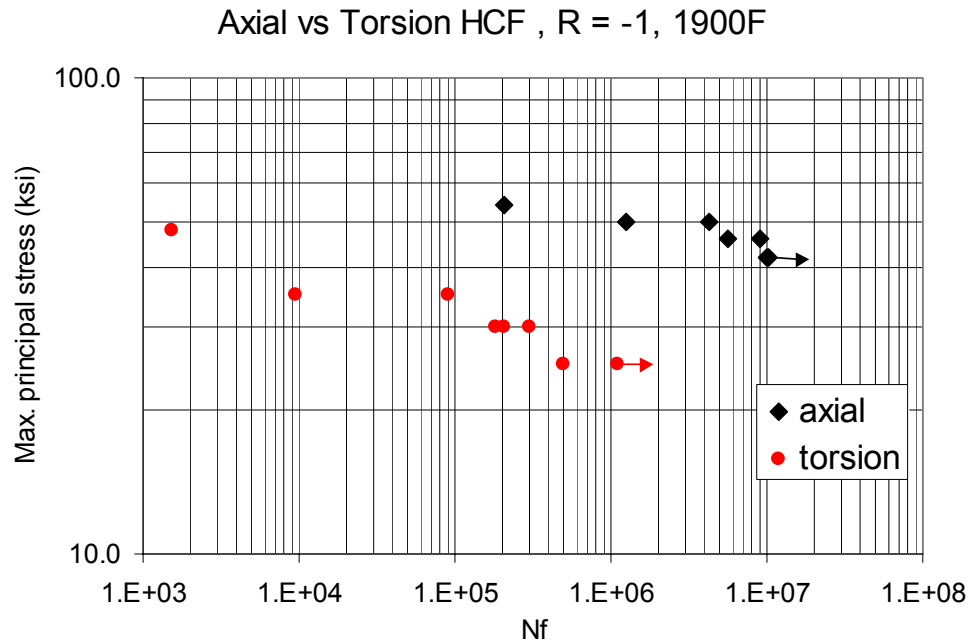
Figure 4.133.   Effect of stress state on 1900°F, R = -1 HCF of PWA 1484
using maximum principal stress.

just the opposite of that seen at 1100°F: At 1900°F effective stress collapses the axial and torsional results very well and the maximum principal stress model does not. Perhaps the change in behavior from 1100°F to 1900°F has to do with the changes in the nature of the deformation at the two temperatures. At 1100°F slip systems are more limited and slip occurs in intense bands on few planes. At 1900°F, additional (cube) slip systems are activated and deformation is more homogeneous. This is reflected in the constitutive behavior, which showed relatively little anisotropy at 1900°F. This more isotropic behavior at 1900°F may make its behavior more like that of polycrystalline isotropic metals which usually follow effective stress models.

4.3.4.3   1900°F HCF – Rupture Interaction

   A. *Objective and Approach*

       Typical turbine blade applications reach temperatures of 1900°F where time-dependent mechanisms, particularly creep, become significant. Creep can cause the initial mean stress levels created by a combination of centrifugal and thermal stresses to vary with time. Variable mean stress history and a high temperature environment

342

complicate prediction of the HCF capability of the blade. The objective of this study was to investigate models to predict HCF-rupture capability at 1900°F under such time-varying loading conditions.

The physical appearance of the crack surfaces from the baseline 1900°F HCF tests (Section 4.3.1.5.*B*) suggests that there are two distinct mechanisms responsible for failure at these test conditions. Figure 4.134 and 4.135 show typical fracture surfaces for a low R HCF test and high R test.
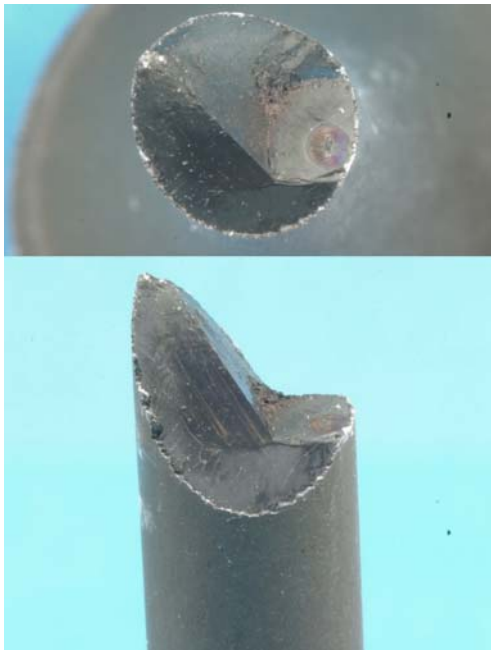
Figure 4.134. Typical Fracture Surface for Low R HCF Test, 1900°F, 59 Hz
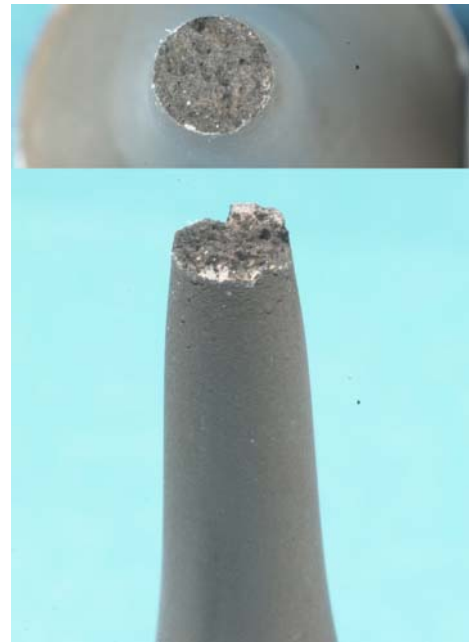
Figure 4.135. Typical Fracture Surface for High R HCF Test, 1900°F, 59 Hz

At low mean stress, the failure process appears to be dictated by fatigue whereby a single crack initiates and grows to critical size. A rupture-like failure mechanism involving internal voiding and necking appears to dominate at high mean stress conditions. At intermediate stress ratios, failure is probably due to some combination of both fatigue and rupture processes.

Based on these observations, the fatigue and rupture behavior of the material were modeled independently. The two models were then combined linearly to create a mean

stress dependent model for the material applicable to all regimes of the Goodman diagram. The fatigue capability of the material was represented with a Walker model. To model the rupture capability of the material, two primary models were considered: 1) a mean stress rupture model and 2) a cumulative summation of rupture damage model as described below. The linear combinations were used to back-predict life for all tests that were performed.

Data from the baseline HCF testing at 1900°F (Section 4.3.1.5.*B*), 1900°F rupture tests (Section 4.3.1.6), and 1900°F frequency effect HCF data at R = 0.1 and R = -1 (Section 4.3.1.2.*B)* were used in generating the models. Additional tests with more complex load histories were also performed to assess the capability of the models. Results for these tests will be given in Section 4.3.4.3.*D*.

B. 1900°F Goodman Diagram and Walker Model

A Goodman diagram was constructed at a life of ten million cycles based on the 1900°F HCF test data presented in Section 4.3.1.5. The stress-life behavior was characterized for each stress ratio using a power law relationship:

$$N_f = k\sigma_{alt}{}^m \tag{4.32}$$

Data was used only from <001> oriented specimens with the exception of eight specimens oriented at <001+15> that were tested at a stress ratio of 0.8. The <001+15> oriented data fall on top of the <001> data and consequently were included in the data set to characterize the R = 0.8 stress-life behavior. Values for the constants k and m for each tested R are shown in Table 4.31, along with the standard error, S_e, in log life.

Table 4.31. Standard Errors for S-N Empirical Fits at 1900°F

R	m	k	Se
-1	-12.4	2.0E+27	0.290
-0.333	-3.0	1.9E+11	0.173
0.1	-5.9	5.6E+14	0.177
0.5	-4.9	1.0E+12	0.084
0.8	-7.5	1.9E+11	0.144

The standard error for each fit was determined using the following formula:

$$S_e = \sqrt{\frac{\Sigma\left(\log N_{pred} - \log N_{obs}\right)^2}{N-2}}$$

(4.33)

where, N is the number of tests and 2 is the number of constants in the model.

Using the empirical S-N relationships, a Goodman Diagram was constructed at a life of ten million cycles (Figure 4.136).
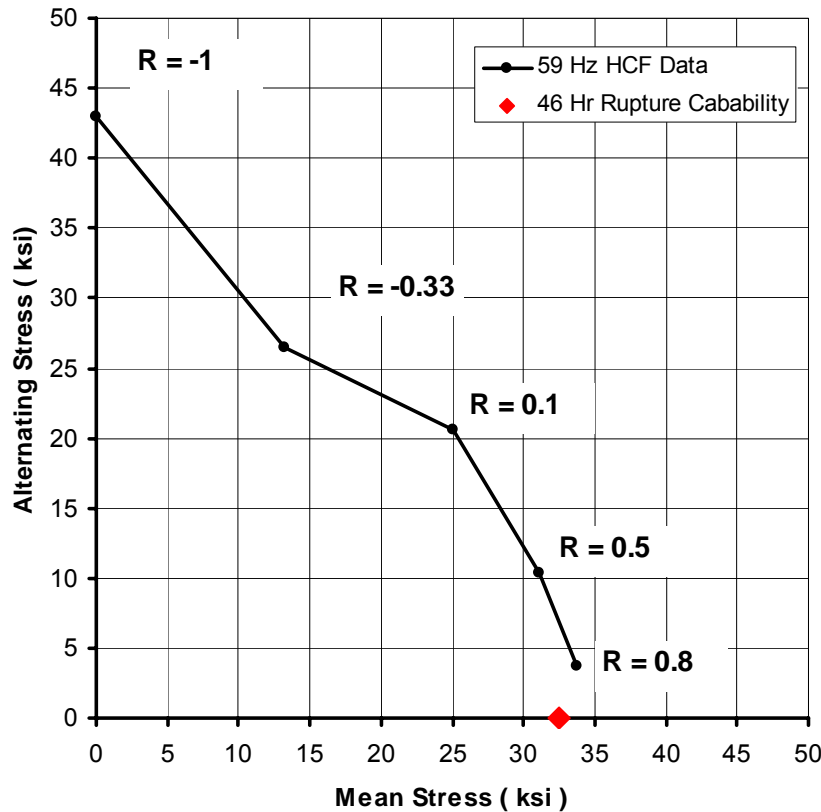
Figure 4.136. 1900°F Goodman Diagram for PWA 1484, 10 Million Cycles.

The Goodman Diagram shows the HCF capability of PWA 1484 at 1900°F for combinations of alternating and mean stress. The shape of the diagram is fairly conventional for single crystal superalloy. A gradual decrease in alternating stress capability is accompanied by an increase in allowable mean stress. Above a stress ratio of 0.5, the alternating stress capability drops off rapidly as the stress rupture capability is

345

approached. The stress rupture capability can be represented as an asymptote at R = 1 at 46 hours, the time for 10^7 cycles at 59 Hz.

A Walker model was used to represent the fatigue behavior of the material. In the Walker model, an equivalent alternating stress is defined to take into account different mean stress conditions. This equivalent alternating stress is then used in the stress-life power law relationship as shown below:

$$N_f = k\sigma_{equivalent\_alt}{}^m \tag{4.34}$$

where, the equivalent alternating stress is given by:

$$\sigma_{equivalent\_alt} = \sigma_{alt}(1-R)^{(w-1)} \tag{4.35}$$

$$R = \frac{\sigma_{min}}{\sigma_{max}} \tag{4.36}$$

The Walker exponent, w, was determined by taking data from several stress ratios and iterating until the standard error in predicted life was minimized. The Walker model collapsed the S-N response over a range of stress ratios. Normally, the Walker exponent is determined over the full range of stress ratio data that is available, in this case R = -1 to R = 0.8. However, the goal was to capture only those specimens failing in a pure fatigue mode. As evident by the HCF fracture surfaces, failure was dominated by fatigue at low stress ratios or low mean stress loading conditions.

Two approaches were considered for fitting the Walker model. The first (termed Walker Model A in what follows) used 59 Hz HCF data at all R ≤ 0.1. A second approach (Walker Model C) was examined because despite the fatigue based appearance of specimens at R = 0.1 tested at 59 Hz, the high frequency HCF results in Section 4.3.1.2 showed that a time-dependent process is present at this test condition. At a constant stress level at R = 0.1, fatigue life in cycles increased as the frequency was increased from 59 Hz to 900 Hz (Section 4.3.1.2). A linear line with a slope of 1:1 approximated the data fairly well indicating a fully time dependent process up to the highest frequency that was tested, 900 Hz. A transition to time-independent behavior with cycles to failure maintaining a constant level may exist just beyond 900 Hz or could

occur well beyond that frequency. As a result, the estimate of the Walker exponent for pure HCF may be affected by using the lower 59 Hz data. Therefore the second approach used only high frequency data (370-400 Hz) at R=0.1 in combination with 59 Hz data at R = -1 and R = -0.333 to represent time independent behavior. Walker model constants for each subset of HCF data are shown in Table 4.32.

Table 4.32. Constants for 1900°F Walker Models

Walker Model	HCF Data Subset	Number of Tests	K	m	Walker exponent, w	Standard Error
Walker A	R ≤ -0.1 @ 59 Hz	24	5.83E16	-7.17	0.165	0.27
Walker C	R ≤ -0.333 @ 59 Hz, R = 0.1 @ 370-400 Hz	20	7.63E16	-6.98	0.3817	0.33

In Figure 4.137, Walker Model A approximates the 59 Hz HCF data fairly well up to an R ratio of 0.1. Walker Model C shows a benefit in alternating stress capability at R = -0.333 and R = 0.1 compared to the other models. Both Walker Models deviate from the 59 Hz Goodman diagram above R = 0.1 as the mean stress increases and time dependent failure mechanisms reduce the cyclic capability of the material.

C. 1900°F Rupture Models

Two approaches were considered in modeling the rupture behavior of PWA 1484 at 1900°F. The first approach assumes that only the applied mean stress contributes to rupture damage. This approach will be referred to as the Mean Stress Rupture Model. The second method, the Cumulative Rupture Model, considers the summation of rupture damage from applied stress over the entire fatigue cycle.

The Mean Stress Rupture Model is represented by the expression in Equation (4.37) that relates mean stress to time to rupture. The expression was derived by fitting a power law relationship to the four tests that were tested at R = 1 until rupture. The equation is shown for reference:

347
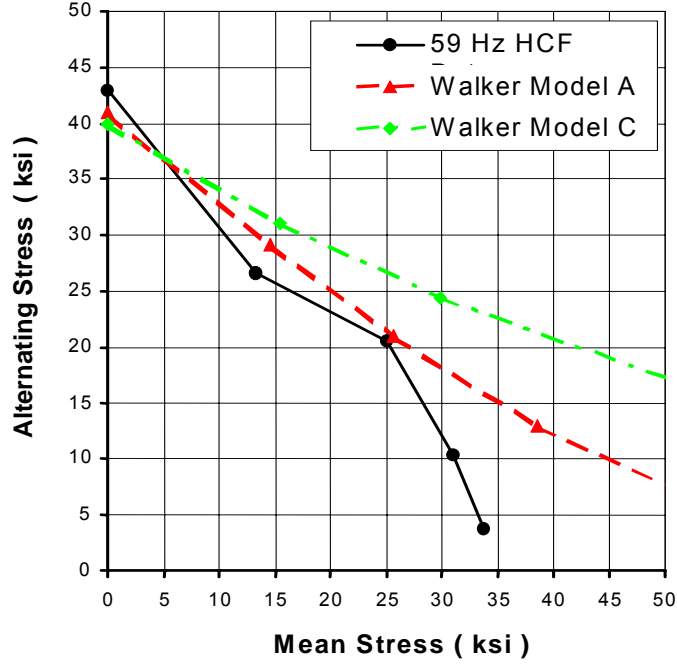
Figure 4.137. Walker Models A and C with 59 Hz 10^7 Cycles Goodman Diagram.

$$t_f = 2.19 x 10^9 \sigma_{mean}^{-5.069} \tag{4.37}$$

where, σ is the applied mean stress in ksi and t_f is the time to failure in hours.

In the Cumulative Rupture Model, the rupture damage due to the applied stress is integrated over the loading history. For a cyclic load, the applied stress is expressed as a sinusoidal function:

$$\sigma = \sigma_{mean} + \sigma_{alt} \sin(\frac{2\pi t}{\tau}) \tag{4.38}$$

where, τ is the period of the cycle in hours.

The load cycle is divided into small time increments, Δt. At each time increment, the applied stress is calculated and the corresponding rupture life is determined using Equation 4.35. The rupture damage for the time increment is calculated using the expression

$$D_{\Delta t} = \frac{\Delta t}{t_{rupture}} = \frac{\Delta t}{k\sigma_{\Delta t}{}^{m}} \tag{4.39}$$

Damage fractions for Δt are summed over the loading cycle. The number of cycles to failure can be calculated using the assumption that failure occurs when the rupture damage equals one.

$$D_{cycle} = \Sigma D_{\Delta t} \tag{4.40}$$

$$D_{failure} = 1 = N_f D_{cycle} \tag{4.41}$$

$$N_f = \frac{1}{D_{cycle}} \tag{4.42}$$

These calculations were performed in Excel or in a program written in BASIC. The period of the cycle was divided into one hundred time increments when using Excel.

When the stress ratio is less than zero, a portion of the loading cycle is compressive. Two scenarios were considered when applying the Cumulative Rupture Model: a) compressive stress is neither damaging nor beneficial to life, and b) compressive stress is damaging to life. As an example, consider a sinusoidal applied stress with mean stress of 5-ksi and alternating stress of 35-ksi. Using the cumulative rupture model when compressive stress does not contribute to damage the time to failure is 91 hours vs. 76 hours if compressive stress is considered damaging. The predicted time to failure is 627,140 hours using the mean stress rupture model where only mean stress contributes to rupture damage. In total, three rupture models were considered: mean stress rupture model, cumulative rupture without compressive damage, and cumulative rupture with compressive damage.

Figure 4.138 shows the rupture model predictions for a constant life of 10 million cycles at 59 Hz compared to the HCF test data. Both cumulative rupture models approximate the shape of the Goodman diagram. The mean stress model predicts a mean stress of 32.5 ksi independent of R for 10^{7} cycles at 59 Hz.
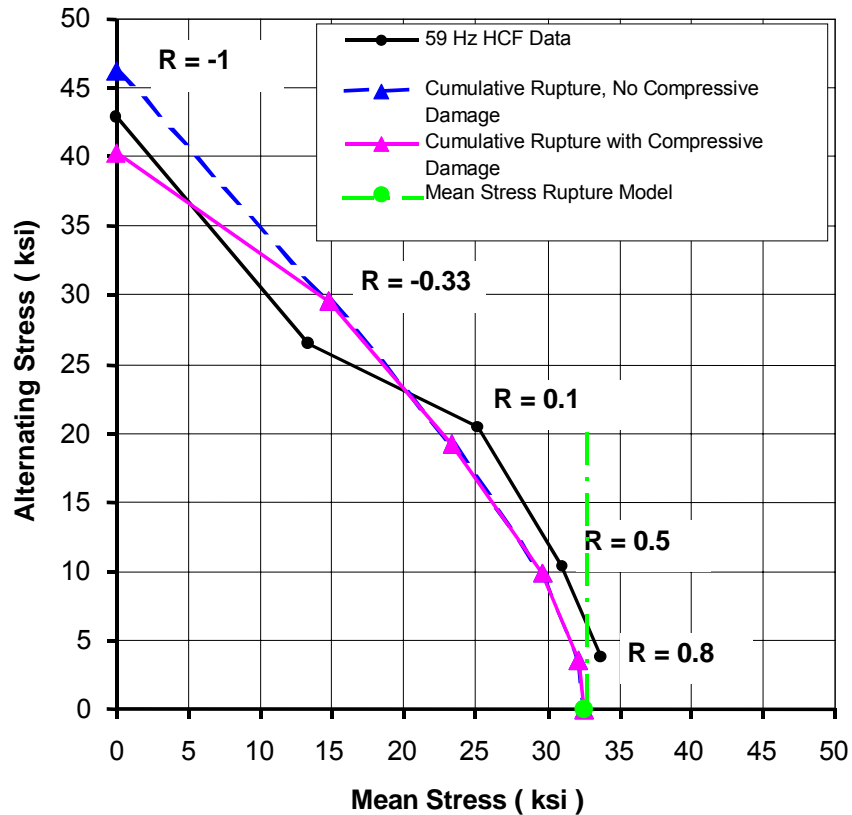
Figure 4.138.   1900°F 10^7 cycle Goodman diagram at 59 Hz with
rupture model predictions.

D. Multi-Step and Variable Mean Stress History Tests

Additional tests were run with multi-step load histories to assess damage
accumulation and loading sequence effects. Cyclic tests were also performed in which
the mean stress was changed linearly as a function of time and the alternating stress was
held constant. These tests were performed to simulate the loading on turbine airfoils
where the mean stress varies with time due to creep effects. PtAl coated cylindrical HCF
specimens were used with a nominal <001> crystal orientation. Testing was performed
at Metcut at 59 Hz at 1900°F.

Results for the multi-step tests and variable mean stress tests are shown in
Tables 4.33 and 4.34. Variable mean stress tests that were started at a mean stress of 0
with high alternating stresses generally had a fracture surface that was typical of fatigue

failures; the fracture surfaces were flat and failure initiated at a single site. For tests started at a high mean stress and low alternating stress, the fracture surfaces were rough and dimpled. Coating cracks were evident in the specimens that were removed before failure.

Table 4.33. Multi-Step HCF Test Results for PWA 1484 at 1900°F

Specimen	1st Loading Condition	Observed Cycles or Time loaded in Rupture for 1st Condition	2nd Loading Condition	Observed Cycles or Time loaded in Rupture for 2nd Condition	Notes	Total Observed Life (hrs)
A2LL9-1	Rupture at 35 ksi	15 hrs	HCF at alt stress 42.5 ksi, R = -1	5,756,158	Failure, Gage	42
A2LLC-4	Rupture at 35 ksi	15 hrs	HCF at alt stress 42.5 ksi, R = -1	3,732,855	Failure, Gage	33
A2LLE-2	HCF at alt stress 42.5 ksi, R = -1	4,510,342	Rupture at 35 ksi	37.8 hrs	Failure, Gage	59
A2LLE-1	HCF at alt stress 42.5 ksi, R = -1	4,460,416	Rupture at 35 ksi	35.6 hrs	Failure, Gage	57
A2LKU-5	HCF at alt stress 7 ksi, R = 0.6	5,136,868	HCF at alt stress 17.2 ksi, R = 0.1	35,000,000	Run out	189
A2LL9-5	HCF at alt stress 17.2 ksi, R = 0.1	8,231,780	HCF at alt stress 7 ksi, R = 0.6	15,044,503	Run out	110
A2LKU-4	HCF at alt stress 10.4 ksi, R = 0.5, 24 hrs	5,097,729	HCF at alt stress 21.0 ksi, R = 0.1	13,140,545	Failure, Gage	86
A2LL9-4	HCF at alt stress 21.0 ksi, R = 0.1, 24 hrs	5,101,208	HCF at alt stress 10.4 ksi, R = 0.5, to failure	11,277,793	Failure, Gage	77
A2LKV-3	HCF at alt stress 10.4 ksi, R = 0.5, 24 hrs	5,098,486	HCF at alt stress 21.0 ksi, R = 0.1	12,676,369	Failure, Gage	84
A2LKV-2	HCF at alt stress 13 ksi, R = 0.409, 16 hrs	3,398,400	HCF at alt stress 13 ksi, R = 0.316, to failure	15,491,220	Run out	89

Table 4.34. Variable Mean Stress Test Results for PWA 1484 at 1900°F

Specimen	Condition	Observed Cycles	Notes	Approximate Mean Stress at Failure or Test Removal (ksi)
A2LLP-3	HCF at alt stress 10.4 ksi, initial mean stress 20.0 ksi, increase mean stress 1 ksi every hour	5,135,071	failure, gage	44
T20W9-1	HCF at alt stress 30 ksi, initial mean stress 0 ksi, increase mean stress 1 ksi every hour	7,211,897	failure, gage	34
T20WA-5	HCF at alt stress 8 ksi, initial mean stress 22 ksi, increase mean stress 0.25 ksi every hour	11,457,556	failure, gage	35
T20W9-2	HCF at alt stress 8 ksi, initial mean stress 22 ksi, increase mean stress 0.25 ksi every hour	11,256,673	failure, gage	35
T20WA-1	HCF at alt stress 30 ksi, initial mean stress 0 ksi, increase mean stress 1 ksi every hour	4,979,607	failure, gage	23
T20W9-5	HCF at alt stress 20 ksi, initial mean stress 0 ksi, increase mean stress 1 ksi every hour	8,235,572	failure, gage	39
T20WA-4	HCF at alt stress 20 ksi, initial mean stress 40 ksi, decrease mean stress 1 ksi every hour	13,378,415	run-out	-23
T20W9-4	HCF at alt stress 8 ksi, initial mean stress 38 ksi, increase mean stress 0.25 ksi every hour	15,625,693	run-out	20

E. Linear Combination of Models

The simplest approach to modeling fatigue-rupture interaction is a linear combination of the respective damage.

$$D_{fatigue} + D_{rupture} = 1 \qquad (4.43)$$

The linear model was used to back-predict life for all tests that were performed. The two variations of the Walker model were considered in combination with the three rupture models for a total of six linearly combined models. The two cumulative rupture models were considered as independent models and were used to back-predict all the tests, making a total of eight model combinations evaluated.

For the linear combination models, life was predicted on a time basis. A time basis was more appropriate to represent the tests with multiple loading conditions that had a pure rupture component. For those tests where two loading conditions were applied to the specimen, life was predicted only for the second leg of the test. Predictions for the two leg tests are detailed below.

The damage for the first loading condition was calculated and designated as D_1. For linear-combination models, this damage is the result of both fatigue and rupture.

$$D_1 = \frac{t_{obs}}{t_{1\_rupt\_pred}} + \frac{t_{obs}}{t_{1\_fatigue\_pred}} \qquad (4.44)$$

The damage for the second loading condition was calculated assuming the total damage to failure is equal to one. Knowing the life fraction left for the second loading condition, the predicted time to failure can be calculated.

$$D_2 = 1 - D_1 \qquad (4.45)$$

$$D_2 = \frac{t_{2\_pred}}{t_{2\_rupt\_pred}} + \frac{t_{2\_pred}}{t_{2\_fatigue\_pred}} \qquad (4.46)$$

$$t_{2\_pred} = \frac{D_{2\_pred}}{\left(\dfrac{1}{t_{rupt\_pred}} + \dfrac{1}{t_{fatigue\_pred}}\right)} \tag{4.47}$$

For pure rupture loading (R = 1), the predicted fatigue life was assumed to be essentially infinite (4700 hours) since there is no alternating stress. Similarly, for cyclic loading with a mean stress of zero the predicted rupture life due to mean stress was assumed to be 10^9 cycles. If the damage fraction for the first loading condition was calculated to be greater than one, then the predicted life for the second loading condition was taken to be zero.

For each test that was performed, the life was predicted with each of the eight models. Models were down-selected by performing an analysis of variance on the log ratio of observed life to predicted life for each set of tests. A test for which the predicted life was exactly equal to the observed life gives a log ratio of 0 (observed time / predicted time = 1, log 1 = 0). Numbers were assigned to each model to facilitate the analysis; model numbers are shown in Table 4.35. The best models for each test type were noted in bold in the tables below.

Table 4.35. Model Names and Assigned Numbers

Model Number	Model
1	Linearly Combined Walker Model A & Mean Stress Rupture Model
2	Linearly Combined Walker Model C & Mean Stress Rupture Model
3	Cumulative Rupture Model with No Compressive Damage
4	Linearly Combined Walker Model A & Cumulative Rupture Model with No Compressive Damage
5	Linearly Combined Walker Model C & Cumulative Rupture Model with No Compressive Damage
6	Cumulative Rupture with Compressive Damage
7	Linearly Combined Walker Model A & Cumulative Rupture Model with Compressive Damage
8	Linearly Combined Walker Model C & Cumulative Rupture Model with Compressive Damage

The capability of these eight models were evaluated with all the test data combined and then with five subsets of the data representing major test types of: 59 hz, high frequency R = -1, high frequency R = 0, multi-step, and variable mean stress.

The models were first evaluated by calculating the overall standard deviation of the log ratio of life with all the test types combined. In total, life predictions were calculated for ninety tests. Figure 4.139 shows the Analysis of Variance for the eight models when considering all test predictions taken together. Model 2 is shown to have a mean of log ratio life that is closest to zero. However, Model 1 has the lowest standard deviation of fit of all the models and has a mean fit close to zero, so it represents a good alternative.

```
Analysis of Variance for log Tobs/Tpred
Source      DF         SS        MS         F          P
Model        7     22.081     3.154     16.80      0.000
Error      712    133.678     0.188
Total      719    155.758
                                        Individual 95% CIs For Mean
                                        Based on Pooled StDev
Level        N       Mean     StDev   ----+---------+---------+--------
-+--
1           90     0.0951    0.3361                    (----*---)
2           90     0.0222    0.4568              (---*----)
3           90    -0.1808    0.5778   (----*---)
4           90     0.2831    0.3495                            (---*----
)
5           90     0.2411    0.3912                            (---*----)
6           90    -0.0872    0.4933          (----*---)
7           90     0.3244    0.4109                              (---*--
--)
8           90     0.2568    0.3989                            (----*---)
                                      ----+---------+---------+--------
-+--
Pooled StDev =    0.4333                 -0.20      0.00       0.20
0.40
```

Figure 4.139. Analysis of variance for all predicted tests at 1900°F fitted to models.

In addition, all eight models were evaluated against data subsets to look for bias in the models. The first subset so evaluated was the baseline 59 Hz 1900°F HCF tests. The analysis of variance on the log of the ratio of observed to predicted life showed that the model type was a significant factor. Of the eight models, Models 1, 3, and 6 had

354

averages that were closest to 0. The standard deviation of all the models were similar.

Figure 4.140 shows the analysis of variance for this type of test.

```
Analysis of Variance for log observed time /predicted time
Source     DF        SS        MS        F        P
Model       7     3.9719    0.5674    10.09    0.000
Error     304    17.0896    0.0562
Total     311    21.0615
                                   Individual 95% CIs For Mean
                                   Based on Pooled StDev
Level       N       Mean     StDev  -+---------+---------+---------+-
----
1          39     0.0326    0.2065            (----*----)
2          39    -0.0845    0.2344  (----*----)
3          39    -0.0488    0.2882     (----*----)
4          39     0.2064    0.2307                      (----*----)
5          39     0.1487    0.2258                  (----*----)
6          39     0.0208    0.2368          (----*----)
7          39     0.2328    0.2350                        (----*----)
8          39     0.1728    0.2314                   (----*----)
                                   -+---------+---------+---------+-
----
Pooled StDev =    0.2371           -0.15     0.00     0.15     0.30
```

Figure 4.140.   Analysis of variance for baseline HCF tests at 1900°F,
59 Hz fitted to models.

The analysis of pure rupture tests fitted with the models is shown in Figure 4.141. All eight models were able to predict pure rupture capability as would be expected.

For varying frequency tests at $R = -1$, the best models on average were Models 1, 4, 5, and 7, as shown in Figure 4.142.

The analysis of variance for varying frequency HCF tests at $R = 0.1$ showed that there was a significant difference between the different models. Figure 4.143 shows that the best models were Models 2, 3, and 6.

Figure 4.144 shows that Models 1, 2, 3, and 6 fitted the multi-step tests best.

The analysis of variance for tests with varying mean stress histories indicated that there was no significant difference between the model capabilities since the p value was greater than 0.05. Models 1, 2, 3, and 6 had average log life ratios closest to 0. Results from the analysis are shown in Figure 4.145.

355

```
Analysis of Variance for log observed time / predicted time
Source      DF       SS        MS        F        P
C2           7  0.000090  0.000013     0.05    1.000
Error       24  0.006412  0.000267
Total       31  0.006502
                                     Individual 95% CIs For Mean
                                     Based on Pooled StDev
Level        N     Mean      StDev  -----+---------+---------+-------
--+-
1            4   0.00025    0.01721   (-------------*-------------)
2            4   0.00025    0.01721   (-------------*-------------)
3            4  -0.00000    0.01715   (-------------*-------------)
4            4   0.00400    0.01726      (-------------*-------------)
5            4   0.00000    0.00000   (-------------*-------------)
6            4   0.00025    0.01721   (-------------*-------------)
7            4   0.00400    0.01726      (-------------*-------------)
8            4   0.00250    0.01893    (-------------*-------------)
                                     -----+---------+---------+-------
--+-
Pooled StDev =  0.01635              -0.012     0.000      0.012
0.024
```

Figure 4.141. Analysis of variance for rupture tests at 1900°F fitted to models.

```
Analysis of Variance for log observed time / predicted time
Source      DF       SS        MS        F        P
C2           7    28.713     4.102    15.17    0.000
Error      120    32.451     0.270
Total      127    61.163
                                     Individual 95% CIs For Mean
                                     Based on Pooled StDev
Level        N     Mean      StDev  --+---------+---------+---------+
1           16   0.0428     0.4415                  (----*---)
2           16   0.3157     0.7698                    (---*----)
3           16  -1.0541     0.5573   (---*----)
4           16   0.1001     0.4358                  (----*---)
5           16   0.1688     0.4332                   (---*---)
6           16  -0.7531     0.5574       (---*----)
7           16   0.1452     0.4352                  (---*----)
8           16   0.2037     0.4333                   (---*----)
                                     --+---------+---------+---------+
Pooled StDev =  0.5200              -1.20     -0.60      0.00
0.60
```

Figure 4.142. Analysis of variance for varying frequency tests at
R = -1, 1900°F fitted to models.

356

```
Analysis of Variance for log observed time / predicted time
Source     DF       SS       MS       F       P
C2          7     5.922    0.846    4.89    0.000
Error      88    15.227    0.173
Total      95    21.149
                                Individual 95% CIs For Mean
                                Based on Pooled StDev
Level      N     Mean     StDev  -+---------+---------+---------+-
1          12    0.3118   0.5151               (------*------)
2          12   -0.0227   0.3624      (-----*------)
3          12   -0.1344   0.5184  (------*------)
4          12    0.5394   0.2860                      (-----*------
)
5          12    0.2667   0.2708              (------*-----)
6          12   -0.0554   0.5904      (-----*------)
7          12    0.5572   0.3209                      (------*-----
-)
8          12    0.3025   0.3348               (------*-----)
                                -+---------+---------+---------+-
Pooled StDev =  0.4160          -0.35     0.00     0.35     0.70
```

Figure 4.143. Analysis of variance for varying frequency tests at R = 0.1, 1900°F fitted to models.

```
Analysis of Variance for log T/T
Source     DF       SS       MS       F       P
C2          7     5.308    0.758    3.67    0.002
Error      72    14.864    0.206
Total      79    20.172
                                Individual 95% CIs For Mean
                                Based on Pooled StDev
Level      N     Mean     StDev  ---+---------+---------+---------
+---
1          10    0.2567   0.2192   (-------*--------)
2          10    0.1970   0.2348  (--------*-------)
3          10    0.3502   0.4133     (-------*-------)
4          10    0.6871   0.3536           (--------*-------)
5          10    0.8200   0.6052             (-------*------
--)
6          10    0.3441   0.2027     (-------*-------)
7          10    0.8614   0.6384              (--------*----
---)
8          10    0.7750   0.6615             (-------*-------
)
                                ---+---------+---------+---------
+---
Pooled StDev =  0.4544           0.00     0.35     0.70
1.05
```

Figure 4.144. Analysis of variance for multi-step tests, 59 Hz, 1900°F fitted to models.

357

```
Analysis of Variance for log Tobs/Tpred
Source      DF       SS        MS        F        P
C2           7     1.263     0.180     1.55    0.169
Error       55     6.394     0.116
Total       62     7.657
                                    Individual 95% CIs For Mean
                                    Based on Pooled StDev
Level       N      Mean     StDev  ----+---------+---------+--------
1           8     0.0631    0.3770          (---------*--------)
2           8    -0.1069    0.6517  (---------*--------)
3           8     0.1424    0.2909            (---------*--------)
4           8     0.3269    0.2011                  (---------*-----
----)
5           8     0.2750    0.2188                 (---------*-------
--)
6           7     0.1624    0.3080            (---------*----------)
7           8     0.3270    0.2011                  (---------*-----
----)
8           8     0.2700    0.2278                 (---------*-------
-)
                                    ----+---------+---------+--------
Pooled StDev =    0.3409           -0.25      0.00      0.25
0.50
```

Figure 4.145 Analysis of variance for variable mean stress tests at 1900°F, 59 Hz

Based on the analysis of variance on log ratio life for each subset of tests, the models were down-selected to Models 1, 2, 3 and 6: Linearly Combined Walker Model A and Mean Stress Rupture, Cumulative Rupture with No Compressive Damage, and Cumulative Rupture with Compressive Damage. Table 4.36 shows the down-selected models and test types for which the model was favorable.

Table 4.36. Models Evaluations Based on Analysis of Variance of Data Subsets

Model No.	HCF 59 Hz	Rupture	High Freq. R = -1	High Freq. R = 0.1	Multi-step Tests	Varying Men Stress
1	x	x	x		x	x
2		x		x	x	x
3	x	x		x	x	x
6	x	x		x	x	x

None of the models performed well in predicting frequency effects at both R = -1 and R = 0.1. Model 1 (Walker A + Mean Stress Rupture) was better suited than others in predicting frequency effects at R = -1 which is dominated by fatigue processes. However, Model 2 (Walker C + Mean Stress Rupture) and the cumulative rupture models, Models 3 and 6, ranked better at predicting frequency effects at R = 0.1 where the failure mechanism is time dependent. Based on the evaluation performed using all the data (Figure 4.139), Models 2 and 1 are preferred over 3 or 6.

Figure 4.146 shows the ratio of observed time to failure to predicted time to failure for Models 1 and 2. The capability of the models to predict experimental lives was very similar across all test types. For frequency tests at R = 0.1, Model 2 showed a tighter scatter band, while for frequency tests at R = -1, Model 1 showed a tighter scatter band.
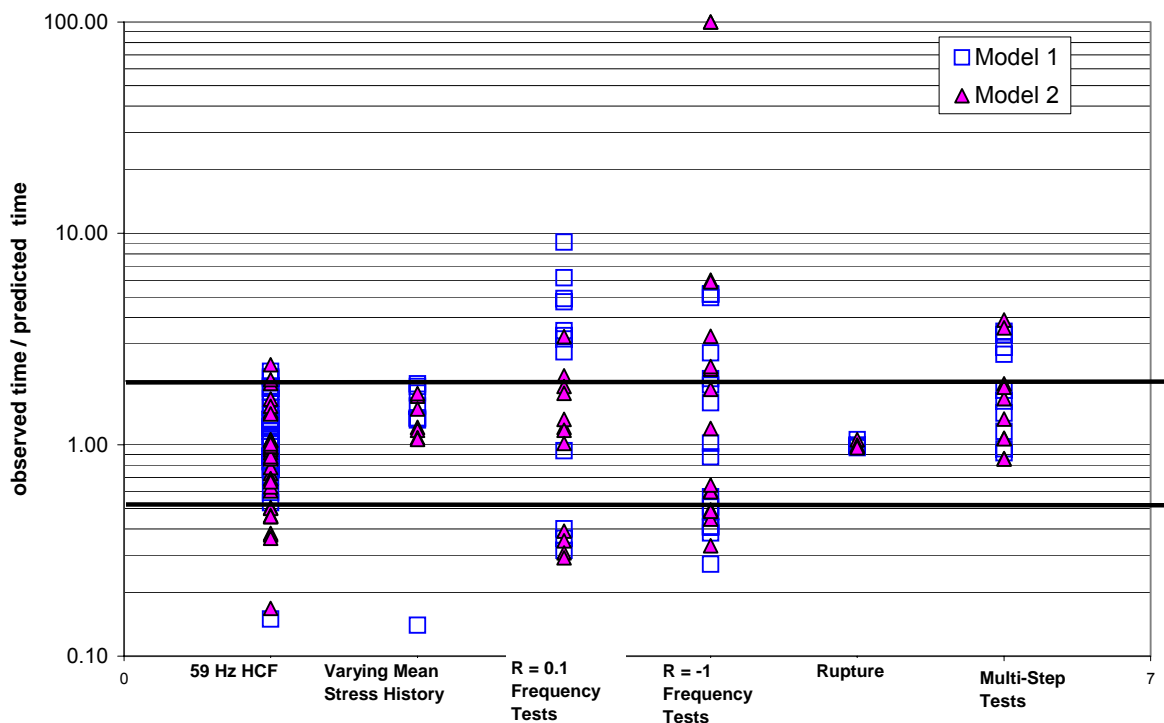
Figure 4.146.   Ratio of observed time to failure to predicted time to failure for Models 1 and 2.

F. Summary and Recommendations

A variety of Rupture-HCF damage interaction models have been evaluated at 1900°F using a wide range of test types from pure rupture to R = -1 HCF to tests with various cyclic frequencies and mixtures of stress ratios.

The models that worked best were based on the Walker Model for the HCF damage combined with a Mean Stress Model for rupture damage (Models 1 and 2). The evaluations against data did not show a clear preference between these two, but Model 2 is conceptually favored since it bases the HCF capability on data which are known to more closely representing pure HCF conditions, that is, high frequency or frequency independent conditions.

All the models that were considered were somewhat biased in the type of tests they were able to accurately predict. No model produced accurate predictions with a tight scatter band across all the tests that were performed. The linear combination models were better in predicting fatigue dominated tests while rupture dominated tests were better predicted by the cumulative rupture models.

Frequency effects clearly need to be considered when predicting HCF capability at high temperatures. Tests that were run with a positive mean stress (R = 0.1) showed a frequency dependence up to 900 Hz. Application of S-N responses characterized at low frequencies (30 Hz – 100 Hz) may underestimate the actual HCF capability of turbine blades which vibrate at much higher frequencies, typically on the order of kilohertz. Additional investigation of shifts in S-N response due to frequency is suggested.

4.4   NOTCH EFFECTS

4.4.1   Critical Plane Modeling of Notched PWA 1484 at 1100°F

4.4.1.1   Double Notch Testing of PWA 1484 at 1100°F

HCF testing for double edge notched PWA 1484 single crystal specimens was conducted at 1100°F and the data is shown in Figures 4.147 and 4.148. The tests were conducted at R = 0.1 and 0.8. The R = 0.8 condition was tested for the k_t = 2.5 specimens only. Two different notch geometries were tested. One notch geometry had a k_t = 2.5 with a notch radius of 0.032 inch and a notch depth of 0.05 inch. The other notch geometry had a k_t = 3.05 with a notch radius of 0.02 inch and a notch depth of 0.05 inch. Furthermore, each notch geometry was tested at two different specimen orientations. One orientation had the specimen axis along the <001> crystal axis with the notches cut in the <010> direction. These specimens were denoted as <001>/<010>. The other orientation had the specimen axis along the <011> crystal axis with the notches cut in the <011> direction. These specimens were denoted as <011>/<011>. The R = 0.8 specimens were tested at maximum cyclic stress levels above 125 ksi (except two which were tested at 116.7 ksi). Since the yield strength at 1100°F is ~124 ksi, it is believed that these data may have been influenced by the effects of cyclic plasticity and creep. The R = 0.8 data were not included in the critical plane analysis below. The data in Figures 4.147 and 4.148 was analyzed using elastic 3-D finite element analysis (FEA) together with the Walls, Shear Stress Range (SSR), and the Chu-Conle-Bonnen (CCB) critical plane damage parameters.

The failed specimens were observed under the scanning electron microscope (SEM) to study fatigue initiation mechanisms. All the specimens were found to have crystallographic initiations. A typical SEM micrograph is shown in Figure 4.149.

4.4.1.2   Finite Element Analysis of Double Notch PWA 1484 Specimens

The two different notch geometries and specimen orientations were analyzed using elastic 3-D FEA. Figure 4.150 shows the 3-D solid model for the double-notched specimen. The refinement of the finite element mesh was checked using isotropic material properties.

PWA 1484, Notched HCF, 1100 F, <001/010>
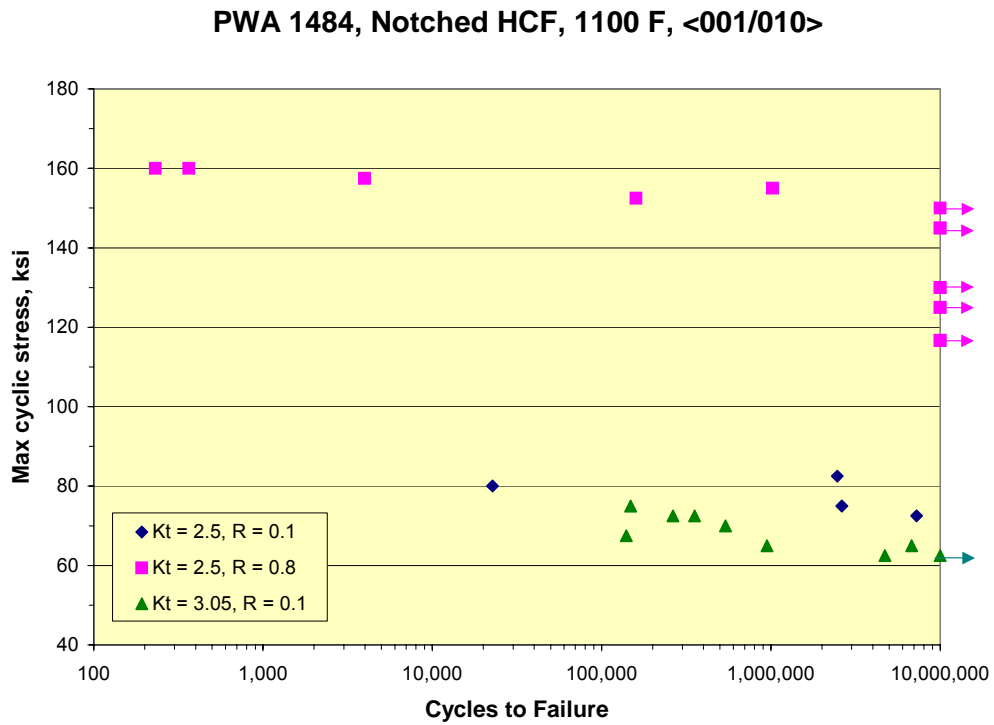
Figure 4.147. Max cyclic stress versus life, PWA 1484, 1100°F, <001>/<010>.

PWA 1484, Notched HCF, 1100 F, <011/0-11>
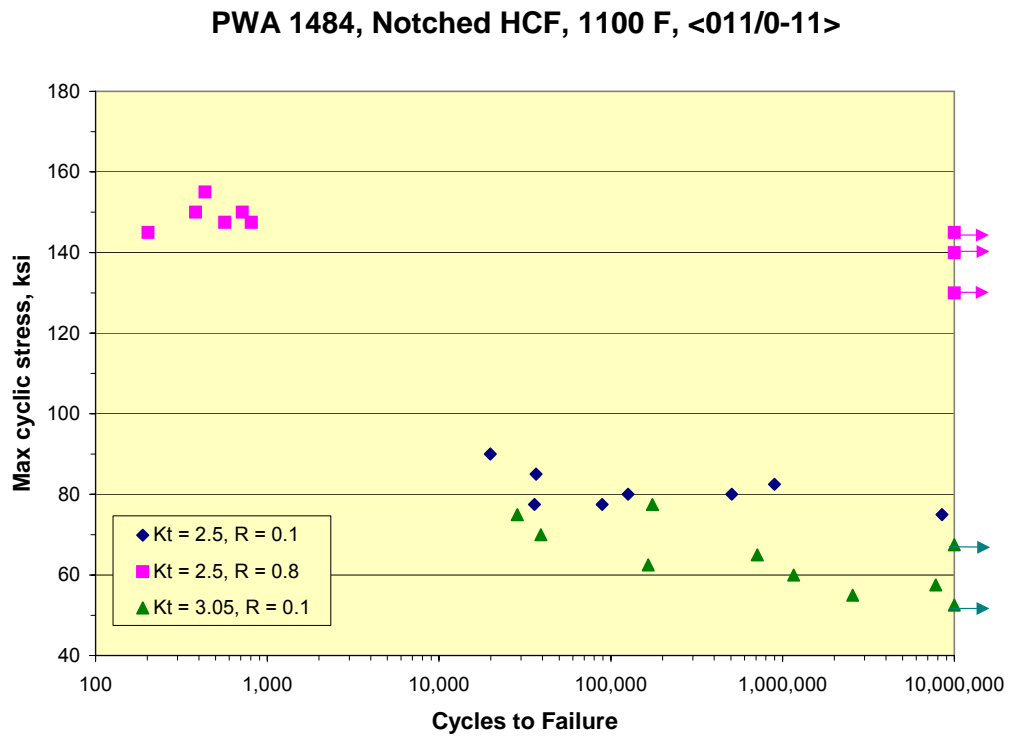
Figure 4.148. Max cyclic stress versus life, PWA 1484, 1100°F, <011>/<011>.
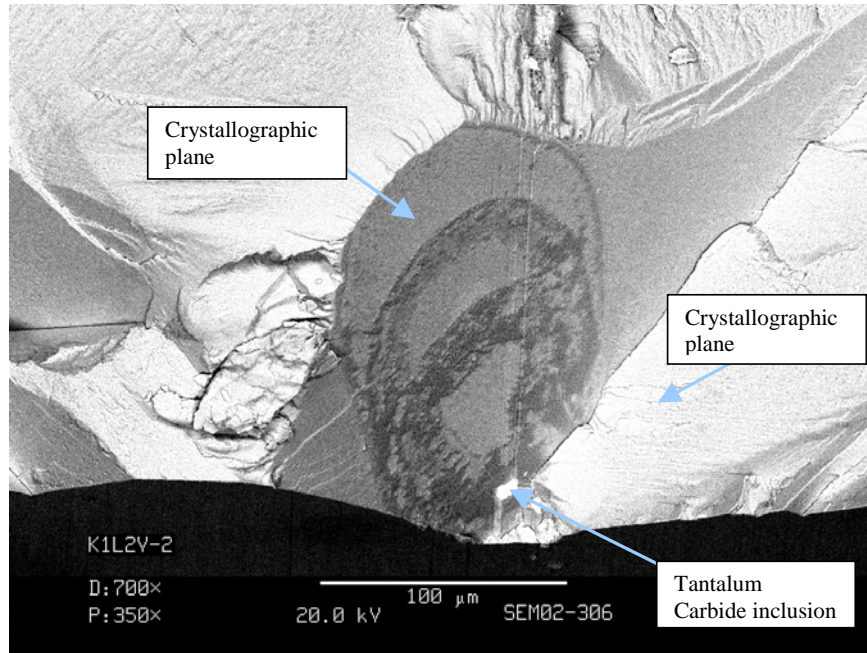
Figure 4.149.   SEM micrograph showing crystallographic initiation in notched HCF specimen, PWA 1484, 1100°F.
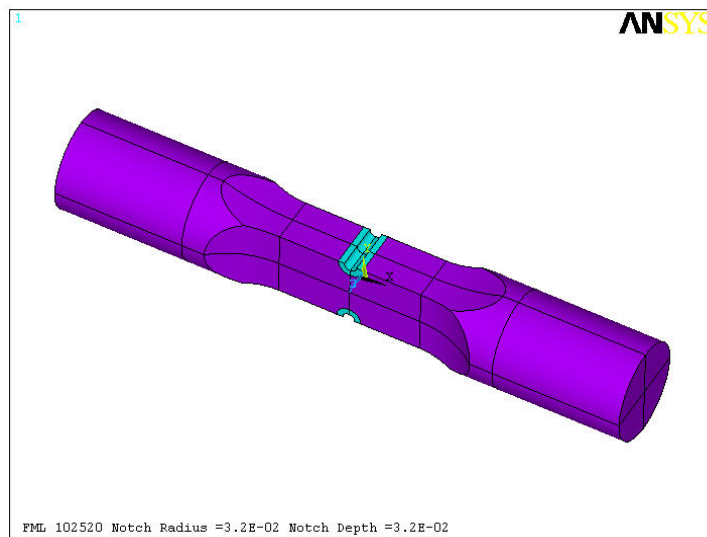
Figure 4.150. FEA 3-D solid model of notched HCF specimen.

The principal stress (σ_1) contours for the $k_t = 2.5$ specimen for the two different orientations are shown in Figures 4.151 and 4.152 for an applied load of 1000 lbs.
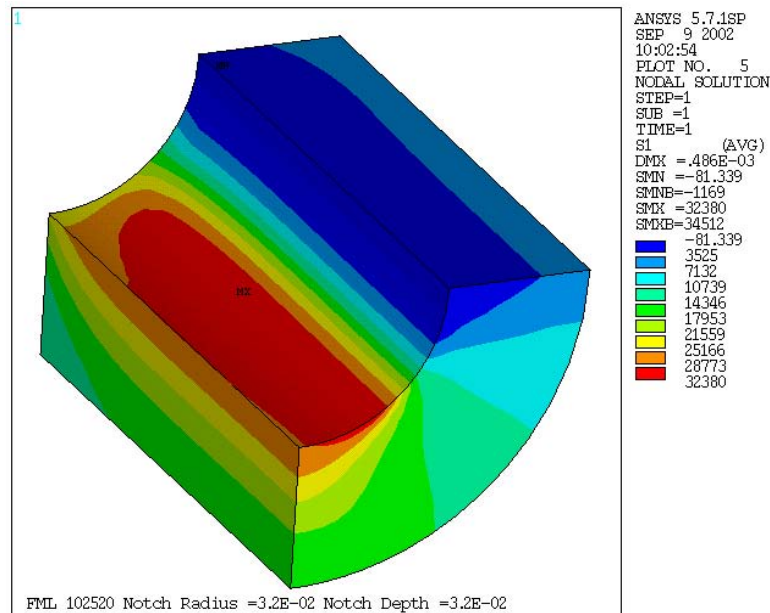
Figure 4.151. Principal stress (σ_1) contours for the $k_t = 2.5$, <001>/<010> notched specimen, applied load = 1000 lbs.
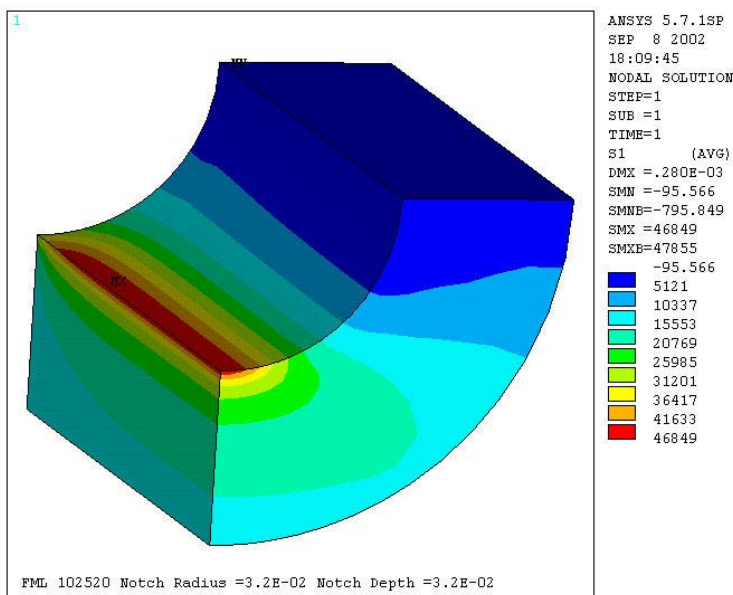
Figure 4.152. Principal stress (σ_1) contours for the $k_t = 2.5$ <011>/<011> notched specimen, applied load = 1000 lbs.

The principal stress (σ_1) contours for the <001>/<010> specimen appear to be symmetrical with respect to the notch central plane. For the <011>/<011> specimen the σ_1 contours appear to be skewed with respect to the notch central plane and also have a higher value of stress concentration. The nature of the stress contours for each specimen orientation was considered in deciding the radial line along which the damage parameter gradients would be analyzed. In order to keep away from the effects of surfaces and edges, only the stresses at mid-thickness were used in the life analysis.

4.4.1.3   Critical Plane Modeling

As shown in Figure 4.149, all specimens showed evidence of crystallographic initiations. Thus a critical plane approach appears to be well suited for analyzing the notch fatigue data. The 3-D FEA results were used together with several critical plane damage stresses parameters to analyze the notched data. Three different critical plane damage parameters were considered in the analysis of the notch specimen data. These were the Walls, the Shear Stress Range (SSR), and the Chu-Conle-Bonnen (CCB) critical plane damage parameters. These three parameters had correlated the smooth PWA 1484 data (at 1100°F) quite well (see Section 4.3.3.5).

A detailed description of these three damage parameters is given in Section 4.3.3.4.*B*. The critical plane search algorithm used for determining the "critical plane" for these damage parameters is described in Section 4.3.3.4.*C* and in Appendix V.

4.4.1.4   Results and Discussion

All the calculations were performed using the following elastic constants, measured along the primary <001> orientations, for PWA 1484 at 1100°F: E = 15.69 msi, ν = 0.3995, G = 15.93 msi. The critical plane damage parameters were calculated for each applied stress level (and stress ratio) using the elastic 3-D FEA stresses. The results shown in Figures 4.153 through 4.158 include the damage parameters calculated at the notch surface (at specimen mid-thickness) and at a critical distance, a_o, along a radial line below the notch surface. For the <001>/<010> oriented specimens, the three damage parameters had a maximum gradient along the specimen mid-length line (between the two notches) and at the specimen mid-thickness. For the <011>/<011> oriented

specimens, the Walls and CCB parameters were found to have a maximum gradient along a radial line, which was at 15 degrees to the specimen mid-length line (between the two notches) and at the specimen mid-thickness. For the <011>/<011> orientation, the SSR parameter had a maximum gradient along the specimen mid-length line between the two notches, as in the case of the <001>/<010> specimen orientation.

The damage parameters calculated at the notch surface were in general not able to correlate the data for the different orientations and notch geometries. However, when the stresses at a critical distance, a_o, were used to calculate the damage parameters, there was reasonably good correlation of the data at different orientations and notch geometries. The critical distance a_o was a function of both the orientation and the notch geometry for all the three damage parameters. For the SSR parameter this critical distance was along the specimen mid-length line between the two notches for both the different orientations. The Walls and CCB parameters had the same critical distance values for the corresponding notch geometry and specimen orientation conditions. Both these parameters also had their maximum gradients along a radial line which was at 15 degrees to the specimen mid-length line (between the two notches) and at the specimen mid-thickness for the <011>/<011> oriented specimens.

All the three parameters did a reasonably good job of correlating the notch HCF data for the two different orientations and two different notch geometries.

4.4.2   Modeling of Notched PWA 1484 at 1900°F

4.4.2.1   Objective and Approach

All turbine blade airfoils contain stress concentrations, whether at the airfoil to root transition, at tip shrouds, or at air-cooling holes. Stress concentrations represent a common region of concern for HCF because stresses are usually highest there. The objective of this portion of the technical effort was to investigate the capability of PWA1484 single crystal in the presence of stress concentrations and to evaluate analytical models for relating baseline unnotched material capability to that of various notch sizes and stress concentration factors.
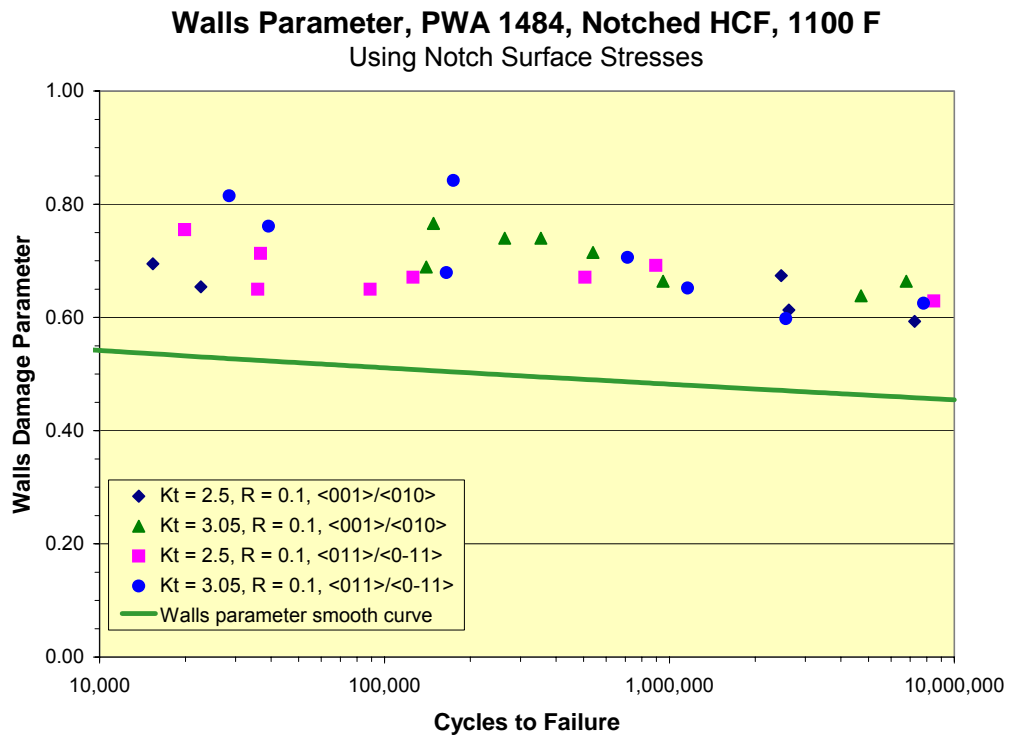
Figure 4.153. The Walls damage parameter calculated at notch surface.
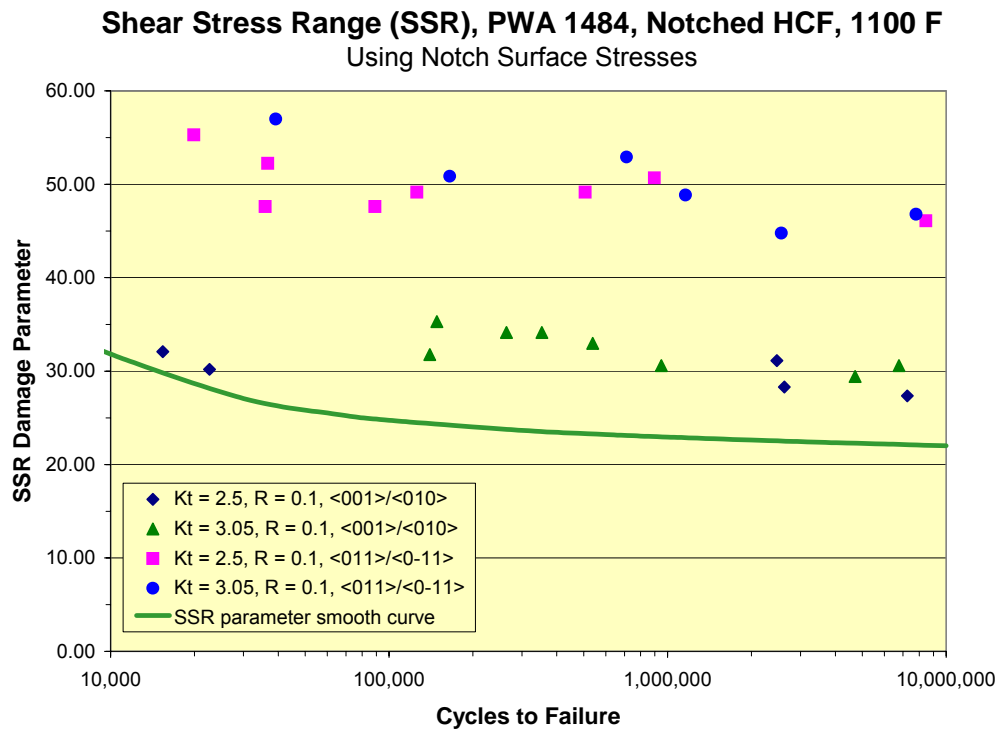
Figure 4.154. The SSR damage parameter calculated at notch surface.

367
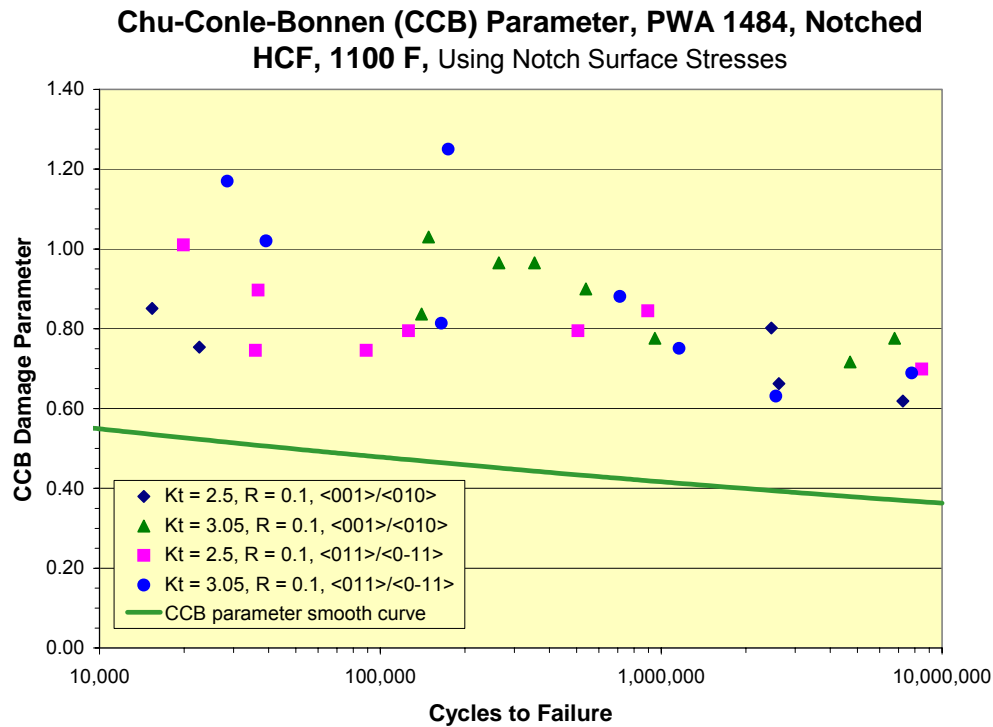
Figure 4.155. The CCB damage parameter calculated at notch surface.
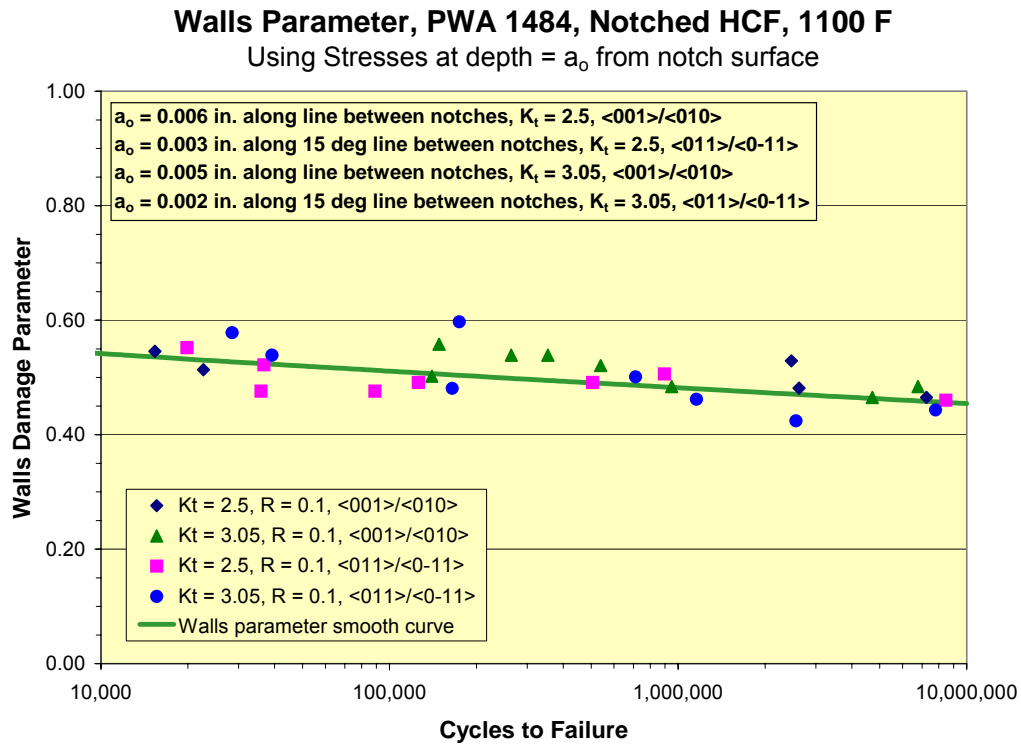
Figure 4.156. The Walls damage parameter calculated at a_o.
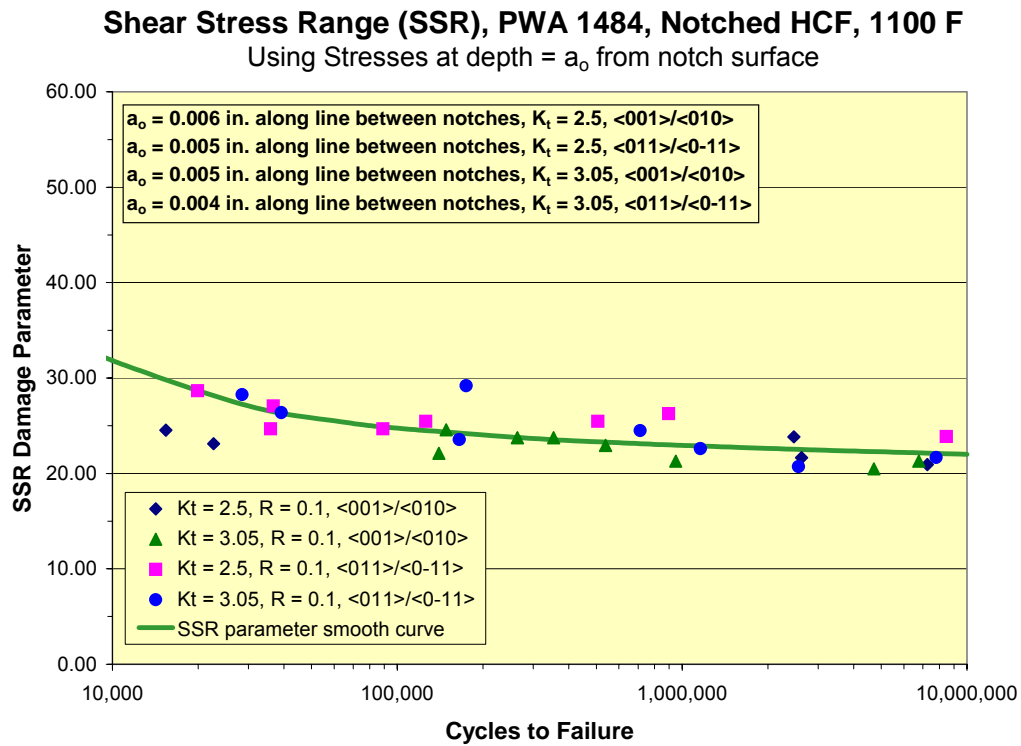
Figure 4.157. The SSR damage parameter calculated at a_o.
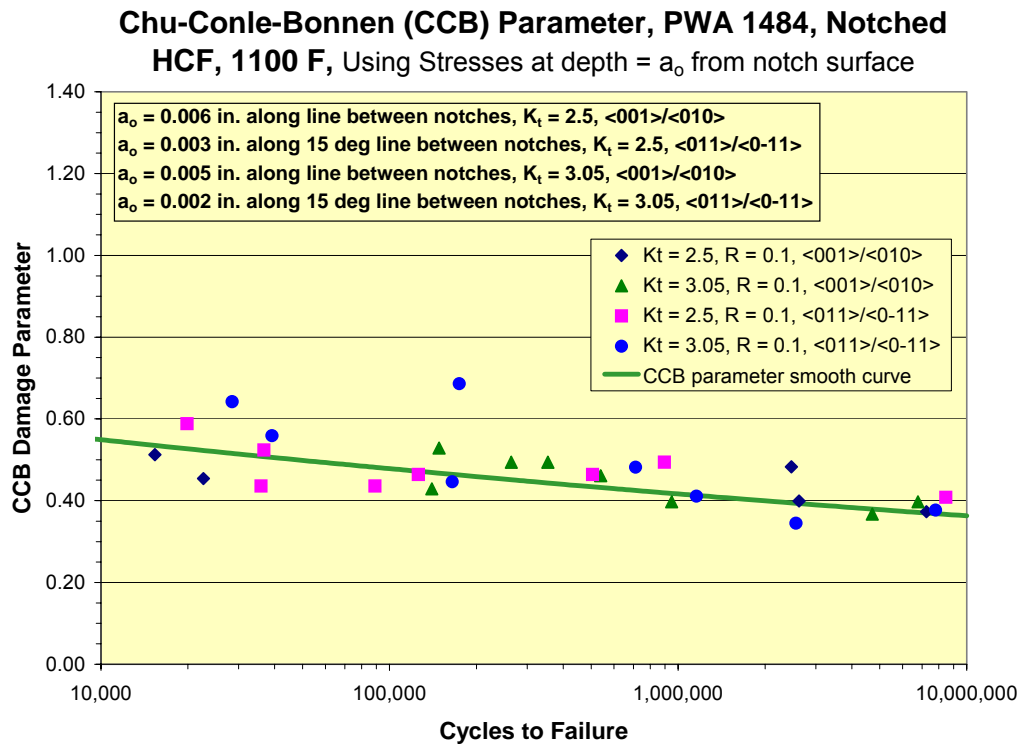
Figure 4.158. The CCB damage parameter calculated at a_o.

While the majority of turbine blade notches are at air cooling holes, which are usually fabricated by EDM or laser drilling processes, and as a result have relatively rough and recast finishes, the approach adopted here was to try to eliminate the variable of surface condition in establishing a notch method. Therefore, all notches were introduced by grinding, rather than conventional blade hole drilling processes. This grinding was used for the baseline specimens, so the differences in surface preparation would be minimized. In addition, like the baseline unnotched specimens, all notched specimens were PtAl coated (Section 4.1.2), which further minimized any differences in surface effects. A simple 2-D notch geometry was chosen. The notched specimen was identical in configuration to a 0.4 inch by 0.168-inch rectangular gage with opposing edge notches. Two different notch geometries were investigated: the 0.065-inch radius notch and a pair of smaller, 0.020-inch radius opposing notches (0.020 inch deep). The latter size was closer to that used for cooling holes, and was felt to be the smallest notch that could be reproducibly ground. Prior ANSYS anisotropic elastic analysis of the 0.065-inch double-notch specimen showed it to have a k_t of 2.04. The k_t of the 0.020-inch notch was estimated at 2.85.

Testing was performed at Metcut Research at 1900°F, 59 Hz, to match the baseline conditions. All specimens had nominal <001> stress axes (within 6°) and a <010> direction normal to the notch face (within 10°). Two stress ratios were tested: R = -1, and R = 0.5.

4.4.2.2 Results

The HCF test results are shown in Table 4.37 and Figures 4.159 and 4.160.

At R = -1, when plotted against nominal alternating stress (unconcentrated stress, based on net section area between notches), the HCF capability in Figure 4.159 shows a significant degradation of capability for both notches. The degradation is slightly more for the smaller (higher k_t) notch. When using concentrated (pseudo) elastic stress the notched capability become slightly superior to that of the unnotched baseline. This suggests that a local stress notch model, like "q" (see Section 4.4.2*A* below) may be applicable.

370

Table 4.37. HCF Results for Notched PWA 1484 at 1900°F, 59 Hz

S/N	Notch Radius (in)	R-ratio	Nom. Alt. stress (ksi)	Nf	Result
A2LPE-2	.065"	-1.0	65.0	1	F.O.L. at 50.3 ksi max
A2LPF-2	.065"	-1.0	41.0	298,653	Failed at Notch
A2LRR-2	.065"	-1.0	36.0	784,801	Failed at Notch
A2LPE-4	.065"	-1.0	31.0	4,134,320	Failed at Notch
T20VT-4	.065"	-1.0	28.0	9,602,775	Failed at Notch
A2LRR-1	.065"	-1.0	27.0	8,645,485	Failed at Notch
A2LPE-3	.065"	0.5	13.0	2,844,490	Failed at Notch
A2LLV-3	.065"	0.5	11.4	825,126	Failed at Notch
A2LPE-5	.065"	0.5	11.0	8,020,485	Failed at Notch
T20VT-5	.065"	0.5	10.0	14,633,628	Failed at Notch
T20VT-3	.065"	0.5	9.0	15,040,417	No failure
Z175P-2	.020"	-1.0	35.0	673,152	Failed at Notch
Z175P-1	.020"	-1.0	32.0	1,426,202	Failed at Notch
Z175P-4	.020"	-1.0	28.0	5,888,317	Failed at Notch
T20VV-4	.020"	-1.0	26.0	9,887,968	Failed at Notch
Z175P-5	.020"	0.5	13.0	1,672,353	Failed at Notch
T20VV-5	.020"	0.5	11.4	3,809,117	Failed at Notch
Z175P-3	.020"	0.5	10.0	5,589,788	Failed at Notch
Z175R-5	.020"	0.5	9.0	13,605,264	Failed at Notch

At R = 0.5, however, the notched and unnotched results are very close in capability when compared on a nominal stress basis, and converge as the life is increased. Since this condition is at a stress ratio where it is known from the unnotched testing that creep can occur, it is quite likely that the local mean stress at the notches has relaxed to a level near that of the average (nominal) level. Thus, although the stress amplitude would still be increased by the notch K_t, the mean stress would be considerably lower in the notched specimens than in the unnotched ones, i.e., although the remote applied stress ratios are the same, the notch roots are not running at the same local stress ratio as the unnotched specimens. This interaction between creep and HCF needs to be more carefully modeled to determine if the combined effects of reduced mean stress and amplified alternating sress at a notch can be used to model 1900°F HCF in PWA 1484.
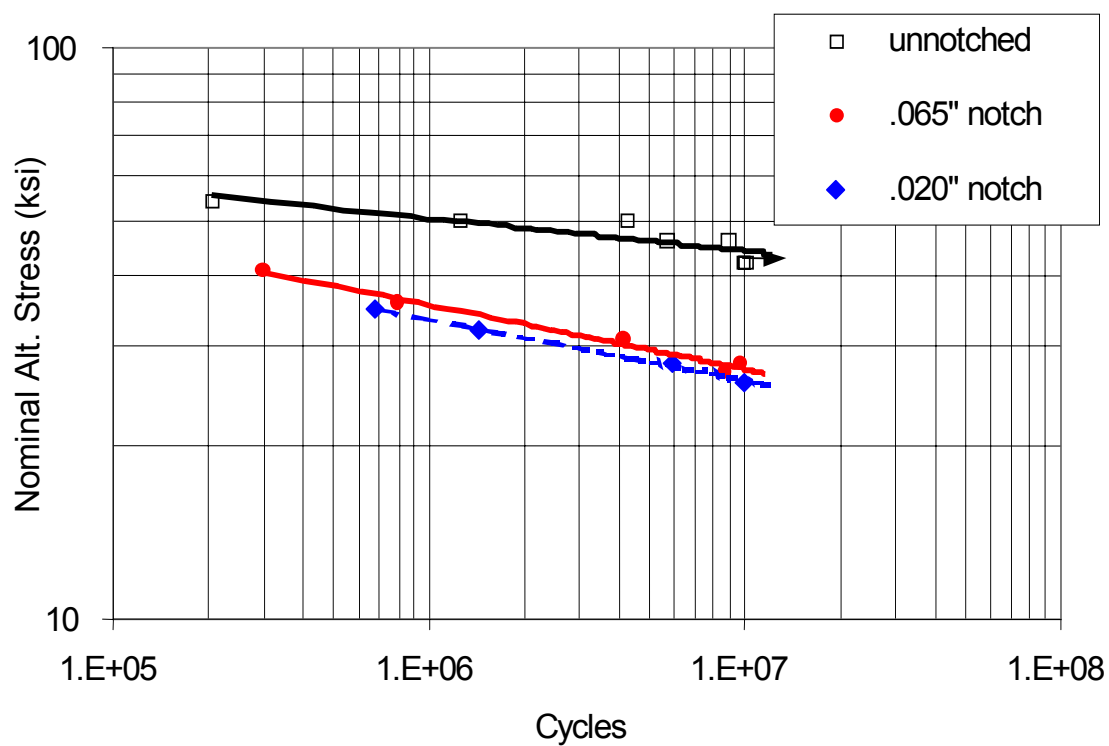
Figure 4.159. Notched HCF of PWA 1484 at 1900°F, R = -1.
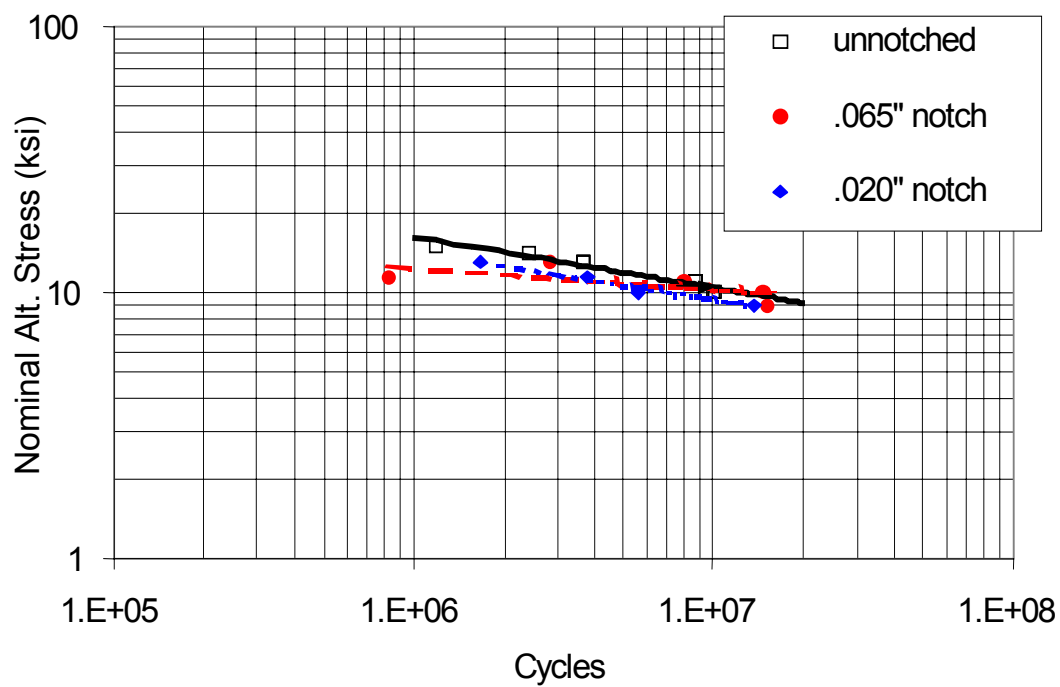
Figure 4.160. Notched HCF of PWA 1484 at 1900°F, R = 0.5.

4.4.2.3   Fractography

Representative fracture surfaces of specimens with both notch geometries and both stress ratios were examined. Examples of each are presented in Figures 4.161 through 4.164.

In general, the cracks always initiated at or near the root of the notch, usually in a broad, frontal manner. Some localization of the crack initiation can be seen in some specimens, but the indications suggest that the initial crack front was much longer than it was deep. In all but one case, crack initiation occurred in the PtAl coating and was intergranular in nature in the coating. One case was seen (not shown) where the crack appeared to have initiated slightly subsurface in the superalloy. The life of this specimen appeared to follow the same trend as the others. The only major trend noted was that at R = -1 the coating cracks were relatively tight, while at R = 0.5 they were noticeably open.

This is presumably due to creep occurring at the notch root under the non-zero mean stress of R = 0.5. The crack propagation surfaces in the superalloy were smooth and oxidized, quite similar in appearance to those of the crack propagation specimens tested at similar conditions. The extent of this flat, featureless region is quite large, especially on the R = 0.5 specimens, and suggests that subcritical crack growth may have occurred to a significant depth.

4.4.2.4   Notched HCF Modeling

Several different models were investigated to try to correlate the notched and unnotched HCF behavior at 1900°F. The simplest of these was based solely on the concentrated elastic notch stress as determined by the elastic notch stress concentration factor, k_t, times the nominal alternating stress, $\sigma_{alt,nom}$. For the unnotched tests, this is the same as the alternating stress. When the unnotched and notched (k_t = 2.04 and 2.85) results were fitted with a power law life relationship: $N_f = k_a(\sigma_{alt,conc})^n$, a rather poor collapsing of these data resulted, Figure 4.165. The predicted lives for the k_t = 2.04 results are on average about an order of magnitude greater than those of k_t = 1 and the k_t = 2.85 predictions were about another order of magnitude greater than that. The

a) Overall view of fracture

b) Origin region
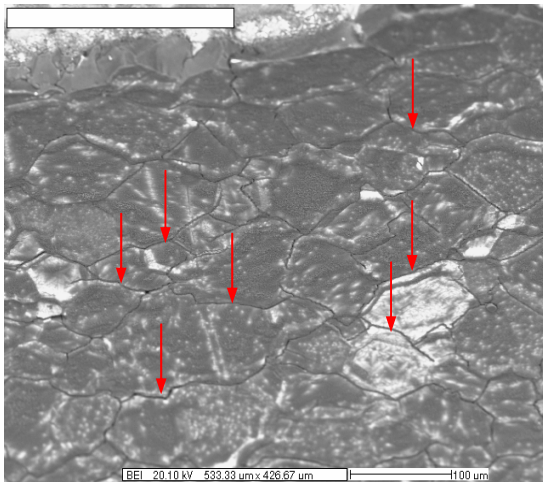
c) coating surface on notch face
   below fracture plane showing
   multiple tight coating cracks
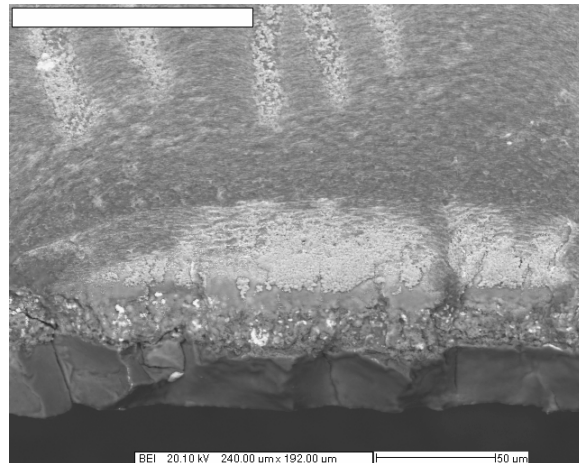
d) Close up of origin from coating

Figure 4.161.   Fracture appearance of notched HCF A2LRR-1, 1900°F,
              k_t = 2.04, R = -1, σ_{alt} = 27 ksi, N_f = 8.6E6

a) Overall view of fracture
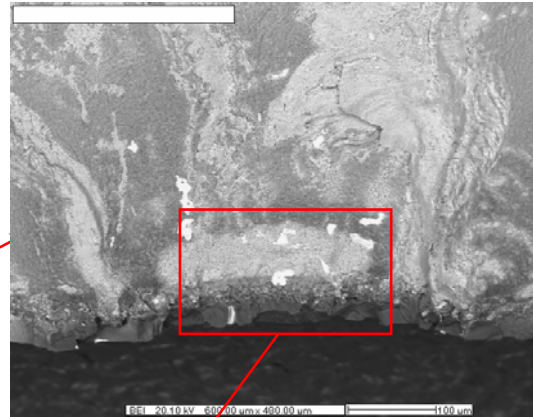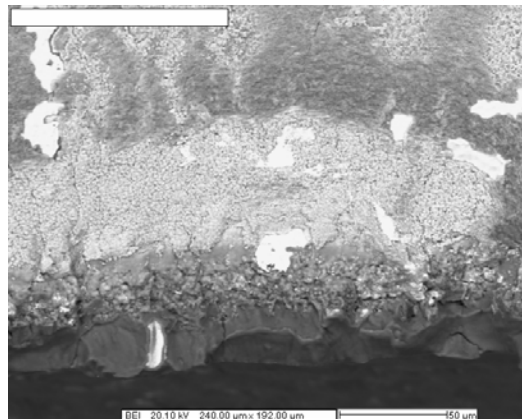
b) Origin region

c) Close up of origin from coating

Figure 4.162. Fracture appearance of notched HCF T20VV-4, 1900°F,
$k_t = 2.85$, $R = -1$, $\sigma_{alt} = 26$ ksi, $N_f = 9.9E6$

a) Overall view of fracture
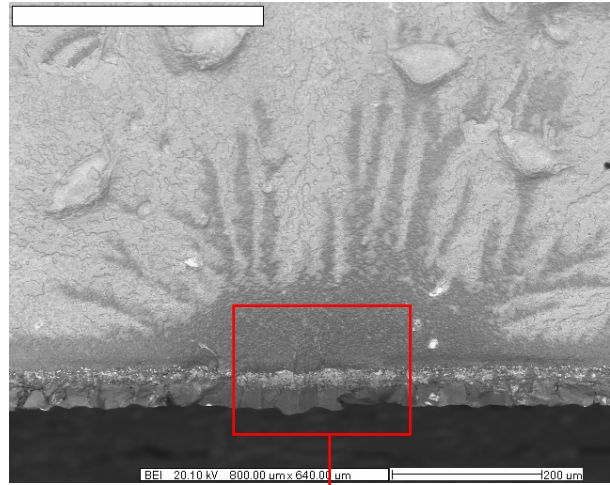
b) Origin region
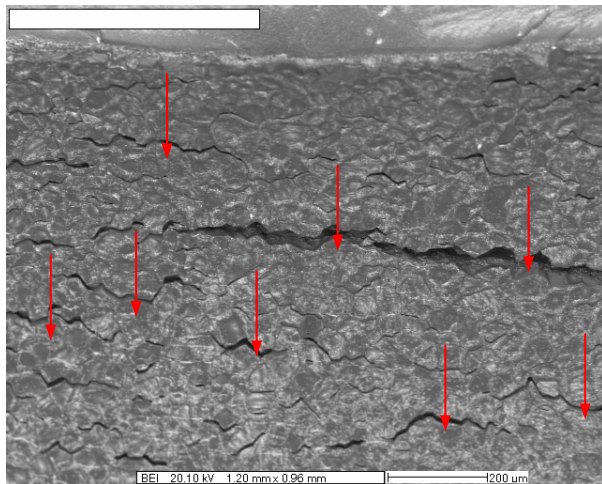
c) Coating surface on notch face
below fracture plane showing
multiple open coating cracks
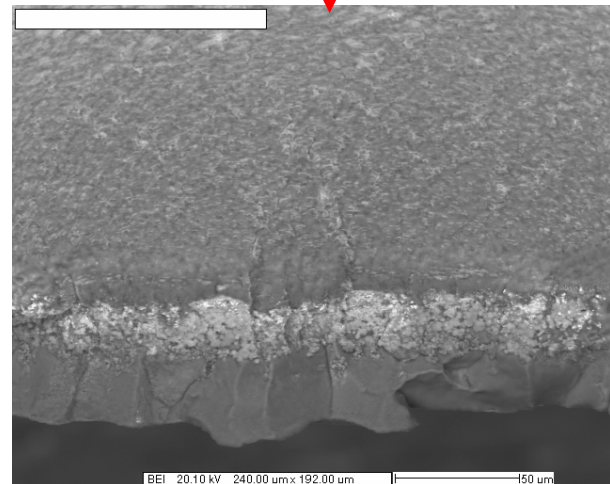
d) Close up of origin from coating

Figure 4.163.   Fracture appearance of notched HCF T20VT-5, 1900°F,
$k_t = 2.04$, R = 0.5, $\sigma_{alt} = 10$ ksi, $N_f = 14.6E6$
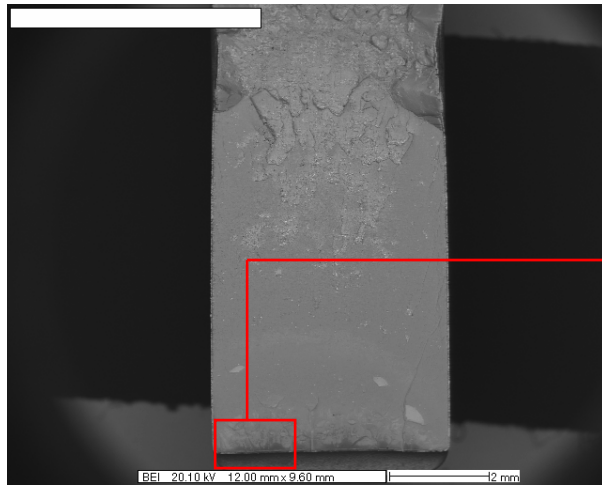
a) Overall view of fracture   b) Origin region
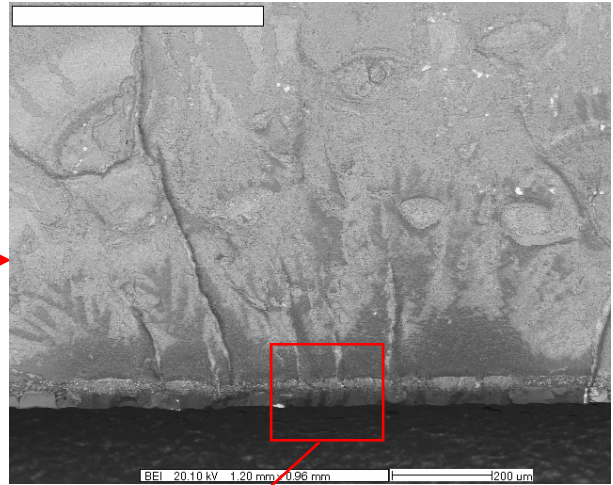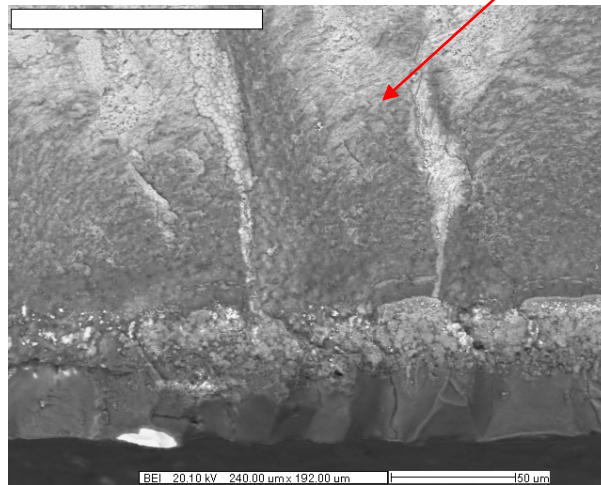
c) Close up of origin from coating

Figure 4.164. Fracture appearance of notched HCF Z175R-5, 1900°F,
$k_t = 2.85$, R = 0.5, $\sigma_{alt} = 9$ ksi, $N_f = 13.6E6$.
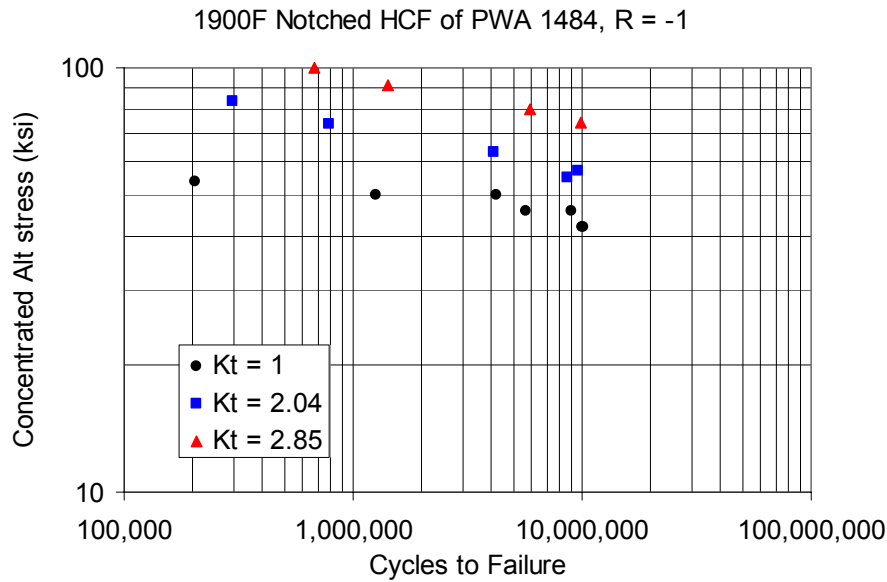
Figure 4.165. Predicted S-N behavior for notched HCF life at 1900°F, R = -1
for concentrated alternating elastic stress model.

standard error of $\log(N_f)$ was 0.57 as shown in Table 4.38. At R = 0.5 the modeled results were similarly spread apart as shown in Figure 4.166, although the standard error of fit was somewhat lower, 0.41 (Table 4.38).

Table 4.38. 1900°F Notched HCF Model Parameters and Standard Errors

Model	R-ratio	Model Parameter	Parameter Value	Standard error in log(Nf)
Concentrated Alternating Stress	-1	none	-	0.57
Concentrated Alternating Stress	0.5	none	-	0.41
q	-1	q	0.365	0.35
q	0.5	q	0.0744	0.23
Fs	-1	α	9.5	0.34
Fs	0.5	α	5.0	0.31
Neuber	-1	none	-	0.49
Neuber	0.5	none	-	0.38
Relaxed notch mean	0.5	w	-.0239	0.36

378
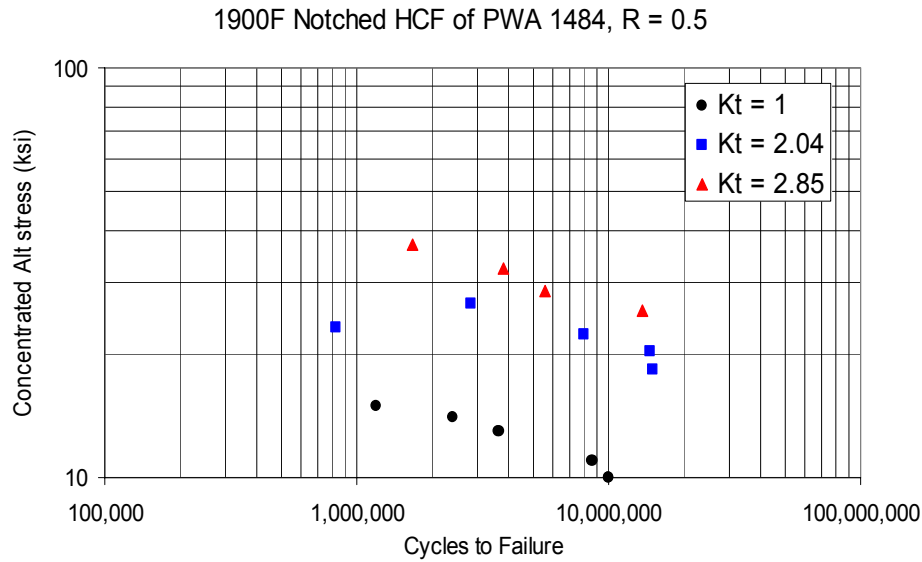
Figure 4.166. Predicted vs. observed notched HCF life at 1900°F, R = 0.5
for concentrated alternating elastic stress model.

The next model investigated was the "q" model, where $q = (k_f - 1)/(k_t - 1)$. Since $k_f = \sigma_{unnotched}/\sigma_{notched} = \sigma_u/\sigma_n$ at constant life, then the predicted unnotched equivalent stress, σ_q can be defined as:

$$\sigma_q = \sigma_n [q (k_t - 1) + 1] \tag{4.48}$$

This σ_q was related to life through a power law relationship, $N_f = k_q(\sigma_q)^n$ and q was allowed to vary to minimize the standard error of curve fit. Using this method, q's for R = -1 and R = 0.5 were 0.365 and 0.0744, respectively, as shown in Table 4.38. The standard error of fit was significantly improved over the concentrated alternating stress approach. At R = -1 some layering of the data by k_t remained (Figure 4.167) but at R = 0.5 no segregation or layering of the predictions was observed (Figure 4.168). Note that optimization of the fits at the two stress ratios required quite different values of q. This is inconvenient since the implication is that q is stress ratio dependent, and a further relationship for this dependence would have to be developed. The very low q obtained at R = 0.5 implies that the material is very notch insensitive at this condition, which agrees with the observed behavior in Figure 4.160.

379
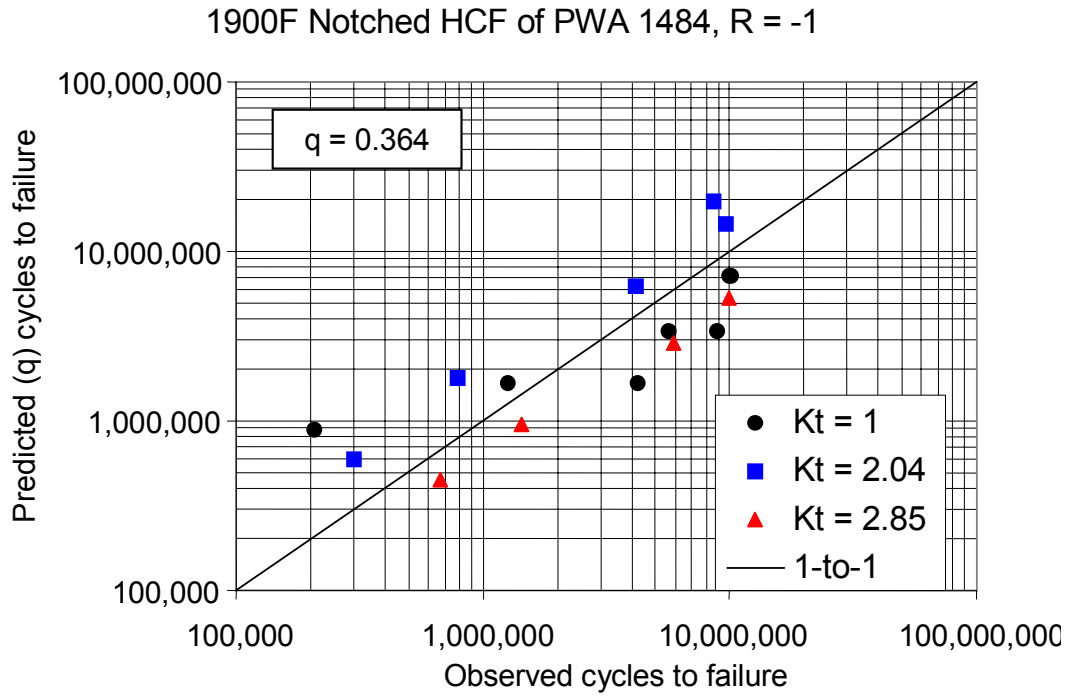
Figure 4.167. Predicted vs. observed notched HCF life at 1900°F, R = -1
for "q" model.
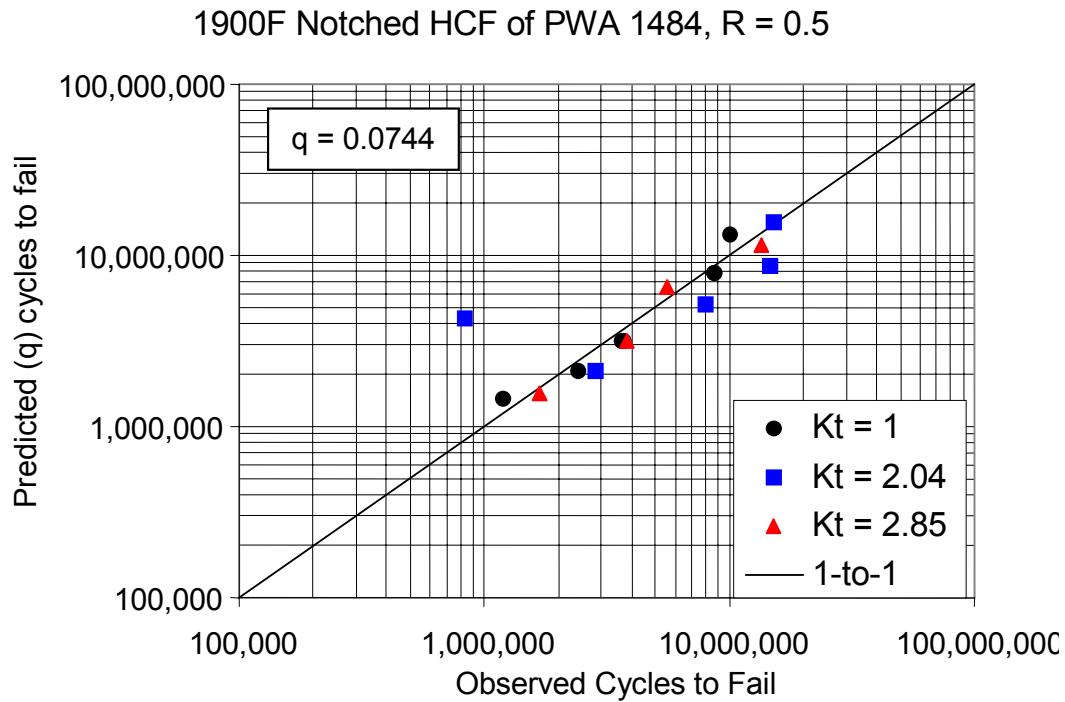
Figure 4.168. Predicted vs. observed notched HCF life at 1900°F, R = 0.5
for "q" model.

The third model considered was the "Fs" model developed in the Titanium portion of this program (see Section 3.3.8). Briefly, the model determines a notch equivalent stress, σ_{Fsi}, based on the stress distribution over the surface area of the notch (obtained from an elastic finite element analysis of the specimen). This equivalent stress is then fit to a stress-life relationship to identify the notch parameter, α, which provides the best fit. The equations are:

$$Fs(geom) = \Sigma[-(\sigma_i/\sigma_{max})^{\alpha}]\Delta A_i \tag{4.49}$$

$$\sigma_{FSi} = (Kt\ \sigma_{alt,nom})(Fs_o/Fs_i)^{(-1/\alpha)} \tag{4.50}$$

The Fs factors were calculated from a finite element analysis of each of the notches, using the stresses on the free surfaces only. These calculations were repeated for different α's to give a table of Fs vs α. Fs_o was the Fs for the unnotched specimen, taken as the surface area of the gage section; $Fs_o = \pi dL_g$. The notch equivalent stress, σ_{FSi}, was calculated for each α value and the resulting σ_{FSi} and N_f data were fitted to a power law equation. The standard error of curve fit was determined for each α and the α that yielded the lowest standard error was selected. These α's and their standard errors of fit are shown in Table 4.38. The standard errors are only slightly higher than those for the "q" model and the Fs model has the advantage of not having to define a far field stress to determine K_t. In some features and stress fields the far field stress level is not obvious. Predicted vs. observed life plots for the Fs model are shown in Figures 4.169 and 4.170.

Again, the two stress ratios require different α's to provide good fits for each, although the R = 0.5 results are not strongly sensitive to α, and a reasonable standard error could be obtained with $\alpha = 9.5$. The standard errors obtained for the two stress ratios are higher that those for the "q" model, but not excessive.

For most of the notched tests, the maximum concentrated notch stress exceeded the yield strength at 1900°F (about 50 ksi per the constitutive property tests described in Section 4.3.2.2). Therefore the use of the elastic stress concentration factor in all of the
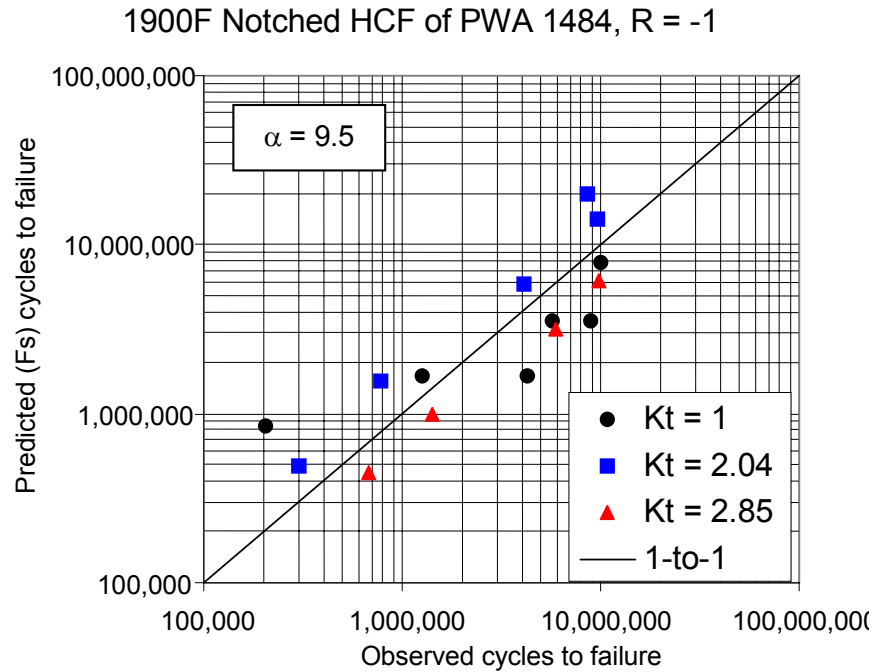
Figure 4.169. Predicted vs. observed notched HCF life at 1900°F, R = -1 for "Fs" model.
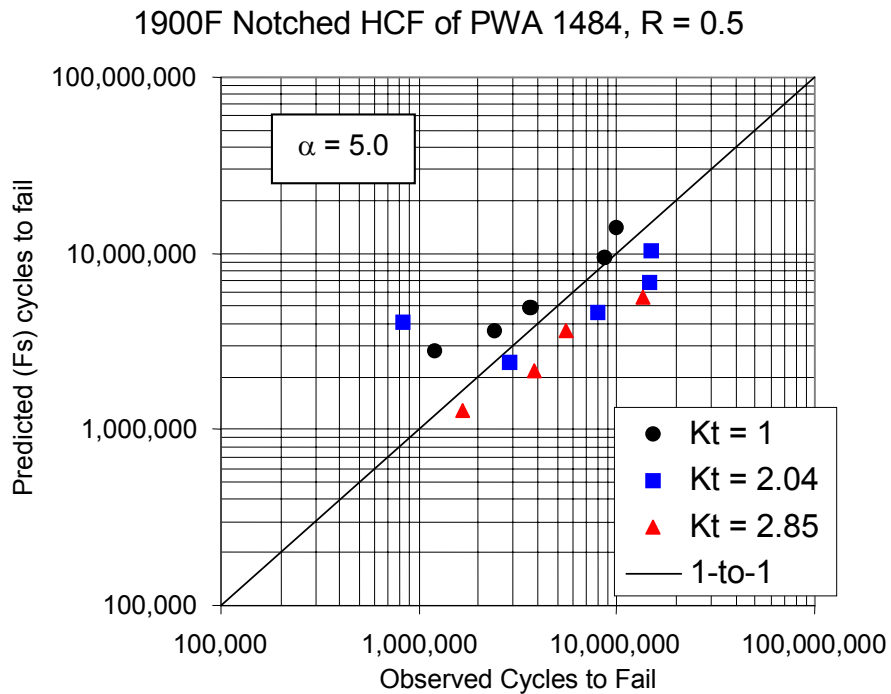
Figure 4.170. Predicted vs. observed notched HCF life at 1900°F, R = 0.5 for "Fs" model.

above models may be erroneous, and the effect of yielding on reducing the maximum stress may need to be incorporated. Indeed, it is possible that this may allow combination of the two stress ratios into one analysis.

The simplest method for evaluating the effect of yielding on notch stress was to perform a one dimensional (isotropic) Neuber analysis on the maximum stress location. To do this requires an elastic-plastic stress-strain curve for the material. Since PWA 1484 is strain rate sensitive at 1900°F, this curve would ideally be at the HCF strain rate, about 1 sec^{-1}. However, the constitutive tests were only performed up to a strain rate of 10^{-3} sec^{-1}. Since the flow behavior at the higher strain rates tested (10^{-5} to 10^{-3} sec^{-1}) were about the same (stress at 10^{-4} was anomalously high, and had other test difficulties, so it was ignored), the stress-strain behavior at 1 sec^{-1} was assumed to be the same as at 10^{-5} to 10^{-3} sec^{-1}.

This curve is shown in Figure 4.171. The fit to the data is seen to be good up to about 1% strain. This was satisfactory for most of the tests, but some of the R = 0.5 tests at high stress had calculated notch root strains exceeding this value so for these tests the maximum stress at the notch may be somewhat overestimated. The point along this curve at which the notch root operated was determined by applying the Neuber condition:

$$\sigma_{max} \, \varepsilon_{max} = (k_t \sigma_{nom})^2 / E \qquad\qquad (4.51)$$

σ_{max} and ε_{max} are determined from the stress-strain curve: $\varepsilon_{max} = \sigma_{max}/E + (\sigma_{max}/K)^{(1/n)}$ and the maximum stress was iterated until the left side of the equation matched the right side. At both stress ratios, the maximum stress in the cycle was used. The notched data were combined with the smooth bar data and the maximum (notch) stresses were related to cycles to failure by fitting them to a power law expression. The standard error of curve
fit of the predicted vs. the actual lives by this approach was decidedly poorer than for the "q" or "Fs" models, Table 4.38. These S-N and predicted vs. observed correlations are shown in Figures 4.171, and 4.172, and 4.173.

Stress-strain response of PWA1484, 1900F <001>

Legend:
- ◇ 1.00E-03
- △ 1.00E-05
- ── model

$$\varepsilon = (\sigma/1.07E7) + (\sigma/8.967E4)^{10.92}$$
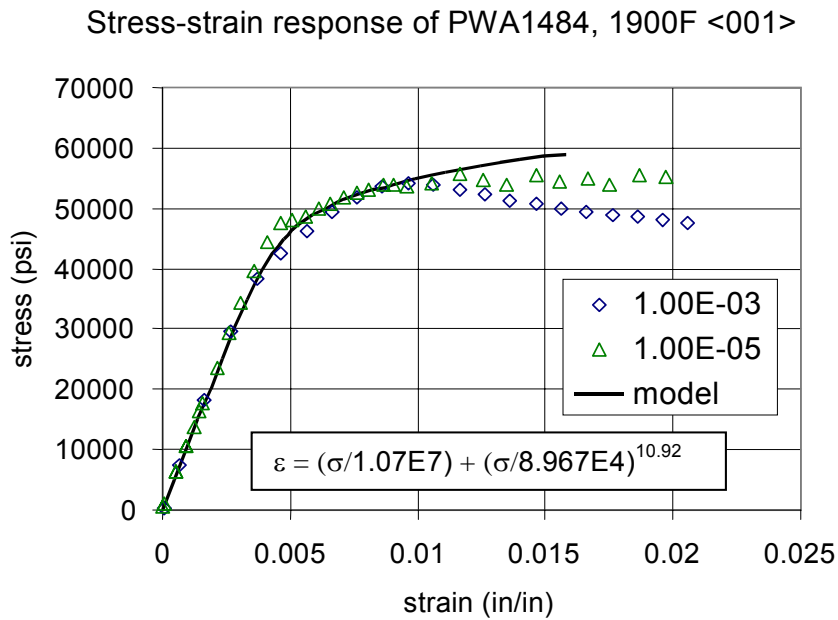
Figure 4.171. Stress-strain curve for <001> PWA 1484 at 1900°F.

1900F Notched HCF of PWA 1484, R = -1

Legend:
- ● Kt = 1
- ■ Kt = 2.04
- ▲ Kt = 2.85
- ── 1-to-1
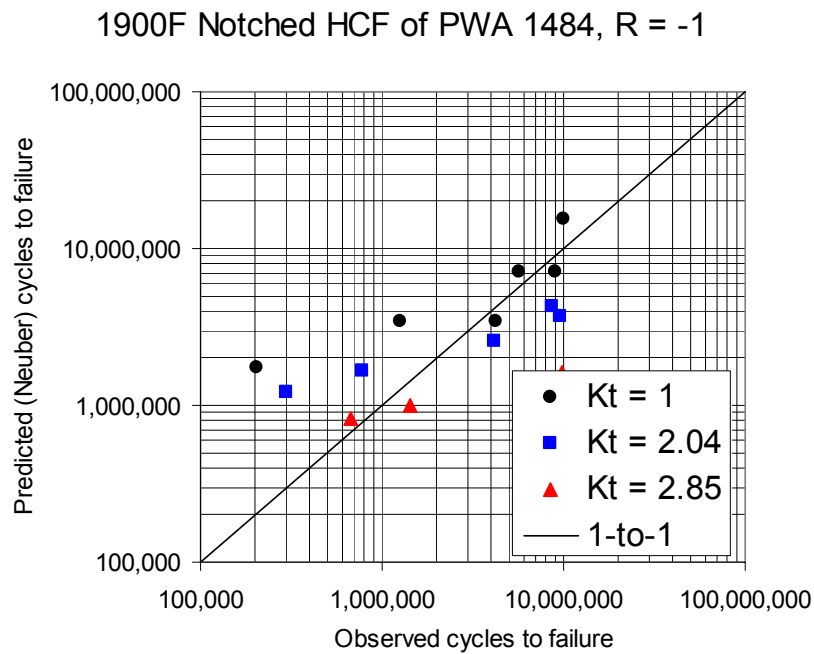
Figure 4.172. Predicted vs. observed notched HCF life at 1900°F,
R = -1 for "Neuber" model.
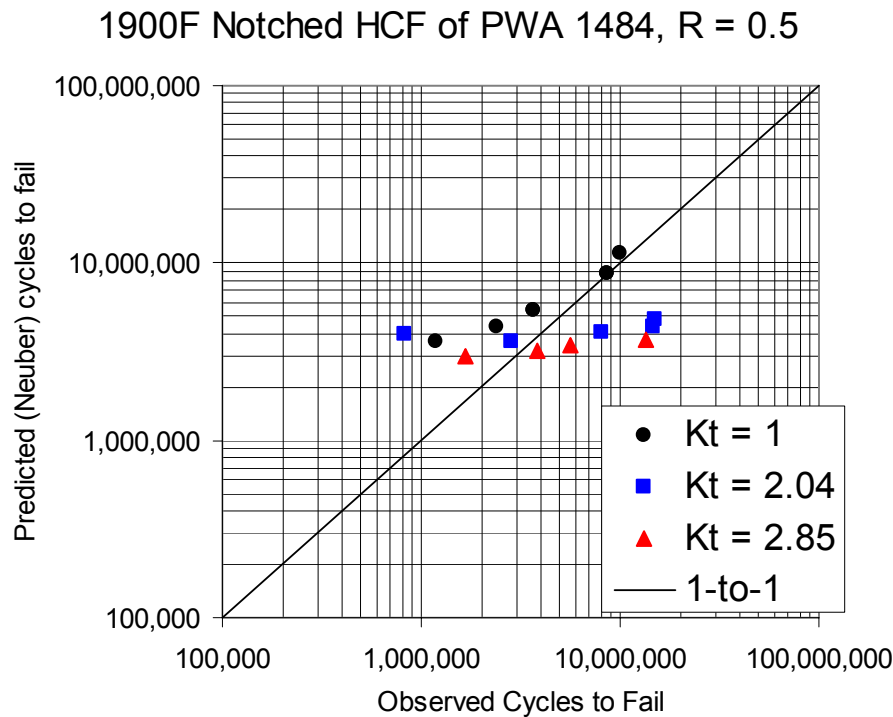
Figure 4.173. Predicted vs. observed notched HCF life at 1900°F,
R = 0.5 for "Neuber" model.

One final modeling approach was tried with the R = 0.5 results. At this elevated mean stress, it is likely that creep will be occurring that will tend to make the stress distribution across the specimen more uniform. In other words, as creep occurs the actual stress concentration will tend to be less than the initial elastic one. In the limit of full stress relaxation, the mean stress will be uniform across the net section of the specimen. This fully relaxed mean stress is simply the nominal (net section) mean stress. The alternating component of stress will not be affected by creep, since it occurs rapidly, so the stress ratio at the notch root effectively shifts (reduces) as the stresses relax. By computing the new stress ratio and using the concentrated alternating stress, it is possible to arrive at a new equivalent stress using a Walker model. This equivalent stress can then be entered into a stress-life relationship to determine the expected life in the presence of the relaxed mean stress.

385

The Walker model used for accounting for effect of the mean stress relaxation on life was:

$$\sigma_{eq} = \sigma_{alt}/(1-R_{rel})^{(1-w')} \tag{4.52}$$

where, R_{rel} is the relaxed stress ratio. For the $K_t = 2.04$ specimens, the relaxed stress ratio became 0.19, and for the $K_t = 2.85$ specimens became 0.026. Since the Walker model does not work well over the entire range of stress ratios studied for PWA 1484 HCF at 1900°F, w' was obtained by fitting only data with R's close to the relaxed R's. For this study, data with R = -0.33, 0.1, and 0.5 were used. A best fit of the Walker model was found with w' = -0.0239. The negative sign is non-standard and reflects the downward concave nature of the Goodman Diagram in this region. Normally Goodman Diagrams derived from Walker models are concave up (w ≥ 0). The equivalent stresses so obtained from the notched tests were combined with the uniform stresses from the unnotched tests at R = 0.5 and all were fitted with a power law equation relating stress and life. The standard error of fit was 0.36, as shown in Table 4.38, and the predicted vs. observed lives are shown in Figure 4.174. As can be seen, the two notched sets of data are collapsed nicely by this method but the predictions fall about a factor of three lower in life than observed. Since this is a bounding condition (the mean stress will fall gradually to the fully relaxed level during the test instead of immediately, as assumed), a prediction based on a more realistic mean stress history would be more pessimistic yet.

Since the R = 0.5 condition is in the regime where rupture or time-dependent behavior dominates, as described in Section 4.3.4, it may be that modeling the effect of the mean stress relaxation using a rupture-based approach like that presented in Section 4.3.4 would provide a better correlation with the observed results.

4.4.2.5   Summary of 1900°F Notch Modeling

None of the notch models examined were fully satisfactory in correlating smooth and notched HCF capability over a range of k_t and stress ratio. The "q" and "Fs" provided the lowest standard errors of fit, and thus appear to be the most attractive. However, both of these models required different values of the parameters (q or α) at
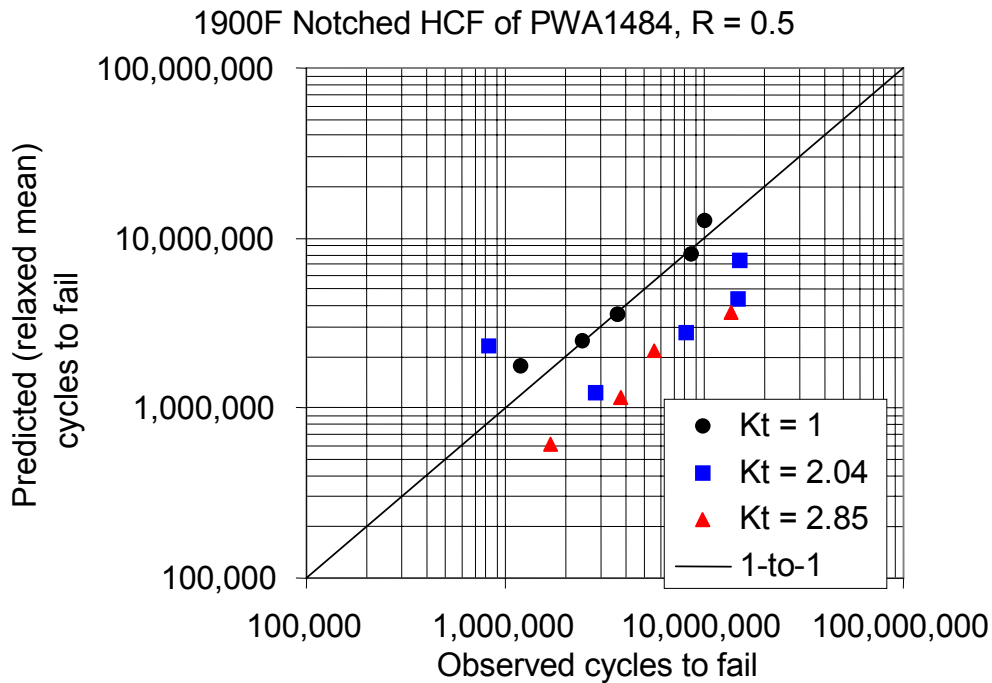
Figure 4.174. Predicted vs. observed notched HCF life at 1900°F,
R = 0.5 for "relaxed notch mean stress" model.

different stress ratios in order to obtain the best fits. Thus for predicting (or correlating) behavior for any notch at any stress ratio, a stress ratio dependence of the parameter must be developed, which is cumbersome. Notch tests were not performed at enough stress ratios to determine the R ratio dependence of these parameters completely.

The Neuber and relaxed notch mean stress models were attempts to remove the stress ratio dependence of the model fitting by determining in more detail the stress conditions at the notch root. However, the model variations examined here did not achieve this. Perhaps a combination of these models with a model such as "q" or "Fs" would provide a better correlation.

The contribution of crack propagation to total life was ignored in these models, as is typical in total life approaches. However, there is some evidence from the fractography that crack propagation may have occupied a non-trivial portion of total life. This should be

investigated further to determine whether a combination of initiation- and propagation-based models would be superior.

4.4.3   Flat Cooling Hole Testing and Verification

4.4.3.1   Introduction

This test program was undertaken to examine the effects of cooling holes on HCF life in a representative nickel base single crystal alloy PWA 1484. About 30 tests were planned to examine the effect of cooling hole orientation and mean stresses on the endurance limits in PWA 1484. The test plan is shown in Table 4.39

Table 4.39. HCF Test Plan

Specimen and test type	Number of specimens
Coated, no holes, R = 0.1	5
Coated, no holes, R = 0.5	5
Coated, normal holes, R = 0.5	5
Coated, skew holes (A), R = 0.5: A = 40 deg	5
Coated skew holes (B), R = 0.5: B = 50 deg	5
Coated, normal holes, R = 0.1	4

Fully heat treated PWA 1484 plates were provided by GEAE. The plates, 6 inch x 3 inch x 0.625 inch and <001> oriented slabs, as per Honeywell Drawing PAP 601225-a, were used to fabricate flat sheet specimens. The blanks were excised such that the tensile testing axis was oriented in the <001> direction. The specimens were milled and ground to final dimensions. A single EDM hole 0.020 inch in diameter was drilled in the middle of the gage section in some of the specimens as per the test plan. The orientation of the hole was representative of what we would expect at the different regions of some of our advanced military engine airfoils.

The measured thickness of the coating as shown in Figure 4.175 is about 0.0019 inch, which is about 9.5% of the total thickness of the specimen. At the test temperature of 1900°F, the PtAl coating and the diffused layer are not expected to be able to support any loads and hence the stresses have been adjusted by changing the net section areas.

Figure 4.175. Cross-section of a test coupon of PWA 1484 showing the PtAl
coating and the diffused layer. The total thickness is about
0.0019 inch.

The recast layer from the hole drilling was removed by light grit blasting and all the
specimens were then sent to Howmet Corporation for a PtAl coating, which was applied by
chemical vapor deposition. The HCF tests on these coated specimens were conducted at
Rockwell Science Center on a servohydraulic test frame capable of operating at 300 Hz. All
testing was done at 1900°F using miniature igniter furnaces that have a hot zone of about 2
inches. Calibration of the hot zone showed uniform temperatures with the temperature gradients
that are less than 1%.

Baseline tests were initiated on the specimens with no holes. Tests were initially run at
300 Hz. At that frequency, a considerable number of contact problems leading to failures at the
grips were encountered as shown in Figure 4.176. Various techniques were investigated to
eliminate the problem, including compliant layers. Although the problem was somewhat
reduced, there were still grip failures. Once the test frequency was reduced to 120 Hz, there
were no additional grip failures. Subsequently all tests were run at 120 Hz. A gage failure is
shown in Figure 4.177.

Figure 4.176. Failure at 300 Hz in the tabs.

Figure 4.177. Failure in the gage section.

4.4.3.2   Experimental Test Setup

A custom-built 300-Hz electrohydraulic axial test machine was used for the evaluation of PWA 1484 specimens in the life regime to 10^9 cycles (Figure 4.178).

Normally, long life fatigue testing is performed in rotating bending or cantilever bending where a stress gradient is imposed on the material. Such testing techniques cannot reveal changes in crack initiation mechanisms that occur with axial loading of bulk volumes where there is no strain gradient. Control was provided through a load cell – computer-controlled A/D

Figure 4.178. Overall view of high cycle fatigue load frame.

feedback system. Feedback correction to loading amplitude and mean was made every 300 cycles at 300 Hertz. Heating to 1900°F was provided by quartz IR heaters mounted adjacent to either flat side of the specimen gage section. The temperature gradient was maintained within ± 1°F across the gage section throughout the duration of each test. All specimens were thermally equilibrated for 15 minutes before cyclic loading. The specimen was gripped with water-cooled, lightweight wedge-collet grips. The lower grip and hydraulic actuator were torsionally constrained to inhibit any non-axial loading. Atmosphere was laboratory air, although capability exists for flowing nitrogen or argon gas. A detailed image of the HCF system with furnace in operation is shown in Figure 4.179. The results of the experiments are summarized in Table 4.40.
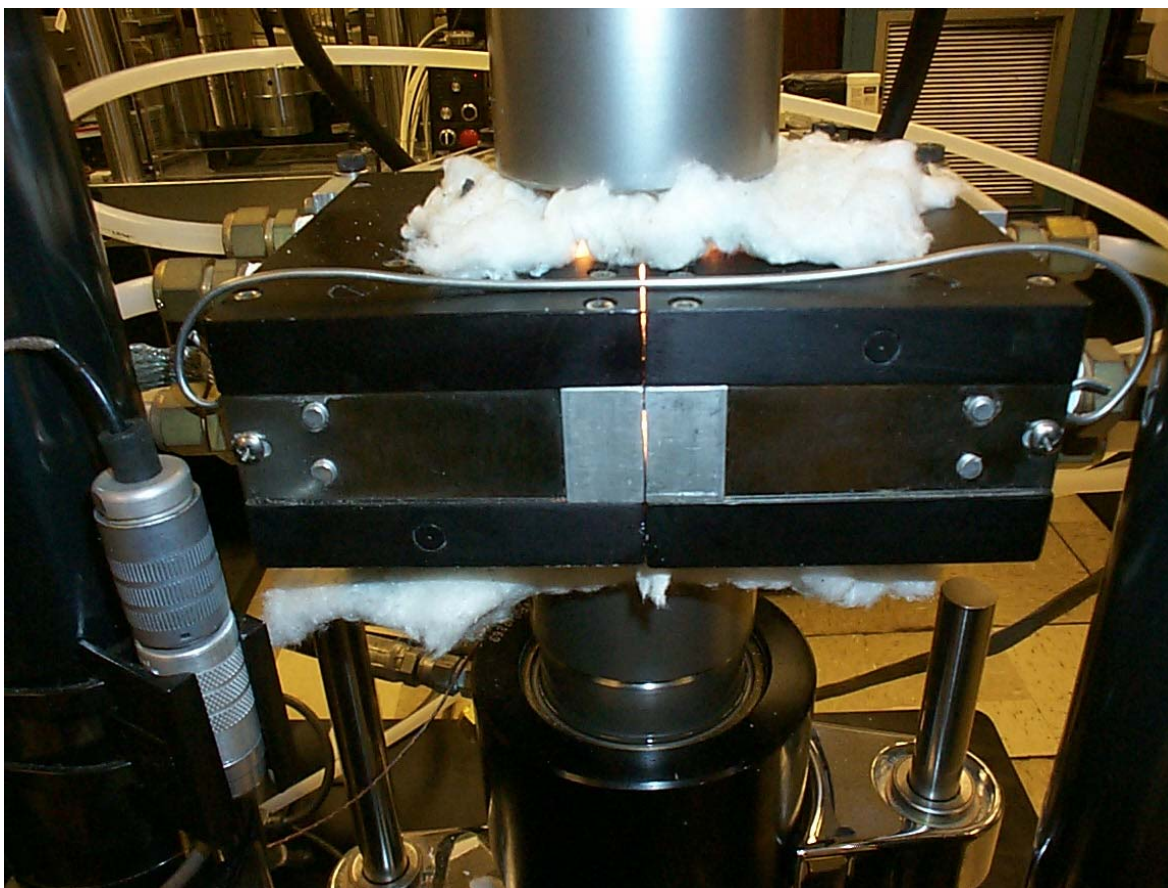
Figure 4.179. Close-up of high-temperature HCF test system.

4.4.3.3   Failure Analysis

The PWA 1484 used in this study is a coated nickel-base single crystal superalloy with nominal composition of 5Cr-10Co-2Mo-6W-9Ta-3Re-5.6Al-0.1Hf-Bal Ni. A typical fatigue initiation site for the no-hole condition is shown in Figure 4.180. Significant oxidation of the crack front is apparent.

The extent of oxide penetration is shown in the backscattered SEM mode of Figure 4.181. Oxide accumulation at the initiation site decreases with crack depth, and correlates with crack front progression (light regions are metallic). All specimens in the no-hole condition exhibited crack initiation at gage section corners.

Table 4.40. Load-Controlled HCF Test Results on PWA 1484 Sheet

Condition	Specimen ID	Frequency --Hz	Gage CSA--in.^{2}	Stress level-- ksi	Account for coating thickness Modified stress-- ksi	Cycles	Comments
No hole,	E-5	150	0.01619	35	37.8	82,781	
R = 0.1		200	0.01619	35	37.8	118,671	Poor test control
		180	0.01619	35	37.8	0	Stopped, temp to RT
		300	0.01619	35	37.8	n/a	Poor test control
		200	0.01619	35	37.8	n/a	Strain gage results confirm good control
	C-5	200	0.01556	32	33.2	1,395,160	Failed outside gage section in grips
	C-6	200	0.01594	32	34.0	10,008,692	
		200	0.01594	34	36.1	1,867,273	Failed outside gage section (not in grips)
	C-7	200	0.01531	32	32.7	10,713,036	
		200	0.01531	34	34.7	10,001,754	
		200	0.01531	36	36.8	2,424,102	Failed in gage section
	E-2	200	0.01575	34	35.7	8,683,789	Failed in grips
90 deg,	C-3	120	0.01573	22	23.1	10,000,000	
R = 0.1		120	0.01573	24	25.2	63,000	
	D-1	120	0.01606	24	25.7	3,397,946	
	D-8	120	0.01571	26	27.2	6,540,000	
	D-6	120	0.01577	22	23.1	12,900,000	
	B-6		0.01621	22	23.8		Broke in grips
30 deg,	A-4	120	0.01578	24	25.2	3,422,115	
R = 0.5	B-4	120	0.01563	22	22.9	7,613,516	
	C-1	120	0.01588	21	22.2	17,132,141	
	C-8	120	0.01578	20	21.0	33,461,862	
	D-3	120	0.01539	23	23.6	14,016,492	

Table 4.40. (continued)
Load-Controlled HCF Test Results on PWA 1484 Sheet

Condition	Specimen ID	Frequency --Hz	Gage CSA--in.^{2}	Stress level-- ksi	Account for coating thickness Modified stress-- ksi	Cycles	Comments
40 deg, R = 0.5	D-2	120	0.01581	28	29.5	775,516	
	E-3	120	0.01581	26	27.4	1,818,984	
	E-7	120	0.01542	24	24.7	2,009,684	
	E-6	120	0.01607	22	23.6	4,273,267	
	E-1	120	0.01608	20	21.4	91,185,941	
90 deg, R = 0.5	A-5	120	0.01616	26	28.0	16,870,431	Failed across hole
	A-6	120	0.01614	24	25.8	42,760,954	Failed across hole
	A-7	120	0.01562	28	29.2	3,310,686	Failed across hole
	A-8	120	0.01620	23	24.8	43,093,656	Failed across hole
	B-3	120	0.01561	22	22.9	80,237,072	Failed across hole
	B-5						
No hole, R = 0.5	A-2	120	0.01625	36	39.0	7,155,826	Failed in gage section
	A-3	120	0.01621	34	36.7	10,043,807	Failed in gage section
	B-1	120	0.01538	30	30.8	20,154,379	Failed in gage section
	C-2	120	0.01594	25	26.6	89,964,131	Failed in gage section
	C-4	120	0.01599	27	28.8	43,095,077	
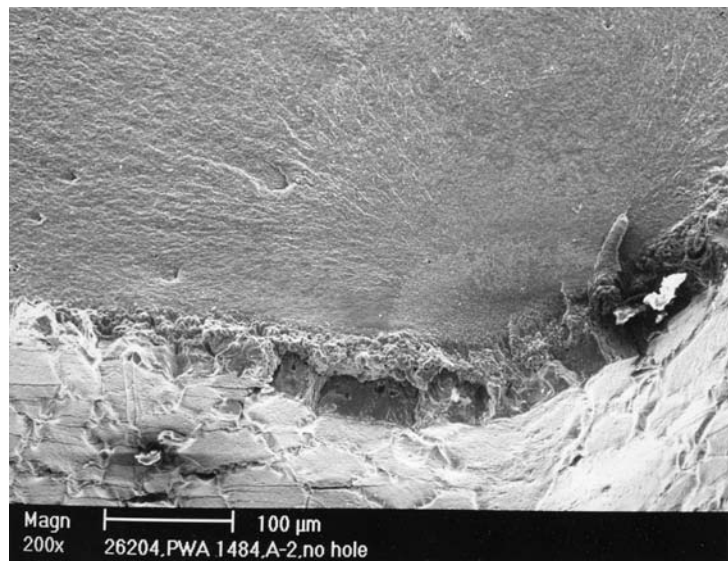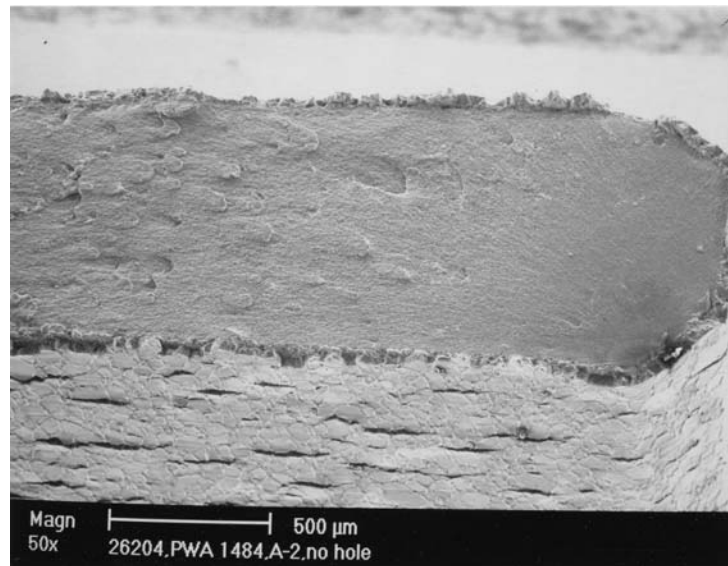
Figure 4.180. SEM image of fatigue crack initiation site (A-2, no hole, R = 0.5).
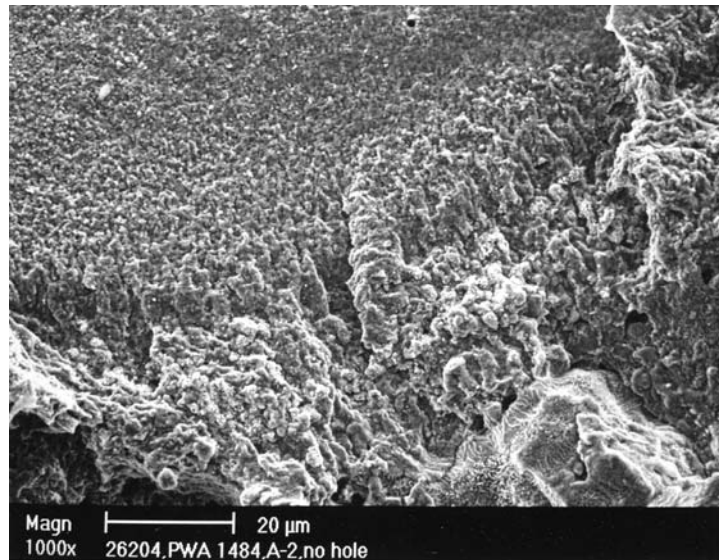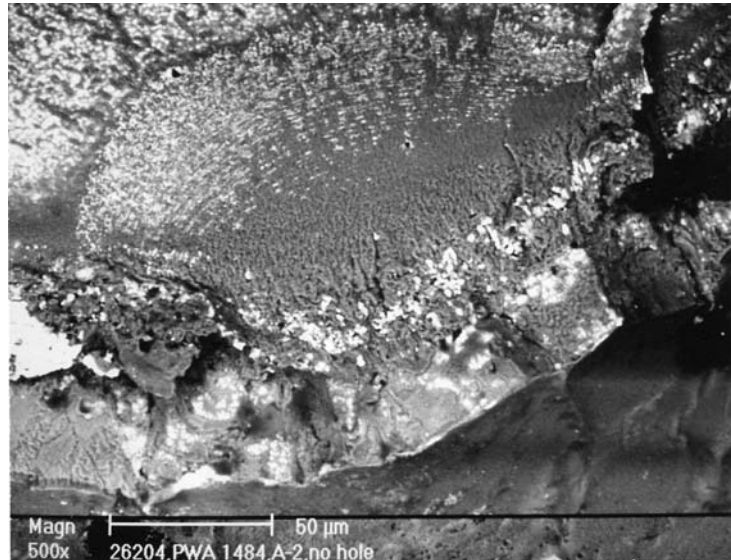
Figure 4.181. Backscatter image of fatigue initiation site
(A-2, no hole, R = 0.5).

Crack propagation in the 30 deg hole specimens was similar. Initiation (for the 30 deg hole condition) was observed at the stress concentration formed by the acute hole entrance (Figures 4.182 and 4.183). In the one case examined, initiation for the 90 deg hole condition was at the hole wall (Figures 4.184 and 4.185).
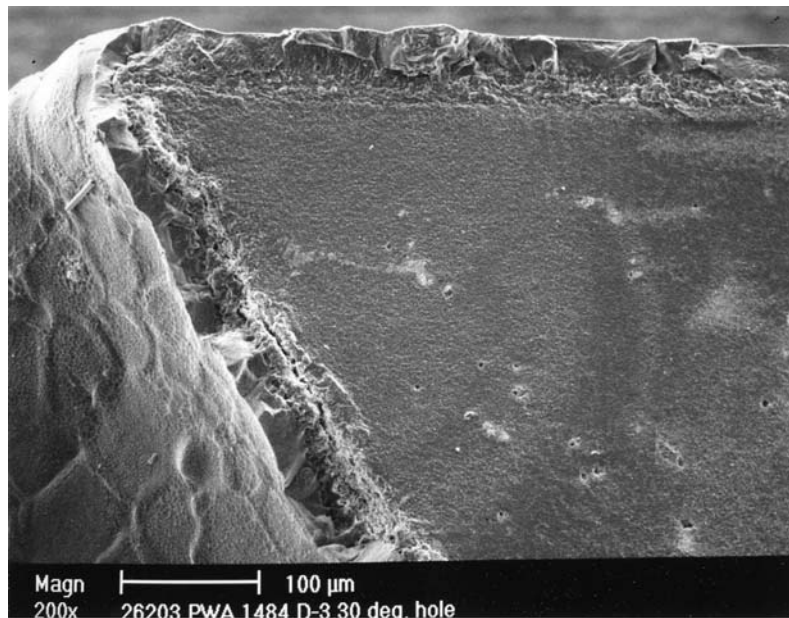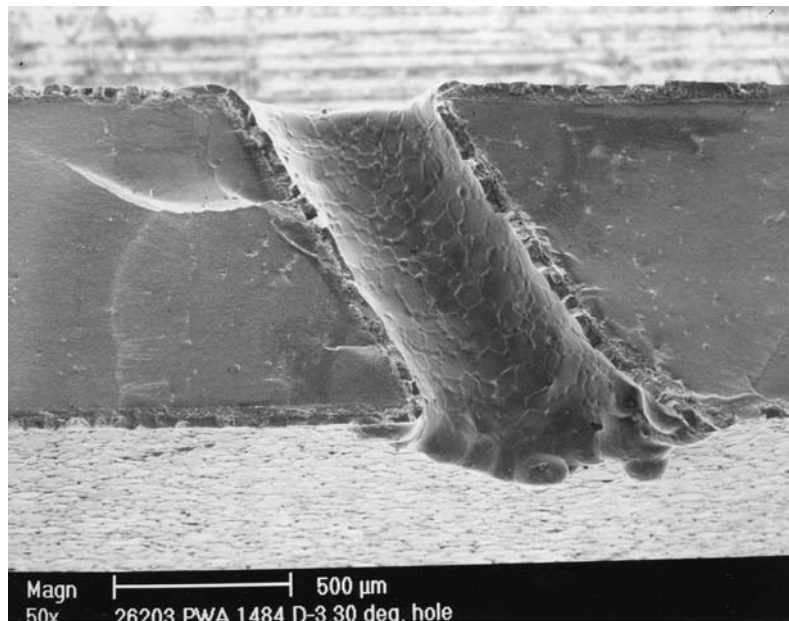
Figure 4.182. SEM image of fatigue crack initiation site (Specimen D-3).

Figure 4.183. Detail SEM image of initiation site (D-3).
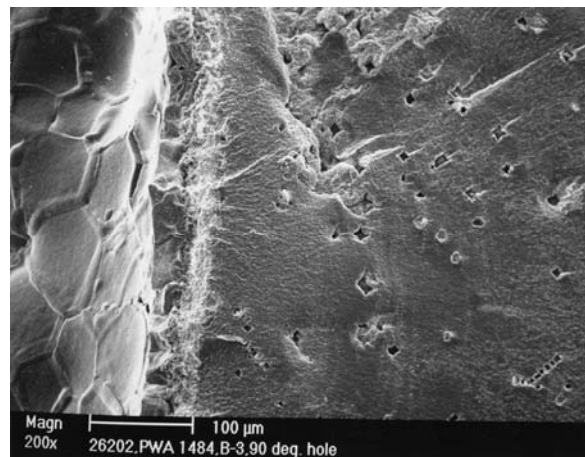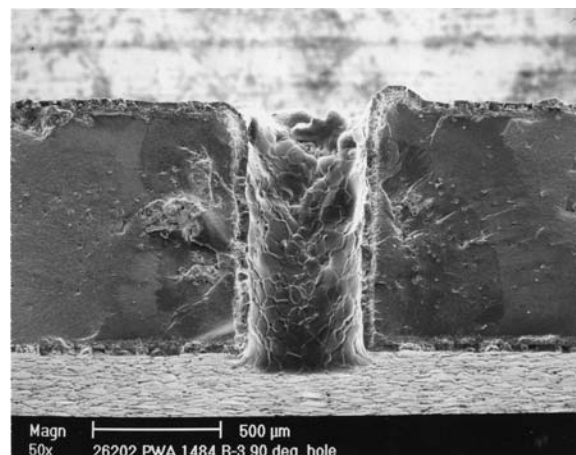
Figure 4184. SEM image of fatigue crack initiation site. (B-3, 90 deg hole, R = 0.5).
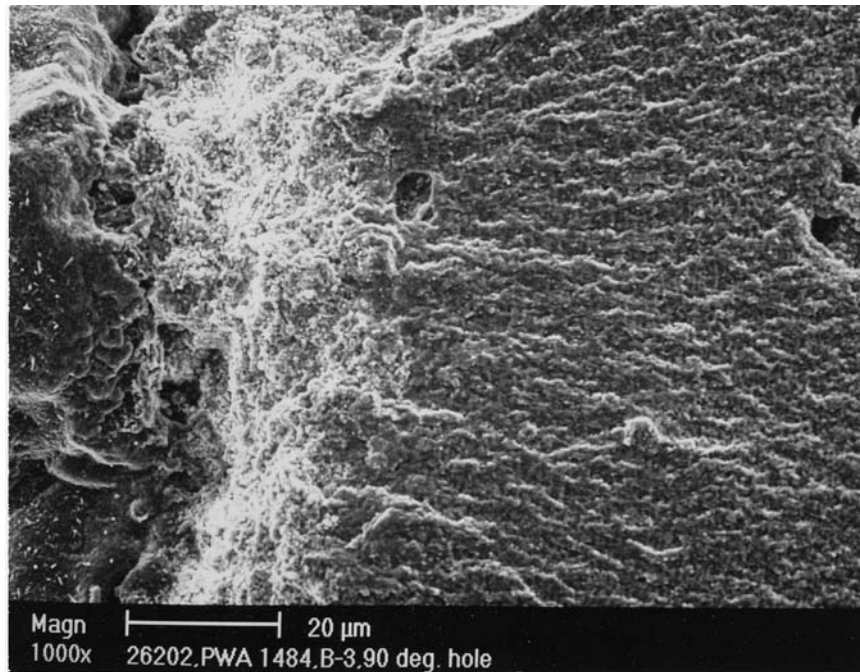
Figure 4.185. Detail SEM image of initiation site (B-3).

4.4.3.4   Results and Discussion

This verification program was an attempt to apply the models developed during the high cycle fatigue program to correlate the results of HCF tests. As described, the single crystal verification study consisted of a number of high cycle fatigue tests conducted on coated PWA 1484 sheet specimens. The specimens were 0.040 inch thick. Four geometries were tested, three with 0.020 inch diameter holes and one with no hole. The plane normal to the loading and at the specimen center contained the holes. The three holes were at an angle to the sheet face; one normal (90 degree) to the sheet while the other two angles were 50 and 60 degrees. The specimen drawing is shown in Figure 4.186. The test results are summarized in Table 4.40.

The results of the verification experiments were evaluated using elastic finite element analysis and the Glinka stress redistribution model. An example of the finite element model for the 90-degree specimen is shown in Figure 4.187. The other models were similar except for the angle of the hole. The principal material directions of the single crystal were assumed to coincide with the axes of the specimen, i.e. along the loading axis and normal to the face. The coating on the specimen was not explicitly modeled.

399

Figure 4.186. Flat specimen drawing for HCF test program.

Figure 4.187 (a). Overall model of flat specimen finite element model.
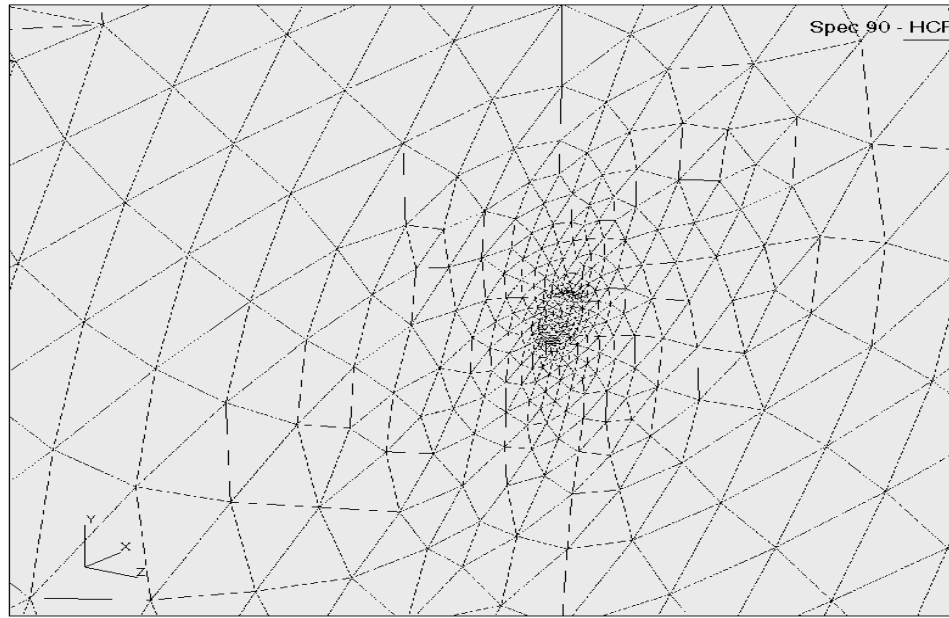
Figure 4.187 (b). Hole region of flat specimen finite element model.

Some results of the initial elastic analysis are shown in Figures 4.188 through 4.190. The figures show the location of the peak effective stress for each hole geometry. In all cases, the maximum value is on the hole surface, some distance from the specimen face. The 60 and 90-degree specimens reach maximums near the front surface while the 50-degree panel has its maximum near the rear face. Based on the elastic stress analysis and the local effective stress, the k_t values are given in Table 4.41.

Table 4.41. Stress Concentration (k_t) Values

Hole angle--	k_t
50	3.63
60	3.27
90	2.74
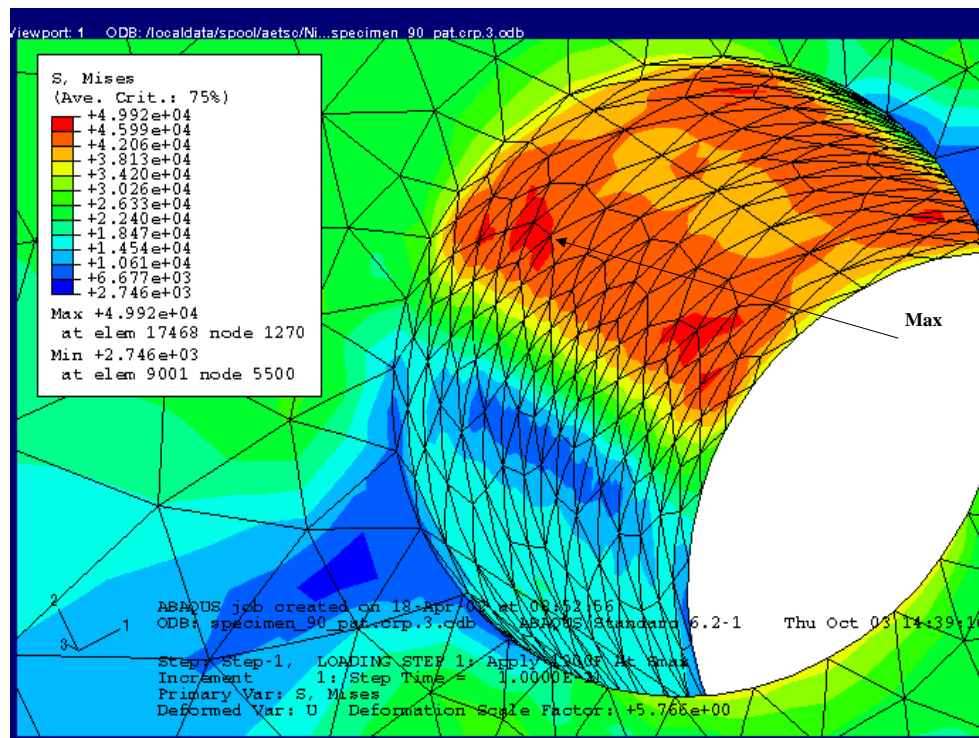
Figure 4.188. Maximum stress location in 90-degree hole specimen model.
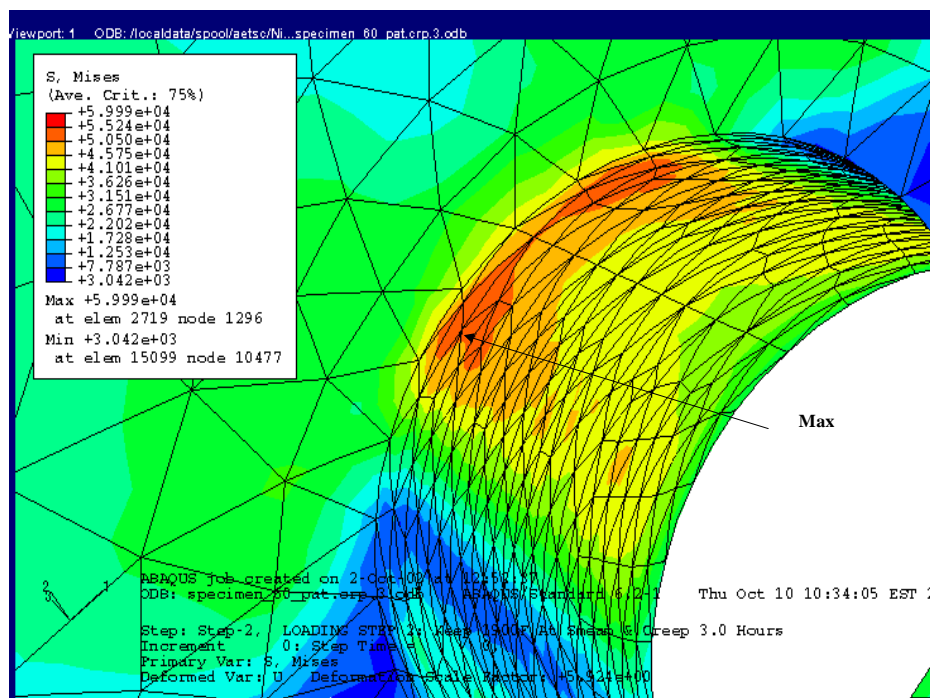
Figure 4.189. Maximum stress location in 60-degree hole specimen model.
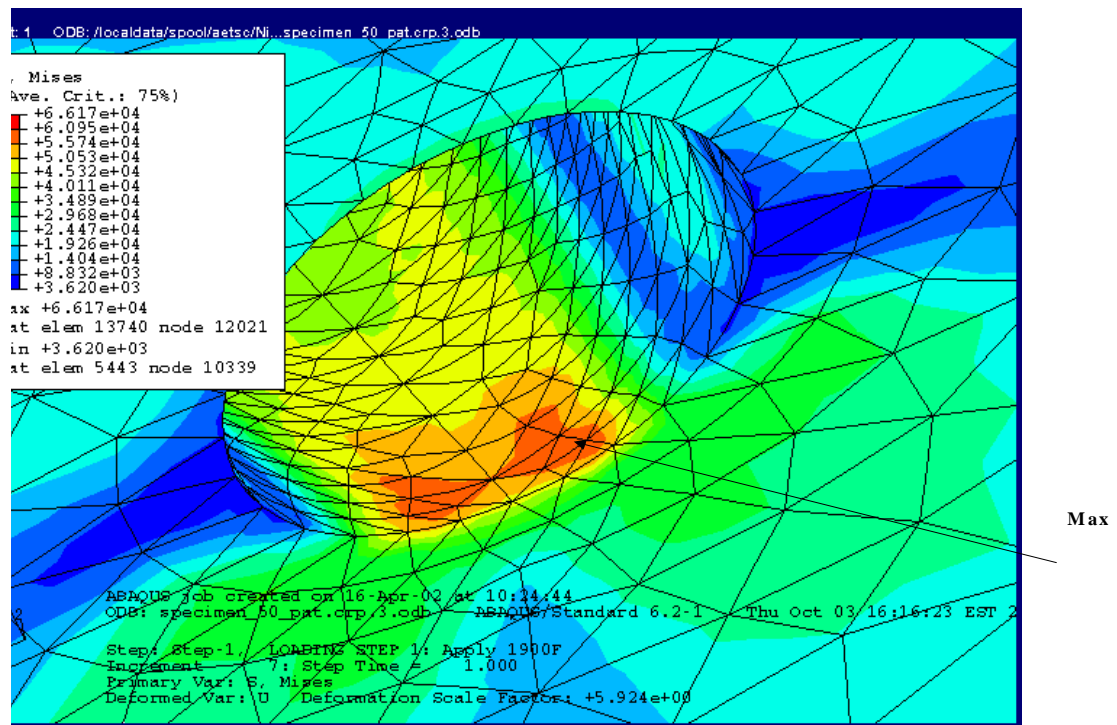
Figure 4190. Maximum stress location in 50 degree hole specimen model.

Throughout the HCF program, extensive work has been conducted to determine the "best" parameter to be used in predicting fatigue life. Generally it has been found that the critical plane approaches have been superior, although the Manson-McKnight method has shown capabilities almost as good. While these methods eventually will be applied to this set of results, it seemed premature to do so at this time since a fully verified anisotropic constitutive model of PWA 1484 was not widely available. Instead, it was decided to rely on HCF parameters, which can be easily calculated using largely elastic methods. The Smith-Watson-Topper (SWT) parameter was used since it accounts for the mean stress, is amenable to calculation from finite element results, and has been applied previously in the program. However, given the high temperature and positive mean stress, it was expected that creep would play a large role in relaxing the stress field around the holes. Thus, some nonlinear analysis was performed to examine the contribution of creep to the HCF process.

The initial effort to correlate the test data of Table 4.40 was to perform a "traditional" notch analysis. This analysis calculated a local stress using the applied stress and stress

concentration factor; this stress was then redistributed through a Glinka/Neuber model. When this analysis was completed and compared to the no hole sheet data, the hole specimen data was located above the baseline data by at least a factor of two.

The next step was to combine the results of the finite element analysis with the Glinka notch model developed in this program. The Glinka model requires three pieces of input data: a material stress-strain curve, a description of the stress gradient at the stress concentration, and the stress increments describing the applied stress cycle. The stress increments were obtained from the finite element models that were subjected to a load cycle of zero-minimum-maximum. The stress component increments were obtained from these load steps and input to the model. The material stress-strain data for PWA 1484 was obtained from GEAE and input as several linear segments. The stress gradient was obtained directly from the ABAQUS output by picking nodes along a path from the hole to the edge of the specimen. This procedure required some smoothing since the models were meshed with 10 node tetrahedrons and thus a straight, planar path could not be selected. The stress vs. distance data was input to a spreadsheet and adjusted to give a monotonic decay. Since the data reflected the particular nodal path chosen, no standard procedure was developed; the smoothing was done manually since only small shifts were needed on most cases.

The results of this procedure are shown in Figure 4.191, a plot of the failure data using the Smith-Watson-Topper parameter calculated for the maximum stress nodes. The results show that the hole specimen data does not correlate with the baseline panel data. The data demonstrate that either the calculated maximum stress or strain range, or both, are too large. This result is very similar to that obtained by the stress concentration and Glinka method. The surface stress obtained in a finite element model is obtained by extrapolation, and when there is a high stress gradient, there is some concern about the magnitude of the surface stress being overestimated. To address this issue, the results were reanalyzed using a subsurface node. The node selected was the first corner node near the surface maximum stress point; the subsurface distance ranged from 0.0045 to 0.0048 inch. The same process was followed. The stress increments at the node, along with its location, were input to the Glinka redistribution code. The result based on the SWT parameter is shown in Figure 4.192. The figure shows some layering of the data but brackets the baseline data rather well.
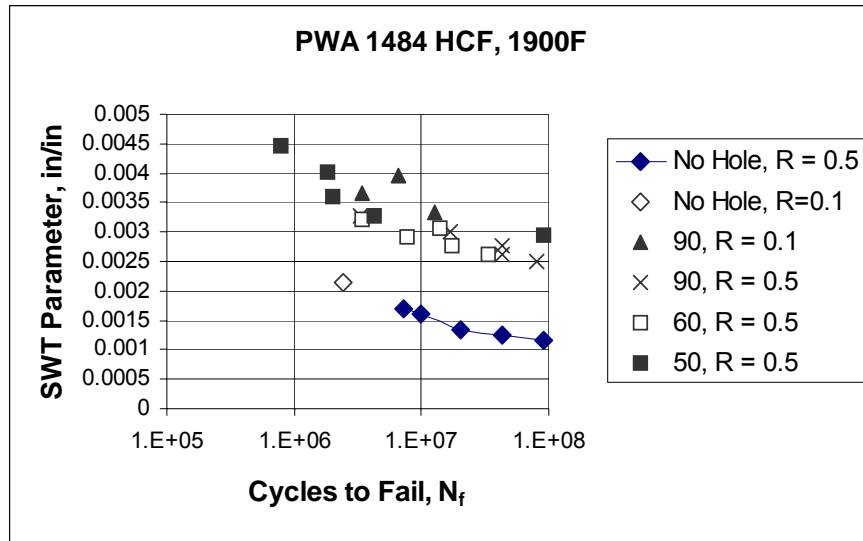
Figure 4.191. Correlation of HCF data with Smith-Watson-Topper parameter, based on surface stresses and the Glinka plasticity adjustment.
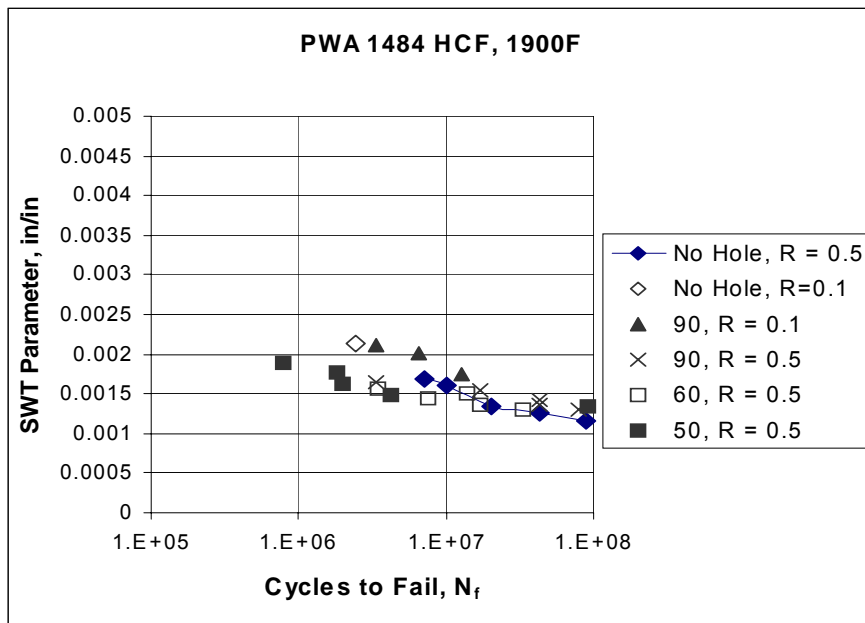
Figure 4.192. Correlation of HCF data with Smith-Watson-Topper parameter, using subsurface stresses, ≈ 0.0045 inch, and the Glinka plasticity adjustment.

Since the calculated surface stress appears to be too high and the choice of the subsurface depth is mesh dependent, it was decided to look at time dependent deformation in the specimens. This was done using two models, one with creep-fatigue loading and one with a three-hour hold at mean load. The creep-fatigue model used the 90 degree hole, R = 0.5, with σ_{max} = 25.2 ksi. The specimen was loaded from zero to minimum, and the ramp from minimum to maximum divided into ten load steps, each 1.17e-7 hours. Creep was turned on during the loading to simulate the local stress relaxation. At the end of the load ramp, the analysis was restarted and the panel was unloaded. Several load-unload steps were run. The changes in stress magnitude are small, about 0.2 percent on the first cycle, and an order of magnitude less 3 cycles later. The changes in creep strain are much larger but the creep strain magnitude is the order of 10^{-7} in/in, and is concentrated at a couple of nodes. The volume of strained material is very small. Because of the size of the analysis files, it is not practical to continue the cycle-by-cycle loading very far. It is difficult to tell if the local creep strain is fully relaxed at this point in the test. Since the extrapolation is over millions of cycles, any small change would result in unrealistically small-predicted stress values.

In an effort to see how much creep would be anticipated over a million or so cycles, the specimens were loaded to their mean load and then held for 3 hours. A typical stress relaxation curve is shown in Figure 4.193. The element stress was taken at an element at the maximum stress location. Clearly the stress decay was not asymptotic after 3 hours but the rate of relaxation significantly drops after 15 minutes. Confirming the earlier creep result, the creep strain was very localized. For the high stress 50 degree hole, the decrease in maximum stress was 43.7% at the critical node but only 7.2% at the adjacent node used for the life calculation of Figure 4.192. The other holes had smaller percent changes. The models indicated that there was a small amount of creep at the holes, which was a very local influence. If the lowered stress level were used in the calculation of the SWT parameter, it would lower the surface values plotted in Figure 4.191. However the problem was determining the appropriate hold time. Given this uncertainty, the extremely local nature of the creep, and the fact that the creep analysis has to be performed for each specimen, the explicit inclusion of creep into the model prediction seemed premature. However, it should be performed as part of the analysis to

determine if there is significant creep in the component. In such a case, the current approach of using the subsurface elastically calculated stresses in the life model would have to be revisited. The results of the verification testing on coated flat sheets of PWA 1484 containing holes through the panels were correlated using elastic finite element results combined with the program-developed Glinka notch model to account for local stress redistribution. It was found that using the surface stress values was grossly conservative but the use of stress components at a subsurface node, approximately 4.5 mils from the surface, led to reasonable correlations. While this makes the approach somewhat model dependent, it is consistent with the very local nature of the calculated high stresses. By using an "average" value, a more representative failure criterion is achieved. In addition, while the test specimens did not include compound skew holes with acute included angles, the success of the SWT parameter in correlating this class of holes suggests that when predictions of actual airfoil cooling holes is attempted, a measure of success can be anticipated.
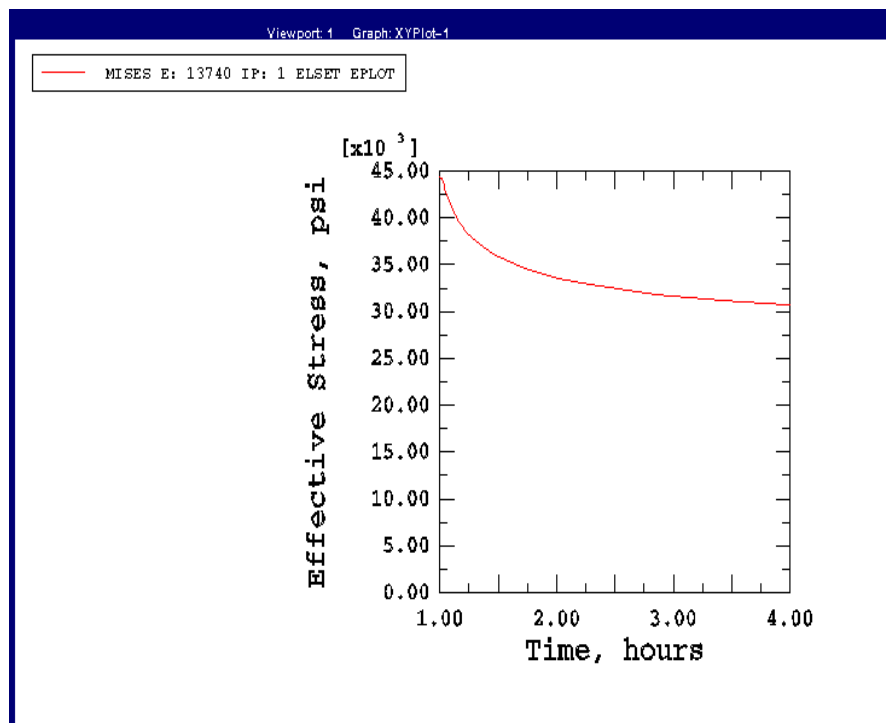
Figure 4.193. Relation of stress at the 50 degree hole over 3 hr accumulated time.

4.4.4   Anisotropic Shakedown Methodology For Bivariant Stress Fields

This section summarizes the development and validation of an anisotropic shakedown methodology for bivariant stress fields where stresses vary in both the *x* and *y* directions. Additional details on the methodology are provided in Appendix J.

Shakedown occurs due to stress relaxation and redistribution arising from plastic strains generated during loading. Plastic deformation can occur in regions of high stress, such as notches and underneath contact surfaces. A compressive residual stress is left in the structure as a consequence of elastic unloading following stress relaxation. This static compressive stress is beneficial in inhibiting both crack initiation and crack propagation by lowering the local stress ratio, *R*, and in helping to increase the critical crack size by reducing the maximum crack-tip driving force.

After the formation of the compressive residual stress the structure is said to have undergone shakedown, and further load excursions will result only in linear-elastic behavior as non-linear behavior has been "shaken out." The analytical shakedown methodology described herein enables elastic-plastic stress and strain distributions to be determined from the results of a linear elastic stress analysis. The shakedown residual stress field is obtained from these solutions by subtracting the linear elastic solution from the analytically estimated elastic-plastic solution.

The advantage of an analytically based shakedown methodology is that it can account for plastic deformation in design and reliability assessments without the need to perform more time consuming and costly elastic-plastic finite element analyses. Although the methodology described herein, and the anisotropic shakedown module developed by SwRI to implement it, are verified against the results of elastic-plastic finite element computations using materials data and constitutive models developed by P&W specifically for the single crystal material PWA 1484, the shakedown module is applicable to a wide variety of other anisotropic materials, provided the appropriate constitutive models are available to describe the relationships between stress and strain in these materials.

4.4.4.1   Anisotropic Shakedown Methodology

The anisotropic shakedown methodology developed by SwRI is an extension of the isotropic shakedown methodology described in the Final Report on titanium material prepared under the first HCF Program [1]. The load shedding and load redistribution schemes employed in the anisotropic shakedown module to allow for the effects of plastic deformation on linear elastic stress solutions are similar to those used in the isotropic shakedown module. The major difference between the isotropic and anisotropic shakedown modules is the algorithm used to determine the stress relaxation at a point (point relaxation) whose formulation depends on the material modeling. The reason for this is that whereas the constitutive behavior of an isotropic material can usually be expressed as a relatively simple relationship between uniaxial stress and uniaxial strain, this is not the case for the more complicated constitutive models that describe anisotropic materials such as PWA 1484.

The shakedown methodology converts incremental linear elastic solutions, corresponding to incremental load changes, into equivalent elastic-plastic solutions while conserving forces and moments resulting from the remote loading. All six components of stress are required for the shakedown analysis. The z-component of stress that is normal to the load bearing area is considered the primary stress of concern. The out-of-plane direction is in the y-direction, and this coordinate along with the x coordinate defines the load bearing section. The designation of stresses conforms to the coordinate system employed in Figure 4.194, which shows the load bearing section (enclosed by dashed lines) corresponding to a notched plate.

Two major tasks are performed in the anisotropic shakedown methodology. The first task determines the stress relaxation at a point on the load bearing area from the linear elastic stress state. This point-relaxation procedure provides an initial approximate solution to the elastic-plastic stress state at each point when load re-distribution and shedding are ignored. The point relaxation procedures are based on Neuber's rule that converts the incremental elastic strain energy density into the equivalent incremental elastic-plastic strain energy density. Neuber's rule states that the incremental product of stress and strain is invariant for each load step irrespective of the constitutive relationship between stress and strain. The second task performs the load shedding that occurs due to point relaxation and re-distributions of the surplus incremental forces and moments over the load bearing area.

409
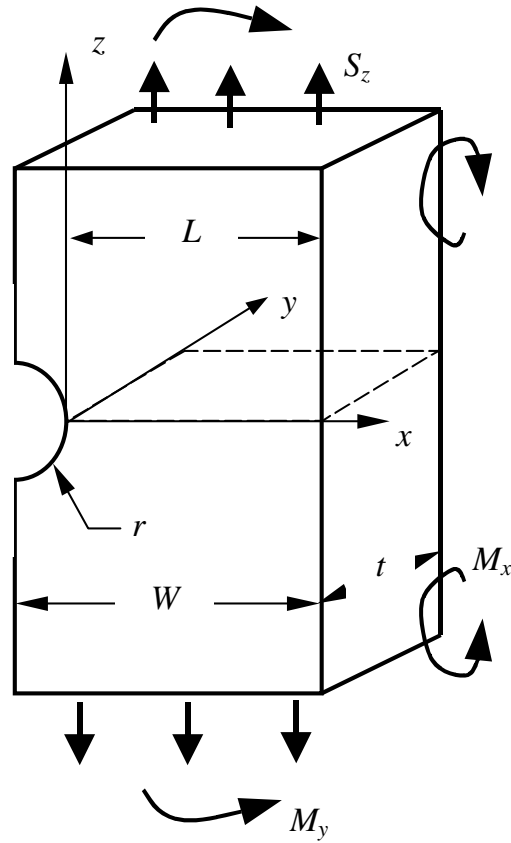
Figure 4.194.   Geometry, coordinate system, and example loading conditions for a typical
                 rectangular structure that can be analyzed using SwRI's anisotropic shakedown
                 module. The crystal axis can be at any angle to the axis of the structure (the z-axis
                 in the figure). In one analysis reported herein to verify the shakedown module the
                 axis of the plate is assumed parallel to the <001> direction, while in another set of
                 calculations the axis of the plate is assumed parallel to the <111> direction.

        The material data needed in the shakedown analysis is composed of discrete pairs of

stress and strain values that define the uniaxial stress and strain behavior of an anisotropic

material under monotonic loading when the direction of loading is along the <001>

crystallographic direction. Along the <001> direction, the anisotropic materials in this study

display "pseudo-isotropic" behavior. The coordinate system that is compatible with the <001>

or equivalent direction is herein called the local coordinate system. In addition, there is a global

coordinate system. The global coordinate system is the system consistent with the external

loading direction, the direction for which the linear elastic stress results are obtained.

The linear elastic stress analysis data that are input to the shakedown module consist of the incremental changes in the global stress components as the applied load(s) are incrementally increased. The point relaxation calculations are performed in the local coordinate system. Hence, the transformation matrix and its transpose that operate on the global stresses to transform them into local stresses, and on the calculated local plastic relaxed stresses to transform them back into the global stresses also have to be input into the module.

Currently, the anisotropic shakedown methodology is limited to isothermal and constant strain rate loading conditions. Thus, the so-called "pseudo-isotropic" stress-strain curve provided by the user needs to be representative of the actual operating temperature and strain rate.

4.4.4.2   Software Module Anisotropic Shakedown

The isotropic shakedown methodology described in [1] is implemented in a software module called SHARP (Shakedown Analysis of Residual Plasticity). The anisotropic shakedown methodology described herein is implemented in a software module called SHARP_AN (Shakedown Analysis of Residual Plasticity Anisotropic). Both shakedown methodologies are based on approximate elastic-plastic stress analyses that are applicable to rectangular load bearing areas, such as that illustrated in Figure 4.194. User provided routines that determine the constitutive behavior of the anisotropic material are needed to interface with SHARP_AN. These constitutive-based routines (called generic interface routines, see Figure 4.195) have to be compatible with material behavior measured on a specimen with its axis parallel to the <001> or equivalent crystallographic direction. In other words, quantities calculated within the user provided routines have to be compatible with the local coordinate system.

A very brief overview of the anisotropic shakedown module and how it interacts with the point relaxation model and three user-provided generic interface routines is shown in Figure 4.195. The purpose of the three generic routines signified as GENERIC_INTF I, GENERIC_INTF II, and GENERIC_INTF III is to provide needed data that is derived from the material constitutive model. Since the derivation of these data are constitutive model dependent, the user is required to develop explicit routines and procedures for extracting the needed data

411

from the constitutive model. This generic interface approach enables users to implement a variety of anisotropic material constitutive relationships. More details are available in Appendix J.

```
┌─────────────────────────────────┐
│ Anisotropic Shakedown Module    │          ┌──────────────────────────────────┐
│ Purpose: perform load shedding  │          │      GENERIC INTERFACE I         │
│         and load re-distribution│ ←─────── │ Purpose: provide values for the  │
└─────────────────────────────────┘          │ material constants used in the   │
                                              │ constitutive model.              │
┌─────────────────────────────────┐          └──────────────────────────────────┘
│ Point Relaxation Module         │
│ Purpose:  convert linear elastic field
│ quantities at a point into elastic-plastic
│ quantities using Neuber's rule  │
└─────────────────────────────────┘

┌──────────────────────────┐      ┌─────────────────────────────────────────┐
│ GENERIC_INTF_III         │      │          GENERIC_INTF_II                │
│ Purpose: determine the   │      │ Purpose: determine the incremental change│
│ equivalent stress from the│     │ in elastic-plastic field quantities      │
│ component values consistent│    │ consistent with the material constitutive│
│ with the material constitutive│ │ model based on the equivalent stress and │
│ relationship             │      │ the equivalent strain.                   │
└──────────────────────────┘      └─────────────────────────────────────────┘
```

Figure 4.195.   An overview of the program structure of SwRI's anisotropic shakedown module and how the shakedown module interfaces with three user provided routines: GENERIC_INTF_I, GENERIC_INTF_II, and GENERIC_INTF_III.

4.4.4.3   Verification of ANSYS User Material Routines

Elastic-plastic finite element analyses were performed using ANSYS to verify the anisotropic shakedown module. To accomplish these analyses, P&W provided SwRI with software modules to link with ANSYS in order to implement the Walker constitutive model for PWA 1484 (see Section 4.3.2.1). Modified versions of these ANSYS user material routines were developed and used by SwRI to validate the anisotropic shakedown methodology. The modified versions corrected incompatibility problems between the received versions and ANSYS that led

412

to overwriting the state variables used internally by ANSYS. The modified versions of P&W's ANSYS user material routines were verified by SwRI as the initial step in the development of the anisotropic shakedown module. This was accomplished by comparing the results of FEA computations with those derived from the analytical solutions for a plate and round bar subjected to uniaxial tensions and shear, respectively. The PWA 1484 material constitutive relationship corresponding to a uniform temperature of 1400°F was used in the computations. Figure 4.196 presents the comparison of the analytical tension results with the finite element results and shows that the FEA results predicted using the SwRI modified material routines are in excellent agreement with the solutions for three strain rates at 1400°F. Also given in the figure (solid line) are the FEA results calculated assuming a temperature of 1100°F. At this temperature, which is typical of the blade attachment area, the stress-strain relationship is independent of the applied strain rate.
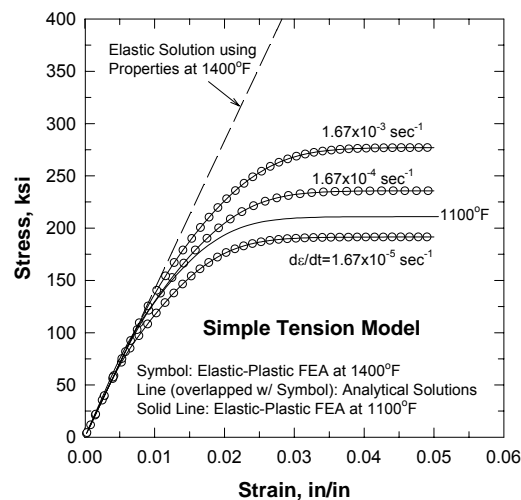
Figure 4.196. Comparison between analytical solutions from the Simple Tension Model, derived from the Walker constitutive equation, and the corresponding finite element analysis.

4.4.4.4   <u>Verification of the Anisotropic Shakedown Module Against Finite Element Results</u>

Three-dimensional elastic-plastic finite element analyses were performed to validate the anisotropic shakedown methodology once the material routines had been verified. The anisotropic shakedown module used, as input, bivariant stress fields determined from three-dimensional anisotropic linear-elastic finite element computations employing ANSYS. The

elastic finite element results were obtained based on the anisotropic linear-elastic relationship derived from the Walker constitutive model.

The validation was performed for a single-edge-notched plate containing a semi-circular through-thickness notch (see Figure 4.194). This plate was subjected to various combinations of tensile load and out-of-plane bending moment, as illustrated in Figure 4.194. Two sets of computations were performed. In one, the axis of the plate was assumed parallel to the <001> direction, while in the other the axis was assumed parallel to the <111> direction. The local and global coordinate systems are identical for the specimens whose axes are parallel to the <001> direction. The nonlinear material behavior used for the anisotropic shakedown module corresponded to a temperature of 1100^oF. At this temperature, the effect of strain rate is minimal (see Figure 4.196). Typical comparisons between the results predicted by the shakedown module and FEA are presented in Figures 4.197 and 4.198. Each figure shows results for different planes through the plate thickness parallel to the two side surfaces. For symmetrical loading conditions and the <001> direction, only results on three planes are plotted. The locations of these planes are at one of the free surfaces (y/r=0), a plane one quarter of the way through the thickness (y/r=1.237), and the mid-thickness (y/r=2.5). For loading parallel to the <111> direction results are not symmetric with respect to the mid-thickness, thus, results are also given on the two additional planes corresponding to about three-quarters of the way through the plate (y/r=3.763) and the other side surface (y/r=5).

The results obtained by applying the anisotropic shakedown module developed by SwRI are, as in the case of the isotropic shakedown module, SHARP, in excellent agreement with the FEA results obtained using Walker's constitutive model, except for the through-thickness (out-of-plane) component of stress, σ_y. The reason that this stress component is not estimated as accurately as it is by the isotropic module is the fact that the out-of-plane multi-axial stress corrections that were developed in that case were not implemented in the anisotropic module. The main reason for this is that evaluation of these corrections for isotropic materials involved performing finite element computations for materials with a range of strain hardening capabilities. This option was not available for anisotropic material studied in the present work because of the nature of the material strain hardening response embodied in the Walker constitutive relationship specifically derived for PWA 1484.

The deficiency of the simple point relaxation predictions is apparent from the results shown in Figures 4.197 and 4.198. However, the deficiency is not as great as that observed under some circumstances in the development of the isotropic shakedown module [1]. The reason is that the anisotropic material investigated herein displays significant strain hardening capability, as illustrated by the stress-strain curve for 1100°F shown in Figure 4.196. The major discrepancies between the point relaxation model predictions and the elastic-plastic finite-element results observed in the isotropic case occurred for materials like Ti-6Al-4V that exhibited little strain hardening capability. As strain hardening capability increases the changes between the linear-elastic and elastic-plastic results become less significant. Thus, materials with a high strain hardening capability result in less load redistribution for a given applied load than do materials with low hardening. This means that the point relaxation model will become more accurate with increasing strain hardening, as borne out by the present results.

4.4.4.5   Verification of the Anisotropic Shakedown Module

The following conclusions are drawn based on the results reported herein.

(1)   The shakedown methodology developed by SwRI for isotropic materials has been successfully extended to anisotropic materials.

(2)   A shakedown software module has been developed for implementing the anisotropic methodology and verified against the results of three-dimensional elastic-plastic computations for structures orientated with their axes parallel to the <001> and <111> crystallographic directions.

(3)   Generic software interfaces have been developed to allow users of the shakedown module to employ anisotropic constitutive models other than the Walker model used herein to validate the shakedown module.

(4)   The shakedown methodology developed by SwRI includes the effects of load shedding and re-distribution due to stress relaxation. It has been shown that the accuracy of the shakedown model is significantly reduced if this capability is not included in the modeling.

415
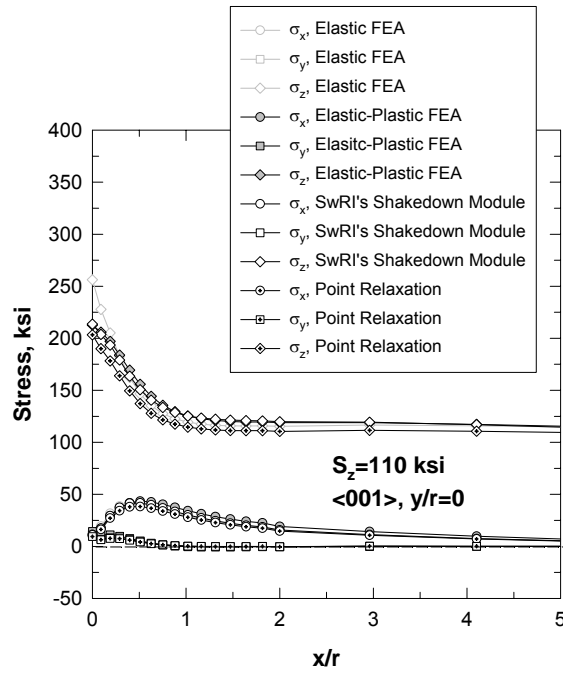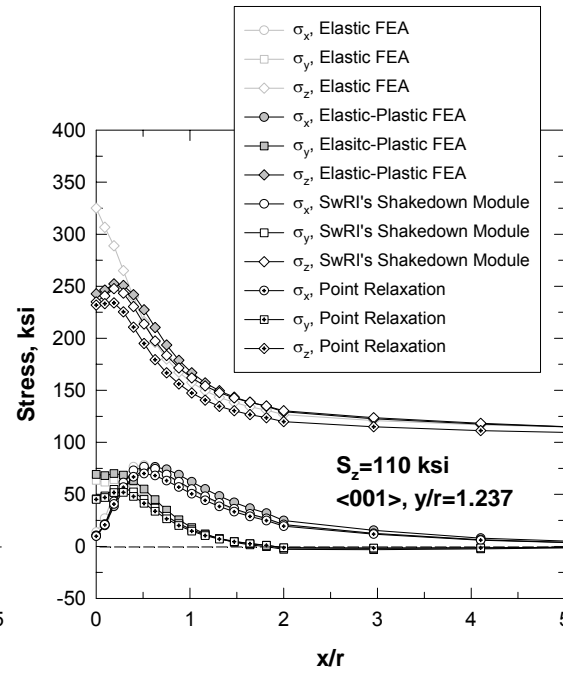
Figure 4.197(a) Figure 4.197(b) Figure 4.197c)
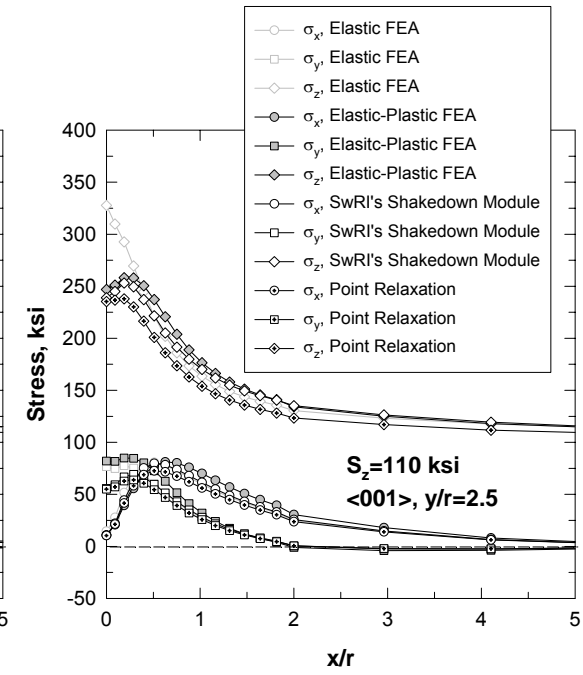
Figure 4.197. Comparison of stress components predicted by SwRI's anisotropic shakedown module with the results obtained from FEA. The results computed from point relaxation are also included to illustrate the effects of load shedding and re-distribution. The notched plate is subjected to a uniform stress, S_z=110 ksi, and the axis of the plate is parallel to the <001> direction. Results in (a) are for the side surface of the plate (y/r=0), results in (b) are for a plane one quarter of the way through the plate thickness (y/r=1.237), and results in (c) are for the mid-thickness (y/r=2.5).
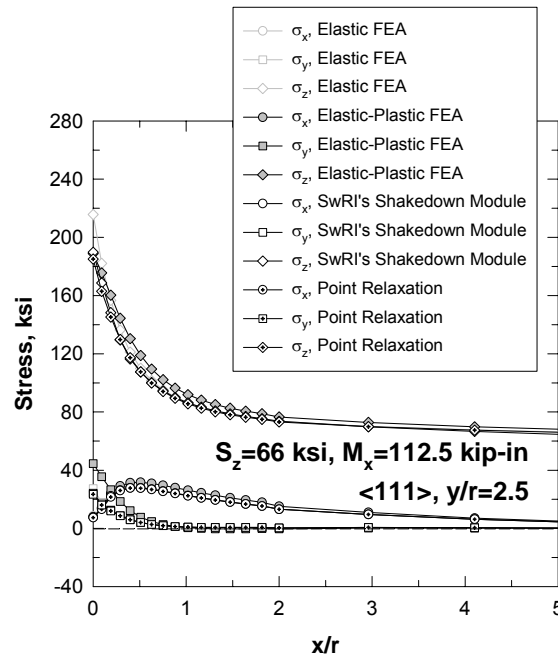
Figure 4.198(a)
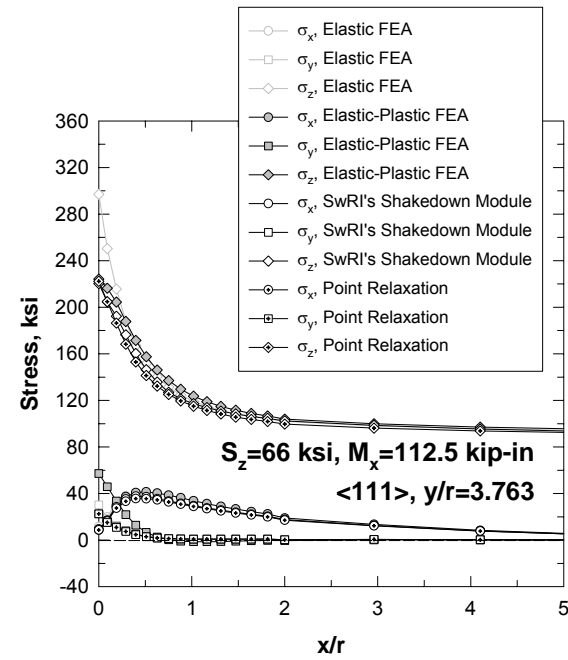
Figure 4.198(b)

Figure 4.198. Comparison of stress components predicted by SwRI's anisotropic shakedown module with the results obtained from FEA. The results computed from point relaxation are also included to illustrate the effects of load shedding and re-distribution. The notched plate is subjected to a uniform stress ,S_z=66 ksi, and a out-of-plane moment, M_x=112.5 kip-in, and the axis of the plate is parallel to the <111> direction. Results in (a) are for the mid-thickness (y/r=2.5) and results in (b) are for a plane about three quarters of the way through the thickness (y/r=3.763).
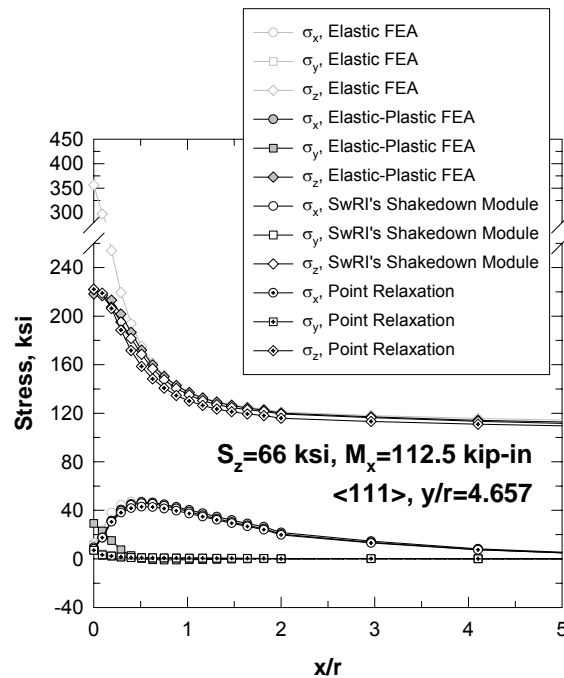
Figure 4.198(c)
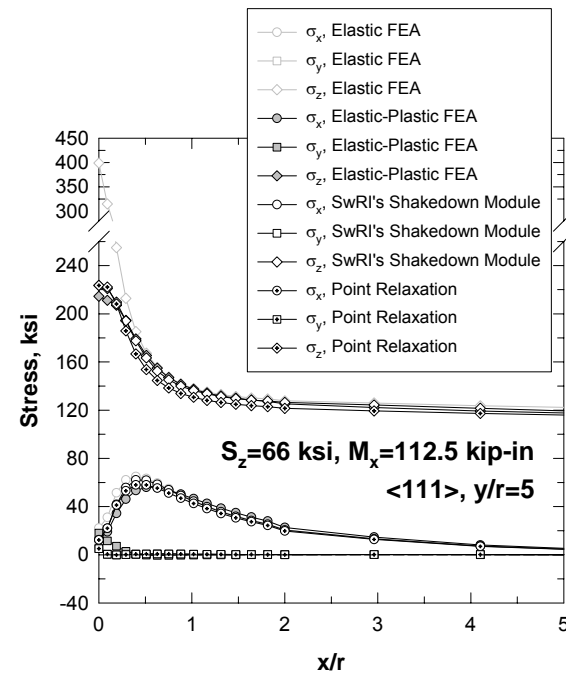
Figure 4.198(d)

Figure 4.198.   (continued). Comparison of stress components predicted by SwRI's anisotropic shakedown module with the results obtained from FEA. Results in (c) are for a plane about seven eights of the way through the thickness (y/r=4.657), and results in (d) are for the other side surface (y/r=5.0). Note the break on the stress axis.

**4.5   ATTACHMENT TESTING, METHOD DEVELOPMENT AND
          CALIBRATION**

Realizing the objective of designing and manufacturing of damage tolerant bladed
rotors within an agile and validated engineering system mandates a computationally efficient
and accurate framework for determining the stress histories near the blade/disk interface.
Such a framework must incorporate the mission-driven morass of static and transient
mechanical, thermal and aerodynamic loads on the blade and rotor components. While
conventional finite element models are used routinely and effectively to define robust airfoil
and rotor structures, they fall far short in resolving adequately the interfacial displacements
and sharp gradients in contact stresses near the edges of the blade/disk interface responsible
for initiating and subsequently propagating fatigue cracks into the blade and disk.

This chapter serves to summarize recent efforts to develop and deploy advanced
mechanics-based modeling tools that ensure the streamlined design of robust attachments by
integrating accurate contact stress modeling in gas turbine engine components with validated
life prediction approaches. Specific attention will be given to highlighting:

- the development and calibration of a design methodology that integrates
  accurate modeling of attachment stress histories in HCF environments with
  validated life prediction models;

- successful efforts to calibrate this approach on well-characterized HCF
  durability shortfall experienced in a fielded bladed-disk design; and

- the fundamental underpinnings of this approach, including advances in
  contact modeling, characterization of the tribology of nickel-based alloys at
  elevated temperature and results from contact specimen and component
  testing.

4.5.1   Accurately Modeling Stress Histories in Bladed-Disk Attachments

4.5.1.1   Continuum Mechanics Approaches to Contact Stress Modeling

Efforts carried out under this program have yielded a set of numerically efficient
and robust tools for modeling the two-dimensional or line contact of nominally flat surfaces
representative of the profiles present in fan, compressor and turbine bladed rotors. These

tools enable solution of the singular integral equations (SIE) rooted in elastic continuum mechanics that govern the interaction between interfacial normal and tangential surface displacements. The interaction among these displacements, associated contact pressure, frictional traction and near-surface stresses drive galling, fretting and fatigue damage in bladed disks.

For the case of contacting surfaces with similar elastic properties (i.e. a fan or compressor stage comprising a titanium disk and blades), the uncoupled system of equations can be solved within a matter of seconds for the near-surface contact stress fields using a Fast Fourier Transform (FFT) algorithm. In the case of contacting components with either dissimilar isotropic or even orthotropic material properties—such as single-crystal turbine blades in an Inconel rotor—a separate, but nearly as efficient, numerical technique can be employed in an incremental fashion to solve the coupled system of singular integral equations that arise. Pertinent details of and results from this latter method will be presented in the context of interpretation of well-controlled fretting fatigue experiments conducted with contacts comprising dissimilar isotropic and single crystal/isotropic pairs.

4.5.1.2   Advances in the Hybrid Approach for Contact Stress Prediction

In transitioning these analytical tools successfully to a design environment where three-dimensional finite element models of bladed rotors are ubiquitous, links must be established between the contact analysis based on efficient numerical solution of singular integral equations and the results readily available from finite element models possessing fidelity compatible with an agile concurrent design environment. Such a hybrid approach would empower designers with mechanics-based insight into the influence of geometric details, manufacturing tolerances and coatings on the subsequent damage tolerance of blade attachments and disk lugs.

As illustrated in Figure 4.199, a global-local hybrid approach that treats axial slices of the blade attachment and disk lug geometries represented in a three-dimensional finite element model as isolated two-dimensional contacts is straightforward to implement for static analyses requisite for LCF-type assessments of mission histories. In this hybrid

420

approach, a coarse blade attachment/disk lug mesh that includes the non-linear influences of frictional contact is used to solve the statically indeterminate eccentric normal and tangential reaction loads between the blade and disk. The reactions over each axial slice then serve as inputs to determine the interfacial tractions and near-surface stress histories. Finally, these stress histories can be interpreted within the context of a validated lifing system and associated criteria.
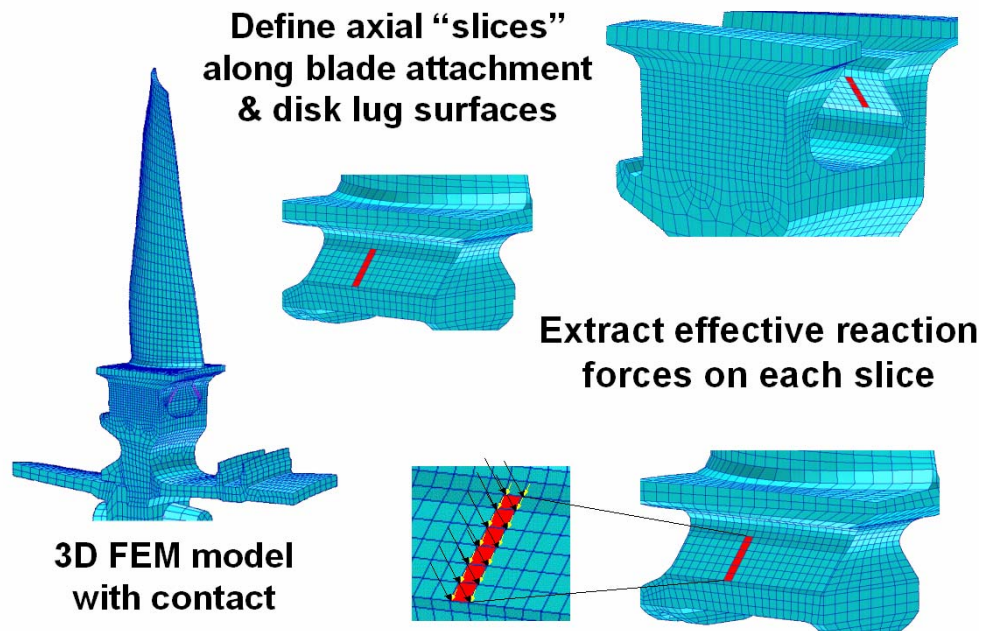
Figure 4.199.   An illustration of the hybrid approach for modeling near-surface contact stresses in blade attachment and disk lug designs.

A. The Hybrid Approach and Single Crystal Blade Attachments

Central to the hybrid approach is treating piecewise segments of a three-dimensional geometry as independent two-dimensional (either plane stress or plane strain) contacting elastic half spaces. Implicit in this two-dimensional analysis is an absence of out-of-plane shear loading, either applied or induced through the in-plane/out-of-plane coupling afforded by anisotropic material properties.

421

The latter influence is of direct relevance to typical turbine blade attachments produced from either directionally solidified or single crystal nickel alloys. In an effort to understand the influence of material anisotropy on in-plane and out-of-plane contact reaction loads, a series of trade studies was conducted with a three-dimensional finite element model of a single-tooth fir tree (STFT) laboratory specimen (Figure 4.200) and associated fixture. The objectives of these studies were to: (1) examine the validity of applying the hybrid approach to anisotropic contacting surfaces by assessing the out-of-plane interfacial reactions, and (2) characterize the sensitivities of both the planar and anti-plane reaction loads (and thus the near-surface contact stress histories) to primary and secondary crystallographic orientations.
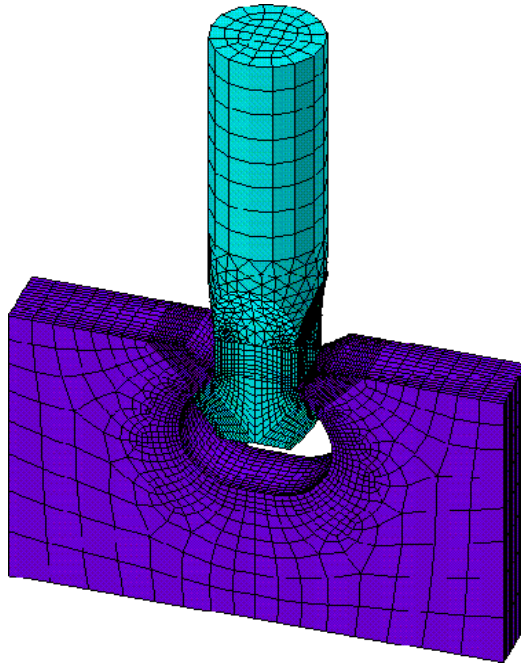
Figure 4.200. The three-dimensional finite element model used in the
single-crystal Nickel single-tooth fir tree trade study analysis.

The model portrayed in Figure 4.200, comprised eight-noded brick elements almost exclusively. Node-to-node contact was established during a non-linear static analysis at 1100°F to resolve the interaction between the STFT specimen feature and fixture during application of a full-load waveform to the buttonhead specimen feature. Both in-plane and out-of-plane relative tangential motions were incorporated using identical friction coefficients of 0.35.

The specimen element material properties were representative of an orthotropic single-crystal nickel alloy, PWA 1484, while the material of the mating fixture was modeled as an isotropic nickel-based superalloy. As detailed in Figure 4.201, the primary and secondary orientations of the crystallographic axes were varied with respect to the specimen/loading axes. Analyses for each of these orientations were carried out for the same specimen load waveform and post-processed to extract the reaction forces at the specimen/fixture interface for three axial locations.

$$\theta = 5°, 10°$$
$$\Phi = 5°, 10°$$
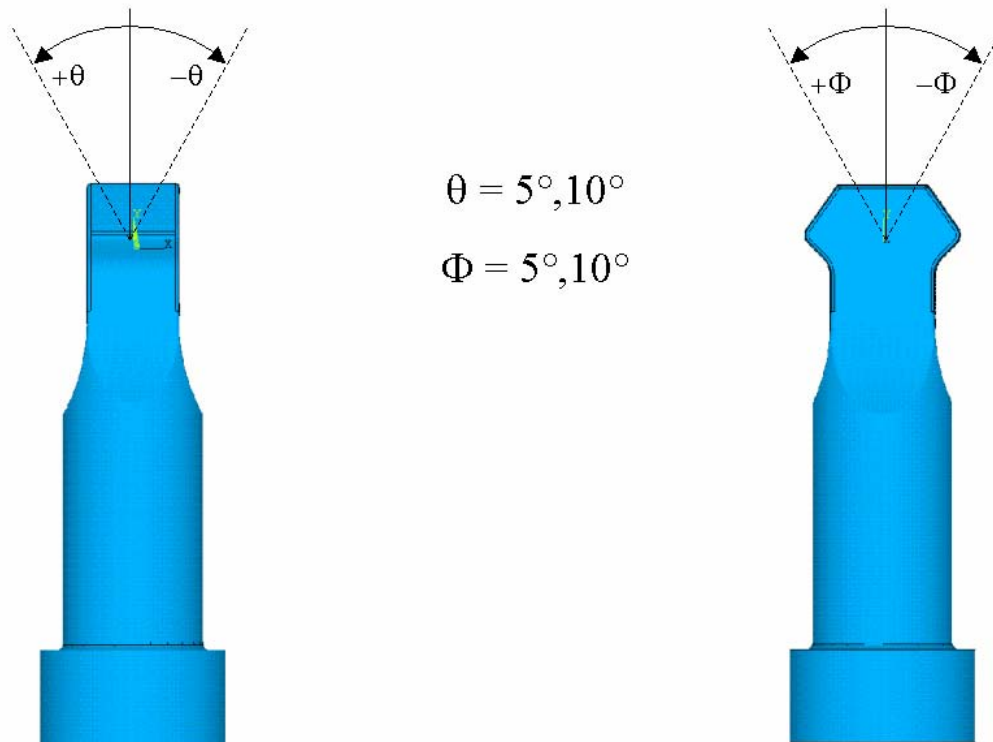
Figure 4.201. Definition of the primary crystallographic axis orientation ranges used in the single-crystal nickel STFT trade studies.

A review of the interfacial antiplane shear loads from these runs provided convincing validation to the applicability of the hybrid method to these contacts: These loads induced through the orthotropic material properties of the single-crystal nickel alloy were negligible compared to their in-plane counterparts. Explicit comparisons of the in-plane reaction loads are shown in Figures 4.202 through 4.204, which present the ratios of reactions from off-axis orientations to those corresponding to the baseline crystallographic orientation. As is clearly evident, the in-plane normal and shear loads show little sensitivity (0% to 5%) over the range of primary axis orientations considered. Changes in primary orientation, however, had a stronger influence over the eccentricity of the normal load distribution, or effective in-plane moment. These sensitivities tend to skew the distributions of contact traction on the surface and can lead to an amplification of stress near the critical edges of contact.
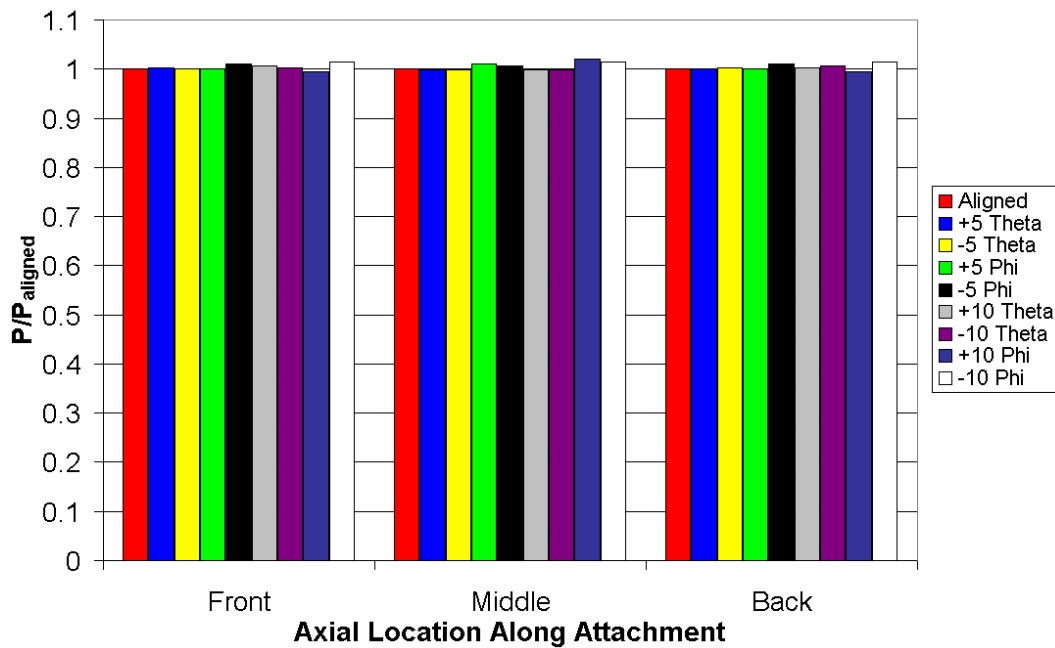
Figure 4.202. A comparison of the normal line loads on the center slice of the single-crystal nickel STFT model for various primary axis.
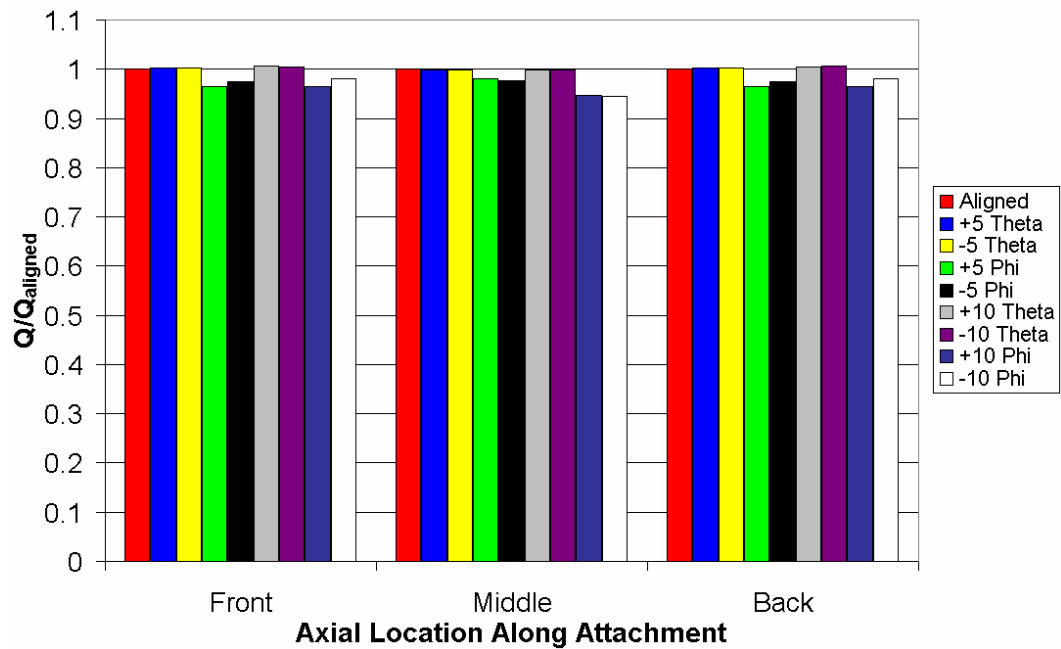
Figure 4.203. A comparison of the shear line loads on the center slice of the single-crystal nickel STFT model for various primary axis orientations.
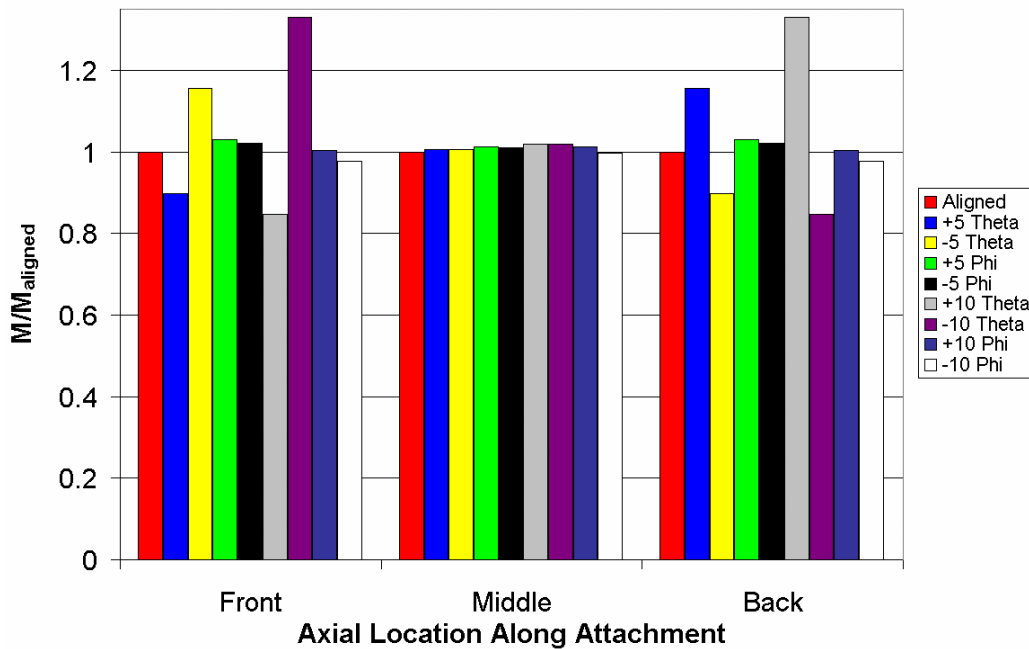
Figure 4.204. A comparison of the unit moment loading on the center slice of the single-crystal nickel STFT model for various primary axis orientations.

Two secondary axis orientations, one aligned to the specimen geometry and one offset by 45 degrees, were also considered as shown in Figure 4.205. The influence of the secondary axis orientation was similar to that of the primary axis, with little effect on the normal and tangential loads, but over a 30% increase in magnitude of in-plane moment.

Aligned

Load Step	Normal Load (lb/in)	Moment (lb-in/in)	Shear (lb/in)
1	9178.3	-93.1	0.0
3	10741.0	-88.0	-1092.1
5	9178.4	-93.1	0.2

45° Offset

Load Step	Normal Load (lb/in)	Moment (lb-in/in)	Shear (lb/in)
1	9503	-116	0
3	10926	-115	-1059
5	9503	-116	0

Difference

Load Step	Normal Load (lb/in)	Moment (lb-in/in)	Shear (lb/in)
1	-4%	-24%	0%
3	-2%	-31%	3%
5	-4%	-24%	0%
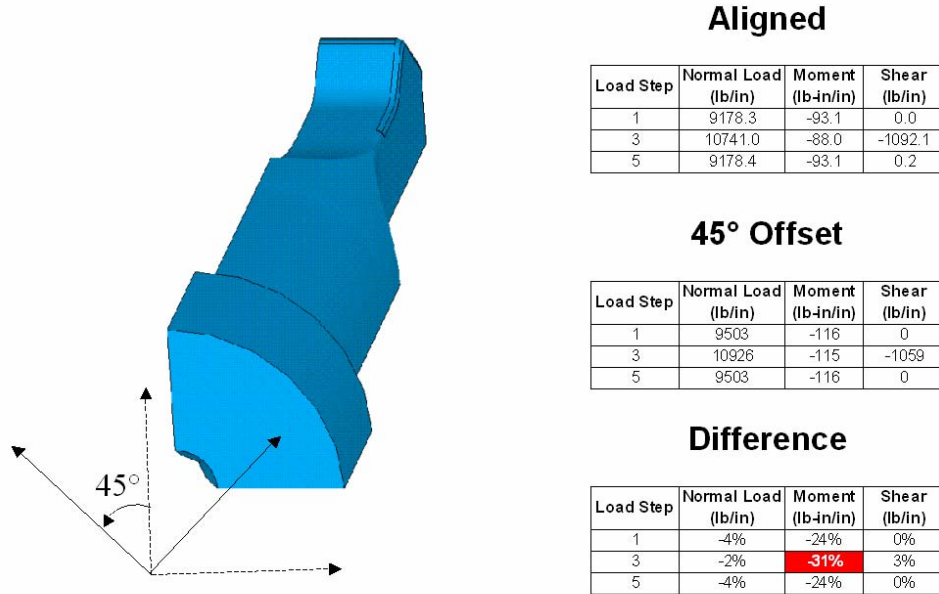
Figure 4.205. A comparison of the contact reactions on the center slice of the single-crystal nickel STFT model for two secondary axis orientations.

B.   *Application to HCF-Environments: Quasi-Dynamic Vibratory Analysis*

To this point, the obvious advantages to the hybrid method of attachment analyses have been illustrated for load and stress histories representative of the LCF mission cycles. Direct application of the hybrid methodology to understand non-linear reaction load and contact stress histories in HCF environments is precluded at first glance by the linear modal analysis used conventionally to characterize stage vibration. These modal results are typically generated by determining solutions of the eigenvalue problem:

$$\left([K] - \omega^2[M]\right)\{\hat{u}\} = 0 \qquad\qquad (4.53)$$

In this equation, [M] is the elemental mass matrix and [K] is the model stiffness matrix that may include non-linear influences such as stress-stiffening and spin-softening associated with high-speed rotation of the bladed disk rotor structure. In such an analysis, the contact interaction at the blade/disk interface is often modeled in a linear fashion with displacement constraint equations that prevent interpenetration of the blade attachment and disk lug nodes; and enforce either a no-slip/infinite friction or pure sliding/zero friction condition in the tangential direction.

A procedure dubbed quasi-dynamic vibratory analysis (QDVA) has been developed to bridge this gap between conventional modal analysis procedures and the need to obtain non-linear interfacial reaction loads for subsequent accurate and efficient characterization of near-surface contact stress histories. As outlined in steps 2 through 5 of the process presented in Figure 4.206, the QDVA process involves conducting an incremental static analysis including frictional contact at the blade/disk interface using a load history comprised of a nodal force history extracted from the modal results. This quasi-dynamic force history is determined by scaling the modal forces generated from the aforementioned eigenvalue problem by either recorded or predicted stage vibration levels (strain gage readings, optical probe tip deflection measurements, etc.); or by design-system criteria defining acceptable vibratory responses.

The scaled modal force history is then enforced over the entire model, save at the blade/disk interface—which is resolved through the use of contact elements on the surfaces of the blade attachment and disk slot. Implicit in this approach is the assumption that the set of interfacial displacement boundary conditions imposed during the modal analysis (and thus used to generate the scaled modal force history) are identical to those during the actual vibratory response of the bladed disk stage.
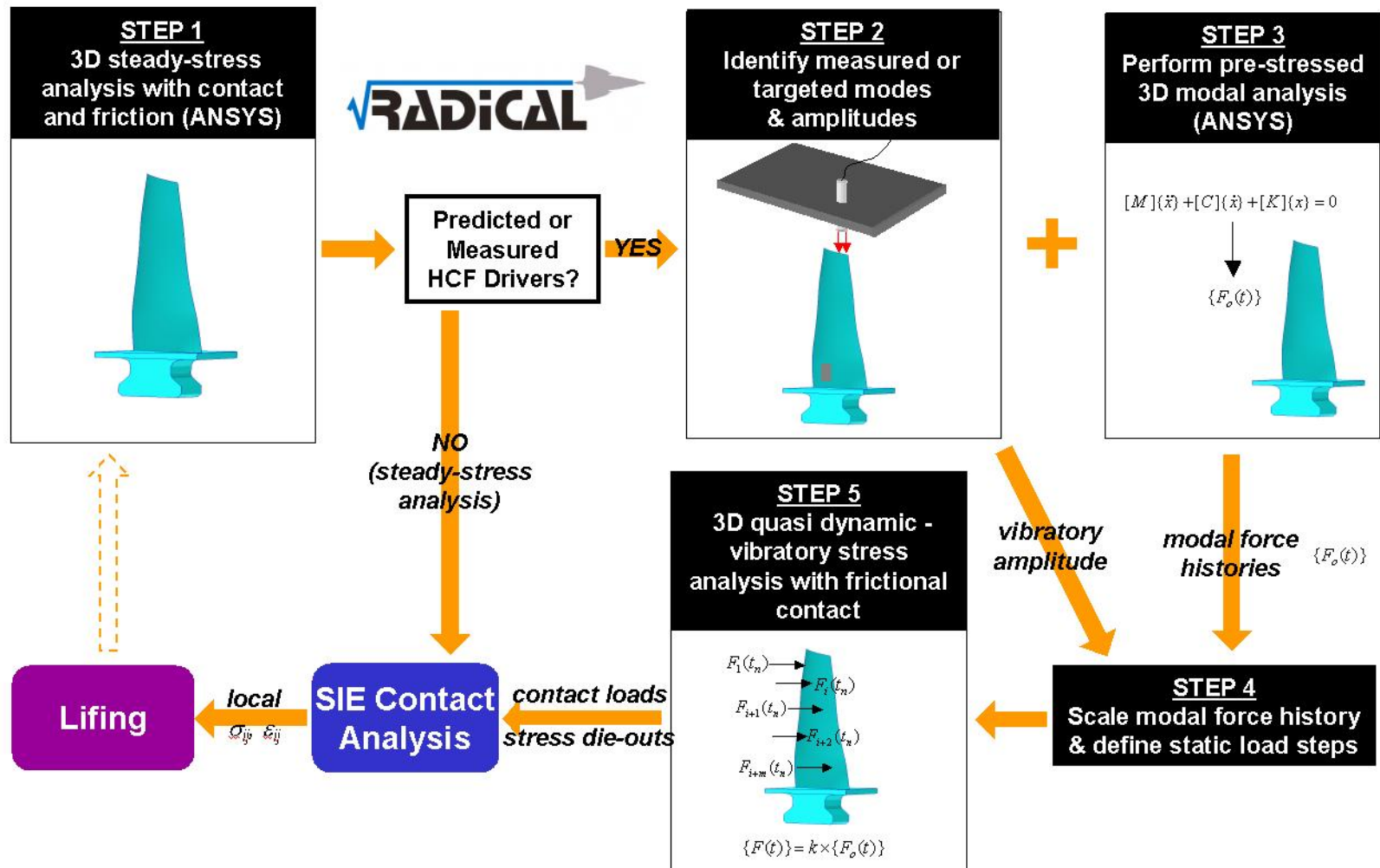
Figure 4.206. A summary of the Pratt & Whitney proprietary radical analytical framework assembled for designing damage tolerant attachments in gas turbine engine bladed disk assemblies.

4.5.1.3   Validating the RADICAL Methodology: F100-PW229 3rd-Stage Fan Analysis

With the development of this approach to determine contact reaction loads during forced vibration, an inclusive compliment of modeling tools now exist to determine both accurately and efficiently the near-surface contact stress histories in bladed-disk attachments during complete mission histories. Juxtaposing these analysis capabilities with the lifing methods presented previously in Chapters 4.2 and 4.3 yields a design-oriented framework for damage tolerant attachment design, as presented in Figure 4.206. While the path outlined in this framework is considered a generic one, a proprietary implementation of this approach dubbed RADICAL—Robust Attachment Design Through the Integration of Contact Analysis and lifing—is being deployed within the standard work instructions of Pratt & Whitney. With these specific efforts detailed in Chapter 4.6, this section focuses on a calibration of the radical approach to a well-characterized and since-eliminated HCF-driven durability shortfall in a military fan application.

A. Background

With an extensive well-characterized set of engine, modeling and mission data available, a recent case of HCF-cracking in both the blade attachments and disk lugs in the 3rd-stage of the F100-PW229 fan provided an excellent baseline for calibrating the radical methodology. These data were used previously to identify root cause for the cracking as an integral stiffwise bending response of the stage at a sea-level mil power rating, driven by bow waves from downstream static hardware. A redesign effort introduced geometric changes in both the rotor and blade attachment to successfully eliminate the incidents of HCF cracks.

Figure 4.207 provides a cross-section of the fan geometry, highlighting not only representative views of the blade and disk cracks, but also instrumentation used to characterize the vibratory responses of the stage, including dynamic strain gages and non-intrusive structural measurement system (NSMS) optically based tip timing probes. Blade attachment cracks initiated at the forward, convex corner, while the disk lug cracks began on both the concave and convex aft corners of the pressure surface.
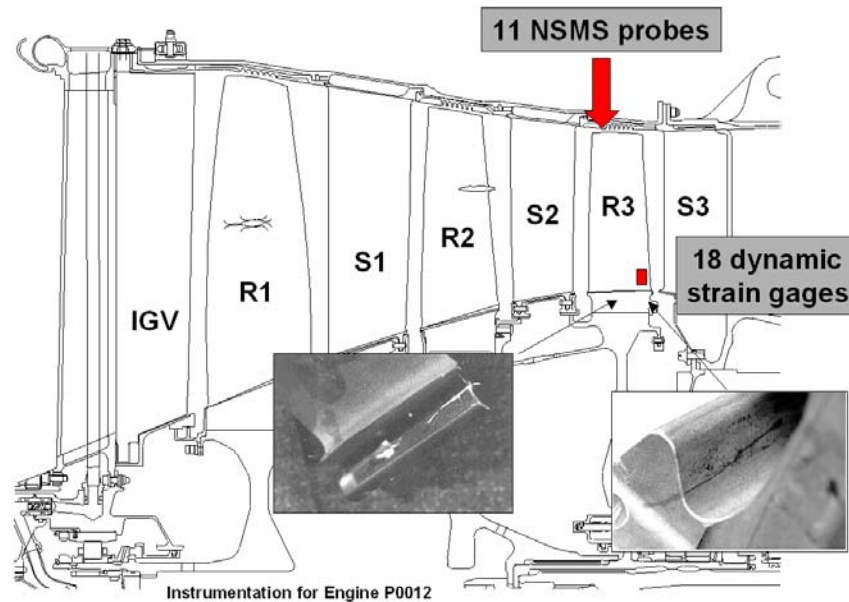
Figure 4.207. Cross-section of F100-PW229 fan, highlighting of 3rd-stage disk
lug and blade attachment HCF cracks and instrumentation used
to characterize the vibratory responses of 3rd stage bladed-disk.

B.   Analysis

A sector model of the bladed disk with appropriate cyclic symmetry
constraints (Figure 4.208) was used to analyze both the static and vibratory responses of the
stage. Similar to the aforementioned single-tooth fir tree models, node-to-node contact was
employed at the blade attachment/disk lug interfaces with a friction coefficient of 0.15. The
finite element analysis consisted of four segments, following the steps outlined in Figure
4.206: (1) a steady-state thermal analysis with an applied rotor and blade temperature
distribution, (2) a non-linear static analysis from idle to the sea-level mil power rating, (3) a
subsequent pre-stressed modal analysis corresponding to the measured 14 nodal diameter
pattern of the stiffwise bending response, and (4) the quasi-dynamic vibratory analysis, using
the modal force history for the stiffwise bending mode scaled using tip deflection
measurements from the leading-edge NSMS probes.
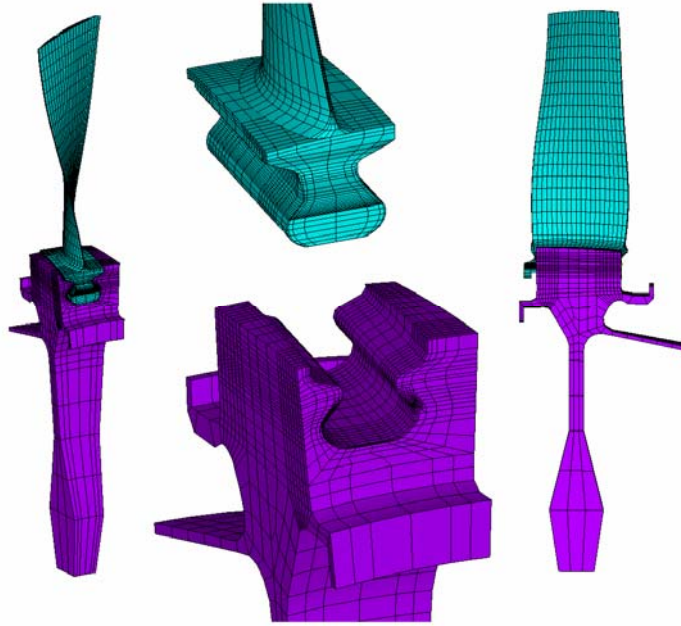
Figure 4.208.   Three-dimensional sector mesh of the 3rd-stage fan.

The reaction force and moment histories on all four contact surfaces (concave sides of blade attachment and disk lug; convex surfaces of blade attachment and disk lug) were generated via an ANSYS macro for each of the 19 axial slices composing the interfaces. These histories served as inputs to the FFT-based contact traction and near-surface stress analysis. It is critical to note that while this fan application involves isotropic titanium components and related application of the FFT-based contact analysis, the modular framework of RADICAL provides for transparent transition to the numerical solution of the governing singular integral equations for either dissimilar isotropic contact pairs or contacts involving anisotropic materials.

Figure 4.209 presents one visual representation of the results from the entire analysis—the evolution of contact pressure on the interface of the disk lug on the concave or suction side of the airfoil. This evolution is presented as a sequence of snapshots proceeding from left to right and top to bottom in the following chronology: (1) ground idle to sea-level mil power (top row), and (2) one complete cycle of a measured stiffwise bending response. It is important to note that the vibratory results in rows 2 through 4 are *not* scaled modal

431
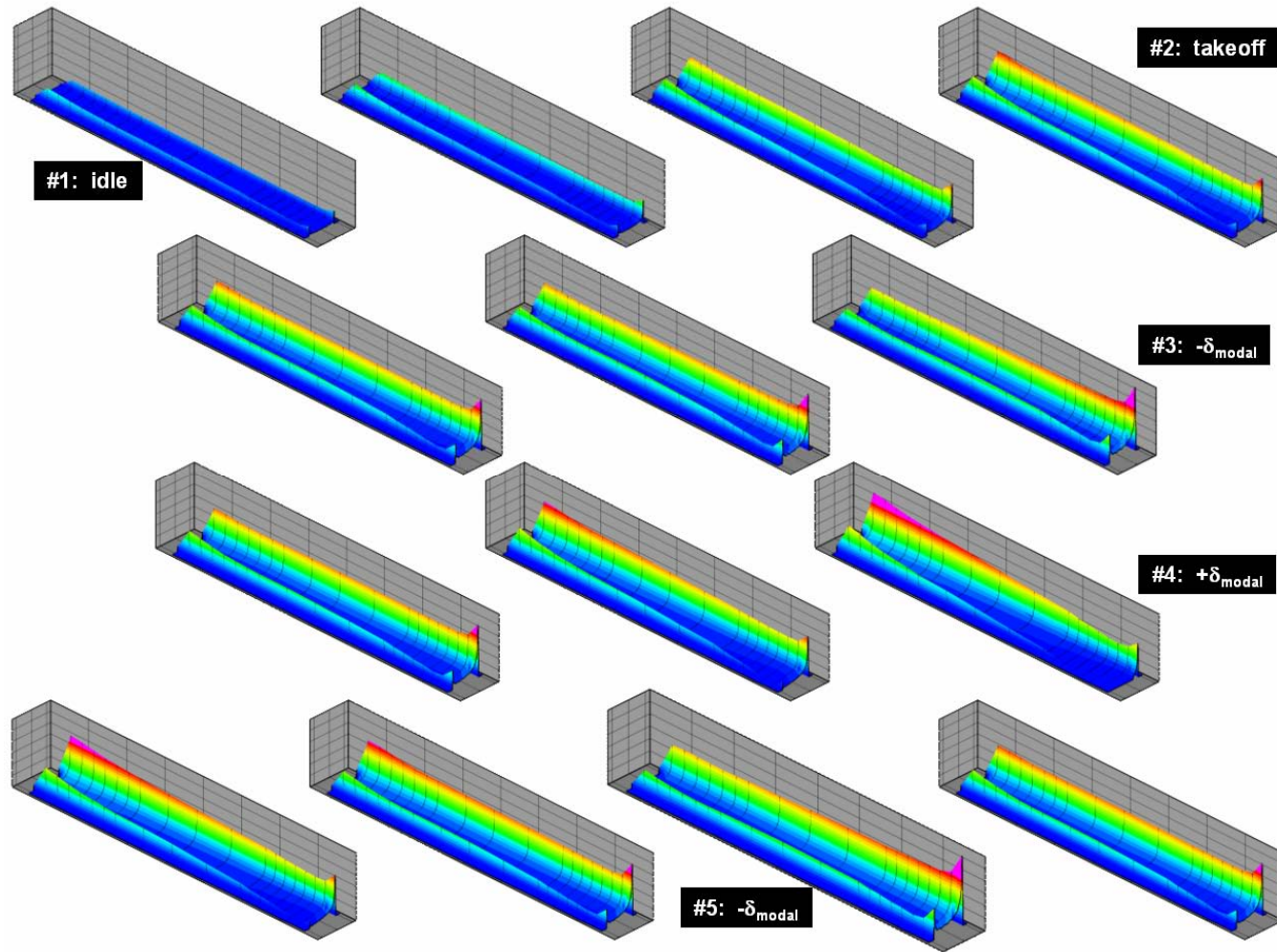
Figure 4.209. Evolution of contact pressure on the concave side disk lug surface during take-off from idle and a Subsequent measured stiffwise bending vibratory response at sea-level mil power rating.

results from the finite element model, but highly accurate analytical contact pressures from the hybrid approach.

The near-surface stress histories associated with the evolution of both this normal pressure and shear traction were then interpreted in the context of the Findley multiaxial life parameter presented earlier in this document. Any influence of residual stress resulting from either shot peening or localized yielding was not included when calculating the life parameters. Figure 4.210 presents contours of this parameter over the surface of the disk lug on the concave side of the airfoil. As highlighted on the plot, the RADICAL approach predicts finite lives ($< 10^8$) in the vicinity of the observed initiation sites. The predictions made to date have fallen short, however, in agreeing with the remaining initiation sites on the convex sides of the disk lug and blade attachment. Future work will be directed at enhancing the approach to incorporating the influence of both history effects induced by simultaneous variation of normal and tangential loading, and surface treatments such as shot peening and coating. Furthermore, additional calibration efforts are required to correlate the actual cycles predicted by the Findley parameter to the estimated exposure to the hardware based on detailed mission analysis.
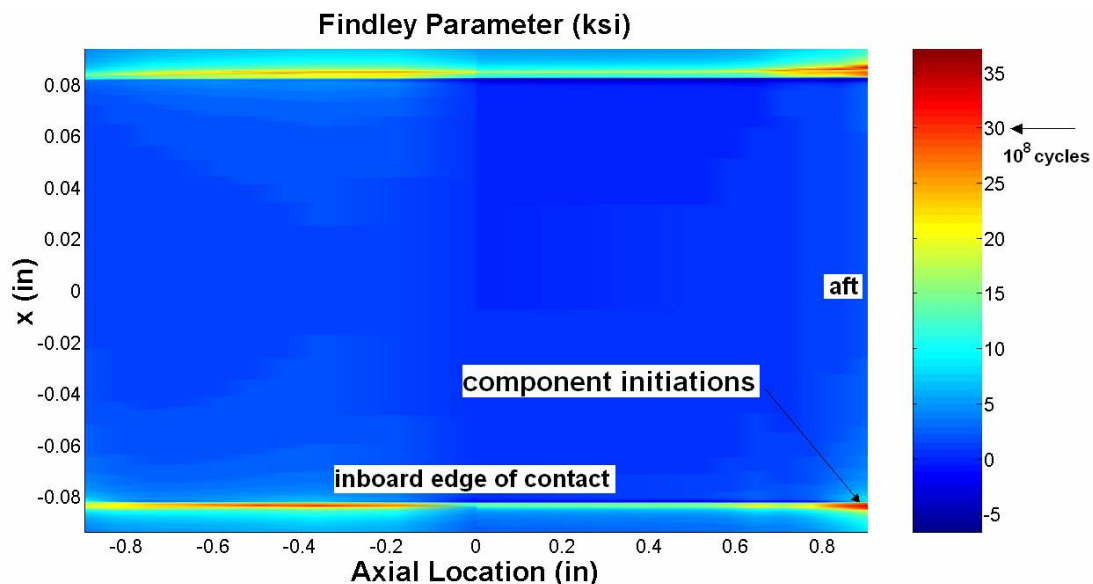
Figure 4.210. Contours of the Findley parameter on the concave disk lug surface, where 10^8 cycles correspond to around a parameter value of 30 ksi. The observed component initiation region corresponds to the lower right corner of the plot, in agreement with the predictions.

4.5.2   Testing

4.5.2.1   Single Tooth Firtree

   A. Background

        The single tooth firtree (STFT) sample is a subcomponent test used to evaluate blade attachment LCF, HCF, and fracture mechanics capability. The STFT consists of a holder and the dovetail shaped specimen as shown in Figure 4.211.
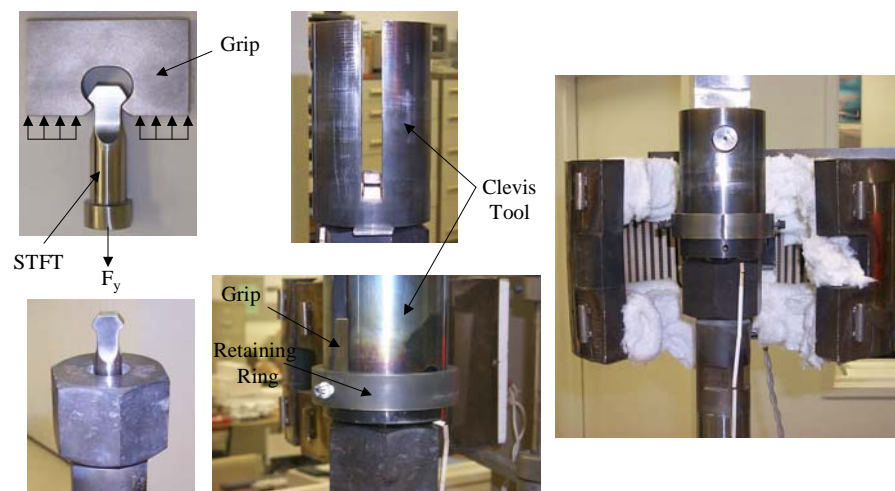
Figure 4.211. Single tooth firtree test hardware.

        Small misalignments and induced bending have a big effect on the true stress at the failure location. This robust geometry for both the holder and the specimen reduces the effect of misalignment. The testing procedure addresses the problem by monitoring misalignment through strain gages that are attached to both sides of the rectangular section of the specimen just above the specimen to holder interface. Then rig alignment is adjusted to reduce gage measured bending where modulus is taken into account in gage measurements.

        Both LCF and HCF testing have been conducted with this sample. The HCF testing was conducted at 1100°F with a stress ratio of 0.70 and at 1200°F with stress ratios of 0.05 and 0.80.

434

The quarter finite element model of the STFT specimen, holder and fixturing is shown in Figure 4.212. The loading cycle modeled for the STFT specimen, which has <001> radial crystalline orientation and a <010> tooth orientation is shown in Figure 4.213. This model was analyzed with a coefficient of friction of 0.35.
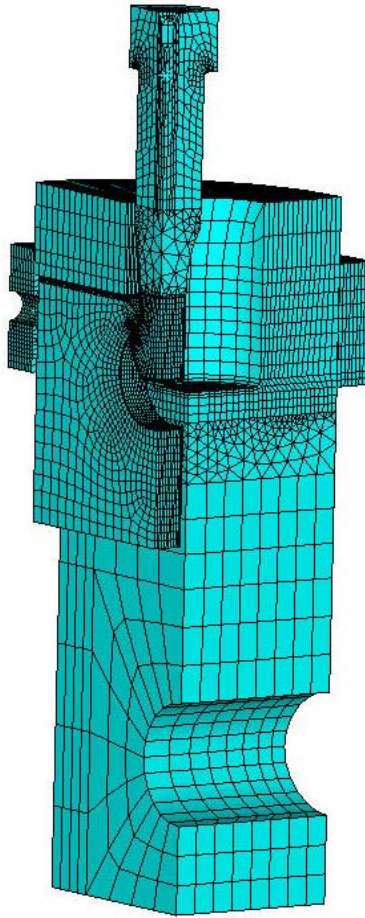
Figure 4.212.   Single tooth firtree stress model.

Single Crystal, mu =0.35

Loading
- Increase Zero to 19775 lbs
- Decrease from 19775 lbs to 15820 lbs
- Increase from 15820 lbs to 19775 lbs
- Decrease from 19775 lbs to 15820 lbs
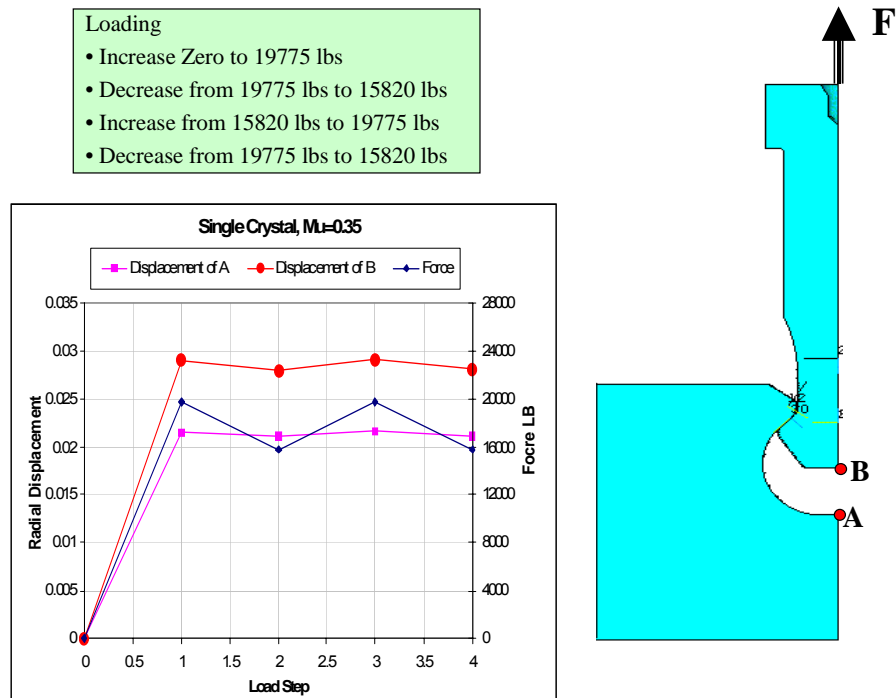
Figure 4.213. Loading cycle and displacement used in single crystal STFT analysis.

Contour plots of the displacements and stresses in the specimen and holder are shown in Figures 4.214 through 4.216.

Step 3: 15820 lbs　　　　　　　　Step 4: 19775 lbs
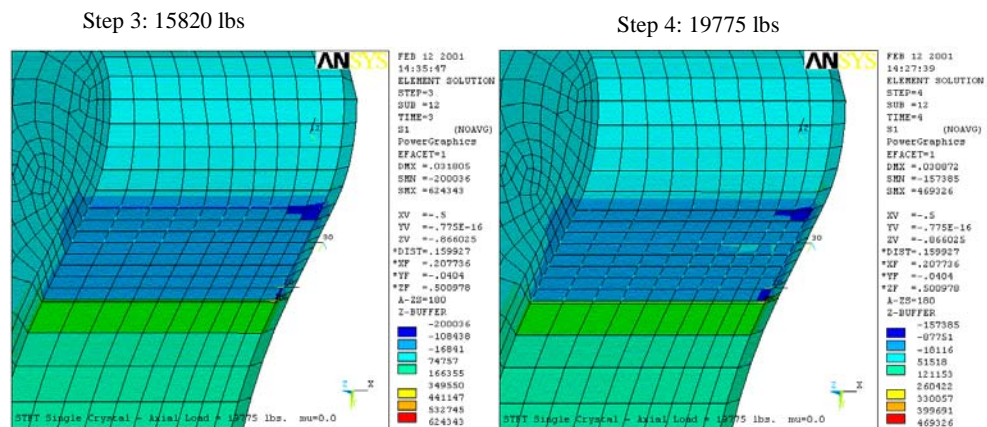
Figure 4.214.   Radial displacement results from the single crystal STFT analysis.

436

Step 3: 15820 lbs

Step 4: 19775 lbs
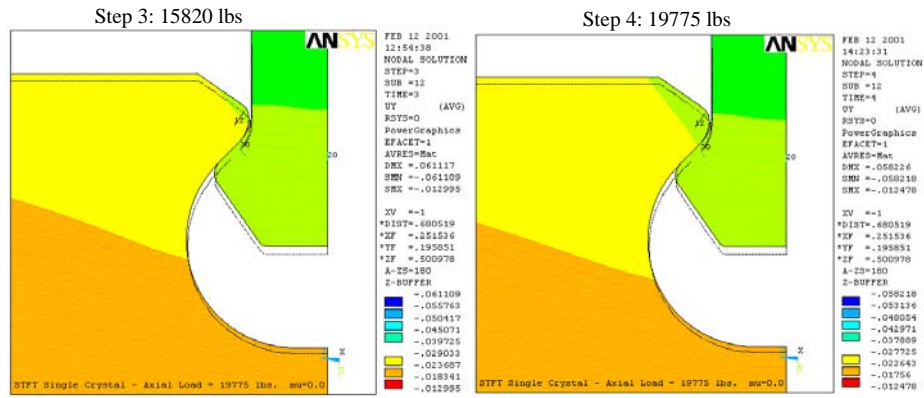
Figure 4.215. Maximum principal stress in the holder for the single crystal STFT test.

Step 3: 15820 lbs

Step 4: 19775 lbs
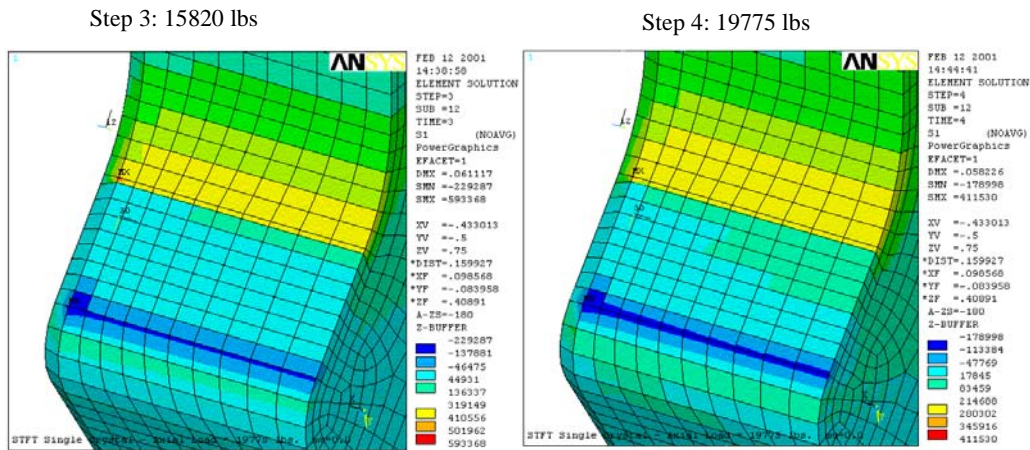
Figure 4.216. Maximum principal stress in the single crystal STFT specimen.

To reduce computer time for a full model of the STFT, holder and fixturing, a mesh refinement study was pursued with 5, 9 and 18 elements across the bearing surface being considered and compared to the load sensitivity, see Figure 4.217. The full model was required so as to study orientation effects on the bearing surface loading. The results of the study are shown in Figure 4.218. Note that with the exception of the shear load, little changed was observed in going to as few as five elements across the bearing surface. The resulting loads produced from the study indicated that the coarse mesh, five elements across the bearing surface, could be used to capture the proper loading for the 360-degree model.

437

5 Elements   9 Elements   18 Elements
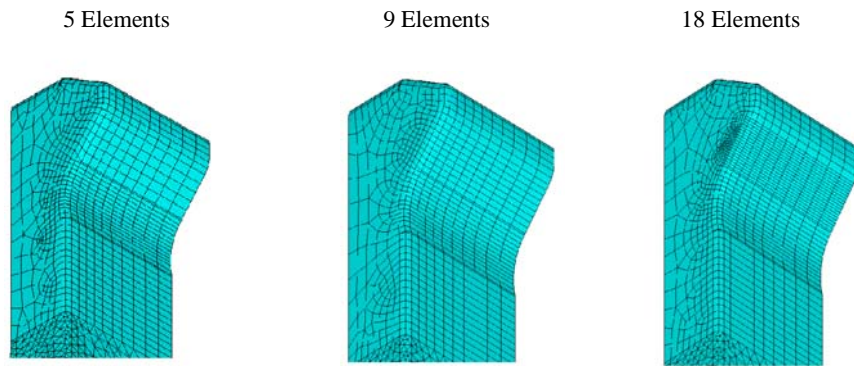
Figure 4.217. Mesh sensitivity study for orientation study.
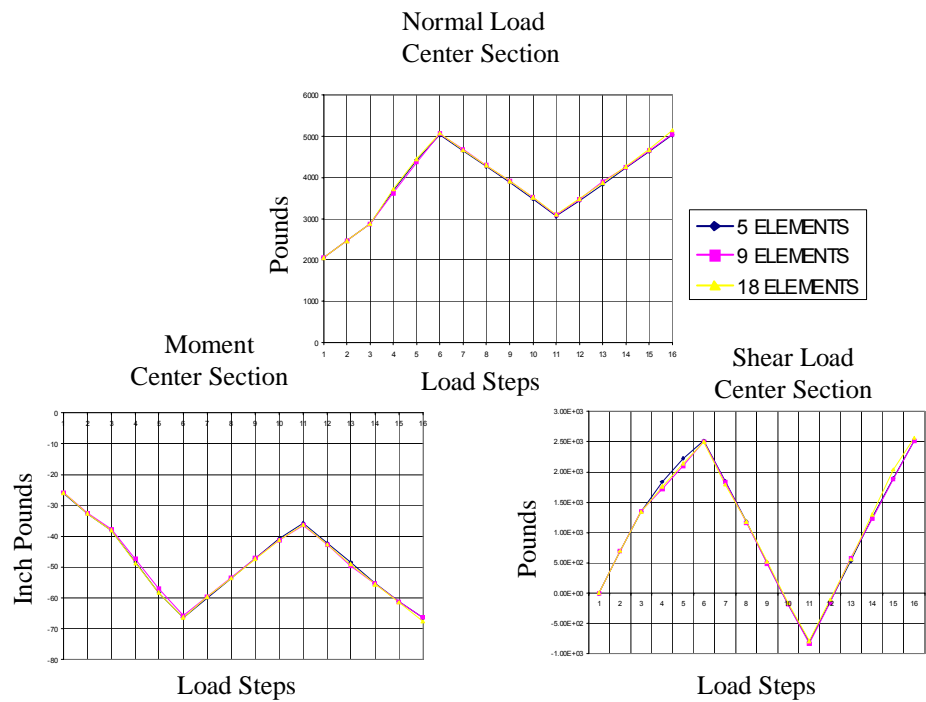
Figure 4.218.   Mesh refinement study for single crystal bearing study.

The full 360-degree model took approximately one week to do a five load step analysis. A mesh density of nine elements was found to be appropriate for modeling contact regions of the blade. Single tooth firtree specimen stiffness is different from conventional

disk geometries and is sensitive to out of plane loading. Care was taken in test set-up to limit out-of-plane loading and in utilizing results in application to turbine disk attachments. This was done through the design of the latest single tooth firtee fixturing and the use of modulus corrected strain gage readings to evaluate alignment.

C. Single Crystal Single Tooth Firtree Test Results

A plot of the data versus a psuedo-Smith Watson Topper parameter where normal bearing stress is used as the input stress is shown in Figure 4.219. This permits the combining of several different stress ratios under which the testing was conducted. Figure 4.220 only includes the edge of contact failure test results. Due to the fact that a critical plane life prediction method for single crystal had not yet been established and that the contact analysis method (CAFDEM) for single crystal had not been evaluated at Pratt and Whitney, predictions for the STFT contact failures could not be made. It is also uncertain as to whether or not plasticity would or would not have had to be considered for the life predictions in single crystal STFT specimens.
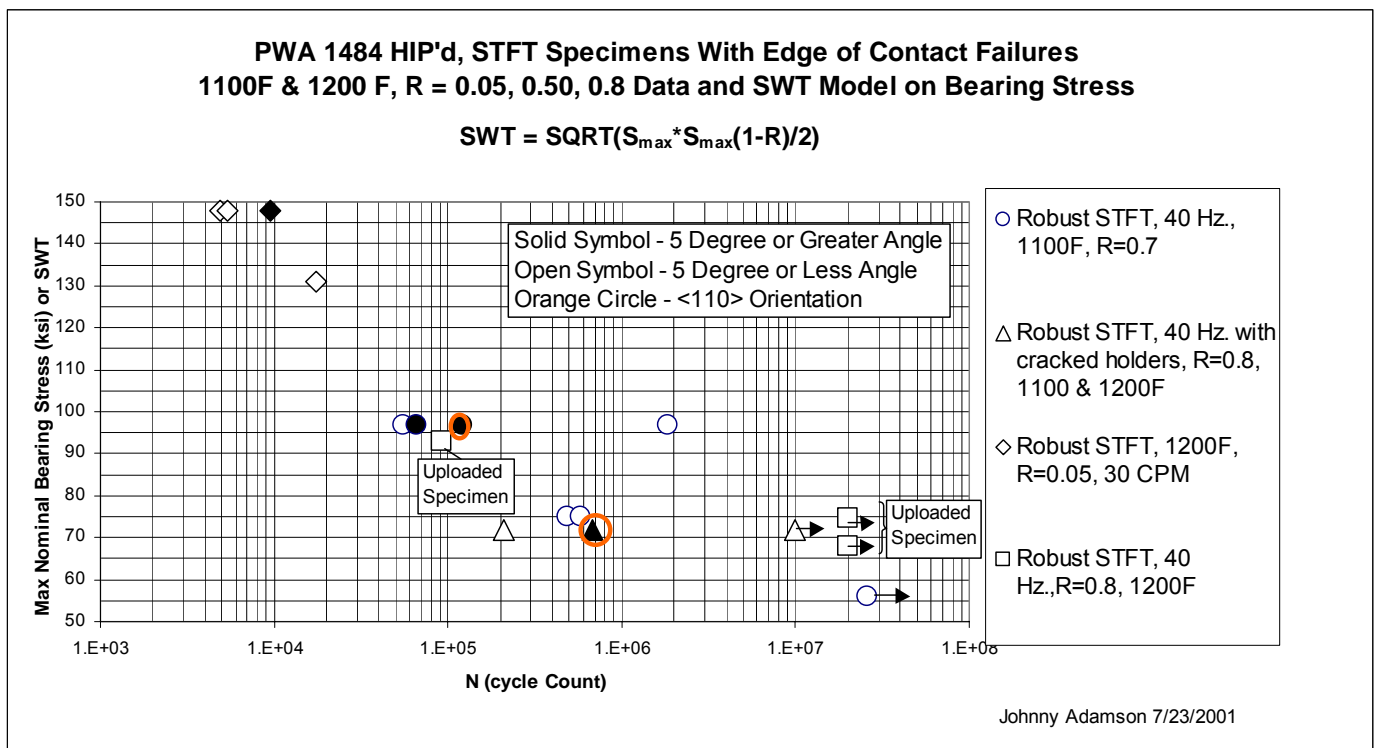
Figure 4.219. Single crystal single tooth firtree HCF test results versus a pseudo Smith Watson Topper parameter.

Bearing symmetry good, octahedral and non crystallographic fracture noted on same specimen:

octahedral   **non- crystallographic**
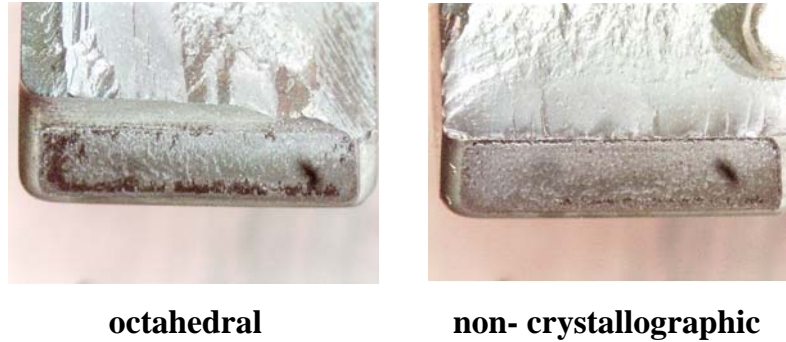
Figure 4.220**.** Fractography of a edge of contact HCF failure site.

4.5.2.2   <u>High Temperature Fretting and Tribology Experiments</u>

      A.   Experimental Development

      Purdue University's standard fretting rig as described in a previous section (see Section 3.5.3.1) had been designed to operate at room temperature. The rig was useful in testing the materials like Ti-6Al-4V, Ti17 and Inco718 that are used in components that operate at lower temperatures. However, advanced alloys like Single Crystal Nickel (SCN) and IN100 are known to have different mechanical fatigue characteristics at high temperature than at room temperature. Therefore, to study the material characteristics, the experiments have to be conducted the elevated temperatures which the material is exposed to. A rig was designed to achieve an elevated temperature of 610°C at the contact region. Figure 4.221 shows a schematic of the rig designed for high temperature tests. Components of the rig closer to the zone of elevated temperature were designed using Ti-6Al-4V alloy. 4140 steel was used to design the components that were far away from the region of high temperature.
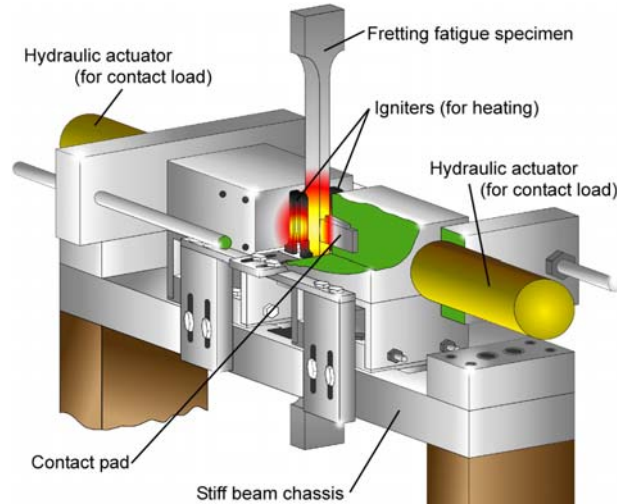
Figure 4.221.   Schematic of rig designed for conducting
experiments at elevated temperatures.

Load transfer in the high temperature rig is based on a principle similar to that of the room temperature fretting rig. The webs connected to the platforms that hold the pads act as membranes. They transfer most of the normal load applied to it, but their stiffness in the tangential direction gives rise to tangential (shear) load at the contact. Normal load is again applied using two hydraulic actuators. Two rods on either side of the contact ensure that the pressure is applied symmetrically to the pads. Since the temperatures that would be encountered during the experiments were high, assembly of different parts using welds or bolts were avoided. Hence the webs and the platforms that hold the pads were machined from a single Ti-6Al-4V block. Further, the pad holder block was not made of two different parts bolted together with the pad in between them, as in the case of the standard room temperature rig. As the normal load is applied, the pads get wedged into a tapered groove (tapered at an angle of 5°) machined in the pad holder block.

The temperature of the local area of contact was increased using a pair of igniters on either side of the specimen. The igniters draw a current of 4.25A to 4.75A at 132V, and the maximum temperature achieved by the igniter surface is 1550°C. The heat transfer from the igniter to the specimen and the pads is through radiation and convection with air as the medium. Temperature of the specimen was measured using a *K type*

441

thermocouple spot-welded onto the specimen, halfway between the two contacts. The voltage output of the thermocouple was used to control the temperature at the contact using an on/off type of control. The controller was set up such that the igniter switches off if the temperature goes up by 1^oC from the desired temperature and switches on if the temperature drops by 0.5^oC. In an on/off type of control, the igniter should reach a very high temperature in a short period of time to minimize the fluctuations in temperature. Hence, an igniter that can achieve the maximum temperature from room temperature in 17 sec. was chosen. However, there was a fluctuation of +/-5^oC when the desired temperature was 610^oC. The fluctuation may be due to air currents affecting the convective heat transfer, in addition to on/off type of control. The influence of air currents was minimized by forming a shield around the zone of elevated temperature with ceramic blocks and sheets. The fluctuation was less than 1% of the desired value so it was neglected.

The surface of the webs and the pad holder block facing the zone of elevated temperature was covered with ceramic sheets glued using high temperature adhesive, hence preventing their exposure to high temperatures. It also prevents absorption of heat by the rig from the elevated temperature zone. Loss of heat to ambient air was further prevented using a shield made of ceramic block placed behind the igniter.

The ceramic shields along with the ceramic sheets covering the rig give rise to a furnace-like environment around the region of contact. In spite of covering the surface of the webs with ceramic sheets, there is some heat transfer to the rig due to air surrounding it that is at very high temperature. In addition, there is a transfer of heat from the pad to the pad holder, by conduction. To absorb the heat generated in the rig, the pad holders are cooled by passing water through channels machined in the block (Figure 4.222). Heat is also conducted to the wedges that hold the specimens. Hence, water-cooled wedges were used for clamping the specimens.
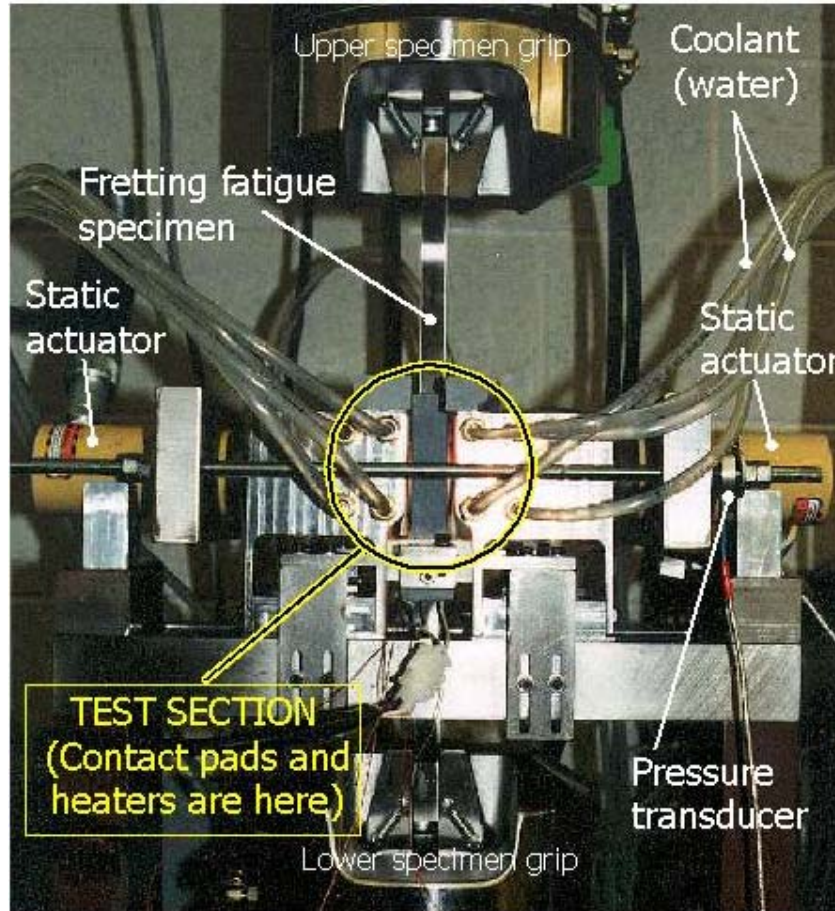
Figure 4.222. A photograph of the rig designed for conducting
experiments at elevated temperature.

Cylindrical rods (7.9 inches long, 1 inch in diameter) cast from SCN were used to machine the fretting fatigue specimens. The primary principal axis (x_0) is possibly tilted from the cylinder axis (x_1) by a small angle ($< 10^o$). A rectangular cross section (0.6 inches times 0.38 inches) oriented at an arbitrary angle about the x_1-axis was machined (Figure 4.223-a). Tabs made from WASP alloy were inertia welded to the ends to produce the specimens. The nominally flat fretting pads were made from IN100.
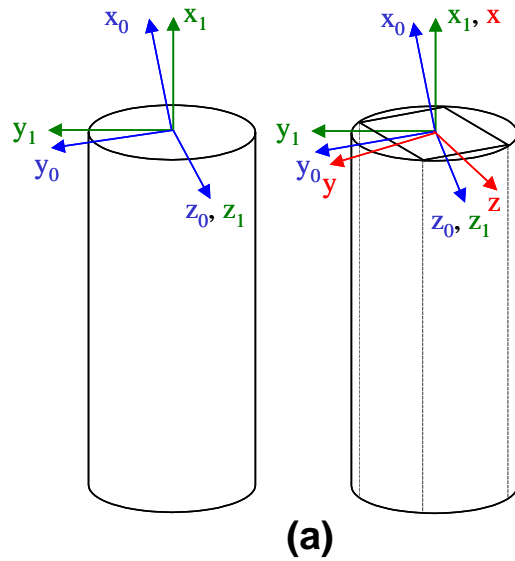
Figure 4.223(a). Schematic showing the material principal axes with respect to the specimen.
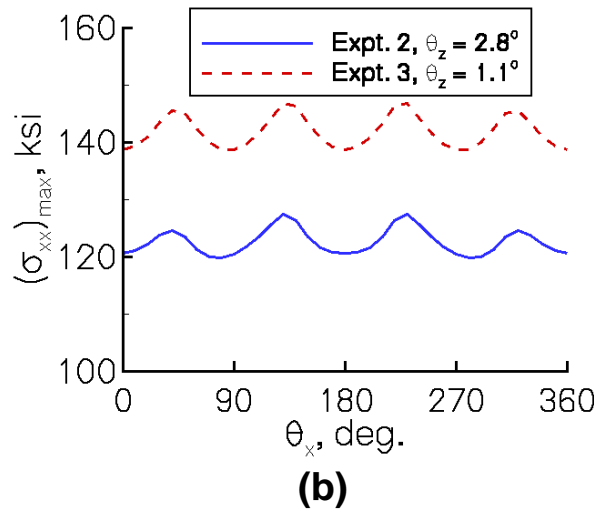
Figure 4.223(b). Effect of the change in orientation of principal axes with respect to contact surface on the subsurface stresses.

B.   *Experimental Results*

The details of the experiments are listed in Table 4.42.

Table 4.42.   Experimental Conditions for High Temperature Fretting Fatigue Experiments with SCN on IN100*

Expt. No.	Controllable Loads			Measured loads				Total
	P (lb/in)	σ^t_{max} (ksi)	σ^t_{min} (ksi)	σ^b_{max} (ksi)	σ^b_{min} (ksi)	Q_{max} (lb/in)	Q_{min} (lb/in)	Life (Cycles)
HTFF01	10695	30.7	7.5	46.9	0.6	4871	-2084	415,000[s]
HTFF02	10575	58.0	7.7	64.1	2.0	1799	-1696	944,495
HTFF03	12522	42.1	11.3	51.9	3.3	2964	-2410	2,000,000[r]
HTFF04	19100	58.2	12.9	77.3	2.1	5733	-3249	174,973
HTFF05	19380	59.0	12.2	72.8	0.1	4128	-3620	169,815
HTFF06	19592	48.9	10.3	64.5	-0.1	4688	-3101	61,900
HTFF07	19791	53.5	14.5	64.0	0.3	3141	-4260	491,292

*(σ^t=stresses measured by top load cell, σ^b=stresses measured by bottom load cell).
[s] gross sliding observed throughout the experiment, [p] partial slip or mixed fretting regime during the experiments.

444

The first experiment provided valuable insight into the mechanics of the rig and the temperature variation at the contact. Based on the behavior of the rig in the first experiment, changes were made in the alignment procedure. The next two experiments served the purpose of verifying the working of the rig. Coefficient of friction was found to be very low (0.17 - 0.23) for the given contacting materials, due to which severe gross sliding (implying $Q= \mu P$) was observed during the course of experiments. It is possible that the relatively large displacements associated with sliding wear introduced non-linearity into the load transfer relationship. Thus P could be smaller than the measured value.

In order to achieve partial slip, representative of the engine hardware, the tangential load has to be decreased such that $Q< \mu P$. Either the length of the specimen between the contact and the top grips could be reduced or the area of cross-section (i.e. the thickness) of the diaphragms could be reduced in order to reduce Q. The length of the specimen was reduced due to the ease of modification. This was achieved by raising the fretting chassis, relative to the specimen, using spacers. By this process, partial slip conditions were achieved in the subsequent experiments. Q/P ratios of up to 0.27 were achieved implying that the coefficient of friction could be higher than what was anticipated from the first few sliding experiments.

As a preliminary study, the effect of the orientation of material principal axes on a sliding contact problem, representative of first two experiments, was studied using the aforementioned SIE approach. The orientation of the primary axis of the material with respect to the axis of the specimen was obtained from the manufacturer. However, since the orientation of the secondary axis with respect to the contacting surface was not known, SIE analysis was performed for all possible orientations. The effect of orientation of the material principal axes on subsurface stresses is significant. Lauè x-ray diffraction method is being used to determine the orientation of the material principal axes to facilitate an accurate stress analysis. Further analysis of the fretting experiments will be conducted after determining the orientation of the material principal axes.

C. Summary

Fretting characteristics of advanced materials at higher temperatures were studied. A new rig has been designed to operate at temperatures representative of the conditions to which the engine components are exposed in the turbine. Load histories clearly illustrated the effect of temperature on tribological behavior through the friction coefficient. The effect of change in the orientation of the secondary axis in the samples provided has been evaluated and a method to determine the orientation of the secondary axis has been discussed. Once the friction coefficient and the orientation of the secondary axis is known, efforts to relate fretting fatigue life to local stresses will be pursued.

4.5.3 Component Stress Prediction

4.5.3.1 Background on HCF Induced Attachment Cracking in Turbine Blade

Validating the advanced modeling tools that integrate accurate contact stress modeling with validated high cycle fatigue (HCF) life prediction is a key part of the single crystal HCF attachment analysis system. Validation cases consist of fretting fatigue data generated by Purdue University and a P&W single tooth firtree (STFT) test. Additional validation cases were conducted after completion of basic work and are reported in Appendix X.

The component considered for the calibration of the single crystal attachment HCF life system is a low turbine blade that experienced considerable vibratory excitation from both a 3E and a non-integral mode. The blade is made of a directionally solidified nickel base material but exhibited initiation from the HCF loading within a single grain. This configuration has since been redesigned to remove this sensitivity to HCF. The fracture surfaces for one of the blades are shown in Figure 4.224 and 4.225. Figure 4.224 is a composite of several blade fracture locations. Sufficient information was available on both fractured and non-fractured parts to develop a comparison for HCF fatigue predictions in the attachment region. In addition, extensive testing was done with a Noninterference Stress Measurement System (NSMS) to determine blade motion, a critical element in applying the RADICAL HCF predictive process.
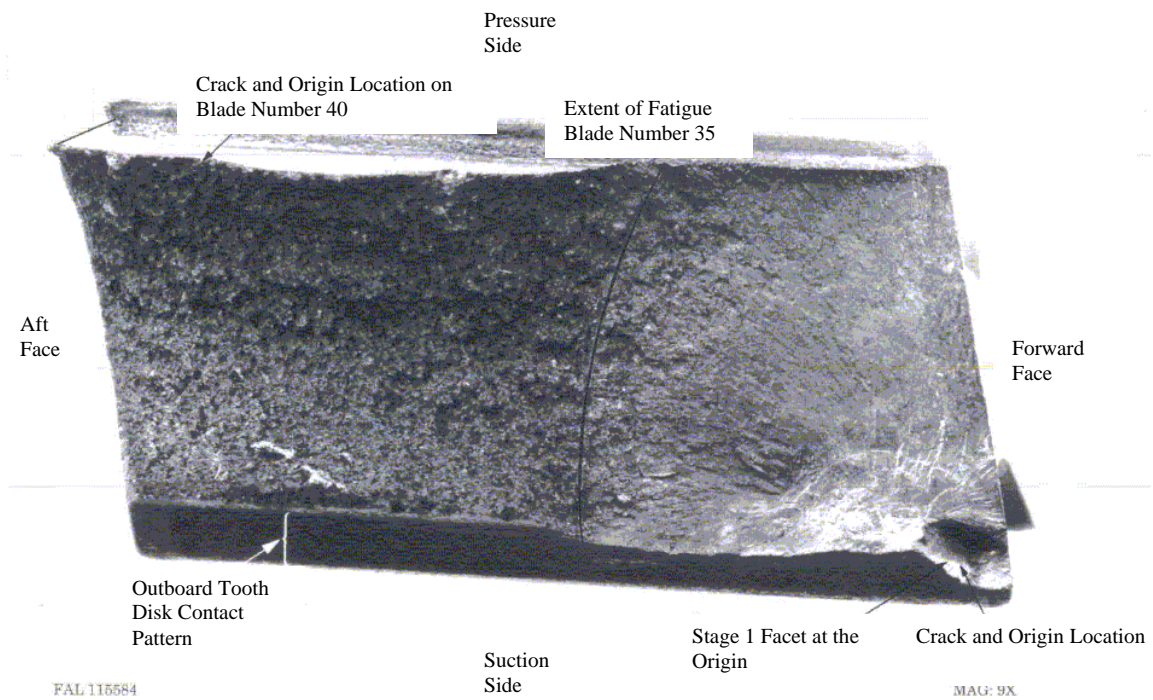
Figure 4.224. Top view of low pressure turbine blade upper tooth fracture surface
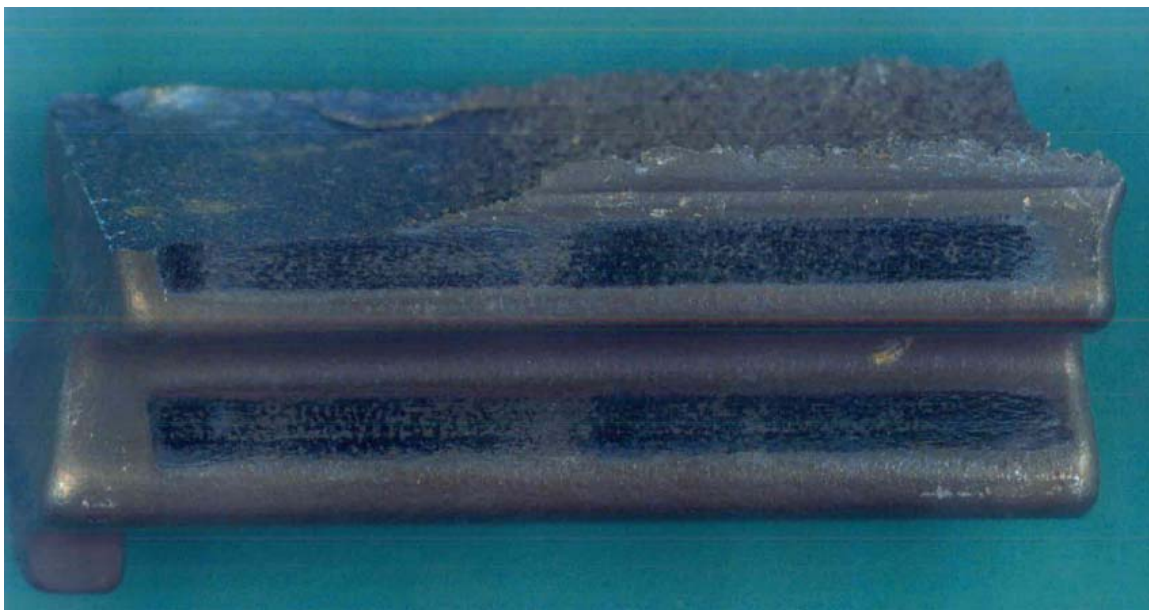
Figure 4.225. Side view of low pressure turbine blade upper tooth fracture surface.

4.5.3.2   Component Stress Prediction

    This section describes the progress made in the stress analysis portion of the RADICAL HCF attachment lifing system validation. This low pressure turbine blade presents some unique challenges in that it has two teeth and is shrouded, whereas the previous analysis work on fan blades contained only one tooth and was unshrouded. The fan analysis was therefore less complicated from a stress analysis and particular boundary condition perspective. The low pressure turbine blade exhibited attachment failure due to high cycle fatigue excitation from a 3E stiffwise bending mode response. The turbine blade, see Figure 4.226, had begun to be subjected to the initial part of the RADICAL analysis process, that is developing the finite element model. This process consists of: (1) three dimensional finite element analyses with and without contact to characterize both static and vibratory responses of bladed disk designs, (2) engine data or aeromechanical predictions characterizing vibratory responses, (3) serial two-dimensional quasi-analytical contact analyses conducted using finite element method input, and (4) interpretation of the accuracy of the stress histories within the context of a validated lifing system. Time limitations prevented the completion of the verification work, therefore this section chronicles progress made towards that end. (Subsequent to this analysis, further work was completed on the validation phase and is documented in Appendix X.)

    Life prediction verification is to be built upon previous studies of the F100-PW-229 4th Turbine Blade [63,64]. These previous studies contained analyses and laboratory testing concluding that blade failure was due to the effect of a 3E stiffwise bending mode upon the blade-to-disk contact surface. Two separate NASTRAN finite element models were used for that work; one for LCF and the other for HCF. The LCF model contained the loads at the 0.6/0K condition for the 3E mode [Reference 63, page 37, Figure 22] but was not suited for robust contact or current modal cyclic symmetry techniques. The HCF model did not contain the required loads but was suited for symmetry and can be modified for robust contact.

    Accurate contact stress analysis verification requires a model having loading conditions simulating 0.6/0K and blade/disk contact. To meet these requirements loads from the NASTRAN LCF model are to be mapped onto the HCF model. In this way the steps for

the RADICAL process can be completed and the necessary contact load and stress dieout data can be extracted from the finite element analysis model for later use.

The NASTRAN models have been successfully translated into ANSYS as shown in Figure 4.226 and 4.227 and the load mapping strategy has been laid out. More work, beyond the scope of this program, is required to complete the verification process. (See Appendix X for updated information on verification of RADICAL process.)
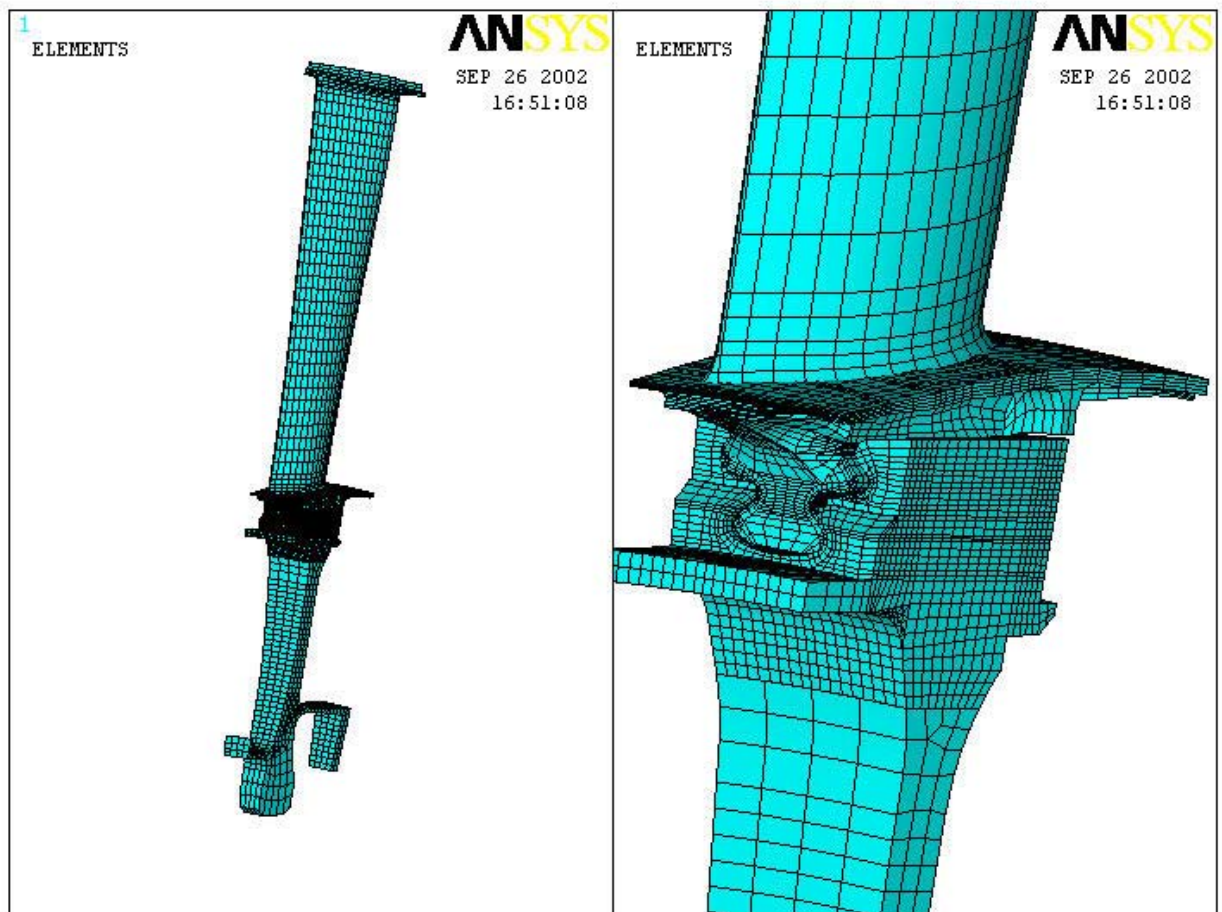
Figure 4.226. 4th blade and disk 3D finite element model (assembled).
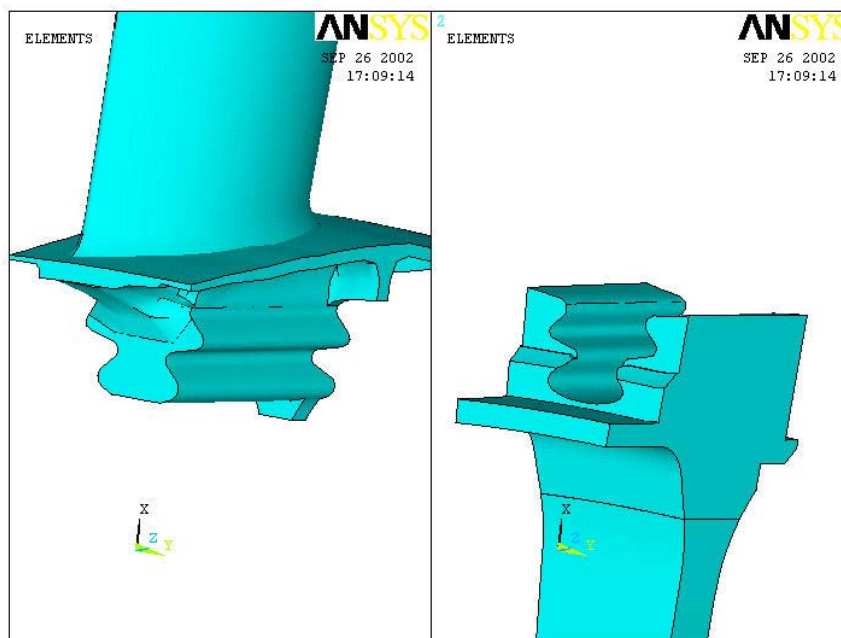
Figure 4.227. 4th blade and Disk 3D Finite Element Model (dis-assembled).

4.5.3.3   HCF Life Prediction Attachment Cracking in Turbine Blade

Subsequent work to the work under the basic program, the RADICAL process has been exercised against several field and laboratory test cases, for which there is attachment EOC cracking experience. The objective is to understand the robustness of the process as well as to calibrate it. A description of the hardware on which the calibration/validation is performed, the analysis assumptions and process, and the results of the analyses are presented in Appendix X. In the case of the turbine blade the single crystal system is adapted to directionally solidified material for both life and contact stress analysis. It was not determined if a plastic analysis involving a constitutive model would be required.

4.6   IMPLEMENTATION INTO DESIGN INVIRONMENT

The technologies developed under this program for single crystal materials are aimed at ultimately improving the design and analysis capabilities of the engine manufacturers for both new designs as well as analysis of existing components in order to insure structural durability. The methods for implementing these technologies involve

450

incorporating them into standard design practice through their inclusion of the design manuals used within the engine companies. Described, below, are the summary comments by Pratt and Whitney and GEAE on the inclusion of single crystal technologies into "Standard Work" and "Best Practices," respectively. In addition to the implementation, technologies developed under this program will be adopted, where appropriate, into the ENSIP specifications.

4.6.1   Deployment into Pratt & Whitney Standard Work

With the development and successful calibration of the RADICAL approach as a solid foundation for contact fatigue, intensive efforts have been underway within both the Compression Systems and Turbine Module Center to deploy, apply and mature this suite of analytical capabilities within the context of the standard work instructions for bladed disks that frame all design and field investigation efforts. The current vision incorporates a subset of the RADICAL approach and criteria into the preliminary design phase and embraces the complete process for detailed design work and field investigations.

Specific steps are being incorporated into the activity pages that define explicit guidelines for modeling and analysis procedures for designers and structural analysts during a concurrent design effort. An overview of the steps is included below:

- Create appropriate three-dimensional sector representation of bladed disk stage with pre-defined mesh features in attachment region

- Run ANSYS non-linear static solution with frictionless node-to-node contact corresponding to initial (idle) condition, followed by a restart with appropriate friction coefficient enforced

- Continue non-linear static solution to mission point corresponding to vibratory crossing

- Reduce convergence tolerance and restart/rerun solution at this point

- Perform a pre-stressed modal analysis and extract modal force history for mode(s) of interest

- Restart analysis at mission point of interest and solve with superposed scaled modal force history until frictional path dependence effects have shaken down

- Extract interfacial reaction load history for complete analysis and execute contact stress analysis & lifing modules corresponding to materials of interest.

Pratt & Whitney's commitment to transferring the technologies and methods developed under the auspices of this contract promise to have immediate, persistent and profound impact on the robust design of bladed disk attachments. As evidence of this, consider that this methodology is being applied currently to over ten commercial and military applications at various stages in their life cycle—from clean-sheet designs, to development components and finally maturing hardware in need of durability improvements.

4.6.2   Development of Best Practices at GE

4.6.2.1   1900°F SX HCF Implementation

Modeling studies have been performed to determine the applicability of the HCF-Rupture Interaction Model developed for PWA1484 (Section 4.3.4.3) to the single crystal alloy, Rene N5, used in GEAE engines. This effort used historical Rene N5 data at 1900°F. The study examined the influence of rupture damage in high mean stress HCF, and the capability to model tests under constant and variable mean stress by the cumulative rupture damage approach shown to be valid for PWA 1484 at high mean stress. Following the method outlined in Section 4.3.4.3, pure rupture data under constant stress was fit with a power law of the form $t_r = k\sigma^m$, where t_r is rupture time, σ is stress, and k and m are empirical constants. The life of 2-step rupture tests (high-low and low-high) was calculated assuming linear damage summation. The lives of HCF tests with different mean and alternating stresses) were calculated assuming rupture was the only damage mechanism and that damage under variable stress conditions could be integrated over each cycle (cumulative rupture model without compressive damage). Tests for two cyclic frequencies were included (60 and 900 Hz). Since the model was based on rupture damage, the lives of these two

frequencies were predicted to be the same on a time basis. This was in good agreement with observations. The life of 2-step HCF tests (high-low mean and low-high mean) was also computed by assuming linear damage accumulation of the two HCF segments (each of which was calculated from rupture). Figure 4.228 shows a comparison of the predicted (y-axis) and observed (x-axis) lives using this approach.

In the key attached to Figure 4.228, "const HCF, s1" refers to 60 Hz HCF at a constant mean stress of s1 (s1 > s2 > s3 > s4) and several different alternating stress levels. (Each test has only one alternating level; there are one or more different tests for each alternating stress.) "Hi Freq HCF" is 900 Hz HCF, also at a constant mean, R >0. "Lo-Hi Rupture" refers to rupture tests in which the specimen is loaded for a fraction of life at a low stress (s3) and then the load is increased to a higher stress(s1). "Lo-Hi HCF" is similar, where the mean stress is changed from s3 to s1 while the alternating stress is kept constant.
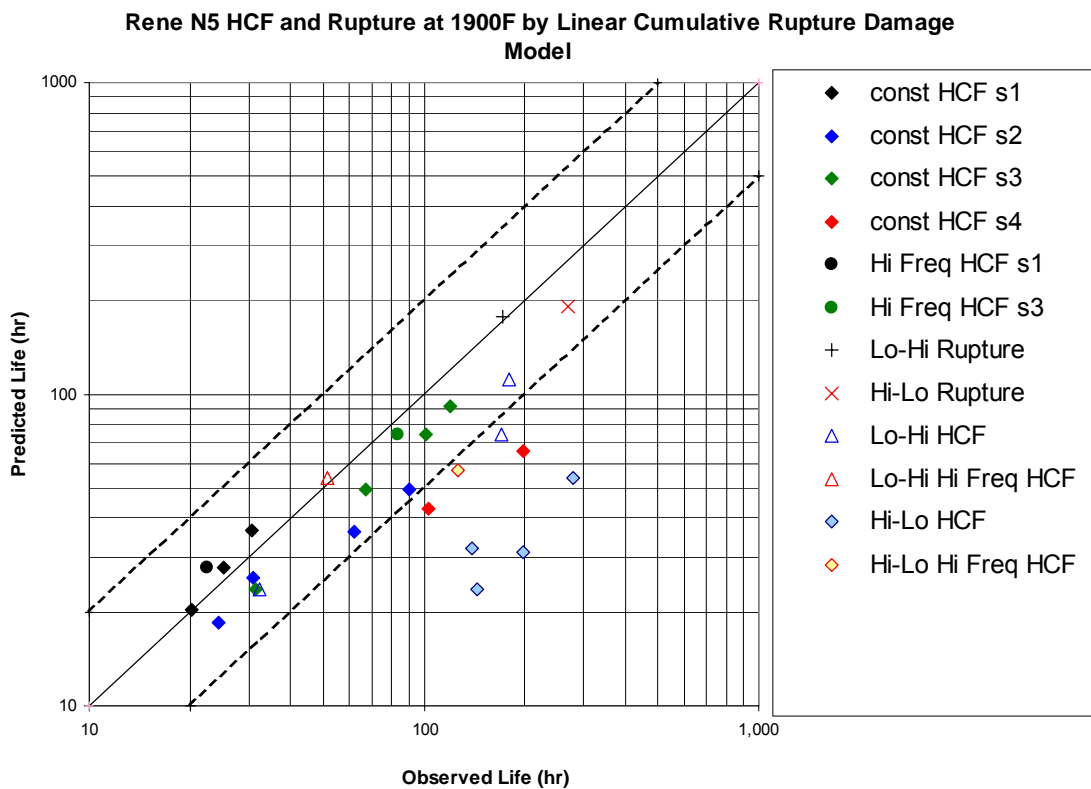
Figure 4.228   Comparison of predictions vs. observed lives (hr) using linearupture damage model for rupture and HCF of Rene N5 at 1900°F.

Overall, this approach performed remarkably well: 18 of the total of 26 test predictions fell within a factor of 2 of the observed lives. The test conditions that are not well predicted are: Hi-Lo HCF and HCF at the lowest mean stress (lowest R). There is also a noticeable trend of increasing conservatism (predicted less than observed) as the stress-ratio is decreased (as mean stress decreases). This might be expected since at lower R the conditions are farther from pure rupture, where the cumulative rupture model is expected to work the best. The reason for the failure of the model to predict Hi-Lo HCF capability is not known but is disturbing since many turbine blades undergo time-varying (relaxing) mean stresses due to creep during engine exposure. One possible reason comes from observation of the test specimens themselves: except for the rupture tests and the HCF tests with the highest mean stresses, the failure modes in these specimens were all fatigue-like (flat, oxidized surface origins) and not rupture-like (rough, dimpled, internally initiated). Thus even though the extent of agreement is relatively good, as shown in Section 3.4.3, a rupture damage-based model alone may not be appropriate for all high temperature HCF conditions. Unfortunately, the low mean stress HCF data representing a pure fatigue capability were not available to construct the Walker HCF model required for lower mean stress HCF modeling. Nevertheless, the extension of the HCF-Rupture modeling approach to other single crystal superalloys is certainly promising and will be pursued under internal company funding.

4.6.3 ENSIP for Single Crystal Materials

The following is a summary statement of the state-of-the-art of some aspects of SX and DS alloys. These observations should be recognized in ENSIP, and specific guidance should be developed on how to deal with these features that are unique to anisotropic materials.

Unlike traditional polycrystalline, isotropic materials, components made from directionally solidified (DS) or single crystals (SX) materials require several special design considerations. The first of these is that DS and SX materials are anisotropic, that is, their properties vary with direction. This is true for elastic, inelastic, and fracture properties. Both material types are fabricated so that one axis of the cubic crystal geometry is approximately parallel to the solidification direction of the part, usually noted by convention as the <001> direction. In a DS material, there are multiple grains, all with the same <001> axis, but with

varying and random transverse orientations. In a SX material there is only one grain or crystal, whose transverse orientation may or may not be controlled by processing.

By virtue of the cubic symmetry of nickel-based superalloys, SX superalloys have cubic symmetry, and thus require three independent elastic constants to fully describe them. Unlike isotropic materials, the shear modulus is not definable in terms of the Young's modulus and Poisson's Ratio. DS materials have lower symmetry due to the random transverse orientation of their grains. This makes them elastically transversely isotropic, and they require 5 constants to define their elastic response. Both types of material symmetry are found in most modern finite element codes and modeling of elastic response should be done with the proper anisotropic description. The elastic anisotropy does not change much with temperature.

The yield and creep behavior of DS and SX materials is also anisotropic due to the strong tendency for these materials to deform on a limited number of slip systems. This response is more complex than the elastic response and much more difficult to model and imbed in stress analysis codes. The plastic and creep anisotropy appears to be greatest at low temperatures (up to about 1400°F) and then diminishes above that, due to the activation of additional slip systems at higher temperatures. In parts where the loading is primarily uniaxial, the properties in the stress direction (usually <001>) can often be used to satisfactorily describe the inelastic response of these materials.

Fracture properties (e.g, rupture, LCF) can also be anisotropic with the extent varying with temperature. Properties can be developed uniaxially for different orientations, but there is no widely agreed-upon method for evaluating the capability of DS or SX materials under complex stress states (as often occur in blades and vanes). In addition to the material anisotropy, DS and especially SX materials can be subject to cracking along crystallographic planes, especially under fatigue cycling. This crystallographic cracking is most pronounced at low temperatures, and introduces a mixed-mode fracture component. For conditions where such crystallographic cracking is anticipated, mixed mode characteristics should be incorporated into the fracture analysis. For many cases, Mode I cracking is observed and conventional Mode I practices suffice.

Most modern turbine airfoils are relatively defect and damage tolerant structures, as evidenced by their ability to function with many cooling holes drilled into them. This tolerance results partly from the need to keep stresses low due to the limited creep-rupture capability at high temperature, and partly to the large component of thermally-generated stress, which tends to make cracking self-limiting. Blade shanks and dovetails are usually more highly stressed, since they are much cooler, and here more attention needs to be paid to defects and damage tolerance.

Both DS and SX materials can have manufacturing defects or in-service damage that may need to be considered in the component capability. Examples of manufacturing defects are: primary grain misorientation, inclusions, porosity, low angle grains, and high angle grains. The latter two are only relevant for SX materials. In-service damage can be from impact, fretting, or erosion. Currently, most of these defect types are managed by placing experimentally determined acceptance limits on them. An example would be manufacturer's limitations on the allowable primary grain misorientation. There is only limited evidence and experience in DS and SX hardware on using fracture mechanics based determinations of allowable defect or damage type or size. Again, consideration needs to be made as to whether the cracking will be Mode I or mixed mode. Grain boundary type defects in SX materials (low angle and high angle grains) do not appear to be well suited for conventional fracture analysis, since the defect geometry is wide by very thin and the grain boundary properties are not easily characterized. These defects are usually governed by experimental or empirical acceptance limits on misorientation, size, or location.

Impact damage is less of a problem for turbine airfoils than for compressor airfoils, since the turbine section is more isolated from the outside environment. Most turbine impact events are domestic in nature, that is, from upstream combustor or airfoil pieces that are liberated inside the engine. Superalloys have high ductility and toughness, so their resistance to such events is generally good. However, when considering low ductility or low toughness materials for turbine airfoils, careful attention must be paid to potential effects of impact.

Calculation of the stress intensity factor, K, or range of K, ΔK, is necessary for crack growth rate computations or fracture toughness evaluation. K calculations are based either on standard solutions found in handbooks or are determined from analytical or numerical

procedures, the latter often based on FEM. Most solutions are based on isotropic material properties and are, therefore, not strictly applicable to anisotropic materials such as SX or DS alloys. In this program, several specific cracked specimen geometries were evaluated using both isotropic as well as anisotropic analysis techniques. For the most part, the isotropic solutions were found to be a reasonable representation of the more accurate anisotropic analysis, primarily for Mode I stress intensity solutions. For this reason, it seems reasonable to use isotropic solutions for geometries and crack lengths where validation of the accuracy of the isotropic solution has been demonstrated and the amount of error is considered to be within acceptable limits. For mixed mode cracks, however, the observed crack path as well as the associated Mode I and Mode II K values can differ from those predicted from isotropic solutions. Again, the use of isotropic solutions can only be justified if it can be demonstrated that the errors in mixed mode K values, as well as crack paths, are well predicted compared to those from the anisotropic solution. It is recommended that future versions of ENSIP provide documentation of cases where isotropic solutions have been compared with anisotropic solutions and present data on the magnitude of the errors for specific cases.

Material properties of SX materials such as threshold or critical K values vary with crystal orientation. General anisotropic models of material properties, developed primarily for anisotropic metals with texture, are not necessarily valid for single crystal materials. Great care should be used in extrapolating properties in a direction in one crystal orientation to another direction using conventional anisotropic models. As an example, extrapolation of threshold ΔK under Mode I can produce significant errors in the value of threshold ΔK under Mode II for the same material orientation and crack direction. Future versions of ENSIP should highlight these differences.

REFERENCES

1.   Gallagher, J.P., et. al., *Improved High Cycle Fatigue (HCF) Life Prediction*, Final Report, Contract No. F33615-96-5269, UDRI Report No. UDR-TR-1999-00079.

2.   Lenets, Y.N. and Bellows, R.S. (2000) *Crack Propagation Life Prediction for Ti-6Al-4V Based on Striation Spacing Measurements*. Int. J. Fatigue, Vol. 22, p. 521.

3.   Lenets, Y.N., Bellows, R.S., and Merrick, H.F. (2000) *Propagation Behavior of Naturally Initiated Fatigue Cracks in Round Bars of Ti-6Al-4V*. In Proceedings of the 5th National Turbine Engine High Cycle Fatigue Conference, HCF'00.

4.   Boyce, B.L. and Ritchie, R.O. (1999) *On the definition of lower-bound fatigue-crack propagation thresholds in Ti-6Al-4V under high cycle fatigue conditions*. In Proceedings of the 4th National Turbine Engine High Cycle Fatigue Conference, HCF'99.

5.   Lenets, Y.N., Nelson, R., and Merrick, H.F. (2001) *Incorporation of "Small" Crack Behavior into Life Prediction Methodology for Military Aircraft Engines*. In Proceedings of the 6th National Turbine Engine High Cycle Fatigue Conference, HCF'01.

6.   Larsen, J.M., Worth, B.D., Annis, Jr., C.G., and Haake, F.K., *An Assessment of the Role of Near-Threshold Crack Growth in High-Cycle Fatigue Life Predictions of Aerospace Titanium Alloys Under Turbine Engine Spectra*, International Journal of Fracture, Vol. 80, 1996, pp. 237-255.

7.   Maxwell, D.C. and Nicholas, T., *A Rapid Method for Generation of a Haigh Diagram for High Cycle Fatigue*, ASTM STP 1321, T. L. Panontin and S. D. Sheppard, ASTM, 1999.

8.   Peterson, R.E., *Stress Concentration Factors*, John Wiley and Sons, New York, 1974.

9.   Southwest Research Institute, Honeywell, General Electric, Pratt & Whitney, Rolls-Royce Allison, Scientific Forming Technologies, Federal Aviation Administration Grant, *Turbine Rotor Material Design Final Report,* 95-G-041, August 1999.

10.   Hudak, Jr., S.J., *Small Crack Behavior and the Prediction of Fatigue Life*, ASME Trans., Journal of Engineering Materials and Technology, Vol. 103, 1982, p.26.

11.   Suresh, S. and Ritchie, R.O., *The Propagation of Short Fatigue Cracks*, Int. Metals Reviews, Vol. 29, p. 445, 1984.

12.   Ritchie, R.O. and Lankford, J., TMS-AIME, *Small Fatigue Cracks*, Warrendale, PA, 1986.

13.   Topper, T.H. and. El Haddad, M.H., *Fatigue Strength Predictions of Notches Based on Fracture Mechanics*, Fatigue Thresholds: Fundamentals and Engineering Applications, Engineering Materials Advisory Services, LTD, Warley, UK, 1982.

14.   Hudak, Jr., S.J., Chell, G.G, Rennick, T.S, McClung, R.S., and Davidson, D.L., *A Damage Tolerance Approach to FOD Based on the Worst Case Notch Concept*, Proceedings of the 4th National Turbine engine High Cycle Fatigue Conference, Monterey, CA, February 1999.

15.   Chell, G.G, Hudak, Jr., S.J., Lee, Y.D., and Feiger, J.J, *An Assessment of the "Worst Case Notch" Model for Prediction of HCF Threshold Stresses in the Presence of Foreign Object Damage*, Proc. of the 5th National Turbine Engine High Cycle Fatigue Conference, Chandler, AZ, March, 2000.

16.   Hudak, Jr., S.J., Chan, K.S., Chell, G.G, Lee, Y.D., and McClung, R.C., *A Damage Tolerance Approach for Predicting the Threshold Stresses for High Cycle Fatigue in the Presence of Supplemental Damage*, Fatigue – David L. Davidson Symposium, Edited by K. S. Chan, P. K. Liaw, R. S. Bellows, T. C. Zogas, W. O. Soboyejo, TMS, 2000.

17.   Chan, K.S., Lee, Y.D., Davidson, D.L. and Hudak, Jr., S.D., *A Fracture Mechanics Approach to High Cycle Fretting Fatigue Based on the Worst Case Fret Concept: Part I – Model Development*, Int. J. of Fracture (to be published).

18.   Chan, K.S., Davidson, D.L., Owen, T.E., Lee, Y.D., Hudak, Jr., S.J., *A Fracture Mechanics Approach to High Cycle Fatigue Based on the Worst Case Fret Concept: Part II – Experimental Evaluation*, Int. J. of Fracture (to be published).

19.   Tanaka, K., Nakai, Y., and Yamashita, M., *Fatigue Growth Threshold of Small Cracks*, International Journal of Fracture, Vol. 17, pp. 519-533, 1981.

20.   Brown, C.W. and Taylor, D., *The Effects of Texture and Grain Size on the Short Fatigue Crack Growth Rates in Ti-6Al-4V*, in Fatigue Crack Growth Threshold Concepts, D. Davidson and S. Suresh, Eds. TMS-AIME, pp. 433-445, 1984.

21.   Southwest Research Institute, DARWIN User's Guide, Version 3.5, Appendix : *Shakedown Residual Stress Methodology and Validation of SHAKEDOWN Module*, 2002.

22.   Amstutz and Seeger, T., *Accurate and Approximate Elastic Stress Distribution in the Vicinity of Notches in Plates Under Tension*. Unpublished results (referenced in G. Savaidis, M. Dankert, and T. Seeger, "An Analytical Procedure for Predicting

Opening Loads of Cracks at Notches," Fatigue Fracture Engineering Materials. Structure", Vol. 18, No. 4, pp. 425-442, 1995).

19.   Hudak, Jr., S.J., Chan, K.S., McClung, R.C., Chell, G.G, Lee, Y.D., and Davidson, D.L., *High Cycle Fatigue of Turbine Engine Materials*, Final Technical Report, U.S. Air Force Contract No. F33615-96-C-5269, UDRI Subcontract No. RI 40098X, 1999.

20.   McVeigh, P.A., Harish, G., Farris, T. N., and Szolwinski, M. P., *Modeling Interfacial Conditions in Nominally-Flat Contacts for Application to Fretting Fatigue of Turbine Engine Components*, International Journal of Fatigue, Vol. 21, pp. 5157-5165, 1999.

21.   Hills, D. A., and Nowell, D., *Mechanics of Fretting Fatigue*, Kluwer Academic Publishers, Drodrecht, Netherlands, 1994.

22.   Murthy, H., Harish, G. and Farris, T.N., *Efficient Modeling of Fretting of Blade/Disk Contacts Including Load History Effects*, ASME Journal of Tribology, In-Press.

23.   Murthy, H., Farris, T.N., and Slavik, D.C., *Fretting Fatigue of Ti-6Al-4V subjected to blade/disk contact loading*, Developments in Fracture Mechanics for the New Century, 50th Anniversary of Japan Society of Materials Science, 2001, pp. 41-48.

24.   Murthy, H., Harish, G. and Farris, T. N., *Influence of Contact Profile on Fretting Crack Nucleation in a Titanium Alloy*, in A Collection of Technical Papers, Proceedings of 41st AIAA/ASME/ASCE/AHS/ASC Structures, Structural Dynamics and Materials Conference, Atlanta, GA, AIAA, Vol. 1, 2000, pp.1326-1333.

25.   Szolwinski, M. P. and Farris, T. N., *Mechanics of Fretting Fatigue Crack Formation*, Wear, Vol. 198, 1996, pp. 93-107.

26.   Szolwinski, M.P. and Farris, T.N., *Observation, Analysis and Prediction of Fretting Fatigue in 2024-T351 Aluminum Alloy*, Wear, 221(1), pp 24-36 (1998)

27.   Doner, M., Bain, K.R., and Adams, J.H., *Evaluation of Methods for the Treatment of Mean Stress Effects on Low-Cycle Fatigue*, Journal of Engineering for Power, 1981, pp 1-9.

28.   Murthy, H., Rajeev, P. T. and Farris, T. N., *Fretting Fatigue of Ti6Al4V/Ti6Al4V and Ti6Al4V/In718 Subjected to Blade/Disk Contact Loading*, Fatigue 2002: The 8th International Fretting Fatigue Congress, Stockholm, Sweden, Ed A.F. Blom, EMAS, Volume 3, pp 2153-2160, 2002.

29.   Golden, P.J., *High Cycle Fatigue of Fretting Induced Cracks*, PhD thesis, Purdue University, West Lafayette, IN, 2001.

30. Cormier, N.G., Smallwood, B.S., Sinclair, G.B., and Meda, G., *Aggressive Submodeling of Stress Concentrations*, Int. J. Numer. Meth. Engrg., Vol 46, 1999, pp 889-909.

31. Neuber, Heinz, *Theoretical Determination of Fatigue Strength at Stress Concentration*, AFML-TR-68-20, April 1968.

32. Sih, G.C., Paris, P.C., Irwin, G.R., On *Cracks in Rectilinearly Anisotropic Bodies*, International Journal of Fracture Mechanics, Vol. 1, pp. 189-203, 1965.

33. Chan, K.S., Cruse, T.A., *Engineering Fracture Mechanics*, Vol. 23, No. 5, pp. 863-874, 1986.

34. Hoenig, A., *Near-Tip Behavior of a Crack in a Plane Anisotropic Elastic Body*, Engineering Fracture Mechanics, Vol. 16, No. 3, pp. 3930403, 1982.

35. Tada, H., Paris, P.C., Irwin, G.K., *The Stress Analysis of Cracks Handbook*, 1st Ed., Del Research Corp. Hellertown, PA, 1973.

36. Johnson H. H., *Calibrating the Electrical Potential Method for studying Slow Crack Growth*, Materials Research and Standards, 442 – 445 (Sept. 1965).

37. Cunningham, S.E., DeLuca, D.P., Haake, F.K., *Crack Growth and Life Prediction In Single Crystal Nickel Superalloys*, Crack Growth and Life Prediction In Single Crystal Nickel Superalloys, Vol. 1, Air Force Wright Aeronautical Laboratory, pps. 86 – 95.

38. Wright, P.K., Jang, H., and Popp, H.G., *Fatigue and Fracture of Advanced Blade Materials*, AFWAL TR-84-4166, Materials Laboratory, Air Force Wright Aeronautical Laboratory, WPAFB, OH, Feb. 1985.

39. DeLuca D.P., and Cowles, B.A., *Fatigue and Fracture of Advanced Blade Materials*" AFWAL TR-84-4167, Materials Laboratory, Air Force Wright Aeronautical Laboratory, WPAFB, OH, Feb. 1985.

40. Cunningham, S.E., Deluca, D.P., Haake, F.K., *Crack Growth and Life Prediction in Single-Crystal Nickel Superalloys*, Volume 1, WL-TR-94-4089, Air Force Wright Laboratory, February 1996.

41. Cunningham, S.E., Deluca, D.P., Hindle, E.H., Sheldon, J.W., Haake, F.K., *Crack Growth and Life Prediction in Single-Crystal Nickel Superalloys*, Volume 2, WL-TR-96-4048, Air Force Wright Laboratory, August 1994.

42. ANSYS Structural Analysis Guide, Chapter 11 "Fracture Mechanics".

43. Leverant, G.R. and Gell, M., *Metal Transactions A*, Vol. 6A, 1975, pp. 367-371.

44. Leverant, G.R. and Gell, M., and Hopkins, S.W., *Mat. Sci. Eng.*, Vol. 8, 1971, pp. 125-133.

45. Telesman, J., and Ghosn, L.J., *Crack Growth and Life Prediction in Single-Crystal Nickel Superalloys*, Vol. 3, WL-TR-94-4090, Pratt & Whitney, West Palm Beach, FL, 1996.

46. DeLuca, D.P., and Annis, C., *Fatigue in Single Crystal Nickel Superalloys*, FR23800, Pratt & Whitney, West Palm Beach, FL, 1995.

47. Wright, P.K., Jang, H., and Popp, H.G., *Fatigue and Fracture of Advanced Blade Materials*, AFWAL-TR-84-4166, General Electric, Cincinnati, OH, 1985.

48. Hudak, Jr., S.J., Chan, K.S., Chell, G.G, Lee, Y.D., and Feiger, J.J., *Advanced HCF Life Assurance Methodologies for Turbine Engine Materials*, SwRI Annual Progress Report to UDRI, UDRI Subcontract No. RSC99008, UDRI Contract No. F49620-99-C-0007, Southwest Research Institute, April 30, 2002.

49. Snyder, M.D. and Cruse, T.A., *Crack Tip Stress Intensity Factors in Finite Anisotropic Plates*, AFML-TR-73-209, 1973.

50. He, M.Y. and Hutchinson, J.W., *Asymmetric Four-Point Crack Specimen*, Journal of Applied Mechanics, Vol. 67, pp. 207-209, 2000.

51. Swenson, D. and James, M., *FRANC2D/L: A Crack Propagation Simulator for Plane Layered Structures*, Kansas State University, Manhattan, Kansas, 1995.

52. Erdogan, F. and Sih, G.C., *Journal of Basic Engineering D*, Vol. 85, 1963, pp. 519-527.

53. Pettit, R., Pratt & Whitney Aircraft, East Hartford, CT, Private communication, December 2001.

54. Telesman, J., Ghosn, L.J. and DeLuca, D.P., *Hydrogen Effects in Materials*, edited by A. W. Thompson and N. R. Moody, TMS, Warrendale, PA, 1996, pp. 943-952.

55. *Behavior of a Single Crystal Ni-Base Superalloy Subjected to Mixed Mode Loading, Mixed-Mode Crack Behavior*, ASTM STP 1359, K. J. Miller and D. L. McDowell, Eds., American Society for Testing and Materials, West Conshohocken, PA, pp. 312-328, 1999.

56. Hussain, M.A., Pu, S.L., and Underwood, J., *Strain Energy Release Rate for a Crack Under Combined Mode I and Mode II*, *ASTM STP 560*, 1974, pp. 23-28.

57. Sih, G.C., *Some Basic Problems in Fracture Mechanics and New Concepts, Eng. Frat. Mech.,* Vol. 3, 1973, p-p. 439-451.

58. Milligan, W.W., Department of Mat. Sci. & Eng., Michigan Technological University, Houghton, MI, Private Communication, August 2000.

59. Milligan, W.W. and Antolovich, S.D., *Yielding and Deformation Behavior of the Single Crystal Superalloy PWA1480*, Metal Transactions A, Vol. 18A, 1987, pp. 85-95.

60. *Life Prediction and Constitutive Models for Engine Hot Section Anisotropic Materials Program*, Final Report, NASA CR-189223, September, 1992.

61. Shah, D., and Duhl, D., *The Effect of Orientation, Temperature, and Gamma Prime Size on the Yield Strength of a Single Crystal Nick Base Superalloy*, Proceedings of the Fifth International Symposium on Superalloys, ASM, Metals Park, Ohio, 1984.

62. Stouffer, Donald C., and Dame, L. Thomas, *Inelastic Deformation of Metals: Models, Mechanical Properties, and Metallurgy*, John Wiley & Sons, Inc., New York, 1996, pp. 413-430.

63. Cap, T. and Martin, S., et al., *F100-PW-229 4th Blade Investigation Engine Test Report,* FTDM #3013, Traceability Number 95AQ052, July 26, 1996.

64. Conner, S. and Cap, T., *F100-PW-229 4th Stage Turbine Blade and Disk Attachment Stress/Life Analysis with Verification Test Results for the Current and Full-Life Blade Designs,* FTDM#2926, Task Number 91QA204, January 29, 1992.

APPENDIX A
Ti-6Al-4V SMALL CRACK BEHAVIOR

A.1   MATERIAL AND EXPERIMENTAL DETAILS

The tests were conducted on a forged Ti-6Al-4V titanium alloy representative of a turbine engine fan blade material fully described in [1] as well as in Section 3.1.1.1 of this report. All experiments were carried out at room temperature in laboratory air on servo-hydraulic, closed-loop test frames operating under load control conditions. Smooth cylindrical specimens of 0.2 inch nominal diameter were subjected to interrupted high cycle fatigue (HCF) tests at different stress ratios (R = 0.1 and 0.5) and a frequency of 60 Hz. During the periodic interruptions, acetate replicas were taken from the entire gage section of a specimen surface. The replication employed 0.0013" thick Bioden RFA Acetyl Cellulose film and methylacetate. Since initial attempts to replicate unprepared electro-polished surface were not successful, subsequent efforts employed a quick (about 20 second) etch with Krolls reagent to enhance the effectiveness of the method. After completion of the test, the replicas were used to track the critical crack backwards to its initiation. In addition to conventional analysis in optical microscope, selected replicas were sputtered with gold and evaluated in a scanning electron microscope.

The replication information was converted into conventional da/dN - a and da/dN - ΔK form. The NASCRAC™ (NASA CRack Analysis Code) software was used to determine the stress intensity factor. Surface cracks were assumed to be semi-circular, so that the length of the surface crack (Figure A1c) was twice the crack depth (Figure A1a). The results obtained were compared to the available data for both compact tension and surface flaw specimens obtained via load shedding technique under constant R as well as constant K_{max} conditions.
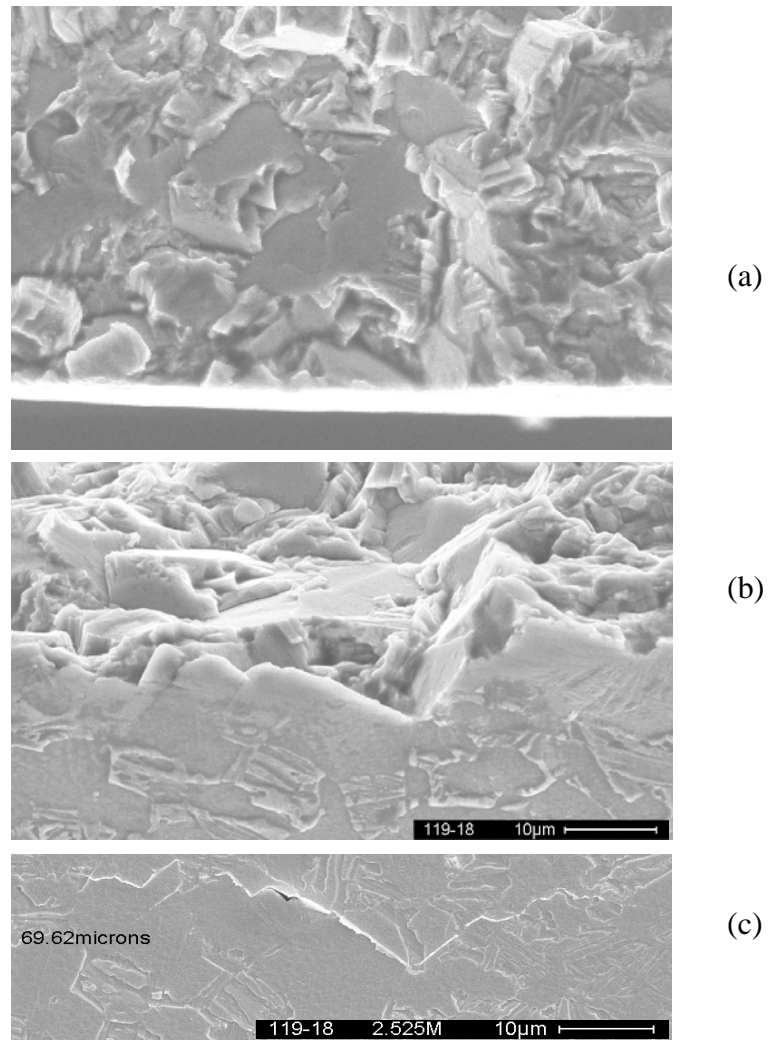
Figure A1. Fractograph of the crack initiation location (a); the same location tilted ~45° (b) and crack profile on the specimen surface (c).

A.2   RESULTS AND DISCUSSION

A representative example of several consecutive replicas taken from the same location is shown in Figure A2. It can be concluded that the fatigue crack in the given specimen initiated between 2,420,000 and 2,440,000 cycles (Figure A2e and A2d, respectively). Also, the rate of subsequent crack propagation on the specimen surface can be readily and very accurately evaluated.
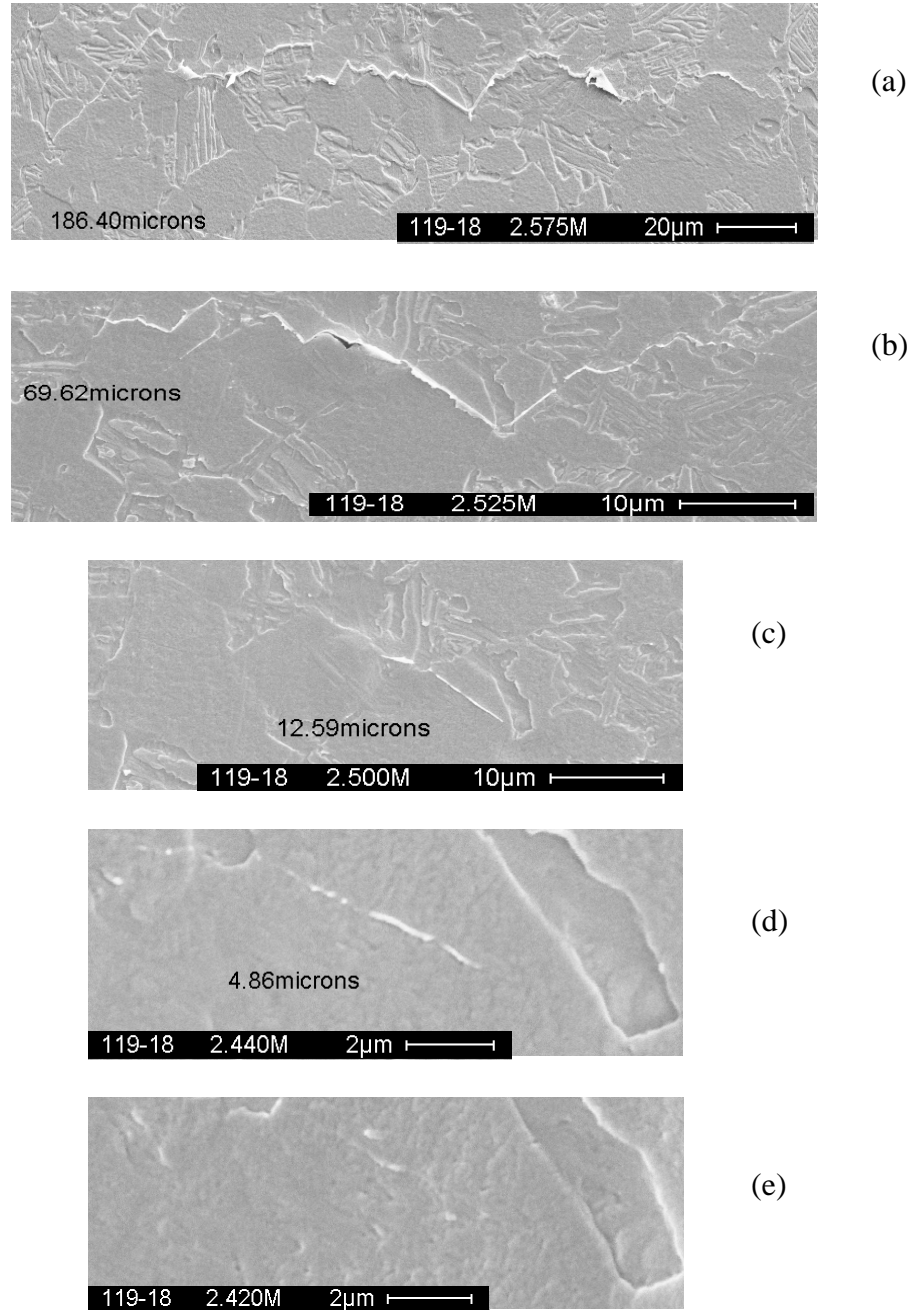
Figure A2. Consecutive replicas taken from the same location of the specimen.

In order to obtain even more information about small crack initiation and propagation behavior, an attempt was made to match the crack profile from the replicas with postmortem observations made on the fracture surface. One example of such exercise is given in Figure A1. The bottom photograph in Figure A1 contains the crack

profile from one of the replicas shown before (see Figure A2b). The top photograph in Figure A1 was taken from the fracture surface at the supposed location of crack initiation. The same location is shown in the middle photograph, however in this case the sample was tilted in the SEM so that both crack profile on the specimen surface and fracture surface can be seen simultaneously. The presence of a very specific feature (almost 90 degrees change in the crack propagation direction) in all three photographs confirms that they were taken from the same location. It is also evident that in this particular specimen intra-granular crack initiation occurred from a relatively large sub-surface grain. Another example (Figure A3) shows similar crack initiation mechanism from a large grain immediately adjacent to the specimen surface.

This fractographic evidence is consistent with common observations for alpha-beta Ti-alloys. According to the current understanding, such behavior can be attributed to the occurrence of heterogeneous plastic deformation in the form of intense slip bands interacting with microstructural constituents of the material [2-4]. This nucleation mechanism should result in intra-alpha-grain initiation. It is interesting to note that in our earlier tests conducted on the same material and microstructure at $R = 0.1$, an inelastic portion of the total strain range was smaller and the dominant crack nucleation event was interface-related separation.

The fatigue crack propagation rate in two different specimens is plotted in Figure A4 as a function of the crack size. Both parameters were evaluated from replicas and, therefore, reflect the crack propagation behavior on the specimen surface. An arrow indicates the size of the crack-initiating grain as determined by post-test fractography. It may appear that the two charts shown in Figure A4 represent different types of interaction between propagating small crack and the microstructure of the material. In the first case (Figure A4a) microstructure-sensitive crack propagation appears to be limited to the first grain, while in the second case (Figure A4b) microstructure-related variability of the crack propagation rate persists well beyond the size of the first, crack-initiating grain.
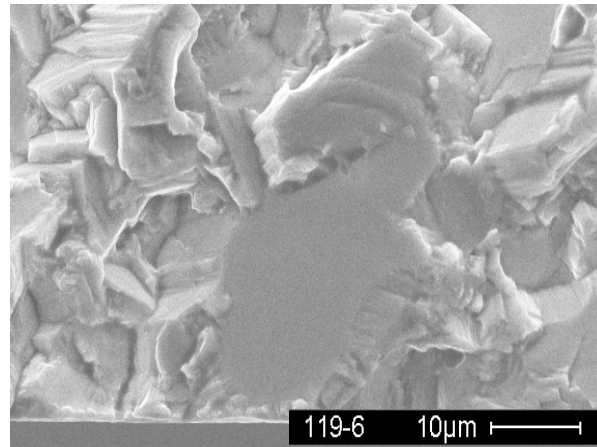
(a)
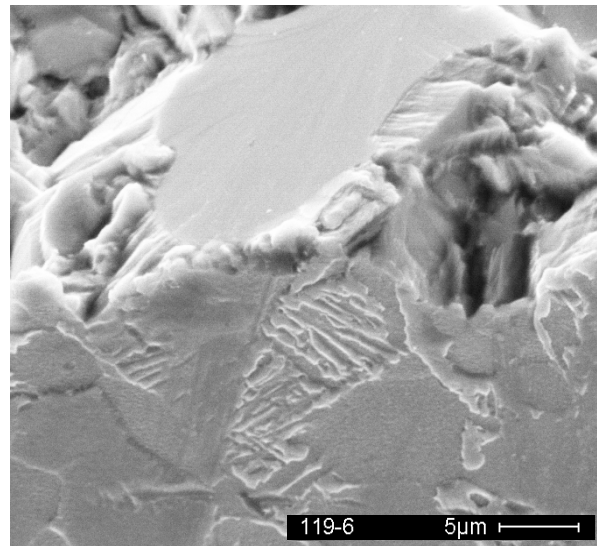
(b)
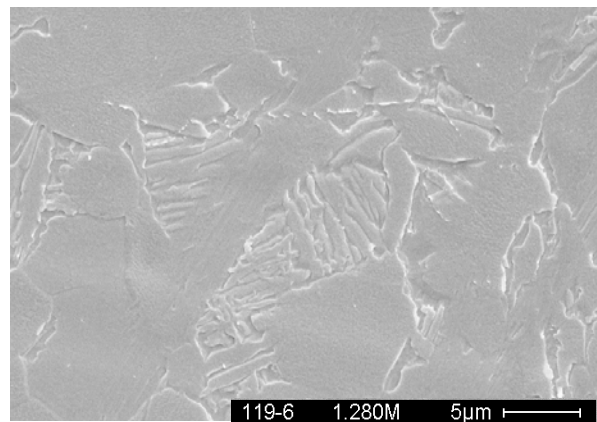
(c)

Figure A3. Fractograph of the crack initiation location (a); the same location tilted ~45°
(b) and crack profile on the specimen surface (c); shows similar crack
initiation mechanism (vs. Figure A1) from a large grain immediately adjacent
to the specimen surface.

119-18, Subsurface crack initiation
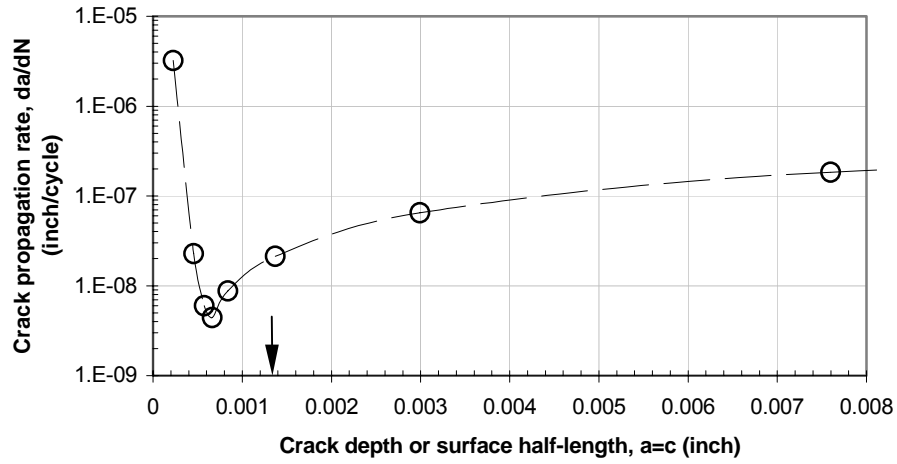
A4a)

119-6, Surface crack initiation
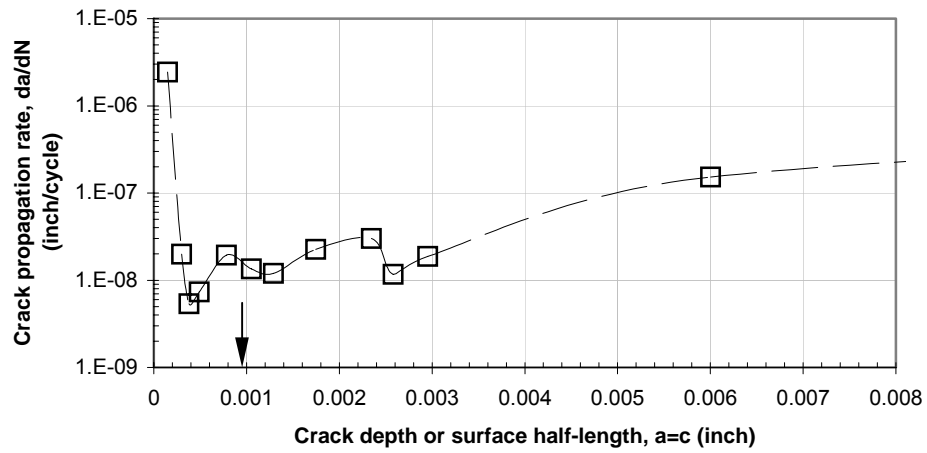
A4b)

Figure A4. Crack propagation rate as a function of crack size. Arrow
indicates the size of the crack-initiating grain.

Additional information about crack initiation mechanism turns out to be very helpful in explaining these observations. In fact, only the latter chart (Figure A4b) represents the true propagation behavior of a small crack. In the former case (see Figure A4a), due to sub-surface crack initiation, an initial (microstructure-sensitive) portion of the crack propagation process could not be monitored by the surface replication method employed in the present study. As a result, an initial crack size measured from the replica corresponds to a larger crack that has already propagated through several grains under the specimen surface, and therefore demonstrates very limited microstructural sensitivity.

The above analysis provides a better understanding of the small crack propagation behavior in Ti-alloys as well as points out some limitations of the surface replication method.

In Figure A5, the fatigue crack propagation rate plotted as a function of the crack size for R = 0.5 (points) is compared to the earlier data for R = 0.1 (lines). No significant difference can be seen between small crack propagation behavior at R = 0.1 and R = 0.5. Similarly, reasonable agreement exists between the raw small crack data for both R = 0.1 and R = 0.5 when plotted in a "da/dN – ΔK" format. At the same time, both sets of small crack data appear to be shifted to the left in respect to the available long crack data for the same material and microstructure.

A recent study [5] of long cracks performed on the same material in the same microstructural condition has shown a significant effect of positive R (0.1-0.95) on fatigue thresholds and near-threshold propagation behavior. In respect to the lower part of the stress ratio range studied (R ≤ 0.5), such observations are consistent with the traditional explanation [6] of stress ratio effects based on the crack closure concept. The same concept can be applied to the results of the present study in order to justify the opposite observation, namely – the absence of any significant effect of stress ratio on the crack propagation behavior.
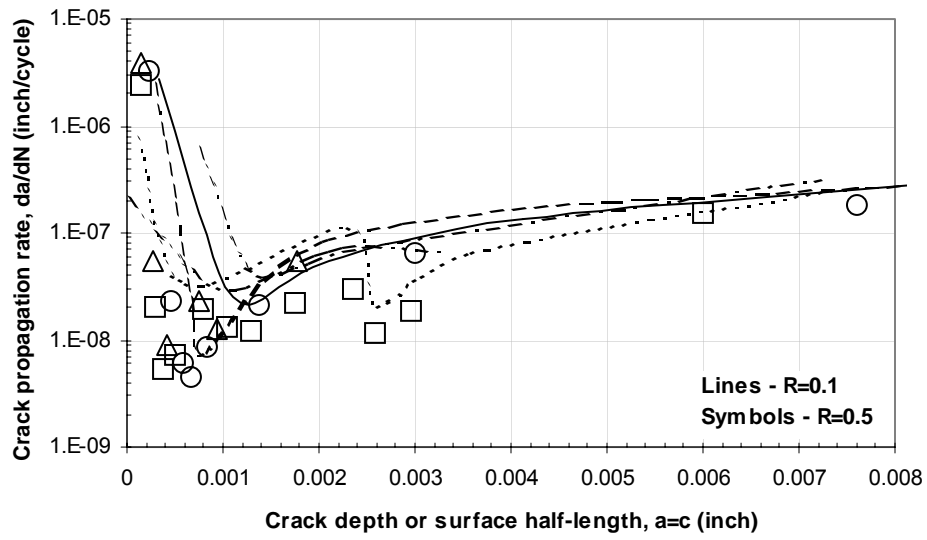
A5a)
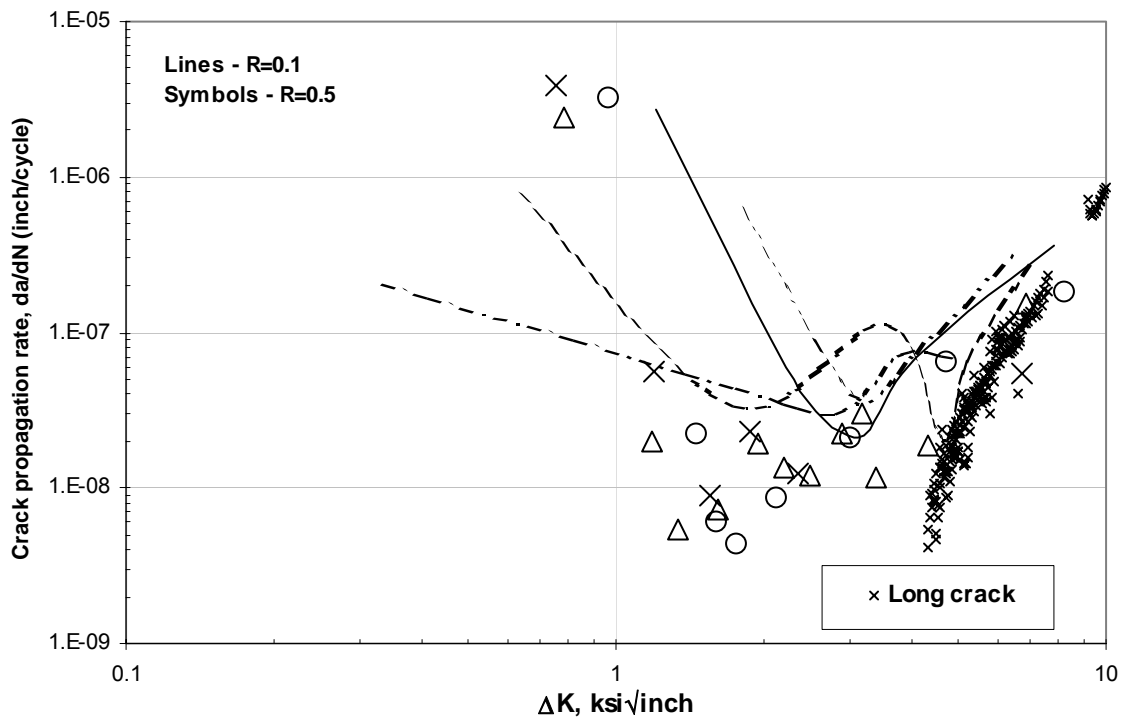
A5b)

Figure A5. Crack propagation rate as a function of crack size (A5a) and ΔK (A5b).

A-8

According to the common perception originally proposed in [10], in the case of a long crack, stress ratio R determines the amount of crack tip shielding (closure) accompanying the process of fatigue crack propagation. This, in turn, will affect the crack propagation rate and threshold, until the value of R becomes high enough to completely eliminate any crack closure. In the case of a small crack, crack closure is absent for all positive values of R. Therefore, the transition from R = 0.1 to R = 0.5 should not cause any change in the crack propagation rate as, indeed, was observed in the present study.

A.3   SUMMARY AND CONCLUSIONS

The results obtained can be summarized as follows:

1.) At R = 0.5, intra-granular crack initiation occurred from relatively large surface or sub-surface alpha grains. In contrast, at R = 0.1, the dominant crack nucleation event was interface-related separation.

2.) An apparent scatter in the microstructural sensitivity of the small crack propagation behavior can be associated with different (surface vs. sub-surface) initiation mechanisms.

3.) No significant difference can be seen between small crack propagation behavior at R = 0.1 and R = 0.5 while presenting replication test results in "da/dN – a'" or "da/dN – ΔK" form. At both stress ratios tested, small cracks are shown to propagate much faster than the long cracks under identical conditions.

4.) The results obtained further confirm the applicability of the K_{max} = constant test method as an effective alternative to the direct study of the naturally initiated small cracks.

A.4   REFERENCES

1.   D. Eylon (1998) Summary of the Available Information on the Processing of the Ti-6Al-4V HCF/LCF Program Plates" University of Dayton Report, Dayton, OH.

2.   J. K. Gregory (1994) in Handbook of Fatigue Crack Propagation in Metallic Structures (Edited by A. Carpinteri), Elsevier, Science, p. 281.

3.   J. A. Hall (1997) Fatigue Crack Initiation in Alpha-Beta Titanium alloys. Int. J. Fatigue. 19, No. 1, S23-S73.

4.   L. Wagner (1994) in Handbook of Fatigue Crack Propagation in Metallic Structures (Edited by A. Carpinteri), Elsevier, Science, p. 837.

5.   B. L. Boyce and R. O. Ritchie (2001) Effect of Load Ratio and Maximum Stress Intensity on the Fatigue Threshold in Ti-6Al-4V. Engng Fract. Mech., Vol. 68, p. 129.

6.   R. A. Schmidt and P. C. Paris (1973) Threshold for Fatigue Crack Propagation and the Effects of Load Ratio and Frequency. Progress in Flaw Growth and Fracture Toughness Testing, ASTM STP 536, ASTM, Philadelphia, p. 79.

APPENDIX B

CHARACTERIZING FATIGUE LIMITS FOR HAIGH DIAGRAMS

Using HCF S-N data collected as part of the Damage Tolerance program we exercise the Random Fatigue Limit model proposed by Pascual and Meeker. Preliminary results are very encouraging and include these observations: 1) the RFL model provides excellent descriptions of S-N behavior over the entire range of data and out-performs competing models in the long-life region; 2) curve-fits that exclude long-life tests ($N > 10^7$) significantly underestimate material capability, indicating that long life tests are necessary; and 3) if tests with lives at least 10^7 cycles are censored (stopped prior to failure) at 10^7 cycles, the fit changes remarkably little from the original fit, suggesting that these tests are important, but the added value of testing them longer than 10^7 cycles is minimal.

B.1   INTRODUCTION

The concept of the Haigh diagram will remain an important element of the design processes being developed to protect against high cycle fatigue (HCF) in turbine engines. In the past, the constant life, fatigue limit stresses of a Haigh diagram have been determined from fits to constant amplitude, stress-life, S-N, data. In [1], the fatigue limit is defined in terms of the median and p^{th} percentile of the limiting distribution of fatigue strengths as N increases without bound. Fatigue strength at N cycles is similarly defined in terms of the stress levels for which p percent of a population of specimens will survive for at least N cycles. These definitions do not provide for the characterization of the fatigue limit in terms of an observable stress property since the result of a fatigue test is the random number of cycles to failure for the fixed stress level that was used in the test. As a result, the distribution properties of fatigue strengths at a fixed, large N have been inferred from the distribution of cyclic lives from specimens that have failed or have reached some economically defined runout life.

There are at least three practical problems in this traditional approach to estimating fatigue limits:

1.) At the stress levels of interest, S-N curves are relatively flat. To get failures below the median fatigue limit requires tests that are potentially orders of magnitude longer than the desired cyclic life. The primary interest, of course, is in a stress level at which one percent or less of the structures would not survive, say, 10^7 cycles. While extrapolation of a median S-N curve to the long life of interest may be acceptable, estimation of the first percentile of the fatigue limit distribution most likely is not.

2.) The variability of fatigue lives increases greatly as test stresses decrease and a general model for this changing scatter has not been accepted. Thus, extrapolation of the percentiles of the fatigue strength to longer lives also requires linking the standard deviation of fatigue lives with stress levels.

3.) Current HCF problems indicate the necessity to define fatigue limits at lives longer than 10^7. The economic burden of testing runout lives to 10^8, or longer, only compounds the first two problems.

Because of the erratic nature of the scatter in lives at the stress levels of prime interest and the expense of testing for lengthening high cycle fatigue lives, alternative methods of estimating and validating fatigue limits are needed.

The step test is one method being investigated to determine the properties of the fatigue strength distribution [2]. In this approach, a specimen is tested at stress conditions slightly below the anticipated fatigue limit for the specified number of cycles. If it does not fail, the cycling is continued at a slightly increased stress. The process is continued until the specimen fails. The failure stress is estimated by interpolating on the number of cycles in the last increment as a ratio of the runout number of cycles. This procedure provides a sample of fatigue strengths which are assumed to represent the population that would be obtained if each specimen failed at the runout stress. There is a continuing discussion concerning the introduction of a step test interaction effect that potentially alters the S-N relationship. While "coaxing" that produces higher fatigue limit stresses, has been considered, the results are inconclusive.

An innovative approach to estimating the fatigue limit distribution has recently been proposed by Meeker and his student Pascual [3]. A random fatigue limit (RFL) model is postulated in which each specimen has its own fatigue limit in much the same way that each specimen has its own fatigue lifetime if tested at a sufficiently high stress. This random fatigue limit is explicitly included in the S-N model. Maximum likelihood methods are then used to estimate the parameters of the S-N equation as well as the parameters of the fatigue limit distribution. The percentiles of the fatigue limit distribution are easily calculated from the estimated parameters. The random fatigue limit model produces the proper shape of the median S-N function and the type of scatter typically seen in fatigue tests at HCF stress levels.

The threefold objective of this paper is to describe the random fatigue limit model, to demonstrate its application using the baseline Ti 6-4 test data from the PRDA V Materials Damage Tolerance HCF Program, and to suggests its further use in describing HCF S-N behavior.

B.2   THE RANDOM FATIGUE LIMIT (RFL) MODEL

Past attempts at modeling the stress-life (S-N) behavior of cyclic fatigue in the long life regime used an equation of the form:

$$\log N_i = \beta_0 + \beta_1 \log (S_i - \beta_2) + \varepsilon_t \qquad\qquad (B1)$$

where, for specimen i, N_i represents cycles to failure, S_i is the applied stress parameter, β_2 is a constant fatigue limit ($S_i > \beta_2$), and ε_i is a random variable representing the scatter in cycles to failure about the predicted life. [4] (Note: all logarithms in this paper are to base e.) Typically, the life random variable, ε, would be represented by a lognormal distribution with zero mean. For this assumption, ε_i is the difference between the log life of specimen i and the log median life at the test stress S_i. The parameters of the median life prediction, β_0, β_1, and β_2 are estimated from test data and β_2 is interpreted as the fatigue limit stress condition. Since β_2 is an asymptote, the S-N curve flattens as S approaches the fatigue limit. This model may be adequate for the median behavior in the long life regime but it is not consistent with the commonly observed increase in the standard deviation of lives as S approaches the constant fatigue limit. But its main

shortcoming is that it doesn't work. Since the single-valued, constant, fatigue limit, β_2, must be less than the lowest stress tested (so that the logarithm of $(S_i - \beta_2)$ is defined) it must be less than even the lowest runout stress tested. This causes the β_2 asymptote to be so low as to produce an unrealistic material model.

The random fatigue limit model [3] is a generalization of Equation (B1) in which the fatigue limit term is modeled as a random variable that can be considered to result from inherent, but unknown, quality characteristics of each specimen in the population. Thus, the fatigue limit is not a single constant, but rather an individual characteristic of each specimen. The RFL model for test specimen i is given by:

$$\log N_i = \beta_0 + \beta_1 \log (S_i - \gamma_i) + \varepsilon_t \qquad (B2)$$

where γ_i is the random fatigue limit for specimen i $(S_i > \gamma_i)$ and is expressed in units of the stress parameter. In this model, ε is the random life variable associated with scatter from specimens that have the same fatigue limit.

The RFL model produces probabilistic S-N curves that have the characteristics commonly seen in HCF data. This is illustrated in Figure B1 which presents the 1st, 25th, 50th, 75th and 99th percentile S-N curves as would be determined from the distribution of fatigue limits. The percentile S-N curves display the commonly observed shape in the HCF regime. Further, it is easily seen in Figure B1 that a difference in test lives from two specimens with slightly different fatigue limits could be quite large. The increased scatter in fatigue lives is explained by different specimens having different fatigue limits and this is true regardless of the scatter in life at higher stresses. Thus, the RFL model accommodates not only the flattening of the S-N curve but also the increased scatter that is typical of HCF lives. To date, little experience has been gained with this model but, intuitively, the fatigue limit scatter would be expected to dominate in the HCF regime when S is close to γ_i while the scatter in life, ε, could be significant when S is large compared to γ_i.
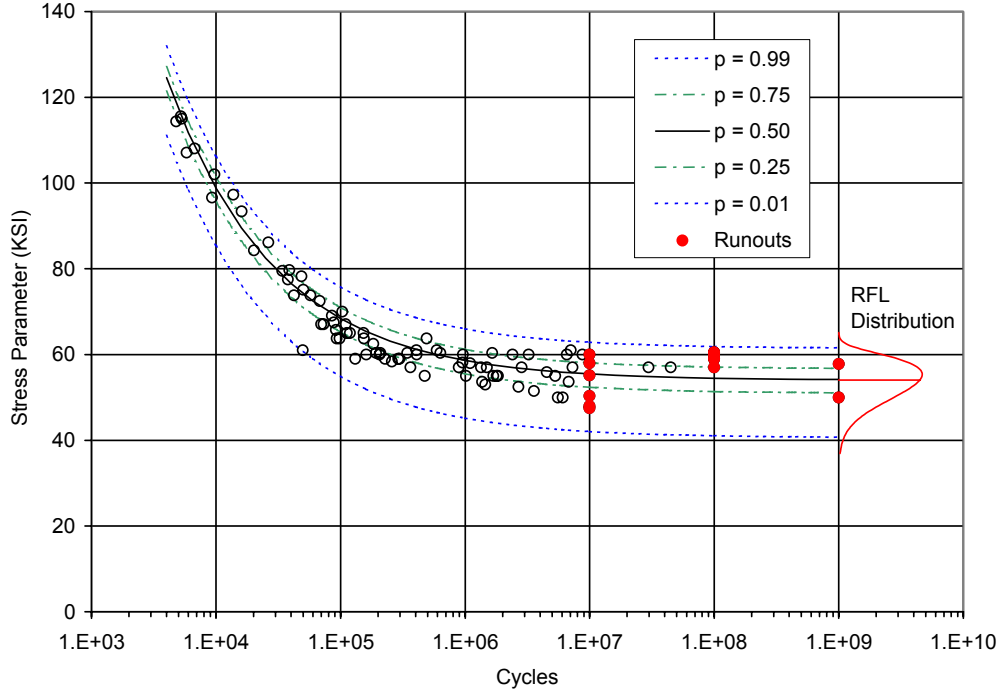
Figure B1. Example S-N curves calculated from percentiles of the Random Fatigue Limit distribution (Scenario 1).

There are two random variables in the RFL model for which probability distributions are needed. In theory, any family of distributions could be used to model either of the distributions and Pascual and Meeker considered several. In this paper, the conditional distribution of cycles to failure given γ will be assumed to have a lognormal distribution with mean equal to $\beta_0 + \beta_1 \log (S - \gamma)$ and standard deviation equal to σ_ε. Then ε is lognormal $(0,\sigma_\varepsilon)$. This assumption is consistent with common practice in the analysis of S-N data.

The random fatigue limit, γ, will be assumed to have a smallest extreme value (SEV) distribution. The SEV distribution has two parameters – location, μ_γ, and scale, σ_γ. The equations for the cumulative distribution and probability density function of the SEV distribution are:

$$F(z) = 1-\exp [-\exp(z)] \tag{B3}$$

$$f(z) = (1/\sigma_\gamma) \exp [z - \exp(z)] \qquad\qquad\qquad (B4)$$

where $z = (\gamma - \mu_\gamma) / \sigma_\gamma$. The pth percentile of the fatigue limit distribution, γ_p, is calculated quite simply from Equation (B3) as

$$\gamma_p = \mu_\gamma + \sigma_\gamma \bullet \ln(-\ln(1\text{-}p)) \qquad\qquad\qquad (B5)$$

Figure B2 shows example SEV probability density functions for fatigue limit distributions. The distribution labeled Scenario 1 was used to generate Figure B1. The SEV distribution was selected as a model for fatigue limits because it has a basis in extreme value theory and it is skewed to the left, i.e., to values smaller than the median. Additionally it is analytically convenient, although convenience was not a selection criterion.
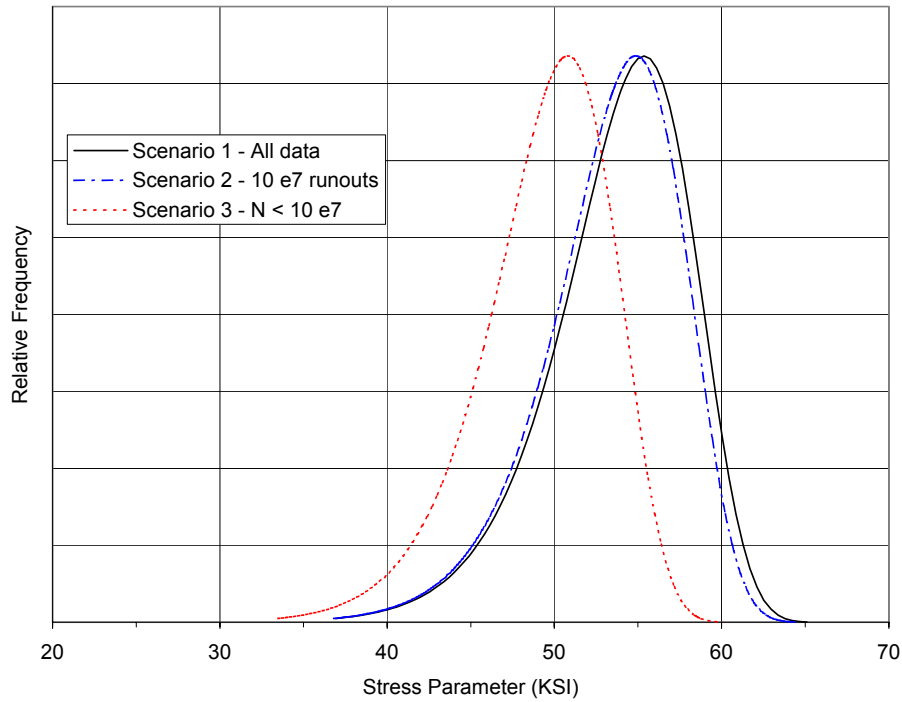
Figure B2. Smallest Extreme Value (SEV) probability density functions.

Intuitively, quality differences can result in distinct fatigue resistance in the long life regime. Quality is more limited on the good side than on the bad side. It is reasonable that upper limit resistance will have a sharper upper bound while the degrees of weakness in the lower tail of the distribution will be more scattered. Thus, the fatigue limit distribution should be skewed to lower values. It might be noted that if the random variable Y has a Weibull distribution then log Y will have an SEV distribution – the SEV is to the Weibull as the lognormal is to the normal.

Given a set of S-N data including runouts, the five parameters of the RFL model can be estimated using maximum likelihood methods. Pascual and Meeker discuss these methods in detail [3]. Maximum likelihood estimates have known, desirable statistical properties and confidence bounds can be calculated when wanted. See, for example [5]. Computer software that works with the S-PLUS statistical analysis program can be obtained from Dr. Meeker (wqmeeker@iastate.edu or http://www.public.iastate.edu/~wqmeeker/other_pages/wqm_software.html).

B.3   EXAMPLE APPLICATION

There are two objectives in presenting the example application of this paper. The prime objective is to demonstrate that the model can produce a valid description of S-N data in the HCF regime. The secondary objective is to demonstrate one use for the model by investigating the necessity of having long runout lives in the analysis.

The smooth bar, baseline S-N data from the PRDA V Materials Damage Tolerance HCF program are used for this example application [6]. The fatigue test data used in the analysis were collected at lab temperature on the same lot of Ti 6-4 material by four organizations at three stress ratios (R = -1, 0.1, and 0.5) and three cyclic frequencies (60, 400, and 1000Hz). For the purposes of this example, the Smith-Watson-Topper (SWT) stress parameter was used to adjust for stress ratio effects [7]. Any potential differences due to the other test factors were investigated and found to be of secondary importance for our purposes. A total of 95 S-N test results were available for estimating the parameters of the RFL model with 15 of these being runouts at 10^7, 10^8, or

10^9 cycles and two that failed between 10^7 and 10^8 cycles; the others had shorter lives. The S-N data used in the analysis are shown in Figure B1.

(It is noted that three of the 1000 Hz S-N specimen lives collected during the PRDA V program were not included in this example application. There is some concern over the actual conditions governing these tests, those reported resulting in significantly reduced fatigue strengths than the other test results. The cause of the differences is being investigated. Since the prime objective of this paper is to illustrate the RFL model, exclusion of these data was deemed warranted.)

Three scenarios were analyzed to investigate the effect of approaches to setting runout test lives. In Scenario 1, all 95 test results were used as originally recorded and provides the best available estimates of the parameters of the model. This scenario included the 15 specimens with runouts at 10^7 or greater and the two failures with lifetimes greater than 10^7. Scenario 1 is the baseline scenario for demonstrating the general application of the RFL model, and is illustrated in Figure B1. In Scenario 2, all lives and runouts greater than 10^7 were treated as though they were runouts (censored) at $N = 10^7$. Scenario 2 addresses the need to test to the extremely long (10^8 and 10^9) runout times. In Scenario 3, only the 78 test failures with lives less than 10^7 (i.e., no runouts) were used in the analysis to address the question of estimating the fatigue limit parameters using only data from higher stress levels. The estimates of the RFL model parameters and three example percentiles of the fatigue limit distribution are presented in Table B1.

Table B1. Estimated RFL Model Parameters and Percentiles under Three Scenarios

RFL Parameter	Scenario 1 - All Data	Scenario 2 – Runouts at 10^7	Scenario 3 – $N < 10^7$
β_0	16.90	17.17	18.55
β_1	-2.022	-2.089	-2.394
σ_ε	0.00246	0.00375	0.00238
μ_γ	4.014	4.005	3.928
σ_γ	0.06757	0.06652	0.06951
$\gamma_{0.01}$	40.6	40.4	36.9
$\gamma_{0.50}$	54.0	53.6	49.5
$\gamma_{0.99}$	61.4	60.7	56.5

The fit of the RFL model for Scenario 1, shown in Figure B1, produces a median curve that is slightly high (2.4 percent). Since maximum likelihood estimates are not necessarily unbiased, there may be a bias in the estimate of the median fatigue limit. In many applications it is possible to develop factors to remove bias. Further development of the model will be required to resolve this issue.

The estimate of the standard deviation of ε, the life random variable in the model, was extremely small ($\sigma_\varepsilon = 0.0025$) and had a negligible effect on the estimates of the percentile curves in the range of the data. Scatter from this factor is introduced as the multiplicative factor, $\exp(z_p \bullet \sigma_\varepsilon)$, where z_p is the pth percentile from the standard normal distribution For example, if $p = 0.01$, $z_p = -2.326$, then $\exp(z_p \bullet \sigma_\varepsilon) = 0.994$ for Scenario 1, a negligible change. A small sensitivity study was performed to investigate the effect of the standard deviation of life, σ_ε, on the 1st and 99th percentile S-N curves. σ_ε was set equal to 0, 0.0025, 0.025, and 0.25. Both γ and ε were set to their respective 0.01 and 0.99 percentiles which will produce S-N plots which are outer bounds for the true p S-N curves. The results of the sensitivity to σ_ε calculations are presented in Figure B3.
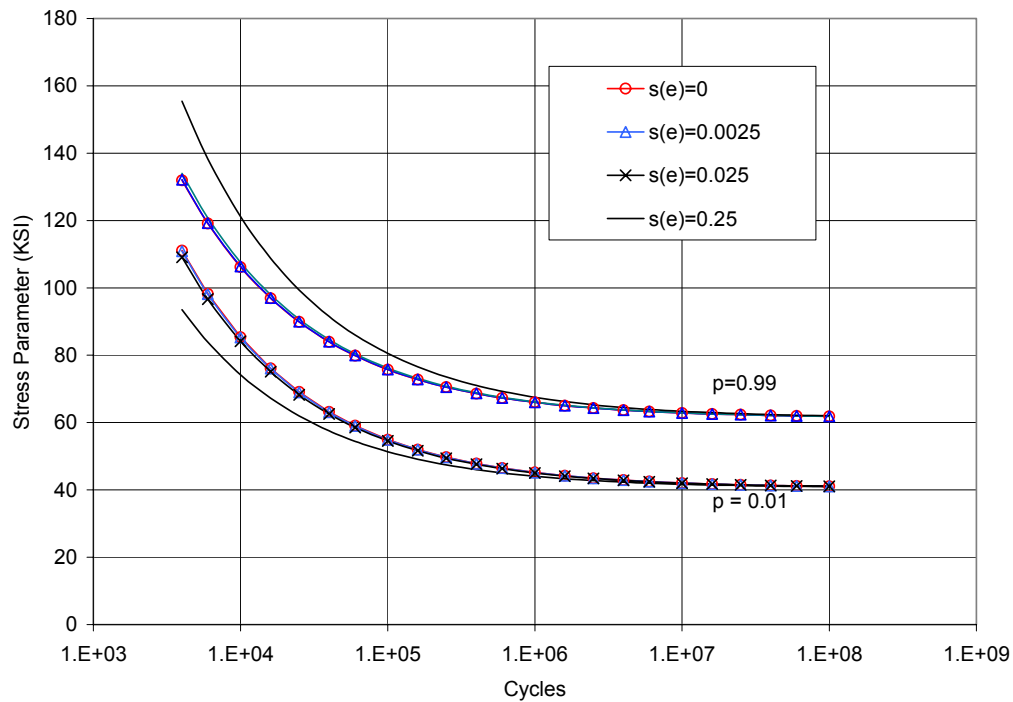
Figure B3.   Sensitivity of Life Variability (SEV) parameter on p S-N Curves, PRDA V, Ti 6-4 smooth bar baseline data.

For the data of this example, for $\sigma_e \leq 0.025$, there is no practical difference in the S-N curves for $p = 0.01$ and 0.99 for lives greater than 10^5 and very little difference over the entire range of the data. Even for a σ_ε value that is two orders of magnitude greater than the estimate, there is little or no difference in the curves when $N > 5 \times 10^6$. This suggests that the observed scatter in HCF lifetime can be almost entirely explained by each specimen's individual fatigue limit for this collection of data.

For these data it is not necessary to include the parameter in the RFL model that adjusts for variability in life at a fixed fatigue limit. As previously noted, there is little experience with the RFL model and it is not known whether or not the extremely small estimate of σ_ε will be typical of S-N data in general. If σ_ε proves to be negligible, the model and analysis can easily be simplified by eliminating this random factor. Negligible σ_ε would indicate that the quality characteristics that determine a specimen's fatigue limit also account for scatter in life that is seen in the LCF regime.

Scenarios 2 and 3 are based on not using the full amount of information that is in the baseline data set. The probability density functions of the three estimates of the fatigue limit distribution are presented in Figure B2. Table B1 lists the estimates of selected percentiles of the fatigue limit distribution that were obtained from the three scenarios. When the tests longer than 10^7 cycles are analyzed as though they were runouts at 10^7 cycles, Scenario 2, the parameter estimates are neither statistically nor practically significantly different from those of the baseline. In this data set, running the tests beyond 10^7 provided little additional information to the characterization of the fatigue limit distribution. In the data of this analysis, very little information was obtained from testing to the longer runout cycles.

Scenario 3 is based on the test results from only those specimens with lives less than 10^7 cycles. The Scenario 3 parameter estimates are statistically and practically different from those of the baseline scenario. Figure B4 presents Scenario 3 and a visual comparison for Scenarios 1 and 3 (Figures B1 and B4) suggests that excluding long-term tests (as might be desired to reduce testing costs) results in considerable underestimation of material capability. The location parameter, μ_γ, is significantly less than the baseline

μ_γ which resulted in an overly conservative estimate of the 0.01 percentile of the fatigue limit distribution. The 1st, 50th, and 99th percentiles from the shorter test result are approximately 9 percent less than those of the baseline scenario. Since if all 17 tests with lives at least 10^7 cycles were censored (stopped prior to failure) at 10^7 cycles, the fit changes remarkably little from the original fit, this suggests that these tests are important, but the added value of testing them longer than 10^7 cycles is minimal.
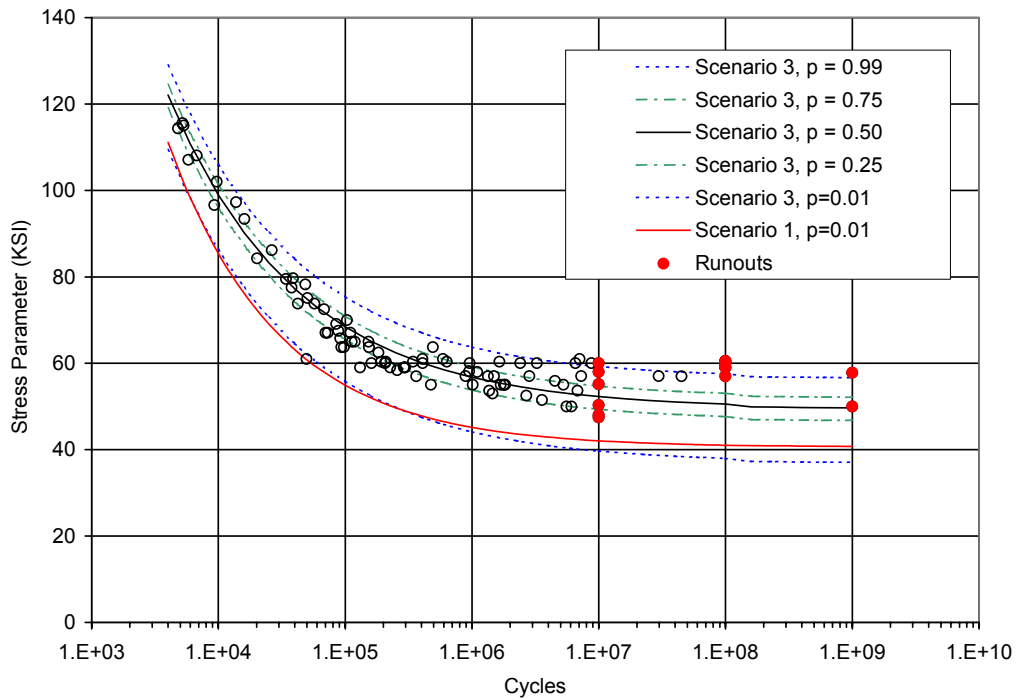
Figure B4. PRDA V smooth bar S-N data and scenario 3 RFL model fit.

B.4   SUMMARY AND CONCLUSIONS

Existing methods for determining the fatigue limits that characterize safe operating stress levels for HCF have traditionally been based on the distribution of cyclic fatigue lives at fixed stress levels. This approach has well recognized problems in obtaining and analyzing data for stress levels below the estimated median fatigue limit. The random fatigue limit model proposed by Pascual and Meeker predicts both the S-N curve shape and scatter in fatigue lives that is observed in the HCF regime. The RFL model is based on the concept that each specimen has an inherent fatigue limit that will

determine its HCF life behavior. Since the fatigue limits are unknown for a population of structural details, they are accounted for by the inclusion of a fatigue limit random term in the S-N model. Modern computerized statistical analysis methods facilitate the estimation of the parameters of the model with confidence bounds on lower percentiles of the fatigue limit distribution, if desired.

The model was demonstrated by fitting it to the Ti 6-4 smooth bar S-N data of the PRDA V HCF Program. An acceptable fit was obtained as the scatter observed in the data was well described by the estimated fatigue limit distribution. Three additional conclusions were drawn from the analyses of this example:

a) The scatter in life of the smooth bar specimens was adequately described by the distribution of the fatigue limit parameter. The inherent quality properties that affect the long life behavior may also dominate cyclic life at higher stresses.

b) The added information from testing to lives greater than a runout life of 10^7 did not significantly change the fatigue limit distribution.

c) Using only lives less than 10^7 in the analysis produced a significantly lower and unreasonable fatigue limit distribution.

The RFL model is not just another curve-fit. The formulation is based on physics, not just arithmetic. Explicitly modeling the random fatigue limit term may provide new insight into the interplay of parameters that primarily influence both LCF ($N<10^7$ cycles) and HCF ($N>>10^7$ cycles).

B.5   ACKNOWLEDGEMENT

B.6 REFERENCES

1. "Standard Definitions of Terms Relating to Fatigue," E 1823, Annual Book of ASTM Standards, Vol. 03.01, American Society for Testing and Materials, Philadelphia, PA, 1999.

2. Maxwell, D.C. and Nicholas, T., "A Rapid Method for Generation of a Haigh Diagram for High Cycle Fatigue," Fatigue and Fracture Mechanics: 29th Volume, ASTM STP 1332, T.L. Panontin and S.D. Sheppard, Eds., American Society for Testing and Materials, 1998.

3. Pascual and Meeker (1999), "Estimating Fatigue Curves with the Random Fatigue-Limit Model," TECHNOMETRICS, Vol. 41, No. 4, with comments, pp.277-302, November 1999.

4. MIL-HDBK-5G, Metallic Materials and Elements for Aerospace Vehicle Structures, Volume 2, 1 November 1994, pp. 9-100.

5. Meeker, W.Q. and Escobar, L.A., Statistical Methods for Reliability Data, John Wiley & Sons, New York, 1998.

6. Gallagher, J.P., et al., "Improved High Cycle Fatigue (HCF) Life Prediction," UDR-TR-1999-00079, University of Dayton, Dayton, Ohio, October, 1999.

7. Smith, K.N., Watson, P., and Topper, T.H., "A Stress-Strain Function for the Fatigue of Metals," *Journal of Materials*, JMLSA, Vol. 5, No. 4, Dec. 1970, pp. 767-778.

APPENDIX C
BIAXIAL FATIGUE OF TI-6-4 AND TI-17-β AT 70 AND 500 $^{\text{o}}$F

C.1   EXPERIMENTAL PROCEDURE

The materials investigated were a Ti-6-4 forged alloy on the PRDA V pedigree and a Ti-17 β anneal. Only some of the Ti-6-4 specimens were tested at 500$^{\text{o}}$F. The forged plates were approximately 20 mm thick. These materials are utilized extensively in the front fan of gas turbine engines. Even though a forged plate is utilized, they are heat treated to resemble airfoil microstructures [1]. Solid biaxial specimens were fabricated with approximate dimensions shown in Figure C1. Grip section diameters were dictated by the thickness of the forging. Hence, the gage section diameter of 12.5 mm was the maximum possible. The choice of a solid bar does make analysis of plastic deformation more difficult, but a tubular specimen would necessitate a wall thickness of less than 1 mm for the thin walled tube approximation to be appropriate. This might have introduced torsional buckling as well as a non-representative cross section from a microstructural perspective. Grain size for the Ti-6-4 material is inferred from the PRDA V pedigree designation, as is specimen stress relief, and subsequently chem-milling. This was done in part to facilitate comparison to existing uniaxial data.

All testing was conducted on a closed loop servo-hydraulic tension-torsion load frame, with an axial load capacity of 445 kN and a torsional load capacity of 5000 N-m. Since anticipated maximum loads were approximately 10% of full scale, load cells were calibrated within this range, and were linear to within 0.05% of the anticipated test range. A hydraulic collet system was utilized to grip the specimens. Solid aluminum bars of the same grip diameter and length were strain gauged in accordance with ASTM E1012-93 to assure alignment of the test frame and grips. Room temperature strains were measured with a modified MTS model 632.85-xx biaxial extensometer with conical points. The modification involved strain gauging existing flexure elements to measure torsional strains. The extensometer's gage length was 25 mm and an axial full scale calibration of 2.5%. Nonlinearly of this measurement was less than 0.2% of full scale. Torsional full-scale rotations of 5 degrees or a shear strain of approximately 4.3%, were linear to within 0.3% of full scale. Maximum cross talk between the axis was 0.5% of either full scale. This

extensometer provides averaging of two locations for both axial and torsional measurements. Elevated temperature strain measurements were obtained utilizing a quartz rod MTS model 632.68C-04 extensometer with full scales of 2.5% axial and 5 degrees rotation.
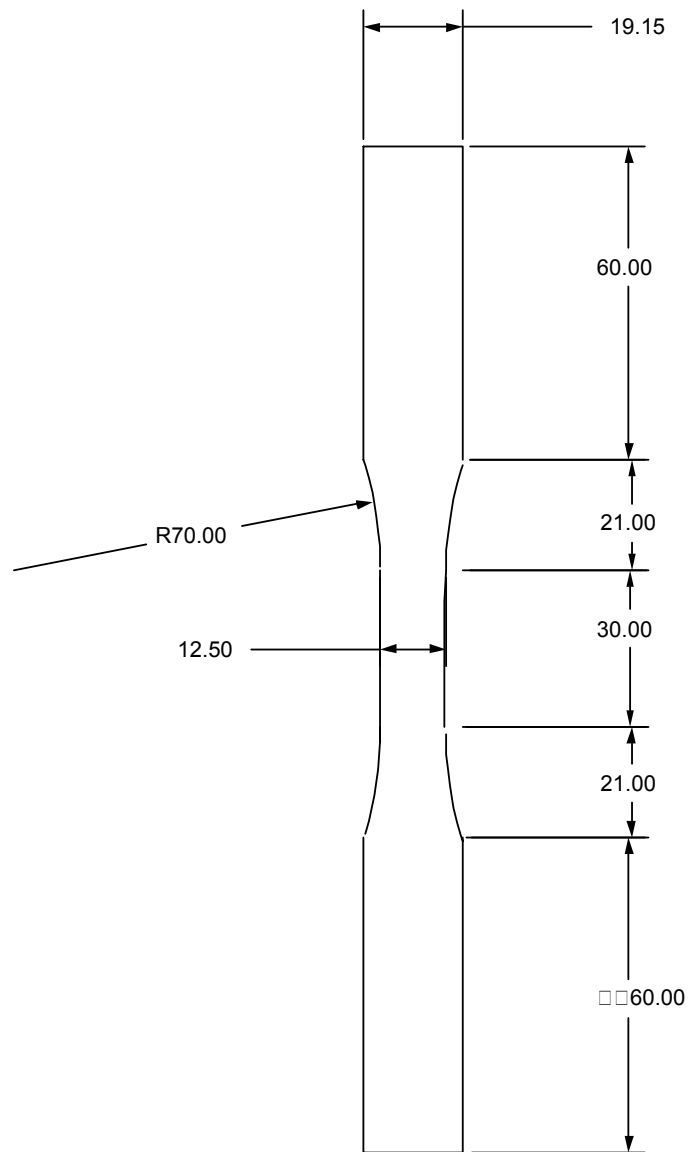
Biaxial Test Specimen
Units in mm

Figure C1. Baseline multiaxial specimen

Cross talk, gage length, and nonlinearty were almost identical to the room temperature extensometer. Small dimples had to be made on the specimen surface to attach

the extensometer. Since fatigue cracks did not originate from these dimples in most cases, their effect on fatigue life is ignored. On specimens where the cracks did originate at the dimple, other similar sized cracks were observed that had other origins. Data acquisition and test path generation was handled by a 32-bit data acquisition/control system.

Specimen dimensions limited the maximum frequency of testing to approximately 1 Hz. The 12.5 mm diameter severely reduces the torsional stiffness of the specimen, which limited frequency of testing. Before conducting any test at the reported levels, 20 cycles of ± 8 kN axial and then ± 40 N-m torsional load were performed. This data was utilized to check both the axial and shear moduli of the specimen and insure the integrity of the extensometer before switching to strain control. These are the values reported in the tables for initial moduli. All tests were conducted in strain control for the entire fatigue life. Not much frequency increase could have been obtained by switching to load or stress control. Some of the non-fully reversed tests displayed ratcheting.

For the elevated temperature tests, one specimen was instrumented with multiple welded thermocouples (Table C1) to verify a quasi-uniform temperature distribution in the gage section of the specimen. Originally, it had been suggested to control temperature via a thermocouple welded to the shank of the specimen.

Table C1. Thermocouple Locations
Case 1: 4-1-4 coil design, 1/8" tubing. Control temp = 152°C 300° F (300° F)

TC-#, Data column	Location (± from midsection)
1	B(-18 mm)
2	T (+12.5 mm)
3	T (+6.25 mm)
4	Midsection (0.0 mm)
5	B (-6.25 mm)
6	B (-12.5 mm)
7	Top Shank (+5 mm)
8	Ambient air

However, temperature gradients from shoulder curvature region to shank were noticeable. Due to different shoulder configurations (i.e. machining from Metcut), this region is not highly amenable to calibration for remote temperature control. Also, slight

shifts (±2 mm) in coil position cause ±5°C differences in shoulder/curvature region
temperatures, and ambient temperature also impacted shoulder/shank temperature stability.
Specimen gage section temperatures were marginally affected (>±1° C) by similar coil
movements. The ensuing graph (Figure C2) shows that in the gage section there is for the
most part a steady temperature (within ±2.5^o C of control temperature). This experiment in
essence verifies the coil design. To avoid fatigue failures emanating from the thermocouple
welds, only one thermocouple was attached to test specimens with fiberglass insulation
tubing at the midsection of the gage length. Similar data was obtained at 75, 205 and 260° C
(150, 400, and 500 ^{o}F).
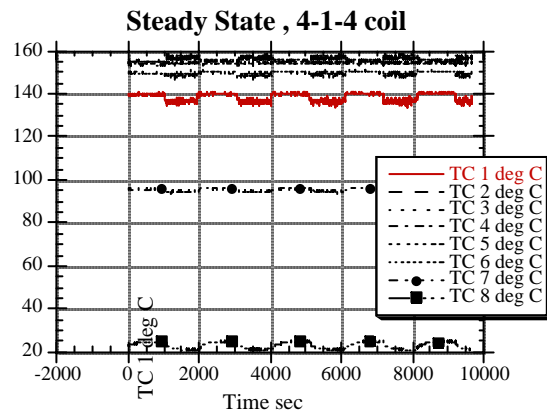
Figure C2. Coil verification test.

C.2   EXPERIMENTAL DATA

Data obtained from this smooth specimen test program is summarized in Tables C2
and C3. Tests are grouped with regard to type of test, not the order in which they were
conducted. As previously noted, specimens were cycled at low load or torque levels prior to
fatigue testing to determine the cyclic modulus. These results are summarized in Table C3,
and presented in a format indicative of a normal distribution in Figures C4 and C5.
Specimen 156-11 was a fully reversed axial test. It was initially the quality control specimen
returned to GEAE after the specimens were machined for phase 1. Before testing it was
instrumented with a 3 element rosette strain gage to determine Poisson's ratio, and verify
extensometer measurements of E and G (Note: these values are not reported). Minimal
insight was also gleaned into specimen size compared to previous smaller uniaxial

specimens. The next group of tests in the phase 1 tables are torsion only experiments. The goal of these experiments was to ascertain if mean shear stresses influence fatigue lives. Quite a bit of mean shear stress relaxation was observed for those tests that were not fully reversed. These tests are also vital to obtain baseline constants for some critical plane multiaxial theories. Next, three proportional combined axial-torsional tests are reported. This is probably the simplest combined loading. Phase 2 proportional testing was intended to fill some gaps in the data that remained after phase 1. Several of the damage parameters did a poor job predicting torsion only data, and it was deemed essential to duplicate some of the experimental results.

It was deemed important to consider non-proportional loading in the testing and life analysis programs. In phase 1, one 90-degree out-of-phase test (Figure C3a) was conducted. Many researchers regard this path as being critical with regard to out-of-phase deformation and fatigue damage.

| a) 90° out-of-phase | b) Triangle path | c) Box path | d) Check path |
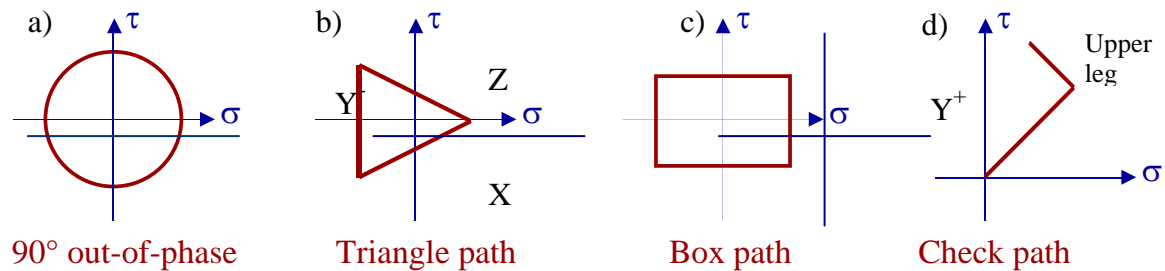
Figure C3. Non-proportional loading paths: a) 90 degree out-of-phase (Phase 1), b) Triangle Path and individual segments X,Y and Z (Phase 1), c) Box path (Phase 2) and d) "Check Mark" path (Phase 2).

The triangle path (Figure C3b) is another out-of-phase approximation of service conditions. The final six non-proportional tests conducted in phase 1 all consist of segments of the triangle path. Since the extrapolation of each path does not pass through the origin of strain space, they are also considered to be out-of-phase. The Y+ or Y- connotation for the cyclic torsion with static axial strain indicates whether the static axial strain is positive or negative. A Y+ segment is not shown in Figure 3Cb, but would be on the other side of the origin in comparison to the Y- segment. Both Y+ and Y- tests were proportionally loaded to the maximum positive shear strain when starting a test. The segments of the triangle path were also conducted so that cumulative damage of the triangle path could be performed

based on the segments. The sequence of loading for the triangle path was on startup to the positive axial stress (zero shear strain), then the X leg, Y- leg and the Z leg were repeated for the duration of the test. Two additional non-proportional paths and subsequent mission histories were introduced in Phase 2. The box path (Figure 3Cc) is a simplification of the edge of contact state of stress, and the 'check mark' path (Figure 3Cd) is derived from blade loading histories. Both are deemed relevant for the application and material under consideration. Simplified mission histories utilize these two non-proportional paths as a basis with either 5 or 50 subcycles. For the box mission history subcycles were located on the Y+ leg of the box, and for the check path the subcycles were located on the upper leg. The subcycles for either mission history did not have the range of ether the Y+ or upper leg shown, but a portion thereof. Both subcycles were skewed toward positive shear stress. The tests were conducted in strain control, even though stress is shown on the ordinates of Figure C3. Minimal plastic deformation for these paths at the levels chosen makes the difference between stress and strain control minimal (see Figures C11-C14).

Table C3 summarizes the experimental deformation results. These materials have monotonic yield strengths in excess of 1000 MPa, resulting in the expectation that many of the tests would incur only elastic cyclic loads. Calculating a plastic strain is straight forward for axial loading of a solid bar, but is somewhat more challenging for torsional loading of the solid bar specimen. The quantities in the τ_{max} and τ_{min} columns in Table C3 are the results of an elastic calculation based on the torque and original specimen dimensions.

Table C2. Life Results for Ti-6-4 and Ti-17- β

Ti-6-4, Phase 1 (old data)

Test #	Spec ID	Freq (Hz)	Temp (F)	Spec Dia (in)	Nf or long crack(cycles)	Comments
1	156-11	0.5	70	0.492	6200	
2	21-11	0.5	70	0.492	72141	
3	21-6	1	70	0.491	241250	
4	156-10	0.5	70	0.492	961806	
5	21-7	0.5	70	0.492	24895	
6	156-5	0.5	70	0.491	150293	
7	156-4	0.5	70	0.491	151598	
8	156-1	0.5	70	0.492	814753	
9	21-4	0.5	70	0.492	141229	outside gage section
10	21-8	0.5	70	0.492	72124	
12	21-3	0.5	70	0.491	73728	
13	21-10	0.5	70	0.492	329058	
14	156-7	0.5	70	0.492	>24576	overload during storm
15	21-1	0.5	70	0.491	67965	
16	156-9	0.5	70	0.492	60514	
17	156-3	0.5	70	0.491	87920	
18	156-8	0.5	70	0.492	111783	90-OP
19	156-2	0.33	70	0.491	38355	triangle
20	21-2	0.33	70	0.492	43009	triangle
21	156-6	0.5	70	0.492	>19864	top-triangle-overload during storm
22	21-9	0.5	70	0.491	71358	top-triangle
23	21-5	0.5	70	0.492	79367	Bottom-triangle

Ti-6-4, Phase 2 (new data)

Test #	Spec ID	Freq (Hz)	Temp (F)	Spec Dia (in)		Nf or long crack(cycles)	Comments
1	142-6	0.75	70	0.491		>2.0 E6	runout
2	142-5	0.75	70	0.492		260657	
3	142-9	0.5	70	0.491		184669	
7	178-3	0.75	70	0.492		843404	
19	178-10	0.5	500	0.492		648181	proport 500 F
20	142-10	0.5	500	0.492		75107	proport 500 F
4	142-8	0.25	70	0.492		59432	R=-1 Box contact simulation
5	142-11	0.33	70	0.492		182149	Reps=-3, Rgam=-1 box
6	178-7	0.25	70	0.492		72360	R=-1 Box contact simulation
8	178-8	0.25	70	0.491		212337	Reps=-3, Rgam=-1 box
9	178-12	0.25	70	0.492		50,568	check mark,R=0
12	178-1	0.25	70	0.491		36920	check mark,R=0
14	178-11	0.25	70	0.492		109848	check mark,R=0
15	178-5	0.25	70	0.492		99418	check mark,R=0
21	142-4	0.25	500	0.492		13859	box, R=-1 500F
22	178-2	0.25	500	0.492		30720	box, R=-1 500F
						Blocks to fail	
10	142-7	0.25	70	0.491		19470	miss 2b, r=-1 box w/50 subcycles
11	178-4	0.25	70	0.491		44544	miss 7, chck w/ 50 sub up
13	178-6	0.25	70	0.492		21422	miss 2b, r=-1 box w/50 subcycles
16	142-3	0.25	70	0.491		49776	miss 7, chck w/ 50 sub up
17	142-1	0.25	70	0.492		48787	miss 2b, r=-1 box w/5 subcycles
18	178-9	0.25	70	0.492		39,480	miss 2b, r=-1 box w/5 subcycles

Table C2. Life Results for Ti-6-4 and Ti-17- β (Continued)

Ti-17-β, Phase 2 (new data)

Test #	Spec ID	Freq (Hz)	Temp (F)	Spec Dia (in)	Nf or long crack(cycles)	Comments
1	4B29K	0.5	70	0.492	46132	
2	4B25K	0.75	70	0.492	80268	
3	5B12K	0.5	70	0.491	36004	
4	5B36K	0.5	70	0.492	53182	
5	5B16k	0.5	70	0.492	47212	
6	5B4K	0.5	70	0.491	386505	outside gage section failure
9	5B13K	0.5	70	0.491	49491	
10	5B24K	0.5	70	0.492	122988	
11	5B28K	0.5	70	0.492	95845	outside gage section failure
7	5B8K	0.5	70	0.491	152285	Check mark
8	5B20K	0.5	70	0.492	159844	check mark

Table C3. UDRI-Ti-6-4 and Ti-17-β Biaxial Deformation-Life Data

Ti-6-4, Phase 1 (old data)

Test #	Spec ID	Freq (Hz)	Temp (F)	Spec Dia (in)	E (ksi)	G (ksi)	εmin (%)	εmax (%)	σmin (ksi)	σmax (ksi)	γ min (%)	γ max (%)	τmin (ksi)	τmax (ksi)	Cycle Count	E (ksi)	G (ksi)	εmin (%)	εmax (%)	σmin (ksi)	σmax (ksi)	γ min (%)	γ max (%)	τmin (ksi)	τmax (ksi)
							first cycle properties if significasntly different than half-life											half life properties at 70F							
1	156-11	0.5	70	0.492	16881	6338												-0.751	0.756	122.3	119.07	0	0	0	0
2	21-11	0.5	70	0.492	17287	6323												0	0	0	0	-0.868	0.866	-55.4	55.98
3	21-6	1	70	0.491	17157	6294												0	0	0	0	-0.61	0.614	-38.43	38.58
4	156-10	0.5	70	0.492	17447	6352												0	0	0	0	-0.563	0.559	-35.82	36.11
5	21-7	0.5	70	0.492	17041	6367					0.166	1.81	-13.78	87.02				0	0	0	0	0.166	1.81	-26.54	72.37
6	156-5	0.5	70	0.491	17056	6396					0.09	1.21	3.92	75.7				0	0	0	0	0.09	1.21	1.16	71.64
7	156-4	0.5	70	0.491	17462	6367					0.15	1.36	1.09	77.44				0	0	0	0	0.15	1.36	-8.7	66.42
8	156-1	0.5	70	0.492	16896	6323												0	0	0	0	0.086	0.958	5.9	61.49
9	21-4	0.5	70	0.492	17447	6323					0.815	1.96	17.4	89.49				0	0	0	0	0.815	1.96	2.75	73.53
10	21-8	0.5	70	0.492	17433	6338												0.089	0.091	14.94	15.81	-0.665	0.666	-41.77	41.91
12	21-3	0.5	70	0.491	17476	6335												0.089	0.090	14.65	15.37	-0.666	0.666	-42.2	42.49
13	21-10	0.5	70	0.492	17448													-0.091	-0.089	-16.82	-15.8	-0.664	0.665	-43.51	40.9
14	156-7	0.5	70	0.492	17475	6367												-0.091	-0.089	-16.53	-15.95	-0.667	0.663	-42.64	42.35
15	21-1	0.5	70	0.491	17331	6352												-0.312	0.312	-54.39	52.94	-0.418	0.416	-27.12	26.83
16	156-9	0.5	70	0.492	17447	6352												0.049	0.462	8.37	78.75	0.055	0.616	4.046	40.03
17	156-3	0.5	70	0.491	17462	6381												0.048	0.464	8.02	77.73	0.055	0.621	4.12	40.61
18	156-8	0.5	70	0.492	17070	6381												-0.302	0.303	-51.48	51.77	-0.409	0.406	-25.82	26.4
19	156-2	0.33	70	0.491	17346	6338	-0.373	0.362	-64.25	62.8	-0.476	0.471	-29.87	29.29				-0.373	0.362	-65.11	61.92	-0.476	0.471	-34.37	25.09
20	21-2	0.33	70	0.492	17389	6338												-0.372	0.364	-65.84	62.36	-0.477	0.471	-30.76	29.73
21	156-6	0.5	70	0.492	17200	6323												-0.361	0.363	-63.09	61.78	0.004	0.476	0.81	30.31
22	21-9	0.5	70	0.491	17462	6323												-0.364	0.364	-64.68	63.37	0.004	0.475	1.32	30.6
23	21-5	0.5	70	0.492	17302	6352												-0.363	0.365	-63.09	62.65	-0.005	-0.475	-31.47	-0.7

Half Life Values for paths

156-2	time pt	ε (%)	σ (ksi)	γ (%)	τ (ksi)
	0	0.362	61.92	0.000	0.00
	1	-0.373	-65.11	0.471	25.09
	2	-0.373	-64.23	-0.476	-34.57

21-2	time pt	ε (%)	σ (ksi)	γ (%)	τ (ksi)
	0	0.364	62.36	0.000	0
	1	-0.372	-65.48	0.471	29.73
	2	-0.372	-65.84	-0.477	-30.76

Table C3. UDRI-Ti-6-4 and Ti-17-β Biaxial Deformation-Life Data (Continued)

Ti-6-4, Phase 2 (new data)

Test #	Spec ID	Freq (Hz)	Temp (F)	Spec Dia (in)	E (ksi)	G (ksi)	εmin (%)	εmax (%)	σmin (ksi)	σmax (ksi)	γ min (%)	γ max (%)	τmin (ksi)	τmax (ksi)	Cycle Count	E (ksi)	G (ksi)	εmin (%)	εmax (%)	σmin (ksi)	σmax (ksi)	γ min (%)	γ max (%)	τmin (ksi)	τmax (ksi)
									first cycle properties												half life properties at 70F				
1	142-6	0.75	70	0.491	16370	6300	0	0	0	0	0.0844	0.99	5.3	62.8	200000		6300	0	0	0	0	0.085	0.98	6.41	62.87
2	142-5	0.75	70	0.492	16530	6330	0	0	0	0	-0.626	0.623	-39.95	39.56	131000		6350	0	0	0	0	-0.62	0.62	-38.46	40.35
3	142-9	0.5	70	0.491	16646	6367	0	0	0	0	0.125	1.263	7.5	79.89	81920		6354	0	0	0	0	0.125	1.25	0.18	71.93
7	178-3	0.75	70	0.492	16715	6390	0	0	0	0	-0.565	0.564	-36.19	36.27	393220		6396	0	0	0	0	-0.559	0.56	-34.37	37.29
19	178-10	0.5	500	0.492	14710	5731	0.0504	0.5313	5.14	77.91	0.0672	0.698	0	36.05	327000	14881	5634	0.051	0.511	1.623	69.95	0.0687	0.687	-9.45	25.36
20	142-10	0.5	500	0.492	14960	5730	0.0544	0.567	-1.2	78.94	0.071	0.733	-2.06	36.08	32768	15050	5691	0.056	0.55	-7.92	66.63	0.0729	0.72	-14.03	23.26
4	142-8	0.25	70	0.492	16570	6370	-0.304	0.292	-51.04	47.6	-0.419	0.418	-26.91	27.36	30720	16565	6394	-0.305	0.306	-51.6	50.15	-0.418	0.418	-27.05	27.01
5	142-11	0.25	70	0.492	16515	6360	-0.462	0.142	-77.43	22.85	-0.419	0.418	-27.15	26.91	88064	16630	6398	-0.459	0.161	-77.27	26.07	-0.417	0.418	-27.36	26.62
6	178-7	0.25	70	0.492	16330	6330	-0.306	0.283	-50.47	45.58	-0.419	0.417	-26.93	26.84	32768	16340	6350	-0.311	0.311	-52.55	49.09	-0.418	0.418	-26.73	27.03
8	178-8	0.25	70	0.491	16500	6385	-0.456	0.149	-76.34	24.01	-0.419	0.417	-27.31	27.06	106500	16632	6405	-0.455	0.156	-79.18	22.92	-0.418	-0.418	-28.4	25.75
9	178-12	0.25	70	0.492	16480	6343	0	0.299	0.03	47.81	0	1.225	-0.14	77.53	25600	15970	6340	0.007	0.298	-0.2	46.58	0.007	1.218	-6.38	70.56
12	178-1	0.25	70	0.491	16380	6375	0	0.298	0.46	46.82	-0.004	1.225	-0.25	77.85	18432	15560	6346	0.004	0.298	8.26	54.37	0.006	1.219	-6.22	70.64
14	178-11	0.25	70	0.492	16605	6485	0	0.238	0	36.61	0	0.963	-0.44	62.93	53248	15253	6492	0.004	0.239	-1.11	34.96	0.005	0.958	5.46	67.34
15	178-5	0.25	70	0.492	16560	6430	0	0.238	0.13	36.34	0	0.962	-0.57	62.2	49152	15080	6451	0.004	0.239	-1.72	34.1	0.006	0.958	3.96	65.47
21	142-4	0.25	500	0.492	15170	5745	-0.3495	0.3370	-54.74	53.14	-0.482	0.479	-30.22	26.16	6144	14840	5515	-0.353	0.354	-56.73	48.35	-0.481	0.48	-28.93	25.3
22	178-2	0.25	500	0.492	14870	5890	-0.3240	0.3110	-50.09	47.4	-0.451	0.449	-28.2	26.18	14336	14595	5781	-0.327	0.328	-49.39	46.46	-0.45	0.449	-30.5	22.58
10	142-7	0.25	70	0.491	16460	6380	-0.305	0.306	-51.03	49.91	-0.419	0.417	-26.94	26.94	9728	16433	6364	-0.308	0.307	-54.09	47.66	-0.418	0.415	-26.19	27.49
															50 subcycle			0.3	0.3	45.96	46.62	-0.11	0.399	-5.78	26.56
11	178-4	0.25	70	0.491	16710	6385	0	0.3	0	47.65	0	1.222	0.2	78.83	22784	17060	6379	0.007	0.298	-1.23	44.75	0.007	1.22	-8.32	68.78
															50 subcycle			0.153	0.277	19.47	41.16	0.853	1.21	48.74	68.48
13	178-6	0.25	70	0.492	16495	6400	-0.305	0.308	-50.75	50.34	-0.418	0.416	-27.12	26.96	10240	16470	6384	-0.308	0.306	-51.05	50.34	-0.419	0.415	-26.14	27.84
															50 subcycle			0.299	0.301	48.64	48.88	-0.107	0.396	-5.49	26.5
16	142-3	0.25	70	0.491	16680	6430	0	0.296	0	44.59	-0.001	1.223	0.25	78.81	32768	16390	6396	0.003	0.298	-4.87	40.19	0.006	1.215	-8.97	68.96
															50 subcycle			0.151	0.278	14.56	37.51	0.8719	1.201	48.83	69.68
17	142-1	0.25	70	0.491	16400	6370	-0.308	0.312	-51.12	50.73	-0.42	0.419	-26.86	27.32	24576	16390	6400	-0.309	0.307	-54.04	47.46	-0.42	0.416	-26.45	27.6
															5 subcycle			0.301	0.302	45.86	46.54	-0.107	0.399	-5.82	26.39
18	178-9	0.25	70	0.492	16570	6400	-0.305	0.308	-51.13	50.58	-0.42	0.418	-27.15	27.13	20480	16560	6430	-0.308	0.306	-54.22	48.12	-0.42	0.416	-27.05	27.28
															5 subcycle			0.3	0.302	46.29	46.96	-0.106	0.4	-6.14	26.17

Half Life Paths, Major cycle-Missions

142-7 box	time pt	ε (%)	σ (ksi)	γ (%)	τ (ksi)
	0	0.3004	46.29	0.4135	27.39
	1	-0.3071	-53.69	0.4148	27.36
	2	-0.3055	-52.97	-0.4175	-26.00
	3	0.3052	47.52	-0.4171	-25.61

178-6 box	time pt	ε (%)	σ (ksi)	γ (%)	τ (ksi)
	0	0.2999	49.37	0.4142	27.55
	1	-0.3070	-50.61	0.4136	28.85
	2	-0.3060	-50.48	-0.4167	-25.85
	3	0.3051	50.25	-0.4163	-25.62

178-4 chk	time pt	ε (%)	σ (ksi)	γ (%)	τ (ksi)
	0	0.0095	-1.005	0.0076	-7.28
	1	0.2977	44.66	0.8244	44.5
	2	0.1530	19.26	1.2162	69.58
	1a*	0.2769	41.05	0.8912	48.65

1a* is where the subcycles start in this test

142-3 chk	time pt	ε (%)	σ (ksi)	γ (%)	τ (ksi)
	0	0.0045	-1.84	0.0084	-6.71
	1	0.2990	41.42	0.8140	44.95
	2	0.1530	14.8	1.2150	70.32
	1a*	0.2776	37.51	0.8719	48.83

142-1 box	time pt	ε (%)	σ (ksi)	γ (%)	τ (ksi)
	0	0.3010	45.88	0.4064	27.07
	1	-0.3080	-53.99	0.4150	27.15
	2	-0.3058	-52.99	-0.4156	-26.25
	3	0.3061	47.39	-0.4183	-25.68

178-9 box	time pt	ε (%)	σ (ksi)	γ (%)	τ (ksi)
	0	0.3010	46.47	0.4140	27.04
	1	-0.3080	-54.43	0.4140	26.79
	2	-0.3050	-53.59	-0.4170	-26.68
	3	0.3060	47.75	-0.4160	-26.17

Half Life Paths

178-12 chk	time pt	ε (%)	σ (ksi)	γ (%)	τ (ksi)
	0	0.0094	0.262	0.0083	-5.31
	1	0.2970	46.48	0.8205	45.41
	2	0.1563	21.98	1.2170	70.56
	1a	0.2976	46.58	0.8254	46.09

178-1 chk	time pt	ε (%)	σ (ksi)	γ (%)	τ (ksi)
	0	0.0090	9.013	0.0085	-5.51
	1	0.2976	54.33	0.8217	45.59
	2	0.1521	29.47	1.2190	70.63
	1a	0.2979	54.34	0.8257	46.27

178-11 chk	time pt	ε (%)	σ (ksi)	γ (%)	τ (ksi)
	0	0.0070	-0.59	0.0056	6.06
	1	0.2390	35.05	0.6400	46.57
	2	0.1200	13.96	0.9570	67.2
	1a	0.2380	34.96	0.6410	47.1

178-5 chk	time pt	ε (%)	σ (ksi)	γ (%)	τ (ksi)
	0	0.0075	-0.83	0.0054	4.58
	1	0.2390	34.1	0.6400	45.32
	2	0.1223	13.14	0.9560	65.45
	1a	0.2385	33.97	0.6460	45.79

142-8 box	time pt	ε (%)	σ (ksi)	γ (%)	τ (ksi)
	0	0.3045	49.46	0.4174	26.83
	1	-0.3044	-51.49	0.4154	26.59
	2	-0.3038	-50.49	-0.4155	-26.84
	3	0.3063	50.11	-0.4158	-26.11

178-7 box	time pt	ε (%)	σ (ksi)	γ (%)	τ (ksi)
	0	0.3080	48.36	0.4153	26.64
	1	-0.3090	-52.37	0.4159	26.42
	2	-0.3079	-51.94	-0.4138	-26.43
	3	0.3103	49.02	-0.4159	-25.99

178-8 box	time pt	ε (%)	σ (ksi)	γ (%)	τ (ksi)
	0	0.1545	22.23	0.4169	25.55
	1	-0.4545	-79.1	0.4168	25.22
	2	-0.4539	-78.52	-0.4162	-28.24
	3	0.1558	22.86	-0.4161	-27.62

142-11 box	time pt	ε (%)	σ (ksi)	γ (%)	τ (ksi)
	0	0.1598	25.53	0.4165	26.3
	1	-0.4583	-77.21	0.4163	26.13
	2	-0.4578	-76.78	-0.4165	-27.2
	3	0.1605	25.99	-0.4163	-26.75

142-4 (500F) box	time pt	ε (%)	σ (ksi)	γ (%)	τ (ksi)
	0	0.3500	47.72	0.4768	25.01
	1	-0.3500	-56.81	0.4759	24.27
	2	-0.3493	-55.85	-0.4791	-28.6
	3	0.3529	48.06	-0.4783	-27.59

178-2 (500F) box	time pt	ε (%)	σ (ksi)	γ (%)	τ (ksi)
	0	0.3250	46.13	0.4430	22.09
	1	-0.3250	-49.15	0.4480	21.7
	2	-0.3230	-48.23	-0.4420	-30.27
	3	0.3270	46.56	-0.4460	-29.01

Table C3. UDRI-Ti-6-4 and Ti-17-β Biaxial Deformation-Life Data (Continued)

Ti-17-β, Phase 2 (new data)

					first cycle properties											half life properties at 70F										G 6281
Test #	Spec ID	Freq (Hz)	Temp (F)	Spec Dia (in)	E (ksi)	G (ksi)	εmin (%)	εmax (%)	σmin (ksi)	σmax (ksi)	γ min (%)	γ max (%)	τmin (ksi)	τmax (ksi)	Cycle Count	E (ksi)	G (ksi)	εmin (%)	εmax (%)	σmin (ksi)	σmax (ksi)	γ min (%)	γ max (%)	τmin (ksi)	τmax (ksi)	E εmin (%)
1	4B29K	0.5	70	0.492	16596	6468	0	0	0	0	-0.91	0.909	-58.94	59.22	16384		6464	0	0	0	0	-0.899	0.899	-58.17	58.35	0.0
2	4B25K	0.75	70	0.492	16550	6440	0	0	0	0	-0.838	0.834	-54.03	53.77	32768		6452	0	0	0	0	-0.83	0.83	-53.42	53.67	0.0
3	5B12K	0.5	70	0.491	16980	6376	0	0	0	0	0.166	1.685	7.16	103.8	16404		6332	0	0	0	0	0.168	1.667	3.23	98.28	0.0
4	5B36K	0.5	70	0.492	16750	6450	0	0	0	0	0.134	1.363	8.69	88.36	16384		6451	0	0	0	0	0.136	1.35	8.825	87.36	0.0
5	5B16k	0.5	70	0.492	16728	6400	0	0.363	-0.07	58.52	0	0.99	0	64.02	16384	16168	6408	0	0.36	0.08	58.25	0.004	0.98	1.43	64.39	0.0
6	5B4K	0.5	70	0.492	16400	6450	-0.002	0.3332	-0.11	53.44	-0.007	0.888	-0.08	57.99	163840	16065	6481	1E-04	0.33	1.6	54.57	-2E-04	0.879	3.15	60.5	0.0
9	5B13K	0.5	70	0.491	16640	6505	0	0.373	0.07	59.47	-0.007	0.939	-0.15	61.85	16384	15923	6541	0	0.37	-0.32	58.57	-1E-04	0.93	-0.42	60.63	0.0
10	5B24K	0.5	70	0.492	16680	6475	0	0	0	0	0.121	1.233	7.93	80.2	65536		6450	0	0	0	0	0.122	1.221	9.08	79.9	0.0
11	5B28K	0.5	70	0.492	16700	6423	0	0	0	0	0.121	1.236	7.9	79.98	49152		6426	0	0	0	0	0.123	1.222	9.06	79.76	
7	5B8K	0.5	70	0.491	16690	6447	0	0.269	-0.23	43.86	-4E-04	1.083	-0.009	70.64	75785	16305	6473	0.007	0.268	1.94	44.78	0.0068	1.078	1.64	71.14	
8	5B20K	0.5	70	0.492	16440	6540	0	0.268	-0.15	42.68	-4E-04	1.082	-0.032	71.77	75776	15887	6565	0.006	0.269	-0.35	41.99	0.0074	1.08	1.73	72.13	
		70																								
		70																								

Half Life Values for paths

5B8K	time pt	ε (%)	σ (ksi)	γ (%)	τ (ksi)
	0	0.0098	2.48	0.0170	2.56
	1	0.2680	44.76	0.7191	47.91
	2	0.1367	22.37	1.0779	71.14
	1a	0.2678	44.77	0.7216	48.14

5B20K	time pt	ε (%)	σ (ksi)	γ (%)	τ (ksi)
	0	0.0095	0.524	0.0194	2.44
	1	0.2689	41.98	0.7167	48.29
	2	0.1360	19.47	1.0784	72.12
	1a	0.2686	41.96	0.7278	49.59
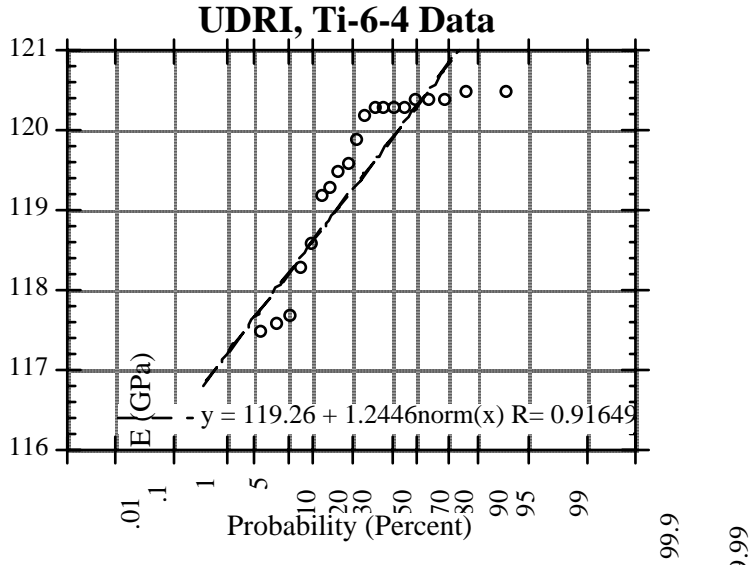
Figure C4. Normal distribution of axial modulus check data.

y = 119.26 + 1.2446norm(x) R= 0.91649

UDRI, Ti-6-4 Data
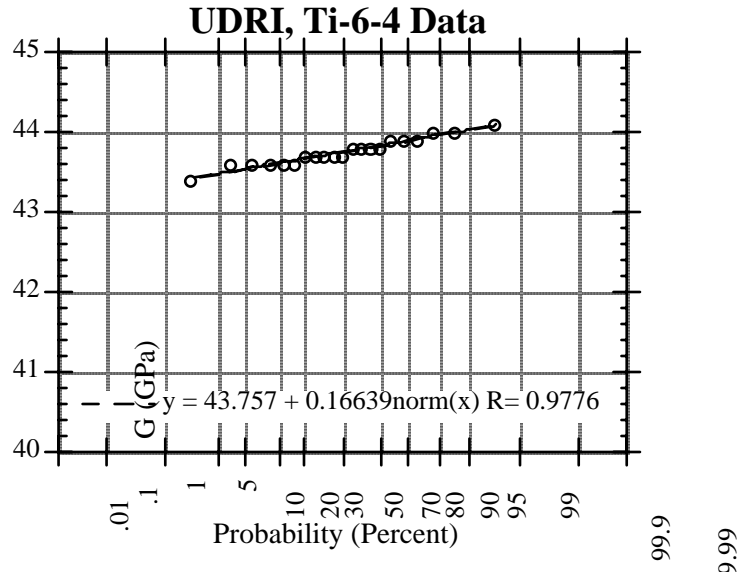
Figure C5. Normal distribution of shear modulus check data.

In order to consider torsional plastic deformation it was necessary to assume a plasticity algorithm. An Armstrong-Frederick based model subsequently refined by Jiang and Kurath [2-6] was implemented. Even the existing uniaxial LCF data did not provide adequate data to fit the modeling constants. A uniaxial specimen was machined from remnants of the forging used for the biaxial specimens. A summary of the deformation results is shown in Figure C6. Notable is the cyclic softening which occurs rapidly after the initial plastic deformation in the first cycle. Both the initial half cycle and half-life data (cycle 1024) were used to obtain two sets of plasticity constants. Note the half-life linear elastic modulus is lower than the initial cycle value in Figure C6.

UDRI, Ti-6-4, Uniaxial
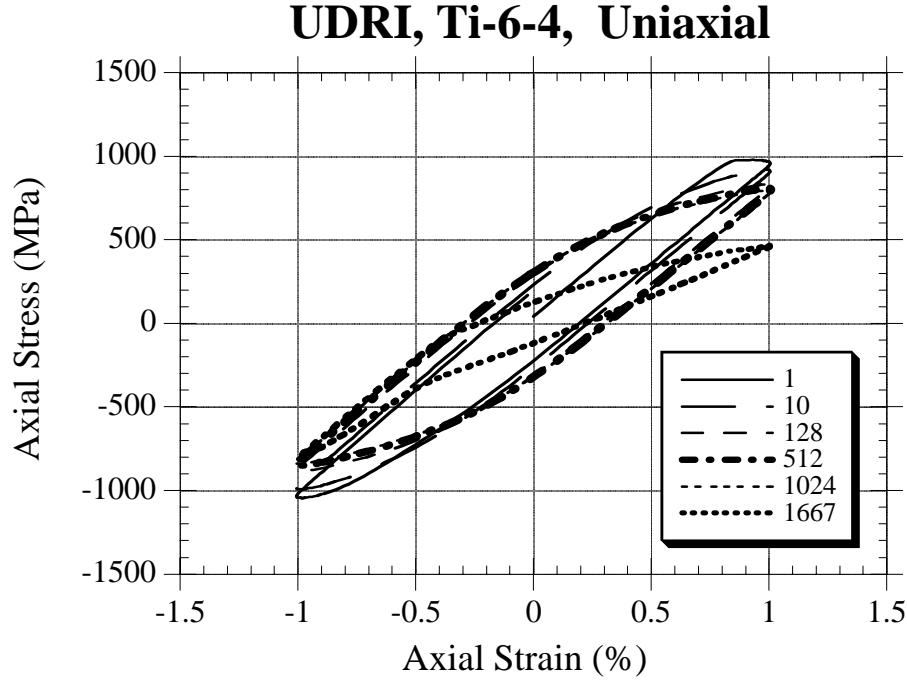
Figure C6. Uniaxial deformation data.

Without laboring over the details in the derivation, the following simple procedure for determining $c^{(i)}$ and $r^{(i)}$ for an A-F type model is forwarded. Select M points from the σ_a - ε_a^p curve from the uniaxial experiment (refer to Figure C7) so that the stress range, $\sigma_{a(i)}$, and plastic strain range, $\varepsilon_{a(i)}^p$, are known for any point i. Generally, half of a representative hysterisis loop is employed to represent the stress strain curve shown in Figure C7. Note that $\varepsilon_{a(i)}^p$ denotes the plastic strain range and $\sigma_{a(i)}$ is the stress range corresponding to $\varepsilon_{a(i)}^p$. The quantities, $c^{(i)}$ and $r^{(i)}$ are determined by the following two equations respectively,

$$c^{(i)} = \sqrt{\frac{2}{3}} \; \frac{1}{\varepsilon_{a(i)}^p} \quad (i=1, 2, ..., M) \tag{C1}$$

$$r^{(i)} = \frac{2}{3} \frac{H_{(i)} - H_{(i+1)}}{c^{(i)}} \quad (i=1, 2, ..., M) \tag{C2}$$

In the previous two equations,

$$H_{(i)} = \frac{\sigma_{a(i)} - \sigma_{a(i-1)}}{\varepsilon_{a(i)}^p - \varepsilon_{a(i-1)}^p} \quad (i=1, 2, ..., M) \tag{C3}$$

C-12

$$\sigma_{a(0)} = \sigma_y = \sqrt{3}\ k \quad ; \quad \Delta\varepsilon_{(0)}^{P} = 0 \quad ; \quad H_{(M+1)} = 0 \tag{C4}$$

The slope between point (i-1) and point i is $H_{(i)}$ (Figure C7), and is often termed the plastic modulus. The yield stress σ_y in Equation C4 is the linear elastic portion in Figure C7. The constant k is the yield stress in pure shear and is related to uniaxial loading via the von Mises criterion. The maximum stress range, $\Delta\sigma_{(M)}$, satisfies the following condition,

$$\sigma_{a(M)} = \sigma_{max} = \sqrt{\frac{3}{2}}\ \square\ \sum_{i=1}^{M} r^{(i)} + \sigma_y \tag{C5}$$

where σ_{max} is the maximum stress range that the model is intended to simulate. For a non-Massing material, the determination of $c^{(i)}$ and $r^{(i)}$ is more complex and involves a series of hysterisis loops, or a "step" test. The constants utilized in the plasticity model are summarized in Table C3 (an M=10 expansion of the backstress was utilized).
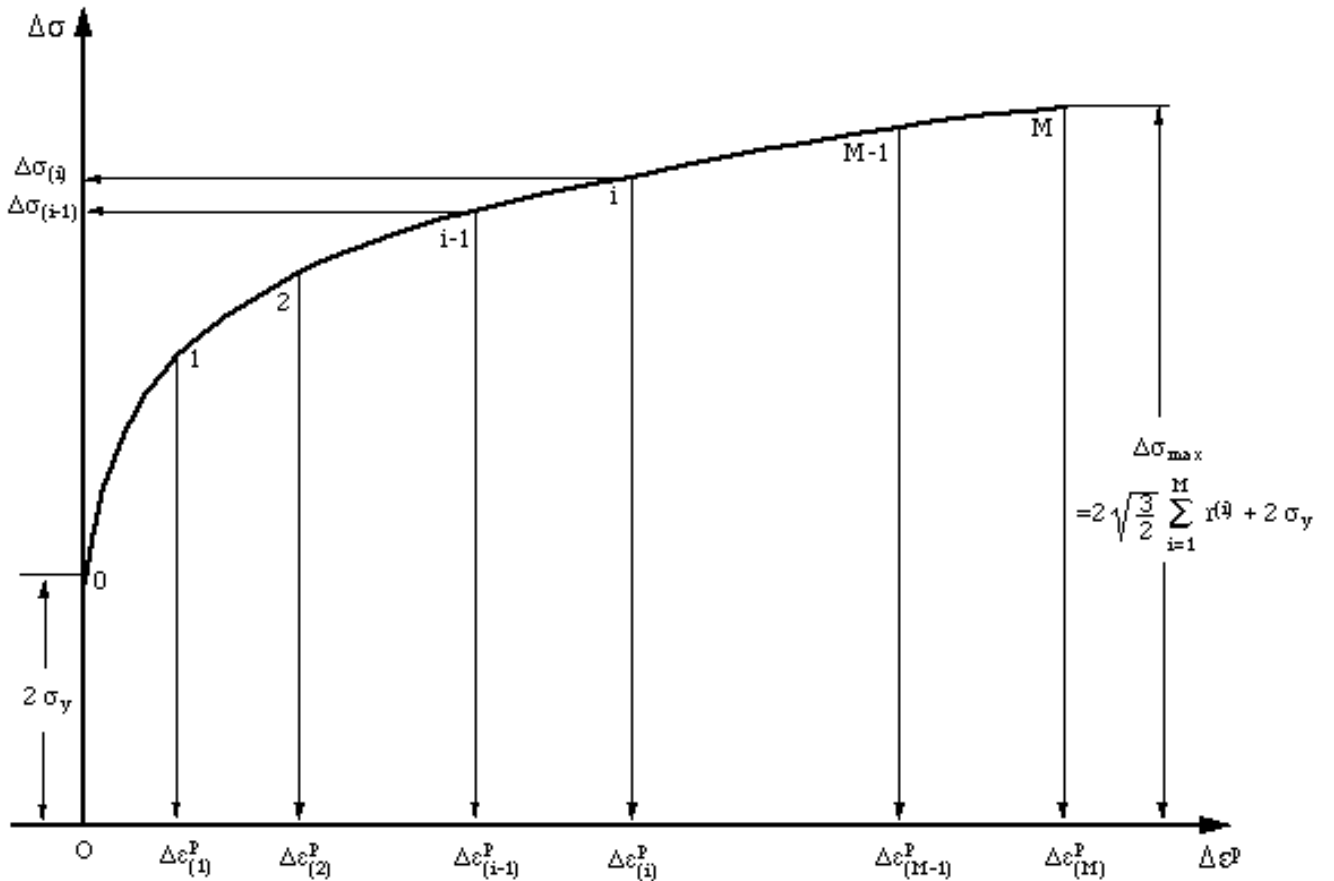
Figure C7. Fitting plasticity modeling constants.

Comparison of the half-life deformation and the model is shown in Figure C8. Coincidence of this data is anticipated since it was employed to fit the plasticity constants. While most of the cyclic biaxial data appears linear elastic when viewed on a cycle by cycle basis, there is appreciable plasticity on the first cycle of many R=0.1 and 0.5 tests. Figure C9 shows a typical torsion only test, showing experimental and analytical results. It should be noted that the y-axis on this plot is torque. The plasticity algorithm is run in "strain" control, and the stresses integrated to give a nominal torque. If the torque values compare favorably, the author implies that the stresses calculated are a reasonable estimate. Table C4 lists the stabilized half-life deformation predicted for all Ti-6-4 multiaxial stress paths.

Table C4. Plasticity Modeling Constants

$c^{(i)}$	$R^{(i)}$ (MPa) Cycle 1 K= 260 (MPa)	$r^{(i)}$ (MPa) Half-life k= 205 (MPa)
3265	150	127
1637	77.7	63.2
820	82.3	63.8
411	85.3	62.4
206	86.4	59.0
103	85.5	54.1
51.8	82.9	48.3
26.0	78.5	42.0
13.0	72.9	35.8
6.53	120	50.9

UDRI, Ti-6-4
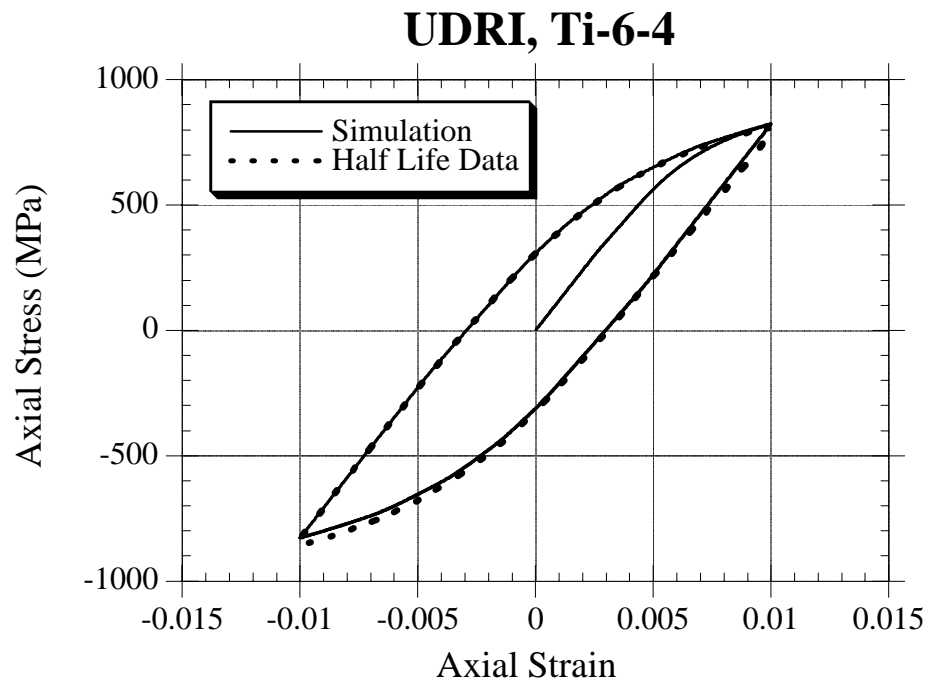
Figure C8. Comparison of modeling and uniaxial data.

UDRI, Ti-6-4, Specimen 21-7
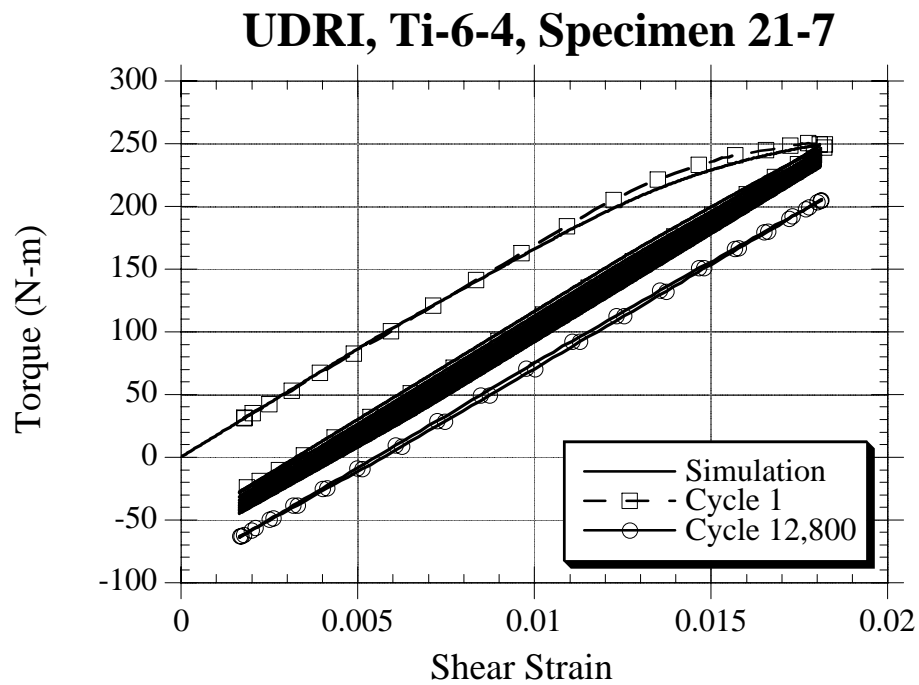
Figure C9. Typical R=0.1 torsion only data.
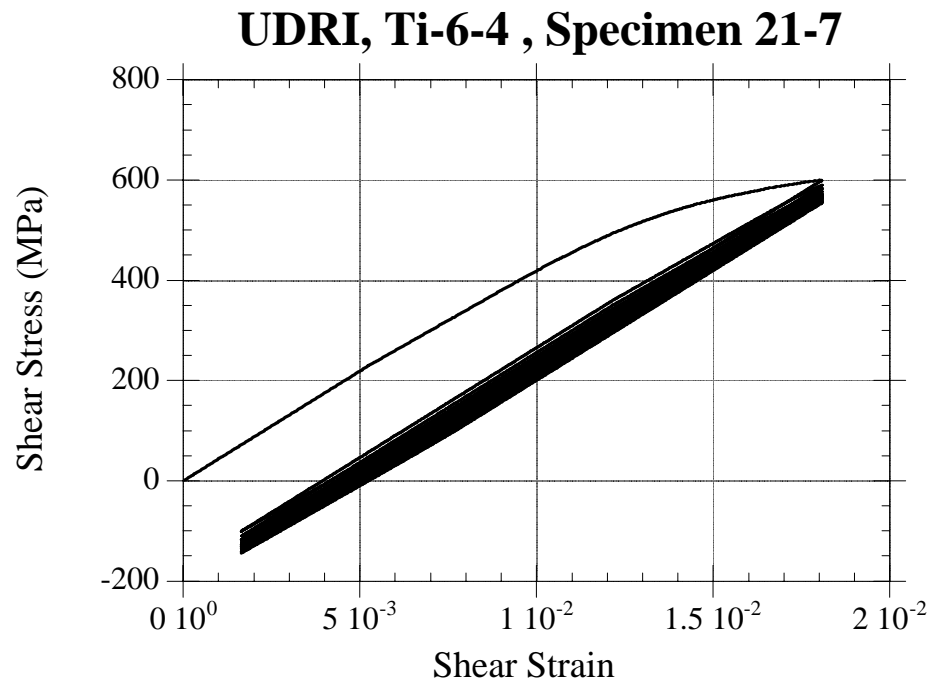
Figure C10. Typical R=0.1 plasticity modeling of torsion only data.
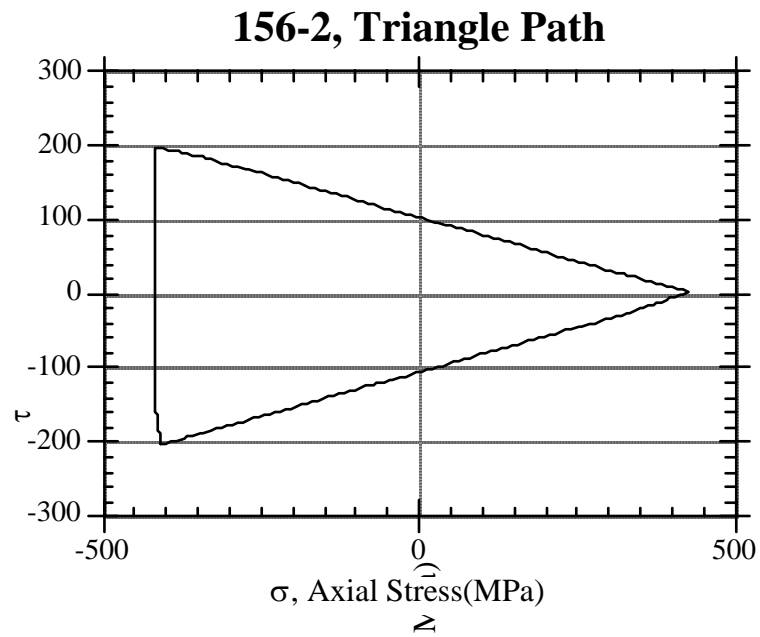
Figure C11. Typical plasticity modeling of triangle path.
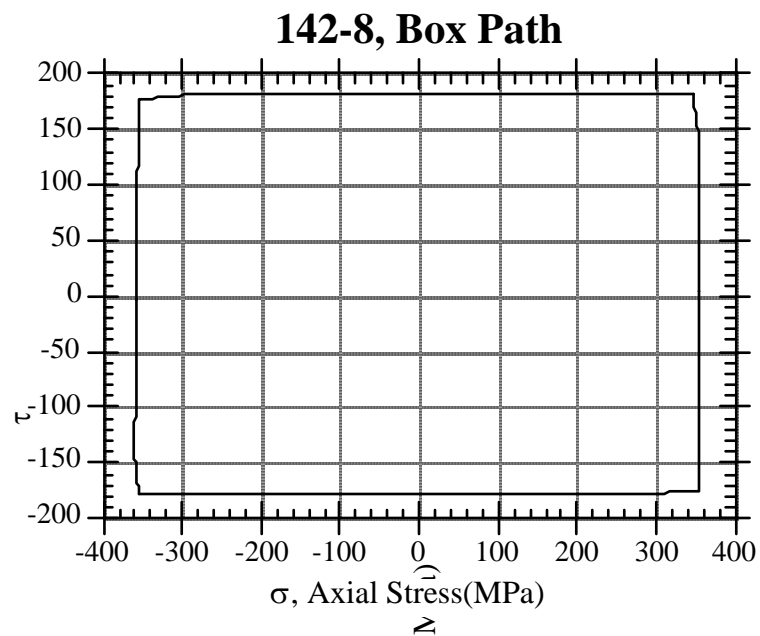
Figure C12. Typical plasticity modeling of box path.

142-11, Mean Stress Box Path
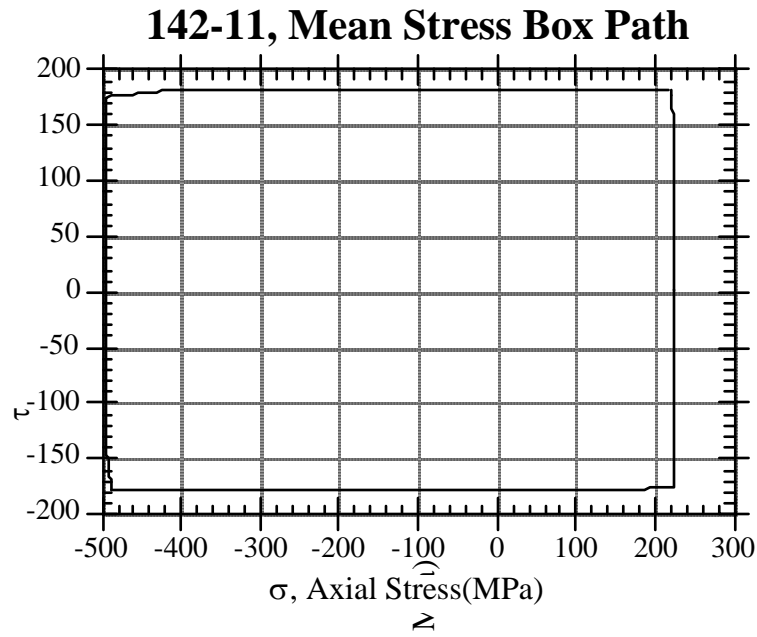
Figure C13. Typical plasticity modeling of axial mean stress box path.
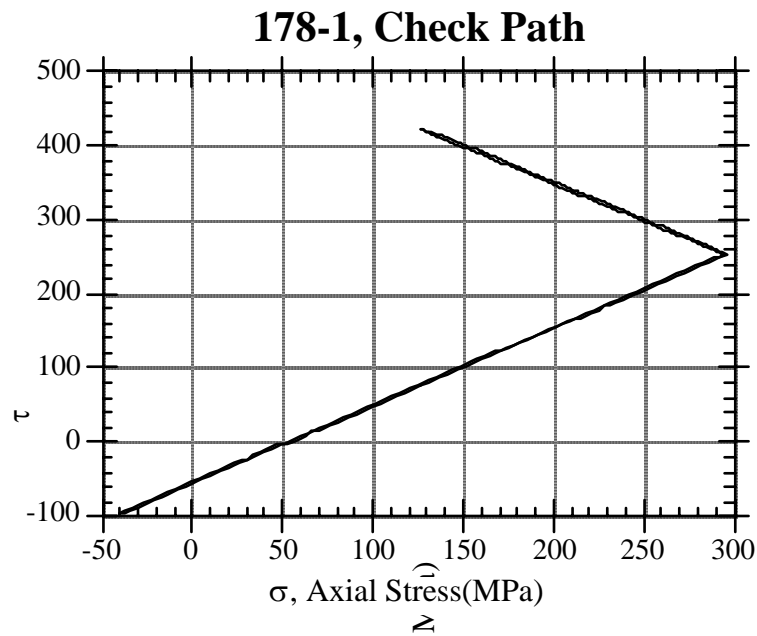
178-1, Check Path

Figure C14. Typical plasticity modeling of check path.

Table C5. Predicted Deformation/Life For Ti-6-4

Spec ID	Endpt Order	Freq (Hz)	ε_θ (%)	ε_z (%)	γ (%)	σ_θ (ksi)	σ_z (ksi)	τ (ksi)	Findley lifespan θ	Findley lifespan cycles	SWT lifespan θ	SWT lifespan cycles	Measured lifespan	Ratio (pred/meas) Findley	Ratio (pred/meas) SWT	Comment
21-11	1	0.5	0.000	0.000	0.866	0.00	0.00	50.66	10	3.045E+04	44	2.224E+05	7.214E+04	0.42	3.08	fully reversed torsion
	2		0.000	0.000	-0.868	0.00	0.00	-50.82								
	3		0.000	0.000	0.866	0.00	0.00	50.73								
21-6	1	1	0.000	0.000	0.614	0.00	0.00	38.25	-10	3.231E+06	--	r/o	2.413E+05			fully reversed torsion
	2		0.000	0.000	-0.610	0.00	0.00	-38.06								
	3		0.000	0.000	0.614	0.00	0.00	38.25								
156-10	1	0.5	0.000	0.000	0.559	0.00	0.00	34.96	10	1.473E+08	--	r/o	9.618E+05			fully reversed torsion
	2		0.000	0.000	-0.563	0.00	0.00	-35.21								
	3		0.000	0.000	0.559	0.00	0.00	34.96								
21-7	1	0.5	0.000	0.000	1.810	0.00	0.00	71.64	-74	2.583E+04	-46	6.455E+04	2.490E+04	1.04	2.59	R=0.1 torsion
	2		0.000	0.000	0.166	0.00	0.00	-28.30								
	3		0.000	0.000	1.810	0.00	0.00	69.12								
156-5	1		0.000	0.000	1.210	0.00	0.00	62.41	-72	8.836E+05	-46	3.149E+06	1.503E+05			R=0.1 torsion
	2		0.000	0.000	0.090	0.00	0.00	-7.73								
	3		0.000	0.000	1.210	0.00	0.00	62.31								
156-4	1	0.5	0.000	0.000	1.360	0.00	0.00	65.56	-72	2.095E+05	-46	5.931E+05	1.516E+05	1.38	3.91	R=0.1 torsion
	2		0.000	0.000	0.150	0.00	0.00	-10.58								
	3		0.000	0.000	1.360	0.00	0.00	65.06								
156-1	1	0.5	0.000	0.000	0.958	0.00	0.00	54.76	-18	2.370E+10	--	r/o	8.148E+05			R=0.1 torsion
	2		0.000	0.000	0.086	0.00	0.00	0.20								
	3		0.000	0.000	0.958	0.00	0.00	54.74								
21-4	1	1	0.000	0.000	1.960	0.00	0.00	73.03	-20	2.034E+05	-46	3.415E+05	1.412E+05	1.44	2.42	R=0.5 torsion
	2		0.000	0.000	0.815	0.00	0.00	1.35								
	3		0.000	0.000	1.960	0.00	0.00	72.96								
21-1	1	0.5	-0.109	0.312	0.416	0.09	52.15	25.70	12	7.308E+04	-22	1.197E+05	6.797E+04	1.08	1.76	fully reversed tension-torsion
	2		0.109	-0.312	-0.418	-0.09	-52.15	-25.81								
	3		-0.109	0.312	0.416	0.09	52.16	25.71								
156-9	1	0.5	-0.166	0.462	0.616	0.28	72.16	35.26	4	2.236E+05	-22	1.776E+05	6.051E+04	3.70	2.94	R=0.1 tension-torsion
	2		-0.021	0.049	0.055	0.29	2.28	0.15								
	3		-0.166	0.462	0.616	0.29	72.11	35.24								
156-3	1	0.5	-0.166	0.464	0.621	0.29	72.36	35.49	4	2.093E+05	-10	3.627E+00	8.792E+04	2.38	0.00	R=0.1 tension-torsion
	2		-0.020	0.048	0.055	0.30	1.97	0.06								
	3		-0.166	0.464	0.621	0.30	72.30	35.46								
156-2	1	0.333	-0.127	0.362	0.000	0.00	61.14	0.00	0	3.637E+04	-8	1.407E+05	3.836E+04	0.95	3.67	non-proportional tension-torsion (triangular path)
	2		0.132	-0.373	0.471	-0.20	-60.40	28.51								
	3		0.132	-0.373	-0.476	-0.37	-58.92	-29.68								
21-2	1	0.333	-0.128	0.364	0.000	0.00	61.48	0.00	-2	3.774E+04	8	1.405E+05	4.301E+04	0.88	3.27	non-proportional tension-torsion (triangular path)
	2		0.131	-0.372	0.471	-0.20	-60.27	28.51								
	3		0.132	-0.372	-0.477	-0.37	-58.78	-29.74								
21-9	1	0.5	-0.128	0.364	0.004	0.00	61.48	0.25	-24	4.467E+04	8	1.467E+05	7.136E+04	0.63	2.06	non-proportional tension-torsion (top segment of triangular path)
	2		0.128	-0.364	0.475	-0.08	-60.33	27.70								
	3		-0.128	0.364	0.004	0.02	61.87	-1.64								
21-5	1	0.5	-0.128	0.365	-0.005	0.00	61.65	-0.28	24	4.315E+04	-6	1.468E+05	7.937E+04	0.54	1.85	non-proportional tension-torsion (bottom segment of triangular path)
	2		0.128	-0.363	-0.475	-0.08	-60.19	-27.70								
	3		-0.128	0.365	-0.005	0.02	62.01	1.60								
21-8	1	0.5	-0.032	0.091	0.666	0.05	15.06	40.66	-10	8.394E+04	-42	7.492E+08	7.212E+04	1.16		non-proportional tension-torsion
	2		-0.031	0.089	-0.665	0.31	12.80	-40.77								
	3		-0.032	0.091	0.666	0.33	13.03	40.82								
21-3	1	0.5	-0.032	0.090	0.666	0.05	14.89	40.66	-12	8.590E+04	-44	1.226E+09	7.373E+04	1.17		reversed torsion + mean tension
	2		-0.031	0.089	-0.666	0.31	12.81	-40.82								
	3		-0.032	0.090	0.666	0.32	12.87	40.82								
21-10	1	0.5	0.031	-0.089	0.665	-0.05	-14.73	40.61	80	5.369E+05	--	r/o	3.291E+05	1.63		reversed torsion + mean compression
	2		0.032	-0.091	-0.664	-0.32	-13.15	-40.72								
	3		0.031	-0.089	0.665	-0.32	-12.71	40.77								
156-8	0	0.5	0.000	0.000	0.406	0.00	0.00	25.39	0	2.400E+05	--	r/o	1.118E+05	2.15		90 deg phase shifted tension-torsion (circle)
	0.1		-0.033	0.094	0.386	0.00	15.88	24.14								
	0.2		-0.062	0.178	0.328	0.00	30.07	20.51								
	0.3		-0.085	0.245	0.239	0.00	41.38	14.95								
	0.4		-0.099	0.288	0.125	0.00	48.64	7.82								
	0.5		-0.106	0.303	0.000	0.00	51.18	0.00								
	0.6		-0.099	0.288	-0.126	0.00	48.64	-7.88								
	0.7		-0.085	0.245	-0.240	0.00	41.38	-15.01								
	0.8		-0.062	0.178	-0.331	0.00	30.07	-20.70								
	0.9		-0.033	0.094	-0.389	0.00	15.88	-24.33								
	1		0.000	0.000	-0.409	0.00	0.00	-25.58								
	1.1		0.032	-0.093	-0.389	0.00	-15.71	-24.33								
	1.2		0.062	-0.178	-0.331	0.00	-30.07	-20.70								
	1.3		0.085	-0.244	-0.240	0.00	-41.21	-15.01								
	1.4		0.099	-0.287	-0.126	0.00	-48.48	-7.88								
	1.5		0.105	-0.302	0.000	0.00	-51.01	0.00								
	1.6		0.099	-0.287	0.125	0.00	-48.48	7.82								
	1.7		0.085	-0.244	0.239	0.00	-41.21	14.95								
	1.8		0.062	-0.178	0.328	0.00	-30.07	20.51								
	1.9		0.032	-0.093	0.386	0.00	-15.71	24.14								
	2		0.000	0.000	0.406	0.00	0.00	25.39								
142-6	1	0.75	0.000	0.000	0.980	0.00	0.00	55.61	-18	5.222E+09	--	r/o	> 2.0E+06			runout
	2		0.000	0.000	0.085	0.00	0.00	-0.39								
	3		0.000	0.000	0.980	0.00	0.00	55.58								
142-5	1	0.75	0.000	0.000	0.620	0.00	0.00	38.55	-10	2.435E+06	--	r/o	2.607E+05			
	2		0.000	0.000	-0.620	0.00	0.00	-38.55								
	3		0.000	0.000	0.620	0.00	0.00	38.55								

C-19

Spec ID	Endpt Order	Freq (Hz)	ε_a (%)	ε_z (%)	γ (%)	σ_θ (ksi)	σ_z (ksi)	τ (ksi)	Findley lifespan θ	cycles	SWT lifespan θ	cycles	Measured lifespan	Ratio (pred/meas) Findley	SWT	Comment
142-9	1	0.5	0.000	0.000	1.250	0.00	0.00	63.33	-18	8.594E+05	-46	4.014E+06	1.847E+05			
	2		0.000	0.000	0.125	0.00	0.00	-7.13								
	3		0.000	0.000	1.250	0.00	0.00	63.23								
178-3	1	0.75	0.000	0.000	0.560	0.00	0.00	35.02	-10	1.946E+08	--	r/o	8.434E+05			
	2		0.000	0.000	-0.559	0.00	0.00	-34.96								
	3		0.000	0.000	0.560	0.00	0.00	35.02								
142-8	1	0.25	-0.107	0.305	0.417	0.07	51.00	25.85	22	1.581E+04	-22	1.306E+05	5.943E+04	0.27	2.20	R=-1 Box contact simulation
	2		0.107	-0.304	0.415	-0.01	-51.34	25.49								
	3		0.108	-0.304	-0.416	-0.14	-51.27	-26.00								
	4		-0.107	0.306	-0.416	0.01	51.67	-25.46								
	5		-0.107	0.305	0.417	0.14	50.57	26.17								
142-11	1	0.33	-0.056	0.160	0.417	0.00	26.99	26.05	24	3.102E+04	-26	1.539E+06	1.821E+05	0.17	8.45	Rgam=-1 box
	2		0.164	-0.458	0.416	-0.29	-71.30	25.39								
	3		0.164	-0.458	-0.417	-0.43	-70.33	-26.17								
	4		-0.052	0.161	-0.416	-0.26	33.05	-25.53								
	5		-0.052	0.160	0.417	-0.11	31.98	26.06								
178-7	1	0.25	-0.054	0.308	0.415	0.08	51.55	25.70	22	1.559E+04	-22	1.332E+05	7.236E+04	0.22	1.84	R=-1 Box contact simulation
	2		0.163	-0.309	0.416	-0.02	-52.05	25.45								
	3		0.163	-0.308	-0.414	-0.15	-51.08	-25.97								
	4		-0.051	0.310	-0.416	0.03	52.24	-25.45								
	5		-0.051	0.308	0.415	0.15	51.06	26.06								
178-8	1	0.25	-0.054	0.155	0.417	0.00	26.10	26.07	24	3.334E+04	-22	2.926E+06	2.123E+05	0.16	13.78	Rgam=-1 box
	2		0.163	-0.455	0.417	-0.29	-70.80	25.51								
	3		0.163	-0.454	-0.416	-0.41	-69.94	-26.13								
	4		-0.051	0.156	-0.416	-0.26	32.15	-25.59								
	5		-0.051	0.155	0.417	-0.13	31.12	26.08								
178-12	2	0.25	-0.106	0.297	0.821	0.34	46.56	47.10	-6	2.969E+04	-42	1.522E+05	5.057E+04	0.59	3.01	check mark,R=0
	3		-0.057	0.156	1.217	0.69	19.08	62.15								
	4		-0.107	0.298	0.825	0.69	42.95	37.66								
	5		-0.006	0.009	0.008	0.67	-5.65	-13.25								
	2*		-0.107	0.297	0.821	0.66	42.83	36.48								
	3*		-0.057	0.156	1.217	0.67	18.96	60.80								
178-1	2	0.25	-0.106	0.298	0.822	0.34	46.63	47.14	-4	2.857E+04	-40	1.547E+05	3.692E+04	0.77	4.19	check mark,R=0
	3		-0.056	0.152	1.219	0.68	18.42	62.23								
	4		-0.107	0.298	0.826	0.68	43.05	37.63								
	5		-0.006	0.009	0.009	0.67	-5.67	-13.27								
	2*		-0.107	0.298	0.822	0.65	42.99	36.50								
	3*		-0.056	0.152	1.219	0.67	18.31	60.85								
178-11	2	0.25	-0.084	0.239	0.640	0.18	39.01	38.46	-6	2.761E+05	-40	3.278E+07	1.098E+05	2.51	298.41	check mark,R=0
	3		-0.043	0.120	0.957	0.32	17.38	54.45								
	4		-0.084	0.238	0.641	0.32	37.31	34.69								
	5		-0.003	0.007	0.006	0.32	-1.71	-5.05								
	2*		-0.085	0.239	0.640	0.32	37.47	34.58								
	3*		-0.043	0.120	0.957	0.32	17.37	54.40								
178-5	2	0.25	-0.084	0.239	0.640	0.18	39.01	38.46	-6	2.630E+05	-42	3.180E+07	9.942E+04	2.64	319.90	check mark,R=0
	3		-0.040	0.122	0.956	0.32	17.75	54.40								
	4		-0.084	0.239	0.646	0.32	37.38	35.01								
	5		-0.004	0.008	0.005	0.32	-1.64	-5.05								
	2*		-0.085	0.239	0.640	0.32	37.45	34.59								
	3*		-0.044	0.122	0.956	0.32	17.74	54.35								
142-7	1	0.25	-0.107	0.300	0.414	0.06	50.97	25.63	-22	1.666E+04	-22	1.377E+05	1.947E+04	0.86	7.07	miss 2b, r=-1 box w/5 subcycles
	2		0.108	-0.307	0.415	-0.02	-51.73	25.45								
	3		0.107	-0.306	-0.418	-0.14	-50.73	-26.16								
	4		-0.107	0.305	-0.417	0.02	51.46	-25.56								
	5		-0.105	0.300	0.414	0.12	50.00	25.98								
	6		-0.105	0.300	-0.110	0.12	49.93	-6.76								
	7		-0.105	0.300	0.399	0.12	49.93	25.07								
178-4	2	0.25	-0.106	0.298	0.824	0.35	46.62	47.27	-6	2.895E+04	-40	1.559E+05	4.454E+04	0.65	3.50	miss 7, chck w/ 5 subcycles
	3		-0.056	0.153	1.216	0.68	18.58	62.15								
	4		-0.100	0.277	0.853	0.68	39.52	39.44								
	5		-0.056	0.153	1.210	0.68	18.58	61.77								
	6		-0.107	0.298	0.824	0.68	42.90	37.65								
	7		-0.006	0.010	0.008	0.66	-5.59	-13.20								
	2*		-0.107	0.298	0.824	0.66	43.05	37.37								
	3*		-0.056	0.153	1.216	0.67	18.50	61.33								
178-6	1	0.25	-0.105	0.300	0.414	0.05	50.34	25.71	-22	1.708E+04	-22	1.442E+05	2.142E+04	0.80	6.73	miss 2b, r=-1 box w/5 subcycles
	2		0.108	-0.307	0.414	-0.03	-51.67	25.42								
	3		0.107	-0.306	-0.417	-0.14	-50.83	-26.10								
	4		-0.107	0.305	-0.416	0.01	51.46	-25.52								
	5		-0.105	0.300	0.414	0.12	49.93	26.02								
	6		-0.106	0.301	-0.107	0.12	50.11	-6.57								
	7		-0.104	0.298	0.396	0.12	49.61	24.88								
142-3	2	0.25	-0.106	0.299	0.814	0.34	46.92	46.78	-8	2.961E+04	-42	1.586E+05	4.978E+04	0.59	3.19	miss 7, chck w/ 5 subcycles
	3		-0.056	0.153	1.203	0.67	18.75	61.84								
	4		-0.100	0.278	0.863	0.67	39.86	40.59								
	5		-0.055	0.151	1.189	0.67	18.41	60.97								
	6		-0.107	0.278	0.863	0.67	43.41	37.50								
	7		-0.004	0.299	0.806	0.66	-6.29	-12.80								
	2*		-0.107	0.299	0.814	0.66	43.42	37.25								
	3*		-0.056	0.153	1.203	0.67	18.69	61.21								
142-1	1	0.25	-0.105	0.301	0.406	0.04	50.58	25.26	-22	1.692E+04	-22	1.460E+05	4.879E+04	0.35	2.99	miss 2b, r=-1 box w/5 subcycles
	2		0.108	-0.308	0.415	-0.04	-51.77	25.53								
	3		0.107	-0.306	-0.416	-0.14	-50.79	-26.05								
	4		-0.107	0.306	-0.418	0.02	51.58	-25.63								
	5		-0.106	0.301	0.406	0.12	50.14	25.59								
	6		-0.106	0.302	-0.107	0.12	50.29	-6.52								
	7		-0.106	0.301	0.399	0.12	50.12	25.58								
178-9	1	0.25	-0.106	0.301	0.414	0.06	50.51	25.69	-22	1.668E+04	-22	1.396E+05	3.948E+04	0.42	3.54	miss 2b, r=-1 box w/5 subcycles
	2		0.108	-0.308	0.414	-0.03	-51.83	25.42								
	3		0.107	-0.305	-0.417	-0.14	-50.65	-26.14								
	4		-0.107	0.306	-0.416	0.02	51.58	-25.50								
	5		-0.106	0.301	0.414	0.13	50.09	26.00								
	6		-0.106	0.302	-0.106	0.13	50.24	-6.52								
	7		-0.106	0.300	0.400	0.13	50.07	25.99								

C.3   LIFE PREDICTION AND DISCUSSION

The goal of the experimental program was to identify a fatigue damage parameter useful for design. While there are a multitude of fatigue damage models, two will be examined as part of this report. Other researchers are conducting a more thorough review of fatigue damage models as another facet of this program. Without undue generalization, there are basically two types of critical plane fatigue approaches: maximum principal stress or strain based and shear dominated. A modified biaxial version of the Smith-Watson-Topper (SWT) principal stress-strain based parameter (a square root and normalization of the stress by dividing by the elastic modulus is the original form proposed by Smith-Watson and Topper (Ref. 7)) follows,

$$\frac{\Delta \varepsilon}{2}\, \sigma_{max} = AN_f^{\,b} + CN_f^{\,d} = Damage \,. \tag{C6}$$

$$\varepsilon_a \sigma_{max} = 223.5 N_f^{-0.6840} + 0.1861 N_f^{-0.0078}$$
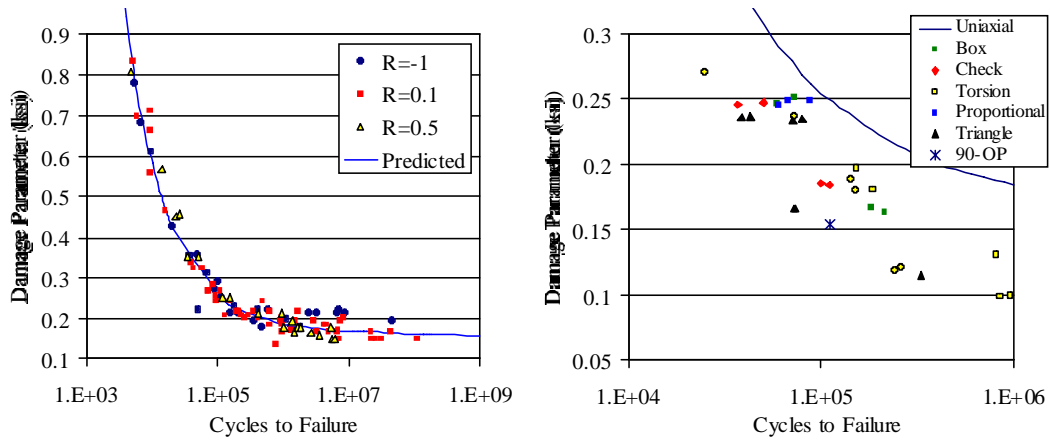
Figure C15. SWT uniaxial and biaxial data (Kallmeyer).

$$\tau_a + k\sigma_{max} = 7191N_f^{-0.6347} + 52.90N_f^{-0.0186} \quad (k = 0.379)$$
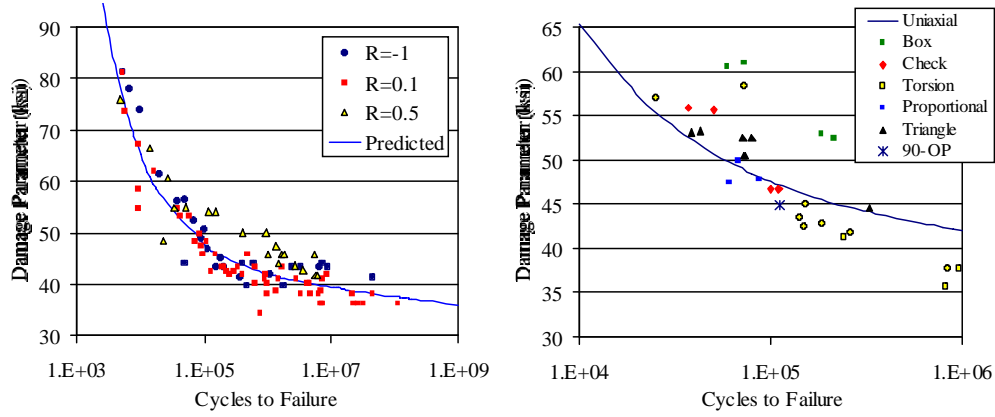
Figure C16. Findley uniaxial and biaxial data (Kallmeyer).

For a shear-based parameter, the Findley (Ref. 8-9) formulation was chosen.

$$\frac{\Delta\tau}{2} + k\sigma_{max} = AN_f^{b} + CN_f^{d} = Damage \tag{C7}$$

Both of the parameters are interpreted as the critical plane being that which has the highest value of damage, rather than the maximum of any individual term. This has more implications when considering Equation C7 than the SWT approach. Collapsing the uniaxial load ratio data is the approach employed to fit either parameter's constants. Constants obtained by Prof. Alan Kallmeyer from the experimental deformation and associated life predictions are shown in Figures C15 and C16. These constants should **not** be confused with the traditional strain life constants. As shown in Phase 1, a shear-based parameter provides a better representation for the range of data, even though the SWT parameter collapsed the uniaxial load ratio data very efficiently. Furthermore, the SWT parameter provides non-conservative life estimates for the majority of the multiaxial tests.

Figures C15 and C16 are based on experimental deformation. The predicted lives in Table C5 are based on the elastic-plastic deformation analysis reported in the same table, rather than the experimental deformation. These data are not identical to that plotted in Figures C15 and C16, which are based on experimentally measured deformations. Finally,

Figures C17 and C18 view various data sets within the context of a lognormal distribution. The basis for comparison for these calculations was the ratio of predicted to experimental values of the damage parameter. Tests that were predicted as runouts in Table C5 are not included in the comparison.
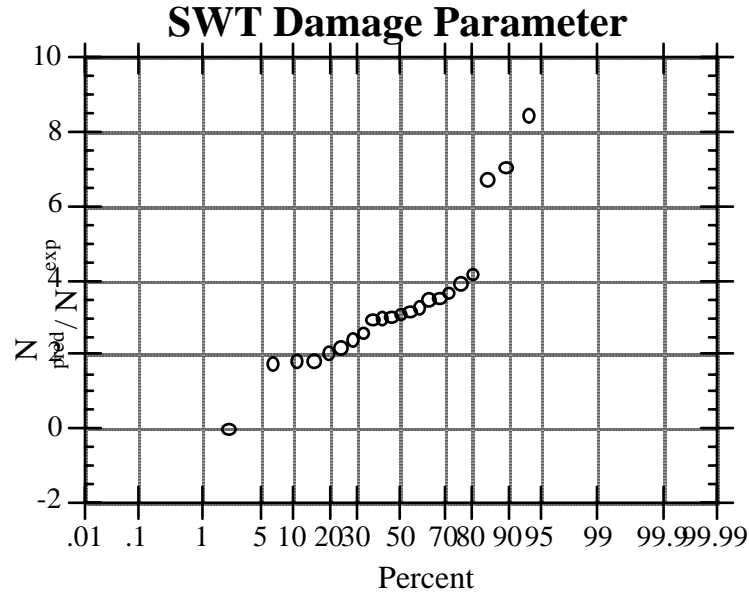
Figure C17. Lognormal presentation biaxial data with SWT parameter.
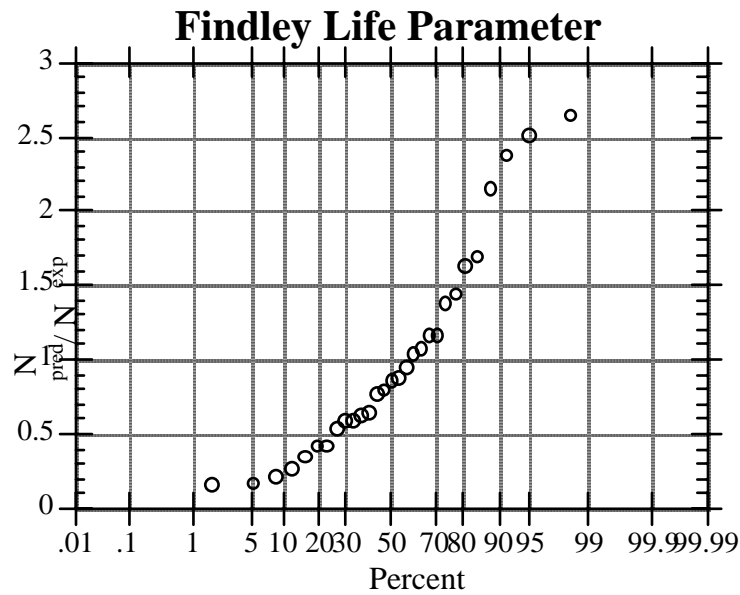
Figure C18. Lognormal presentation biaxial data with Findley parameter.

Current computational capabilities finally make implementation of the critical plane approach reasonable for realistic loadings. Of all the predictions, some of the most interesting are those for the "mission histories". The major cycle was chosen to be identical to those run at constant amplitude (~5 x10^4 cycles). The subcycle levels were chosen to give a life of approximately 10^8 cycles per event. With either 5 or 50 subcycles per block Miner's linear damage accumulation algorithm would predict almost no change in life. For the check path this hypothesis appears reasonable from the experimental data. However, the box mission history was detrimentally impacted by the presence of the subcycles, above and beyond that attributable to scatter in the fatigue data. This indicates that there are still some unresolved issues with regard to event interaction.

Minimal elevated temperature testing has been conducted. While the Findley critical plane parameter seems to provide the best overall representation of the experimental data at room temperature, its validity over the anticipated range of service (~0 to 450 ^{o}C) temperatures has not been ascertained. It would be desirable to somehow normalize the damage with regard to temperature, so that thermal fluctuations could be accommodated within the current fatigue event identification (rainflow counting) and subsequent damage assignment based on the event identified.

C.4   REFERENCES

1.   Ruschau, J.J., Nicholas, T. and Thompson, S.R., "Influence of Foreign Object Damage (FOD) on the Fatigue Life of Simulated Ti-6Al-4V Airfoils," International Journal of Impact Engineering, Vol. 25, pp. 233-250, 2001.

2.   Kurath, P. and Jiang, Y., "Analysis of Residual Stresses and Cyclic Deformation for Induction Hardened Components," SAE Technical Paper Series No. 950707, Society of Automotive Engineers, Warrendale, PA , 15 pp., 1995.

3.   Jiang, Y. and Kurath, P., "Characteristics of the Armstrong-Frederick Type Plasticity Models," International Journal of Plasticity, Vol. 12, No. 3, pp. 387-415, 1996.

4.   Jiang, Y. and Kurath, P., "A Theoretical Evaluation of the Incremental Plasticity Hardening Algorithms for Cyclic Non-proportional Loading," Acta Mechanica, Vol 118, pp. 213-234, 1996.

5.   Jiang, Y. and Kurath, P., "An Investigation of Cyclic Transient Behavior and Implications on Fatigue Life Estimates," ASME Transactions, Journal of Engineering Materials and Technology,Vol. 119, 1997.

6.   Jiang, Y. and Kurath, P., " Non-Proportional Cyclic Deformation: Critical Experiments and Analytical Modeling," International Journal of Plasticity, Vol. 13, No. 5, 1997.

7.   Smith, K. N., Watson, P. and Topper, T. H., "A Stress-Strain Function for the Fatigue of Metals," Journal of Materials, Vol. 5, No. 4, pp. 767-778, 1970.

8.   Findley, W.N., "A Theory for the Effect of Mean Stress on Fatigue of Metals Under Combined Torsion and Axial Loading or Bending," Journal of Engineering for Industry , pp. 301-306, 1959.

9.   Kurath,P., Jiang, Y. and Fatemi, A., "Strain Path Influence on Multiaxial Deformation and Fatigue Damage," Chapter 8-2, SAE AE-14++, Society of Automotive Engineers, Warrendale, PA, To be published May 1999.

APPENDIX D
MULTIAXIAL MODELING

D.1   INTRODUCTION

Despite the substantial amount of research that has been devoted to understanding the mechanisms associated with fatigue damage and the development of methods for modeling the evolution of this damage, fatigue failures continue to be a significant concern in engineering design. Historically, the majority of fatigue research has been directed towards experiments involving uniaxial stress states. This research has resulted in an improved understanding of the mechanisms associated with fatigue crack nucleation and propagation, a wealth of uniaxial test data, and reasonably reliable fatigue life prediction models for uniaxial loadings. However, many critical engineering components, such as crankshafts, axles, rotor and turbine blades, and notched components, are routinely subjected to multiaxial cyclic stress states. In many cases the loading is non-proportional or may involve multidimensional mean stresses. The successful design and analysis of such components requires that appropriate methods be available that can reliably estimate the fatigue life of materials under multiaxial states of stress.

Recently, increased emphasis has been placed on the development of robust fatigue models that are applicable to multiaxial stress states. Many of the classical multiaxial fatigue parameters utilize an effective-stress term with a possible modification for mean stress, which were developed in an era when the experiments were dominated by proportional loadings in the elastic regime (commonly referred to as high cycle fatigue, HCF). More recently, a number of critical-plane fatigue models have been proposed in the technical literature. However, most of these models were developed to fit data from common steel and aluminum alloys under loading conditions that result in significant plastic deformations (typically resulting in failures identified in the low cycle fatigue (LCF) regime) [1,2]. With the increasing use of high-performance materials in applications where high cycle fatigue conditions prevail and the loadings are often non-proportional, there is a pressing need to identify multiaxial fatigue models capable of predicting the long-term behavior of such materials. Since different damage mechanisms may be present under HCF and LCF

conditions, the simple extrapolation of data and extension of models from the LCF to the HCF regime may not suffice. A thorough and systematic effort is required to review, evaluate, and/or develop new or existing multiaxial fatigue models for use with advanced materials in the HCF regime.

This appendix presents the findings of a comprehensive study into the applicability and accuracy of a variety of multiaxial fatigue models in predicting the fatigue damage or life of common aircraft engine materials under complex loading conditions. A thorough review of the literature was conducted to identify multiaxial fatigue parameters that appeared promising for the types of load conditions experienced in aircraft engines. These parameters, which included both equivalent (effective)-stress and critical-plane approaches, were evaluated by comparing fatigue life/damage predictions to experimental uniaxial and biaxial fatigue data from two common titanium alloys, generated as part of the HCF program. The majority of the fatigue data used for model evaluations were obtained from Ti-6Al-4V at room temperature. However, some data were also available for Ti-6Al-4V at 500°F and Ti-17 at room temperature. A small number of biaxial notched specimen tests and simulated mission history tests on Ti-6Al-4V were also conducted to further evaluate the applicability of certain models under more severe loading conditions (stress gradients or variable loading).

D.2   MULTIAXIAL FATIGUE MODELS

A robust fatigue model must be capable of providing accurate life predictions, or allowable design stresses, under complex cyclic stress states, including non-proportional loadings. As the focus of this research was on HCF loading conditions, the multiaxial fatigue models considered here were primarily stress-based models, or models that could be modified to meet such conditions. Based on these criteria, a total of 22 multiaxial fatigue algorithms were selected for evaluation in this study. These models can be classified into two categories, which are described in the following paragraphs: (1) equivalent (effective) stress models and (2) critical-plane models.

The equivalent-stress models are essentially extensions of static yield criteria, such as the von Mises criterion, in which the multiaxial stresses are reduced to an equivalent cyclic scalar value. The equivalent stress history is then used in conjunction with uniaxial stress-

life data, along with an appropriate mean stress model (e.g., modified Goodman criterion), to predict the corresponding fatigue life. However, a difficulty arises with this type of procedure in the definition of a mean stress, which becomes vague within a multiaxial stress state. Consequently, these types of models have often had limited success when applied to complex loading histories. Nevertheless, due to their popularity, familiarity, and ease of implementation, several equivalent-stress based models were evaluated in this study.

The critical-plane models were developed in conjunction with phenomenological observations of fatigue crack development, where it has been found that fatigue cracks often nucleate on critical planes (such as planes of maximum alternating shear stress or strain). It has also been observed that secondary quantities, such as the normal stress or strain on the critical plane, can have an influence on the nucleation and progression of fatigue cracks. As a result, critical-plane damage parameters typically make use of some combination of normal and shear stresses or strains on a given plane. The critical-plane approaches currently appear to be receiving the most attention among active researchers because of their good correlation with multiaxial test data. Consequently, the majority of the models evaluated in this study were critical-plane models.

The models selected for evaluation in this study are briefly described in the following sections, and are shown in equation form in Table D1. The nomenclature used in these equations, and throughout the remainder of this report, is first summarized below.

D.2.1 Nomenclature

DP	Damage parameter, relating stress/strain components to fatigue life
N_f	Fatigue life (cycles)
A,b,C,d	Fatigue-life curve-fitting parameters
$\sigma_x, \sigma_y, \tau_{xy}$, etc.	Stress components, referred to specimen axes
$\sigma_1, \sigma_2, \sigma_3$	Principle stresses
σ_{eq}	Equivalent (effective) stress
σ_h	Hydrostatic stress
σ_a	Cyclic normal stress amplitude on critical plane or equivalent stress amplitude
σ_m	Cyclic normal mean stress on critical plane or equivalent mean stress
$\sigma_{m,vm}$	Multiaxial cyclic mean stress, using von Mises stress definition
$\sigma_{m,h}$	Multiaxial cyclic mean stress, using hydrostatic stress definition
R	Cyclic stress ratio ($\sigma_{min}/\sigma_{max}$ or τ_{min}/τ_{max})
σ_y	Tensile yield strength

σ_{ut}	Tensile ultimate strength
σ_f'	Axial fatigue strength coefficient
τ_f'	Torsional fatigue strength coefficient
MF	Multiaxiality factor
TF	Triaxiality factor
$\Delta\sigma_{psu}$	Alternating "pseudostress" range for modified Manson-McKnight model
β	Term defining the sign of the mean stress in modified Manson-McKnight model
τ_a	Cyclic shear stress amplitude on critical plane
τ_m	Cyclic shear mean stress on critical plane
τ_y	Torsional (shear) yield strength
τ_{ut}	Torsional (shear) ultimate strength
σ_{max}	Maximum normal stress on critical plane
τ_{max}	Maximum shear stress on critical plane
γ_a	Cyclic shear strain amplitude on critical plane
ε_a	Cyclic normal strain amplitude on critical plane
k	Adjustable material parameter for various fatigue models

D.2.2 Equivalent-Stress Models

Most equivalent stress models utilize the von Mises definition in the calculation of the alternating component of equivalent stress from a multiaxial cyclic stress state:

$$\sigma_{eq} = \frac{1}{\sqrt{2}}\left[\left(\sigma_x - \sigma_y\right)^2 + \left(\sigma_y - \sigma_z\right)^2 + \left(\sigma_z - \sigma_x\right)^2 + 6\left(\tau_{xy}^2 + \tau_{xz}^2 + \tau_{yz}^2\right)\right]^{1/2} \qquad (D1)$$

where the alternating component of each stress term is used in calculating the equivalent stress amplitude. This is the definition that causes the nuances of non-proportional loading to be neglected. To account for mean stress effects, the equivalent mean stress component can also be defined from Eq. D1 using each mean stress rather than an alternating component. However, the von Mises mean stress defined via Eq. D1 will always be positive. As it is well known that normal mean stresses are more damaging in tension than in compression, some have suggested the use of the hydrostatic component in the definition of the multiaxial mean stress [3]:

$$\sigma_h = \frac{\sigma_1 + \sigma_2 + \sigma_3}{3} \qquad (D2)$$

where σ_1, σ_2, and σ_3 are the mean principle stresses. Traditional uniaxial mean stress models include the Goodman, Gerber, and Soderberg relations [4]. These concepts are modified for multiaxial loadings by using both the von Mises definition for mean stress (models 1(a)-(c)) and the hydrostatic definition for mean stress (models 2(a)-(c)), as shown in Table D1. When using the von Mises definition, it is necessary to somehow differentiate between a tensile and compressive value of the equivalent multiaxial mean stress. Extending a method suggested by Sines and Ohgi [3], the sign of the equivalent mean stress term in this study was dictated by the sign of the hydrostatic mean stress.

An improvement to this type of approach has been suggested by Manson and Jung [5], who proposed using a multiaxiality factor, MF, which is a function of the principle stresses,

$$ MF = \frac{1}{2 - TF} \quad (TF \le 1) \quad \text{or} \quad MF = TF \quad (TF > 1) \tag{D3} $$

where

$$ TF = \frac{\sqrt{2}(\sigma_1 + \sigma_2 + \sigma_3)}{\left[(\sigma_1 - \sigma_2)^2 + (\sigma_2 - \sigma_3)^2 + (\sigma_1 - \sigma_3)^2\right]^{1/2}} \tag{D4} $$

The quantities in Eq. D4 are maximum principle stresses. The original paper is unclear as to which quantities to use in this equation. Employing minimum principle or mean principle stresses in this equation changes the triaxiality factor, but not the overall trends of the method. This approach is shown as model 3 in Table D1.

The final equivalent stress model considered here is the modified Manson-McKnight (MMM) model [6,7] (model 4 in Table D1). This model uses an alternating "pseudostress" range, $\Delta\sigma_{psu}$, defined from Eq. D1 with the range of each stress component, and a maximum stress, σ_{max}, defined as the mean stress plus $0.5\Delta\sigma_{psu}$. The sign of the mean stress term in the MMM model is defined by multiplying Eq. D1 by the term $\beta/2$, where β is defined as

$$ \beta = \frac{\left(\sum \sigma_1 + \sum \sigma_3\right)}{\left(\sum \sigma_1 - \sum \sigma_3\right)} \tag{D5} $$

where $\Sigma\sigma_1$ and $\Sigma\sigma_3$ are the sum of the first and third principle stresses, respectively, at the maximum and minimum points in the cycle. As shown in Table D1, the pseudostress range and maximum stress values are modified by an exponent, w. This exponent is an adjustable material parameter that is optimally determined from a least-squares fit to the uniaxial data at all stress ratios tested; i.e., the value that best collapses all the uniaxial data into a single curve.

D.2.3   Critical-Plane Models

The critical-plane models investigated in this study are also shown in Table D1. For these models, all stress and strain components are defined on a particular (critical) plane. The critical-plane definition employed in this investigation is the plane experiencing the maximum value of the entire damage parameter, not an individual component.

The Morrow model, model 5, is a strain-based model commonly used to represent uniaxial data [8]. Although not originally intended for use as a critical-plane model, it can be interpreted as the critical plane being dependent on normal stress-strain quantities. In this study, the model was modified into a stress-based form that uses the stress amplitude (σ_a) and mean stress (σ_m) calculated on a given orientation, as shown in Table D1. The Smith, Watson, Topper (SWT) parameter [9], model 6, is another common strain-based uniaxial model. A similar interpretation utilizing the normal strain amplitude (ε_a) and the maximum normal stress (σ_{max}) as the relevant parameters in the calculation of the damage parameter was implemented. Models 7(a)-(c) are the Goodman, Gerber, and Soderberg relations, defined in terms of the normal stress amplitude, σ_a, and mean stress, σ_m, calculated on a given plane, rather than in terms of equivalent stresses. Conceptually they are similar to the Morrow model, except with an alternate measure of damage assigned to the mean stress. Models 8(a)-(c) mirror models 7(a)-(c), but are modified by replacing the normal stress components with shear stress components, τ_a and τ_m.

The rest of the critical-plane damage parameters investigated can be differentiated from the previously discussed models in that they involve stress and/or strain components from more than one direction for any given orientation. In some sense these parameters reflect the premise that crack nucleation and small crack growth is a mixed-mode

phenomenon. The Kandil, Brown, Miller (KBM) parameter [10], model 9, considers the maximum alternating shear strain (γ_a) to be the primary damage component on a plane, with the normal strain amplitude (ε_a) on this plane acting as a secondary damage component. Findley [11] considered the maximum alternating shear stress (τ_a) to be the primary damage component on a plane, with the maximum normal stress on this plane (σ_{max}), modified by an adjustable material parameter (k), acting as a secondary damage component, shown as model 10. The McDiarmid parameter [12], model 11, is similar to the Findley parameter, with k defined as a constant in terms of the material's ultimate strength (σ_{ut}). The Fatemi, Socie, Kurath (FSK) [13] model 12, assumes the maximum alternating shear strain (γ_a) is the primary damage component on a plane, with the maximum normal stress (σ_{max}) on this plane (modified by an adjustable parameter, k, and the material's yield strength, σ_y) acting as a secondary damage component. The designation of primary or secondary damage variable has more to do with cycle counting for more complex histories, than their relative importance in the damage computation.

The Chu, Conle, Bonnen (CCB) parameter [14], is an extension of the SWT parameter, in which a shear term ($2\gamma_a\tau_{max}$) is added to the normal stress/strain term. This parameter can be considered to represent a portion of the strain energy, as it involves the multiplication of corresponding stress and strain components. In this study, a slight modification was made to the CCB hypothesis, model 13, by multiplying the second term ($\varepsilon_a\sigma_{max}$) by an empirical factor, k, to allow for an adjustment in the influence of this term. It was found that this modification significantly improved the accuracy of this model. Another similar type of parameter, but one which considers only the shear component of energy, was defined by Glinka, Wang, and Plumtree (GWP), model 14 [15]. This parameter is defined as the product of the shear strain amplitude (γ_a) and shear stress amplitude (τ_a) on a plane, and a mean stress modification with terms involving the maximum shear and normal stresses (τ_{max} and σ_{max}) on that plane. σ_f' and τ_f' are baseline strain-life fatigue constants obtained from uniaxial or torsional fatigue data.

Table D1. Multiaxial Fatigue Models

Model	Damage Parameter $DP = f(N_f) = A(N_f)^b + C(N_f)^d$
Equivalent-Stress Models	
1a) Goodman (v. Mises mean stress) [4]	$\sigma_a\left[1-\left(\sigma_{m,vm}/\sigma_{ut}\right)\right]^{-1} = f(N_f)$
1b) Gerber (v. Mises mean stress) [4]	$\sigma_a\left[1-\left(\sigma_{m,vm}/\sigma_{ut}\right)^2\right]^{-1} = f(N_f)$
1c) Soderberg (v. Mises mean stress) [4]	$\sigma_a\left[1-\left(\sigma_{m,vm}/\sigma_y\right)\right]^{-1} = f(N_f)$
2a) Goodman (hydrostatic mean stress)[4]	$\sigma_a\left[1-\left(\sigma_{m,h}/\sigma_{ut}\right)\right]^{-1} = f(N_f)$
2b) Gerber (hydrostatic mean stress) [4]	$\sigma_a\left[1-\left(\sigma_{m,h}/\sigma_{ut}\right)^2\right]^{-1} = f(N_f)$
2c) Soderberg (hydrostatic mean stress)[4]	$\sigma_a\left[1-\left(\sigma_{m,h}/\sigma_y\right)\right]^{-1} = f(N_f)$
3) Multiaxiality factor [5]	$\sigma_a = \dfrac{A}{MF^{b/d}}(N_f)^b + \dfrac{C}{MF}(N_f)^d$
4) Modified Manson-McKnight [6, 7]	$\dfrac{1}{2}\Delta\sigma_{psu}^{1-w}\sigma_{max}^{w} = f(N_f)\quad(w = 0.433)$
Critical-Plane Models	
5) Morrow [8]	$\sigma_a\left[1-\left(\sigma_m/\sigma_f'\right)\right]^{-1} = f(N_f)$
6) Smith-Watson-Topper [9]	$\varepsilon_a\sigma_{max} = f(N_f)$
7a) Goodman (normal stress)	$\sigma_a\left[1-\left(\sigma_m/\sigma_{ut}\right)\right]^{-1} = f(N_f)$
7b) Gerber (normal stress)	$\sigma_a\left[1-\left(\sigma_m/\sigma_{ut}\right)^2\right]^{-1} = f(N_f)$
7c) Soderberg (normal stress)	$\sigma_a\left[1-\left(\sigma_m/\sigma_y\right)\right]^{-1} = f(N_f)$
8a) Goodman (shear stress)	$\tau_a\left[1-\left(\tau_m/\tau_{ut}\right)\right]^{-1} = f(N_f)$
8b) Gerber (shear stress)	$\tau_a\left[1-\left(\tau_m/\tau_{ut}\right)^2\right]^{-1} = f(N_f)$
8c) Soderberg (shear stress)	$\tau_a\left[1-\left(\tau_m/\tau_y\right)\right]^{-1} = f(N_f)$
9) Kandil-Brown-Miller [10]	$\gamma_a + \varepsilon_a = f(N_f)$
10) Findley [11]	$\tau_a + k\sigma_{max} = f(N_f)$
11) McDiarmid [12]	$\tau_a\left[1-\left(\sigma_{max}/2\sigma_{ut}\right)\right]^{-1} = f(N_f)$
12) Fatemi-Socie-Kurath [13]	$\gamma_a\left[1+k\left(\sigma_{max}/\sigma_y\right)\right] = f(N_f)$
13) Chu-Conle-Bonnen [14]	$2\gamma_a\tau_{max} + k\varepsilon_a\sigma_{max} = f(N_f)$
14) Glinka-Wang-Plumtree [15]	$\gamma_a\tau_a\left[\left(1-\tau_{mx}/\tau_f'\right)^{-1} + \left(1-\sigma_{mx}/\sigma_f'\right)^{-1}\right] = f(N_f)$

The models shown in Table D1 were evaluated based on their ability to correlate both the uniaxial and multiaxial test data. Note that each of these models is expressed in the form of a "damage parameter" (DP) that may include some mean stress modification. This parameter is then related to the fatigue life, N_f, by a mathematical function that provides an adequate representation of the data. Historically, fatigue data have often been fit with a power-law type of expression. Due to the broad range of data (LCF and HCF) available for the titanium alloys considered in this study, a generic two-term power-law expression was adopted to provide greater flexibility in the fitting of the data. This expression took the following form:

$$DP = A(N_f)^b + C(N_f)^d \tag{D6}$$

The constants A, b, C, and d are curve-fitting (least squares) parameters. Although this expression is similar in form to the conventional strain-life equation, no attempt was made here to relate A, b, C, and d to the strain-life constants σ_f', ε_f', b, and c. The details of the fatigue data, implementation methodologies, and corresponding results and comparisons, are discussed in following sections.

D.3   FATIGUE DATA (Ti-6Al-4V)

The models described in the previous section were initially evaluated using fatigue data generated in the HCF program for Ti-6Al-4V at room temperature (RT). Subsequent model evaluations included Ti-6Al-4V data at 500°F and Ti-17 data at RT. Details regarding microstructural aspects of the titanium alloys, specimen machining, and test procedures can be found elsewhere in the report. A summary of the pertinent RT data for Ti-6Al-4V required for the model evaluations is included here.

D.3.1   Uniaxial Data for Ti-6Al-4V at Room Temperature

Over 100 data points from uniaxial fatigue tests of Ti-6Al-4V at RT were obtained. These tests were conducted by P&W, GEAE, and ASE, and included both stress-controlled (HCF) and strain-controlled (LCF) tests at ratios of R = −1, 0.1, and 0.5. The experimental fatigue lives ranged from approximately 5000 to 1×10^9 cycles. Test frequencies ranged from

0.33 Hz (strain-controlled, short life tests) to 1000 Hz (load-controlled, long life tests). Although these frequencies are very high, minimal specimen heating was observed during testing. Further, the data generated in this program suggest that the fatigue life of Ti-6Al-4V does not significantly depend on frequency within the range tested.

The uniaxial fatigue data are shown in Figure D1. There is a very smooth transition between the strain-controlled and stress-controlled data, indicating primarily linear-elastic behavior within the region of data overlap. The concurrence of the data in the overlap region also indicates that crack nucleation rather than long crack growth dominates in this region. It is also worth noting that there is a distinct separation in the data between the stress ratios tested, particularly at longer fatigue lives. Clearly, the presence of a tensile mean stress significantly alters the allowable stress amplitude for Ti-6Al-4V. The fully-reversed uniaxial data were used to provide a baseline reference for comparison of the multiaxial fatigue models, and to further evaluate their capabilities when mean stresses occur. Note that, in this study, no step-test data were used in evaluating the models.
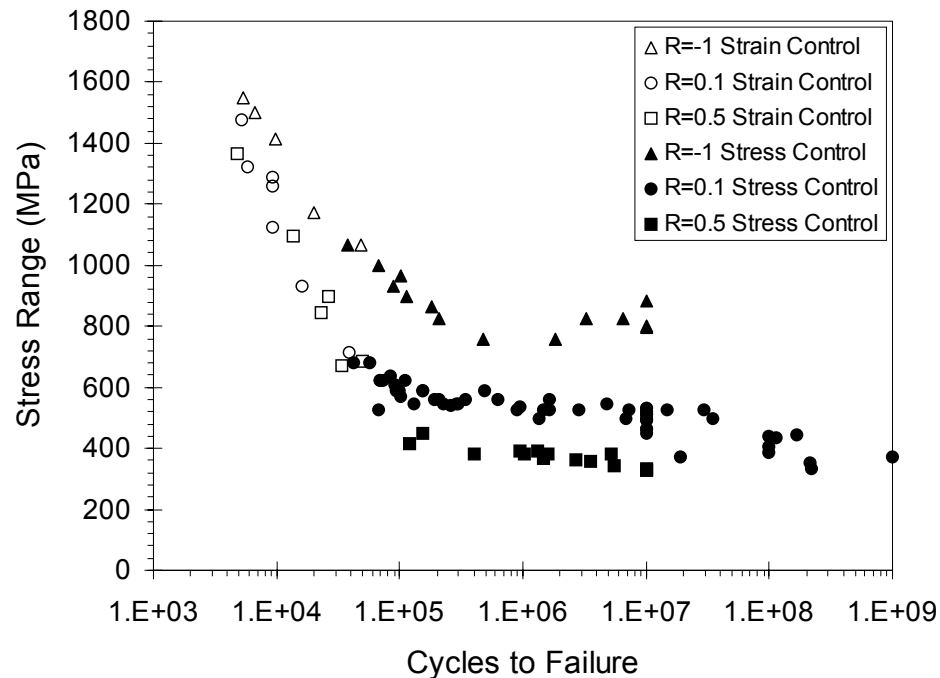
Figure D1. Uniaxial fatigue data for Ti-6Al-4V at RT.

D.3.2 Biaxial Data for Ti-6Al-4V at Room Temperature

The RT biaxial fatigue data for Ti-6Al-4V, generated by the University of Illinois, are summarized in Table D2, grouped according to type of test. For each test, the pertinent "corner" points of the cycle are included. The first group of tests in the table (21-11 to 21-4) represents torsion-only experiments at various stress ratios. These tests were performed to ascertain whether mean shear stresses influence fatigue lives. A common assumption that torsional mean stresses do not affect fatigue lives was a result of investigations at loading levels close to the endurance limit for low carbon steels. However, it has been reported that when the maximum shear stress (the mean plus alternating) exceeds about 80% of the torsional yield strength, the allowable stress amplitude in bending or torsion is reduced relative to the fully-reversed case. For levels of maximum stress less than 80% of the torsional yield strength, a static or mean shear stress has little effect on the fatigue strength of metals [3]. To determine the effects of mean shear stresses on the fatigue behavior of Ti-6Al-4V, torsion tests were conducted at stress ratios (τ_{min}/τ_{max}) of R = −1, 0.1, and 0.5.

The next three tests (21-1 to 156-3) represent proportional, combined axial-torsion experiments. These tests were utilized to evaluate the combined mean stress performance of the damage parameters, where the torsional mean stresses would be considered damaging on the basis of the previous set of experiments. The remaining tests are non-proportional and some include multidimensional mean stresses. These load paths are illustrated in Figure D2. Specimen 156-8 was loaded 90 degrees out-of-phase (circle path); that is, a 90º sinusoidal lag between the shear and axial strain. This load path is often considered to be critical with regard to deformation and fatigue damage [1, 16]. Specimens 156-2 through 21-10 were loaded in a triangle path (or certain segments), an out-of-phase approximation of service conditions. Specimens 142-8 through 178-8 were loaded in a box path, which is representative of the stress state produced near the edge-of-contact region in fretting fatigue simulations. The remaining specimens were loaded in a check path, another approximation of observed service events.

The definition of failure used in the biaxial test program was specimen separation, which was identical with that used in the uniaxial test program. Examination of the load/torque response from the strain-controlled biaxial tests revealed that the life fraction at

which load shedding occurred at the end of the tests was less than 5% of the total life in all cases. Torsion-only tests displayed the highest fraction (i.e., 5%), while combined loading tests were always lower. While the onset of these compliance changes does not indicate that no cracks were present prior to fracture, it may at least be assumed that the cracks were small relative to the gage section diameter of the biaxial specimens. Gage section diameters of the biaxial and uniaxial specimens were within a factor of two, indicating that small crack nucleation, rather than long crack growth, dominated the fatigue lives for both sets of specimens within the life regime considered.

The stresses and strains reported in Table D2 represent stabilized, half-life values on the outer surface of the specimen. Most specimens experienced only elastic strains during the cyclic loading. For these specimens, the values of σ and τ reported in Table D2 were obtained analytically from measured load and torque values. However, a few specimens did incur plastic strains on the first reversal. An elastic-plastic finite element analysis was performed for those tests. This analysis used a multilinear kinematic hardening rule with a Ramberg-Osgood representation of the cyclic stress-strain curve. The resulting stresses obtained from the finite element analysis, which were used in this study, are shown in Table D2. The material properties used in the analysis are shown below.

Modulus of elasticity	$E = 16{,}870$ ksi
Poisson's ratio	$\nu = 0.349$
Cyclic strain hardening coefficient	$K' = 124$ ksi
Cyclic strain hardening exponent	$n' = 0.0149$
Cyclic yield strength	$\sigma_y' = 109.2$ ksi
Monotonic yield strength	$\sigma_y = 134.9$ ksi
Ultimate strength	$\sigma_{ut} = 141.8$ ksi

It should be noted that the presence of an elastic-plastic boundary within the specimen induces additional stresses near the interface due to the difference in dilatation between the elastic and plastic regions in the material. In the specimens tested in this study, the plastic deformations were small, and the finite element analysis took into account these additional stresses.

Table D2. Biaxial Fatigue Data for Ti-6Al-4V at RT

Spec ID	ε (%)	γ (%)	σ (ksi)	τ (ksi)	Life (N_f)	Test Type
21-11	0.000	0.866	0.00	54.50	72,141	R = -1 Torsion
	0.000	-0.868	0.00	-54.63		
21-6	0.000	0.614	0.00	38.64	241,250	R = -1 Torsion
	0.000	-0.61	0.00	-38.39		
156-10	0.000	0.559	0.00	35.18	961,806	R = -1 Torsion
	0.000	-0.563	0.00	-35.43		
142-5	0	0.62	0.00	39.02	260,657	R = -1 Torsion
	0	-0.62	0.00	-39.02		
178-3	0	0.56	0.00	35.24	843,404	R = -1 Torsion
	0	-0.559	0.00	-35.18		
142-9	0	1.25	0.00	64.40	184,669	R = 0.1 Torsion
	0	0.125	0.00	-5.72		
21-7	0.000	1.810	0.00	65.93	30,007	R = 0.1 Torsion
	0.000	0.166	0.00	-36.53		
156-5	0.000	1.210	0.00	64.17	150,293	R = 0.1 Torsion
	0.000	0.090	0.00	-5.63		
156-4	0.000	1.360	0.00	65.02	151,598	R = 0.1 Torsion
	0.000	0.150	0.00	-10.39		
156-1	0.000	0.958	0.00	60.29	814,753	R = 0.1 Torsion
	0.000	0.086	0.00	5.41		
142-9	0	1.25	0.00	64.40	184,669	R = 0.1 Torsion
	0	0.125	0.00	-5.72		
21-4	0.000	1.960	0.00	66.08	141,229	R = 0.5 Torsion
	0.000	0.815	0.00	-5.28		
21-1	0.312	0.416	52.98	26.18	67,965	R = -1 Proportional
	-0.312	-0.418	-52.98	-26.31		
156-9	0.462	0.616	78.45	38.77	60,514	R = 0.1 Proportional
	0.0486	0.055	8.25	3.46		
156-3	0.464	0.621	78.79	39.08	87,920	R = 0.1 Proportional
	0.0476	0.055	8.08	3.46		
156-2	0.362	0	61.47	0.00	38,355	Triangle Path
	-0.373	0.471	-63.34	29.64		
	-0.373	-0.476	-63.34	-29.96		
21-2	0.364	0	61.81	0.00	43,009	Triangle Path
	-0.372	0.471	-63.17	29.64		
	-0.372	-0.477	-63.17	-30.02		
21-9	0.364	0.004	61.81	0.25	71,358	Triangle Path (top leg)
	-0.364	0.475	-61.81	29.89		
21-5	0.365	-0.0045	61.98	-0.28	79,367	Triangle Path (bottom leg)
	-0.363	-0.475	-61.64	-29.89		
21-8	0.091	0.666	15.37	41.92	72,124	Triangle Path (right leg)
	0.089	-0.665	15.16	-41.85		

21-3	0.090	0.666	15.28	41.92	90,988	Triangle Path (right leg)
	0.089	-0.666	15.11	-41.92		
21-10	-0.089	0.665	-15.11	41.85	329,058	Triangle Path (left leg)
	-0.091	-0.664	-15.45	-41.79		
156-8	0.000	0.406	0.00	25.39	111,783	Circle Path
	0.303	0.000	51.12	0.00		
	0.000	-0.409	0.00	-25.57		
	-0.302	0.000	-50.95	0.00		
142-8	0.3045	0.4174	51.70	26.27	59,432	$R_\epsilon = R_\gamma = -1$ Box Path
	-0.3044	0.4154	-51.69	26.14		
	-0.3038	-0.4155	-51.59	-26.15		
	0.3063	-0.4158	52.01	-26.17		
178-7	0.308	0.4153	52.30	26.14	72,360	$R_\epsilon = R_\gamma = -1$ Box Path
	-0.309	0.4159	-52.47	26.17		
	-0.3079	-0.4138	-52.28	-26.04		
	0.3103	-0.4159	52.69	-26.17		
142-11	0.1598	0.4165	27.13	26.21	182,149	$R_\epsilon = -3$, $R_\gamma = -1$ Box Path
	-0.4583	0.4163	-77.82	26.20		
	-0.4578	-0.4165	-77.73	-26.21		
	0.1605	-0.4163	27.25	-26.20		
178-8	0.1545	0.4169	26.23	26.24	212,337	$R_\epsilon = -3$, $R_\gamma = -1$ Box Path
	-0.4545	0.4168	-77.17	26.23		
	-0.4539	-0.4162	-77.07	-26.19		
	0.1558	-0.4161	26.45	-26.19		
178-12	0.0094	0.0083	-3.26	-12.17	50,568	$R = 0$ Check Path
	0.297	0.8205	45.58	38.45		
	0.1563	1.217	21.68	63.16		
	0.2976	0.8254	45.68	38.76		
178-1	0.009	0.0085	-3.26	-12.21	36,920	$R = 0$ Check Path
	0.2976	0.8217	45.75	38.48		
	0.1521	1.219	21.04	63.24		
	0.2979	0.8257	45.80	38.73		
178-11	0.007	0.0056	1.19	0.35	109,848	$R = 0$ Check Path
	0.239	0.64	40.58	40.28		
	0.12	0.957	20.38	60.23		
	0.238	0.641	40.41	40.34		
178-5	0.0075	0.0054	1.27	0.34	99,418	$R = 0$ Check Path
	0.239	0.64	40.58	40.28		
	0.1223	0.956	20.77	60.17		
	0.2385	0.646	40.50	40.66		
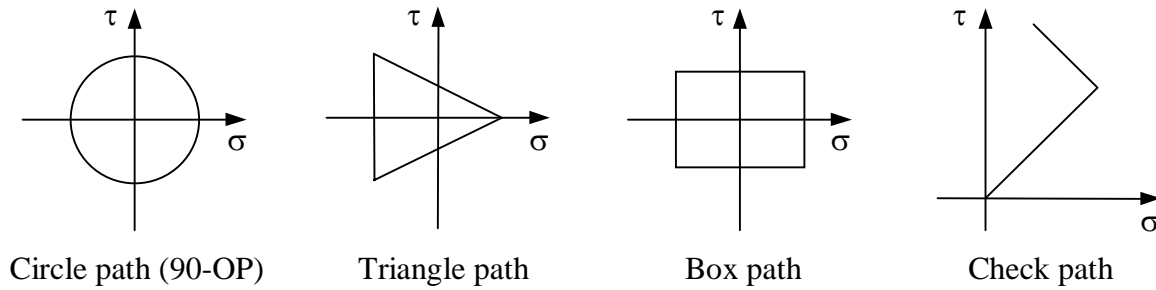
Figure D2. Non-proportional biaxial load paths.

D.4   IMPLEMENTATION OF MODELS

The multiaxial fatigue models were evaluated based on their ability to correlate both the uniaxial and multiaxial fatigue data. This was accomplished by calculating the damage parameter for each model (shown as the left-hand side of the equations in Table D1), from the stress and strain values associated with each of the experimental tests. The calculated damage parameters were then plotted vs. the corresponding experimental fatigue lives. An effective fatigue model (damage parameter) can be considered to be one that essentially collapses all the data (i.e., uniaxial data at different stress ratios and multiaxial data) into a single curve, assumed here to be of the form shown in Eq. D6. Traditionally, this curve would coincide with the uniaxial, fully-reversed (R = −1) fatigue data, which are often considered to represent the baseline fatigue behavior (zero mean stress). Since a successful parameter collapses all the load ratio data, the definition of baseline data being fully reversed is not required. Many critical plane parameters require data other than one stress state and/or load ratio to ascertain the adjustable constant. However, it may be useful to have the baseline load ratio mimic the perceived service load conditions.

D.4.1   Implementation for Uniaxial and Proportional Multiaxial Tests

The evaluation of the damage parameters for the uniaxial and proportional multiaxial tests was straightforward. The pertinent stress or strain components were calculated at the maximum and minimum points (reversal points) in the cycle. For the equivalent stress models, the principle stresses at the reversal points were calculated, from which the corresponding maximum and minimum equivalent stress values were determined. Next, the alternating and mean components of the equivalent stresses were calculated in the

conventional manner. The damage parameters were then calculated from the equivalent alternating and mean components using the equations in Table D1.

The critical plane models required implementation of stress and strain rotation procedures to identify the critical plane. Since all stress states were uniaxial or biaxial, a two-dimensional transformation was used to rotate the stresses and strains within the plane. The use of this simplification assumes that cracks would propagate perpendicular to the surface, into the specimen. This assumption was supported by observations made during the multiaxial test program [6].

To perform the stress transformations, the half-life stresses at the reversal points in the cycle were rotated onto planes at 1° increments, from 0° to 90°, using the following set of equations:

$$\sigma_{x'} = \frac{\sigma_x + \sigma_y}{2} + \frac{\sigma_x - \sigma_y}{2}\cos 2\phi + \tau_{xy}\sin 2\phi$$

$$\sigma_{y'} = \frac{\sigma_x + \sigma_y}{2} - \frac{\sigma_x - \sigma_y}{2}\cos 2\phi - \tau_{xy}\sin 2\phi \quad\quad\quad (D7)$$

$$\tau_{x'y'} = -\frac{\sigma_x - \sigma_y}{2}\sin 2\phi + \tau_{xy}\cos 2\phi$$

To transform the strains, the y-component of strain was first calculated as $\varepsilon_y = -\nu_{eff}\varepsilon_x$, where the effective Poisson's ratio is used to account for plasticity,

$$\nu_{eff} = \frac{\nu_e \varepsilon_e + \nu_p \varepsilon_p}{\varepsilon_t} \quad\quad\quad (D8)$$

The strains (at the reversal points in the cycle) were then rotated onto the same planes using the following equations:

$$\varepsilon_{x'} = \varepsilon_x \cos^2 \phi + \varepsilon_y \sin^2 \phi + \gamma_{xy}\sin\phi\cos\phi$$

$$\varepsilon_{y'} = \varepsilon_y \cos^2 \phi + \varepsilon_x \sin^2 \phi - \gamma_{xy}\sin\phi\cos\phi \quad\quad\quad (D9)$$

$$\gamma_{x'y'} = 2(\varepsilon_y - \varepsilon_x)\sin\phi\cos\phi + \gamma_{xy}(\cos^2 \phi - \sin^2 \phi)$$

From the maximum and minimum stress and strain components on each plane, the amplitude and mean of the shear and normal stresses and strains were calculated. The damage parameters for the critical plane models were then calculated on each plane, according to the equations in Table D1. In this study, the critical plane was defined to be the plane experiencing the maximum value of the damage parameter, rather than the maximum value of a particular stress or strain component. The value of the damage parameter on the critical plane was then used in the evaluation of the model.

D.4.2 Implementation for Non-proportional Multiaxial Tests

The implementation of the fatigue models for the non-proportional multiaxial tests was more involved, since the individual stress and strain components did not reach maximum values at the same time (i.e., the principle stress directions rotated during the cycle). As a result, a "time-stepping" or incremental procedure was implemented, in which each loading cycle was discretized into 20 to 30 increments. At each increment, the applied stress and strain components were specified. The applied stress histories were then used to calculate the damage parameters, as described below.

For the equivalent stress models, the principle stresses were calculated at each increment. The principle stresses were then used to calculate the equivalent stresses at each point. Next, the maximum and minimum values of the equivalent stresses during the cycle were identified, and the alternating and mean values were then determined in the conventional manner. In the calculation of the mean stress using the von Mises criterion, the sign of the stress was defined to be the same as the sign of the mean hydrostatic stress. The damage parameters, as shown in Table D1, were then calculated from these alternating and mean components.

For the critical plane models, the same stress and strain transformation equations previously listed were used to calculate the stress and strain components on planes at 2° increments from 0° to 90° (rotated about a line perpendicular to the surface of the specimen). These components were calculated at each time-increment on each plane. The maximum and minimum values of normal and shear stress and strain were determined on each plane, from which the alternating and mean components were calculated. The damage parameters for

each of the critical plane models were then determined on each plane, and the critical plane was identified as the plane with the maximum value of the damage parameter.

D.5   MODEL EVALUATIONS USING RT Ti-6Al-4V DATA

D.5.1   Preliminary Model Comparisons

A preliminary assessment of the models listed in Table D1 was performed using the RT Ti-6Al-4V data listed in Section D.3. This preliminary assessment was performed to identify the multiaxial parameters that possessed a reasonable ability to collapse both the uniaxial and biaxial data sets. Those models would subsequently be considered for more detailed evaluation using additional data sets. At the time the preliminary assessments were made, not all the biaxial data listed in Table D2 were available (only one of the non-proportional check path tests had been performed). Thus, the preliminary assessments evaluated the ability of the models to collapse the uniaxial data (at various stress ratios) and available biaxial data (torsion, proportional, and non-proportional) to the fully-reversed uniaxial baseline.

A broad qualitative summary of the results of the preliminary evaluation is provided in Table D3. Three measures of the adequacy of each model at correlating the fatigue data are shown. In the second column, the ability of each model to correlate the uniaxial data (i.e., collapse the data for each stress ratio onto the fully-reversed curve) is rated using a simple good/fair/poor scale. The last two columns summarize the ability of the models to correlate the biaxial data to the baseline curve, in terms of two indicators. The first indicator (mean) gives a measure of how well the data were centered about the baseline curve; i.e., if the data were roughly centered about the curve, or if the data tended to fall below (low) or above (high) the baseline curve. This measure gives an indication of whether the model tends to be conservative (high) or non-conservative (low) when predicting the damage or fatigue life under a multiaxial state of stress. The last indicator (scatter) provides a qualitative measure of the degree of scatter or spread in the biaxial data about the mean.

Table D3. Preliminary Model Comparisons using RT Ti-6Al-4V Data

Model	Correlation of Uniaxial Data	Correlation of Biaxial Data	
		Mean	Scatter
Equivalent-Stress Models			
1a) Goodman (v. Mises mean stress)	Fair	Centered	High
1b) Gerber (v. Mises mean stress)	Poor	Centered	High
1c) Soderberg (v. Mises mean stress)	Fair	Centered	High
2a) Goodman (hydrostatic mean stress)	Poor	Centered	High
2b) Gerber (hydrostatic mean stress)	Poor	Centered	High
2c) Soderberg (hydrostatic mean stress)	Poor	Centered	High
3) Multiaxiality factor	Poor	Centered	High
4) Modified Manson-McKnight	Good	Centered	Moderate
Critical-Plane Models			
5) Morrow	Fair	Centered	Moderate
6) Smith-Watson-Topper	Fair	Low	Moderate
7a) Goodman (normal stress)	Fair	Low	Moderate
7b) Gerber (normal stress)	Poor	Low	Moderate
7c) Soderberg (normal stress)	Fair	Low	Moderate
8a) Goodman (shear stress)	Fair	High	High
8b) Gerber (shear stress)	Poor	Centered	High
8c) Soderberg (shear stress)	Fair	High	High
9) Kandil-Brown-Miller	Poor	High	Moderate
10) Findley	Good	Centered	Low
11) McDiarmid	Poor	Centered	Moderate
12) Fatemi-Socie-Kurath	Fair	Centered	Low
13) Chu-Conle-Bonnen	Fair	Centered	Moderate
14) Glinka-Wang-Plumtree	Poor	Centered	High

It is evident from the results shown in Table D3 that the critical plane models, in general, were more successful at correlating the broader spectrum of fatigue data than the equivalent stress models. Of the equivalent or effective stress models, only the modified Manson-McKnight formulation (model 4) provided a good correlation of the uniaxial data, and correlated the biaxial data with a moderate amount of scatter. Conversely, several critical plane models demonstrated some desirable characteristics, such as good or fair correlation of the uniaxial data coupled with low to moderate scatter in the biaxial data. The Findley, FSK, and modified CCB parameters all include a variable, k, which was taken to be a constant for the life range under consideration. It has been shown over a broader range of lives that k may vary [13, 17]. In the preliminary analysis, the optimal values of k for each

model were determined by an incremental procedure. For the Findley parameter, k was varied from 0.15 to 0.55, in increments of 0.05. For the FSK parameter, k was varied from 0.5 to 8.0 in increments of 0.1, while k was varied from 0.5 to 4.0, in increments of 0.1, for the modified CCB model. The optimal k values, which provided the best overall correlation of both the uniaxial and biaxial data, were found to be 0.35 for the Findley model, 6.0 for the FSK model, and 2.7 for the modified CCB model.

Upon consideration of the results shown in Table D3, six of the multiaxial models were selected for more detailed study. These models were chosen due to their good agreement with the experimental data, or because of their familiarity and frequent use in fatigue analysis. They also include sufficient breadth to illustrate the rating system forwarded in Table D3. The models selected for more detailed consideration were the modified Manson-McKnight (MMM) model (4), the SWT model (6), the Goodman critical plane model, based on normal stresses (7a), the Findley model (10), the FSK model (12), and the modified CCB model (13). The fatigue life/damage predictions for these models, in comparison to the experimental data, are presented graphically in Figures D3 – D8. Two plots are shown for each model, depicting (1) the uniaxial data for several stress ratios, and (2) the biaxial data compared to the uniaxial baseline. These were essentially the criteria that were employed to evaluate the parameters. Note that the curves in the plots represent the best fit to all of the stress ratios for the uniaxial data. These curves were generated by a least-squares fit to the entire set of uniaxial data, utilizing the two-term power law relationship between damage parameter and fatigue life shown in Eq. D6.
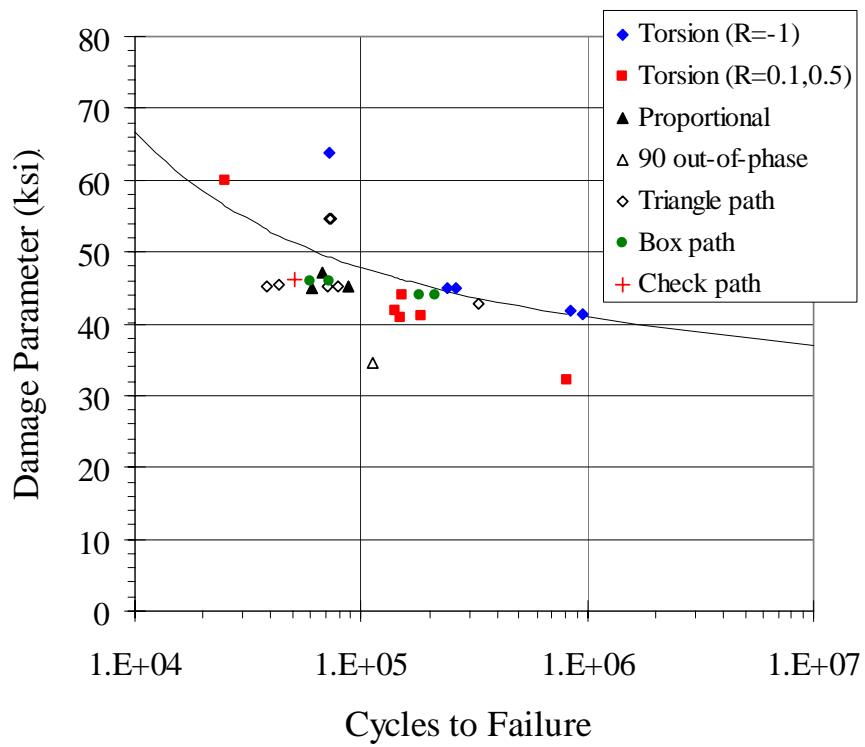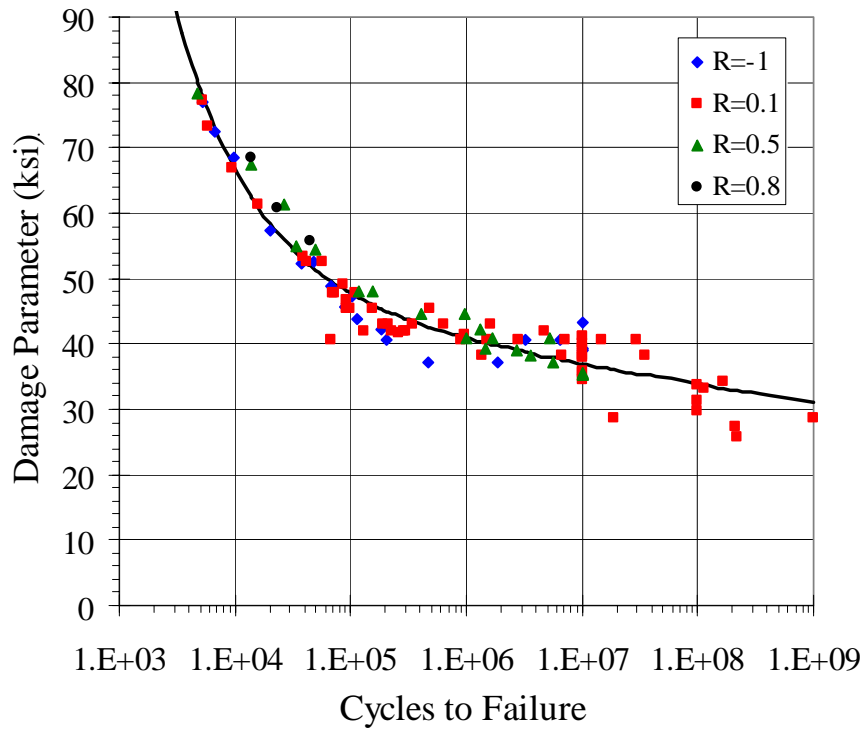
Figure D3. Modified Manson-McKnight model applied to
RT Ti-6Al-4V: (a) uniaxial data and (b) biaxial data.
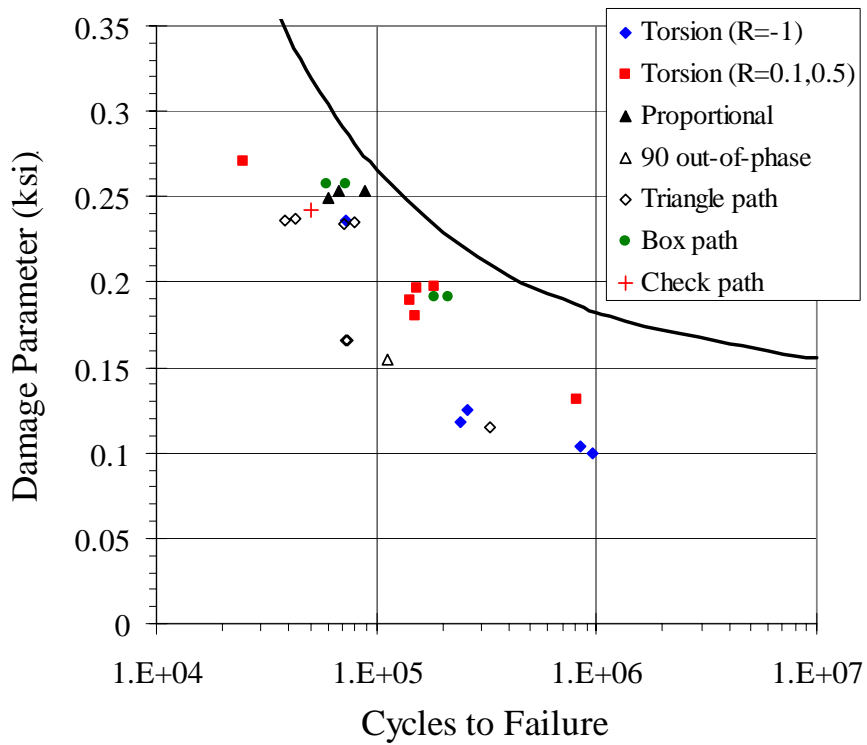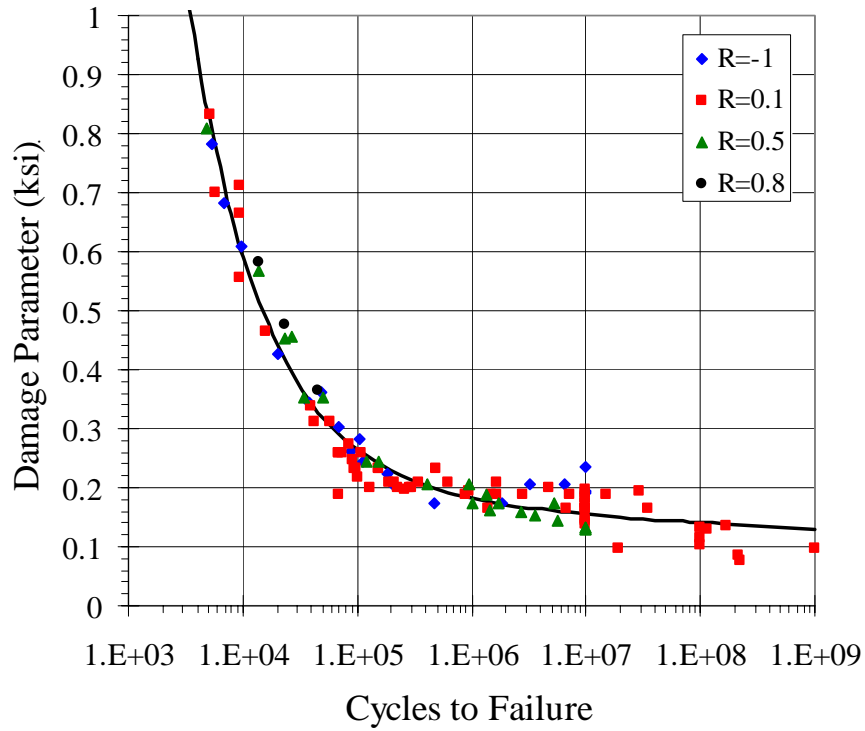
Figure D4. Smith-Watson-Topper (SWT) model applied to
RT Ti-6Al-4V: (a) uniaxial data and (b) biaxial data.
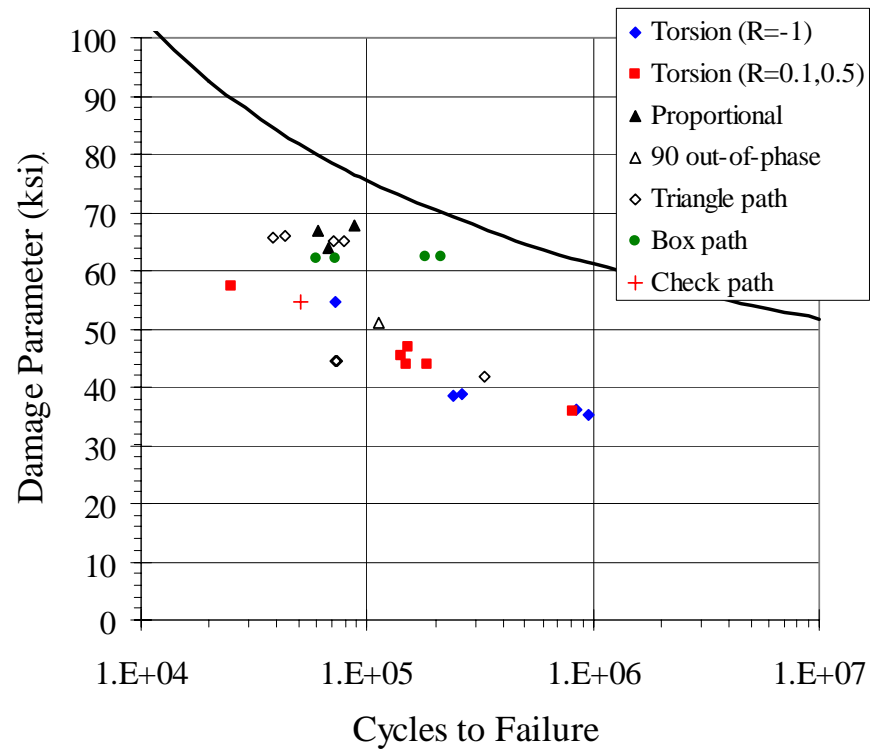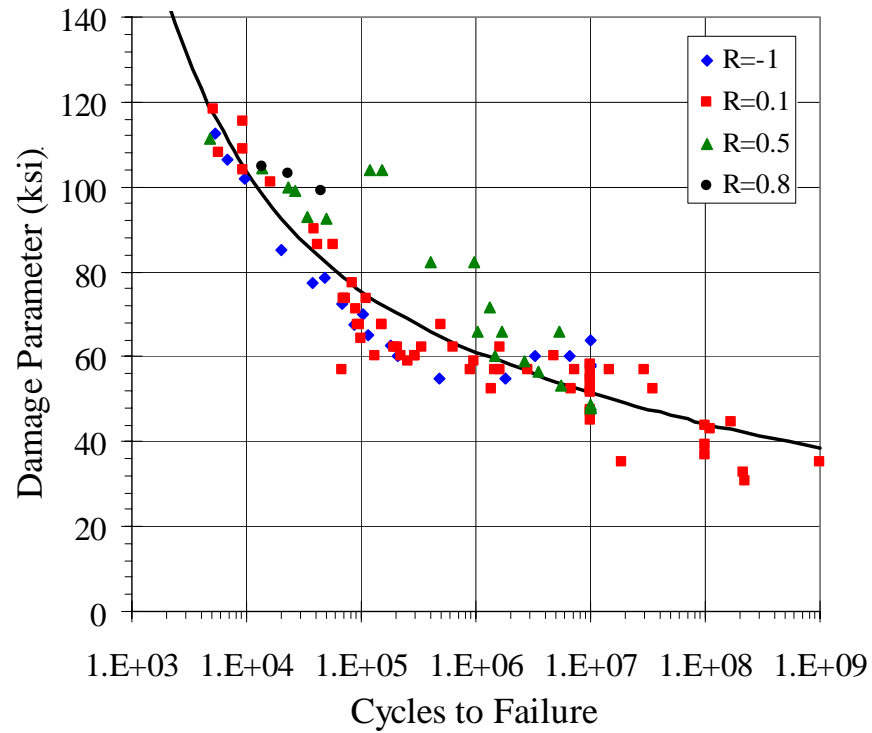
Figure D5. Goodman critical plane model (normal stresses) applied to RT Ti-6Al-4V: (a) uniaxial data and (b) biaxial data.
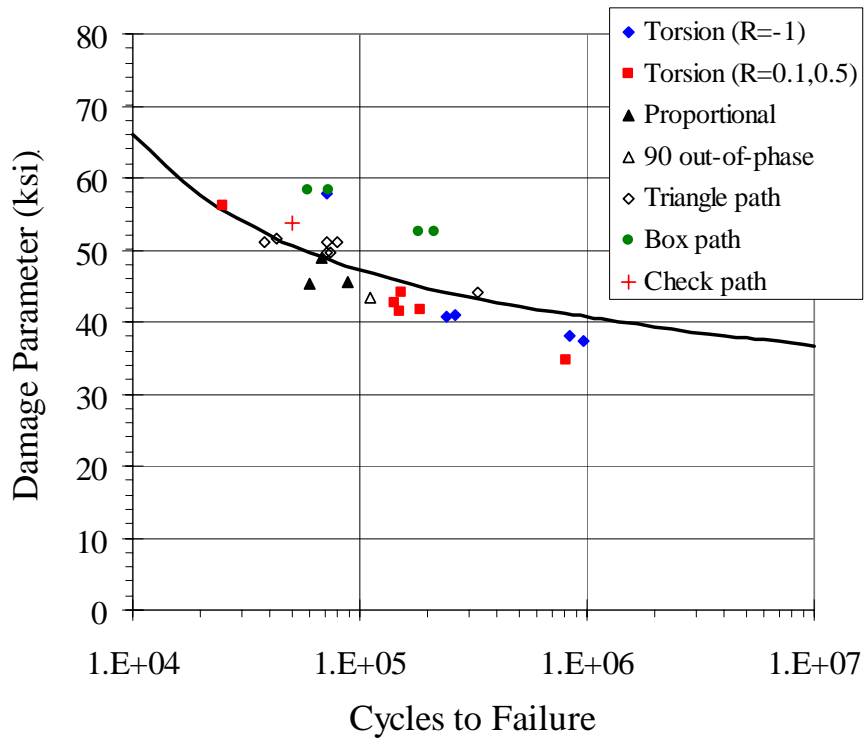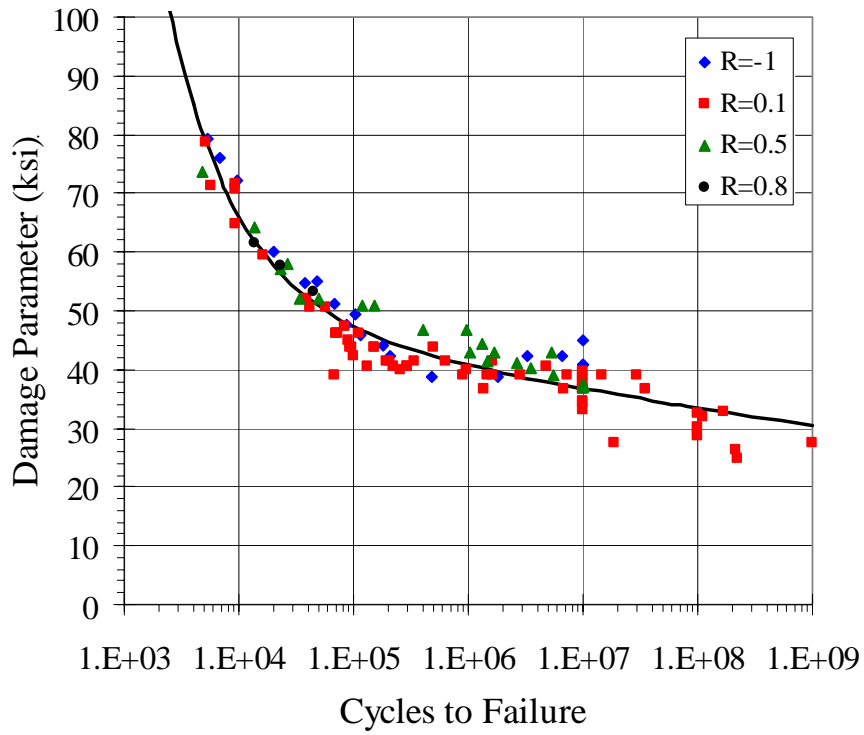
Figure D6. Findley model, with k = 0.35, applied to RT
Ti-6Al-4V: (a) uniaxial data and (b) biaxial data.
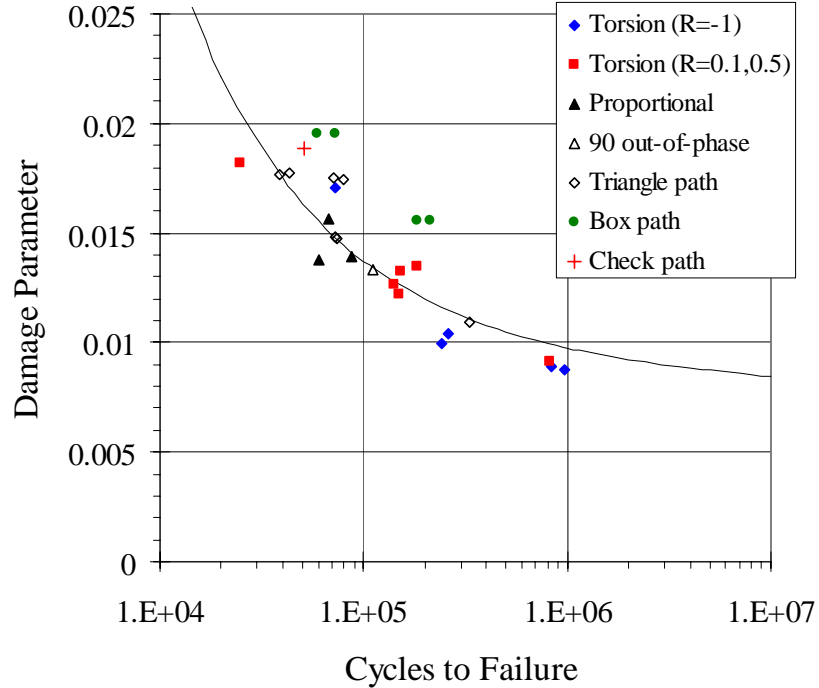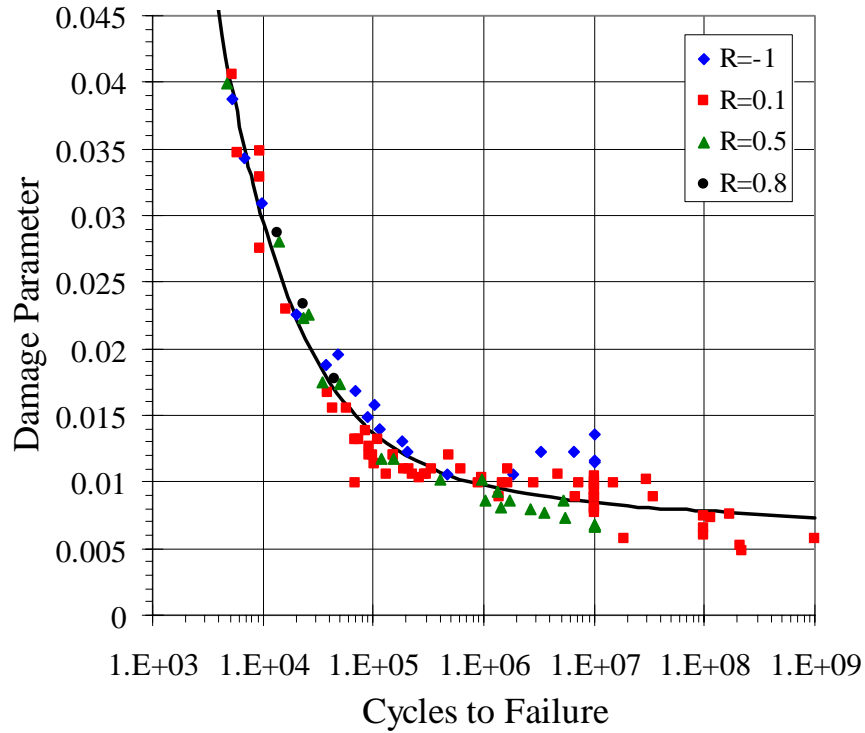
Figure D7. Fatemi-Socie-Kurath (FSK) model, with k = 6.0, applied
to RT Ti-6Al-4V:(a) uniaxial data and (b) biaxial data.
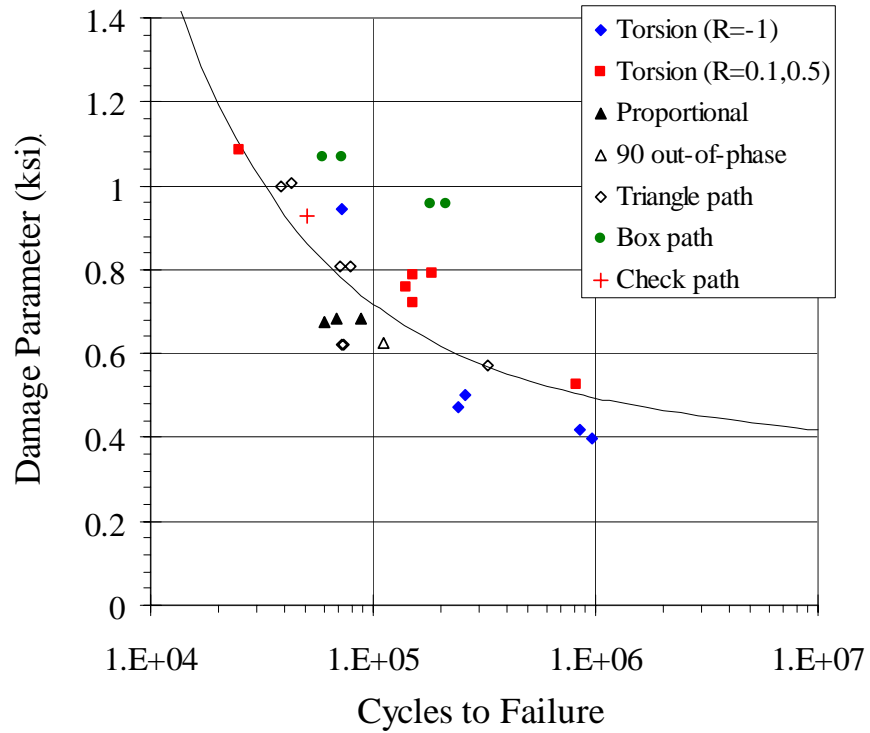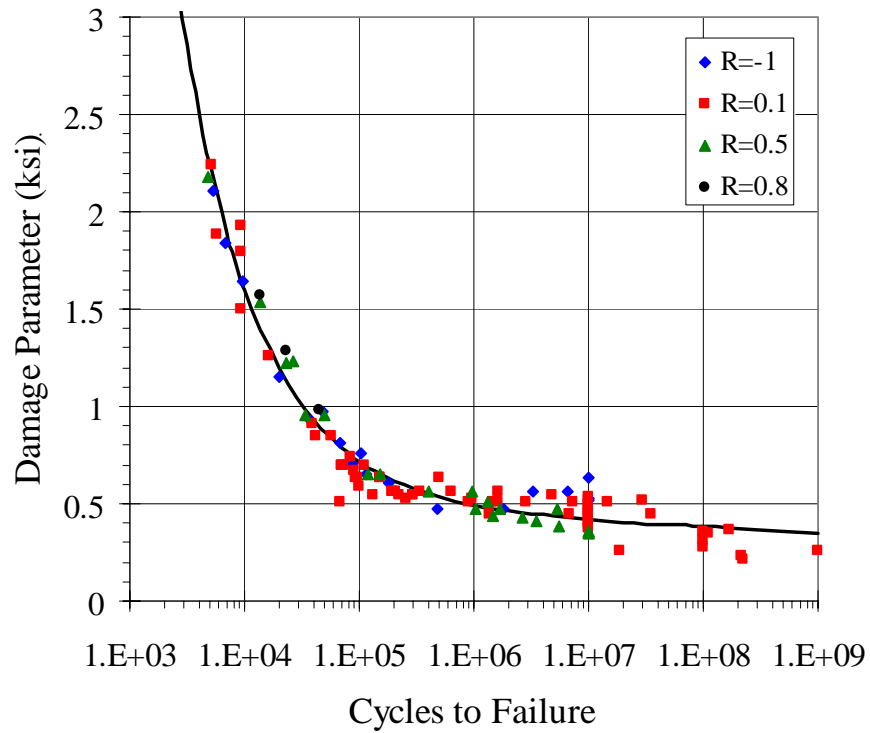
Figure D8. Modified Chu-Conle-Bonnen (CCB) model, with k = 2.7,
applied to RT Ti-6Al-4V: (a) uniaxial data and (b) biaxial data.

As is evident from Figures D3 through D8, most of the models were fairly successful at correlating the uniaxial data over the various stress ratios, although there appears to be a bit more scatter with the Goodman model at the higher stress ratios. However, there were significant differences in the abilities of the models to correlate the biaxial data. The Findley parameter (Fig. D6) and FSK parameter (Fig. D7) provide the best overall correlation of the biaxial data, in that the uniaxial curves roughly pass through the center of the data and the scatter around the curves is relatively small. The FSK model does appear to suffer from some "layering" of the uniaxial data by stress ratio, but the overall correlation can be considered to be quite good. Considering the modified Manson-McKnight (Fig. D3) and modified CCB models (Fig. D8), the uniaxial curves are fairly well centered about the biaxial data, but there is more scatter around the curves. For the SWT and Goodman models (Figs. D4 and D5), the uniaxial curves pass above the biaxial data, meaning the biaxial stress states are more damaging than the models would predict. As both of these models are normal stress-based models, this would indicate that tensile-stress driven cracks did not dominate the initiation phase in the biaxial tests. The success of the mixed-mode parameters (e.g., Findley and FSK) at correlating the biaxial data suggests that crack nucleation was driven by shear or mixed-mode cyclic stresses in this material.

Due to the nature of the loading, experimental verification of the cracking modes in the biaxial specimens cannot be reliably provided. Small crack development and growth were not monitored during the tests. Furthermore, for biaxial loadings with a torsional component, traditional fatigue fracture surface characteristics are not always evident, making identification of crack initiation sites and orientations difficult. It has also been shown that classical long crack growth data (i.e., rates and orientations) often provide a poor representation of the behavior of small cracks [18, 19]. Compliance measurements made during the testing indicate that the vast majority of the fatigue lives were consumed by small crack nucleation and growth, which is assumed to be represented by the damage parameter vs. cycles approach presented here. Thus, it would be unreasonable to attribute the final long-cracking pattern to short crack behavior in order to justify the use of a particular damage parameter.

Since qualitative observations can be misleading, a quantitative comparison between the models was made by considering the magnitude of the error between the experimental

and predicted values of the damage parameters at equivalent fatigue lives. An experimental value of the damage parameter was calculated based on the elastic-plastic stresses and strains reported in Table D2, and the predicted value was taken from the baseline data curve at the experimental life. For each model, the percent error between the experimental value of the damage parameter and the predicted value was determined for each data point as

$$\text{Error(\%)} = \frac{\text{DP}_{exp} - \text{DP}_{pred}}{\text{DP}_{exp}} \times 100 \qquad\qquad (\text{D10})$$

The mean and standard deviation of the error values were then determined, from both the uniaxial and biaxial data sets, for each model. The results are shown in Table D4. Using these criteria, the mean value provides an indication of the offset of the curve from the data set, while the standard deviation provides a measure of the degree of scatter in the data about the curve. An optimal model would be one with small errors in the predicted damage parameters, resulting in small values for both the mean and standard deviation.

**Table D4. Statistical Analysis of Percent Error
in Predicted Values of Damage Parameters**

Model	Uniaxial Data		Biaxial Data	
	Mean	Stand. Dev.	Mean	Stand. Dev.
Modified Manson-McKnight	-0.54	7.51	-5.91	11.75
Smith-Watson-Topper	-2.45	17.26	-41.46	26.11
Goodman	-1.64	12.70	-46.48	23.56
Findley	-0.68	8.37	-0.15	9.36
Fatemi-Socie-Kurath	-2.42	16.27	2.86	12.25
Modified Chu-Conle-Bonnen	-2.45	17.26	1.36	19.03

Although fatigue models have traditionally been evaluated based on comparisons of predicted and experimental fatigue lives, a comparison of damage parameters was used here because in most design situations, a required fatigue life would be specified and an allowable value of the design parameter would be calculated. The value of the damage parameter in some sense reflects the allowable nominal loading. Having statistical data for the damage parameter would allow probabilistic methods to be incorporated to assess the reliability under changes in nominal loading. Thus, viewing how the data are utilized rather than generated is

the basis for this comparison, which allows the reader to contemplate the change in loading parameters for a given life.

The results shown in Table D4 verify the qualitative observations made previously. The mean error values for the uniaxial data were small in all cases, which is to be expected since the curves represent the best fit to the uniaxial data. However, there is significant variation in the scatter in the data (represented by the standard deviation values) between the models, with the Findley and modified Manson-McKnight models showing the best correlation of the uniaxial data. Considering the biaxial data, the Findley model produced the lowest scatter, followed by the FSK and modified Manson-McKnight models. Note that the Goodman and SWT models, in addition to having a higher degree of scatter, also showed a significant mean offset between the biaxial data and uniaxial curve, as discussed previously.

It is also worth noting that, based on the results shown in Table D2, mean shear stresses do appear to have some effect on the fatigue life of Ti-6Al-4V. This is evidenced by the fact that, at equivalent shear stress amplitudes (e.g., specimens 156-10 and 156-5), the presence of a mean shear stress (156-5) reduced the fatigue life relative to the fully-reversed case (156-10). These tests were conducted at stress levels where Sines and Ohgi [3] predict the observed behavior.

D.5.2 Effect of Critical Plane Definition

The question of how to define the critical plane has been raised by many in the field of multiaxial fatigue, and is rooted in the observations made by early researchers regarding the nature of fatigue crack nucleation. It has been observed that fatigue cracks often tend to nucleate on planes in which either the normal stress/strain amplitude is a maximum or the shear stress/strain amplitude is a maximum, depending on the material. This is easily seen in a uniaxial test, where fatigue cracks may nucleate on planes perpendicular to the axis of loading (maximum normal stress) or at 45º to this axis (maximum shear stress). It was such observations that led to the development of critical-plane fatigue models for multiaxial loading; i.e., determine the plane with the maximum alternating normal or shear stress (strain), and this is defined as the critical plane, on which fatigue calculations should be carried out. For example, Findley [11] proposed that his parameter $(\Delta\tau/2 + k\sigma_n^{max})$ be defined on the plane of maximum shear stress amplitude. On the other hand, the SWT

parameter [$(\Delta\varepsilon/2)\sigma_n^{max}$], when used as a critical plane parameter, would be defined on the plane of maximum normal strain amplitude.

The shortfall with this definition of the critical plane is the potential to underestimate the damage caused by a particular multiaxial stress state, by minimizing the impact of the secondary terms in the damage parameter (e.g., the maximum normal stress on the critical plane in the Findley and SWT models). For example, considering the Findley parameter, a plane on which the shear stress amplitude is large (but not maximized), with a large tensile normal stress, may be more at risk for fatigue crack nucleation than the plane on which the shear stress amplitude is maximum, if that plane has a small or compressive normal stress. As a result, many researchers have advocated defining the critical plane as the one on which the damage parameter is maximized, and not necessarily the plane with the maximum normal or shear stress/strain amplitude. The approach used in this study was based on the definition of the critical plane as the plane of maximum damage parameter.

To justify the approach taken here, the critical-plane models selected for detailed evaluation (Findley, FSK, Goodman, SWT, and CCB) were also analyzed based on the definition of the critical plane as the plane containing the appropriate maximum stress or strain amplitude. By comparison of the results from the two methods, the latter definition of the critical plane (based on maximum stress/strain amplitude) reduced the accuracy of the damage calculations, for the most part. For the Goodman and SWT models, the differences were negligible. However, for the Findley and FSK parameters, the accuracy of the models at correlating the biaxial data was noticeably reduced. In addition, for the CCB models, the latter definition of the critical plane (maximum shear strain amplitude) produced very poor correlation of the biaxial data. This is likely due to the ambiguous choice of the shear strain amplitude as the primary damage-causing component. This damage parameter involves both normal and shear strain amplitudes, and it is not clear which component should be used to define the critical plane. Consequently, for this model, it is imperative that the critical plane be defined in terms of the maximum value of the damage parameter. It is evident that the "maximum-damage-parameter" definition of the critical plane should be adopted when using the critical plane models for Ti-6Al-4V.

D.5.3 Detailed Model Evaluations

Based on the results presented in Section D.5.1, four models were selected for detailed evaluation using the RT Ti-6Al-4V data, as well as using the other data sets for Ti-6Al-4V and Ti-17. In this final evaluation, one effective-stress model and three critical-plane models were considered, plus three additional variations of one critical-plane model. The selected models are as follows:

1) <u>Modified Manson-McKnight (MMM) model</u>. This model represents the most promising of the "effective-stress" models considered in this program. The damage parameter for this model is defined as:

$$DP = \frac{1}{2} \Delta\sigma_{psu}^{1-w} \sigma_{max}^{w} \tag{D11}$$

2) <u>Smith, Watson, Topper (SWT) critical-plane model</u>. Although this model has been shown to be in poor agreement with the experimental fatigue data for titanium alloys, it has been included in the final comparison because it is representative of the normal stress/strain based critical-plane models, and because it is a well-known, highly utilized parameter. The damage parameter for this model has the form

$$DP = \varepsilon_a \sigma_{max} \tag{D12}$$

3) <u>Findley critical-plane model</u>. This shear-stress based model was found to possess the best agreement with experimental data of all the critical-plane models. In addition to the original model, three other variations have been considered. These variations involve modifications to the normal stress term in the damage parameter,

$$DP = \tau_a + k\sigma \tag{D13}$$

The original and modified models are as follows, with reference to Figure D9:

a) σ = maximum algebraic normal stress over the entire cycle, on the critical plane; i.e., $\sigma = \sigma_{max} = \sigma_C$ (see Fig. D9). This was the original definition of the Findley parameter.

b) σ = maximum normal stress at the two shear reversal points of the cycle, on the critical plane; i.e., σ = maximum algebraic value of σ_A and σ_B (σ_B in the example shown in Fig. D9).

c) σ = average (integrated) normal stress over the entire cycle, on the critical plane; i.e., $\sigma = \dfrac{1}{T}\int_0^T \sigma \, dt$, where T is the elapsed time for 1 cycle (T = 1/f where f is the frequency).

d) σ = average normal stress at the two shear reversal points, on the critical plane; i.e., $\sigma = (1/2)(\sigma_A + \sigma_B)$ (see Fig. D9).

4) Fatemi, Socie, Kurath (FSK) critical plane model. This shear-strain based critical-plane model also produced good agreement with experimental data, and provides an alternative to the stress-based models. The damage parameter for this model is as follows:

$$DP = \gamma_a \left(1 + k \frac{\sigma_{max}}{\sigma_y} \right) \tag{D14}$$
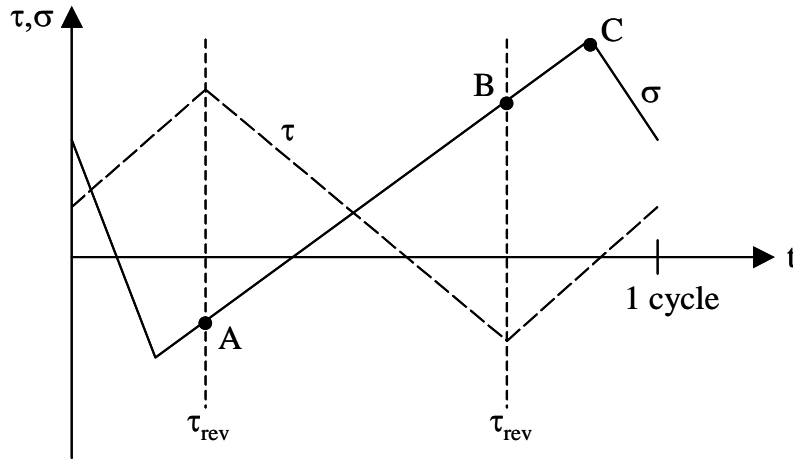
Figure D9. Example biaxial stress history over 1 cycle, showing different methods used to define the normal stress term in the Findley model. The dashed line is the shear stress and the solid line is the normal stress.

As in the preliminary evaluations, the damage parameter for each model was assumed to be related to the fatigue life by an equation of the form

$$DP = A(N)^b + C(N)^d \qquad\qquad (D15)$$

However, in this phase of the study, the optimal model and curve-fit parameters (A, b, C, d, and k where appropriate) for each model were determined by fitting only the uniaxial data, at all stress ratios. This was a departure from the method used previously, in which both the uniaxial and biaxial data sets were utilized to optimize the model constants. In this comparison, the uniaxial data were used exclusively because this provides a more realistic assessment of the models for practical situations. Typically, uniaxial fatigue data (at various stress ratios) will be available for fitting model constants, while reliable multiaxial fatigue data are likely to be in limited supply. Models that can accurately predict the multiaxial fatigue behavior of materials with only uniaxial data required as input are clearly desirable to those models that require extensive multiaxial data for fitting necessary constants. The adjustable parameter for the MMM model (w), along with the damage parameter values for each test, were obtained directly from GEAE.

Algorithms were developed for each model to calculate the optimal parameters (A, b, C, d, k) using the least-squares minimization technique. All parameters were simultaneously optimized by minimizing the sum of the squared errors between predicted and experimental values of the damage parameters at a given life. The experimental damage parameters were calculated from the appropriate equation, D11 – D14, using the measured or calculated values of stress and strain for each test. The predicted values were calculated from Eq. D15 using the experimental fatigue life from each test. For the critical-plane models, the "critical plane" itself also had to be identified; i.e., the plane on which the damage parameter was maximized. Under general conditions of biaxial loading, this requires an iterative approach (the plane cannot be analytically determined). However, under uniaxial loading conditions, the plane can be determined analytically by expressing stress and strain components on an arbitrary plane (at an angle of ϕ to the loading direction) as a function of the applied stress and strain (σ and ε), differentiating the damage parameter with respect to ϕ, and setting the

result equal to zero. Using this procedure, the following equations can be derived for the critical plane orientation (ϕ) under a uniaxial loading (σ, ε) for each critical plane model:

SWT Model:
$$\phi = 0 \qquad\qquad\qquad \text{(D16)}$$

Findley Model, version (a) and (b):
$$\tan 2\phi = \frac{\sigma_a}{k\sigma_{max}} \qquad\qquad \text{(D17)}$$

Findley Model, version (c) and (d):
$$\tan 2\phi = \frac{\sigma_a}{k\sigma_m} \qquad\qquad \text{(D18)}$$

FSK Model:
$$\cos 2\phi = -\frac{\sigma_y}{2k\sigma_{max}} - \frac{1}{4} \pm \frac{1}{2}\sqrt{\frac{\sigma_y^2}{k^2\sigma_{max}^2} + \frac{\sigma_y}{k\sigma_{max}} + \frac{5}{4}} \qquad \text{(D19)}$$

Note that, under uniaxial or proportional biaxial loading conditions, versions (a) and (b) of the Findley model are identical, as are versions (c) and (d). These models only differ when the loading is non-proportional. Also note that in the Findley and FSK models, the critical plane orientation depends on the value of k, which complicates the optimization procedure.

After analyzing the four variations of the Findley model, it was determined that neither of the average stress definitions for the normal stress term produced improved correlations for the uniaxial and biaxial data. Consequently, the results for these versions are not included here. The predictions from the remaining four models for the uniaxial Ti-6Al-4V data at RT are shown in Figures D10 – D13.

The predictions are presented in two formats for each model. The DP vs. N curves show the experimental damage parameter, calculated from the measured stress or strain values, vs. experimental life, along with the best-fit curves using Eq. D15. A sound model will collapse all the variable mean stress data into a single curve that can be adequately represented by this equation. However, direct comparison of the models using these plots is difficult due to the widely differing definitions of the damage parameters. Consequently, a second approach was devised to provide a direct comparison of the models for the uniaxial data. In this approach, the maximum uniaxial cyclic stress level for a given stress ratio (R) was calculated from the predicted value of the damage parameter at a given fatigue life (N).

This value was then plotted against the actual (measured) value of the maximum stress at that life. These results are shown in the form of plots of predicted σ_{max} vs. actual σ_{max}. For some of the models, this latter approach required the assumption of elastic conditions for stress-strain calculations; consequently, only the HCF (load-control) data were used for these comparisons.
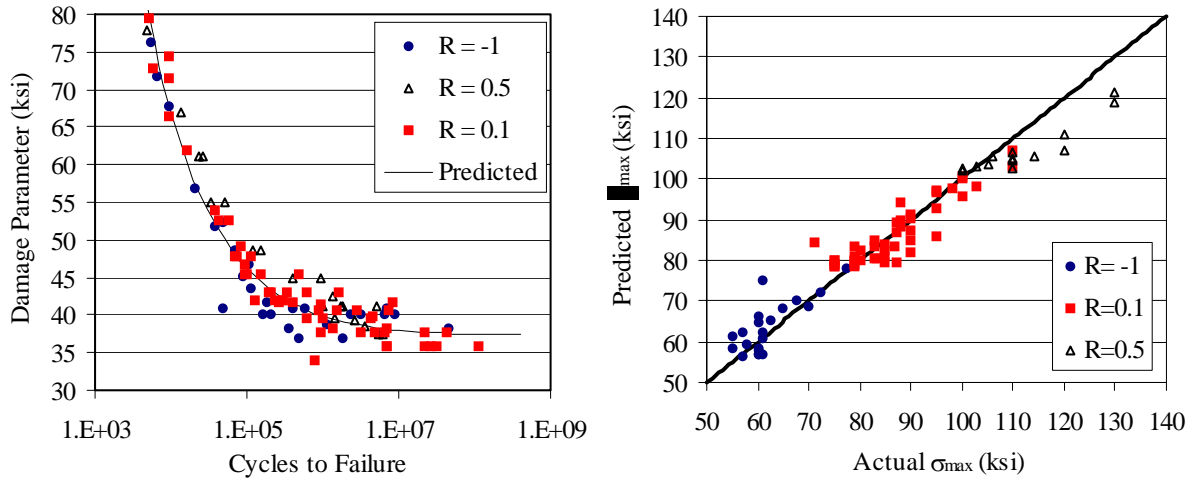
Figure D10. Modified Manson-McKnight (MMM) model applied to uniaxial Ti-6Al-4V RT data.
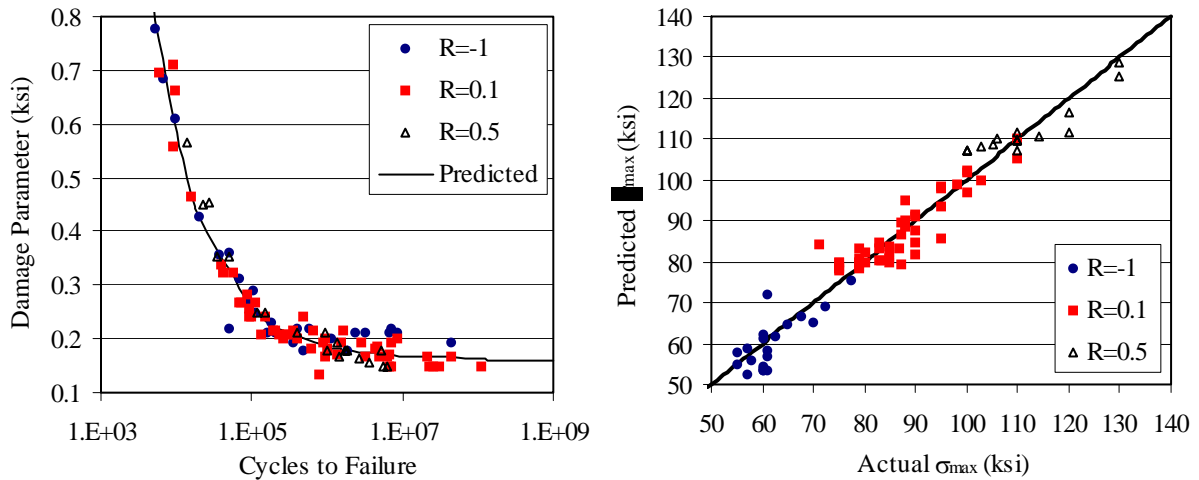
Figure D11. Smith-Watson-Topper (SWT) model applied to uniaxial Ti-6Al-4V RT data.
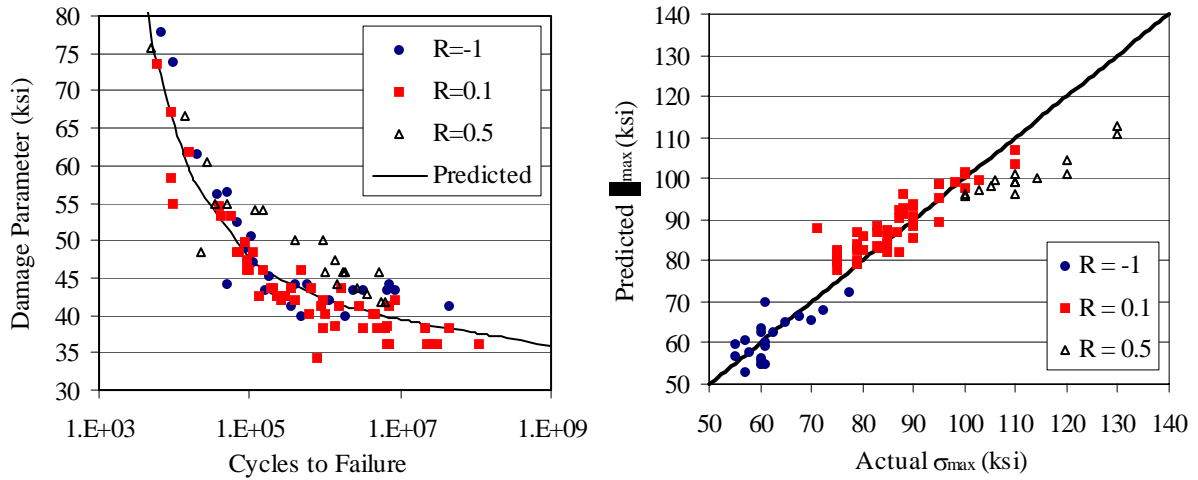
Figure D12. Findley model applied to uniaxial Ti-6Al-4V RT data.
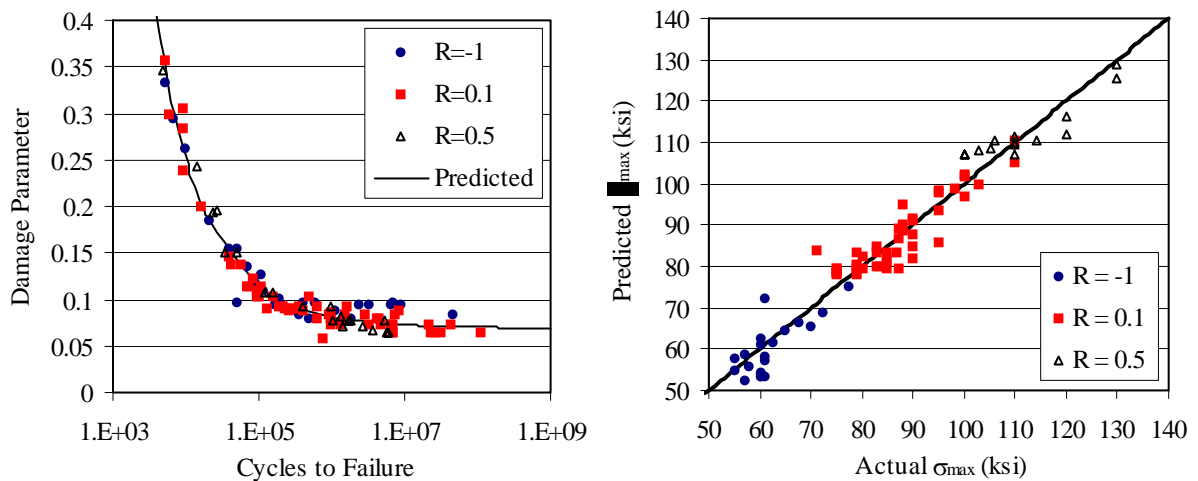
Figure D13. Fatemi-Socie-Kurath (FSK) model applied to uniaxial Ti-6Al-4V RT data.

As is evident from Figs. D10 – D13, all four models provided reasonable correlations of the uniaxial data. A quantitative comparison between the models is included in Table D5. For each model, the ratio of actual to predicted σ_{max} was calculated for every uniaxial data point. The average and standard deviation of the group of data are shown in the table for each model. As would be expected, the average value is very near unity for each model, since the predicted values were generated from a least-squares curve fit to the data. The standard deviation values are more useful for comparison, as they represent the degree of scatter in the data about the predicted curve. Note that the MMM, SWT, and FSK models all

D-36

have similar standard deviations, while the Findley model displays a slightly higher value. This is primarily due to the fact that the Findley model under-predicted the allowable stress levels for the R = 0.5 data, as can be seen in Fig. D12. The MMM model also displayed the same tendency, although to a lesser degree (Fig. D10).

Table D5. Comparison of Models for Uniaxial Ti-6Al-4V RT Data:
Actual/Predicted σ_{max}

Model	MMM	SWT	Findley	FSK
A/P σ_{max} (average)	1.002	1.008	1.008	1.009
A/P σ_{max} (stand. dev.)	0.056	0.056	0.072	0.058

The model predictions for the biaxial Ti-6Al-4V RT data are shown in Figs. D14 – D18. The curve in each figure represents the best fit to the uniaxial data.
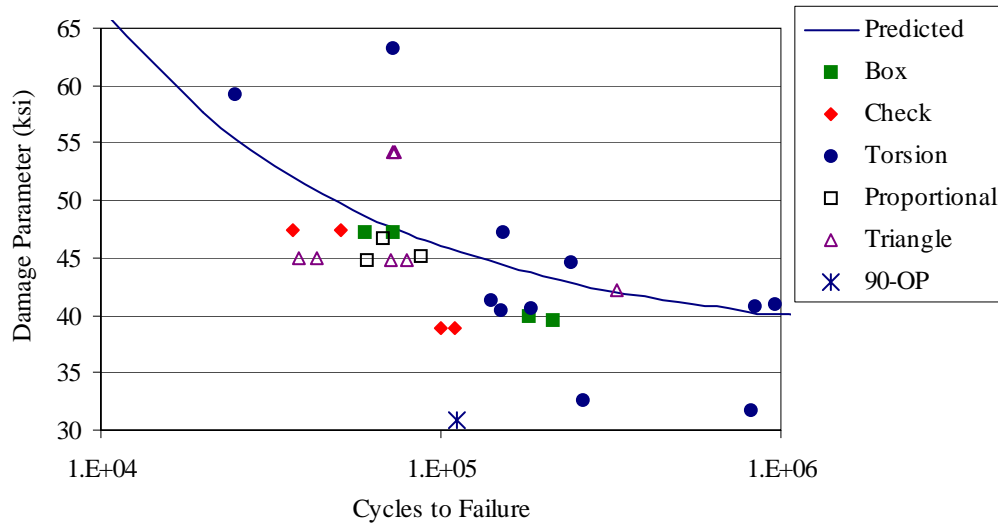
Figure D14. MMM model applied to biaxial Ti-6Al-4V RT data.
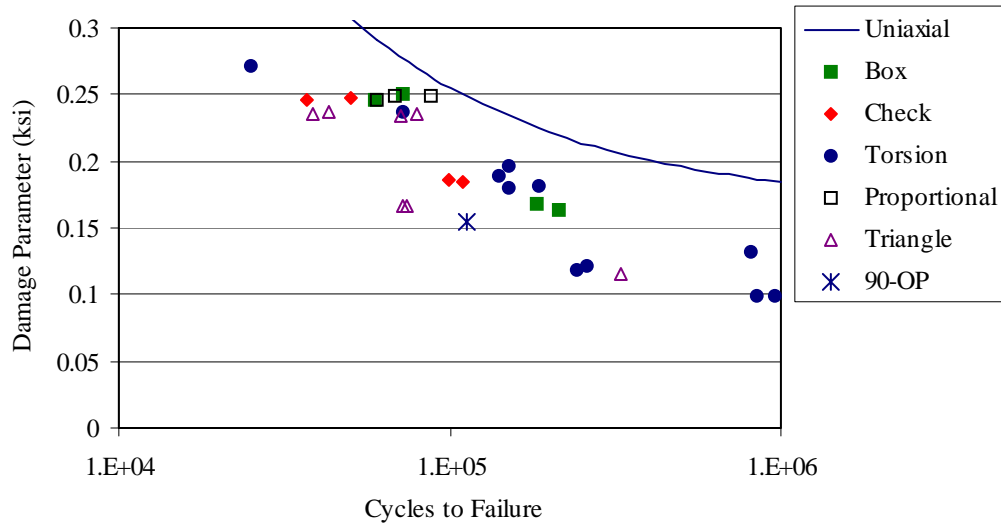
Figure D15. SWT model applied to biaxial Ti-6Al-4V RT data.
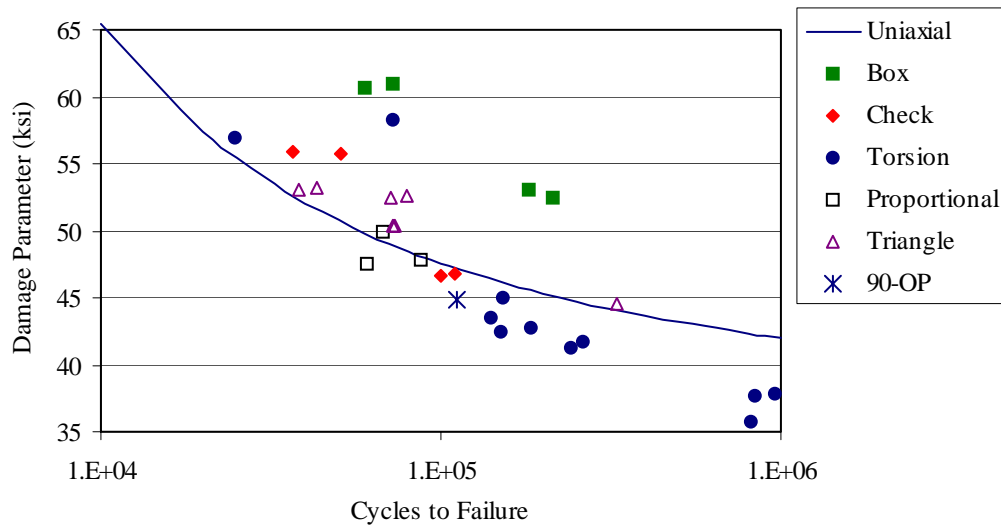
Figure D16. Findley model, version (a), applied to biaxial Ti-6Al-4V RT data.
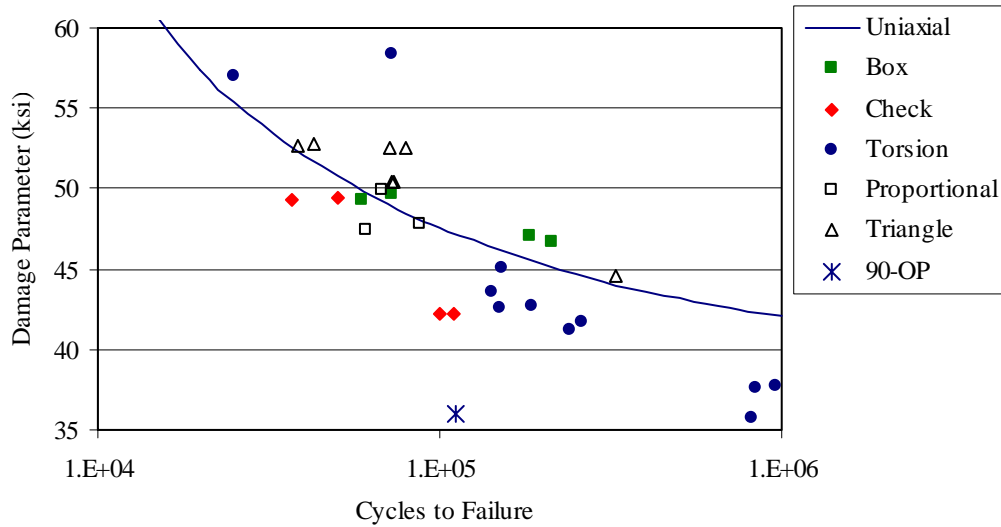
Figure D17. Findley model, version (b), applied to biaxial Ti-6Al-4V RT data.
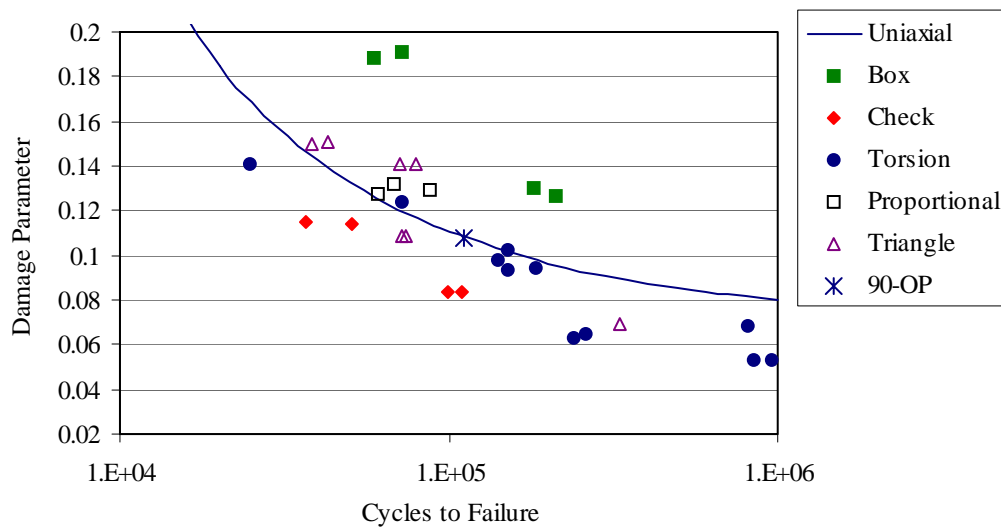
Figure D18. FSK model applied to biaxial Ti-6Al-4V RT data.

The differences between the models are more pronounced when comparing the calculations for the biaxial data. With the exception of the SWT model, the biaxial data are reasonably centered about the uniaxial baseline curves. The SWT model is noticeably non-conservative, in that the biaxial tests were more damaging than predicted by the uniaxial curve. The MMM model had difficulty correlating the torsion data, and was highly non-

conservative in its damage prediction of the circle (90–OP) path. The Findley model, version

(a), produced fairly good predictions for most of the load paths, with the notable exception of

the box path, in which the damage estimates were highly conservative. Version (b) of the

Findley model produced substantially improved predictions for the box path; however, the

predictions for the check and circle paths worsened. Similar to version (a) of the Findley

model, the FSK model was also found to be conservative in its damage predictions for the

box path.

      Due to the complexity of the biaxial load paths and the differing definitions of

damage parameter for each model, direct quantitative comparisons cannot be made between

the models as was done for the uniaxial data. Indirect comparisons can be made, however,

by considering the average value and standard deviation of the set of actual/predicted damage

parameter ratios from each model for the biaxial data. These values are shown in Table D6,

along with the curve-fit parameters for each model. These results show that the two versions

of the Findley model produced the lowest overall scatter in the data (lowest standard

deviation in the actual/predicted DP values). Of the two variations, version (b) produced

significantly lower scatter about the mean than version (a) due to the improved predictions

for the box path tests, as is evident by comparison of Figures D16 and D17. The MMM and

SWT models also produced reasonably low scatter, but the SWT model had a very low

average value, indicating the model is non-conservative when used to predict biaxial fatigue

damage.

**Table D6. Curve-Fit Parameters and Model Comparisons for
Biaxial Ti-6Al-4V RT Data: Actual/Predicted Damage Parameter**

Model	k	A	b	C	d	A/P DP (avg.)	A/P DP (std. dv.)
MMM	--	3501.8	-0.5164	36.74	0.00068	0.953	0.122
SWT	--	223.46	-0.6840	0.1861	-0.00783	0.737	0.121
Find., v. (a)	0.379	7190.8	-0.6347	52.896	-0.0186	1.011	0.101
Find., v. (b)	0.379	7190.8	-0.6347	52.896	-0.0186	0.967	0.079
FSK	54.3	91.074	-0.6783	0.0795	-0.00695	1.025	0.229

      From a mechanistic perspective, the improved correlations using version (b) of the

Findley parameter, relative to version (a), provide further evidence that shear stresses drive

the crack initiation process in Ti-6Al-4V. In version (b), the maximum normal stress at a shear reversal point (when the shear stress is maximum) is used in the parameter, rather than the overall maximum normal stress in the cycle. This indicates that it is not the peak normal stress that is driving the process, but rather the peak shear stress. The tensile stress present at the point of maximum shear stress plays a secondary effect, in that it reduces frictional forces between crack surfaces, which accelerates the development and growth of small shear cracks. This argument is further supported by the poor predictions for the biaxial damage using the SWT parameter, which is a normal stress/strain based model.

D.6   MODEL EVALUATIONS USING 500°F Ti-6Al-4V DATA

A limited number of uniaxial and biaxial fatigue data points for Ti-6Al-4V at 500°F were also generated for model evaluations. As with the RT evaluations, no uniaxial step-test data were included in this analysis due to the uncertainty associated with those results. Excluding the step-test data, 16 uniaxial data points at R = −1, 0.1, and 0.5 were available. In addition, four biaxial tests were conducted: two proportional tests at R = 0.1 and two non-proportional box-path tests.

Model correlations for both the uniaxial and biaxial 500°F data using the SWT, Findley [version (a)], and FSK critical-plane models are shown in Figures D19 – D21. The solid curve in each figure represents the best fit to the uniaxial data assuming an equation of the form shown in Eq. D15. In all cases, the model predictions were quite poor for this set of data. The uniaxial data appear to exhibit an increasing slope with increasing life, which is not well accounted for by any of the models. A complication with this data set was the lack of measured strain values from the uniaxial tests. As a result, all strains were estimated from elastic relations, which likely introduced significant errors in the analysis for the FSK and SWT models.

Note that the Findley model (Fig. D20) generated relatively good damage predictions for this data set, with the exception of the box path data. In this case, the damage predictions were made using version (a) of the Findley model, rather than version (b). Based on the results of the RT Ti-6Al-4V model predictions, it would be anticipated that the box path calculations for this data set would improve substantially using the latter definition of the

Findley damage parameter. It should also be noted that the SWT model provided better predictions for the biaxial data than either the Findley or FSK models. However, more accurate strain calculations would be required before greater confidence could be placed in these analyses.
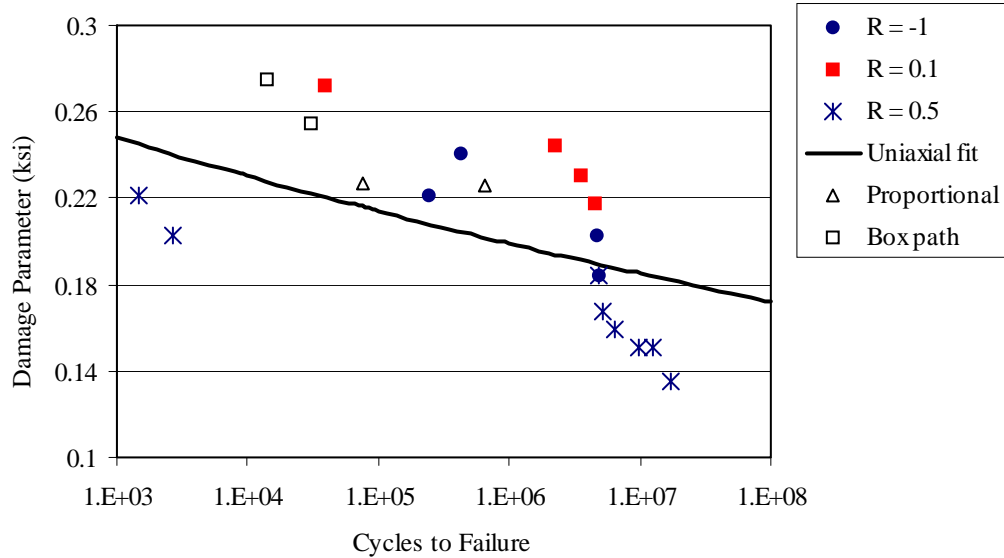
Figure D19. SWT model applied to uniaxial and biaxial Ti-6Al-4V 500°F data.
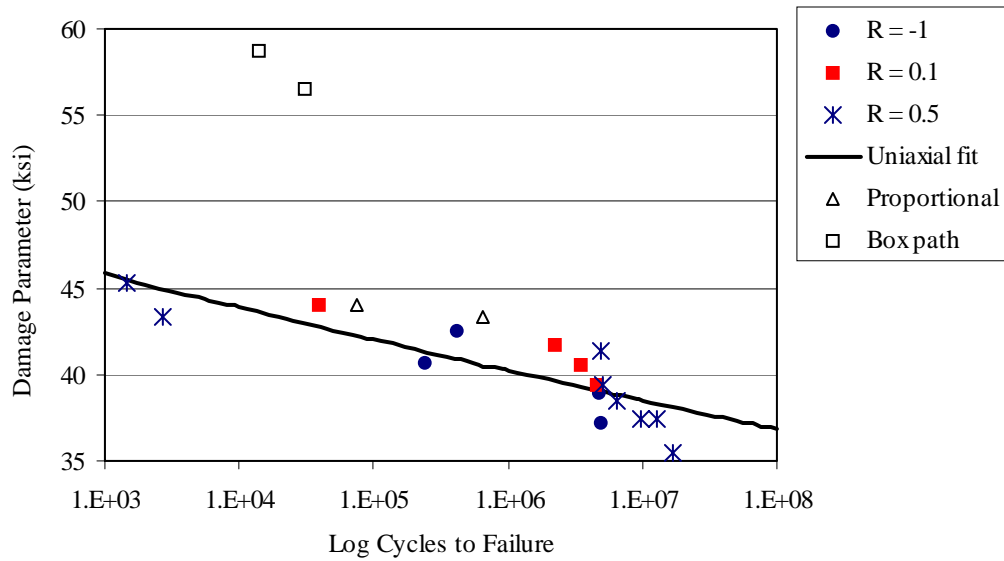
Figure D20. Findley model, v. (a) applied to uniaxial and biaxial Ti-6Al-4V 500°F data.
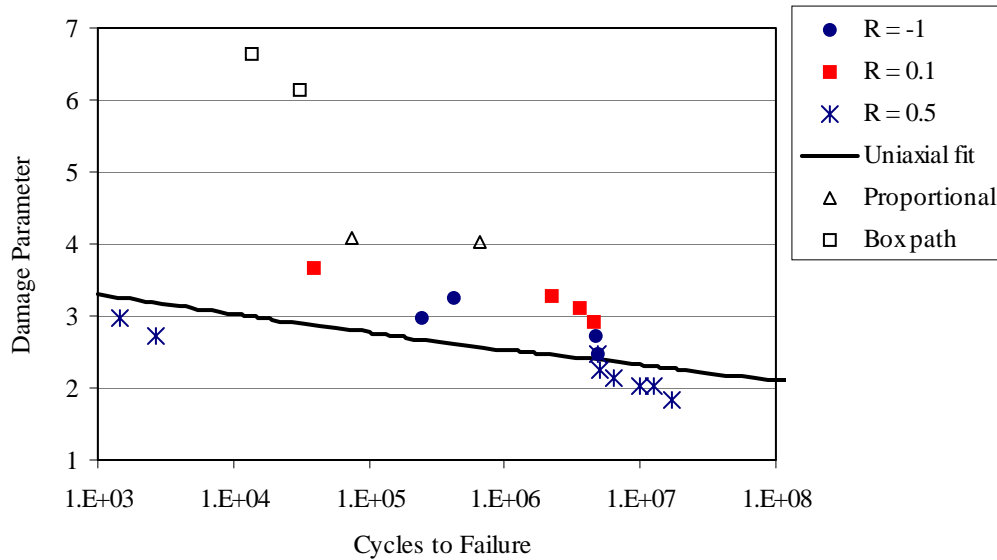
Figure D21. FSK model applied to uniaxial and biaxial Ti-6Al-4V 500°F data.

D.7   MODEL EVALUATIONS USING RT Ti-17 DATA

The three critical-plane fatigue models (Findley v. (a), FSK and SWT) were also evaluated using a set of uniaxial and biaxial fatigue data for Ti-17 at room temperature (RT). As before, no step data were included in the evaluations. The uniaxial set consisted of strain-controlled (LCF) and stress-controlled (HCF) data at stress ratios of R = −1, 0.1, 0.5, and 0.8. The biaxial set included torsion data (R = −1, 0.1), proportional tension-torsion data (R = 0), and non-proportional check path data. The results of the model correlations are shown in Figures D22 – D24. The curves shown in each plot represent a best fit to the uniaxial data, assuming an equation of the form shown in Eq. D15.

As with the Ti-6Al-4V RT data, all three models adequately collapsed the variable mean stress uniaxial data, although there appears to be a little more separation of the data by stress ratio, most noticeably between R = −1 and R = 0.1 data at longer lives. When applied to the biaxial data, the SWT critical plane model was again generally non-conservative, indicating that fatigue crack initiation may be driven primarily by shear stresses in Ti-17. The Findley and FSK models produced better overall damage predictions for the biaxial data, although both models tended to underestimate the fatigue damage caused by the torsion tests.
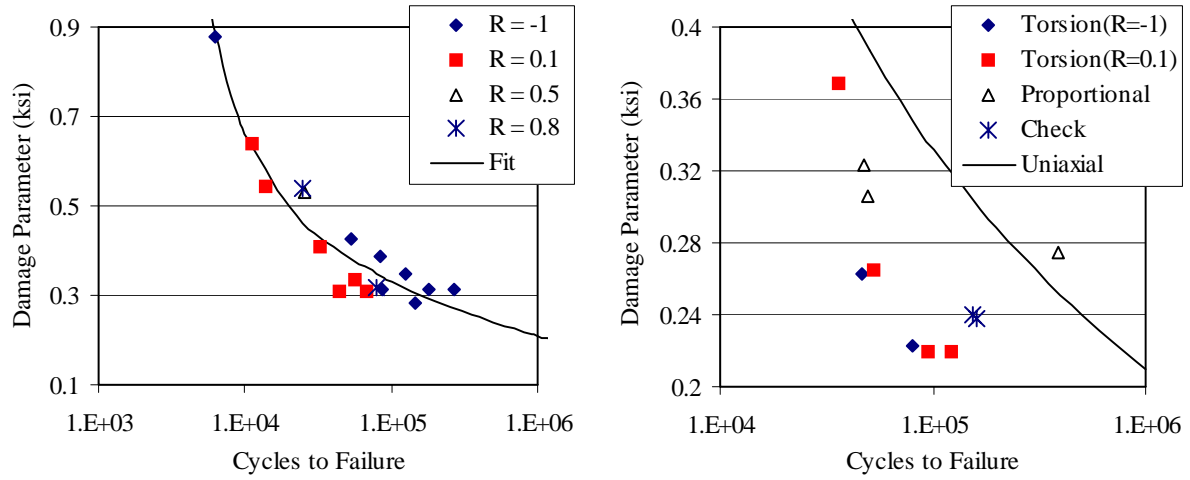
Figure D22. SWT model applied to uniaxial and biaxial Ti-17 RT data.
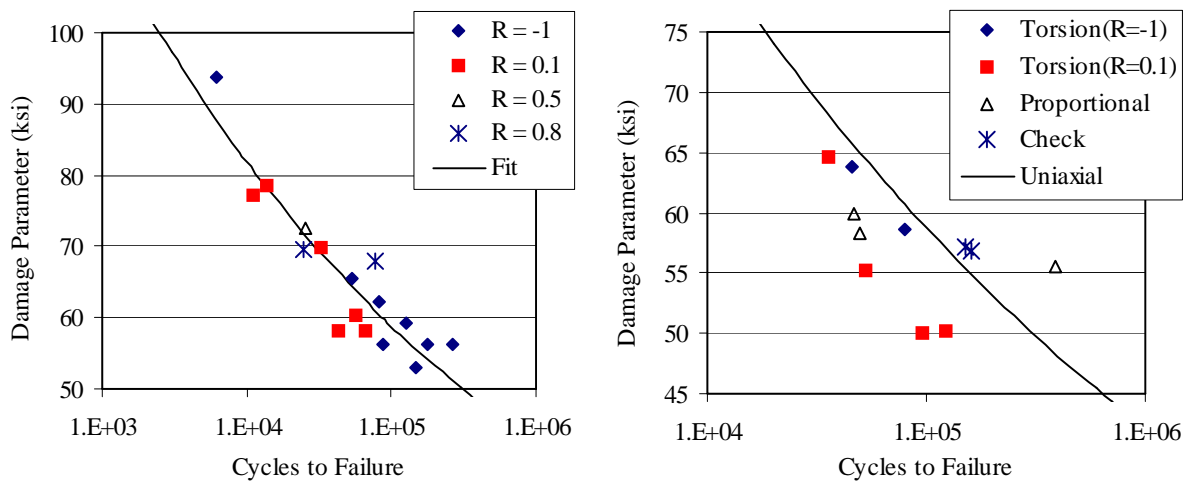
Figure D23. Findley model applied to uniaxial and biaxial Ti-17 RT data.
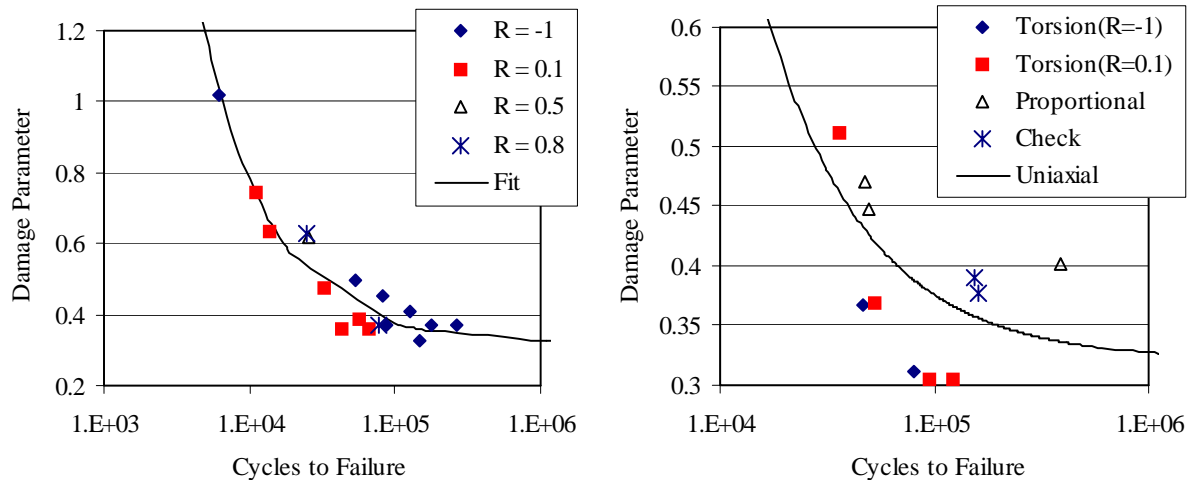
Figure D24. FSK model applied to uniaxial and biaxial Ti-17 RT data.

D.8   MULTIAXIAL FATIGUE LIFE PREDICTION METHODS FOR NOTCHED BARS OF Ti-6Al-4V

The prediction of fatigue lives for notched components presents additional challenges that must be overcome. It is generally recognized that in a notched component, both the maximum (notch-root) stresses as well as the stress gradients affect the fatigue behavior. A number of methodologies have been proposed to account for the influence of the stress gradients under uniaxial loadings. Probably the most common approach is based on the use of a fatigue stress concentration factor, K_f, which is defined in terms of a notch-sensitivity factor, q. In general, the sharper a notch, the higher the stress concentration factor (K_t), but the steeper the elastic stress-strain gradient. In essence, these concepts assume the maximum principle stress is the relevant damage parameter and serve to reduce the maximum value of the damage parameter (due to the stress gradient), such that $K_f \leq K_t$. While these techniques have been successfully applied to uniaxially-loaded notched components, the extension to multiaxial loadings is ambiguous.

More recently, a number of investigators have proposed notched fatigue prediction methods that rely on an averaging or weighting of the stresses or damage parameter over some critical region, or the calculation of the appropriate damage parameter at some specified distance below the notch root [20, 21]. These techniques, collectively referred to as "critical-distance" methods, are more readily extendable to multiaxial loadings since there is no reliance on a particular stress component (as there is in the definition of K_f). In this study,

the multiaxial models considered previously for smooth specimens were also applied to evaluate their abilities at predicting the fatigue lives of notched bars of Ti-6Al-4V. These models were applied within the general framework of the critical-distance methodology.

D.8.1 Experimental Program

Five circumferentially notched round bars with a notch net section diameter of 0.5 in. (12.5 mm), a notch depth of 0.128 in. (3.25 mm), and a notch radius of 0.098 in. (2.5 mm) were biaxially loaded along the load paths shown in Figure D25. Theoretical stress concentration factors of $K_\sigma = 1.85$ (axial) and $K_\tau = 1.35$ (torsion) are associated with this geometry [22]. Specimen preparation was identical to the uniaxial and multiaxial smooth specimens tested previously. The individual test data are summarized in Table D7.
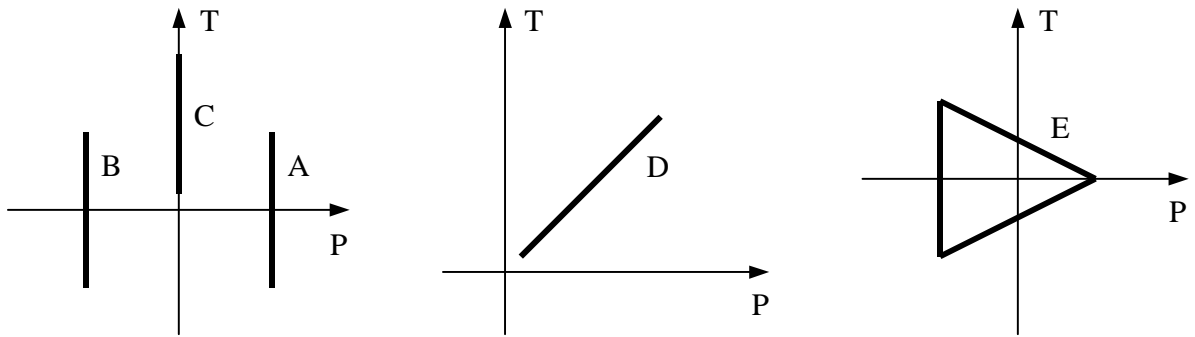
Figure D25. Load paths for notched specimen tests.

Table D7. Notched Specimen Test Conditions and Fatigue Lives

Spec/Path	P_{max} (lb)	P_{min} (lb)	T_{max} (lb-in)	T_{min} (lb-in)	N_f (cycles)
132-4/A	2000	2000	750	−750	369,700
132-3/B	−2000	−2000	750	−750	$>1.8\times10^6$
132-1/C	0	0	1500	75	627,000
132-2/D	9000	1000	750	90	123,800
132-5/E	6500	−6500	550	−550	416,200

D.8.2 Notch Fatigue Analysis and Results

Based on the results of the smooth-specimen evaluations discussed previously, four models were selected for consideration in the notch study: the MMM effective-stress model, and the Findley, FSK, and modified CCB critical-plane parameters. Application of the critical-distance methods requires that the full stress and strain distributions (gradients) be calculated below the notch root. Consequently, a finite element analysis was performed for each of the five specimens listed in Table D7. In this study, ANSYS was utilized with a tetrahedral 10-node element. A sensitivity analysis was conducted to ensure convergence of the stress solutions, using meshes that varied from approximately 5,000 to over 17,000 elements for the entire specimen. In the final mesh, shown in Figure D26, the average element side length in the notch root was approximately 20 mil (0.5 mm). The results of the elastic analyses indicated that one of the tests (test C in Table D7) experienced plastic deformation during the loading. For this test, an elastic-plastic analysis was conducted in ANSYS using a multilinear kinematic hardening rule, assuming the plastic deformation was restricted to the first reversal. The Ramberg-Osgood relation was used to model the cyclic stress-strain curve, using the material properties listed in Section D.3.2. Figure D27 shows a typical von Mises contour stress plot for test A, while Figure D28 shows the stress components as a function of radial position through the notch section for tests A and C. These stress components were used to calculate a value for each damage parameter.
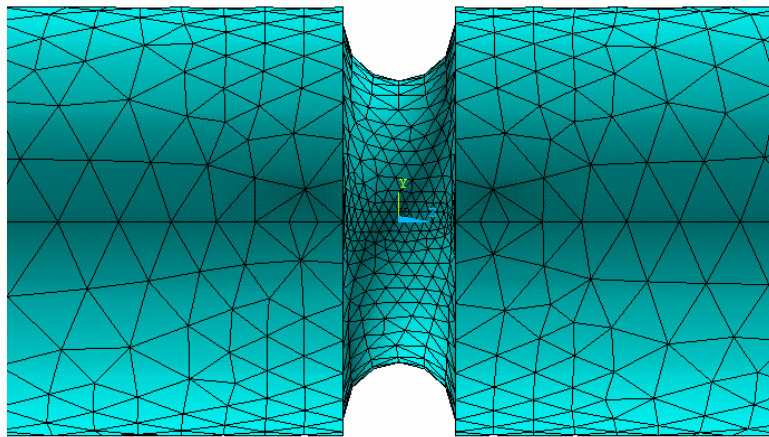
Figure D26. Finite element mesh of notched specimen.
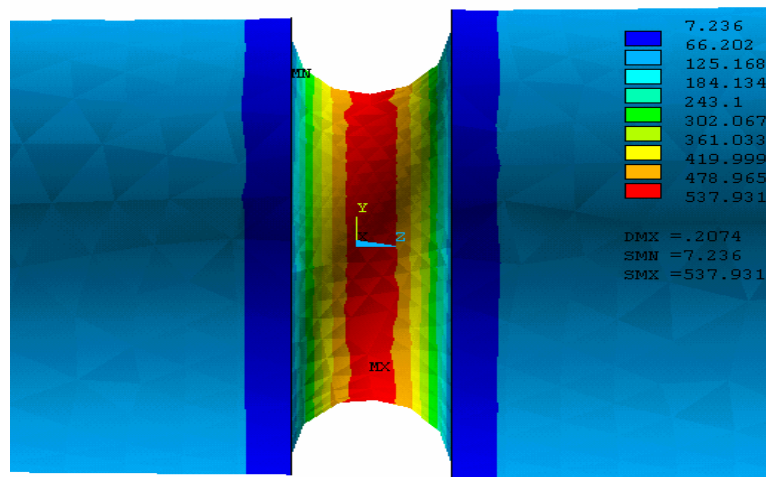
Figure D27. Sample plot of von Mises stress distribution (test A).
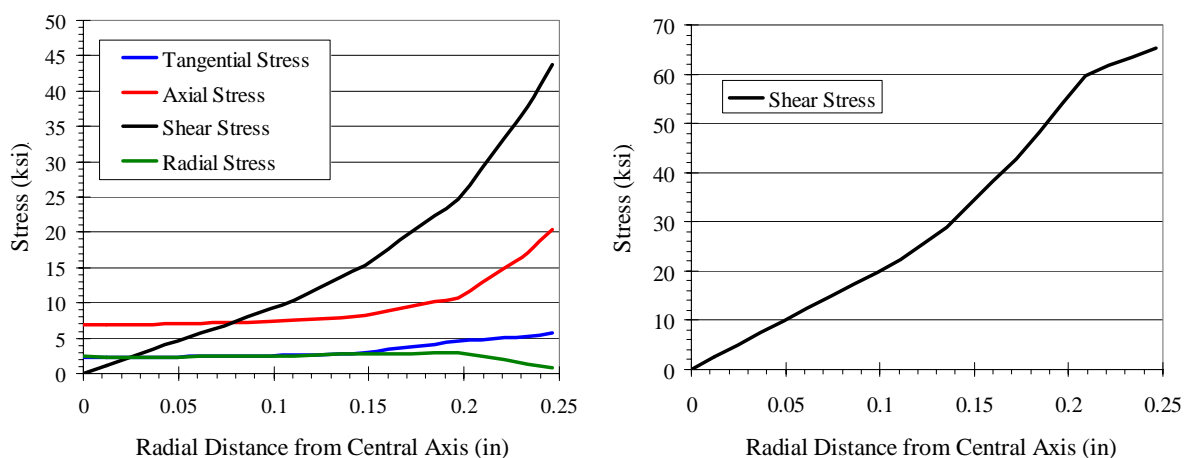
Figure D28. Plots of stress distribution vs. depth under the notch
for tests A (left) and C (right).

Figures D29 through D32 show the radial damage predicted for each damage
algorithm utilizing the individual stress-strain components determined from the finite
element analysis. The solid point on each curve shows the location of the damage parameter
calculated using the experimental life and the baseline damage curve. The fact that these
points are all located subsurface indicates that the damage predicted employing surface
stresses and strains is conservative. They also render some insight as to a depth over which
the damage needs to be assessed. Using 2 mil (0.05 mm) increments, the subsurface damage
was calculated, and Eq. D10 was utilized to calculate a percent error for each test. The

optimized depth, which best correlates all the notched specimen data to the uniaxial baseline curve, was chosen to minimize the percent error. In other words, the mean of the notched data was chosen to correspond to the baseline uniaxial data. These results, along with the surface damage calculations, are shown in Figures D33 through D36 for each of the damage parameters under consideration.
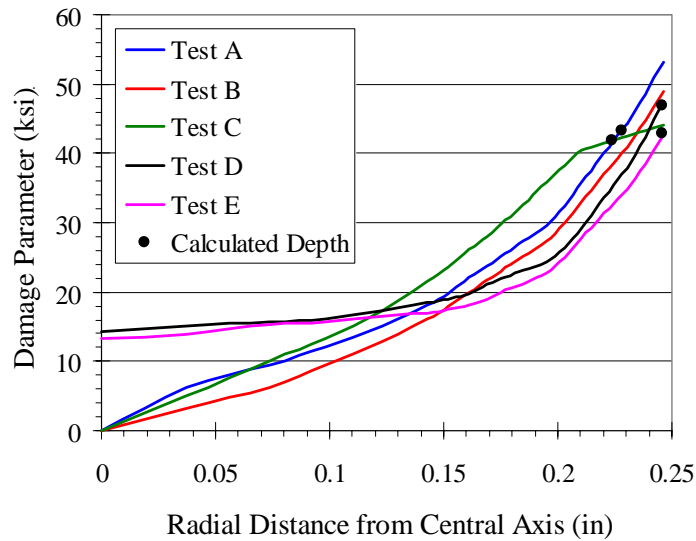
Figure D29. Damage parameter vs. depth under notch for the modified Manson-McKnight model, and depth at which damage parameters correspond with experimental lives.
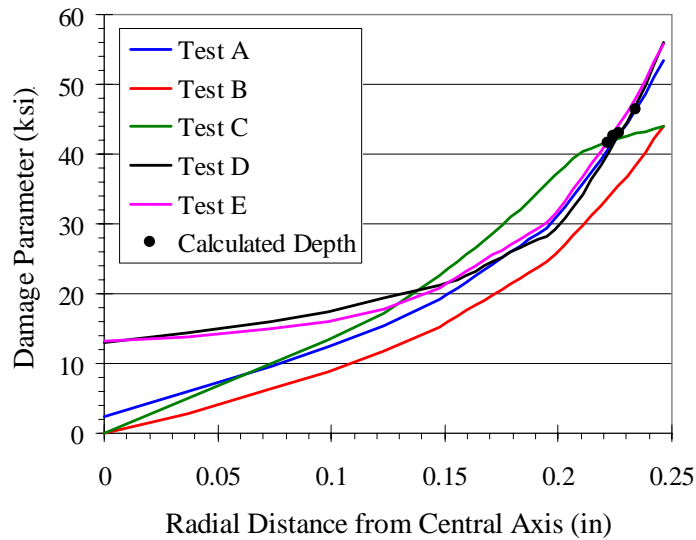
Figure D30. Damage parameter vs. depth under notch for the Findley model, and depth at which damage parameters correspond with experimental lives.
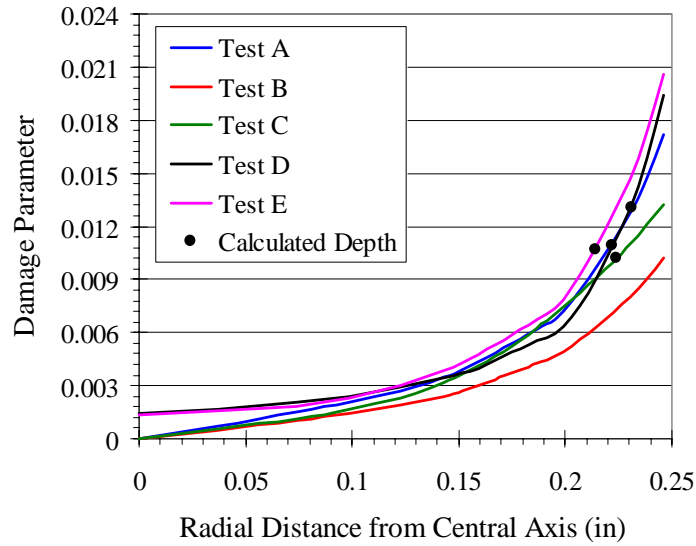
Figure D31. Damage parameter vs. depth under notch for the Fatemi-Socie-Kurath model, and depth at which damage parameters correspond with experimental lives.
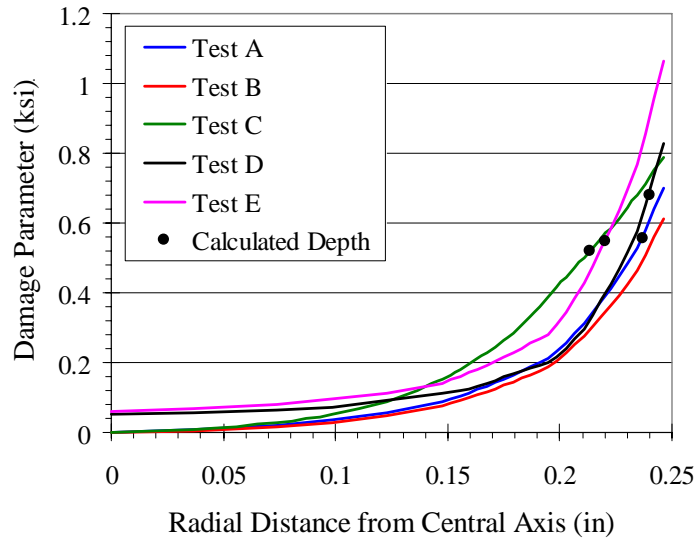
Figure D32. Damage parameter vs. depth under notch for the modified Chu-Conle-Bonnen model, and depth at which damage parameters correspond with experimental lives.
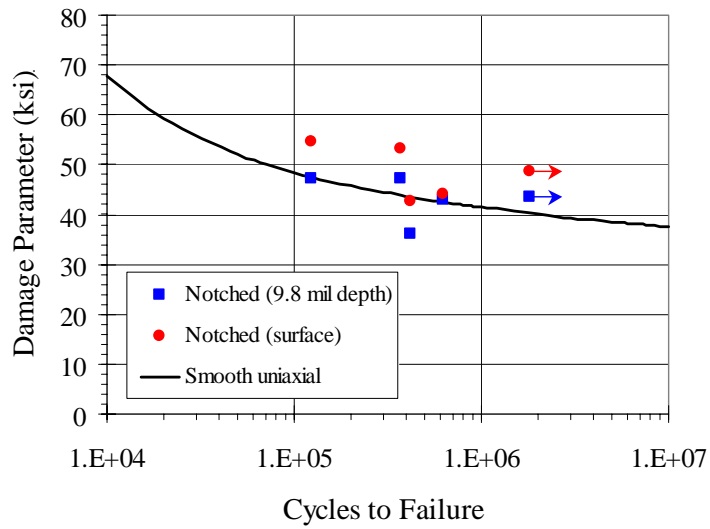
Figure D33. Comparison of damage parameters from the modified Manson-
McKnight model calculated at the surface and a depth of
9.8 mil (0.25 mm).
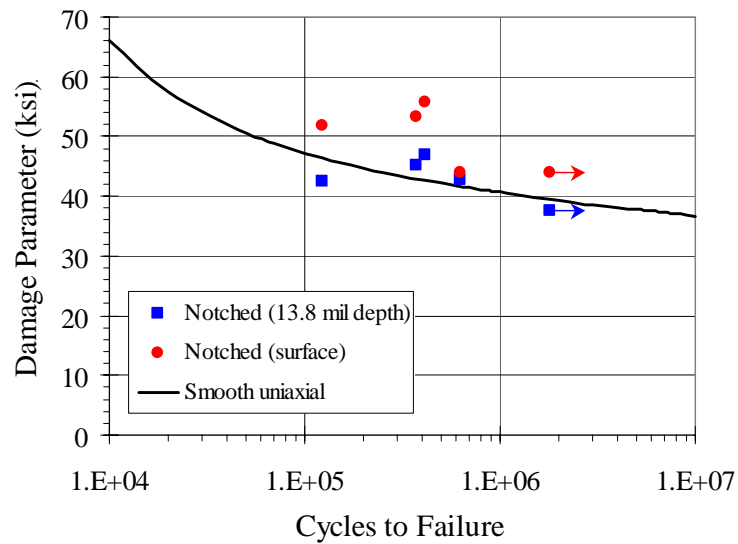
Figure D34. Comparison of damage parameters from the Findley model
calculated at the surface and a depth of 13.8 mil (0.35 mm).
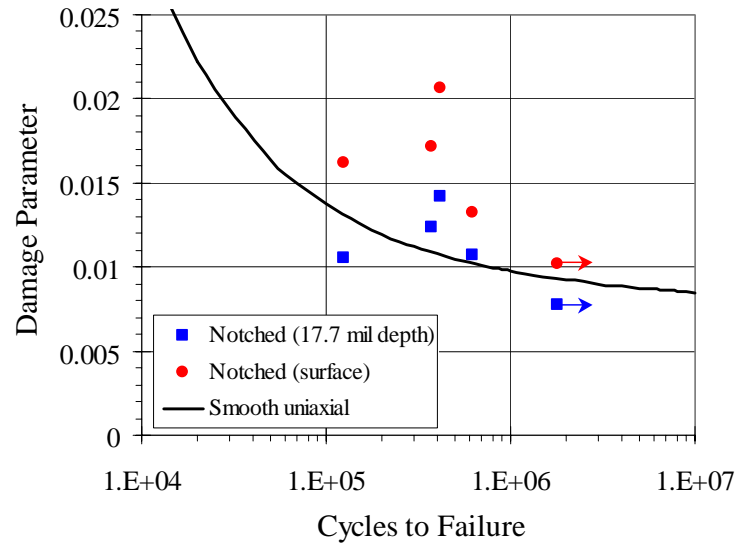
Figure D35. Comparison of damage parameters from the Fatemi-Socie-Kurath model calculated at the surface and a depth of 17.7 mil (0.45 mm).
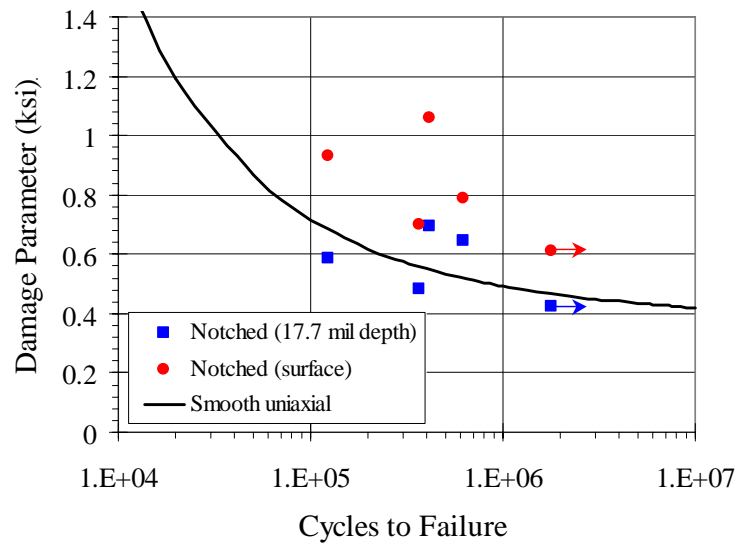
Figure D36. Comparison of damage parameters from the modified Chu-Conle-Bonnen model calculated at the surface and a depth of 17.7 mil (0.45 mm).

Notch acuity was shown to be influential in uniaxial experiments and theories previously presented. The observation that, in these tests, the torsional and axial stress concentrations differ could cause some of the "depth" discrepancy observed here.

Depending on the parameter evaluated, the optimal "damage depth" varied from 9.8 mil (0.25 mm) to 17.7 mil (0.45 mm). While these dimensions seem large compared to prior values assigned in the literature, it should be noted that the stress concentration factors in the current experiments were lower than most considered in the literature. The low value of K_t also tends to cause the stress-strain gradient to be shallow, but cover a significant portion of the net section of the specimen (Fig. D28). Hence, the dimensions cited here should be interpreted in the context of the geometry of notches tested.

Rather than assign a specific depth value to the damage, another methodology involves integrating the value of the damage parameter over a depth beneath the surface, r*, to obtain an averaged damage.

$$\overline{Damage} = \frac{1}{r^*} \int_{r_o - r^*}^{r_o} (Damage)\, dr \qquad (D20)$$

where r_o is the outer radius at the notch section. The results of this analysis are presented in Figures D37 through D40, and closely resemble the results of the point-depth analysis. A similar increment in depth and methodology to place the mean notched life on the uniaxial baseline curve was employed in this analysis. The depths, or r*, ranged from 15.8 mil (0.4 mm) with the modified Manson-McKnight parameter to 47.2 mil (1.2 mm) for the Fatemi-Socie-Kurath parameter. Again these are somewhat higher than those reported in the literature. A statistical comparison of the point and line depth averaging techniques is summarized in Table D8. As before, lower values of the mean and standard deviation are desirable.

Table D8. Statistical Comparison of Multiaxial Models for Notched Specimen Data

Model	DP calculated at notch root surface (% Error)		DP calculated at critical depth (% Error)		DP averaged over critical length (% Error)	
	Mean	St. Dev.	Mean	St. Dev.	Mean	St. Dev.
Mod. M-M	8.84	8.47	0.51	11.24	0.043	10.45
Findley	16.3	6.39	0.47	7.44	1.1	8.06
FSK	32.04	12.77	-0.67	20.93	-0.75	19.39
Mod. CCB	31.06	12.45	0.003	18.84	-1.37	21.69
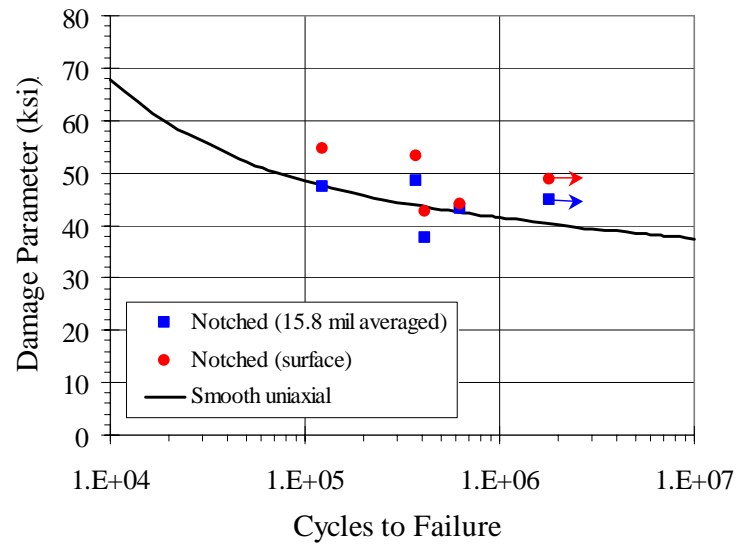
Figure D37. Comparison of damage parameters from the modified Manson-McKnight model calculated at the surface and averaged over 15.8 mil (0.4 mm) depth.
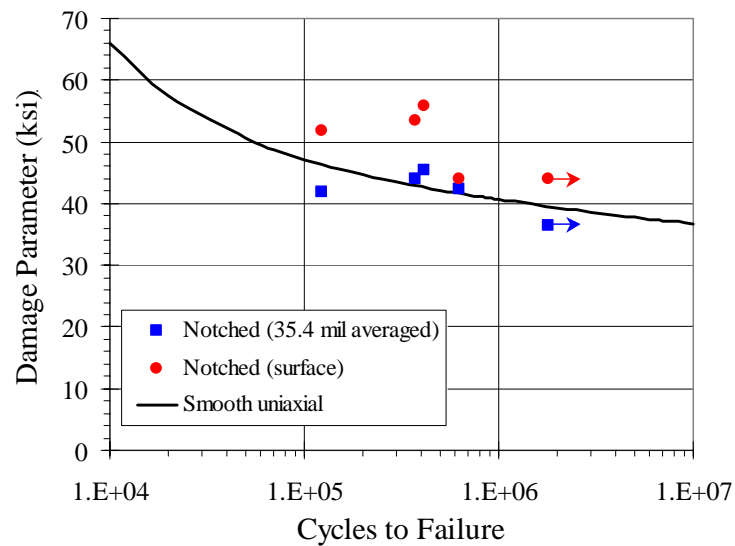
Figure D38. Comparison of damage parameters from the Findley model calculated at the surface and averaged over 35.4 mil (0.9 mm) depth.
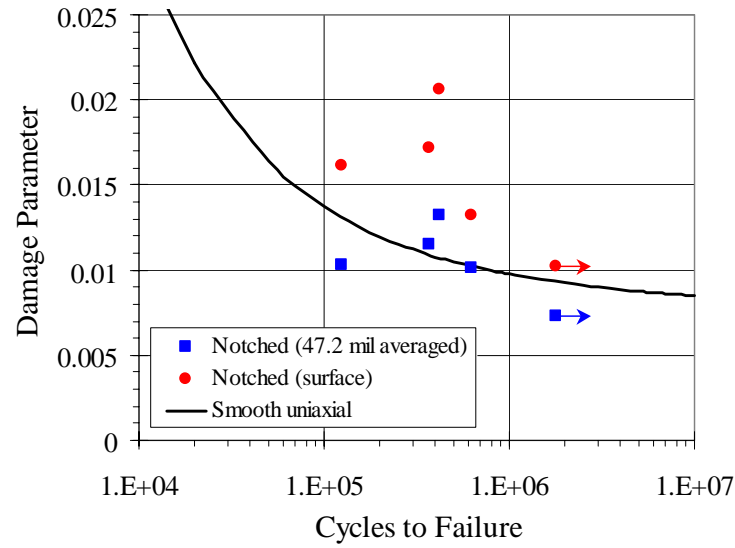
Figure D39. Comparison of damage parameters from the Fatemi-Socie-Kurath model calculated at the surface and averaged over 47.2 mil (1.2 mm) depth.
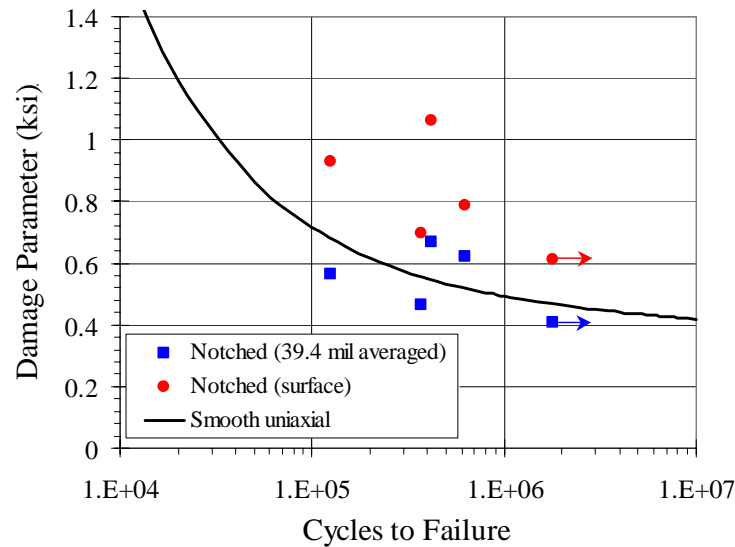
Figure D40. Comparison of damage parameters from the modified Chu-Conle-Bonnen model calculated at the surface and averaged over 39.4 mil (1 mm) depth.

While the line-averaged results look similar to the point results, the line-average method has the conceptual advantage of somewhat accounting for the differences in axial and torsional stress concentration factors that result in different stress and strain gradients. The

stress state of the geometry tested is two dimensional at the surface, but three dimensional below the surface. Neglecting the circumferential stress would have introduced significant errors in the calculations, but the effects of the radial stress below the surface were negligible. Due to the symmetry of the loading and stress state near the notch, the critical plane orientation remained approximately constant over the depths considered here. For more complex loading and a general geometry, an averaging scheme over a "critical" volume of dimension V* may be required. However, it seems that averaging or integrating the value of the damage parameter has inherent advantages over modifying the stress-strain state, especially for more complex loading. A major drawback at this juncture is that no overall methodology has been developed to determine the critical distance, line length or volume for a general multiaxial loading and geometry.

D.9   LCF/HCF INTERACTIONS AND FATIGUE DAMAGE ASSESSMENTS FOR MULTIAXIAL MISSION LOADINGS

The interaction between LCF (high damage) and HCF (low damage) cycles in a variable load history, or "mission" history, is another area of concern when developing fatigue damage assessment methods for turbine engine materials. The consideration of such interaction effects within multiaxial loadings gives rise to some additional challenges. For example, the definition of a cyclic event can be ambiguous when different components of the stress tensor are cycling out-of-phase of one another. Furthermore, the use of a critical-plane model for damage assessment can add additional complications when different events in the history cause maximum damage on different planes.

Past research has demonstrated that damage summation methods utilizing traditional multiaxial fatigue damage parameters and linear damage accumulation rules are often highly non-conservative, indicating an interaction effect between LCF and HCF cycles. These effects are more pronounced when out of phase loading comprises one of the cyclic events. Similar LCF/HCF interaction effects have been observed under uniaxial loading conditions. A variety of techniques have been proposed to accommodate experimental observations, including non-linear damage rules, modification of the baseline damage curve, and extended interpretation of the damage parameter.

In an attempt to better understand the potential interaction effects between LCF and HCF cycles in Ti-6Al-4V under a multiaxial stress state, several biaxial mission tests were conducted on similar specimens as used in the previous biaxial testing. The mission histories were constructed from the non-proportional load paths discussed previously, and consisted of a relatively small number of high damage (LCF) cycles coupled with a larger number of low damage (HCF) cycles. Based on the results of the previous analyses, the Findley model [version (b)] was selected to predict the damage caused by each cycle. To evaluate the LCF/HCF interaction effect, mission lives were subsequently calculated and compared to experimental results. In this study, two damage summation algorithms were used, the first based on the assumption of linear damage accumulation, and the second using a nonlinear cumulative damage rule.

The damage predictions using version (b) of the Findley model are repeated for the smooth bar data in Figure D41, with the uniaxial data shown in the upper plot and the biaxial data in the lower plot. There are two additional features that need clarification in the uniaxial (top) figure. First, the "step-test" data located at the higher end of the failure life are shown on this plot, but were not included in the calculation of the best-fit curve. It was noted that these tests appeared to result in slightly higher stress levels at long life than the single-load tests. Second, a "threshold" line is shown on the plot. This line indicates the level of the Findley parameter below which the applied loadings are assumed to have negligible effect on the fatigue life of the specimen. As can be seen from the figure, the prediction curve continues to drop at higher life, even though there are no data to suggest the continued trend above 10^9 cycles. This results in overly conservative life predictions when extrapolating the curve to long-life regions. Examining the calculated Findley parameters and observing that no failure occurred below 34 ksi, a lower bound to failure was established at this level.
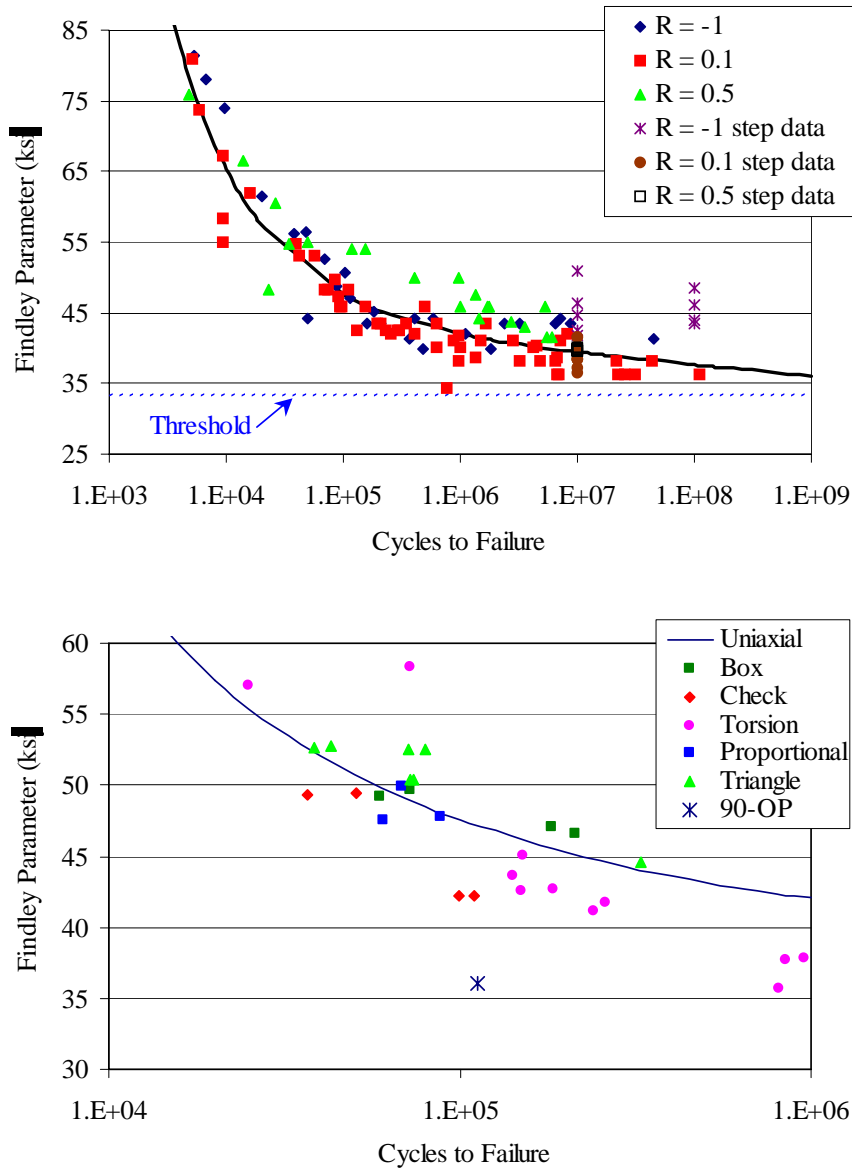
Figure D41. Findley model, version (b), applied to Ti-6Al-4V uniaxial data (top) and biaxial data (bottom).

D.9.1   Mission Histories: Results and Model Comparisons using Linear Damage Rule

Two variations of mission histories were tested, each designed to represent the effects a component could experience while in service. In these histories, a relatively few high-damage (LCF) cycles were applied periodically within a larger number of low-damage (HCF) cycles. The LCF load path is what gives rise to the mission type. As illustrated in Figure D42, the two mission histories were based on the box path and the check path (LCF

cycles). The HCF cycles were defined as small portions of the LCF cycles. The differences between the LCF and HCF cycle shapes and amplitudes generated different critical planes within a loading cycle, as predicted by the Findley model, and provided a differentiation among the fatigue damage produced by each cycle. The stress levels were applied to produce LCF lives in the range of 10^4 to 10^5 cycles, while the HCF stress levels were selected to produce lives on the order of 10^8 to 10^9 cycles, as per the Findley model predictions.
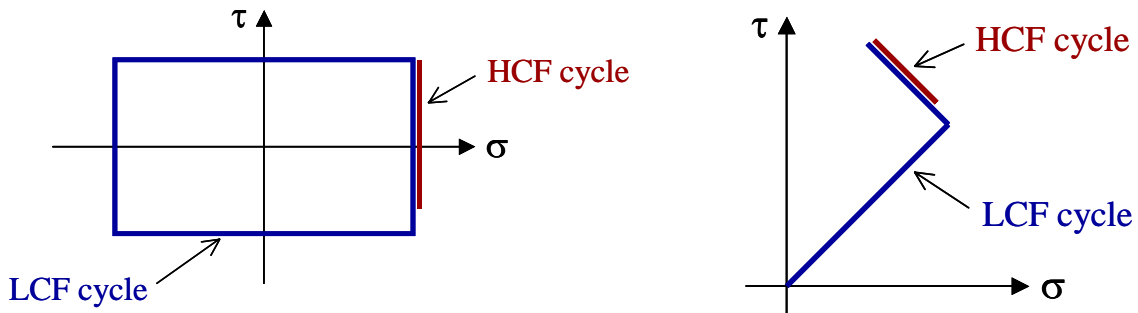
Figure D42. Simulated mission histories, showing LCF and HCF cycles
for the box path and the check path.

Three sets of mission history tests were conducted, two based on the box path and one based on the check path. Two samples were run at each load level. Each mission history consisted of one LCF cycle followed by a larger number of HCF cycles. For the two box path histories, one consisted of 50 HCF subcycles (Box 1) and the other consisted of 5 HCF subcycles (Box 2). It should be noted the same subcycle was utilized in both missions. The check path consisted of 50 subcycles in addition to the LCF cycle. These mission histories were repeatedly applied to round bar specimens of Ti-6Al-4V until fracture. The number of LCF cycles completed before failure is defined as the mission life.

The experimental results for the mission histories are shown in Table D9, along with the corresponding mission life predictions using the Findley model in conjunction with a linear cumulative damage rule. As is evident from these results, the predicted mission lives were essentially identical to the predicted LCF lives in all cases, when a linear damage assumption was used. This is not surprising, since the HCF lives were predicted to be roughly four orders of magnitude larger than the LCF lives. Thus, utilizing a linear damage

rule, a substantial number of HCF cycles would need to be applied before they would begin to influence the mission life.

The experimental data, however, indicate different results. For the two box missions, the HCF cycles substantially influenced the mission lives. Specifically, when 50 HCF cycles were applied (Box 1), the mission lives decreased by a factor of three relative to the LCF lives. When only 5 HCF cycles were applied, the mission lives still decreased by roughly 33%. This indicates a significantly nonlinear damage accumulation rate in the box path. However, in the case of the check path, 50 HCF cycles did not produce any reduction in the mission life, even though they were predicted to cause similar damage levels as the subcycles in the box path. Thus, it is evident that the damage accumulation rate, and the effects of LCF/HCF interactions, are load path dependent.

**Table D9. Mission History Results and Model Comparisons
using the Findley Parameter with Linear Cumulative Damage Rule**

Cycle/Mission	Mission Histories		
	Box 1 1 LCF/50 HCF	Box 2 1 LCF/5 HCF	Check 1 LCF/50 HCF
Experimental LCF Lives Average	59,432 / 72,360 65,900	59,432 / 72,360 65,900	50,568 / 36,920 43,700
Predicted LCF Life (Plane)	66,900 (122°)	65,500 (122°)	66,900 (12°)
Predicted HCF Life (Plane)	3.0×10^8 (10°)	2.3×10^8 (10°)	1.9×10^8 (48°)
Experimental Mission Life Average	19,420 / 21,422 20,400	48,787 / 39,480 44,100	44,544 / 49,776 47,200
Pred. Mission Life (Plane)	66,900 (122°)	65,400 (122°)	66,600 (12°)

By consideration of the results in Table D9, it is evident that two factors merit further attention. The first pertains to the observed effect of the load path dependence on the damage accumulation rate; i.e., the HCF cycles are much more damaging in the case of the box path than in the check path. The second factor relates to the damage accumulation method itself; i.e., a nonlinear cumulative damage rule is required to account for the nonlinear nature of the LCF/HCF interactions.

D.9.2 Load Path Dependence on LCF/HCF Interactions

To address the issue of load path dependence, an evaluation was performed for both the box path and check path to determine which plane experiences the most damage from the combined LCF and HCF cycles, according to the Findley model. As illustrated in Figure D43, the box path exhibits four LCF maxima representing approximately the same damage value. Thus, it is reasonable to expect that there would be an equal probability that a crack may initiate on any of these four planes. When incorporated into a mission history containing LCF and HCF cycles, it would subsequently be expected that the plane of maximum damage potential would be the LCF critical plane experiencing the maximum damage from the HCF subcyles. From Figure D43, it is evident that the LCF critical plane at 12° also nearly coincides with an HCF critical plane; i.e., the LCF and HCF damage curves experience a peak at roughly the same plane orientation.

A similar evaluation was performed with the check mission, shown in Figure D44. In this instance there were only two peaks associated with the LCF parameter. Note, however, that the peak in the HCF curve did not correspond closely to a peak in the LCF curve. Further examination revealed that the maximum HCF Findley parameter on an LCF critical plane was only 32.6 ksi. This value falls below the prescribed threshold of 34 ksi determined earlier. Therefore, the damage associated with the HCF subcycles would be predicted to have a negligible effect on the fatigue life of the specimen.

This distinction of the applied HCF damage on the LCF critical plane validates the experimental evidence showing a load path dependence on the influence of the HCF cycles. In other words, even though both HCF cycles were predicted to cause the same degree of damage on their corresponding critical planes, the fact that the HCF critical plane for the box path coincided with an LCF critical plane caused the box missions to be much more influenced by the HCF cycles than the check mission, where the LCF and HCF critical planes did not coincide. It should be noted that a multiaxial parameter that does not identify critical plane orientations would not be capable of recognizing the load path dependence of HCF damage observed in this study. This is an important point in regard to equivalent-stress based multiaxial parameters, which do not distinguish critical plane orientations with respect to fatigue damage.
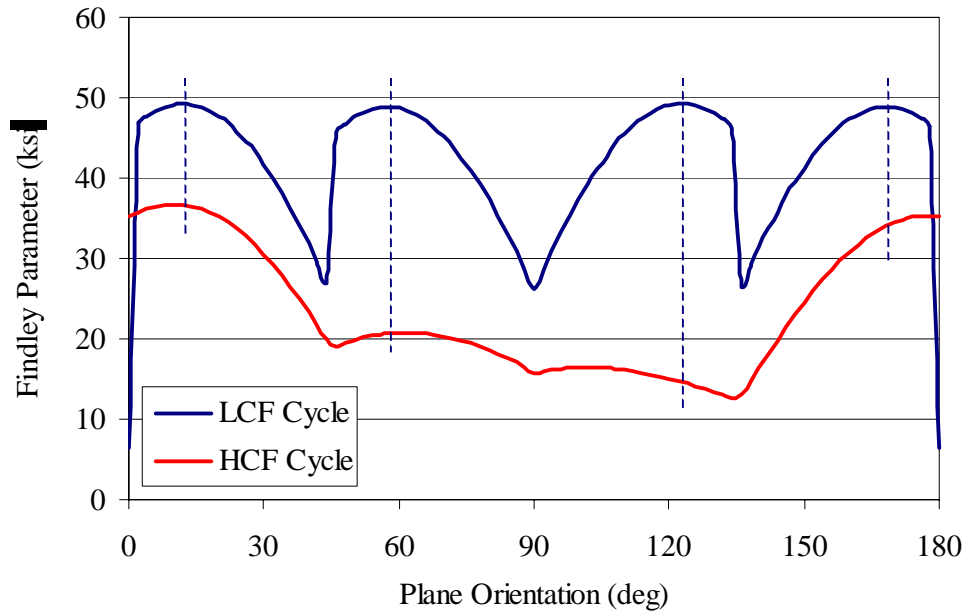
Figure D43. Variation of the Findley Parameter with plane orientation for
the box path (LCF and HCF cycles).
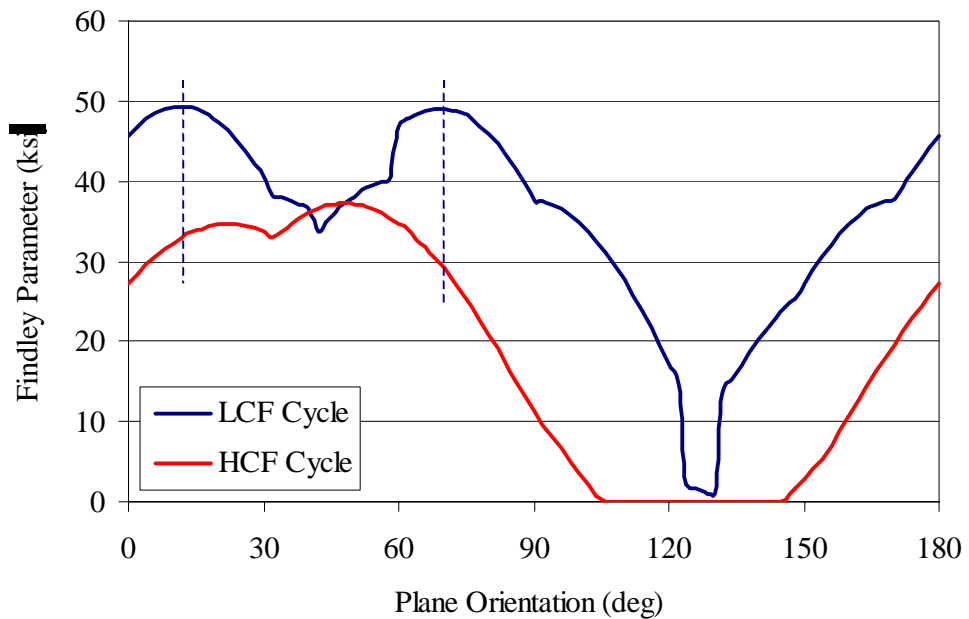
Figure D44. Variation of the Findley Parameter with plane orientation for
the check path (LCF and HCF cycles).

D.9.3 Nonlinear Damage Accumulation Rule

The manner in which damage was initially determined for the multiaxial loadings was to sum up all of the LCF and HCF cycles as per the Palmgren-Miner Rule. However, the discrepancy between experimental and predicted mission lives for the box path indicates the damage likely accumulates nonlinearly. Recent work [23, 24] has expressed the possibility of two models that possess the likelihood of reducing this difference, the Double Linear Damage Rule (DLDR) and the Damage Curve Approach (DCA). The DLDR proposes to create two separate linear damage relations; one for Phase I and one for Phase II crack growth. The difficulty in utilizing this model is the failure to distinguish between crack initiation and crack propagation. Consequently, in this study the DCA model was implemented. This model makes use of relative damage and employs the concept of remaining life for a specimen. The DCA approach can be seen in its general form in Eq. D21, where n is the number of applied cycles, N_f is the number of cycles to failure, N_{ref} is the life level at which damage accumulates linearly, and α is a material parameter. Since the point at which damage accumulates in a linear manner is an unknown, N_{ref} can be taken as 1, which has the added effect of simplifying the general equation [24].

$$D = \left(\frac{n}{N_f}\right)^{\left(\frac{N_f}{N_{ref}}\right)^{\alpha}} \tag{D21}$$

The following form of the DCA equation, Eq. D22, describes a two-level loading condition in which one cycle experiences a stress of a given magnitude followed by another cycle(s) of different (either larger or smaller) stress magnitude. As can be seen, this expression predicts greater nonlinearity in damage accumulation as the difference between N_1 and N_2 increases. In this equation, n_1 and n_2 are the number of applied cycles for one mission. N_1 and N_2 are the number of cycles to failure corresponding to the first and second loading blocks (in this case the number of LCF and HCF cycles), respectively. Again, α is a material property that needs to be determined. According to McGaw [24], α is generally taken to be 0.4 based on two-level load testing of steel and titanium alloys. However,

analysis of the DCA approach in this study yielded an α of 0.72 when applied to the box and check missions.

$$\frac{n_2}{N_2} = 1 - \left(\frac{n_1}{N_1}\right)^{\left(\frac{N_1}{N_2}\right)^{\alpha}}$$ (D22)

Figure D45(a) illustrates the general DCA model. Notice that damage develops earlier and at a faster rate when N is smaller, which is indicative of an LCF loading block. Also shown is the DCA for a two-level loading history, Fig. D45(b). As the difference between N_1 and N_2 decreases the damage accumulation becomes more linear until, when N_1 equals N_2, the DCA reduces to the Palmgren-Miner Rule.

(a)   (b)
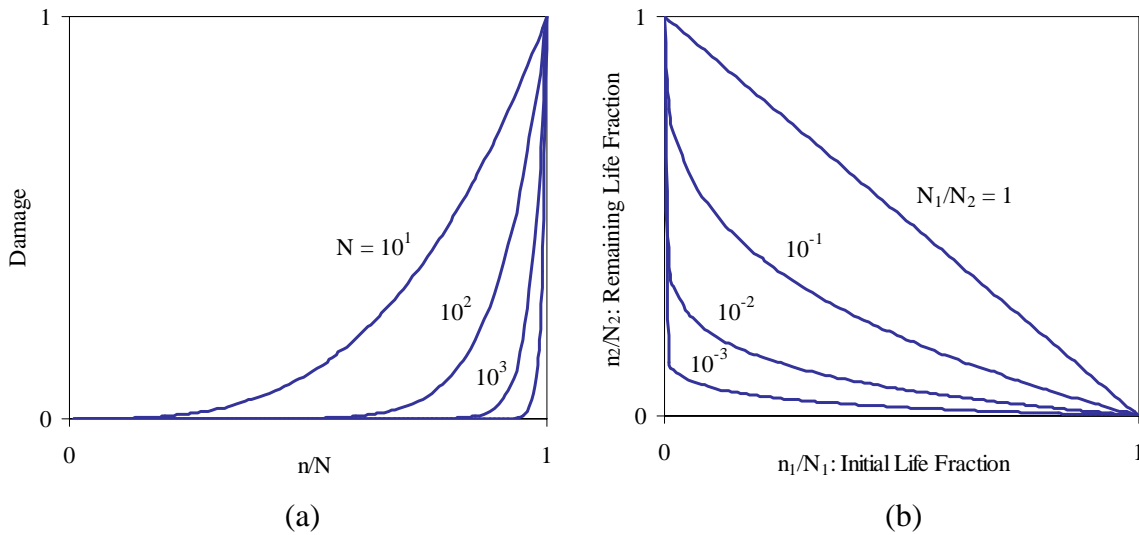
Figure D45. Graphical interpretation of the DCA model.

An important feature of the DCA model is the manner in which the loads are applied. McGaw [24] evaluated the effects on damage for both a two-level single-block loading and a two-level multi-block loading (Figure D46). The result indicated the multi-block loading experienced a more nonlinear rate of damage accumulation. Note that the testing conditions for the box and check path mission histories consisted of this two-level multi-block loading.

Therefore, these histories would be expected to exhibit significant nonlinear damage accumulation.
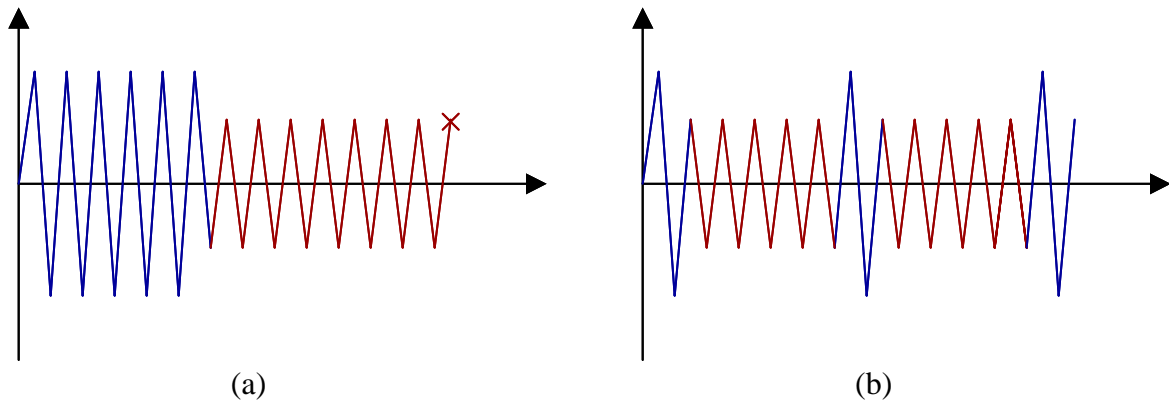
Figure D46. Loading patterns: (a) two-level single-block loading, and
(b) two-level multi-block loading.

The results of the mission-history life predictions, using the Findley model with the threshold stress level in conjunction with the DCA model, are shown in Table D10 along with the experimental results. As previously noted, a value of $\alpha = 0.72$ was found to provide the best correlation with experimental results. It can be seen that the predicted mission lives for the two box histories are in excellent agreement with the experimental lives using the DCA model.

In the case of the check mission, since the HCF Findley parameter on the LCF critical plane was less than the threshold value, the HCF life on that plane was taken as infinite. Thus, the DCA model predicted no effect of the HCF cycles on the check mission life. Although the predicted and experimental mission lives for the check history were not in as good agreement as for the box history, the discrepancy was due to the LCF life prediction, not due to the failure of the nonlinear damage model. Nevertheless, it should be noted that all the life predictions using the Findley model and Damage Curve Approach are within reasonable bounds.

**Table D10. Mission History Results and Model Comparisons using
Findley Parameter with Nonlinear Cumulative Damage Rule (DCA)**

Cycle/Mission	Mission Histories		
	Box 1 1 LCF/50 HCF	Box 2 1 LCF/5 HCF	Check 1 LCF/50 HCF
Experimental LCF Lives	59,432 / 72,360	59,432 / 72,360	50,568 / 36,920
Average	65,900	65,900	43,700
Predicted LCF Life (Plane)	66,900 (12°)	65,500 (12°)	66,900 (12°)
Pred. HCF Life on LCF Plane	3.0×10^8	2.3×10^8	∞
Experimental Mission Life	19,420 / 21,422	48,787 / 39,480	44,544 / 49,776
Average	20,400	44,100	47,200
Pred. Mission Life (Plane)	18,260 (12°)	45,880 (12°)	66,900 (12°)

D.10   SUMMARY AND CONCLUSIONS

Twenty-two multiaxial fatigue algorithms were initially evaluated in their ability to
correlate uniaxial mean stress and biaxial fatigue data for Ti-6Al-4V. Both equivalent-stress
and critical-plane parameters were considered. Based on the results of the initial evaluation,
a smaller number of models were selected for more detailed study. The majority of the
selected multiaxial fatigue models were reasonably successful at predicting mean stress
effects in Ti-6Al-4V and Ti-17 under uniaxial loading conditions. However, significant
differences were noted between models in their ability to predict multiaxial fatigue lives or
damage. Of the equivalent-stress models, only the modified Manson-McKnight model
provided reasonably good multiaxial predictions. The Findley critical-plane model provided
the best overall correlations with experimental data for multiaxial loadings; however, the
definition of the maximum normal stress in the cycle is important, and affects the
correlations. Since the normal (tensile) stress based critical-plane models were all highly
non-conservative in their multiaxial predictions, it can be inferred that fatigue crack
development in these titanium alloys is driven primarily by cyclic shear stresses.

The application of multiaxial fatigue methodologies to notched components presents
some additional challenges. It was demonstrated here that methods based on the critical-
distance concept, in conjunction with a variety of multiaxial parameters, hold potential.

However, a significant limitation involves the determination of the critical distance, or depth at which the damage parameter should be calculated or averaged.

The limited data pertaining to LCF/HCF interactions in Ti-6Al-4V indicate that small (HCF) cycles can cause significantly more damage than predicted by a linear cumulative damage rule, but the effect of the HCF cycles on the LCF mission life is dependent on the load path. When used in conjunction with a linear damage rule, none of the multiaxial models were successful at predicting the observed experimental behavior. However, a nonlinear damage rule was evaluated (Damage Curve Approach), and produced very good results when used with the Findley critical-plane parameter. It was noted that, in order to account for the observed load-path dependence on LCF/HCF interactions, the relationships between the LCF and HCF critical planes must be taken into account. This finding poses a severe limitation in the use of equivalent-stress models, which are incapable of distinguishing such nuances in the load path.

D.11 REFERENCES

1. Garud, Y. S., 1981, "Multiaxial Fatigue: A Survey of the State of the Art," *Journal of Testing and Evaluation*, **9**, pp. 165-178.

2. You, B. R., and Lee, S. B., 1996, "A Critical Review on Multiaxial Fatigue Assessments of Metals," *International Journal of Fatigue*, **18**, pp. 235-244.

3. Sines, G., and Ohgi, G., 1981, "Fatigue Criteria under Combined Stresses or Strains," *ASME Journal of Engineering Materials and Technology*, **103**, pp. 82-90.

4. Shigley, J. E., and Mischke, C. R., 1989, *Mechanical Engineering Design*, McGraw-Hill, New York.

5. Manson, S. S., and Jung, K., 1994, "Progress in the Development of a Three-Dimensional Fatigue Theory Based on the Multiaxiality Factor," *Material Durability/Life Prediction Modeling: Materials for the 21st Century*, American Society of Mechanical Engineers, **290**, pp. 85-93.

6. Slavik, D., and Kurath, P., 2000, "Fatigue Crack Initiation Modeling in Ti-6Al-4V for Smooth and Notched Specimens under Complex Stress States," *Fifth National Turbine Engine HCF Conference*, Chandler, AZ.

7. McKnight, R. L., and Slavik, D. C., 2000, General Electric Aircraft Engines, personal communication.

8.   Morrow, J., 1968, *Fatigue Design Handbook, SAE AE-6*, J. A. Graham, ed., Society of Automotive Engineers, pp. 17-58.

9.   Smith, R. N., Watson, P., and Topper, T. H., 1970, "A Stress-Strain Function for the Fatigue of Metals," *Journal of Materials*, **5**, pp. 767-778.

10.   Kandil, F. A., Brown, M. W., and Miller, K. J., 1982, "Biaxial Low-Cycle Fatigue Fracture of 316 Stainless Steel at Elevated Temperatures," The Metals Society, London, **280**, pp. 203-210.

11.   Findley, W. N., 1957, "Fatigue of Metals Under Combinations of Stresses," *ASME Transactions*, **79**, pp. 1337-1348.

12.   McDiarmid, D. L., 1991, "A General Criterion for High Cycle Multiaxial Fatigue Failure," *Fatigue Fract. Engng. Mater. Struct*., **14**, pp. 429-453.

13.   Fatemi, A., and Kurath, P., 1988, "Multiaxial Fatigue Life Predictions Under the Influence of Mean Stresses," *ASME Journal of Engineering Materials and Technology*, **110**, pp. 380-388.

14.   Chu, C. C., Conle, F. A., and Bonnen, J. J. F., 1993, "Multiaxial Stress-Strain Modeling and Fatigue Life Prediction of SAE Axle Shafts," *Advances in Multiaxial Fatigue, ASTM STP 1191*, D. L. McDowell and R. Ellis, eds., American Society for Testing and Materials, Philadelphia, PA, pp. 37-54.

15.   Glinka, G., Wang, G., and Plumtree, A., 1995, "Mean Stress Effects in Multiaxial Fatigue," *Fatigue Fract. Engng. Mater. Struct*., **18**, pp. 755-764.

16.   Socie, D., 1993, "Critical Plane Approaches for Multiaxial Fatigue Damage Assessment," *Advances in Multiaxial Fatigue, ASTM STP 1191*, D. L. McDowell and R. Ellis, eds., American Society for Testing and Materials, Philadelphia, PA, pp. 7-36.

17.   Kurath, P., and Jiang, Y., "Analysis of Residual Stresses and Cyclic Deformation for Induction Hardened Components," *SAE Technical Paper Series No. 950707, Journal of Materials and Manufacturing, SAE Transactions*, Society of Automotive Engineers, Warrendale, PA, **5**, pp. 603-617.

18.   Forsyth, P. J. E., 1969, *The Physical Basis of Metal Fatigue*, American Elsevier Publishing Company, Inc., New York.

19.   Ritchie, R. O., and Peters, J. O., 2001, "Small Fatigue Cracks: Mechanics, Mechanisms and Engineering Applications," *Materials Transactions*, **42**, pp. 58-67.

20.   Slavic, D. C., Dunyak, T., Griffiths, J., and Kurath, P., 2000, "Fatigue Crack Initiation Modeling in Ti-6Al-4V for Smooth and Notched Geometries," *Proceedings of the 5ᵗʰ National Turbine Engine High Cycle Fatigue Conference*, Arizona.

21.	Taylor, D., 1999, "Geometrical Effects in Fatigue: A Unifying Theoretical Model," *International Journal of Fatigue*, **21**, pp. 413-420.

22.	Peterson, R. E., 1974, <u>Stress Concentration Factors</u>, Wiley Interscience.

23.	Manson, S. S., and Halford, G. R., "Practical Implementation of the Double Linear Damage Rule and Damage Curve Approach for Treating Cumulative Fatigue Damage," Int. J. of Fracture, **17**, 1981, pp. 169-192.

24.	McGaw, M. A., "Approaches to Cumulative Damage Analysis," Material Durability/Life Prediction Modeling: Materials for the 21st Century, ASME PVP-Vol. 290, 1994, pp. 95-106.

APPENDIX E

CLOSED-FORM EQUATIONS FOR CRITICAL PLANE ORIENTATION AND PARAMETERS

E.1 INTRODUCTION

In an effort to make critical plane calculations more efficient, P&W developed closed-form equations for determining the orientations of the critical planes and also the values of the critical plane parameters. We have focused on two different critical plane parameters:

> (i) Smith-Watson-Topper (SWT) and
> (ii) Findley (FIN).

The SWT parameter is more suited to model normal stress induced cracking while the FIN parameter is more suited for modeling shear stress dominated cracking. Currently, these parameters (like all critical plane parameters) are evaluated by using a search algorithm in which the "critical plane" is determined by sweeping through plane orientations between 0 – 180 degrees (in increments of either 1, 2, or 5 degrees) for each time step in the fatigue cycle. This procedure can be implemented in a computer program. However, conducting such a calculation at each Gauss point in a finite element structural analysis for large mission loadings, encountered in engine components, could lead to very large computer run times. The closed-form solutions presented in this report are expected to alleviate this problem and lead to an efficient implementation of critical plane theories in the life analysis of aero-engine components.

E.2 THE SWT PARAMETER

The SWT parameter is calculated as the product of the maximum normal strain amplitude, ε_a, on a 'critical plane' and the maximum normal stress, σ_{max}, on the critical plane:

$$SWT = \sqrt{\sigma_{max} \varepsilon_a E} \qquad (E1)$$

where, E is the Young's modulus.

E.2.1   SWT Parameter and Critical Plane Using the Double Search Algorithm

The 'double search' algorithm computes the critical plane by computing the SWT parameter (for all time steps in the fatigue cycle) along planes with orientation angles ranging from 0 – 180 degrees with respect to the axial loading direction. Along each plane the max normal ε_a and the max normal σ_{max} are computed over the entire fatigue cycle, using appropriate transformation equations for stress and strain. The plane on which the SWT parameter is the maximum (for all time steps of the loading cycle) is then the 'critical plane' for the given loading cycle.

E.2.2   SWT Parameter and Critical Plane Using Closed-Form Equations

A more efficient way to calculate the SWT parameter is by using closed-form equations. For the case of two dimensional, proportional, in-phase loading consisting of σ_x, σ_y, and τ_{xy} stresses, it is possible to derive direct equations to calculate the SWT parameter and the critical plane.

Consider a general state of stress in which the material is being subjected to cyclic loading in all the three stress components σ_x, σ_y, and τ_{xy}. Each of the stress components are in-phase and consist of a sinusoidal wave form described by a stress amplitude given by σ_{xa}, σ_{ya}, and τ_a and a mean stress given by σ_{xm}, σ_{ym}, and τ_m. Further, consider that the material is subjected to cyclic strain amplitudes given by ε_{xa}, ε_{ya}, and γ_a and mean strains given by ε_{xm}, ε_{ym}, and γ_m. For this applied stress and strain state, the critical plane, θ_{SWT}, can be derived by maximizing the strain amplitude, $\varepsilon_{xa}(\theta)$, as function of the orientation angle θ. It is assumed that the plane on which the strain amplitude is maximized will provide a good approximation for the plane on which the SWT parameter peaks. Maximizing the strain amplitude, $\varepsilon_{ya}(\theta)$, also provides the same equation for the critical plane which is given by:

$$\theta_{SWT} = \frac{1}{2}\tan^{-1}\left(\frac{\gamma_a}{\varepsilon_{xa} - \varepsilon_{ya}} \right) \tag{E2}$$

The SWT parameter is then computed on this critical plane, θ_{SWT}. Since both σ_x and σ_y, could be acting in a general stress state, the required SWT parameter needs to be computed using both the stress and strain components as:

$$SWT = \max \{SWT1, SWT2\} \text{ where,}$$

$$SWT1 = \sqrt{\sigma_{x,\max} \varepsilon_{xa,\max} E} , \quad \text{and} \quad SWT2 = \sqrt{\sigma_{y,\max} \varepsilon_{ya,\max} E} \tag{E3}$$

where, $\varepsilon_{xa,\max}$ and $\varepsilon_{ya,\max}$ are the max x and y strain amplitudes on the critical plane, θ_{SWT}. $\sigma_{x,\max}$ and $\sigma_{y,\max}$ are the max normal x- and y-stresses on the critical plane, θ_{SWT}. The max strain amplitudes and max normal stresses on the critical plane are given by the following equations:

$$\sigma_{x,\max} = (\sigma_{xa} + \sigma_{xm})\cos^2(\theta_{SWT}) + (\sigma_{ya} + \sigma_{ym})\sin^2(\theta_{SWT}) + (\tau_a + \tau_m)\sin(2\theta_{SWT})$$

$$\varepsilon_{xa,\max} = \frac{1}{2}\left((\varepsilon_{xa} + \varepsilon_{ya}) + (\varepsilon_{xa} - \varepsilon_{ya})\cos(2\theta_{SWT}) + \gamma_a \sin(2\theta_{SWT})\right)$$

$$\sigma_{y,\max} = (\sigma_{xa} + \sigma_{xm})\sin^2(\theta_{SWT}) + (\sigma_{ya} + \sigma_{ym})\cos^2(\theta_{SWT}) - (\tau_a + \tau_m)\sin(2\theta_{SWT})$$

$$\varepsilon_{ya,\max} = \frac{1}{2}\left((\varepsilon_{xa} + \varepsilon_{ya}) - (\varepsilon_{xa} - \varepsilon_{ya})\cos(2\theta_{SWT}) - \gamma_a \sin(2\theta_{SWT})\right)$$

$$\tag{E4}$$

E.3 THE FINDLEY (FIN) PARAMETER

The FIN parameter is calculated using the maximum shear stress amplitude, τ_a, on a 'critical plane' and the maximum normal stress, $\sigma_{\max}$, on the critical plane:

$$FIN = \tau_a + k \, \sigma_{\max} \tag{E5}$$

where, k is a fitting parameter. For the present study, k = 0.28 was used.

Findley Parameter and Critical Plane Using the Double Search Algorithm:

The 'double search' algorithm can be used to compute the critical plane and the maximum Findley parameter over the fatigue cycle using the same procedure described above for the SWT parameter.

E.3.1 Findley Parameter and Critical Plane Using Closed-Form Equations:

A more efficient way to calculate the Findley parameter is by using closed-form equations. For the case of two dimensional, proportional, in-phase loading consisting of σ_x, σ_y, and τ_{xy} stresses, it is possible to derive direct equations to calculate the FIN parameter and the critical plane.

Consider the cyclic stress state in which each of the stresses consists of a sinusoidal wave form described by a stress amplitude given by σ_{xa}, σ_{ya}, and τ_a and a mean stress given by σ_{xm}, σ_{ym}, and τ_m. For this applied in-phase stress state, the critical planes, θ_{FIN1}, and, θ_{FIN2}, can be derived by maximizing the Findley parameters, FIN1(θ) and FIN2(θ), as functions of the orientation angle θ. The two critical planes result from the stress components σ_x and σ_y, which may be present on a critical plane in a general stress state. The closed-form equation for the critical angle, θ_{FIN1}, is given by:

$$\theta_{FIN1} = \frac{1}{2}\tan^{-1}\left(\frac{2k(\tau_a + \tau_m) - (\sigma_{xa} - \sigma_{ya})}{2\tau_a + k((\sigma_{xa} + \sigma_{xm}) - (\sigma_{ya} + \sigma_{ym}))}\right) \qquad (E6)$$

The corresponding equation for the Findley parameter, FIN1, is:

$$FIN1 = \tau_a \cos(2\theta_{FIN1}) - \frac{1}{2}(\sigma_{xa} - \sigma_{ya})\sin(2\theta_{FIN1})$$
$$+ k((\sigma_{xa} + \sigma_{xm})\cos^2(\theta_{FIN1}) + (\sigma_{ya} + \sigma_{ym})\sin^2(\theta_{FIN1}) + (\tau_a + \tau_m)\sin(2\theta_{FIN1}))$$
$$(E7)$$

The closed-form equation for the critical angle, θ_{FIN2}, is given by:

$$\theta_{FIN2} = \frac{1}{2}\tan^{-1}\left(\frac{2k(\tau_a + \tau_m) + (\sigma_{xa} - \sigma_{ya})}{-2\tau_a + k((\sigma_{xa} + \sigma_{xm}) - (\sigma_{ya} + \sigma_{ym}))}\right) \qquad (E8)$$

The corresponding equation for the Findley parameter, FIN2, is:

$$FIN2 = \tau_a \cos(2\theta_{FIN2}) - \frac{1}{2}(\sigma_{xa} - \sigma_{ya})\sin(2\theta_{FIN2})$$
$$+ k((\sigma_{xa} + \sigma_{xm})\sin^2(\theta_{FIN2}) + (\sigma_{ya} + \sigma_{ym})\cos^2(\theta_{FIN2}) - (\tau_a + \tau_m)\sin(2\theta_{FIN2}))$$
$$(E9)$$

For the general state of stress considered above, the maximized Findley parameter, FIN, is given by:

$$FIN = \max(FIN1, FIN2) \qquad (E10)$$

E.4   RESULTS AND DISCUSSION

The above closed form equations were used to compute the critical angles and parameters for the proportionally loaded, in-phase tension-torsion test cases from the PRDA V test program. The details of the stress states analyzed are given in Table E1. The results from the closed-from equations are compared with the results from the double search algorithm in Table E2.

For the SWT parameter, using the maximum strain amplitude to search for the critical plane was found to be adequate in determining the appropriate critical planes for the cases analyzed. For the Findley parameter, there was excellent agreement between the closed-form equation results for the critical plane and the maximized parameter.

Table E1. Tension-Torsion Proportionally Loaded Test Cases from the PRDA V Program

Spec. ID	σ_{xa}	σ_{xm}	τ_a	τ_m	ε_{xa}	ε_{xm}	γ_a	γ_m
Multiaxial In-phase Loading Cases
156-11/S	120.67	-1.60	0.00	0.00	0.00754	0.00002	0.00000	0.00000
21-11/S	0.00	0.00	54.55	-0.05	0.00000	0.00000	0.00867	-0.00001
21-6-S/L	0.00	0.00	38.50	0.10	0.00000	0.00000	0.00612	0.00002
156-10-S	0.00	0.00	35.30	-0.10	0.00000	0.00000	0.00561	-0.00002
21-7/S	0.00	0.00	34.78	31.13	0.00000	0.00000	0.00822	0.00988
156-5S	0.00	0.00	34.92	29.29	0.00000	0.00000	0.00560	0.00650
156-4-S	0.00	0.00	37.70	27.30	0.00000	0.00000	0.00605	0.00755
156-1	0.00	0.00	32.86	27.45	0.00000	0.00000	0.00436	0.00522
21-4-S/L	0.00	0.00	35.69	30.41	0.00000	0.00000	0.00573	0.01388
21-1-S	53.00	0.00	26.25	-0.05	0.00312	0.00000	0.00417	-0.00001
156-9-S	35.08	43.33	17.67	21.13	0.00207	0.00255	0.00281	0.00336
156-3/S	35.36	43.44	17.82	21.28	0.00208	0.00256	0.00283	0.00338

Table E2. Comparison of the Closed-form Equation Results with the Double Search Algorithm

Spec. ID	Double Search		Closed-Form		Double Search		Closed-Form	
	θ_{cr}	SWT	θ_{cr}	SWT	θ_{cr}	Findley	θ_{cr}	Findley
156-11/S	45.00	123.03	0.00	123.03	37.00	79.26	-37.28	79.26
21-11/S	45.00	63.19	45.00	63.13	8.00	56.65	7.81	56.64
21-6-S/L	45.00	44.64	45.00	44.64	98.00	39.99	7.84	39.99
156-10-S	45.00	40.93	45.00	40.81	98.00	36.66	7.80	36.65
21-7/S	45.00	67.60	45.00	67.60	14.00	39.37	13.98	39.37
156-5S	45.00	55.07	45.00	55.07	14.00	39.27	13.62	39.27
156-4-S	45.00	57.59	45.00	57.59	13.00	41.86	12.88	41.86
156-1	45.00	47.09	45.00	47.09	14.00	36.94	13.60	36.94
21-4-S/L	45.00	56.50	45.00	56.50	14.00	40.20	13.71	40.20
21-1-S	112.0	65.41	26.60	66.71	75.00	46.16	-14.82	46.16
156-9-S	112.0	64.93	26.81	66.24	83.00	40.39	-6.56	40.39
156-3/S	113.0	65.37	26.83	66.69	173.00	40.66	-6.57	40.66

APPENDIX F

COMPARISON OF APPROXIMATE ELASTIC-PLASTIC
NOTCH ANALYSIS METHODS

F.1   INTRODUCTION

The ability to assess the effect of a notch or other stress concentration on the fatigue resistance of components is largely dependent on the ability to accurately determine the stress/strain distributions or gradients in the vicinity of the notch. Although elastic stress and strain distributions can be efficiently generated using finite element techniques, localized plastic deformation often occurs in the vicinity of sharp notches and discontinuities. The inclusion of nonlinear elastic-plastic material behavior into finite element models requires significantly greater computational resources (i.e., memory and time), particularly in cases in which cyclic plasticity must be accounted for. Furthermore, the models often require greater attention to details such as mesh refinement, element shape, and nonlinear solution procedures. Due to the added complexities and computational requirements involved in elastic-plastic finite element analysis, approximate methods that can efficiently and accurately model the stress redistribution resulting from plastic deformation near notches are highly desirable. However, such methods must be validated using proven and reliable techniques.

Two approximate elastic-plastic notch analysis codes have been independently developed as part of the HCF Damage Tolerance Program. The first code, developed by Prof. G. Glinka at the University of Waterloo, was designed to approximate the multiaxial elastic-plastic stress and strain fields in notched, isotropic components subjected to proportional and non-proportional cyclic loadings (see Sec. 3.3.4). The second code, developed by Southwest Research Institute (SwRI), extended the Glinka code to include the consideration of anisotropic materials, but in the delivered form is more restrictive in the types of component geometries and load histories that can be analyzed (see Sec. 3.3.5).

In this Appendix, an independent assessment and comparison of the two approximation codes, hereafter referred to as the Glinka and SwRI codes, is presented. The codes were evaluated by comparing the approximate elastic-plastic stresses obtained from each code to the results obtained from elastic-plastic finite element analyses of several notched component

geometries subjected to a variety of loading conditions. In each case, the elastic stress-strain distributions from the FEA analysis served as input to the codes. The elastic-plastic stress-strain distributions on the notch section were then compared and used as validation measures. Presented here are more complete details of the finite element procedure discussed briefly in Sec. 3.3.3 as well as comparisons between approximation codes and FEM results briefly outlined in Sec. 3.3.6. This Appendix compares the results from the Glinka and SwRI codes under a wide variety of geometry and loading conditions.

F.2 ELASTIC-PLASTIC FEA OF NOTCHED COMPONENTS

All finite element analyses of notched components were conducted using the commercial software ANSYS. A multilinear kinematic hardening rule was used in conjunction with the cyclic stress-strain curve for Ti-6Al-4V at room temperature obtained from half-life LCF data generated in this program. Applying a Ramberg-Osgood fit to the data, the cyclic stress-strain curve for Ti-6Al-4V can be expressed as

$$\varepsilon = \frac{\sigma}{E} + \left(\frac{\sigma}{K}\right)^{\frac{1}{n}} = \frac{\sigma}{16870} + \left(\frac{\sigma}{124}\right)^{\frac{1}{0.0149}} \tag{F1}$$

where σ has units of ksi, and the cyclic yield strength was taken as $\sigma_y = 109.2$ ksi. From this equation, cyclic stress-strain values were calculated and used as input for the models. The stress-strain values are shown in Table F1.

Table F1. Stress/Strain Values used in ANSYS Elastic-Plastic Analyses (Kinematic Hardening)

Stress (ksi)	109.22	113.0	114.0	115.5	116.3	116.8	117.2	117.6	118.3	119.7	121.0
Strain (in/in)	.006474	.008659	.01030	.01536	.02043	.02497	.02965	.03551	.04951	.1007	.2004

All models were constructed using 8-node, three-dimensional structural solid elements with extra displacement shapes included for better accuracy. A mesh refinement study was performed on each model to verify that the discretization error was sufficiently small. For each of the elastic-plastic analyses in which cyclic plasticity was anticipated, 10 to 20 cycles were run to ensure the local (notch-root) plastic strains reached a cyclically stable state. This was verified by examining the equivalent plastic strain and the largest principal plastic strain at the root of the

notch at the end of each load cycle. In most cases, it was found that negligible changes in these values occurred after the fifth cycle, and the analysis was subsequently terminated after 10 cycles. In a few cases involving large-scale, nonproportional plastic straining, 20 cycles were completed to ensure a stable state had been reached.

Four notched component geometries were selected to evaluate the elastic-plastic approximation methods developed by Glinka and SwRI. These geometries were selected with the intent of providing a variety of loading conditions to thoroughly evaluate the accuracy and limitations of the approximation methods. Loading combinations and levels were chosen to produce an array of cyclic elastic-plastic stress/strain states, ranging from small scale, first-reversal proportional plasticity to large scale, non-proportional cyclic plasticity. For each of the models, both elastic and elastic-plastic finite element analyses were conducted. The elastic stress and strain distributions across the notch section were used as inputs to the approximation codes, and the resulting elastic-plastic approximate solutions were compared to the elastic-plastic finite element results for accuracy.

Of the two codes evaluated in this program, the Glinka code is more versatile in its present form, as it is not restricted by notch or component geometry or type of loading; i.e., it can be used to analyze proportional or non-proportional cyclic loading applied to any notched component. While the SwRI methodology is not restricted on its theoretical basis to certain notched component geometries or loadings, the delivered code was limited to the analysis of a rectangular cross-section under monotonic loading (not cyclic). Consequently, different notch geometries and loadings were used in the evaluation of each code.

F.3   NOTCHED COMPONENT GEOMETRIES AND LOADING

Four notched component geometries were analyzed for the purposes of model validation. The Glinka code was evaluated against geometries 1 – 3, while the SwRI code was evaluated against geometries 1 and 4. The details of the component geometries, loading, and FE models are summarized below.

F.3.1   Geometry 1: Flat Plate with Center Hole (Uniaxial Tension)
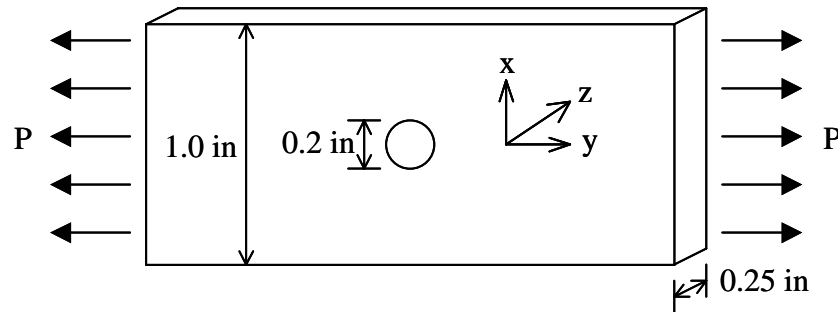
Figure F1.   Geometry 1 for Glinka and SwRI code validation: flat plate with center hole in uniaxial tension.

This geometry was selected to provide a baseline validation test for both the Glinka and SwRI approximation methods. The stress gradients around the hole are not too severe, and typical of those found in many service components. The notch plasticity levels were controlled by varying the magnitude of the remote axial load, P. In all cases, the loading was applied cyclically at R = 0 (R = P_{min}/P_{max}, P_{min} = 0). The following nominal stress levels ($\sigma = P_{max}/A$, with A defined as the gross cross-sectional area) were used for this analysis:

P_{max}/A = 20 ksi   (elastic loading, scaleable to any level)
P_{max}/A = 40 ksi   (local plasticity at notch root on first reversal, followed by elastic cycling)
P_{max}/A = 60 ksi
P_{max}/A = 80 ksi
P_{max}/A = 100 ksi   (full notch section plasticity with local cyclic plasticity)

In the finite element analysis, symmetry on three planes was used to reduce the model to a 1/8 section of the full component. The final model was comprised of 6,720 elements. A close-up view of the elements in the notch region is shown in Figure F2. For this geometry, the elastic-plastic stress gradients were compared along a line through the notch section at both the midplane and outer surface of the specimen.
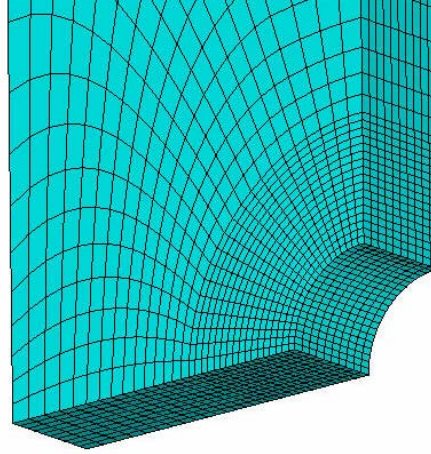
Figure F2.   Element plot of notch region for geometry 1.

F.3.2   Geometry 2: Large Circumferential Notch in a Round Bar (Tension/Torsion Loading)
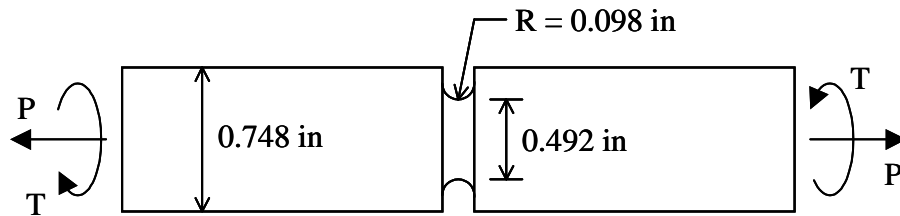
Figure F3. Geometry 2 for Glinka code validation: round bar with large circumferential notch in tension/torsion.

This geometry represents the notched tension/torsion specimen tested by the University of Illinois as part of the HCF program. This component provides a more thorough validation of the multiaxial capabilities of the approximation methods. A variety of multiaxial stress/strain gradients were produced in the notch section by varying the relative axial and torsion load levels. Four cyclic loading cases were considered for this geometry:

1) Axial loading only (R = 0)
2) Torsion loading only (R = 0)
3) Proportional loading (R = 0, with $\sigma_{max} \approx \tau_{max}$ at notch root)
4) Non-proportional loading (box path with R = −1)

The box path consists of a four-point cycle, with load levels ordered as follows: (1) P_{max}, T_{max}, (2) $-P_{max}$, T_{max}, (3) $-P_{max}$, $-T_{max}$, (4) P_{max}, $-T_{max}$. For each load case, one elastic analysis and three elastic-plastic analyses were performed. Plasticity levels ranged from first-reversal local yielding with elastic cycling to large-scale yielding with local cyclic plasticity. The specific load levels are shown in Table F2.

Table F2. Load Levels for Geometry 2

Load Case		Elastic	Elastic-Plastic		
Axial	P_{max} (lb)	8,000	18,000	23,000	28,000
	T_{max} (lb-in)	0	0	0	0
Torsion	P_{max} (lb)	0	0	0	0
	T_{max} (lb-in)	800	1,200	1,600	2,000
Proportional	P_{max} (lb)	4,000	6,400	8,200	10,000
	T_{max} (lb-in)	700	1,120	1,435	1,750
Box Path	P_{max} (lb)	4,000	6,400	8,200	10,000
	T_{max} (lb-in)	700	1,120	1,435	1,750

For the finite element analysis, a small "wedge" was created as shown in Figure 4. The wedge consisted of a 4° sector with the nodal displacements on adjacent surfaces coupled to take advantage of the axisymmetric geometry. The final model was comprised of 11,420 elements. A close-up view of the elements in the notch region is shown in Figure F4. For this geometry, the elastic-plastic stress gradients were compared along a radial line through the notch section.
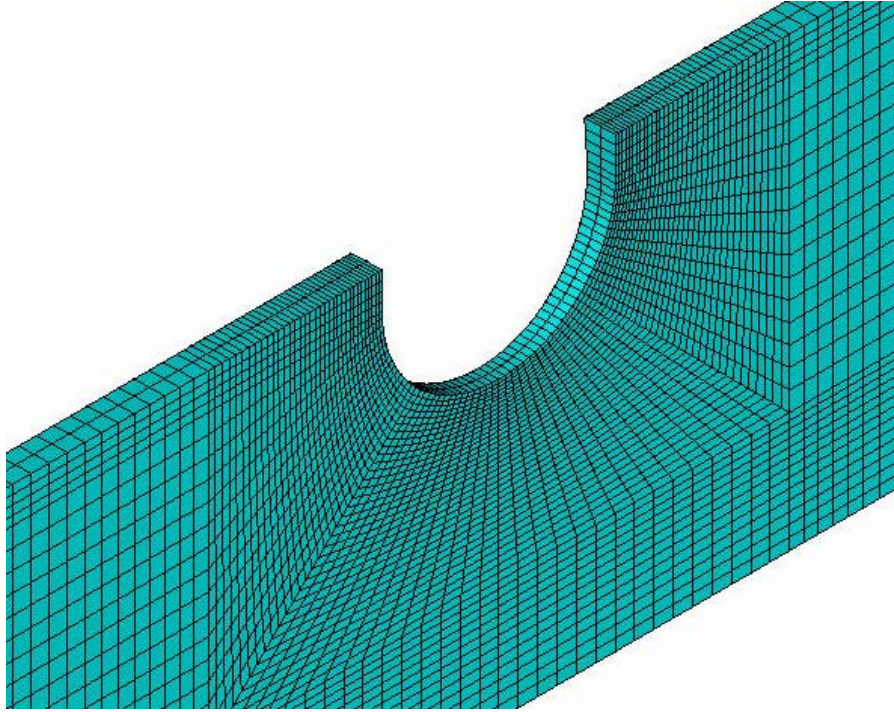
Figure F4.   Element plot of notch region for geometry 2.

F.3.3   Geometry 3: Small Circumferential Notch in a Round Bar (Tension/Torsion Loading)
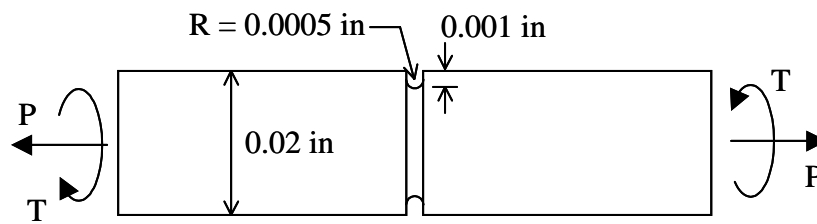
Figure F5. Geometry 3 for Glinka code validation: round bar with small circumferential notch in tension/torsion.

This component is similar to geometry 2, except the circumferential notch is smaller and sharper. This geometry was designed to produce stress gradients similar to those experienced near edge of contact (EOC) fretting locations. Based on a previous analysis by GEAE, typical EOC stress magnitudes and gradients were achieved in the notch section by applying certain combinations of axial and torsional loads coupled with a radial pressure applied

normal to the notch surface. For the present study, the radial pressure term was not included due to potential differences in how ANSYS and the approximation module may treat this boundary condition. However, the nature of the stress gradients in the notch region due to the axial and torsional loads are still similar to those found near EOC conditions. This geometry is intended to provide a more critical validation of the approximation module under loading conditions commonly experienced in aircraft turbine engines.

Two cyclic loading conditions were considered for this geometry:

1) Proportional loading (R = 0, with $\tau_{max} \approx 0.6\sigma_{max}$ at notch root)
2) Non-proportional loading (box path with R = −1)

For each load case, one elastic analysis and three elastic-plastic analyses were performed. Plasticity levels ranged from first-reversal local yielding with elastic cycling to large-scale yielding with local cyclic plasticity. The specific load levels are shown in Table F3.

Table F3. Load Levels for Geometry 3

Load Case		Elastic	Elastic-Plastic		
Proportional	P_{max}/A (ksi)	12	30	40	60
	T_{max} (lb-in)	0.018	0.045	0.06	0.09
Box Path	P_{max}/A (ksi)	12	30	40	60
	T_{max} (lb-in)	0.018	0.045	0.06	0.09

For the finite element analysis, a small "wedge" was created in the same manner as was done for the previous model. The wedge consisted of a 4º sector with the nodal displacements on adjacent surfaces coupled to take advantage of the axisymmetric geometry. The final model was comprised of 11,840 elements. A close-up view of the elements in the notch region is shown in Figure F6. For this geometry, the elastic-plastic stress gradients were compared along a radial line through the notch section.
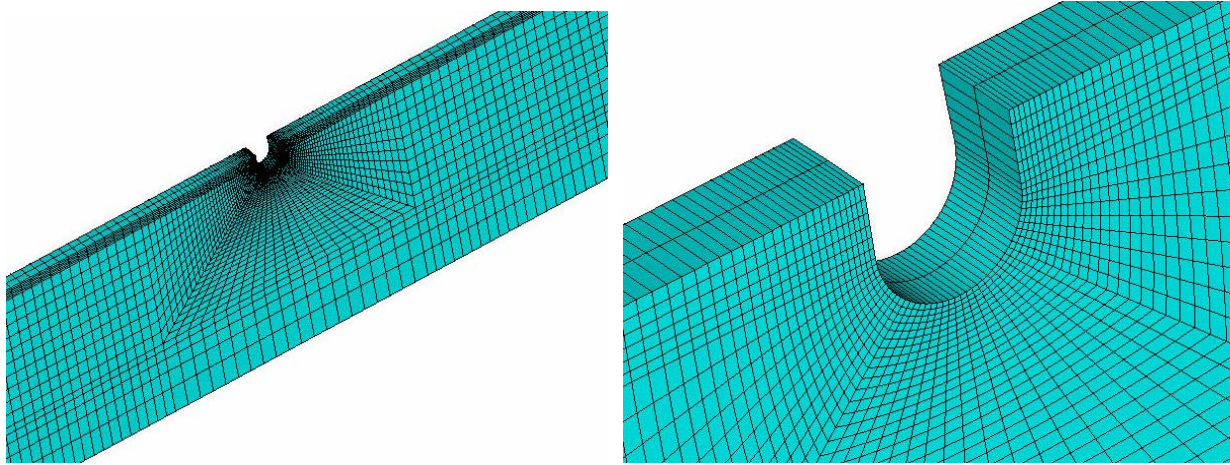
Figure F6.   Element plot of notch region for geometry 3.

F.3.4   Geometry 4: Rectangular Bar with Edge Notch (Tension/Torsion Loading)
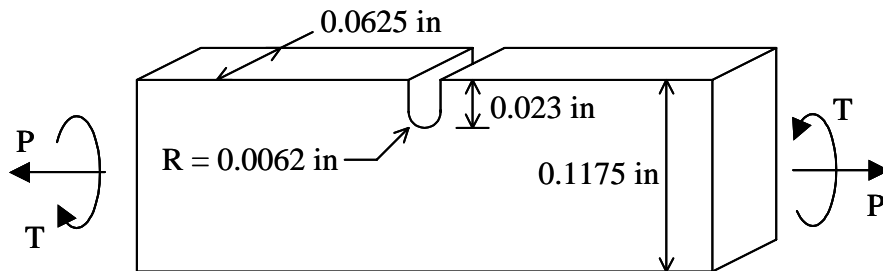
Figure F7.   Geometry 4 for SwRI code validation: rectangular bar with edge notch in tension/torsion.

This geometry was created and analyzed to evaluate the SwRI approximation module, due to the aforementioned geometric restrictions of the code. The small edge notch in the component produced much steeper stress gradients than those encountered in Geometry 1. Two monotonic loading conditions were considered for this geometry:

1)   Axial loading
2)   Combined axial/torsion (proportional) loading

For each load case, one elastic analysis and three elastic-plastic analyses were performed. The specific load levels are shown in Table F4.

Table F4. Load Levels for Geometry 4

Load Case		Elastic	Elastic-Plastic		
Axial	P_{max}/A (ksi)	15	40	60	80
Axial/Torsion	P_{max}/A (ksi)	10	20	30	40
	T_{max} (lb-in)	1.5	3.0	4.5	6.0

The finite element model for this geometry was comprised of 95,088 elements. A close-up view of the elements in the notch region is shown in Figure F8. For this geometry, the elastic-plastic stress gradients were compared along a line through the notch section at both the midplane and outer surface of the specimen.
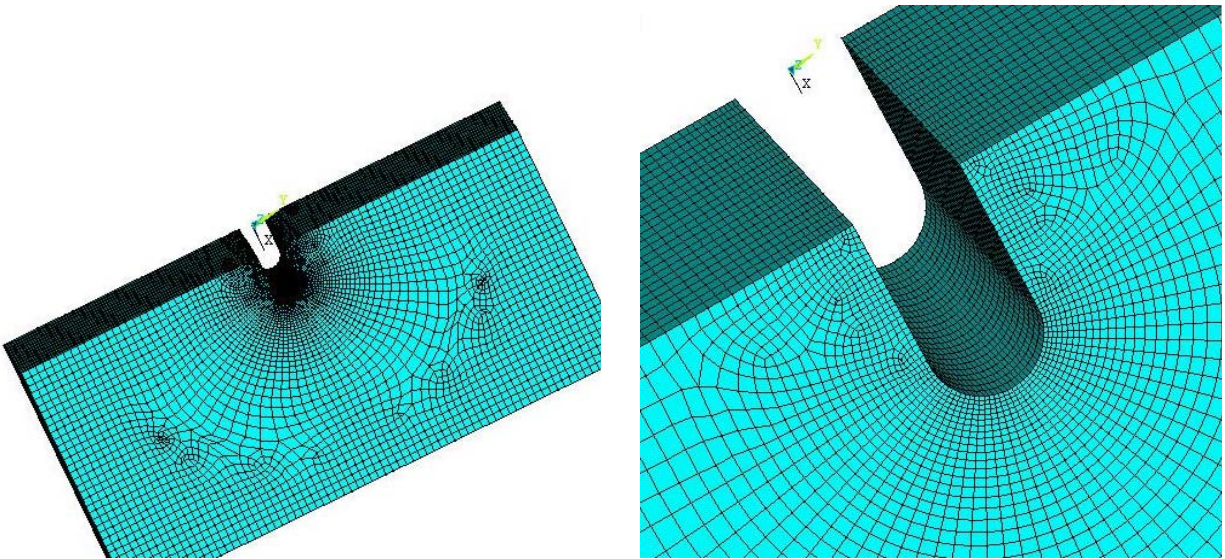
Figure F8. Element plot of notch region for geometry 4.

F.4 ASSESSMENT OF GLINKA CODE

Comparisons between the elastic-plastic stresses obtained from the finite element analyses and the Glinka approximation code for Geometries 1 – 3 are shown in Figures F9 – F40. For Geometry 1 (Figures F9 – F16), the y-axis corresponds to the axial (loading) direction, while the x-axis is directed along the notch section and the z-axis is directed through the thickness (see Figure F1). For Geometry 2 (Figures F17 – F31), x represents the tangential (hoop) direction, y

represents the radial direction, and z represents the longitudinal (axial) direction. The same coordinate system applies for geometry 3 (Figures F32 – F40).

F.4.1   Summary of Glinka Results: Geometry 1

The comparisons between the Glinka code and FEA results for geometry 1 are shown in Figures F9 – F16. Even at low loads, there were noticeable discrepancies between the Glinka stresses and FEA stresses for this geometry. In general, the Glinka code predicted a greater yield zone depth near the notch than FEA. In some cases, the depth of the plastic zone predicted by Glinka was approximately twice the depth calculated by FEA (see Figures F11 – F14, for example). Although the stresses at the notch root were, in most cases, reasonably accurate, the sub-surface stresses were often in disagreement. The errors become particularly significant at minimum load (unloading), even at low loads. For example, in Figures F9 and F11 (P/A = 40 and 60 ksi, respectively), the subsurface residual stresses calculated by the Glinka code are much greater than those calculated by FEA. It is also interesting to observe that, at high loads, the errors change in sign from the center of the notch section to the outer edge. Note that, in Figures F15 and F16 (P/A = 100 ksi), while the equivalent stress (σ_{eqv}) is in good agreement, the individual components (σ_x, σ_y, and σ_z) calculated by the Glinka code are less than the FEA stresses at the center of the notch section, but greater than the FEA stresses at the edge of the notch section.

The errors in the Glinka code for geometry 1 are likely due to the method by which this code redistributes the stresses across the notch section. The Glinka code utilizes the elastic equivalent stress distribution along a single line through the notch section, rather than considering the elastic stress distribution over the entire cross-section. If stress gradients only exist in one direction, such as under axisymmetric loading, this method is sufficient. However, for this notch geometry, the stress distribution on the notch section varies not only along the width of the component but also through the thickness of the component, due to the constraint near the notch. In this case, the stress redistribution due to yielding must take into account the gradients in two directions. The Glinka code, in the current form, cannot fully account for bi-directional stress gradients.

F.4.2   Summary of Glinka Results: Geometry 2

The comparisons between the Glinka code and FEA results for geometry 2 are shown in Figures F17 – F31. In general, the Glinka stress approximations for this geometry were in much better agreement with FEA results than those for geometry 1. For the cases of pure tension, pure torsion, and proportional (combined tension/torsion) loading (Figures F17 – F19, F20 – F22, and F23 – F25, respectively), the approximate stresses from the Glinka code are, in most cases, in quite good agreement. However, some discrepancies appear at the higher load levels. For example, the hoop stress (σ_x) is underpredicted by the Glinka code at higher levels of axial loading. Under torsion and proportional loading, the depth of the yield zone is underpredicted at the highest load levels (Figures F22 and F25), resulting in substantial errors in the estimated subsurface residual stresses upon unloading.

The non-proportional box path proved to be a greater challenge for the Glinka code. At low load levels (Figures F26 – F27), where the extent of plasticity was very localized, the Glinka stress approximations were in good agreement with FEA. However, as the load levels were increased (Figures F28 – F31), the Glinka stresses deviated from the FEA stresses at certain points. This is especially noticeable in the axial stress (σ_z). Also, at the highest load level, the yield depth is underpredicted by the Glinka code, and the error in the radial stress (σ_y) at the notch root appears to increase at each successive point in the cycle (the radial stress should be zero at the notch root).

F.4.3   Summary of Glinka Results: Geometry 3

The comparisons between the Glinka code and FEA results for geometry 3 are shown in Figures F32 – F40. This geometry was similar to geometry 2, although the notch was much sharper. This resulted in steeper stress gradients near the notch root, making the stress redistribution due to yielding more difficult to calculate. For the case of proportional (combined tension/torsion) loading (Figures F32 – F34), there were slight discrepancies noted between the Glinka and FEA results for some stress components even at lower loads (for example, the hoop stress, σ_x, near the notch root). At the highest load level (Figure 34), the subsurface stresses deviated considerably, and the yield zone depth was again underpredicted by the Glinka code.

Similar discrepancies were found for the non-proportional box path load cycle (Figures F35 – F40). At the lowest load level, slight errors between the Glinka and FEA stresses are

evident near the notch root (note, however, that the notch root stresses for the Glinka code shown in Figure F36 are unreasonable, and may be due to an error in the analysis). At the highest load level (Figures F39 and F40), the differences between the Glinka and FEA results are severe, even subsurface. At this load level, the Glinka code failed to generate stress results near the notch root. However, it should be noted that this loading case represents a very severe state of plastic deformation that would not likely be encountered in aircraft engine components.
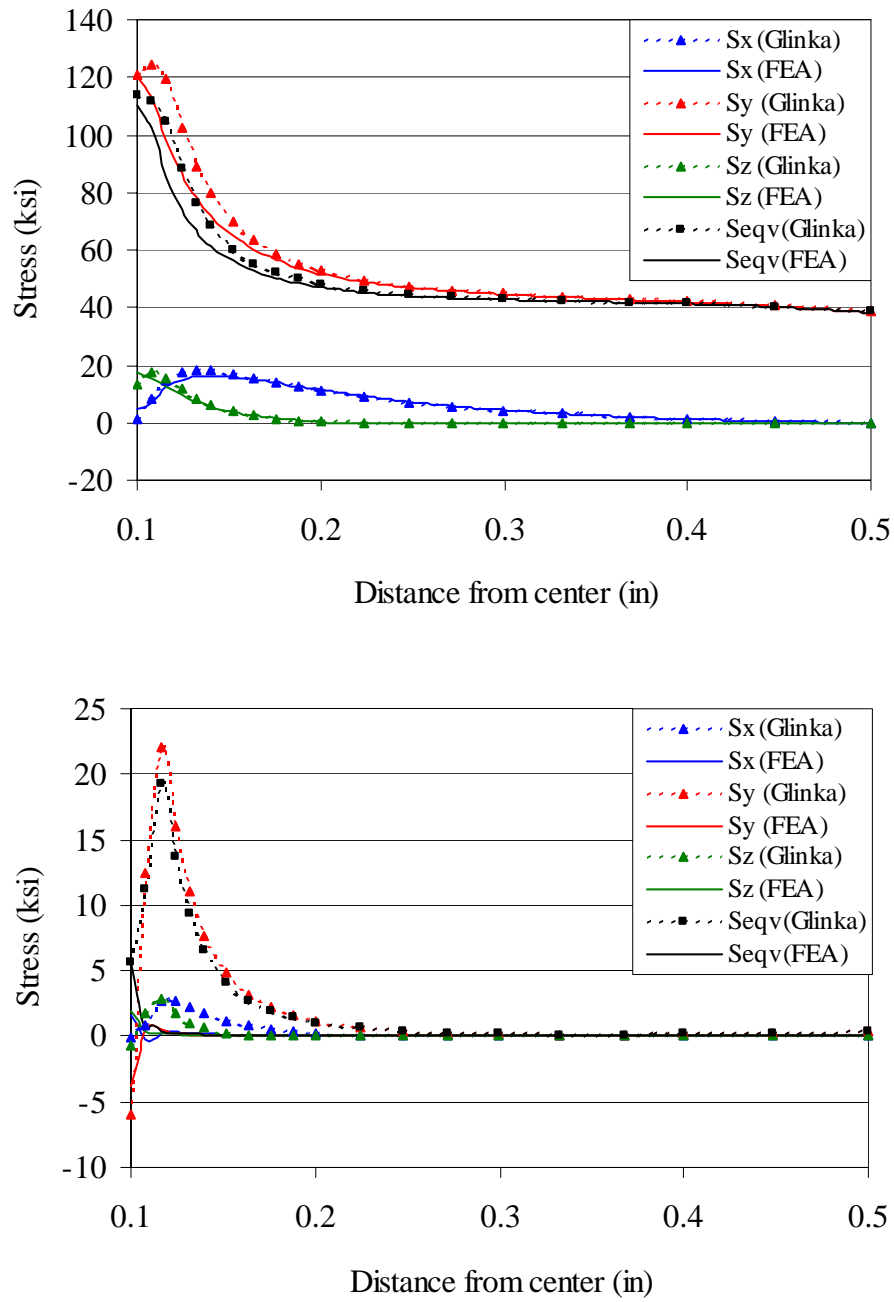
Figure F9. Comparisons between FEA and Glinka stresses for geometry 1, P/A = 40 ksi, center of notch section at maximum load (top) and minimum load (bottom).
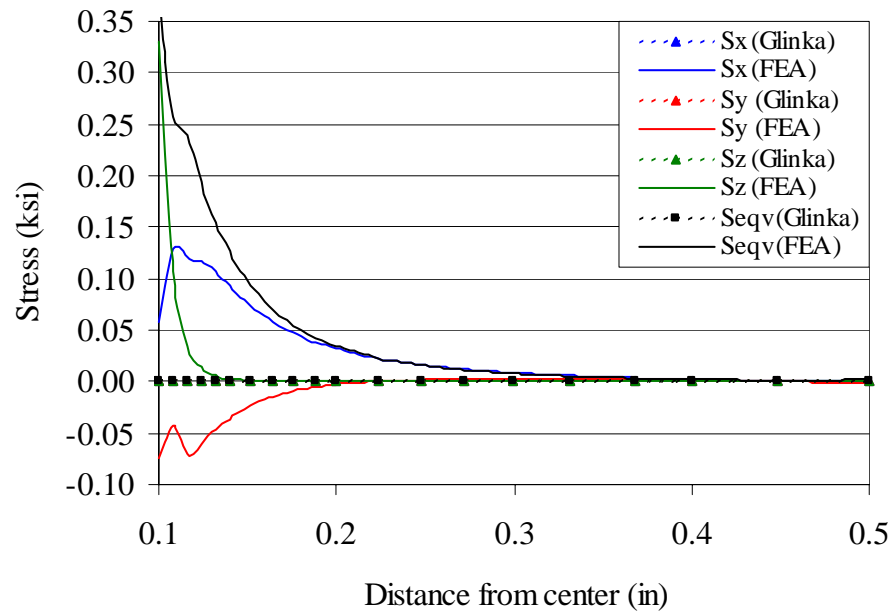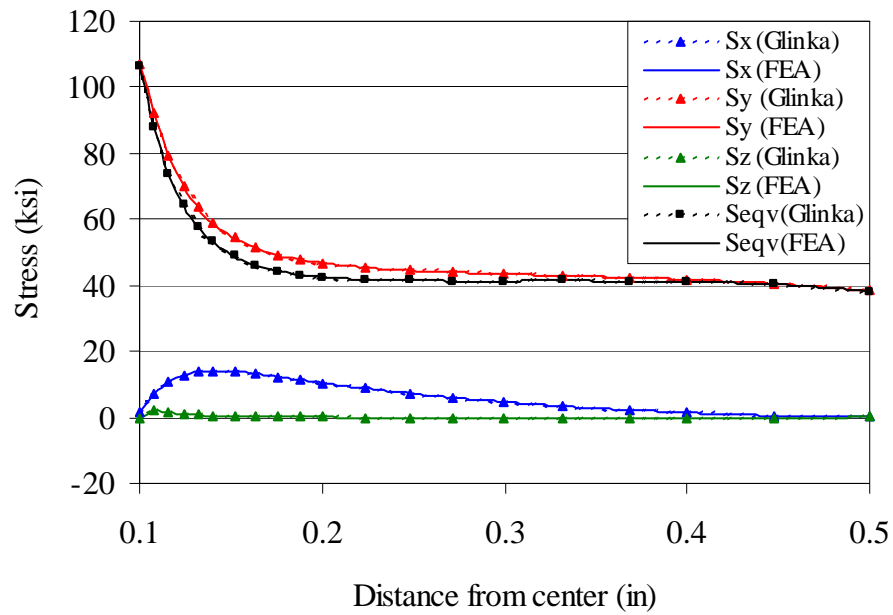
Figure F10. Comparisons between FEA and Glinka stresses for geometry 1, P/A = 40 ksi, edge of notch section at maximum load (top) and minimum load (bottom).
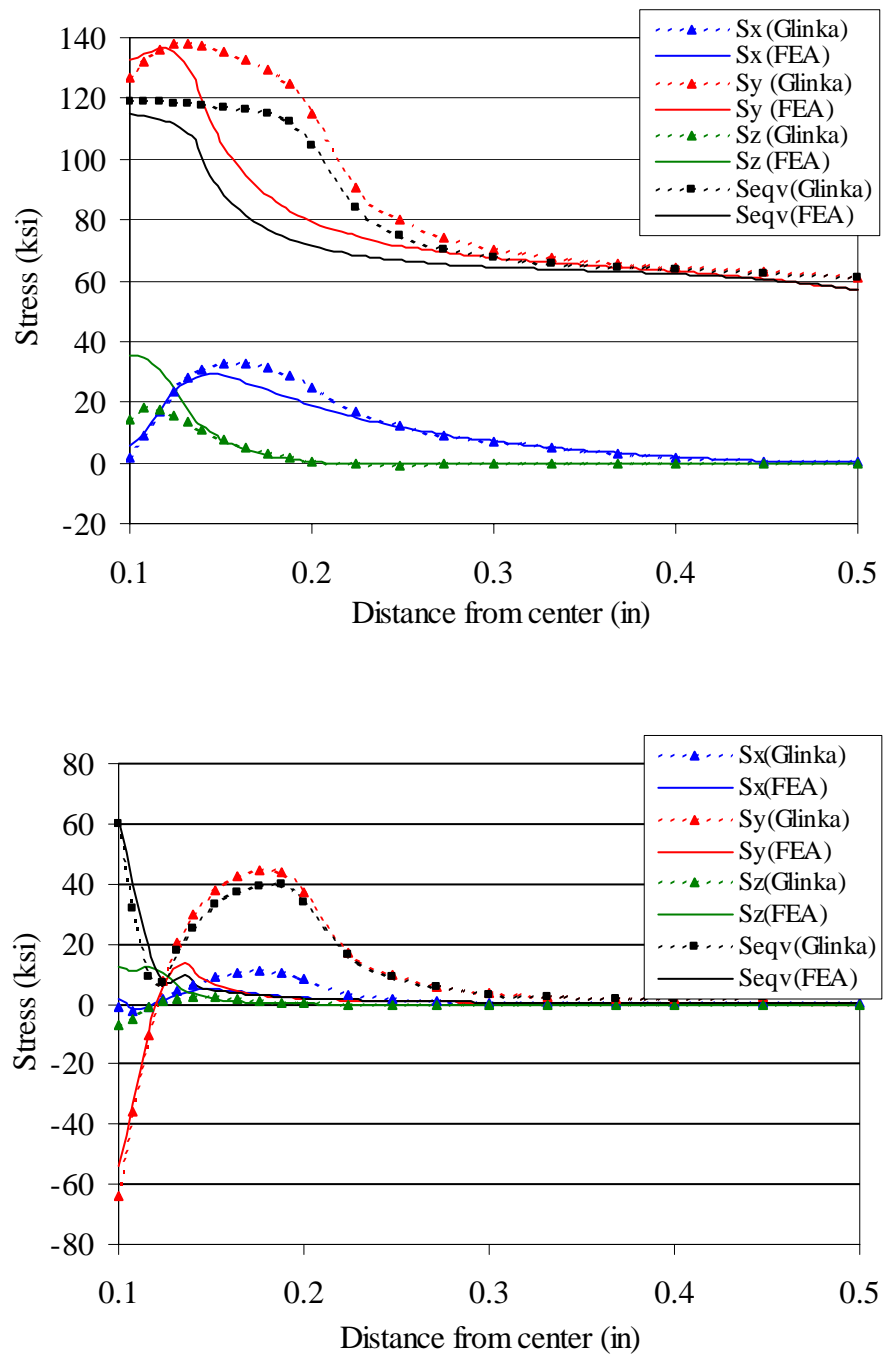
Figure F11. Comparisons between FEA and Glinka stresses for geometry 1, P/A = 60 ksi, center of notch section at maximum load (top) and minimum load (bottom).
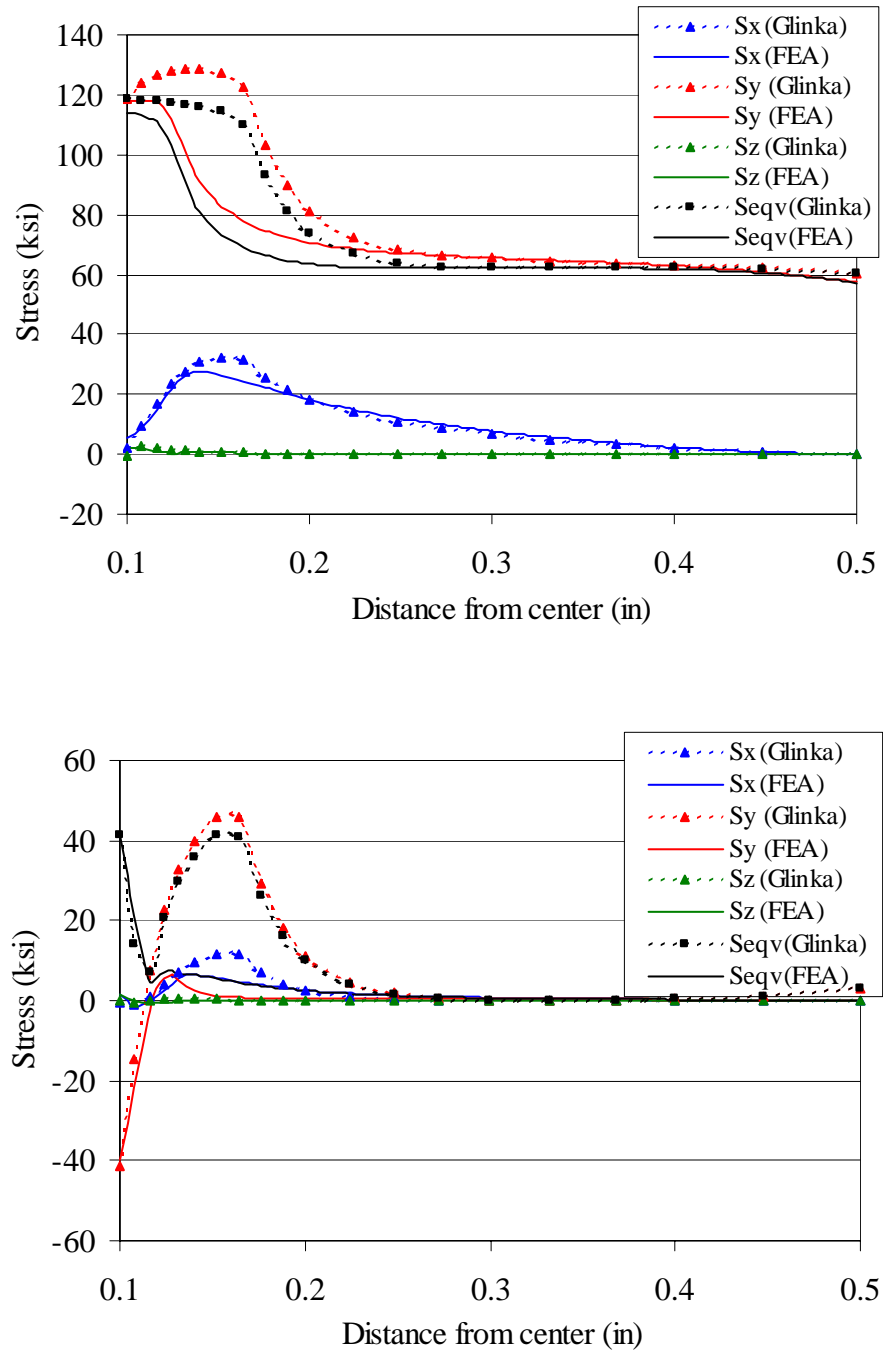
Figure F12. Comparisons between FEA and Glinka stresses for geometry 1, P/A = 60 ksi, edge of notch section at maximum load (top) and minimum load (bottom).
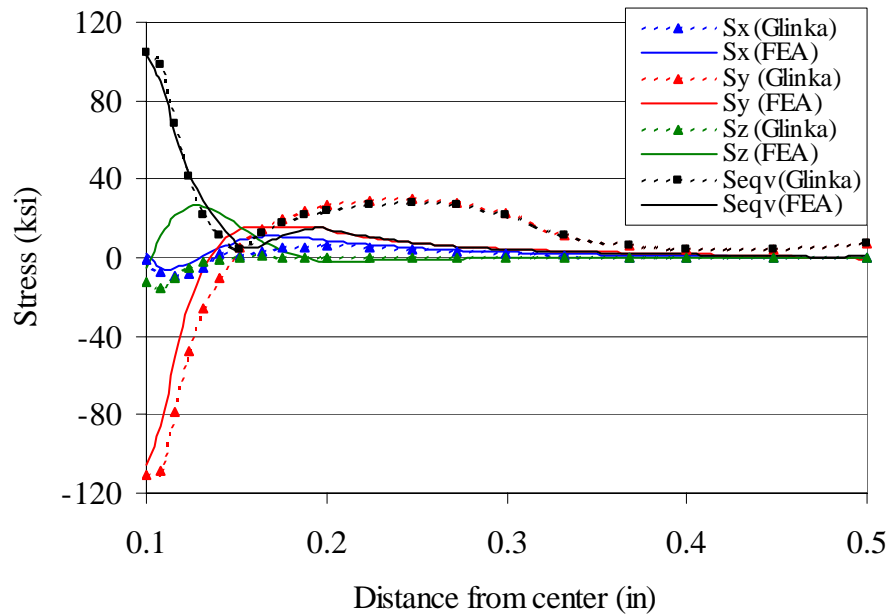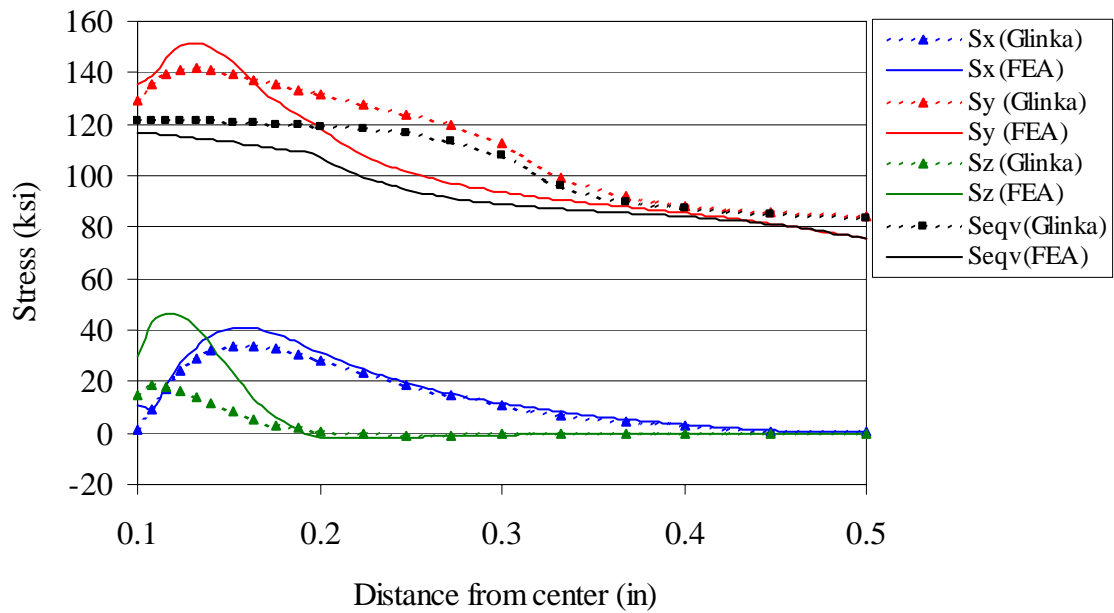
Figure F13. Comparisons between FEA and Glinka stresses for geometry 1, P/A = 80 ksi, center of notch section at maximum load (top) and minimum load (bottom).
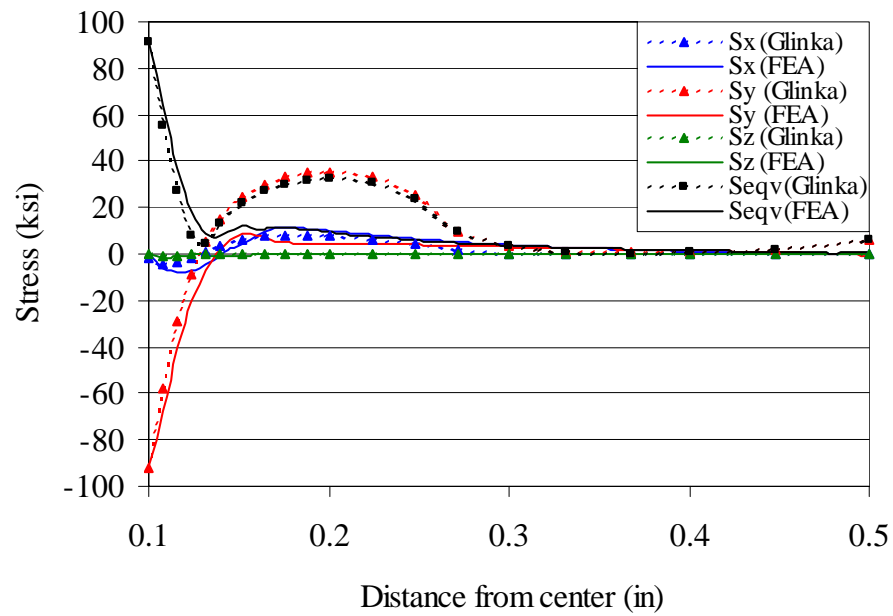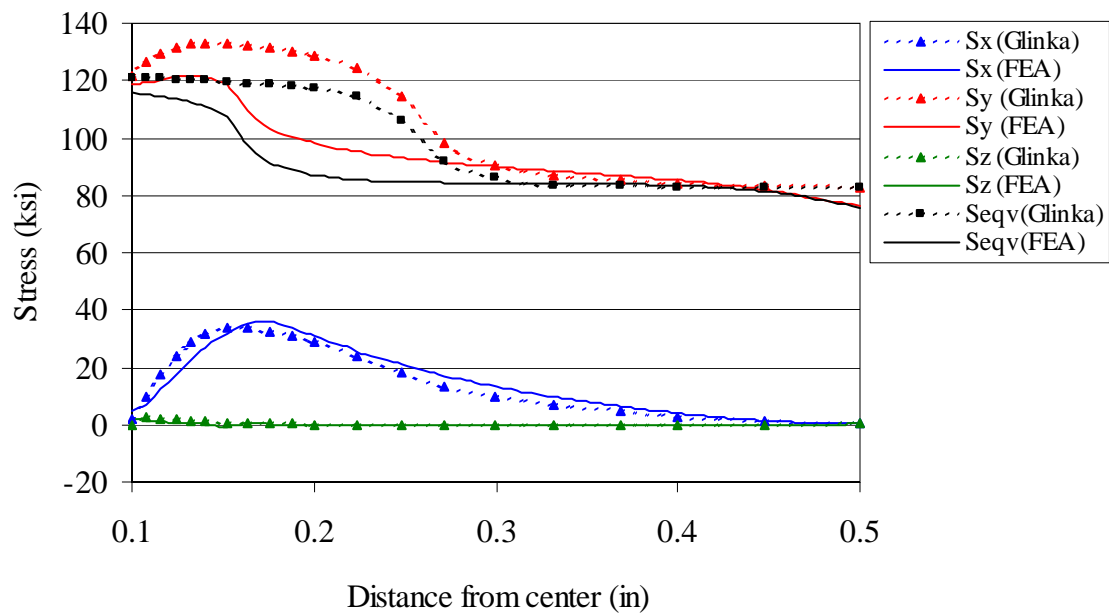
Figure F14. Comparisons between FEA and Glinka stresses for geometry 1, P/A = 80 ksi, edge of notch section at maximum load (top) and minimum load (bottom).
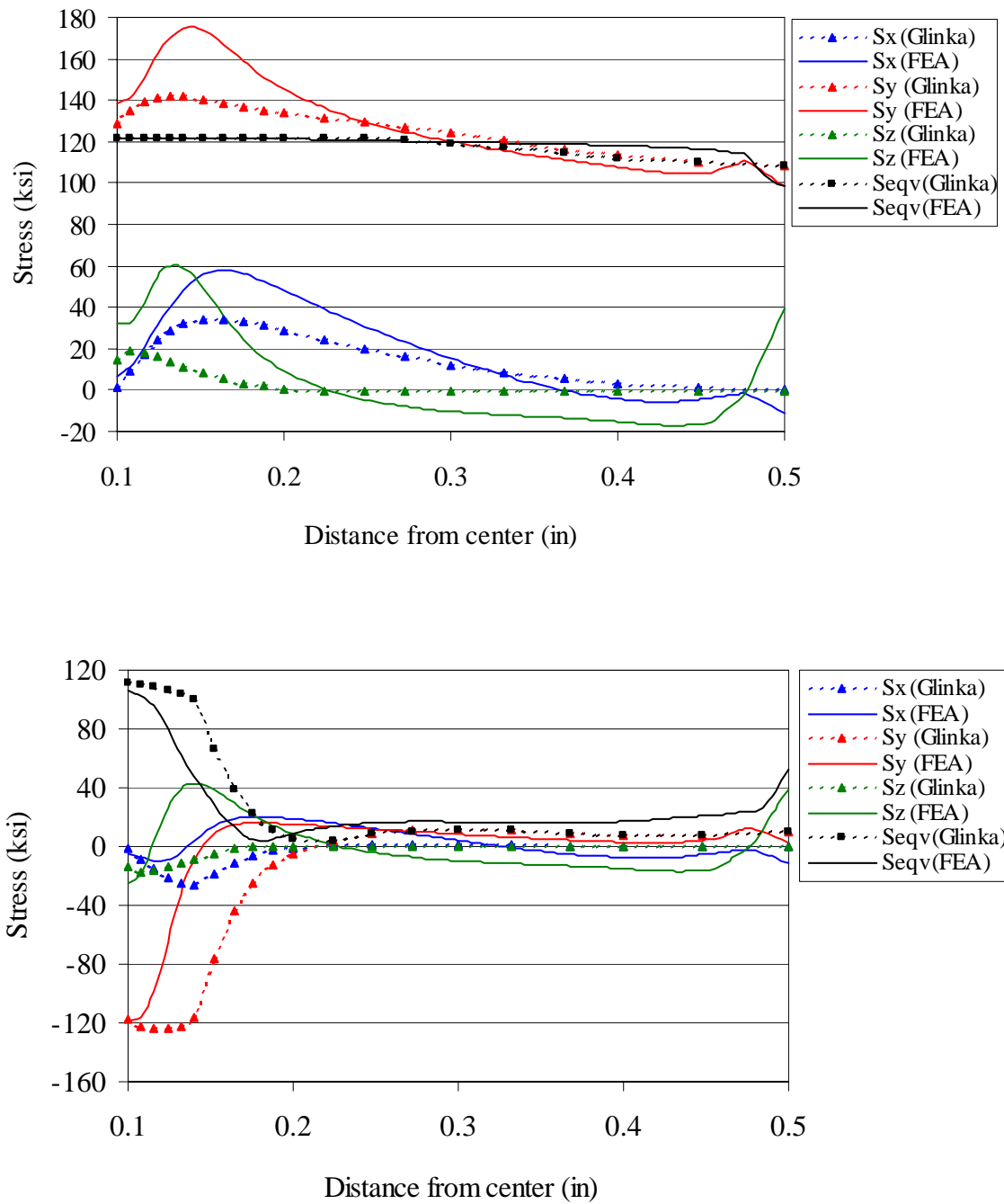
Figure F15. Comparisons between FEA and Glinka stresses for geometry 1, P/A = 100 ksi, center of notch section at maximum load (top) and minimum load (bottom).
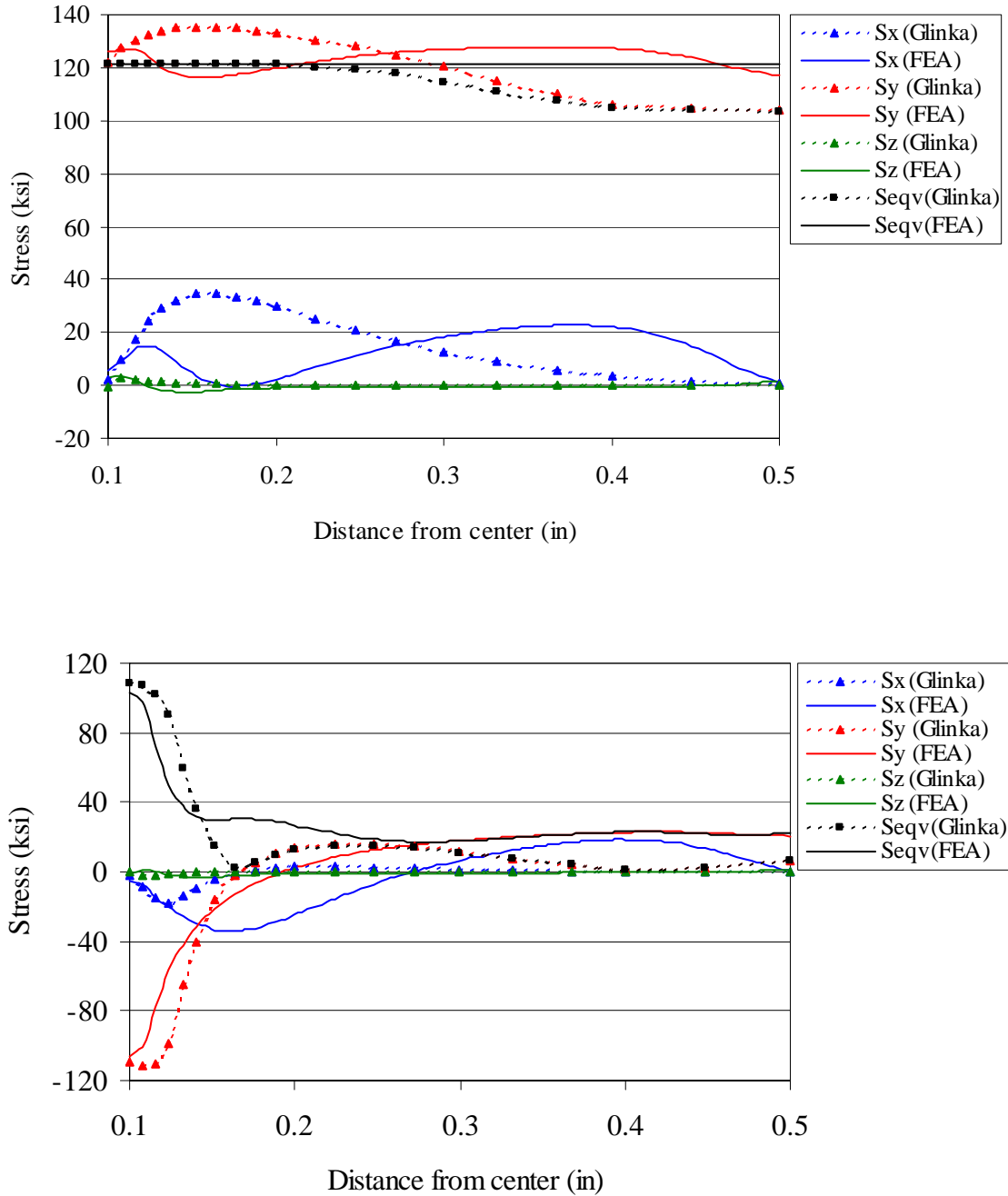
Figure F16. Comparisons between FEA and Glinka stresses for geometry 1, P/A = 100 ksi, edge of notch section at maximum load (top) and minimum load (bottom).
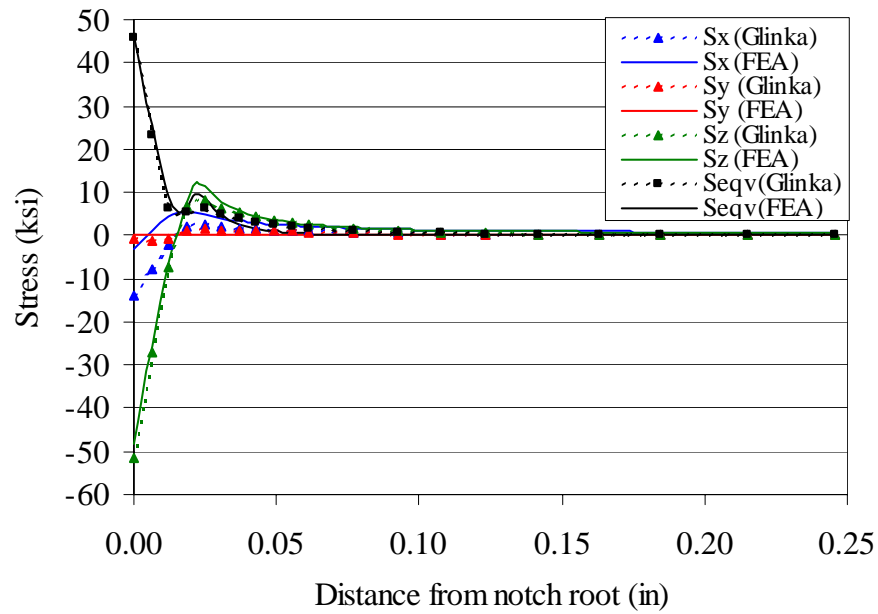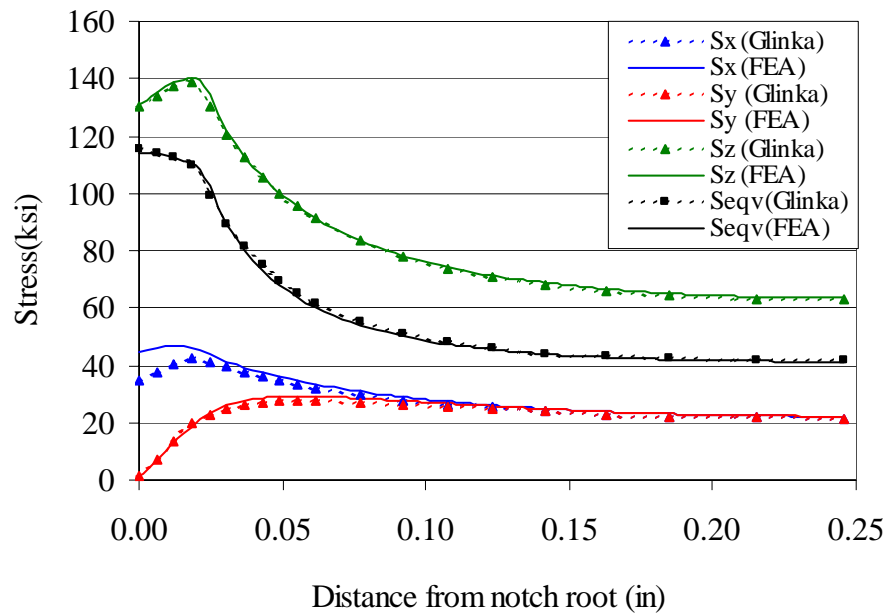
Figure F17. Comparisons between FEA and Glinka stresses for geometry 2, axial loading (P = 18,000 lb) at maximum load (top) and minimum load (bottom).
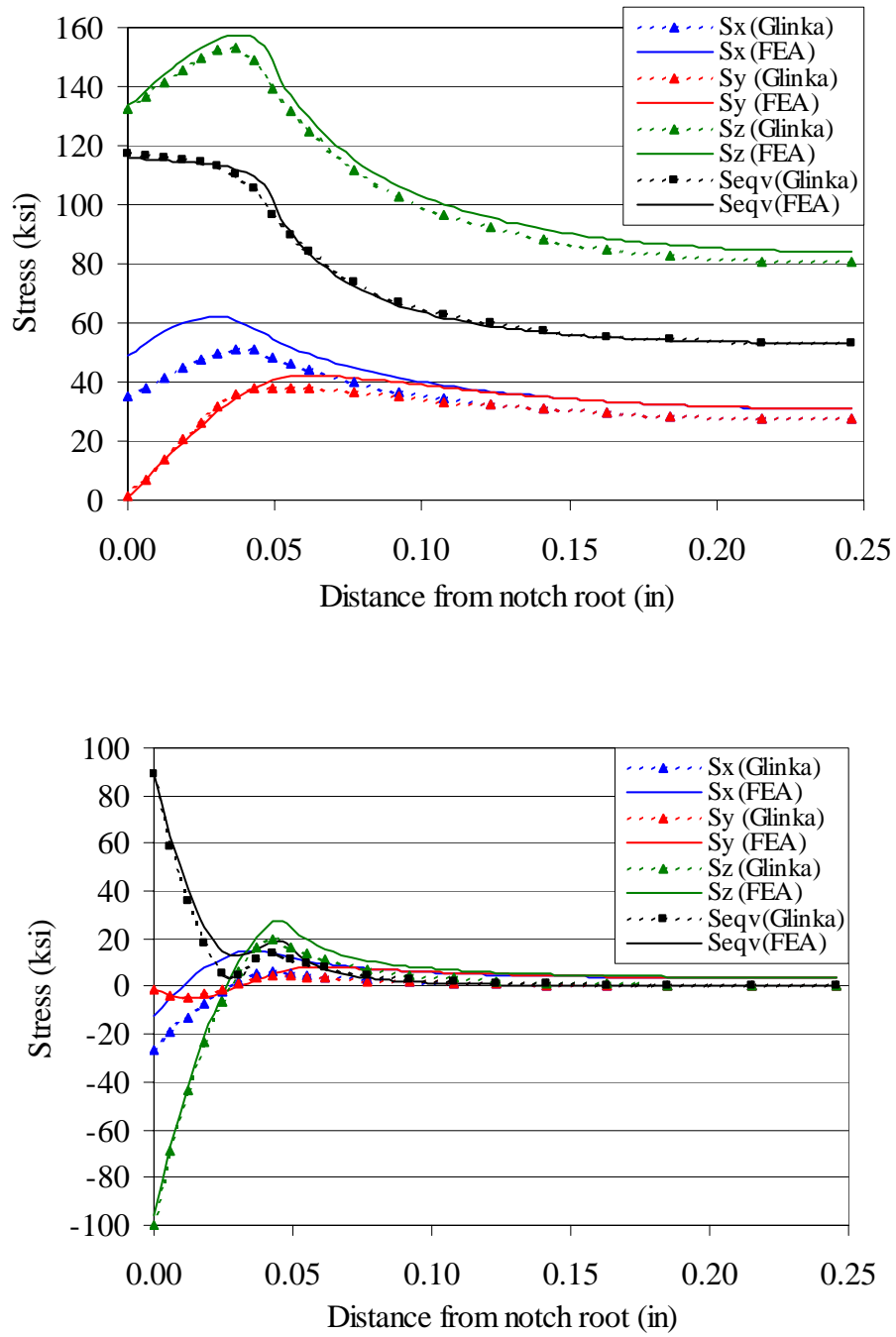
Figure F18. Comparisons between FEA and Glinka stresses for geometry 2, axial loading (P = 23,000 lb) at maximum load (top) and minimum load (bottom).
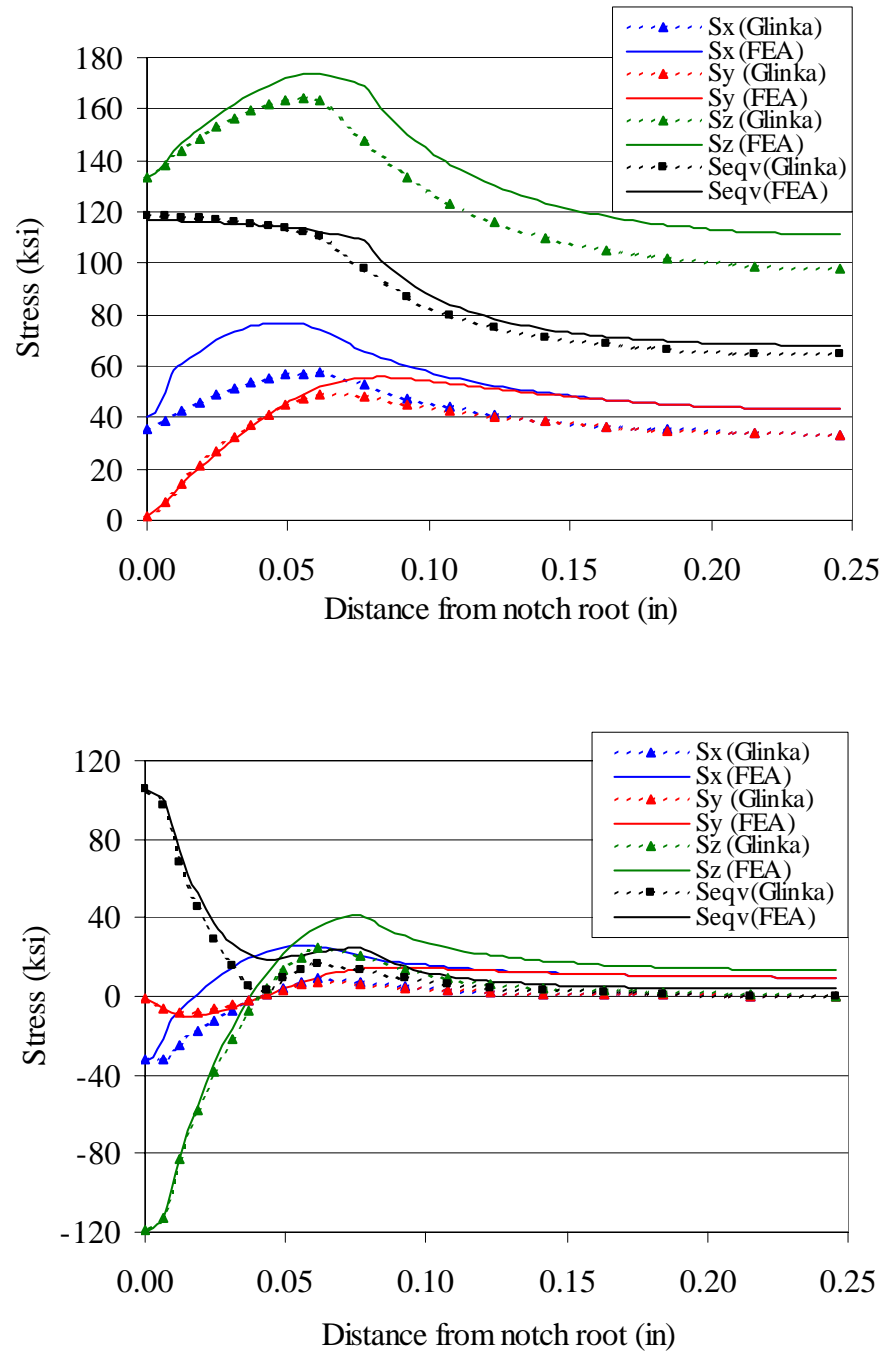
Figure F19. Comparisons between FEA and Glinka stresses for geometry 2, axial loading (P = 28,000 lb) at maximum load (top) and minimum load (bottom).
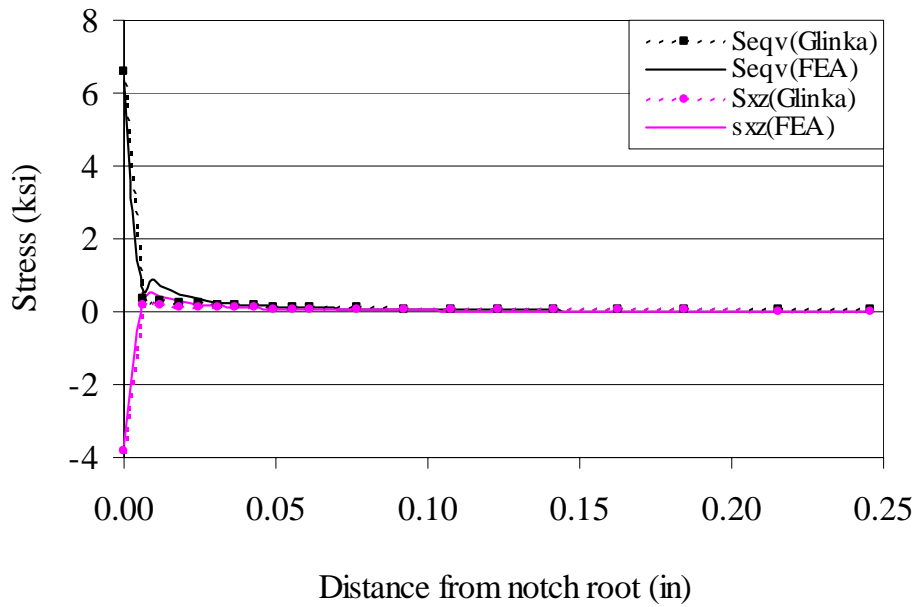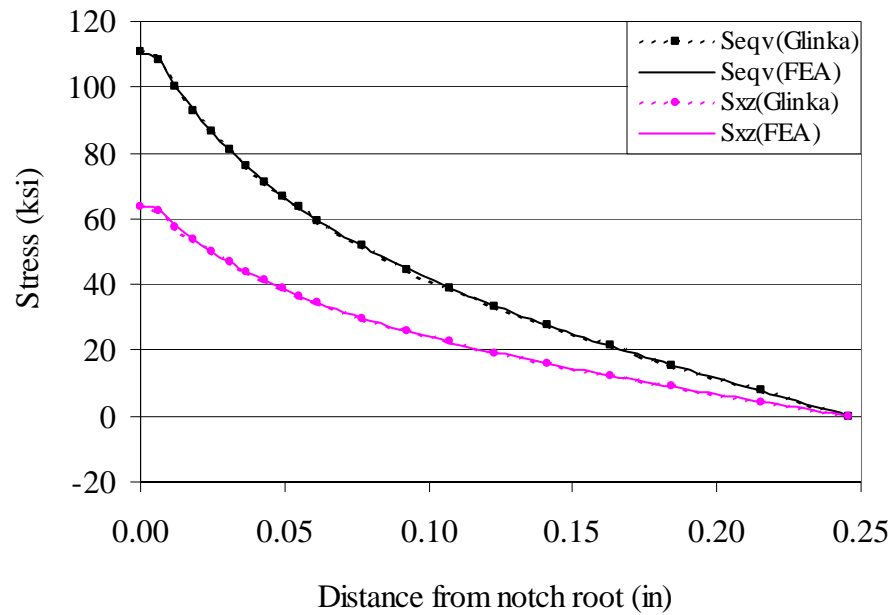
Figure F20. Comparisons between FEA and Glinka stresses for geometry 2, torsion loading (T = 1200 lb-in) at maximum load (top) and minimum load (bottom).
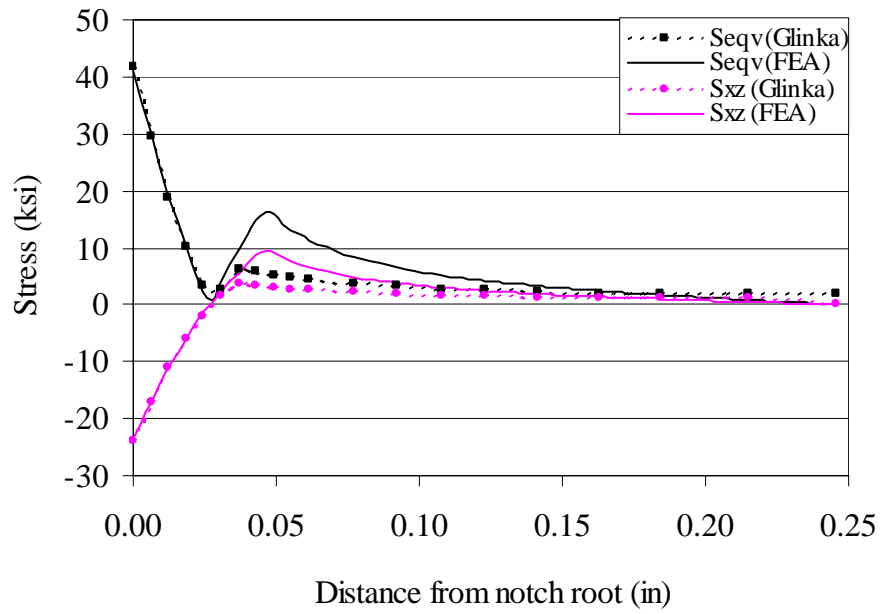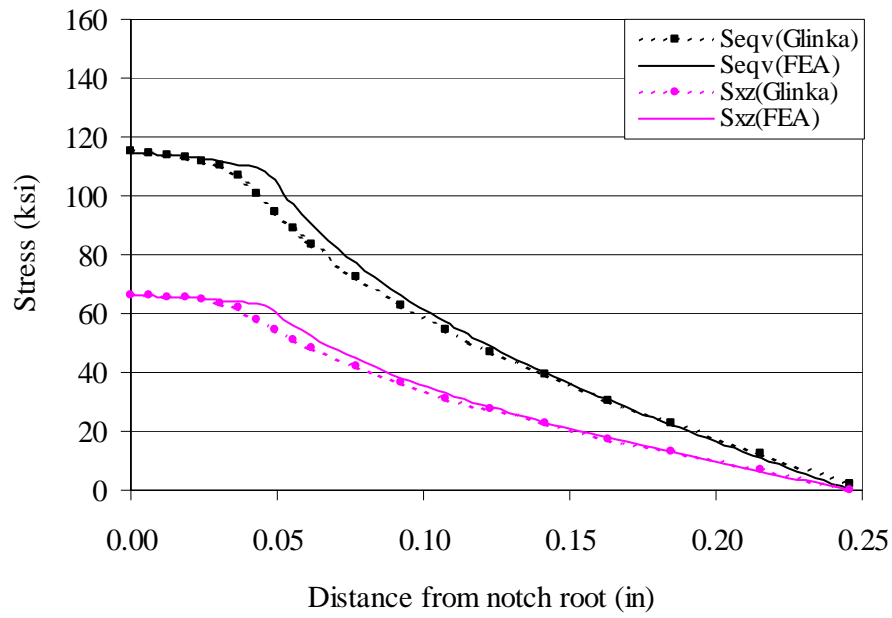
Figure F21. Comparisons between FEA and Glinka stresses for geometry 2, torsion loading (T = 1600 lb-in) at maximum load (top) and minimum load (bottom).
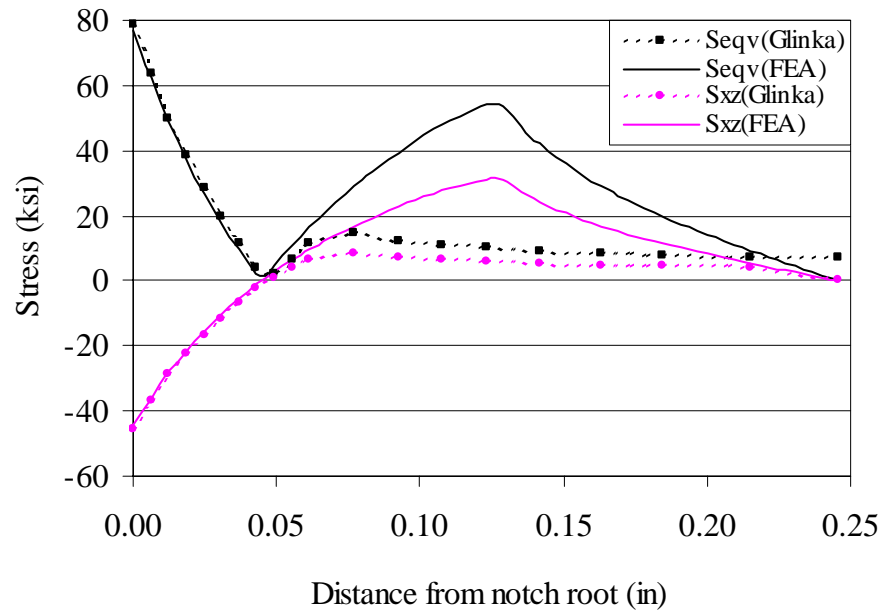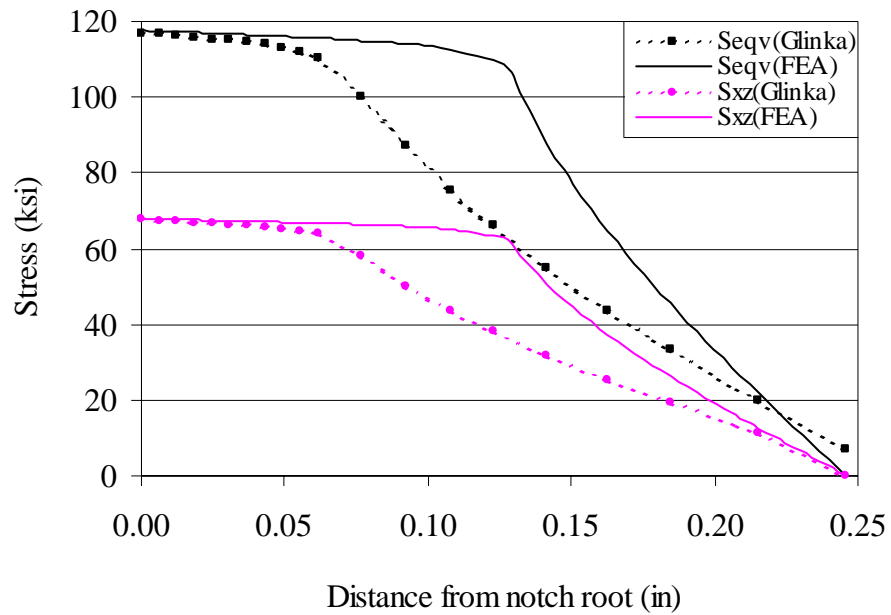
Figure F22. Comparisons between FEA and Glinka stresses for geometry 2, torsion loading (T = 2000 lb-in) at maximum load (top) and minimum load (bottom).
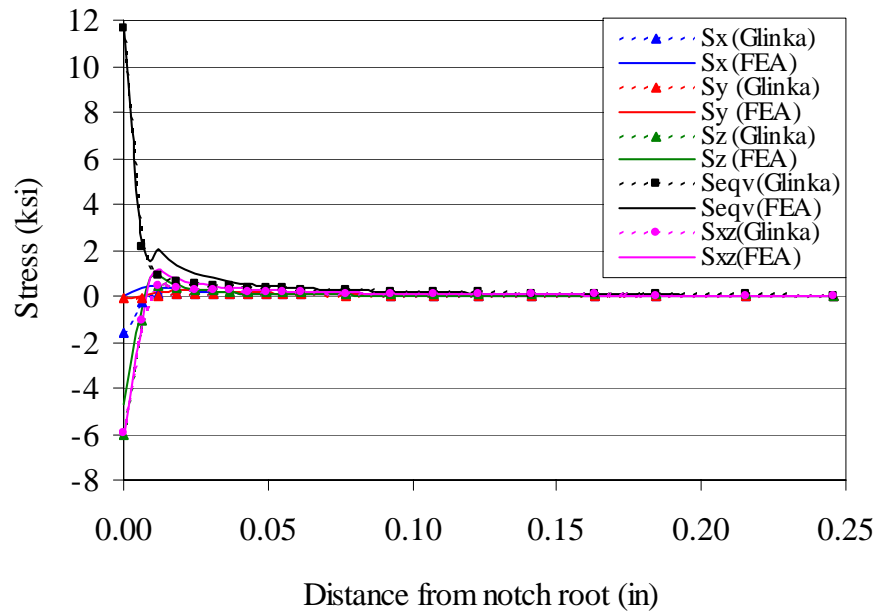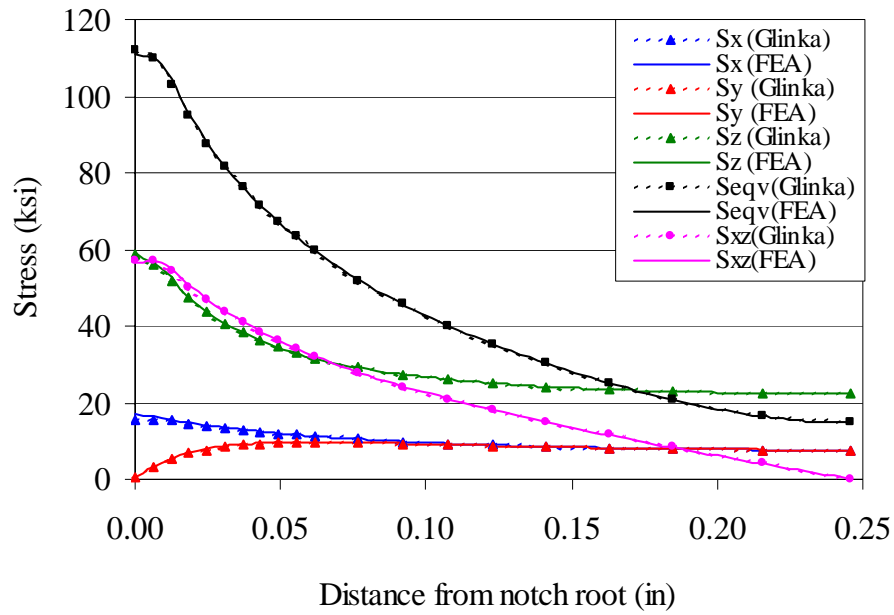
Figure F23. Comparisons between FEA and Glinka stresses for geometry 2, proportional loading (P = 6400 lb, T = 1120 lb-in) at maximum load (top) and minimum load (bottom).
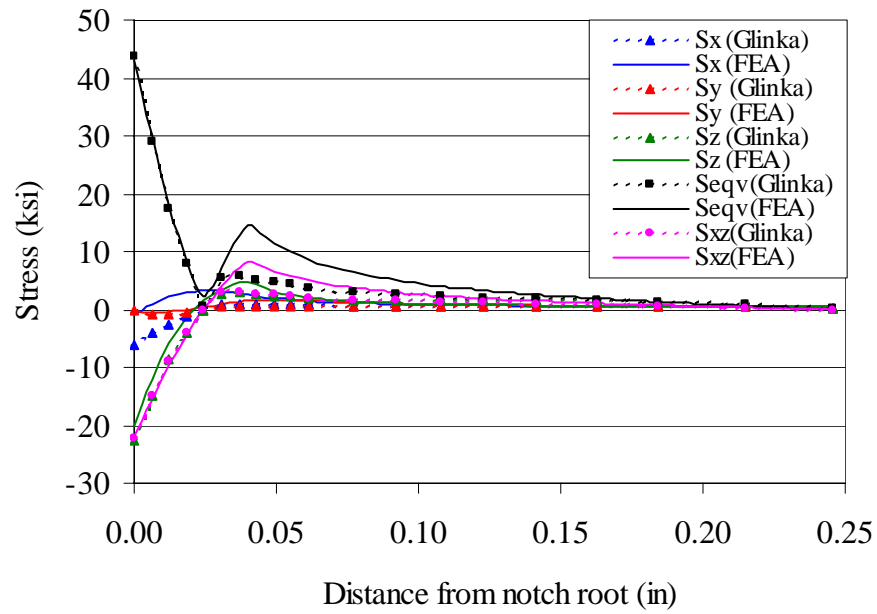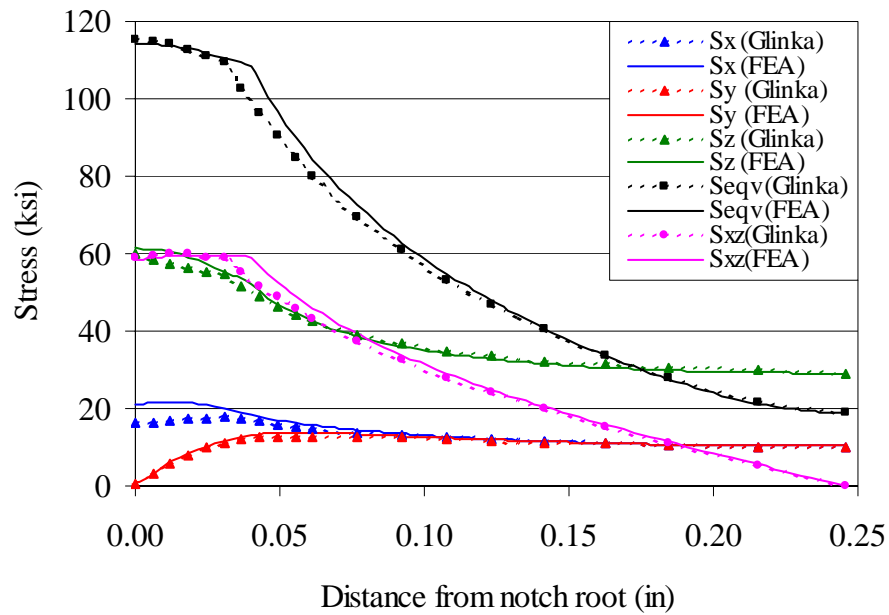
Figure F24. Comparisons between FEA and Glinka stresses for geometry 2, proportional loading
(P = 8200 lb, T = 1435 lb-in) at maximum load (top) and minimum load (bottom).
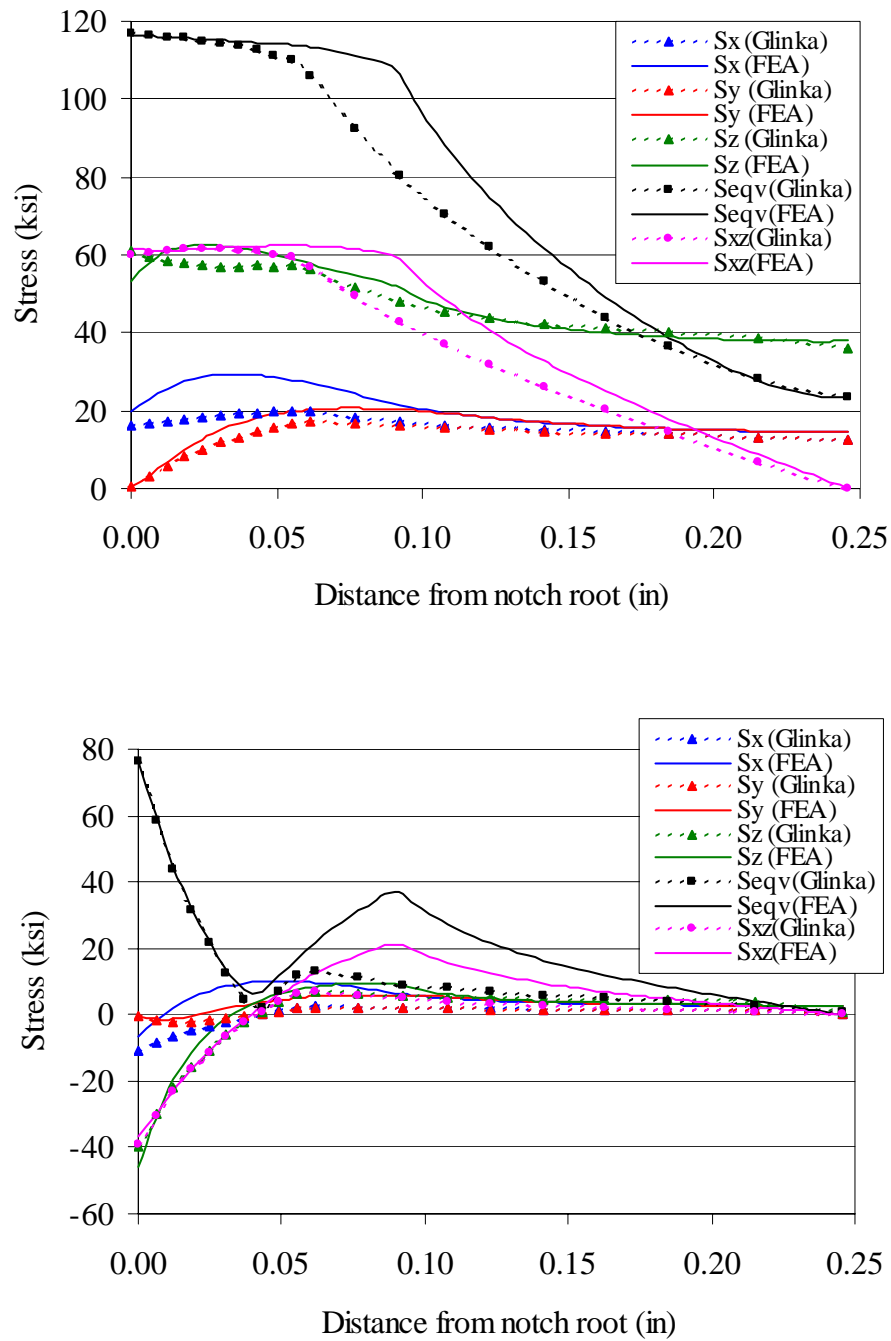
Figure F25. Comparisons between FEA and Glinka stresses for geometry 2, proportional loading (P = 10,000 lb, T = 1750 lb-in) at maximum load (top) and minimum load (bottom).
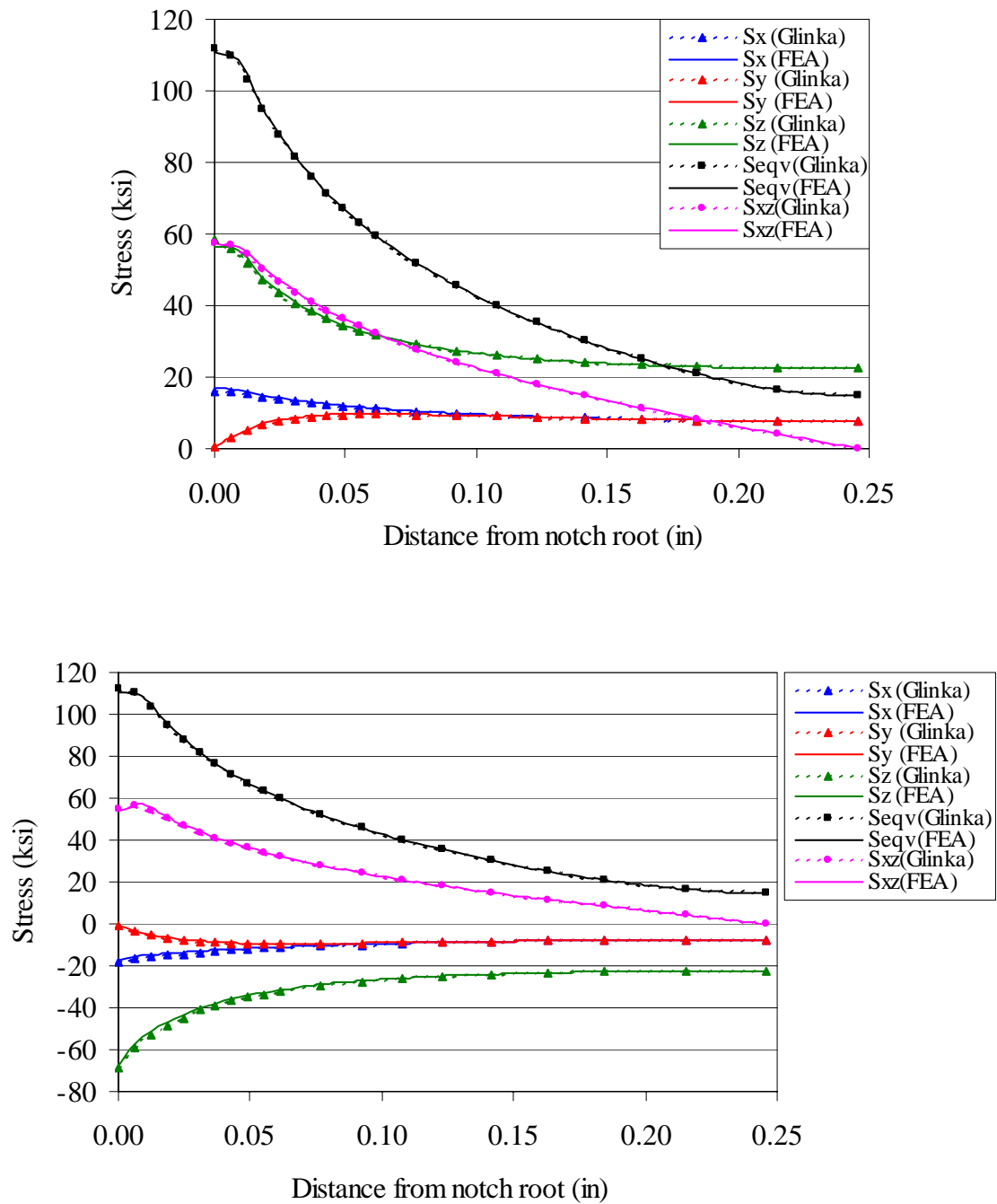
Figure F26. Comparisons between FEA and Glinka stresses for geometry 2, box path (P = 6400 lb, T = 1120 lb-in) at point 1 (top) and point 2 (bottom).
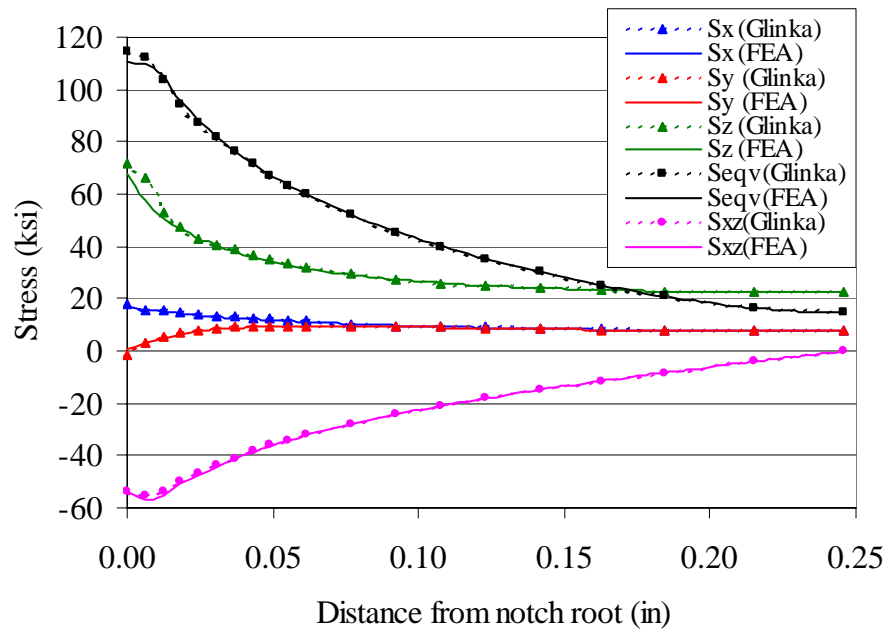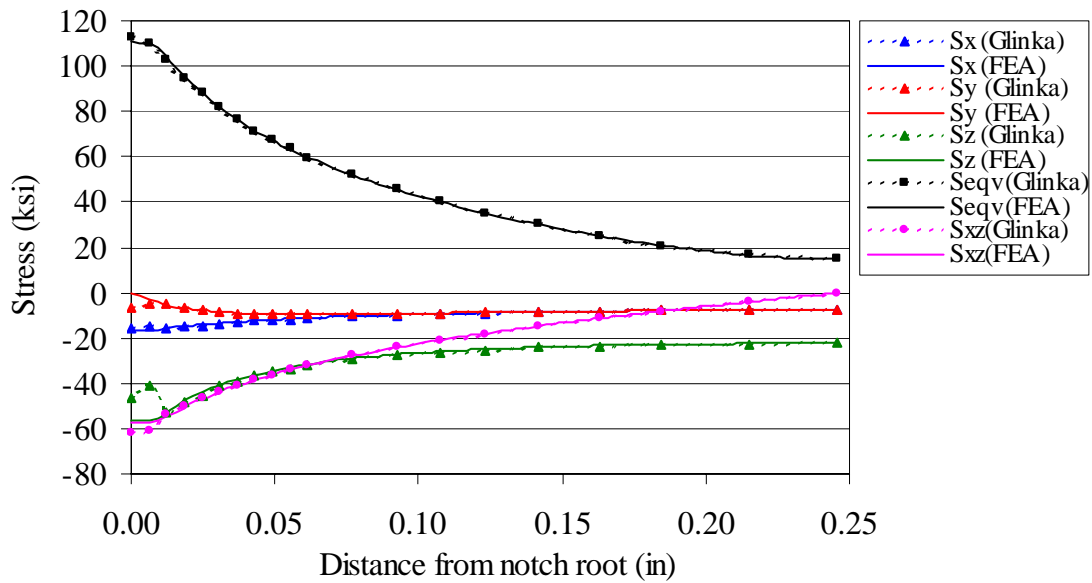
Figure F27. Comparisons between FEA and Glinka stresses for geometry 2, box path (P = 6400 lb, T = 1120 lb-in) at point 3 (top) and point 4 (bottom).
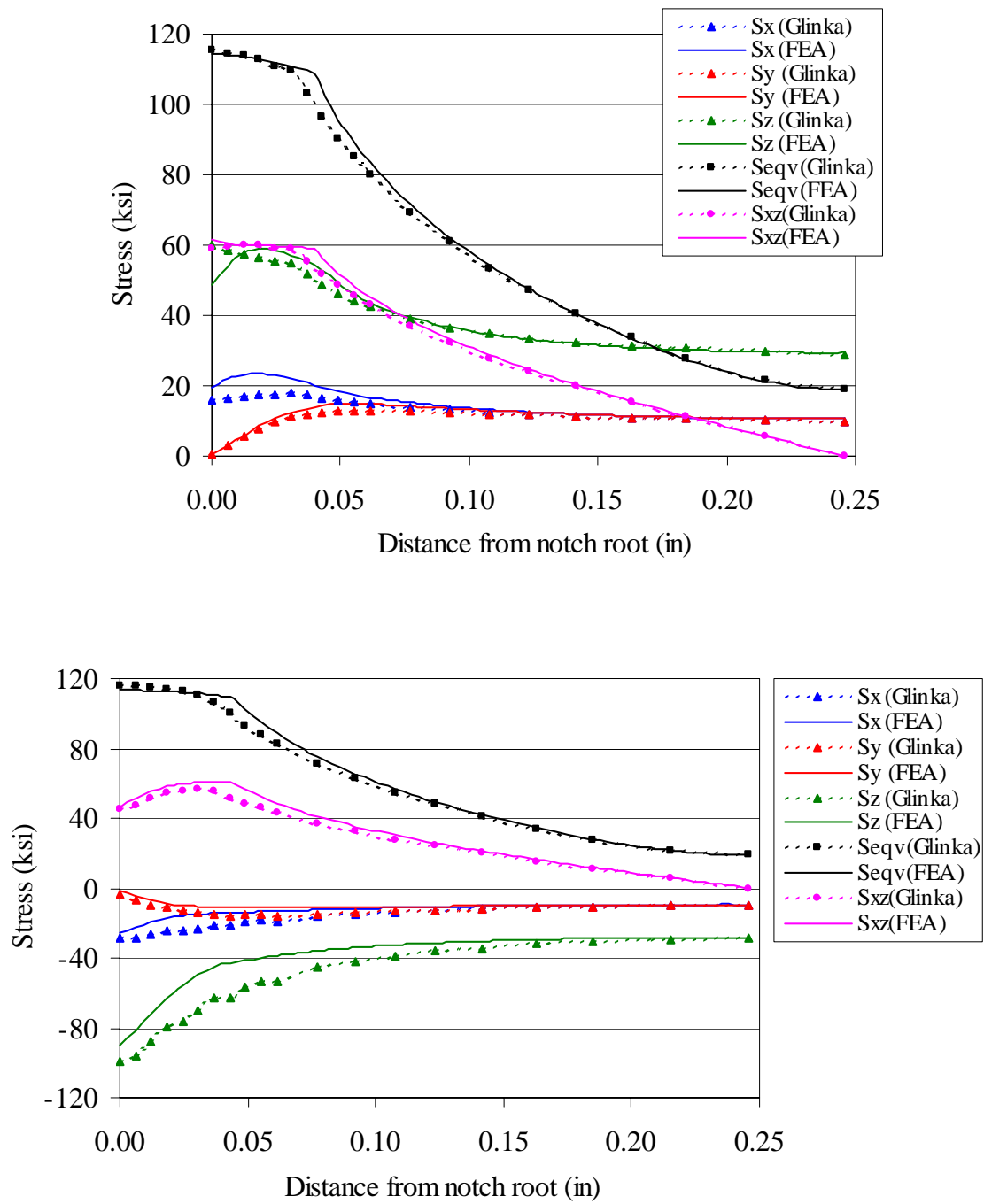
Figure F28. Comparisons between FEA and Glinka stresses for geometry 2, box path (P = 8200 lb, T = 1435 lb-in) at point 1 (top) and point 2 (bottom).
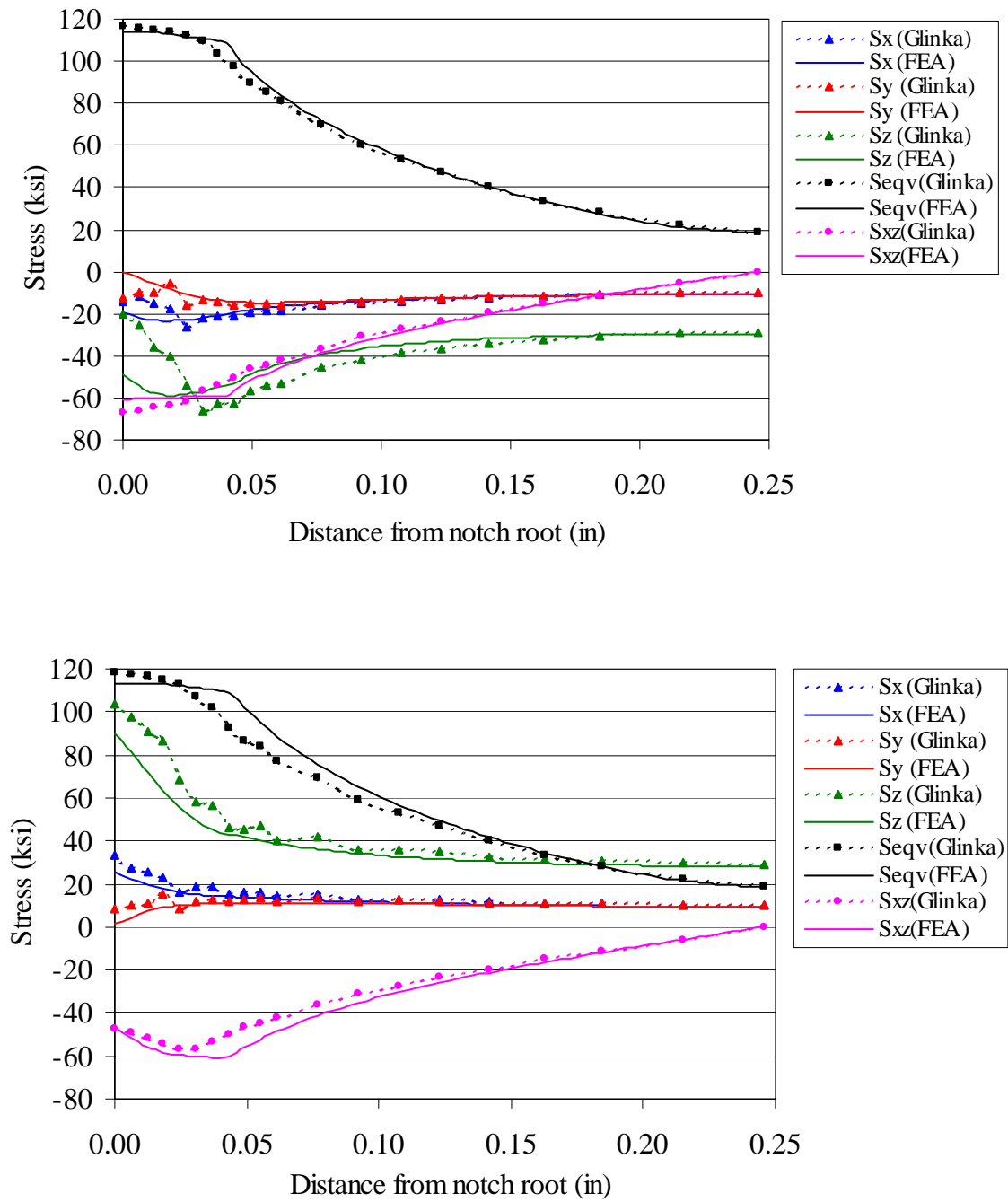
Figure F29. Comparisons between FEA and Glinka stresses for geometry 2, box path (P = 8200 lb, T = 1435 lb-in) at point 3 (top) and point 4 (bottom).
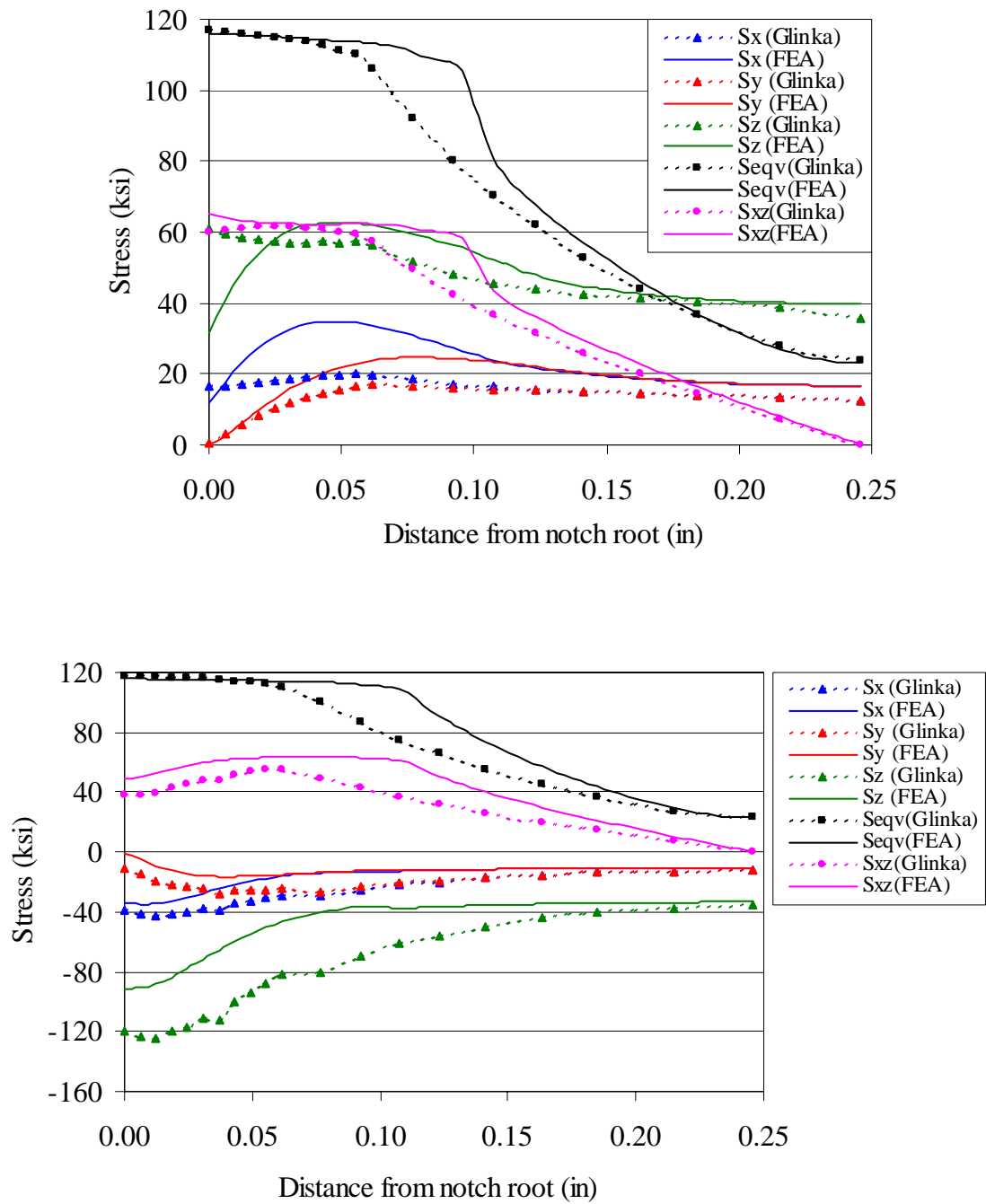
Figure F30. Comparisons between FEA and Glinka stresses for geometry 2, box path (P = 10,000 lb, T = 1750 lb-in) at point 1 (top) and point 2 (bottom).
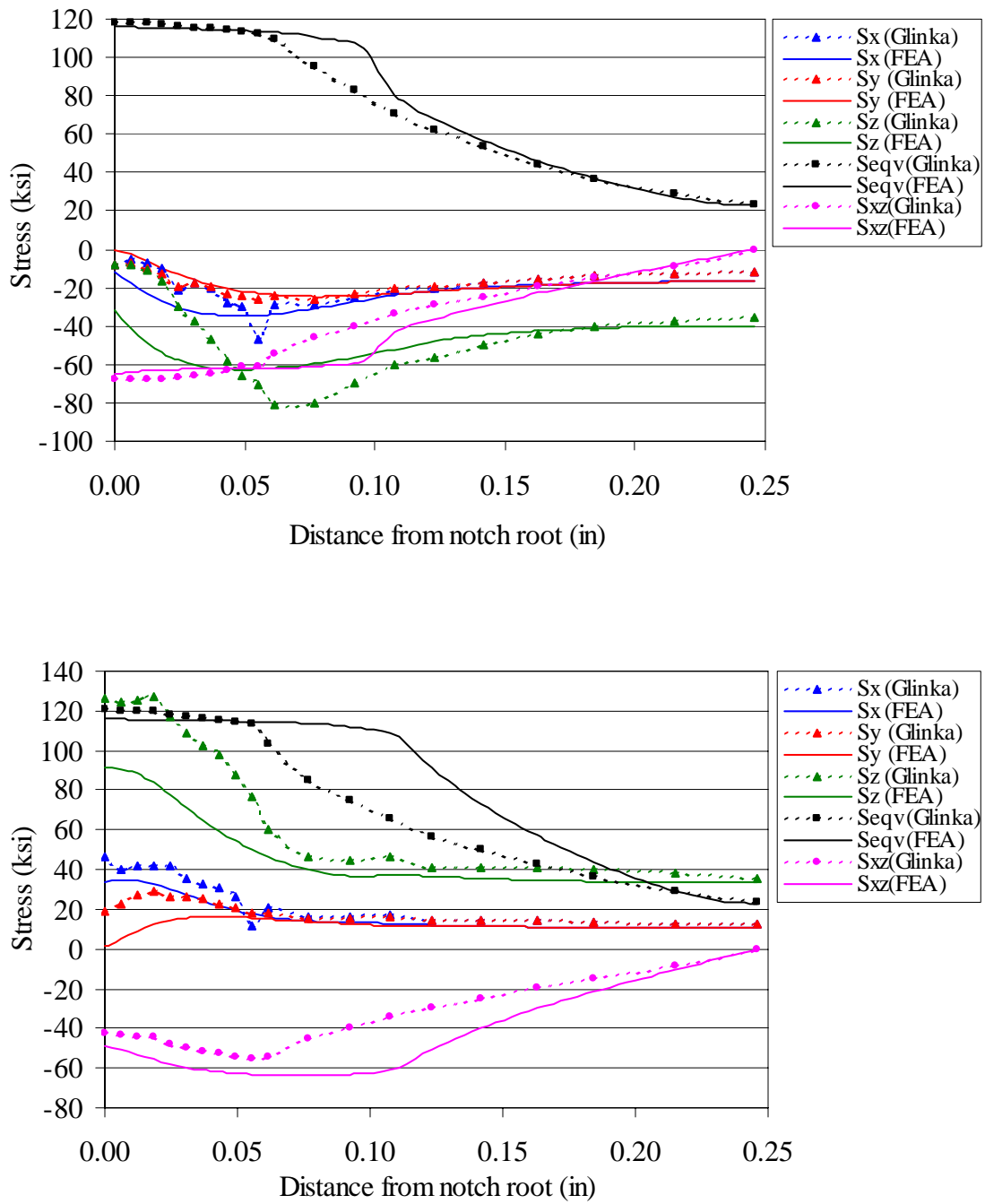
Figure F31. Comparisons between FEA and Glinka stresses for geometry 2, box path (P = 10,000 lb, T = 1750 lb-in) at point 3 (top) and point 4 (bottom).
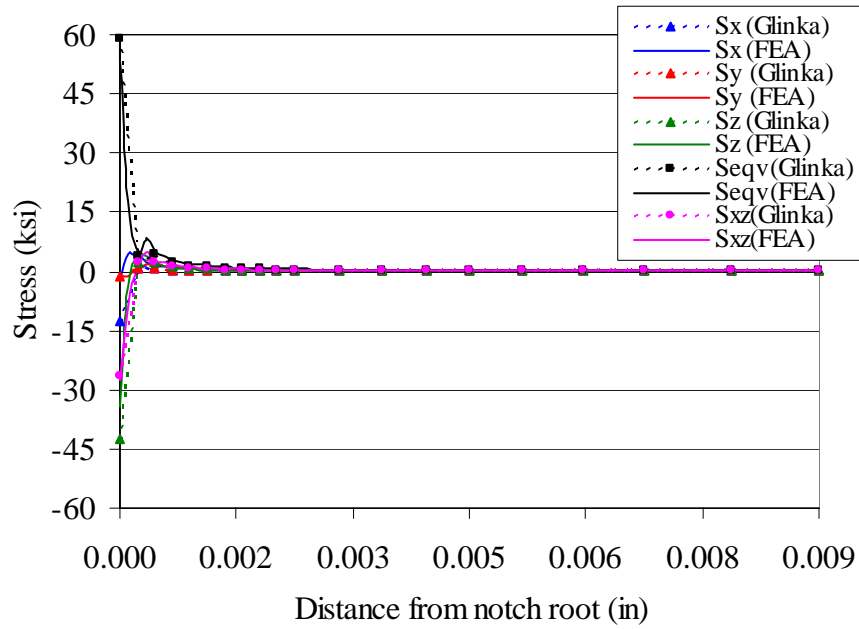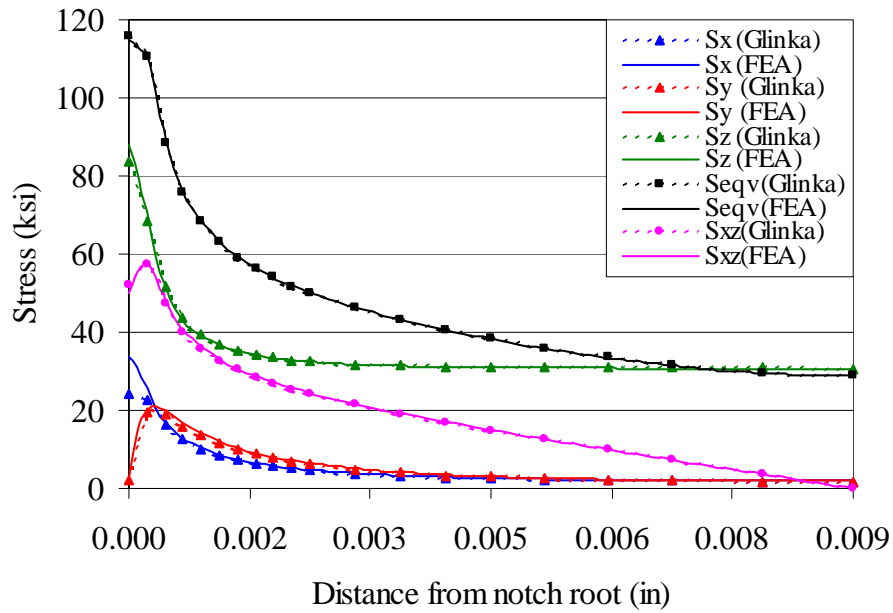
Figure F32. Comparisons between FEA and Glinka stresses for geometry 3, proportional loading (P/A = 30 ksi, T = 0.045 lb-in) at maximum load (top) and minimum load (bottom).
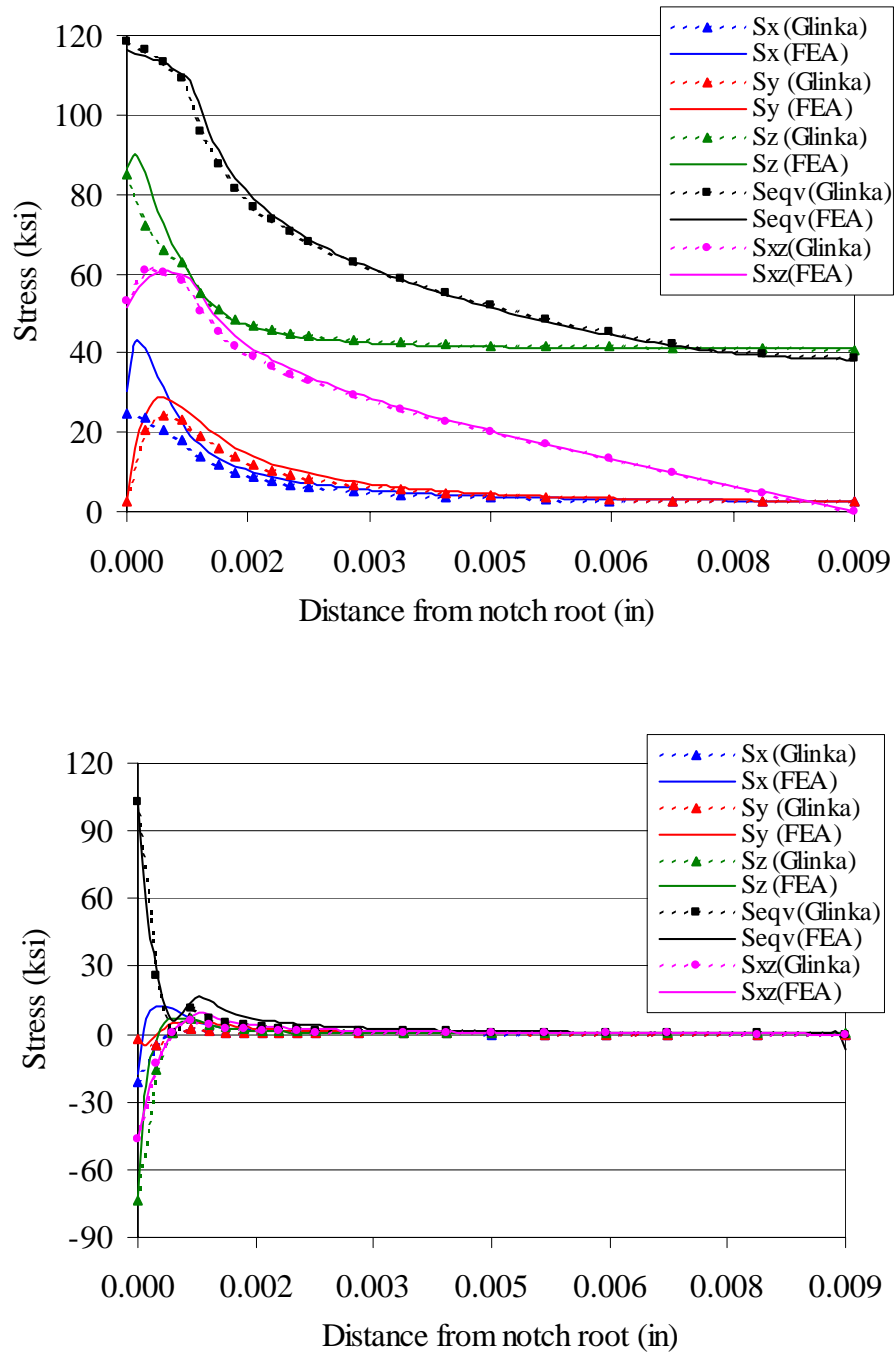
Figure F33. Comparisons between FEA and Glinka stresses for geometry 3, proportional loading (P/A = 40 ksi, T = 0.06 lb-in) at maximum load (top) and minimum load (bottom).
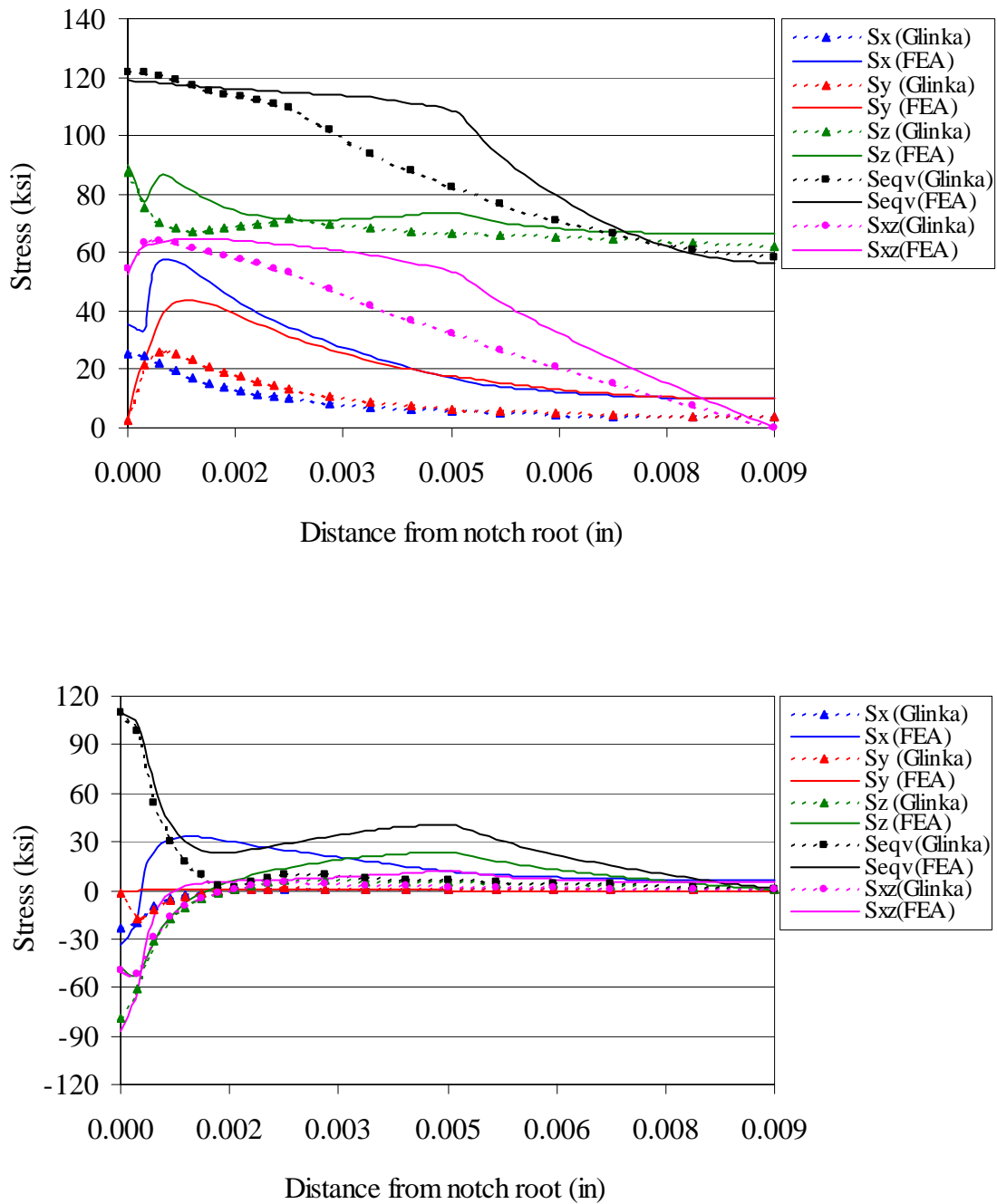
Figure F34. Comparisons between FEA and Glinka stresses for geometry 3, proportional loading (P/A = 60 ksi, T = 0.09 lb-in) at maximum load (top) and minimum load (bottom).
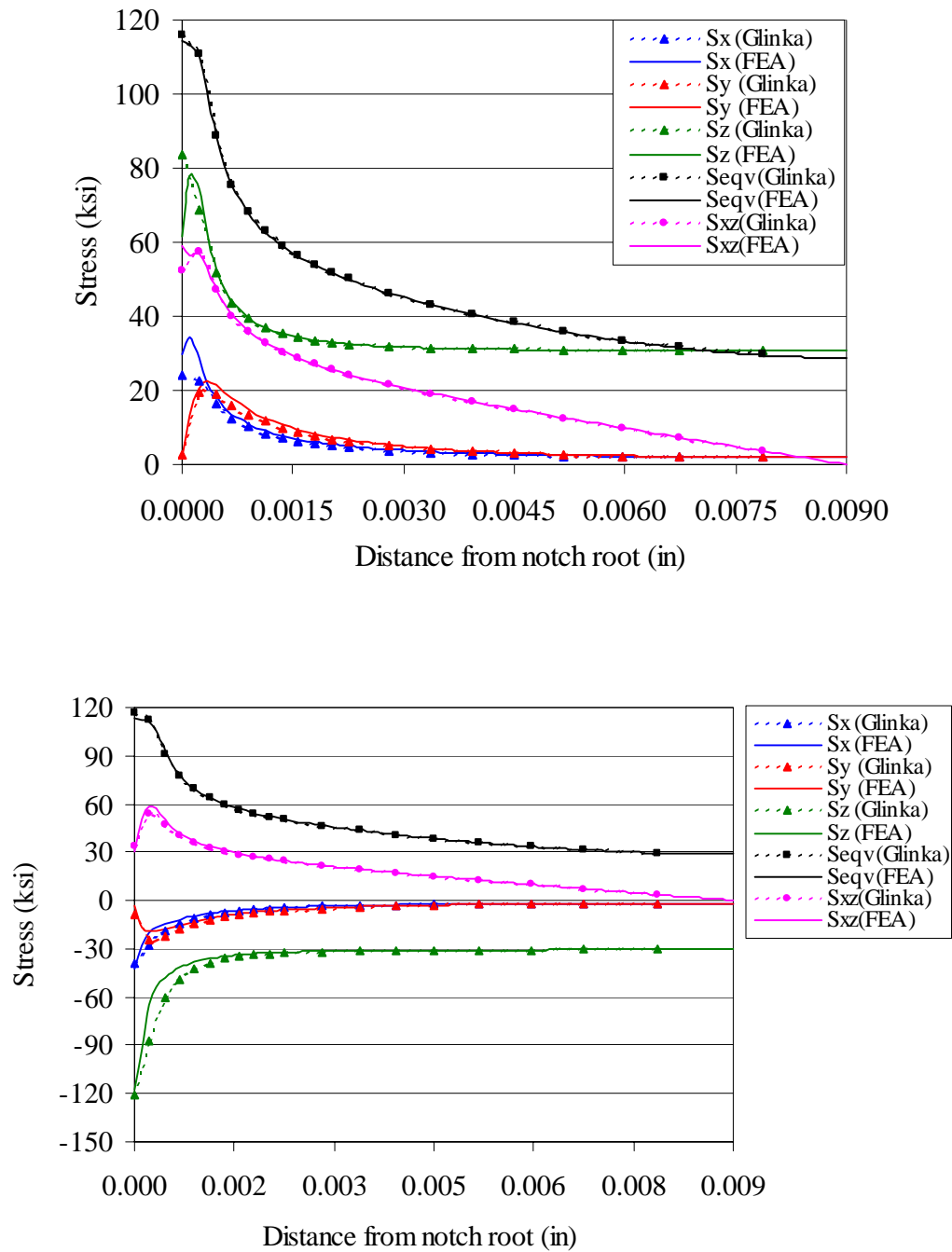
Figure F35. Comparisons between FEA and Glinka stresses for geometry 3, box path (P/A = 30 ksi, T = 0.045 lb-in) at point 1 (top) and point 2 (bottom).
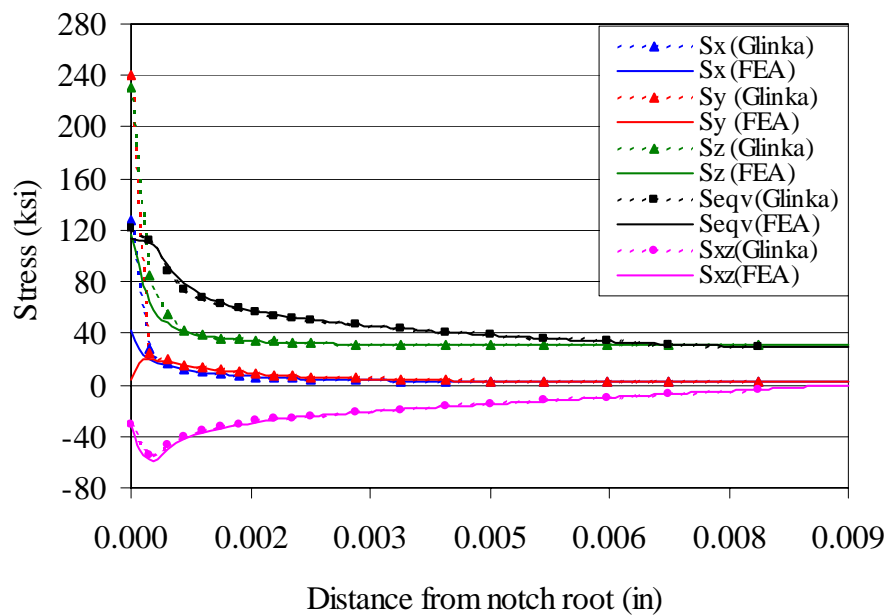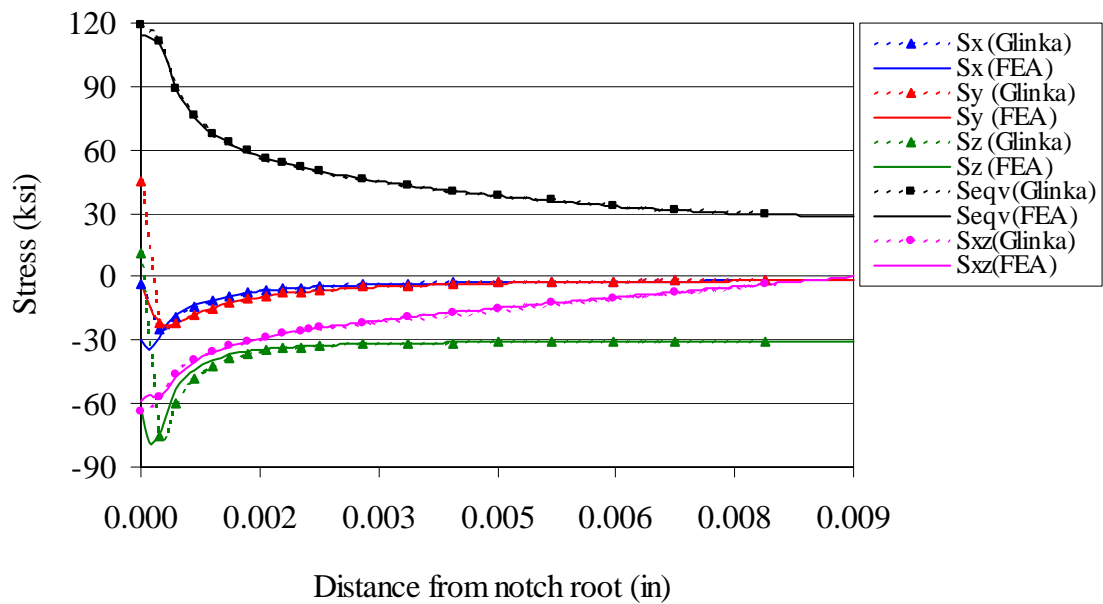
Figure F36. Comparisons between FEA and Glinka stresses for geometry 3, box path (P/A = 30 ksi, T = 0.045 lb-in) at point 3 (top) and point 4 (bottom).
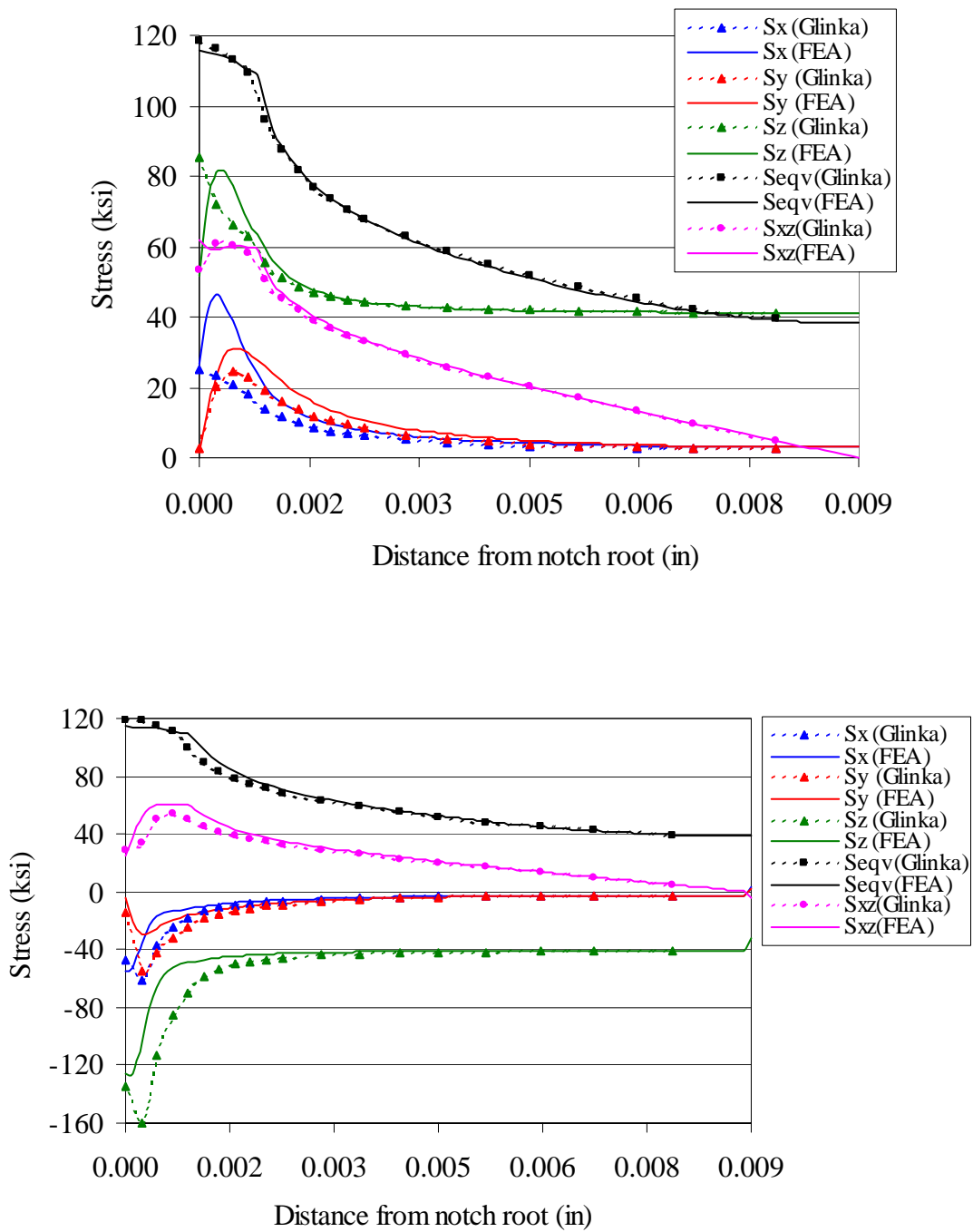
Figure F37. Comparisons between FEA and Glinka stresses for geometry 3, box path (P/A = 40 ksi, T = 0.06 lb-in) at point 1 (top) and point 2 (bottom).
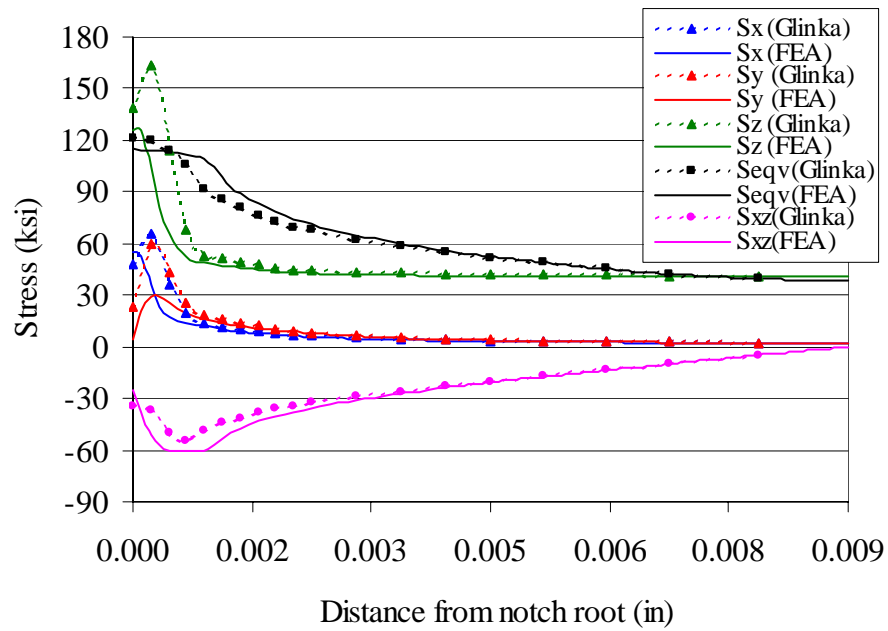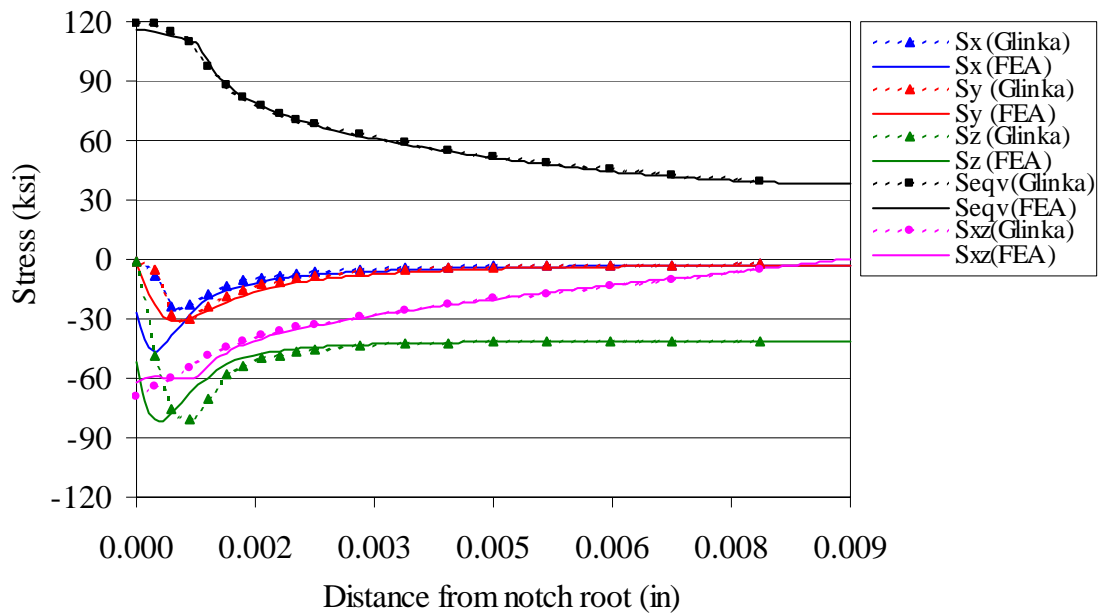
Figure F38. Comparisons between FEA and Glinka stresses for geometry 3, box path (P/A = 40 ksi, T = 0.06 lb-in) at point 3 (top) and point 4 (bottom).
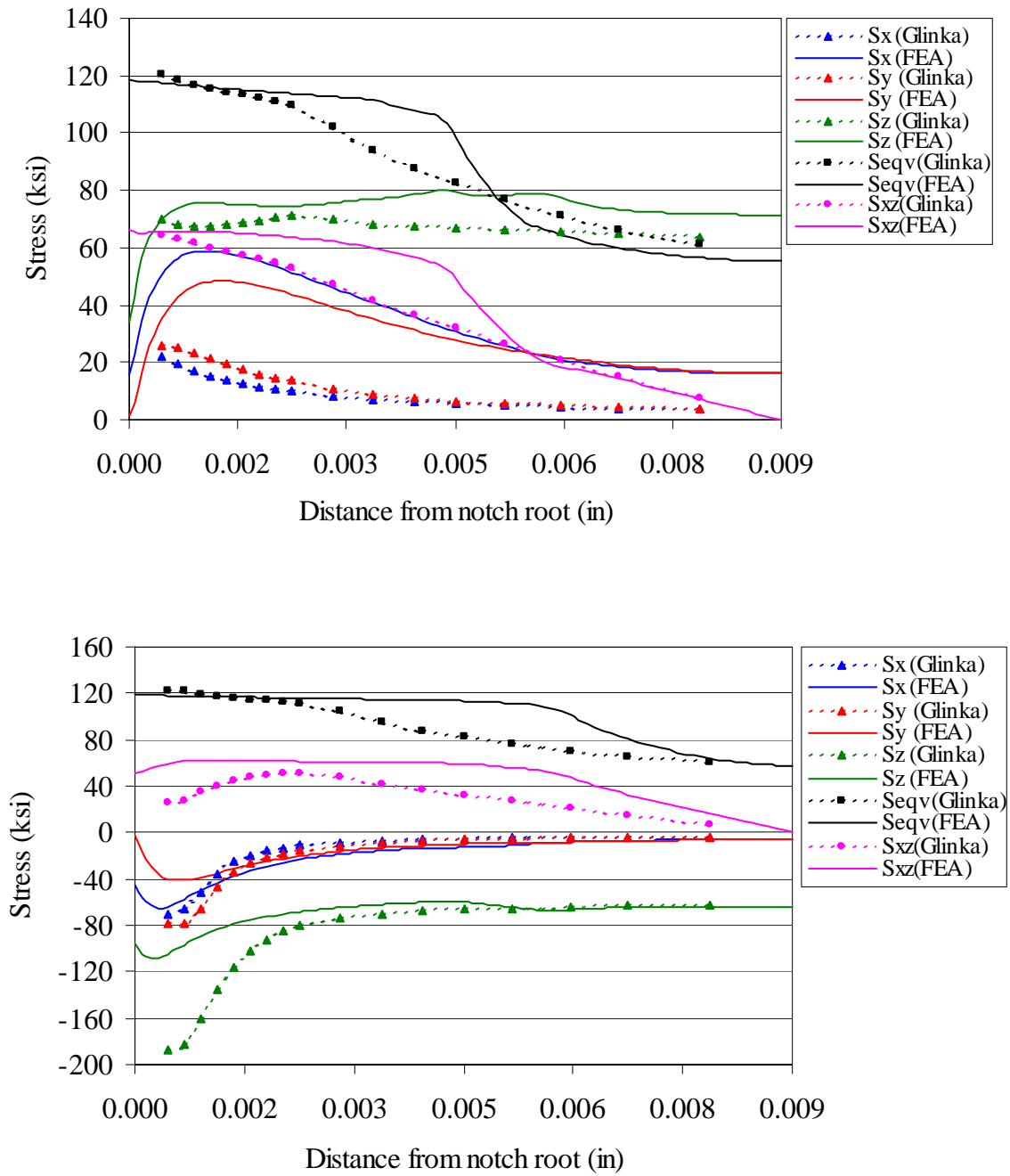
Figure F39. Comparisons between FEA and Glinka stresses for geometry 3, box path (P/A = 60 ksi, T = 0.09 lb-in) at point 1 (top) and point 2 (bottom).
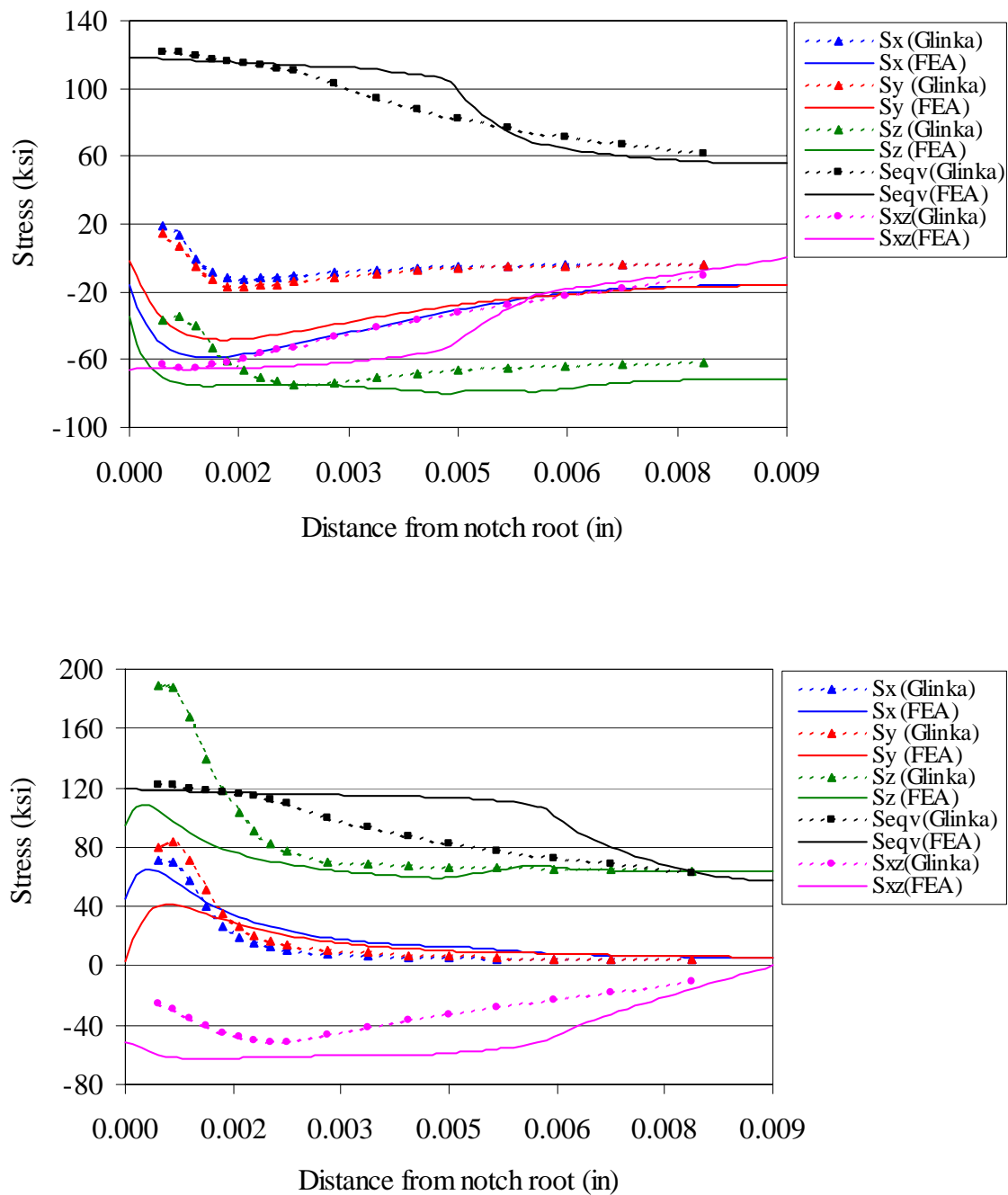
Figure F40. Comparisons between FEA and Glinka stresses for geometry 3, box path (P/A = 60 ksi, T = 0.09 lb-in) at point 3 (top) and point 4 (bottom).

F.5   ASSESSMENT OF SWRI CODE

As previously mentioned, the SwRI code, in the delivered form, was limited to the
analysis of a rectangular cross-section under monotonic loading (not cyclic). Consequently, the
assessment and validation of this code was more limited than for the Glinka code. Only
geometries 1 and 4 could be analyzed by this code, as geometries 2 and 3 contained circular
cross-sections at the notch. Furthermore, the applied load cases were restricted to tension,
torsion, and proportional combined tension-torsion, with comparisons only made at the point of
maximum load (no unloading or cyclic loading).

Comparisons between the elastic-plastic stresses obtained from the finite element
analyses and the SwRI approximation code for geometries 1 and 4 are shown in Figures 41 – 49.
For geometry 1 (Figures F41 – F43), the z-axis corresponds to the axial (loading) direction,
while the x-axis is directed along the notch section and the y-axis is directed through the
thickness (note the y and z axes have been interchanged relative to the Glinka comparisons).
The same coordinate system applies for geometry 4 (Figures F44 – F49).

F.5.1   Summary of SwRI Results: Geometry 1

The comparisons between the SwRI code and FEA results for geometry 1 are shown in
Figures F41 – F43. The results shown are for tensile loading with P/A ranging from 40 to 80 ksi.
Due to the extensive yielding on the notch section that occurred at P/A = 100 ksi, the code was
not able to generate an elastic-plastic stress approximation at the highest load. However, at the
lower load levels, the stress calculations from the SwRI code were in much better agreement
with the FEA results than those from the Glinka code. Some discrepancies in σ_y and σ_z near the
notch root were observed along the specimen centerline, but the depth of the plastic zone was
reasonably well approximated, and the stresses along the edge of the component were in fairly
close agreement with FEA results.

The better accuracy for geometry 1 displayed by the SwRI code, relative to the Glinka
code, is likely due to the method by which the SwRI code redistributes the stresses on the notch
section. In approximating the elastic-plastic stresses from the elastic solution, the SwRI code
takes into account the full stress distribution on the entire component cross-section, rather than
along a single line as the Glinka code does. Thus, full equilibrium is maintained as the stresses
are redistributed across the section due to yielding. As a result, the stress gradient through the

thickness of the part (from the centerline to the edge), which affects the magnitudes of the stress components and the depth of the plastic zone, is better accounted for by the SwRI code, leading to more accurate elastic-plastic stress estimates in components with a rectangular cross-section. For axisymmetric components, in which a stress gradient occurs in only one direction (radial), the differences between the two codes would likely be much less. This could not be verified, however, as the SwRI code was not formulated to analyze such components.

F.5.2   Summary of SwRI Results: Geometry 4

The comparisons between the SwRI code and FEA results for geometry 4 are shown in Figures F44 – F49. As with geometry 1, the stresses predicted by the SwRI code were in reasonable agreement with FEA results in most cases, although there were slightly larger discrepancies found in certain stress components at higher loads. For example, under axial loading (Figures F44 – F46), the through-the-thickness stress (σ_y) predicted by the SwRI code along the centerline was substantially smaller than the FEA value near the notch root, while the axial stress (σ_z) was also slightly underpredicted at the higher load levels. However, the depth of the plastic zone was in good agreement with FEA. Under combined axial/torsional loads (Figures F47 – F49), similar results were found at the higher loads, with σ_z and σ_y underpredicted along the centerline near the notch root. With the exception of σ_x, the stress predictions along the edge of the component were in very good agreement with FEA results at all load levels.
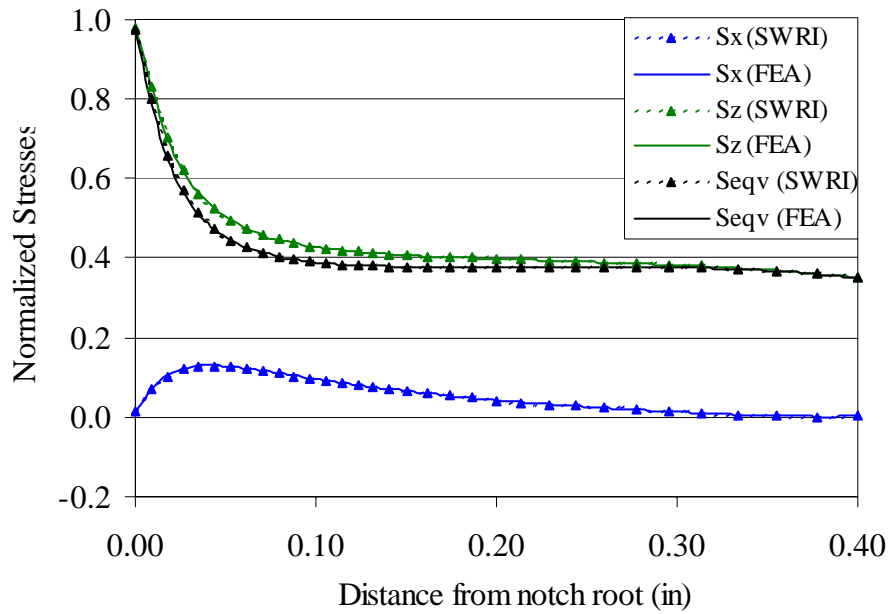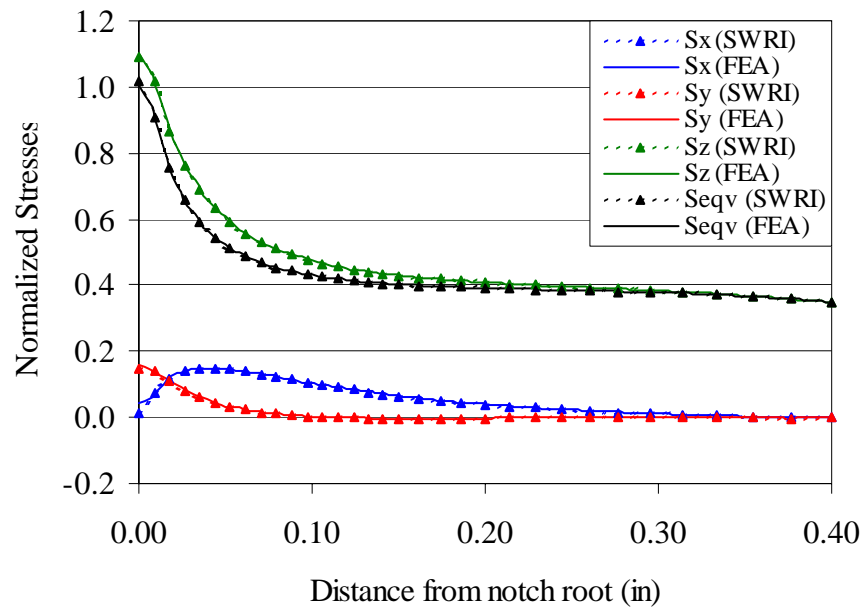
Figure F41. Comparisons between FEA and SwRI stresses for geometry 1, P/A = 40 ksi, center of notch section (top) and edge of notch section (bottom).
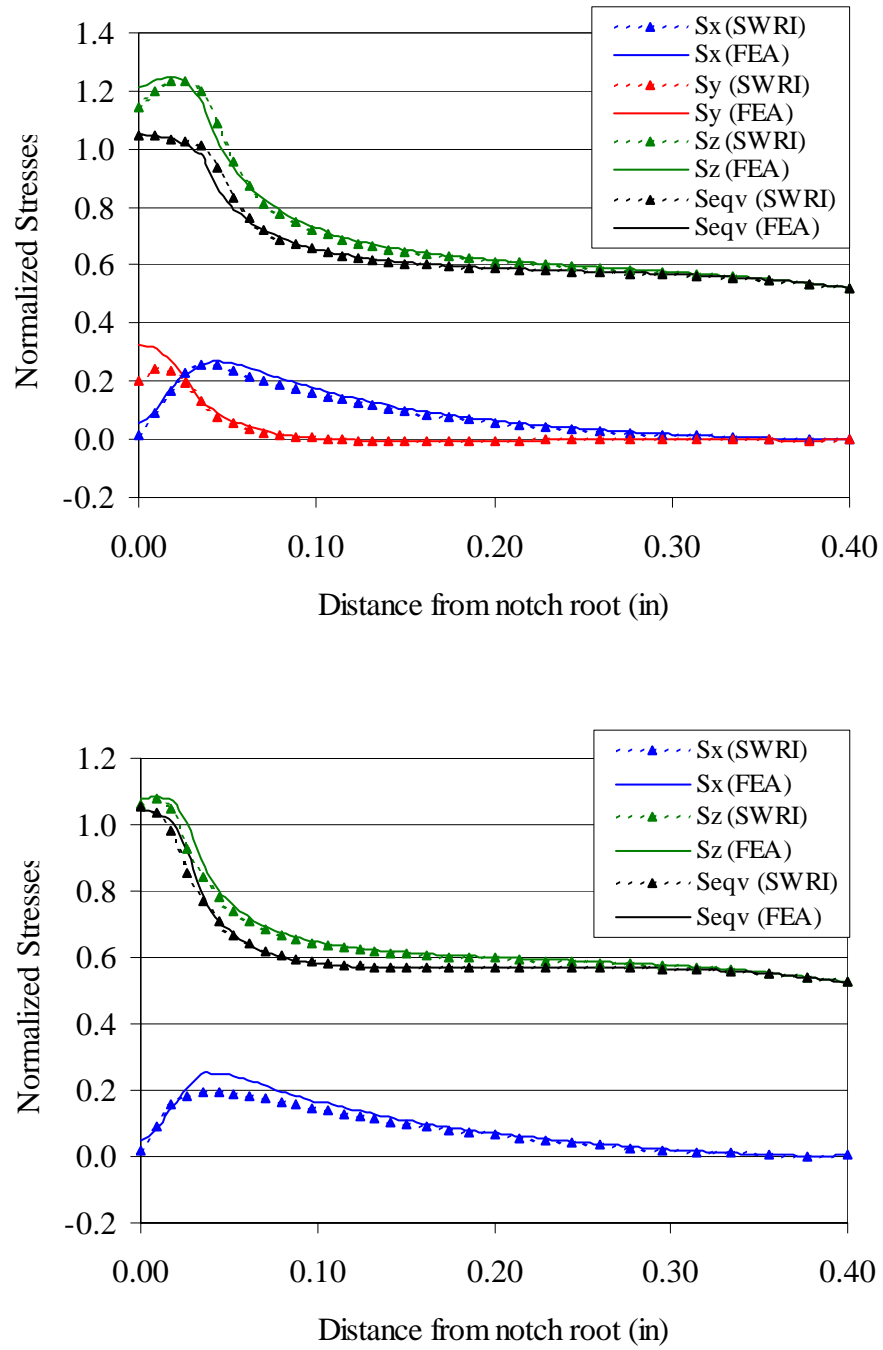
Figure F42. Comparisons between FEA and SwRI stresses for geometry 1, P/A = 60 ksi, center of notch section (top) and edge of notch section (bottom).
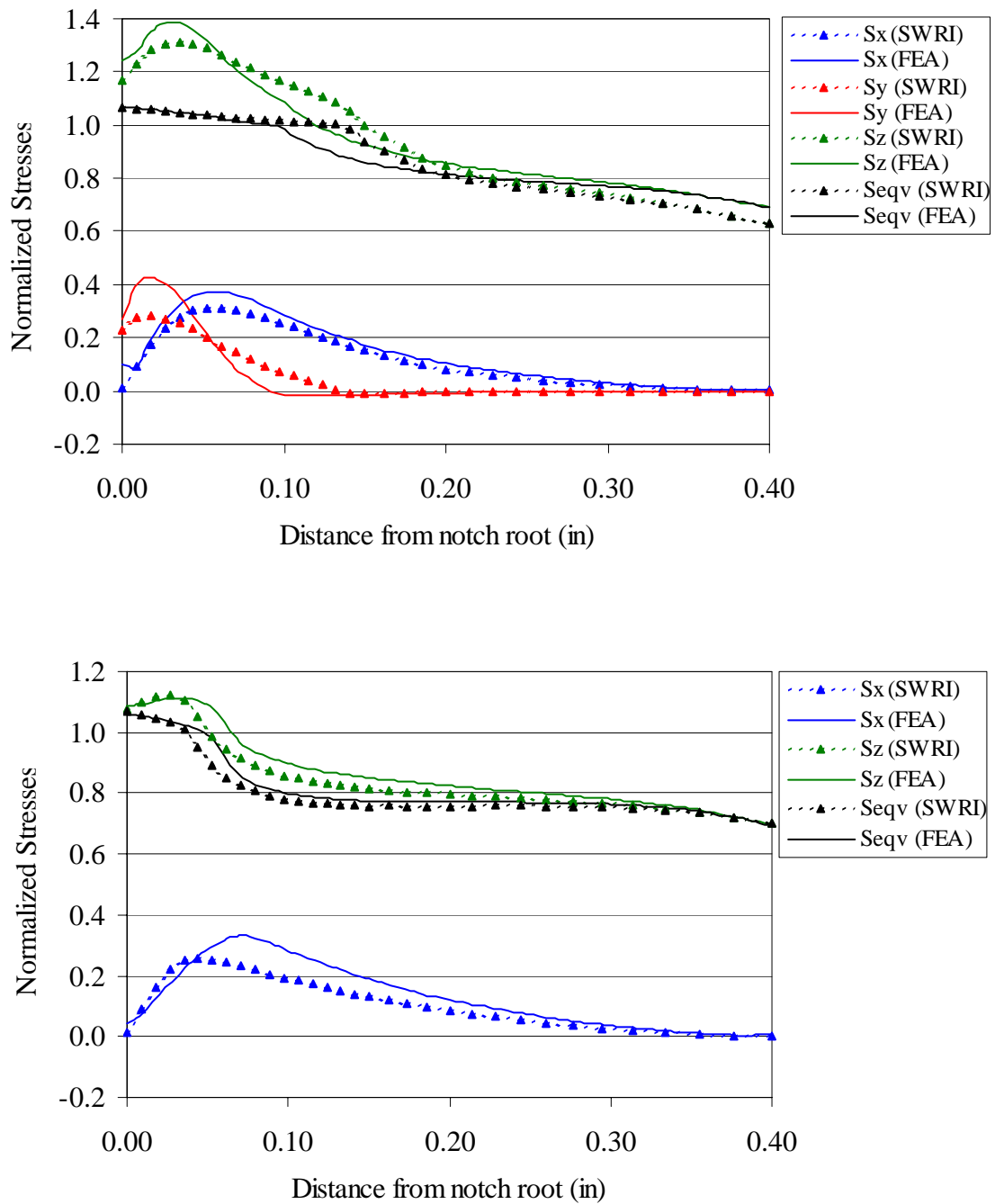
Figure F43. Comparisons between FEA and SwRI stresses for geometry 1, P/A = 80 ksi, center
of notch section (top) and edge of notch section (bottom).
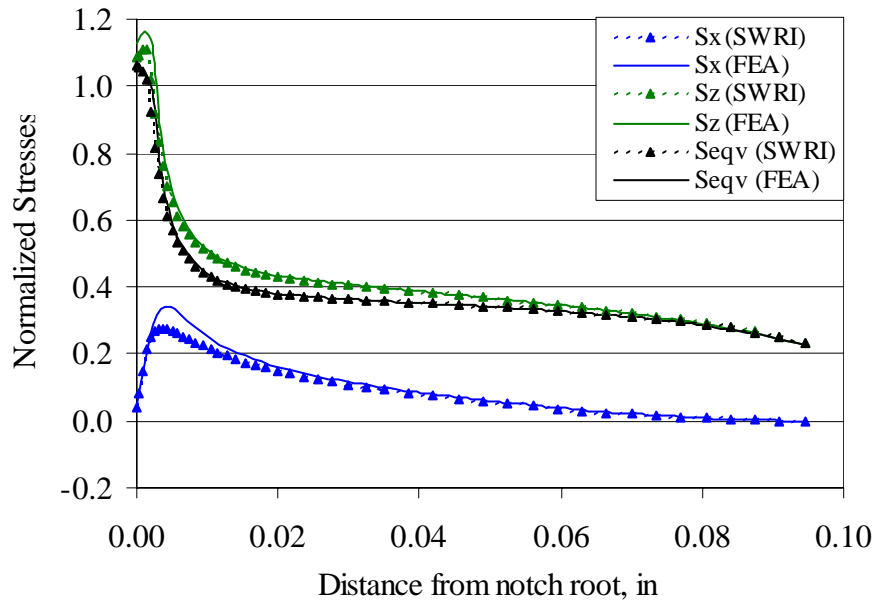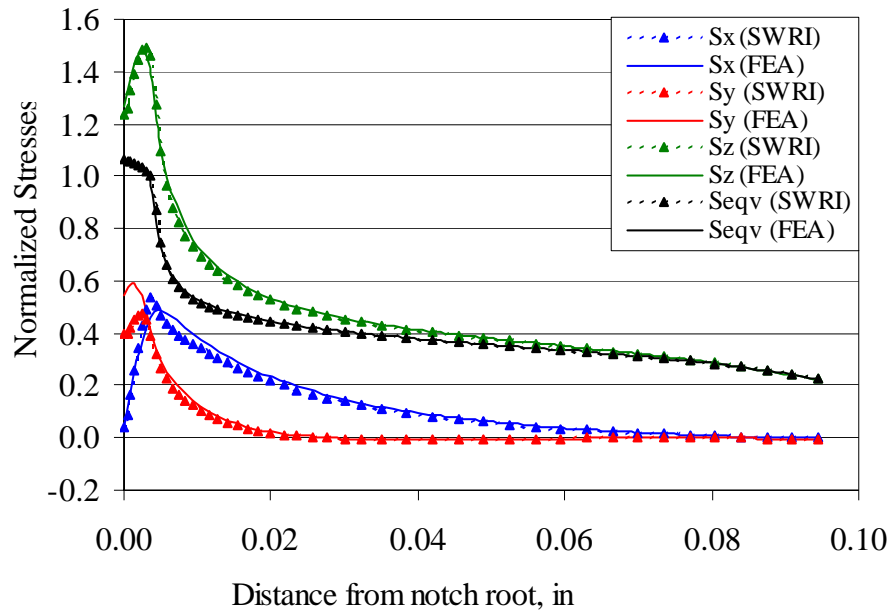
Figure F44. Comparisons between FEA and SwRI stresses for geometry 4, axial loading (P/A = 40 ksi), center of notch section (top) and edge of notch section (bottom).
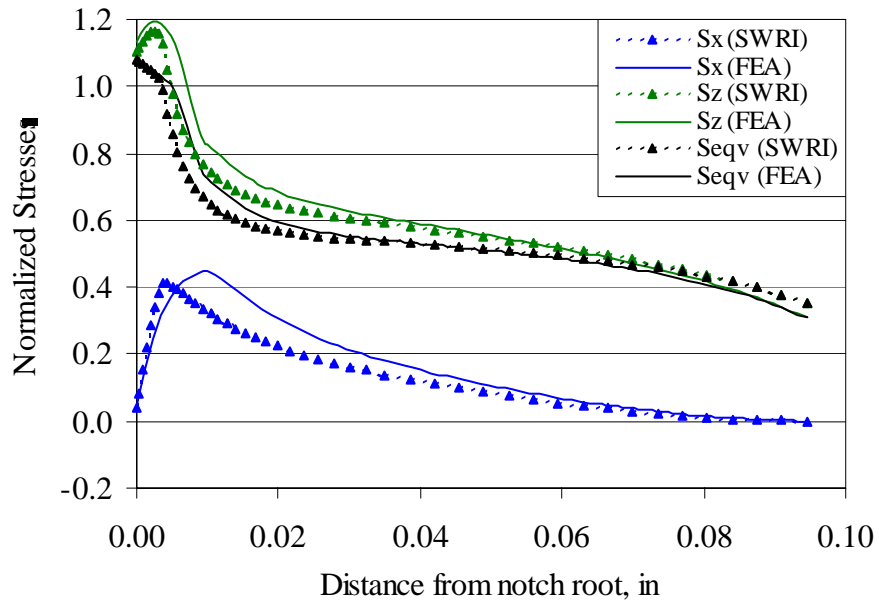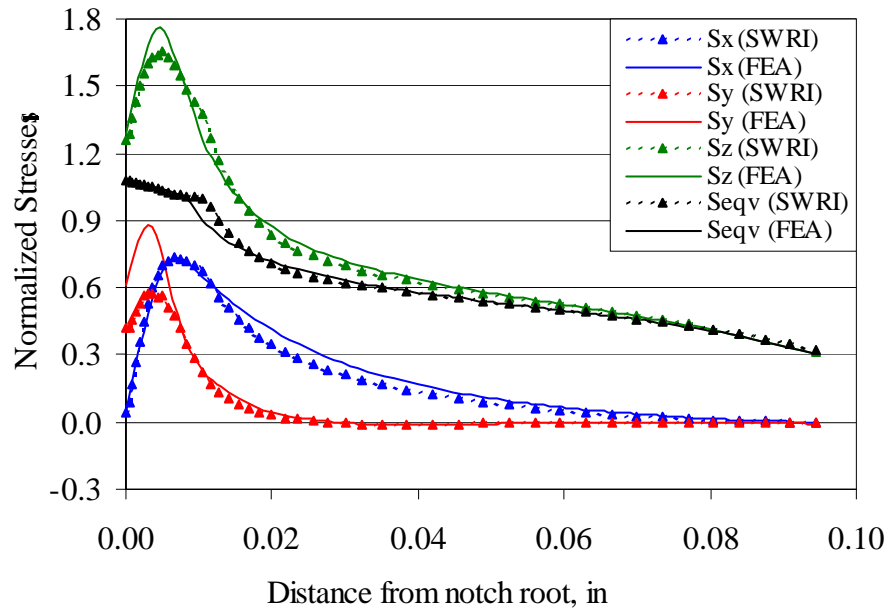
Figure F45. Comparisons between FEA and SwRI stresses for geometry 4, axial loading (P/A = 60 ksi), center of notch section (top) and edge of notch section (bottom).
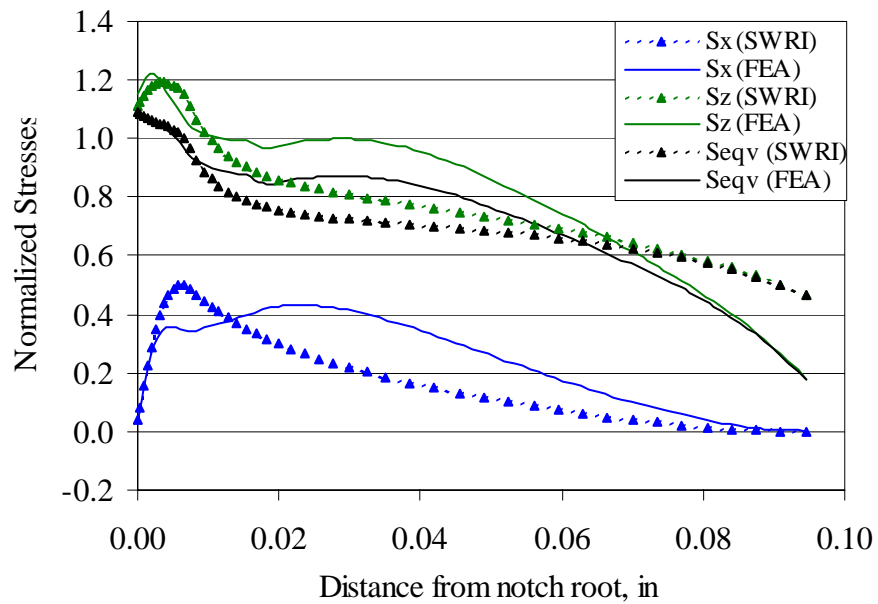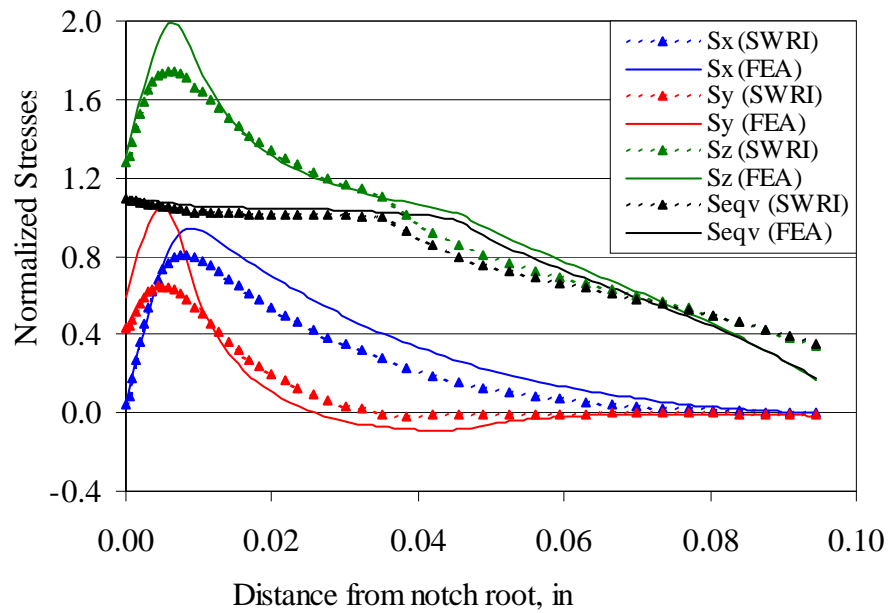
Figure F46. Comparisons between FEA and SwRI stresses for geometry 4, axial loading (P/A = 80 ksi), center of notch section (top) and edge of notch section (bottom).
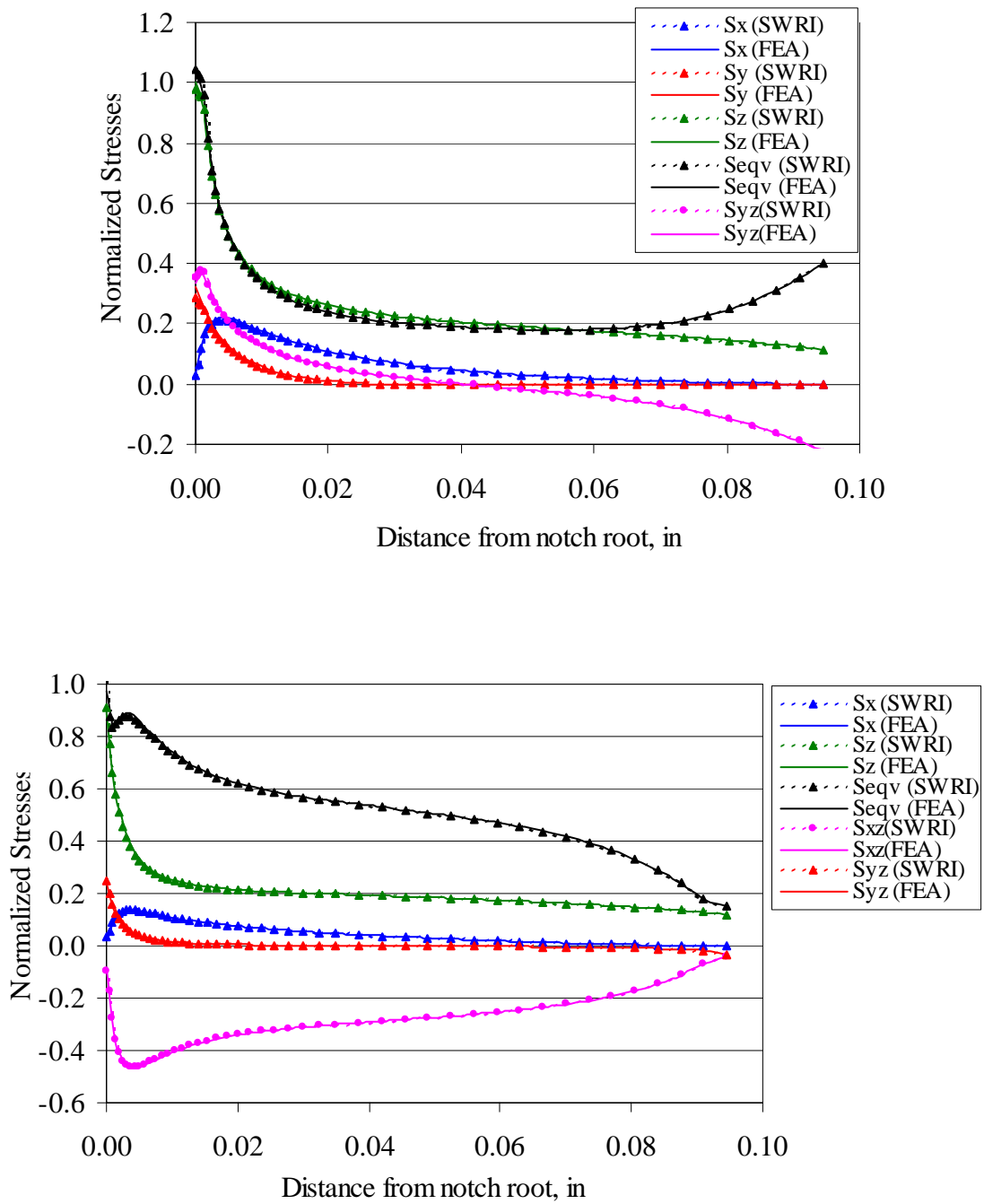
Figure F47. Comparisons between FEA and SwRI stresses for geometry 4, proportional loading (P/A = 20 ksi, T = 3.0 lb-in), center of notch section (top) and edge of notch section (bottom).
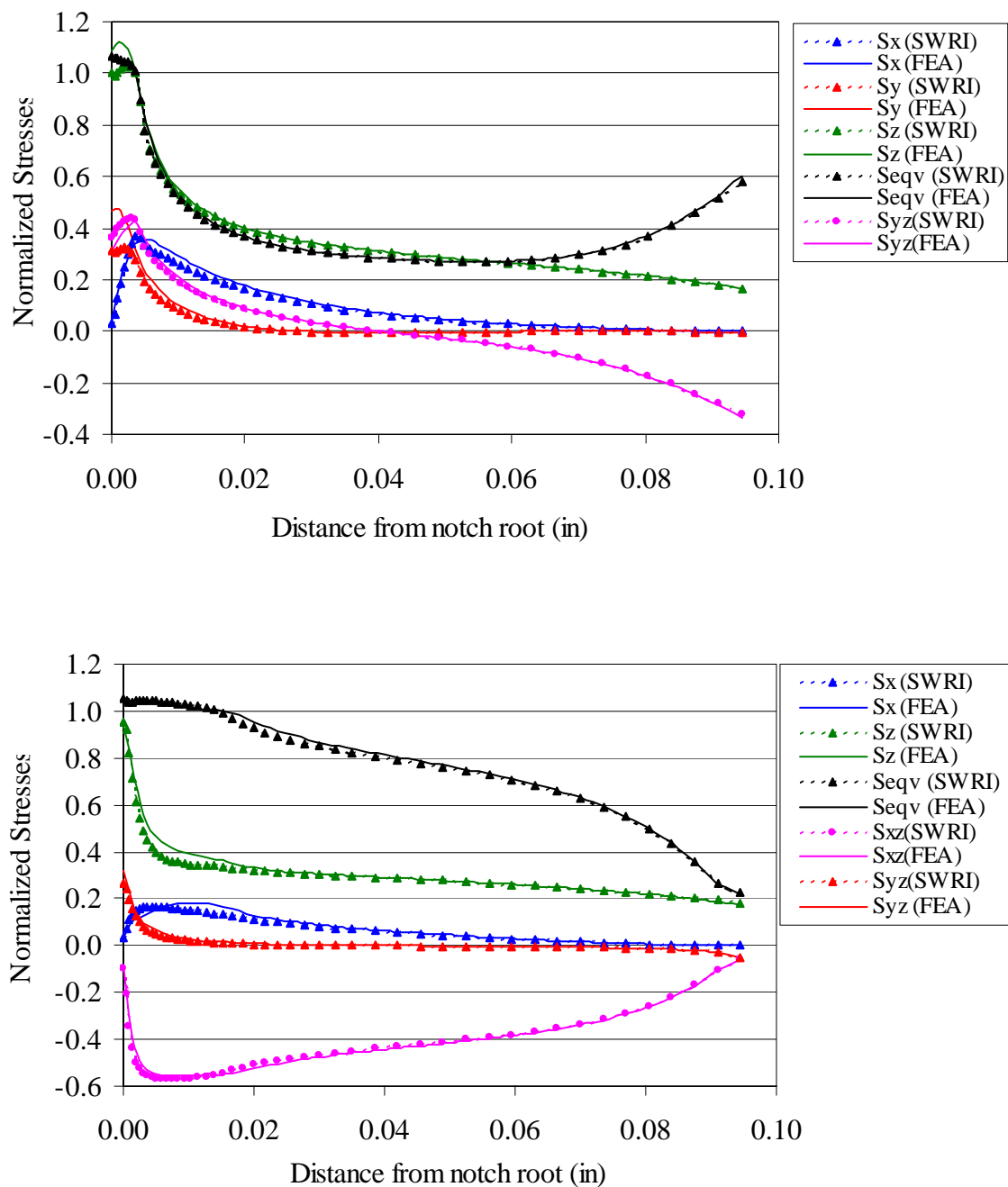
Figure F48. Comparisons between FEA and SwRI stresses for geometry 4, proportional loading (P/A = 30 ksi, T = 4.5 lb-in), center of notch section (top) and edge of notch section (bottom).
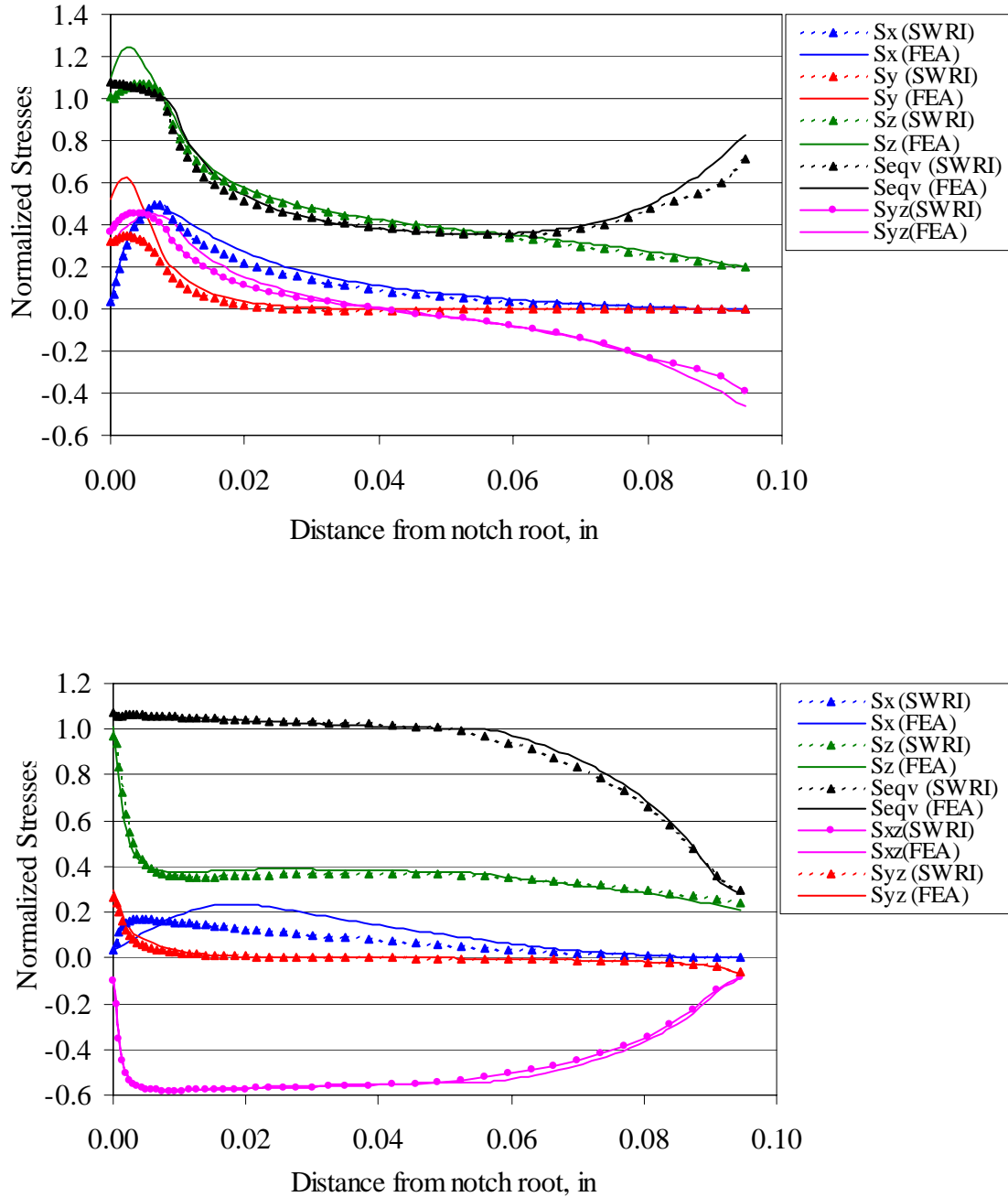
Figure F49. Comparisons between FEA and SwRI stresses for geometry 4, proportional loading (P/A = 40 ksi, T = 6.0 lb-in), center of notch section (top) and edge of notch section (bottom).

F.6   SUMMARY AND CONCLUSIONS

The two approximate elastic-plastic notch analysis methods considered here both displayed promising results under certain conditions. The Glinka code provided reasonable stress estimates for axisymmetric components (such as circumferentially notched round bars), in which the stress gradients are limited to one direction. However, for non-axisymmetric components, in which the stress gradients may be bi-directional, the Glinka approximations were much less accurate. The SwRI code provided better overall stress approximations for components with a rectangular cross-section. However, in the current form, the SwRI program is more limited in its versatility, as it has not been coded to analyze non-rectangular sections or handle loading conditions that result in cyclic plasticity. In addition, some problems were encountered in running the SwRI code under loading conditions that produced very large-scale plasticity. This should not be considered a serious drawback, however, as the primary intent of the approximation code is to analyze notched components under conditions of fairly localized yielding.

APPENDIX G
SMALL NOTCH MODELING USING Fs

G.1   INTRODUCTION

The prediction of the fatigue life or fatigue limit loading for notched components has received considerable attention over the years. It has long been recognized that the use of the peak notch-root stress, calculated using the theoretical stress concentration factor K_t, results in overly conservative life-predictions. Even when localized plasticity at the notch root (resulting in shakedown) is taken into account, the peak stress alone is still insufficient to predict the fatigue life or limiting stress from smooth bar data. Although there are a number of contributing factors, it is generally acknowledged that the stress gradients in the vicinity of the notch play a significant role. Evidence has shown that the steeper the stress gradient, the more non-conservative the prediction using K_t. This phenomenon can be explained by recognizing that, under equivalent peak stress conditions, a steeper stress gradient results in a smaller area (volume) of material subjected to the high stress levels. Utilizing a stochastic viewpoint of the fatigue process, cracks would be less likely to initiate from a smaller highly-stressed volume of material, than in a larger (highly-stressed) volume such as found in smooth, axially loaded specimens.

A common design methodology that has been used to account for the observed behavior defines a "fatigue notch factor," K_f, where $K_f \leq K_t$. K_f is often defined in terms of a "notch sensitivity factor," q, which is dependent on the material and the notch root radius (which affects the stress gradients). As the notch radius decreases, q decreases, reflecting a greater deviation between K_t and K_f. Although this approach has been successfully applied to some common notch geometries under uniaxial loading conditions, the definition of q and K_f are ambiguous for more complex notch/component geometries or under multiaxial loading conditions.

An alternative technique for analyzing the fatigue characteristics of notched components makes use of the amount of highly stressed surface area in the vicinity of a notch [1]. The stressed-surface-area, or Fs approach, accounts for the stress gradient effect through consideration of the stress distribution on the surface of a component in the vicinity of the

notch. In applying this method, a factor is calculated that provides a correction to the peak notch root stress as determined by theoretical, numerical (e.g., FEA) or experimental techniques. The corrected notch root stress may then be used in conjunction with conventional fatigue life/strength prediction methods employed for unnotched components.

The Fs method has been successfully used to predict the fatigue life or fatigue limit loads for a variety of notched components containing mild to moderate stress gradients [1, 2]. However, one area of particular concern in the design of aircraft engines is foreign-object damage (FOD), which can result in very small, sharp notches (with severe stress gradients) on the leading edges of fan or turbine blades. To evaluate the capabilities of the Fs method in predicting allowable fatigue-limit (threshold) stress levels for components containing FOD-like notches, the method was used to estimate the threshold (long-life) stress levels for the small, sharp-notch Ti-6Al-4V specimens tested by SwRI. The details regarding the implementation of this method, and the resulting threshold stress predictions, are discussed in this appendix.

G.2   STRESSED-SURFACE-AREA (Fs) METHOD

The Fs method makes use of a geometry dependent factor (Fs_{notch}), which provides a measure of the amount of highly stressed surface area in the vicinity of a notch [1, 2]. In the general case, this factor is calculated by integrating the ratio of the maximum principle stress to the peak notch-root stress (raised to a power) over the surface area of the component. When calculated from a finite element model, the integral is replaced by a summation over the elements adjacent to a free surface on the component, resulting in the following expression

$$Fs_{notch} = \sum_{i=1}^{n} \left(\frac{\sigma_{1,i}}{\sigma_{max}} \right)^{\alpha} A_i \qquad (G1)$$

where $\sigma_{1,i}$ is the first principle stress on the free surface of element i (averaged at the nodes), A_i is the free-surface area of element i, σ_{max} is the maximum notch root stress (first principle stress), and α is a material constant obtained by correlating smooth and notched test data. Since Fs_{notch} is calculated from a ratio of stresses, it does not change appreciably with load

level provided notch root yielding is small. Thus, σ_{max} is often calculated from an elastic analysis.

The factor Fs_{notch} is then used to determine the adjusted notch root stress,

$$\sigma_{notch}^{Fs,adjusted} = \left(\frac{Fs_{notch}}{Fs_{ref}} \right)^{1/\alpha} \sigma_{notch}^{peak} \tag{G2}$$

where Fs_{ref} is the value of Fs for a baseline axial specimen and σ_{notch}^{peak} is the peak notch root stress at a particular load level. The peak stress in Eq. G2 must take into account localized yielding, and must therefore be calculated from an elastic-plastic analysis. The adjusted notch root stress can then be used in conjunction with conventional stress-life data to estimate the corresponding fatigue life or fatigue limit load for a particular notched specimen.

G.3 FINITE ELEMENT MODELING OF SMALL-NOTCH SPECIMENS

The small-notch Ti-6Al-4V specimens tested by SwRI and modeled in this analysis consisted of a double-edge notched specimen with rectangular cross-section, with gross-section dimensions of 0.235 in × 0.125 in. The notch geometry is illustrated in Fig. G1. For this analysis, notch dimensions (ρ and b) were chosen to correspond to the average measured notch dimensions of the specimens tested by SwRI. These notch dimensions correspond to the eleven configurations of notch-type 1 originally identified for testing by SwRI. The notch dimensions and associated elastic stress concentration factors (obtained from elastic FEA solutions) for the notched specimens considered in this study are shown in Table G1. Two values of K_t are included in the table for each specimen, one based on the net-section area through the notch (the traditional definition of K_t), and the other based on the gross-section area (0.235 in × 0.125 in). The net-section K_t values range from approximately 2.7 to 5.
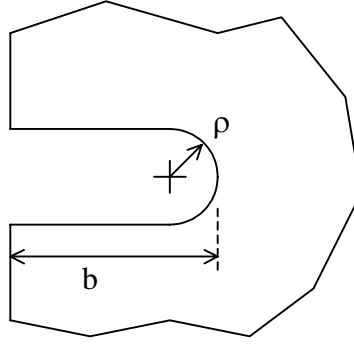
Figure G1. Small notch details.

Table G1. Small Notch Dimensions and Elastic Stress Concentration Factors

Notch ID	ρ (in)	b (in)	K_t (net section)	K_t (gross section)
1	0.0047	0.0041	2.94	3.04
2	0.0049	0.0080	3.59	3.86
3	0.0035	0.0023	2.70	2.76
4	0.0038	0.0085	4.07	4.39
5	0.0054	0.0040	2.77	2.87
6	0.0064	0.0080	3.24	3.48
7	0.0062	0.0230	4.56	5.67
8	0.0064	0.0490	4.99	8.55
9	0.0090	0.0090	2.96	3.21
10	0.0090	0.0240	3.94	4.95
11	0.0090	0.0500	4.27	7.43

For each of the notched specimens identified in Table G1, three-dimensional elastic and elastic-plastic finite element analyses were conducted using the commercial software ANSYS. All of the FE models were constructed using 8-node, three-dimensional structural solid elements with extra displacement shapes included for better accuracy. Symmetry of the specimens (on three planes) was taken advantage of to reduce the size of the FE models. A mesh refinement study was performed on each model to verify that the discretization error was sufficiently small. To facilitate the collection of the free-surface stresses required by the Fs model (Eq. G1), special 3-D Structural Surface Effect Elements (SURF154 in ANSYS) were overlaid on all the solid elements adjacent to a free surface. These additional elements did not affect the results of the analyses, but simply provided a convenient mechanism for identifying the surface stresses and surface area of each element along a free-surface of the

component. Sample FE meshes for specimens 6 and 11 (Table G1) are shown in Figures G2 and G3.
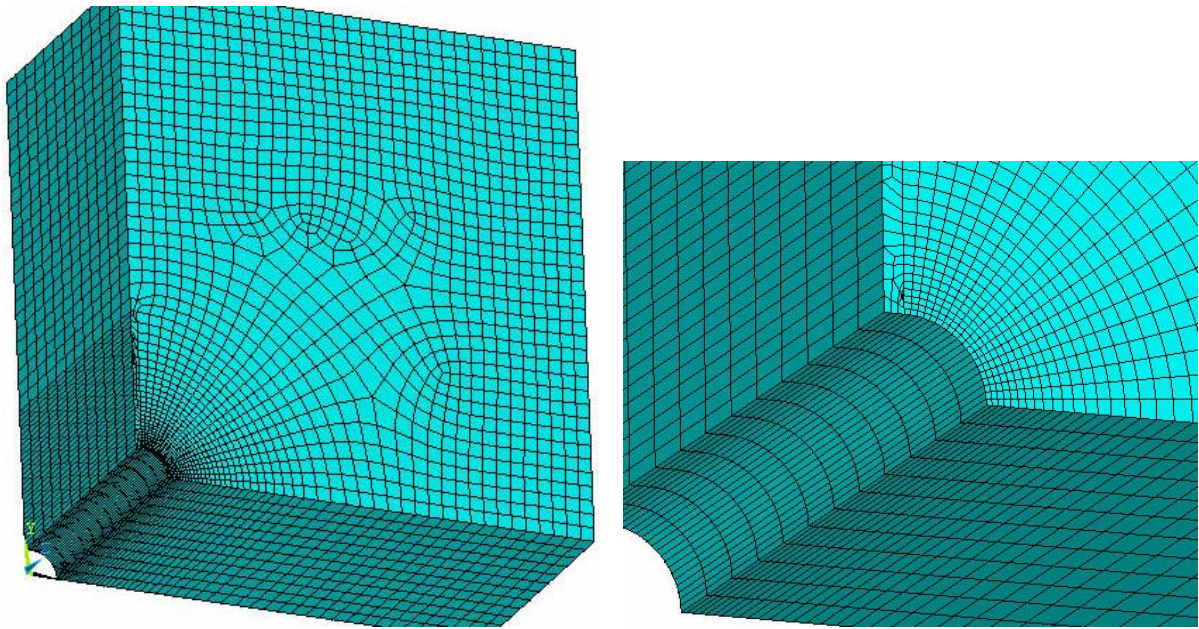
Figure G2. Finite element mesh for specimen #6.
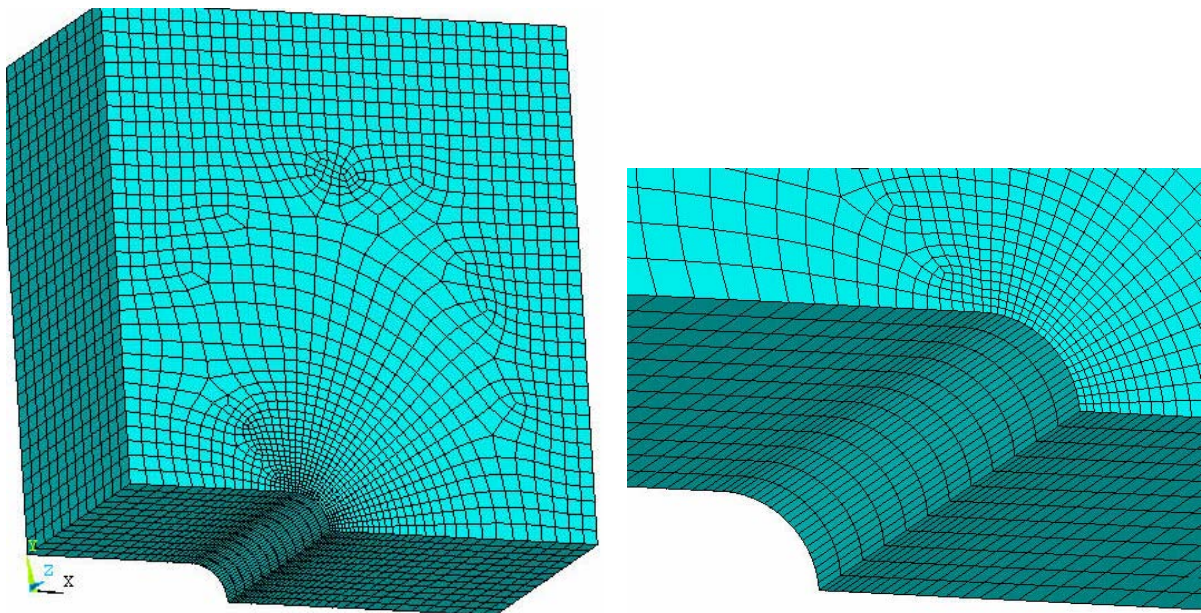
Figure G3. Finite element mesh for specimen #11.

A static, linear-elastic analysis was first performed on each specimen to determine the K_t values shown in Table G1 and to calculate the geometry factor Fs_{notch} from Eq. G1. The material properties used in this analysis were $E = 16,780$ ksi and $\nu = 0.349$. To calculate the adjusted notch root stresses from Eq. G2, a cyclic elastic-plastic analysis was required for each specimen. For these analyses, a multilinear kinematic hardening rule was used in conjunction with the cyclic stress-strain curve for Ti-6Al-4V at room temperature obtained from half-life LCF data generated in the HCF program. Applying a Ramberg-Osgood fit to the data, the cyclic stress-strain curve for Ti-6Al-4V can be expressed as

$$\varepsilon = \frac{\sigma}{E} + \left(\frac{\sigma}{K}\right)^{\frac{1}{n}} = \frac{\sigma}{16870} + \left(\frac{\sigma}{124}\right)^{\frac{1}{0.0149}} \qquad (G3)$$

where σ has units of ksi, and the cyclic yield strength was taken as $\sigma_y = 109.2$ ksi. From this equation, cyclic stress-strain values were calculated and used as input for the models. The stress-strain values are shown in Table G2. For each of the elastic-plastic analyses, 10 load cycles were run to ensure the local (notch-root) plastic strains reached a cyclically stable state. This was verified by examining the equivalent plastic strain and the largest principle plastic strain at the root of the notch at the end of each load cycle.

Table G2. Stress/Strain Values used in Ansys Elastic-Plastic Analyses

Stress (ksi)	109.22	113.0	114.0	115.5	116.3	116.8	117.2	117.6	118.3	119.7	121.0
Strain (in/in)	.006474	.008659	.01030	.01536	.02043	.02497	.02965	.03551	.04951	.1007	.2004

The purpose of this study was to determine the nominal threshold stress levels for the notched specimens corresponding to a fatigue life of 10^7 cycles at a stress ratio of $R = 0.5$. Due to the biaxial stress state occurring at the center of the notch root, the peak and adjusted notch root stresses in Eq. G2 were calculated in terms of an equivalent stress, with $\alpha = 35$ and $Fs_{ref} = 0.161$ [1]. For the cyclic loading condition, the equivalent stress was incorporated into the modified Manson-McKnight (MMM) model [2]. The MMM parameter was related to the fatigue life of Ti-6Al-4V using the following function, with $w = 0.42$:

$$0.5(\Delta\sigma_{psu})^w (\sigma_{max})^{1-w} = 3501.8 N^{-0.5164} + 36.74 N^{0.00068} \qquad (G4)$$

To determine the threshold stress levels corresponding to $N = 10^7$ cycles, an iterative study was needed. That is, an initial load level was applied, the adjusted notch-root stresses were calculated from Eqs. G1 and G2, and the fatigue life was then determined from Eq. G4. This process was repeated until a value sufficiently close to $N = 10^7$ was found.

G.4 RESULTS AND COMPARISONS TO EXPERIMENTAL DATA

The predicted threshold stress levels for the 11 notched specimens, based on the gross cross-section dimensions, are shown in Table G3. Also included in this table, where applicable, are the experimentally determined values obtained by SwRI for notches of similar dimensions. The experimental values represent the 10^7-cycle notch fatigue strength at R = 0.5 obtained using a step-test approach. Due to experimental difficulties, not all notch configurations originally planned were tested. It should also be noted that, in most cases, the measured notch dimensions deviated somewhat from the values used in this study. Thus, direct comparison between the experimental and predicted threshold stress levels must be done with caution.

Table G3. Threshold Stress Estimates for Notched Specimens using the Fs Approach

	Predicted				Experimental			
No.	ρ (in)	b (in)	σ_{max} (ksi)	$\Delta\sigma$ (ksi)	$\Delta\sigma$ (ksi)	Spec. ID	ρ (in)	b (in)
1	0.0047	0.0041	51.0	25.5				
2	0.0049	0.0080	39.6	19.8				
3	0.0035	0.0023	57.4	28.7				
4	0.0038	0.0085	35.0	17.5				
5	0.0054	0.0040	53.0	26.5				
6	0.0064	0.0080	43.2	21.6	16.3	153-39	0.0064	0.0089
7	0.0062	0.0230	26.2	13.1	11.1	153-42	0.0060	0.0236
8	0.0064	0.0490	17.5	8.75	6.0	153-43	0.0064	0.0495
					7.9	153-44	0.0064	0.0484
9	0.0090	0.0090	45.4	22.7				
10	0.0090	0.0240	29.5	14.75				
11	0.0090	0.0500	19.9	9.95				

Although limited in number, the comparisons between experimental and predicted threshold stress levels provide some useful information concerning the capabilities and

accuracy of the Fs approach. In all cases, the predicted threshold stress levels exceeded the experimental values. However, the differences between the actual and modeled notch dimensions may have contributed to the discrepancies to some degree. For example, the actual (experimental) notch depth for specimen #6 was approximately 10% greater than the modeled value, and the actual notch for specimen #7 was slightly sharper and deeper than modeled. These effects would increase the effective stress concentration factors (peak notch root stresses), thereby reducing the nominal threshold stress levels for these specimens.

The limited results presented in this study indicate that the Fs method is slightly non-conservative when applied to components containing very small, sharp notches resulting in severe stress gradients, such as may arise from foreign object damage to fan and compressor blades. However, this may possibly be corrected by modifying the material dependent parameter α used in the Fs model; i.e., the value of α used for moderate stress gradients may not be adequate for notches with steep stress gradients. Nevertheless, the predicted threshold stress levels obtained here can be considered to be reasonably close to the experimental values, indicating that the Fs method, with some modification, has the potential to account for the severe stress gradients encountered in the vicinity of small, sharp notches.

G.5   REFERENCES

1.   Slavik, D., personal communication, March 2002.

2.   Slavik, D., and Kurath, P., "Fatigue Crack Initiation Modeling in Ti-6Al-4V for Smooth and Notched Specimens under Complex Stress States," *Fifth National Turbine Engine HCF Conference*, Chandler, AZ, 2000.

APPENDIX H

AN ANALYSIS OF ELASTO-PLASTIC STRAINS AND STRESSES IN NOTCHED BODIES SUBJECTED TO NON-PROPORTIONAL LOADING

H.1   INTRODUCTION

The report contains the theoretical principles of the equivalent strain energy density method developed for the elasto-plastic stress-strain analysis of notched bodies subjected to multiaxial non-proportional loading paths and results of its experimental and numerical validation.

The first module (NEU34) developed within the project dealt with stresses and strains at the notch tip only enabling to reduce the analysis to two dimensional stress (three non-zero stress components) state because it was assumed that the surface of the notch tip contour was stress free.

The second module (NPC30) was developed for complete three dimensional stress states making it possible to analyze six non-zero stress components.

Each module was extensively validated using independent numerical data.

H.2   NOTATION

E   - modulus of elasticity

ESED   - equivalent strain energy density

e_{ij}^{a} - actual elastic-plastic strains at the notch tip

e_{ij}^{e} - hypothetical elastic strains at the notch tip

G   - shear modulus of elasticity

K'   - cyclic strength coefficient

K_F - stress concentration factor due to axial load

K_T - stress concentration factor due to torsional load

k, n   - load increment number

n'   - cyclic strain hardening exponent

δ_{ij} - Kronecker delta, $\delta_{ij} = 1$ for $i = j$ and $\delta_{ij} = 0$ for $i \neq j$

$\Delta\varepsilon_{ij}{}^p$ - plastic strain increments

$\Delta\varepsilon_{ij}{}^e$ - elastic strain increments

$\Delta\varepsilon_{ij}{}^a$ - actual elastic-plastic strain increments

$\Delta\varepsilon_{eq}{}^{pa}$ - equivalent plastic strain increment

$\Delta\sigma_{ij}{}^e$ - pseudo-elastic stress components

$\Delta\sigma_{ij}{}^a$ - actual stress components

$\Delta\sigma_{eq}{}^a$ - actual equivalent stress increment

$S_{ij}{}^e$ - deviatoric stresses of the elastic input

$S_{ij}{}^a$ - actual deviatoric stresses

$\varepsilon_{eq}{}^{pa}$ - actual equivalent plastic strain

$\varepsilon_{ij}{}^a$ - actual elasto-plastic notch-tip strains

$\varepsilon_{ij}{}^e$ - elastic notch tip strain components

ε_n - nominal strain

ν - Poisson's ratio

$\sigma_{eq}{}^a$ - actual equivalent stress at the notch tip

$\sigma_{ij}{}^a$ - actual stress tensor components in the notch tip

$\sigma_{ij}{}^e$ - notch tip stress tensor components of the elastic input

σ_o - parameter of the material stress-strain curve

P - axial load

T - torque

R - radius of the cylindrical specimen

H.3 THEORETICAL BASIS FOR THE TWO-DIMENSIONAL (2-D) ELASTO-PLASTIC NOTCH TIP MODEL

Notches and other geometrical irregularities cause significant stress concentration. Such an increase of stresses results often in localized plastic deformation, leading to premature initiation of fatigue cracks. Therefore, the fatigue strength and durability estimations of notched components require detail knowledge of stresses and strains in such regions. The stress state in the notch tip region is in most cases multiaxial in nature. Axles and shafts may experience, for example, combined out of phase torsion and bending loads.

Although modern Finite Element commercial software packages make it possible to determine notch tip stresses in elastic and elastic plastic bodies with a high accuracy for short loading histories such methods are still impractical in the case of long loading histories experienced by machines in service. A representative cyclic loading history may contain from a few thousands to a few millions of cycles. Therefore incremental elastic-plastic finite element analysis of such a history would require prohibitively long computing time. For this reason more efficient methods of elastic-plastic stress analysis are necessary in the case of fatigue life estimations of notched bodies subjected to lengthy cyclic stress histories. One such a method, suitable for calculating multiaxial elastic-plastic stresses and strains in notched bodies subjected to proportional and non-proportional loading histories, is proposed below.

H.3.1   Loading Histories

The notch tip stresses and strains are dependent on the notch geometry, material properties and the loading history applied to the body. If all components of a stress tensor change proportionally, the loading is called *proportional.* When the applied load causes the directions of the principal stresses and the ratio of the principal stress magnitudes to change after each load increment, the loading is termed *non-proportional.* If plastic yielding takes place at the notch tip then almost always the stress path in the notch tip region is non-proportional regardless whether the remote loading is proportional or not. The non-proportional loading/stress paths are usually defined by successive increments of load/stress parameters and all calculations have to be carried out incrementally. In addition the material stress-strain response to non-proportional cyclic loading paths has to be simulated, including the material memory effects.

H.3.2   The Stress State at the Notch Tip

For the case of general multiaxial loading applied to a notched body, the state of stress near the notch tip is tri-axial. However, the stress state at the notch tip is bi-axial because of the notch-tip stress free surface (Figure H1). Since equilibrium of the infinitesimal element at the notch tip must be maintained, i.e. $\sigma_{23} = \sigma_{32}$ and $\varepsilon_{23} = \varepsilon_{32}$, there are three non-zero stress components and four non-zero strain components. Therefore there are seven

unknowns all together and a set of seven independent equations is required for the determination of all stress and strain components at the notch tip.

$$\sigma_{ij}^a = \begin{bmatrix} 0 & 0 & 0 \\ 0 & \sigma_{22}^a & \sigma_{23}^a \\ 0 & \sigma_{32}^a & \sigma_{33}^a \end{bmatrix} \quad and \quad \varepsilon_{ij}^a = \begin{bmatrix} \varepsilon_{11}^a & 0 & 0 \\ 0 & \varepsilon_{22}^a & \varepsilon_{23}^a \\ 0 & \varepsilon_{32}^a & \varepsilon_{33}^a \end{bmatrix} \quad\quad \text{(H1)}$$

The material constitutive relationships provide four equations, leaving three additional equations to be established.
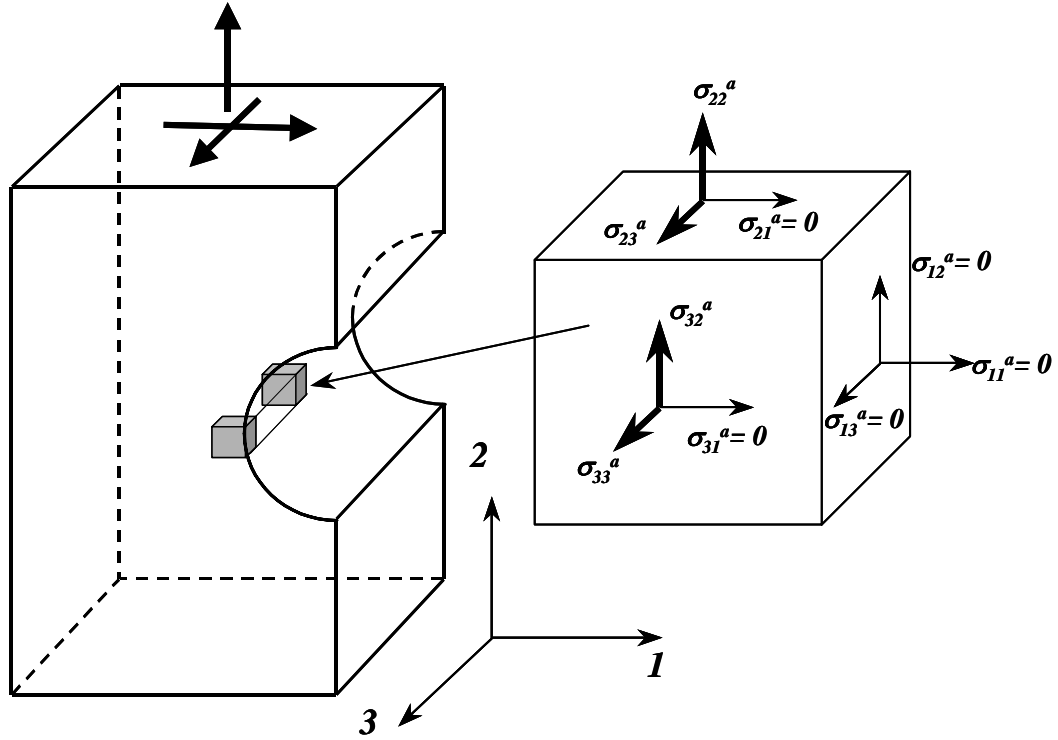
Figure H1. Stress state at a notch tip (notation).

H.3.3   Material Constitutive Model

In the case of proportional or nearly proportional notch tip stress path the Hencky total deformation equations of plasticity can be used in the analysis.

$$\varepsilon_{ij}^a = \frac{1+\nu}{E}\sigma_{ij}^a - \frac{\nu}{E}\sigma_{kk}^a \delta_{ij} + \frac{3}{2}\frac{\varepsilon_{eq}^{pa}}{\sigma_{eq}^a}S_{ij}^a \quad\quad \text{(H2)}$$

where: $S_{ij}^{a} = \sigma_{ij}^{a} - \dfrac{1}{3}\sigma_{kk}^{a}\delta_{ij}$

The most frequently used model of incremental plasticity is the Prandtl-Reuss flow rule. For an isotropic body, the Prandtl-Reuss strain-stress relationships can be expressed as:

$$\Delta\varepsilon_{ij}^{a} = \frac{1+\nu}{E}\Delta\sigma_{ij}^{a} - \frac{\nu}{E}\Delta\sigma_{kk}^{a}\,\delta_{ij} + \frac{3}{2}\frac{\Delta\varepsilon_{eq}^{pa}}{\sigma_{eq}^{a}}S_{ij}^{a} \qquad (H3)$$

The multiaxial incremental stress-strain relation (H3) is obtained from the uniaxial stress-strain curve by relating the equivalent plastic strain increment to the equivalent stress increment such that:

$$\Delta\varepsilon_{eq}^{pa} = \frac{d\,f(\sigma_{eq}^{a})}{d\,\sigma_{eq}^{a}}\Delta\sigma_{eq}^{a}. \qquad (H4)$$

The function, $\varepsilon_{eq}^{P} = f(\sigma_{eq})$, is identical to the plastic strain – stress relationship obtained experimentally from uni-axial tension test.

H.3.4   The Load-Notch Tip Stress-Strain Relationships

The load or the load parameter, in the case of notched bodies, is usually represented by the nominal or reference stress being proportional to the remote applied load. In the case of notched bodies in plane stress or plane strain state the relationship between the load and the elastic-plastic notch tip strains and stresses in the localized plastic zone is often approximated by the Neuber rule [1] or the Equivalent Strain Energy Density (ESED) equation [2]. It was shown [3, 4] that both methods can also be extended for multiaxial proportional and non-proportional modes of loading. Similar approaches were proposed by Hoffman and Seeger [5] and Barkey et al. [6]. All methods consist of two parts namely the constitutive equations and the relationships linking the fictitious linear elastic stress-strain state $(\sigma_{ij}^{e},\varepsilon_{ij}^{e})$ at the notch tip with the actual elastic-plastic stress-strain response $(\sigma_{ij}^{a},\varepsilon_{ij}^{a})$ as shown in Figure H2.
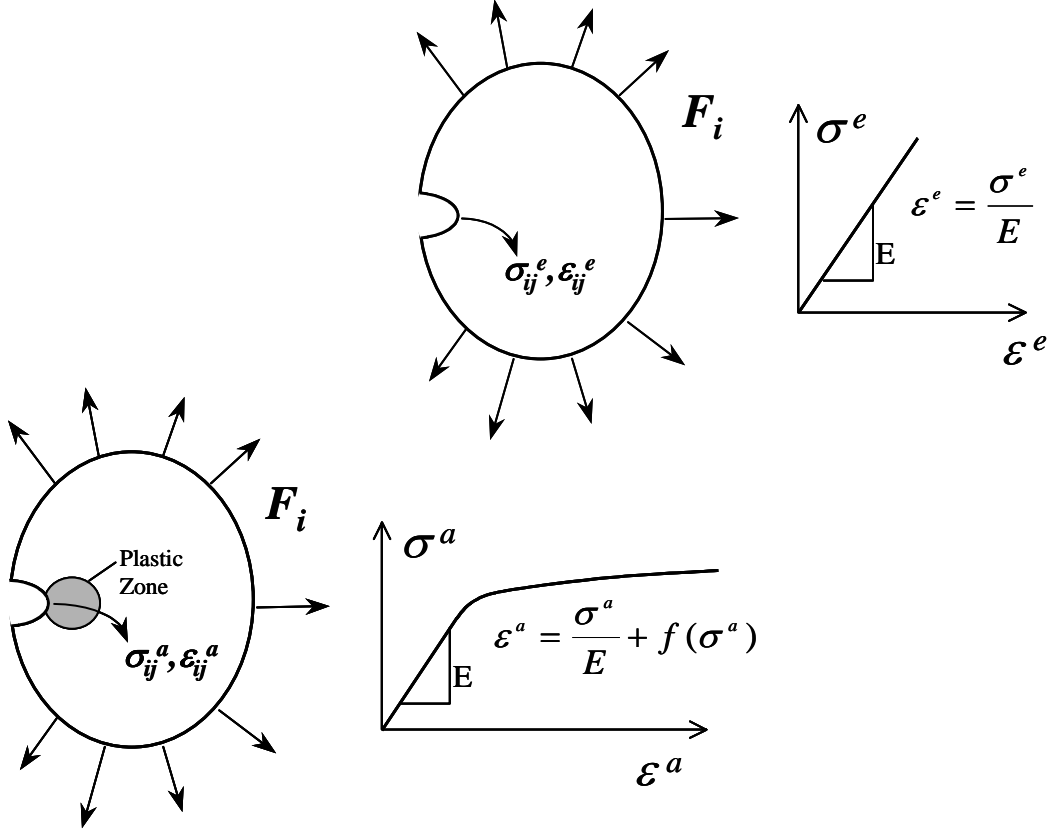
Figure H2. Stress states in geometrically identical elastic and elastic-plastic bodies subjected to identical boundary conditions.

For proportional loading the Neuber rule [2,3], where the Hencky stress-strain relationships are applicable, can be written for the uni-axial and multiaxial stress state in the form of equations (H5a) and (H5b) respectively.

$$\sigma_{22}^{e}\varepsilon_{22}^{e} = \sigma_{22}^{a}\varepsilon_{22}^{a} \tag{H5a}$$

$$\sigma_{ij}^{e}\varepsilon_{ij}^{e} = \sigma_{ij}^{a}\varepsilon_{ij}^{a} \tag{H5b}$$

The Neuber rule (H5a) represents the equality of the total strain energy (the strain energy & the complimentary strain energy density) at the notch tip, represented by the rectangles A and B in Figure H3a.

The ESED method (H6a) is based on the equivalence of the strain energy density, which can be interpreted as the equality between the strain energy density at the notch tip of

a linear elastic body (Figure H2) and the notch tip strain energy density of a geometrically identical elastic-plastic body subjected to the same load.

$$\int_0^{\varepsilon_{22}^e} \sigma_{22}^e d\varepsilon_{22}^e = \int_0^{\varepsilon_{22}^a} \sigma_{22}^a d\varepsilon_{22}^a \tag{H6a}$$

This relationship is shown graphically in Figure H3b, and represents the equality of the area under the linear-elastic curve and the area under the actual elastic-plastic σ_{22}^a-ε_{22}^a material curve.
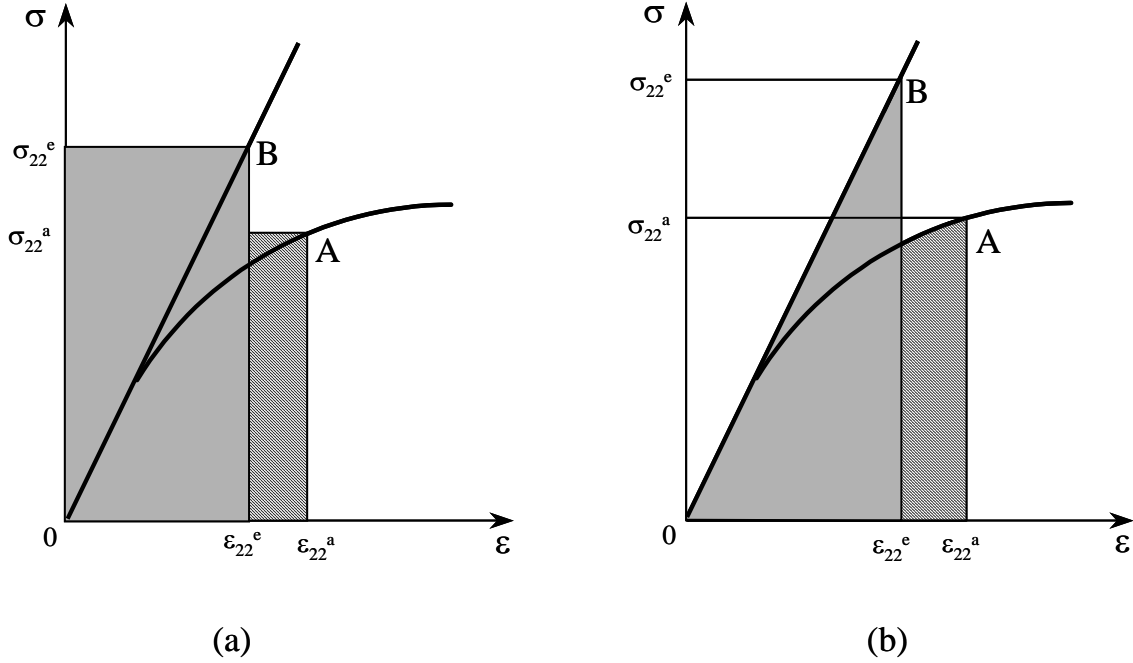
Figure H3. Graphical interpretation of (a) Neuber's rule, and (b) the equivalent strain energy density (ESED) method.

In the case of multiaxially stressed notches the strain energy density equations can be written as:

$$\int_0^{\varepsilon_{ij}^e} \sigma_{ij}^e d\varepsilon_{ij}^e = \int_0^{\varepsilon_{ij}^a} \sigma_{ij}^a d\varepsilon_{ij}^a \tag{H6b}$$

The overall strain energy density equivalence, equation (H5b) or (H6b), relating the pseudo-elastic and the actual elastic-plastic notch tip strains and stresses at the notch tip has been generally accepted as a good approximation rule but the additional conditions, necessary for the complete formulation of a multiaxial stress state problem, are being the subject of controversy. Hoffman and Seeger [5] assumed that the ratio of the actual principal strains at the notch tip is to be equal to the ratio of the fictitious elastic principal strain components while Barkey et al. [6] suggested to use the ratio of principal stresses. The data presented by Moftakhar [7] found that the accuracy of the stress or strain ratio based analysis depended on the degree of constraint at the notch tip. Therefore, Moftakhar and co-workers proposed [7] to use the ratios of strain energy density contributed by each pair of corresponding stress and strain components. It was confirmed later by Singh et.al. [4] that the accuracy of the additional energy equations was also good when used in an incremental form. Because the ratios of strain energy density increments seem to be less dependent on the geometry and constraint conditions at the notch tip than the ratios of stresses or strains the analyst is not forced to make any arbitrary decisions about the constraint while using these equations. However, the additional strain energy density equations [4, 7] have a theoretical drawback indicated by Chu [8], namely the estimated elastic-plastic notch tip strains and stresses may depend on the selected system of coordinates. Fortunately, the dependence is not very strong and with suitably chosen system of axis it could be sufficiently accurate for a variety of engineering applications. It was also found that the set of seven equations involving the strain, stress and the strain energy density increments can be singular at some specific ratios of stress components, which is due to the conflict between the plasticity model (normality rule) and strain energy density equations. Such a conflict can be avoided if the principal idea of Neuber is implemented in the incremental form. Namely, it should be noted that the original Neuber rule (H5a) was derived for bodies in pure shear stress state. It means that the Neuber equation states the equivalence of only distortional strain energies. Therefore, in order to formulate the set of necessary equations for a multiaxial non-proportional analysis of elastic-plastic stresses and strains at the notch tip, the equality of increments of the total *distortional strain energy density* should be used. Thus all equations should be written in terms of deviatoric stresses and strains.

H.3.5 Deviatoric Stress-Strain Relationships

The notch tip deviatoric stresses of the hypothetical linear-elastic input are determined as:

$$S_{ij}^e = \sigma_{ij}^e - \frac{1}{3}\sigma_{kk}^e \delta_{ij} \tag{H7}$$

The elastic deviatoric strains and strain increments can be calculated from the Hooke law.

$$\Delta e_{ij}^e = \frac{\Delta S_{ij}^e}{2G} \tag{H8}$$

The actual deviatoric stress components in the notch tip can analogously be defined as:

$$S_{ij}^a = \sigma_{ij}^a - \frac{1}{3}\sigma_{kk}^a \delta_{ij} \tag{H9}$$

The incremental deviatoric stress-strain relations based on the associated Prandtl-Reuss flow rule can be subsequently written as:

$$\Delta e_{ij}^a = \frac{\Delta S_{ij}^a}{2G} + S_{ij}^a d\lambda. \tag{H10}$$

where:

$$d\lambda = \frac{3}{2}\frac{\Delta \varepsilon_{eq}^{pa}}{\sigma_{eq}^a}; \qquad \left(\sigma_{eq}^a\right)^2 = \frac{3}{2}S_{ij}^a S_{ij}^a;$$

$$\Delta \varepsilon_{eq}^{pa} = \frac{df\left(\sigma_{eq}^a\right)}{d\sigma_{eq}^E}\Delta \sigma_{eq}^a;$$

The form and specific parameters of the stress-strain function, $\varepsilon_{eq}^P = f(\sigma_{eq})$, must be obtained experimentally from an uniaxial cyclic test.

H.3.6 Equivalence of Increments of the Total Distortional Strain Energy Density

It is proposed, analogously to the original Neuber rule, to use the equivalence of increments of the total distortional strain energy density contributed by each pair of associated stress and strain components, i.e.,

$$S^e_{22}\Delta e^e_{22} + e^e_{22}\Delta S^e_{22} = S^a_{22}\Delta e^a_{22} + e^a_{22}\Delta S^a_{22}$$
$$S^e_{33}\Delta e^e_{33} + e^e_{33}\Delta S^e_{33} = S^a_{33}\Delta e^a_{33} + e^a_{33}\Delta S^a_{33} \quad . \tag{H11}$$
$$S^e_{23}\Delta e^e_{23} + e^e_{23}\Delta S^e_{23} = S^a_{23}\Delta e^a_{23} + e^a_{23}\Delta S^a_{23}$$

The equalities of strain energy increments for each set of corresponding hypothetical elastic and actual elastic-plastic strains and stress increments at the notch tip can be shown graphically (Figure H4) as the equality of surface areas of the two pairs of rectangular elements representing the increments of strain energy density. The area of dotted rectangles represents the total strain energy increment of the hypothetical elastic notch tip input stress while the area of the hatched rectangles represents the total strain energy density of the actual elastic-plastic material response at the notch tip.

Figure H4. Graphical representation of the incremental Neuber rule.

Equations (H10) and (H11) form a set of seven simultaneous equations from which all deviatoric strain and stress increments can be determined, based on the linear hypothetical elastic notch tip stress path data, i.e. increments $\Delta\sigma_{ij}^e$, obtained from the linear-elastic analysis and the constitutive stress-strain curve (H3).

$$
\left\{
\begin{aligned}
\Delta e_{11}^a &= \frac{\Delta S_{11}^a}{2G} + \frac{3}{2}\frac{\Delta\varepsilon_{eq}^a}{\sigma_{eq}^a} S_{11}^a \\[2ex]
\Delta e_{22}^a &= \frac{\Delta S_{22}^a}{2G} + \frac{3}{2}\frac{\Delta\varepsilon_{eq}^a}{\sigma_{eq}^a} S_{22}^a \\[2ex]
\Delta e_{33}^a &= \frac{\Delta S_{33}^a}{2G} + \frac{3}{2}\frac{\Delta\varepsilon_{eq}^a}{\sigma_{eq}^a} S_{33}^a \\[2ex]
\Delta e_{23}^a &= \frac{\Delta S_{23}^a}{2G} + \frac{3}{2}\frac{\Delta\varepsilon_{eq}^a}{\sigma_{eq}^a} S_{23}^a \\[3ex]
S_{22}^e \Delta e_{22}^e &+ e_{22}^e \Delta S_{22}^e = S_{22}^a \Delta e_{22}^a + e_{22}^a \Delta S_{22}^a \\
S_{33}^e \Delta e_{33}^e &+ e_{33}^e \Delta S_{33}^e = S_{33}^a \Delta e_{33}^a + e_{33}^a \Delta S_{33}^a \\
S_{23}^e \Delta e_{23}^e &+ e_{23}^e \Delta S_{23}^e = S_{23}^a \Delta e_{23}^a + e_{23}^a \Delta S_{23}^a
\end{aligned}
\right.
\tag{H12}
$$

For each increment of the external load, represented by the increments of pseudo-elastic deviatoric stresses, ΔS_{ij}^e, the deviatoric elastic-plastic notch tip strain and stress increments, Δe_{ij}^a and ΔS_{ij}^a, are computed from the equation set (H12). With the help of equation (H9) the calculated deviatoric stress increments, ΔS_{ij}^a, can subsequently be converted into the actual stress increments, $\Delta\sigma_{ij}^a$,

$$
\begin{aligned}
\Delta S_{22}^a &= \Delta\sigma_{22}^a - \frac{1}{3}\left(\Delta\sigma_{22}^a + \Delta\sigma_{33}^a\right) \\[2ex]
\Delta S_{33}^a &= \Delta\sigma_{33}^a - \frac{1}{3}\left(\Delta\sigma_{22}^a + \Delta\sigma_{33}^a\right) \\[2ex]
\Delta S_{23}^a &= \Delta\sigma_{23}^a
\end{aligned}
\tag{H13}
$$

The deviatoric and the actual stress components S_{ij}^a and σ_{ij}^a at the end of given load increment are determined from equations (H14-H15).

$$S_{ij}^{an} = S_{ij}^{ao} + \sum_{k=1}^{n-1} \Delta S_{ij}^{ak} + \Delta S_{ij}^{an} , \qquad (H14)$$

$$\sigma_{ij}^{an} = \sigma_{ij}^{ao} + \sum_{k=1}^{n-1} \Delta\sigma_{ij}^{ak} + \Delta\sigma_{ij}^{an} \qquad (H15)$$

where: n denotes the load increment number.

The actual strain increments, $\Delta\varepsilon_{ij}{}^a$, can finally be determined from the constitutive equation (H3).

H.3.7   Cyclic Plasticity Model

In order to predict the notch tip stress-strain response of a notched component subjected to multiaxial cyclic loading, the incremental equations discussed above have to be linked with the cyclic plasticity model. Several plasticity models are available in the literature. The most popular is the model [9] proposed by Mroz. According to Mroz [9] the uniaxial stress-strain material curve can be represented in a multiaxial stress space by a set of work-hardening surfaces.

$$\sigma_{eq,i}^a = \sqrt{\frac{3}{2} S_{ij}^a S_{ij}^a} \qquad (H16)$$

In the case of a two-dimensional stress state, such as that one at a notch tip, the work-hardening surfaces can be represented by ellipses on the coordinate plane for which the axes are defined by the directions principal stress components (Figure H5). The equation of each work-hardening ellipse in the principal stress space is:

$$\sigma_{eq}^a = \sqrt{\left(\sigma_2^a\right)^2 - \sigma_2^a\sigma_3^a + \left(\sigma_2^a\right)^2} \qquad (H17)$$

The essential elements of the plasticity model can be presented in such a case graphically in a two-dimensional stress space.
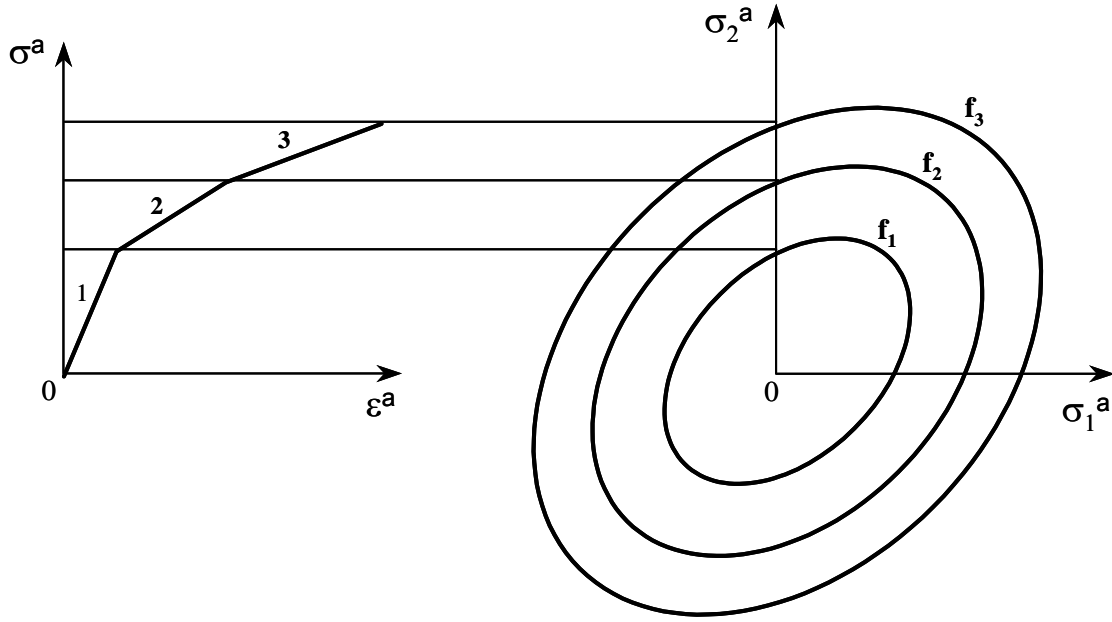
Figure H5. Piecewise linearization of the material $\sigma-\varepsilon$ curve and the corresponding work hardening surfaces.

The load path dependency effects are modeled by prescribing a translation rule for the translation of ellipses in the σ_1^a-σ_2^a plane. The translation of these ellipses is assumed to be caused by the sought stress increment, which can be represented in the principal stress space as a vector. The ellipses can be translated with respect to each other over distances dependent on magnitude of the stress/load increment. The ellipses move within the boundaries of each other, but they do not intersect. If an ellipse comes in contact with another, they move together as one rigid body.

However, it has been found that the ellipses in the original Mroz model may sometimes intersect each other, which is not permitted. Therefore, Garud proposed [10] an improved translation rule that prevents any intersections of plasticity surfaces. The principle idea of the Garud translation rule is illustrated in Figure H6.

a.)   The line of action of the stress increment, $\Delta\sigma^a$, is extended to intersect the next larger non-active surface, f_2, at point B_2.

b.)   Point B_2 is connected to the center, O_2, of the surface f_2.

c.) A line is extended through the center of the smaller active surface , O_1, parallel to the line O_2B_2 to find point B_1 on surface f_1.\

d.) The conjugate points B_1 and B_2 are connected by the line B_1B_2.

e.) Surface f_1 is translated from point O_1 to point O_1' such that vector O_1O_1' is parallel to line B_1B_2. The translation is complete when the end of the vector defined by the stress increment, $\Delta\sigma$, lies on the translated surface f_1'.
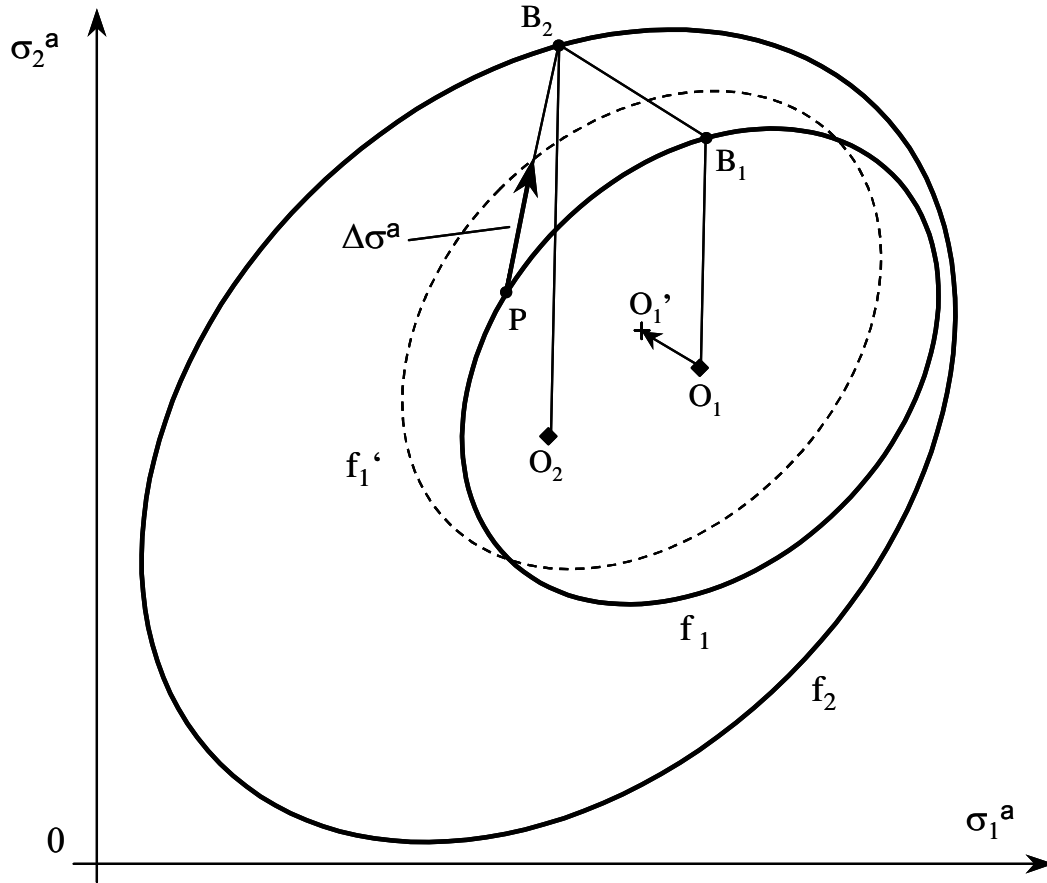
Figure H6. Geometrical illustration of the translation rule in the Garud incremental plasticity model.

The mathematics reflecting these operations can be found in the original paper of Mroz [9] or Garud [10] or in any recent textbook on the theory of plasticity. The Mroz and Garud models are relatively simple but they are not very efficient numerically, especially in the case of long load histories with a large number of small increments. If the computation

time is of some concern the model based on infinite number of plasticity surfaces proposed by Chu [11] can be used in lengthy fatigue analyses.

The cyclic plasticity models enable the, $\Delta\varepsilon_{eq}{}^p$-$\Delta\sigma_{eq}{}^a$, relationship to be established providing the actual plastic modulus for given stress/load increment, $\Delta\sigma_i$. In other words the plasticity model determines which piece of the stress-strain curve (Figure H5) has to be utilized during given stress/load increment. Two or more tangent ellipses translate together as rigid bodies and the largest moving ellipse indicates which linear piece of the constitutive relationship should be used for a given stress increment. The slope of the actual element of the stress-strain curve defines the plastic modulus, $\Delta\sigma_{eq}$ /$\Delta\varepsilon_{eq}{}^p$, necessary for the determination of parameter, $d\lambda$, in the constitutive equation (H10). The plasticity models are described in most publications, as algorithms for calculating strain increments that result from given series of stress increments or vice versa. This is called as the stress or strain controlled input. In the case of the notch analysis neither stresses nor strains are directly inputted into the plasticity model. The input is given in the form of the total deviatoric strain energy density increments and both the deviatoric strain and stress increments are to be found simultaneously by solving the equation set (H12). Therefore, the plasticity model is needed only to indicate which work-hardening surface is going to be active during the current load increment, which subsequently determines the instantaneous value of the parameter $d\lambda$. In order to find the elastic-plastic deviatoric stress and strain increment $\Delta\sigma_{ij}{}^a$ and $\Delta e_{ij}{}^a$ from the equation set (H12) the value of parameter $d\lambda$ is determined first based on the current configuration of plasticity surfaces. After calculating the stress increments, $\Delta\sigma_{ij}{}^a$, and the resultant stress increment, $\Delta\sigma^a$, the plasticity surfaces are translated as shown in Figure H6. The process is repeated for each subsequent increment of the "elastic" input, $\Delta\sigma_{ij}{}^e$.

The Mroz and Garud models were chosen here as an illustration. Obviously, any other plasticity model can be associated with the incremental stress-strain notch analysis proposed above.

H.4   VALIDATION OF THE TWO-DIMENSIONAL (2 – D) MODEL

The first set of data was obtained for multiaxial non-proportional monotonic load (no unloading) in order to check whether the method and code are qualitatively and

quantitatively correct. For that purpose several Finite Element analyses have been carried out involving various material models and load paths.

The second set of data was obtained for non-proportional cyclic loading paths and the calculated results were compared with experimentally measured elastic-plastic strains at the notch tip.

H.4.1 Comparison of Calculated Elastic-Plastic Notch Tip Strains and Stresses with Finite Element Data Obtained under Non-proportional Monotonically Increasing Load

In the case of monotonic (no unloading) non-proportional stress path the qualitative correctness and accuracy of the method was demonstrated by comparing the calculated notch tip stress-strain histories to those obtained from the finite element method. The elastic-plastic finite element stress results of reference [4] were obtained using the ABAQUS finite element package. The isotropic strain-hardening plasticity model was used for calculations. The geometry of the notched element was that of the circumferentially notched bar shown in Figure H7.
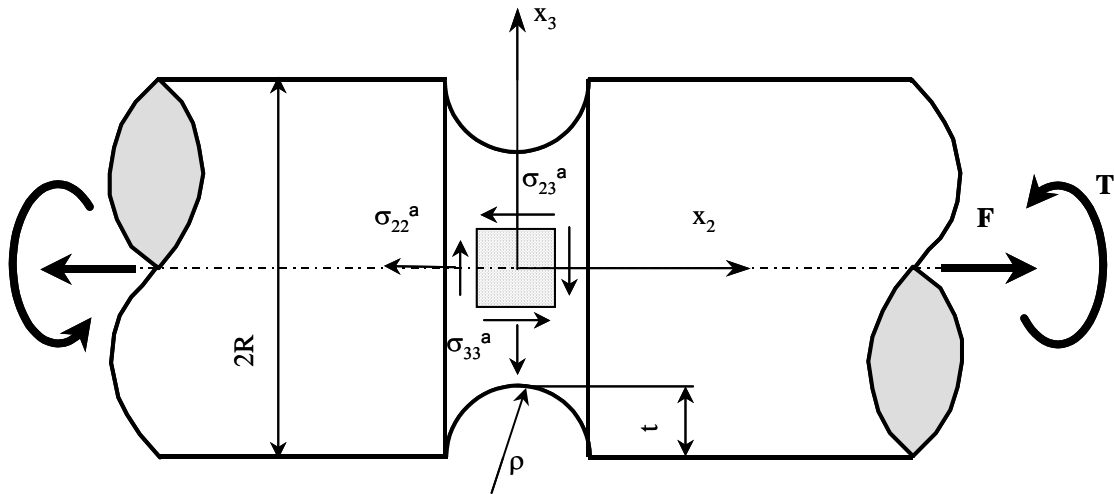
Figure H7. Geometry and dimensions of the notched bar tested under non-proportional tension and torsion loading.

The basic proportions of the cylindrical component were $\rho/t = 0.3$ and $R/t = 7$ resulting in the torsional and tensile stress concentration factor $K_T = 3.31$ and $K_F = 1.94$

respectively. The ratio of the notch tip hoop to axial stress under tensile loading was σ_{33}^{e} /σ_{22}^{e} = 0.284. The stress concentration factors for the axial and torsion loads were defined as:

$$K_F = \frac{\sigma_{22}^{e}}{\sigma_{nF}} \quad and \quad K_T = \frac{\sigma_{32}^{e}}{\tau_{nF}} \tag{H18}$$

While the nominal stresses in the net cross section were determined as:

$$\sigma_n = \frac{F}{\pi(R-t)^2} \quad and \quad \tau_n = \frac{2T}{\pi(R-t)^3} \tag{H19}$$

The loads applied to the bar were monotonically increasing torsion in the first phase and then increasing tension in the second phase with the torsion load being kept constant as shown in Figure H8.
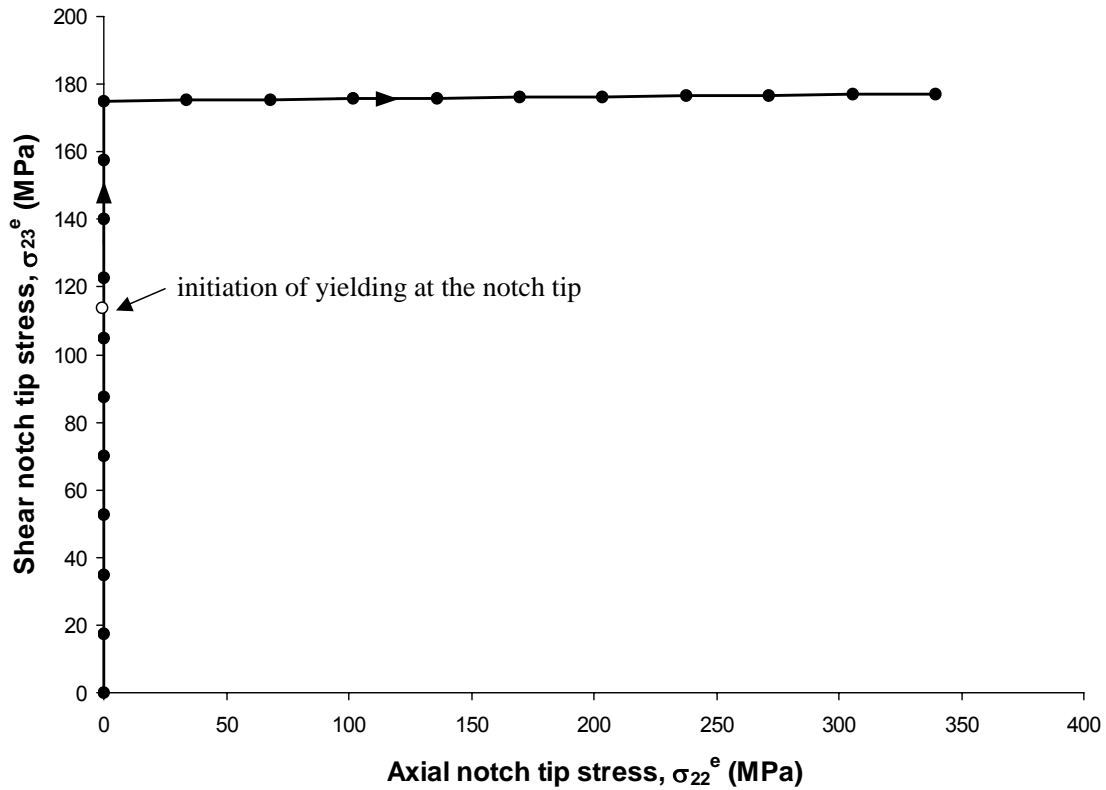
Figure H8. The input stress path increments of the monotonic non-proportional stress-time history.

The torque T induced the 'linear elastic' shear stress σ_{23}^{e} at the notch tip and the axial load F induced the normal stress components σ_{22}^{e} and σ_{33}^{e}. The increments of the

hypothetical 'elastic" stress components σ_{23}^e, σ_{22}^e and σ_{33}^e and associated strains were used as the input data. The pseudo elastic equivalent stress of the input at the notch tip was increasing throughout the entire loading process to ensure monotonic loading path. The material for the notched bar was SAE 1045 steel with a cyclic stress-strain curve approximated by the Ramberg- Osgood relation. The material properties were: E = 202 GPa, ν = 0.3, S_Y = 202 MPa, n=0.208, and K = 1258 MPa..

$$\varepsilon = \frac{\sigma}{E} + \left(\frac{\sigma}{K}\right)^{\frac{1}{n}} \tag{H20}$$

The maximum applied load levels were chosen to be 50% higher than it would be required to induce yielding at the notch tip if each load was applied separately.

The calculated and the FEM determined strain components, ε_{22}^a and ε_{23}^a, and the stress components, σ_{22}^a and σ_{23}^a, are shown in Figures H9 - H10.
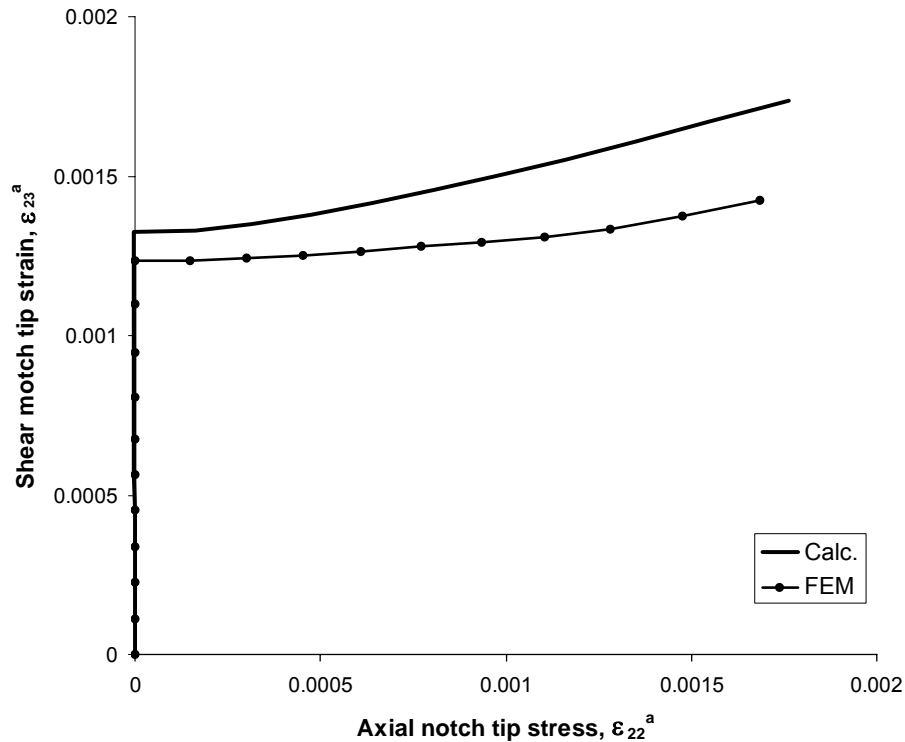
Figure H9.   Comparison of the calculated and FEM determined strain paths for the monotonic non-proportional torsion-tension input stress history.

Note, that the calculated stresses and strains and the results of the finite element analysis are identical in the elastic range. This is expected since the model converges to the elastic solution in the elastic range. Just beyond the onset of yielding at the notch tip, the strain results that were predicted using the proposed model and the finite element data begin gradually to diverge. It can be concluded that the method based on the equivalence of the total strain energy increments overestimates the actual notch tip strains but the predicted strains are reasonably close to the numerical FEM data.
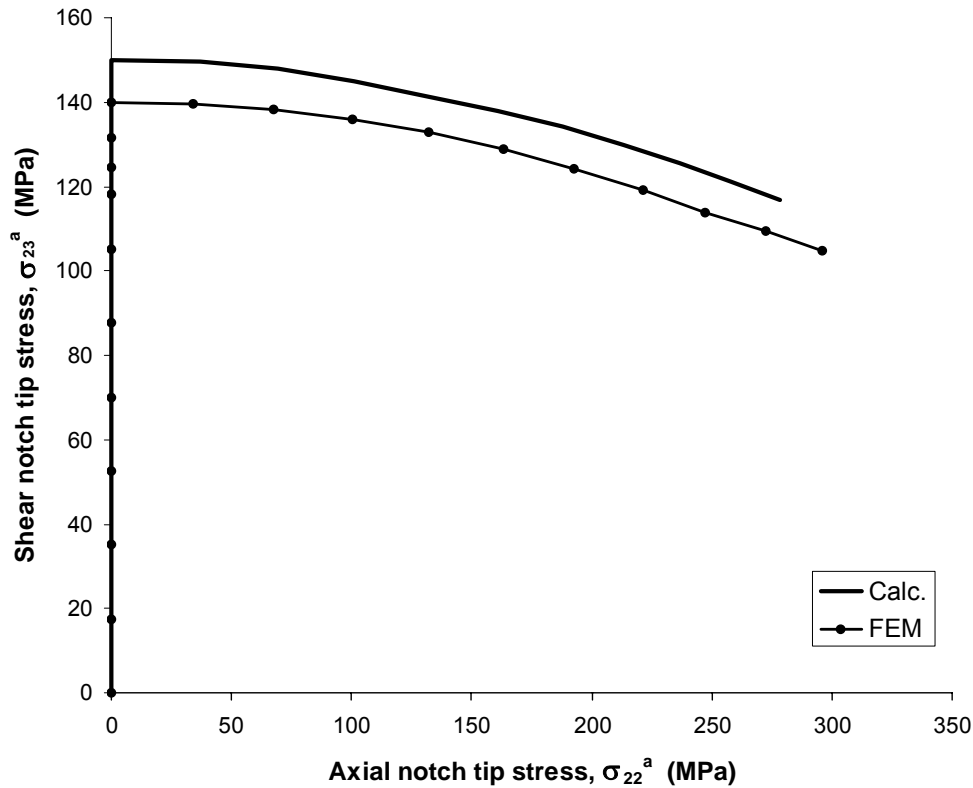
Figure H10. Comparison of the calculated and FEM determined stress paths for the monotonic non-proportional torsion-tension input stress history.

H.4.2 Comparison of Calculated Elastic-Plastic Notch Tip Strains with Experimentally Measured Elastic-Plastic Strains at the Notch Tip Induced by Cyclic Non-proportional Stress Paths

The experimental data concerning measured notch tip strains induced by non-proportional cyclic loading histories were obtained by Barkey [12] who used a cylindrical bar with a circumferential notch similar to that one shown in Figure H7. The basic proportions of

the cylindrical specimen were $\rho/t = 1$ and $R/t = 2$ resulting in the tensile and torsion stress concentration factor $K_F = 1.41$ and $K_T = 1.15$ respectively. The ratio of the notch tip hoop stress to the axial stress under tensile axial loading was $\sigma_{33}^e / \sigma_{22}^e = 0.184$. The actual radius of the cylindrical specimen was R=25.4 mm.

The material for the notched bar was SAE 1070 steel with a cyclic stress-strain curve approximated by the Ramberg- Osgood relation (H18). The material properties were: E = 210 GPa, $\nu = 0.3$, $S_Y = 242$ MPa, n'=0.199, and K' = 1736 MPa..

The first box-type cyclic stress path of the pseudo-elastic notch tip stresses, σ_{22}^e - σ_{23}^e, is shown in Figure (H11).

Rectangular Stress Path
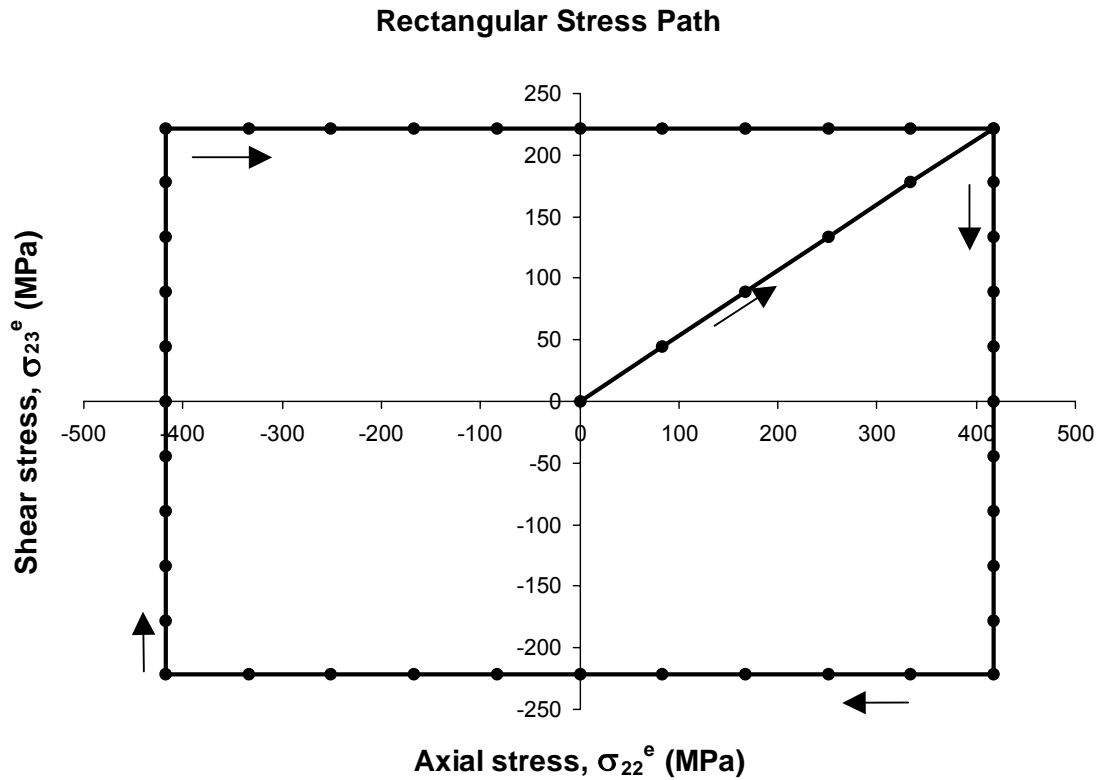
Figure H11. Non-proportional "box" type cyclic stress/load history (path).

The rectangular box path was repeated counter-clockwise more than hundred times while recording the strains in the notch tip. The notch tip stress components were measured using electric resistance strain gauges mounted at the notch tip. The maximum nominal

tensile stress and the nominal torsion stresses were $\sigma_n = 296$ MPa and $\tau_n = 193$ MPa respectively. The corresponding notch tip pseudo-elastic input stresses were $\sigma_{22}^e = 417.3$ MPa and $\sigma_{23}^e = 221.9$ MPa respectively. Comparison of the measured and calculated notch tip strain paths are shown in Figure (H12). The pseudo-elastic input strain path has been also included as a reference. It can be noted that the agreement between the calculated and measured strain paths is qualitatively and quantitatively good. The experimental solid lines represent notch tip strains measured during the 1st and the 50th loading cycle. The remaining experimental data is not shown in order to preserve the clarity of the diagram. The measured strain path is not symmetric with respect to the center of coordinates and the yielding during the first make up cycle, which is always slightly different from the subsequent cyclically stabilized material response, might cause this shift. This might be the reason of the offset of one part of the measured strain path with respect to the calculated symmetric strain path, which was obtained from the stabilized cyclic stress-strain curve.
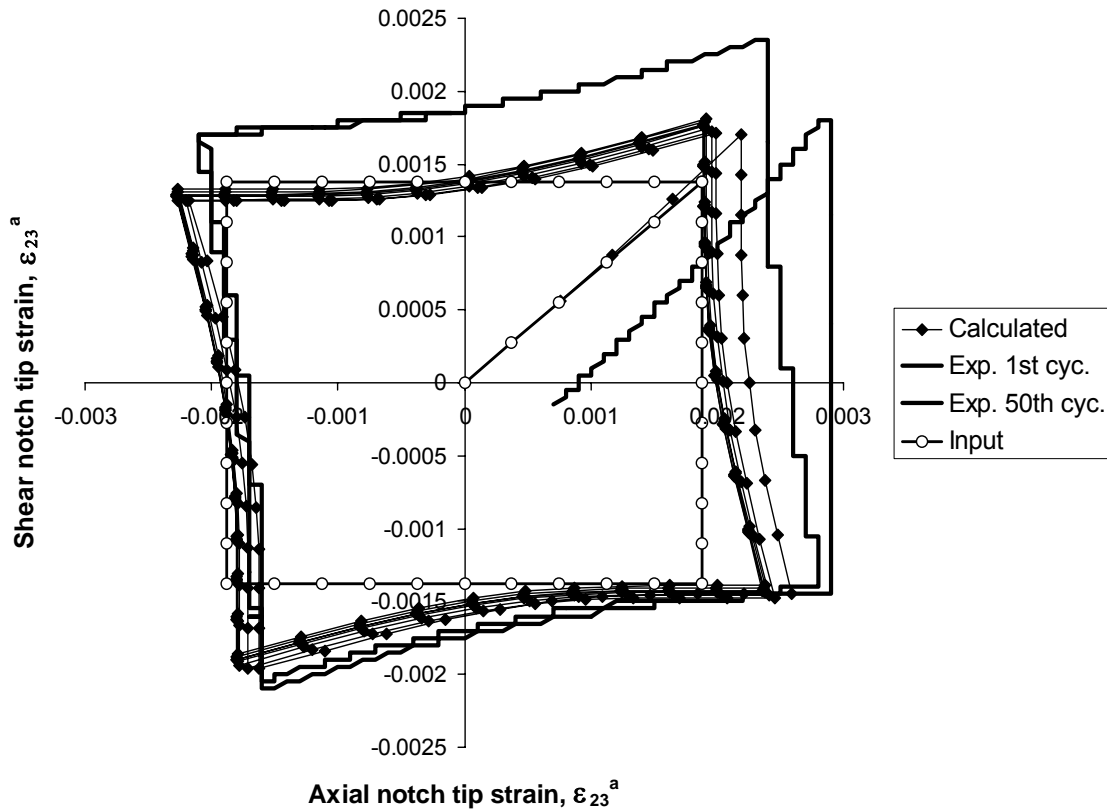
Figure H12. Measured and calculated strain paths in the notch tip induced by the "box" input-loading path.

The second cyclic stress path of Barkey (H12) is shown in Figure (H13). The resulting elastic-plastic notch tip strain paths are shown in Figure (H14). The maximum nominal stresses were $\sigma_n = 296$ MPa and $\tau_n = 193$ MPa. Again the qualitative and quantitative agreement between the measured and calculated strain histories was good as in the case of the box stress path.

Unequal- Frequency Stress Path
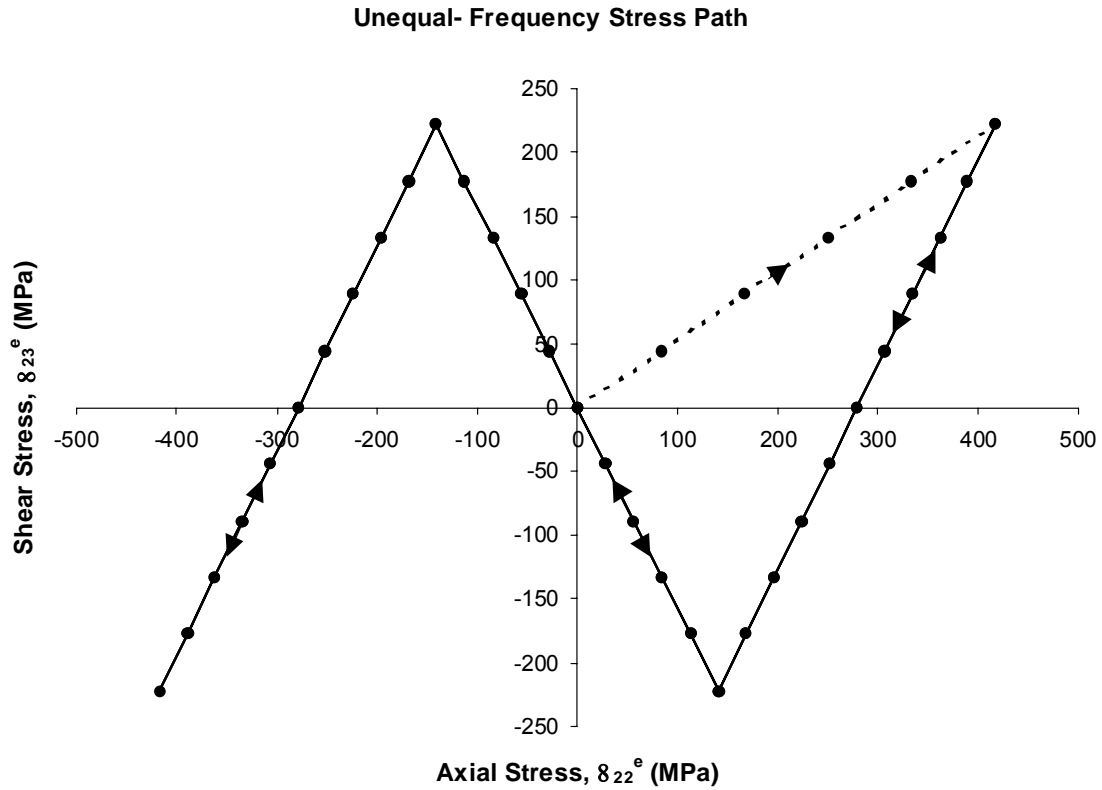
Figure H13. Unequal frequency tension-torsion stress/loading path.
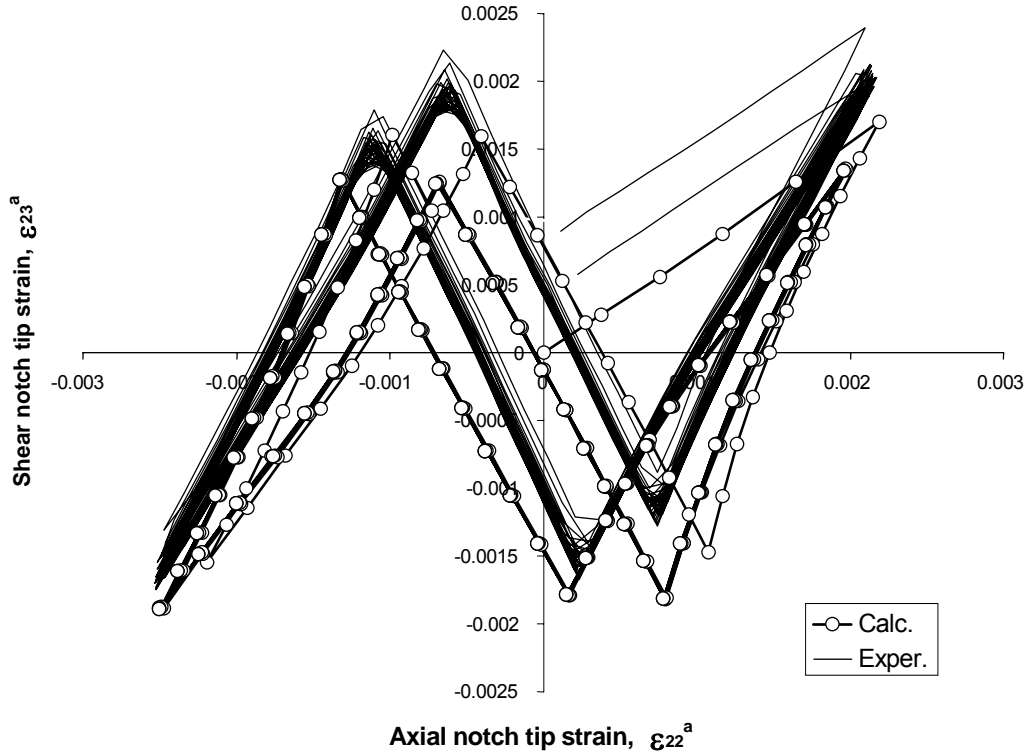
Figure H14. Measured and calculated strain paths in the notch tip induced by the unequal frequency tension-torsion input-loading path.

H.5   THE 2-D NOTCH TIP COMPUTER CODE (NEU34)

The computer code for solving the required set of incremental equation has been written in FORTRAN 77. The executable file has been created using the WATCOM - WATFOR87 compiler.

The Computer Code Data Files

There are two files necessary to run the calculations, i.e. the MATERIAL STRESS-STRAIN CURVE file and the STRESS PATH file. Both of them are text files.

The material stress-strain curve is given by series of points having stress and strain $(\sigma - \varepsilon)$ values as coordinates (Figure H15). The first data point (i.e. the first line) in the material file has to be that one above the yield limit, S_0, (or proportionality limit) because the yield limit, the modulus of elasticity, E, and the Poisson ratio, ν, are inputted from the keyboard. The format of the material data file is given below.
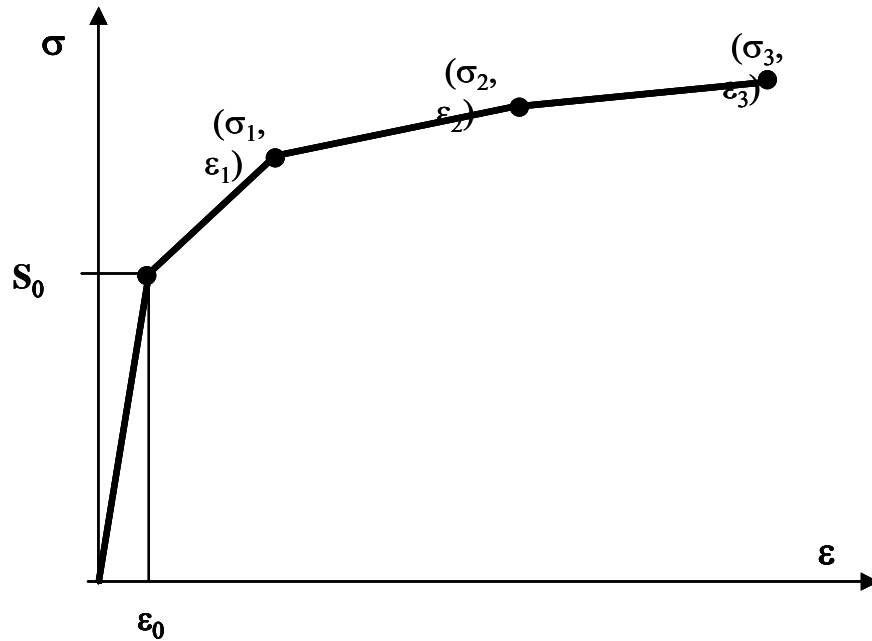
Figure H15. Stress-strain coordinates for the material stress-strain input file.

The stress-strain curve is approximated by a series of linear pieces. The maximum number of linear elements of the stress-strain curve was set to 100.

Material Stress-Strain File (the format):

File name (example: 13ab.dat) – length of the file name 6 characters;

Stress coordinate, σ, in the first column;

Strain coordinate, ε, in the second column.

The first linear segment (piece) from 0 to S_0 should not be given in the data file. The data file must start with the coordinates of the end of the second linear piece or the beginning of the third one (see Figure H15). Columns in the material data file must be separated by coma. The material data file below (attached also in an electronic form) has been prepared for a material with the modulus of elasticity $E = 200000$ MPa and the yield limit of $S_0 = 400$ MPa and the Poisson ratio $v=0.3$ and it has been approximated by 15 linear pieces.

Example of the material data file

432,0.0023
460,0.0027
490,0.0033
512,0.004
540,0.0055
575,0.009
605,0.015
620,0.024
640,0.04
660,0.08
700,0.16
750,0.3
800,0.45
850,0.6
1000,1.2

The stress path data is given (Figure H16) in terms of elastic stress increments, $\Delta\sigma_i$, at the notch tip. The first two columns are reserved for the increments of the normal stress components σ_{22} and σ_{33}. The third column is reserved for the increments of the shear stress, σ_{23}. The remaining stress components are zero. The stress columns in the stress path data file must be separated by coma. An example of a stress path data file (CROSS.DAT) is given below.
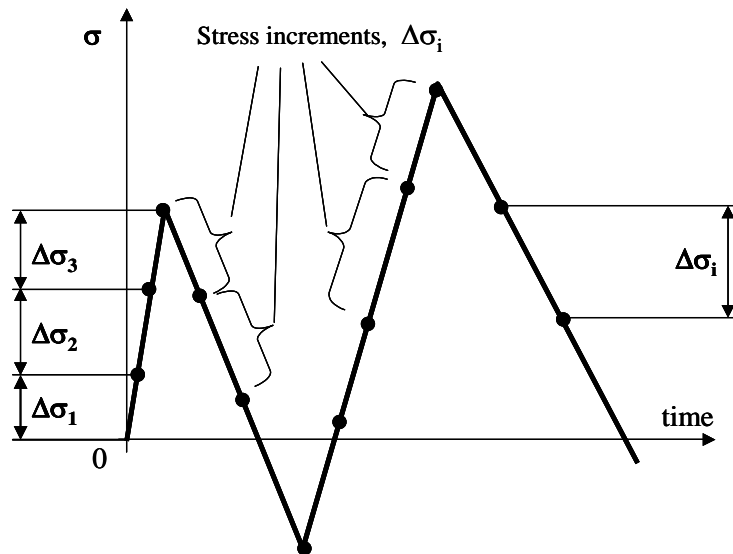
Figure H16. The input stress path increments of the stress-time history.

Stress Path Data File - Cross.dat (Increments!):

$\Delta\sigma_{22}$, $\Delta\sigma_{33}$, $\Delta\sigma_{23}$

The data………..
80.01,8.001,59.436
80.01,8.001,59.436
80.01,8.001,59.436
80.01,8.001,59.436
80.01,8.001,59.436
80.01,8.001,59.436
-80.01,-8.001,-59.436
-80.01,-8.001,-59.436
-80.01,-8.001,-59.436
-80.01,-8.001,-59.436
-80.01,-8.001,-59.436
-80.01,-8.001,-59.436
-80.01,-8.001,59.436
-80.01,-8.001,59.436
-80.01,-8.001,59.436
-80.01,-8.001,59.436
-80.01,-8.001,59.436
-80.01,-8.001,59.436
80.01,8.001,-59.436
80.01,8.001,-59.436
80.01,8.001,-59.436
80.01,8.001,-59.436
80.01,8.001,-59.436
80.01,8.001,-59.436
-80.01,-8.001,-59.436
-80.01,-8.001,-59.436
-80.01,-8.001,-59.436
-80.01,-8.001,-59.436
-80.01,-8.001,-59.436
-80.01,-8.001,-59.436
80.01,8.001,59.436
80.01,8.001,59.436
80.01,8.001,59.436
80.01,8.001,59.436
80.01,8.001,59.436
80.01,8.001,59.436
80.01,8.001,-59.436
80.01,8.001,-59.436
80.01,8.001,-59.436

The output file (Cross.out) gives subsequent values of the elastic-plastic stress and strain components corresponding to the end of each stress increment inputted from the stress path data file.

Data Inputted from the Keyboard:

At the beginning of the execution of the program the following data (bold characters) has to be inputted from the keyboard: the modulus of elasticity E, Poisson's ratio ν, yield limit S_0, name of the material input file, name of the (loading) stress path file and name of the output file.

The Screen Output:

MATERIAL PROPERTIES:

YOUNG MODULUS E=**200000**
POISSON`s RATIO ENI=**0.3**
PLASTICITY LIMIT So=**400**
CONSTITUTIVE LAW DATA FILE : **13ab.dat**
LOADING DATA FILE : **cross.dat**
NAME THE OUTPUT DATA FILE : **cross.out**

All data files have to reside in the same directory as the executable file (NEU34.EXE)! The output file (example given below) will be written in the same directory were the executable program file resides.

Example of the 2-D Notch Tip Output File Contents:

cross.out						
EPS(1,1)	EPS(2,2)	SIG(2,2)	EPS(2,3)	SIG(2,3)	EPS(3,3)	SIG(3,3)
0.00E+00	0.00E+00	0.00E+00	0.00E+00	0.00E+00	0.00E+00	0.00E+00
-1.32E-04	3.88E-04	8.00E+01	3.86E-04	5.94E+01	-8.00E-05	8.00E+00
-2.64E-04	7.76E-04	1.60E+02	7.73E-04	1.19E+02	-1.60E-04	1.60E+01
-3.96E-04	1.16E-03	2.40E+02	1.16E-03	1.78E+02	-2.40E-04	2.40E+01
-6.11E-04	1.63E-03	2.87E+02	1.67E-03	2.13E+02	-3.87E-04	2.87E+01
-9.37E-04	2.25E-03	3.14E+02	2.37E-03	2.34E+02	-6.18E-04	3.14E+01
-1.36E-03	3.00E-03	3.31E+02	3.25E-03	2.47E+02	-9.19E-04	3.31E+01
-1.22E-03	2.61E-03	2.51E+02	2.86E-03	1.87E+02	-8.39E-04	2.51E+01
-1.09E-03	2.23E-03	1.71E+02	2.47E-03	1.28E+02	-7.59E-04	1.71E+01
-9.59E-04	1.84E-03	9.08E+01	2.09E-03	6.82E+01	-6.79E-04	9.08E+00
-8.27E-04	1.45E-03	1.08E+01	1.70E-03	8.79E+00	-5.99E-04	1.08E+00
-6.95E-04	1.06E-03	-6.92E+01	1.31E-03	-5.06E+01	-5.19E-04	-6.92E+00
-5.63E-04	6.74E-04	-1.49E+02	9.29E-04	-1.10E+02	-4.39E-04	-1.49E+01
-4.31E-04	2.86E-04	-2.29E+02	1.31E-03	-5.06E+01	-3.59E-04	-2.29E+01
-2.99E-04	-1.02E-04	-3.09E+02	1.70E-03	8.79E+00	-2.79E-04	-3.09E+01
-1.13E-04	-5.50E-04	-3.72E+02	2.09E-03	6.96E+01	-1.56E-04	-3.72E+01
1.39E-04	-1.05E-03	-4.04E+02	2.48E-03	1.20E+02	1.99E-05	-4.04E+01
4.72E-04	-1.66E-03	-4.20E+02	2.94E-03	1.60E+02	2.59E-04	-4.20E+01
9.01E-04	-2.40E-03	-4.22E+02	3.55E-03	1.88E+02	5.71E-04	-4.22E+01
7.69E-04	-2.01E-03	-3.42E+02	3.17E-03	1.29E+02	4.91E-04	-3.42E+01
6.37E-04	-1.62E-03	-2.62E+02	2.78E-03	6.94E+01	4.11E-04	-2.62E+01
5.05E-04	-1.24E-03	-1.82E+02	2.39E-03	1.00E+01	3.31E-04	-1.82E+01
3.72E-04	-8.47E-04	-1.02E+02	2.01E-03	-4.94E+01	2.51E-04	-1.02E+01
2.40E-04	-4.59E-04	-2.19E+01	1.62E-03	-1.09E+02	1.71E-04	-2.19E+00
1.08E-04	-7.09E-05	5.81E+01	1.23E-03	-1.68E+02	9.04E-05	5.81E+00
2.17E-04	-4.28E-04	-2.63E+01	7.55E-04	-2.11E+02	1.53E-04	-2.63E+00
3.50E-04	-8.08E-04	-1.02E+02	1.57E-04	-2.39E+02	2.34E-04	-1.02E+01
5.26E-04	-1.23E-03	-1.60E+02	-5.21E-04	-2.57E+02	3.50E-04	-1.60E+01
7.76E-04	-1.74E-03	-2.02E+02	-1.35E-03	-2.67E+02	5.24E-04	-2.02E+01
1.09E-03	-2.35E-03	-2.32E+02	-2.31E-03	-2.75E+02	7.47E-04	-2.32E+01
1.44E-03	-3.00E-03	-2.55E+02	-3.33E-03	-2.82E+02	9.97E-04	-2.55E+01
1.31E-03	-2.61E-03	-1.75E+02	-2.95E-03	-2.22E+02	9.17E-04	-1.75E+01
1.18E-03	-2.22E-03	-9.52E+01	-2.56E-03	-1.63E+02	8.36E-04	-9.52E+00
1.04E-03	-1.83E-03	-1.52E+01	-2.17E-03	-1.03E+02	7.56E-04	-1.52E+00
9.12E-04	-1.45E-03	6.49E+01	-1.79E-03	-4.41E+01	6.76E-04	6.49E+00
7.80E-04	-1.06E-03	1.45E+02	-1.40E-03	1.54E+01	5.96E-04	1.45E+01

H.6 THEORETICAL BASIS FOR THE THREE-DIMENSIONAL (3-D) ELASTO-PLASTIC NEAR NOTCH TIP MODEL

The 2-D approach makes it possible to analyze elastic-plastic stresses and strains at the notch tip only where at least three stress components are being zero. However, away from the notch tip there are more unknown stress components than three. Therefore if elasto-plastic stresses and strains across the notch tip plastic zone need to be determined the complete stress and strain tensor must be considered. It means that all stress and strain components have to be included into the mathematical formulation of the problem.

H.6.1 The Stress State in the Notch Tip Region

For the case of general multiaxial loading applied to a notched body, the state of stress in the notch tip region is tri-axial. There are in general six unknown stress (Figure H17) and six strain components. As a result there are twelve unknowns all together and a set of twelve independent equations is required for the determination of all stress and strain components at the notch tip.

$$
\sigma_{ij}^a =
\begin{bmatrix}
\sigma_{11}^a & \sigma_{12}^a & \sigma_{13}^a \\
\sigma_{21}^a & \sigma_{22}^a & \sigma_{23}^a \\
\sigma_{31}^a & \sigma_{32}^a & \sigma_{33}^a
\end{bmatrix}
\quad and \quad
\varepsilon_{ij}^a =
\begin{bmatrix}
\varepsilon_{11}^a & \varepsilon_{12}^a & \varepsilon_{13}^a \\
\varepsilon_{21}^a & \varepsilon_{22}^a & \varepsilon_{23}^a \\
\varepsilon_{31}^a & \varepsilon_{32}^a & \varepsilon_{33}^a
\end{bmatrix}
\tag{H21}
$$

The material constitutive relationships provide six equations, leaving six additional equations to be established.
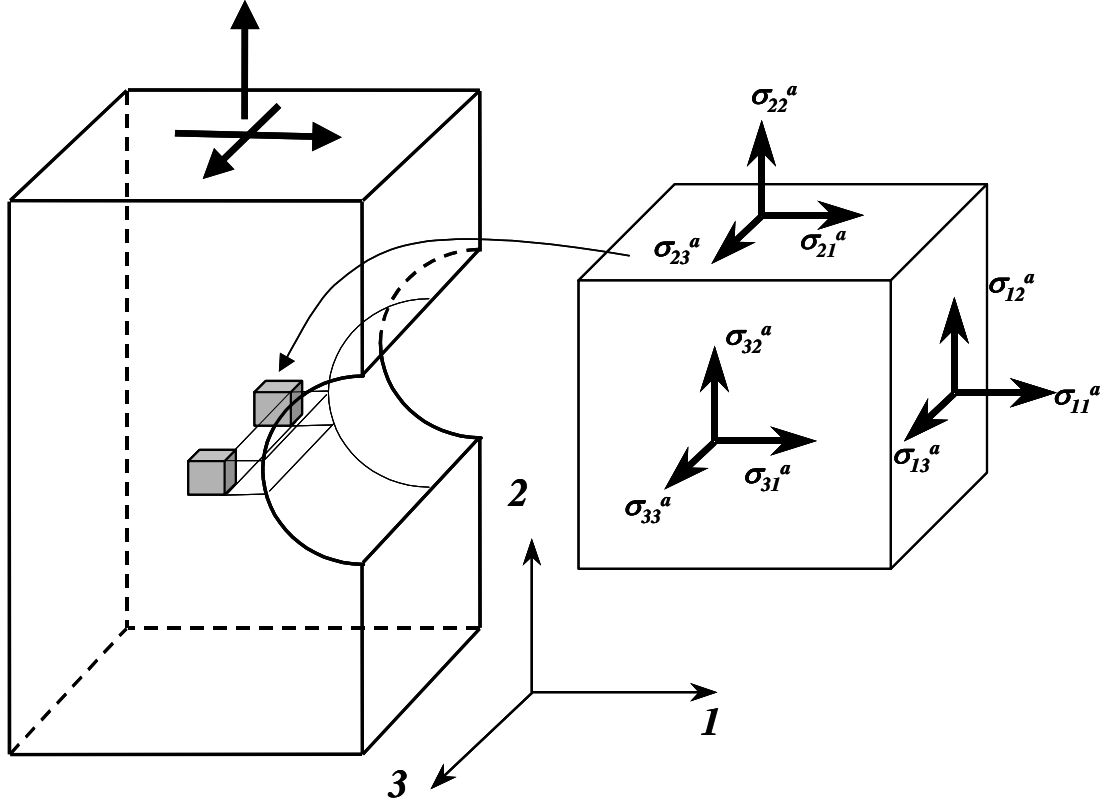
Figure H17. Stress state in the notch tip region.

H.6.2   Material Constitutive Model

In the case of proportional or nearly proportional notch tip stress path the Hencky total deformation equations of plasticity can be used in the analysis.

$$\varepsilon_{ij}^{a} = \frac{1+\nu}{E}\sigma_{ij}^{a} - \frac{\nu}{E}\sigma_{kk}^{a}\,\delta_{ij} + \frac{3}{2}\frac{\varepsilon_{eq}^{pa}}{\sigma_{eq}^{a}}S_{ij}^{a} \tag{H22}$$

where: $S_{ij}^{a} = \sigma_{ij}^{a} - \dfrac{1}{3}\sigma_{kk}^{a}\delta_{ij}$

The most frequently used model of incremental plasticity is the Prandtl-Reuss flow rule. For an isotropic body, the Prandtl-Reuss strain-stress relationships can be expressed as:

$$\Delta\varepsilon_{ij}^{a} = \frac{1+v}{E}\Delta\sigma_{ij}^{a} - \frac{v}{E}\Delta\sigma_{kk}^{a}\,\delta_{ij} + \frac{3}{2}\frac{\Delta\varepsilon_{eq}^{pa}}{\sigma_{eq}^{a}}S_{ij}^{a} \qquad (\text{H23})$$

The multiaxial incremental stress-strain relation (H3) is obtained from the uniaxial stress-strain curve by relating the equivalent plastic strain increment to the equivalent stress increment such that:

$$\Delta\varepsilon_{eq}^{pa} = \frac{d\,f(\sigma_{eq}^{a})}{d\,\sigma_{eq}^{a}}\Delta\sigma_{eq}^{a}. \qquad (\text{H24})$$

The function, $\varepsilon_{eq}^{p} = f(\sigma_{eq})$, is identical to the plastic strain – stress relationship obtained experimentally from uni-axial tension test.

H.6.3 The Load-Notch Tip Stress-Strain Relations

The load or the load parameter, in the case of notched bodies, is usually represented by the nominal or reference stress being proportional to the remote applied load. Analogously to the 2-D formulation for the notch tip it was anticipated that the relationship between the load and the elastic-plastic notch tip strains and stresses in the localized plastic zone can also be approximated by the Neuber rule [1] or the Equivalent Strain Energy Density (ESED) equation [2]. Both methods consist of two parts namely the constitutive equations and the relationships linking the fictitious linear elastic stress-strain state (σ_{ij}^{e},ε_{ij}^{e}) near the notch tip with the actual elastic-plastic stress-strain response (σ_{ij}^{a},ε_{ij}^{a}) as shown in Figure H2. The Neuber rule [2,3] for proportional loading, where the Hencky stress-strain relationships are applicable, can be written for the multiaxial stress state in the form of equations (H25).

$$\sigma_{ij}^{e}\varepsilon_{ij}^{e} = \sigma_{ij}^{a}\varepsilon_{ij}^{a} \qquad (\text{H25})$$

The Neuber rule (H25) represents the equality of the total strain energy (the strain energy & the complimentary strain energy density) at the notch tip, represented by the rectangles A and B in Figure H3a. The total strain energy density equation written in engineering notation takes the form of expression (H26).

$$\begin{aligned}
&\sigma_{11}^{e}\varepsilon_{11}^{e} + \sigma_{12}^{e}\varepsilon_{12}^{e} + \sigma_{13}^{e}\varepsilon_{13}^{e} + \sigma_{22}^{e}\varepsilon_{22}^{e} + \sigma_{23}^{e}\varepsilon_{23}^{e} + \sigma_{33}^{e}\varepsilon_{33}^{e}\\
&\quad = \sigma_{11}^{a}\varepsilon_{11}^{a} + \sigma_{12}^{a}\varepsilon_{12}^{a} + \sigma_{13}^{a}\varepsilon_{13}^{a} + \sigma_{22}^{a}\varepsilon_{22}^{a} + \sigma_{23}^{a}\varepsilon_{23}^{a} + \sigma_{33}^{a}\varepsilon_{33}^{a}
\end{aligned} \qquad (\text{H26})$$

The overall strain energy density equivalence, equation (H26), relating the pseudo-elastic and the actual elastic-plastic notch tip strains and stresses at the notch tip has been generally accepted as a good approximation rule but the additional conditions, necessary for the complete formulation of a multiaxial stress state problem, are being the subject of controversy as far as the 2-D formulation is concerned. However, nobody tried according to the authors knowledge to formulate the complete 3-D problem in terms of the Neuber or the ESED hypothesis. The method described below uses the ratios of strain energy density contributed by each pair of corresponding stress and strain components. In order to analyze non-proportional loading paths the energy equations were written in an incremental form. Because the ratios of strain energy density increments seem to be less dependent on the geometry and constraint conditions at the notch tip than the ratios of stresses or strains the analyst is not forced to make any arbitrary decisions about the constraint while using these equations. Because plastic yielding is dependent mainly on deviatoric stresses the entire formulation has been written in deviatoric stress space involving deviatoric stresses and strains, analogously to the original Neuber's idea.

H.6.4 Deviatoric Stress-Strain Relationships

The notch tip deviatoric stresses of the hypothetical linear-elastic input are determined as:

$$S_{ij}^e = \sigma_{ij}^e - \frac{1}{3}\sigma_{kk}^e \delta_{ij} \tag{H27}$$

The elastic deviatoric strains and strain increments can be calculated from the Hooke law.

$$\Delta e_{ij}^e = \frac{\Delta S_{ij}^e}{2G} \tag{H28}$$

The actual deviatoric stress components in the notch tip can analogously be defined as:

$$S_{ij}^a = \sigma_{ij}^a - \frac{1}{3}\sigma_{kk}^a \delta_{ij} \tag{H29}$$

The incremental deviatoric stress-strain relations based on the associated Prandtl-Reuss flow rule can be subsequently written as:

$$\Delta e_{ij}^a = \frac{\Delta S_{ij}^a}{2G} + S_{ij}^a d\lambda \tag{H30a}$$

In engineering notation the deviatoric stress-strain relations are written in the form:

$$
\begin{cases}
\Delta e_{11}^a = \dfrac{\Delta S_{11}^a}{2G} + S_{11}^a d\lambda \\[2mm]
\Delta e_{12}^a = \dfrac{\Delta S_{12}^a}{2G} + S_{12}^a d\lambda \\[2mm]
\Delta e_{13}^a = \dfrac{\Delta S_{13}^a}{2G} + S_{13}^a d\lambda \\[2mm]
\Delta e_{22}^a = \dfrac{\Delta S_{22}^a}{2G} + S_{22}^a d\lambda \\[2mm]
\Delta e_{23}^a = \dfrac{\Delta S_{23}^a}{2G} + S_{23}^a d\lambda \\[2mm]
\Delta e_{33}^a = \dfrac{\Delta S_{33}^a}{2G} + S_{33}^a d\lambda
\end{cases}
\tag{H30b}
$$

where:

$$
d\lambda = \frac{3}{2}\frac{\Delta \varepsilon_{eq}^{pa}}{\sigma_{eq}^a}; \qquad \left(\sigma_{eq}^a\right)^2 = \frac{3}{2} S_{ij}^a S_{ij}^a;
$$

$$
\Delta \varepsilon_{eq}^{pa} = \frac{df\left(\sigma_{eq}^a\right)}{d\sigma_{eq}^E}\Delta\sigma_{eq}^a;
$$

The form and specific parameters of the stress-strain function, $\varepsilon_{eq}{}^p = f(\sigma_{eq})$, must be obtained experimentally from uniaxial cyclic test.

H.6.5   The Equivalence of Increments of the Total Distortional Strain Energy Density

It is proposed, analogously to the original Neuber rule, to use the equivalence of increments of the total distortional strain energy density contributed by each pair of associated stress and strain components.

$$
\begin{cases}
S_{11}^e \Delta e_{11}^e + e_{11}^e \Delta S_{11}^e = S_{11}^a \Delta e_{11}^a + e_{11}^a \Delta S_{11}^a \\[1mm]
S_{12}^e \Delta e_{12}^e + e_{12}^e \Delta S_{12}^e = S_{12}^a \Delta e_{12}^a + e_{12}^a \Delta S_{12}^a \\[1mm]
S_{13}^e \Delta e_{13}^e + e_{13}^e \Delta S_{13}^e = S_{13}^a \Delta e_{13}^a + e_{13}^a \Delta S_{13}^a \\[1mm]
S_{22}^e \Delta e_{22}^e + e_{22}^e \Delta S_{22}^e = S_{22}^a \Delta e_{22}^a + e_{22}^a \Delta S_{22}^a \\[1mm]
S_{23}^e \Delta e_{23}^e + e_{23}^e \Delta S_{23}^e = S_{23}^a \Delta e_{23}^a + e_{23}^a \Delta S_{23}^a \\[1mm]
S_{33}^e \Delta e_{33}^e + e_{33}^e \Delta S_{33}^e = S_{33}^a \Delta e_{33}^a + e_{33}^a \Delta S_{33}^a
\end{cases}
\tag{H31}
$$

The equalities of strain energy increments for each set of corresponding hypothetical elastic and actual elastic-plastic strains and stress increments at the notch tip can be shown graphically (Figure H4) as the equality of surface areas of the two pairs of rectangular elements representing the increments of strain energy density. The area of dotted rectangles represents the total strain energy increment of the hypothetical elastic notch tip input stress while the area of the hatched rectangles represents the total strain energy density of the actual elastic-plastic material response at the notch tip.

Equations (H30)-(H31) form a set of twelve simultaneous equations from which all deviatoric strain and stress increments can be determined, based on the linear hypothetical elastic notch tip stress path data, i.e. increments $\Delta\sigma_{ij}{}^{e}$, obtained from the linear-elastic analysis and the constitutive stress-strain curve (H3).

$$
\begin{cases}
\Delta e_{11}^{a} = \dfrac{\Delta S_{11}^{a}}{2G} + \dfrac{3}{2}\dfrac{\Delta\varepsilon_{eq}^{a}}{\sigma_{eq}^{a}} S_{11}^{a} \\[2mm]
\Delta e_{12}^{a} = \dfrac{\Delta S_{12}^{a}}{2G} + \dfrac{3}{2}\dfrac{\Delta\varepsilon_{eq}^{a}}{\sigma_{eq}^{a}} S_{12}^{a} \\[2mm]
\Delta e_{13}^{a} = \dfrac{\Delta S_{13}^{a}}{2G} + \dfrac{3}{2}\dfrac{\Delta\varepsilon_{eq}^{a}}{\sigma_{eq}^{a}} S_{13}^{a} \\[2mm]
\Delta e_{22}^{a} = \dfrac{\Delta S_{22}^{a}}{2G} + \dfrac{3}{2}\dfrac{\Delta\varepsilon_{eq}^{a}}{\sigma_{eq}^{a}} S_{22}^{a} \\[2mm]
\Delta e_{23}^{a} = \dfrac{\Delta S_{23}^{a}}{2G} + \dfrac{3}{2}\dfrac{\Delta\varepsilon_{eq}^{a}}{\sigma_{eq}^{a}} S_{23}^{a} \\[2mm]
\Delta e_{33}^{a} = \dfrac{\Delta S_{33}^{a}}{2G} + \dfrac{3}{2}\dfrac{\Delta\varepsilon_{eq}^{a}}{\sigma_{eq}^{a}} S_{33}^{a} \\[2mm]
S_{11}^{e}\Delta e_{11}^{e} + e_{11}^{e}\Delta S_{11}^{e} = S_{11}^{a}\Delta e_{11}^{a} + e_{11}^{a}\Delta S_{11}^{a} \\[1mm]
S_{12}^{e}\Delta e_{12}^{e} + e_{12}^{e}\Delta S_{12}^{e} = S_{12}^{a}\Delta e_{12}^{a} + e_{12}^{a}\Delta S_{12}^{a} \\[1mm]
S_{13}^{e}\Delta e_{13}^{e} + e_{13}^{e}\Delta S_{13}^{e} = S_{13}^{a}\Delta e_{13}^{a} + e_{13}^{a}\Delta S_{13}^{a} \\[1mm]
S_{22}^{e}\Delta e_{22}^{e} + e_{22}^{e}\Delta S_{22}^{e} = S_{22}^{a}\Delta e_{22}^{a} + e_{22}^{a}\Delta S_{22}^{a} \\[1mm]
S_{23}^{e}\Delta e_{23}^{e} + e_{23}^{e}\Delta S_{23}^{e} = S_{23}^{a}\Delta e_{23}^{a} + e_{23}^{a}\Delta S_{23}^{a} \\[1mm]
S_{33}^{e}\Delta e_{33}^{e} + e_{33}^{e}\Delta S_{33}^{e} = S_{33}^{a}\Delta e_{33}^{a} + e_{33}^{a}\Delta S_{33}^{a}
\end{cases}
\tag{H32}
$$

For each increment of the external load, represented by the increments of pseudo-elastic deviatoric stresses, ΔS_{ij}^e, the deviatoric elastic-plastic notch tip strain and stress increments, Δe_{ij}^a and ΔS_{ij}^a, are computed from the equation set (H32). Then the calculated deviatoric stress increments, ΔS_{ij}^a, are converted into the actual stress increments, $\Delta\sigma_{ij}^a$,

$$\Delta S_{11}^a = \Delta\sigma_{11}^a - \frac{1}{3}\left(\Delta\sigma_{11}^a + \Delta\sigma_{22}^a + \Delta\sigma_{33}^a\right)$$

$$\Delta S_{22}^a = \Delta\sigma_{22}^a - \frac{1}{3}\left(\Delta\sigma_{11}^a + \Delta\sigma_{22}^a + \Delta\sigma_{33}^a\right)$$

$$\Delta S_{33}^a = \Delta\sigma_{33}^a - \frac{1}{3}\left(\Delta\sigma_{11}^a + \Delta\sigma_{22}^a + \Delta\sigma_{33}^a\right) \qquad\text{(H33)}$$

$$\Delta S_{12}^a = \Delta\sigma_{12}^a$$

$$\Delta S_{13}^a = \Delta\sigma_{13}^a$$

$$\Delta S_{23}^a = \Delta\sigma_{23}^a$$

The deviatoric and the actual stress components S_{ij}^a and σ_{ij}^a at the end of given load increment are determined from equations (H34-H35).

$$S_{ij}^{an} = S_{ij}^{ao} + \sum_{k=1}^{n-1}\Delta S_{ij}^{ak} + \Delta S_{ij}^{an}, \qquad\text{(H34)}$$

$$\sigma_{ij}^{an} = \sigma_{ij}^{ao} + \sum_{k=1}^{n-1}\Delta\sigma_{ij}^{ak} + \Delta\sigma_{ij}^{an} \qquad\text{(H35)}$$

where: n denotes the number of the load increment.

The actual strain increments, $\Delta\varepsilon_{ij}^a$, can finally be determined from the constitutive equation (H3). The same cyclic plasticity model has been implemented as in the case of the 2-D formulation.

H.6.6 Correction for the Stress Redistribution in the Notch Tip Region

Plastic yielding near the notch tip causes stress re-distribution of the hypothetical linear elastic field used as a base in the proposed methodology. The stress redistribution results in an increase of plastic zone size by amount of Δx_p (Figure H18) in comparison to that one (denoted x_p) resulted from the hypothetical linear elastic stress notch tip field.

$$\sigma_{eq} = \frac{1}{\sqrt{2}} \sqrt{\frac{\left(\sigma_{11} - \sigma_{22}\right)^2 + \left(\sigma_{22} - \sigma_{33}\right)^2}{+\left(\sigma_{33} - \sigma_{11}\right)^2 + 6\left(\sigma_{12}^2 + \sigma_{13}^2 + \sigma_{23}^2\right)}}$$
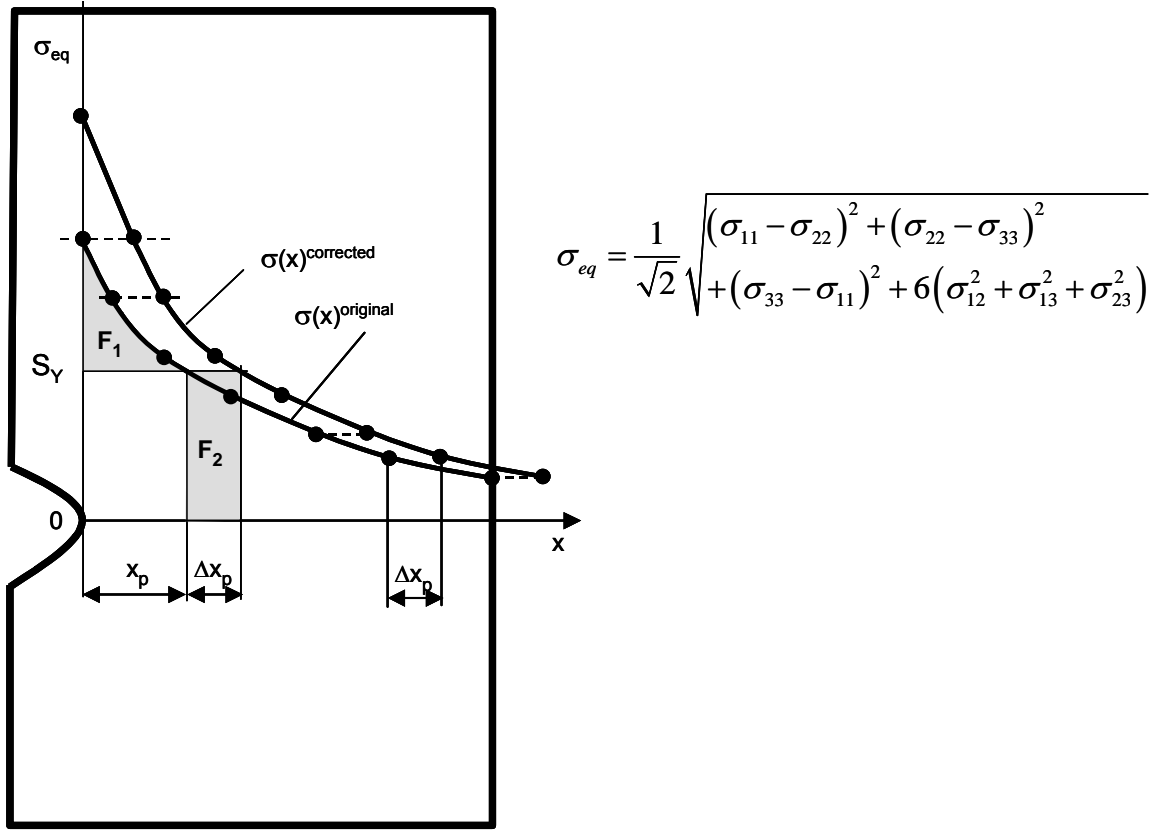
Figure H18. The original and corrected equivalent stress distribution.

Such an increase of the plastic zone size can be interpreted, analogously with Irwin [13], as an increase of the hypothetical elastic notch tip stresses. The plasticity induced increase of stress near the notch tip Irwin proposed to estimate by shifting horizontally (Figure H18) the original linear elastic stress field over the distance equal to the increment of the plastic zone size Δx_p caused by the stress redistribution. The increase of the stress at given co-ordinate x was determined as:

$$C_p = \frac{\sigma(x)^{corrected}}{\sigma(x)^{original}} \tag{H36}$$

Thus, in order to calculate the plastic zone correction factor, C_p, one has to determine the plastic zone size, x_p, and plastic zone increment, Δx_p. The plastic zone size, x_p, can be estimated from the distribution of the equivalent (von Mises) stress in the near notch tip

region. Therefore the distribution of the equivalent stress has to be supplied as an additional input data. The plastic zone increment, Δx_p, can be subsequently determined from the equilibrium condition in the near notch tip region.

If the plastic flow is localized and the elastic field surrounding the plastic zone is relatively large the stress redistribution occurs predominantly in the near notch tip region. Therefore the force, F_1, denoted as area, F_1, in Figure H18, has to be transferred by adjacent material over the distance, Δx_p. Thus, forces F_1 and F_2 represented by areas F_1 and F_2 in Figure H18 have to be equal.

$$F_1 = F_2 \tag{H37}$$

Because equivalent stress in the plastic zone is approximately equal to the yield limit, S_Y, then the increment, Δx_p, can by easily determined from equation (H38) representing the equality of the two generalized forces F_1 and F_2.

$$F_1 = F_2 \quad i.e.$$
$$\int_0^{x_p} \sigma(x)_{eq} \, dx - S_Y x_p = S_Y \Delta x_p \tag{H38}$$

The plastic zone increment, Δx_p, can be finally determined from expression (H39).

$$\Delta x_p = \frac{1}{S_Y} \int_0^{x_p} \sigma(x)_{eq} \, dx - x_p \tag{H39}$$

A special numerical routine has been written for calculating the integral in expression (H39) and the plastic zone increment, Δx_p.

The original distribution of the equivalent stress, $\sigma(x)^{\text{original}}$ is subsequently shifted away from the notch tip by distance, $x = \Delta x_p$, resulting in the corrected equivalent stress distribution, $\sigma(x)^{\text{corrected}}$. Knowing both equivalent stress distributions makes it possible to determine the correction factor, C_p, for any coordinate, x, according to expression (H36).

The original increments of the input stress history are then multiplied by the plastic zone correction factor, C_p, before they are inputted into the Neuber strain energy density equations. All calculations are in effect carried out later for stress increments increased by the correction factor C_p.

H.7 VALIDATION OF THE THREE DIMENTIONAL (3 – D) NOTCH MODEL

The linear elastic and elasto-plastic stresses and strains in several notched components have been determined using a variety of geometry and material configurations. The SWRI (G. Chell) and the North Dakota State University (A. Kallmeyer) carried out the Finite Element (FE) analyses. Both the elastic and elastic plastic stress distributions were determined and made available for independent analysis.

The SWRI data (G. Chell) were obtained for only one stress reversal (monotonic loading) and the data supplied corresponded to the maximum load. The applied load was proportional in all instances. Only the stress data was supplied by the SWRI. The strain data was not made available.

The data supplied by the NDSU (A. Kallmayer) included both proportional and non-proportional loading and unloading and non-proportional cyclic load paths. Both strains and stresses were made available for the validation.

H.7.1 The Geometry of SWRI Notched Components

The data supplied by the SWRI concerns three cases. Stresses for the notch tip region for Cases A and B were obtained for a two-dimensional configuration in the form of a plate with a circular hole (Figures H19a-H19b) subjected to uni-axial and bi-axial tension respectively. The two-dimensional cases A and B were analyzed under imposed condition of plane strain. The third case C was a single edge notch in a plate and the component was analyzed as a three-dimensional problem (Figure H19c) without imposing any specific condition concerning the resultant stress state in the notch tip region.
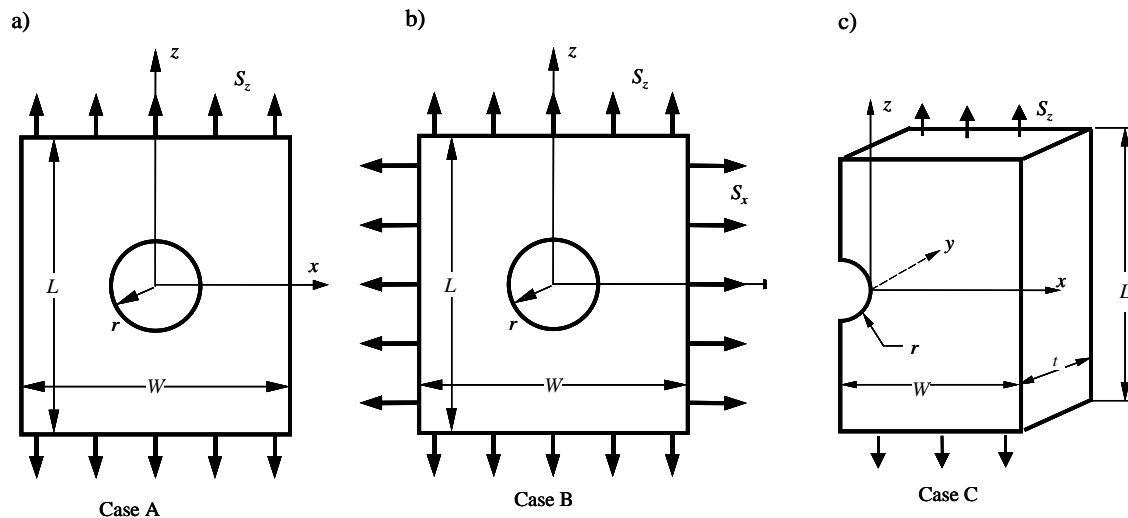
Figure H19. The SwRI two-dimensional (2-D) finite element models: a.) Case A; b.) Case B; and c.) Case C.

H.7.2 The Material Stress-Strain Curves Used in the SWRI Analyses

Two nonlinear material behaviors are included in the comparison. They are shown in Figure H20.
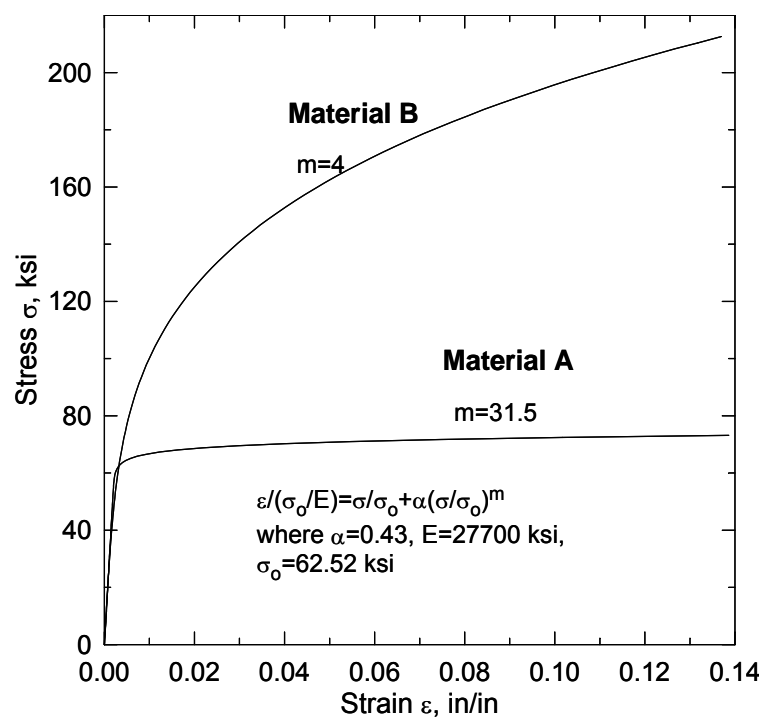
Figure H20. The material stress-strain curves used in the SwRI finite element (FE) analysis.

Material A behaves more like a perfect plastic material while Material B demonstrates a strong material hardening. The same curves were used in the Neuber based program NCP340 described below. However some caution has to be taken while dividing the material curve into a series of linear pieces. It has been found that the yield strength, S_Y, can not be considered as the upper limit for the linear segment of the stress –strain curve (Figures H21-H22). This is due to the fact that the nonlinearly below the standard yield limit has to be taken into account as well. This is particularly true for notch tip strains and stresses not significantly exceeding the yield limit - as it should be the case in most practical engineering applications. Therefore two limits characterizing the stress-strain curve are used in the proposed methodology, i.e. the standard yield strength, S_Y, and the linearity limit, σ_0. Assumption that the stress-strain curve is linear up to the yield limit ($\sigma < S_Y$) results in non-conservative notch tip strain and stress predictions.

Two different piecewise representations of both strain-stress curves are shown in Figures H21 – H22. The smooth curves with the non-linearity starting at stress $\sigma > \sigma$ were used in the Neuber based calculations. Unfortunately it is know what kind of representations of the stress-strain curve was exactly used by the SWRI-FE package.

SWRI - material curve A
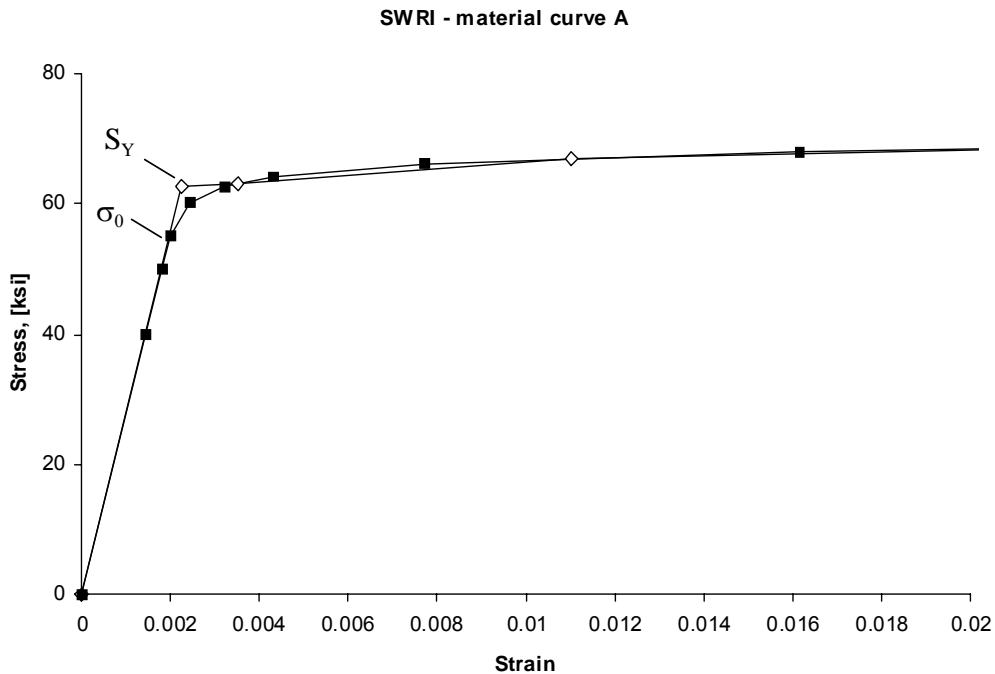
Figure H21. Piecewise representations of the stress-strain curve; SwRI-material A.

SWRI - material curve B
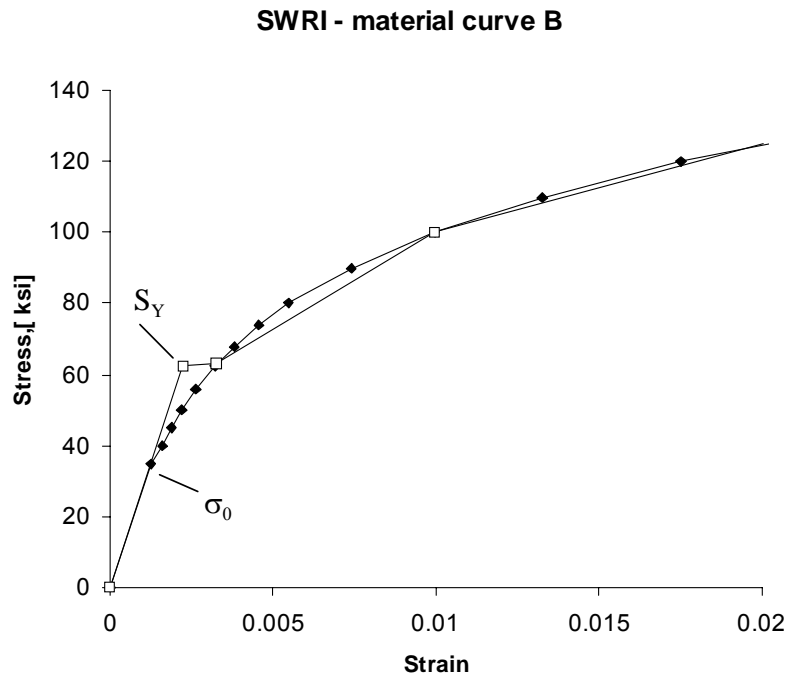
Figure H22. Piecewise representations of the stress-strain curve; SwRI-material B

H.7.3   The Load/Stress Paths

The elastic stress path input was given in terms of a set of stress increments for each stress component determined at given point near the notch for an ideal elastic material behavior. All input files are to be delivered separately in the form of EXCEL files. Examples of stress path input files are discussed below.

However, one feature of the stress-input files should be looked at with some caution. Namely, several input files used by the SWRI contained inaccurate stress values such as non-zero stress components on a free surface. The deviations from zero stress values were relatively small and they were probably resulting from the FE averaging process but when included into the Neuber based analysis these inaccuracies invoked noticeable accumulated error at the end of the load path. This was particularly true in the case of the transverse (through the thickness) stress component.

H.7.4   The Comparisons of the SWRI - FE and the Neuber-Based Near Notch Tip Stresses

The comparison of results obtained by SWRI and those obtained from the NPC30 program are shown in Figures H23-H32. In the case of the 3-D model (Case C – Figures H27-H32) stresses were determined in three planes: in the side plane (y/r = 0), in the plane at ¼ of the plate thickness (y/r = 1.237) and in the plane at the mid-thickness of the plate (y/r = 2.5). It can be noticed that the transverse stress SIGyy is under-predicted by the proposed method. However, the Neuber based analysis for y/r = 0 predicted the transverse stress zero, as it should be, while the FE analysis predicted non-zero stress normal to the free surface. It is therefore thought that the FE data concerning the transverse stress are inaccurate and over-predicted.

The plasticity model used in the Neuber based methodology was the isotropic-kinematic model proposed by Garud [10]. There was no specific information concerning the plasticity model incorporated into the FE package used by the SWRI. Therefore some differences may also be caused by the incompatibility of the basic plasticity models used in the study.
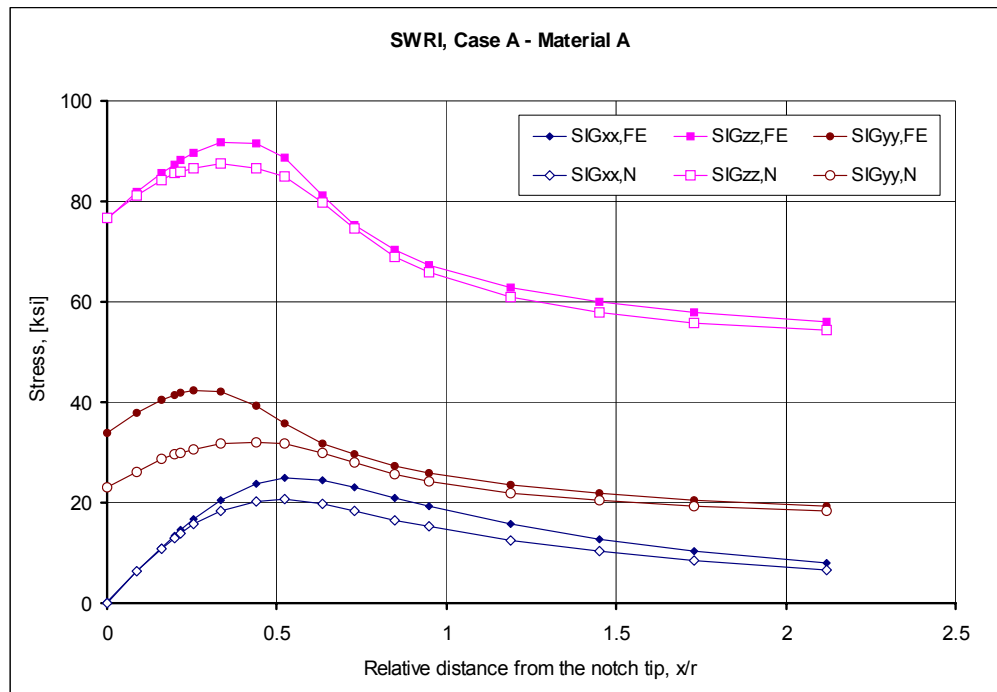
Figure H23. Comparison of SwRI finite element stress data with the Neuber based estimations; Case A – material A.
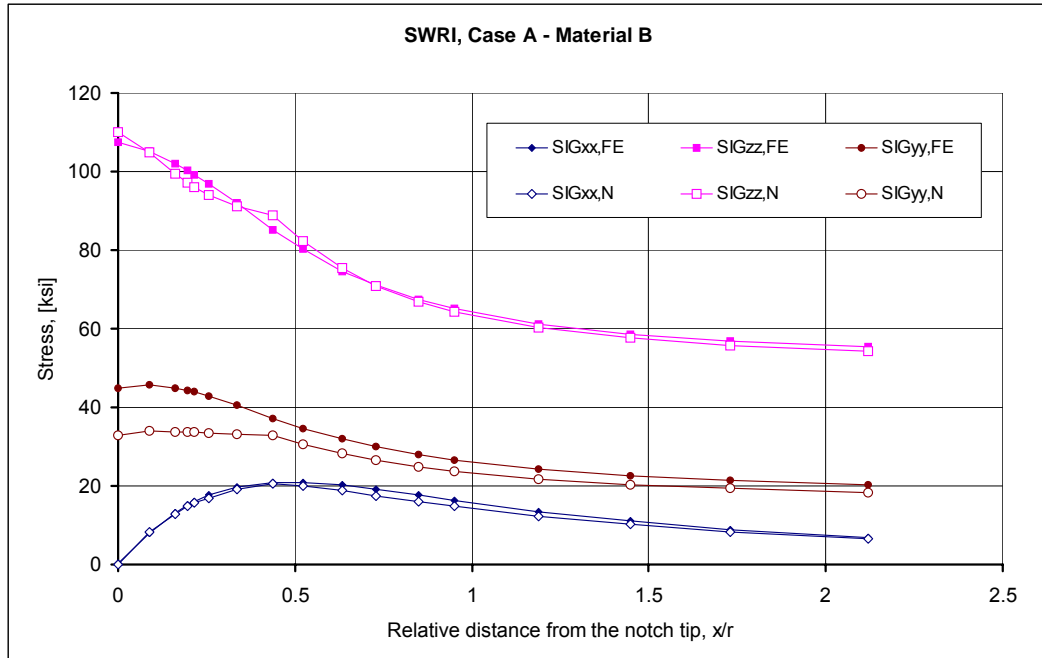
Figure H24. Comparison of SwRI finite element stress data with the Neuber based estimations; Case A – material B.
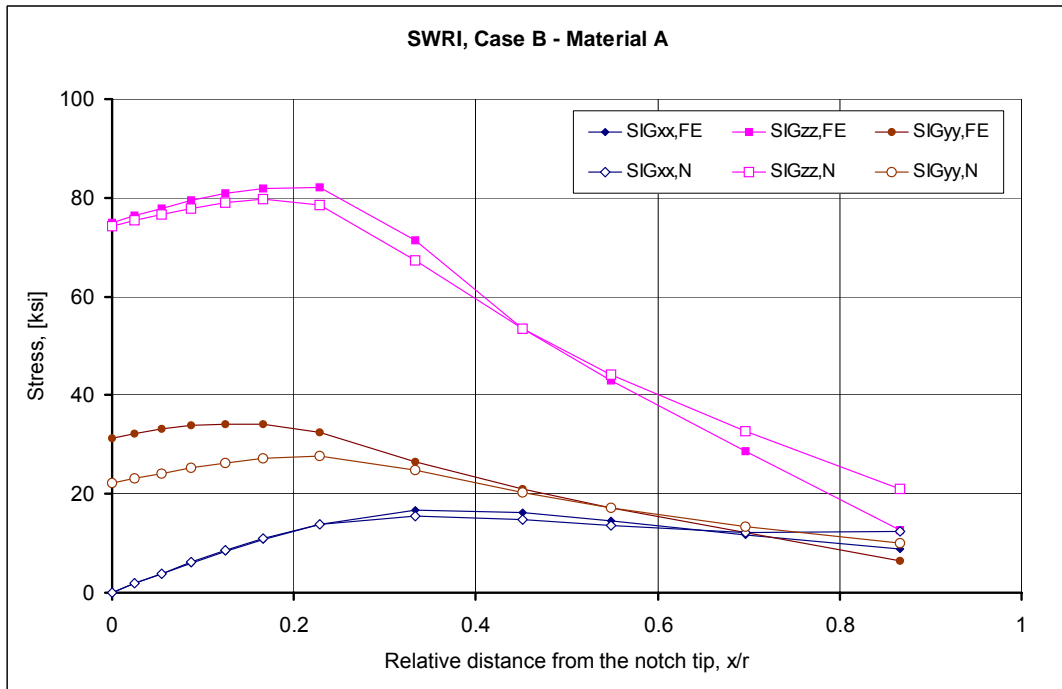
Figure H25. Comparison of SwRI finite element stress data with the Neuber based estimations; Case B – material A.
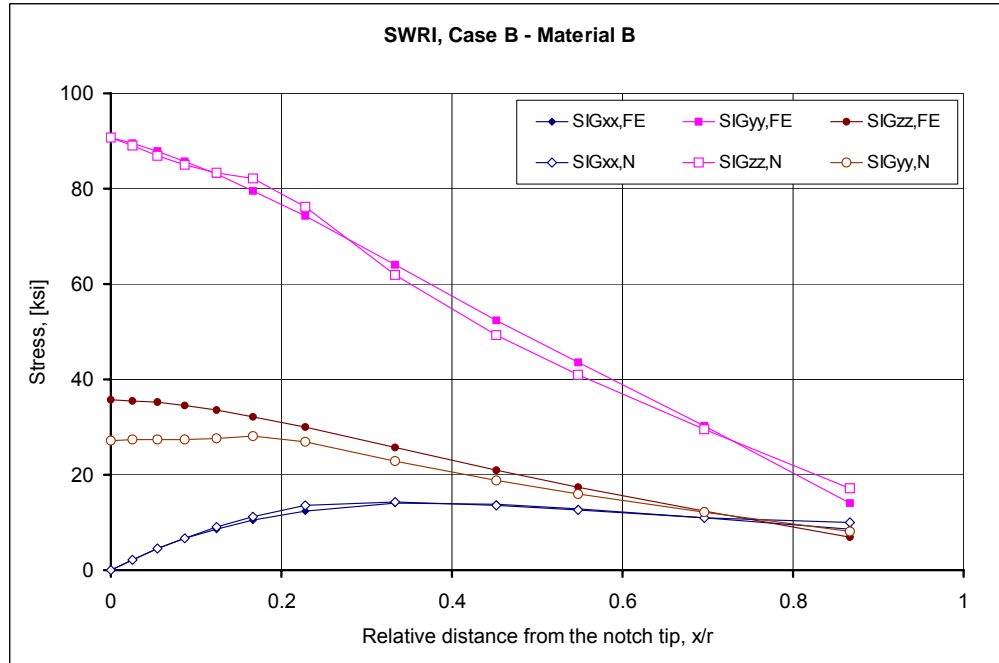
Figure H26. Comparison of SwRI finite element stress data with the Neuber based
estimations; Case B – material B.
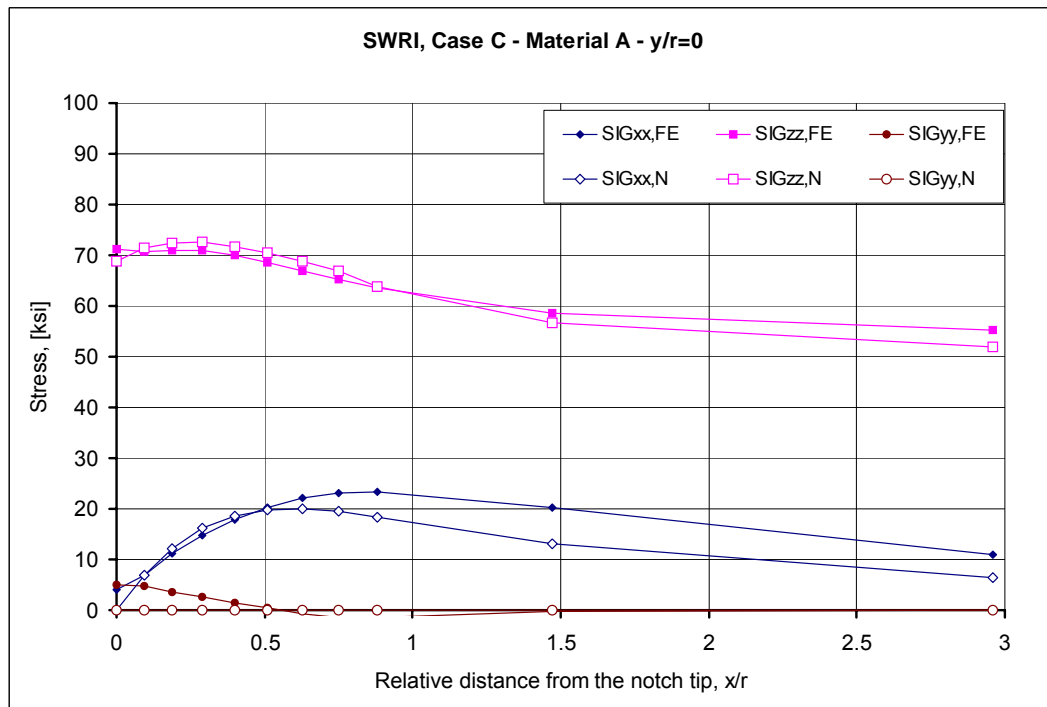
Figure H27. Comparison of SwRI FE stress data with the Neuber based estimations;
Case C – material A, y/r=0.
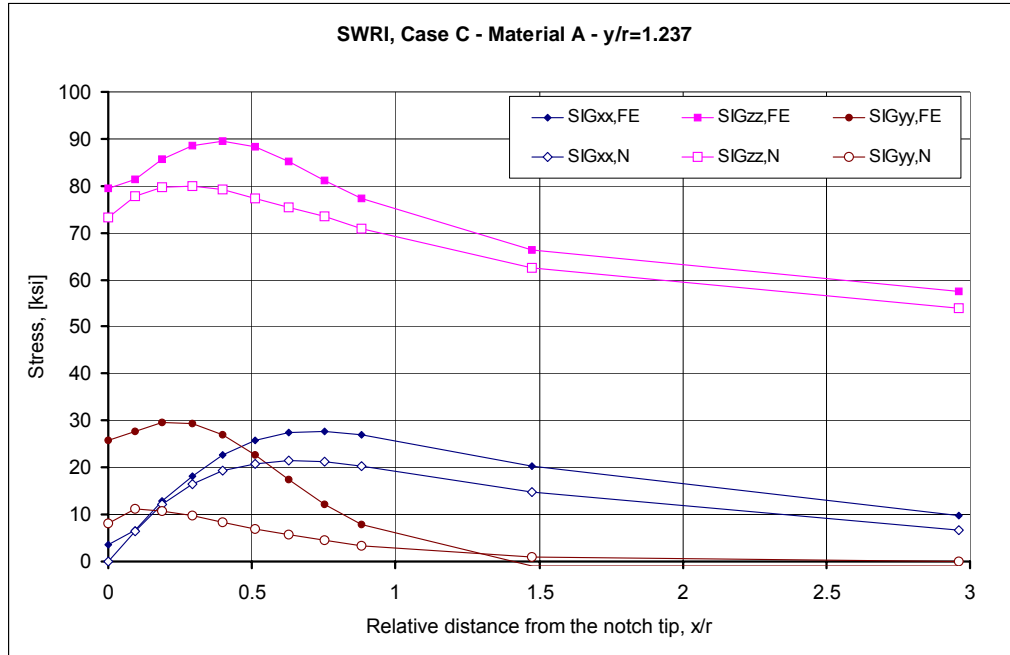
Figure H28.   Comparison of SwRI FE stress data with the Neuber based estimations; Case C – material A, y/r=1.237.
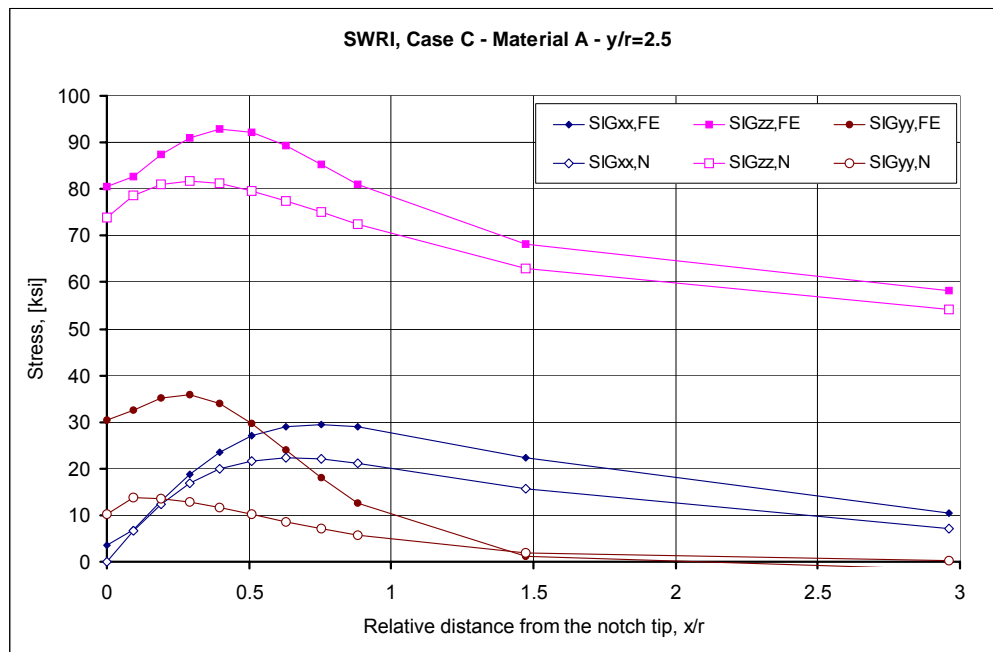
Figure H29.   Comparison of SwRI FE stress data with the Neuber based estimations; Case C – material A, y/r=2.5.
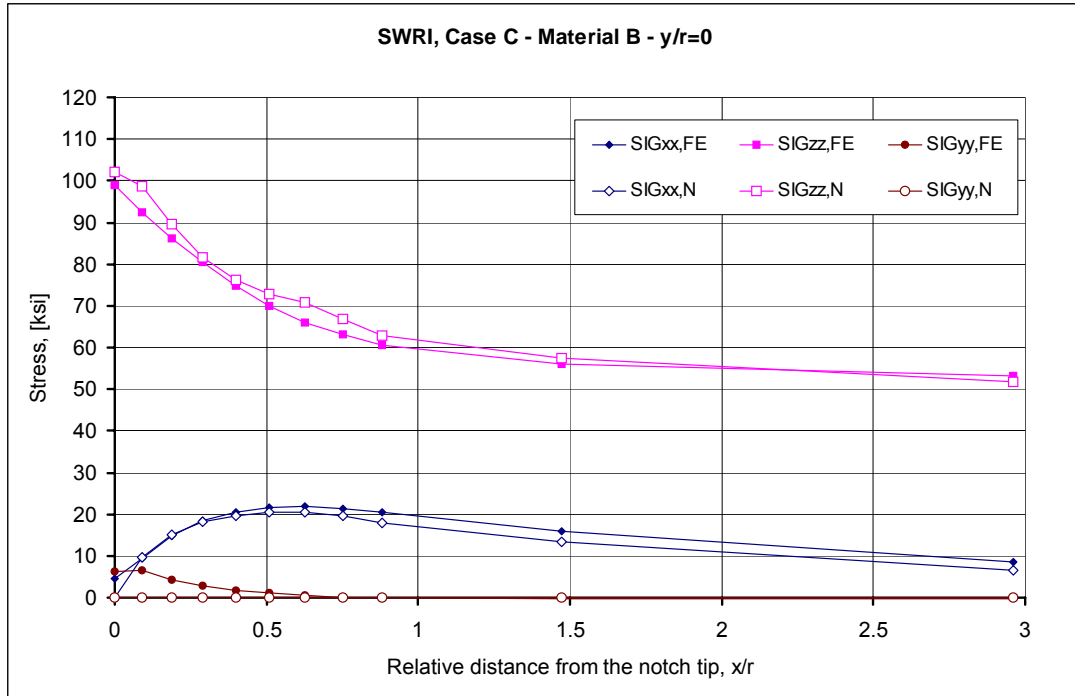
Figure H30. Comparison of SwRI FE stress data with the Neuber based estimations; Case C – material B, y/r=0.
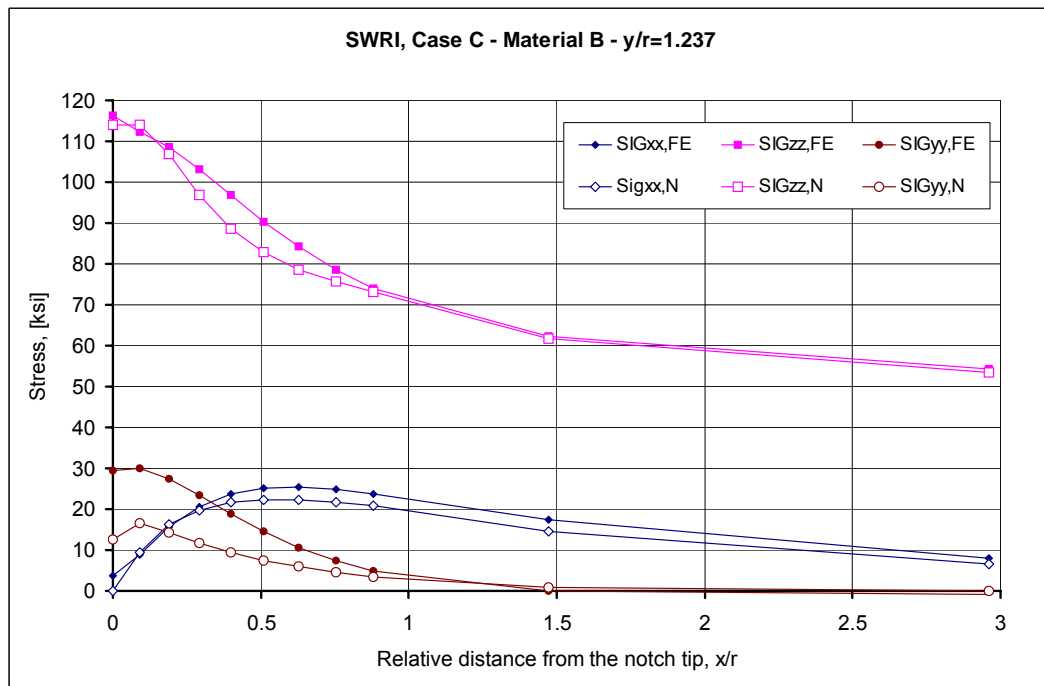
Figure H31. Comparison of SwRI FE stress data with the Neuber based estimations; Case C – material B, y/r=1.237.
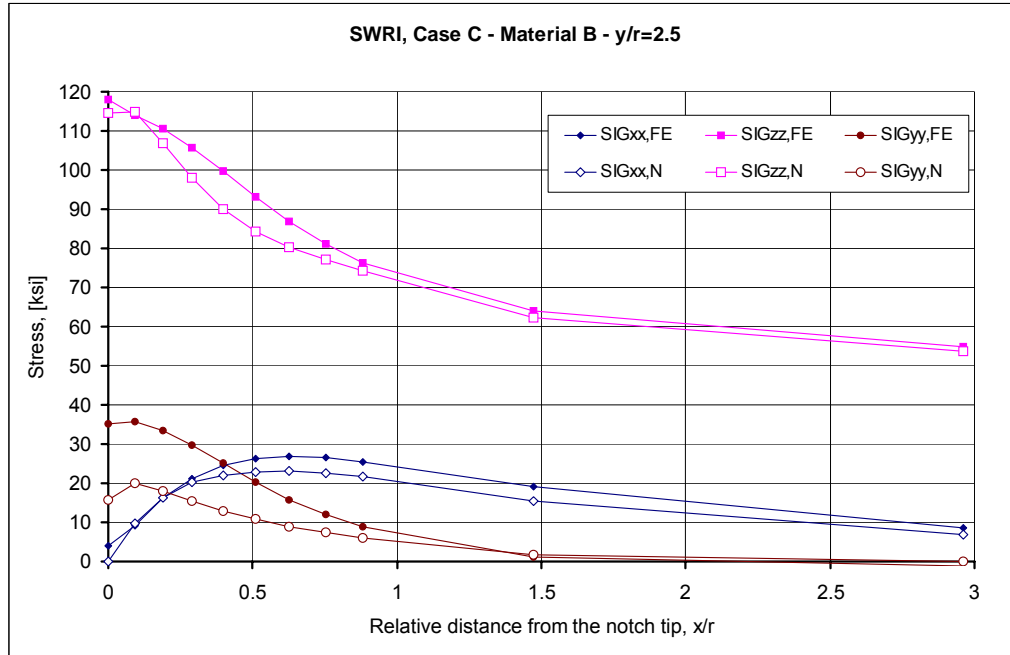
Figure H32.   Comparison of SwRI FE stress data with the Neuber based estimations; Case C – material B, y/r=2.5.

H.7.5   The Geometry of NDSU Notched Components

The data supplied by NDSU also concerned a three dimensional analysis of plate with a circular notch (Figure H33) but subjected to cyclic axial loading (loading and unloading). The cylindrical specimen shown in Figure H33 was subjected to two loading modes, i.e. torsion and axial load. Both proportional and non-proportional cyclic loading paths were studied and all the stress and strain components were made available for comparisons.

H.7.6   The Material Stress-Strain Curve Used in the NDSU Analyses

The finite element analyses of NDSU were conducted in Ansys using a multilinear kinematic hardening rule in conjunction with the cyclic stress-strain curve for Ti-6Al-4V at room temperature. The original cyclic stress-strain curve used in the FE analysis is shown in Figure H34. The analogous piecewise stress-strain curve used in the Neuber based analysis is shown in Figure H35.
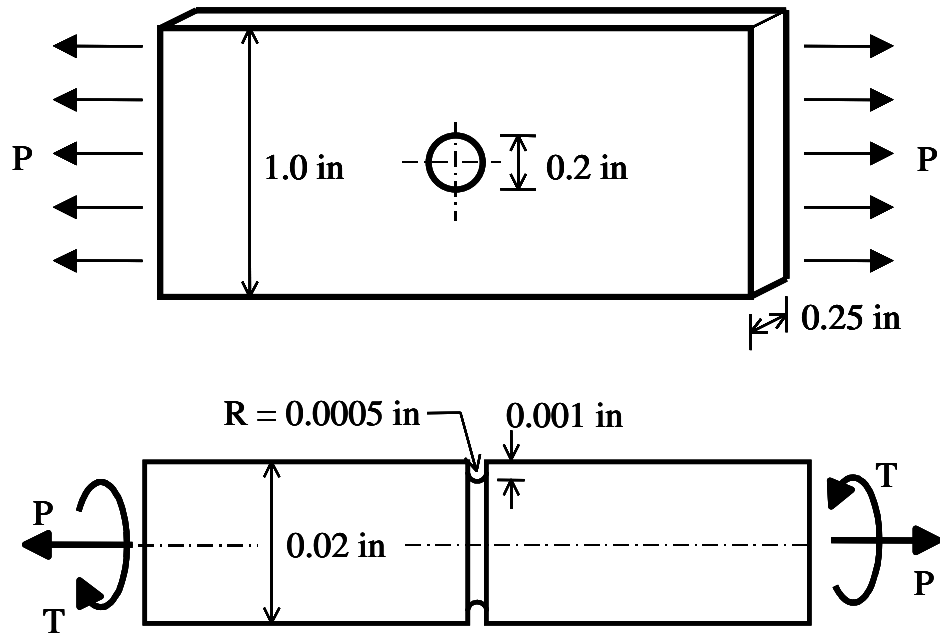
Figure H33. The NDSU three-dimensional (3-D) finite element models.
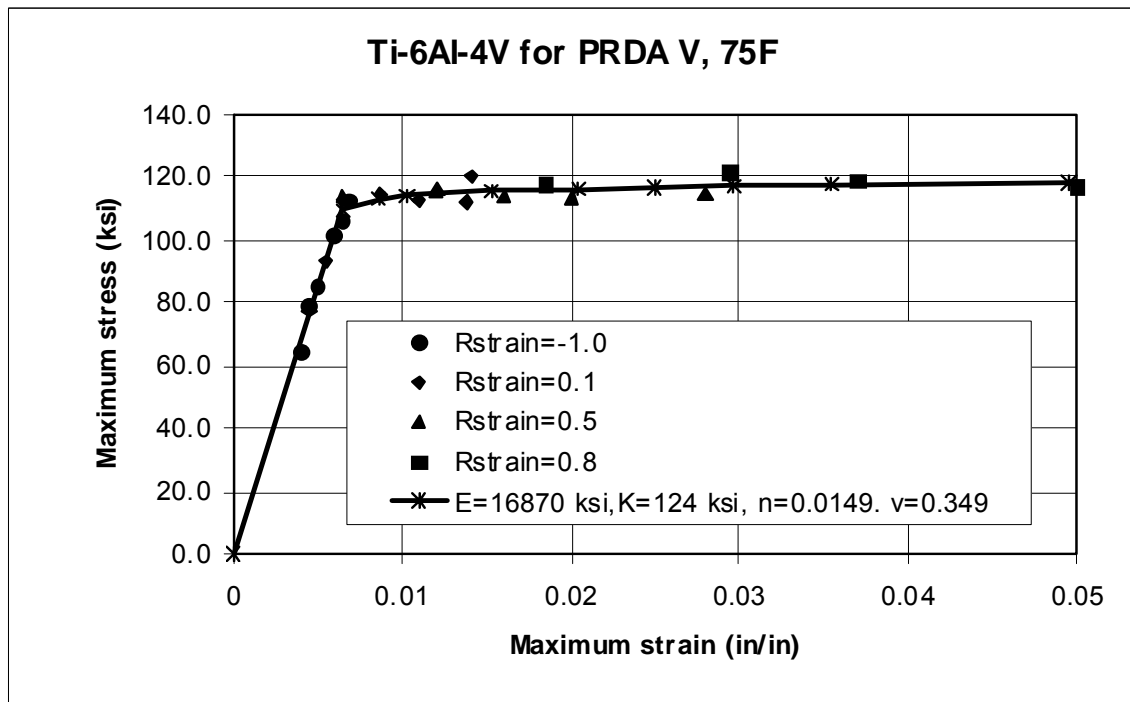
Figure H34. The original material stress-strain curve used in the NDSU finite element (FE) analyses.

NDSU material curve MatTi6
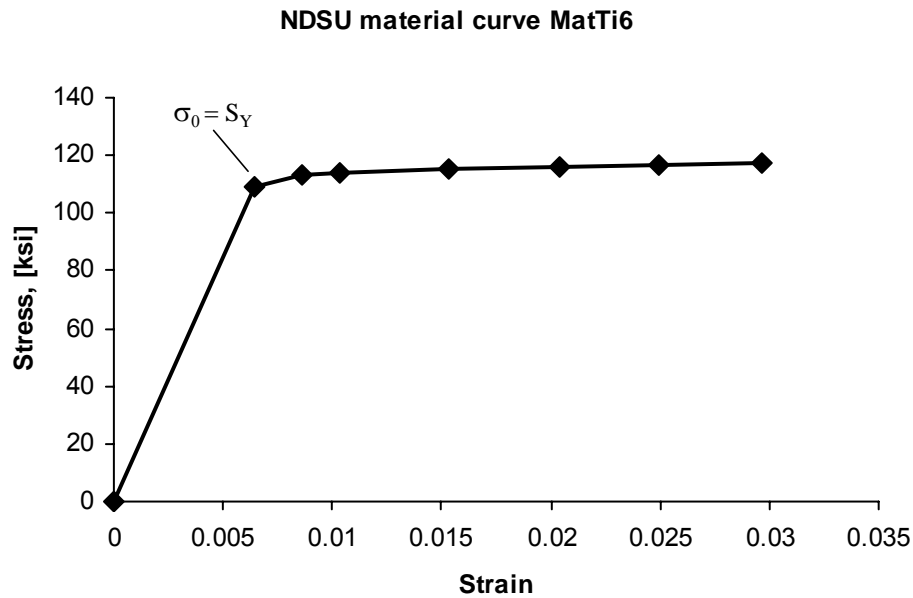
Fig. 35. The piecewise stress-strain material curve used in the Neuber based analyses

Figure H35. The piecewise stress-strain material curve used in the Neuber based analyses.

H.7.7 The NDSU Loading Paths

The stress path for the plate with the circular hole was simple loading from zero to maximum load and unloading to zero (zero-maximum-zero). The comparison was carried out for stresses and strains corresponding to the maximum and the minimum load (Figure H36). In the case of the non-proportional box type loading path the stresses and strains were obtained for loads corresponding to the values at each corner of the box load path denoted as Point 1, Point 2, Point 3 and Point 4.

H.7.8 The Comparisons of the SWRI - FE and the Neuber-Based Near Notch Tip Stresses

The comparison of results generated by the NDSU and those obtained from the Neuber based NPC30 code is shown in Figures H37-H69. The NDSU-FE and the Neuber based stress component values are close to each other even in the case of the non-proportional cyclic load path. The data used in the comparisons was that one corresponding to the 10-th cycle of cyclic loads path. The strains are usually over-predicted by the proposed methodology as it should be expected in the case of the Neuber type formulation.
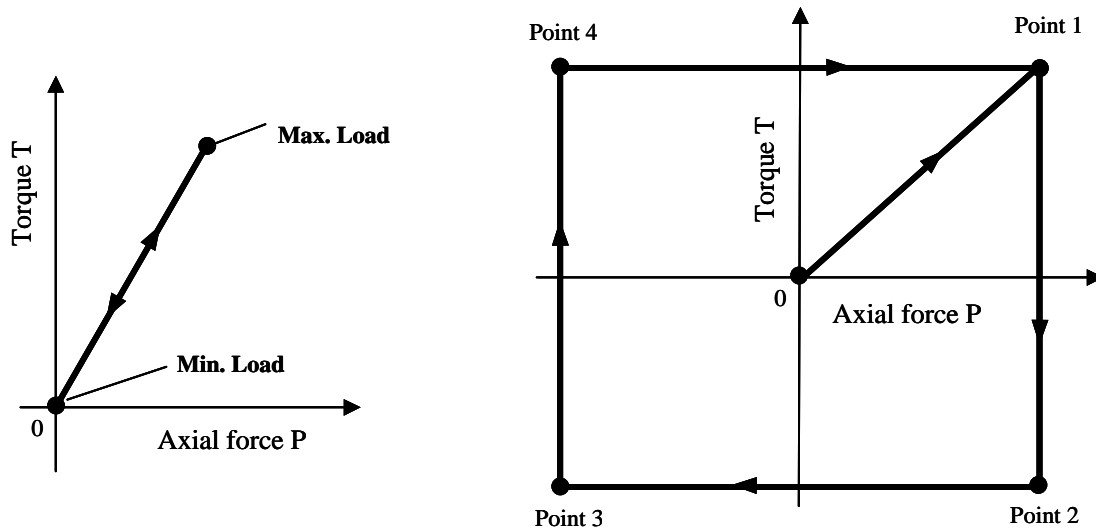
Figure H36. The proportional and the box-type non-proportional multiaxial cyclic loading paths analyzed by the NDSU.
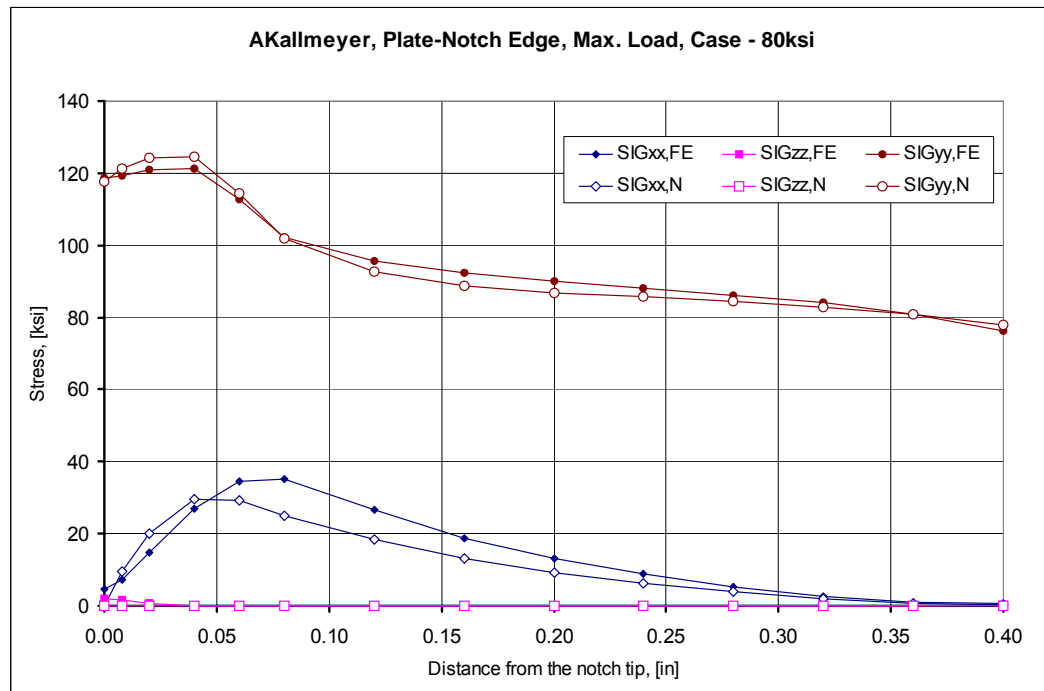
Figure H37. Comparison of stresses in plate with circular hole; in the plane coinciding with the side free surface; at max. load.

H-50
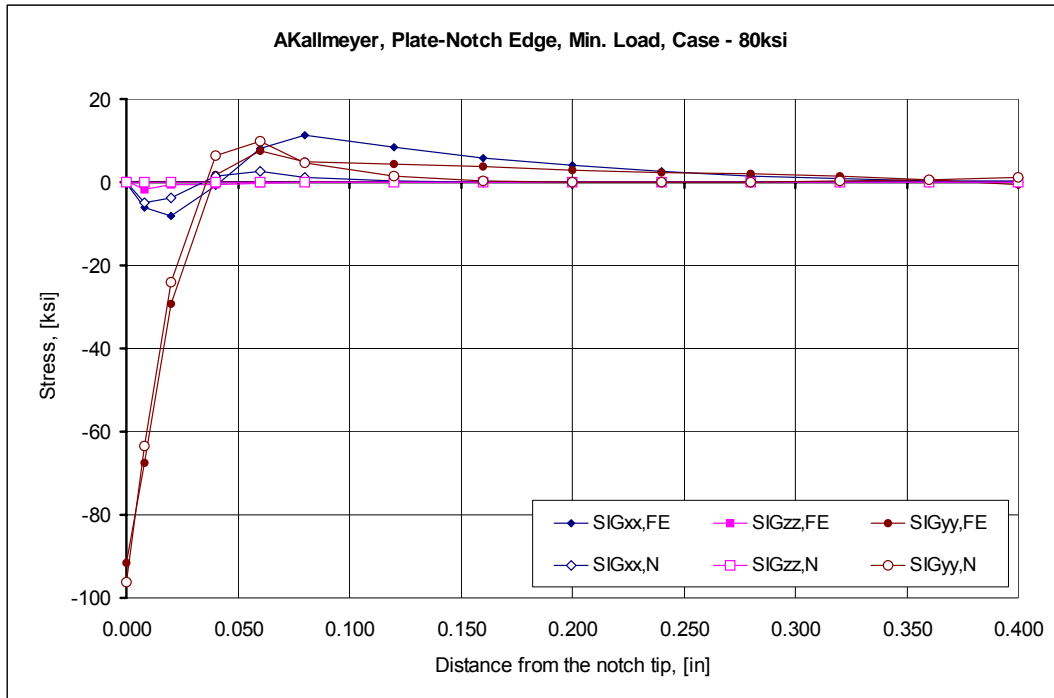
Figure H38. Comparison of strains in the plate with circular hole; in the plane
coinciding with the side free surface; at max load.
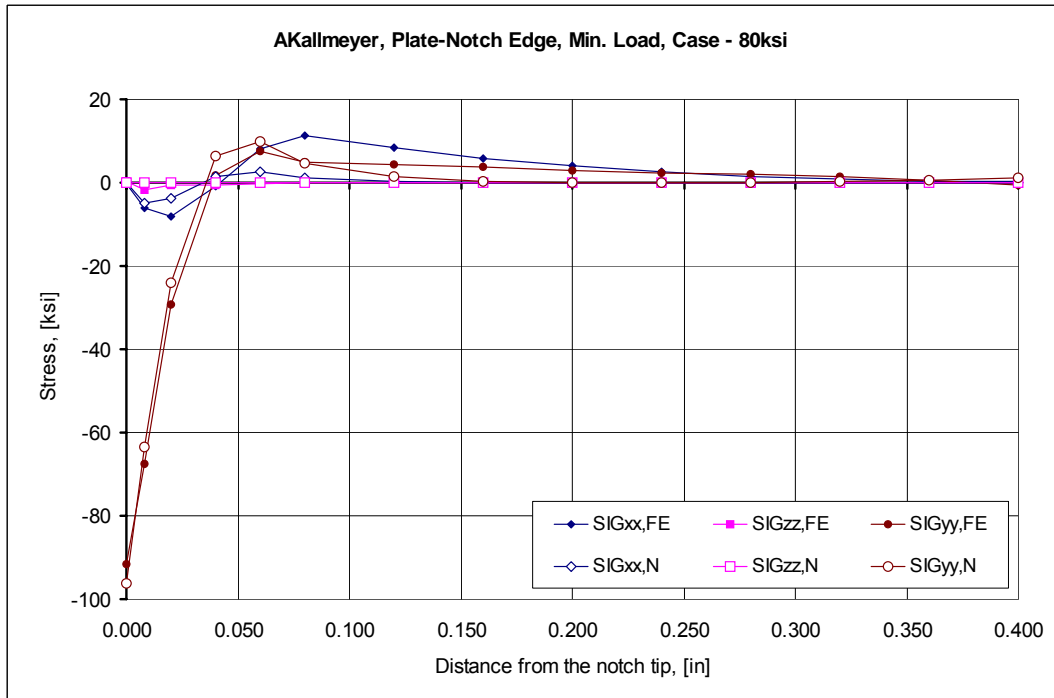
Figure H39. Comparison of stresses in the plate with circular hole; in the plane
coinciding with the side free surface; at min. load.

H-51
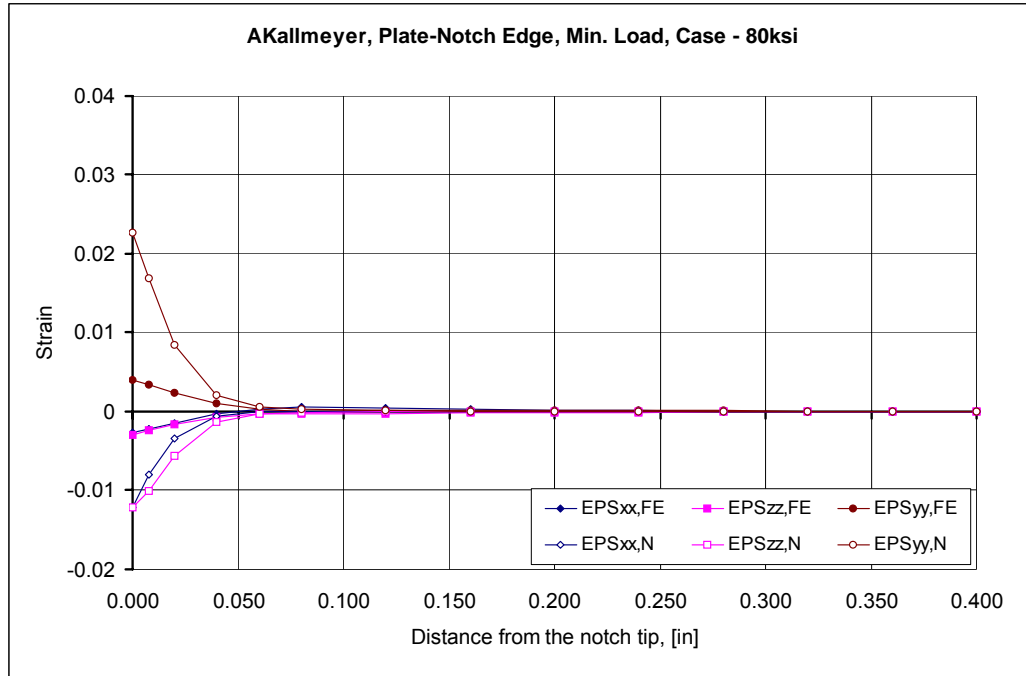
Figure H40. Comparison of strains in the plate with circular hole; in the plane coinciding with the side free surface; at min. load.
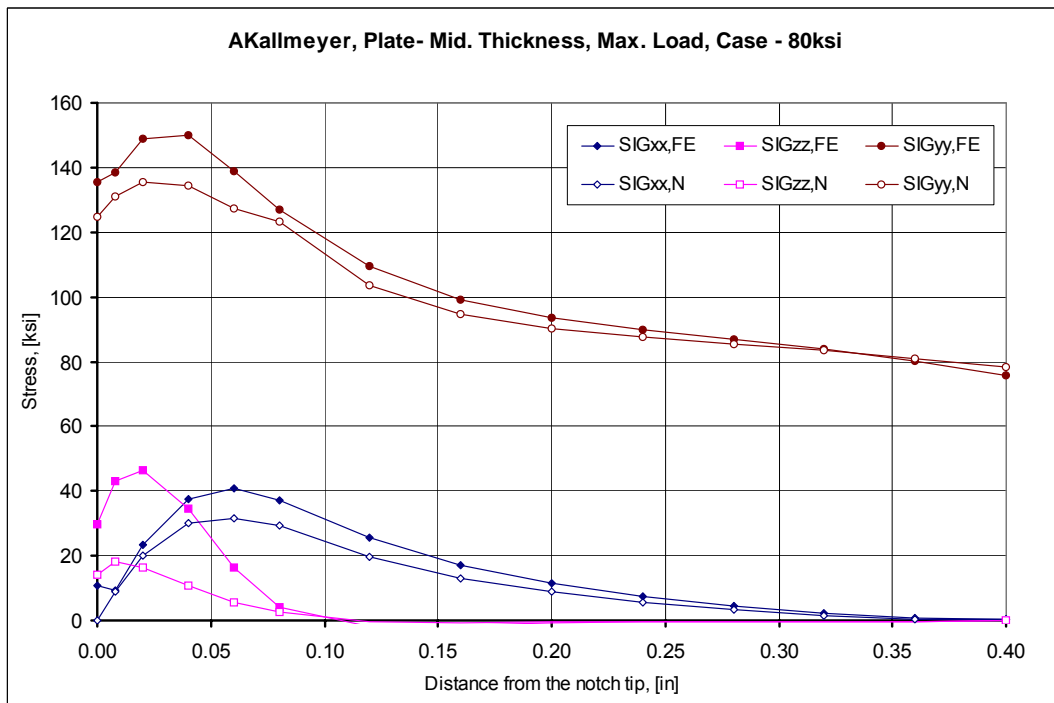
Figure H41. Comparison of stresses in the plate with circular hole; in the mid-thickness plane; at max load.
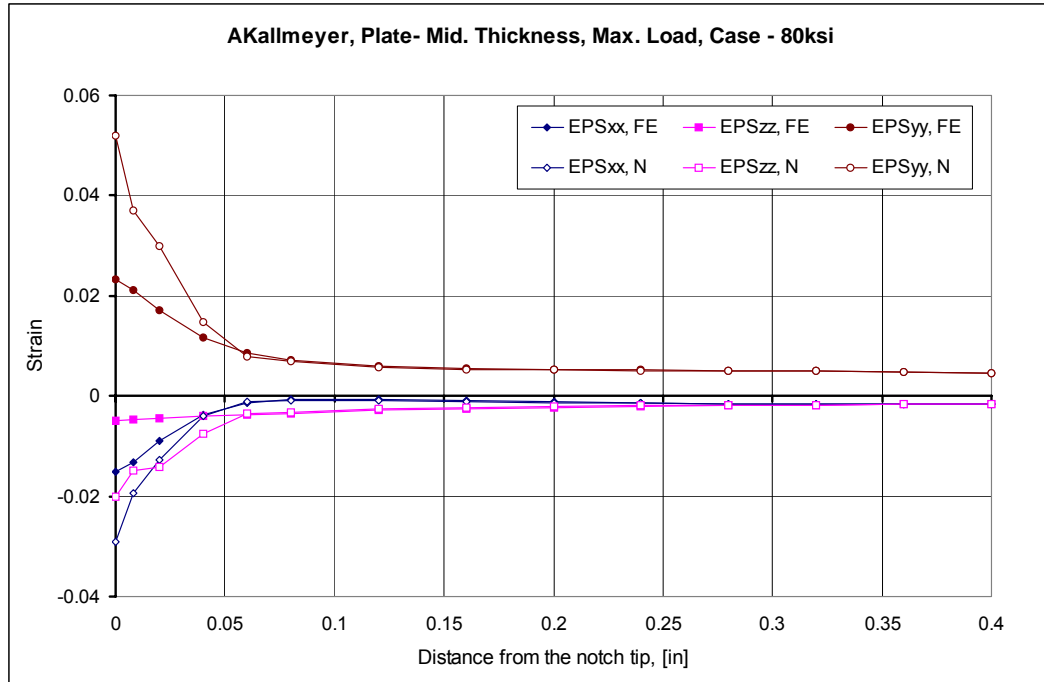
Figure H42. Comparison of strains in the plate with circular hole; in the mid-thickness plane; at max load.
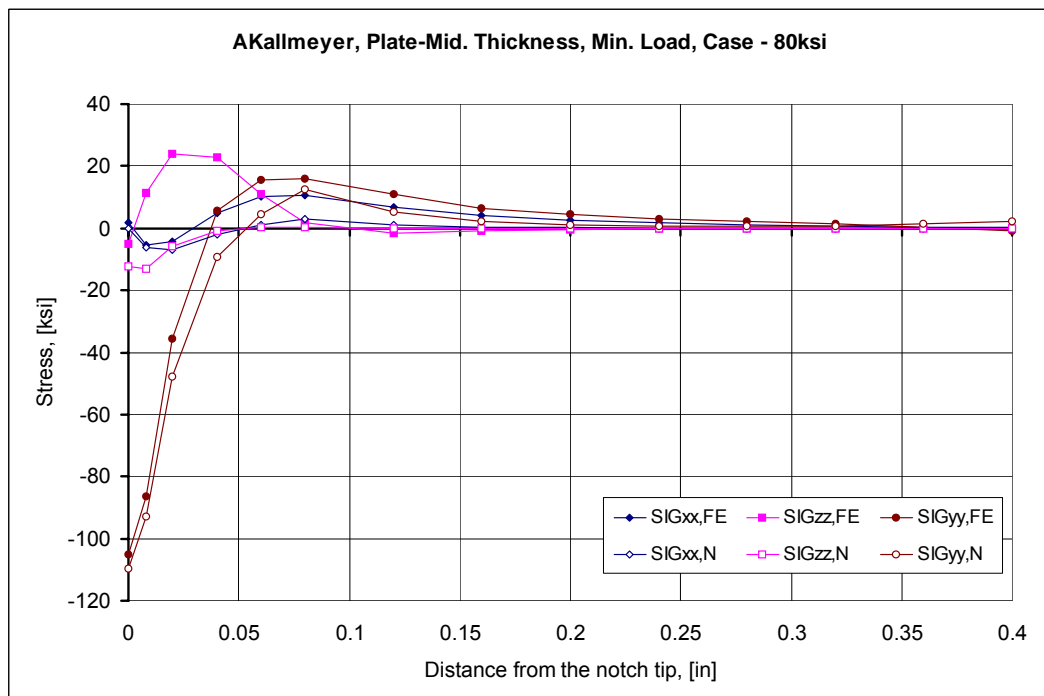
Figure H43. Comparison of stresses in the plate with circular hole; in the mid-thickness plane; at min. load.
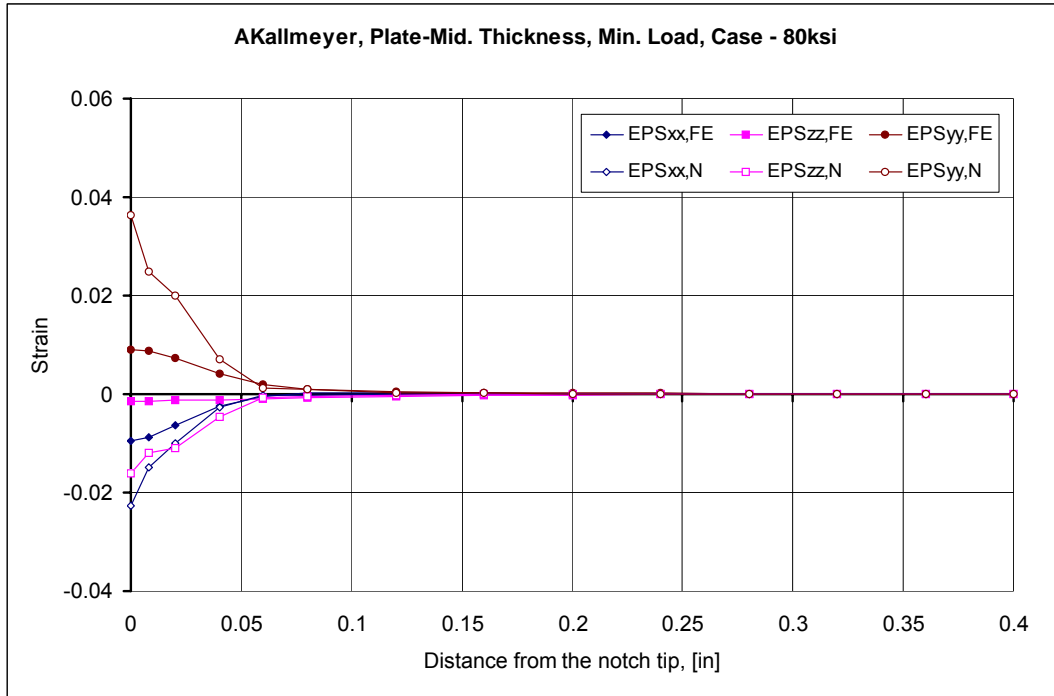
Figure H44. Comparison of strains in the plate with circular hole; in the mid-thickness plane; at min. load.
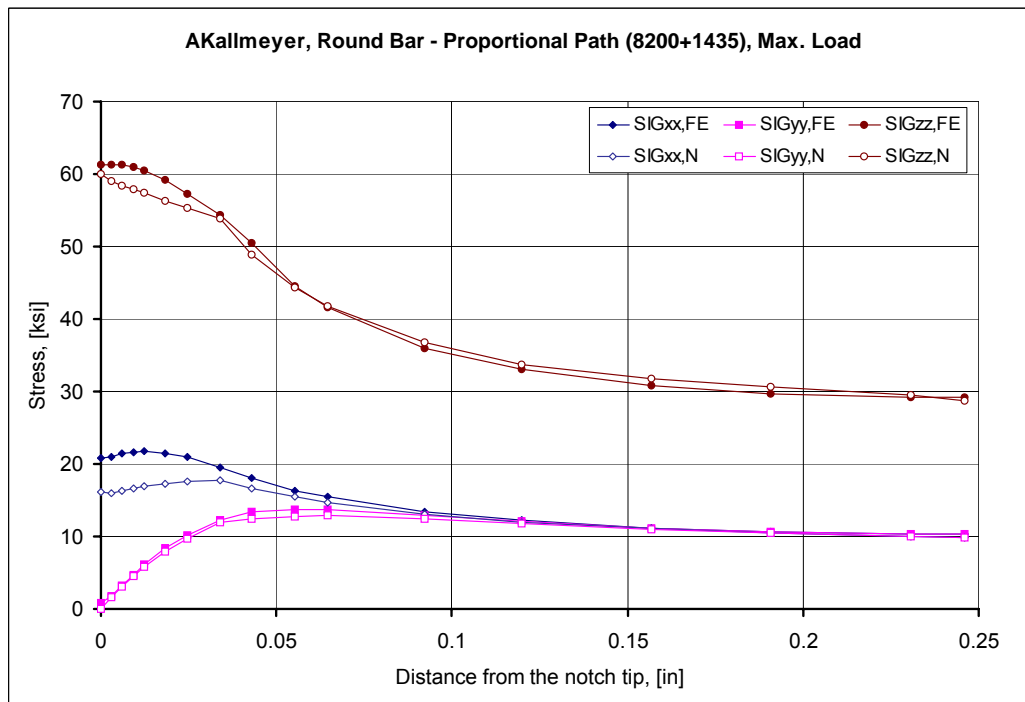
Figure H45. Comparison of normal stresses in the cylindrical bar; at maximum of proportional loading.
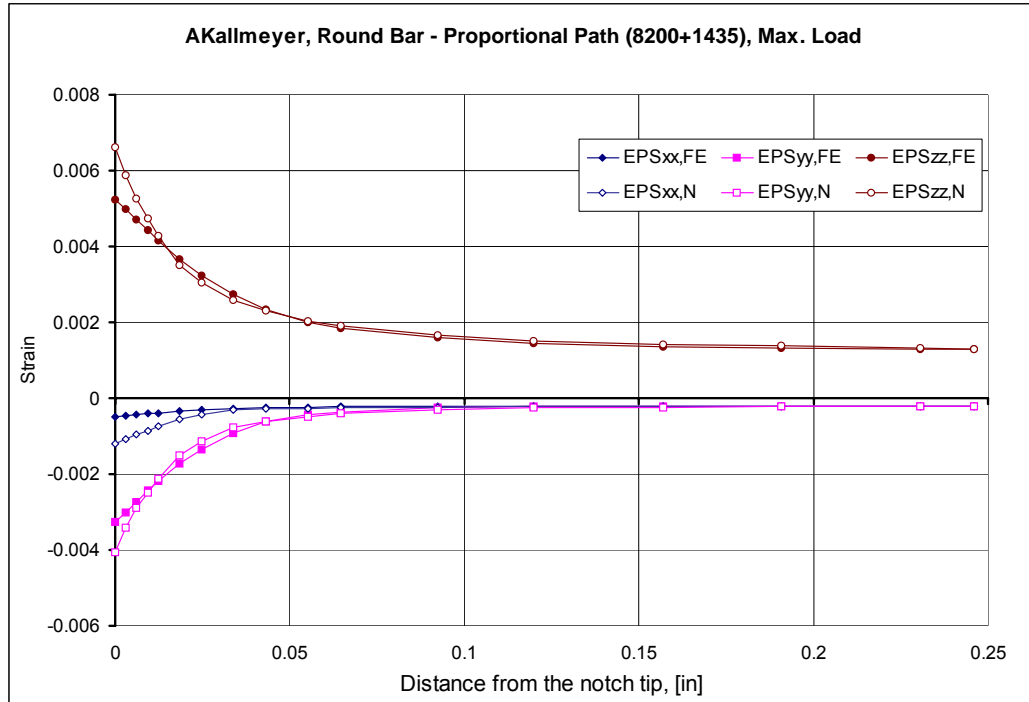
Figure H46. Comparison of normal strains in the cylindrical bar; at maximum of proportional loading.
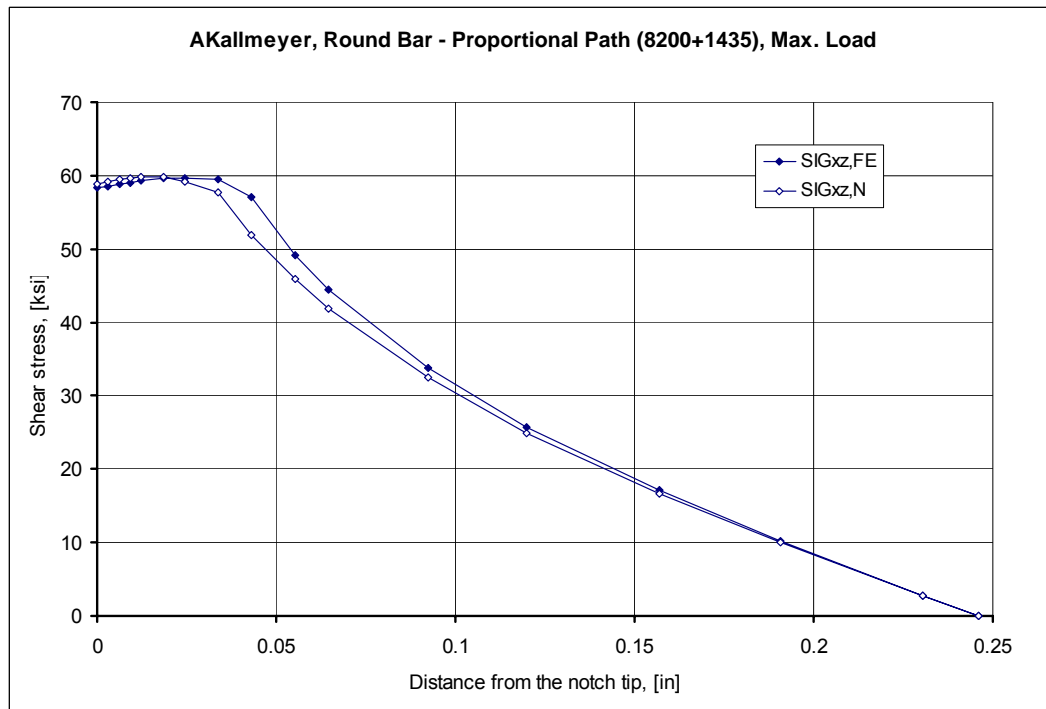
Figure H47. Comparison of shear stresses in the cylindrical bar; at maximum of proportional loading.
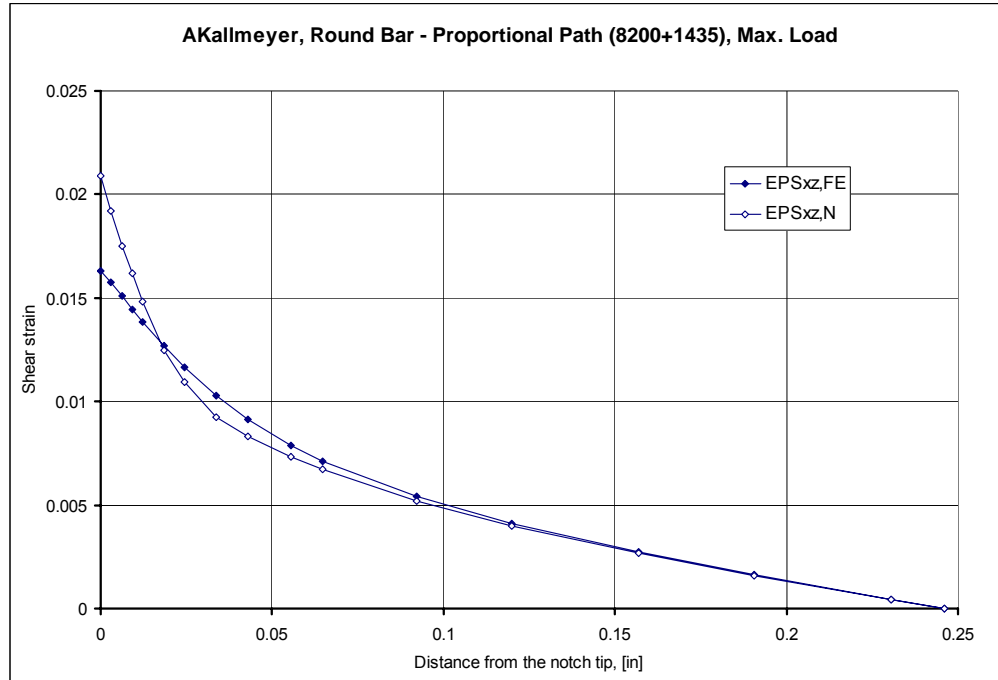
Figure H48. Comparison of shear strains in the cylindrical bar; at maximum of proportional loading.
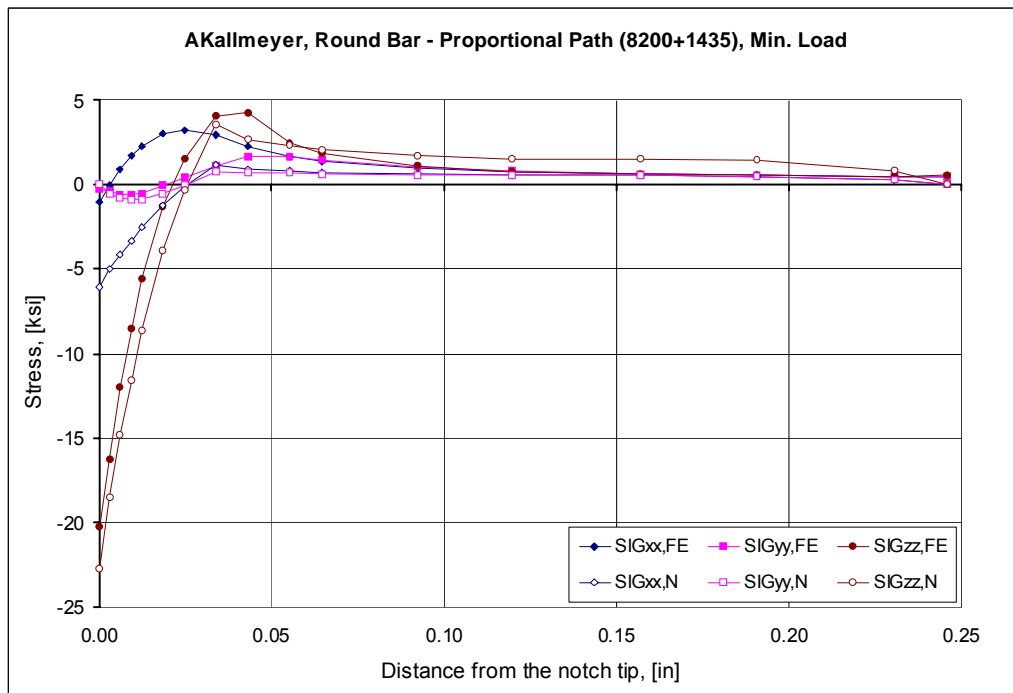
Figure H49. Comparison of normal stresses in the cylindrical bar; at minimum of proportional loading.
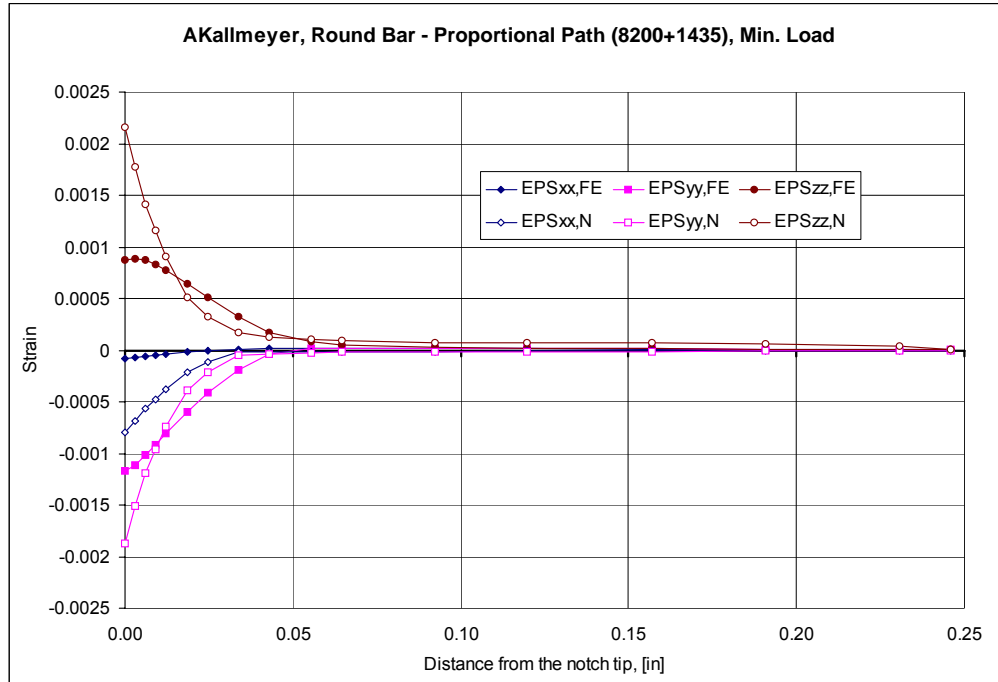
Figure H50. Comparison of normal strains in the cylindrical bar; at minimum of
proportional loading.
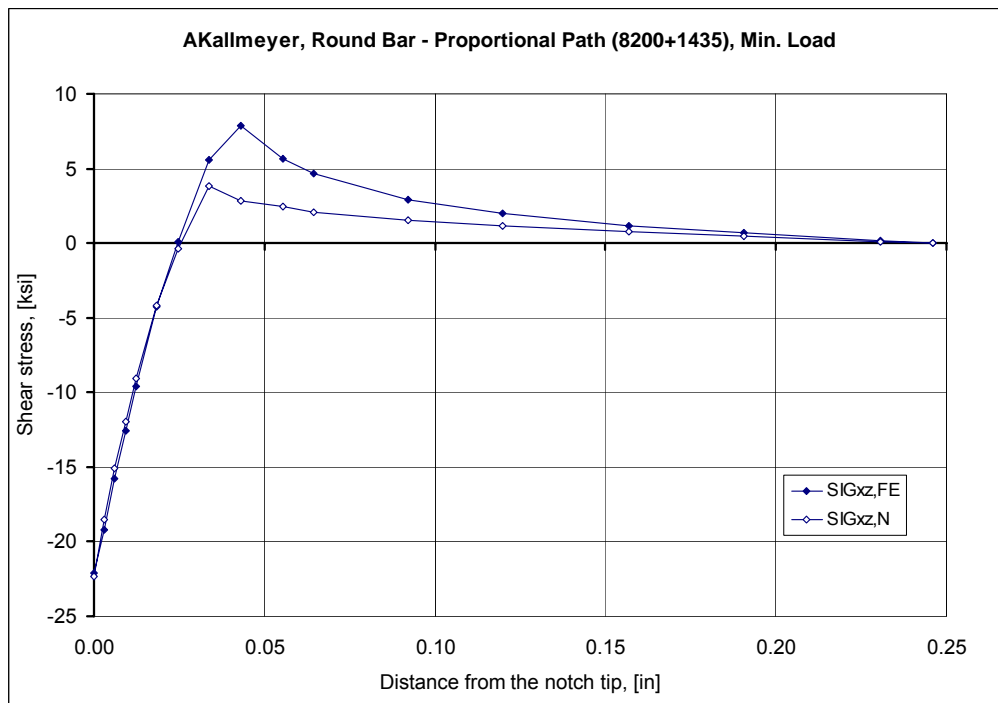
Figure H51. Comparison of shear stresses in the cylindrical bar; at minimum of
proportional loading.
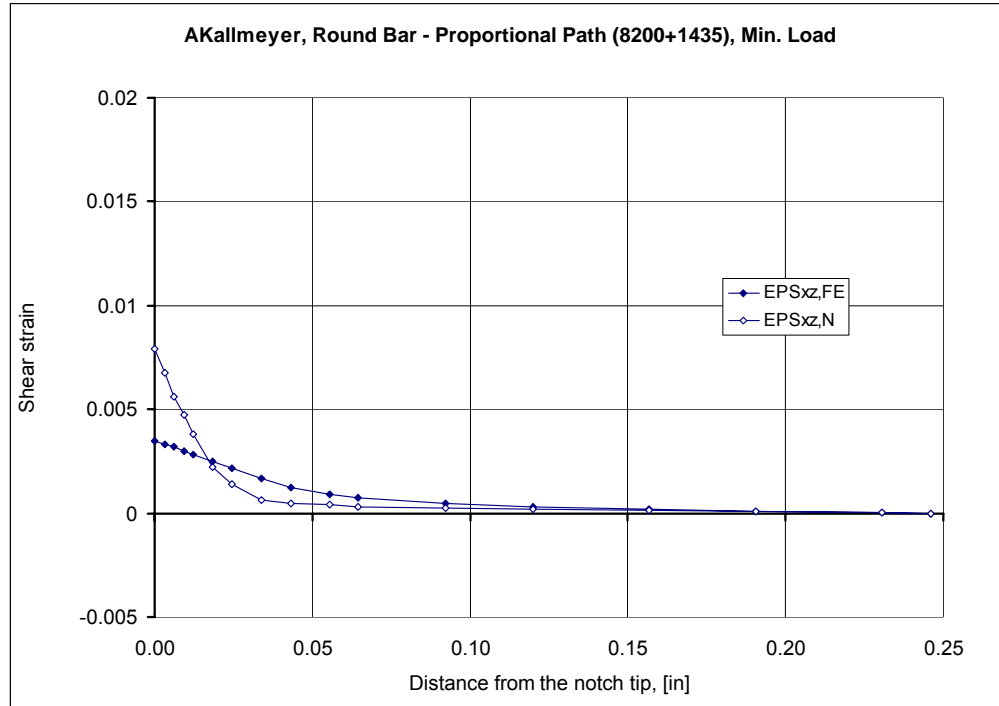
Figure H52. Comparison of shear strains in the cylindrical bar; at minimum of proportional loading.
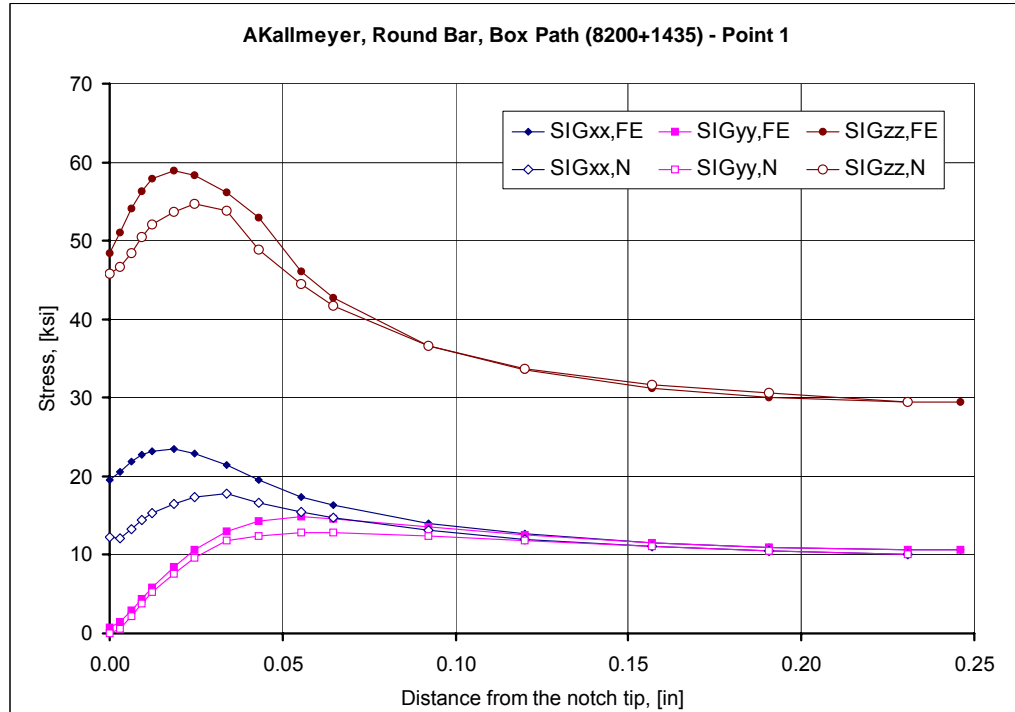
Figure H53. Comparison of normal stresses in the cylindrical bar; at Point 1 of the box type loading path.
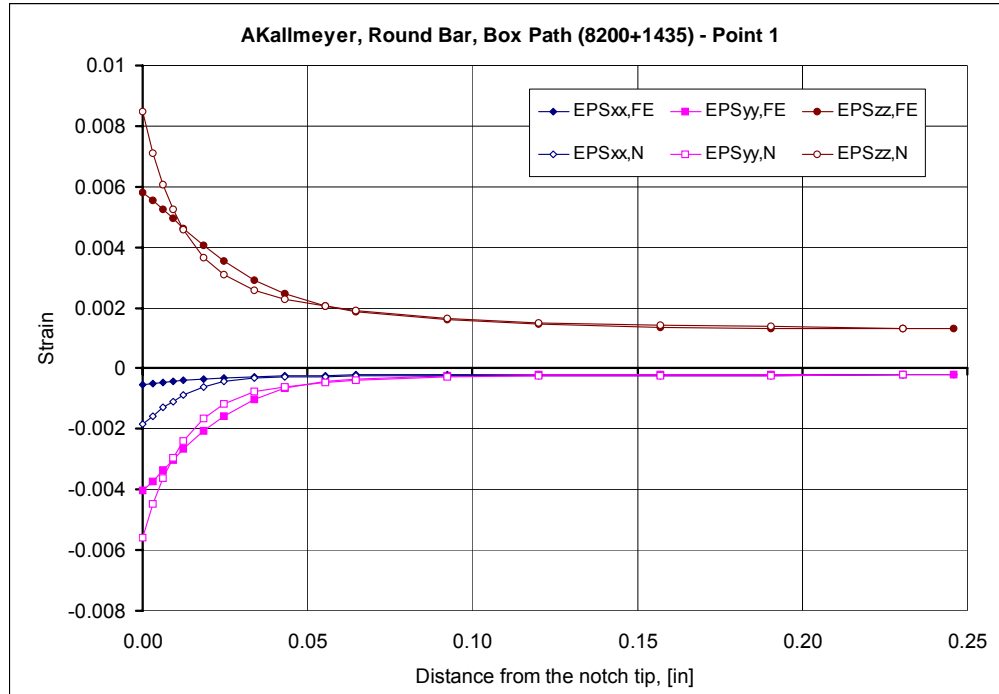
Figure H54. Comparison of normal strains in the cylindrical bar; at Point 1 of the box type loading path.
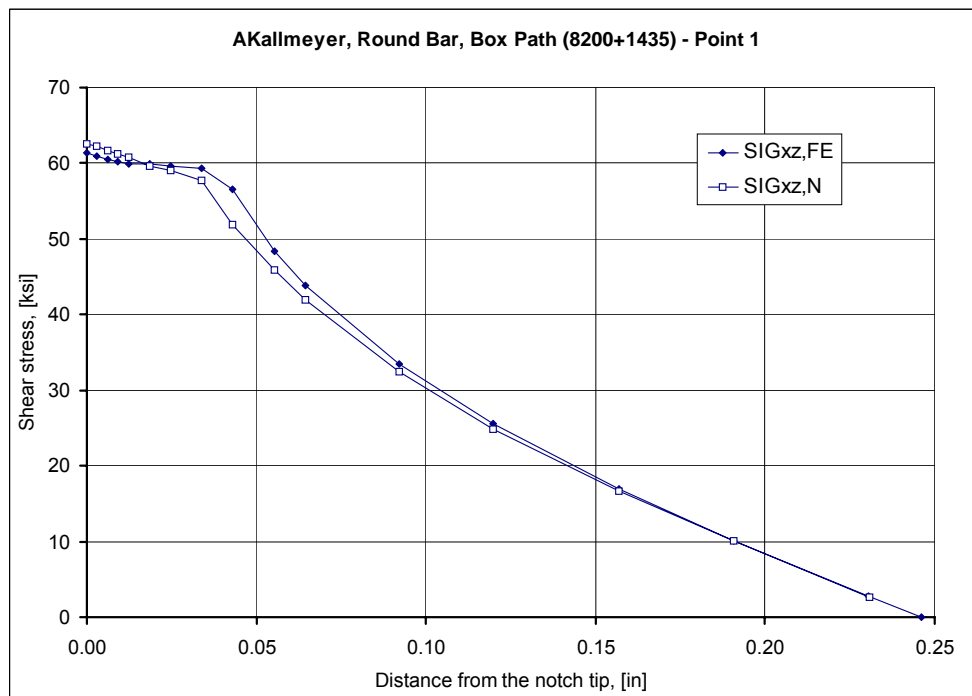
Figure H55. Comparison of shear stresses in the cylindrical bar; at Point 1 of the box type loading path.
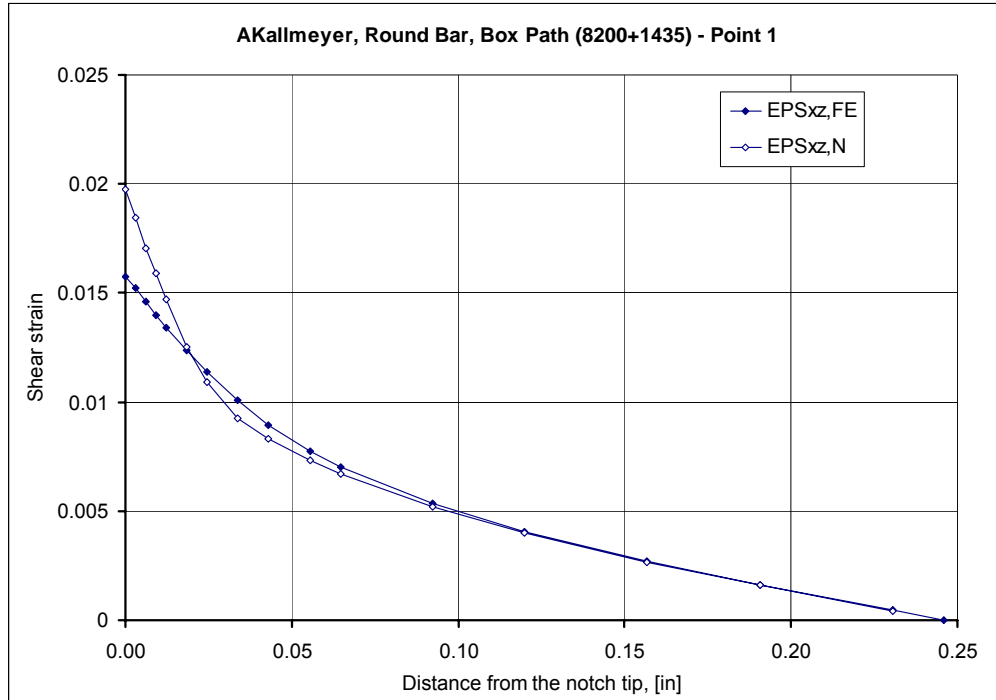
Figure H56. Comparison of shear strains in the cylindrical bar; at Point 1 of the box type loading path.
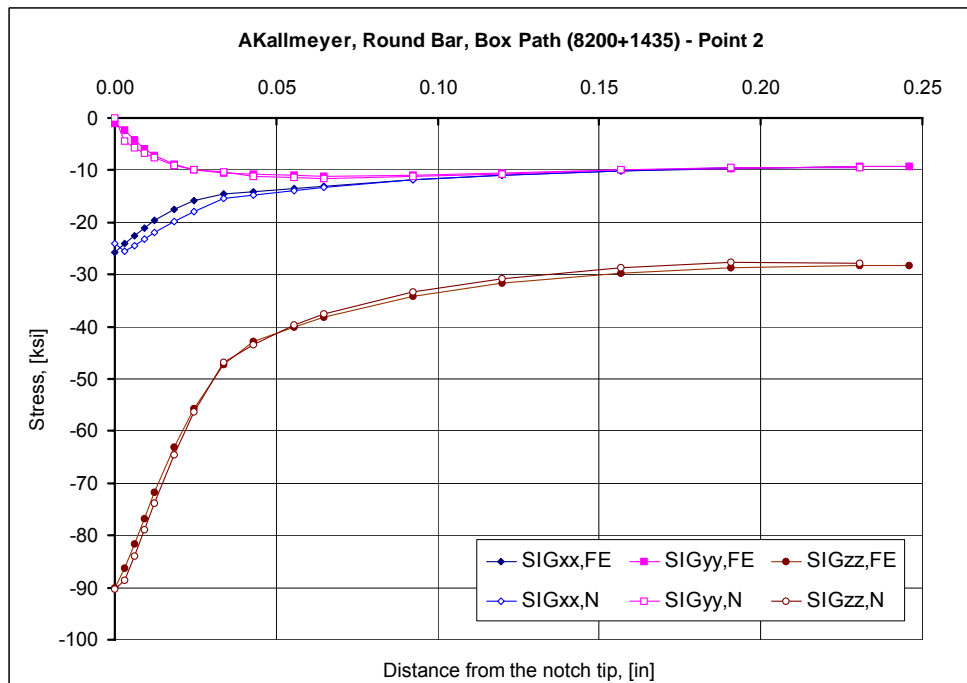
Figure H57. Comparison of normal stresses in the cylindrical bar; at Point 2 of the box type loading path.
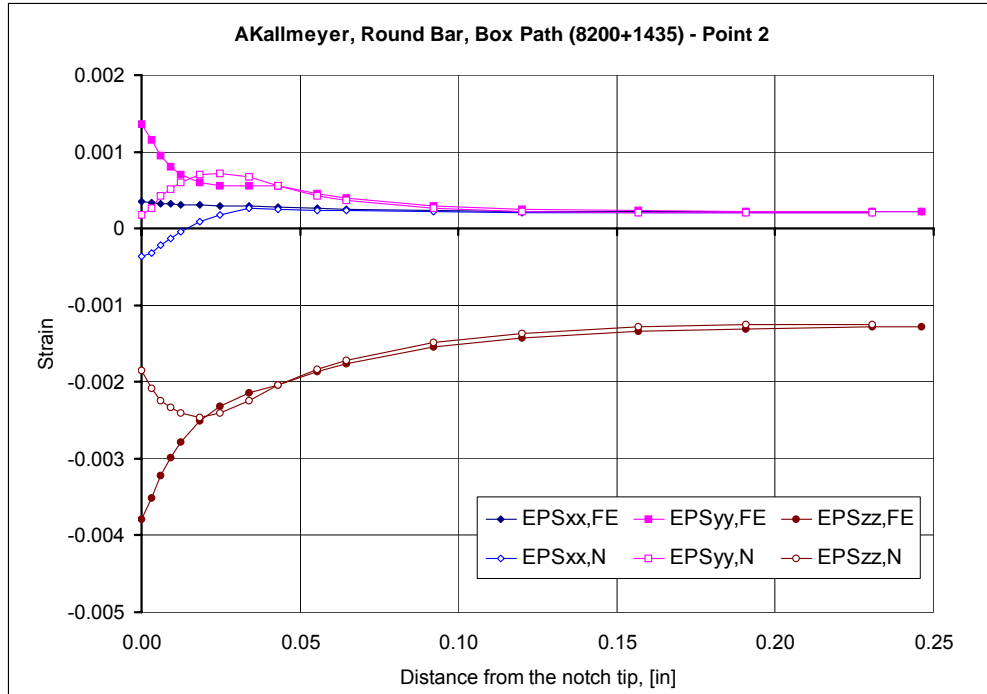
Figure H58. Comparison of normal strains in the cylindrical bar; at Point 2 of
the box type loading path.
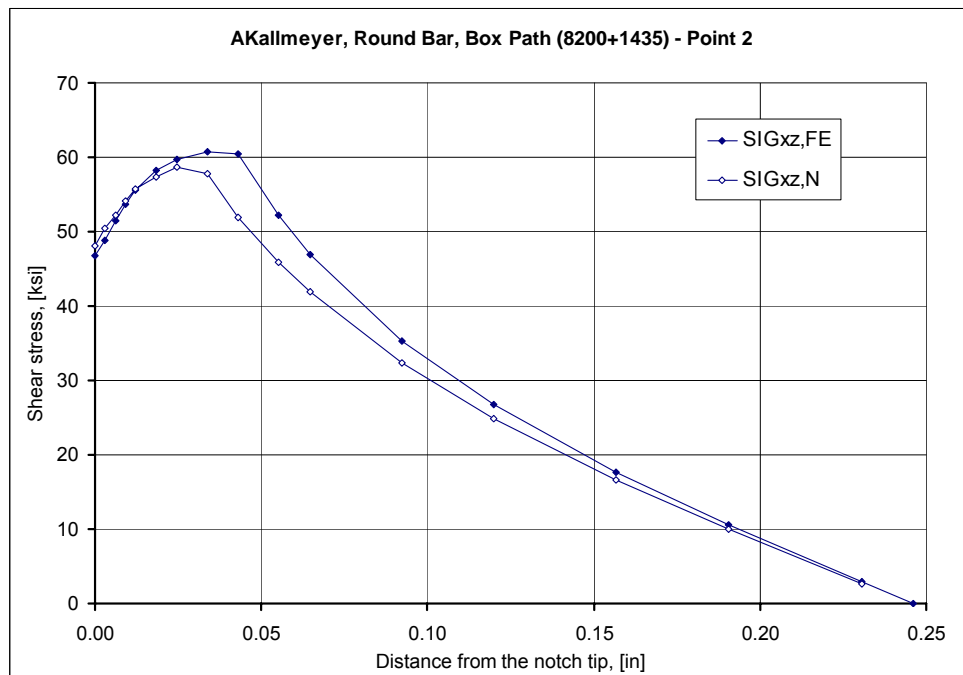
Figure H59. Comparison of shear stresses in the cylindrical bar; at Point 2 of
the box type loading path.

H-61
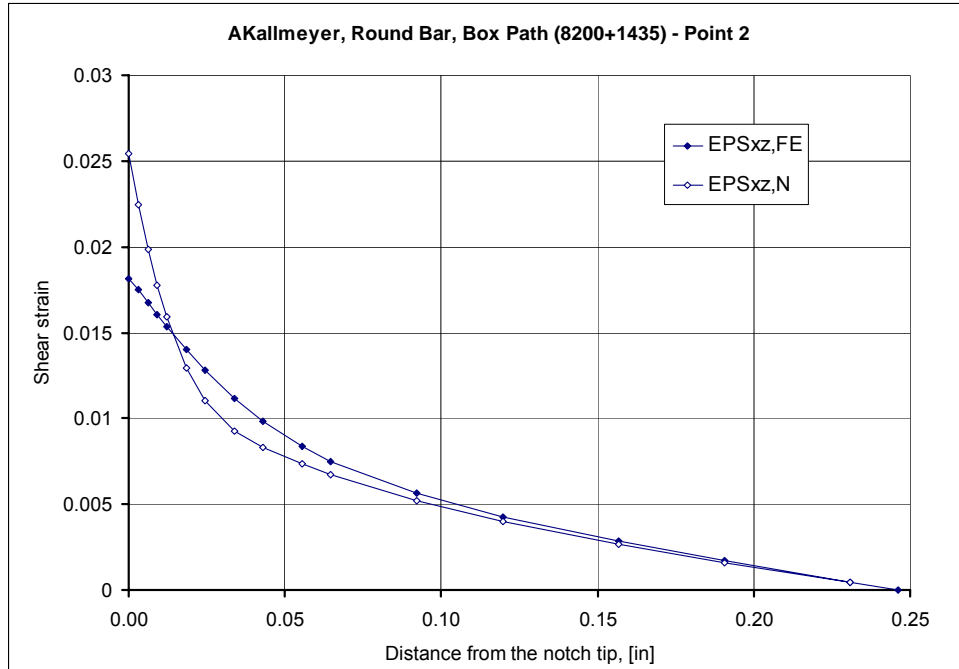
Figure H60. Comparison of shear strains in the cylindrical bar; at Point 2 of the box type loading path.
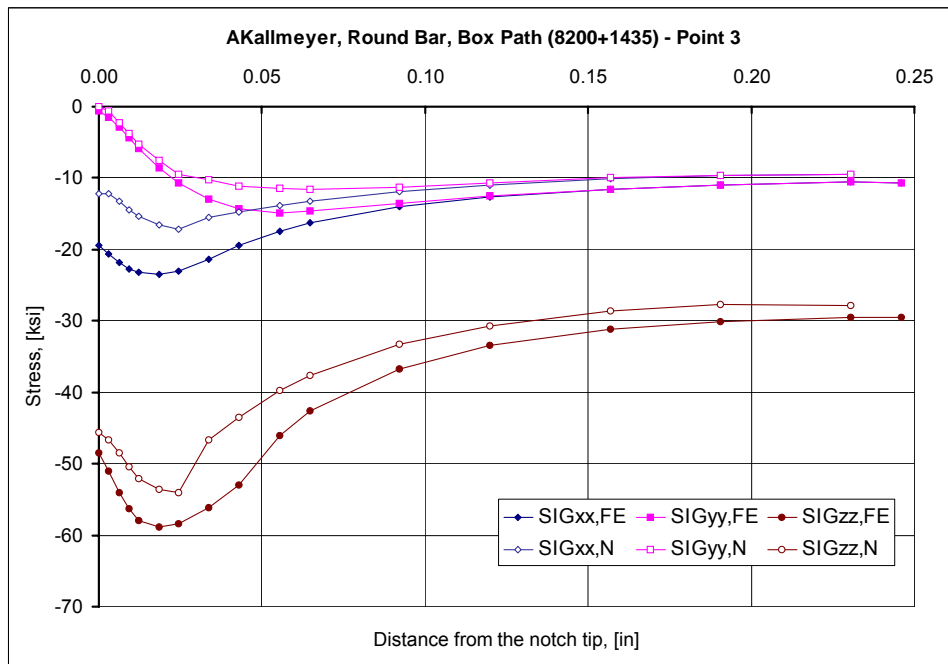
Figure H61. Comparison of normal stresses in the cylindrical bar; at Point 3 of the box type loading path.
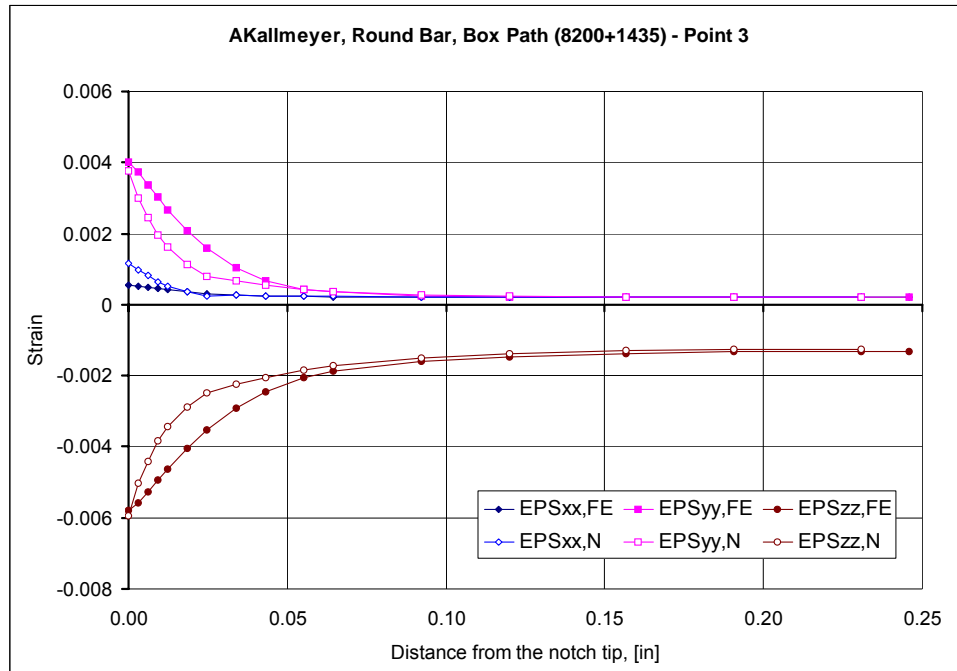
Figure H62. Comparison of normal strains in the cylindrical bar; at Point 3 of the box type loading path.
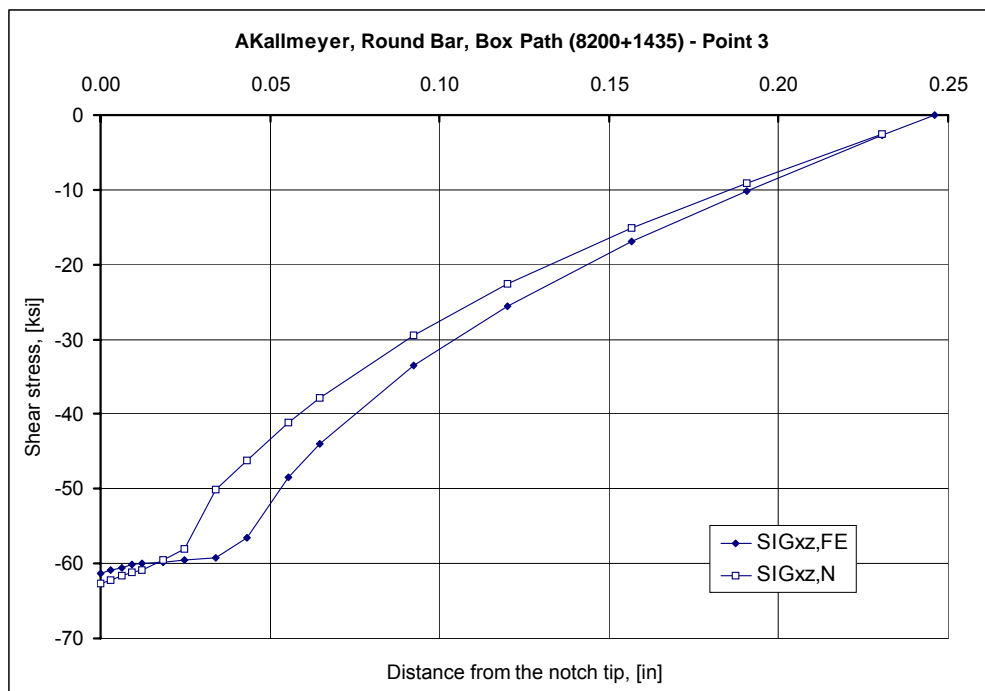
Figure H63. Comparison of shear stresses in the cylindrical bar; at Point 3 of the box type loading path.

H-63
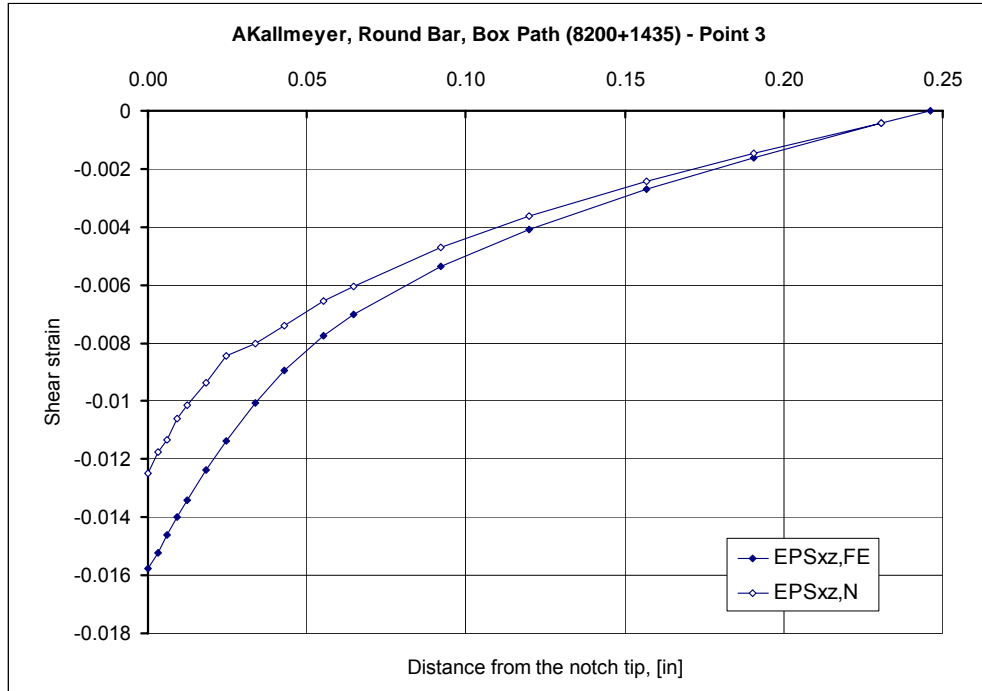
Figure H64. Comparison of shear strains in the cylindrical bar; at Point 3 of the box type loading path.
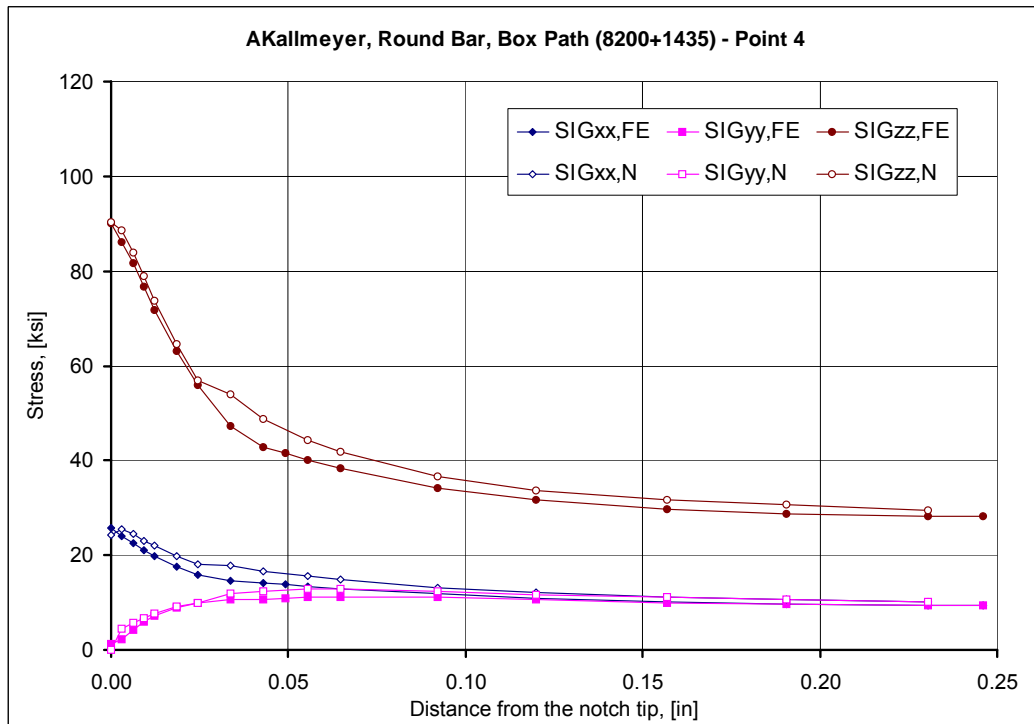
Figure H65. Comparison of normal stresses in the cylindrical bar; at Point 4 of the box type loading path.

H-64
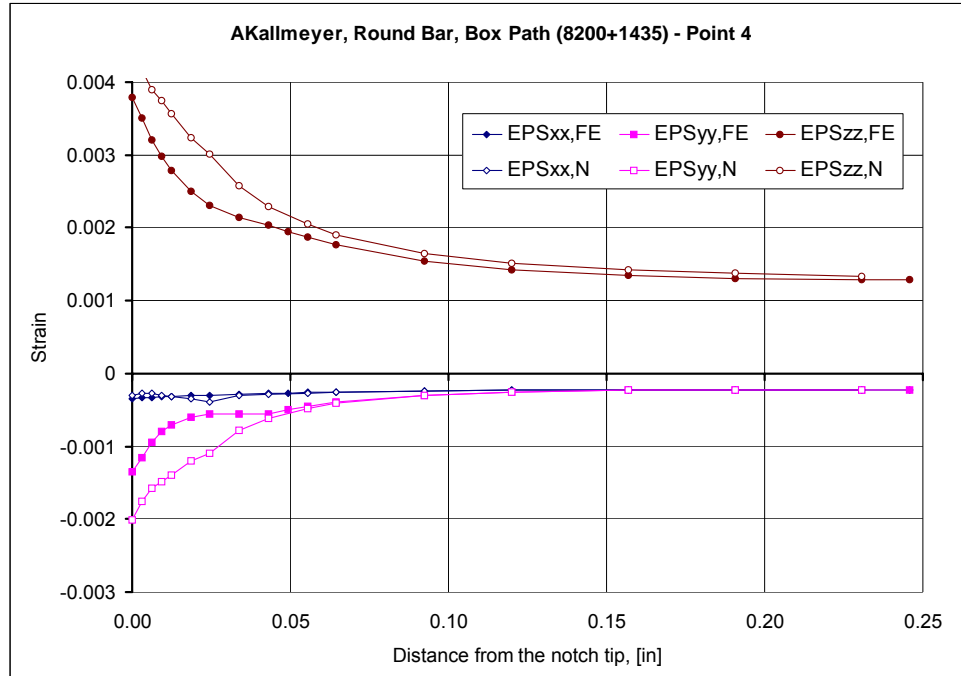
Figure H66. Comparison of normal strains in the cylindrical bar; at Point 4 of the box type loading path.
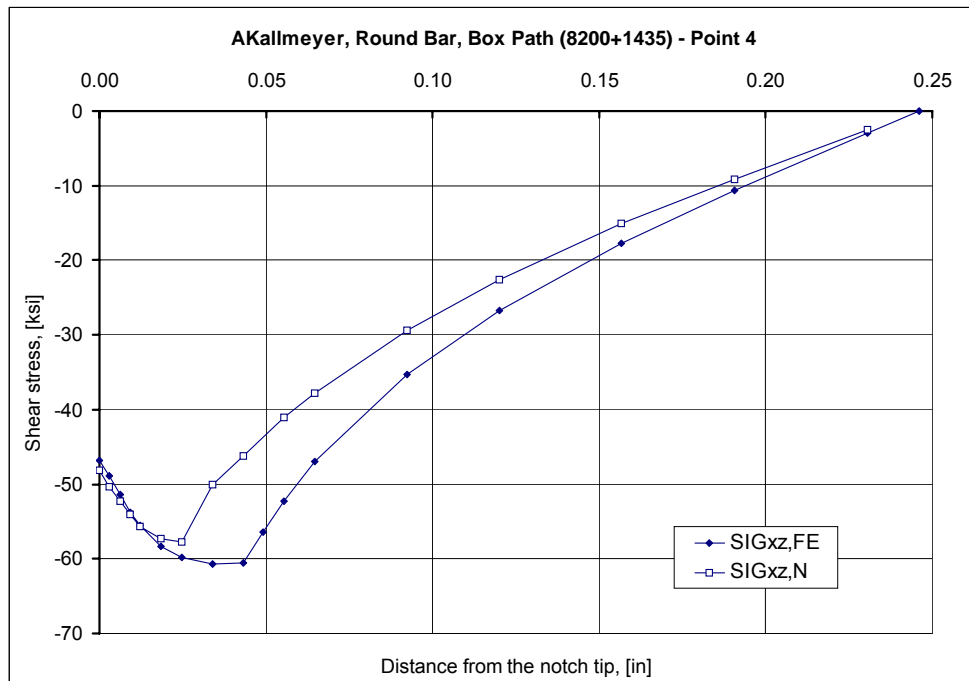
Figure H67. Comparison of shear stresses in the cylindrical bar; at Point 4 of the box type loading path.
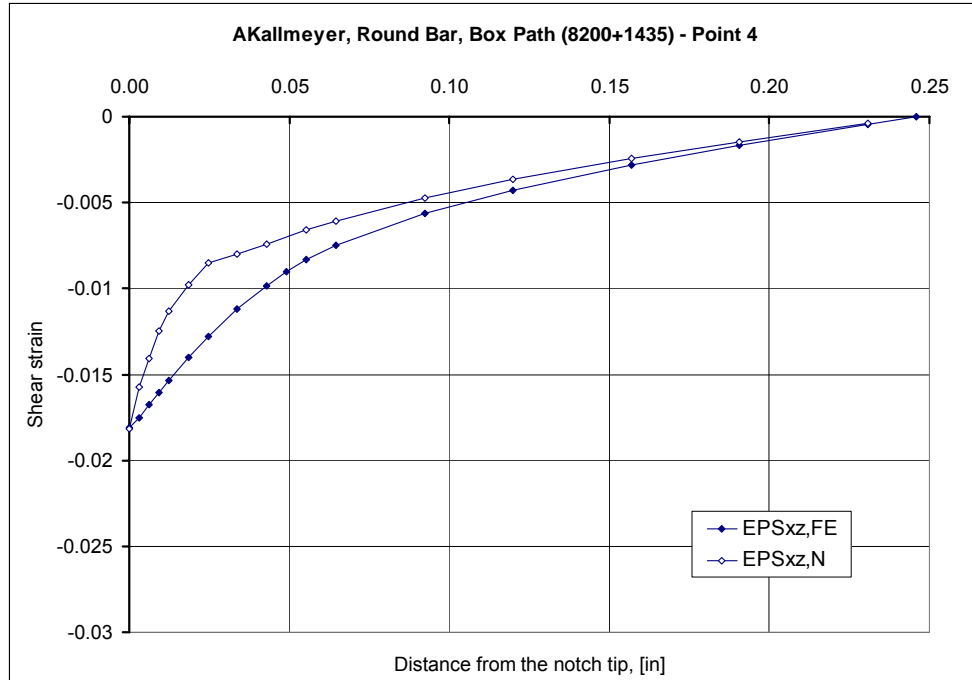
Figure H68. Comparison of shear strains in the cylindrical bar; at Point 4 of the box type loading path.

$$\sigma_{eq} = \frac{1}{\sqrt{2}} \sqrt{\left(\sigma_{11} - \sigma_{22}\right)^2 + \left(\sigma_{22} - \sigma_{33}\right)^2 + \left(\sigma_{33} - \sigma_{11}\right)^2 + 6\left(\sigma_{12}^2 + \sigma_{13}^2 + \sigma_{23}^2\right)}$$
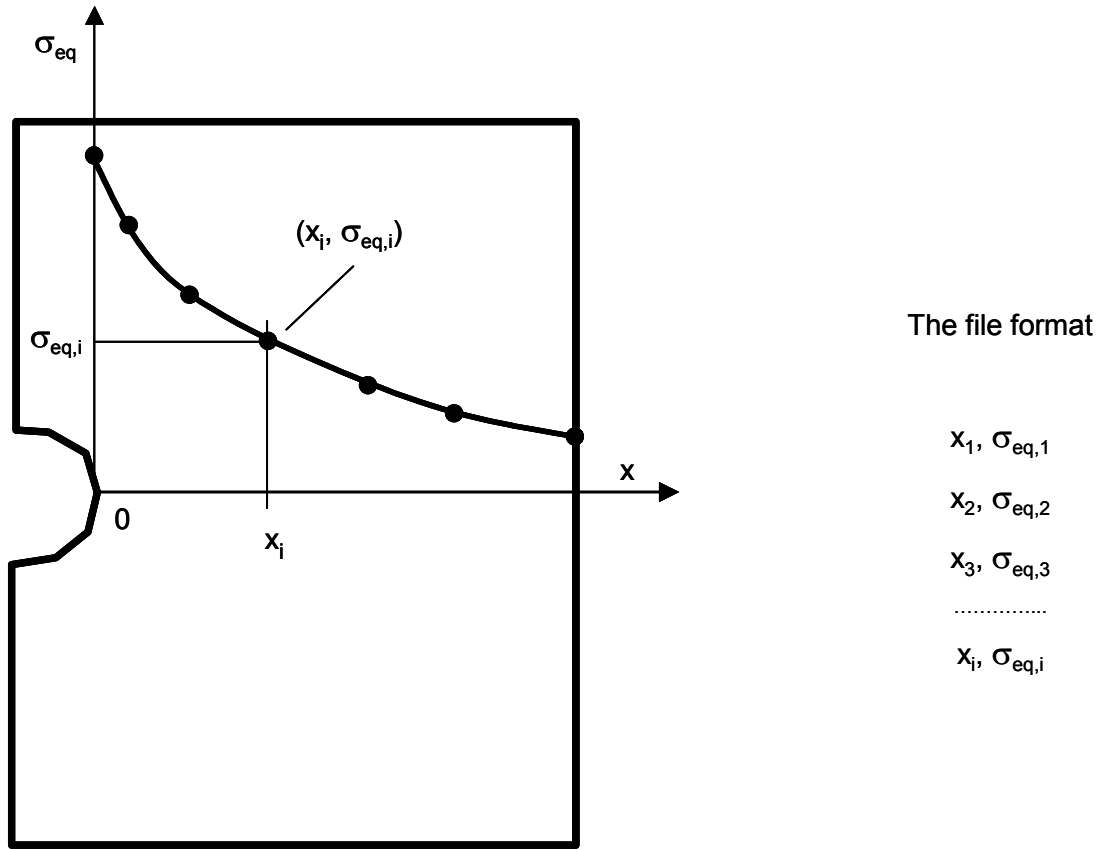
Figure H69. The distribution of the equivalent stress and the input file.

H.8   THE 3-D NEAR THE NOTCH TIP COMPUTER CODE (NPC30)

The computer code for solving the required set of incremental equation has been written in FORTRAN 77. The executable file has been created using the WATCOM WATFOR87 compiler.

The Computer Code Data Files:

There are three input files necessary to run the calculation, i.e. the MATERIAL STRESS-STRAIN CURVE file, the distribution of the EQUIVALENT STRESS in the cross section file and the STRESS PATH file. All of them are text files.

The material stress strain curve is given by series of points with stress-strain (σ - ε) coordinates (Figure H15). The first data point in the material file has to be above the linearity limit (or proportionality limit) because the proportionality limit, σ_0, the yield limit, S_Y, the modulus of elasticity, E, and the Poisson ratio, ν, are inputted from the keyboard. The format of the material file is the same as in the case of the NUE34 code discussed earlier.

The stress-strain curve is approximated by a series of linear pieces. The maximum number of linear elements of the stress-strain curve was set to 100.

Material Stress-Strain File (the format):

File name (example: 13ab.dat) – length of the file name 6 characters;

Stress coordinate, σ, in the first column;

Strain coordinate, ε, in the second column.

The first linear segment (piece) from 0 to σ_0 should not be given in the data file. The data file must start with the coordinates of the end of the first linear piece or the beginning of the second one (see Figure H15). Columns in the material data file must be separated by coma. The material data file below (attached in electronic form) has been prepared for a material with modulus of elasticity E = 200000 MPa and the yield limit of σ_0= 400 MPa and it is approximated by 15 linear pieces.

Example Material Data File:

432,0.0023
460,0.0027
490,0.0033
512,0.004
540,0.0055
575,0.009
605,0.015
620,0.024
640,0.04
660,0.08
700,0.16
750,0.3
800,0.45
850,0.6
1000,1.2

The Stress Path File

The stress path data is given (Figure H16) in terms of elastic stress increments, $\Delta\sigma_{ij}$, at the point, x_i, where the elastic-plastic stress and strains have to be determined. Each of the six columns is reserved for the increments of one stress component. The stress columns in the stress path data file must be separated by coma. The notation for the stress/columns order is as follows:

Column 1 – stress increments of component σ_{11},

Column 2 – stress increments of component σ_{12},

Column 3 – stress increments of component σ_{13},

Column 4 – stress increments of component σ_{22},

Column 5 – stress increments of component σ_{23},

Column 6 – stress increments of component σ_{33},

An example of a stress path data file is given below.

*Stress Path Data File – **Ld31a31.csv** (Increments!):*

$\Delta\sigma_{11}$, $\Delta\sigma_{12}$, $\Delta\sigma_{13}$, $\Delta\sigma_{22}$, $\Delta\sigma_{23}$, $\Delta\sigma_{33}$

The data………..

```
0.0065083,0.00062707,0.00026852,-0.00004694,-0.00000535,0.05176030
0.0065083,0.00062707,0.00026852,-0.00004694,-0.00000535,0.05176030
0.0065083,0.00062707,0.00026852,-0.00004694,-0.00000535,0.05176030
0.0065083,0.00062707,0.00026852,-0.00004694,-0.00000535,0.05176030
0.0065083,0.00062707,0.00026852,-0.00004694,-0.00000535,0.05176030
0.0065083,0.00062707,0.00026852,-0.00004694,-0.00000535,0.05176030
0.0065083,0.00062707,0.00026852,-0.00004694,-0.00000535,0.05176030
0.0065083,0.00062707,0.00026852,-0.00004694,-0.00000535,0.05176030
0.0065083,0.00062707,0.00026852,-0.00004694,-0.00000535,0.05176030
0.0065083,0.00062707,0.00026852,-0.00004694,-0.00000535,0.05176030
```
…………………………………………

The output file contains header with complete set if information concerning the input data and subsequent values of the elastic-plastic stress and strain components corresponding to the end of each stress increment inputted from the stress path data file.

The Distribution of the Equivalent Stress over the Entire Cross Section

The equivalent stress distribution has to be given by a series of points - equivalent stress value, $\sigma_{eq,i}$, and corresponding coordinate, x_i -(see Figure H69). The equivalent stress distribution can be determined for any load level applied to the component or it can be given in non-dimensional form (divide all values by any reference stress). The equivalent stress

distribution file is used for scaling the actual equivalent stress depending on the current stress magnitude at given point near the notch tip. Therefore only the relative values are needed (the actual values of the equivalent stress are OK but not necessary).

An example of the equivalent stress file is given below. The stress file below is given in a non-dimensional form obtained by division of all equivalent stresses by the peak value occurring at the notch tip. However, the actual stress values can be given as well. The first column in the equivalent stress data file contains coordinates, x, and the second column contains the absolute or relative values of the equivalent stress at those points.

Example of Equivalent Stress Distribution File:

```
0.000,1.00000
0.092,0.78864
0.189,0.64553
0.291,0.55130
0.398,0.48833
0.510,0.44518
0.628,0.41506
0.752,0.39348
0.882,0.37794
1.473,0.34971
2.961,0.34386
5.462,0.34210
9.000,0.31616
```

H.9   REFERENCES

1.   Neuber, H., " Theory of Stress Concentration of Shear Strained Prismatic Bodies with Arbitrary Non Linear Stress-Strain Law", *ASME Journal of Applied Mechanics,* vol. 28, 1961, pp. 544-550.

2.   Molski, K. and Glinka, G., " A Method of ElasticPlastic Stress and Strain Calculation at a Notch Root", *Material Science and Engineering,* vol. 50, 1981, pp. 93-100.

3.   Moftakhar, A., Buczynski, A. and Glinka, G., "Calculation of Elasto-Plastic Strains and Stresses in Notches under Multiaxial Loading", *International Journal of Fracture,* vol. 70, 1995, pp. 357-373.

4.   Singh, M.N.K., "Notch Tip Stress-Strain Analysis in Bodies Subjected to Non-Proportional Cyclic Loads", *Ph.D. Dissertation,* Dept. Mech. Eng., University of Waterloo, Ontario, Canada, 1998.

5. Seeger, T. and Hoffman, M., "The Use of Hencky's Equations for the Estimation of Multiaxial Elastic-Plastic Notch Stresses and Strains", *Report No. FB-3/1986,* Technische Hochschule Darmstadt, Darmstadt, 1986.

6. Barkey, M.E., Socie, D.F. and Hsia, K.J., "A Yield Surface Approach to the Estimation of Notch Strains for Proportional and Non-proportional Cyclic Loading", *ASME Journal of Engineering Materials and Technology,* vol. 116, 1994, pp. 173-180.

7. Moftakhar, A. A., "Calculation of Time Independent and Time-Dependent Strains and Stresses in Notches", *Ph. D. Dissertation,* University of Waterloo, Department of Mechanical Engineering, Waterloo, Ontario, Canada, 1994.

8. Chu, C. -C., "Incremental Multiaxial Neuber Correction for Fatigue Analysis"*, International Congress and Exposition,* Detroit, 1995, SAE Technical Paper No.950705, Warrendale, 1995.

9. Mroz, Z., "On the Description of Anisotropic Workhardening", *Journal of Mechanics and Physics of Solids*, vol. 15, 1967, pp. 163-175.

10. Garud, Y. S. "A New Approach to the Evaluation of Fatigue under Multiaxial Loading", *Journal of Engineering Materials and Technology*, ASME, vol. 103, 1981, pp. 118-125.

11. Chu, C. -C., "A Three-Dimensional Model of Anisotropic Hardening in Metals and Its Application to the Analysis of Sheet Metal Forming", *Journal of Mechanics and Physics of Solids*, vol.32, 1984, pp. 197-212.

12. Barkey, M. E., "Calculation of Notch Strains under Multiaxial Nominal Loading", *Ph. D.Dissertation*, Department of Theoretical and Applied Mechanics, University of Illinois at Urbana-Champaign, Urbana, 1993.

13. Irwin , G. R., "Linear Fracture Mechanics, Fracture Transition and Fracture Control", Engineering Fracture Mechanics, vol.1, 1986, pp. 241-257

14. Glinka, G., "Calculation of Inelastic Notch-Tip Strain-Stress Histories under Cyclic Loading", Engineering Fracture Mechanics, vol. 22, 1985, pp. 839-854.

APPENDIX I

ISOTROPIC SHAKEDOWN METHODOLOGY FOR BIVARIANT STRESS FIELD

I.1 INTRODUCTION

The shakedown methodology developed herein is based on an approximate elastic-plastic stress analysis that is applicable to rectangular load bearing areas that are subjected to bivariant stressing. (Bivariant stress distributions occur in a structure when the stresses in the load bearing section vary with both x and y coordinates, as in Figure I1) The input data needed to apply the methodology and to run the computer program SHARP (Shakedown Analysis for Residual Plasticity) that performs the stress analysis consists of three parts: structural dimensions, material properties and linear elastic stress analysis results. The structural data consists of specifying the coordinates of the rectangular load bearing section. The material data consists of the uniaxial stress-strain curve for monotonic loading and discrete points on the stress-strain curve that define the plasticity surfaces for use with the Garud yield criterion. The linear elastic stress analysis data consists of the incremental changes in the stress components at the grid points or nodes of the elements that form a two-dimensional model of the load bearing section as the applied load(s) are incrementally increased. The elements have to be rectangular in shape but not necessarily of equal size. For example, they could coincide with the elements on the load bearing section corresponding to the finite element modeling of that plane.

The shakedown methodology converts the incremental linear elastic solutions into equivalent elastic-plastic solutions while conserving forces and moments resulting from the remote loading. All six components of stress are required for the shakedown analysis. The z-component of stress that is normal to the load bearing area is considered the primary stress of concern. The out-of-plane direction is in the y-direction, and this coordinate along with the x coordinate defines the load bearing section. The designation of stresses conforms to the coordinate system employed in Figure I1, which shows the load bearing section (enclosed by dashed lines) corresponding to a notched plate.
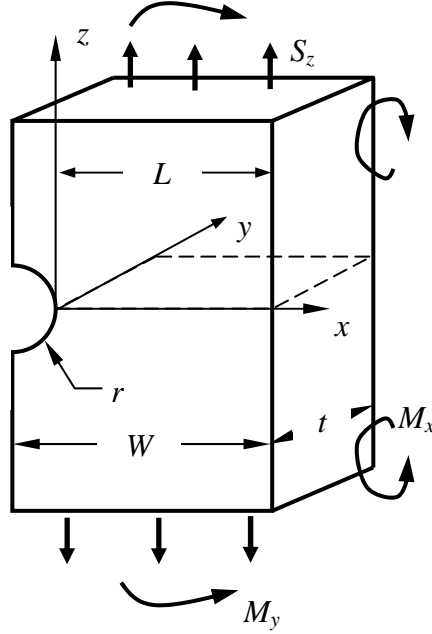
Figure I1. Geometry, coordinate system, and loading conditions for finite
element analysis used to verify SwRI's isotropic shakedown module.
Various combinations of tensile stresses and moments were applied
to the notched plate (see Table I8).

The load bearing section is defined by a rectangle bounded on one side by the x-coordinate with a width (L) extending from x_{min} to x_{max}, and on the other side by the y-coordinate with a depth (t) extending from y_{min} to y_{max}. The incremental elastic stress state is specified at the points (nodes) defined by the intersecting perpendicular gridlines that define $(n_x-1)\times(n_y-1)$ small rectangular elements corresponding to n_x and n_y gridlines that originate from the x- and y-axes, respectively. The nodal coordinates are signified by (x_i,y_j) where i varies from 1 to n_x and j from 1 to n_y, and a rectangle element is represented by four corner nodes whose coordinates are given by (x_i, y_j), (x_{i+1}, y_j), (x_{i+1}, y_{j+1}), and (x_i, y_{j+1}).

Two major tasks are performed in the isotropic shakedown methodology. The first task determines the stress relaxation at each nodal position using the linear elastic stress state. This procedure is referred to herein as the point relaxation procedure and it provides an approximate solution to the elastic-plastic stress state at each nodal position for the current load step from the corresponding incremental change in the applied linear elastic solution. The point relaxation procedures are based on the point relaxation module originally developed by Professor Glinka and subsequently modified and enhanced by SwRI. The

I-2

modifications made by SwRI included changing the Neuber method from one based on the incremental change in each component of stress, to one based on the incremental change in the equivalent stress, and the introduction of a parameter that characterizes the degree of stress triaxiality to capture the mixed plane stress/plane strain conditions that prevail in three-dimensional structures. The second task performs the load shedding that occurs due to point relaxation and re-distributes the surplus incremental forces and moments over the load bearing area. A more detailed description of each of these tasks now follows.

I.2 STRESS RELAXATION AT A POINT (POINT RELAXATION)

The point relaxation process is accomplished by applying Neuber's rule using the linear elastically determined equivalent stress and equivalent strain increments. Neuber's rule states that the incremental product of stress and strain is invariant for each load step irrespective of the constitutive relationship between stress and strain. In terms of incremental stresses, which is more appropriate to multi-axial stressing and non-proportional loading, Neuber's rule can be formulated[1] as

$$^{(k)}\Delta\left(\sigma_{eq}^{ep}\varepsilon_{eq}^{ep}\right) = {}^{(k)}\Delta\left(\sigma_{eq}^{E}\varepsilon_{eq}^{E}\right) \implies {}^{(k)}\Delta\sigma_{eq}^{ep}\cdot{}^{(k-1)}\varepsilon_{eq}^{ep} + {}^{(k-1)}\sigma_{eq}^{ep}\cdot{}^{(k)}\Delta\varepsilon_{eq}^{ep} = {}^{(k)}\Delta\left(\sigma_{eq}^{E}\varepsilon_{eq}^{E}\right) \tag{I1}$$

where stress and strain are denoted by σ and ε, ${}^{(k)}\Delta\sigma_{eq}^{ep} = {}^{(k)}\sigma_{eq}^{ep} - {}^{(k-1)}\sigma_{eq}^{ep}$ and ${}^{(k)}\Delta\varepsilon_{eq}^{ep} = {}^{(k)}\varepsilon_{eq}^{ep} - {}^{(k-1)}\varepsilon_{eq}^{ep}$. The superscript k denotes the current step number. The superscripts E and ep signify elastic and elastic-plastic quantities, and the subscript, eq, represents an equivalent quantity; for example, σ_{eq}^{ep} is used to denote the equivalent elastic-plastic stress. The equivalent elastic stress and the equivalent elastic stress increment are defined, respectively, as

$$\sigma_{eq}^{E} = \sqrt{\frac{1}{2}\left\{\left(\sigma_{x}^{E}\right)^2 + \left(\sigma_{y}^{E}\right)^2 + \left(\sigma_{z}^{E}\right)^2 - 2\left(\sigma_{x}^{E}\sigma_{y}^{E} + \sigma_{x}^{E}\sigma_{z}^{E} + \sigma_{y}^{E}\sigma_{z}^{E}\right) + 6\left[\left(\sigma_{xy}^{E}\right)^2 + \left(\sigma_{xz}^{E}\right)^2 + \left(\sigma_{yz}^{E}\right)^2\right]\right\}}$$
$$\tag{I2}$$

and

---

[1] This approach is different from the approach used in the original point relaxation module by Glinka in which Neuber's rule was applied to every component of stress and strain instead of to the equivalent stress and equivalent strain. In Glinka's formulation for multiaxial stressing, Neuber's rule becomes ${}^{(k)}\Delta\left(S_{ij}^{ep}e_{ij}^{ep}\right) = {}^{(k)}\Delta\left(S_{ij}^{E}e_{ij}^{E}\right)$ where i and j are summation indices for the stress and strain components, while S and e denote the deviatoric stress and strain.

$$^{(k)}\Delta\sigma_{eq}^{E} = {}^{(k)}\sigma_{eq}^{E} - {}^{(k-1)}\sigma_{eq}^{E} \tag{I3}$$

The Ramberg-Osgood equation is used to represent the constitutive relationship between stress and strain. Using this equation, the expression for the equivalent elastic-plastic strain in terms of the equivalent elastic-plastic stress is given by

$$^{(k)}\varepsilon_{eq}^{ep} = \varepsilon_o \left[\frac{{}^{(k)}\sigma_{eq}^{ep}}{\sigma_o} + \alpha \left(\frac{{}^{(k)}\sigma_{eq}^{ep}}{\sigma_o} \right)^{\beta} \right] \tag{I4}$$

in which σ_o and ε_o are the yield stress and the elastic strain at yield, respectively, and α and β are material constants.

Neuber's rule can be solved for the current equivalent elastic-plastic stress, $^{(k)}\sigma_{eq}^{ep}$, using the elastic-plastic stresses and strains determined at the end of the previous load step together with the user-specified elastic stresses and strains. (In the SHARP module, the elastic strains are derived from the stresses using the elastic modulus matrix). The required solution is in the form of one of the roots of a non-linear equation derived by applying Neuber's rule. This root needs to be determined using numerical methods. The bisection method is used in the isotropic shakedown module. After the root is found, the elastic-plastic equivalent strain $^{(k)}\varepsilon_{eq}^{ep}$ and the elastic-plastic equivalent strain increment $^{(k)}\Delta\varepsilon_{eq}^{ep}$ can be computed from the constitutive relationship.

The following procedure was implemented[2] to derive the incremental elastic-plastic stress components $\Delta\sigma_{ij}^{ep}$ from the calculated equivalent incremental elastic-plastic stress $\Delta\sigma_{eq}^{ep}$. In the following, the superscript k is removed to signify that the step number is referring to the k-th step, which is the current step number. The process involves two steps: (1) determining a triaxiality parameter at each nodal position based on the linear elastic solutions, and (2) solving for the components of the relaxed elastic-plastic stress increment at the current step.

---

[2] Glinka's point relaxation module uses a proportional relationship to determine the elastic-plastic stress increment based on the equation $\Delta\sigma_{ij}^{ep} = \left(\xi_{ij}^{ep} \Delta S_{ij}^{ep} / \xi_{ij}^{ep} \Delta S_{ij}^{E} \right) \cdot \sigma_{kk}^{E} / 3 + \Delta S_{ij}^{ep}$ where $\xi_{ij}^{ep} = S_{ij}^{ep} - \alpha_{ij}$ and α_{ij} is the center of the plasticity surface in deviatoric space.

A triaxiality parameter, ω, is employed to characterize the multi-axial stress state that exists at notches in 3-D structures, such as the plane stress conditions at free surfaces and the near plane strain conditions in the interior of a structure. The evaluation of ω is position-dependent and is based on the linear elastic analysis results provided as input data. The parameter is given by the equation

$$\omega = \frac{\Delta\sigma_y^E}{\sqrt{\left(\Delta\sigma_x^E\right)^2 + \left(\Delta\sigma_z^E\right)^2}} \tag{I5}$$

In practice, a normalized value of ω, called $\overline{\omega}$, that varies from 0 to 1 is used. The normalized value is equal to the point value of ω divided by the maximum value of ω on the load bearing section. As can be seen from the foregoing equation, the triaxial parameter has a value near zero adjacent to free surfaces where plane stress conditions prevail ($\Delta\sigma_y^E = 0$, no out-of-plane stress).

Solving for the incremental changes in the components of elastic-plastic stress at the current step requires an iterative procedure to ensure that the set of solutions for the incremental stress components is consistent with the incremental change in equivalent stress determined from Neuber's rule.

The iteration starts with an initial estimate for the incremental change in the elastic-plastic stress components based on the ratio of the equivalent elastic-plastic stress increment to the equivalent elastic stress increment times the changes in the elastic stress components during the current load step, as shown in the equation:

$$\left(\Delta\sigma_{ij}^{ep}\right)^{ESTIMATE} = \frac{\Delta\sigma_{eq}^{eq}}{\Delta\sigma_{eq}^E} \cdot \Delta\sigma_{ij}^E \tag{I6}$$

The iteration process proceeds by finding a suitable set of solutions for the three major stress components; i.e., $\Delta\sigma_x^{ep}$, $\Delta\sigma_y^{ep}$, and $\Delta\sigma_z^{ep}$ while $\Delta\sigma_x^{ep}$ remains unchanged. During the iteration, the following two equations are used to determine the intermediate values until the convergence criteria are met:

$$\left(\Delta\sigma_y^{ep}\right)^{NEW} = \left(\Delta\sigma_y^{ep}\right)^{OLD}\left(1-\overline{\omega}\right) + \xi\cdot\overline{\omega}\cdot\nu_{eff}\cdot\left[\left(\Delta\sigma_z^{ep}\right)^{OLD} + \Delta\sigma_x^{ep}\right] \tag{I7}$$

and

$$\left(\Delta\sigma_z^{ep}\right)^{NEW} = \frac{1}{2}\left\{\left[\Delta\sigma_x^{ep} + \left(\Delta\sigma_y^{ep}\right)^{NEW}\right] + \right.$$

$$\left. \sqrt{-3\left[\left(\Delta\sigma_x^{ep}\right)^2 + \left(\left(\Delta\sigma_y^{ep}\right)^{NEW}\right)^2\right] + 6\Delta\sigma_x^{ep}\left(\Delta\sigma_y^{ep}\right)^{NEW} + 4\left(\Delta\sigma_{eq}^{ep}\right)^2 - 12\left[\left(\Delta\sigma_{xy}^{ep}\right)^2 + \left(\Delta\sigma_{xz}^{ep}\right)^2 + \left(\Delta\sigma_{yz}^{ep}\right)^2\right]}\right\} \qquad (\text{I8})$$

These two equations have three unknowns, ξ, $\left(\Delta\sigma_y^{ep}\right)$ and $\left(\Delta\sigma_z^{ep}\right)$. It is shown below how a value of ξ is chosen so that the three unknowns are reduced to two.

In the first iteration, the initial estimated values are used for $\left(\Delta\sigma_x^{ep}\right)^{OLD}$, $\left(\Delta\sigma_y^{ep}\right)^{OLD}$ and $\left(\Delta\sigma_z^{ep}\right)^{OLD}$. The effective Poisson's ratio, which interpolates between the elastic and plastic Poisson ratio values, is defined by

$$\nu_{eff} = \frac{\nu^E\left(\Delta\varepsilon_{eq}^{ep}\right)^{elastic} + 0.5\cdot\left(\Delta\varepsilon_{eq}^{ep}\right)^{plastic}}{\Delta\varepsilon_{eq}^{ep}} \qquad (\text{I9})$$

This quantity remains unchanged during the iteration (as do $\Delta\sigma_x^{ep}$ and all shear components of the stress increment). The superscripts *elastic* and *plastic* signify elastic and plastic components, respectively. The user specifies the elastic value of Poisson's ratio, ν^E, but the plastic value is taken as 0.5. The updated values for $\Delta\sigma_y^{ep}, \Delta\sigma_z^{ep}$, $\left(\Delta\sigma_y^{ep}\right)^{NEW}$ and $\left(\Delta\sigma_z^{ep}\right)^{NEW}$ after each iteration are assigned as the old values, $\left(\Delta\sigma_y^{ep}\right)^{OLD}$ and $\left(\Delta\sigma_z^{ep}\right)^{OLD}$, and used in the next iteration until convergence is attained. The equation for $\left(\Delta\sigma_z^{ep}\right)^{NEW}$ is derived from the quadratic equation for the equivalent elastic-plastic stress increment.

To reduce the three unknowns, ξ, $\left(\Delta\sigma_y^{ep}\right)$ and $\left(\Delta\sigma_z^{ep}\right)$ to two, the following empirically derived procedure is followed. The factor ξ is initially taken as 1. After $\left(\Delta\sigma_y^{ep}\right)$ and $\left(\Delta\sigma_z^{ep}\right)$ have been determined for this ξ value, the value of ξ is increased, and the iterative procedure with the new ξ value is repeated. This process continues until the root searching process fails to find a solution for $\left(\Delta\sigma_y^{ep}\right)$ and $\left(\Delta\sigma_z^{ep}\right)$. The maximum value of ξ, ξ_{max}, for which a solution for $\left(\Delta\sigma_y^{ep}\right)$ and $\left(\Delta\sigma_z^{ep}\right)$ is found and the calculated values of

$\Delta\sigma_x^{ep}$, $\Delta\sigma_y^{ep}$, $\Delta\sigma_z^{ep}$, $\Delta\sigma_{xy}^{ep}$, $\Delta\sigma_{yz}^{ep}$ and $\Delta\sigma_{xz}^{ep}$ corresponding to $\xi = \xi_{max}$ are used to determine the final value of $\Delta\sigma_{eq}^{ep}$. However, in order to decompose $\Delta\sigma_{eq}^{ep}$ into the incremental changes in the elastic-plastic stress components, an adjusted value of ξ, ξ_{adj}, that depends on ξ_{max} and the material hardening exponent, β, is used based on the following empirically derived equation:

$$
\xi_{adj} = \begin{cases} \dfrac{\xi_{max}}{2}, & \beta < 4 \\ \xi_{max}, & \beta > 31.5 \\ \xi_{max}\left[0.5579\left(\log_{10}\beta - 0.6021\right) + 0.5\right], & 4 \le \beta \le 31.5 \end{cases} \tag{I10}
$$

Once the incremental elastic-plastic stress components are determined, the loci of plasticity surfaces can be updated. Consistent with the point relaxation module developed by Glinka, the approach proposed by Garud is used. Assume there are n functions that define the field of plasticity of the von-Mises type. They are specified by

$$
f_m(S_{ij}^{ep}, (\alpha_{ij})_m, R_m) = \frac{3}{2}\left[S_{ij}^{ep} - (\alpha_{ij})_m\right] \cdot \left[S_{ij}^{ep} - (\alpha_{ij})_m\right] - R_m^2 \tag{I11}
$$

where $f_m = 0$ defines the m-th plasticity surface in deviatoric stress space ($m=1, 2, \ldots, n$), S_{ij}^{ep} is the deviatoric elastic-plastic stress components, $(\alpha_{ij})_m$ denotes the current center of the m-th plasticity surface, and R_m is the yield stress associated with the m-th plasticity surface. It is assumed that during plastic straining the size and shape of the plasticity surfaces do not change. Let f_ℓ be the current "active" plasticity surface; i.e., the current state of stress is on f_ℓ. During plastic straining, the applied elastic-plastic stress increment leads to the following shift in the center of the ℓ-th plasticity surface.

$$
(\Delta\alpha_{ij})_\ell = p \cdot d_{ij} \tag{I12}
$$

where d_{ij} is related to the proportionality scalar $\dfrac{R_l}{R_{l+1}}$ by

$$
d_{ij} = \left(1 - \frac{R_\ell}{R_{\ell+1}}\right) \cdot \left[S_{ij}^{ep} - (\alpha_{ij})_{\ell+1} + \kappa\Delta S_{ij}^{ep}\right] + \left[(\alpha_{ij})_{\ell+1} - (\alpha_{ij})_\ell\right] \tag{I13}
$$

κ is a scalar parameter defined by the positive root of $f_{\ell+1}\left(S_{ij}^{ep} + \kappa\Delta S_{ij}^{ep}, \left(\alpha_{ij}\right)_{\ell+1}, R_{\ell+1}\right) = 0$. The

κ parameter provides an estimate of the factor that the current elastic-plastic stress increment

has to be multiplied by to reach the next plasticity surface, $f_{\ell+1}$ and to determine the

translation direction (shift) of the center of the current plasticity surface, d_{ij}, if indeed the

current load step is sufficiently large to cause the stress state to fall on the next plasticity

surface. The p parameter is determined while the size and shape of the current plasticity

surface, f_ℓ, remain unchanged while the plasticity center is translated by an amount

determined according to the applied elastic-plastic stress increment. Mathematically, the

scalar parameter p can be determined as the positive root of the equation:

$$f_\ell\left(S_{ij}^{ep} + \Delta S_{ij}^{ep}, \left(\alpha_{ij}\right)_\ell + p\cdot d_{ij}, R_\ell\right) = 0 \tag{I14}$$

The centers of the plasticity surfaces f_r are shifted by

$$\left(\Delta\alpha_{ij}\right)_r = \left(S_{ij}^{ep} + \Delta S_{ij}^{ep}\right) - \frac{R_r}{R_\ell}\left\{\left(S_{ij}^{ep} + \Delta S_{ij}^{ep}\right) - \left[\left(\alpha_{ij}\right)_\ell + \left(\Delta\alpha_{ij}\right)_\ell\right]\right\} - \left(\alpha_{ij}\right)_r \tag{I15}$$

for $r=1, 2, \ldots, \ell-1$, and $\left(\Delta\alpha_{ij}\right)_r = 0$ for $\ell+1 \le r \le n$.

This hardening rule used in the Garud procedure ensures that the material undergoes

kinematic hardening before the next plasticity surface is reached. However, when the

applied stress increment is large enough to result in a stress state beyond the current plasticity

surface, the plasticity surface expands to the next one and employs the center of this surface.

In this sense, the material behaves as if it is following an isotropic hardening rule.

I.3   LOAD SHEDDING AND LOAD RE-DISTRIBUTION

The methodology for load shedding and load re-distribution that was developed by

SwRI in previous work for P&W needed to be modified for the current work. The previous

method was based on assuming history independent non-linear behavior and applying

Neuber's rule to only the final stress state. The present problem involves applying Neuber's

rule to load history dependent incremental loading. Implementation of the version of the

load shedding and load re-distribution methodology developed for the incremental loading

history problem addressed herein can be resolved into the eight steps listed below. The steps
reference sub-steps where more detailed descriptions of the procedure are given.

Step (1)   Interpolation of the incremental linear elastic stress values for the current load
           step to generate stress values at the nodal points of a much finer mesh of
           rectangular elements than the original mesh defined by finite element modeling of
           the load bearing section. (Sub-Section I.3.1).

Step (2)   Evaluation of the incremental increase in forces and moments for the current load
           step from the incremental change in the linear elastic stress and the estimated
           elastic-plastic stress state for the previous load step (Sub-Section I.3.2).

Step (3)   Estimation of the plastic zone size on the load bearing area based on the
           equivalent stress derived from the applied incremental linear elastic stress for the
           current load step and the elastic-plastic stress derived in the previous load step
           (Section I.3.3).

Step (4)   Splitting the stress range (defined as the difference between the maximum and
           minimum values of an equivalent stress) on the load bearing section into specific
           stress bands, determining the area of the load bearing section occupied by each of
           the bands, and assigning the equivalent stress in each element of the fine mesh to
           one of the stress bands (Section I.3.4).

Step (5)   Evaluation of the areas over which load shedding will occur for each equivalent
           stress band (Section I.3.5).

Step (6)   Determination of the plastically relaxed stresses for each equivalent stress band
           (Section I.3.6)

Step (7)   Redistribution (load shedding) of the excess incremental load arising from plastic
           stress relaxation over the area associated with each equivalent stress band
           (Section I.3.7).

Step (8)   Calculation and re-distribution of the global incremental loads needed to maintain
           force and moment balance after the plastic stress relaxation process is completed
           over the load bearing section (Section I.3.8)

I.3.1   Generation of a New Bivariant Incremental Stress Array

This procedure is required to provide a fine mesh consisting of small element sizes
in order to increase the accuracy of the plastic stress relaxation and load shedding procedures
detailed in Sections I.3.5 and I.3.7. The stress values provided at the corner points of the
elements constituting the user-defined mesh are interpolated to provide stress values at the
corner points of the elements constituting a finer mesh. The distribution of incremental
stress, $\Delta \sigma_{ij}^{E}(x, y)$, across an element is assumed to be linear. This means that if (x,y) is a
coordinate position within an element of the user-defined mesh then the incremental stress
within that element will vary as $\Delta \sigma_{ij}^{E}(x, y) = b_1 + b_2 x + b_3 y + b_4 xy$, where the coefficients b_1, b_2,

I-9

b_3, and b_4 are determined by the incremental stress values at the coordinates of the four corner points of the element. The shakedown methodology utilizes the results for the finer mesh which is specified to have m_x nodes (m_x-1 elements) along the x-axis between $x=x_{min}$ and $x=x_{max}$, and m_y nodes (m_y-1 elements) along the y-axis between $y=y_{min}$ and $y=y_{max}$. In general, $m_x>n_x$ and $m_y>n_y$, where n_x and n_y are the number of nodes along the x-axis and y-axis, respectively, in the user-specified mesh.

I.3.2 Evaluation of the Applied Incremental Force and Moments at the Current Load Step

The evaluation of the applied force F_z and moments M_x, M_y, at the current load step is based on the elastically determined stress increments at the current load step and the elastic-plastic stress solution determined from the previous load step. The equations are given by

$$
\begin{aligned}
^{(k)}F_z = \frac{1}{4}\sum_{i=1}^{m_x-1}\sum_{j=1}^{m_y-1}(x_{i+1}-x_i)(y_{j+1}-y_j)\Big[&{}^{(k-1)}\sigma_z^{ep}(x_i,y_j)+{}^{(k)}\Delta\sigma_z^{E}(x_i,y_j)+ \\
&{}^{(k-1)}\sigma_z^{ep}(x_i,y_j)+{}^{(k)}\Delta\sigma_z^{E}(x_i,y_j)+{}^{(k-1)}\sigma_z^{ep}(x_{i+1},y_j)+{}^{(k)}\Delta\sigma_z^{E}(x_{i+1},y_j)+ \\
&{}^{(k-1)}\sigma_z^{ep}(x_{i+1},y_{j+1})+{}^{(k)}\Delta\sigma_z^{E}(x_{i+1},y_{j+1})+{}^{(k-1)}\sigma_z^{ep}(x_i,y_{j+1})+{}^{(k)}\Delta\sigma_z^{E}(x_i,y_{j+1})\Big]
\end{aligned}
$$

$$
\begin{aligned}
^{(k)}M_y = \frac{1}{8}\sum_{i=1}^{m_x-1}\sum_{j=1}^{m_y-1}(x_{i+1}^2-x_i^2)(y_{j+1}-y_j)\Big[&{}^{(k-1)}\sigma_z^{ep}(x_i,y_j)+{}^{(k)}\Delta\sigma_z^{E}(x_i,y_j)+ \\
&{}^{(k-1)}\sigma_z^{ep}(x_i,y_j)+{}^{(k)}\Delta\sigma_z^{E}(x_i,y_j)+{}^{(k-1)}\sigma_z^{ep}(x_{i+1},y_j)+{}^{(k)}\Delta\sigma_z^{E}(x_{i+1},y_j)+ \\
&{}^{(k-1)}\sigma_z^{ep}(x_{i+1},y_{j+1})+{}^{(k)}\Delta\sigma_z^{E}(x_{i+1},y_{j+1})+{}^{(k-1)}\sigma_z^{ep}(x_i,y_{j+1})+{}^{(k)}\Delta\sigma_z^{E}(x_i,y_{j+1})\Big]
\end{aligned}
\tag{I16}
$$

$$
\begin{aligned}
^{(k)}M_x = \frac{1}{8}\sum_{i=1}^{m_x-1}\sum_{j=1}^{m_y-1}(x_{i+}-x_i)(y_{j+1}^2-y_j^2)\Big[&{}^{(k-1)}\sigma_z^{ep}(x_i,y_j)+{}^{(k)}\Delta\sigma_z^{E}(x_i,y_j)+ \\
&{}^{(k-1)}\sigma_z^{ep}(x_i,y_j)+{}^{(k)}\Delta\sigma_z^{E}(x_i,y_j)+{}^{(k-1)}\sigma_z^{ep}(x_{i+1},y_j)+{}^{(k)}\Delta\sigma_z^{E}(x_{i+1},y_j)+ \\
&{}^{(k-1)}\sigma_z^{ep}(x_{i+1},y_{j+1})+{}^{(k)}\Delta\sigma_z^{E}(x_{i+1},y_{j+1})+{}^{(k-1)}\sigma_z^{ep}(x_i,y_{j+1})+{}^{(k)}\Delta\sigma_z^{E}(x_i,y_{j+1})\Big]
\end{aligned}
$$

These equations are based on the interpolated values at the corner points of the elements constituting a finer mesh that has (m_x-1) elements along x-axis and (m_y-1) elements along y-axis. The symbols used to designate the stress component normal to the load bearing section are $\Delta\sigma_z$ for stress increment and σ_z for stress. The superscript E denotes the linear elastic solutions derived from the data provided by the user, and the superscript ep represents

the elastic-plastic solutions determined from the isotropic shakedown module. The current
and previous load steps are denoted by superscripts k and $(k-1)$, respectively.

I.3.3   Estimation of the Plastic Zone Size

The plastic zone size, a_y, is the area of the load bearing section where the equivalent
stress values, σ_{eq}, equal or exceed the yield stress, σ_{yield}. An element is only included in this
area if the equivalent stress values at all four corner points of the element satisfy this
criterion. A pseudo von-Mises type of equivalent stress, σ_{eq}^{pseudo}, composed of the current
elastic stress increment and the elastic-plastic stress from the previous step is is defined by
the equation

$$\sigma_{eq}^{pseudo} = \sqrt{\frac{3}{2}\xi_{ij}^{pseudo}\,\xi_{ij}^{pseudo}} = \sqrt{\frac{3}{2}\left(S_{ij}^{pseudo}-\alpha_{ij}\right)\cdot\left(S_{ij}^{pseudo}-\alpha_{ij}\right)} \qquad (\text{I}17)$$

where $\xi_{ij}^{pseudo} = S_{ij}^{pseudo}-\alpha_{ij}$. The term S_{ij}^{pseudo} is a pseudo deviatoric stress based on the
current linear elastic stress increment $^{(k)}\Delta\sigma_{ij}^{E}$ and the elastic-plastic stress $^{(k-1)}\sigma_{ij}^{ep}$ obtained
from the previous load step. Its tensor representation is given by

$$S_{ij}^{pseudo} = \left(^{(k-1)}\sigma_{ij}^{ep}+{}^{(k)}\Delta\sigma_{ij}^{E}\right)-\delta_{ij}\cdot\left(^{(k-1)}\sigma_{kk}^{ep}+{}^{(k)}\Delta\sigma_{kk}^{E}\right)/3 \qquad (\text{I}18)$$

with $\delta_{ij}=1$, if $i=j$, or $\delta_{ij}=0$, if $i\neq j$. α_{ij} is the coordinate of the center of the current
plasticity surface in the deviatoric space coordinate.

I.3.4   Determination of the Stress Bands for Load Shedding

The equivalent stress range $\left(\sigma_{eq}\right)_{max}^{pseudo}-\left(\sigma_{eq}\right)_{min}^{pseudo}$ is divided into n_r levels (i.e., n_r-1
stress bands) where the subscripts *max* and *min* denote the maximum and minimum
equivalent stresses, respectively. The areas occupied by each of the stress bands is
determined and elements of the fine mesh that fall within each area are identified. Thus, the
elements that fall within an area contain equivalent stresses with values between the upper
and lower bounds that define the stress band. If a_y is the area over which the equivalent
stress exceeds the yield stress, σ_{yield}, and a_{total} is the area of the load bearing section, then the
number of stress bands, n_l, that contain equivalent stresses that exceed σ_{yield} is

$$n_l = \frac{a_y}{a_{total}} n_r \tag{I19}$$

The stress ranges corresponding to each of the stress bands where yielding has occurred are defined as

$$\sigma_{inc} = \frac{\left(\sigma_{eq}\right)_{max} - \sigma_{yield}}{n_l} \tag{I20}$$

It follows that the number of stress bands where the equivalent stress is lower than σ_{yield} is $n_r - n_l$ and the stress ranges associated with these bands is

$$\sigma_{inc} = \frac{\sigma_{yield} - \left(\sigma_{eq}\right)_{min}}{n_r - n_l} \tag{I21}$$

Once a stress band is determined, the associated area a_k occupied by elements which have equivalent stress values above the lower limit of the band is evaluated. During this process, each element is assigned to and associated with a specific stress band.

I.3.5 Evaluation of Load Shedding Areas

The plastic stress relaxation process, load shedding and stress re-distribution, start in the area of the load bearing section that has the maximum equivalent stress, $\left(\sigma_{eq}\right)_{max}^{pseudo}$. It then proceeds to the area with a stress band equal to the second highest equivalent stress, and so on until the area of the load bearing section containing the minimum equivalent stress, $\left(\sigma_{eq}\right)_{min}^{pseudo}$, is reached. During this process, load shedding due to plastic stress relaxation transfers incremental loads onto adjacent load bearing areas. The size of these areas, or re-distribution zones, $a^{relax}(a_k)$, for the k-th equivalent stress band is defined by

$$a^{relax}(a_k) = f(a_k) \cdot a_y \tag{I22}$$

where $f(a_k)$ is a dimensionless multiplication factor calculated from the equation

$$f(a_k) = \frac{\alpha_{high} - \alpha_{low}}{2} \tanh\left(\frac{a_k - a_y}{a_y \zeta}\right) + \frac{\alpha_{high} + \alpha_{low}}{2} \tag{I23}$$

This empirical factor acts as a smoothing function that re-distributes surplus incremental loads from locations inside the plastic zone over areas comparable to a_y, and re-

distributes incremental loads from locations outside the plastic zone over areas many times greater than a_y. The forms for the parameters α_{high}, α_{low}, and ζ are empirically chosen based on exploratory investigations using the results of elastic-plastic finite element stress analyses of notched plates for material behaviors with significantly different strain-hardening capacities.

The final forms are given by

$$\zeta = 0.03^{\frac{\beta-1}{\beta+1}}, \quad \alpha_{low} = \frac{\beta+1}{\beta-1}, \quad \alpha_{high} = 20\alpha_{low} \tag{I24}$$

where β is the Ramberg-Osgood strain hardening exponent (see Section I.2)

I.3.6 Determination of the Plastically Relaxed Stresses

The plastically relaxed stresses are calculated from the following stresses:

(1) Linear elastic stress solution at the end of previous load step, $^{(k-1)}\sigma_{ij}^{E}$.

(2) Linear elastic stress increment for the current load step, $^{(k)}\Delta\sigma_{ij}^{E}$.

(3) Elastic-plastic stress solution at the end of previous load step, $^{(k-1)}\sigma_{ij}^{ep}$.

The computation of the plastically relaxed stresses is performed using the point relaxation module. For more details, refer to Section I.2.

I.3.7 Redistribution of Local Incremental Loads Resulting from Load Shedding

The reduction of the pseudo stress component σ_z^{pseudo} within each element belonging to a given stress band, is converted into an incremental load which is then re-distributed over an area that encompasses smaller stress bands. The increment of load re-distributed, ΔF_m, within the m-th stress band is calculated by the difference between the pseudo elastic-plastic stress state $\left[^{(k-1)}\sigma_z^{ep} + ^{(k)}\Delta\sigma_z^{E}\right]$ and the relaxed stress state $^{(k)}\Delta\sigma_z^{ep}$ for the elements belonging to the stress band using a simple Trapezoidal rule

$$\Delta F_m = \frac{1}{4}\sum_{i=1}^{n_m} A_i \Delta\sigma_i \tag{I25}$$

In this equation, n_m denotes the number of elements within the m-th stress band, A_i stands for the area of the i-th element, and $\Delta\sigma_i$ the sum of the incremental reductions in the stress

component normal to the load bearing section, $\left[\left({}^{(k-1)}\sigma_z^{ep} + {}^{(k)}\Delta\sigma_z^E\right) - {}^{(k)}\Delta\sigma_z^{ep}\right]$, evaluated at the four corner points of the i-th element. The excess load is redistributed as an increment of stress, $\Delta\sigma_z(a_j, a_m)$, whose magnitude linearly varies over the redistribution zone size $a^{relax}(a_m)$ according to the rule

$$\Delta\sigma_z(a_j, a_m) = \frac{2\Delta F_m}{a^{relax}(a_m)}\left[1 - \frac{a_j - a_m}{a^{relax}(a_m)}\right] , \quad a_m \leq a_j \leq a^{relax}(a_m) + a_m \qquad (I26)$$

The increments $\Delta\sigma_z(a_j, a_m)$ are added to the incremental stress component $\Delta\sigma_z^E$ of those nodes whose element belongs to the j-th stress band. Thus at the time when the plastic stress relaxation calculation for the m-th stress band is completed, the total stress consists of the pseudo elastic-plastic stress component at the end of the previous step, ${}^{(k-1)}\sigma_z^{ep} + {}^{(k)}\Delta\sigma_z^E$, plus the sum of all the incremental stresses $\Delta\sigma_z(a_j, a_m)$ resulting from load shedding.

I.3.8   Balance of Force and Moments, and Load Re-distribution

After the stress relaxation calculations have been completed over the load bearing section, conservation of the force normal to the section, and conservation of moments with respect to the x- and y-axes, are checked. In this procedure, the force and moments are compared with the force and moments evaluated before stress relaxation according to Section I.3.2. If the difference in force is denoted by ΔF_z and the differences in moments by ΔM_x and ΔM_y, then these are globally re-distributed as an incremental stress distribution $\Delta\sigma_z(x, y)$ over the whole load bearing section, where $\Delta\sigma_z(x, y)$ is evaluated according to the following rule:

$$\Delta\sigma_z(x, y) = C_{30}x + C_{31}y + C_{32}\sigma_z^{ep}(x, y) \qquad (I27)$$

where the coefficients C_{ij} are given by

$$\begin{Bmatrix} C_{32} \\ C_{31} \\ C_{30} \end{Bmatrix} = \begin{bmatrix} q_{11} & q_{12} & q_{13} \\ q_{21} & q_{22} & q_{23} \\ q_{31} & q_{32} & q_{33} \end{bmatrix}^{-1} \begin{Bmatrix} \Delta F_z \\ \Delta M_y \\ \Delta M_x \end{Bmatrix} \qquad (I28)$$

with

$$q_{11} = \sum_{i=1}^{n_x-1}\sum_{j=1}^{n_y-1}\frac{1}{2}\left(x_{i+1}^2 - x_i^2\right)\cdot\left(y_{j+1} - y_j\right) \tag{I29}$$

$$q_{12} = \sum_{i=1}^{n_x-1}\sum_{j=1}^{n_y-1}\frac{1}{2}\left(x_{i+1} - x_i\right)\cdot\left(y_{j+1}^2 - y_j^2\right)$$

$$q_{13} = \sum_{i=1}^{n_x-1}\sum_{j=1}^{n_y-1}\frac{1}{4}\left(x_{i+1} - x_i\right)\cdot\left(y_{j+1} - y_j\right)\left[\sigma_z^{ep}\left(x_i, y_j\right) + \sigma_z^{ep}\left(x_{i+1}, y_j\right) + \sigma_z^{ep}\left(x_{i+1}, y_{j+1}\right) + \sigma_z^{ep}\left(x_i, y_{j+1}\right)\right]$$

$$q_{21} = \sum_{i=1}^{n_x-1}\sum_{j=1}^{n_y-1}\frac{1}{4}\left(x_{i+1} + x_i\right)^2\left(x_{i+1} - x_i\right)\cdot\left(y_{j+1} - y_j\right)$$

$$q_{22} = \sum_{i=1}^{n_x-1}\sum_{j=1}^{n_y-1}\frac{1}{4}\left(x_{i+1}^2 - x_i^2\right)\cdot\left(y_{j+1}^2 - y_j^2\right)$$

$$q_{23} = \sum_{i=1}^{n_x-1}\sum_{j=1}^{n_y-1}\frac{1}{8}\left(x_{i+1}^2 - x_i^2\right)\cdot\left(y_{j+1} - y_j\right)\left[\sigma_z^{ep}\left(x_i, y_j\right) + \sigma_z^{ep}\left(x_{i+1}, y_j\right) + \sigma_z^{ep}\left(x_{i+1}, y_{j+1}\right) + \sigma_z^{ep}\left(x_i, y_{j+1}\right)\right]$$

$$q_{31} = \sum_{i=1}^{n_x-1}\sum_{j=1}^{n_y-1}\frac{1}{4}\left(x_{i+1}^2 - x_i^2\right)\cdot\left(y_{j+1}^2 - y_j^2\right)$$

$$q_{32} = \sum_{i=1}^{n_x-1}\sum_{j=1}^{n_y-1}\frac{1}{4}\left(x_{i+1} - x_i\right)\cdot\left(y_{j+1} + y_j\right)^2\left(y_{j+1} - y_j\right)$$

$$q_{33} = \sum_{i=1}^{n_x-1}\sum_{j=1}^{n_y-1}\frac{1}{8}\left(x_{i+1} - x_i\right)\cdot\left(y_{j+1}^2 - y_j^2\right)\left[\sigma_z^{ep}\left(x_i, y_j\right) + \sigma_z^{ep}\left(x_{i+1}, y_j\right) + \sigma_z^{ep}\left(x_{i+1}, y_{j+1}\right) + \sigma_z^{ep}\left(x_i, y_{j+1}\right)\right]$$

After the global re-distribution, the stress relaxation process is repeated starting with a new "pseudo" stress state given by

$$\sigma_z^{pseudo}\left(x, y\right) = {}^{(k-1)}\sigma_z^{ep} + {}^{(k)}\Delta\sigma_z^E + \Delta\sigma_z\left(x, y\right)$$

This process is repeated until the convergence criterion is met.

I.4 INTERFACING WITH SwRI's ISOTROPIC SHAKEDOWN MODULE

As part of the current program SwRI developed and validated under monotonic loading conditions a computer module, SHARP that performs an approximate shakedown analysis for three-dimensional structures where a bivariant stress distribution is induced on the load bearing section of interest. The program enhances the point relaxation module developed by Prof. Glinka to include the effects of load relaxation and load re-distribution

over the load bearing area while maintaining force and moment balance on that area. An executable version of the routine SHARP has been delivered to the HCF Team. This section describes how the SHARP routine can be interfaced with a calling program so that the module may be integrated into HCF related software that requires a shakedown analysis for its execution.

Two data transfer mechanisms are used to pass information to and receive results from the isotropic shakedown module, SHARP. One mechanism is through a COMMON data structure that contains arrays with prescribed dimensions, and the other mechanism is through the argument list of the routine itself. To demonstrate the data passing mechanisms, several segments of computer code are listed below that illustrate the type of coding that the user should include in the program driving the isotropic shakedown module.

The computer code listed in Table I1 shows the parameters and the associated array sizes required to call the isotropic shakedown module. A description of the arrays and parameters listed in Table I1 is provided in Table I2. The declaration for the data type employs the default Fortran 77 style.

Depending on how the shakedown module is driven by the calling program, the declarations of the arrays listed in Table I1 can be placed in different routines in the calling program. For large data arrays, the Fortran COMMON data structure is used for storage efficiency. Comments are used in Table I1 to separate the COMMON and DIMENSION declarations into two Code Segments, A and B. The arrays declared in Code Segment A are used by the isotropic shakedown module and the elements of these arrays need to have their values initialized as illustrated in Code Segment C that is contained in Table I3. The parameters and arrays declared in Code Segment B are either input values specified by the user or output values of the plastically relaxed stress components (output), σ_{ij}^{ep}, calculated by the shakedown module.

The arrays declared in Code Segment A need to be initialized before the isotropic shakedown module is called for the first time. The initialization should be placed outside of the loop driving the incremental loading. A segment of code illustrating how to properly initialize the arrays declared in Code Segment A listed in Table I3.

Specification of the plasticity surfaces used in the Garud model described in Section I.2 is needed before the isotropic shakedown module can be called. These plasticity surfaces should be specified outside of the incremental loading loop that calls SHARP, as indicated in Code Segment D shown in Table I4. An example of a subroutine that will calculate the plastic modulus for a specified stress and the corresponding strain is illustrated Table I5. This routine will automatically increase the number of discrete stress and strain pairs specified by the user if refinements in stress/strain data are deemed necessary. The routine arranges the stress and strain data pairs in an ascending order, and calculates the effective plastic modulus from the piecewise line segments representing the uniaxial stress-strain behavior.

The statement to drive the isotropic shakedown routine is shown in Code Segment E of Table I4. There are five parameters in the argument list of the routine SHARP. A description of each of the arguments can be found in Table I6. Note should be taken of the fact that since the two-dimensional stress arrays that contain the linear elastic results for an incremental increase in load are used in the calculations for the current load step, a segment of code may be needed to assign the incremental stress values to these stress arrays from global stress arrays that may contain all the linear elastic stress results for every load step.

A non-zero error code generated by the isotropic shakedown module indicates an error is detected in the module. A sample subroutine is provided to show what the various error codes represent. The listing of these error descriptions is displayed in Table I7.

Table I1. Listing of Computer Code Indicating How the Array Dimensions are Declared

```
c====================================================================
c   Parameter and arrays required to drive SHARP
c
        Implicit real (a-h,o-z)
        parameter (nso=100,nnx=200,nny=200,max_pt=nnx*nny,max_seq=40,max_rv=5)
c
c *** CODE SEGMENT A ***
c arrays used by the isotropic shakedown module.  They are declared outside the module
c for initialization.  The initialization can be found in Code Segment A.
c
        dimension a1vb(max_pt,max_seq,6),ipv(max_pt),sigv(max_pt,6),epsv(max_pt,6),
     +          sigev(max_pt,6),dfdsv(max_pt,6),irv(max_pt,6),sezv(max_pt,6),
     +          sazv(max_pt,6),eazv(max_pt,6),dsmv(max_pt,6),serv(max_pt,max_rv,6),
     +          sarv(max_pt,max_rv,6),earv(max_pt,max_rv,6),x1v(max_pt,6)
        common/global_/a1v,sigv,epsv,sigev,dfdsv,sezv,sazv,eazv,
     +          dsmv,serv,sarv,earv,x1v,ipv,irv
c
c   *** CODE SEGMENT B ***
c
        dimension seq(max_seq), etp(max_seq)
        common/mpd/E,eni,etp
        common/RO_law/alpha,beta,sigo,epso,tri_max,tri_min,iduck
        common/sig_out/ss11r(nso,nso),ss12r(nso,nso),ss13r(nso,nso),
     +          ss22r(nso,nso),ss23r(nso,nso),ss33r(nso,nso)
        common/ds_old/xo(nso),yo(nso),dsxx(nso,nso),dsxy(nso,nso),
     +          dsxz(nso,nso),dsyy(nso,nso),dsyz(nso,nso),dszz(nso,nso)
c====================================================================
```

Table I2.   Descriptions for Parameters and Arrays Listed in Code Segment B Using the Default Fortran 77 Style

Parameter Name	Data Type	Status	Description
E	real	User-specified	Young's module
Eni	real	User-specified	Poisson's ratio
Etp	real array	User-specified	One-dimensional array of size *max_seq* used to store the effective plastic modulus corresponding to the user-specified discrete stress values contained in array *seq*. The effective plastic modulus is defined as $$\left.\frac{d\sigma}{d\varepsilon_{plastic}}\right|_{\sigma,\varepsilon_{plastic}}$$. The *etp* and *seq* array values define piecewise line segments of the user-specified Ramberg-Osgood equation used to represent the uniaxial stress-strain relationship. Hence the stress-strain points defined by the values of *etp* and *seq* should all fall on the Ramberg-Osgood curve. The values of *etp* and *seq* define the plasticity surfaces employed in the Garud model.
seq	real array	User-specified	One-dimensional array of size *max_seq* used to store the discrete stress values corresponding to the values of the plasticity modulus, *etp*. The element values of the arrays *etp* and *seq*, define the piecewise line segments representing the uniaxial stress-strain relationship defined through the Ramberg-Osgood equation (see description of *etp*).
$alpha$	real	User-specified	Coefficient appearing in the plastic strain component of the Ramberg-Osgood stress-strain equation.
$beta$	real	User-specified	Exponent appearing in the plastic strain component of the Ramberg-Osgood stress-strain equation.
$sigo$	real	User-specified	Yield stress parameter appearing in the Ramberg-Osgood stress-strain equation.
$epso$	real	User-specified	Yield strain parameter appearing in the Ramberg-Osgood stress-strain equation where *epso=sigo/E.*.

Table I2. Descriptions for Parameters and Arrays Listed in Code Segment B Using the Default Fortran 77 Style (continued)

Parameter Name	Data Type	Status	Description
xo	real array	User-specified	One-dimensional array of size *nso* used to store the x-coordinates of the user-defined bivariant stress distribution. The values of x should be stored in the ascending order from the minimum value, x_{min}, to the maximum value, x_{max}. The array needs not to be fully populated with *nso* non-zero values. However, if there are only n_x values of x, the array elements indexed from (n_x+1) to *nso* should be filled with zeros.
yo	real array	User-specified	One-dimensional array of size *nso* used to store the y-coordinates of the user-defined bivariant stress distribution. The values of y should be stored in the ascending order from the minimum value, y_{min}, to the maximum value, y_{max}. The array needs not to be fully populated with *nso* non-zero values. However, if there are only n_y values of y, the array elements indexed from (n_y+1) to *nso* should be filled with zeros.
dsxx	real array	User-specified	Two-dimensional array of size *nso×nso* used to store values of the incremental linear elastic stress component, $\Delta\sigma_x$, of the bivariant stress field corresponding to position coordinates (x,y) contained in the arrays *xo* and *yo*. The array should contain $n_x \times n_y$ values, and the remaining elements should contain zero values.
dsxy	real array	User-specified	Two-dimensional array of size *nso×nso* used to store values of the incremental linear elastic stress component, $\Delta\sigma_{xy}$, of the bivariant stress field corresponding to position coordinates (x,y) contained in the arrays *xo* and *yo*. The array should contain $n_x \times n_y$ values, and the remaining elements should contain zero values.
dsxz	real array	User-specified	Two-dimensional array of size *nso×nso* used to store values of the incremental linear elastic stress component, $\Delta\sigma_{xz}$, of the bivariant stress field corresponding to position coordinates (x,y) contained in the arrays *xo* and *yo*. The array should contain $n_x \times n_y$ values, and the remaining elements should contain zero values.

Table I2. Descriptions for Parameters and Arrays Listed in Code Segment B Using the Default Fortran 77 Style (continued)

Parameter Name	Data Type	Status	Description
dsyy	real array	User-specified	Two-dimensional array of size *nso×nso* used to store values of the incremental linear elastic stress component, $\Delta\sigma_{yy}$, of the bivariant stress field corresponding to position coordinates (*x,y*) contained in the arrays *xo* and *yo*. The array should contain $n_x \times n_y$ values, and the remaining elements should contain zero values.
dsyz	real array	User-specified	Two-dimensional array of size *nso×nso* used to store values of the incremental linear elastic stress component, $\Delta\sigma_{yz}$, of the bivariant stress field corresponding to position coordinates (*x,y*) contained in the arrays *xo* and *yo*. The array should contain $n_x \times n_y$ values, and the remaining elements should contain zero values.
dszz	real array	User-specified	Two-dimensional array of size *nso×nso* used to store values of the incremental linear elastic stress component, $\Delta\sigma_{z}$, of the bivariant stress field corresponding to position coordinates (*x,y*) contained in the arrays *xo* and *yo*. The array should contain $n_x \times n_y$ values, and the remaining elements should contain zero values.
ss11r	real array	Output	Two-dimensional array of size *nso×nso* used to store values of the plastically relaxed stress component, σ_x^{ep}, of the bivariant stress field corresponding to position coordinates (*x,y*) contained in the arrays *xo* and *yo*.
ss12r	real array	Output	Two-dimensional array of size *nso×nso* used to store values of the plastically relaxed stress component, σ_{xy}^{ep}, of the bivariant stress field corresponding to position coordinates (*x,y*) contained in the arrays *xo* and *yo*.
ss13r	real array	Output	Two-dimensional array of size *nso×nso* used to store values of the plastically relaxed stress component, σ_{xz}^{ep}, of the bivariant stress field corresponding to position coordinates (*x,y*) contained in the arrays *xo* and *yo*.

Table I2. Descriptions for Parameters and Arrays Listed in Code Segment B Using the Default Fortran 77 Style (continued)

Parameter Name	Data Type	Status	Description
ss22r	real array	Output	Two-dimensional array of size *nso×nso* used to store values of the plastically relaxed stress component, σ_y^{ep}, of the bivariant stress field corresponding to position coordinates (*x*,*y*) contained in the arrays *xo* and *yo*.
ss23r	real array	Output	Two-dimensional array of size *nso×nso* used to store values of the plastically relaxed stress component, σ_{yz}^{ep}, of the bivariant stress field corresponding to position coordinates (*x*,*y*) contained in the arrays *xo* and *yo*.
ss33r	real array	Output	Two-dimensional array of size *nso×nso* used to store values of the plastically relaxed stress component, σ_z^{ep}, of the bivariant stress field corresponding to position coordinates (*x*,*y*) contained in the arrays *xo* and *yo*.
tri_max, tri_min	real	Declaration	Parameters allocated for SHARP
iIduck	integer	Declaration	Parameter allocated for SHARP

Table I3. Segment of Computer Code Illustrating How to Initialize the Arrays Declared in Code Segment A

```
c====================================================================
c  *** CODE SEGMENT C ***: Initializing the arrays declared in Code Segment A
c
        do i=1,max_pt
           do i1=1,max_seq
              do j=1,6
                   a1v(i,i1,j)=0.
               End do
           End do
        End do
        do i=1,max_pt
           ipv(i)=0
           do j=1,6
               x1v(i,j)=0.
               irv(i,j)=0
               sigv(i,j)=0.
               epsv(i,j)=0.
               sigev(i,j)=0.
               dfdsv(i,j)=0.
               dsmv(i,j)=0.
               sezv(i,j)=0.
               sazv(i,j)=0.
               eazv(i,j)=0.
           End do
        End do
        do i=1,max_pt
           do i1=1,max_rv
              do j=1,6
                 serv(i,i1,j)=0.
                 sarv(i,i1,j)=0.
                 earv(i,i1,j)=0.
              End do
           End do
        End do
c====================================================================
```

Table I4. Segment of Computer Code Showing How to Call SwRI's Isotropic Shakedown Module

```
c====================================================================
c ***CODE SEGMENT D ***
c  User needs to provide a segment of code to define the plasticity surfaces
       **** CODE FOR THE DEFINITION OF PLASTICITY SURFACES
c
c  before calling the isotropic shakedown module, set kinit=0
c
       kinit=0
c
c====================================================================
c  *** CODE SEGMENT E *** : Computing loop starts from here
c
       do istep=1,nstep
c
c   User needs to provide a segment of code here to read the linear elastic stress increment
       **** CODE FOR THE INPUT OF STRESS INCREMENT ****
c
          print '(a,i3)','---  Processing Step ',istep
           call SHARP (kinit,istep,seq,in,ierr)
          end do
c====================================================================
```

Table I5. A Sample Subroutine Used to Define the Plasticity Surfaces

```fortran
c======================================================================
      SUBROUTINE MDI(IN,SEQ,sige0)
c
c   Modified from Glinka's MDI routine
c
      parameter(max_seq=40)
      DIMENSION SEQ(max_seq),EEQ(max_seq),ETP(max_seq),
     +        SEQ1(max_seq),EEQ1(max_seq)
      common/mpd/E,eni,etp
      in1=1
      seq1(1)=sige0
      EEQ1(1)=SEQ1(1)/E
      SEQ(1)=SEQ1(1)
      EEQ(1)=EEQ1(1)
      IN=1
31    IN=IN+1
      READ(10,*,END=41) ss1,ee1
        SEQ1(IN)=ss1
        EEQ1(IN)=ee1
        IF(SEQ1(IN) .LE. SEQ1(IN-1).OR.EEQ1(IN) .LE. EEQ1(IN-1))
     +      STOP '[ERROR]: SEQ(I) < SEQ(I-1) or EEQ(I) < EEQ(I-1)!'
      GOTO 31
41    IN=IN-1
      DO 20 I=2,IN
        SQP=SEQ1(I)
        IN2=0
71      DSEQ=(SQP-SEQ1(I-1))/SEQ1(I-1)
        IF(DSEQ .GT. 0.01D1)THEN
         IN2=IN2+1
         SQP=SEQ1(I-1)+(SQP-SEQ1(I-1))/0.2D1
         GOTO 71
        ENDIF
        IN2=2**IN2
        DSEQ=SQP-SEQ1(I-1)
        DEQP=(EEQ1(I)-EEQ1(I-1))/DBLE(IN2)
        DO 30 I2=1,IN2
         IN1=IN1+1
         if(in1.gt.max_seq) stop '[ERR]: exceed the preset!'
         SEQ(IN1)=SEQ(IN1-1)+DSEQ
         EEQ(IN1)=EEQ(IN1-1)+DEQP
30      CONTINUE
20    CONTINUE
      IN=IN1
c
c   plastic modulus
c
      DO 40 I=2,IN
        ETP(I)=(EEQ(I)-EEQ(I-1))/(SEQ(I)-SEQ(I-1))-0.1D1/E
        ETP(I)=0.1D1/ETP(I)
40    CONTINUE
      close(10)
      RETURN
      END
```

Table I6. Parameters and Arrays Passed Through the Argument List of the Isotropic Shakedown Module

SUBROUTINE SHARP (*kinit, istep, seq, in, ierr*)			
Parameter Name	Data Type	Status	Description
Kinit	integer	User-specified Initially	Set to zero (0) initially for SHARP to generate *x*- and *y*-coordinates constituting a finer mesh. After the first increment, it is automatically reset to one (1) within SHARP.
Istep	integer	User-specified	Current load increment number
Seq	real array	User-specified	See Table A.2 for description.
In	integer	User-specified	Number of data points for *seq* and *etp*.
Ierr	integer	Output	Error code (see Table A.7)

Table I7. Sample Error Code Handler

```
c===================================================================
      subroutine errmsg(ierr)
      if(ierr.eq.0) return
      open(23,file='error.msg')
      if(ierr.eq.1) then
        write(23,101)
      elseif(ierr.eq.2) then
        write(23,102)
      elseif(ierr.eq.3) then
        write(23,103)
      elseif(ierr.eq.4) then
        write(23,104)
      elseif(ierr.eq.5) then
        write(23,105)
      elseif(ierr.eq.7) then
        write(23,107)
      elseif(ierr.eq.8) then
        write(23,108)
      endif
      close(23)
101   format('[ERROR]: too few data points to generate a new bi-',/,
     +   '         variant stress array! At least 2 by 2 required')
102   format('[ERROR]: the values of the x-coordinate array are not',/,
     +   '         in ascending order!')
103   format('[ERROR]: the values of the y-coordinate array are not',/,
     +   '         in ascending order!')
104   format('[ERROR]: reach the max. declared array size. Increase',/,
     +   '         the value of nbmax in the parameter statement!')
105   format('[ERROR]: reach max. number of iterations (13)!')
107   format('[ERROR]: no single root found when searching for the',/,
     +   '         equivalent stress using Neuber rule!')
108   format('[ERROR]: iterations exceeded when searching for the',/,
     +   '         equivalent stress using Neuber rule!')
      return
      end
```

I.5   VALIDATION OF ISOTROPIC SHAKEDOWN MODULE AGAINST THREE-DIMENSIONAL FINITE-ELEMENT RESULTS

New and existing three-dimensional elastic-plastic finite element analyses were used to validate the isotropic shakedown methodology. The isotropic shakedown module used as input bivariant stress fields derived from three dimensional linear elastic finite element computations employing ABAQUS. The validation was performed for a single edge notched plate of width (W) equal to 10 inches, thickness (t) equal to 5 inches, and height (h) equal to 20 inches, containing a semi-circular through-thickness notch with a radius (r) equal to 1 inch (see Figure I1). This plate was subjected to various combinations of tensile loads and applied in-plane and out-of-plane moments, as illustrated in Figure I1. The combinations of loads used in the validation analyses are listed in Table I8.

Validation computations have been performed for materials with different strain hardening capabilities. As can be seen in Figure I2, two extreme types of material strain hardening behaviors (Materials A and B) were used for all of the load cases listed in Table I8. For material behaviors displaying intermediate strain hardening between these two extremes (Materials C to F), only the results for the notched plate subjected to remote tension (Load Case A) were generated and used for validation. Table I9 lists the Ramberg-Osgood parameters governing these constitutive relationships.

Comparison of the results derived from the isotropic shakedown methodology with those evaluated using three-dimensional EPFEA is shown in Figure I3 to I42. The figure number pertaining to a specific loading condition and material type can be located from Table I8. Included for comparison are the results derived from the as-received Glinka's point relaxation module.

Figures from I3 to I22 show the comparison of the distribution (in terms of contours) of the elastic-plastic stress component normal to the load bearing section predicted by the isotropic shakedown module and the FEA results. In each figure, Figure (a) contains the FEA results, Figure (b) contains the results predicted by the isotropic shakedown module, and Figure (c) shows Glinka's point relaxation results (available only for Materials A and B). The agreement between the results obtained using SHARP and FEA is far better than the agreement between Glinka's point relaxation module and the FEA results, when these comparisons are measured with respect to either the positions of peaks and valleys in the

stress distributions or the peak stress magnitudes. Glinka's point relaxation module consistently predicts much lower peak values than those computed by the EPFEA and the isotropic shakedown module. This conclusion can be drawn by observing the contour values and the stress gradients around the stress peaks when comparing Figures (a), (b) and (c).

Figures I23 to I42 show the variations of the three normal stress components along the plate width direction from the notch tip. These figures illustrate how the enhancements made by SwRI to account for the stress triaxiality and to maintain force/moment balance during incremental loading produced a significant improvement in the point relaxation module developed by Glinka. In each figure, three plots are displayed. The results in Figure (a) are for y/r=0 (the free surface at the side of the plate), those in Figure (b) are for y/r=1.237 (a plane one quarter of the way through the plate), and those in Figure (c) are for y/r=2.5 (at the mid-plane). As can be seen, for the loading conditions leading to a small scale of yielding near the notch tip (Load Cases A, B and C, see Table A.5.1), the agreement between the FEA results and SHARP in reference to the locations of the peak stress values and the stress variation with distance is excellent.

For loading conditions resulting in a large scale of yielding (Load Cases D to H), the agreement between the FEA results and SHARP depends on the strain hardening capacity of the material. For materials displaying large strain hardening capacity; *e.g*., Material B, the agreement remains excellent—for example, see Figures I34 to I38. However, there is a reduction in accuracy of the SHARP solutions for materials displaying very little strain hardening capacity (nearly perfectly plastic behavior) when large scale yielding occurs at the notches—for example, see Figures I28 to I30. This is because in these cases a large amount of surplus load needs to be re-distributed over the load bearing area where deformations remain elastic. The load re-distribution method developed by SwRI was not intended for use in these situations. However, it should be recognized that these are extreme cases where the plastic zone is on the order of 25% to 50% of the load-bearing section. This situation is not likely to occur in engine components.

The variation of the out-of-plane stress predicted by Glinka's point relaxation method tends to follow the linear elastic solution with the result that this method does not capture the actual elastic-plastic multiaxial stress state in the plastic zone at a notch.

Consequently, this approach predicts much lower stress values in most cases than does the FEA results.

Table I8. **Load Combinations Used in the Verification of SwRI Isotropic Shakedown Module**

Material	Load Case	Applied Loads			Figure No. Showing the Comparison of Contours of Elastic-Plastic Stress Component normal to the Load Bearing Section	Figure No. Showing the Comparison of the Distributions of Three Normal Stress Components
		S_z (ksi)	M_x (kip-in)	M_y (kip-in)		
A	A	50	0	0	I.3	I.23
	B	25	0	2500	I.4	I.24
	C	25	1600	0	I.5	I.25
	D	20	1800	1800	I.6	I.26
	E	55	0	0	I.7	I.27
	F	30	0	3500	I.8	I.28
	G	30	2500	0	I.9	I.29
	H	25	2400	2400	I.10	I.30
B	A	50	0	0	I.11	I.31
	B	25	0	2500	I.12	I.32
	C	25	1600	0	I.13	I.33
	D	20	1800	1800	I.14	I.34
	E	55	0	0	I.15	I.35
	F	30	0	3500	I.16	I.36
	G	30	2500	0	I.17	I.37
	H	25	2400	2400	I.18	I.38
C	A	50	0	0	I.19	I.39
D	A	50	0	0	I.20	I.40
E	A	50	0	0	I.21	I.41
F	A	50	0	0	I.22	I.42

Table I9. Ramberg-Osgood Parameters Used to Generate Various Material Constitutive Relationships

Material ID	E (ksi)	σ_o (ksi)	α	β
A				31.5
B				4
C	27700	62.52	0.43	25.63
D				14.7
E				8.53
F				4.92
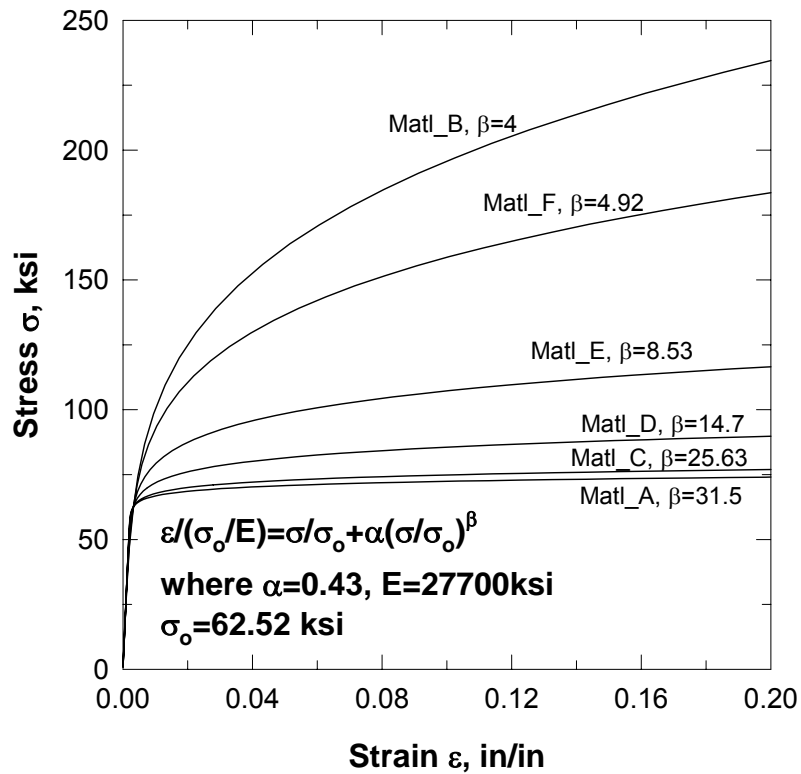
Figure I2.   Material constitutive relationships with various capacities of strain hardening used for validation of isotropic shakedown methodology against three-dimensional finite element results.

Fig. I3(a)   FEA results

Fig. I3 (b)   Predicted results by SwRI's isotropic shakedown module.

Fig. I3 (c)   Predicted results by as-received Glinka's point relaxation module.

Figure I3.   Comparison of the distribution of the elastic-plastic stress component normal to the load bearing section predicted by SwRI's isotropic shakedown module with FEA results for the notched plate subjected to S_z=50 *ksi*, and M_x=M_y=0; Material A. The results predicted by the as-received Glinka's point relaxation module are also included to demonstrate the enhancements made by SwRI to account for stress triaxiality at the notches and to maintain force/moment balance through load shedding and re-distribution.

Fig. I4(a)   FEA results   Fig. I4(b)   Predicted results by SwRI's   Fig. I4(c)   Predicted results by as-received
                                                    isotropic shakedown module.   Glinka's point relaxation
                                                                                                         module.

Figure I4.   Comparison of the distribution of the elastic-plastic stress component normal to the load bearing section predicted by
              SwRI's isotropic shakedown module with FEA results for the notched plate subjected to S_z=25 *ksi*, M_x=0, and M_y=2500 *kip-
              in*; Material A. The results predicted by the as-received Glinka's point relaxation module are also included to demonstrate
              the enhancements made by SwRI to account for stress triaxiality at the notches and to maintain force/moment balance
              through load shedding and re-distribution.

Fig. I5(a)   FEA results

Fig. I5 (b)   Predicted results by SwRI's isotropic shakedown module.

Fig. I5 (c)   Predicted results by as-received Glinka's point relaxation module.

Figure I5. Comparison of the distribution of the elastic-plastic stress component normal to the load bearing section predicted by SwRI's isotropic shakedown module with FEA results for the notched plate subjected to S_z=25 *ksi*, M_x=1600 *kip-in*, and M_y=0; Material A. The results predicted by the as-received Glinka's point relaxation module are also included to demonstrate the enhancements made by SwRI to account for stress triaxiality at the notches and to maintain force/moment balance through load shedding and re-distribution.

Fig. I6(a)   FEA results

Fig. I6(b)   Predicted results by SwRI's isotropic shakedown module.

Fig. I6(c)   Predicted results by as-received Glinka's point relaxation module.

Figure I6.   Comparison of the distribution of the elastic-plastic stress component normal to the load bearing section predicted by SwRI's isotropic shakedown module with FEA results for the notched plate subjected to S_z=20 *ksi*, M_x=1800 *kip-in*, and M_y=1800 *kip-in*; Material A. The results predicted by the as-received Glinka's point relaxation module are also included to demonstrate the enhancements made by SwRI to account for stress triaxiality at the notches and to maintain force/moment balance through load shedding and re-distribution.

Fig. I7(a)   FEA results

Fig. I7(b)   Predicted results by SwRI's isotropic shakedown module.

Fig. I7(c)   Predicted results by as-received Glinka's point relaxation module.

Figure I7.   Comparison of the distribution of the elastic-plastic stress component normal to the load bearing section predicted by SwRI's isotropic shakedown module with FEA results for the notched plate subjected to S_z=55 ksi, and M_x=M_y=0; Material A. The results predicted by the as-received Glinka's point relaxation module are also included to demonstrate the enhancements made by SwRI to account for stress triaxiality at the notches and to maintain force/moment balance through load shedding and re-distribution.

Fig. I8(a)   FEA results   Fig. I8(b)   Predicted results by SwRI's   Fig. I8(c)   Predicted results by as-received
                                                         isotropic shakedown module.   Glinka's point relaxation
                                                                                                          module.
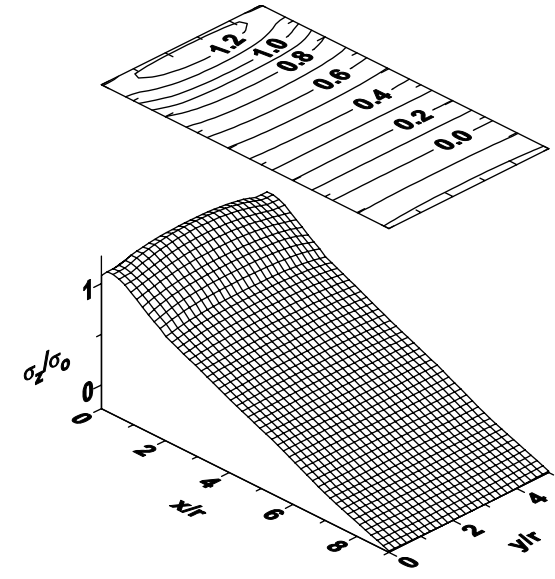
Figure I8.   Comparison of the distribution of the elastic-plastic stress component normal to the load bearing section predicted by
              SwRI's isotropic shakedown module with FEA results for the notched plate subjected to S_z=30 *ksi*, M_x=0 and M_y=3500 *kip-in*; Material A. The results predicted by the as-received Glinka's point relaxation module are also included to demonstrate
              the enhancements made by SwRI to account for stress triaxiality at the notches and to maintain force/moment balance
              through load shedding and re-distribution.

Fig. I9(a)   FEA results

Fig. I9(b)   Predicted results by SwRI's isotropic shakedown module.
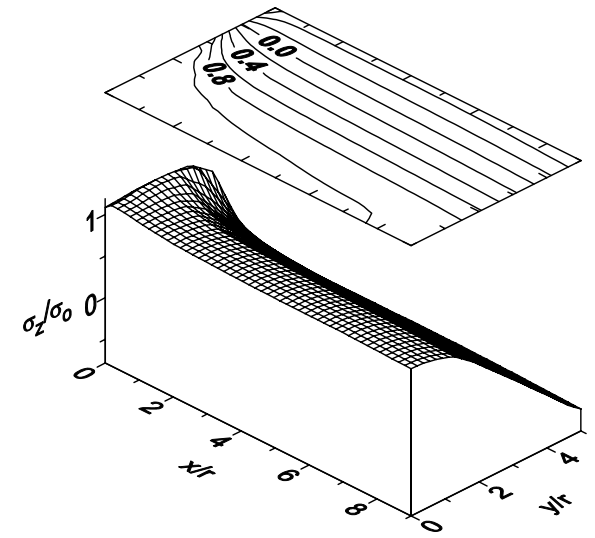
Fig. I9(c)   Predicted results by as-received Glinka's point relaxation module.

Figure I9.   Comparison of the distribution of the elastic-plastic stress component normal to the load bearing section predicted by SwRI's isotropic shakedown module with FEA results for the notched plate subjected to S_z=30 *ksi*, M_x=2500 *kip-in* and M_y=0; Material A. The results predicted by the as-received Glinka's point relaxation module are also included to demonstrate the enhancements made by SwRI to account for stress triaxiality at the notches and to maintain force/moment balance through load shedding and re-distribution.

Fig. I10(a)   FEA results   I10(b)   Predicted results by SwRI's isotropic shakedown module.   Fig. I10(c)   Predicted results by as-received Glinka's point relaxation module.
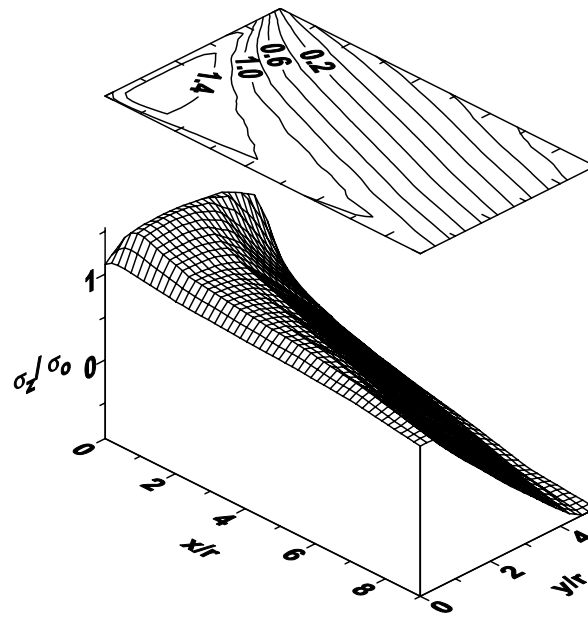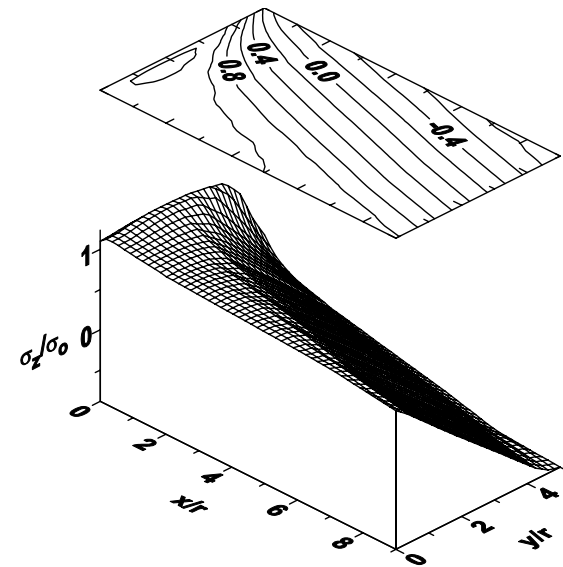
Figure I10.   Comparison of the distribution of the elastic-plastic stress component normal to the load bearing section predicted by SwRI's isotropic shakedown module with FEA results for the notched plate subjected to S_z=25 *ksi*, M_x=2400 *kip-in* and M_y=2400 *kip-in*; Material A. The results predicted by the as-received Glinka's point relaxation module are also included to demonstrate the enhancements made by SwRI to account for stress triaxiality at the notches and to maintain force/moment balance through load shedding and re-distribution.
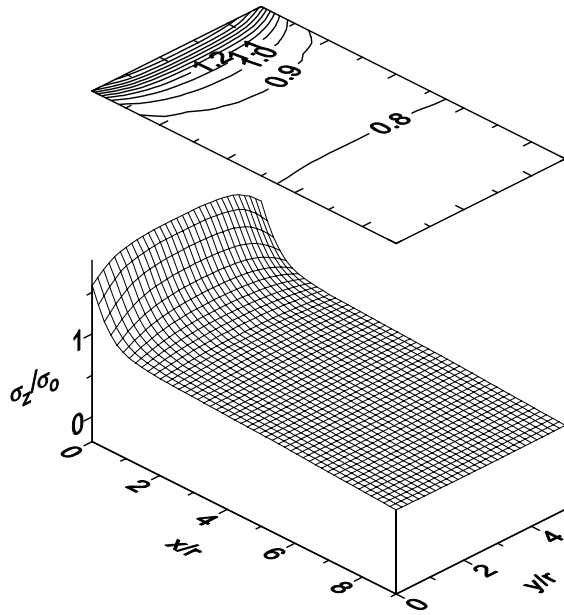
Fig. I11(a)   FEA results
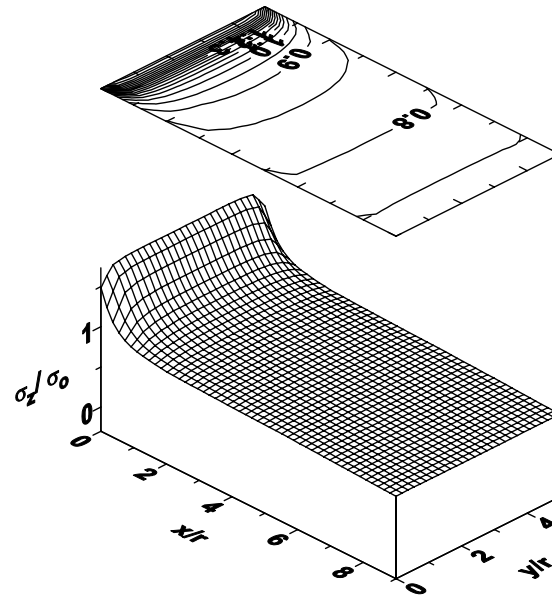
Fig. I11(b)   Predicted results by SwRI's isotropic shakedown module.
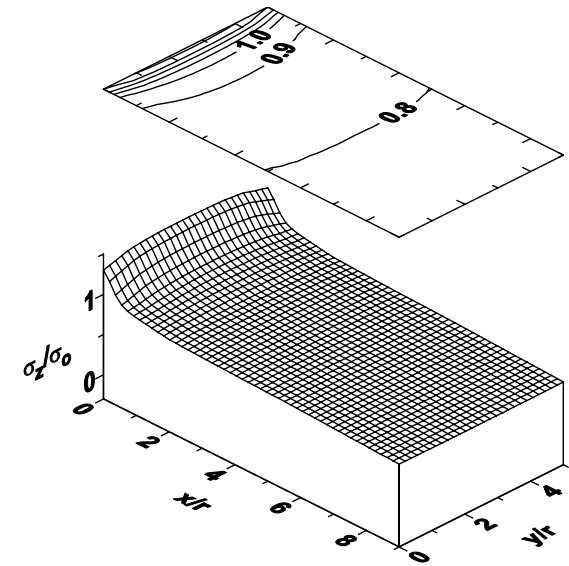
Fig. I11(c)   Predicted results by as-received Glinka's point relaxation module.

Figure I11.   Comparison of the distribution of the elastic-plastic stress component normal to the load bearing section predicted by SwRI's isotropic shakedown module with FEA results for the notched plate subjected to S_z=50 *ksi*, and $M_x=M_y=0$; Material B. The results predicted by the as-received Glinka's point relaxation module are also included to demonstrate the enhancements made by SwRI to account for stress triaxiality at the notches and to maintain force/moment balance through load shedding and re-distribution.
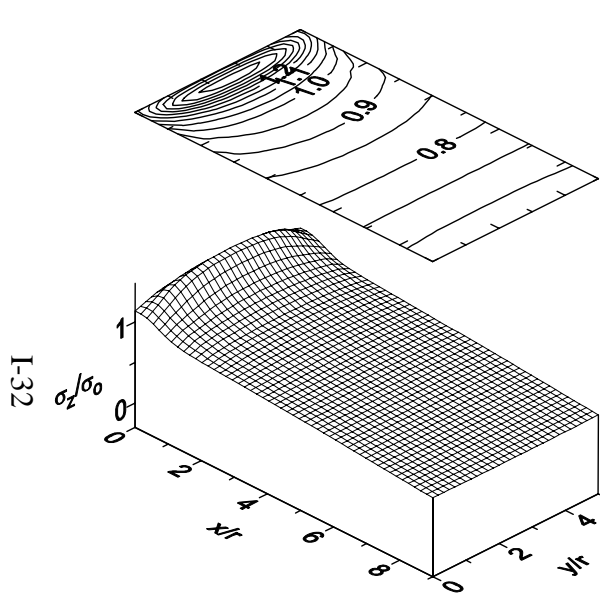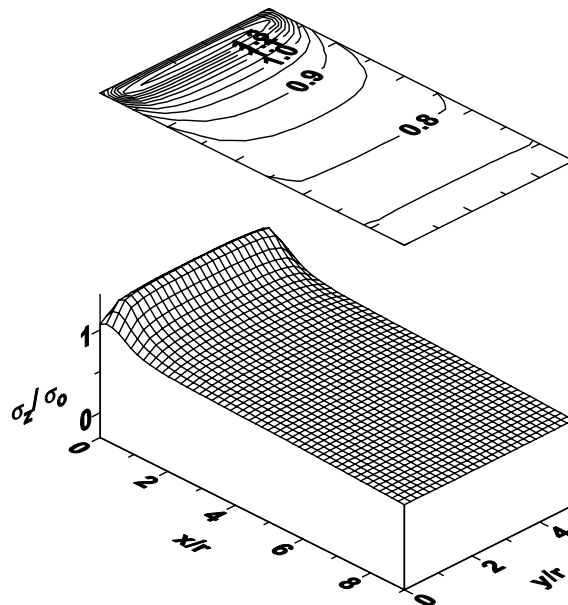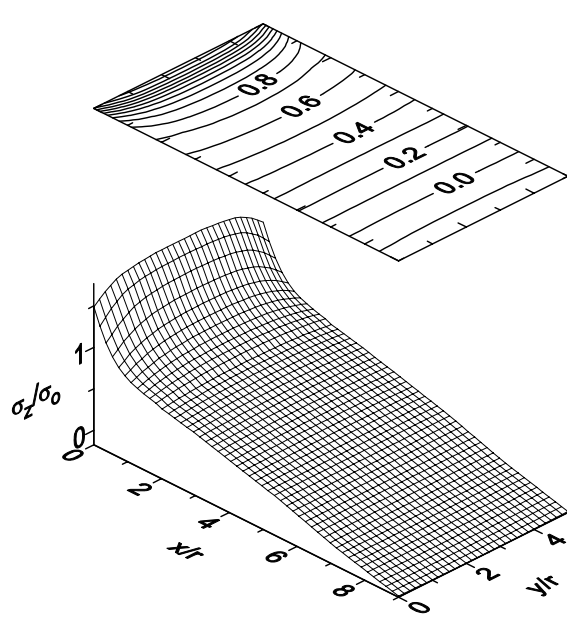
Fig. I12(a)   FEA results
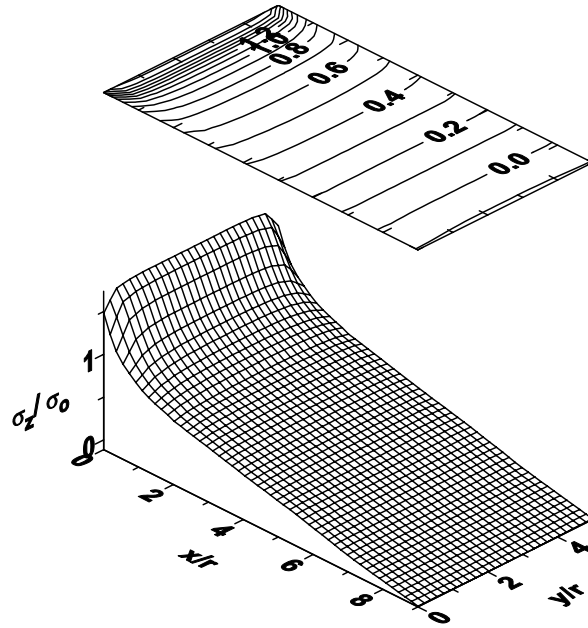
Fig. I12 (b)   Predicted results by SwRI's isotropic shakedown module.
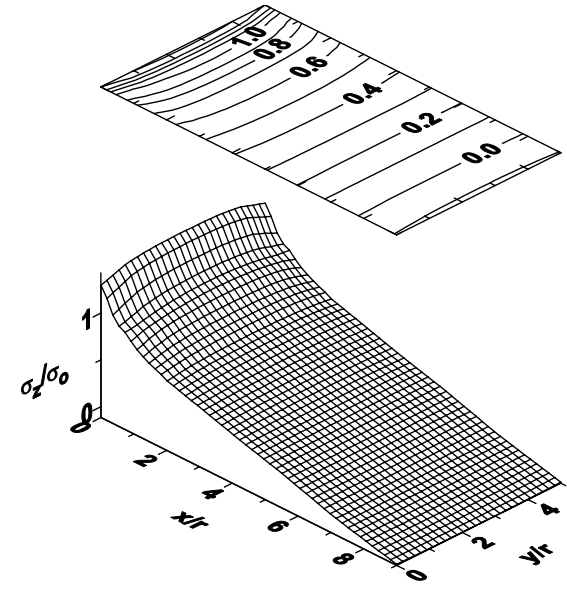
Fig. I12 (c)   Predicted results by as-received Glinka's point relaxation module.

Figure I12.   Comparison of the distribution of the elastic-plastic stress component normal to the load bearing section predicted by SwRI's isotropic shakedown module with FEA results for the notched plate subjected to S_z=25 *ksi*, M_x=0, and M_y=2500 *kip-in*; Material B. The results predicted by the as-received Glinka's point relaxation module are also included to demonstrate the enhancements made by SwRI to account for stress triaxiality at the notches and to maintain force/moment balance through load shedding and re-distribution.
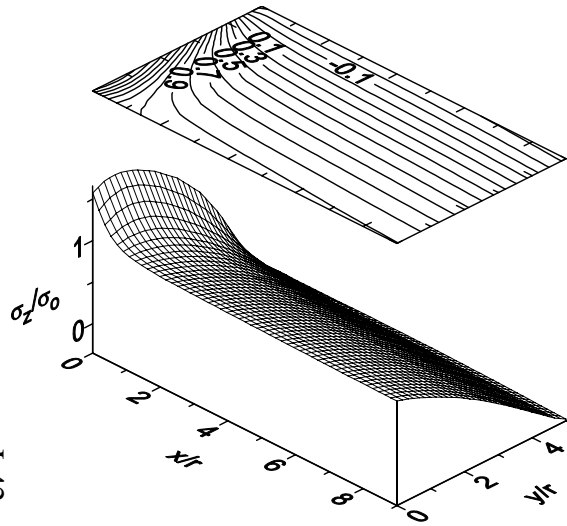
Fig. I13(a)   FEA results
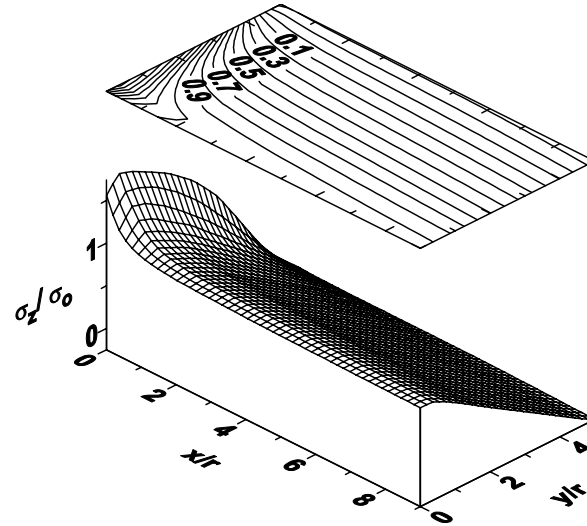
Fig. I13 (b)   Predicted results by SwRI's isotropic shakedown module.
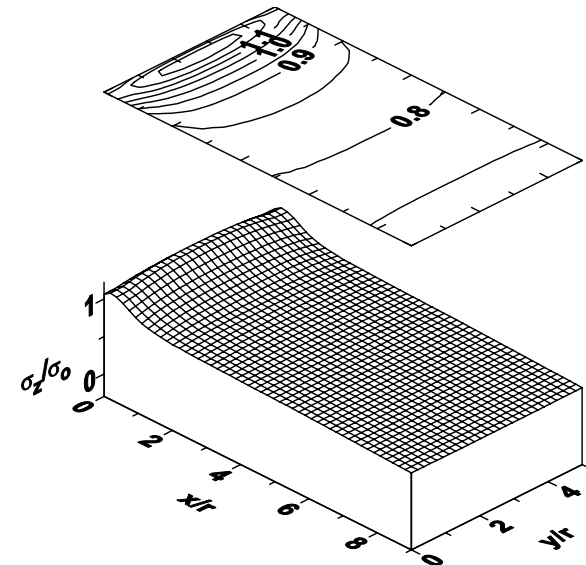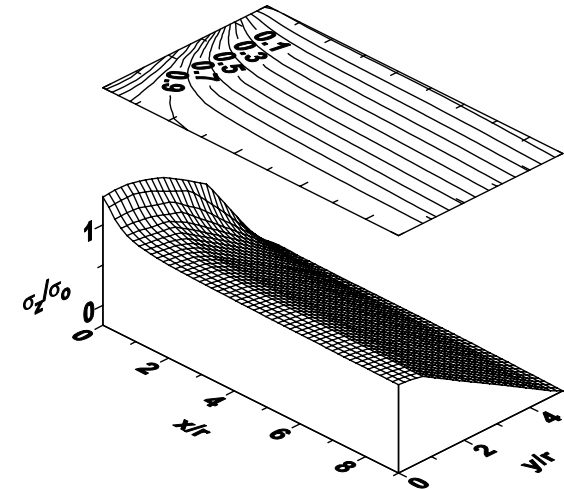
Fig. I13 (c)   Predicted results by as-received Glinka's point relaxation module.

Figure I13.   Comparison of the distribution of the elastic-plastic stress component normal to the load bearing section predicted by SwRI's isotropic shakedown module with FEA results for the notched plate subjected to S_z=25 *ksi*, M_x=1600 *kip-in*, and M_y=0; Material B. The results predicted by the as-received Glinka's point relaxation module are also included to demonstrate the enhancements made by SwRI to account for stress triaxiality at the notches and to maintain force/moment balance through load shedding and re-distribution.
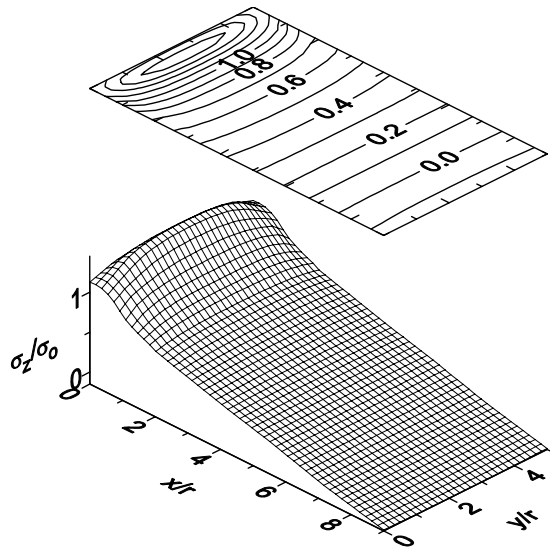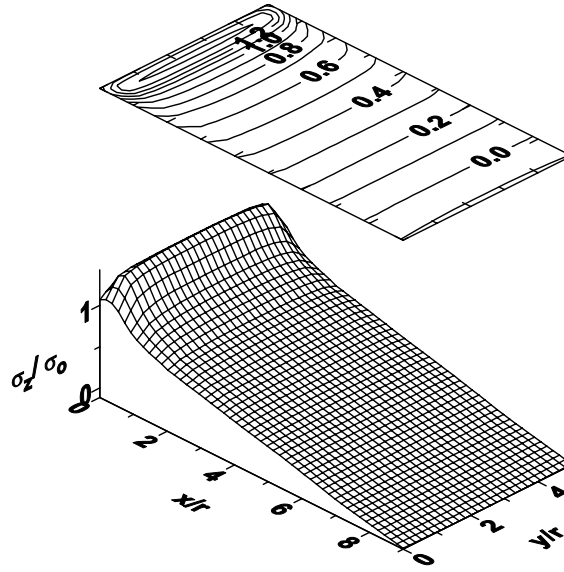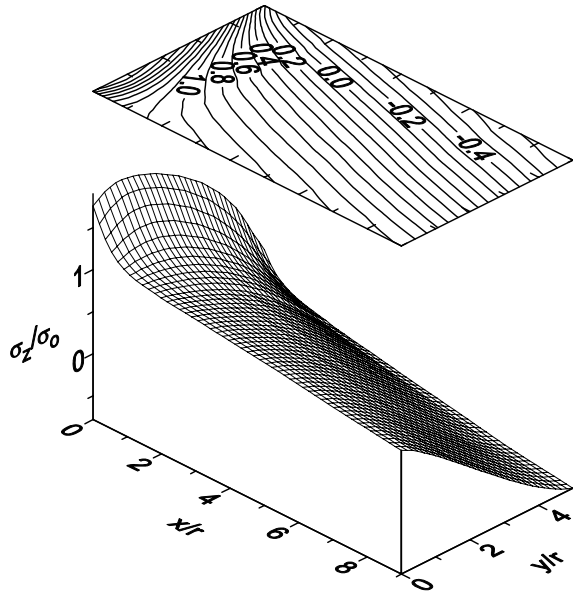
Fig. I14 (a) FEA results
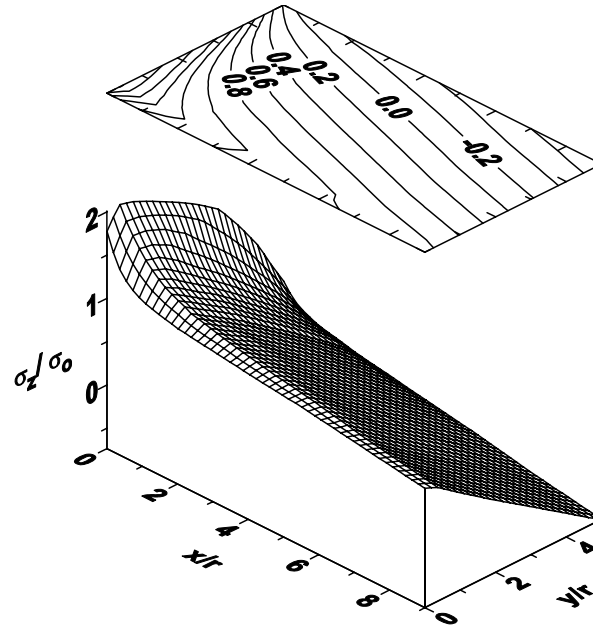
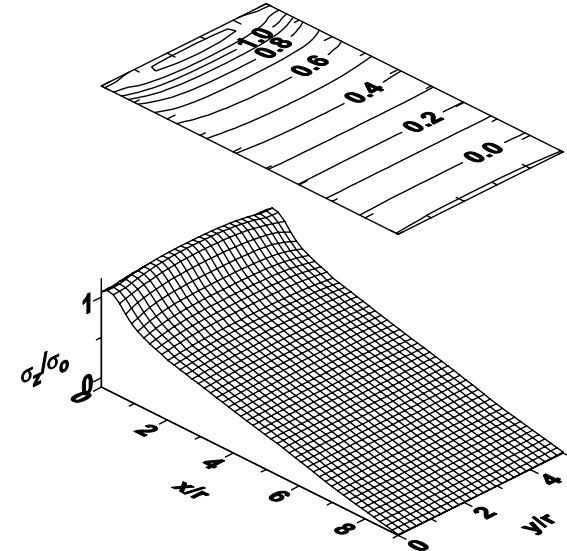Fig. I14 (b)   Predicted results by SwRI's isotropic shakedown module.
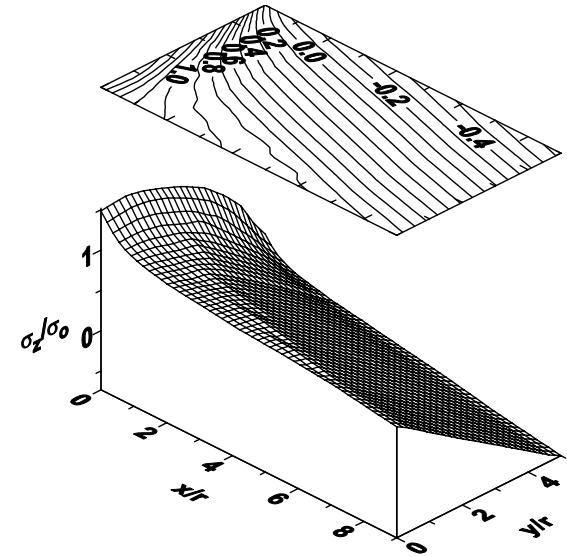
Fig. I14 (c)   Predicted results by as-received Glinka's point relaxation module.

Figure I14.   Comparison of the distribution of the elastic-plastic stress component normal to the load bearing section predicted by SwRI's isotropic shakedown module with FEA results for the notched plate subjected to $S_z=20$ *ksi*, $M_x=1800$ *kip-in*, and $M_y=1800$ *kip-in*; Material B. The results predicted by the as-received Glinka's point relaxation module are also included to demonstrate the enhancements made by SwRI to account for stress triaxiality at the notches and to maintain force/moment balance through load shedding and re-distribution.
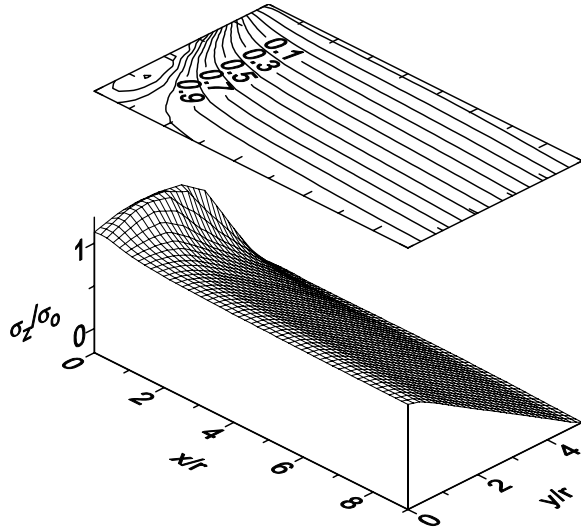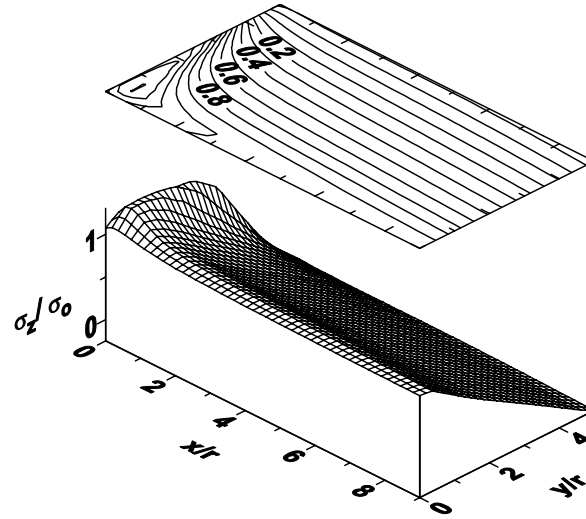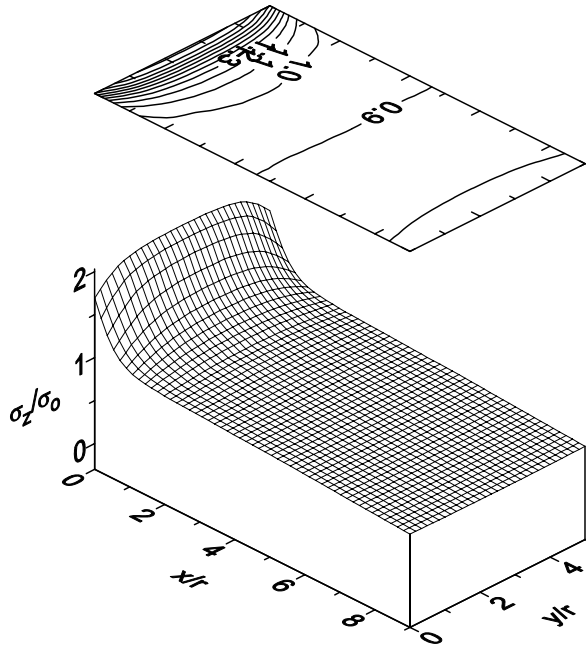
Fig. I15(a) FEA results
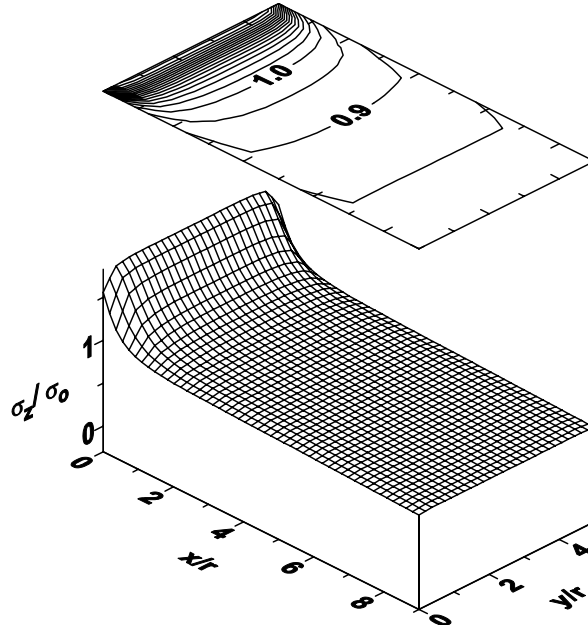
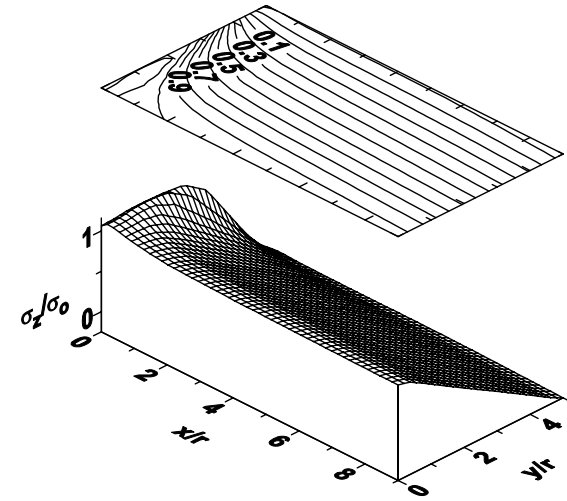Fig. I15 (b) Predicted results by SwRI's isotropic shakedown module.
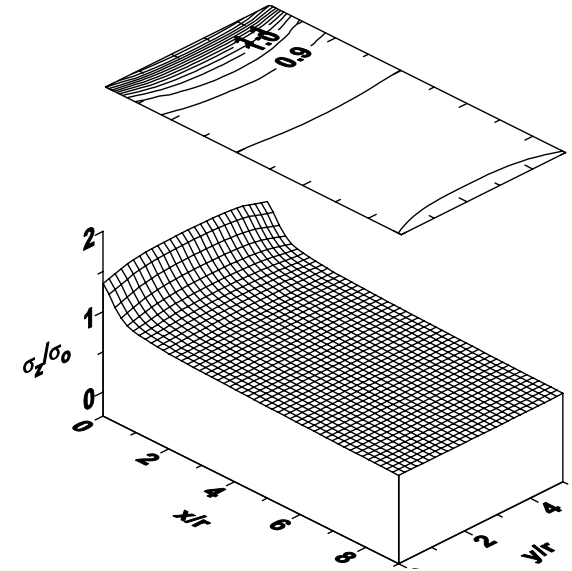
Fig. I15 (c) Predicted results by as-received Glinka's point relaxation module.

Figure I15. Comparison of the distribution of the elastic-plastic stress component normal to the load bearing section predicted by SwRI's isotropic shakedown module with FEA results for the notched plate subjected to S_z=55 *ksi*, and M_x=M_y=0; Material B. The results predicted by the as-received Glinka's point relaxation module are also included to demonstrate the enhancements made by SwRI to account for stress triaxiality at the notches and to maintain force/moment balance through load shedding and re-distribution.
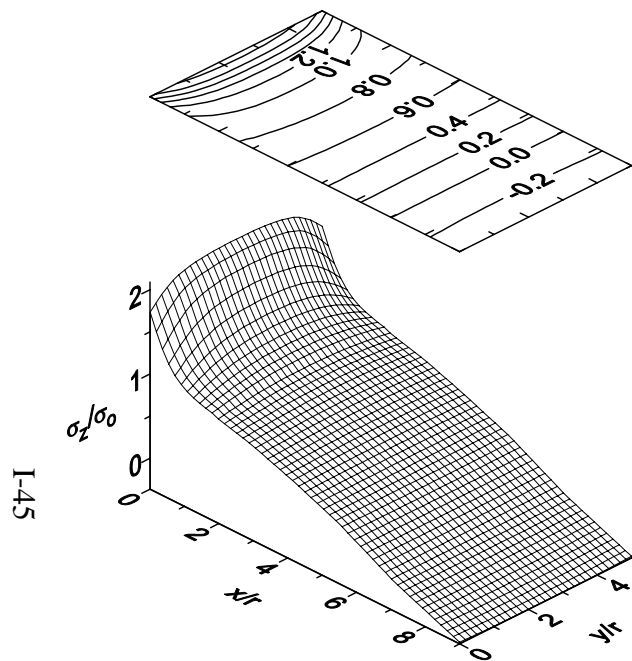
Fig. I16(a) FEA results
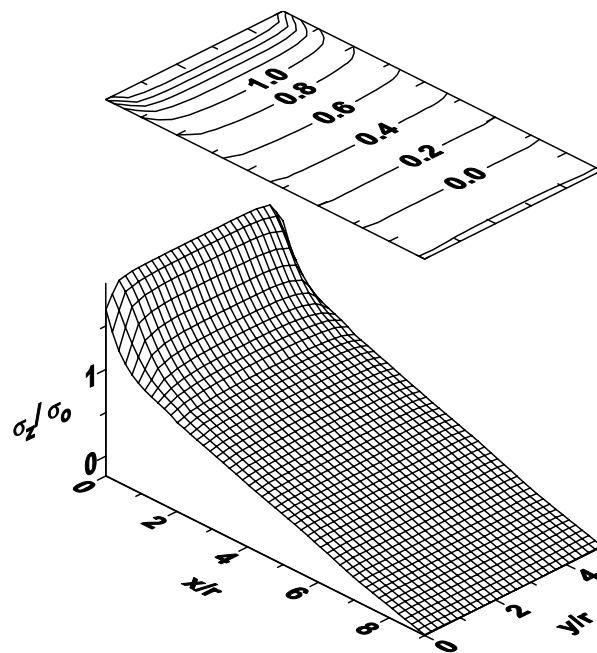
Fig. I16 (b)   Predicted results by SwRI's isotropic shakedown module.
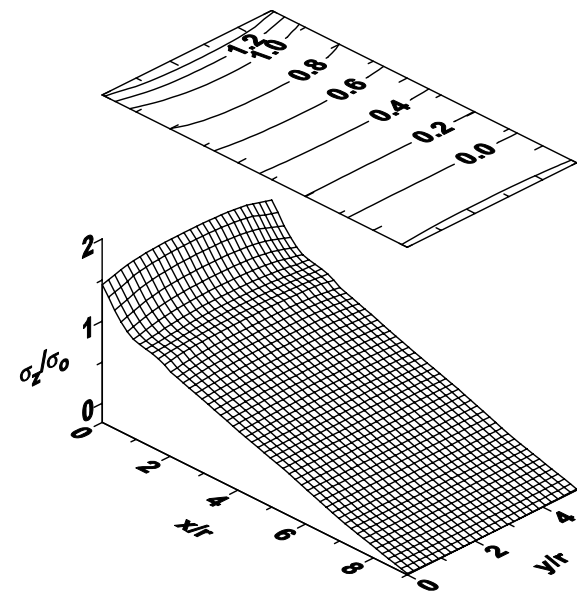
Fig. I16 (c)   Predicted results by as-received Glinka's point relaxation module.

Figure I16.   Comparison of the distribution of the elastic-plastic stress component normal to the load bearing section predicted by SwRI's isotropic shakedown module with FEA results for the notched plate subjected to $S_z=30$ *ksi*, $M_x=0$ and $M_y=3500$ *kip-in*; Material B. The results predicted by the as-received Glinka's point relaxation module are also included to demonstrate the enhancements made by SwRI to account for stress triaxiality at the notches and to maintain force/moment balance through load shedding and re-distribution.
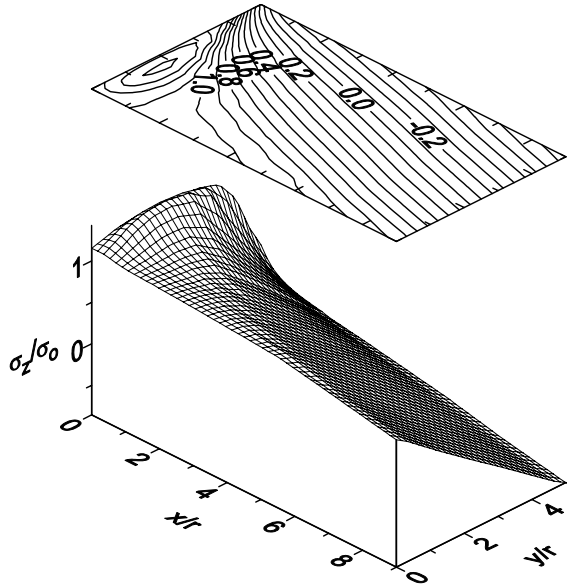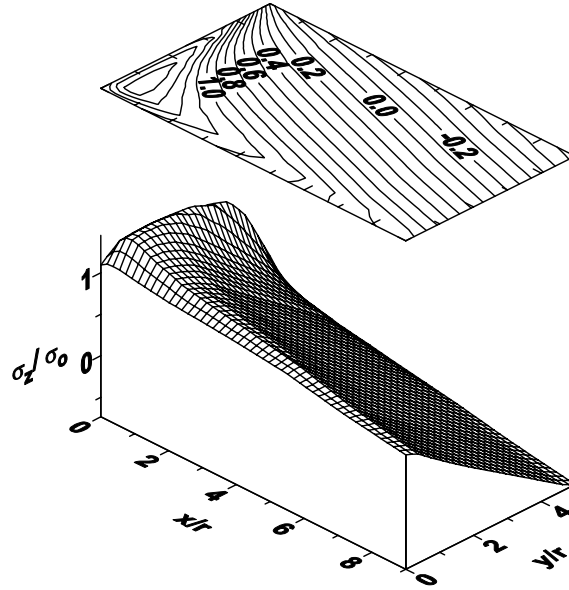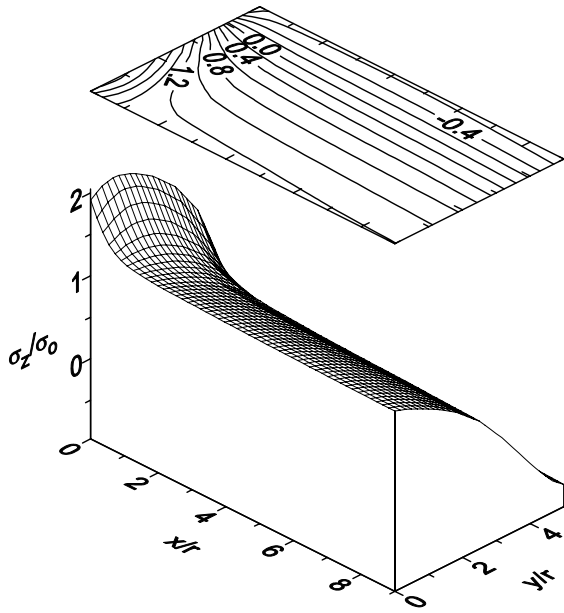
Fig. I17(a) FEA results
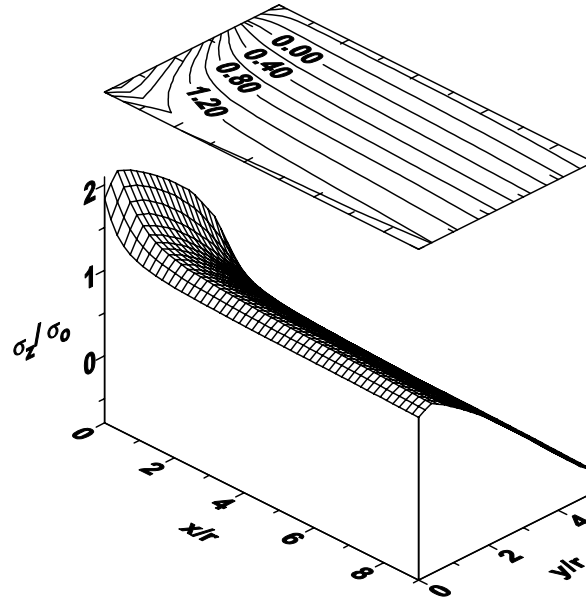
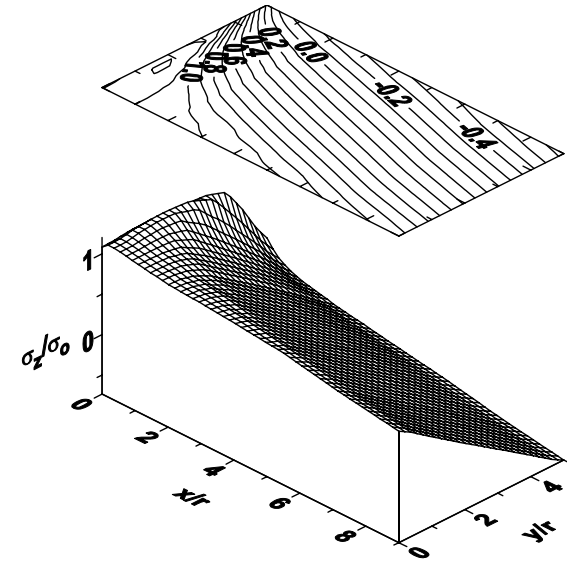Fig. I17 (b)   Predicted results by SwRI's isotropic shakedown module.
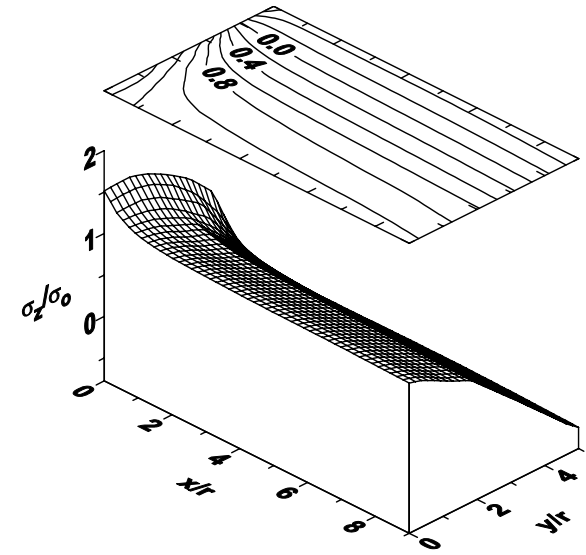
Fig. I17 (c)   Predicted results by as-received Glinka's point relaxation module.

Figure I17.   Comparison of the distribution of the elastic-plastic stress component normal to the load bearing section predicted by SwRI's isotropic shakedown module with FEA results for the notched plate subjected to S_z=30 *ksi*, M_x=2500 *kip-in* and M_y=0; Material B. The results predicted by the as-received Glinka's point relaxation module are also included to demonstrate the enhancements made by SwRI to account for stress triaxiality at the notches and to maintain force/moment balance through load shedding and re-distribution.
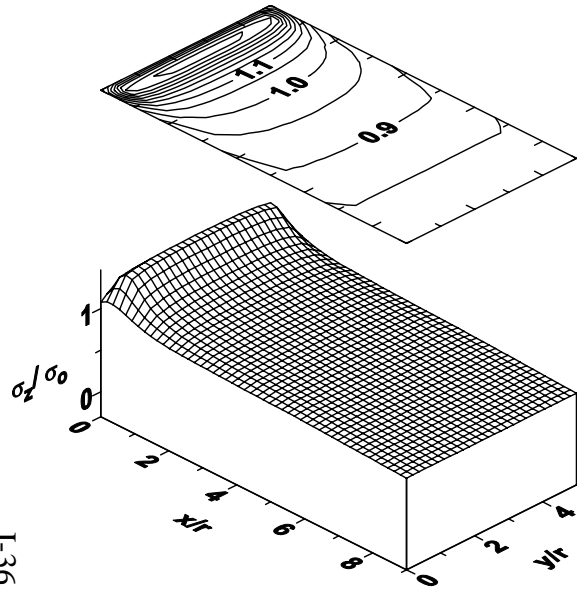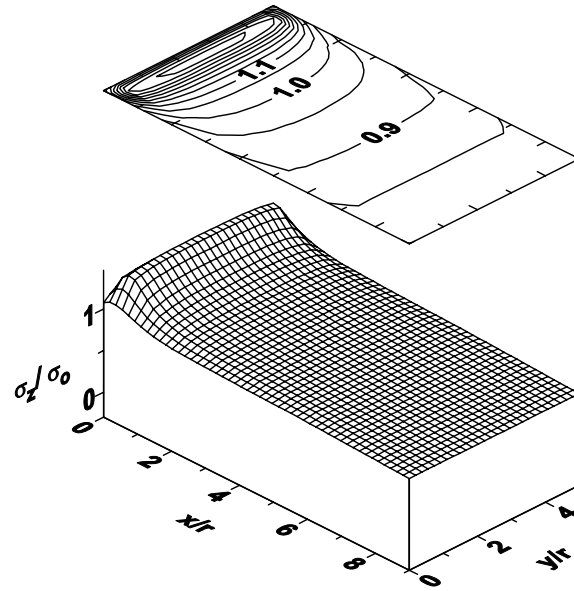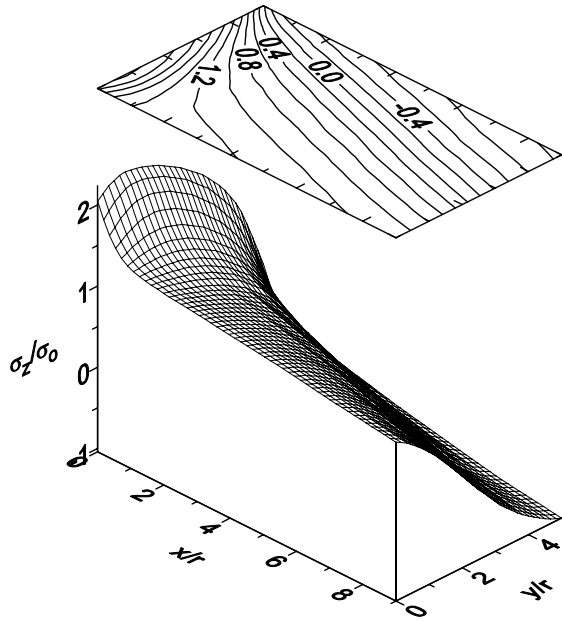
Fig. I18(a) FEA results
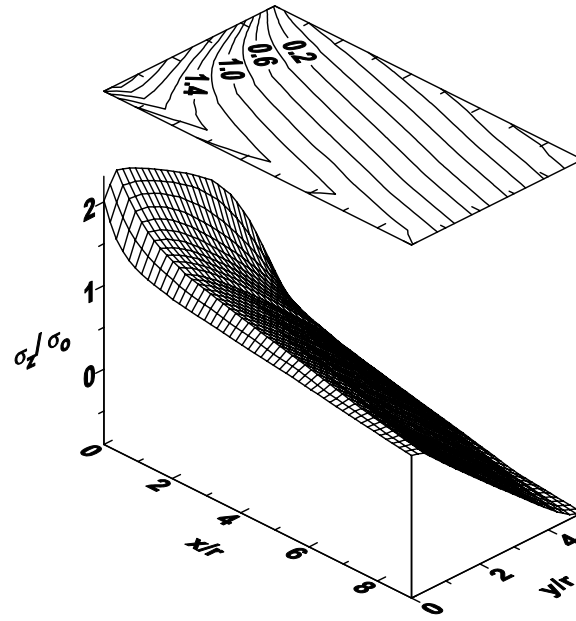
Fig. I18(b)   Predicted results by SwRI's isotropic shakedown module.
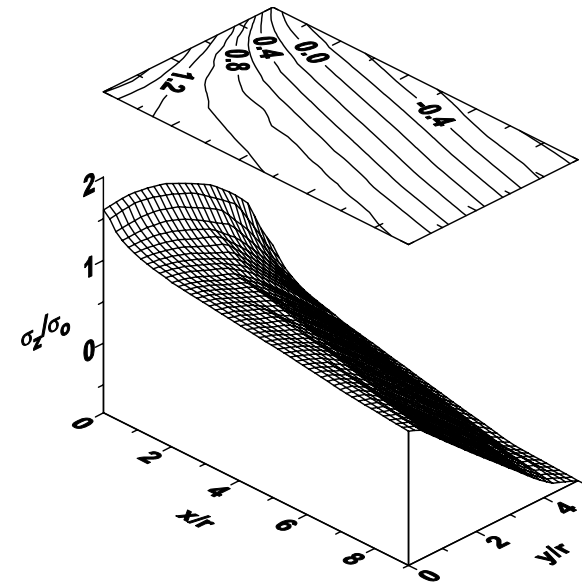
Fig. I18(c)   Predicted results by as-received Glinka's point relaxation module.

Figure I18.   Comparison of the distribution of the elastic-plastic stress component normal to the load bearing section predicted by SwRI's isotropic shakedown module with FEA results for the notched plate subjected to S_z=25 *ksi*, M_x=2400 *kip-in* and M_y=2400 *kip-in*; Material B. The results predicted by the as-received Glinka's point relaxation module are also included to demonstrate the enhancements made by SwRI to account for stress triaxiality at the notches and to maintain force/moment balance through load shedding and re-distribution.
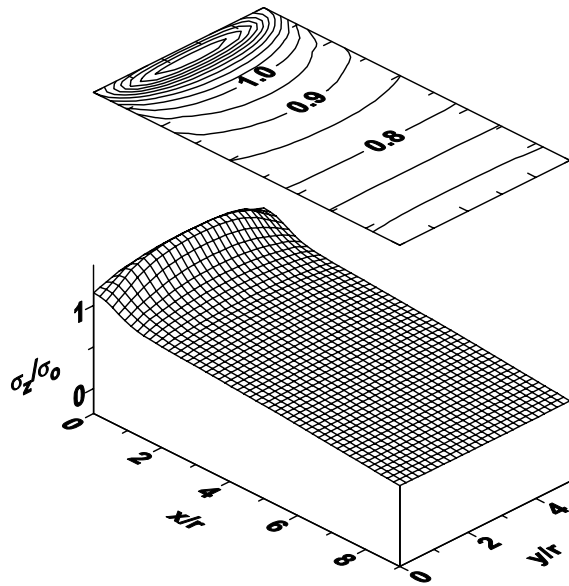
Fig. I19(a) FEA results   Fig. I19(b)   Predicted results by SwRI's
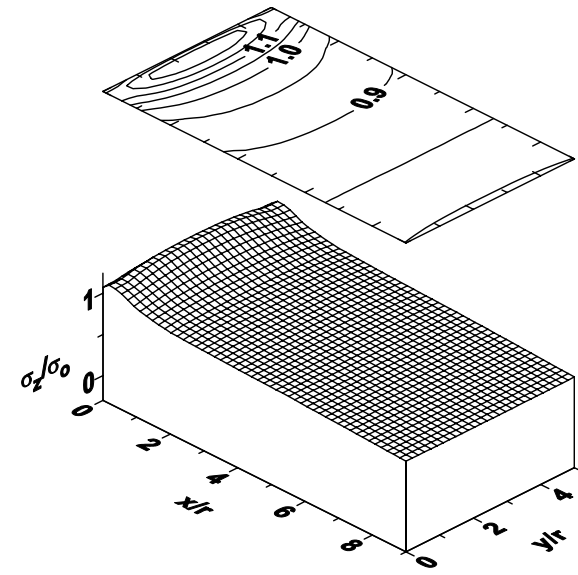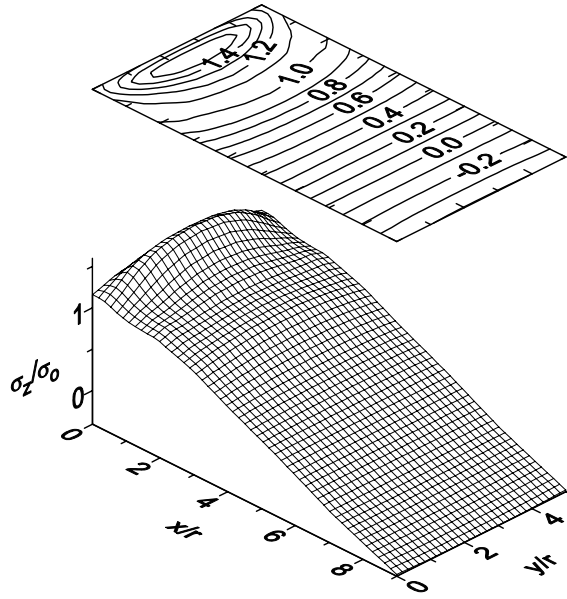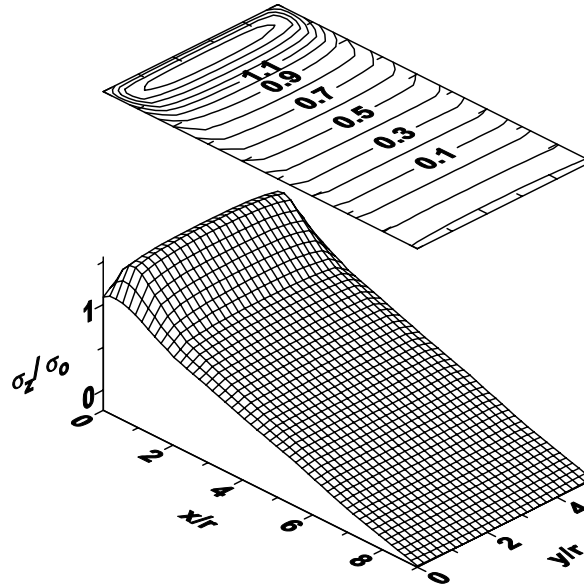   isotropic shakedown module.
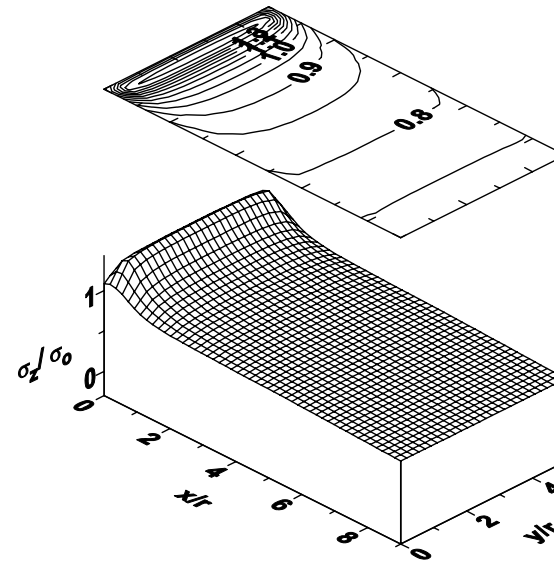
Figure I19.   Comparison of the distribution of the elastic-plastic stress component normal to the load bearing section predicted by
                  SwRI's isotropic shakedown module with FEA results for the notched plate subjected to S_z=50 *ksi*, and M_x=M_y=0;
                  Material A.
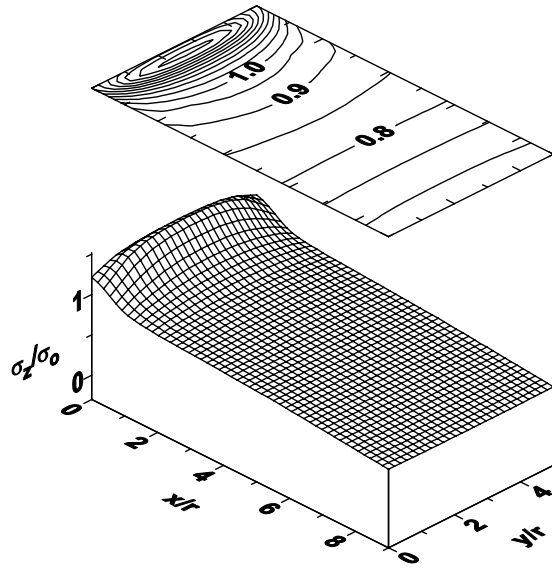
Fig. I20(a)   FEA results
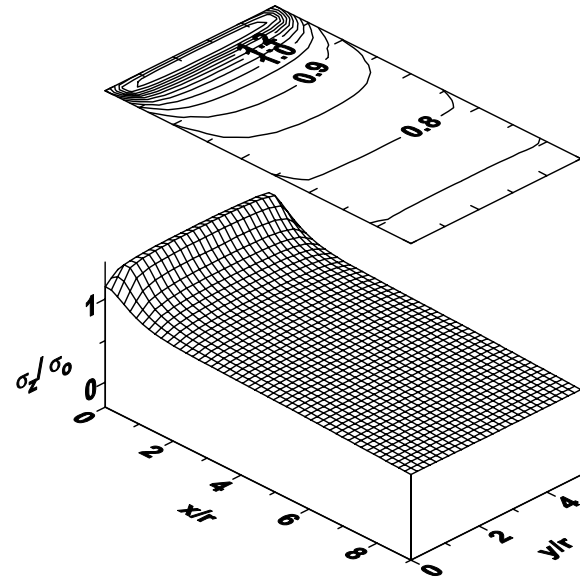
Fig. I20(b)   Predicted results by SwRI's isotropic shakedown module.

Figure I20.   Comparison of the distribution of the elastic-plastic stress component normal to the load bearing section predicted by SwRI's isotropic shakedown module with FEA results for the notched plate subjected to $S_z=50$ *ksi*, and $M_x=M_y=0$; Material D.
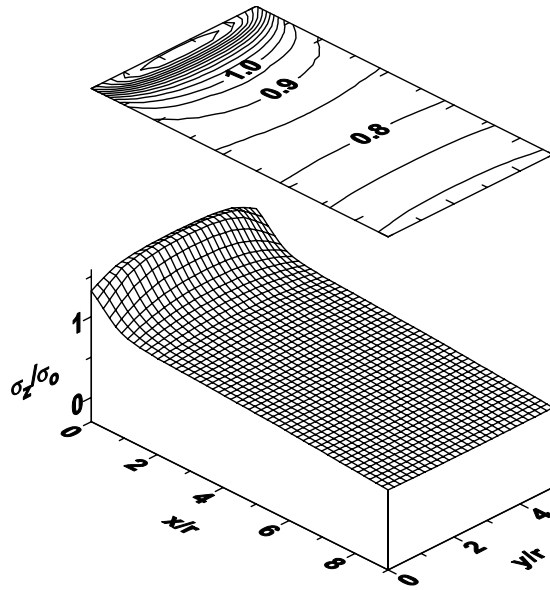
Fig. I21(a) FEA results
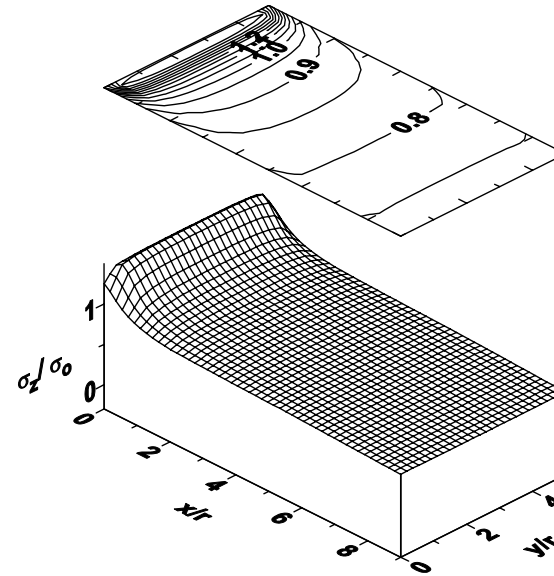
Fig. I21(b) Predicted results by SwRI's isotropic shakedown module.

Figure I21. Comparison of the distribution of the elastic-plastic stress component normal to the load bearing section predicted by SwRI's isotropic shakedown module with FEA results for the notched plate subjected to S_z=50 *ksi*, and M_x=M_y=0; Material E.
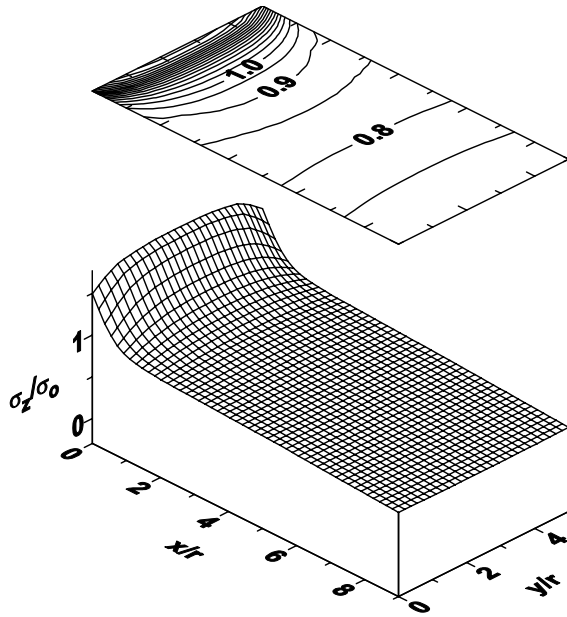
Fig. I22(a) FEA results
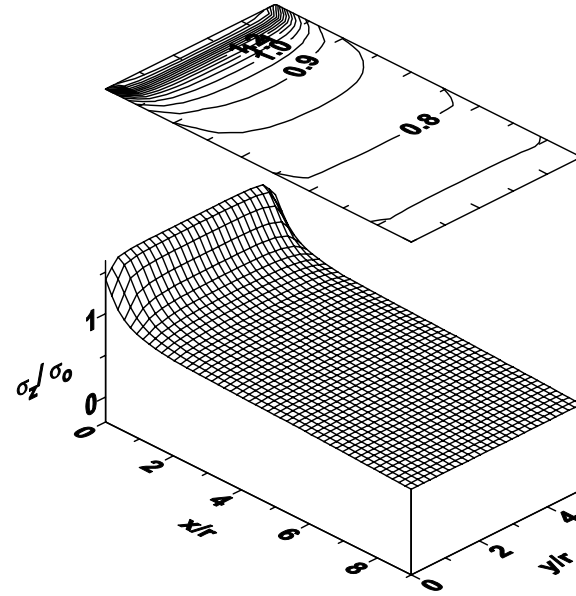
Fig. I22(b) Predicted results by SwRI's isotropic shakedown module.

Figure I22. Comparison of the distribution of the elastic-plastic stress component normal to the load bearing section predicted by SwRI's isotropic shakedown module with FEA results for the notched plate subjected to $S_z=50$ *ksi*, and $M_x=M_y=0$; Material F.

Figure I23(a)   Figure I23(b)   Figure I23(c)

Figure I23.   Comparison of stress components predicted by SwRI's isotropic shakedown module with the results obtained from FEA. The results computed from Glinka's point relaxation are also included. The notched plate is subjected to S_z=50 *ksi*, and M_x=M_y=0; Material A. Results in Figure A.5.22(a) are for *y/r*=0 (the free surface at the side of the plate), A.5.22(b) are for *y/r*=1.237 (a plane one quarter of the way through the plate), and A.5.22(c) are for *y/r*=2.5 (at the mid-plane). In Figure A.5.22(a), the results predicted by SwRI's isotropic shakedown module can not be visually differentiated from the point relaxation results.
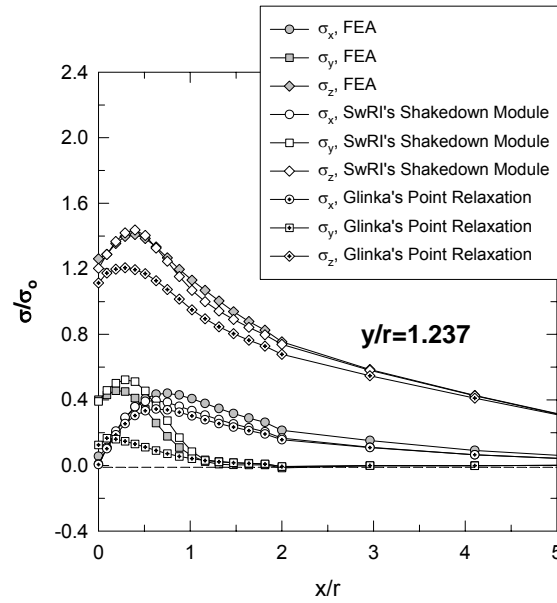
Figure I24(a)   Figure I24(b)   Figure I24(c)
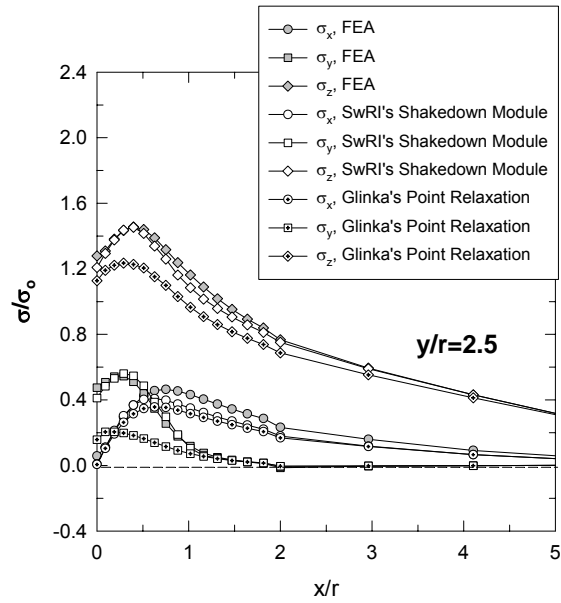
Figure I24.   Comparison of stress components predicted by SwRI's isotropic shakedown module with the results obtained from FEA. The results computed from Glinka's point relaxation are also included. The notched plate is subjected to S_z=25 *ksi*, M_x=0, and M_y=2500 *kip-in*; Material A. Results in Figure A.5.23(a) are for *y/r*=0 (the free surface at the side of the plate), A.5.23(b) are for *y/r*=1.237 (a plane one quarter of the way through the plate), and A.5.23(c) are for *y/r*=2.5 (at the mid-plane). In Figure A.5.23(a), the results predicted by SwRI's isotropic shakedown module can not be visually differentiated from the point relaxation results.
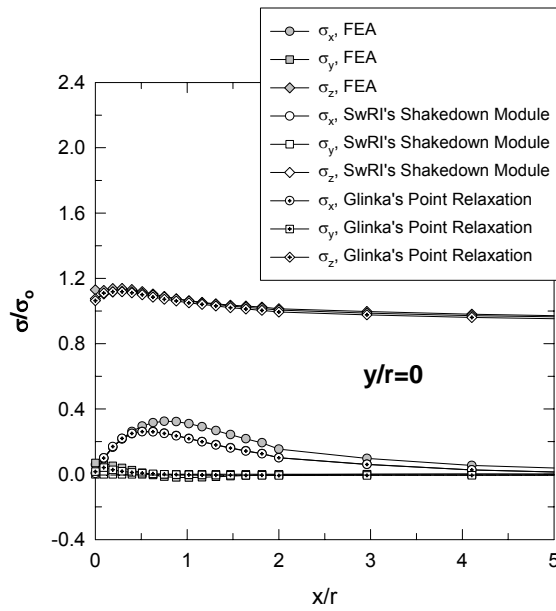
Figure I25(a)
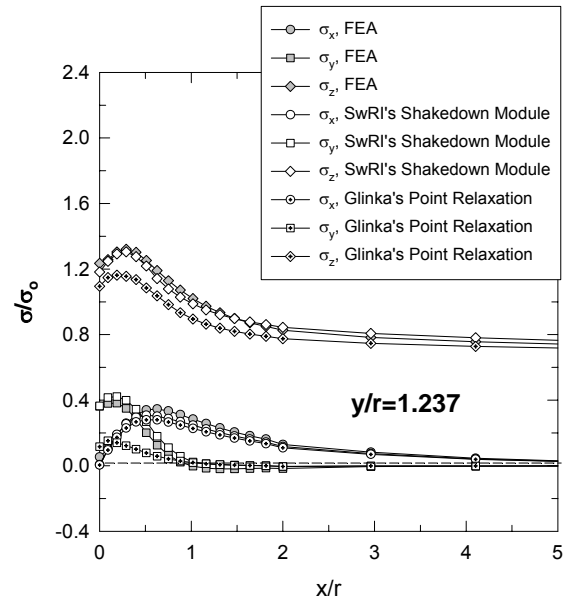
Figure I25 (b)
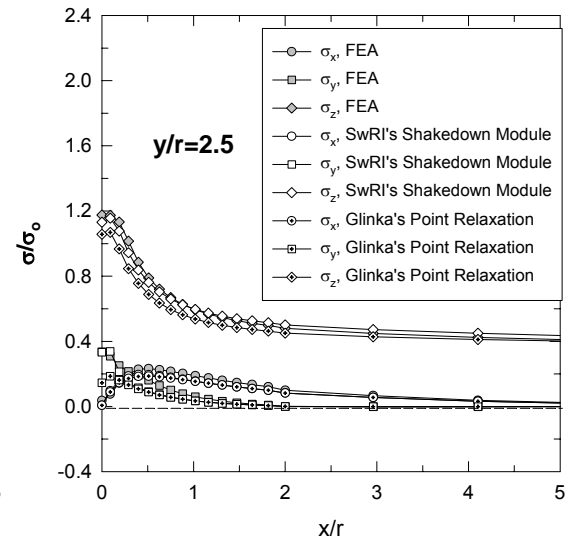
Figure I25 (c)

Figure I25.   Comparison of stress components predicted by SwRI's isotropic shakedown module with the results obtained from FEA. The results computed from Glinka's point relaxation are also included. The notched plate is subjected to S_z=25 *ksi*, M_x=1600 *kip-in*, and M_y=0; Material A. Results in Figure A.5.24(a) are for *y/r*=0 (the free surface at the side of the plate), A.5.24(b) are for *y/r*=1.237 (a plane one quarter of the way through the plate), and A.5.24(c) are for *y/r*=2.5 (at the mid-plane). In Figure A.5.24(a), the results predicted by SwRI's isotropic shakedown module can not be visually differentiated from the point relaxation results.
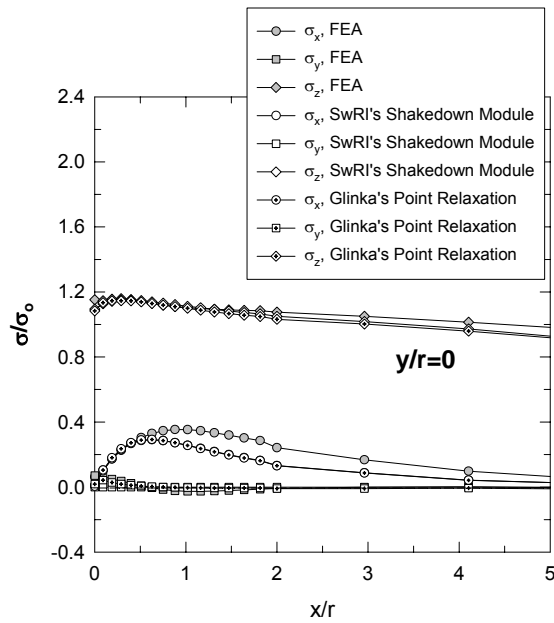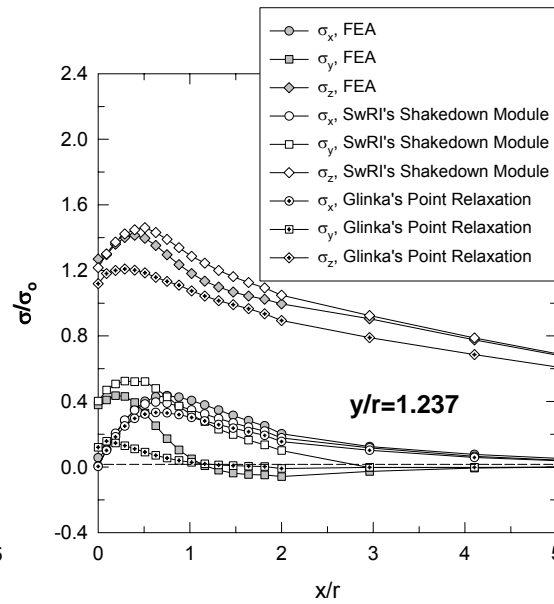
Figure I26 (a)   Figure I26 (b)   Figure I26 (c)
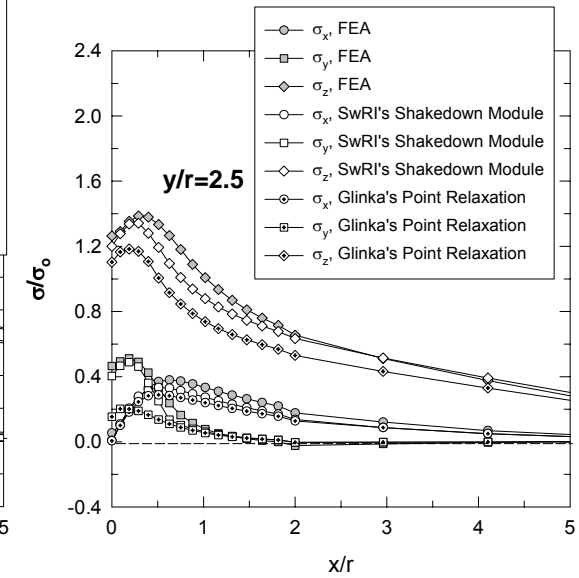
Figure I26.   Comparison of stress components predicted by SwRI's isotropic shakedown module with the results obtained from FEA. The results computed from Glinka's point relaxation are also included. The notched plate is subjected to S_z=20 *ksi*, M_x=1800 *kip-in*, and M_y=1800 *ksi-in*; Material A. Results in Figure A.5.25(a) are for *y/r*=0 (the free surface at the side of the plate), A.5.25(b) are for *y/r*=1.237 (a plane one quarter of the way through the plate), and A.5.25(c) are for *y/r*=2.5 (at the mid-plane). In Figure A.5.25(a), the results predicted by SwRI's isotropic shakedown module can not be visually differentiated from the point relaxation results.
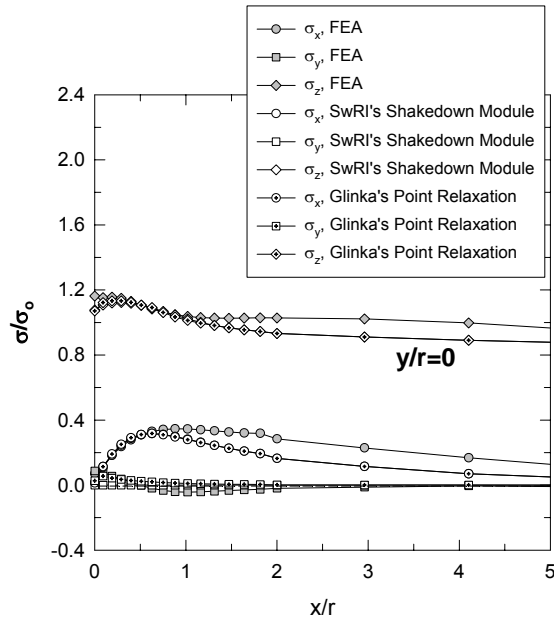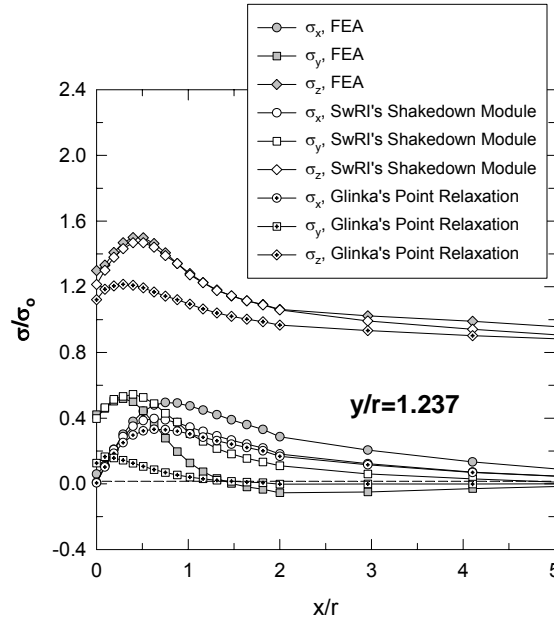
Figure I27 (a)   Figure I27 (b)   Figure I27 (c)
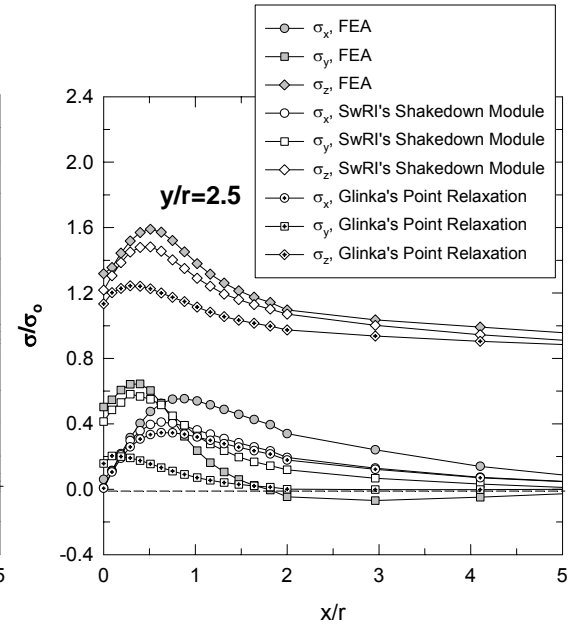
Figure I27.   Comparison of stress components predicted by SwRI's isotropic shakedown module with the results obtained from FEA. The results computed from Glinka's point relaxation are also included. The notched plate is subjected to S_z=55 *ksi*, M_x=M_y=0; Material A. Results in Figure A.5.26(a) are for y/r=0 (the free surface at the side of the plate), A.5.26(b) are for y/r=1.237 (a plane one quarter of the way through the plate), and A.5.26(c) are for y/r=2.5 (at the mid-plane). In Figure A.5.26(a), the results predicted by SwRI's isotropic shakedown module can not be visually differentiated from the point relaxation results.
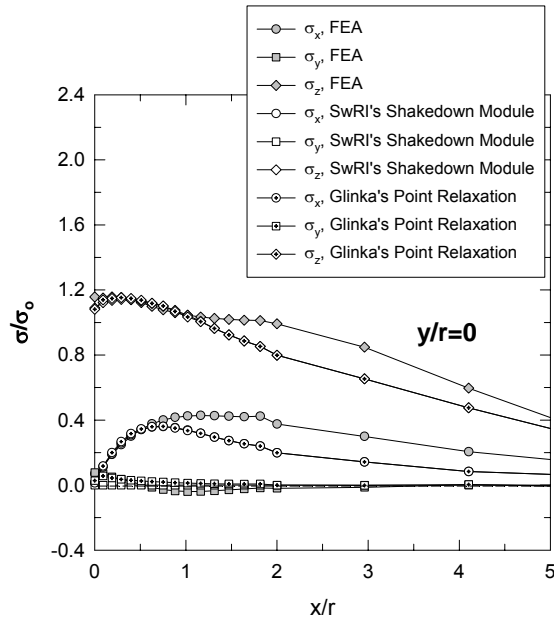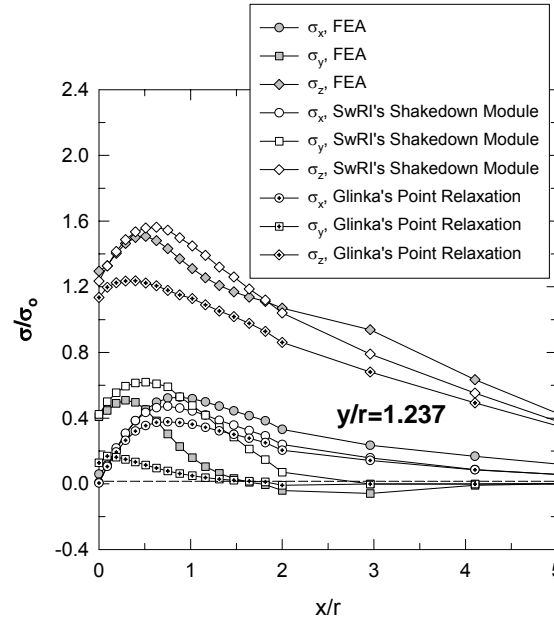
Figure I28(a)   Figure I28(b)   Figure I28(c)
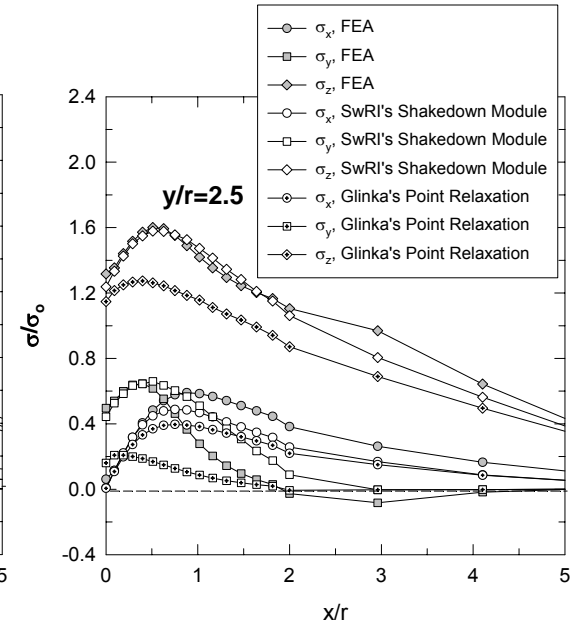
Figure I28.   Comparison of stress components predicted by SwRI's isotropic shakedown module with the results obtained from FEA. The results computed from Glinka's point relaxation are also included. The notched plate is subjected to S_z=30 *ksi*, M_x=0, and M_y=3500 *kip-in*; Material A. Results in Figure A.5.27(a) are for *y/r*=0 (the free surface at the side of the plate), A.5.27(b) are for *y/r*=1.237 (a plane one quarter of the way through the plate), and A.5.27(c) are for *y/r*=2.5 (at the mid-plane). In Figure A.5.27(a), the results predicted by SwRI's isotropic shakedown module can not be visually differentiated from the point relaxation results.
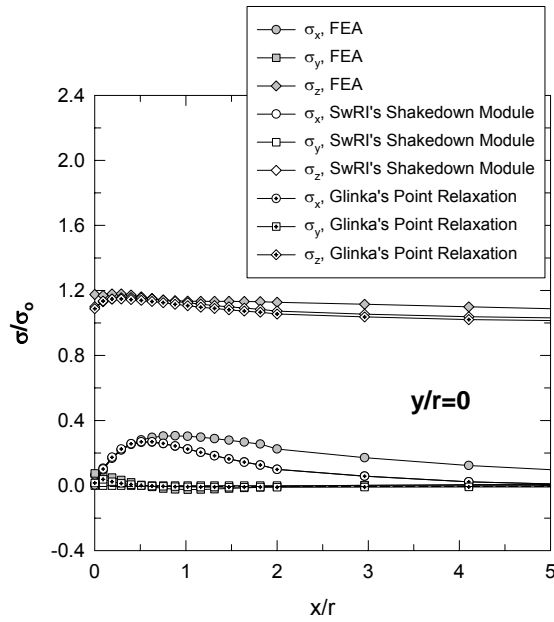
Figure I29(a)
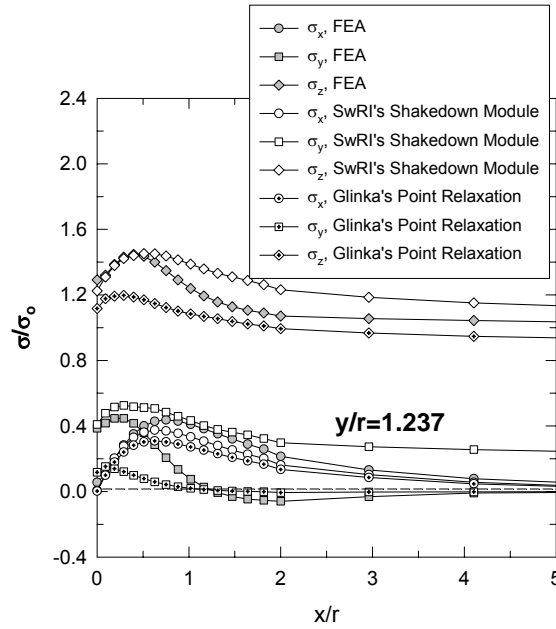
Figure I29(b)
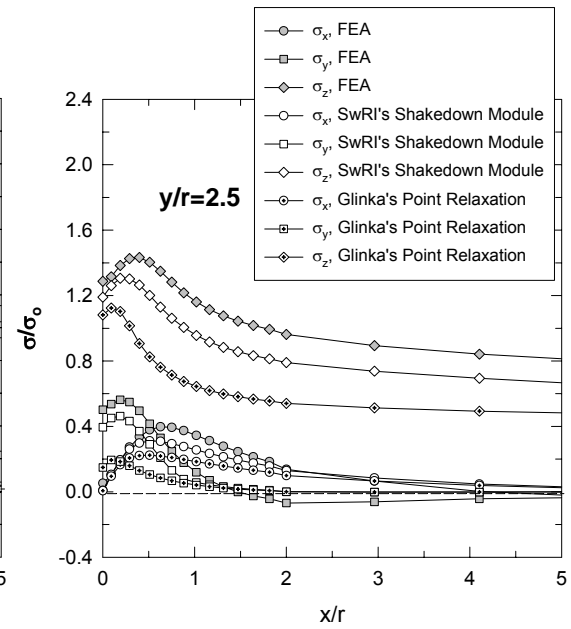
Figure I29(c)

Figure I29.   Comparison of stress components predicted by SwRI's isotropic shakedown module with the results obtained from FEA. The results computed from Glinka's point relaxation are also included. The notched plate is subjected to S_z=30 *ksi*, M_x=2500 *kip-in*, and M_y=0; Material A. Results in Figure A.5.28(a) are for *y/r*=0 (the free surface at the side of the plate), A.5.28(b) are for *y/r*=1.237 (a plane one quarter of the way through the plate), and A.5.28(c) are for *y/r*=2.5 (at the mid-plane). In Figure A.5.28(a), the results predicted by SwRI's isotropic shakedown module can not be visually differentiated from the point relaxation results.
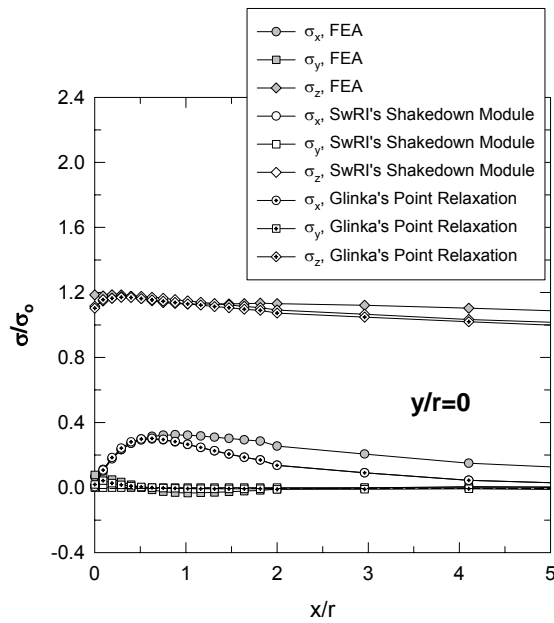
Figure I30 (a)
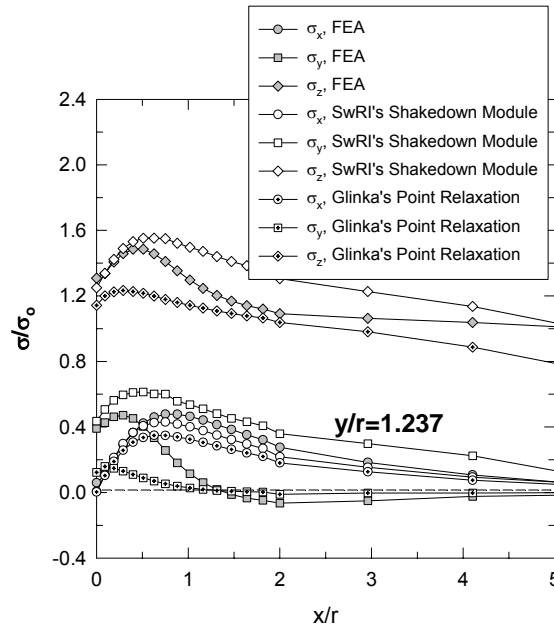
Figure I30 (b)
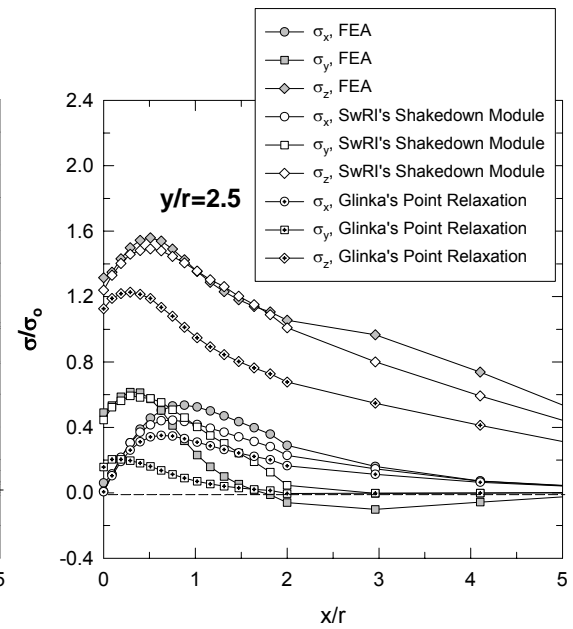
Figure I30 (c)

Figure I30.   Comparison of stress components predicted by SwRI's isotropic shakedown module with the results obtained from FEA. The results computed from Glinka's point relaxation are also included. The notched plate is subjected to S_z=25 *ksi*, M_x=2400 *kip-in*, and M_y=2400 *kip-in*; Material A. Results in Figure A.5.29(a) are for *y/r*=0 (the free surface at the side of the plate), A.5.29(b) are for *y/r*=1.237 (a plane one quarter of the way through the plate), and A.5.29(c) are for *y/r*=2.5 (at the mid-plane). In Figure A.5.29(a), the results predicted by SwRI's isotropic shakedown module can not be visually differentiated from the point relaxation results.
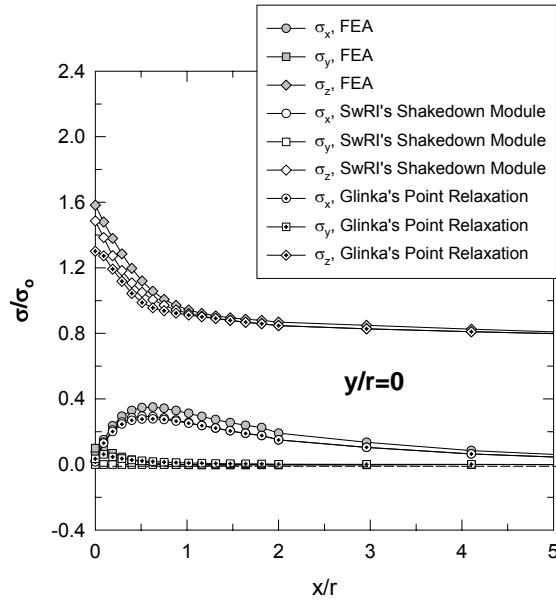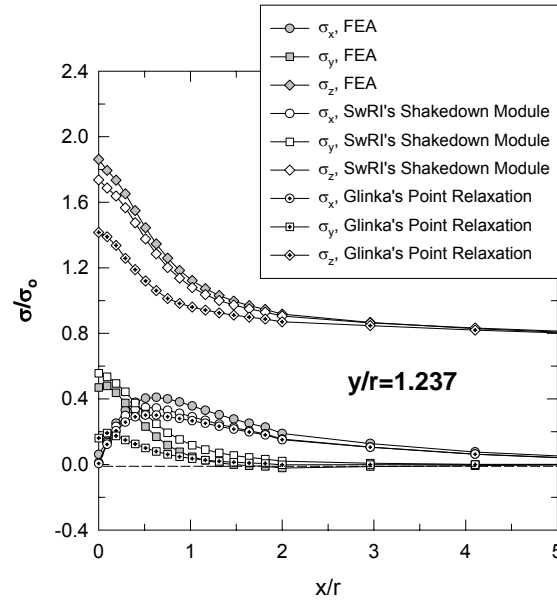
Figure I31 (a)   Figure I31 (b)   Figure I31 (c)
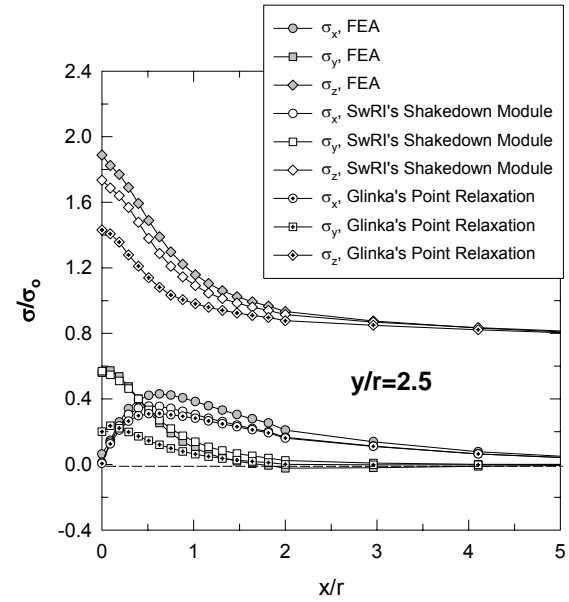
Figure I31.   Comparison of stress components predicted by SwRI's isotropic shakedown module with the results obtained from FEA. The results computed from Glinka's point relaxation are also included. The notched plate is subjected to $S_z=50$ *ksi*, and $M_x=M_y=0$; Material B. Results in Figure A.5.30(a) are for $y/r=0$ (the free surface at the side of the plate), A.5.30(b) are for $y/r=1.237$ (a plane one quarter of the way through the plate), and A.5.30(c) are for $y/r=2.5$ (at the mid-plane). In Figure A.5.30(a), the results predicted by SwRI's isotropic shakedown module can not be visually differentiated from the point relaxation results.
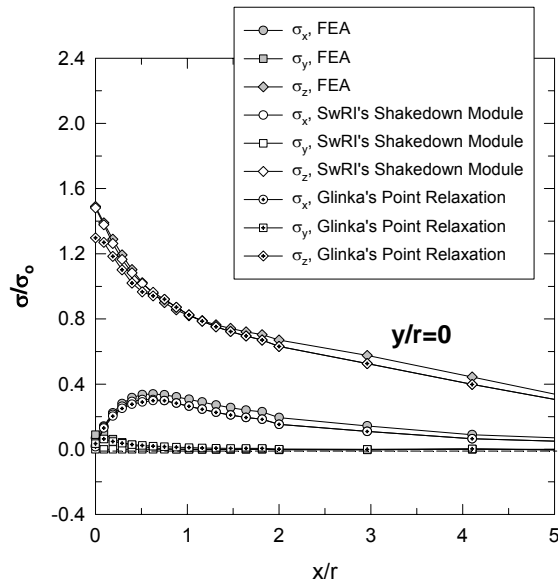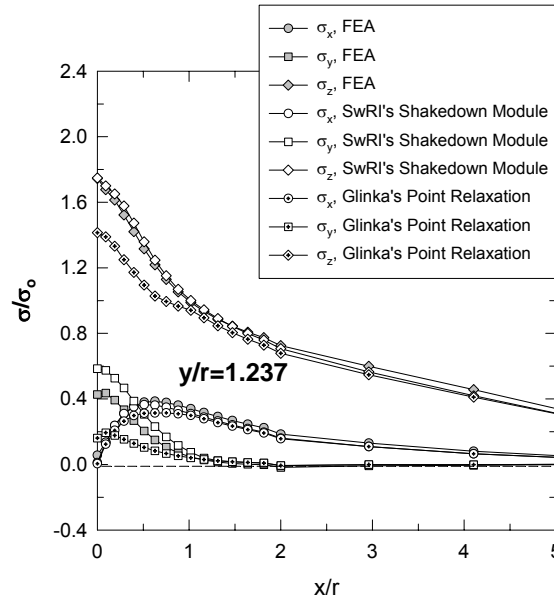
Figure I32 (a)　　　　　　　　Figure I32 (b)　　　　　　　　Figure I32 (c)
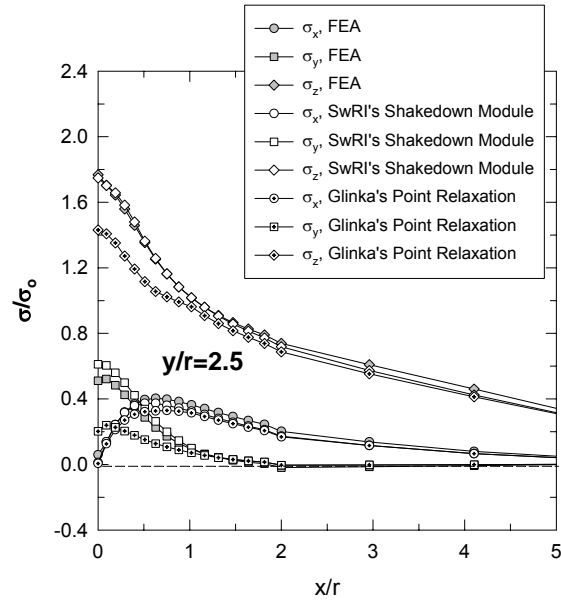
Figure I32.　　Comparison of stress components predicted by SwRI's isotropic shakedown module with the results obtained from FEA. The results computed from Glinka's point relaxation are also included. The notched plate is subjected to S_z=25 *ksi*, M_x=0, and M_y=2500 *kip-in*; Material B. Results in Figure A.5.31(a) are for *y/r*=0 (the free surface at the side of the plate), A.5.31(b) are for *y/r*=1.237 (a plane one quarter of the way through the plate), and A.5.31(c) are for *y/r*=2.5 (at the mid-plane). In Figure A.5.31(a), the results predicted by SwRI's isotropic shakedown module can not be visually differentiated from the point relaxation results.
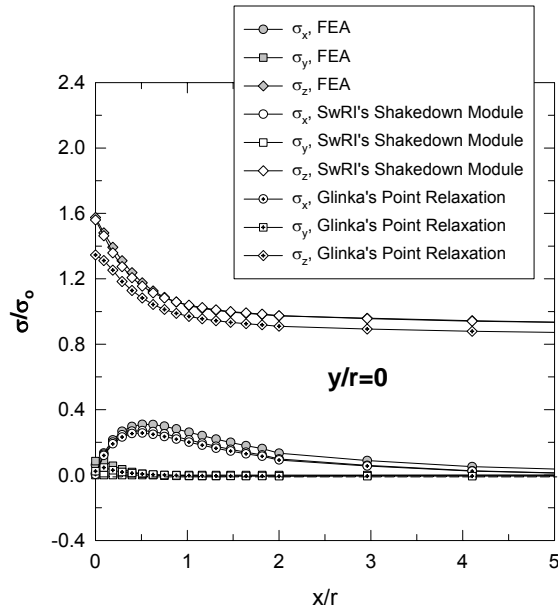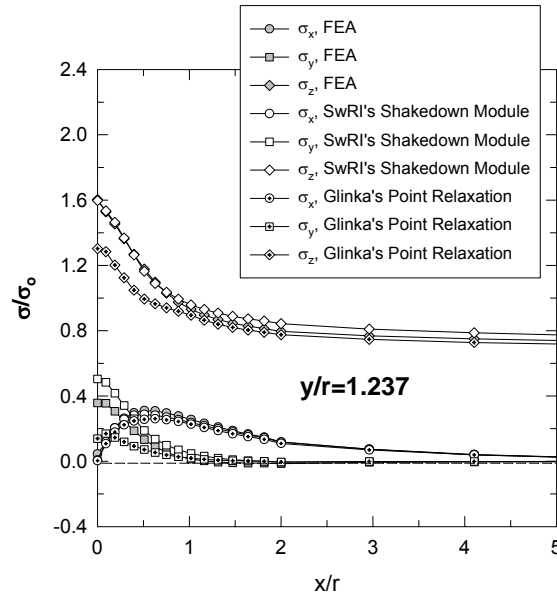
Figure I33 (a) Figure I33 (b) Figure I33c)
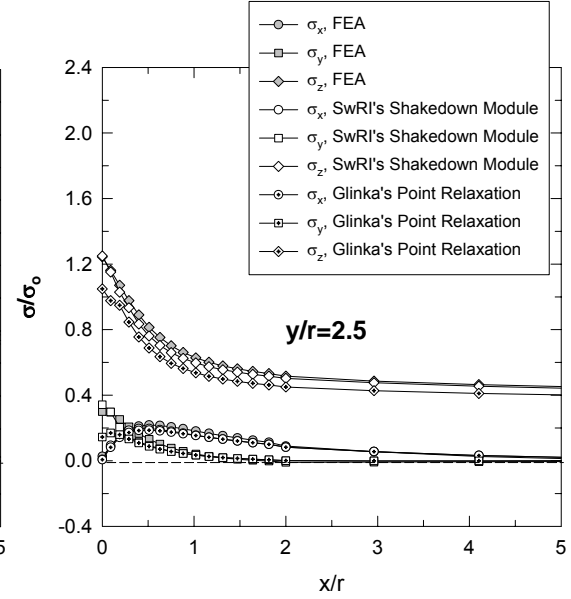
Figure I33.   Comparison of stress components predicted by SwRI's isotropic shakedown module with the results obtained from FEA. The results computed from Glinka's point relaxation are also included. The notched plate is subjected to S_z=25 *ksi*, M_x=1600 *kip-in*, and M_y=0; Material B. Results in Figure A.5.32(a) are for y/r=0 (the free surface at the side of the plate), A.5.32(b) are for y/r=1.237 (a plane one quarter of the way through the plate), and A.5.32(c) are for y/r=2.5 (at the mid-plane). In Figure A.5.32(a), the results predicted by SwRI's isotropic shakedown module can not be visually differentiated from the point relaxation results.
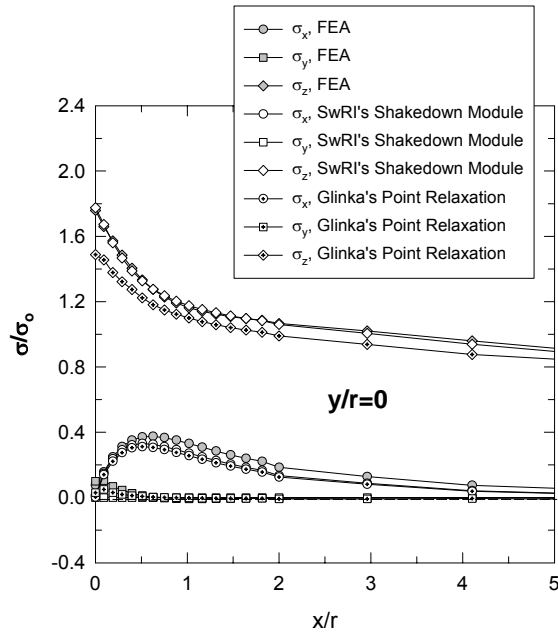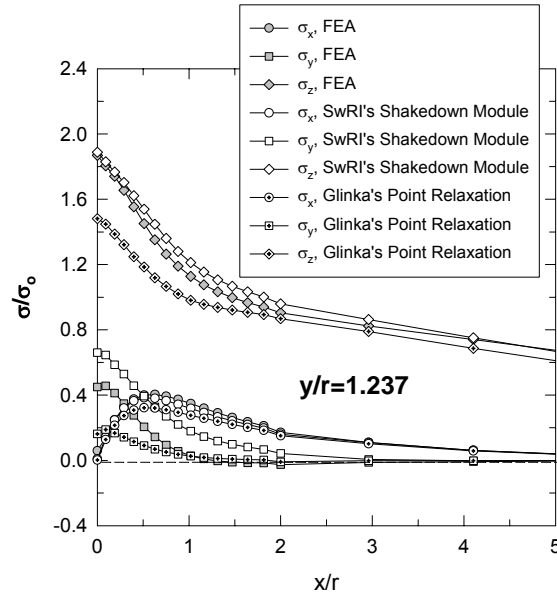
Figure I34 (a)   Figure I34 (b)   Figure I34 (c)
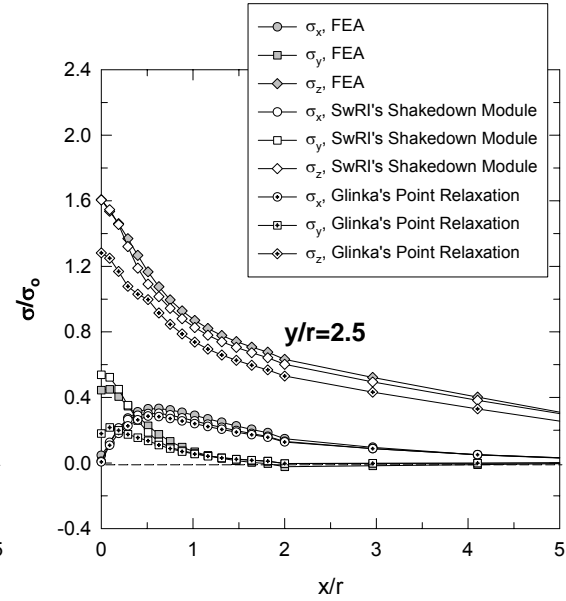
Figure I34.   Comparison of stress components predicted by SwRI's isotropic shakedown module with the results obtained from FEA. The results computed from Glinka's point relaxation are also included. The notched plate is subjected to S_z=20 *ksi*, M_x=1800 *kip-in*, and M_y=1800 *kip-in*; Material B. Results in Figure A.5.33(a) are for *y/r*=0 (the free surface at the side of the plate), A.5.33(b) are for *y/r*=1.237 (a plane one quarter of the way through the plate), and A.5.33(c) are for *y/r*=2.5 (at the mid-plane). In Figure A.33(a), the results predicted by SwRI's isotropic shakedown module can not be visually differentiated from the point relaxation results.
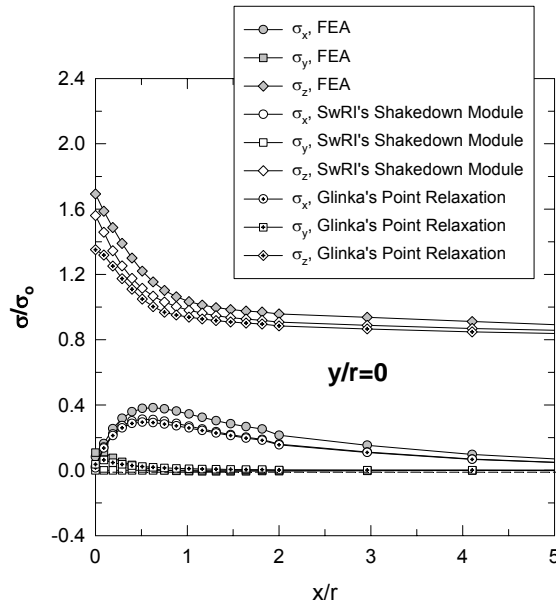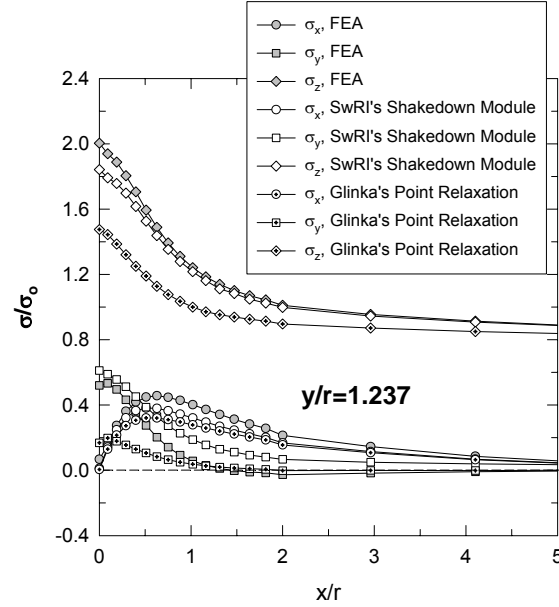
Figure I35(a)   Figure I35b)   Figure I35(c)
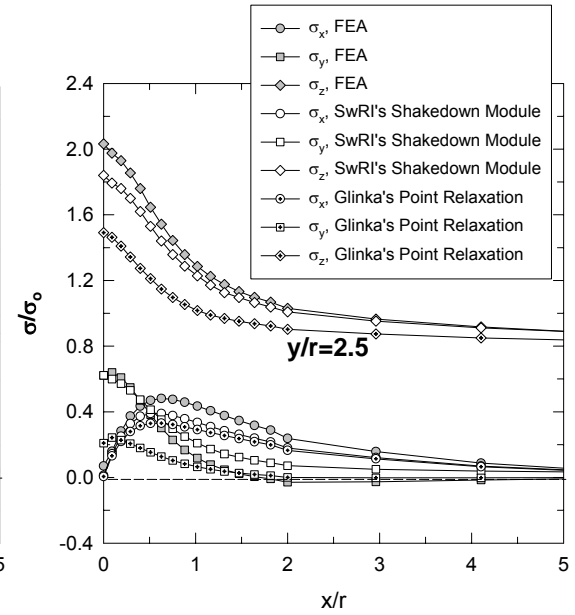
Figure I35.   Comparison of stress components predicted by SwRI's isotropic shakedown module with the results obtained from FEA. The results computed from Glinka's point relaxation are also included. The notched plate is subjected to S_z=55 *ksi*, and M_x=M_y=0; Material B. Results in Figure A.5.34(a) are for *y/r*=0 (the free surface at the side of the plate), A.5.34(b) are for *y/r*=1.237 (a plane one quarter of the way through the plate), and A.5.34(c) are for *y/r*=2.5 (at the mid-plane). In Figure A.5.34(a), the results predicted by SwRI's isotropic shakedown module can not be visually differentiated from the point relaxation results.
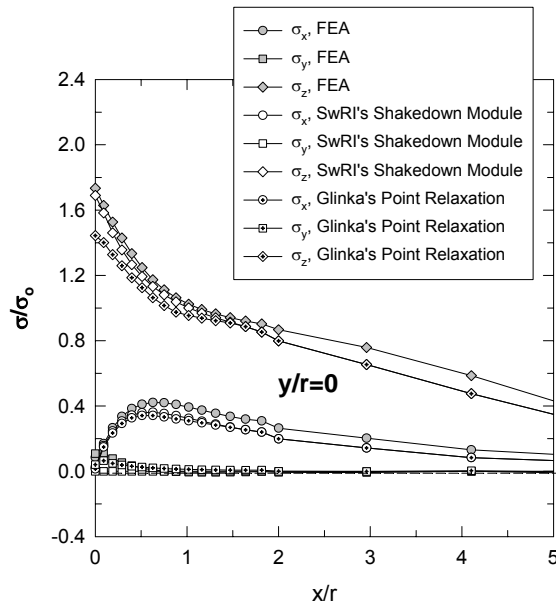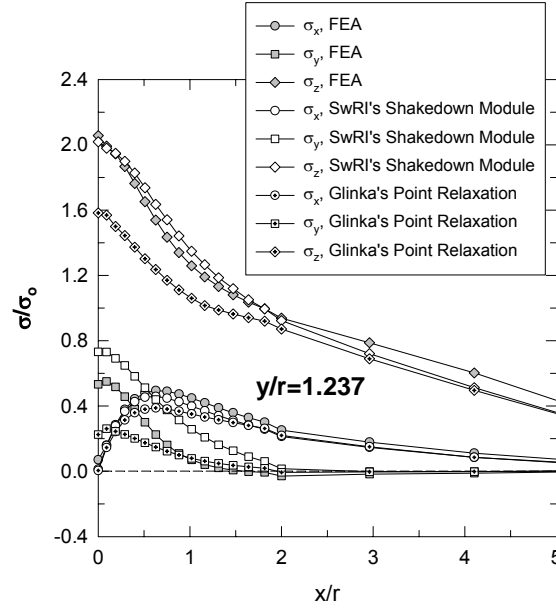
Figure I36 (a)   Figure I36(b)   Figure I36(c)
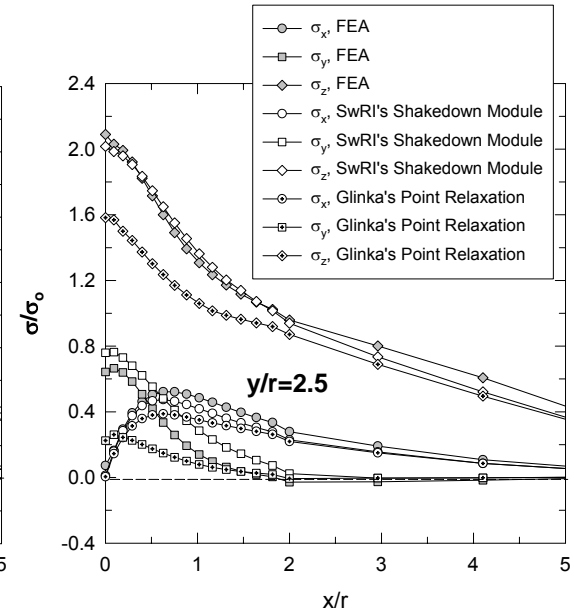
Figure I36.   Comparison of stress components predicted by SwRI's isotropic shakedown module with the results obtained from FEA. The results computed from Glinka's point relaxation are also included. The notched plate is subjected to $S_z=30$ *ksi*, $M_x=0$, $M_y=3500$ *kip-in*; Material B. Results in Figure A.5.35(a) are for *y/r*=0 (the free surface at the side of the plate), A.5.35(b) are for *y/r*=1.237 (a plane one quarter of the way through the plate), and A.5.35(c) are for *y/r*=2.5 (at the mid-plane). In Figure A.5.35(a), the results predicted by SwRI's isotropic shakedown module can not be visually differentiated from the point relaxation results.
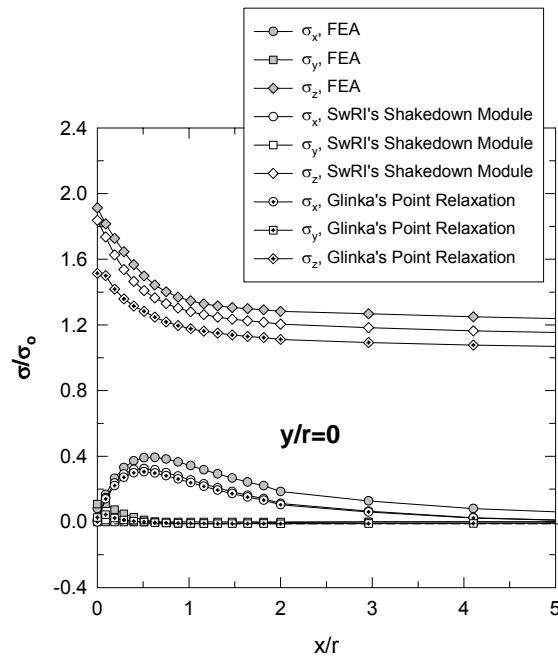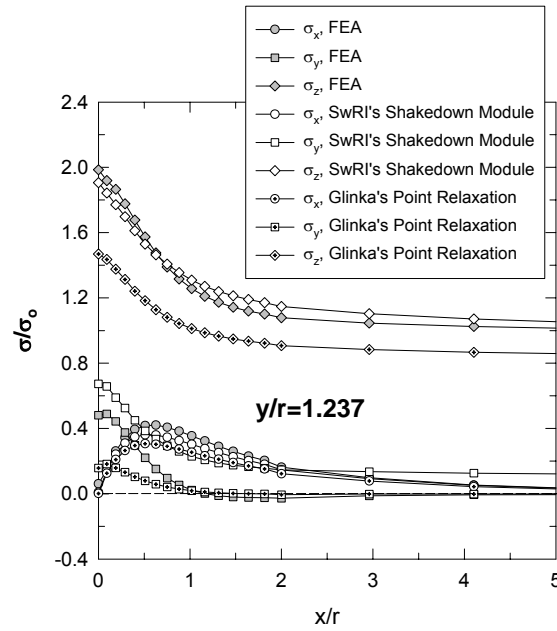
Figure I37a)   Figure I37 (b)   Figure I37 (c)
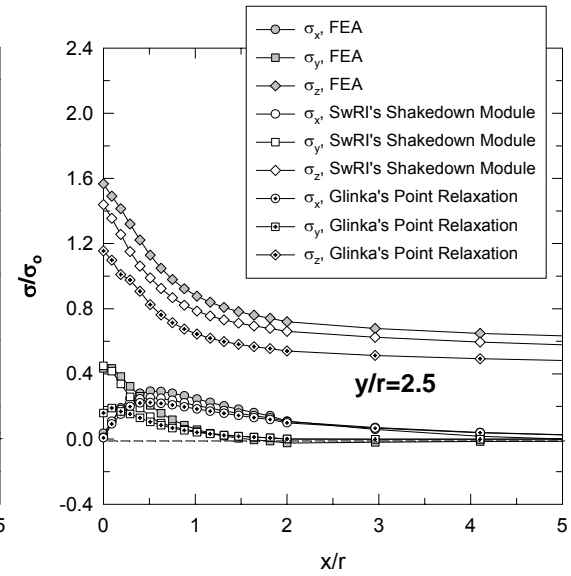
Figure I37.   Comparison of stress components predicted by SwRI's isotropic shakedown module with the results obtained from FEA. The results computed from Glinka's point relaxation are also included. The notched plate is subjected to S_z=30 *ksi*, M_x=2500 *kip-in*, and M_y=0; Material B. Results in Figure A.5.36(a) are for *y/r*=0 (the free surface at the side of the plate), A.5.36(b) are for *y/r*=1.237 (a plane one quarter of the way through the plate), and A.5.36(c) are for *y/r*=2.5 (at the mid-plane). In Figure A.5.36(a), the results predicted by SwRI's isotropic shakedown module can not be visually differentiated from the point relaxation results.
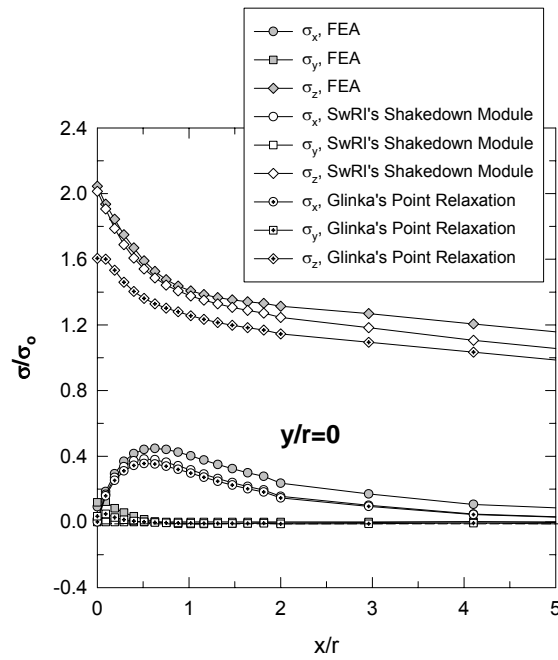
Figure I38 (a)
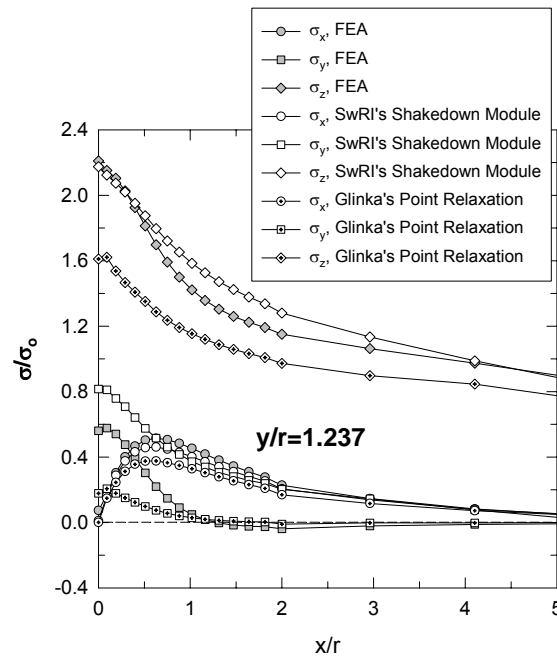
Figure I38 (b)
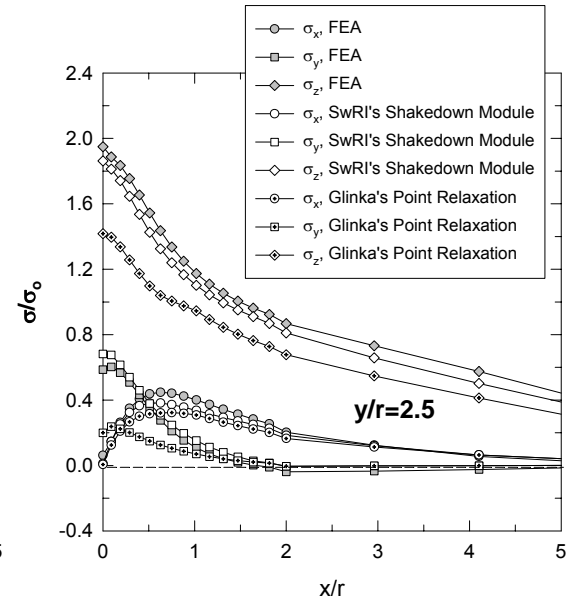
Figure I38 (c)

Figure I38.   Comparison of stress components predicted by SwRI's isotropic shakedown module with the results obtained from FEA. The results computed from Glinka's point relaxation are also included. The notched plate is subjected to S_z=25 *ksi*, M_x=2400 *kip-in*, M_y=2400 *kip-in*; Material B. Results in Figure A.5.37(a) are for y/r=0 (the free surface at the side of the plate), A.5.37(b) are for y/r=1.237 (a plane one quarter of the way through the plate), and A.5.37(c) are for y/r=2.5 (at the mid-plane). In Figure A.5.37(a), the results predicted by SwRI's isotropic shakedown module can not be visually differentiated from the point relaxation results.
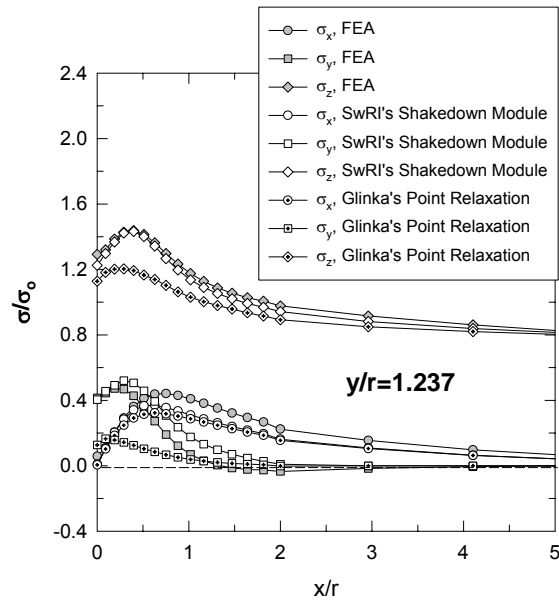
Figure I39(a)
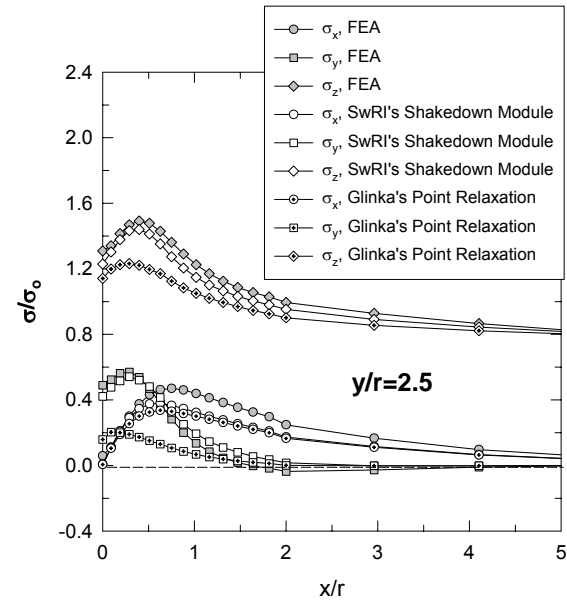
Figure I39(b)

Figure I39.   Comparison of stress components predicted by SwRI's isotropic shakedown module with the results obtained from FEA. The results computed from Glinka's point relaxation are also included. The notched plate is subjected to S_z=50 *ksi*, and M_x=M_y=0; Material A. Results in Figure A.5.38(a) are for y/r=1.237 (a plane one quarter of the way through the plate), and A.5.38(b) are for y/r=2.5 (at the mid-plane).
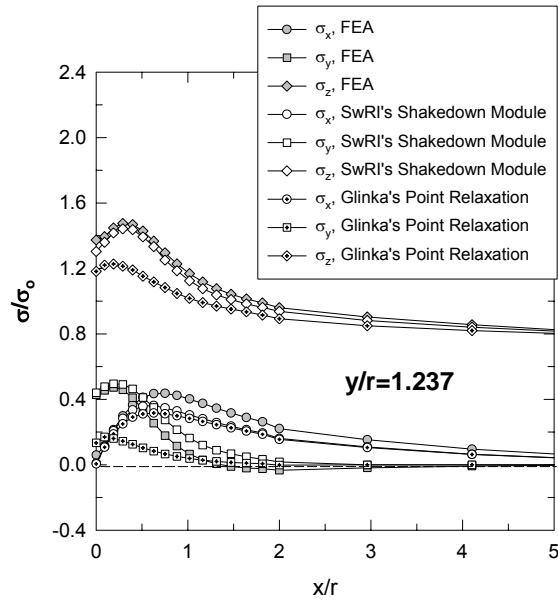
Figure I40 (a)
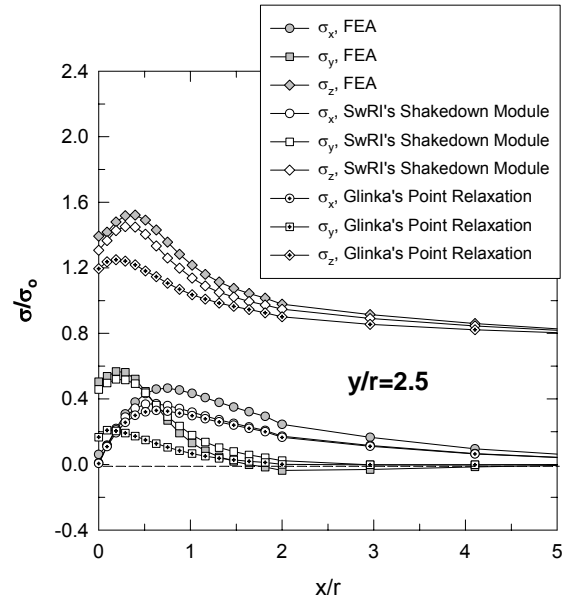
Figure I40 (b)

Figure I40.   Comparison of stress components predicted by SwRI's isotropic shakedown module with the results obtained from FEA. The results computed from Glinka's point relaxation are also included. The notched plate is subjected to S_z=50 *ksi*, and M_x=M_y=0; Material D. Results in Figure A.5.39(a) are for *y/r*=1.237 (a plane one quarter of the way through the plate), and A.5.39(b) are for *y/r*=2.5 (at the mid-plane).
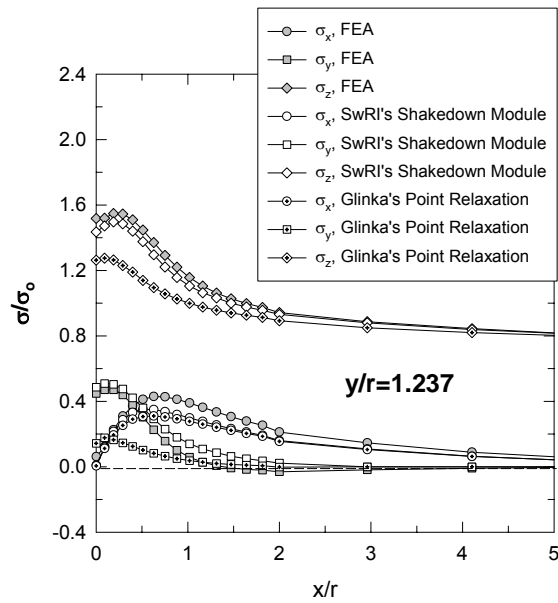
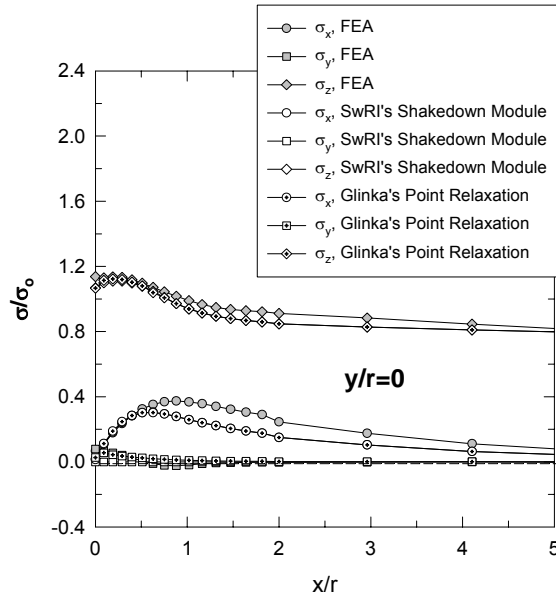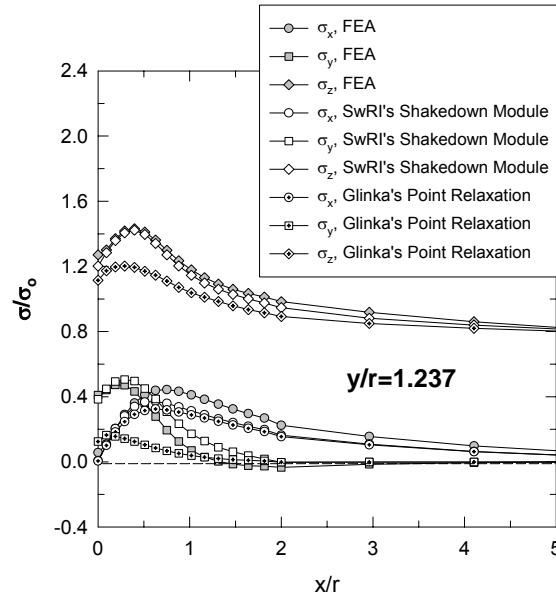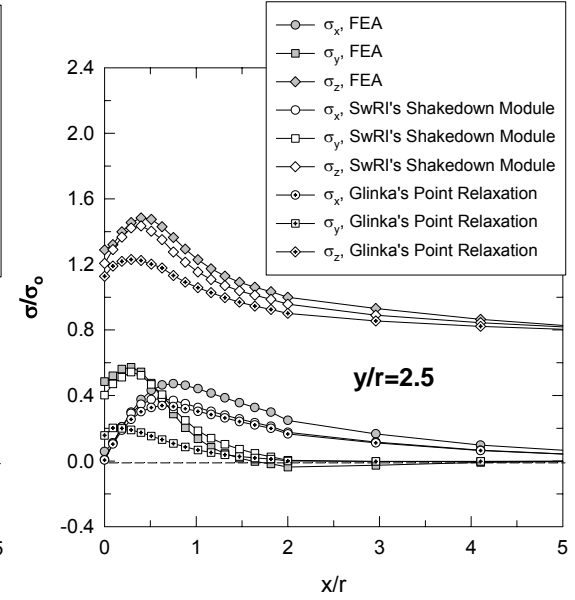Figure I41 (a)
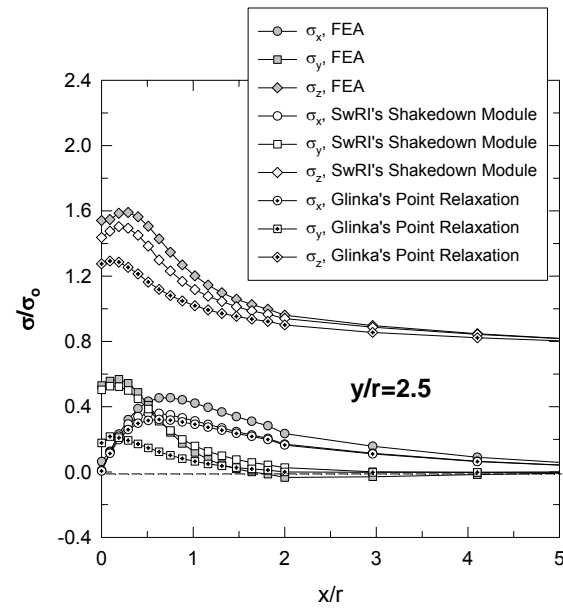
Figure I41 (b)

Figure I41.   Comparison of stress components predicted by SwRI's isotropic shakedown module with the results obtained from FEA. The results computed from Glinka's point relaxation are also included. The notched plate is subjected to S_z=50 *ksi*, and M_x=M_y=0; Material E. Results in Figure A.5.40(a) are for *y/r*=1.237 (a plane one quarter of the way through the plate), and A.5.40(b) are for *y/r*=2.5 (at the mid-plane).
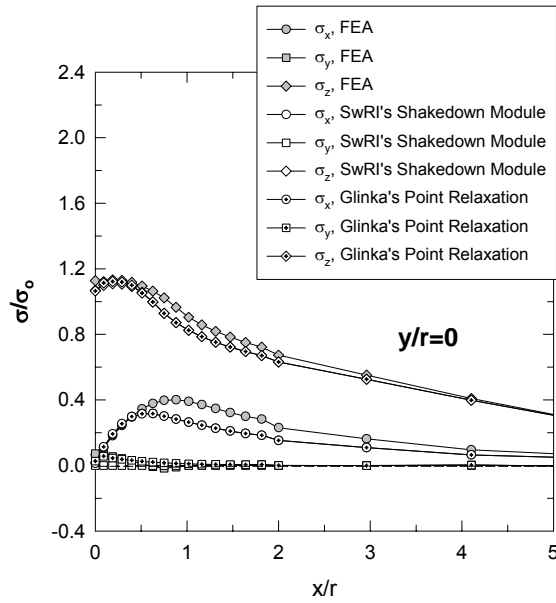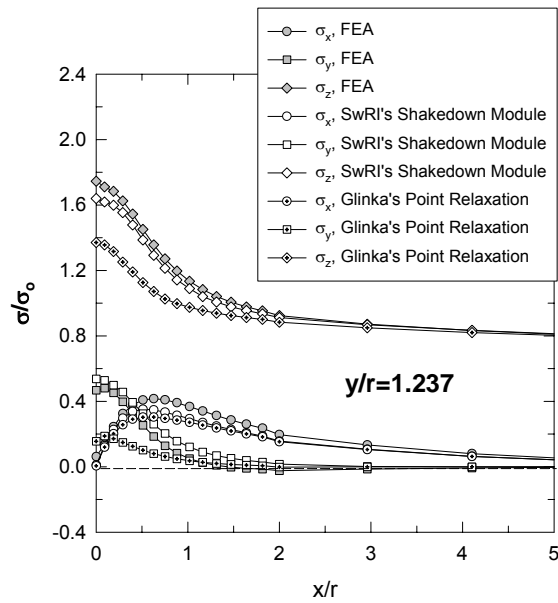
Figure I42 (a)
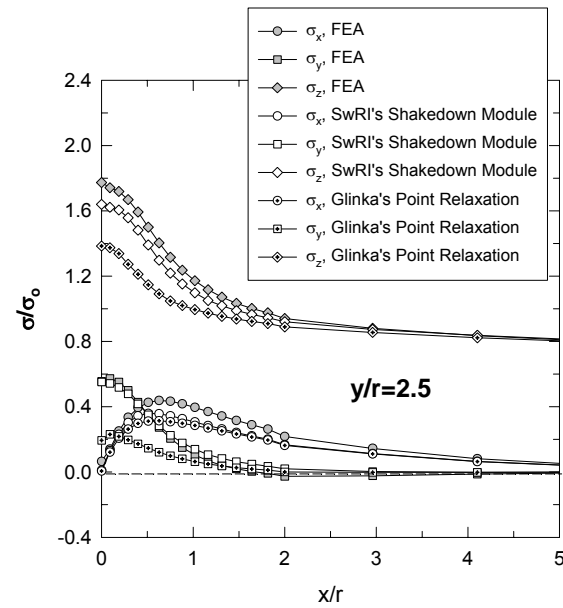
Figure I42 (b)

Figure I42.   Comparison of stress components predicted by SwRI's isotropic shakedown module with the results obtained from FEA. The results computed from Glinka's point relaxation are also included. The notched plate is subjected to S_z=50 *ksi*, and M_x=M_y=0; Material F. Results in Figure A.5.41(a) are for *y/r*=1.237 (a plane one quarter of the way through the plate), and A.5.41(b) are for *y/r*=2.5 (at the mid-plane).

APPENDIX J

ANISOTROPIC SHAKEDOWN METHODOLOGY FOR BIVARIANT STRESS FIELD

J.1   INTRODUCTION

The anisotropic shakedown methodology is an extension of the isotropic shakedown methodology described in the Quarterly Progress Report for April 1 through June 30, 2002, to account for material anisotropy. The load shedding and load redistribution schemes employed in the anisotropic shakedown module are similar to those used in the isotropic shakedown module. The major difference between these two modules is the algorithm to determine the stress relaxation at a point (point relaxation) whose formulation depends on the material modeling. Hence, the accuracy of the developed anisotropic shakedown module should be similar to the accuracy obtained by the isotropic shakedown module, provided the associated anisotropic constitutive relations accurately describe the materials' behavior.

The isotropic shakedown methodology is implemented in a software module called SHARP (Shakedown Analysis of Residual Plasticity). The anisotropic shakedown methodology is implemented in a software module called SHARP_AN (Shakedown Analysis of Residual Plasticity _ Anisotropic). This module is available through AFRL/MLLMN or directly from Southwest Research Institute.

The shakedown methodology converts the incremental linear elastic solutions into equivalent elastic-plastic solutions while conserving forces and moments resulting from the remote loading. All six components of stress are required for the shakedown analysis. The z-component of stress that is normal to the load bearing area is considered the primary stress of concern. The out-of-plane direction is in the y-direction, and this coordinate along with the x coordinate defines the load bearing section. The designation of stresses conforms to the coordinate system employed in Figure J1, which shows the load bearing section (enclosed by dashed lines) corresponding to a notched plate.
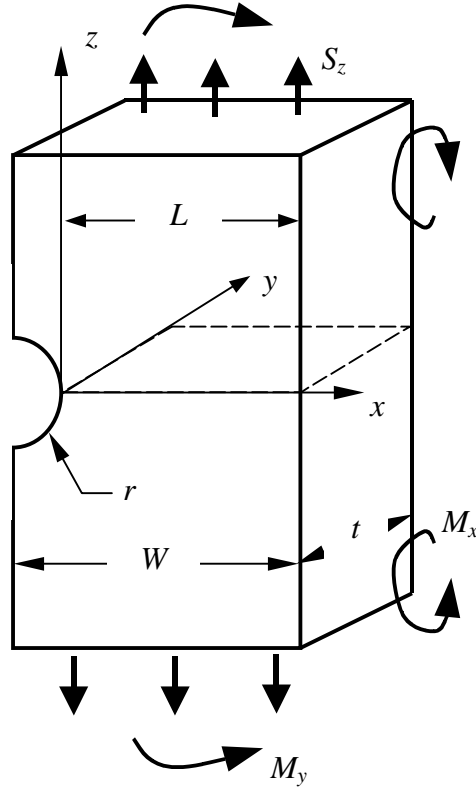
Figure J1. Geometry, coordinate system, and loading conditions for finite element analysis used to verify SwRI's anisotropic shakedown module. Various combinations of tensile stresses and moments were applied to the notched plate. In one set of calculations, the axis of the plate (z-direction) was assumed parallel to the <001> (so that the local and global coordinate systems are identical), while in another set of calculations the axis of the plate was assumed parallel to the <111> direction (so that the local and global coordinate systems were different).

Two major tasks are performed in the anisotropic shakedown methodology. The first task determines the stress relaxation at each nodal position using the linear elastic stress state. This procedure is referred to herein as the point relaxation procedure and it provides an approximate solution to the elastic-plastic stress state at each nodal position for the current load step from the corresponding incremental change in the applied linear elastic solution. The point relaxation procedures are based on Neuber's rule that converts the incremental elastic strain energy density to the incremental elastic-plastic strain energy density. The second task performs the load shedding that occurs due to point relaxation and re-distributions the surplus incremental forces and moments over the load bearing area. A more detailed description of each of these tasks in given in Section J.2.

The shakedown methodology developed herein is based on an approximate elastic-plastic stress analysis that is applicable to rectangular load bearing areas. The input data needed to apply the methodology and to run the computer program SHARP_AN that performs the stress analysis consists of three parts: structural dimensions, material properties and linear elastic stress analysis results, each of which is outlined below.

J.1.1 Structural Data Requirements

The structural data consists of specifying the coordinates of the rectangular load bearing section. The load bearing section is defined by a rectangle bounded on one side by the x-coordinate with a width (L) extending from x_{min} to x_{max}, and on the other side by the y-coordinate with a depth (t) extending from y_{min} to y_{max}. The incremental elastic stress state is specified at the points (nodes) defined by the intersecting perpendicular gridlines that define $(n_x-1) \times (n_y-1)$ small rectangular elements corresponding to n_x and n_y gridlines that originate from the x- and y-axes, respectively. The nodal coordinates are signified by (x_i, y_j) where i varies from 1 to n_x and j from 1 to n_y, and a rectangle element is represented by four corner nodes whose coordinates are given by (x_i, y_j), (x_{i+1}, y_j), (x_{i+1}, y_{j+1}), and (x_i, y_{j+1}).

J.1.2 Material Data Requirements

The material data is composed of discrete pairs of stress and strain values that define the uniaxial stress and strain behavior of an anisotropic material under monotonic loading when the direction of loading is along the <001> crystallographic direction. Along the <001> direction, the anisotropic materials in this study display "pseudo-isotropic" behavior. The coordinate system that is compatible with the <001> or equivalent direction is herein called the local coordinate system. The stress-strain data should be measured at a strain rate typical of the strain rate experienced by the material in the application of interest. A routine that determines the constitutive behavior of the anisotropic material and that can be interfaced with SHARP_AN is also needed. This constitutive routine should be compatible with material behavior measured on a specimen with its axis parallel to the <001> or equivalent direction. The routine should implicitly contain the elastic stiffness matrix for the material and calculate the plastic response in the <001> direction. The specification for this interface is described in more detail in Subsection J.2.1. Finally, the user has to provide the elastic stiffness matrix with respect to the global coordinate system. The global coordinate

system is the system consistent with the external loading direction, the direction for which the linear elastic stress results are obtained. The 6×6 global elastic stiffness matrix is needed in order to derive the global strain components from the global stress components.

J.1.3   Stress Data Requirements

The linear elastic stress analysis data consists of the incremental changes in the global stress components at the grid points or nodes of the elements that form a two-dimensional model of the load bearing section as the applied load(s) are incrementally increased. The elements have to be rectangular in shape but not necessarily of equal size. For example, they could coincide with the elements on the load bearing section corresponding to the finite element modeling of that plane. The point relaxation calculations are performed in the local coordinate system. Hence, the final stress analysis data provided by the user is the transformation matrix, Q, and its transpose, Q^t, that operate on the global stresses, σ^{global}, to transform them into local stresses, σ^{local} ($Q^t\sigma^{global}Q=\sigma^{local}$), and on the calculated local plastic relaxed stresses, to transform them back into the global stresses ($Q\sigma^{local}Q^t=\sigma^{glcbal}$).

J.2   STRESS RELAXATION AT A POINT (POINT RELAXATION)

The point relaxation process is accomplished by applying Neuber's rule using the linear-elastically determined equivalent stress and equivalent strain increments. Neuber's rule states that the incremental product of stress and strain is invariant for each load step irrespective of the constitutive relationship between stress and strain. In contrast to the approach used in the isotropic counterpart SHARP, the anisotropic version SHARP_AN determines the plastic point relaxation of the stress components in the local coordinate system. Thus, all stresses and strains defined in the global coordinate system are transformed to the local system before applying Neuber's rule.

In terms of incremental stresses, which is more applicable to multi-axial stressing and non-dimensional loading, Neuber's rule can be formulated as

$$^{(k)}\Delta\left(\sigma_{eq}^{ep}\varepsilon_{eq}^{ep}\right)=^{(k)}\Delta\left(\sigma_{eq}^{E}\varepsilon_{eq}^{E}\right) \;\Rightarrow\; ^{(k)}\Delta\sigma_{eq}^{ep}\cdot{}^{(k-1)}\varepsilon_{eq}^{ep}+{}^{(k-1)}\sigma_{eq}^{ep}\cdot{}^{(k)}\Delta\varepsilon_{eq}^{ep}=^{(k)}\Delta\left(\sigma_{eq}^{E}\varepsilon_{eq}^{E}\right)$$

where stress and strain are denoted by σ and ε, $^{(k)}\Delta\sigma_{eq}^{ep} = {}^{(k)}\sigma_{eq}^{ep} - {}^{(k-1)}\sigma_{eq}^{ep}$ and $^{(k)}\Delta\varepsilon_{eq}^{ep} = {}^{(k)}\varepsilon_{eq}^{ep} - {}^{(k-1)}\varepsilon_{eq}^{ep}$. The superscript k denotes the current step number. The superscripts E and ep signify elastic and elastic-plastic quantities, and the subscript, eq, represents an equivalent quantity; for example, σ_{eq}^{ep} is used to denote the equivalent elastic-plastic stress.

Currently, the anisotropic shakedown methodology is limited to isothermal and constant strain rate loading conditions. Thus, the so-called "pseudo-isotropic" stress-strain curve provided by the user needs to be representative of the actual operating temperature and strain rate. This curve should be expressed mathematically in the form of the Ramberg-Osgood equation

$$^{(k)}\varepsilon_{eq}^{ep} = \varepsilon_o \left[\frac{^{(k)}\sigma_{eq}^{ep}}{\sigma_o} + \alpha \left(\frac{^{(k)}\sigma_{eq}^{ep}}{\sigma_o} \right)^\beta \right] \tag{J1}$$

in which σ_o, ε_o, α and β are material parameters. σ_o and ε_o may be considered as the yield stress and strain in reference to the behavior of this "pseudo-isotropic" curve.

Neuber's rule can be solved for the current equivalent elastic-plastic stress, $^{(k)}\sigma_{eq}^{ep}$, using the elastic-plastic stresses and strains determined at the end of the previous load step together with the user-specified elastic stresses and strains. (In the SHARP_AN module, the elastic strains are derived from the stresses using the elastic modulus matrix). The required solution is in the form of one of the roots of a non-linear equation derived by applying Neuber's rule. This root needs to be determined using numerical methods. The bisection method is used in the point relaxation module. After the root is found, the elastic-plastic equivalent strain $^{(k)}\varepsilon_{eq}^{ep}$ and the elastic-plastic equivalent strain increment $^{(k)}\Delta\varepsilon_{eq}^{ep}$ can be computed from the constitutive relationship. The incremental elastic-plastic stress components can thus be approximately determined by

$$^{(k)}\Delta\sigma_{ij}^{ep} = \frac{^{(k)}\Delta\sigma_{eq}^{eq}}{^{(k)}\Delta\sigma_{eq}^{E}} \cdot {}^{(k)}\Delta\sigma_{ij}^{E} \tag{J2}$$

J.2.1   Generic Interface for the User-Specified Material Routines

An overview of the anisotropic shakedown module is shown in Figure J2. This figure illustrates the interaction among the main shakedown routine, the point relaxation module and the user-specified material routines. The user-specified material routines consist of three parts, as follows:

GENERIC_INTF_I –   Contains a subroutine that updates the basic material
                     properties;

GENERIC_INTF_II –   Contains a subroutine that determines the incremental elastic-
                     plastic quantities after the equivalent stress and the equivalent
                     strain are defined. It may involve some elaborate analytical
                     work to derive the appropriate equations from the material
                     constitutive model;

GENERIC_INTF_III –   Contains a function that defines the equivalent stress for the
                     specific anisotropic material model.
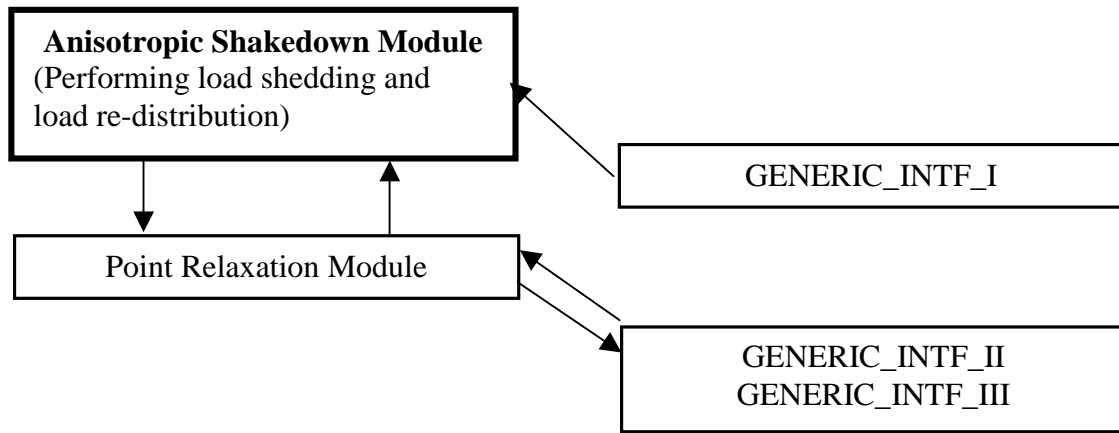
Figure J2.   An overview of the program structure of SwRI's anisotropic shakedown module
             with the user-specified material routines; GENERIC_INTF_I,
             GENERIC_INTF_II, and GENERIC_INTF_III.

The derivation on the Walker constitutive model is provided in Section J.2.2 as an example of how to make use of these user-specified routines.

The generic interfaces for the user-specified material routines are provided so that users can implement a variety of anisotropic material constitutive relationships. The

descriptions of the parameters that form the arguments of the routines enabling them to interface with the main shakedown module are listed in Tables J1 to J3. The routines presented herein to illustrate examples of possible interface routines are in FORTRAN, and floating point computation is in double precision. These routines are provided as guidelines on how to construct the routines conforming to the generic interface.

The material constants are declared and stored in the array argument CONSTANT of GENERIC_INTF_I and passed out into GENERIC_INTF_II. The double precision function ANISO_SEQ contained in GENERIC_INTF_III provides the formulation for the equivalent stress for the given material model. Note that S11, S12, …, and S33 are regular stress components, and, in contrast, A11, A12, …, and A33 (which signify the coordinates of the center of plasticity surface) are in deviatoric space. Quantities in deviatoric space are defined by subtracting the dilatational component from the original quantities. For example, the deviatoric stresses S_{ij} are defined by $S_{ij} = \sigma_{ij} - \sigma_{kk}\delta_{ij}$ in which the dilatational component is defined by $\sigma_{kk} = (\sigma_{11} + \sigma_{22} + \sigma_{33})/3$, and $\delta_{ij} = 1$ for $i = j$, and $\delta_{ij} = 0$ for $i \neq j$ where the subscripts i and j vary from 1 to 3. Table J4 shows the general program structure of the user-specified material routines.

Table J1. Definition of Arguments Used in the User Provided Routine GENERIC_INTF_I

SUBROUTINE GENERIC_INTF_I($D6,Q,Qt,CONSTANT,TEMP$)			
Argument Name	**Data Type**	**Status**	**Description**
$D6$	Double precision array	Output	Two-dimensional array of size 6×6 used to store the elements in the elastic stiffness matrix relating the strains to the stresses in the global coordinate system.
Q	Double precision array	Output	Two-dimensional array of size 3×3 used to store the transformation matrix that converts the tensors in the global coordinate system to those in the local coordinate system.
Q^t	Double precision array	Output	Two-dimensional array of size 3×3 used to store the transpose of Q.
Constant	Double precision array	Output	One-dimensional array used to store user-specified material constants that are needed by the constitutive model. These constants are passed as input arguments to the routines GENERIC_INTF_II and GENERIC_INTF_III. The maximum permissible dimension for this array is 2000.
Temp	Double precision	User-specified	Temperature passed into GENERIC_INTF_I to allow for the fact that the constitutive model may incorporate the variation of material properties with temperature.

Table J2. Definition of Arguments Used in the User Provided Routine
GENERIC_INTF_II

SUBROUTINE GENERIC_INTF_II (*CONSTANT, SIG_PTC, DSIG_PTC,* *DEPS_ETC, OMEGA_PTC, EPS_PTC, DRTOTAL, TEMP, DTIME*)			
Argument Name	**Data Type**	**Status**	**Description**
Constant	Double precision array	Input from GENERIC_INTF_I	One-dimensional array used to store user-specified material constants that are needed by the constitutive model. The constants are defined in GENERIC_INTF_I. The maximum permissible dimension is 2000.
Sig_ptc	Double precision array	Input from anisotropic shakedown module	Two-dimensional array of size 3×3 used to store the predicted local elastic-plastic stress at the current load step determined by the anisotropic shakedown module.
Dsig_ptc	Double precision array	Input from anisotropic shakedown module	Two-dimensional array of size 3×3 used to store the predicted local elastic-plastic stress increment at the current load step determined by the anisotropic shakedown module.
Deps_etc	Double precision array	Input from anisotropic shakedown module	Two-dimensional array of size 3×3 used to store the computed local elastic strain increment used when applying Neuber's rule in the shakedown analysis at the current load step. The value can be different from the user-specified value due to the adjusted time increment, *dtime*.
Omega_ptc	Double precision array	Input/Output	Two-dimensional array of size 3×3 used to store the calculated translation of the center of the plastic surface according to the user-specified anisotropic material model. The quantities are defined in deviatoric space and with respect to the local coordinate system.
Eps_ptc	Double precision array	Input/Output	Two-dimensional array of size 3×3 used to store the calculated local elastic-plastic strain according to the user-specified anisotropic material model.

Table J2 (continued). Definition of Arguments Used in GENERIC_INTF_II

SUBROUTINE GENERIC_INTF_II (*CONSTANT, SIG_PTC, DSIG_PTC, DEPS_ETC, OMEGA_PTC, EPS_PTC, DRTOTAL, TEMP, DTIME*)			
Argument Name	**Data Type**	**Status**	**Description**
DRtotal	Double precision	Input/Output	Total local plastic strain.
Temp	Double precision	Input from GENERIC_INTF_I	Temperature used to determine the material properties (passed in from GENERIC_INTF_I).
Dtime	Double precision	Input from anisotropic shakedown module	Time increment for integration.

Table J3. Definition of Arguments Used in the User Provided Routine GENERIC_INTF_III

DOUBLE PRECISION FUNCTION ANISO_SEQ (CONSTANT, S11, S12, S13, S22, S23, S33, A11, A12, A12, A22, A23, A33)			
Argument Name	**Data Type**	**Status**	**Description**
Constant	Double precision array	Input from GENERIC_INTF_I	One-dimensional array used to store user-specified specified material constants that are needed by the constitutive model. These constants are defined in GENERIC_INTF_I.
S11	Double precision	Input	x-component of stress
S12	Double precision	Input	xy-component of stress
S13	Double precision	Input	xz-component of stress
S22	Double precision	Input	y-component of stress
S23	Double precision	Input	yz-component of stress
S33	Double precision	Input	z-component of stress
A11	Double precision	Input	x-component of the center of plasticity surface*
A12	Double precision	Input	xy-component of the center of plasticity surface*
A13	Double precision	Input	xz-component of the center of plasticity surface*
A22	Double precision	Input	y-component of the center of plasticity surface*
A23	Double precision	Input	yz-component of the center of plasticity surface*
A33	Double precision	Input	z-component of the center of plasticity surface*

(*) in deviatoric space.

Table J4. The General Program Structure of the User-Specified Material Routines for SwRI's Anisotropic Shakedown Module, SHARP_AN

```
!====================================================================
subroutine Generic_intf_I(d6global,Q,Qt,constant,temp)
!
!  Generic Interface Part I - basic anisotropic material properties
!
     implicit none
     double precision, intent(in)  ::  temp
     double precision, intent(out) ::  d6global(6,6),Q(3,3),Qt(3,3),constant(11)
!
!  user-specified algorithm here
!
end  subroutine Generic_intf_I

!====================================================================
subroutine Generic_intf_II(constant,sig_ptc,dsig_ptc,deps_etc,omega_ptc, eps_ptc,   &
               dRtotal, temp, dtime)
!
!   Generic Interface Part II  -  material constitutive model
!
     implicit double precision (a-h,o-z)
     double precision, intent(in)   ::  temp, dtime, constant(11), sig_ptc(3,3),   &
                            dsig_ptc(3,3), deps_etc(3,3)
     double precision, intent(inout)::  dRtotal, omega_ptc(3,3), eps_ptc(3,3)
!
!  user-specified algorithm here
!
end subroutine Generic_intf_II


!====================================================================
double precision function aniso_seq(constant,s11,s12,s13,s22,s23,s33,a11,   &
                    a12,a13,a22,a23,a33)
!
!  Generic interface Part III – equivalent stress definition for anisotropic material
!
     implicit none
     double precision, intent(in) :: constant(11),s11,s12,s13,s22,s23,s33,  &
                    a11,a12,a13,a22,a23,a33
     double precision           :: M11mM12, M44, dev, xi11, xi12, xi13,   &
                    xi22, xi23, xi33
!
!  user-specified algorithm here
!
 end function aniso_seq
!====================================================================
```

J.2.2 Derivation of Example Generic Interface Routines Using Walker's Constitutive Model

A material constitutive model routine developed by Walker that is compatible with the requirements of a user provided material routine for the ANSYS[1] stress analysis program was provided by Pratt & Whitney to SwRI to enable validation of the anisotropic shakedown module. This constitutive model also served to guide SwRI in developing the specification for the generic interface routines listed in Tables J1 to J3. The constitutive model is herein called the Walker model, although it was adopted by Walker from Nouailhas and Freed's viscoplastic theory for anisotropic materials[2]. These routines and the values of the material constants used in them are proprietary to P&W and are not delivered to the HCF Team as part of the shakedown module. However, Walker's constitutive model for an anisotropic material is used herein to demonstrate the procedures to be followed when constructing the generic material interface routines for the shakedown module.

As used in the validation of the shakedown module, Walker's constitutive model is defined by the following differential equations:

$$\Delta\sigma_{ij} = D_{ijkl}\left(\Delta\varepsilon_{kl} - \Delta\varepsilon_{kl}^{plasitc}\right) \tag{J3}$$

$$\Delta\varepsilon_{ij}^{plastic} = \frac{3}{2}\left\langle\frac{f}{K}\right\rangle^{n} \frac{M_{ijkl}\left(S_{kl} - \Omega_{kl}\right)}{\sqrt{\frac{3}{2}\left(S_{pq} - \Omega_{pq}\right)M_{pquv}\left(S_{uv} - \Omega_{uv}\right)}} \tag{J4}$$

$$f = \sqrt{\frac{3}{2}\left(S_{pq} - \Omega_{pq}\right)M_{pquv}\left(S_{uv} - \Omega_{uv}\right)} - \kappa \tag{J5}$$

$$\Delta\Omega_{ij} = \frac{2}{3}N_{ijkl}\Delta\varepsilon_{kl}^{plastic} - Q_{ijkl}\Omega_{kl}\Delta R \tag{J6}$$

$$\Delta R = \sqrt{\frac{2}{3}\Delta\varepsilon_{ij}^{plastic}M_{ijkl}^{-1}\Delta\varepsilon_{kl}^{plastic}} = \left\langle\frac{f}{K}\right\rangle^{n} \tag{J7}$$

---

[1] ANSYS is a commercially available FEM software package.
[2] D. Nouailhas and A. D. Freed, "A Viscoplastic Theory for Anisotropic Materials," Journal of Engineering Materials and Technology, Vol. 114, pp. 97-104, 1992

where the angle bracket notation is used to denote the Heaviside step function, $\langle x \rangle = x H(x)$, Δ denotes an incremental change in a quantity, $[D]$ represents the elastic stiffness matrix relating the elastic strain to the stress, f is a yield function, exponents m and n and the quantities K and k are material constants, and $[M]$, $[N]$, and $[Q]$ are material properties expressed as fourth rank tensors, denoted by the square brackets. ΔR signifies the equivalent plastic strain increment. All material properties used in the foregoing equations are assumed determined with respect to the local coordinate system (*e.g.*, measured with the axis of the specimen parallel to the <001> or equivalent direction).

The relationship of the Walker Model parameters to the arguments in the generic interface routines, GENERIC_INTF_I, GENERIC_INTF_I and GENERIC_INTF_III, is clarified in Table J5.

Table J5. Relationship of Walker Model Parameters to the Arguments of the Routines GENERIC_INTF_I, GENERIC_INTF_I and GENERIC_INTF_III

Argument	Description	Subroutine(s) Used	Relationship to Walker Model
Constant	Array that contains material constants	GENERIC_INTF_I GENERIC_INTF_II GENERIC_INTF_III	Contains values for κ, K, and the non-zero elements of the tensors [D], [M], [N], and [Q].
Omega_ptc	Center of plasticity surface in deviatoric space	GENERIC_INTF_II	Used in Equation (J6) to determine the current incremental change, $\Delta\Omega_{ij}$ in the center of the plasticity surface Ω_{ij} so this can be updated and the new value returned.
Eps_ptc	Total strain.	GENERIC_INTF_II	The incremental change in plastic strain, $\Delta\varepsilon_{ij}^{plastic}$, is computed using Equations (J4) and (J5) and added to the total strain, ε_{ij}, which is then returned as the updated value. The elastic component, $\Delta\varepsilon_{ij}^{elastic}$ of the total strain is computed by inverting Equation (J3) to give the following expression for the total strain increment, $$\Delta\varepsilon_{ij} = D_{ijkl}^{-1}\Delta\sigma_{kl} + \Delta\varepsilon_{ij}^{plastic}$$
DRtotal	Total equivalent plastic strain.	GENERIC_INTF_II	Equation (J7) is used to determine the incremental change in the equivalent plastic strain and this is then added to the current total value and the new value returned.
Function ANISO_SEQ	Equivalent stress	GENERIC_INTF_III	The user provides a function that defines the equivalent stress in terms of material constants, the stress components and deviatoric stress components that define the center of the plasticity surface. The function should be consistent with the anisotropic constitutive model. In the Walker model the equivalent stress is given by the first term on the right hand side of Equation (J5), i.e. $\sqrt{\dfrac{3}{2}\left(S_{pq} - \Omega_{pq}\right)M_{pquv}\left(S_{uv} - \Omega_{uv}\right)}$ (see Equation (J9)).

J.3 LOAD SHEDDING AND RE-DISTRIBUTION

The methodology for load shedding and load re-distribution in SHAPR_AN is identical to the isotropic shakedown methodology developed in SHARP except that the equivalent stress used in the anisotropy constitutive model is different from that employed in the isotropic model. However, for completeness, the load shedding and re-distribution procedures used in SHARP are summarized here. As indicated in Section J.2, although the point relaxation employed in SHARP_AN is performed in the local coordinate system, the corresponding load shedding and re-distribution are accomplished in the global coordinate system.

The following steps reference corresponding section of the report where more detailed descriptions of the load shedding procedures are given.

Step (1)   Interpolation of the incremental linear elastic stress values for the current load step to generate stress values at the nodal points of a much finer mesh of rectangular elements than the original mesh defined by finite element modeling of the load bearing section. (Section J.3.1).

Step (2)   Evaluation of the incremental increase in forces and moments for the current load step from the incremental change in the linear elastic stress and the estimated elastic-plastic stress state for the previous load step (Section J.3.2).

Step (3)   Estimation of the plastic zone size on the load-bearing area based on the equivalent stress derived from the applied incremental linear elastic stress for the current load step and the elastic-plastic stress derived in the previous load step (Section J.3.3).

Step (4)   Splitting the stress range (defined as the difference between the maximum and minimum values of an equivalent stress) on the load bearing section into specific stress bands, determining the area of the load bearing section occupied by each of the bands, and assigning the equivalent stress in each element of the fine mesh to one of the stress bands (Section J.3.4).

Step (5)   Evaluation of the areas over which load shedding will occur for each equivalent stress band (Section J.3.5).

Step (6)   Determination of the plastically relaxed stresses for each equivalent stress band (Section J.3.6)

Step (7)   Redistribution (load shedding) of the excess incremental load arising from plastic stress relaxation over the area associated with each equivalent stress band (Section J.3.7).

Step (8)   Calculation and re-distribution of the global incremental loads needed to maintain force and moment balance after the plastic stress relaxation process is completed over the load bearing section (Section J.3.8)

J.3.1 Generation of a New Bivariant Incremental Stress Array

This procedure is required to provide a fine mesh consisting of small element sizes in order to increase the accuracy of the plastic stress relaxation and load shedding procedures detailed in Sections J.3.5 and J.3.7. The stress values provided at the corner points of the elements constituting the user-defined mesh are interpolated to provide stress values at the corner points of the elements constituting a finer mesh. The distribution of incremental stress, $\Delta\sigma_{ij}^{E}(x, y)$, across an element is assumed to be linear. This means that if (x,y) is a coordinate position within an element of the user-defined mesh then the incremental stress within that element will vary as $\Delta\sigma_{ij}^{E}(x, y) = b_1 + b_2x + b_3y + b_4xy$, where the coefficients b_1, b_2, b_3, and b_4 are determined by the incremental stress values at the coordinates of the four corner points of the element. The shakedown methodology utilizes the results for the finer mesh which is specified to have m_x nodes (m_x-1 elements) along the x-axis between $x=x_{min}$ and $x=x_{max}$, and m_y nodes (m_y-1 elements) along the y-axis between $y=y_{min}$ and $y=y_{max}$. In general, $m_x > n_x$ and $m_y > n_y$, where n_x and n_y are the number of nodes along the x-axis and y-axis, respectively, in the user-specified mesh.

J.3.2 Evaluation of the Applied Incremental Force and Moments at the Current Load Step

The evaluation of the applied force F_z and moments M_x, M_y, at the current load step is based on the elastically determined stress increments at the current load step and the elastic-plastic stress solution determined from the previous load step. The equations are given by

$$
\begin{aligned}
^{(k)}F_z = \frac{1}{4}\sum_{i=1}^{m_x-1}\sum_{j=1}^{m_y-1}(x_{i+1}-x_i)(y_{j+1}-y_j)\Big[& {}^{(k-1)}\sigma_z^{ep}(x_i,y_j)+{}^{(k)}\Delta\sigma_z^{E}(x_i,y_j)+ \\
& {}^{(k-1)}\sigma_z^{ep}(x_i,y_j)+{}^{(k)}\Delta\sigma_z^{E}(x_i,y_j)+{}^{(k-1)}\sigma_z^{ep}(x_{i+1},y_j)+{}^{(k)}\Delta\sigma_z^{E}(x_{i+1},y_j)+ \\
& {}^{(k-1)}\sigma_z^{ep}(x_{i+1},y_{j+1})+{}^{(k)}\Delta\sigma_z^{E}(x_{i+1},y_{j+1})+{}^{(k-1)}\sigma_z^{ep}(x_i,y_{j+1})+{}^{(k)}\Delta\sigma_z^{E}(x_i,y_{j+1})\Big]
\end{aligned}
\tag{J8a}
$$

$$
\begin{aligned}
^{(k)}M_y = \frac{1}{8}\sum_{i=1}^{m_x-1}\sum_{j=1}^{m_y-1}(x_{i+1}^2-x_i^2)(y_{j+1}-y_j)\Big[& {}^{(k-1)}\sigma_z^{ep}(x_i,y_j)+{}^{(k)}\Delta\sigma_z^{E}(x_i,y_j)+ \\
& {}^{(k-1)}\sigma_z^{ep}(x_i,y_j)+{}^{(k)}\Delta\sigma_z^{E}(x_i,y_j)+{}^{(k-1)}\sigma_z^{ep}(x_{i+1},y_j)+{}^{(k)}\Delta\sigma_z^{E}(x_{i+1},y_j)+ \\
& {}^{(k-1)}\sigma_z^{ep}(x_{i+1},y_{j+1})+{}^{(k)}\Delta\sigma_z^{E}(x_{i+1},y_{j+1})+{}^{(k-1)}\sigma_z^{ep}(x_i,y_{j+1})+{}^{(k)}\Delta\sigma_z^{E}(x_i,y_{j+1})\Big]
\end{aligned}
\tag{J8b}
$$

$$^{(k)}M_x = \frac{1}{8}\sum_{i=1}^{m_x-1}\sum_{j=1}^{m_y-1}(x_{i+}-x_i)(y_{j+1}^2-y_j^2)\Big[^{(k-1)}\sigma_z^{ep}(x_i,y_j)+^{(k)}\Delta\sigma_z^E(x_i,y_j)+$$

$$^{(k-1)}\sigma_z^{ep}(x_i,y_j)+^{(k)}\Delta\sigma_z^E(x_i,y_j)+^{(k-1)}\sigma_z^{ep}(x_{i+1},y_j)+^{(k)}\Delta\sigma_z^E(x_{i+1},y_j)+ \qquad \text{(J8c)}$$

$$^{(k-1)}\sigma_z^{ep}(x_{i+1},y_{j+1})+^{(k)}\Delta\sigma_z^E(x_{i+1},y_{j+1})+^{(k-1)}\sigma_z^{ep}(x_i,y_{j+1})+^{(k)}\Delta\sigma_z^E(x_i,y_{j+1})\Big]$$

These equations are based on the interpolated values at the corner points of the elements constituting a finer mesh that has (m_x-1) elements along the x-axis and (m_y-1) elements along the y-axis. The symbols used to designate the stress component normal to the load bearing section are $\Delta\sigma_z$ for stress increment and σ_z for stress. The superscript E denotes the linear elastic solutions derived from the data provided by the user, and the superscript ep represents the elastic-plastic solutions determined from the anisotropic shakedown module. The current and previous load steps are denoted by superscripts k and $(k-1)$, respectively.

J.3.3   Estimation of the Plastic Zone Size

The plastic zone size, a_y, is the area of the load bearing section where the equivalent stress values, σ_{eq}, equal or exceed the yield stress, σ_{yield}. An element is only included in this area if the equivalent stress values at all four corner points of the element satisfy this criterion. A pseudo von-Mises type of equivalent stress, σ_{eq}^{pseudo}, composed of the current elastic stress increment and the elastic-plastic stress from the previous step is defined by the equation

$$\sigma_{eq}^{pseudo} = \sqrt{\frac{3}{2}\xi_{ij}^{pseudo}M_{ijkl}\xi_{kl}^{pseudo}} = \sqrt{\frac{3}{2}\left(S_{ij}^{pseudo}-\Omega_{ij}\right)M_{ijkl}\left(S_{kl}^{pseudo}-\Omega_{kl}\right)} \qquad \text{(J9)}$$

where $\xi_{ij}^{pseudo} = S_{ij}^{pseudo}-\Omega_{ij}$. M_{ijkl} describes the material properties in terms of a fourth rank tensor [see Equation J4]. The term S_{ij}^{pseudo} is a pseudo deviatoric stress based on the current linear elastic stress increment $^{(k)}\Delta\sigma_{ij}^E$ and the elastic-plastic stress $^{(k-1)}\sigma_{ij}^{ep}$ obtained from the previous load step. Its tensor representation is given by

$$S_{ij}^{pseudo} = \left(^{(k-1)}\sigma_{ij}^{ep}+^{(k)}\Delta\sigma_{ij}^E\right)-\delta_{ij}\cdot\left(^{(k-1)}\sigma_{kk}^{ep}+^{(k)}\Delta\sigma_{kk}^E\right)/3 \qquad \text{(J10)}$$

with $\delta_{ij} = 1$, if $i=j$, or $\delta_{ij} = 0$, if $i \neq j$. Ω_{ij} is the coordinate of the center of the current plasticity surface in the deviatoric space coordinate.

J.3.4   Determination of the Stress Bands for Load Shedding

The equivalent stress range $\left(\sigma_{eq}\right)_{\max}^{pseudo} - \left(\sigma_{eq}\right)_{\min}^{pseudo}$ is divided into n_r levels (i.e., n_r-1 stress bands) where the subscripts *max* and *min* denote the maximum and minimum equivalent stresses, respectively. The area occupied by each of the stress bands is determined and elements of the fine mesh that fall within each of the areas that are identified. Thus, the elements that fall within an area contain equivalent stresses with values between the upper and lower bounds that define the stress band. If a_y is the area over which the equivalent stress exceeds the yield stress, σ_{yield}, and a_{total} is the area of the load bearing section, then the number of stress bands, n_l, that contain equivalent stresses that exceed σ_{yield} is

$$n_l = \frac{a_y}{a_{total}} n_r \qquad (J11)$$

The stress ranges corresponding to each of the stress bands where yielding has occurred are defined as

$$\sigma_{inc} = \frac{\left(\sigma_{eq}\right)_{\max} - \sigma_{yield}}{n_l} \qquad (J12)$$

It follows that the number of stress bands where the equivalent stress is lower than σ_{yield} is $n_r - n_l$ and the stress ranges associated with these bands is

$$\sigma_{inc} = \frac{\sigma_{yield} - \left(\sigma_{eq}\right)_{\min}}{n_r - n_l} \qquad (J13)$$

Once a stress band is determined, the associated area a_k occupied by elements which have equivalent stress values above the lower limit of the band is evaluated. During this process, each element is assigned to, and associated with, a specific stress band.

J.3.5   Evaluation of Load Shedding Areas

The plastic stress relaxation process, load shedding, and stress re-distribution, start in the area of the load bearing section that has the maximum equivalent stress, $\left(\sigma_{eq}\right)_{\max}^{pseudo}$. It then proceeds to the area with a stress band equal to the second highest equivalent stress, and so on until the area of the load bearing section containing the minimum equivalent stress,

$\left(\sigma_{eq}\right)_{min}^{pseudo}$, is reached. During this process, load shedding due to plastic stress relaxation transfers incremental loads onto adjacent load bearing areas. The size of these areas, or re-distribution zones, $a^{relax}(a_k)$, for the k-th equivalent stress band is defined by

$$a^{relax}(a_k) = f(a_k) \cdot a_y \qquad (J14)$$

where $f(a_k)$ is a dimensionless multiplication factor calculated from the equation

$$f(a_k) = \frac{\alpha_{high} - \alpha_{low}}{2} \tanh\left(\frac{a_k - a_y}{a_y \zeta}\right) + \frac{\alpha_{high} + \alpha_{low}}{2} \qquad (J15)$$

This empirical factor acts as a smoothing function that re-distributes surplus incremental loads from locations inside the plastic zone over areas comparable to a_y, and re-distributes incremental loads from locations outside the plastic zone over areas many times greater than a_y. The forms for the parameters α_{high}, α_{low}, and ζ are empirically chosen based on exploratory investigations using the results of elastic-plastic finite element stress analyses of notched plates for material behaviors with significantly different strain-hardening capacities. The final forms are given by

$$\varsigma = 0.03^{\frac{\beta-1}{\beta+1}}, \quad \alpha_{low} = \frac{\beta+1}{\beta-1}, \quad \alpha_{high} = 20\alpha_{low} \qquad (J16)$$

where β is the Ramberg-Osgood strain hardening exponent (see Section J.2)

J.3.6   Determination of the Plastically Relaxed Stresses

The plastically relaxed stresses are calculated from the following stresses:

(1)   Linear elastic stress solution at the end of previous load step, $^{(k-1)}\sigma_{ij}^{E}$.

(2)   Linear elastic stress increment for the current load step, $^{(k)}\Delta\sigma_{ij}^{E}$.

(3)   Elastic-plastic stress solution at the end of previous load step, $^{(k-1)}\sigma_{ij}^{ep}$.

The computation of the plastically relaxed stresses is performed using the point relaxation module. For more details, refer to Section J.2.

J.3.7   Redistribution of Local Incremental Loads Resulting from Load Shedding

The reduction of the pseudo stress component σ_z^{pseudo} within each element belonging to a given stress band, is converted into an incremental load which is then re-distributed over an area that encompasses smaller stress bands. The increment of load re-distributed, ΔF_m, within the m-th stress band is calculated by the difference between the pseudo elastic-plastic stress state $\left[{}^{(k-1)}\sigma_z^{ep} + {}^{(k)}\Delta\sigma_z^{E} \right]$ and the relaxed stress state ${}^{(k)}\Delta\sigma_z^{ep}$ for the elements belonging to the stress band using a simple Trapezoidal rule

$$\Delta F_m = \frac{1}{4}\sum_{i=1}^{n_m} A_i \Delta\sigma_i \qquad (J17)$$

In this equation, n_m denotes the number of elements within the m-th stress band, A_i stands for the area of the i-th element, and $\Delta\sigma_i$ the sum of the incremental reductions in the stress component normal to the load bearing section, $\left[\left({}^{(k-1)}\sigma_z^{ep} + {}^{(k)}\Delta\sigma_z^{E} \right) - {}^{(k)}\Delta\sigma_z^{ep} \right]$, evaluated at the four corner points of the i-th element. The excess load is redistributed as an increment of stress, $\Delta\sigma_z\left(a_j, a_m\right)$, whose magnitude linearly varies over the redistribution zone size $a^{relax}\left(a_m\right)$ according to the rule

$$\Delta\sigma_z\left(a_j a_m\right) = \frac{2\Delta F_m}{a^{relax}\left(a_m\right)}\left[1 - \frac{a_j - a_m}{a^{relax}\left(a_m\right)}\right] , \quad a_m \le a_j \le a^{relax}\left(a_m\right) + a_m \qquad (J18)$$

The increments $\Delta\sigma_z\left(a_j, a_m\right)$ are added to the incremental stress component $\Delta\sigma_z^{E}$ of those nodes whose element belongs to the j-th stress band. Thus, at the time when the plastic stress relaxation calculation for the m-th stress band is completed, the total stress consists of the pseudo elastic-plastic stress component at the end of the previous step, ${}^{(k-1)}\sigma_z^{ep} + {}^{(k)}\Delta\sigma_z^{E}$, plus the sum of all the incremental stresses $\Delta\sigma_z\left(a_j, a_m\right)$ resulting from load shedding.

J.3.8   Balance of Force and Moments, and Load Re-distribution

After the stress relaxation calculations have been completed over the load bearing section, conservation of the force normal to the section, and conservation of moments with respect to the x- and y-axes, are checked. In this procedure, the force and moments are compared with the force and moments evaluated before stress relaxation according to Section J.3.2. If the difference in force is denoted by ΔF_z and the differences in moments by ΔM_x

and ΔM_y, then these are globally re-distributed as an incremental stress distribution $\Delta \sigma_z(x, y)$ over the whole load bearing section, where $\Delta \sigma_z(x, y)$ is evaluated according to the following rule:

$$\Delta \sigma_z(x, y) = C_{30}x + C_{31}y + C_{32}\sigma_z^{ep}(x, y) \tag{J19}$$

where the coefficients C_{ij} are given by

$$\begin{Bmatrix} C_{32} \\ C_{31} \\ C_{30} \end{Bmatrix} = \begin{bmatrix} q_{11} & q_{12} & q_{13} \\ q_{21} & q_{22} & q_{23} \\ q_{31} & q_{32} & q_{33} \end{bmatrix}^{-1} \begin{Bmatrix} \Delta F_z \\ \Delta M_y \\ \Delta M_x \end{Bmatrix} \tag{J20}$$

with

$$q_{11} = \sum_{i=1}^{n_x-1} \sum_{j=1}^{n_y-1} \frac{1}{2}\left(x_{i+1}^2 - x_i^2\right) \cdot \left(y_{j+1} - y_j\right)$$

$$q_{12} = \sum_{i=1}^{n_x-1} \sum_{j=1}^{n_y-1} \frac{1}{2}\left(x_{i+1} - x_i\right) \cdot \left(y_{j+1}^2 - y_j^2\right)$$

$$q_{13} = \sum_{i=1}^{n_x-1} \sum_{j=1}^{n_y-1} \frac{1}{4}\left(x_{i+1} - x_i\right) \cdot \left(y_{j+1} - y_j\right)\left[\sigma_z^{ep}\left(x_i, y_j\right) + \sigma_z^{ep}\left(x_{i+1}, y_j\right) + \sigma_z^{ep}\left(x_{i+1}, y_{j+1}\right) + \sigma_z^{ep}\left(x_i, y_{j+1}\right)\right]$$

$$q_{21} = \sum_{i=1}^{n_x-1} \sum_{j=1}^{n_y-1} \frac{1}{4}\left(x_{i+1} + x_i\right)^2\left(x_{i+1} - x_i\right) \cdot \left(y_{j+1} - y_j\right)$$

$$q_{22} = \sum_{i=1}^{n_x-1} \sum_{j=1}^{n_y-1} \frac{1}{4}\left(x_{i+1}^2 - x_i^2\right) \cdot \left(y_{j+1}^2 - y_j^2\right)$$

$$q_{23} = \sum_{i=1}^{n_x-1} \sum_{j=1}^{n_y-1} \frac{1}{8}\left(x_{i+1}^2 - x_i^2\right) \cdot \left(y_{j+1} - y_j\right)\left[\sigma_z^{ep}\left(x_i, y_j\right) + \sigma_z^{ep}\left(x_{i+1}, y_j\right) + \sigma_z^{ep}\left(x_{i+1}, y_{j+1}\right) + \sigma_z^{ep}\left(x_i, y_{j+1}\right)\right]$$

$$q_{31} = \sum_{i=1}^{n_x-1} \sum_{j=1}^{n_y-1} \frac{1}{4}\left(x_{i+1}^2 - x_i^2\right) \cdot \left(y_{j+1}^2 - y_j^2\right)$$

$$q_{32} = \sum_{i=1}^{n_x-1} \sum_{j=1}^{n_y-1} \frac{1}{4}\left(x_{i+1} - x_i\right) \cdot \left(y_{j+1} + y_j\right)^2\left(y_{j+1} - y_j\right)$$

$$q_{33} = \sum_{i=1}^{n_x-1} \sum_{j=1}^{n_y-1} \frac{1}{8}\left(x_{i+1} - x_i\right) \cdot \left(y_{j+1}^2 - y_j^2\right)\left[\sigma_z^{ep}\left(x_i, y_j\right) + \sigma_z^{ep}\left(x_{i+1}, y_j\right) + \sigma_z^{ep}\left(x_{i+1}, y_{j+1}\right) + \sigma_z^{ep}\left(x_i, y_{j+1}\right)\right] \tag{J21}$$

After the global re-distribution, the stress relaxation process is repeated starting with a new "pseudo" stress state given by

$$\sigma_z^{pseudo}(x, y) = {}^{(k-1)}\sigma_z^{ep} + {}^{(k)}\Delta\sigma_z^{E} + \Delta\sigma_z(x, y) \tag{J22}$$

This process is repeated until the convergence criterion is met.

J.4   INTERFACING WITH SwRI's ANISOTROPIC SHAKEDOWN MODULE

As part of the current program, SwRI developed and validated under monotonic loading conditions a computer module, SHARP_AN, that performs an approximate shakedown analysis for three-dimensional structures with material anisotropy where a bivariant stress distribution is induced on the load bearing section of interest. The program enhances the simple point relaxation procedure that makes use of Neuber's rule by including the effects of load relaxation and load re-distribution over the load bearing area while maintaining force and moment balance on that area. The object files accompanied with this report can be used to link with a driver and user-specified routines to conduct anisotropic shakedown analyses. This section describes how the SHARP_AN routine can be interfaced with a calling program so that the module may be integrated into HCF related software that requires a shakedown analysis for its execution.

Two data transfer mechanisms are used to pass information to and receive results from the anisotropic shakedown module. One mechanism is through a COMMON data structure that contains arrays with prescribed dimensions, and the other mechanism is through the argument list of the routine itself. To demonstrate the data passing mechanisms, several segments of computer code are listed below that illustrate the type of coding that the user should include in the program driving the anisotropic shakedown module.

The computer code listed in Table J6 shows the parameters and the associated array sizes required to call the anisotropic shakedown module. A description of the arrays and parameters listed in Table J6 is provided in Table J7. The declaration for the data type employs the default Fortran 77 style.

Depending on how the shakedown module is driven by the calling program, the declarations of the arrays listed in Table J7 can be placed in different routines in the calling program. For large data arrays, the Fortran COMMON data structure is used for storage

efficiency. Comments are used in Table J6 to separate the COMMON and DIMENSION declarations into two Code Segments, A and B. The arrays declared in Code Segment A are used by the anisotropic shakedown module and the elements of these arrays need to have their values initialized as illustrated in Code Segment C contained in Table J8. The parameters and arrays declared in Code Segment B are either input values specified by the user or output values of the plastically relaxed stress components (output), σ_{ij}^{ep}, calculated by the shakedown module. As can be seen from the declared dimensions, the current version limits the maximum dimension of the user-defined linear elastic stress arrays to be 100 by 100, and the maximum dimension of the interpolated stress arrays to be 200 by 200.

Table J6. Listing of Computer Code Indicating How the Array Dimensions are Declared

```
c====================================================================
c   Parameter and arrays required to drive SHARP_AN (Anisotropic Version of SHARP)
c
        Implicit double precision (a-h,o-z)
        parameter (nso=100,nnx=200,nny=200,max_pt=nnx*nny)
c
c *** CODE SEGMENT A ***
c arrays used by the anisotropic shakedown module.  They are declared outside the module
c for initialization.  The initialization can be found in Code Segment C.
c
        dimension a1v(max_pt,6),sigvc(max_pt,6),sigv(max_pt,6),
     +          epsvc(max_pt,6),epsv(max_pt,6),sigev(max_pt,6),
     +          epsev(max_pt,6),erefv(max_pt)
        common/global_/a1v,sigvc,sigv,epsvc,epsv,sigev,epsev,erefv
c
c   *** CODE SEGMENT B ***
c
        common/RO_law/E_eff,alpha,beta,sigo,epso,tri_max,tri_min,iduck
        common/sig_out/ss11r(nso,nso),ss12r(nso,nso),ss13r(nso,nso),
     +          ss22r(nso,nso),ss23r(nso,nso),ss33r(nso,nso)
        common/ds_old/xo(nso),yo(nso),dsxx(nso,nso),dsxy(nso,nso),
     +          dsxz(nso,nso),dsyy(nso,nso),dsyz(nso,nso),dszz(nso,nso)
c====================================================================
```

Table J7. Descriptions for Parameters and Arrays Listed in Code Segment B

Parameter Name	Data Type	Status	Description
E_eff	Double precision	User-specified	Young's module
Alpha	Double precision	User-specified	Coefficient appearing in the plastic strain component of the Ramberg-Osgood stress-strain equation.
Beta	Double precision	User-specified	Exponent appearing in the plastic strain component of the Ramberg-Osgood stress-strain equation.
Sigo	Double precision	User-specified	Yield stress parameter appearing in the Ramberg-Osgood stress-strain equation.
Epso	Double precision	User-specified	Yield strain parameter appearing in the Ramberg-Osgood stress-strain equation where $epso=sigo/E\_eff$.
Xo	Double precision array	User-specified	One-dimensional array of size nso used to store the x-coordinates of the user-defined bivariant stress distribution. The values of x should be stored in the ascending order from the minimum value, x_{min}, to the maximum value, x_{max}. The array does not need to be fully populated with nso non-zero values. However, if there are only n_x values of x, the array elements indexed from (n_x+1) to nso should be filled with zeros.
Yo	Double precision array	User-specified	One-dimensional array of size nso used to store the y-coordinates of the user-defined bivariant stress distribution. The values of y should be stored in the ascending order from the minimum value, y_{min}, to the maximum value, y_{max}. The array does not need to be fully populated with nso non-zero values. However, if there are only n_y values of y, the array elements indexed from (n_y+1) to nso should be filled with zeros.
Dsxx	Double precision array	User-specified	Two-dimensional array of size $nso \times nso$ used to store values of the incremental linear elastic stress component, $\Delta\sigma_x$, of the bivariant stress field corresponding to position coordinates (x,y) contained in the arrays xo and yo. The array should contain $n_x \times n_y$ values, and the remaining elements should contain zero values.

Table J7 (continued). Descriptions for Parameters and Arrays Listed in Code Segment B

Parameter Name	Data Type	Status	Description
dsxy	Double precision array	User-specified	Two-dimensional array of size *nso×nso* used to store values of the incremental linear elastic stress component, $\Delta\sigma_{xy}$, of the bivariant stress field corresponding to position coordinates (x,y) contained in the arrays *xo* and *yo*. The array should contain $n_x \times n_y$ values, and the remaining elements should contain zero values.
dsxz	Double precision array	User-specified	Two-dimensional array of size *nso×nso* used to store values of the incremental linear elastic stress component, $\Delta\sigma_{xz}$, of the bivariant stress field corresponding to position coordinates (x,y) contained in the arrays *xo* and *yo*. The array should contain $n_x \times n_y$ values, and the remaining elements should contain zero values.
dsyy	Double precision array	User-specified	Two-dimensional array of size *nso×nso* used to store values of the incremental linear elastic stress component, $\Delta\sigma_{yy}$, of the bivariant stress field corresponding to position coordinates (x,y) contained in the arrays *xo* and *yo*. The array should contain $n_x \times n_y$ values, and the remaining elements should contain zero values.
dsyz	Double precision array	User-specified	Two-dimensional array of size *nso×nso* used to store values of the incremental linear elastic stress component, $\Delta\sigma_{yz}$, of the bivariant stress field corresponding to position coordinates (x,y) contained in the arrays *xo* and *yo*. The array should contain $n_x \times n_y$ values, and the remaining elements should contain zero values.
dszz	Double precision array	User-specified	Two-dimensional array of size *nso×nso* used to store values of the incremental linear elastic stress component, $\Delta\sigma_z$, of the bivariant stress field corresponding to position coordinates (x,y) contained in the arrays *xo* and *yo*. The array should contain $n_x \times n_y$ values, and the remaining elements should contain zero values.

Table J7 (continued). **Descriptions for Parameters and Arrays Listed in Code Segment B**

Parameter Name	Data Type	Status	Description
ss11r	Double precision array	Output	Two-dimensional array of size *nso×nso* used to store values of the plastically relaxed stress component, σ_x^{ep}, of the bivariant stress field corresponding to position coordinates (*x,y*) contained in the arrays *xo* and *yo*.
ss12r	Double precision array	Output	Two-dimensional array of size *nso×nso* used to store values of the plastically relaxed stress component, σ_{xy}^{ep}, of the bivariant stress field corresponding to position coordinates (*x,y*) contained in the arrays *xo* and *yo*.
ss13r	Double precision array	Output	Two-dimensional array of size *nso×nso* used to store values of the plastically relaxed stress component, σ_{xz}^{ep}, of the bivariant stress field corresponding to position coordinates (*x,y*) contained in the arrays *xo* and *yo*.
ss22r	Double precision array	Output	Two-dimensional array of size *nso×nso* used to store values of the plastically relaxed stress component, σ_y^{ep}, of the bivariant stress field corresponding to position coordinates (*x,y*) contained in the arrays *xo* and *yo*.
ss23r	Double precision array	Output	Two-dimensional array of size *nso×nso* used to store values of the plastically relaxed stress component, σ_{yz}^{ep}, of the bivariant stress field corresponding to position coordinates (*x,y*) contained in the arrays *xo* and *yo*.
ss33r	Double precision array	Output	Two-dimensional array of size *nso×nso* used to store values of the plastically relaxed stress component, σ_z^{ep}, of the bivariant stress field corresponding to position coordinates (*x,y*) contained in the arrays *xo* and *yo*.
tri_max, tri_min	Double precision	Declaration	Parameters allocated for SHARP_AN
iIduck	Integer	Declaration	Parameter allocated for SHARP_AN

The arrays declared in Code Segment A need to be initialized before the anisotropic shakedown module is called for the first time. The initialization should be placed outside of the loop that drives the incremental loading. A segment of code illustrating how to properly initialize the arrays declared in Code Segment A is listed in Table J8.

To specify the pseudo elastic-plastic stress and strain curve, the data pairs corresponding to the discrete points of stress and strain need to be defined. The curve should be specified outside of the incremental loading loop that calls SHARP_AN, as indicated in Code Segment D shown in Table J9. An example of such a routine in a form of FORTRAN SUBROUTINE is illustrated in Table J10. The routine reads the data pairs from a text file whose file unit is denoted by *iunit* and interprets the data whose plastic strains are within 1% to estimate the effective Young's modulus, *E_eff*, and Ramberg-Osgood parameters, *sigo*, *epso*, *alpha*, and *beta* (see Table J7).

The statement to drive the anisotropic shakedown routine is shown in Code Segment E of Table J9. There are six parameters in the argument list of the routine SHARP_AN. A description of each of the arguments can be found in Table J11. Note that since the linear elastic stress increments relative to the stress state at the previous step are used in the calculations for the elastic-plastic stress increments for the current step, a segment of code may be needed to assign the incremental stress values to these stress arrays from global stress arrays that may contain all the linear elastic stress results for every load step.

A non-zero error code generated by the anisotropic shakedown module indicates an error is detected in the module. A sample subroutine is provided to show what the various error codes represent. The listing of these error descriptions is displayed in Table J12.

Table J8. Segment of Computer Code Illustrating How to Initialize the Arrays Declared in Code Segment A

```
c===================================================================
======
c  *** CODE SEGMENT C ***: Initializing the arrays declared in Code Segment A
c
        do i=1,max_pt
          erefv(i)=0.
          do j=1,6
              a1v(i,j)=0.
              sigvc(i,j)=0.
              sigv(i,j)=0.
              epsvc(i,j)=0.
              epsv(i,j)=0.
              sigev(i,j)=0.
              epsev(i,j)=0.
          End do
        End do
c===================================================================
======
```

Table J9. Segment of Computer Code Showing How to Call SwRI's Anisotropic Shakedown Module

```
c=====================================================================
c ***CODE SEGMENT D ***
c  User needs to provide a segment of code to define the pseudo
c  stress-strain curve
c
        call pseudo_curve(inunit)
c
c  before calling the anisotropic shakedown module, set kinit=0
c
kinit=0
c
c=====================================================================
c  *** CODE SEGMENT E *** : Computing loop starts from here
c
do istep=1,nstep
c
c   User needs to provide a segment of code here to read the linear elastic stress increment
          **** CODE FOR THE INPUT OF STRESS INCREMENT ****
c
    print '(a,i3)','---  Processing Step ',istep
     call SHARP_AN(kinit,istep,iopt,ierr,dtt,temp)
end do
c=====================================================================
```

Table J10.   A Sample Subroutine Used to Estimate the Ramberg-Osgood Parameters Based on the Provided Pseudo Stress/Strain Curve

```
c==================================================
      subroutine pseudo_curve(iunit)
      implicit none
      integer iunit,ndat,nfit,iduck,i,i1,i2
      double precision se_mono,ee_mono,smono,emono,
     +        E_eff,alpha,beta,sigo,epso,tri_max,tri_min,a,b,
     +        a11,a12,a21,a22,c1,c2,det,ep,pp1,pp2
      common/RO_law/E_eff,alpha,beta,sigo,epso,tri_max,tri_min,
     +        iduck
      common/mono_se_curve/se_mono(150),ee_mono(150),ndat
*
*   read the pseudo- stress/strain curve
*
      ndat=0
11    read(iunit,*,end=12) smono,emono
      ndat=ndat+1
      se_mono(ndat)=smono
      ee_mono(ndat)=emono
      goto 11
12    continue
      E_eff=(se_mono(2)-se_mono(1))/(ee_mono(2)-ee_mono(1))
      do 13 i=1,ndat-1
        i1=i
        i2=i1+1
        pp1=ee_mono(i1)-se_mono(i1)/E_eff
        pp2=ee_mono(i2)-se_mono(i2)/E_eff
        if(pp1.le.0.002.and.pp2.ge.0.002) then
          sigo=(se_mono(i2)-se_mono(i1))/(pp2-pp1)*(0.002-pp1)+
     +       se_mono(i1)
          goto 14
        endif
13    continue
14    epso=sigo/E_eff
*
*   determine the beta factor by selecting plastic strain less than 1%
*
      nfit=0
      a11=0.

      a12=0.
      a21=0.
      a22=0.
      c1=0.
      c2=0.
      do 100 i=1,ndat
        ep=ee_mono(i)-se_mono(i)/E_eff
        if(ep.gt.0.and.ep.le.0.01) then
          nfit=nfit+1
          a12=a12+dlog10(ep)
          a21=a21+dlog10(ep)
          a22=a22+dlog10(ep)**2
          c1=c1+dlog10(se_mono(i))
          c2=c2+dlog10(se_mono(i))*dlog10(ep)
        endif
100   continue
      if(nfit.eq.0) stop '[ERROR.pseudo]: no data within [0,1%]!'
      a11=nfit
*
*   assume y=a+b*x
*
      det=a11*a22-a12*a21
      a=(a22*c1-a12*c2)/det
      b=(-a21*c1+a11*c2)/det
      beta=1./b
      alpha=sigo**beta/epso*10.**(-a*beta)
      return
      end
```

Table J11.   Parameters and Arrays Passed Through the Argument List of the Anisotropic Shakedown Module

SUBROUTINE SHARP_AN(*kinit, istep, iopt, ierr, dtt, temp*)			
Parameter Name	**Data Type**	**Status**	**Description**
Kinit	Integer	User-specified Initially	Set to zero (0) initially for SHKDN_3D_HCF to generate *x*- and *y*-coordinates constituting a finer mesh. After the first increment, it is automatically reset to one (1) within SHKDN_3D_HCF.
Istep	Integer	User-specified	Current load increment number
Iopt	Integer	Dummy	Hard-coded to check the force and moments balance
Ierr	Integer	Output	Error code (see Table C.4.7)
Dtt	Double precision	User-specified	Time increment associated with the stress and strain increment
Temp	Double precision	User-specified	Operating temperature

Table J12. Sample Error Code Handler

```
c======================================================================
    subroutine errmsg(ierr)
    if(ierr.eq.0) return
    open(23,file='error.msg')
    if(ierr.eq.1) then
      write(23,101)
    elseif(ierr.eq.2) then
      write(23,102)
    elseif(ierr.eq.3) then
      write(23,103)
    elseif(ierr.eq.4) then
      write(23,104)
    elseif(ierr.eq.5) then
      write(23,105)
    elseif(ierr.eq.7) then
      write(23,107)
    elseif(ierr.eq.8) then
      write(23,108)
    endif
    close(23)
101  format('[ERROR]: too few data points to generate a new bi-',/,
    +      '         variant stress array! At least 2 by 2 required')
102  format('[ERROR]: the values of the x-coordinate array are not',/,
    +      '         in ascending order!')
103  format('[ERROR]: the values of the y-coordinate array are not',/,
    +      '         in ascending order!')
104  format('[ERROR]: reach the max. declared array size. Increase',/,
    +      '         the value of nbmax in the parameter statement!')
105  format('[ERROR]: reach max. number of iterations (13)!')
107  format('[ERROR]: no single root found when searching for the',/,
    +      '         equivalent stress using Neuber rule!')
108  format('[ERROR]: iterations exceeded when searching for the',/,
    +      '         equivalent stress using Neuber rule!')
    return
    end
c======================================================================
```

J.5   VERIFICATION OF P&W's ANSYS USER MATERIAL ROUTINES

A modified version of the ANSYS user material subroutines provided by P&W was used to validate the anisotropic shakedown methodology. The modified version corrected incompatibility problems between the received version and the current version of ANSYS that led to overwriting the state variables used internally by ANSYS. The modified ANSYS user material routines implement a constitutive model for the anisotropic material PWA 1484 developed by Walker for P&W. This routine was linked with ANSYS to create a linked-by-licensee version that facilitated finite element stress analysis based on the Walker material model. The modules consist of a user routine (USERPL) for interfacing the Walker anisotropic constitutive model of PWA 1484 with ANSYS, and a software module (HYPELA) that is called by USERPL to implement the anisotropic constitutive relationship for PWA 1484. The following summarizes the major activities associated with the verification of P&W's ANSYS user material routines as part of the development of SwRI's anisotropic shakedown module:

J.5.1   Derivation of Simple Analytical Stress Solutions for the Verification of Linked-by-Licensee FEA

Two analytical one-dimensional stress solutions, denoted as Simple Tension Model (STM) and Simple Shear Model (SSM), were derived using Walker's material model assuming that the axis of the structure was parallel to the <001> crystallographic plane. The derived solutions were used to benchmark results from finite element analysis. The two solutions are in incremental form and require several iterations to converge.

The STM solution represents a tensile bar with square cross-section subjected to a displacement-controlled loading in its longitudinal direction. Under the assumption that the material responses to such a loading are identical throughout the whole specimen, the following conditions prevail:

$$\sigma_1 = \sigma \neq 0, \sigma_2 = \sigma_3 = \sigma_{12} = \sigma_{13} = \sigma_{23} = 0$$

$$\Delta\varepsilon_1^p \neq 0, \Delta\varepsilon_2^p = \Delta\varepsilon_3^p = -\frac{1}{2}\Delta\varepsilon_1^p, \text{ and } \Delta\varepsilon_{12}^p = \Delta\varepsilon_{13}^p = \Delta\varepsilon_{23}^p = 0 \qquad (J23)$$

where σ_{ij} denote the stress components, ε_{ij} are the strain components, and Δ is used to represent an incremental change in the variable. The superscript p signifies the plastic

component of strain. The subscripts 1, 2, and 3 stand for the stressing direction; i.e., σ_1 stands for the normal stress applied to the surface perpendicular to the loading direction.

Such a simple loading condition leads to further simplification of the differential equations employed in Walker's constitutive model. The deviatoric stresses and the location of the center of the plasticity surface become

$$S_{11} = \frac{2}{3}\sigma, S_{22} = S_{33} = -\frac{1}{3}\sigma, S_{12} = S_{23} = S_{13} = 0$$

$$\Omega_{11} = \frac{2}{3}\Omega, \Omega_{22} = \Omega_{33} = -\frac{1}{3}\Omega, \Omega_{12} = \Omega_{23} = \Omega_{13} = 0 \qquad (J24)$$

where Ω represents the unit-directional change of the center of the plasticity surface in the regular stress domain in contrast to Ω_{ij} in the deviatoric space. The plastic strain increment derived from Equation (J4) is given by

$$\Delta\varepsilon_{11}^{plastic} = \left\langle \frac{\left| \sigma - \Omega \right| \sqrt{M_{11} - M_{12}} - \kappa}{K} \right\rangle^{n} \cdot \sqrt{M_{11} - M_{12}} \cdot sign(\sigma - \Omega) \cdot \Delta t \qquad (J25)$$

and $\Delta\varepsilon_{22}^{plastic} = \Delta\varepsilon_{33}^{plastic} = -\frac{1}{2}\Delta\varepsilon_{11}^{plastic}$ due to the incompressibility. The change of the center of plasticity surface is given by Equation (J6) and becomes

$$\Delta\Omega_{11} = \frac{2}{3}(N_{11} - N_{12})\Delta\varepsilon_{11}^{plastic} - (Q_{11} - Q_{12})\Omega_{11}\Delta R$$

(J26)

with $\Delta R = \left\langle \dfrac{\left| \sigma - \Omega \right| \sqrt{M_{11} - M_{12}} - \kappa}{K} \right\rangle^{n} \cdot \Delta t$. Expanding the differential equation (J3) leads to a system of equations for $\Delta\sigma_{11}$, $\Delta\varepsilon_{22}$, and $\Delta\varepsilon_{33}$. The equations are given by

$$\begin{bmatrix} 1 & -D_{12} & -D_{12} \\ 0 & -D_{11} & -D_{12} \\ 0 & -D_{12} & -D_{11} \end{bmatrix} \cdot \begin{Bmatrix} \Delta\sigma_{11} \\ \Delta\varepsilon_{22} \\ \Delta\varepsilon_{33} \end{Bmatrix} = \begin{Bmatrix} D_{11}\Delta\varepsilon_{11} + (D_{12} - D_{11})\Delta\varepsilon_{11}^{plastic} \\ D_{12}\Delta\varepsilon_{11} + (D_{12} - D_{11})\Delta\varepsilon_{22}^{plastic} \\ D_{12}\Delta\varepsilon_{11} + (D_{12} - D_{11})\Delta\varepsilon_{33}^{plastic} \end{Bmatrix} \qquad (J27)$$

The STM solution can be determined by integration over time using the above system of equations in which D_{ig} denote the elements of the elastic stiffness matrix defined in Equation. (J3).

The SSM solution represents a torsion bar with circular cross-section subjected to a shear displacement linearly varying from the center of the circular cross-section to the exterior surface. In this condition, all normal stress and strain components are zero. Assuming that only shear stress and strain components denoted by τ and γ, respectively, are induced in the bar, then the following conditions prevail:

$$\sigma_{31} = \tau \neq 0, \sigma_1 = \sigma_2 = \sigma_3 = \sigma_{12} = \sigma_{23} = 0$$

$$\Delta\varepsilon_{31} = \Delta\gamma \neq 0, \Delta\varepsilon_1 = \Delta\varepsilon_2 = \Delta\varepsilon_3 = \Delta\varepsilon_{12} = \Delta\varepsilon_{23} = 0 \tag{J28}$$

Further simplification based on this one-dimensional model reduces the variables to

$$S_{ij} = 0, \text{ except } S_{13} = \sigma_{13} = \tau \neq 0$$

$$\Omega_{ij} = 0, \text{ except } \Omega_{13} = \Omega \neq 0 \tag{J29}$$

The only non-zero plastic strain component is given by [see Equation (J4)]

$$\Delta\varepsilon_{13}^{plastic} = \frac{3}{2}\left\langle \frac{\sqrt{3M_{44}} \cdot |\tau - \Omega| - \kappa}{K} \right\rangle^n \cdot \sqrt{\frac{M_{44}}{3}} \cdot sign(\tau - \Omega) \tag{J30}$$

and the change of the center of the plasticity surface becomes

$$\Delta\Omega_{13} = \frac{2}{3} N_{44} \Delta\varepsilon_{12}^{plastic} - Q_{44}\Omega_{13}\Delta R$$

where $\Delta R = \left\langle \dfrac{\sqrt{3M_{44}} \cdot |\tau - \Omega| - \kappa}{K} \right\rangle^n$. The shear stress can be determined by integration over the time domain using the simplified equation (J6) for this one-dimensional model reduces to

$$\Delta\sigma_{13} = D_{44}\left(\Delta\varepsilon_{13} - \Delta\varepsilon_{13}^{plastic}\right) \tag{J32}$$

The stress response can thus be determined through step-by-step integration over time. Note that the strain increments are provided by the user with the corresponding time increments.

J-33

J.5.2   Verification for User Material Routines for ANSYS against Analytically-Derived Solutions

The validation of the enhanced USERPL was performed against the one-dimensional STM and SSM solutions.   The material constitutive relationship was specified according to the corrected P&W routine, HYPELA, at a uniform temperature of 1400°F.

Figure J3 shows the finite element modeling used to simulate the STM. The tensile bar has a 1"×1" square cross-section with a length 5". One end of it was fixed and free to expand or contract in the *xy*-plane. The other end was subjected to a displacement-controlled loading. Three applied strain rates were employed over time steps of 30 sec, 300 sec, and 3000 sec, respectively, such that at the end of the loading the final elongation was always δ_z=0.25 inch, which corresponds to a final strain ε_z=0.05 in/in.

Figure J4 presents the comparison of the STM results with the finite element results and shows that the FEA results predicted using USERPL and HYPELA are in exact agreement with the STM analytical solutions. The results also demonstrate that at 1400°F there is a significant effect of strain rate on the stress-strain relationship. Also given in the figure (solid line) are the FEA results calculated assuming a temperature of 1100°F. At this temperature, which is typical of the blade attachment area, the stress-strain relationship is independent of the applied strain rate.

A finite-element model of the SSM is shown in Figure J5 where the cylindrical bar has a radius of 1" and is 5" long. The applied torsion is displacement-controlled and is applied over time intervals of 30 sec, 300 sec, and 3000 sec, respectively, at loading rates that result in a final angular rotation of 0.25 radian at one end of the bar. The other end of the bar is rigidly fixed.

Figure J6 shows the comparison of the SSM solutions with the finite element results. The agreement between the two sets of results is excellent.
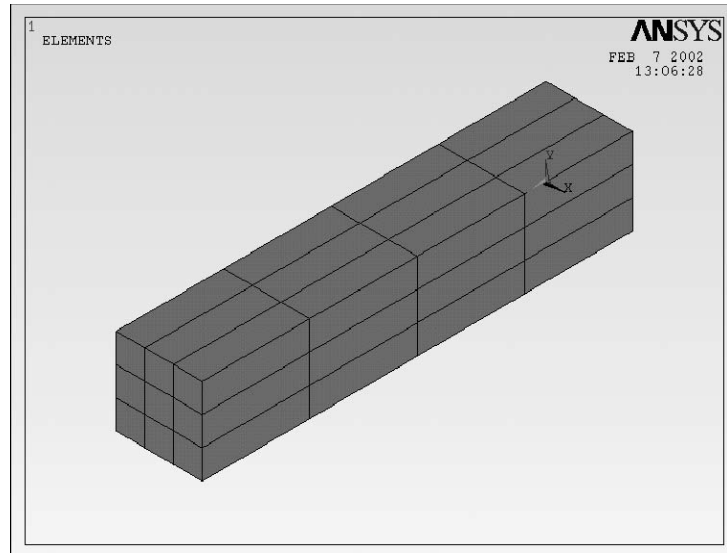
Figure J3. One-dimensional finite element modeling used to validate the P&W user routines linked with ANSYS by licensee; Simple Tension Model.
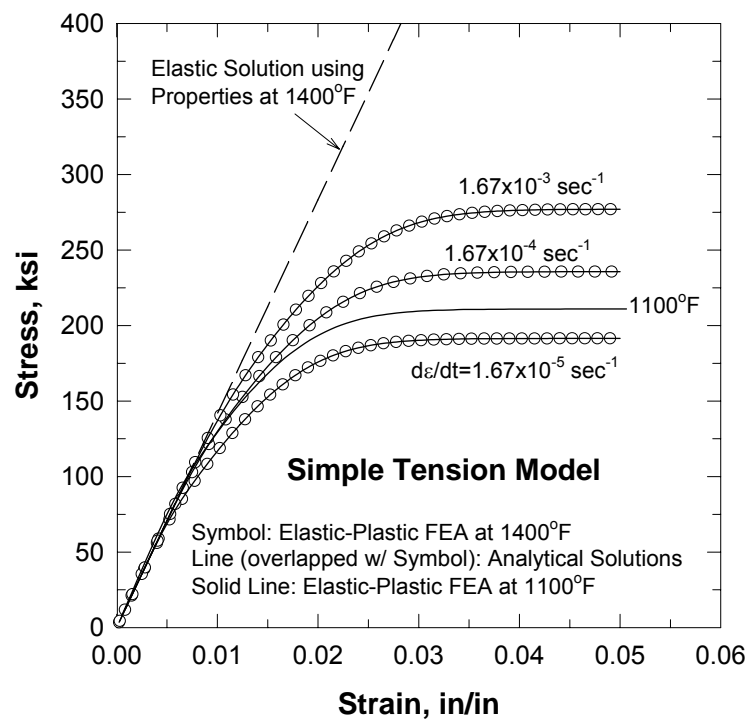
Figure J4. Comparison between the STM analytical solutions and the FEA results using a linked-by-licensee version of ANSYS.
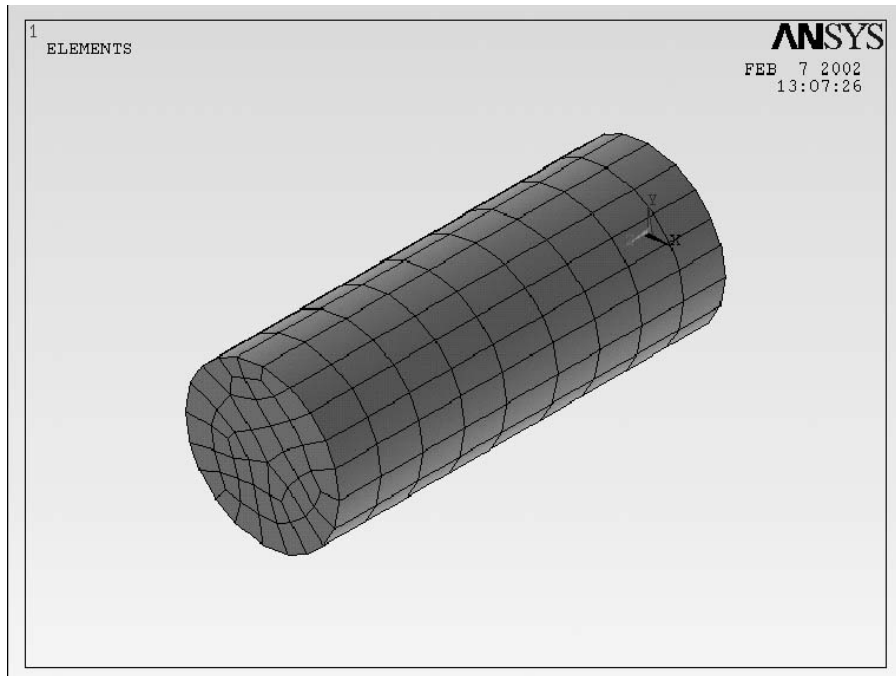
Figure J5. One-dimensional finite-element modeling used to validate the P&W user routines linked with ANSYS by licensee; Pure Shear Model.
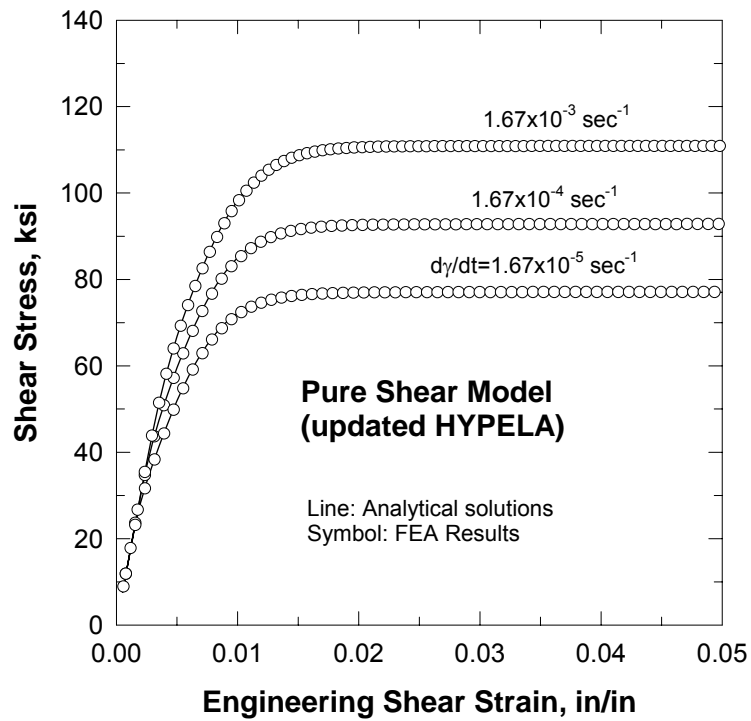
Figure J6. Comparison between the SSM solutions and the FEA results using a linked-by-licensee version of ANSYS.

J.6   VERIFICATION OF THE ANISOTROPIC SHAKEDOWN MODULE AGAINST FINITE ELEMENT RESULTS

Three-dimensional elastic-plastic finite element analyses were performed to validate the anisotropic shakedown methodology. The anisotropic shakedown module used as input bivariant stress fields derived from three dimensional anisotropic linear elastic finite element computations employing ANSYS. The elastic finite element results were obtained based on the anisotropic linear elastic relationship derived from the Walker's constitutive model. In the finite element elastic analyses, the USERPL and HYPELA provided by P&W were modified so that only the elastic stiffness matrix instead of the instantaneous tangential matrix was passed back to ANSYS.

The validation was performed for a single edge notched plate of width (*W*) equal to 10 inches, thickness (*t*) equal to 5 inches, and height (*h*) equal to 20 inches, containing a semi-circular through-thickness notch with a radius (*r*) equal to 1 inch (see Figure J1). This plate was subjected to various combinations of tensile load and out-of-plane bending moment, as illustrated in Figure J1. The combinations of loads used in the validation analyses are listed in Table J13. Two sets of computations were performed. In one, the axis of the plate was assumed parallel to the <001> direction, while in the other the axis was assumed parallel to the <111> direction. The local and global coordinate systems are identical for the specimens whose axes are parallel to the <001> direction. The nonlinear material behavior used for the anisotropic shakedown module is the one at 1100°F that was included in Figure J4. At this temperature, the effect of strain rate is minimal. The comparison between the predicted results by the shakedown module and the FEA results for a variety of load combinations can be found in Figures J7 to J11. Figure numbers associated with specific load combinations and crystallographic planes can be found in Table J13.

Each figure shows the comparison of predicted results by SwRI's anisotropic shakedown module with FEA results for different planes parallel to the free surfaces through the plate thickness. For symmetrical loading conditions and the <001> direction, only results on three planes are plotted. The locations of these planes are *y/r*=0. (at the free surface), *y/r*=1.237 (a plane one quarter of the way through the plate), and *y/r*=2.5 (the mid-plane). For loading parallel to the <111> direction, results are also given on the two additional planes corresponding to *y/r*=3.763 (about three-quarters of the way through the plate) and *y/r*=5 (the other free surface).

The results obtained by applying the anisotropic shakedown module developed by SwRI are, as in the case of the isotropic shakedown module, SHARP, in excellent agreement with the FEA results obtained using the link-by-licensee version of ANSYS with Walker's constitutive model, except for the through-thickness (out-of-plane) component of stress, σ_y. The reason that this stress component is not estimated as accurately as it is by the isotropic module is the fact that the out-of-plane friability corrections that were developed in that case were not implemented in the anisotropic module. The main reason for this is that evaluation of these corrections for isotropic materials involved performing finite element computations for materials with a range of strain hardening capabilities by varying the exponent in the Ramberg-Osgood equation to simulate low and high strain hardening capacities. This option was not available for anisotropic material studied in the present work because the material strain hardening response for this material is embodied in the Walker constitutive relationship and is dictated by material constants that are propriety to P&W. In addition, whereas strain hardening capacity is easily changed in a Ramberg-Osgood equation by changing the exponent, it is not clear which parameters in the Walker constitutive model influence strain hardening and whether these parameters could be readily characterized by a one parameter term equivalent to the Ramberg-Osgood exponent.

The deficiency of the simple point relaxation is also apparent from the results shown in Figures J7 to J11. However, the deficiency is not as great as that observed under some circumstances in the development of the isotropic shakedown module. The reason is that the anisotropic material investigated herein displays significant strain hardening capability, as illustrated by the stress-strain curve for 1100°F shown in Figure J4. The major discrepancies between the point relaxation model predictions and the finite-element results observed in the isotropic case occurred for materials like Ti-6Al-4V that exhibited little strain hardening capability (high Ramberg-Osgood exponents). As strain hardening capability increases, the Ramberg-Osgood exponent decreases, and the changes between linear elastic and elastic-plastic results becomes less significant. (In the limit of the Ramberg-Osgood exponent becoming one, the material behaves in a linear elastic manner.) Thus, materials with a high strain hardening capability result in less load redistribution for a given applied load than do materials with low hardening. This means that the point relaxation model will become more accurate with increasing strain hardening, as borne out by the present results.

Table J13. Load Combinations Used in the Verification of SwRI's Anisotropic Shakedown Module

Orientation of Specimen Axis	Load Case	Applied Loads		Figure No. Showing the Comparison of the Distributions of Three Normal Stress Components
		S_z (ksi)	M_x (kip-in)	
<001>	A	105	0	Figure J7
	B	110	0	Figure J8
<111>	A	105	0	Figure J9
	B	110	0	Figure J10
	C	66	112.5	Figure J11
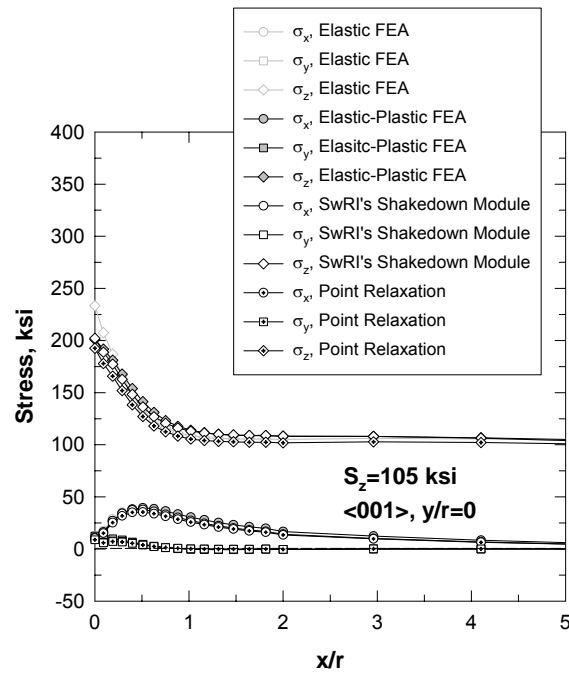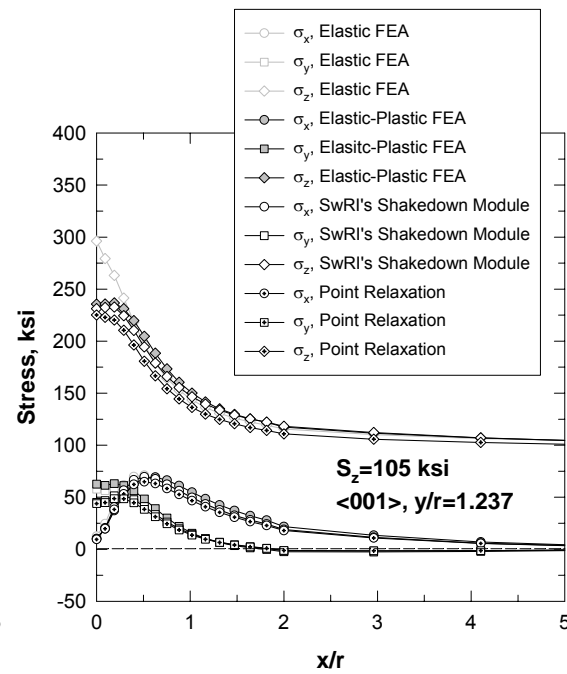
Figure J7(a)   Figure J7(b)   Figure J7(c)
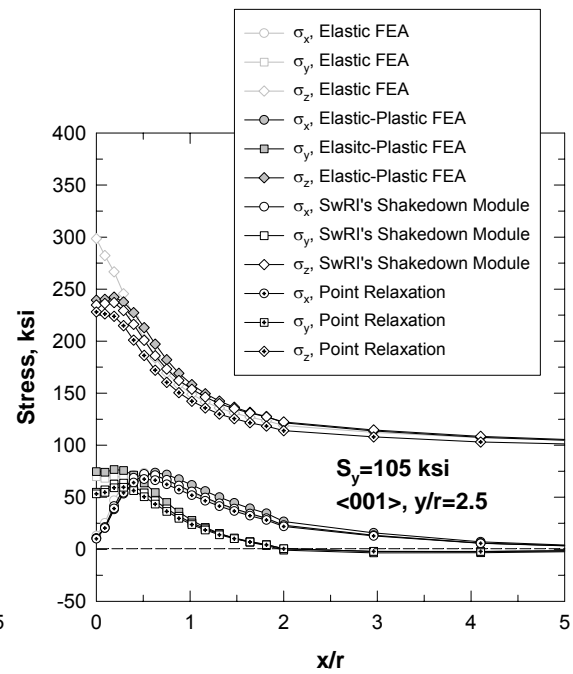
Figure J7.   Comparison of stress components predicted by SwRI's anisotropic shakedown module with the results obtained from FEA. The results computed from point relaxation are also included to show the effects of load shedding and re-distribution. The notched plate is subjected to S_z=105 ksi, and the axis of the plate is parallel to the <001> direction. Results in Figure J7(a) are for y/r=0 (the free surface at the side of the plate), J7(b) are for y/r=1.237 (a plane one quarter of the way through the plate), and J7(c) are for y/r=2.5 (at the mid-plane).
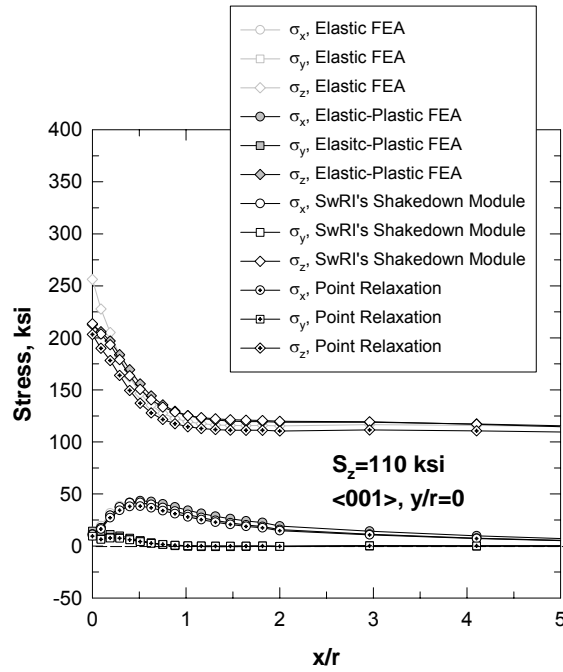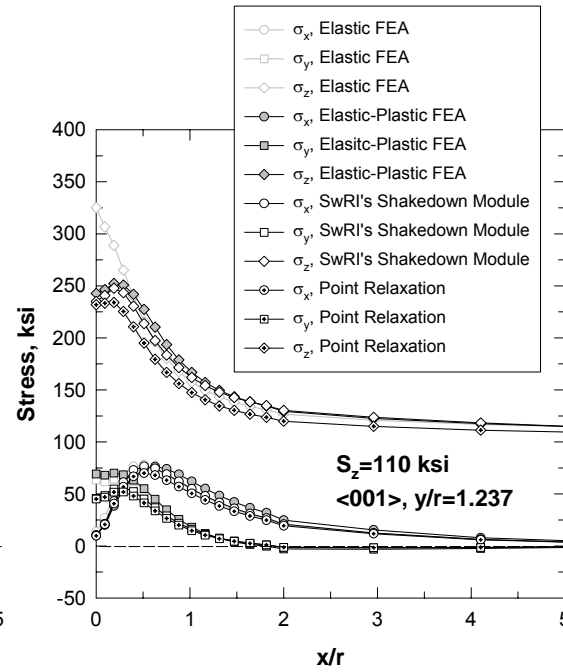
Figure J8(a)   Figure J8(b)   Figure J8(c)
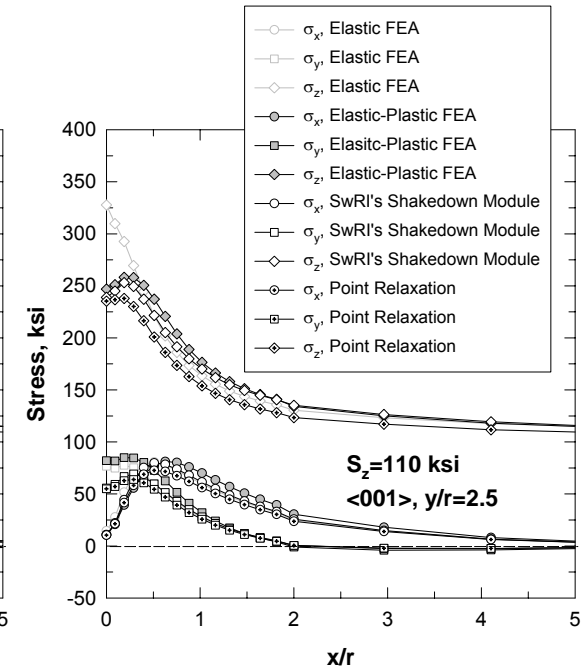
Figure J8.   Comparison of stress components predicted by SwRI's anisotropic shakedown module with the results obtained from FEA. The results computed from point relaxation are also included to show the effects of load shedding and re-distribution. The notched plate is subjected to S_z=110 ksi, and the axis of the plate is parallel to the <001> direction. Results in Figure J8(a) are for y/r=0 (the free surface at the side of the plate), J8(b) are for y/r=1.237 (a plane one quarter of the way through the plate), and J8(c) are for y/r=2.5 (at the mid-plane).
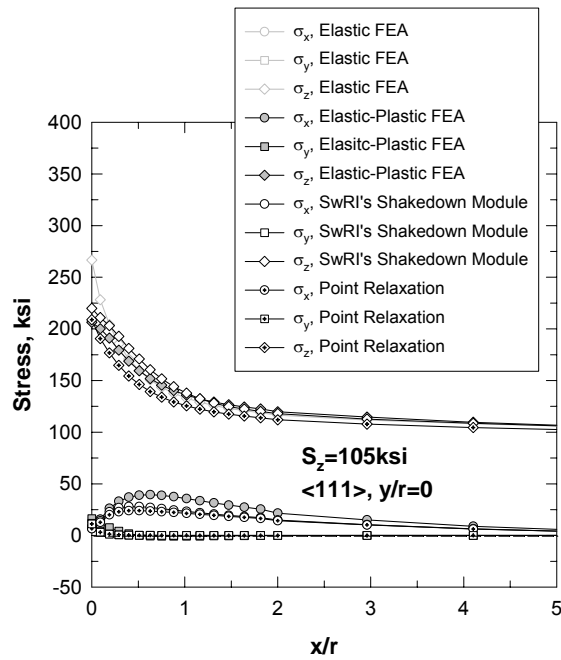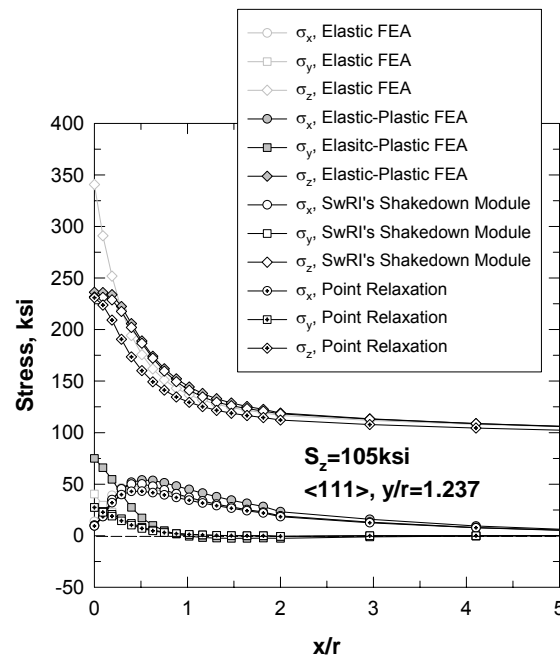
Figure J9(a)　　　　　　　　Figure J9(b)　　　　　　　　Figure J9(c)
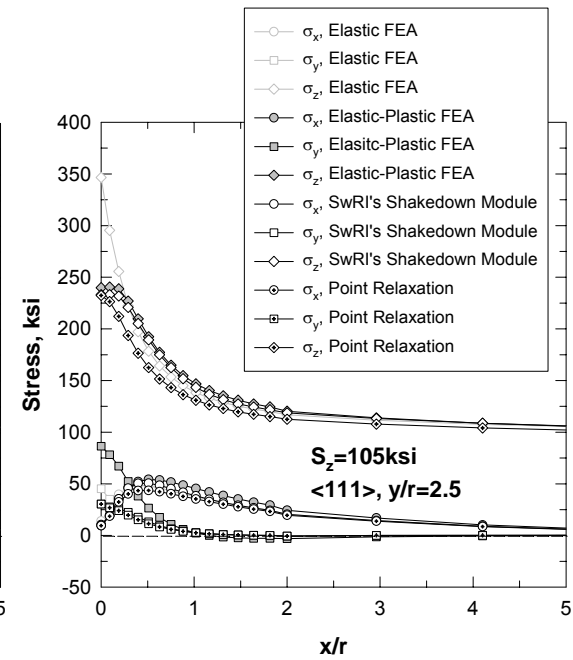
Figure J9.　　　Comparison of stress components predicted by SwRI's anisotropic shakedown module with the results obtained from FEA. The results computed from point relaxation are also included to show the effects of load shedding and re-distribution. The notched plate is subjected to S_z=105 ksi, and the axis of the plate is parallel to the <111> direction. Results in Figure J9(a) are for y/r=0 (the free surface at the side of the plate), J9(b) are for y/r=1.237 (a plane one quarter of the way through the plate), and J9(c) are for y/r=2.5 (at the mid-plane).
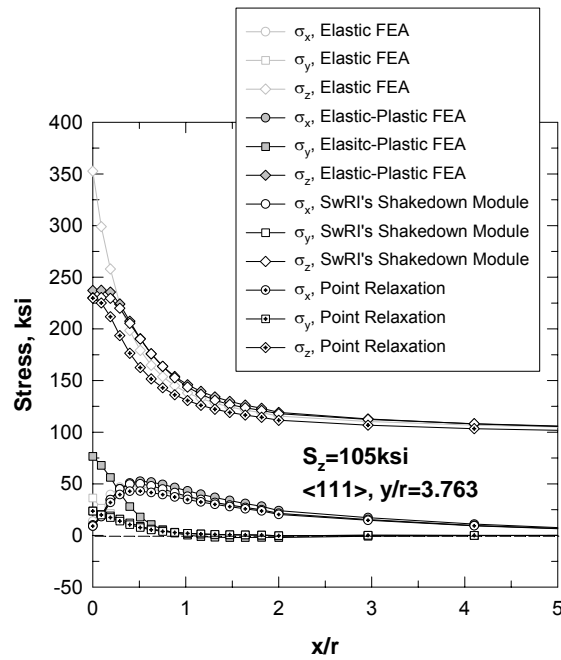
Figure J9(d)
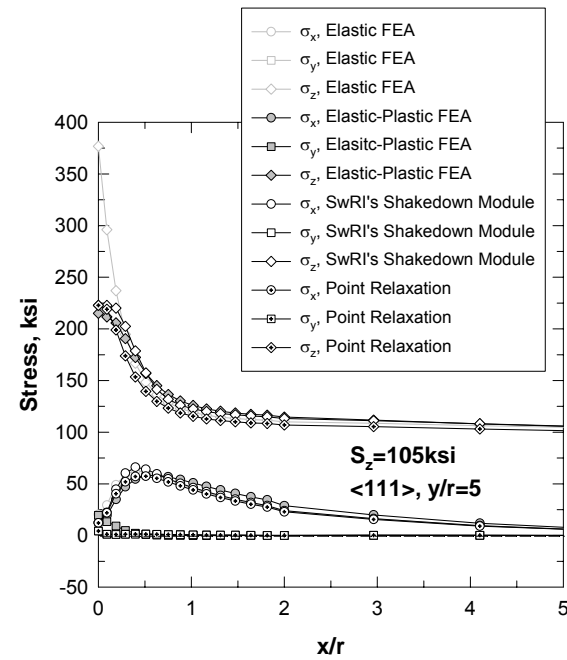
Figure J9(e)

Figure J9.   (continued) Comparison of stress components predicted by SwRI's anisotropic shakedown module with the results obtained from FEA. The results computed from point relaxation are also included to show the effects of load shedding and re-distribution. The notched plate is subjected to S_z=105 ksi, and the axis of the plate is parallel to the <111> direction. Results in Figure J9(d) are for y/r=3.763 (a plane about three quarters of the way through the plate), and J9(e) are for y/r=5.0 (at the other free surface).
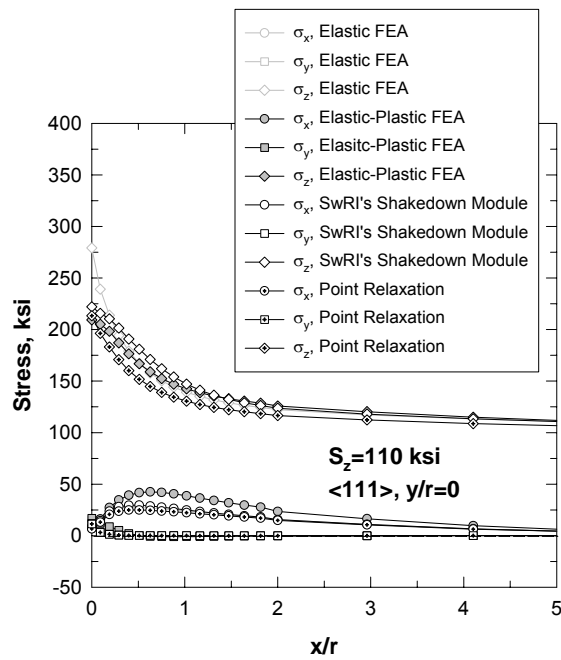
Figure J10(a)
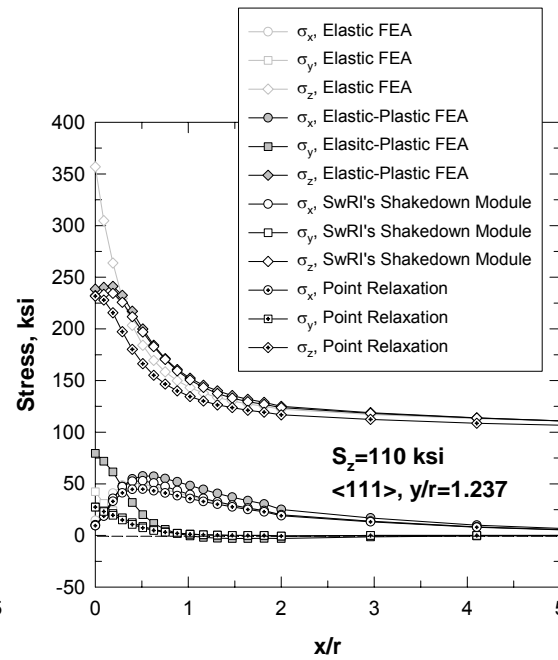
Figure J10(b)
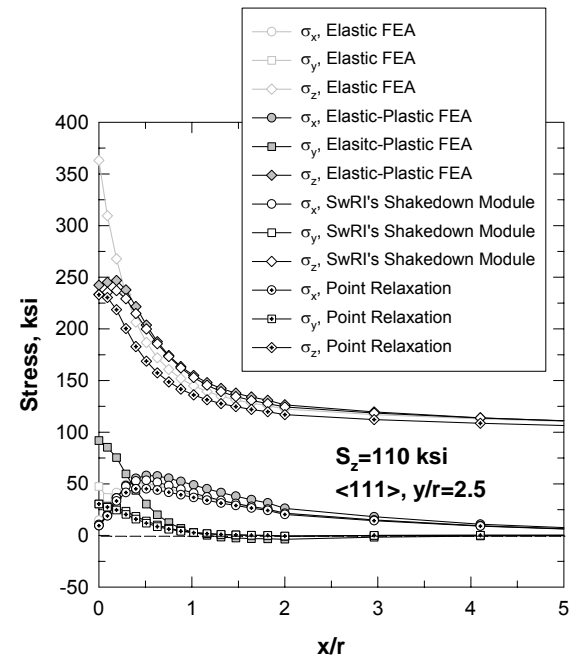
Figure J10(c)

Figure J10.   Comparison of stress components predicted by SwRI's anisotropic shakedown module with the results obtained from FEA. The results computed from point relaxation are also included to show the effects of load shedding and redistribution. The notched plate is subjected to S_z=110 ksi, and the axis of the plate is parallel to the <111> direction. Results in Figure J10(a) are for y/r=0 (the free surface at the side of the plate), J10(b) are for y/r=1.237 (a plane one quarter of the way through the plate), and J10(c) are for y/r=2.5 (at the mid-plane).
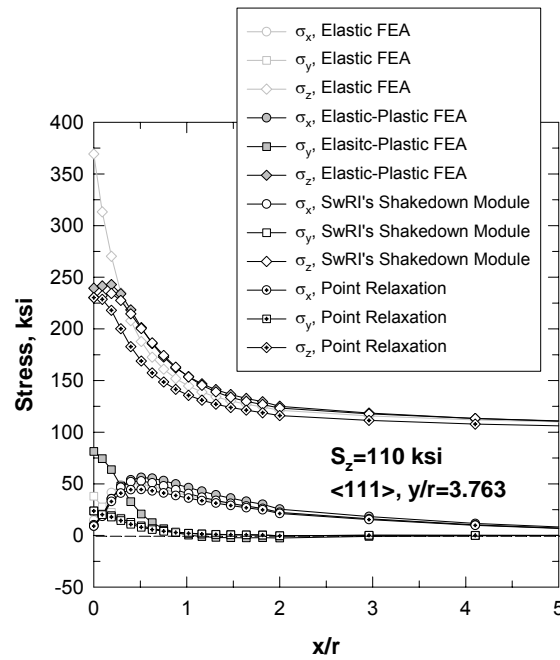
Figure J10(d)
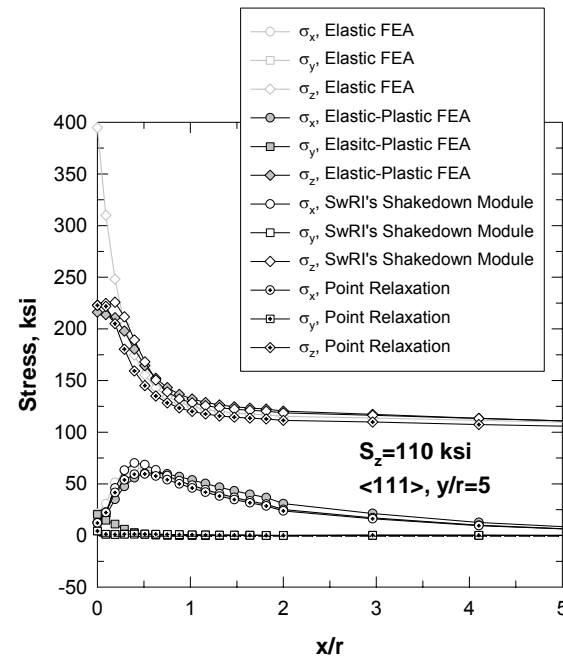
Figure J10(e)

Figure J10. (continued) Comparison of stress components predicted by SwRI's anisotropic shakedown module with the results obtained from FEA. The results computed from point relaxation are also included to show the effects of load shedding and re-distribution. The notched plate is subjected to S_z=110 ksi, and the axis of the plate is parallel to the <111> direction. Results in Figure J10(d) are for y/r=3.763 (a plane about three quarters of the way through the plate), and J10(e) are for y/r=5.0 (at the other free surface).
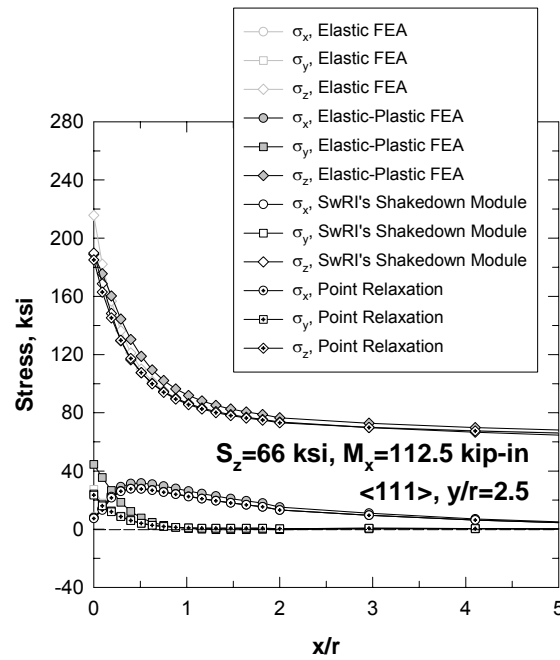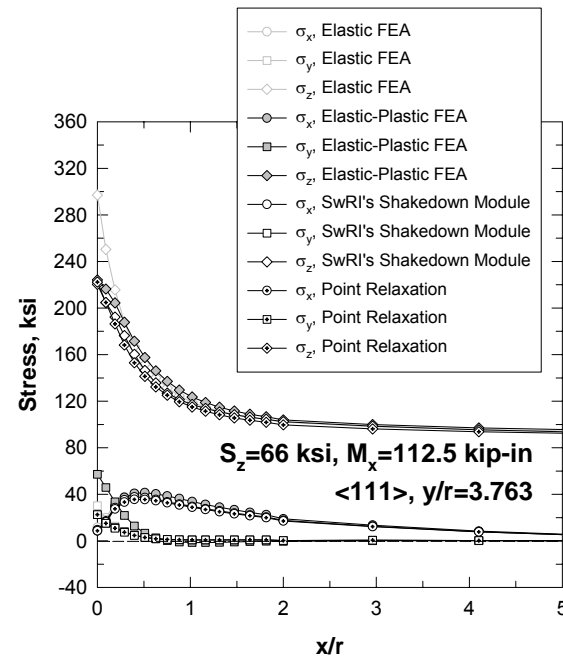
Figure J11(a)   Figure J11(b)

Figure J11.   Comparison of stress components predicted by SwRI's anisotropic shakedown module with the results obtained from
                FEA. The results computed from point relaxation are also included to show the effects of load shedding and re-
                distribution. The notched plate is subjected to S_z=66 ksi and M_x=112.5 kip-in, and the axis of the plate is parallel to
                the <111> direction. Results in Figure J11(a) are for y/r=2.5 (at the mid-plane) and J11(b) are for y/r=3.763 (a plane
                about three quarters of the way through the plate).
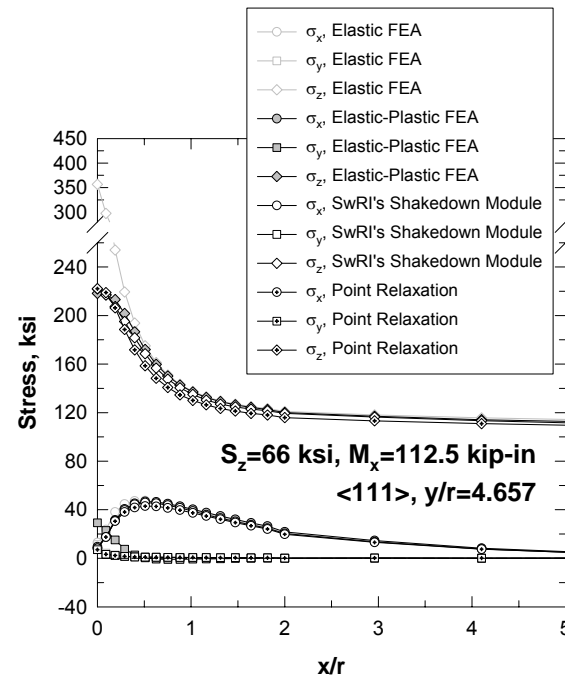
Figure J11(c)
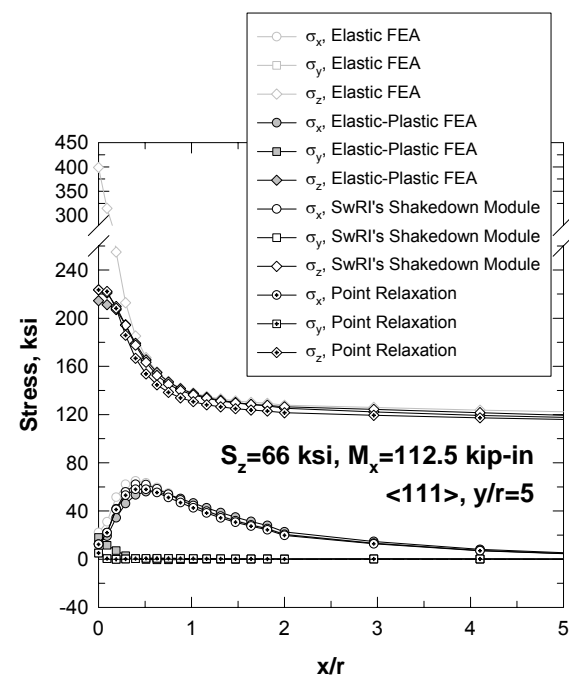
Figure J11(d)

Figure J11.   (continued) Comparison of stress components predicted by SwRI's anisotropic shakedown module with the results obtained from FEA. The results computed from point relaxation are also included to show the effects of load shedding and re-distribution. The notched plate is subjected to S_z=66 ksi and M_x=112.5 kip-in, and the axis of the plate is parallel to the <111> direction. Results in Figure J11(c) are for y/r=4.657 (a plane about one-eight of the way through the plate from the other free surface), and J11(d) are for y/r=5.0 (at the other free surface).

APPENDIX K

ENHANCEMENT OF THE WORST CASE NOTCH (WCN) MODEL TO INCLUDE THREE-DIMENSIONAL CRACK GROWTH AND NOTCH PLASTICITY

Recent fracture mechanics analyses of sharp notches based on the so-called worst case notch (WCN) model have demonstrated the HCF threshold cyclic stresses for sharp notch-like features are no longer simply given by the smooth specimen endurance limit ($\Delta\sigma_e$) divided by k_t [1]. In order to predict threshold behavior, it is necessary to include the local stress gradient in the modeling, and to take account of the crack growth behavior of initiated cracks. The WCN approach [2-3] is based on predicting whether initiated microcracks will propagate to failure or arrest within the notch stress field.

K.1   WCN MODEL

The WCN approach assumes that cracks can initiate relatively early in the life of a component containing a notch-like feature, such as FOD. As illustrated in Figure K1, the method enables the boundaries between crack initiation, crack growth followed by arrest, and crack growth to failure to be defined. The classical S-N approach for a notch with stress concentration factor, k_t, predicts that crack initiation occurs at a remotely applied threshold cyclic stress $\Delta S_{th}(R_{local})$ given by

$$\Delta S_{th}(R_{local}) = \frac{\Delta\sigma_e(R_{local})}{k_t} \tag{K1}$$

where $\Delta\sigma_e$ is the smooth bar endurance limit, $R_{local} = \dfrac{S_{min}^{local}}{S_{max}^{local}}$ is the local stress ratio

determined at the notch tip, and S_{min}^{local} and S_{max}^{local} are the local notch-tip stresses at maximum and minimum load corresponding to the remotely applied stresses S_{min}^{remote} and S_{max}^{remote}, respectively. In the absence of notch plasticity and residual stresses at the notch, $S_{min}^{remote} = S_{min}^{local}/k_t$ and $S_{max}^{remote} = S_{max}^{local}/k_t$.
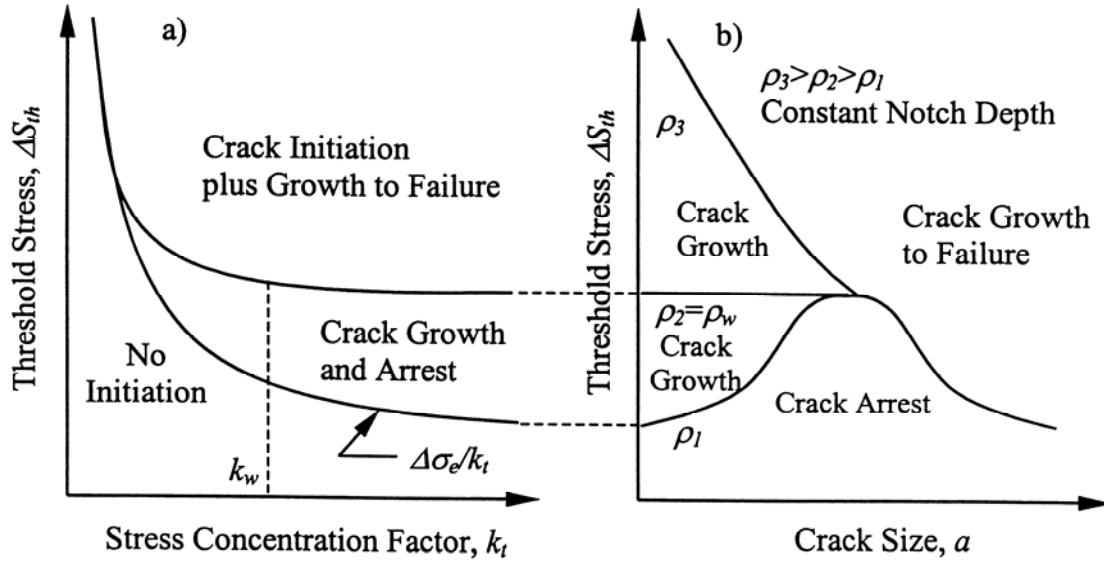
Figure K1. Schematic representation of the Worst Case Notch (WCN) concept.

The growth/arrest boundary in Figure K1 is determined by equating the effective applied cyclic stress intensity factor (ΔK_{eff}) to the threshold cyclic stress intensity factor for fatigue crack propagation (ΔK_{th}). The effective stress intensity factor (SIF) is related to the total range SIF, ΔK, corrected for stress ratio effects.

In the WCN approach, ΔK_{th} is modified for the behavior of small fatigue cracks through the introduction of a crack-size dependence. This means that for a three-dimensional crack (e.g., a semi-elliptical surface flaw), ΔS_{th}, is not only a function of the notch geometry (notch depth, b, root radius, ρ), R, and material variables, but also of the crack depth, a, its surface length, $2c=l$, and two so-called small crack parameters, a_o and c_o associated with the deepest and surface points on the crack. In the case of two-dimensional cracks (e.g. through-thickness flaws) only one small crack parameter, a_o, is needed to apply the WCN model and its definition is unambiguous. However, for three-dimensional cracks, there are several possible ways of defining a_o and c_o within the WCN crack growth model. The approach adopted herein is to define a_o and c_o so that the resulting 3-D WCN model predictions are consistent with the following:

(a)   The threshold cyclic stress range for crack initiation is equal to the value predicted by the classical *S-N* approach;

(b)   At the instant of crack initiation, the initiated crack has the same cyclic crack tip driving forces at the deepest and surface points;

(c)   At notches with very high stress concentrations, the predicted values of the threshold cyclic stresses that would just propagate an initiated crack to failure are independent of the stress concentration factor, consistent with the WCN predictions for 2-D cracks;

(d)   In the limit that an initiated crack is specified to have an aspect ratio *a/c=0* the 3-D WCN model becomes identical to the original 2-D WCN model.

In the 2-D WCN model, the parameter a_o appears in the definition of a small crack cyclic threshold SIF. In order to satisfy the foregoing conditions (a) through (d), the parameters a_o and c_o that appear in the 3-D WCN model are introduced into the definition of two crack-size-dependent, small-crack cyclic threshold SIFs, $\Delta K_{th,a}^{sc}$ and $\Delta K_{th,c}^{sc}$, which are defined through the equations:

$$\Delta K_{th,a}^{sc}\left(a,a_o,R_i\right) = \Delta K_{th}\left[\frac{a}{a+a_o\left(R_i\right)}\right]^{1/2} \tag{K2a}$$

$$\Delta K_{th,c}^{sc}\left(a,c,,c_o,R_i\right) = \Delta K_{th}\left[\frac{a}{a+c_o\left(R_i\right)}\right]\left[\frac{c+c_o\left(R_i\right)}{c}\right]^{1/2} \tag{K2b}$$

In these equations, the subscript *i* signifies that the stress ratio, *R*, is that corresponding to the initiation of cracking, whereas *R* corresponds to the instantaneous value of the ratio, K_{min}/K_{max}, determined for a propagating crack. The subscripts *a* and *c* signify the crack-tip positions corresponding to the deepest and surface points on the crack front, respectively.

The form of Equation (K2) is dictated by the condition that equation (K1) is recovered as the initiated crack goes to zero size (*a→0, c→0*) so that the crack initiation

endurance at a notch with stress concentration factor, k_t goes to a value given by the classical *S*-N approach as $\Delta\sigma_e/k_t$.

Explicit expressions for the parameters a_o and c_o can be derived from the following equations that govern the conditions for crack propagation in the 3-D WCN model in the limit of a vanishing small crack $(a \rightarrow 0, c \rightarrow 0)$,

$$\Delta K_{eff,a}(a,c,\Delta\sigma_e(R_i),k_t) = \Delta K_{th,a}^{sc}(a,a_o,R_i)$$
$$\Delta K_{eff,c}(a,c,\Delta\sigma_e(R_i),k_t) = \Delta K_{th,c}^{sc}(a,c,c_o,R_i)$$

(K3)

by writing

$$\Delta K_{eff,a} = (\pi a)^{1/2} \frac{\Delta\sigma_e(R_i)}{k_t} F_a(a,c,k_t) f_R(R_i)$$

$$\Delta K_{eff,c} = (\pi a)^{1/2} \sqrt{\frac{a}{c}} \frac{\Delta\sigma_e(R_i)}{k_t} F_c(a,c,k_t) f_R(R_i)$$

(K4)

where F_a and F_c are combined shape and free surface magnification factors that also take account of the stress gradient at the notch, and f_R is a function that incorporates the effects of stress ratio. From Equations (K3), (K4) and (K2)

$$a_o(a/c,R_i) = \frac{1}{\pi} \left[\frac{k_t \Delta K_{th}}{\Delta\sigma_e(R_i) F_a(a \rightarrow 0, c \rightarrow 0, a/c = \text{constant}, k_t) f_R(R_i)} \right]^2$$

$$c_o(a/c,R_i) = \frac{1}{\pi} \left[\frac{k_t \Delta K_{th}}{\Delta\sigma_e(R_i) F_c(a \rightarrow 0, c \rightarrow 0, a/c = \text{constant}, k_t) f_R(R_i)} \right]^2$$

(K5)

Note that a_o and c_o depend on the assumed aspect ratio of a vanishing small initiated crack through the dependence of the functions F_a and F_c on aspect ratio. As the crack size goes to zero, then the stress gradient at a notch is no longer important and F_a and F_c can be written as:

$$F_a(a \rightarrow 0, c \rightarrow 0, k_t) = k_t f_a(a \rightarrow 0, c \rightarrow 0)$$
$$F_c(a \rightarrow 0, c \rightarrow 0, k_t) = k_t f_c(a \rightarrow 0, c \rightarrow 0)$$

and Equation (K5) becomes

K-4

$$a_o(a/c, R_i) = \frac{1}{\pi} \left[\frac{\Delta K_{th}}{\Delta \sigma_e(R_i) f_a(a \to 0, c \to 0, a/c = \text{constant}) f_R(R_i)} \right]^2$$

$$c_o(a/c, R_i) = \frac{1}{\pi} \left[\frac{\Delta K_{th}}{\Delta \sigma_e(R_i) f_c(a \to 0, c \to 0, a/c = \text{constant}) f_R(R_i)} \right]^2$$

(K6)

It is clear from this equation, that a_o and c_o are independent of notch geometry.

The terms f_a and f_c represent the magnification factors for surface cracks emanating from planar surfaces. Typical values for f_a and f_c for thumbnail (three-dimensional) and through-thickness (two-dimensional) cracks are given in Table K.1, these values bound the likely aspect ratios of initiated cracks. Note also that a_o and c_o will have different values because of the different values of f_a and f_c due to surface interaction effects.

Table K1. **Example Values for the Functions f_a and f_c for Thumbnail and Through-Thickness Cracks, and Typical Values for a_o and c_o for Ti-6-4**

Thumbnail				Through-thickness a/c=0			
f_a	f_c	a_o (mils)	c_o (mils)	f_a	f_c	a_o (mils)	c_o (mils)
1.04(2/π)	1.22(2/π)	3.16	2.65	1.12	---	1.10	---

K.2   DETERMINING THRESHOLD STRESSES USING THE WCN MODEL

In the case of cracks that have a single degree of freedom (e.g. $a/c=0$), then, as demonstrated in [1], the WCN model can be applied without explicitly performing fatigue crack growth calculations. However, for the two degree of freedom cracks addressed in the present work on 3-D WCN modeling, the crack arrest/propagation behavior of initiated cracks can only be predicted by performing explicit crack growth evaluations to identify the values of ΔS_{th} that result in growth leading to arrest, and growth leading to failure. These computations are performed as described below, where it is assumed that a static residual stress may be present from shakedown following first application of the maximum load.

(1)   Determine the value of ΔS_{th} at the initiation of crack growth. This is straightforward if there are no residual stresses at the notch tip. In this case,

$$\Delta S_{th}(R_{local}) = \frac{\Delta \sigma_e(R_{local})}{k_t}, \quad R_{local} = \frac{S_{min}^{local}}{S_{max}^{local}} = R_{remote} = \frac{S_{min}^{remote}}{S_{max}^{remote}}$$

The subscript *remote* signifies quantities based on the remote loading conditions.

If the local notch-tip stress conditions result in yielding, then R_{local} and R_{remote} are no longer equal. In this case it is necessary to perform an elastic-plastic shakedown analysis to obtain the stress state at the notch tip from which R_{local} can be determined. If $\sigma(x=0)$ represents the stress at a notch tip normal to the plane containing an initiated crack obtained from a shakedown analysis, then

$$S_{max}^{local} = \sigma, \; S_{min}^{local} = \sigma - k_t \Delta S^{remote}, \; \Delta S^{remote} = S_{max}^{remote} - S_{min}^{remote} \quad,$$

In this equation, it is assumed that shakedown occurred at the notch tip from stress relaxation due to plasticity at the first application of the maximum remote load. This assumption implies that further deformation changes at the notch due to load cycling remain elastic.

Assuming that R_{remote} remains constant during cycling, then the value of ΔS_{th} corresponding to crack initiation can be derived by iteration as follows. First, as an initial guess set $R_{local} = R_{remote}$, then

(a)   Evaluate $\Delta S^{remote} = \dfrac{\Delta \sigma_e(R_{local})}{k_t}$ and hence $S_{max}^{remote} = \dfrac{\Delta S^{remote}}{(1 - R_{global})}$ and

$S_{max}^{local} = k_t S_{max}^{remote}$;

(b)   Apply an elastic-plastic stress analysis to determine the maximum local notch stress $\sigma(x)$ after shakedown and the residual stress field $\sigma_{residual}(x)$ at the notch due to shakedown, where

$$\sigma_{residual}(x) = \sigma(x) - \sigma_{notch}(S_{max}^{remote}, x, \rho, k_t).$$

In this equation, $\sigma_{notch}(S_{max}^{remote}, x, \rho, k_t)$ is the elastically calculated stress field at the notch at maximum load.

(c)   Re-evaluate $R_{local} = \dfrac{\sigma(x=0) - k_t \Delta S^{remote}}{\sigma(x=0)}$ and return to step (a) until R_{local}

differs insignificantly from its previous value.

(2)   Set $R_i=R_{local}$ and determine a_o and c_0 using equation (K6) for an assumed initial

aspect ratio, a/c, and calculate $\Delta S_{th}^{initiation}(R_i) = \dfrac{\Delta \sigma_e(R_i)}{k_t}$

(3)   Incrementally increase the value of the remote threshold cyclic stress range, ΔS_{th} ,

from a starting value of $\Delta S_{th}^{initiation}(R_i)$, and at each step perform a shakedown

analysis to obtain the new value of the plastically relaxed stress, $\sigma(x)$ (from which

the value of R_{local} and $\sigma_{residual}(x)$ can be determined).

(4)   Perform a fatigue crack growth calculation using the small crack threshold SIFs

given by Equation (K2) and an effective applied cyclic SIF that takes appropriate

account of stress ratio effects and any shakedown residual stress as the crack

propagates. The effective cyclic SIF is given by

$$\Delta K_{eff,a} = (\pi a)^{1/2} \Delta S_{th} F_a(a,c,k_t) f_R(R_a)$$

$$\Delta K_{eff,c} = (\pi a)^{1/2} \sqrt{\frac{a}{c}} \Delta S_{th} F_c(a,c,k_t) f_R(R_c)$$

The instantaneous stress ratios R_a and R_c during propagation are defined by the

equations

$$R_a = \frac{K_a(a,c,\sigma) - K_a(a,c,\sigma_{residual})}{K_a(a,c,\sigma)}, R_c = \frac{K_c(a,c,\sigma) - K_c(a,c,\sigma_{residual})}{K_c(a,c,\sigma)} \quad (K7)$$

Note that during the crack growth calculations, the following conditions can arise

$\Delta K_{eff,a} \geq \Delta K_{th,a}^{sc}, \quad \Delta K_{eff,c} \geq \Delta K_{th,c}^{sc}$: crack growth occurs at crack tips a and c

$\Delta K_{eff,a} \geq \Delta K_{th,a}^{sc}, \quad \Delta K_{eff,c} < \Delta K_{th,c}^{sc}$: crack growth occurs at tip a, arrest at tip c

$\Delta K_{eff,a} < \Delta K_{th,a}^{sc}, \quad \Delta K_{eff,c} \geq \Delta K_{th,c}^{sc}$: crack growth occurs at tip c, arrest at tip a

$\Delta K_{eff,a} < \Delta K_{th,a}^{sc}, \quad \Delta K_{eff,c} < \Delta K_{th,c}^{sc}$: crack arrest occurs at tips a and tip c

(5)   Observe in the calculations the value, $\Delta S_{th}^{failure}$, when propagation to failure is first observed. Then:

Crack initiation is predicted when : $\Delta S_{th} = \Delta S_{th}^{initiation}$

Crack propagation leading to arrest is predicted when : $\Delta S_{th}^{initiation} < \Delta S_{th} < \Delta S_{th}^{failure}$

Crack propagation to failure is predicted when : $\Delta S_{th} \geq \Delta S_{th}^{failure}$

K.3   2-D WCN MODEL

It is informative to compare the explicit crack growth approach developed for 3-D cracks to the methodology applied for 2-D through-thickness cracks. In the latter case, an explicit crack growth calculation is not required in the absence of residual stresses and the crack arrest/propagation condition can be determined from the equation:

$$\Delta S_{th}(a) = \frac{\Delta K_{th}}{\left(\pi(a+a_o)\right)^{1/2} F_a(a,c,k_t) f_R(R_i)} \tag{K8}$$

by seeking the maximum value of $\Delta S_{th}(a)$ as the crack depth increases from zero where $\Delta S_{th} = \Delta S_{th}^{initiation}$. This maximum value is equal to $\Delta S_{th}^{failure}$. For notches that are shallow but have k_t values greater than k_w, where

$$k_w = \left(1 + \frac{0.122}{\left(1+\left(\frac{a_o}{b}\right)^{1/4}\right)^{5/2}}\right)\left(1+2\left(\frac{b}{a_o}\right)^{1.4}\right) \tag{K9}$$

then it was shown previously [1] that $\Delta S_{th}^{failure}$ can be approximately determined from the equation

$$\Delta S_{th}^{failure}(k_t > k_w) = \Delta S_{th}^{saturation} = \frac{f_R(R_i)\Delta K_{th}}{1.12(\pi)^{1/2}\left(\sqrt{a_o} + \sqrt{b}\right)} \tag{K10}$$

where b is the depth of the notch. Note that the value of $\Delta S_{th}^{failure}$ predicted by this equation is independent of k_t. This means that for notches or FOD that satisfy the condition $k_t > k_w$ the 2-

D WCN model predicts saturation threshold cyclic stresses, $\Delta S_{th}^{saturation}$ that have a value that varies only with the notch or FOD depth, b.

K.4   ASPECTS OF FATIGUE CRACK GROWTH AND THE WCN MODEL

K.4.1   Notch Stresses

The following approximate expressions for determining the linear elastic stress field at notches derived from the work of Amstutz and Seeger [4] have been described and validated in [1]. The stress concentration factors for surface notches that are typical of FOD and have root radii ρ are given by the equation

$$k_t = 1 + \frac{0.122}{\left(1+\sqrt{\dfrac{\rho}{b}}\right)^{\frac{5}{2}}} \left[\frac{A(0)}{A(b)} + \frac{2K(b)}{1.122\sigma_{remote}\sqrt{\pi\rho}}\right] \tag{K11}$$

where $A(b)$ is the load bearing area for a notch of depth b, and $A(0)$ is the load bearing area in the absence of a notch (b=0)..

The stress field at a distance x from a notch tip is approximately given by the expression

$$\sigma_{notch}\left(\sigma_{remote},\frac{x}{\rho},k_t\right) = \sigma_{remote}\left[1 + \frac{k_t-1}{\left(1+\Phi x/\rho\right)^{\psi}}\right] \tag{K12}$$

where

$$\psi = \frac{1}{\Phi}\frac{2k_t+1}{k_t-1}$$

$$\Phi = 0.226 + 0.394(k_t-1)^{3.0457}, 1 < k_t < 2$$

$$\Phi = 3.226 - \frac{2.706}{(k_t-0.9224)^{0.5018}}, 2 < k_t < 50$$

K.4.2   Shakedown Residual Stresses

To allow for shakedown, an approximate elastic-plastic stress analysis is needed that can be used at every incremental increase in applied cyclic stress range to determine the local notch-tip stress state. The methodology used here was based on the shakedown module included in the computer code, DARWIN^{TM} developed previously by SwRI [5]. Alternatively, one could use the shakedown analysis developed in the current program (see Appendix A). (However, the shakedown analysis in Appendix A was not available when the current WCN analysis was developed.) The DARWIN^{TM} shakedown module is applicable to uniaxially varying stress fields. It includes the effects of multi-axial stressing due to the three principal stresses but not the influence of shear stresses. The latter are considered to have insignificant effects on the plastic relaxation of stress fields at notches due to applied remote tension loading. The shakedown module requires as input the elastic stress field ahead of a notch. This was derived using the method of Amstutz and Seeger, as described in the Section B.4.1. The Amstutz and Seeger equations only predict the stress component, σ_z, normal to the plane containing the notch. The other two principal stress components, σ_y and σ_x used in the shakedown analysis were obtained from the following equations based on the plane strain stress fields ahead of a round hole subject to tension loading:

$$\sigma_x = \sigma_z \left[\frac{\sigma_x^{hole}}{\sigma_z^{hole}} \right] \quad , \quad \sigma_y = \nu(\sigma_z + \sigma_x) \tag{K13a}$$

$$\frac{\sigma_x^{hole}}{\sigma_z^{hole}} = \frac{1.5\left(\rho/(\rho + x)^2\right)\left(1 - \rho/(\rho + x)^2\right)}{0.5\left(2 + \rho/(\rho + x)^2 + 3\rho/(\rho + x)^4\right)} \tag{K13b}$$

where x is the distance from the notch tip, and ν is Poisson's ratio. A Ramberg-Osgood equation containing constants applicable to Ti-6-4 was used to describe the uniaxial stress-strain behavior. Typical results of a shakedown analysis based on this methodology are presented in Figure K2.
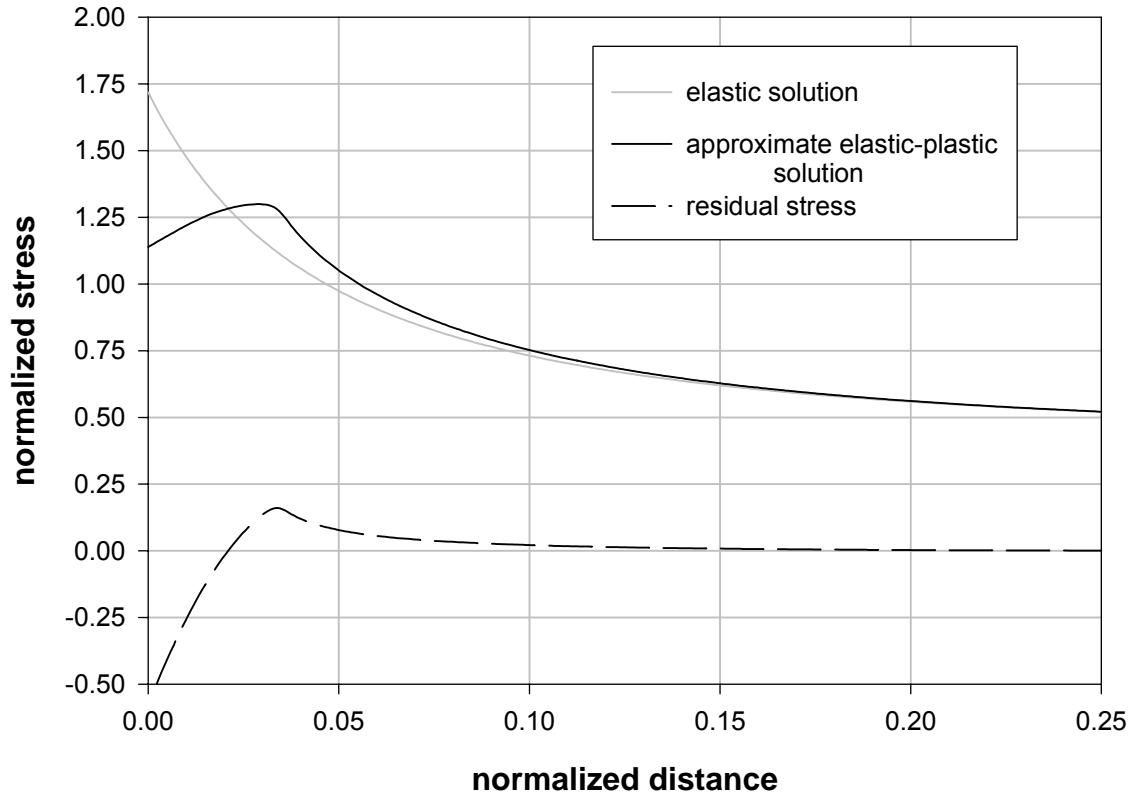
Figure K2.   Example results obtained from applying the shakedown module from DARWIN^{TM} to predicting the residual stress at a notch tip due to stress relaxation and re-distribution from plastic deformation.

K.4.3   Stress Intensity Factors

The steep stress gradients associated with sharp notches and residual stress fields at notches that have undergone shakedown mean that SIF's for cracks at these notches have to be determined using the weight function (WF) method. The WFs used in the present work are a combination of the WFs derived in Reference 1 for through-thickness cracks, and the WFs for surface cracks in plates contained in NASGRO [6]. If the WFs for the *a* and *c* locations on surface cracks are denoted as $W_a(x,a/c,a/\rho,\rho/b)$ and $W_c(x,a/c,a/\rho,\rho/b)$, then the corresponding SIFs for surface cracks at notches subjected to an arbitrary univariant stress can be written as

$$K_a\left(a, \frac{a}{c}, \frac{a}{\rho}, \frac{\rho}{b}\right) = \int_0^a W_a\left(x, \frac{a}{c}, \frac{a}{\rho}, \frac{\rho}{b}\right)\sigma_{arbitrary}(x)dx \qquad \text{(K14a)}$$

$$K_c\left(a, \frac{a}{c}, \frac{a}{\rho}, \frac{\rho}{b}\right) = \int_0^a W_c\left(x, \frac{a}{c}, \frac{a}{\rho}, \frac{\rho}{b}\right)\sigma_{arbitrary}(x)dx \qquad \text{(K14b)}$$

In the current studies, $\sigma_{arbitrary}$ is equal to the elastic notch stress field given by Equation (K12), the shakedown stress field corresponding to the maximum load, $\sigma(x)$, or the shakedown residual stress, $\sigma_{residual}(x)$.

K.4.4 Fatigue Crack Growth

To implement the WCN model described above it is necessary to specify a fatigue crack growth equation. In the present work, the following equation was employed:

$$\frac{da}{dN} = A\left(\frac{\Delta K_{eff}}{\Delta K_{th}^{sc}}\right)^p \left[\ln\left(\frac{\Delta K_{eff}}{\Delta K_{th}^{sc}}\right)\right]^q \left[\ln\left(\frac{K_{crit}}{K_{max}}\right)\right]^d \qquad \text{(K15)}$$

where K_{crit} is the fracture toughness and K_{max} the SIF at maximum load. This general equation covers crack growth behavior from fatigue initiation at threshold through to failure from the onset of static failure modes. In the case of surface cracks, crack growth and crack shape evolution are governed by the fatigue crack propagation rates at the deepest and surface points. Thus, once crack growth was predicted to initiate at a notch, the aspect ratio of the growing crack can change, and arrest could be occur at one crack tip position while growth continued at the other. However, use of Equation (K6) guarantees that crack initiation occurs at both crack tip positions simultaneously.

The predicted lifetime of a notch containing an initiated crack is not calculated in the WCN analysis, as the parameter of interest is $\Delta S_{th}^{failure}$. However, it is necessary to specify an initial crack size and crack shape for the start of the fatigue crack growth calculations. The size chosen for the depth of the initial crack was $a=1\times10^{-8}b$, with half the surface length set equal to

K-12

this value divided by the assumed initial aspect ratio (a/c) of the flaw. Although the choice of initial flaw size effects the lifetime, the value chosen was small enough not to change the calculated value of $\Delta S_{th}^{failure}$.

A method of refining and coarsening the time step used in the crack growth integration scheme was employed in order to reduce computation time. The ability to automatically coarsen an integration step was important since the majority of the computation time is taken in determining the growth of very small cracks. The accuracy of the crack growth integration procedure was maintained by automatically refining the integration step as the crack size increased. This was necessary because the crack propagation rate per cycle increased as the crack size increased, and errors in the integration routine would have accumulated without step refinement because of the coupled nature of the growth at the deepest and surface points on the crack.

K.5   WCN MODEL PREDICTIONS

K.5.1   Saturation Threshold Cyclic Stress

When applied to a 2-D crack problem (a crack with one degree of freedom), the 2-D WCN model predicts a saturation threshold cyclic stress that becomes independent of k_t for a constant notch depth, b, and decreasing notch radius, ρ, consistent with the predictions of Equation (K10). The 3-D WCN model developed herein also predicts this kind of threshold behavior when a/c is set to zero to simulate a through-thickness crack. The results of an analysis illustrating this point are shown in Figure K3. In this figure, the cyclic threshold stress is normalized by the saturation threshold value obtained for a notch with a high k_t. The value of this saturation cyclic threshold stress obtained from explicit crack growth calculations was found to be equal to the saturation value, $\Delta S_{th}^{saturation}$, predicted by Equation (K10).

K.5.2   Effect of Shakedown on Threshold Behavior

Two sets of results are shown in Figure K3. One corresponds to the case where the notch conditions are assumed to remain elastic, and the other to the case where shakedown is allowed to occur. The threshold values determined for the two cases are not equal at the

initiation of cracking for k_t greater than eight, and the two sets of values differ slightly at the saturated threshold stress, $\Delta S_{th}^{saturation}$, corresponding to failure at high k_t values. The reason for this can be seen from the plot of the local stress ratio that is also presented on the figure. At the higher cyclic stresses needed to initiate and propagate cracks to failure, shakedown has occurred at the notch tip and changed the local stress ratio at initiation so that it is no longer simply related to the remote stress ratio, specified as being 0.5 in this example. Indeed, at high k_t values, the local stress ratio becomes negative. Although these negative stress ratios will increase the threshold cyclic stress needed to initiate cracking, they clearly do not significantly influence the threshold needed to cause propagation to failure. This is a consequence of the fact that the residual stress field due to shakedown is still localized at the notch tip, and cracks can readily propagate to depths where the localized residual stress has little influence on the cyclic SIF. Threshold cyclic stresses that fall between the initiation and failure envelopes shown in Figure K3 will initiate cracks either on the initiation envelope, or at cyclic stress values above this envelope if shakedown occurs, but these cracks are predicted to eventually arrest.
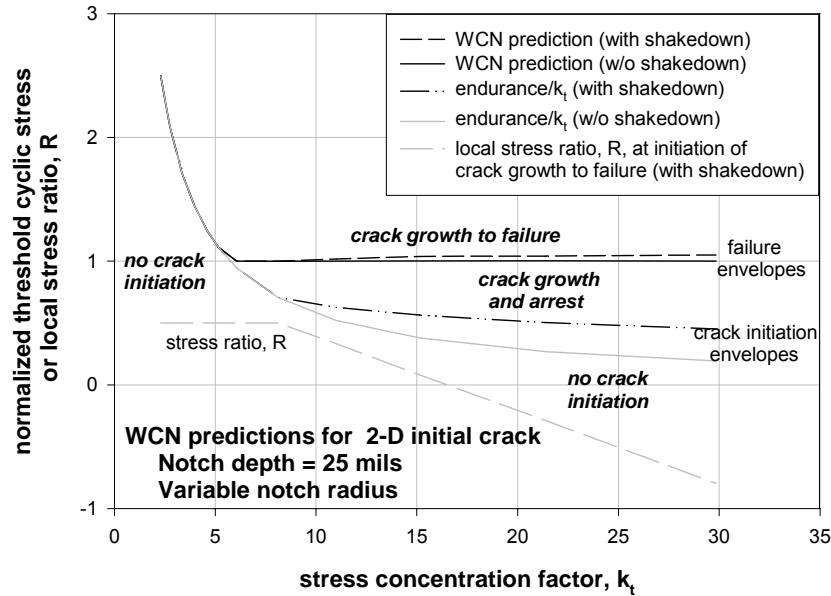
Figure K3. Results of applying the three-dimensional WCN model to predicting the effects of increasing notch severity on the crack growth behavior of two-dimensional cracks with one degree of freedom. Two sets of results are presented, with and without shakedown (i.e., with and without stress relaxation at the notch tip due to plastic deformation).

K.5.3 Through-thickness versus Thumbnail Cracks

The results of an example application of the 3-D WCN model assuming that thumbnail cracks with two degrees of freedom initiate are shown in Figure K4. Also shown on this figure are the predictions for 2-D crack with the one-degree of freedom presented in Figure K3. Although the threshold behaviors in the two cases are similar, the thumbnail crack model for notches with high k_t values predicts that failure will occur at threshold cyclic stresses less than those predicted for the 2-D crack. It should be noted that the calculated values of a_o and c_o are different for the two cracks, and that in the fatigue crack growth calculations the 3-D thumbnail crack was allowed to grow at both the deepest and surface locations of the crack front, so that situations could occur during growth where one location was propagating when the other crack-tip location was not, and vice versa.
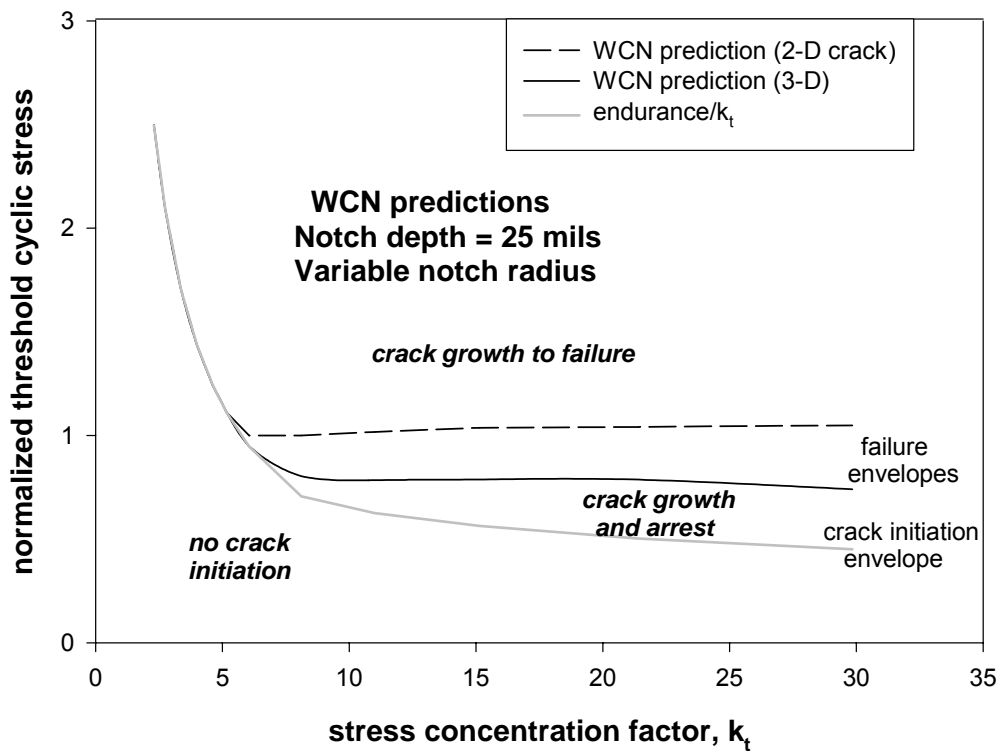
Figure K4.   Results of applying the three-dimensional WCN model to predicting the effects of increasing notch severity on the crack growth behavior of two-dimensional (2-D) and three-dimensional (3-D) cracks, including the effects of shakedown.

This point is illustrated in Figure K5 that shows values of applied effective cyclic SIF's and threshold values plotted against half the surface length, c, of a crack for a cyclic stress range just less than $\Delta S_{th}^{saturation}$. In this example, the deepest point on the crack is predicted to arrest even though the surface point continues to grow until its applied cyclic SIF falls below the threshold value for the surface point and the whole crack is arrested.

If the values for a_o given in Table K1 for thumbnail and through-thickness cracks are substituted into Equation (K10) using a value b=25mils, then the ratio of the saturated thresholds for thumbnail to through-thickness cracks is predicted to be 0.89. In other words, the difference in the a_o values for thumbnail and through-thickness cracks is sufficient to produce a saturated threshold cyclic stress for the former that is significantly lower than the saturation value for the latter, assuming that the thumbnail crack rapidly grows into a through-thickness crack after initiation.

Figure K6 illustrates the predicted crack growth behaviors for the deepest points on thumbnail and through-thickness cracks for a cyclic SIF equal to the $\Delta S_{th}^{saturation}$ corresponding to each type of flaw. Although the cyclic SIF for the deepest point on the thumbnail crack is less than that for the through-thickness crack, nevertheless, the thumbnail crack propagates to failure because the threshold cyclic SIF at the deepest point is less than that for the through-thickness crack.

K.5.4   Effect of Initiated Crack Geometry on Threshold Stress

The effect of different initiated crack aspect ratios on threshold behavior is illustrated in Figure K7. These results, which were calculated assuming shakedown did not occur, demonstrate how the value of $\Delta S_{th}^{saturation}$ increases as the aspect ratio of the cracks decreases.

K.5.5   Effect of Yield Stress on Threshold Stress

The effect of increasing severity of plastic shakedown on threshold behavior is shown in Figure K8 were the predicted results of applying the 3-D WCN model is displayed. The increase in plastic shakedown severity is simulated in the calculations by reducing the yield stress. It can be seen that the decrease in stress ratio, R, due to shakedown can be drastic, in some
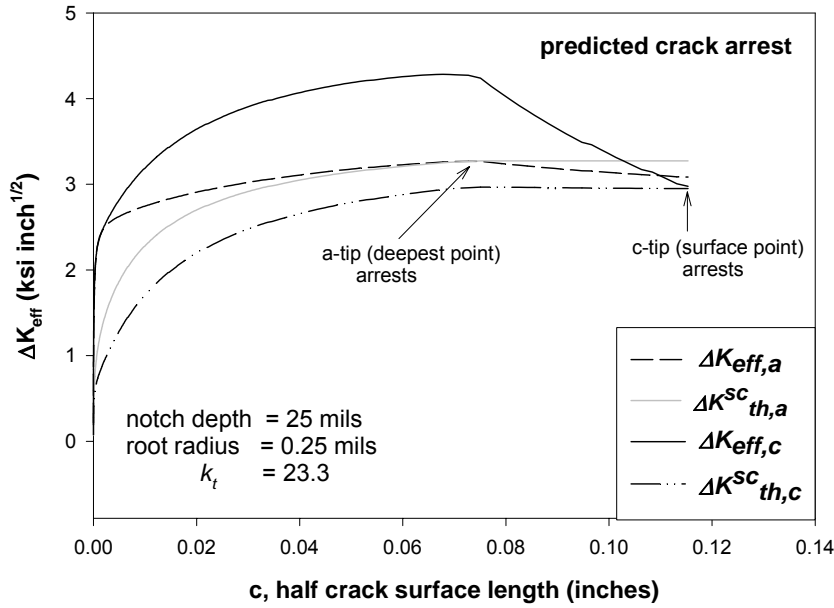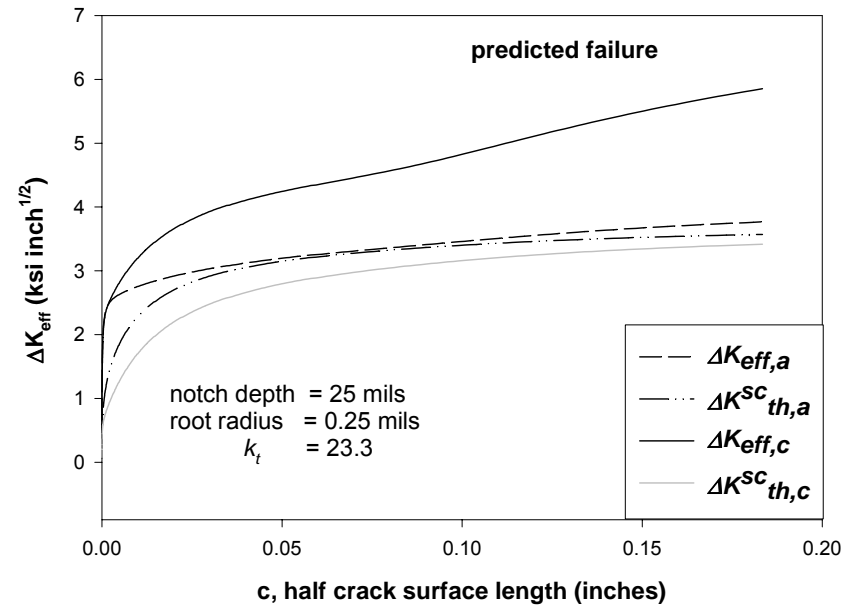
Figure K5.   This example application of the 3-D WCN model illustrates (a) arrest at the deepest point on a crack prior to arrest at the surface point and total arrest of the crack at a cyclic stress range just below $\Delta S_{th}^{saturation}$, and (b) the condition when the cyclic stress range equals $\Delta S_{th}^{saturation}$ and arrest is just avoided at the deepest point and the crack continues to propagate to failure.
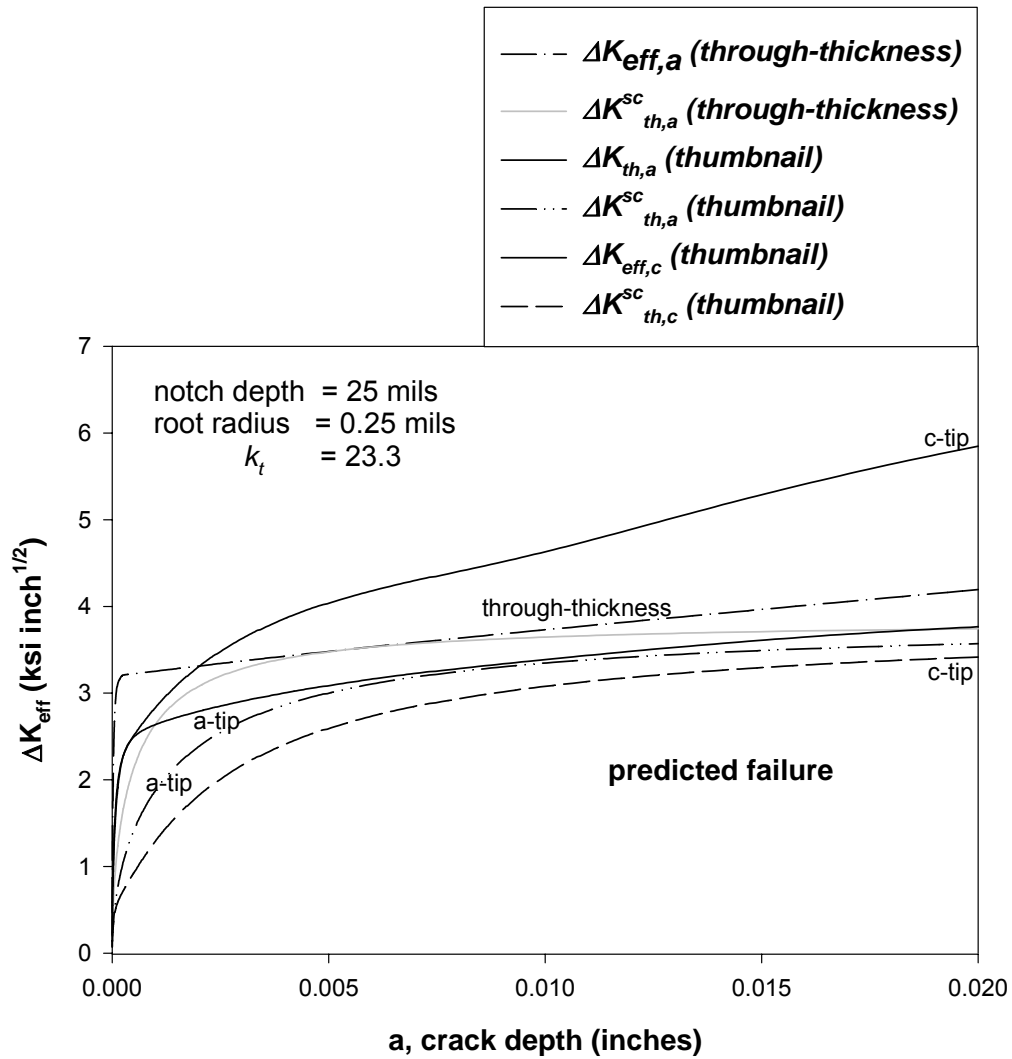
Figure K6. Comparison of the crack growth behaviors of thumbnail (3-D) and through-thickness (2-D) cracks at a cyclic stress range equal to $\Delta S_{th}^{saturation}$. The results illustrate that although the cyclic SIF at the deepest point on the thumbnail is less than that for the through-thickness crack, it still propagates to failure because $\Delta K_{th,a}^{sc}$ is lower for the thumbnail than for the through-thickness crack.
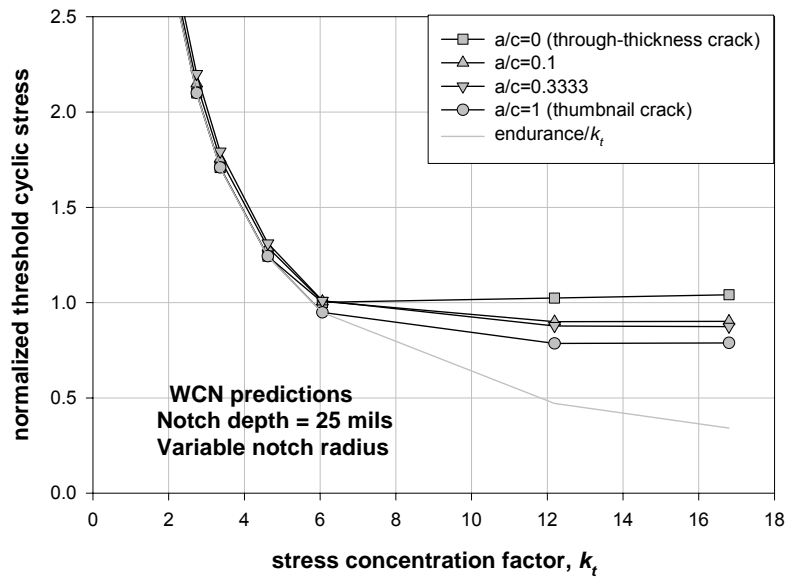
Figure K7.   Application of the 3-D WCN model to illustrate the effects of different assumed aspect ratios for initiated cracks on the threshold cyclic stress.
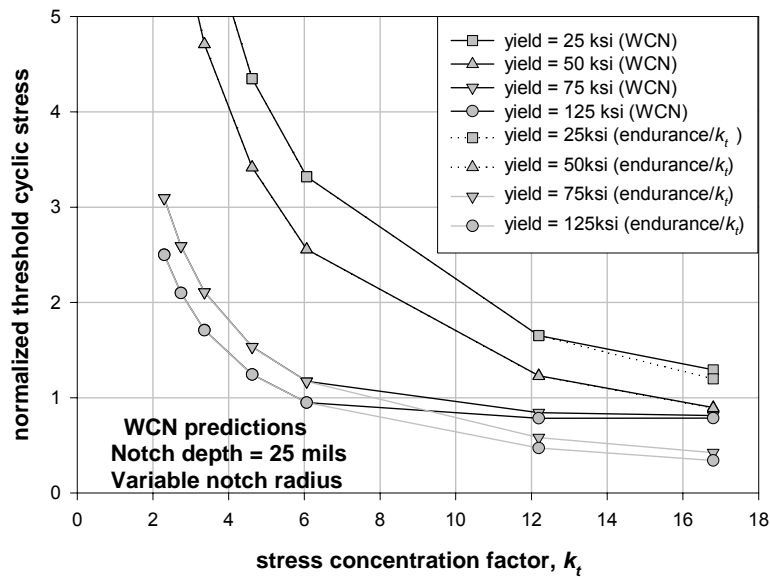
Figure K8.   Application of the 3-D WCN model to illustrate the effects of changes in yield stress on the threshold cyclic stress. In these calculations, the effects of decreasing yield stress are to increase plastic deformation at the notch tip and increase the relative severity of the compressive residual stress due to shakedown, causing the stress ratio, R, at the notch tip to become increasingly negative.

K-19

cases elevating the initiation threshold values above the values of $\Delta S_{th}^{saturation}$ for calculations involving higher yield stresses.

K.6 SUMMARY AND CONCLUSIONS

1.   A 3-D WCN model has been developed for cracks with two degrees of freedom, such as surface flaws. In order to implement the model it is necessary to perform explicit fatigue crack growth calculations to determine whether initiated cracks will propagate to failure or arrest.

2.   The model reproduces the predicted crack initiation and growth behavior of 2-D cracks with one degree of freedom, such as through-thickness flaws, that were predicted using the 2-D WCN model described in Reference 1.

3.   In order to implement the 3-D WCN model it is necessary to determine two small crack parameters, a_o and c_o, that are associated with the deepest and surface points on the crack front, respectively. In the 3-D WCN model, these parameters are defined within the context of a crack-size dependent small crack cyclic threshold SIF so that the smooth specimen endurance is predicted when an initiated crack becomes vanishing small, and so that the 2-D WCN model is recovered for cracks with one degree of freedom.

4.   The 3-D WCN model has also been extended to include the effects of residual stresses from shakedown at the notch tip. Shakedown occurs when plastic yielding occurs at the notch. The effects of shakedown are to change the local stress ratio at the notch so that it is no longer equal to the remotely applied stress ratio.

5.   For notches with high k_t values, the threshold cyclic stress that results in crack propagation to failure is predicted to saturate at a value $\Delta S_{th}^{saturation}$ and become independent of the severity of the notch. This is predicted to be the case for cracks with both one and two degrees of freedom.

6.   The saturation threshold $\Delta S_{th}^{saturation}$ is lower for 3-D thumbnail cracks than for 2-D through-thickness cracks, partly due to the fact that the parameter a_o for a thumbnail is greater than that for a through-thickness crack.

7.   Plastic shakedown is predicted to have a significant effect on threshold behavior by causing compressive residual stresses at the notch tip that elevate the cyclic threshold stress ranges for crack initiation and propagation.

K.7   REFERENCES

1.   S. J. Hudak, Jr., K. S. Chan, R. C. McClung, G. G. Chell, Y-D. Lee, and D. L. Davidson, "High Cycle Fatigue of Turbine Engine Materials," Final Technical Report, August 31, 1999, U.S. Air Force Contract No. F33615-96-C-5269, UDRI Subcontract No. RI 40098X.

2.   T. H. Topper and M. H. El Haddad, "Fatigue Strength Predictions of Notches Based on Fracture Mechanics," *Fatigue Thresholds: Fundamentals and Engineering Applications*, Engineering Materials Advisory Services, LTD, Warley, U.K., 1982. Also see T. H. Topper and M. H. El Haddad, "Fatigue Strength Predictions of Notches Based on Fracture Mechanics," *Fatigue Thresholds: Fundamentals and Engineering Applications*, Engineering Materials Advisory Services, LTD, Warley, U.K., 1982

3.   G. G. Chell, S. J. Hudak, Jr., Y.-D. Lee, and J. J. Feiger, "An Assessment of the 'Worst Case Notch' Model for Prediction of HCF Threshold Stresses in the Presence of Foreign Object Damage," *Proc. of the 5th National Turbine Engine High Cycle Fatigue Conference*, Chandler, AZ, March 2000

4.   Amstutz, H., and Seeger, T., "Accurate and Approximate Elastic Stress Distribution in the Vicinity of Notches in Plates Under Tension" Unpublished Results. (referenced in Savaidis, G., Dankert, M., and Seeger, T., "An Analytical Procedure for Predicting Opening Loads of Cracks at Notches. Fatigue," *Fract. Engng. Mater. Struct.*, Vol. 18, No. 4, pp. 425-442, 1995)

5.   Southwest Research Institute, DARWIN User's Guide, Version 3.5, 2002, Appendix C: Shakedown Residual Stress Methodology and Validation of SHAKEDOWN Module.

6.   I. S. Raju, S. R. Mettu, and V. Shivakumar, "Stress Intensity Factor Solutions for Surface Cracks in Flat Plates Subjected to Nonuniform Stresses," *Fracture Mechanics: Twenty-Fourth Volume*, ASTM STP 1207, J. D. Landes, D. E. McCabe, and J. A. M. Boulet, Eds., American Society for Testing and Materials, Philadelphia, 1994, pp. 560-580.

APPENDIX L

ANALYTICAL INVESTIGATION OF AIRFOIL LEADING EDGE FOREIGN OBJECT DAMAGE EVENTS

L.1   INTRODUCTION

Under the High Cycle Fatigue (HCF) Initiative, the U.S. Air Force selected gas turbine engine manufacturers and academia have been investigating high cycle fatigue behavior of engine components with a goal of achieving twice the damage tolerance of current components. A major source of concern in the high cycle fatigue behavior of gas turbine airfoils is the introduction of damage from foreign object impact events. In order to better understand the factors influencing high cycle fatigue crack growth emanating from foreign object damage (FOD) impact sites in gas turbine engine airfoils, an analytical study was conducted with the commercial explicit finite element code MSC/DYTRAN [1]. DYTRAN, a commercial explicit finite element package, is utilized to model hard body foreign object damage events of titanium airfoils. The titanium airfoils are simulated by tapered specimens with representative airfoil leading edge radii and are impacted with a 1.33mm steel ball or equal mass steel cube. The analysis includes rate dependent material properties and utilizes a simple material failure model. FOD specimen geometries contained in this analysis correspond to actual test specimens used in FOD experiments and post-FOD fatigue testing. All of the impact experiments and the corresponding analysis were conducted at room temperature ($\approx 22°C$). These impact events can generate significant deformation and correspondingly high residual stresses. These residual stresses play a major role in the resulting post-FOD fatigue life of the airfoils. Of particular interest is the residual stress state in the airfoil after impact and the calculated fatigue life to failure of the damaged specimens.

Characteristic materials, airfoil leading edge geometries and impact conditions representing gas turbine compressor fan blades were selected for the analytical investigation. Titanium (Ti-6Al-4V) specimens with representative leading edge radii were impacted with a steel ball and cube at angles and velocities typical of compressor airfoils. A design study of impactor shape, speed, angle, specimen leading edge radii, centrifugal load, and impact site

location was conducted with DYTRAN. The results of the analysis and the relative effects of these variables will be presented.

L.2   FOD ANALYSIS PAST HISTORY

Two specimen geometries representing typical compressor fan airfoil leading edges were selected for this program and were machined for impact testing. A "sharp" edge specimen with a 0.127 mm (0.005 in) leading edge radius (LER) and a "blunt" edge specimen with a 0.381 mm (0.015 in) LER as shown in Figure L1 were modeled. The angle of impact relative to the specimen cross-section was varied from 0° to 60° as shown in Figure L2, and the impact velocity was varied from 182.9 m/s (600 ft/s) to 365.8 m/s (1200 ft/s).

Sharp Edge Specimen

19.05 mm Constant
X-Section Gage

0.127 mm Edge Radius

Section A-A

Blunt Edge Specimen

19.05 mmConstant
X-Section Gage

0.381 mm Edge Radius

Section B-B
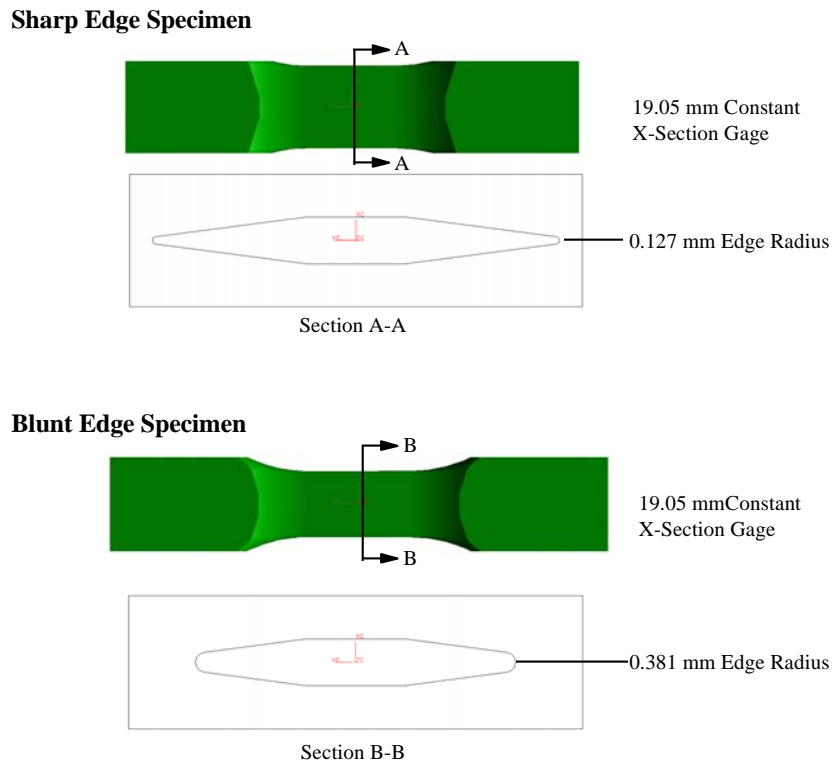
Figure L1. Leading edge specimen geometries.
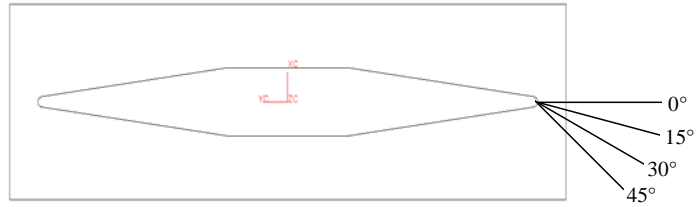
Figure L2. Impact angles.

Past analysis in the HCF Final Report [2] documents the development of the finite element models for the explicit DYTRAN analysis. Figure L3 shows a representative finite element mesh for a sharp edged specimen being impacted at 30°. As with all finite element analysis, whether it is explicit or implicit, the density of the mesh plays a role in the stress predictions.
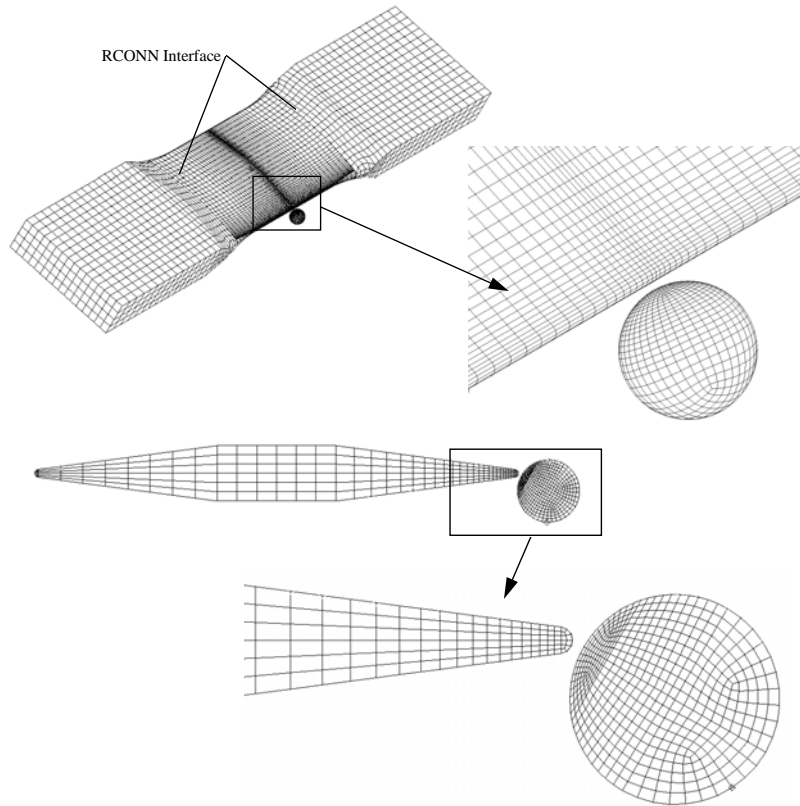
Figure L3. Finite element model of sharp edge specimen impacted at 30°.

The past HCF Final Report [2] documents a specimen mesh refinement study conducted with the ball mesh density kept constant. Figure L4 shows three successively finer meshes used in the past refinement study. The past mesh density study determined that the medium mesh

density predicted the experimental deformation results with the most accuracy. As a result of this past mesh refinement study, the medium mesh density model was selected for this follow-on analytical investigation.
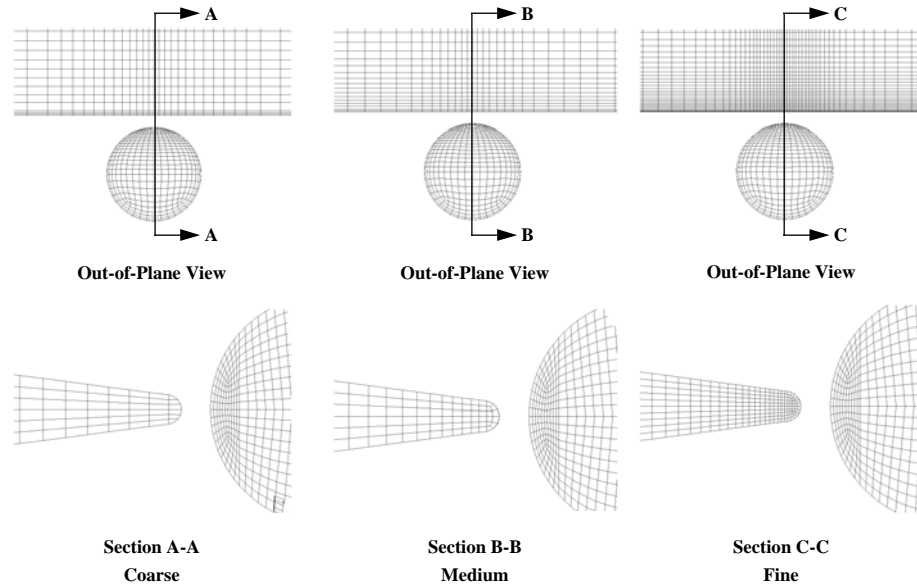
Figure L4. Specimen mesh refinement.

L.2.1   Material Modeling

Ballistic events introduce high strain rates and titanium has been shown to be highly rate sensitive. The same strain rate dependent constitutive material model used in the past HCF Final Report [2] was used for this analysis. The material model allows for the modeling of a nonlinear, plastic material with isotropic hardening and the von Mises flow rule. Strain rate dependent stress-strain curves are supplied to the analysis. The strain rate dependent bilinear stress-strain response input into the DYTRAN analysis is shown in Figure L5. This material model has an elastic modulus of 114 GPa (16.6 Msi), a tangent modulus of 1.1 GPa (0.160 Msi), and a quasistatic yield stress of 951 MPa (138 Ksi).
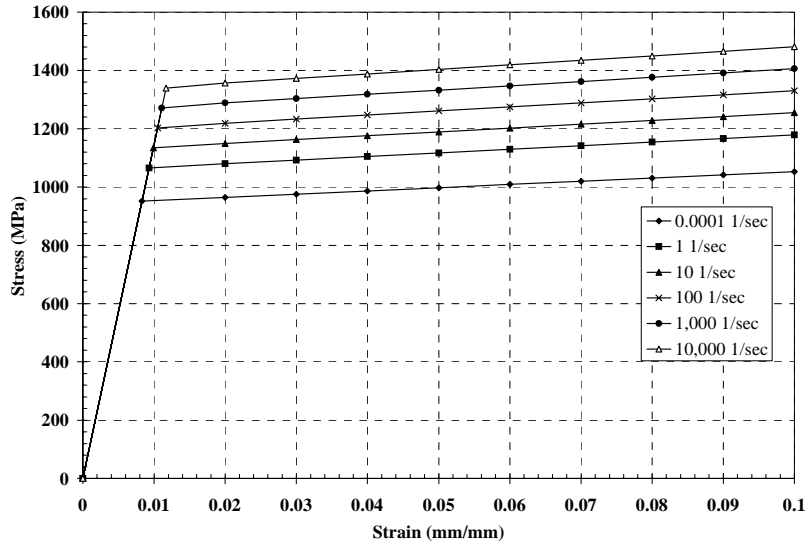
Figure L5. Rate dependent stress-strain behavior utilized in analysis.

Material failure can be modeled in DYTRAN; however, the failure routines are not sophisticated and cannot accurately model the failure process. This means stipulations must be placed on the failure prediction. A basic material failure model based on the Von Mises yield function was selected for evaluation. This chosen material model allows for failure of the element by specifying the effective plastic strain at failure. Once the failure limit is reached, the element looses all its strength. The single effective plastic strain variable utilized does not distinguish between different deformation modes. Once the limit is reached regardless if it is tension, compression, shear, or mixed, the elements fails. The high strain rate effective plastic strain at failure utilized in this analysis is 35%. The selection of 35% was based on a combination of literature surveys and finite element correlation with impact specimens exhibiting failure. The steel ball and cube were modeled as linear elastic with a modulus of 204 GPa (29.6 Msi) and a density of 7832 kg/m^3 (0.283 lb/in^3).

L.2.2   Fatigue Life to Failure Material Model Characterization

The residual stress field resulting from the impact and it's affect on the fatigue life of the specimen is of great interest. To investigate this a **cycles to failure** model based upon a Walker methodology has been developed. The Walker strain equation is shown below. Figure L6 illustrates the consolidated Walker fatigue curve. Walker material constants for

the consolidated room temperature HCF-LCF fatigue model have been developed for fatigue life predictions made within this report.

$$\varepsilon_{Walker} = \sigma_{max}/E * (\Delta\varepsilon_{eq}E/\sigma_{max})^m$$

Where:

ε_{Walker} = Walker strain
σ_{max} = Max stress
E = Modulus of elasticity
m = Walker strain exponent
$\Delta\varepsilon_{eq}$ = Equivalent strain range
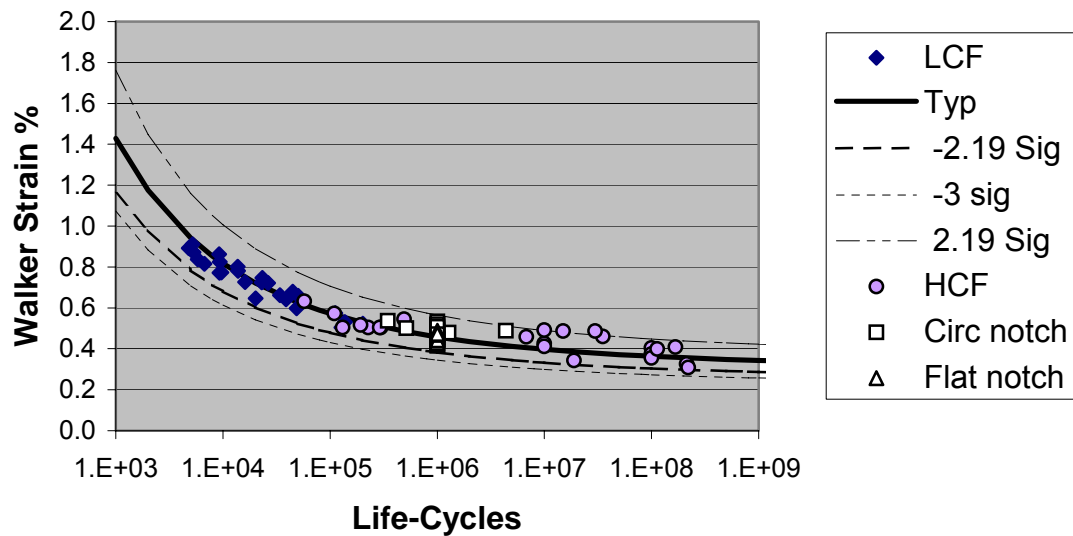
Figure L6. TI64-L RT consolidated HCF and LCF PRDA fatigue results

The ±2.19 sigma curves are the expected scatter band of the smooth data based upon a median ranks prediction. As can be seen, at longer lives the Walker curve becomes flatter and the effect of scatter on the HCF lives is much greater than the effect on LCF lives. Overall consolidating both LCF and HCF material data into a single Walker fatigue model that matched specimen lives from 1000 to 1E9 cycles produced a good fit. The Walker model shown in Figure L6 is used to perform fatigue life investigations for the following analytical studies.

L.3   ANALYTICAL RESULTS

Past analysis documented in the HCF Final Report [2] calibrated the mesh densities used in this analysis with selected ballistic experiments performed by UDRI. This past correlated mesh density has been carried forward and used in the analytical studies performed here. It should be noted that mesh density as well as the simple material failure model affect the analytical results. Results will be presented but it should be noted that the results are subject to the previously discussed modeling limitations.

L.3.1   Centrifugal Loading Analytical Study

This analytical study involves investigating the effect that centrifugal loading might have on the local residual stress field around the impact site. The centrifugal (CF) load was simply simulated as a mean stress by applying a tensile load to the specimen. This was done for modeling simplicity, possible future test comparisons, and to eliminate a CF load stress gradient effect. The sharp edge (0.005" radius) specimen is used in this study. Specimens are impacted at different angles and impact velocities while experiencing 0ksi, 20ksi, and 40ksi static stress fields simulating the blade CF load. The specimens are then statically loaded to a nominal 40ksi stress after impact for comparison of the local stress fields. Figures L7 through L9 show cross sections of the blade specimen at the impact site. In these figures the blade has been sectioned through the airfoil to reveal the internal spanwise stress distribution in the 3 direction denoted by the S_{33} symbol on the legend. Figures L7 through L9 are for impact angles of 0° and 30°. The 1.33 mm steel ball with a 1000 ft/sec velocity was used. Figure L7 shows the case where the blade was not preloaded during impact. The blade is then statically loaded to the nominal 40 ksi for comparison. Figure L8 shows the case where the blade is preloaded to 20 ksi at impact, and than statically loaded to 40 ksi for comparison. Figure L9 shows the case where the blade is preloaded to 40 ksi at impact.

Figures L7 through L9 clearly illustrate the effect of blade preloading on the local stress distribution around the impact site. Higher blade preloading seems to produce regions of locally higher tensile and compressive spanwise stress. These findings are controlled to a degree by the type of material failure model used in the analysis, and while the details of the stress distribution might change, the interaction of the FOD and CF stress fields would be similar.

0° Impact 40 ksi Nominal Stress **30° Impact 40 ksi Nominal Stress**
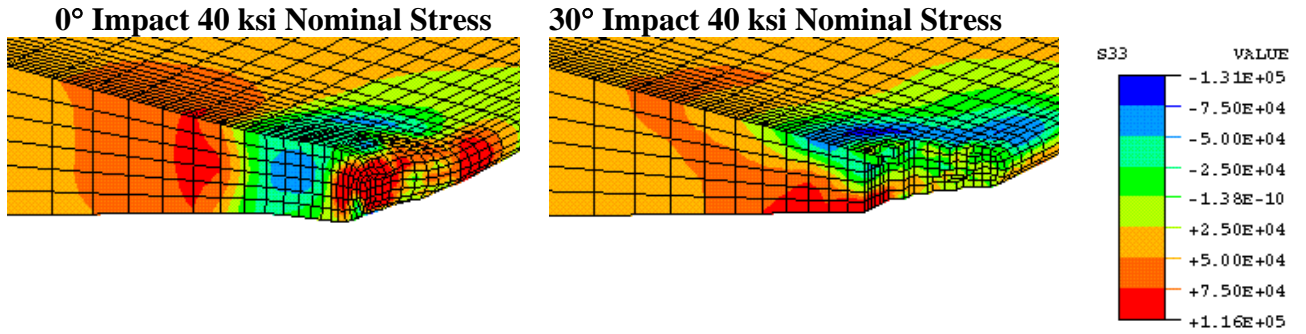
Figure L7. Impact occurred under a 0ksi Preload condition.

0° Impact 40 ksi Nominal Stress **30° Impact 40 ksi Nominal Stress**
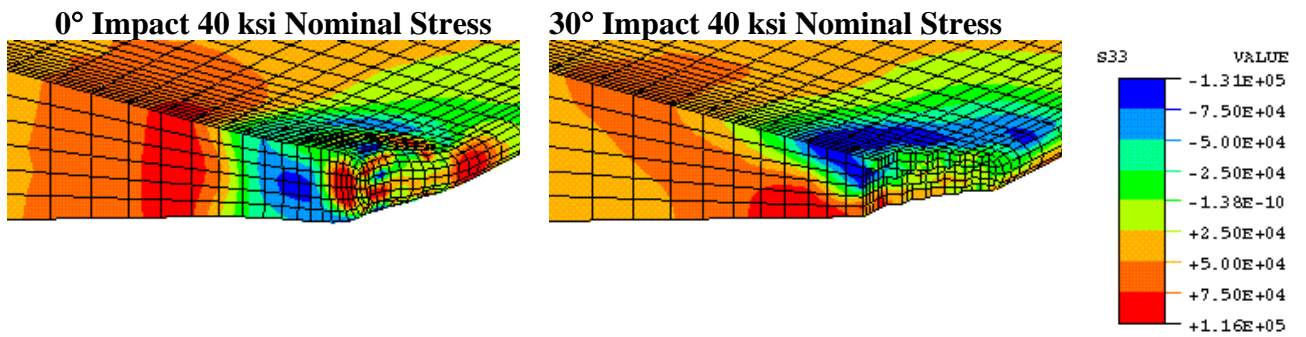
Figure L8. Impact occurred under a 20 ksi Preload condition.

0° Impact 40 ksi Nominal Stress **30° Impact 40 ksi Nominal Stress**
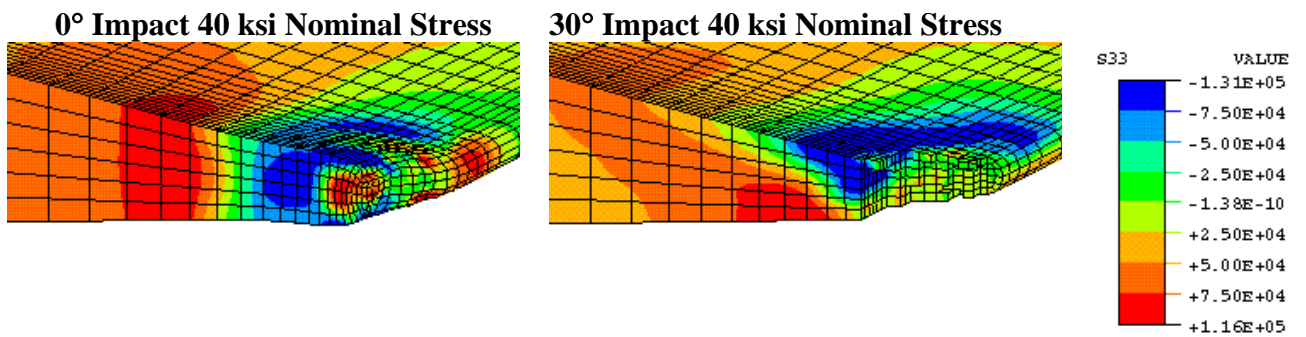
Figure L9. Impact occurred under a 40 ksi Preload condition.

The fatigue life investigation of the preloaded blades uses the Walker model shown in Figure L6. Figure L10 shows the predicted fatigue life to failure for the three preloaded blade conditions investigated. After impact at a preloaded condition, the blade is cycled between 0 ksi and 20 ksi nominal stress levels to investigate the fatigue life to failure effects. Figure L10 compares the predicted life with and without residual stress effects, as well as, 0°, 30°, and 60° impact angle information. Figure L10 results are based on a 1000 ft/sec impact velocity with a 1.33 mm steel ball and the sharp blade 0.005" radius.

Figure L10 illustrates that the fatigue lives for the cases with residual stress are not influenced greatly by blade CF load levels. This finding is subject to the analysis assumptions and further analysis needs to be done. A more refined material failure model may affect the residual stress distribution and therefore produce a different conclusion regarding fatigue life. FOD analysis refinement and experimental testing need to be done in order to predict and correlate how CF load really affects the fatigue life of a damaged blade.

Figure L10 also compares effects on fatigue life with and without residual stress. Including the residual stress distribution has a significant effect on predicted fatigue life. On average, the fatigue life is several orders of magnitude less when residual stresses are included. The "without residual stress" curves show a great deal of variance in predicted life. Including residual stress smoothes out the curves, and reduces the predicted fatigue life. The large variance in life of the "without residual stress" curves might be partly attributed to the mesh density at the FOD site that actually is a faceted surface. The material failure model has a great impact on the residual stress distribution, and therefore the fatigue life prediction also.

Figure L11 illustrates that as the cyclic stress increases to 0 ksi – 40 ksi – 0 ksi, residual stress due to impact has less effect on the predicted life. Comparing Figures L10 and L11 suggests that residual stress is more critical in the HCF regime than the LCF regime. Figure L11 shows that as impact angle increases, fatigue life decreases.
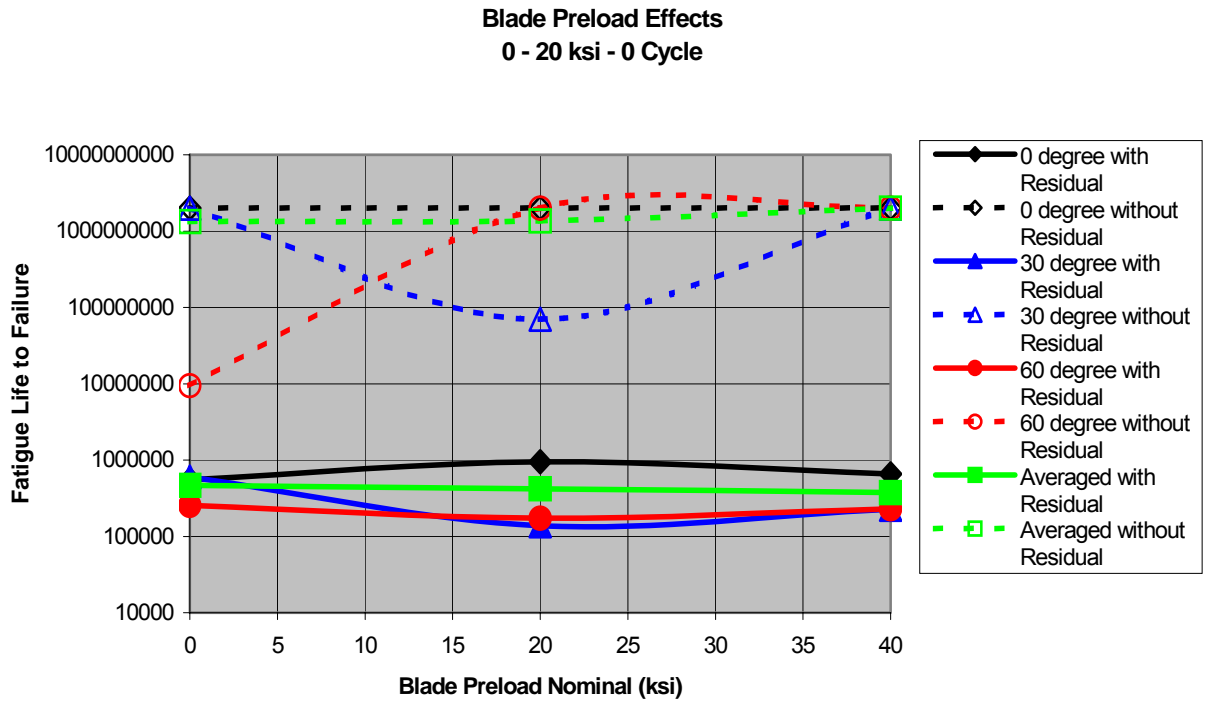
Figure L10. Predicted fatigue life of preloaded blade.
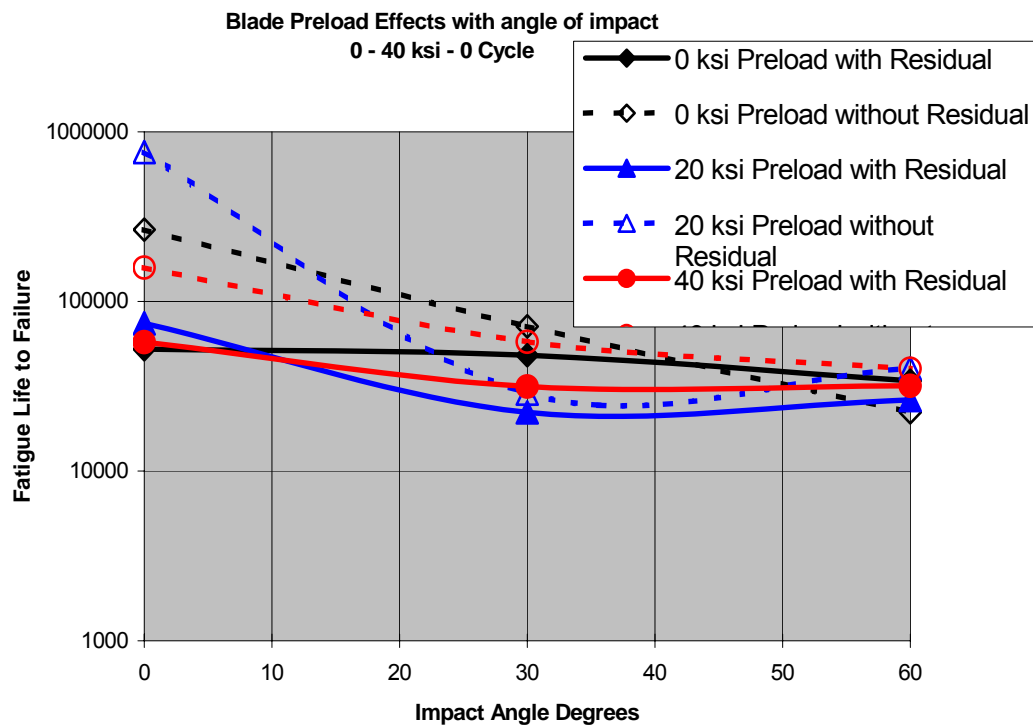
Figure L11. Predicted fatigue life of preloaded blade cycled to 40 ksi nominal stress.

L.3.2   Sphere versus Cube Impact Analytical Study

A comparison study of a sphere impactor to an equal mass cube was performed. The sharp edge blade specimen was used for this study. This study fixed the impact angle at 45°, and used the 1.33 mm steel ball. Figure L12 compares the two local model mesh geometries. The cube is oriented such that a sharp cube edge impacts the blade specimen leading edge. This produces the characteristic V – notch FOD.
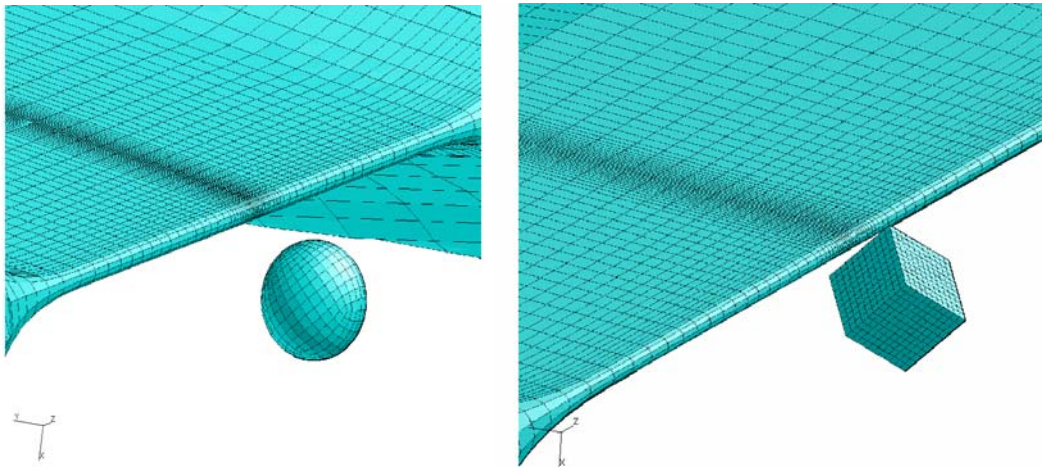
Figure L12. Local sphere and cube impact models.

Figures L13 through L15 compare blade spanwise stress results of impacts due to a sphere and a cube. Here the impact velocity was 1000 ft/sec. Local FOD site geometric differences and chord wise stress distributions are visually compared.

Figure L13 shows that the sphere impact produces more local bending distortion around the FOD site, while the cube impact creates a deeper notch effect. The local bending distortion is produced by an interaction of blade edge radius, impactor radius, and impactor velocity. Slower and larger impactors produce more local bending distortion around the FOD site. As velocity increases, less local bending distortion is observed. Figure L13 shows that the exit side (top) compressive stress distributions are different for the two impactors. The sphere impact produced compressive stress all around the surface of the exit side while the cube impact created a very slight tensile stress at the exit side surface notch location with compressive stresses produced deeper into the blade specimen.

Sphere Impact, 45°, 1000 ft/sec   Cube Impact, 45°, 1000 ft/sec
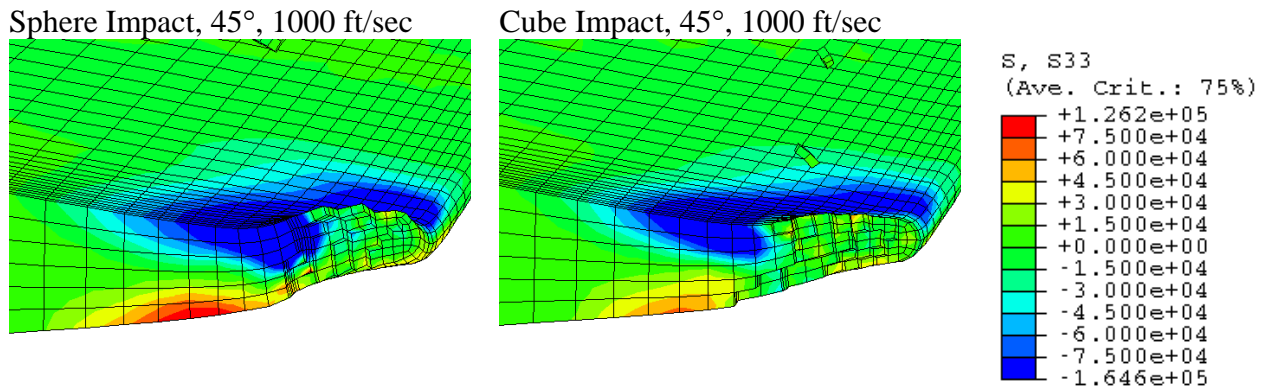
Figure 13 – Comparison of Residual Stress Fields After Impact (No Nominal Load)

Sphere Impact, 45°, 1000 ft/sec   Cube Impact, 45°, 1000 ft/sec
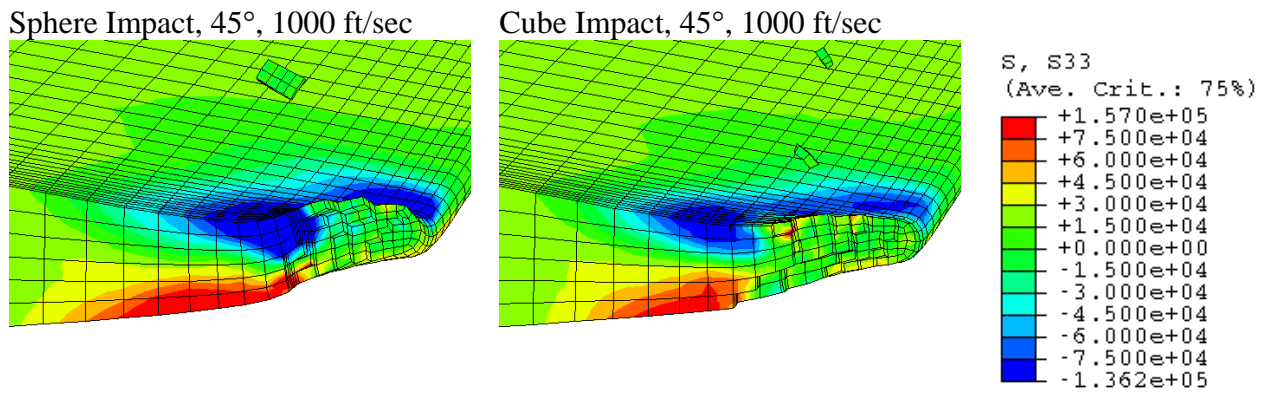
Figure 14 – Comparison of Residual Stress Fields After Impact (20 ksi Nominal Load)

Sphere Impact, 45°, 1000 ft/sec   Cube Impact, 45°, 1000 ft/sec
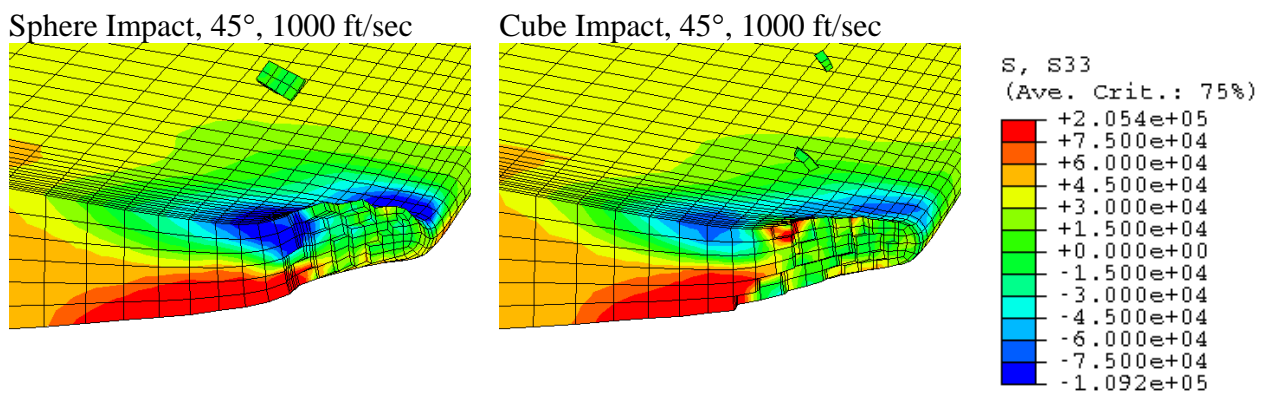
Figure 15 – Comparison of Residual Stress Fields After Impact (40 ksi Nominal Load)

Figure L14 compares the two models loaded to a nominal 20 ksi stress level. Both models show tensile stresses on the projectile entrance side. The cube model shows the localized tensile stress at the exit side notch location. Figure L15 shows that the 40 ksi nominal stress significantly reduces the compressive stress field on the exit side of the cube impact, and the very localized tensile stress at the exit side notch root is clearly observed. The sphere impact still shows a large zone of compressive stress at the exit side.

Fatigue life to failure was investigated comparing the sphere impact to the cube impact. 600 ft/sec, 800 ft/sec, 1000 ft/sec, and 1200 ft/sec velocity cases were investigated for the 45° impact angle. Figure L16 shows the effect of the cube and the sphere on fatigue life to failure.
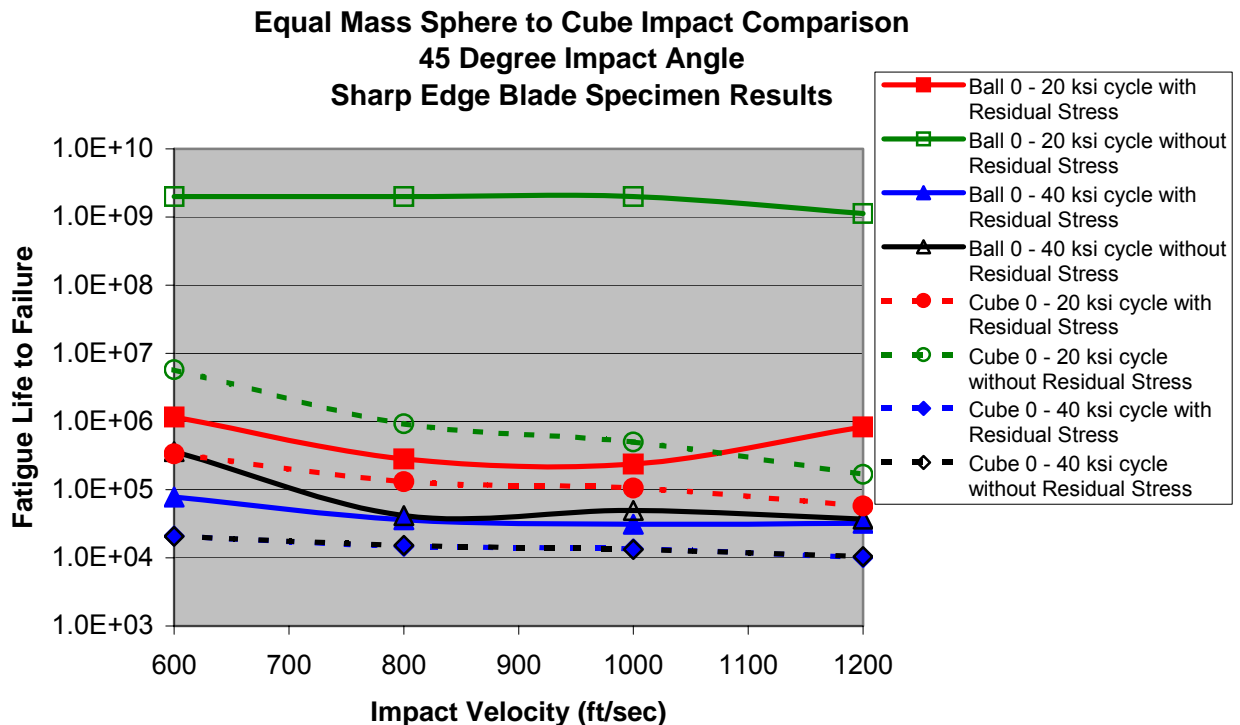
Figure L16. Fatigue life comparison of cube impact to sphere impact.

Figure L16 plots calculated fatigue life for the 0ksi – 20ksi cycle and the 0ksi – 40ksi cycle. The effect of "with and without residual stress" is also shown. Figure L16 clearly shows that the cube impact is more damaging to fatigue life than the sphere impact. Figure L16 shows that fatigue life decreases for the increasing velocity, but the curves also

appear to be converging as velocity increases. This suggests a possible upper limit on velocity for a minimum fatigue life point. For all cases, including residual stress reduced the predicted fatigue life to failure. The difference in fatigue life between "with and without residual stress" decreases as the cyclic stress range increases. This is observed by comparing the cube 0 ksi – 40 ksi "with and without residual stress" curves.

L.3.3   Impact Site Perturbation Study

FOD test results have shown a great deal of scatter in the fatigue life of specimens that were impacted in a similar fashion. It has proven to be very difficult to reproduce exactly the same FOD damage from one test specimen to the next. Given this, it was decided to perform an impact site perturbation study. The first study is an investigation of the effect on fatigue life for the 0° impact angle of the blunt edge radius (.381mm/0.015in) blade specimen. Figure L17 defines how the perturbation study was performed. A 1.33 mm ball with a velocity of 1000 ft/sec was investigated.
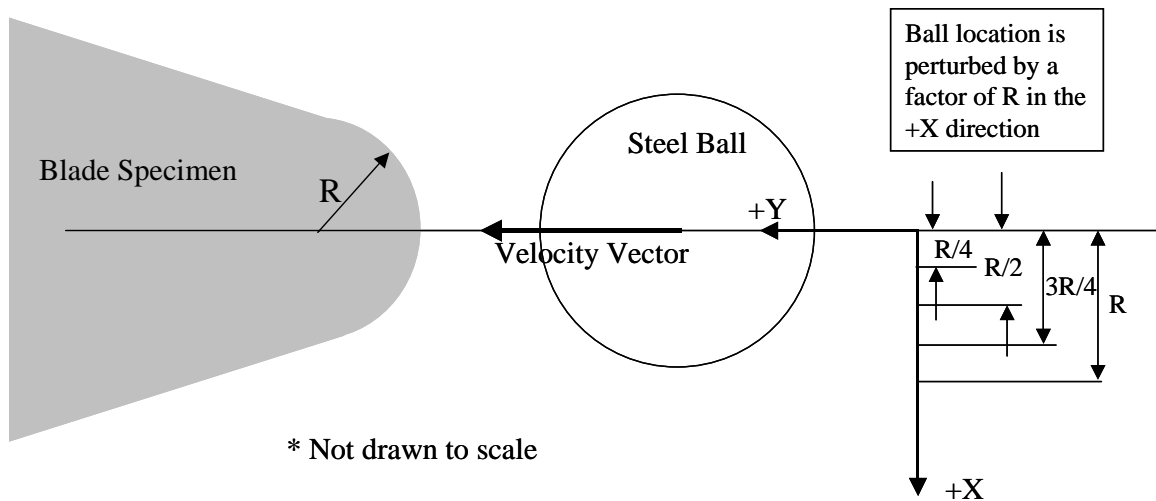
Figure L17. Perturbation study definition for the 0° impact angle study.

Figure L17 shows that the study involves looking at X=0, R/4, R/2, 3R/4, and R ball offset conditions where R is the blunt edge blade specimen radius. Figure L18 is a comparison of the offset impact effect on residual stress distribution in the cross section of the blade.

L-14
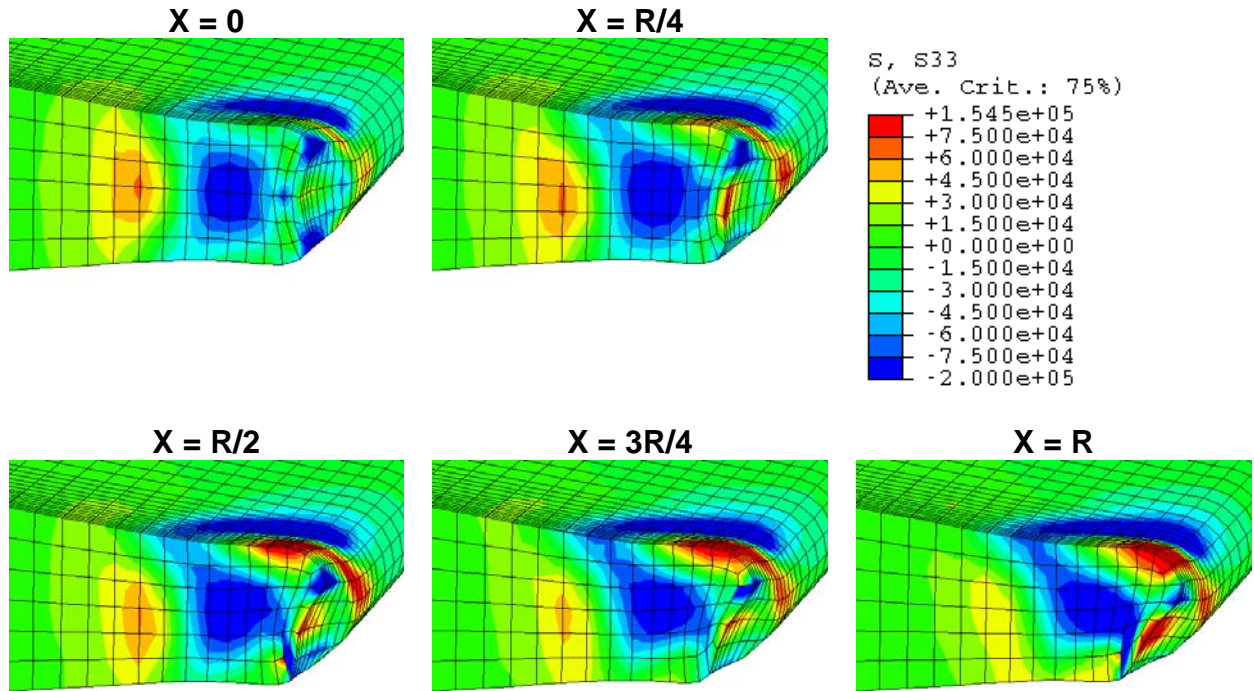
Figure L18. Perturbation study contour plots of 0° impact.

As shown in Figure L18, increased impact site offset in the +X direction(down) produces increased tensile residual stress on the top side of the blade.

Figure L19 compares the fatigue life as impact site offset increases. Figure L19 illustrates that with increased impact site offset there is a reduction in fatigue life. For the X=0 location, the 0 ksi – 20 ksi case fatigue life is calculated to be 3,370,000 cycles, increasing the offset to X = R fatigue life decreases by a factor of 2.9 to 1,180,000 cycles. The 0° perturbation study suggests that a good deal of fatigue life variation could be observed due to imperfect impacts.
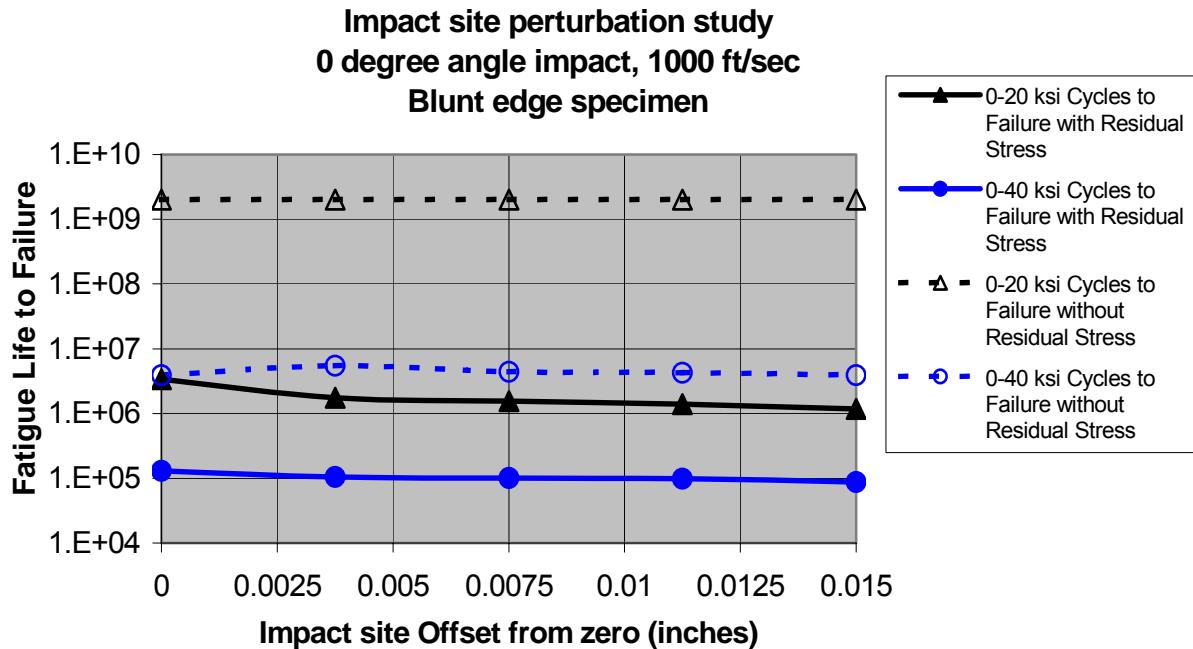
Figure L19. 0° Impact site offset study on fatigue life.

The 30° impact angle perturbation study definition is shown in Figure L20. In this study the steel ball is perturbed along the Y direction as shown, while the 30° angle is held constant. Five impact cases are investigated with the blunt edge specimen. Figure L21 compares residual stress distributions in the blade cross-section for the five cases. As Y goes from –R/2 to +R/2 the depth of the FOD site increases. The –R/2 and –R/4 impacts have removed elements through the thickness of the blade tip. For Y = 0 and greater some elements remain on the exit side of the impact, and there are more elements removed at the entrance side. The compressive stress distribution seems to be driven from a more interior distribution for Y= -R/2 toward a surface distribution for Y = R/2. Figure L22 compares the fatigue life results for this perturbation study.   For the 0 ksi – 20 ksi cyclic case with residual stresses the calculated maximum number of cycles to failure was 980,000 cycles at the Y = -R/4 location. The minimum of 200,000 cycles occurred at the Y = 0 location. There is a factor of 4.9 between the maximum and minimum calculated fatigue life.

Ball location is perturbed by a factor of R in the ±Y direction

Blade Specimen

R

+Y

30°

Velocity Vector

Steel Ball

+R/4 -R/4

* Not drawn to scale

+R/2   -R/2

+X
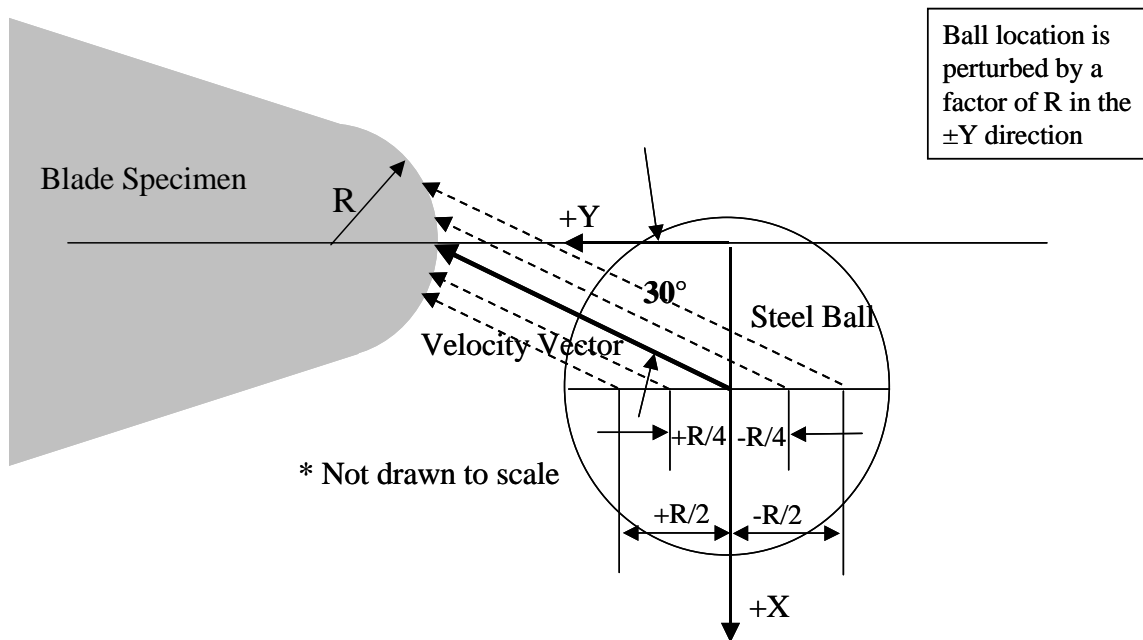
Figure L20. Perturbation study definition for the 30° impact angle study.

Y = -R/2

Y = -R/4

S, S33
(Ave. Crit.: 75%)
+1.095e+05
+7.500e+04
+6.000e+04
+4.500e+04
+3.000e+04
+1.500e+04
+0.000e+00
-1.500e+04
-3.000e+04
-4.500e+04
-6.000e+04
-7.500e+04
-1.912e+05

Y = 0

Y = R/4

Y = R/2
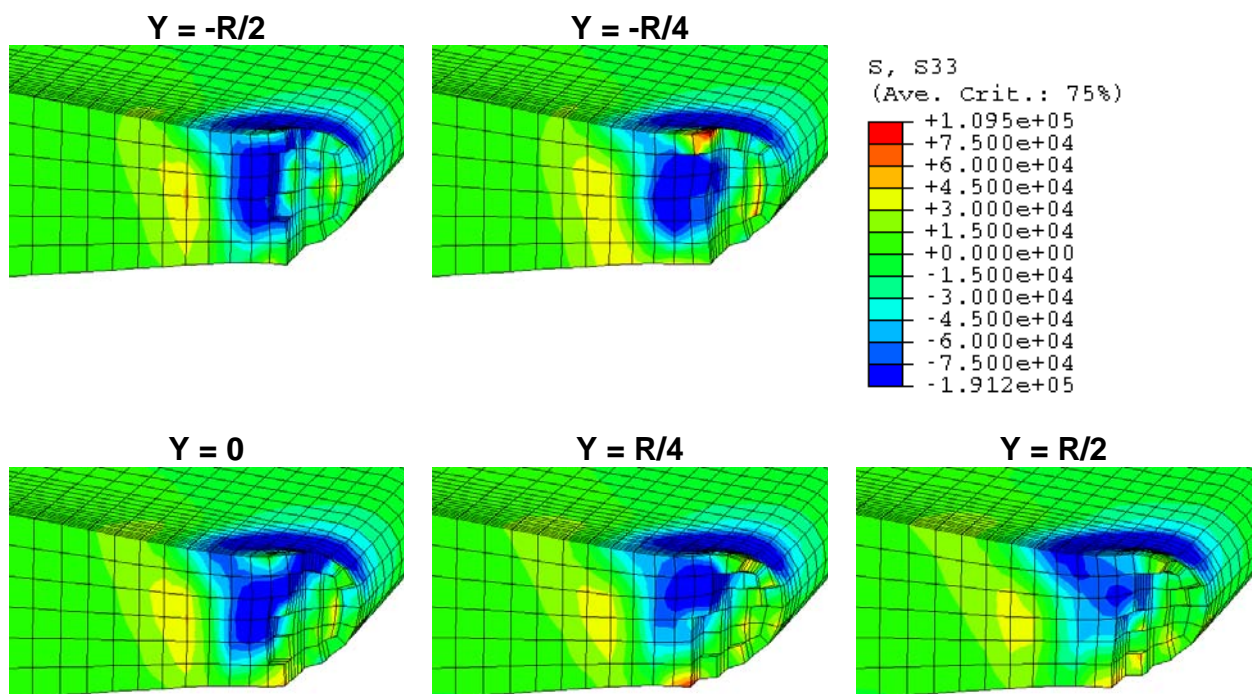
Figure L21. Perturbation study contour plots of 30° impact.
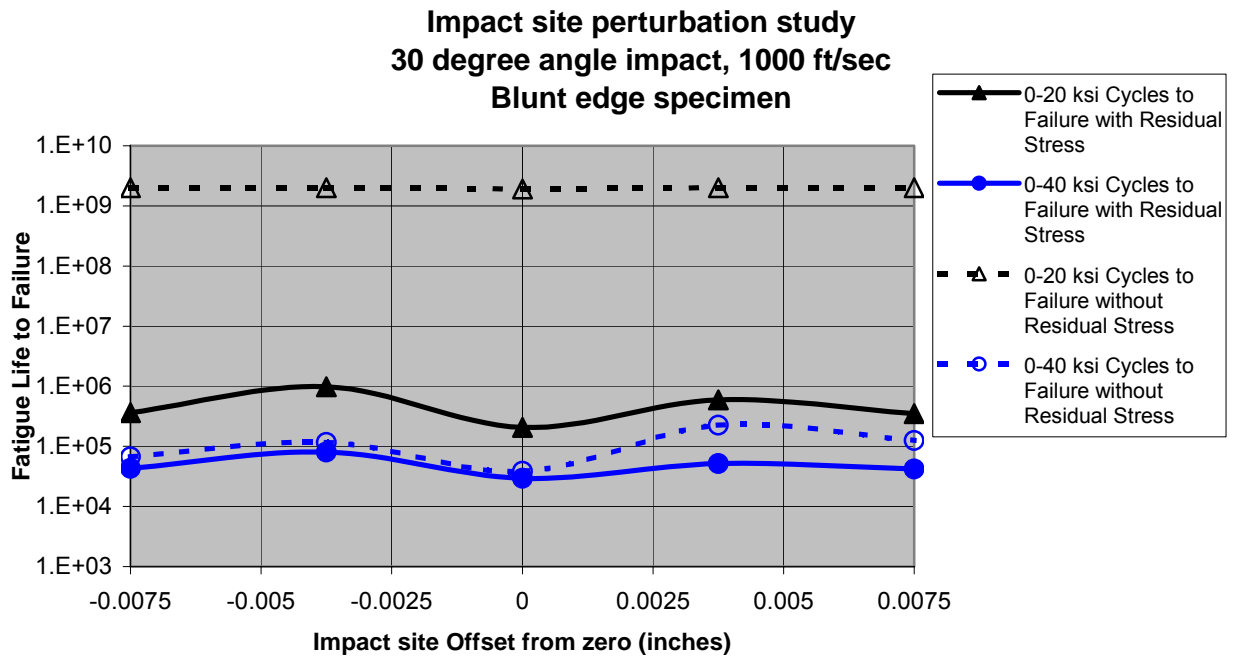
Figure L22. 30° Impact site offset study on fatigue life.

L.4 CONCLUSIONS

Conclusions stated here are predicated on a simple material failure model. Findings presented are subject to that limitation. A Walker LCF – HCF fatigue life to failure model was developed to investigate fatigue life. The effect of scatter on the HCF lives is much greater than the effect on LCF lives. The centrifugal loading study illustrated that there is an effect on the local stress distribution around the FOD site due to blade preload being present at the time of impact. A trend of how preload effects fatigue life was not observed. Analytical studies performed here show that including residual stress distribution around the FOD site does significantly reduce the estimated fatigue life (Figure L10). Increasing the impact angle as shown in Figure L11 from 0° to 60° causes a decrease in fatigue life for the sharp radius specimen.

The cube versus sphere study determined that FOD geometry has a significant effect on fatigue life, local residual stress distribution, and FOD site geometry. Velocity was also investigated within the cube versus sphere study. It was found for the 45° impact of the

sharp edge specimen that as impact velocity increased fatigue life decreased. It was also observed that the fatigue life curves in Figure L16 for the cube results were converging as velocity increased. Figure L16 also shows that including residual stress has a greater impact in the HCF versus LCF regimes. This is observed in Figure L16 by the decreasing gap between "with" and "without residual stress" curves as the load is increased from the 0 ksi – 20 ksi to the 0 ksi – 40 ksi cycle.

The impact site perturbation studies show that there can be a significant difference in predicted fatigue life given an imperfect impact. The 0° impact angle perturbation study of the blunt edge specimen shows a 2.9 factor between the maximum and minimum calculated fatigue life values. For the 0° impact, fatigue life decreased as offset increased. For the 30° impact of the blunt edge specimen, a 4.9 factor between the maximum and minimum fatigue life was observed. The two impact site perturbation studies performed here suggest there is a variation in fatigue life due to imperfect impacts. Further analysis would need to be done to more accurately address the actual magnitude of the variation.

L.5   ACKNOWLEDGMENTS

L.6   REFERENCES

1.   *MSC/DYTRAN Version 4.7 User's Manual*, The MacNeal-Schwendler Corporation, 1999.

2.   HCF Final Report, Chapter 5, Appendix 5B

APPENDIX M

CAFDEM

M.1 GENERAL FORMULATION OF CONTACT STRESS MODEL

A schematic of two elastic bodies in contact is shown in Figure M1. Let the displacements in the x and y directions be given by $_{i}u_x$ and $_{i}u_y$ respectively ($i = 1, 2$). The relative slip between the two bodies, $s(x)$, and the initial gap function, $H(x)$, in the contact zone are related to the displacements as,

$$s(x) = {}_2u_x - {}_1u_x \tag{M1}$$

$$H(x) + C_1\, x = {}_2u_y - {}_1u_y + H_0 \tag{M2}$$

where H_0 is a constant and C_1 is a rotation term. Equation M1 defines slip as difference in tangential surface displacement of two bodies. Equation M2 states that the normal displacement of the bodies must lead to continuity between the two bodies without interpenetration. Using equations of elasticity for plane-strain half spaces, the contact pressure, $p(x)$, and the shear traction, $q(x)$, can be related to $H(x)$ and $s(x)$ as:

$$\frac{\partial s}{\partial x} = \frac{k_2}{\pi} \int_{a_1}^{a_2} \frac{q(t)}{t - x} dt + k_1 p(x) \tag{M3}$$

$$\frac{\partial H}{\partial x} + C_1 = -k_1 q(x) + \frac{k_2}{\pi} \int_{a_1}^{a_2} \frac{p(t)}{t - x} dt \tag{M4}$$

where the Dundurs constants [1] k_1 and k_2 are obtained from the Young's modulus (E) and Poisson's ratio (v) of the two bodies as:

$$k_1 = \frac{(1 - 2v_2)(1 + v_2)}{E_2} - \frac{(1 - 2v_1)(1 + v_1)}{E_1} \tag{M5}$$

$$k_2 = -\frac{2(1 - v_2^2)}{E_2} - \frac{2(1 - v_1^2)}{E_1} \tag{M6}$$

Please note that $k_1 = 0$ when both the contacting bodies are made from similar isotropic materials which means that Equation M3 and M4 are de-coupled so that the contact pressure is independent of the tangential load. If the initial gap function and the slip function are

known, Equations M3 and M4 can be solved for the contact tractions. The initial gap function, $H(x)$, can be obtained from a knowledge of the undeformed geometry of the contacting bodies but the slip function, $s(x)$, is more complicated.
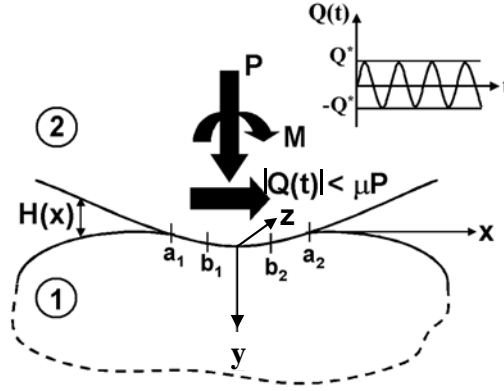
Figure M1.   Schematic of two elastic bodies in partial slip contact, a_1 and a_2 denote the ends of the contact zone and b_1 and b_2 denote the end of the stick zones.

For Coulomb's law of friction to be obeyed at the edge of contact and for there not to be any interpenetration of the contacting surfaces, there has to be some amount of relative sliding between the contacting surfaces. The most common scenario is that there is a central *stick* zone in which no relative slip takes place surrounded by a *slip* zone in which the tangential traction is limited by the available friction. In a given load increment, these conditions can be written as:

$$\frac{\partial s(x,t)}{\partial t} = 0 \qquad\qquad x \in (b_1, b_2) \qquad\qquad\qquad (M7)$$

$$|q(x)| = \mu \,|\, p(x)\,| \qquad\qquad x \in \{(a_1, b_1) \cup (b_2, a_2)\} \qquad\qquad (M8)$$

where b_1 and b_2 are the ends of the stick zone and a_1 and a_2 are the ends of the contact zone as shown in Figure M1. If the next load increment at a given instant in time is such that the size of the stick zone grows into the slip zone then the accumulated slip in the newly added regions to the stick zone gets "locked in". Thus, the contact pressure and shear stress distribution are load path or history dependent.

This point is illustrated in Figure M2 for the case of normal indentation ($Q = 0$) of an elastic half space by a rigid punch. As the applied load P increases, the point A on the surface of the half-space slips against the rigid surface until the stick zone extends to include that point. From that time onward, any increase in the load does not result in additional slip, i.e., the slip is locked in. To solve Equations M3 and M4 for the contact tractions, we need to have knowledge of the accumulated slip function, $s(x,t)$, at the current instant of time. For the most general loading/unloading paths there is no way of knowing the slip function *a priori*. Hence Equations M3 and M4 have to be solved incrementally.
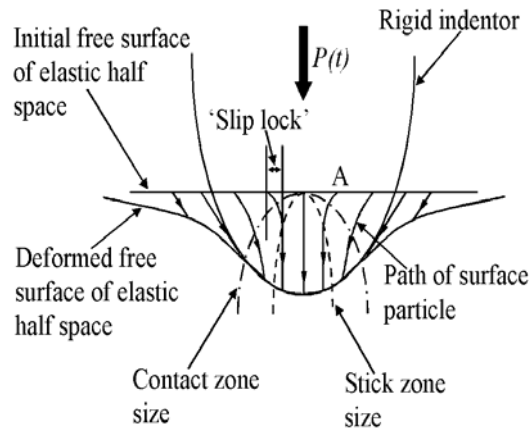
Figure M2. The evolution of the contact and stick zones and the "slip lock" phenomenon that occurs during the incremental indentation of anelastic half space by a rigid surface.

M.2   VERIFICATION OF FORMULATION USING POWER LAW INDENTER WITH Q = 0

The governing singular integral equations (Equations M3 and M4) are solved numerically [2-3]. The numerical implementation is verified by comparing to a solution available in the literature. Spence (1973) [4] gives the contact tractions and the size of the stick zone when an elastic half space is indented by a rigid power law indentor ($H(x)=Ax^n$) under the influence of normal load alone, i.e., $Q=0$. Under such conditions the solution is symmetric with respect to contact pressure and anti-symmetric with respect to the shear traction. Hence the ends of the contact zone and the ends of the stick zone will be located

symmetrically about the origin, i.e., $a_2=-a_1=a$ *and* $b_2=-b_1=b$. Exploiting the self-similarity of the problem, Spence reasoned that the ratio of the size of the stick zone to the size of the contact area remains fixed irrespective of the shape, given by the index *n*, of the power law indentor. Moreover this ratio depends only on the Poisson's ratio (ν) of the half-space and the coefficient of friction (μ).

The present analysis technique is applied to this problem by incrementally indenting an elastic half-space by a rigid parabolic punch ($n=2$). The indentation is continued till the contact size $a=1$. The normal load, applied incrementally using 40 load steps of equal magnitude with the relative slip function calculated at the end of the current step used as input to the next step. The slip function in the first step is assumed to be zero within the stick zone. The analysis is performed for different values of μ and two different values of ν (=0.0, 0.3). The results of the current analysis (Figure M3) are in good agreement with Spence's results for this reduced problem providing partial justification of numerical convergence. Further details on numerical implementation and convergence are given in Rajeev (2001) [5].
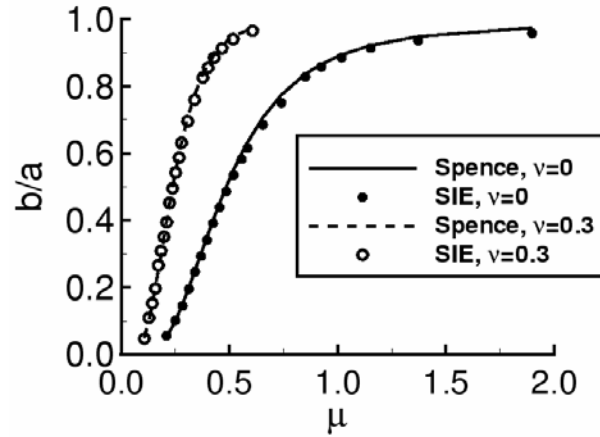
Figure M3.   Stick zone size as a function of the coefficient of friction. The values of b/a obtained by solving the coupled singular integral equations incrementally are in good agreement to those obtained by Spence (1973) [4] using a self-similar analysis.

M.3   VERIFICATION OF FORMULATION CONSIDERING LOAD HISTORY EFFECTS

Consider the following two scenarios: 1) a cylindrical punch with radius (R) of 7 inches is brought in contact with a half-space under the action of a normal load, P, and then a shear load, Q $(<\mu P)$, is applied to the punch, and 2) the cylindrical punch is brought in contact with the half-space by applying P and Q together, i.e., an oblique load. If the punch and the half-space are made from similar isotropic materials, a central stick zone is produced in the first case whereas the entire contact is in stick in the second case [6-7].

For the case of dissimilar materials the contact tractions for the above two load histories have to be obtained numerically. The shear traction results when a rigid cylinder is brought into contact with a Ti-6Al-4V half-space ($E=16.8\ Msi,\ \nu = 0.32$) subject to the load history shown in Figure M4.
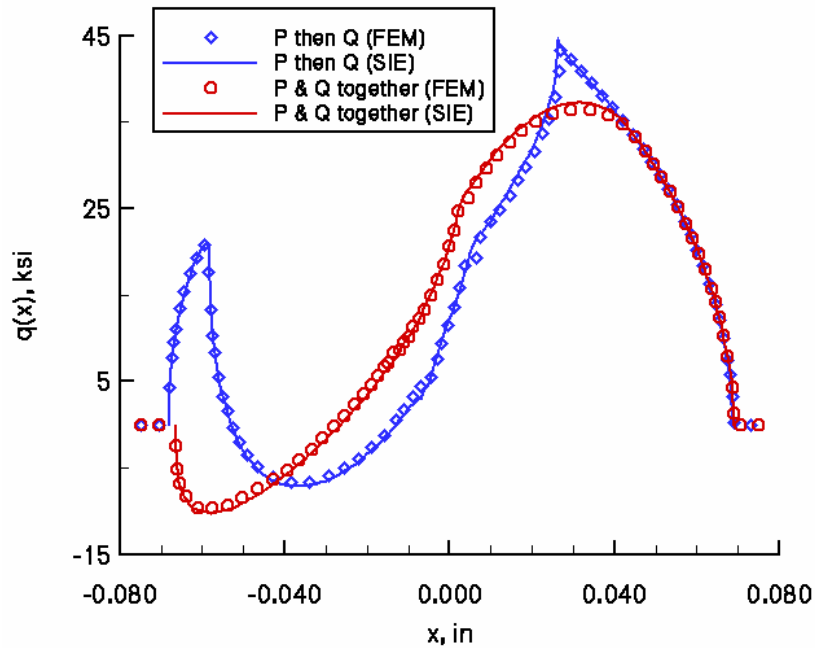
Figure M4.   Shear traction results when a rigid cylinder is brought into contact with a Ti-6Al-4V half-space for two different load histories (P = 10,000 lb/in, Q = 3000 lb/in).

The coefficient of friction is $\mu = 0.5$ and cylinder radius is $R = 7$ inches in these subsequent calculations unless otherwise indicated. Note that the SIE results are in good agreement with the FEM results. Figure M5 represents the shear traction results when a cylindrical punch made from Inco718 alloy ($E = 30.2Msi,\ v = 0.31$) is brought into contact with a Ti-6Al-4V half-space. The "kinks" in the central region of the shear traction distributions are a result of assuming that the relative slip function is identically zero in the stick zone in the very first load increment. They can be confined to smaller regions by increasing the number of load increments. It must be noted that, for the same reason, these "kinks" exist in FEM analyses as well (Figure M4). Small slip zones are present near the edges of contact that are not present in the similar material case.
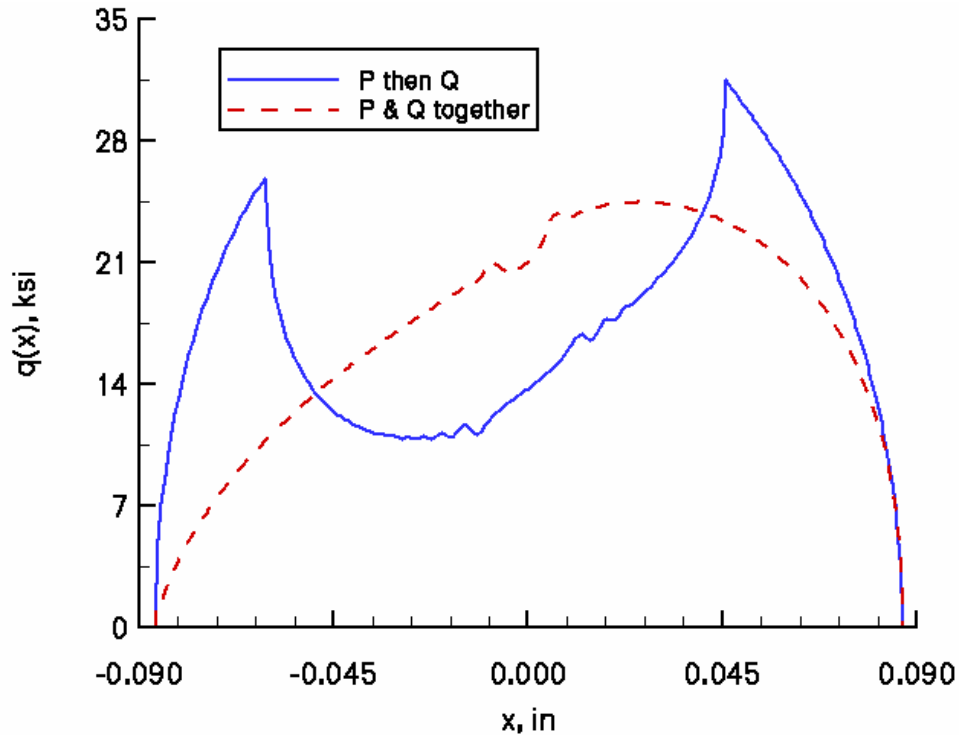
Figure M5. Shear traction results when a cylinder made from Inco718 alloy is brought into

M.4   REFERENCES

1.   Dundurs, J., and Comninou, M., "Some Consequences of the Inequality Conditions in Contact and Crack Problems", *Journal of Elasticity*, Vol. 9(1), 1979, pp.71-82.

2.   Rajeev, P.T., and Farris, T.N., "Two Dimensional Contact of Dissimilar/Anisotropic Materials", in *Proc. Of 42nd AIAA/ASME/ASCE/AHS/ASC Structures, Structural Dynamics and Materials Conference*, Seattle, WA, AIAA, Vol. 1, 2001, pp. 515-522.

3.   Rajeev, P.T. and Farris, T.N., "Numerical Analysis of Fretting Contacts of Dissimilar Isotropic and Anisotropic Materials," *Journal of Strain Analysis*, In-Press.

4.   Spence, D.A., "An Eigenvalue Problem for Elastic Contact with Finite Friction", *Proceedings of the Cambridge Philosophical Society*, Vol. 73, 1973, pp. 249-268.

5.   Rajeev, P.T., Fretting Contact of Dissimilar Isotropic/Anisotropic Materials, *PhD thesis*, Purdue University, 2001.

6.   Hills, D. A., and Nowell, D., "Mechanics of Fretting Fatigue", Kluwer Academic Publishers, Drodrecht, Netherlands, 1994.

7.   Murthy, H., Harish, G. and Farris, T.N., "Efficient Modeling of Fretting of Blade/Disk Contacts Including Load History Effects," *ASME Journal of Tribology,* In-Press.

APPENDIX N

OVERVIEW AND APPLICATION OF CONTACT STRESS APPROACH TO ATTACHMENTS

This Appendix summarizes efforts at Pratt and Whitney (P&W) to develop and deploy advanced modeling tools that integrate accurate contact stress modeling with validated high cycle fatigue (HCF) life prediction. Included in this summary are: (1) advances in characterizing the evolution of contact stresses associated with mission load histories, including during periods of forced vibration, (2) predicting fatigue crack initiation driven by these near-surface stress fields and (3) validating an automated, design-oriented framework dubbed radical—robust attachment design integrating contact and lifing that melds achievements in these two areas with conventional finite element modeling techniques. Validation cases consist of fretting fatigue data generated by Purdue University, a P&W single tooth firtree (STFT) test, and a third stage fan disk and blade attachments from an F100 engine.

N.1 ACCURATELY MODELING STRESS HISTORIES IN BLADED-DISK ATTACHMENTS

The nominally flat geometry of conventional blade attachment and disk lug designs, while conducive for manufacturing and assembly, leads to highly concentrated stresses at and around the edges of the blade/disk contact interface. As detailed in [1] and [2], the computational expense associated with resolving these stresses accurately is daunting for two-dimensional geometries and prohibitive currently for three-dimensional models used routinely to analyze bladed-disk designs.

N.2 CONTINUUM MECHANICS APPROACHES TO CONTACT STRESS MODELING

Previous efforts have yielded a set of numerically efficient and robust tools for modeling the two-dimensional or line contact of nominally flat surfaces [3-4]. These tools enable solution of the singular integral equations (SIE) rooted in the theory of elasticity that govern the interaction between normal and tangential surface displacements

associated with fretting and galling and the resulting contact pressure, frictional traction and edge-of-contact stresses that drive fatigue damage. For the case of contacting surfaces with similar elastic properties (i.e. a fan or compressor stage comprising a titanium disk and blades), the uncoupled system of equations can be solved within a matter of seconds for the near-surface contact stress fields using a Fast Fourier Transform (FFT) algorithm. P&W has adapted the contact analysis code which embodies these principals, CAPRI, for use in predicting blade and disk attachment contact stresses.

N.3 QUASI-DYNAMIC VIBRATORY ANALYSIS (QDVA) FOR HCF ENVIRONMENTS

Procedures for modeling near surface elastic contact stresses both accurately and efficiently for two-dimensional contacts subjected to spectral or mission-type tangential *and* eccentric normal loads representative of bladed-disk attachments, also had to be developed. In transitioning such a tool to a design environment where three-dimensional finite element models of bladed disks are ubiquitous, links must be established between the FFT-based contact analysis and such finite element models, empowering designers with mechanics-based insight into the influence of factors like geometric details, manufacturing tolerances and coatings on damage tolerance of blade attachments and disk lug configurations.

Such a global-local hybrid approach that treats axial slices of the blade attachment and disk lug geometries represented in a three-dimensional finite element model as isolated two-dimensional contacts has been proposed and implemented successfully for static analyses requisite for LCF-type assessments of mission histories. In this hybrid approach, a coarse blade attachment/disk lug mesh that includes the non-linear influences of frictional contact is used to solve the statically indeterminate eccentric normal and tangential reaction loads between the blade and disk—reactions which are then used as inputs to the FFT-based contact analysis.

Direct application of this methodology to understand non-linear reaction load and contact stress histories during forced responses of the bladed-disk is precluded, given that such responses are typically characterized by first obtaining modal results from a linear solution of the eigenvalue problem:

$$\left([K] - \omega^2 [M]\right)\{\hat{u}\} = 0 \tag{N1}$$

where [M] is the elemental mass matrix and [K] is the model stiffness matrix that may include influences such as stress-stiffening and spin-softening associated with high-speed rotation of the rotor structure. In such an analysis, the contact interaction at the blade/disk interface is often modeled in a linear fashion with displacement constraint equations that prevent interpenetration of the blade attachment and disk lug nodes; and enforce either a no-slip/infinite friction or pure sliding/zero friction condition in the tangential direction.

A procedure with the moniker quasi-dynamic vibratory analysis (QDVA) is being proposed to bridge this gap between conventional modal analysis procedures and the need to obtain contact reaction loads for the FFT-based contact analysis. As outlined in steps 2 through 5 portrayed in Figure N1, the QDVA process involves conducting an incremental static analysis including Figure N1 – Robust Attachment Design Integrating Contact and Lifing frictional contact at the blade/disk interface using a load history comprised of a nodal force history determined by scaling the modal force history generated from the aforementioned eigenvalue problem. This scaling factor may be determined from either recorded or predicted stage vibration levels (strain gage readings, tip deflection measurements, etc.); or by design-system criteria for acceptable vibratory responses. This scaled modal force history is enforced over the entire model, save at the blade/disk interface—which is resolved through the use of contact elements on the surfaces of the blade attachment and disk slot. Implicit in this approach is the assumption that the set of interfacial displacement boundary conditions imposed during the modal analysis (and thus used to generate the scaled modal force history) are identical to those during the actual vibratory response of the airfoil. Figure N2 presents the simulated evolution of contact pressure on the surface of a disk lug slot from an idle condition (Point #1), to sea level takeoff conditions (Point #2), through one-and-one-half cycles of a blade-dominant vibratory response.
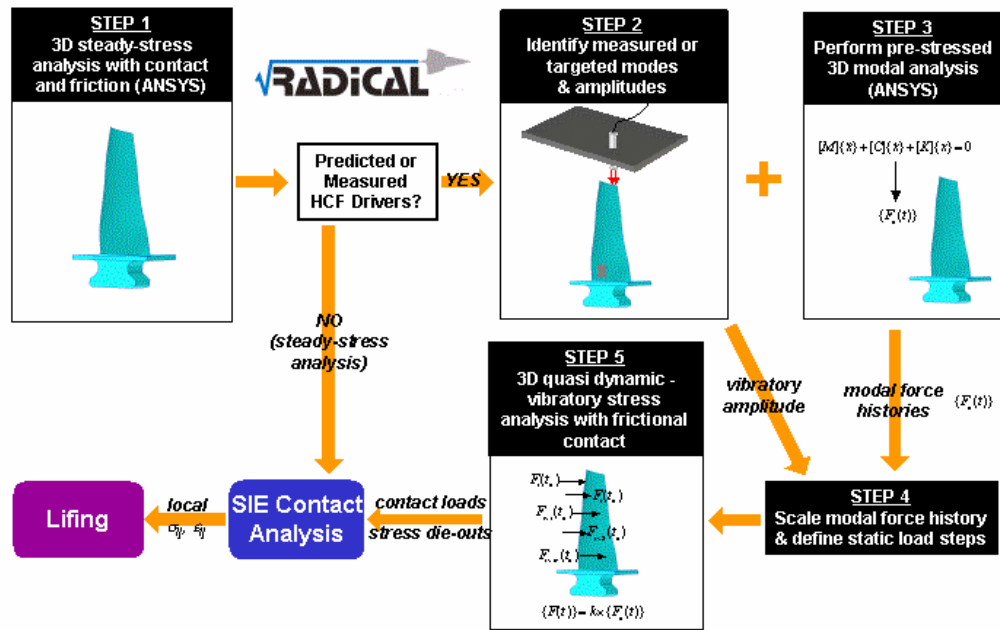
Figure N1. RADICAL overall procedural flow chart.
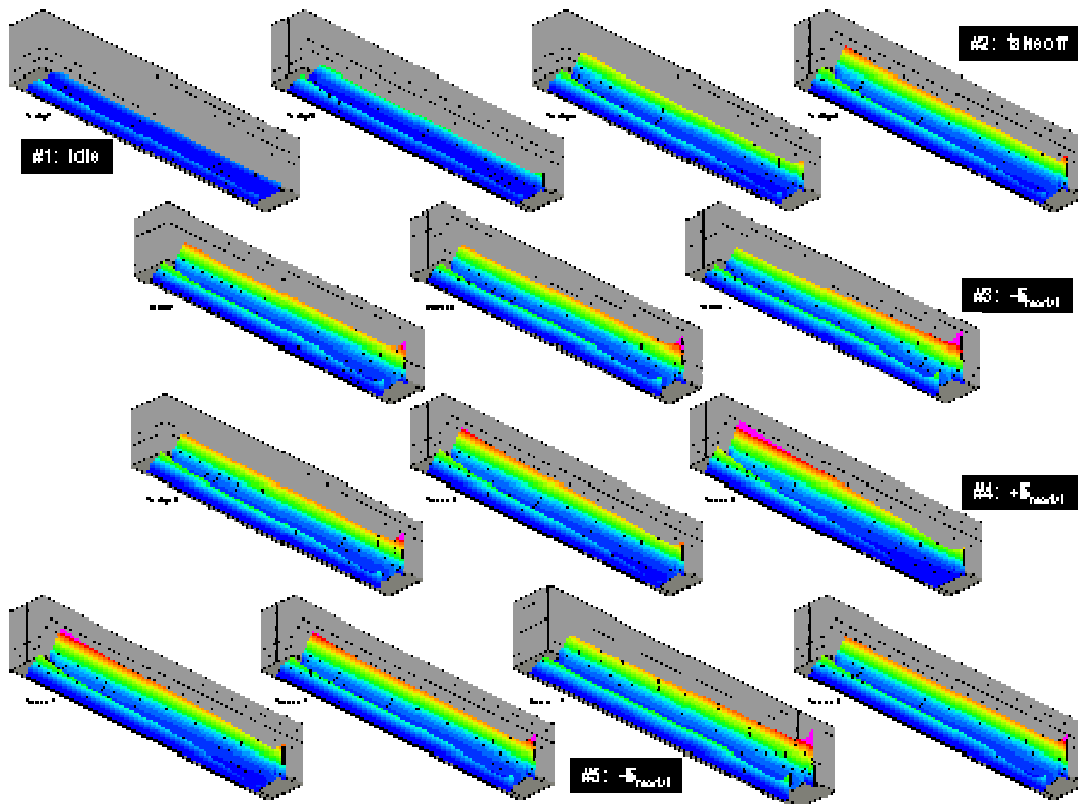
Figure N2. Evolution of contact pressures through mission loading.

N.4   OVERVIEW OF CONTACT STRESS APPROACH

Robust Attachment Design Integrating Contact And Lifing (RADICAL) - The RADICAL analytical procedure was developed in an effort to better characterize contact loads during an HCF event. An overall flowchart of the procedure is shown in Figure N1.

The 'SIE Contact Analysis' and the subsequent lifing uses these contact loads and extracted bulk stresses to calculate edge of contact stresses in locations affected by the 'unsteady' or vibratory loads. Since it is difficult to meld the vibratory and steady stress analyses the quasi-dynamic-vibratory RADICAL procedure was developed. The 'Outline of Steps for the RADICAL Process' (shown below) gives a step by step explanation of the way in which the vibratory loads are added to the critical condition while preserving an abbreviated mission history. This mission history must be preserved in order to get the proper load path for the frictional contact.

N.5   OUTLINE OF STEPS FOR THE RADICAL PROCESS

1.   Setup Finite Element Model with appropriate features.

2.   Run ANSYS solution of 'Initial Condition' (ex. Idle, …)

3.   Restart and rerun 'Initial Condition' solution with appropriate coefficients of friction (μ) applied.

4.   Complete solution of FEM ramped to 'Critical Condition' (ex. Conditions at appropriate spin of critical HCF driver) for each μ from the 'Initial Condition.'

5.   Tighten Convergence tolerance and restart/rerun 'Critical Condition' Solution.

6.   Use 'Critical Condition' results to run a static pre-stress analysis for each μ. If necessary include large deformation effects.

7.   Vibratory analysis – For each pre-stress conditions complete a modal analysis, with or without cyclic symmetry effects for the given frequency and nodal diameter.

8.   Extract loads from Vibratory Analysis

9.   Apply Vibratory Load to 'Critical Condition' Static Analysis.

10.   Restart 'Critical Condition' and solve with added vibratory load.

11.   Restart last solution with vibratory load subtracted.

12.   Add/Subtract vibratory load until friction effects have been shaken out.

13.   Extract

N.6   AUTOMATION OF THE HCF/EDGE OF CONTACT ZONE LIFE PREDICTION PROCESS

To aid in conducting routine contact stress analyses and HCF life prediction a macro has been developed at P&W for analysts. The analysis procedure works with ANSYS and calls the CAPRI code to produce contact stresses. The contact area in the 3D finite element model is broken into a number of two-dimensional slices and loading information extracted. This information is fed to CAPRI and the contact stresses determined at the surface and into the depth of the contact region. The contact stresses are then combined with the existing stresses or bulk stresses, which are not the result of the surface contact phenomena, to produce stresses for the life prediction methodology. Features included in this analysis code include:

- GUI dialog box pops up to select input file
- Input deck parsed for requisite geometry, "material" properties, and job info

N.7   PREDICTING FATIGUE CRACK INITIATION UNDER MULTI-AXIAL LOADING

By melding this QDVA process with the global-local hybrid approach and FFT-based analysis for calculating continuum-level contact stresses, the stated goal of developing a computationally efficient framework for characterizing accurately the near surface conditions that drive fatigue cracking in bladed-disk attachments is realized. For this information to be employed effectively within an agile design system to produce optimized and damage tolerant components, these near surface conditions must be interrogated through the use of lifing metrics or criteria.

The complex nature of the thermal and mechanical influences on the bladed disk, in addition to the influence of frictional contact, typically results in a highly non-

proportional and multiaxial near surface stress history in the attachment components. This fact, coupled with the desired to support a lifing system based on timely and cost-effective specimen data, mandates the use of lifing approaches that collapse specimen data generated over a range of stress ratios and load histories into a single parameter or set of parameters.

N.8 VALIDATION OF THE RADICAL METHODOLOGY

Several approaches, including various critical plane multiaxial fatigue parameters [5] or stress-invariant approaches [6], have been proposed for handling the multiaxial stress histories experienced by bladed-disk attachments. It has been established that there is excellent correlation between the Findley parameter predicted initial life and the observed specimen total lives. Gaining confidence in this multiaxial fatigue life parameter solidifies the last component in the framework for robust attachment design through the integration of contact analysis and lifing (RADICAL), as outlined on Figure N1. Three efforts to validate this design framework at P&W were evaluated and two have been completed successfully to date.

N.9 FRETTING FATIGUE DATA CALIBRATION (P&W)

The goal of the first of these efforts was to predict failure lives in a set of well-characterized fretting fatigue tests conducted on the same pedigreed titanium alloy used to establish the multiaxial fatigue model. The contact geometry and loads in this series of tests were selected to generate conditions typical of those in bladed-disk attachments [6]. Furthermore, a separate series of careful experiments were conducted to establish the steady-state coefficient of friction ($\mu = 0.5$) present at the contact interface for nearly the entire duration of the test, thereby completing the set of requisite parameters for the FFT-based contact stress analysis. Figure N3 reveals an excellent correlation among the observed total lives of the fretting fatigue specimens and predictions made applying the Findley parameter to near-surface stresses averaged over a 0.003" depth. The actual over predicted strength capability is shown in Figure N4.
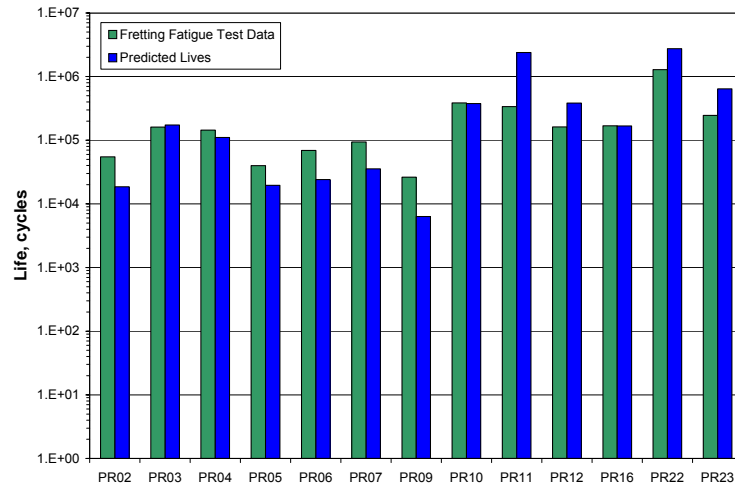
Figure N3. Comparison of fretting fatigue data to predictions at mean level.
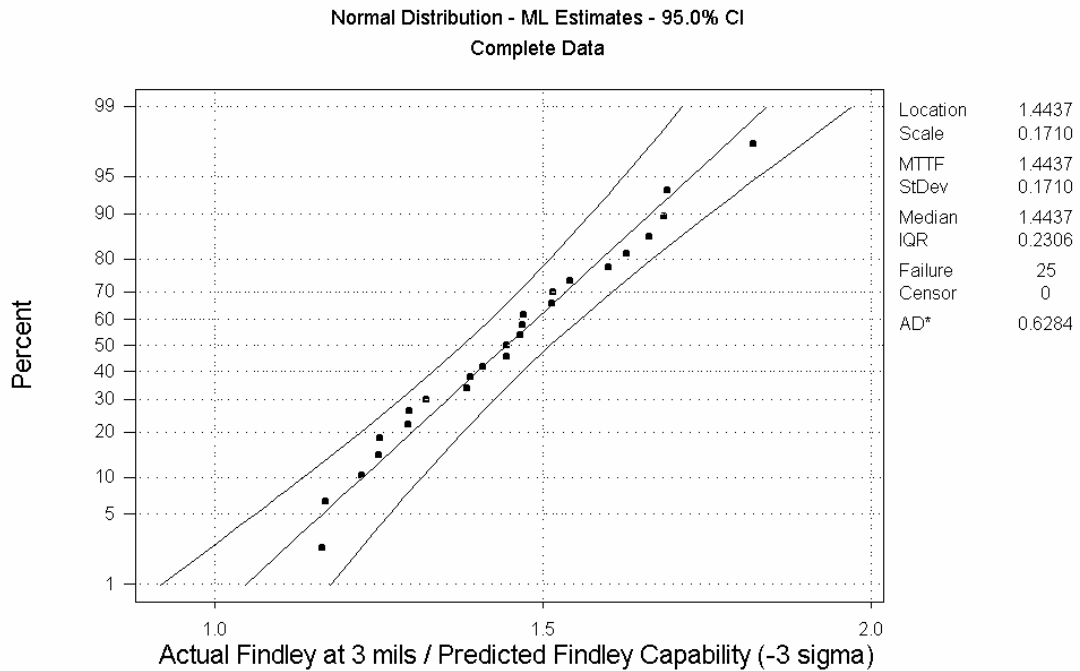
N4. Actual/predicted on fatigue capability for fretting fatigue data.

N.10   SINGLE TOOTH FIRTREE FATIGUE DATA CALIBRATION

Figure N5 provides a similar comparison for a separate specimen configuration designed to directly simulate the conditions in a bladed-disk attachment.
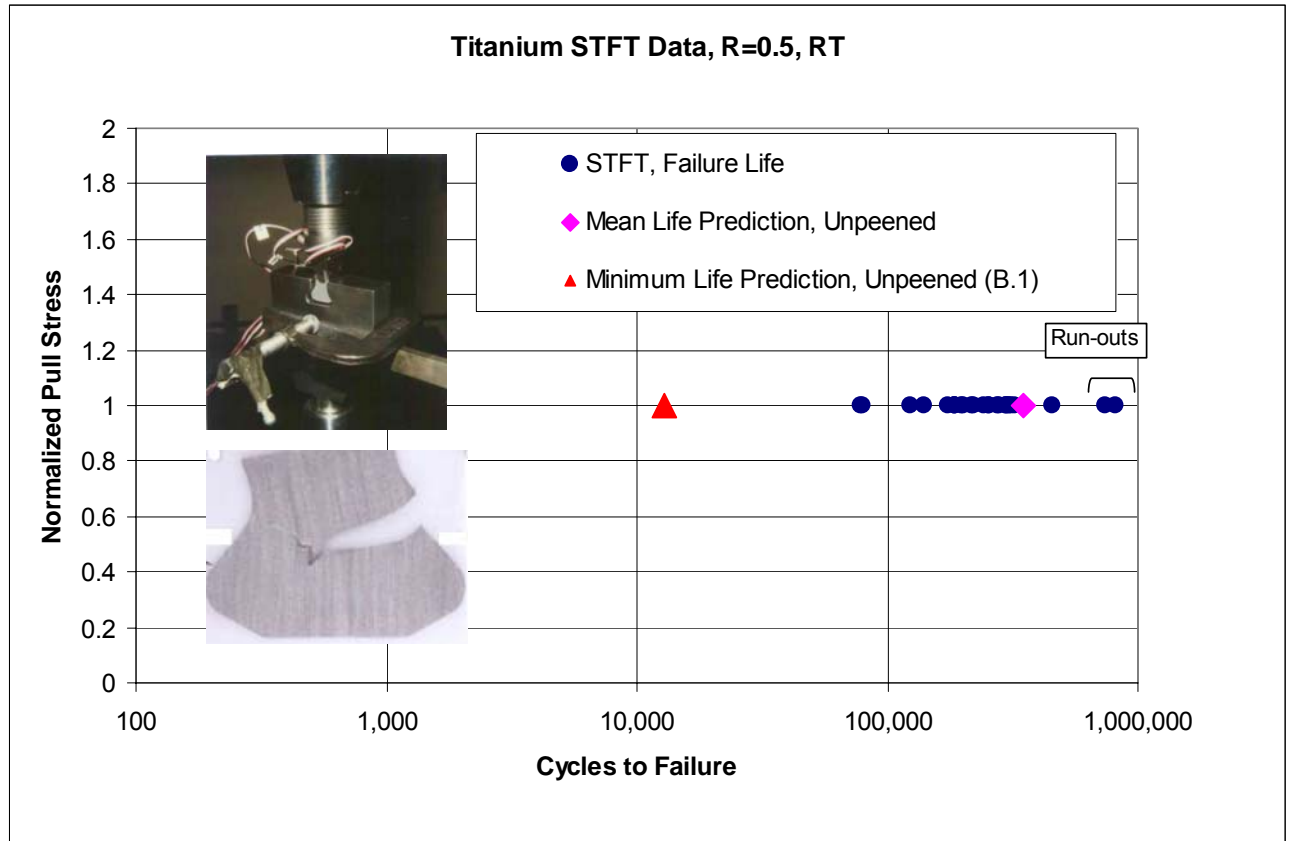
Figure N5. Comparison of titanium STFT fatigue data to predictions.

A quarter-symmetry finite element model of this single-tooth fir tree specimen was used to provide the contact reaction loads at the tooth/lug interface as the specimen was subjected to a remote pull load cycled between 2000 and 8000 lb., as shown in Figure N6.   It must be noted that obtaining direct and accurate measurements of the eccentric normal and tangential loads in this type of setup is virtually untenable; as with bladed-disk attachments, the finite element method provides the best alternative for resolving the statically indeterminate problem. Upon obtaining contact surface reaction

forces associated with a friction coefficient of μ = 0.25, corresponding contact stress histories were determined. These contact stresses were interrogated in the same manner as those from the fretting fatigue tests—by averaging the near surface stress gradients over a depth into the surface (0.0015") and calculating the associated Findley parameter. As seen clearly on Figure N5 the life predictions made using mean and -3σ fatigue capability characterize conservatively the range of observed total lives. The ratio of the Findley value at 1.5 mils below the surface over the Findley fatigue strength (-3σ) is 1.47. The analysis not only predicted the proper failure location, but the life prediction was comparable to the actual test experience as well on a mean basis.
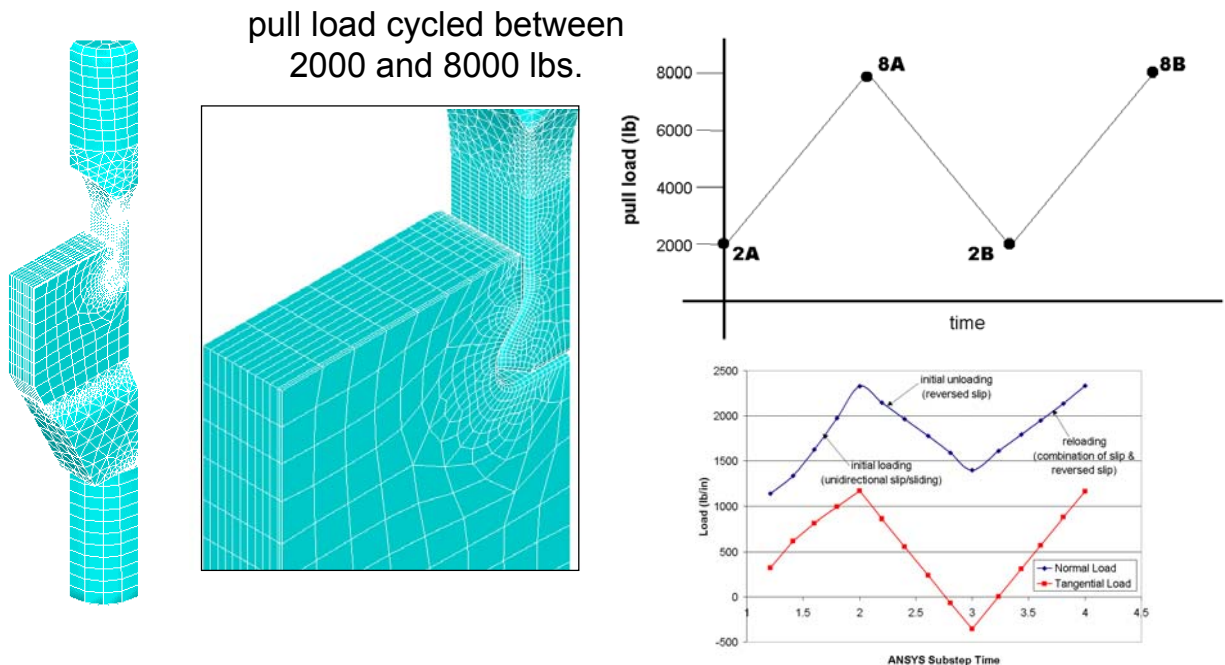
Figure N6. Titanium STFT Finite Element Model, cycle, and contact stresses.

N.11   F100 ENGINE THIRD STAGE FAN DISK / BLADE ATTACHMENT FROM AN DATA CALIBRATION

The F100-PW-229 3rd stage fan disk and blade, see Figure N7, has been put through the initial part of the RADICAL analysis process. This process consists of: (1) three dimensional finite element analyses with and without contact to characterize both static and vibratory responses of bladed disk designs, (2) engine data or aeromechanical

predictions characterizing vibratory responses, (3) serial two-dimensional quasi-analytical contact analyses conducted using finite element method input, and (4) interpretation of the accuracy of the stress histories within the context of a validated lifing system.
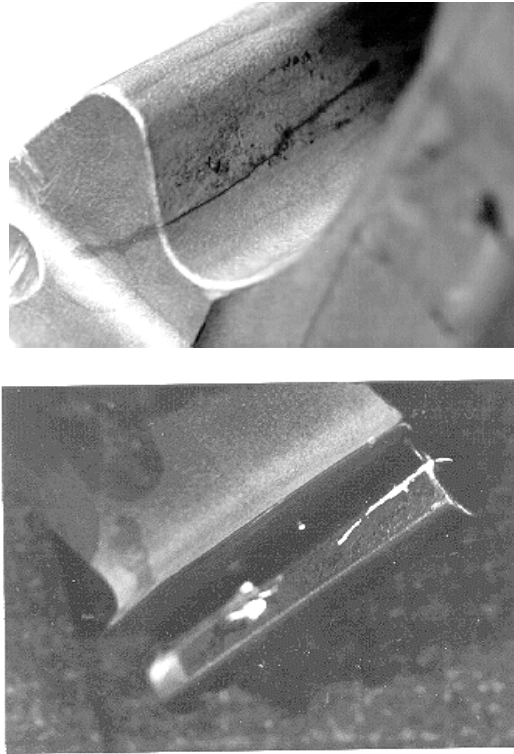
N7. Cracked disk and 3rd stage fan blade.

The root cause analysis identified the problem as a 14E 3rd blade resonance from the intermediate case struts bow wave. This was confirmed with strain gage and NSMS testing, analytical modeling, and lab testing / stress ratios at the attachment, see Figures N8 and N9. Figures N10 and N11 show the finite element models of the 3rd stage fan disk and blade used for the analysis. Resulting vibratory loadings from the NSMS testing were applied to these models to determine loading in the contact area of the attachment.

1995 Strain Gauge Testing Identified Stiffwise Bending as Having Highest Attachment Stress

PW229 3rd Blade Campbell Diagram
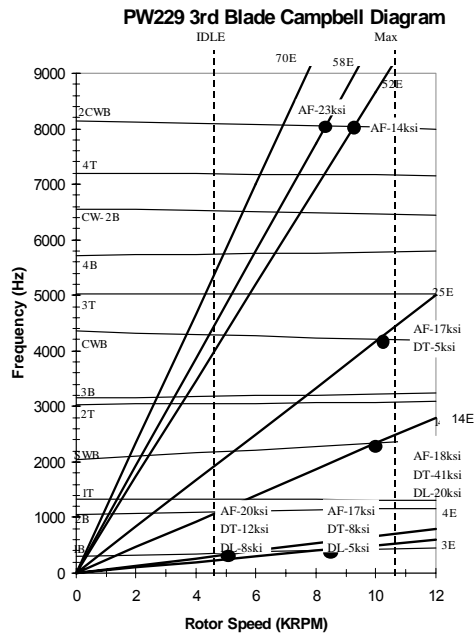
- Maximum Measured Vibratory Stress for Stiffwise Bending Mode

- Excited by 14 Intermediate Case Struts

- 14E resonance occurs at SL Mil power

- Max Stress measured in 1997 on FX178 with NSMS and verified 14E 3rd attachment cracking driver.

Figure N8. Strain gage results indicate 14E stiffwise bending as driver.

F100-PW-229 Fan (P0012) Instrumentation Summary
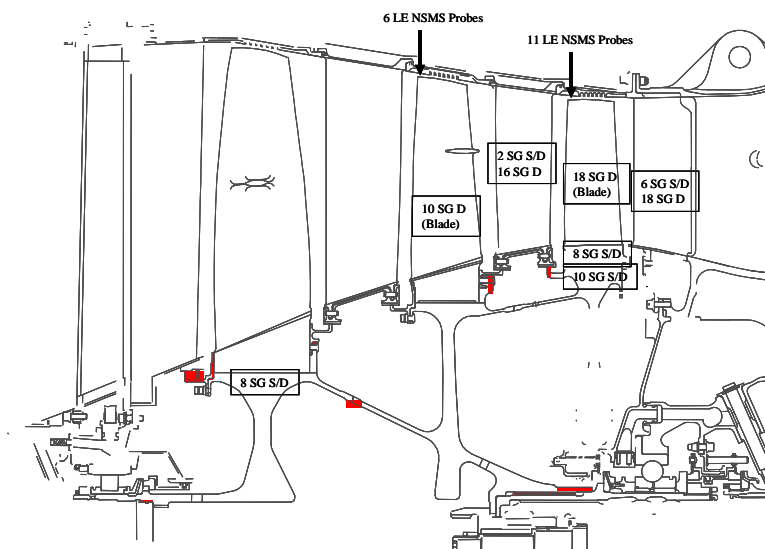
Figure N9. Location of NSMS probes for fan.
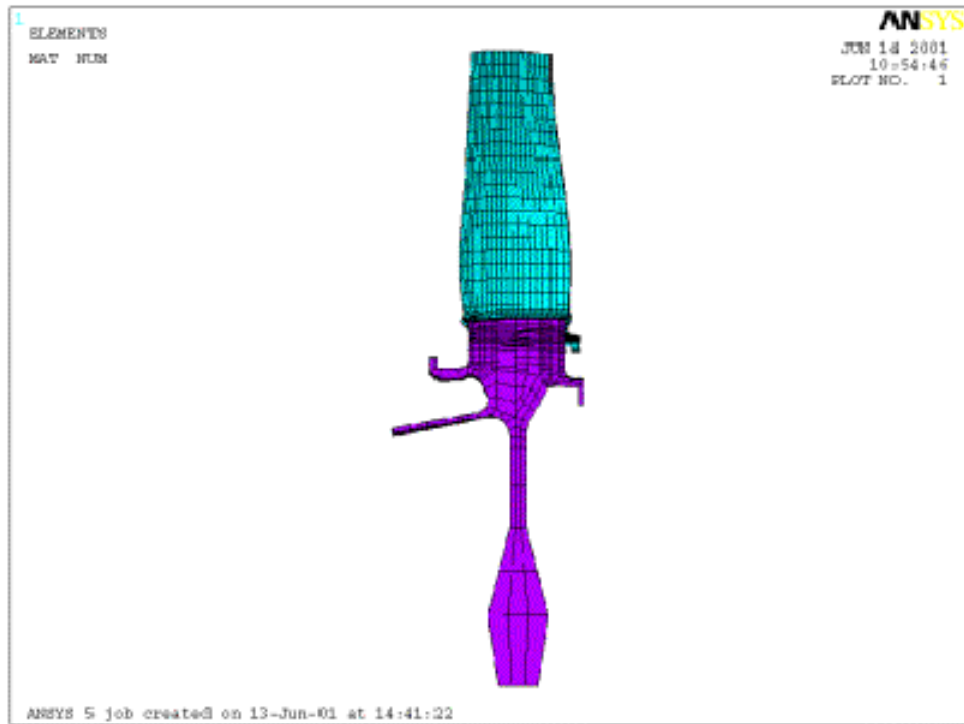
Figure N10. Finite element model of 3rd stage fan disk.
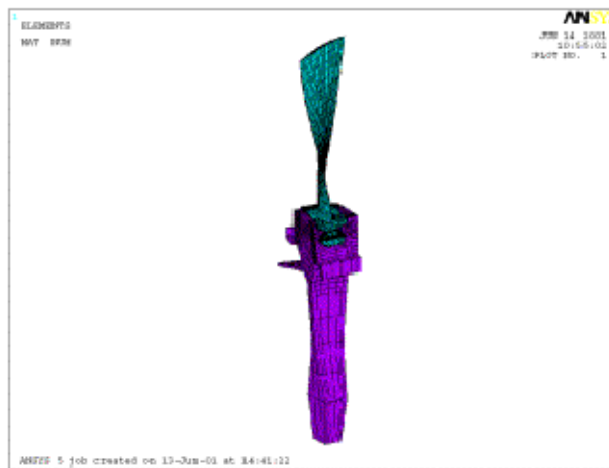
Figure N11. Finite element model of 3rd stage fan blade.

A key consideration in understanding the amount of HCF exposure each of the blades experienced is which engines saw accelerated mission testing (AMT). The number of engines affected has been identified and cyclic time on each of the engines in the fleet at the time the cracking incidents occurred has been collected. Figure N12 shows how the AMT engines experienced additional vibratory exposure because of the engine test cycle. This added exposure to 14E put the AMT affected engines at the extreme of the overall distribution based HCF cycles accumulated as indicated in Figure N13.

Time at Resonance Different for AMT's vs Fleet Average

N1 — AMT's repetitive in nature

N1 — Field is unique in nature. N1 affected by changes in Mn, Alt, Temp, and Press

Time in Resonance In 4000 TACs

1.86X — 1x13⁹ cycles

Time in Resonance (hours)

AMTs — Avg Field — Individual Bases

• Evaluations of flight data has shown cracked AMT's spent more time on average in the resonance speed range 9,700-9,950 (Mil + time) than field

• N1 on AMT relatively constant (PT2, TT2, Mn and Alt)

• N1 varies on field engines as PT2, TT2, Mn and altitude change.

• Typical field engine is in resonance range for 84 hrs in 4000 TAC's

• Avg AMT time at resonance is 156 hrs in 4000 TAC's

Figure N12. Affect of AMT cycle on HCF exposure levels.
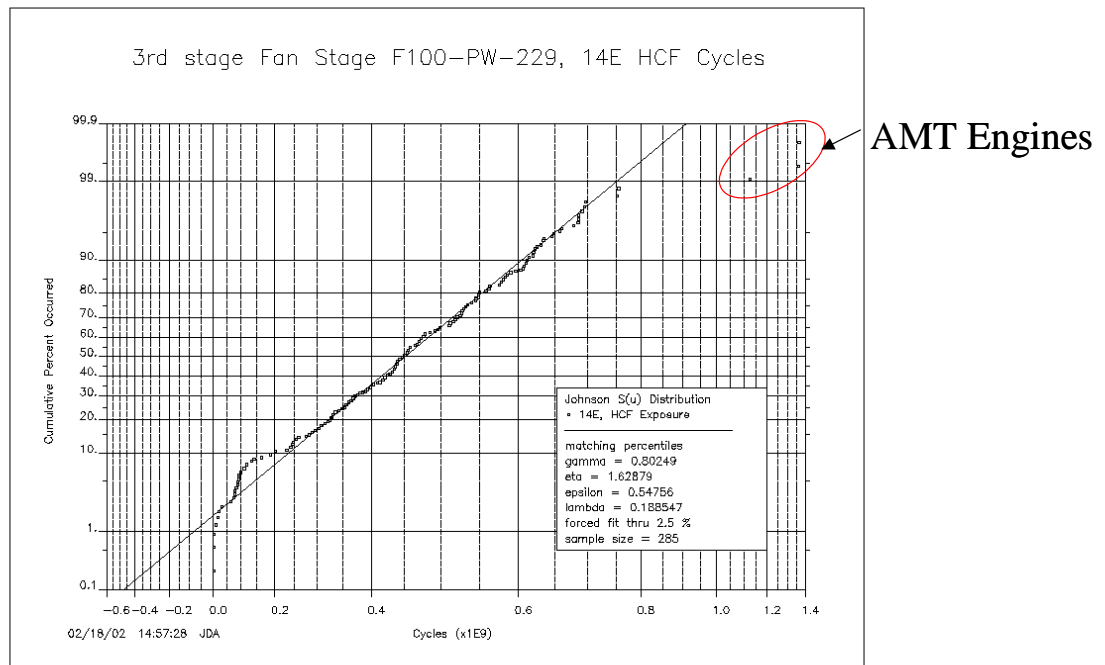
Figure N13. HCF exposure levels for fleet.

Interpretation of the life results in the context of applying both the total life and threshold based fracture predictive system was attempted. The early analysis results indicated that the proper location of cracking in both the blade and disk attachment was not correctly predicted. A review of the contact analysis procedures for the angled slot has not yet been completed but is suspected to be the problem.

N.12   SUMMARY

Validation of the HCF life system has been completed up to the subcomponent level. Modification of the contact analysis processor for angled slots in the 3rd stage fan disk have not yet been completed, but are expected to resolve the issue on proper prediction of the cracking location. Once that has been accomplished then a comparison to HCF field experience can be completed.

N.13 REFERENCES

1. McVeigh, P. A. and Farris, T. N., "Finite Element Analysis of Fretting Stresses," *Journal of Tribology*, Vol. 119, No. 4, 1997, pp. 797-801.

2. Griffin, J., Sinclair, G. B., Comier, N. G. and Meda, G., "Contact Stresses in Dovetail Attachments: Finite Element Modeling", in proceedings of <u>1999 International Gas Turbine and Aeroengine Congress and Exposition</u>, Indianapolis, IN, 1999, 99-GT-387.

3. McVeigh, P. A., Harish, G., Farris, T. N., and Szolwinski, M. P., "Modeling Interfacial Conditions in Nominally Flat Contacts for Application to Fretting Fatigue of Turbine Engine Components," *International Journal of Fatigue*, Vol. 21, Supplement 1, 1999, pp. S157-S166.

4. Rajeev, P. T. and Farris, T. N., "Numerical Analysis of Fretting Contacts of Dissimilar Isotropic and Anisotropic Materials," *Journal of Strain Analysis*, In-Press.

5. Szolwinski, M. P. and Farris, T. N., "Mechanics of Fretting Fatigue Crack Formation," *Wear*, Vol. 198, 1996, pp. 93-107.

6. H. Murthy, T. N. Farris, and D. C. Slavik. "Fretting fatigue of Ti-6Al-4V subjected to blade/disk contact loading", <u>Developments in Fracture Mechanics for the New Century</u>, 50th Anniversary of Japan Society of Materials Science, 2001, pp. 41-48.

APPENDIX O

UNCOATED HCF BEHAVIOR AND MODELING

O.1   BACKGROUND

The 1900F portion of the work on Total Life approaches was initially planned to be executed with uncoated specimens. Even though most airfoil surfaces exposed to 1900F conditions are coated for environmental protection, this decision was based on the desire to keep the materials aspects as simple as possible and to avoid having to choose one of many different coating systems. Thus the work in that task was started with uncoated specimens. After completing the testing and analysis described below, it became apparent that the lack of a coating was significantly affecting the behavior of the material, and that to produce models which were relevant to turbine blade airfoil behavior, it would be necessary to apply an environmental coating. Thus the remainder of the program was completed using a PtAl diffusion aluminide coating.

O.2   APPROACH

The effort described in this Appendix reports the work performed on uncoated material prior to the decision to coat, and while not directly applicable to the effort described in the main body of the report, was nevertheless instructive and helpful in guiding the coated effort. The technical approach was similar to that adopted for the coated effort: testing was performed at 1900F to determine frequency effects and to identify HCF-rupture interactions.

O.3   RESULTS

O.3.1   Frequency Effects

High frequency HCF testing was performed at GE-AE using <001> oriented specimens of the type shown in Figure 4.77 (see Section 4.3.1.1*B*). Testing was at 1900°F, at frequencies of 59, 200, and 900 Hz. A stress ratio of R = -1 was used to eliminate or reduce contributions of rupture damage which could occur with positive mean stresses. The test results are shown in Table O1. Figure O1 shows the results plotted on a cycles to failure basis. This figure suggests that for uncoated material cycles to failure may be dependent on frequency since the results at

900 Hz tend to show better HCF capability than at 59 or 200 Hz, especially at longer lives. On the other hand, 59 and 200 Hz results are essentially comparable. Some coated results from later tests are shown for comparison.

Table O1. Uncoated PWA 1484 HCF Results, 1900°F, R = -1

S/N	Freq (hz)	Alt stress (ksi)	Nf
A2LLA-2	59	40.0	11,225,134
A2LLA-4	59	35.0	12,014,373
A2LLB-2	59	45.0	4,927,212
A2LLB-4	59	35.0	17,408,933
A2LLC-2	59	35.0	21,437,295
A2LPZ-3	200	39.0	7,194,950
A2LRC-2	200	37.0	8,406,463
A2LR1-2	200	35.0	8,377,436
A2LRB-1	200	32.0	28,264,688
A2LRB-5	900	40.0	59,662,836
A2LR2-2	900	50.0	4,896,538
A2LR1-4	900	46.0	6,844,156
A2LPZ-5	900	43.0	7,150,000
A2LRC-4	900	42.0	3,421,975
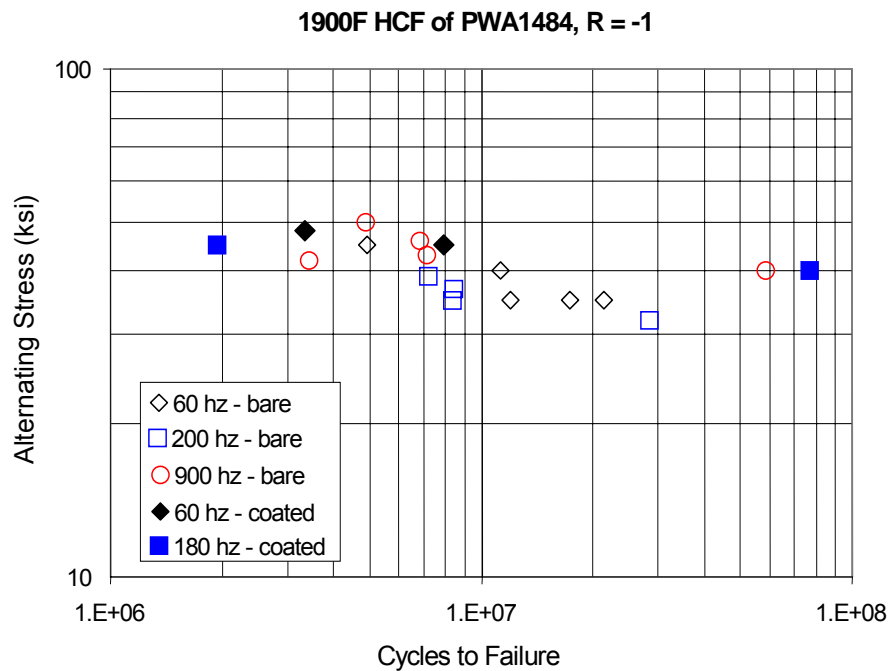
Figure O1. 1900F HCF of uncoated and coated PWA 1484 at various frequencies; R = -1.

Figure O2 shows the same results plotted as <u>time</u> to failure. Here the data are ordered differently, with 59 Hz lying above 200 and 900 Hz. Power law curve fits through each frequency separately yielded the curves shown, with correlation coefficients, R, of 0.92 for 200 Hz and 0.54 for 900 Hz. The reason for the greater variability at 900 Hz is not known at present. However, the data from 200 and 900 Hz are not far apart; treating them as a combined single population leads to a power law fit with a correlation coefficient of 0.87. This is a respectably large value that suggests that when treated on a time-to-failure basis the behavior over this frequency range may be similar. This is similar to behavior seen by GE on Rene' N5 at higher mean stress.
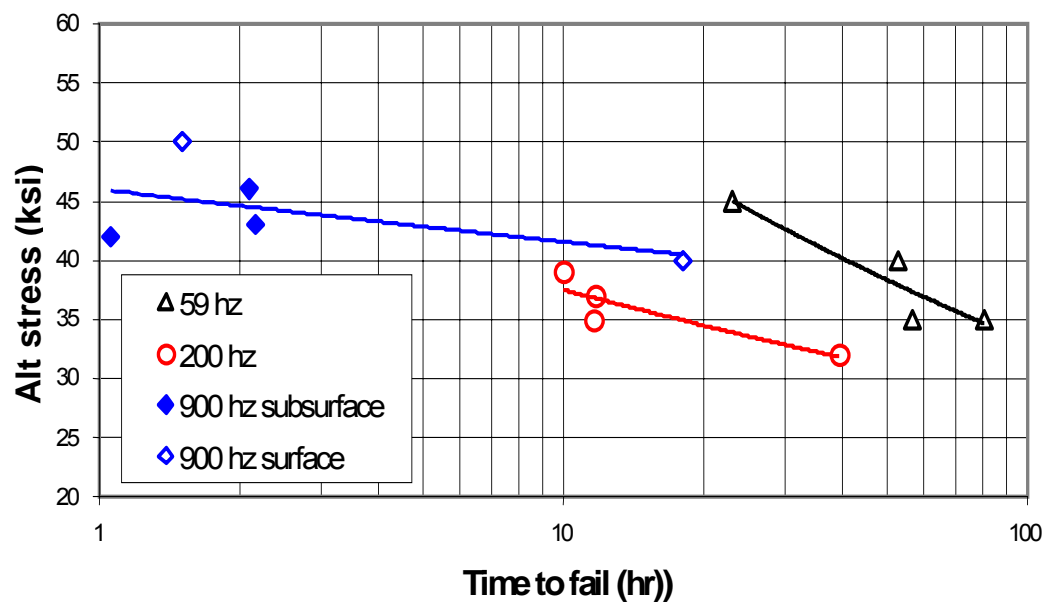
Figure O2.   1900F, R = -1 HCF capability of PWA 1484 plotted as alternating
stress vs. time to failure for various frequencies.

Failure analysis was performed on these specimens. All specimens were examined visually and classified as having either surface or subsurface origins (examples of both will be shown). Figure O2 shows that all of the specimens with subsurface origins (filled points) failed in fairly short times, while all but one of the surface failures (open points) occurred at longer lives. The one short time surface failure (900 Hz, 50 ksi alternating stress) had an unusual amount of oxidation compared to others with similar failure times; it is possible, though not confirmed, that it spent extra time at temperature during test setup. While the three subsurface failures at 900 Hz fell on the same stress-time to failure line in Figure O2 as the 200 Hz data, this

seems fortuitous, since the failure modes are different. A comparison of the 900 Hz surface failures with the 200 Hz surface failures suggests that the frequency effects are not purely time dependent in this regime, but that the 900 Hz surface failures are about 2X longer life than the 200 Hz surface failures.

A more detailed SEM and metallographic examination was performed on 3 representative specimens: one at 200 Hz (39 ksi, 7.2 x10^6 cycles, 10 hr life), a second at 900 Hz with approximately the same cycles to failure (43 ksi, 7.1 x10^6 cycles, 2.2 hr) and a third at 900 Hz with approximately the same time to failure as the 200 Hz specimen (40 ksi, 58.6 x10^6 cycles, 18.1 hr).

Figure O3 shows that the 200 Hz specimen failed from the surface (bottom of Figure O.3) in a flat, relatively featureless mode, transitioning into a <111> crystallographic mode at
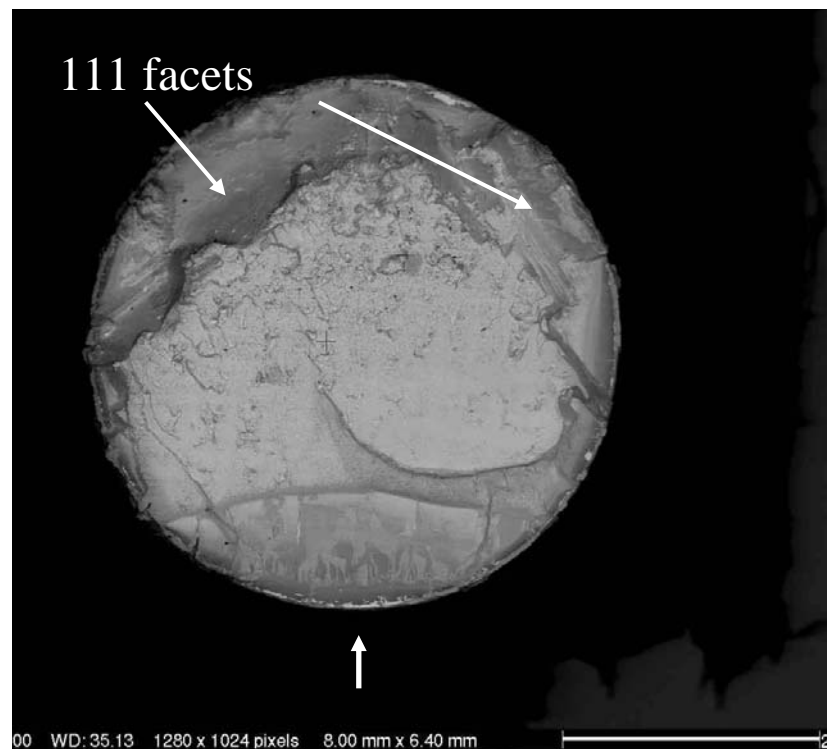
Figure O3.   Fracture surface of 200 Hz specimen (7.2 x10^6 cycles, 10 hr life) showing oxidized surface origin (arrow), flat propagation mode, and crystallographic overload cracking.

final fracture (top of Figure O3). The surface of the specimen was covered with uniformly spaced linear oxidized ridges perpendicular to the stress, Figure O4. Metallographic sectioning parallel to the specimen axis showed (Figure O5) that these ridges were oxide nodules protruding from the surface, and were the source of regularly spaced cracks (average of 137 µm) extending into the specimen. An etched view of the same area, Figure O6, shows that the cracks were often associated with the interdendritic regions of the microstructure and the crack spacing was similar to the secondary dendrite arm spacing (130 µm). This appearance is identical to that reported in [1] for LCF of uncoated Rene N4.
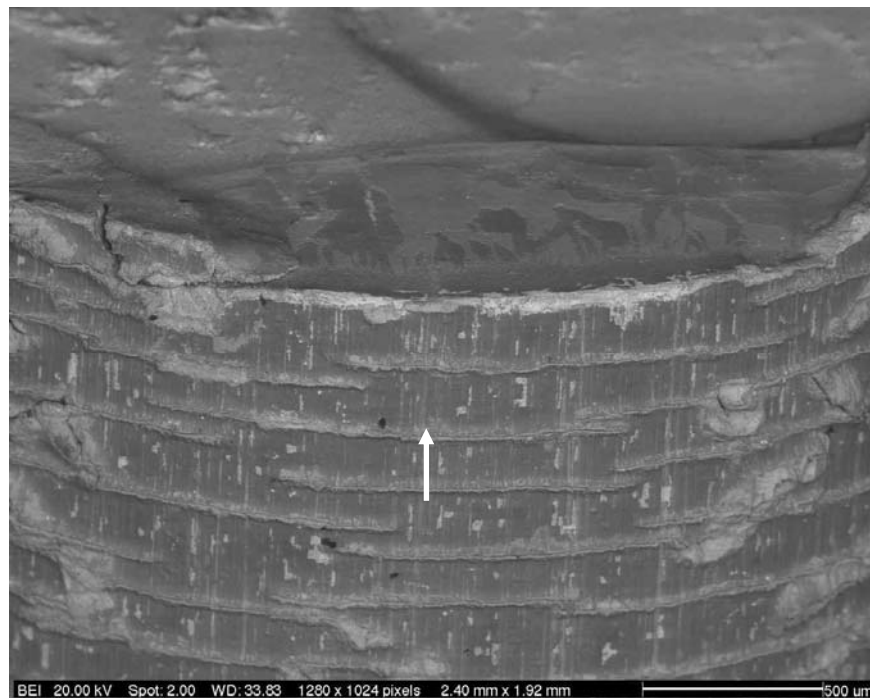
Figure O4.   Regularly spaced oxide ridges and cracks on surface of 200 hz specimen (7.2 x10^6 cycles, 10 hr life) below the origin (arrow).
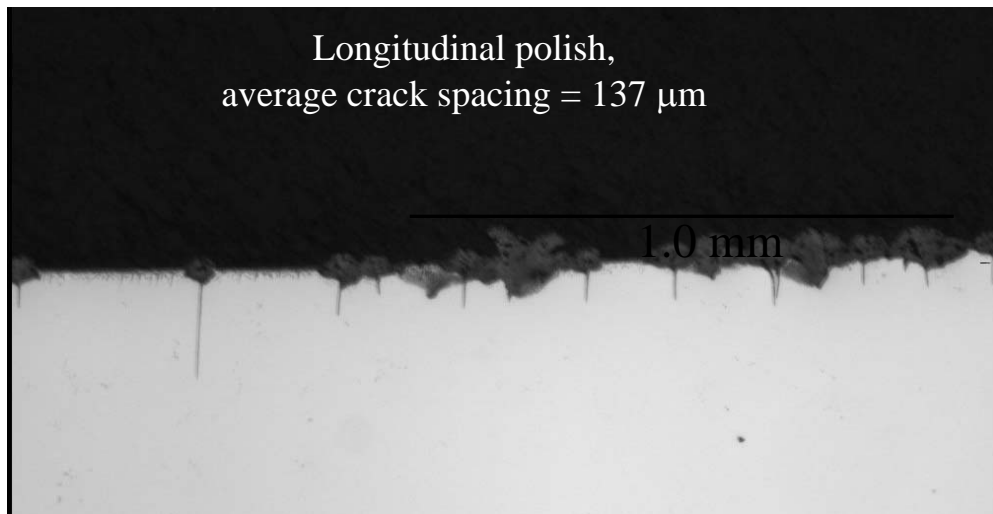
Figure O5. Metallographic section of 200 Hz specimen (7.2 x10^6 cycles, 10 hr life) showing regularly spaced oxide ridges and surface cracks.
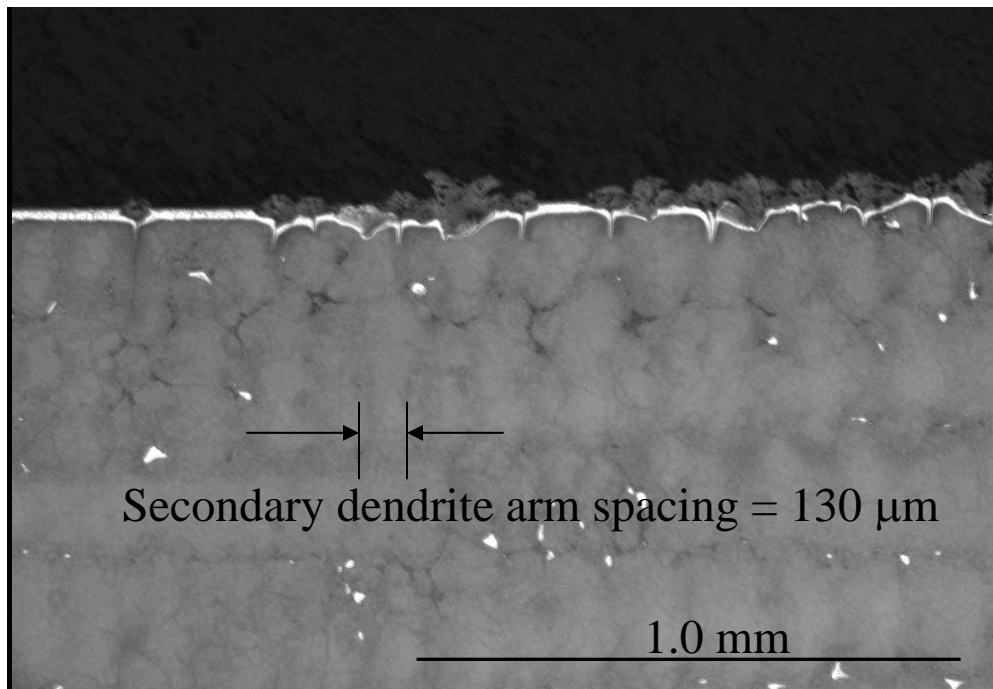
Figure O6. Etched metallographic section of 200 Hz specimen (7.2 x10^6 cycles, 10 hr life)showing similar spacing of surface cracks and secondary dendrite arms.

The high stress, shorter life 900 Hz specimen, Figure O7, failed from an internal site whose nature was not identified. The cracking transitioned into a crystallographic mode more quickly than for the 200 Hz specimen, and the majority of the fracture surface was covered by <111> facets. Figure O8 shows these facets, as well as the initial development of a pattern of uniformly spaced surface cracks. The time of this test, 2.2 hr, is less than that of the 200 Hz test (10 hr) so the oxidation-driven surface cracking had not developed yet.

Figure O7. Fracture surface of high stress 900 Hz specimen (7.2 x10^6 cycles, 2.2 hr life) showing internal origin (black arrow), and transition to crystallographic cracking.
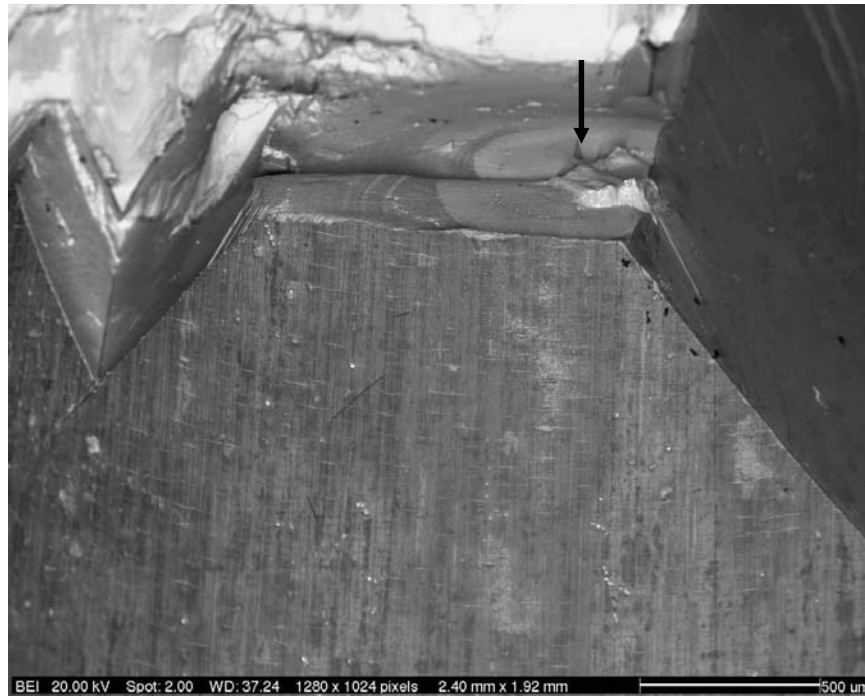
Figure O8.   Surface of high stress 900 Hz specimen (7.2 x10^6 cycles, 2.2 hr life) showing internal origin (black arrow), and early development of regular surface cracks.

The lower stress, longer life 900 Hz specimen showed a surface origin, Figure O9, like the 200 Hz specimen, and extensive surface oxidation, Figure O10. The heavy surface oxide obscured a pattern of regular, 130 μm spaced cracks extending in from the surface, Figure O11, with appearance similar to that of Figures O5 and O6.
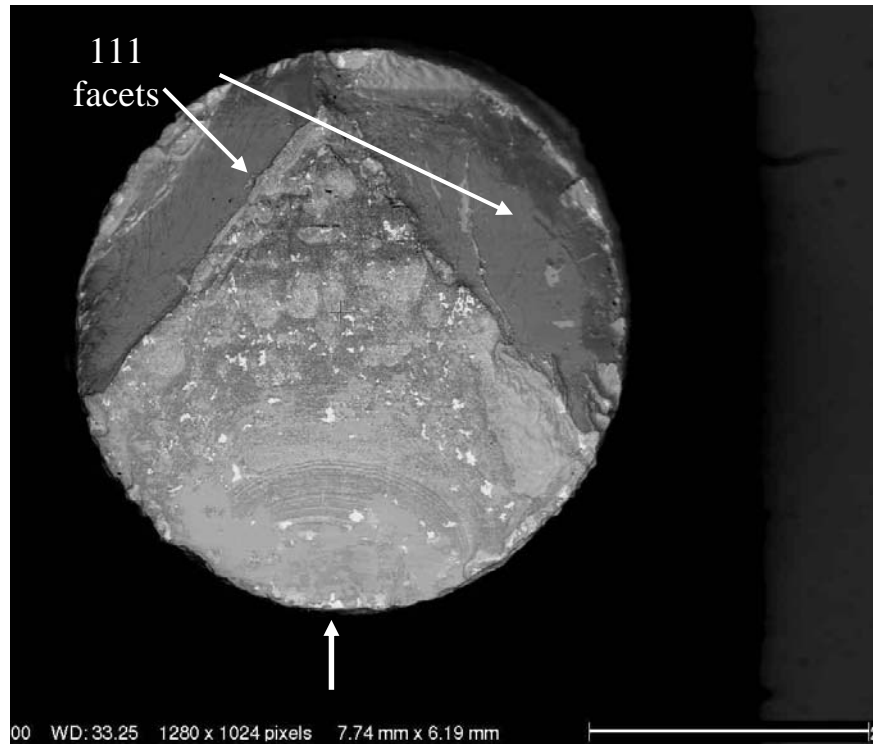
Figure O9. Fracture surface of low stress 900 Hz specimen (58.6 x10^6 cycles, 18.1 hr) showing surface origin (arrow), and transition to crystallographic cracking.
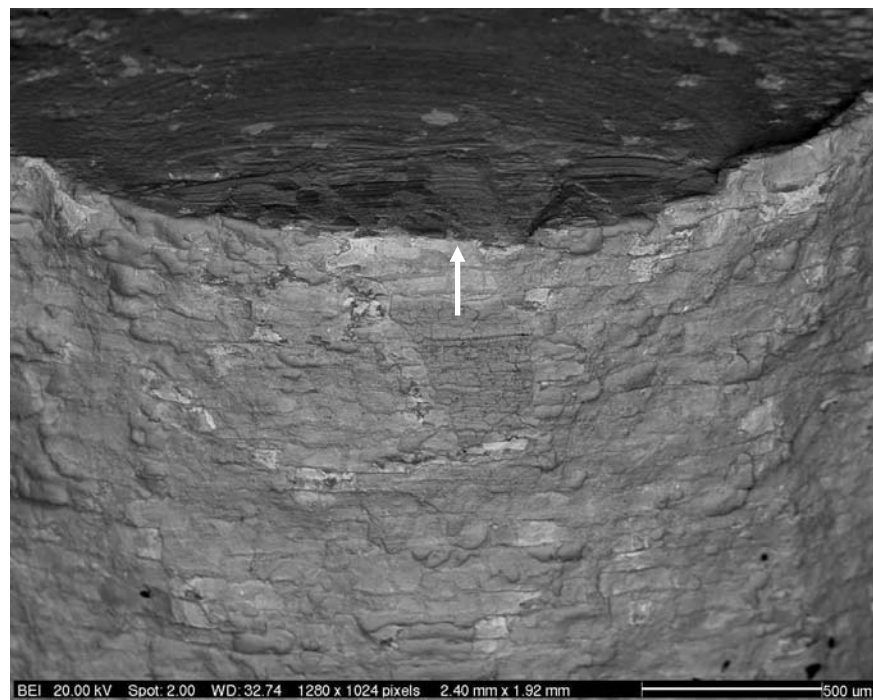
Figure O10. Fracture surface of low stress 900 Hz specimen (58.6 x10^6 cycles, 18.1 hr) showing surface origin (arrow), and heavy, cracked surface oxidation.
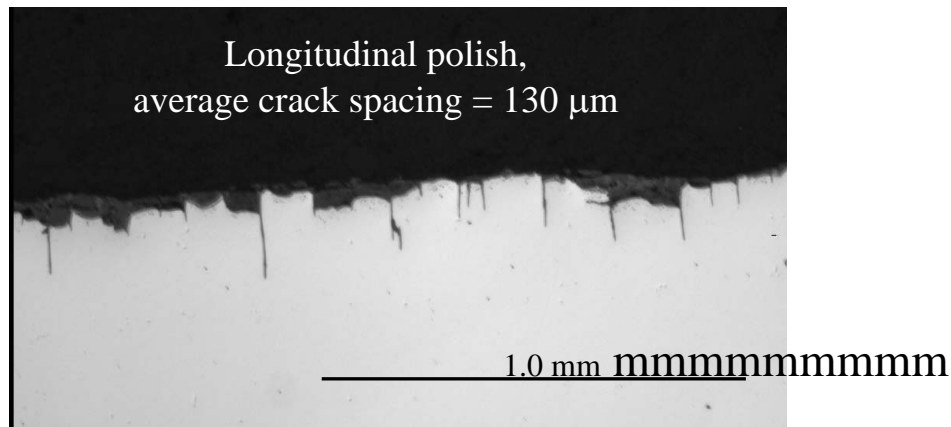
Figure O11. Metallographic section of low stress 900 Hz specimen (58.6 x10^6 cycles, 18.1 hr) showing regular pattern of cracks extending from surface oxidation.

O.3.2   HCF-Rupture Interactions

Creep rupture testing of uncoated PWA 1484 was performed at 1900F to define the time-dependent component of failure. Creep-rupture tests were performed on <001> oriented specimens of the type shown in Figure 4.76 (see Section 4.3.1.1*B*) at 25, 30 and 35 ksi, with results shown in Figure O12. Creep curve shape was typical for single crystal superalloys at high temperature: small amounts of primary creep followed by a long period of increasing creep rate to failure. The times to failure at a given stress were shorter than expected for PWA 1484; this may have been from the relatively coarse microstructure of the large castings (6" x 3" x 5/8") from which these specimens were made.

Tests with combinations of HCF and rupture damage were also performed on uncoated PWA 1484 with <001> orientation. The results of these are shown in Table O2. Tests with only HCF at R = -1, 59 Hz (A2LR2-3), tests with only rupture (A2LLG-2, -3, and –4), and tests with fractional exposures in rupture followed by HCF at R = -1, 59 Hz (A2LLP-, A2LLS-, and A2LLT- specimens) were performed. Attention was focused on one stress level, 35 ksi. Figure O13 shows that prior exposure in stress rupture decreased the HCF capability in a nearly linear fashion when based on percent time exposure. The only exception was one test after 80% rupture life exposure (A2LLT-2) which showed less reduction in HCF life than the others. However, a companion specimen (A2LLT-3) followed the trend, so A2LLT-s's behavior must be

regarded as unusual. Figure O13 shows that there is a strong interaction between HCF and rupture at 1900F for uncoated PWA 1484, and that a damage law of the form: D_r (rupture damage) + D_f (fatigue damage) = D_{tot} (total damage) is appropriate.

SX PWA1484
1900°F / Air / Creep Tests in Servohydraulic Machine
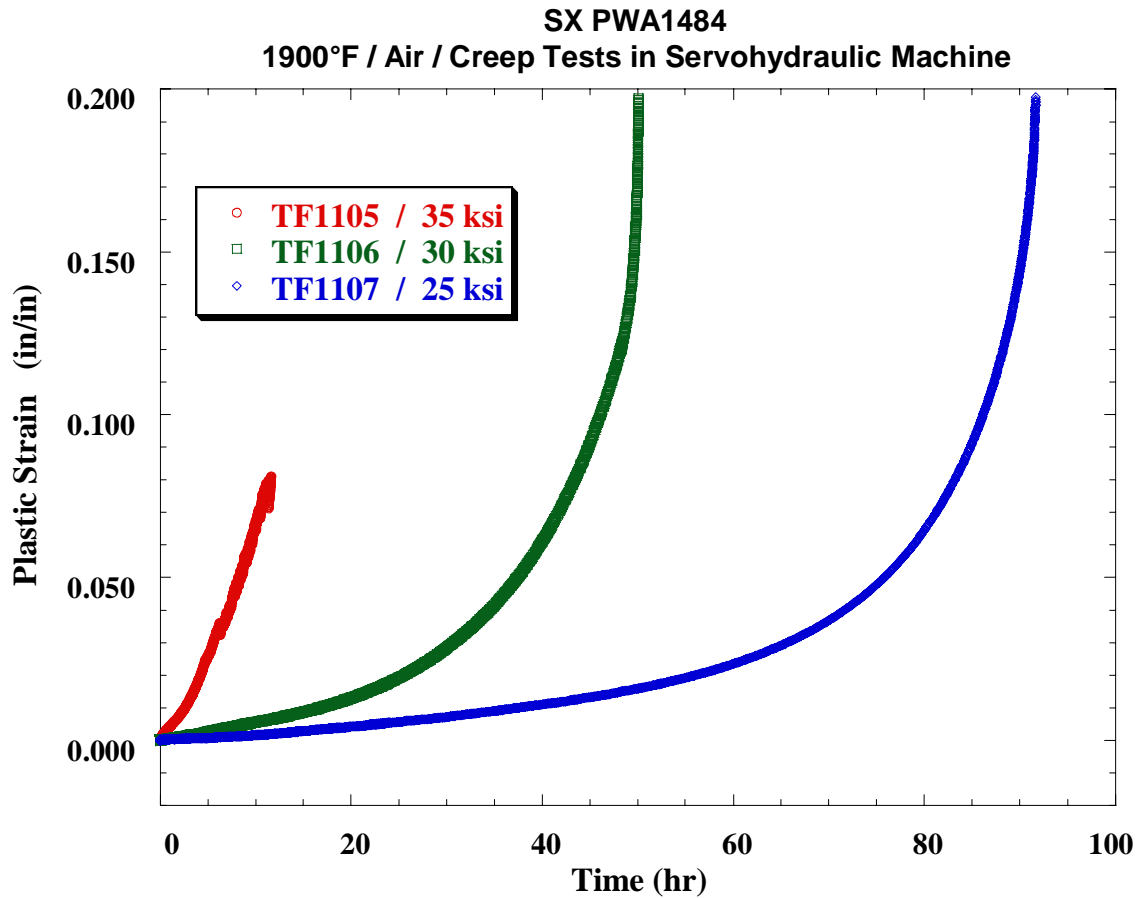
Figure O12. Creep behavior of <001> PWA 1484 at 1900F.

Table O2. 1900F Uncoated PWA 1484 HCF/Rupture Interaction Tests

S/N	1st (Rupture) leg			2nd (59 hz HCF) leg		
	Stress	hrs	result	R	alt stress	Nf
A2LLA-2	-	-	-	-1	40	11,225,134
A2LLA-4	-	-	-	-1	35	12,014,373
A2LLB-2	-	-	-	-1	45	4,927,212
A2LLB-4	-	-	-	-1	35	17,408,933
A2LLC-2	-	-	-	-1	35	21,437,295
A2LR2-3	-	-	-	-1	35	17,581,215
A2LLP-4	35	18.75	to 2nd leg	-1	35	3,759,937
A2LLS-2	35	18.75	to 2nd leg	-1	35	5,135,918
A2LLS-4	35	12	to 2nd leg	-1	35	7,924,504
A2LLS-3	35	12	to 2nd leg	-1	35	6,967,535
A2LLP-4	35	18.75	to 2nd leg	-1	35	3,759,937
A2LLS-2	35	18.75	to 2nd leg	-1	35	5,135,918
A2LLT-2	35	24	to 2nd leg	-1	35	7,158,154
A2LLT-3	35	24	to 2nd leg	-1	35	2,353,050
A2LLH-2	35	12	removed	-	-	-
A2LLH-4	35	12	removed	-	-	-
A2LLP-2	35	18.75	removed	-	-	-
A2LLH-3	35	24	removed	-	-	-
A2LLF-4	35	24	removed	-	-	-
A2LLG-2	35	31.0	failed	-	-	-
A2LLG-3	35	33.4	failed	-	-	-
A2LLG-4	35	25.4	failed	-	-	-
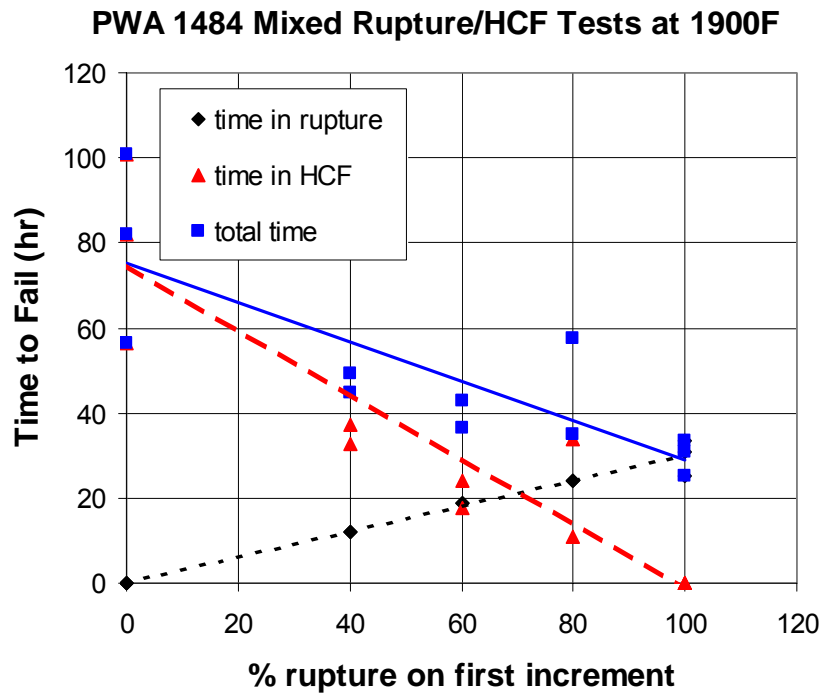
Figure O13. Effect of rupture exposure on PWA 1484 HCF at 1900F/35 ksi.

In addition, some tests with only rupture exposure (A2LLH-2,3,4, A2LLP-2, and A2LLF-4) were terminated prior to rupture to determine if precursor signs of damage could be detected. It was theorized that the prior rupture exposure might be generating small internal voids that would serve as HCF crack initiation sites. However, metallographic and SEM examination of polished cross sections from the gage sections did not reveal any voiding or other signs of internal damage that might explain the effect of prior rupture exposure on HCF. If voiding is occurring, it is on a much smaller scale than observable by these techniques. It is also possible that the oxidation occurring during the rupture exposure would pre-dispose the specimen surface to earlier HCF crack initiation, but no unstressed pre-exposures were performed to test this idea.

O.4　REFERENCES

1.　Wright, P.K., "Oxidation-Fatigue Interaction in a Single-Crystal Superalloy", *Low Cycle Fatigue, ASTM STP 942*, H.D.Solomon, G.R. Halford, L.B. Kaisand, and B.N. Leis, Eds, American Society for Testing and Materials, Philadelphia, 1988, pp.558-575.

APPENDIX P

REVIEW OF ANISOTROPIC ELASTICITY

Due to the elastic anisotropy of single crystal materials, the calculation of Stress Intensity Factors (SIFs) is somewhat more complex than for isotropic materials, and the SIF solutions may differ. The present study was undertaken to evaluate the significance of this difference.

The 3D deformation of an anisotropic or generally oriented orthotropic material can be described in terms of 21 elastic constants A_{ij}

$$
\begin{Bmatrix} \varepsilon_x \\ \varepsilon_y \\ \varepsilon_z \\ \gamma_{yz} \\ \gamma_{zx} \\ \gamma_{xy} \end{Bmatrix} = \begin{bmatrix} A_{11} & A_{12} & A_{13} & A_{14} & A_{15} & A_{16} \\ & A_{22} & A_{23} & A_{24} & A_{25} & A_{26} \\ & & A_{33} & A_{34} & A_{35} & A_{36} \\ & & & A_{44} & A_{45} & A_{46} \\ & & & & A_{55} & A_{56} \\ sym & & & & & A_{66} \end{bmatrix} \cdot \begin{Bmatrix} \sigma_x \\ \sigma_y \\ \sigma_z \\ \tau_{yz} \\ \tau_{zx} \\ \tau_{xy} \end{Bmatrix}
$$
(P1)

The 2D anisotropic solution utilized herein [1] is only valid if the plane normal to the crack front is a plane of elastic symmetry[1]. In this case,

$$
A_{34} = A_{35} = A_{36} = A_{46} = A_{56} = 0
$$
(P2)

For 2D mode I/II fracture analyses, only those terms describing the in-plane response are considered.

$$
\begin{Bmatrix} \varepsilon_x \\ \varepsilon_y \\ \gamma_{xy} \end{Bmatrix} = \begin{Bmatrix} \sigma_x \\ \sigma_y \\ \tau_{xy} \end{Bmatrix}^T \begin{bmatrix} A_{11} & A_{12} & A_{16} \\ & A_{22} & A_{26} \\ sym & & A_{66} \end{bmatrix}
$$
(P3)

---

[1] A more complete solution, valid for general crystalline orientations has been given more recently by Hoenig [2], but is not treated here.

In order to analyze cracks with this level of generality, we will first consider a more restricted problem where the 2D principal elastic axes are aligned with x and y. In this case, A_{16} and A_{26} also vanish and the remaining terms can be given in terms of the engineering elastic constants. For plane stress,

$$A = \begin{bmatrix} \dfrac{1}{E_1} & \dfrac{-v_{12}}{E_1} & 0 \\ & \dfrac{1}{E_2} & 0 \\ sym & & \dfrac{1}{G} \end{bmatrix}$$

(P4)

For plane strain, the applicable elastic constants can be obtained by

$$A'_{ij} = A_{ij} - (A_{i3} A_{j3}/A_{33}) \quad [i=1,2,6].$$

(P5)

(In the following, primed notation will be omitted, with the understanding that the applicable constants will be used for plane stress or plane strain). The stress for a crack in a 2D anisotropic material (Figure P1) with the restrictions described above can be written as.

$$\begin{Bmatrix} \sigma_x \\ \sigma_y \\ \tau_{xy} \end{Bmatrix} = \frac{1}{\sqrt{2\pi r}} \begin{bmatrix} d_{11} & d_{12} \\ d_{21} & d_{22} \\ d_{61} & d_{62} \end{bmatrix} \cdot \begin{Bmatrix} K_I \\ K_{II} \end{Bmatrix}$$

$$d_{11} = \mathrm{Re}\left[\frac{\mu_1 \mu_2}{\mu_1 - \mu_2} \left(\frac{\mu_2}{b_2} - \frac{\mu_1}{b_1} \right) \right] \qquad d_{12} = \mathrm{Re}\left[\frac{1}{\mu_1 - \mu_2} \left(\frac{\mu_2^2}{b_2} - \frac{\mu_1^2}{b_1} \right) \right]$$

$$d_{21} = \mathrm{Re}\left[\frac{1}{\mu_1 - \mu_2} \left(\frac{\mu_1}{b_2} - \frac{\mu_2}{b_1} \right) \right] \qquad d_{22} = \mathrm{Re}\left[\frac{1}{\mu_1 - \mu_2} \left(\frac{1}{b_2} - \frac{1}{b_1} \right) \right]$$

$$d_{61} = \mathrm{Re}\left[\frac{\mu_1 \mu_2}{\mu_1 - \mu_2} \left(\frac{1}{b_1} - \frac{1}{b_2} \right) \right] \qquad d_{62} = \mathrm{Re}\left[\frac{1}{\mu_1 - \mu_2} \left(\frac{\mu_1}{b_1} - \frac{\mu_2}{b_2} \right) \right]$$

$$b_i = \sqrt{\cos\theta + \mu_i \sin\theta} \quad i = 1,2 \tag{P6}$$

and μ_1 and μ_2 are the two roots with positive imaginary parts from

$$A_{11}\mu^4 - 2A_{16}\mu^3 + (2A_{12} + A_{66})\mu^2 - 2A_{26}\mu + A_{22} = 0 \tag{P7}$$

Equations (P6) through (P7) are applicable to the more general case of (P3). However, for the more restricted case of (P4), two terms drop out, and Equation (P7) can be solved by the quadratic formula to obtain

$$\mu_1^o, \mu_2^o = \pm\sqrt{\frac{-(2A_{12} + A_{66}) \pm \sqrt{(2A_{12} + A_{66})^2 - 4A_{11}A_{22}}}{2A_{11}}} \tag{P8}$$

For an orthotropic laminate with the x (crack) axis oriented at angle β to the principal material axis (as shown in Figure P1), it has been shown [3] that μ_1 and μ_2 can be obtained from μ_1^o and μ_2^o by

$$\mu_i = \frac{\mu_i^o \cos\beta - \sin\beta}{\cos\beta + \mu_i^o \sin\beta} \tag{P9}$$
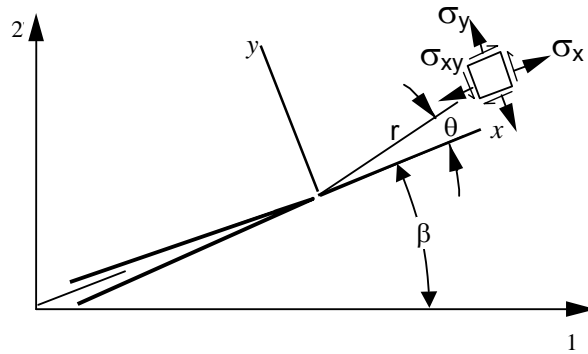
Figure P1. Crack tip coordinate system (x-y) rotated from principal orthotropic material axes (1-2).

REFERENCES

1.   Sih, G.C., Paris, P.C., Irwin, G.R., *On Cracks in Rectilinearly Anisotropic Bodies*, International Journal of Fracture Mechanics, Vol. 1, pp. 189-203, 1965.

2.   Hoenig, A., *Near-Tip Behavior of a Crack in a Plane Anisotropic Elastic Body*, Engineering Fracture Mechanics, Vol. 16, No. 3, pp. 3930403, 1982.

3.   Lekhnitski, S. G., *Theory of an Anisotropic Elastic Body,* Holden-Day, San Francisco, 1963.

APPENDIX Q

FRACTURE RESISTANCE ORTHOTROPY IN TWO DIMENSIONS

Q.1   FRACTURE RESISTANCE ORTHOTROPY IN TWO DIMENSIONS

In general, materials may exhibit elastic anisotropy as well as anisotropy in fracture resistance. Monocrystalline materials can exhibit both, while other materials, such as wrought metal products, are virtually isotropic elastically, but may have a preferred direction of (mode I) crack propagation resulting from the manner in which the material is processed. In either case, the processing and/or crystalline structure is often of symmetric character, and the two-dimensional relation describing the crack growth resistance as a function of orientation can be considered to have two (perpendicular) axes of symmetry. This special case is referred to hereafter as two-dimensional fracture resistance orthotropy, and will be the focus of the present discussion. Following the work of Buczek and Herakovich [1], the fracture resistance relation must:

> 1. Be independent of orientation for an isotropic material.

> 2. Return the principal fracture resistances for cracks in the corresponding principal orientations.

> 3. Be symmetric about the principle material axes.

Expressing the orientation of the crack in two-dimensions as the angle, θ measured from a principal material axis, Chen [2] gave an expression that satisfies the criteria given above

$$K_p(\theta) = \left(\frac{\cos^2 \theta}{K_p(0°)^n} + \frac{\sin^2 \theta}{K_p(90°)^n} \right)^{-\frac{1}{n}} \tag{Q1}$$

where, n is a constant exponent available as a fitting parameter. K_p is taken to represent the stress intensity at which the crack propagates. It is proposed [3], that K_p is a material-dependent function of the orientation of the crack tip consistent with the regime of crack growth. Thus, for fatigue crack growth, K_p represents the stress intensity at which the crack propagates at a given rate; for stable tearing, K_p represents the fracture toughness. For the present study, we are

interested in threshold fatigue crack growth (the stress intensity at which the crack growth rate approaches zero).

In the context of a maximum stress theory, Buczek and Herakovich suggested a fracture orthotropy relation equivalent to setting $n = (-1)$. Kfouri [4] used the more familiar form of an ellipse ($n = 2$). For moderate orthotropy ratios ($0.7 \leq K_p(90°)/K_p(0°) \leq 1.5$) representative of a wide variety of engineering materials, exponents within this range produce a nearly identical oblong shape in polar coordinates as illustrated in Figure Q1.
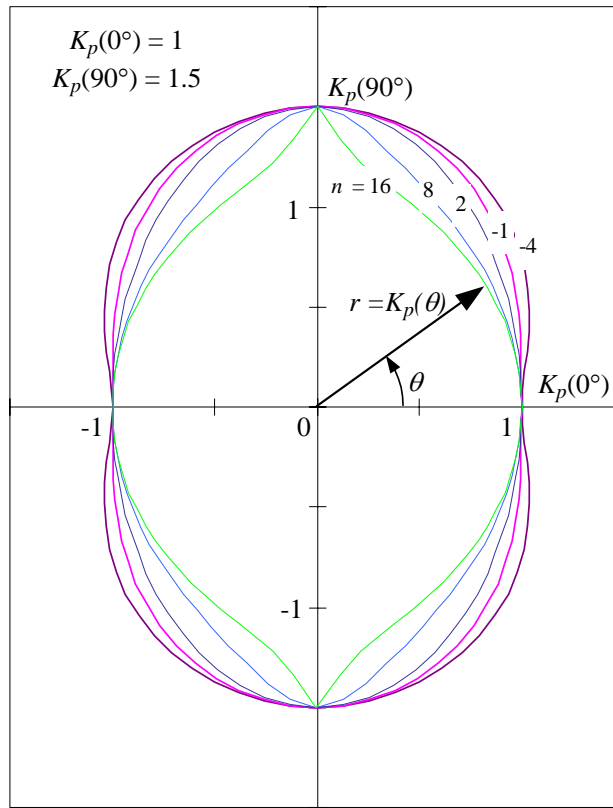
Figure Q1. Polar plots of crack growth resistance function (Equation Q1) given by Chen [2] with various values of the fitting parameter, n.

A drawback of this function is that the if $K_p(90°) = K_p(0°)$, the function becomes isotropic (circular) independent of the fitting parameter. Particularly for monocrystalline materials, it seems plausible that this condition may be too restrictive. A modified form of the crack growth resistance function is thus suggested [5]

$$K_p(\theta) = \left[\left(\frac{\cos^2 \theta}{K_p(0°)^2} \right)^n + \left(\frac{\sin^2 \theta}{K_p(90°)^2} \right)^n \right]^{-\frac{1}{2n}} \qquad (Q2)$$

This function is plotted for an orthotropy ratio of 1.5 and various values of n in Figure Q2. Note that to obtain the isotropic condition, the principal fracture resistance values must be equal *and* the fitting exponent must be unity. Other values of n produce shapes ranging from a star as $n \to 0$ to a rectangle as $n \to \infty$. Note also that Equation (Q1) with $n = 2$ is identical to Equation (Q2) with $n = 1$.
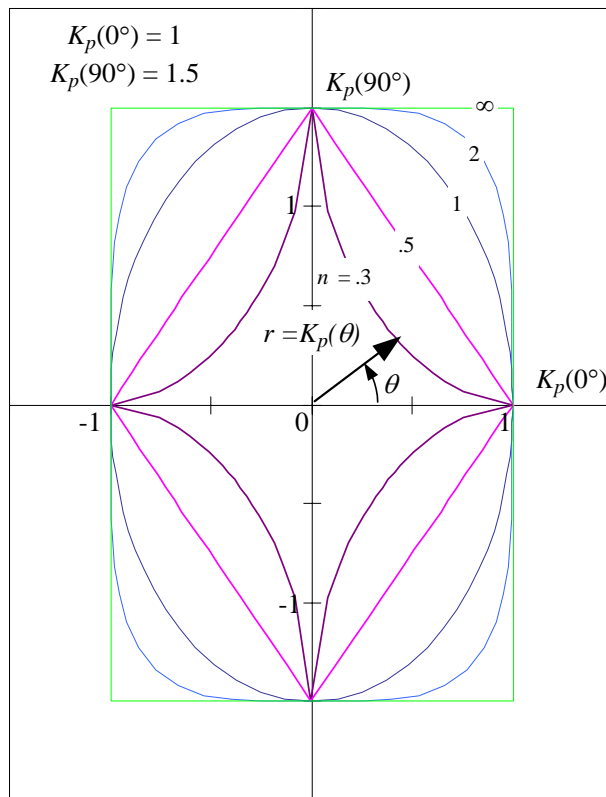

Figure Q2. Polar plots of modified crack growth resistance function (Equation Q2) with various values of the fitting parameter, n.

Q-3

Q.2   EXTENSION TO THREE DIMENSIONS

In a three-dimensional body a crack may be non-planar, and oriented arbitrarily. At any point along the crack front in an orthotropic material, however, we can characterize the local orientation in terms of the crack tangent plane (defined by its normal), and the direction of crack propagation within that plane (see Figure Q3), defined relative to the principal axes of the material.

Materials such as a rolled or extruded plate, or cubic monocrystalline materials may be considered to have three orthogonal planes of symmetry. Within each of these planes there are thus two orthogonal axes of symmetry. This results in six principal fracture resistance values. The material is assumed to be homogeneous, thus the toughness for a given orientation relative to these principal planes is invariant with regard to translation.

Figure Q3. Geometry of crack orientation at a point on an arbitrary crack front.

Following the convention established for wrought metals [6], the principle values of fracture resistance are written in a two-letter code (i-j) where the first letter refers to the principle axis normal to the c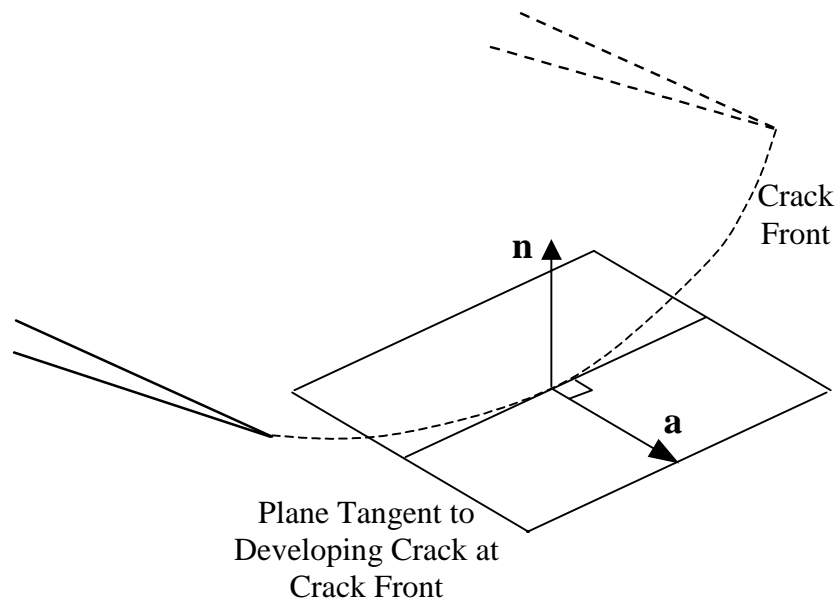rack plane, and the second subscript identifies the principle axis corresponding to the direction of propagation. The standard principal axes for rectangular products (plate, extrusion and forging) correspond to the longitudinal grain orientation (L), the long transverse grain orientation (T), and the short transverse grain orientation (S). Thus, a crack growing normal to the width in the rolling direction of a plate corresponds to the T-L orientation. The (mode I) fracture resistance in this direction we shall designate as K_{TL}. For convenience and generality, we will use numeric subscripts (1,2,3) in place of the metallurgical (L, T, S). The six principal fracture resistances are thus K_{12}, K_{21}, K_{23}, K_{32}, K_{13}, and K_{31}. For cubic monocrystalline materials, we further associate the (x_1,x_2,x_3) axes with the crystallographic (<100>, <010>,<001>) axes.

What is needed is a function to interpolate the fracture resistance for any arbitrary orientation in terms of the principal values. As illustrated in Figure Q3, a crack (or a point on an arbitrary crack front) may propagate in an arbitrary direction defined by unit vector

$$\mathbf{a} = a_1\mathbf{i} + a_2\mathbf{j} + a_3\mathbf{k} \tag{Q3}$$

where, $\mathbf{i}$, $\mathbf{j}$, and $\mathbf{k}$ are unit vectors corresponding to the principal material axes x_1, x_2, and x_3. Vector $\mathbf{a}$ lies within a plane tangent to the developing crack surface at the crack front, which plane is uniquely described by its unit normal vector

$$\mathbf{n} = n_1\mathbf{i} + n_2\mathbf{j} + n_3\mathbf{k} \tag{Q4}$$

The crack orientation is uniquely defined by the direction cosines n_i and a_i. The interpolation function to determine the fracture resistance for this orientation must meet the requirements of Buczek and Herakovich as previously discussed. Presumably such a function must revert to a two-dimensional form similar to Equations (Q1) or (Q2). Pettit [7] developed the following three-dimensional relationship based on the two-dimensional form of Equation (Q1) assuming $n = -1$.

The fracture resistance components corresponding to the trace of **a** in each of the principal planes (as illustrated in Figure Q4) are given by

$$K_1(\mathbf{a}) = \frac{1}{1 - a_1^2}\left(K_{12}a_2^2 + K_{13}a_3^2\right)$$

$$K_2(\mathbf{a}) = \frac{1}{1 - a_2^2}\left(K_{23}a_3^2 + K_{21}a_1^2\right) \qquad\qquad (Q5)$$

$$K_3(\mathbf{a}) = \frac{1}{1 - a_3^2}\left(K_{31}a_1^2 + K_{32}a_2^2\right)$$

from which the fracture resistance in an arbitrary orientation is given by

$$K_p(\mathbf{n}, \mathbf{a}) = K_1 n_1^2 + K_2 n_2^2 + K_3 n_3^2 \qquad\qquad (Q6)$$

Equations (Q5 and Q6) are an attempt to satisfy the outlined requirements with the simplest formulation possible.

Preliminary attempts to fit single-crystal PWA 1484 mode I threshold crack growth data to Equations (Q5 and Q6) showed the need for additional fitting parameters to obtain an acceptable fit. This motivated development of a three-dimensional interpolating function based on the two-dimensional form of Equation (Q2).

Following [7], the angles (using right hand rule) describing the trace of **a** on the principle planes are given by

$$\tan(\theta_1) = \frac{a_3}{a_2} \qquad \tan(\theta_2) = \frac{a_1}{a_3} \qquad \tan(\theta_3) = \frac{a_2}{a_1} \qquad\qquad (Q7)$$

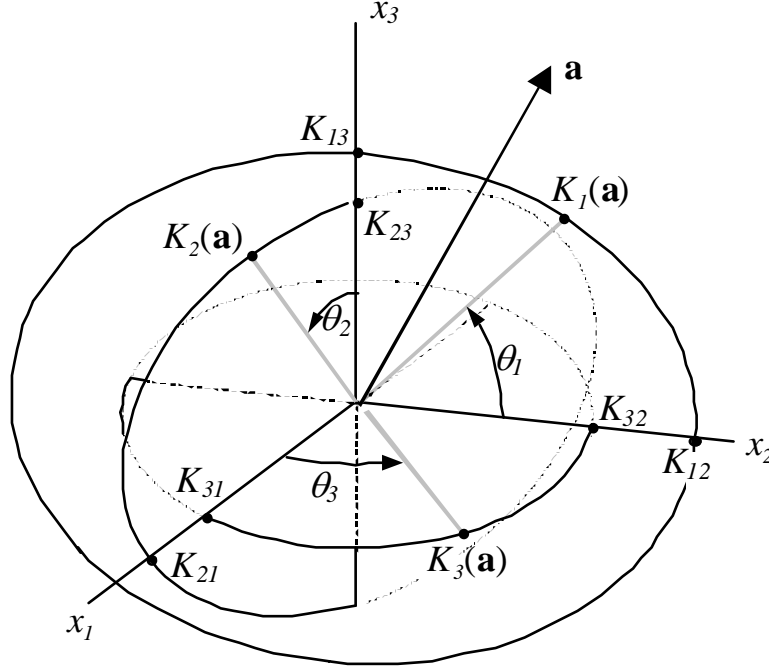where, the angle subscript refers to the axis normal to the principal plane.

Figure Q4.   Principal orthotropic components of crack growth resistance for crack growth parallel to unit vecto*r* a.

The fracture resistance of a crack, were it to lie in a principal plane normal to axis x_k and propagate in the direction of the corresponding trace defined in (Q7), can be interpolated in two dimensions in a manner analogous to Equation (Q2)[1]

$$K_k(\theta_k) = \left[\left(\frac{\cos^2\theta_k}{K_{ki}^{\,2}} \right)^m + \left(\frac{\sin^2\theta_k}{K_{kj}^{\,2}} \right)^m \right]^{-\frac{1}{2m}} \quad (i,j,k \text{ cyclic, non-repeating}) \qquad (Q8)$$

Further observing the trigonometric identity

$$\cos^2\left(\tan^{-1}\frac{b}{c} \right) = \frac{c^2}{b^2 + c^2}$$

$$\sin^2\left(\tan^{-1}\frac{b}{c} \right) = \frac{b^2}{b^2 + c^2}$$

$$(Q9)$$

---

[1] In the three-dimensional form, two fitting exponents will be used, *m* for in-plane rotations, and *n* for out of plane rotations of the crack orientation relative to principal orientations.

and the property of direction cosines

$$a_1{}^2 + a_2{}^2 + a_3{}^2 = 1 \qquad\qquad\qquad\qquad (Q10)$$

we can combine to write

$$K_i(\mathbf{a}) = \frac{\sqrt{1 - a_i{}^2}}{\left[\left(\dfrac{a_j{}^2}{K_{ij}{}^2}\right)^m + \left(\dfrac{a_k{}^2}{K_{ik}{}^2}\right)^m\right]^{\frac{1}{2m}}} \text{ (non-repeating)} \qquad\qquad (Q11)$$

In this case, the K_i may be considered as the fracture resistance components of $\mathbf{a}$ in the principal planes corresponding to the two-dimensional form of Equation (Q2). In order to obtain the fracture resistance for a general orientation, these must be combined in some sort of weighted average based on the orientation of the normal vector, $\mathbf{n}$, similar to Equation (Q6). The use of (Q6), however, is unacceptable, because it does not revert to the form Equation (Q2) for interpolation between any two principal fracture planes when the fracture resistance component in the third plane is zero. In order for the fracture resistance relation to degenerate properly, the expression for the fracture resistance must be of the form

$$K_p(\mathbf{n}, \mathbf{a}) = \left[\left(\frac{n_1{}^2}{K_1{}^2}\right)^n + \left(\frac{n_2{}^2}{K_2{}^2}\right)^n + \left(\frac{n_3{}^2}{K_3{}^2}\right)^n\right]^{-\frac{1}{2n}} \qquad\qquad (Q12)$$

where, the K_i are given by Equation (Q11).

One last observation pertaining to the application of interest is that single crystal materials are fabricated by a casting process, with solidification and dendrite growth proceeding in the <001> direction. While the elastic properties are virtually identical along all three principal axes, inelastic response to load oriented along the <001> axis may differ from the <100> and <010> axes. Nevertheless, these secondary axes would be expected to behave in like

manner to each other (the dendrite symmetry is often compared to a "bundle of pencils" oriented along the <001>). We can thus conclude from the process symmetry that

$$K_{12} = K_{21}$$
$$K_{23} = K_{13}$$ (Q13)
$$K_{31} = K_{32}$$

Thus, for a given single crystal material state, only three unique principal fracture resistance values are needed to characterize the fracture resistance in three dimensions (in practice, more are needed to determine fitting exponents m and n).

Q.3   SPECIFICATION/DETERMINATION OF THE CRACK ORIENTATION

Inasmuch as fracture resistance is sensitive to material orientation, the test program must include fracture threshold values obtained from test specimens of various specified crack orientations. Two methods of specifying nominal crack orientations will be discussed. A second issue, however, is that due to manufacturing tolerances on the crystalline orientation within a specimen, fracture threshold values obtained from test specimens are affected by deviations from the intended specimen orientation. A method of correcting for crystalline misalignment will also be given.

For test specimens, the crack orientation is usually specified using crystalline indices. The components of the unit vectors (**n,a**) denoting the desired crack orientation can be directly inferred from the indices, as given in several examples are given in Table Q1.

$$< i_1\, i_2\, i_3 > \Rightarrow \left(\frac{i_1}{d}\ ,\frac{i_2}{d}\ ,\frac{i_3}{d} \right) \text{ where, } d = \sqrt{i_1^{\,2} + i_2^{\,2} + i_3^{\,2}}$$ (Q14)

Table Q1. Unit Vector Components Corresponding to Various Crystallographic Crack Orientations

Crystallographic Orientation	**n**	**a**
<001/010>	(0,0,1)	(0,1,0)
<0-11/011>	$(0, -\frac{1}{\sqrt{2}}, \frac{1}{\sqrt{2}})$	$(0, \frac{1}{\sqrt{2}}, \frac{1}{\sqrt{2}})$
<001/110>	(0,0,1)	$(\frac{1}{\sqrt{2}}, \frac{1}{\sqrt{2}}, 0)$
<-1-11/112>	$(-\frac{1}{\sqrt{3}}, -\frac{1}{\sqrt{3}}, \frac{1}{\sqrt{3}})$	$(\frac{1}{\sqrt{6}}, \frac{1}{\sqrt{6}}, \frac{2}{\sqrt{6}})$

In other situations, it is sometimes convenient to express the components of the vectors (**n**,**a**) in terms of a series of rotations imposed upon a crack starting from a standard orientation. For the present study, we will assume a reference crack orientation corresponding to K_{21}, or <010/100> in crystallographic notation. That is, the reference plane of the crack is normal to the <010> axis, with crack propagation directed (normal to the crack front) along the <100> axis. The crack is rotated from this standard position to represent an arbitrary orientation as shown in Figure Q5.

The components of unit vectors **n** = **y**, and **a** = **x** are given in terms of the rotation angles by

$$\begin{bmatrix} n_1 \\ n_2 \\ n_3 \end{bmatrix} = \begin{bmatrix} -\sin\theta\cos\alpha - \cos\theta\sin\beta\sin\alpha \\ \cos\theta\cos\alpha - \sin\theta\sin\beta\sin\alpha \\ \cos\beta\sin\alpha \end{bmatrix} \qquad (Q15)$$

$$\begin{bmatrix} a_1 \\ a_2 \\ a_3 \end{bmatrix} = \begin{bmatrix} \cos\theta\cos\beta \\ \sin\theta\cos\beta \\ \sin\beta \end{bmatrix} \qquad (Q16)$$
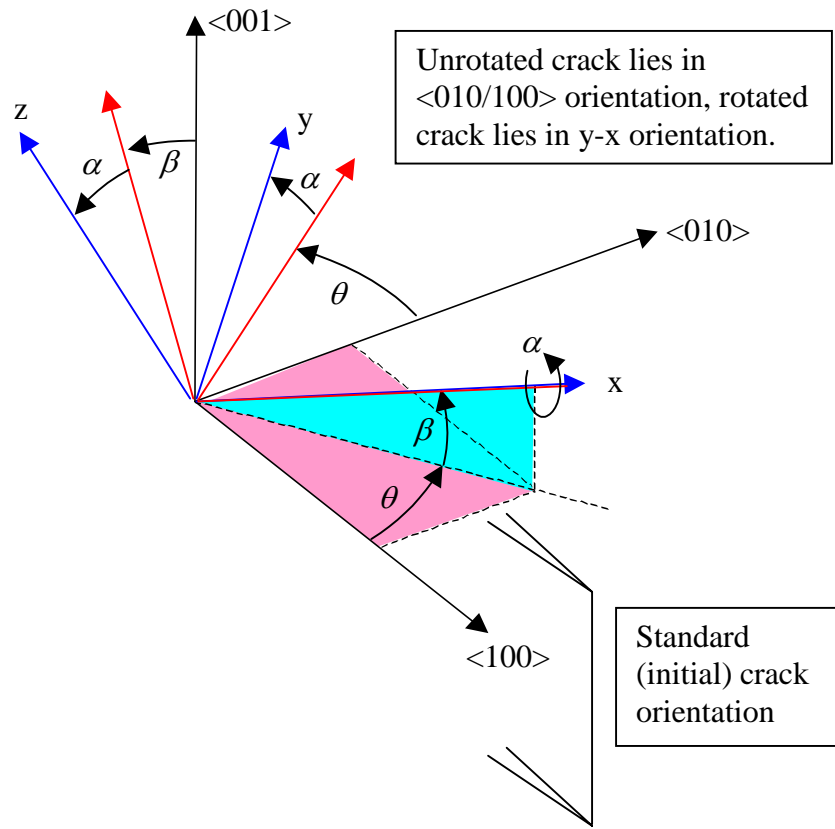
Figure Q5.   System of rotations for defining arbitrary crack orientation in crystallographic coordinates

The above methods are typically used to specify the *intended* crack orientation. In actuality, this may deviate from the *true* crack orientation in the crystal because the material coordinates are typically misaligned somewhat relative to the specimen geometry. In order to use actual crystalline orientation data in the reduction of the threshold test data, it is necessary to determine the actual crack normal and tangential vectors (**n,a**) in crystalline coordinates based on Laue data. An illustration of these vectors is shown in Figure Q3 at a point on an arbitrary crack front. For the purpose of reducing specimen test data, the crack front is assumed to be straight, thus (**n,a**) are assumed constant along the crack front.

In many cases, Laue information for individual specimens described was not available, and actual specimen orientation is estimated from (Honeywell) Laue results obtained for the casting from which the specimen was cut, as well as the cutout orientation specified. The details

of the transformations required to obtain the crack orientation unit vectors (**n,a**) in crystallographic coordinates are as follows (if actual specimen data is available, "specimen" may be substituted for "casting" in the discussion below).

Denoting the basis of the vector space in casting coordinates (the coordinate system resulting if all the casting Laue angles were zero) as

$$\mathbf{e} = \begin{bmatrix} e_1 \\ e_2 \\ e_3 \end{bmatrix} \tag{Q17}$$

and in crystallographic coordinates (for non-zero Laue angles) as

$$\bar{\mathbf{e}} = \begin{bmatrix} \bar{e}_1 \\ \bar{e}_2 \\ \bar{e}_3 \end{bmatrix} \tag{Q18}$$

A transformation matrix **B** exists such that

$$\bar{\mathbf{e}} = \mathbf{B}\mathbf{e} \tag{Q19}$$

For Laue angles defined as shown in Figure Q6, **B** is given by

$$\mathbf{B} = \begin{bmatrix} b_{11} & b_{12} & b_{13} \\ b_{21} & b_{22} & b_{23} \\ b_{31} & b_{32} & b_{33} \end{bmatrix} = \begin{bmatrix} b_{22}b_{33} - b_{23}b_{32} & b_{23}b_{31} - b_{21}b_{33} & b_{21}b_{32} - b_{22}b_{31} \\ \sin\psi \sin\beta & \sin\psi \cos\beta & -\cos\psi \\ \sin\delta & \cos\delta \sin\gamma & \cos\delta \cos\gamma \end{bmatrix} \tag{Q20}$$

where,

$$\psi = \tan^{-1}\left(\frac{\cos\delta \cos\gamma}{\sin\delta \sin\beta + \cos\beta \cos\delta \sin\gamma} \right) \tag{Q21}$$

for a crack with normal **n**, and trajectory **a** in casting coordinates (based on the specimen cutout orientation specified), we obtain $\bar{\mathbf{n}}$ and $\bar{\mathbf{a}}$ in crystallographic coordinates by the inverse transpose transformation

$$\begin{aligned} \bar{\mathbf{n}} &= \left(\mathbf{B}^{-1}\right)^T \mathbf{n} \\ \bar{\mathbf{a}} &= \left(\mathbf{B}^{-1}\right)^T \mathbf{a} \end{aligned} \tag{Q22}$$
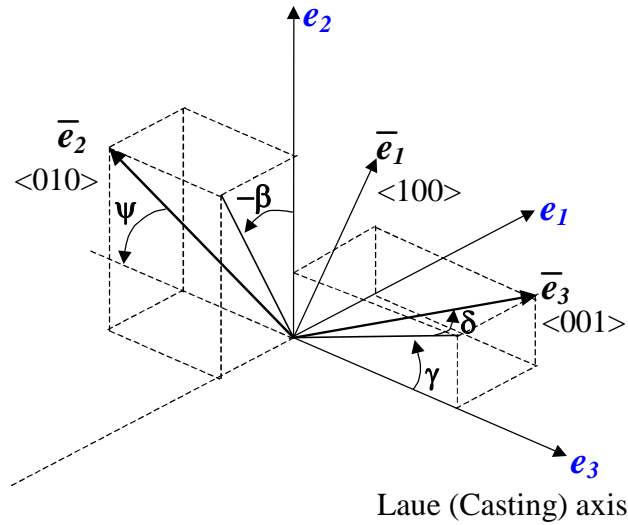
Figure Q6. Laue angles describing rotation from casting basis to crystallographic basis.

Q.4 REFERENCES

1. M. B. Buczek , C. T. Herakovich, "A Normal Stress Criterion for Crack Extension Direction in Orthotropic Composite Materials", *J. Composite Materials*, Vol. 19, pp. 544-553, 1985.

2. C.-S. Chen, *Crack Growth Simulation and Residual Strength Prediction in Thin Shell Structures*, Ph. D. Dissertation, Cornell University, January, 1999.

3. R. G. Pettit, J. J. Wang, C. Toh, *Integral Airframe Structures (IAS)—Validated Feasibility Study of Integrally Stiffened Metallic Fuselage Panels for Reducing Manufacturing Cost*, Boeing Report CRAD-9306-TR-4542, NASA contract NAS1-20014, Task 34, November, 1998 (See also NASA CR-2000-209342, May 2000).

4. A. P. Kfouri, "Crack Extension Under Mixed-Mode Loading in an Anisotropic Mode-Asymmetric Material in Respect of Resistance to Fracture", *Fatigue & Fracture of Engineering Materials & Structures*, Vol. 19, No. 1, pp. 27-38, 1996.

5. R. G. Pettit, unpublished notes, Cornell University, 2000.

6. Standards (MIRSA)", *ASTM*, Vol. 12, No. 9, 1972. (see also ASTM E1823).

7. R. G. Pettit, *Crack Turning in Integrally Stiffened Aircraft Structures*, Ph. D. Dissertation, Cornell University, August, 2000.

APPENDIX R

MIXED-MODE FATIGUE CRACK GROWTH IN SINGLE CRYSTAL Ni-ALLOYS

Fatigue crack growth (FCG) in Ni-based single crystals can occur on crystallographic or transprecipitate noncrystallographic (TPNC) planes, depending on temperature, stress state, crystal orientation, and stress intensity range. Near the fatigue threshold, fatigue crack growth occurs by propagation of a Mode I crack in the γ matrix. At higher stress intensity ranges, fatigue crack growth tends to occur by propagation of mixed-mode cracks on octahedral (111) planes either on the microscopic or macroscopic scale. Differences in the fatigue failure processes lead to different fatigue crack growth responses, particularly in the near threshold regime. Identifying the regime where these various fatigue failure processes occur is an important first step in developing fracture mechanics methods to treat crack growth in single crystal materials since these processes control, among other things, the cracking mode and resulting threshold stress intensity factors.

The transition of a mixed-mode (111) crack to a Mode I crack occurs by a thermally activated process. This was first demonstrated by Leverant and Gell [1] for low-cycle fatigue of Mar-M200 single crystals. The fatigue crack growth mode transition and the corresponding strain rate and frequency effects [1, 2] have been attributed to a change of slip character from heterogeneous planar (111) slip at high strain rates and low temperatures to homogeneous, wavy slip at slow strain rates and high temperatures. Similar fatigue crack growth mode transitions have also been reported for other single crystal alloys, including PWA 1480 [3-6], PWA 1484 [3-6], and Rene N4 [7]. Currently, there are no methods for quantitatively treating mixed-mode fatigue crack growth and fatigue crack growth mode transitions in Ni-based single crystal alloys.

The objective of this task was to develop a methodology for treating the effects of stress state, frequency, crystal orientation, and temperature on the near threshold FCG response of PWA 1484 single crystals subjected to high cycle fatigue. An integrated analytical and experimental approach was used to achieve this objective. The analytical efforts included stress intensity factor computation for cracks in single crystal

alloy PWA 1484, mapping of fatigue crack growth modes, and model development. The analytical efforts were linked to an experimental program to determine the mixed-mode fatigue crack growth threshold of PWA 1484 as a function of stress state and crystal orientation. Mixed-mode fatigue crack growth on (010) and (111) planes was characterized at 1100°F using an asymmetric four-point bend (AFPB) test technique. Stress intensity solutions of these crack geometries in PWA 1484 were obtained using a BIE fracture mechanics code, [8], and an FEM code, FRANC2D/L [9] for anisotropic materials. The influence of mode mixity on the FCG threshold of PWA 1484 was determined as a function of stress state ranging from pure Mode I to pure Mode II. Both the analytical and experimental results were used to develop a fracture mechanics approach for treating high-cycle, mixed-mode fatigue crack growth in single crystal blade material.

R.1   ANALYTICAL

Anisotropic fracture mechanics codes were utilized to compute the stress intensity factors for mixed-mode cracks in PWA 1484. Two crack specimens were considered, which included single-edge notched specimens and asymmetric four-point bend (AFPB) specimens. These results were used to establish: (1) the range of mode mixity that could be achieved as a function of crack length/specimen width ratio, and (2) the applicability of isotropic K solutions to PWA 1484. After a comparison of the K solutions, the AFPB crack specimen was chosen for the mixed-mode crack growth threshold tests because the entire range of mode mixity (pure Mode I to pure Mode II) could be attained in the crack geometry.

R.1.1   Stress Intensity Factor Computation

R.1.1.1   Single-Edge-Notched Specimen

Stress intensity factor (K) solutions for mixed-mode cracks for single edge notched (SEN) specimens were computed using the BIECRX code [8]. New K solutions were obtained for angled cracks at 22.5°, 45°, 60°, and 67.5° to the loading axis. The crack configurations for two 45° cracks at different crystallographic orientations are illustrated in Figures R1 and R2. As shown in Figure R1, α and β are the angles the X-axis makes with the $<E_{11}>$ direction and X'-axis (the crack), respectively, where E_{11} is a principal direction of the elastic properties. The K_I and K_{II} solutions for a mixed-mode crack in isotropic materials

and in PWA 1484 single crystals for {111} and {010} cracks are compared in normalized form in Figure R3. Also shown in Figure R3 are the published isotropic solutions for a 45° crack in a semi-infinite plate [10, 11] and in a finite-width specimen [12, 13]. There is good agreement between the BIECRX solutions and the more-limited published results. Comparison of the BIECRX solutions for isotropic and single crystal materials indicates only small differences, which increase with increasing a/W, as shown in Figure R3. The Mode I, F_I, and Mode II, F_{II}, boundary correction factors were obtained by fitting the K solutions for isotropic materials to 3rd-order polynomial equations, leading to

$$K_I = F_I \ \sigma_N \sqrt{\pi a} \qquad\qquad (R1)$$

and

$$K_{II} = F_{II} \ \sigma_N \sqrt{\pi a} \qquad\qquad (R2)$$

where

$$F_I = 0.6649 + 0.8962(a/W) - 1.5056(a/W)^2 + 3.8710(a/W)^3 \qquad (R3)$$

$$F_{II} = 0.3697 - 0.3970(a/W) - 0.4317(a/W)^2 + 1.16(a/W)^3 \qquad (R4)$$

where a is crack depth, W is specimen width, and σ_N is the nominal stress. The agreement is exceptionally good for a/W less than 0.6. Elastic anisotropy and finite width geometry influence the K solutions only for deep cracks ($a/W > 0.7$). Figure R4 presents the BIECRX results of K_{II}/K_I and the phase angle, $\phi = \arctan (K_{II}/K_I)$, as a function of a/W. It shows that the mode mixity ratio, K_{II}/K_I, and the phase angle, ϕ, decrease slightly with increasing a/W.
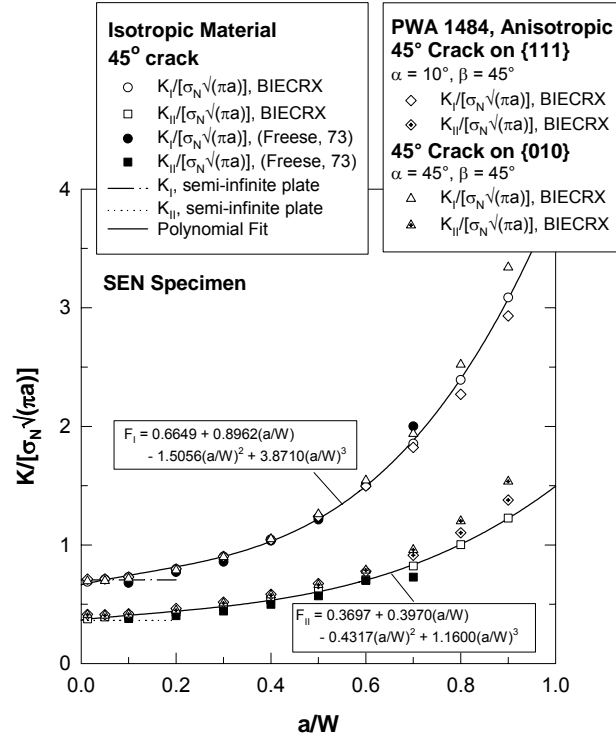
Figure R1.   Proposed SEN specimen with a 45° angled crack for studying fatigue crack growth on the {010} plane in the <100> direction under mixed-mode loading.

Figure R2.   Proposed SEN specimen with a 45° angled crack for studying fatigue crack growth on the {111} plane in the <211> direction under mixed-mode loading.

Figure R3. Normalized stress intensity factors as a function of crack depth, a, normalized by specimen width, *W*, for a SEN specimen with a 45º angled crack subjected to a remote tension, σ_N. BIECRX results are in agreement with literature solutions for semi-finite [10, 11] and finite-width plates [12].
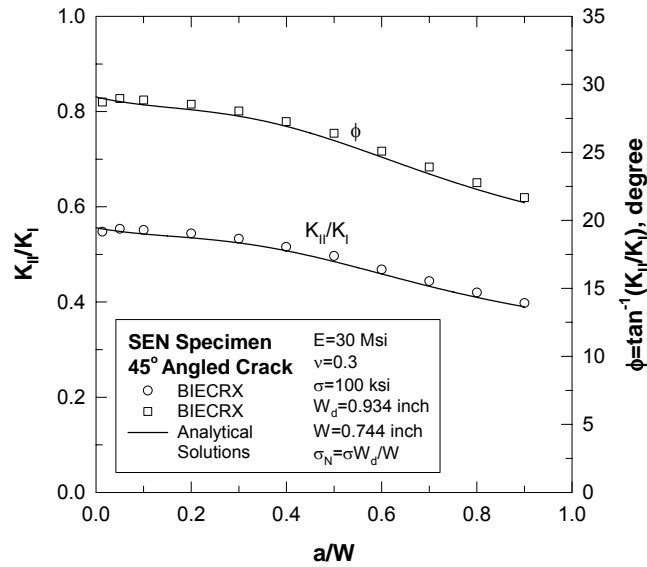
Figure R4. The mode-mixity ratio, K_{II}/K_I, and the phase angle, $\phi = \tan^{-1} (K_{II}/K_I)$, as a function of *a/W* for a SEN specimen with a 45º angled crack.

Additional K solutions were also obtained for 22.5, 60, and 67.5° angled cracks in SEN specimens. Figure R5 illustrates that the BIECRX K solutions are in agreement with published results [12,13] for various angled cracks in isotropic materials, ranging from 0°, 22.5°, 45°, and 60° for *a/W* from 0.1 to 0.7. There are no published solutions for *a/W* > 0.7. Fourth order polynomial expressions were used to fit both the BIECRX and published data [12,13].
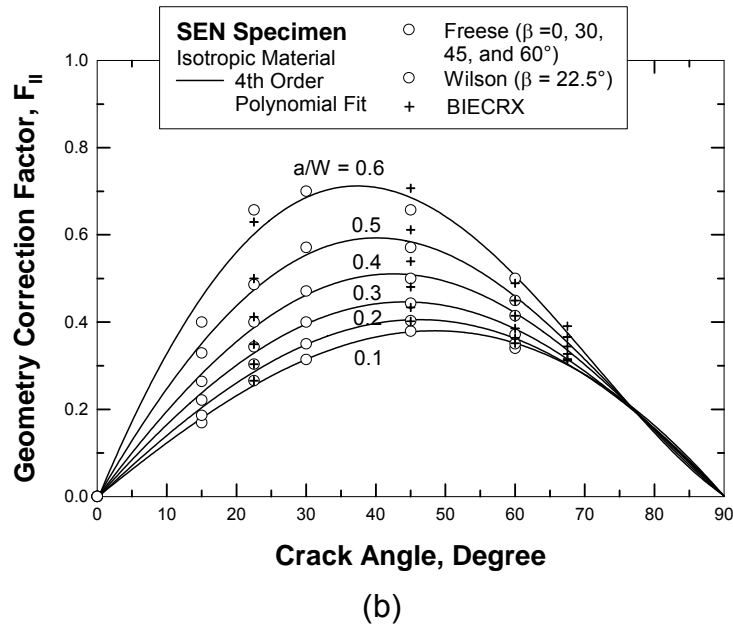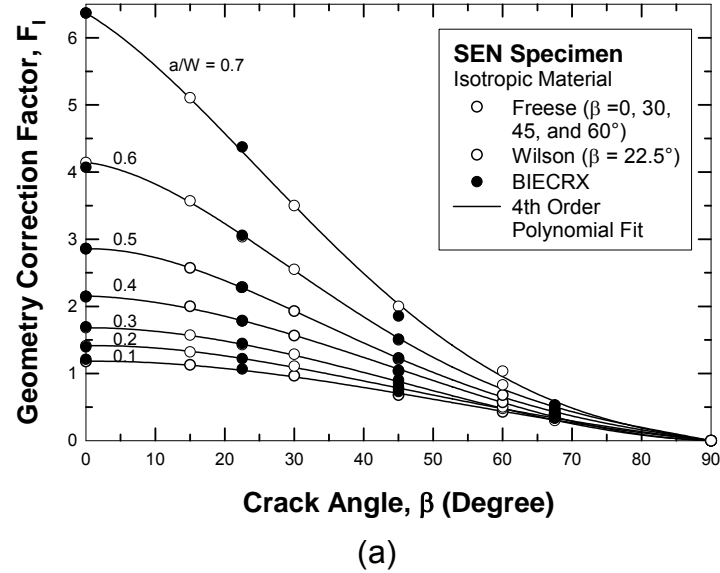

(a)

(b)

Figure R5.   Boundary correction factors as a function of crack angle, β, specimen with an angled crack: a) Mode I, and b) Mode II. BIECRX results are in agreement with literature solutions for a finite-width plate [12,13].

R.1.1.2   Asymmetric Four-Point-Bend (AFPB) Crack Specimen

      Stress intensity solutions of the AFPB crack specimens were obtained for isotropic materials and PWA 1484 single crystals. The BIE mesh for these K calculations is presented in Figure R6. Pin loading was simulated by applying a distributed normal force, T_y, on three boundary segments, while imposing $T_x = 0$ in the horizontal (x) direction. The size of these three boundary segments were made very small, such that the distributed force essentially acted as a point load. The displacements of a small segment located at the lower left of the specimen were prescribed; the vertical (u_y) and horizontal (u_x) displacements of the left node of this boundary segment were maintained to be zero, while only $u_y = 0$ was maintained at the right node of this boundary segment. Reaction force at this boundary segment was computed based on load equilibrium.
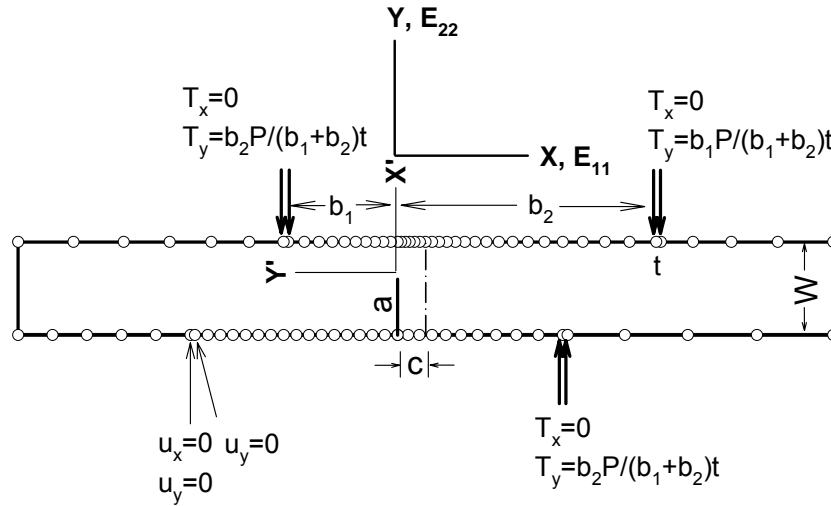

Figure R6.   BIE mesh for the AFPB crack specimen showing the offset distance, c, of the crack from the symmetry line, crack depth, a, and the specimen width, W for an isotropic material.

      For this crack geometry and these specimen dimensions, the important parameters are the offset distance, c, and the crack depth a. Both c and a influence the mode mixity as well as the values of K_I and K_{II}. The K solutions were, therefore, generated as a function of a/W and c/W. The normalized stress intensity factor solutions for isotropic materials are plotted as a function of the normalized crack depth, a/W, in Figures R7, R8, and R9 for c/W values of 0, 0.1, and 0.2, respectively. The case of $c/W = 0$ corresponds to pure Mode II.

The amount of Mode I component increases with increasing values of the *c/W* ratio. The expressions for the normalized stress intensity factors are

$$\frac{K_I}{\left[\dfrac{6q}{W}\sqrt{\pi a}\right]} = \left(\frac{c}{W}\right) F_I \left(a/W\right) \tag{R5}$$

$$\frac{K_{II}}{\left[\dfrac{q\left(a/W\right)^{1.5}}{\sqrt{W\left(1-a/W\right)}}\right]} = F_{II} \left(a/W\right) \tag{R6}$$

which are based on the reference solutions in terms of the load, *P*, per thickness, from the paper by He and Hutchinson [14]. Expressions for the shear force, *q*, and the boundary correction factors, F_I (*a/W*) and F_{II} (*a/W*), are as follows:

$$q = \frac{P\left(b_2 - b_1\right)}{b_1 + b_2} \tag{R7}$$

$$F_I\left(a/W\right) = 1.122 - 1.121\left(a/W\right) + 3.74\left(a/W\right) + 3.873\left(a/W\right)^3 - 19.05\left(a/W\right)^4 + 22.55(a/W)^5$$

for a/W ≤ 0.7 (R8)

and

$$F_{II}\left(a/W\right) = 7.264 - 9.37\left(a/W\right) + 2.74\left(a/W\right)^2 + 1.87\left(a/W\right)^3 - 1.04\left(a/W\right)^4 \ \ for \ 0 \le a/W \le 1$$
(R9)

The BIECRX results are in excellent agreement with the analytic solutions reported by He and Hutchinson [14], as shown in Figures R7 through R9.
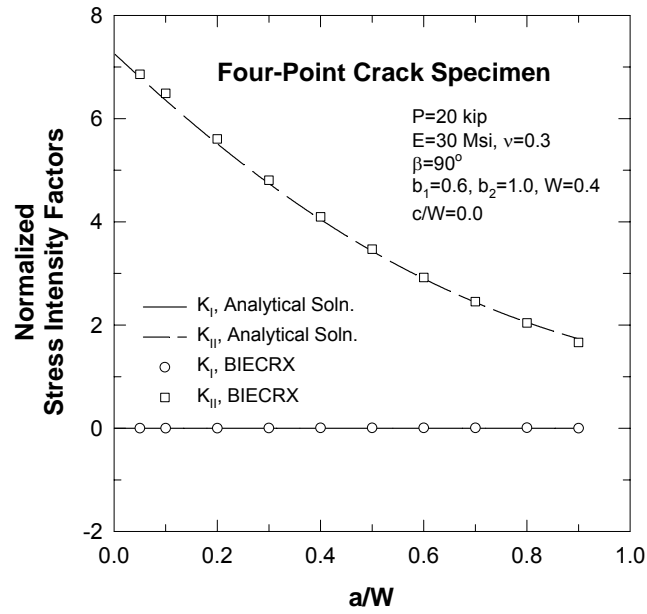
Figure R7. Normalized K_I and K_{II} as a function of *a/W* for isotropic material and an asymmetric four-point bend crack specimen with *c/W* = 0.
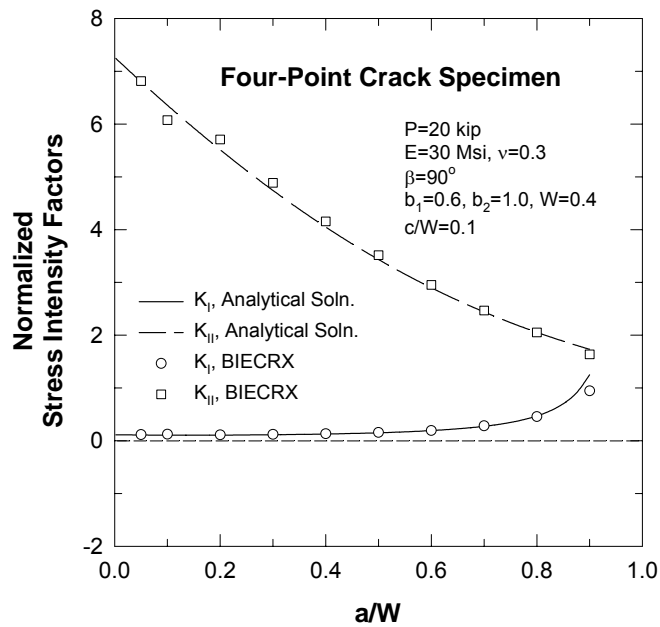

Figure R8. Normalized K_I and K_{II} as a function of *a/W* for isotropic material and an asymmetric four-point bend crack specimen with *c/W* = 0.1.
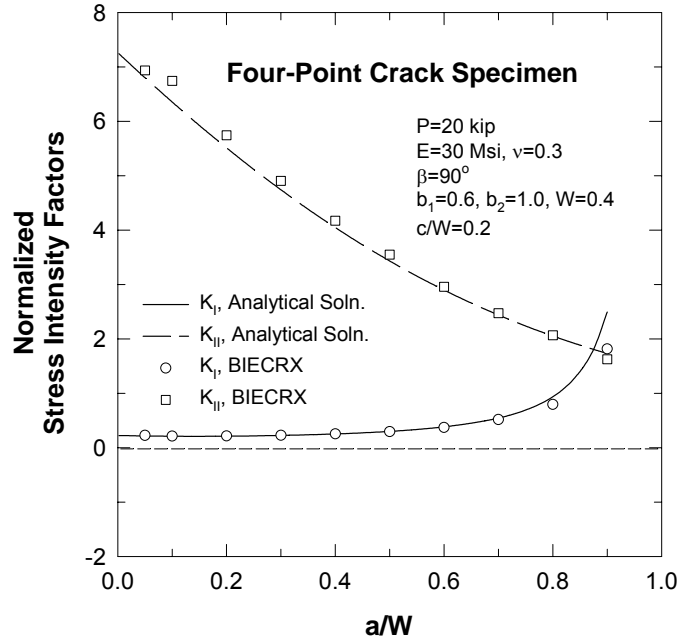
Figure R9. Normalized K_I and K_{II} as a function of *a/W* for isotropic material and an asymmetric four-point bend crack specimen with *c/W* = 0.2.

Stress intensity factor solutions for the AFPB crack specimen of PWA 1484 single crystals were also obtained for (010) and (111) cracks. K solutions for the crystallographic cracks of several crystallographic orientations, crack depths (*a*), and crack offset distances (*c*) were computed. Figure R10 shows the BIE mesh for a (111) crack in an asymmetric four-point bend (AFPB) specimen of width, *W*. Figures R11 and R12 present the results for the (111) crack subjected to pure shear and mixed Mode I and II loading, respectively. Also shown in these figures are the analytical solutions for isotropic materials based on the beam theory from He and Hutchinson [14]. A comparison of the anisotropic and isotropic K solutions indicate that the K solutions are essentially identical for the two cases. In the cases considered, elastic anisotropy in PWA 1484 does not cause significant changes to the K solutions for *a/W* ≤ 0.8. Thus, the analytical K solutions for isotropic materials can be used for PWA 1484 for *a/W* ≤ 0.8.
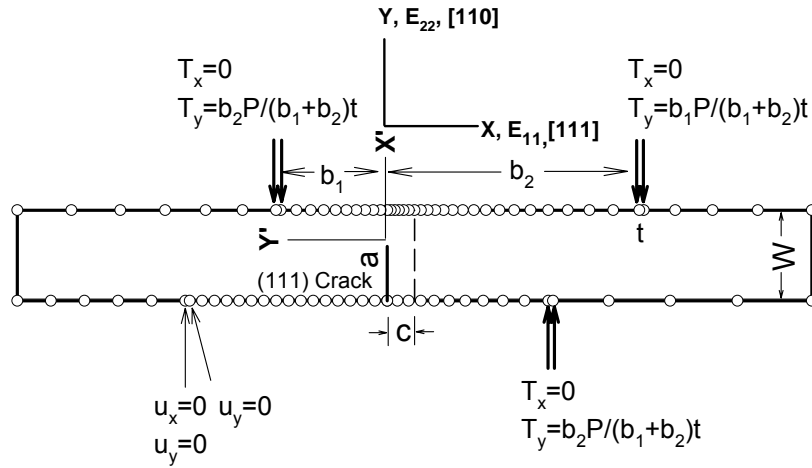
Figure R10. A BIE mesh of the AFPB crack specimen showing the crack depth *a*, the offset distance *c*, the specimen width *W*, the crack coordinate system (X' - Y'), and the material coordinate (X-Y) system for an anisotropic material.
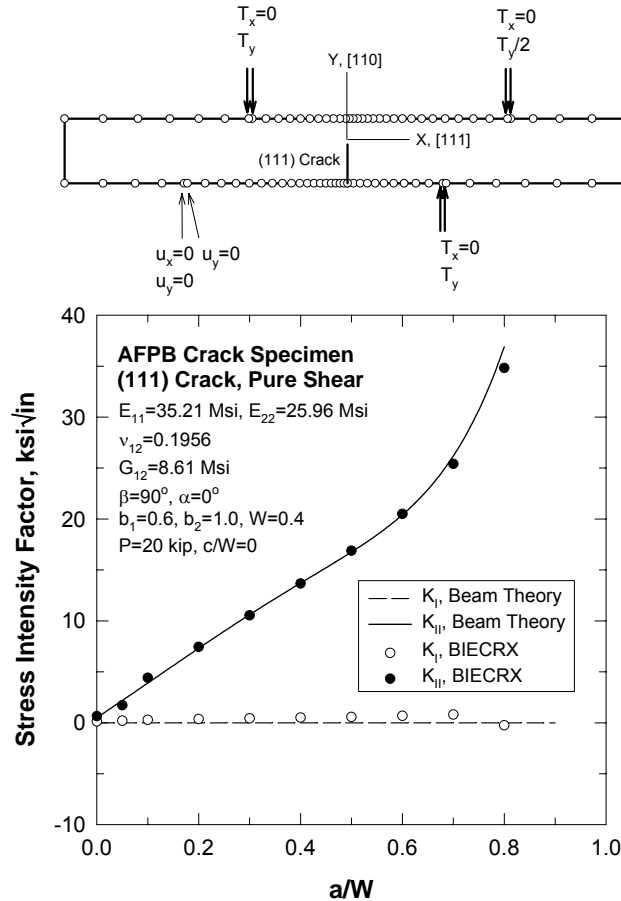

Figure R11. Comparison of the anisotropic BIECRX solutions of stress intensity factors of an (111) crack subjected to pure shear (*c/W* = 0) and the analytical solutions of He and Hutchinson [14] based on isotropic beam theory.
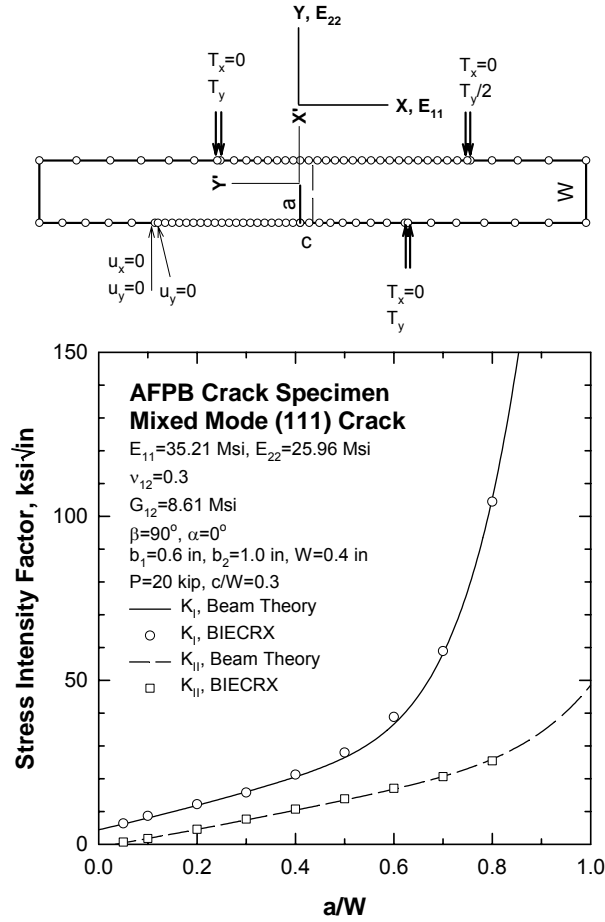
Figure R12.   Comparison of the anisotropic BIECRX solutions of stress intensity factors of an (111) crack subjected to mixed-mode loading ($c/W = 0.3$) and the analytical solutions of He and Hutchinson [14] based on isotropic beam theory.

In addition to c/W, the mode mixity of a crack in the AFPB specimen varies with the a/W ratio. This point is illustrated in Figure R13, which shows the K_{II}/K_I ratio and the phase angle, $\phi = \arctan(K_{II}/K_I)$; both increase with increasing normalized crack depth, reach a maximum at an a/W ratio of about 0.4–0.5, and then decrease with increasing a/W. This mode-mixity gradient is distinctly different from that of the SEN specimen with an angled crack. There is a minor discrepancy between the BIECRX result and the analytical solution obtained by He and Hutchinson using the isotropic beam theory [14] for $a/W = 0.9$. The discrepancy can be ignored since it occurs at a crack depth that is too large for practical use in testing. For this study, $a/W \leq 0.8$ was used and the two K solutions are in good agreement for $a/W \leq 0.8$. The mode-mixity parameter, K_{II}/K_I, and the phase angle, ϕ, were also computed as a function of a/W and c/W using the analytical expressions of K solutions for

isotropic materials obtained by He and Hutchinson using beam theory [14]. These results are presented in Figures R14 and R15, which indicate that both the K_{II}/K_I and the phase angle, ϕ, increase with *a/W*, reach a maximum, and then decrease with increasing *a/W*. To maintain a relatively constant K_{II}/K_I or phase angle, the *a/W* needs to be limited to within a certain range. For $\phi = 22.5$-$67.5°$, it is required that $0.25 < a/W < 0.7$.
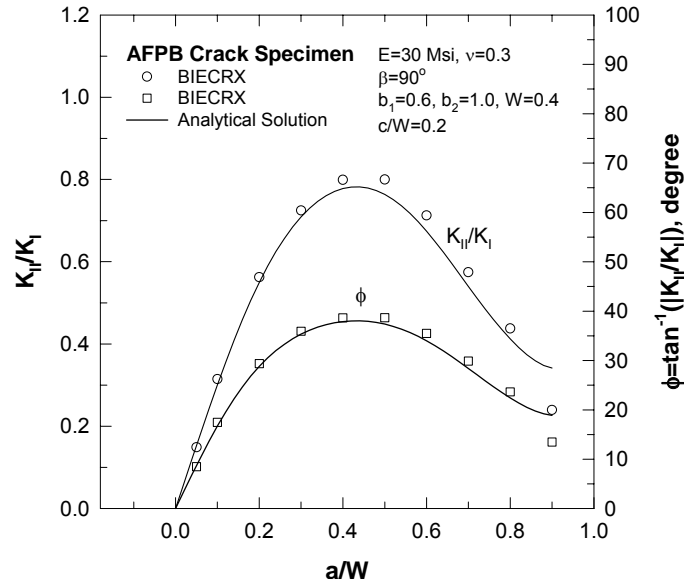

Figure R13.   The mode-mixity ratio, K_{II}/K_I, and the phase angle, $\phi = \tan^{-1} (K_{II}/K_I)$, as a function of *a/W* for the AFPB crack specimen.
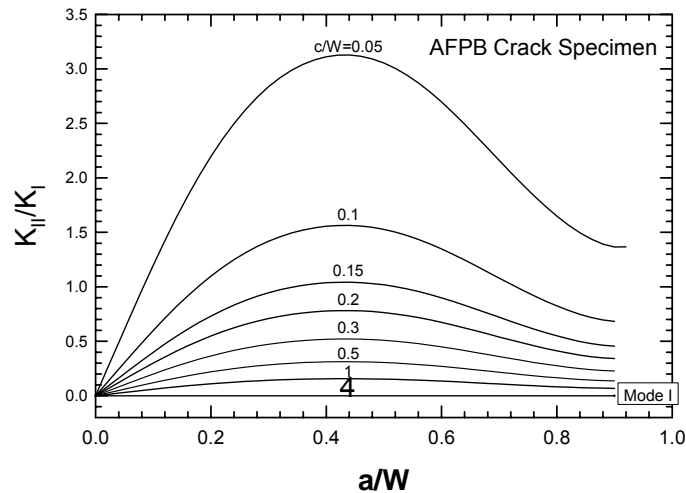

Figure R14.   Mode mixity parameters, K_{II}/K_I, as a function of crack depth, *a*, normalized by specimen width, *W*, of the AFPB specimen for various *c/W* ratios, where *c* is the offset distance of the crack from the symmetry line in the AFPB fatigue fixture.
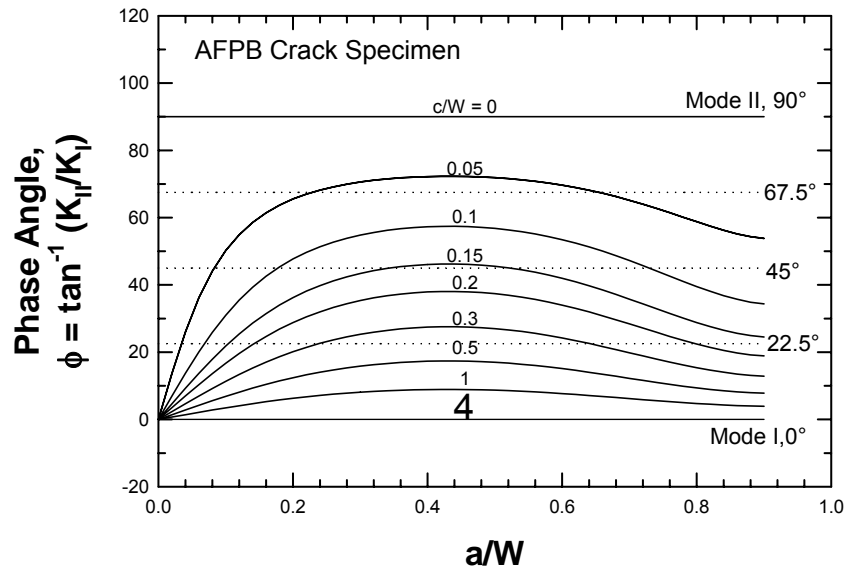
Figure R15.   Phase angle, N = tan^{-1} (K_{II}/K_{I}), as a function of *a/W* for the AFPB crack specimen for various *c/W* ratios. Dashed lines indicate selected phase angles used in the mixed-mode experiments.

R.2   MIXED-MODE FATIGUE CRACK GROWTH THRESHOLD EXPERIMENTS

An experimental program for determining the mixed-mode fatigue crack growth thresholds of PWA 1484 single crystals was developed after consultation with team leaders at P&W and GEAE. The test matrix, shown in Table R1, was designed to measure the fatigue crack growth thresholds for TPNC and macroscopic (111) cracking as a function of mode mixity, frequency, temperature, and crystal orientation. The asymmetric four-point bend (AFPB) test technique was selected because a wide range of mode mixity could be attained. In particular, it was used to generate fatigue crack growth threshold for different values of the phase angle, $\phi = \tan^{-1} (\Delta K_{II}/\Delta K_{I})$, ranging from 0° (pure Mode I) to 90° (pure Mode II). The mixed-mode tests were performed in air at 1100°F. The test frequency was 20 Hz at a stress ratio, R, of 0.5.

Table R1. Test Matrix for Subtask S.1.4.2.1

Work Package	Primary Orientation, Y	Secondary Orientation, X	Crack Plane, Y′	Growth Direction, X′	R	T	Freq., Hz	Mixed Mode Phase Angle {arctan (K_{II}/K_I)}	No. Tests	Single Crystal Number	Specimen Number
Multiaxial Fatigue Crack Growth (Asy, Four Pt Bend)	<010> <010> <111> <111> 10° off <010>*	<100> <110> <211> <110> 10° off <011>**	{010} {010} {111} <111> {111}	<100> <110> <211> <110> <211>	0.5	1100°F	20	0, 22.5, 45, 60, 80, 90, 0, 22.5, 45, 60, 80, 90 0, 45, 60, 80, 90 0, 22.5, 45, 60, 80, 90 0, 45, 60, 80, 90	6 6 5 6 5	AL2KS #A, #B T20WK #1, #2, #3, #4 T20×9 #1, #2, #3 T20×9, #6, #7, #8, #9, #10, #11 T20WK #7, #8	SC-1, SC-2, SC-3, SC-4 SC-5, SC-6, SC-7, SC-8 SC-9, SC-10, SC-11 SC-13, SC-14, SC-15, SC-16, SC-17 SC-19, SC-20

* Near <711>
** Near <133>

The crystallographic orientations were selected to promote (010) decohesion, (111) cracking, or the competition between (010) decohesion and (111) cracking. As reported earlier [3, 4, 6], (010) decohesion was determined to be the primary fatigue mechanism in the near threshold regime of PWA 1480 and PWA 1484. The other important fatigue mechanism is (111) crystallographic cracking, which occurs at lower temperatures and possibly higher frequencies. The possible transition of (010) Mode I cracks to (111) crystallographic cracking was examined using single crystal specimens oriented at 10° off (010) for which a (111) plane was oriented at a 45° angle from both the loading direction and the initial Mode I notch

R.2.1 Asymmetric Four-Point Bend Test Fixture

A schematic of the AFPB test fixture is shown in Figure R16, which is a modification of the UC-Berkeley design [15] to accommodate elevated temperature testing. The entire fixture was fabricated from a single block of AD98 alumina, while the loading pins were fabricated from silicon carbide. Dimensions of the AFPB crack specimen are shown in Figure R17. Both testing and data acquisition are computer-controlled and fully automated. A commercial computer software package made by Fracture Technology Associates was used to control the automated fatigue crack growth threshold testing. Since the AFPB specimen was not part of the standard software package, stress intensity solutions for the AFPB crack specimen were coded and incorporated into the control software. Control of the test machine was based on the equivalent stress intensity factor, ΔK_{eq}, defined as

$$\Delta K_{eq} = \left[\Delta K_I^2 + \Delta K_{II}^2\right]^{1/2} \tag{R10}$$

where ΔK_I and ΔK_{II} are the Mode I and Mode II stress intensity factor ranges, respectively. A clam-shell furnace with resistance heating was used to provide the high temperature capability for the AFPB test fixture. Figure R18 shows the set-up of the AFPB test fixture for high-temperature fatigue crack growth threshold testing.
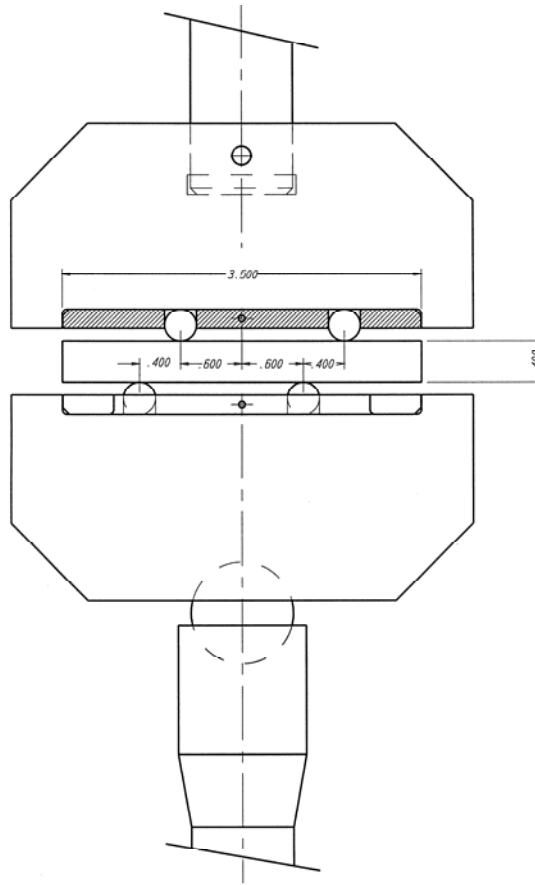
Figure R16.   Schematic of the high-temperature asymmetric four-point bend fatigue test fixture designed at SwRI®.
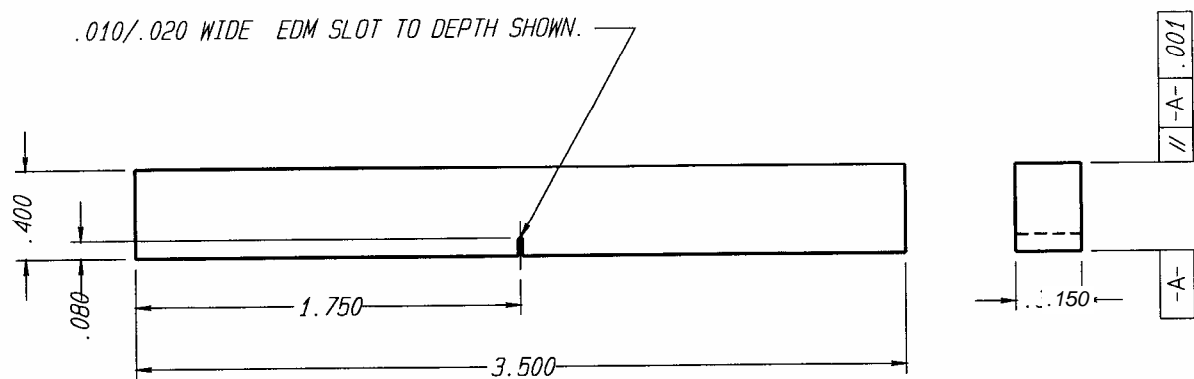

Figure R17.   Dimensions of the AFPB crack specimen for mixed-mode fatigue crack growth testing of PWA 1484 at elevated temperature. All dimensions in inches.

Figure R18.   Set-up of the high-temperature asymmetric four-point bend test fixture for mixed-mode fatigue crack growth studies developed at SwRI.

R.2.2   Stress Intensity Factors

The procedure for computing the stress intensity factors of mixed-mode fatigue cracks in single crystals PWA 1484 during asymmetric four-point bend (AFPB) fatigue testing is summarized in this section. Two different procedures were used to compute the stress intensity factors of mixed-mode cracks in PWA 1484: (1) for straight self-similar cracks, and (2) for deflected or kinked cracks. The first procedure was used during fatigue threshold testing since crack deflection could not be predicted prior to testing or corrected during testing. The second procedure was applied to deflected cracks in post-test data analysis after the crack deflection angle had been determined.

R.2.2.1   Self-Similar Cracks

This K computation methodology is applicable to straight mixed-mode cracks that exhibit self-similar crack growth along the original crack plane. In this circumstance, the measured crack lengths are the actual crack lengths. The computed stress intensity factor ranges and the fatigue crack growth rates represent the actual crack driving force and the growth resistance of the material. Self-similar crack growth has been observed in PWA 1484 for certain crystal orientations and loading conditions.

For most crystal orientations and loading conditions studied, mixed-mode cracks in PWA 1484 are non-straight and propagate in a non-self-similar manner. Even though these cracks were not self-similar after deflection, the methodology outlined here was used because the crack measurement technique, which was a potential drop technique, measured the projected crack length when a crack deflects. In addition, it was not feasible to compute the stress intensity factors of deflected cracks during testing because the crack deflection angle could not be determined until after the test had been completed. Although this methodology did not give the correct local stress intensity ranges and fatigue crack growth rates for deflected cracks during testing, these calculations were needed during the test to perform the decreasing-K test procedure. Post-testing data analyses after the crack deflection angle had been measured were subsequently used to compute the local stress intensity factors for deflected cracks.

Figure R19 shows the geometry of the AFPB test specimen subjected to a cyclic load, ΔP. The width of the specimen is W and its thickness is B. The offset distance of the crack measured from the symmetry plane of the loading configuration is designated as c, while the initial crack length after Mode I fatigue precracking is a_i. Under mixed-mode fatigue loading, the fatigue crack deflects to propagate at an inclined angle, θ, measured from the reference axis X, as shown in Figure R20. The projected crack length, a_p, is calculated as

$$a_p = a_i + a_K \cos\theta \qquad\qquad (R11)$$

while the actual crack length, a, is computed as

$$a = a_i + a_K \qquad\qquad (R12)$$

where a_K is the actual length of the kinked crack.

The mixed-mode fatigue crack growth threshold tests were performed by applying the cyclic load, ΔP, under a constant stress ratio, $R = P_{min}/P_{max}$, where P_{max} is the maximum load and P_{min} is the minimum load. The crack lengths were measured using a potential drop technique that measures the projected crack length, denoted as a_p in Figures R19 and R20, when crack growth is not self-similar. Both the crack growth rates and the stress intensity factors were computed based on the projected crack length, a_p. Since the K solutions generated for anisotropic materials using an

anisotropic fracture mechanics code (BIECRX [8]) are in agreement with analytical solutions for isotropic materials [14], the Mode I and II stress intensity ranges were computed using the analytical equations for isotropic materials, which are given by [14]

$$\Delta K_I = \left[\frac{6\Delta q}{W}\right]\left(\frac{c}{W}\right)(\pi a_p)^{1/2} F_I\left(a_p/W\right) \tag{R13}$$

and

$$\Delta K_{II} = \left[\frac{\Delta q\left(a_p/W\right)^{3/2}}{\sqrt{W\left(1 - a_p/W\right)}}\right] F_{II}\left(a_p/W\right) \tag{R14}$$

with

$$\Delta q = \frac{\Delta P(b_2 - b_1)}{B(b_1 + b_2)} \tag{R15}$$

$$F_I\left(a_p/W\right) = 1.122 - 1.121\left(a_p/W\right) + 3.74\left(a_p/W\right)^2 + 3.873\left(a_p/W\right)^3 - 19.05\left(a_p/W\right)^4$$
$$+ 22.55\left(a_p/W\right)^5 \text{ for } a_p/W \leq 0.7 \tag{R16}$$

and

$$F_{II}\left(a_p/W\right) = 7.264 - 9.37\left(a_p/W\right) + 2.74\left(a_p/W\right)^2 + 1.87\left(a_p/W\right)^3 - 1.04\left(a_p/W\right)^4$$

$$\text{for } 0 \leq a_p/W \leq 1 \tag{R17}$$

An equivalent stress intensity factor, ΔK_{eq}, defined on the basis of the elastic energy release rate range, ΔG, can be expressed as

$$\Delta K_{eq} = \left[\Delta K_I^2 + \Delta K_{II}^2\right]^{1/2} \tag{R18}$$

where ΔK_I and ΔK_{II} are the Mode I and Mode II stress intensity factor ranges, respectively. The corresponding load ratio, R, is given by

$$R = \frac{P_{min}}{P_{max}} = \frac{K_{I,min}}{K_{I,max}} \tag{R19}$$

where $K_{I,min}$ and $K_{I,max}$ are the minimum and maximum values of the Mode I stress intensity factors, respectively. The phase angle, ϕ, that indicates the mode mixity is computed as

$$\phi = \tan^{-1}\left(\frac{\Delta K_{II}}{\Delta K_I}\right) \qquad (R20)$$

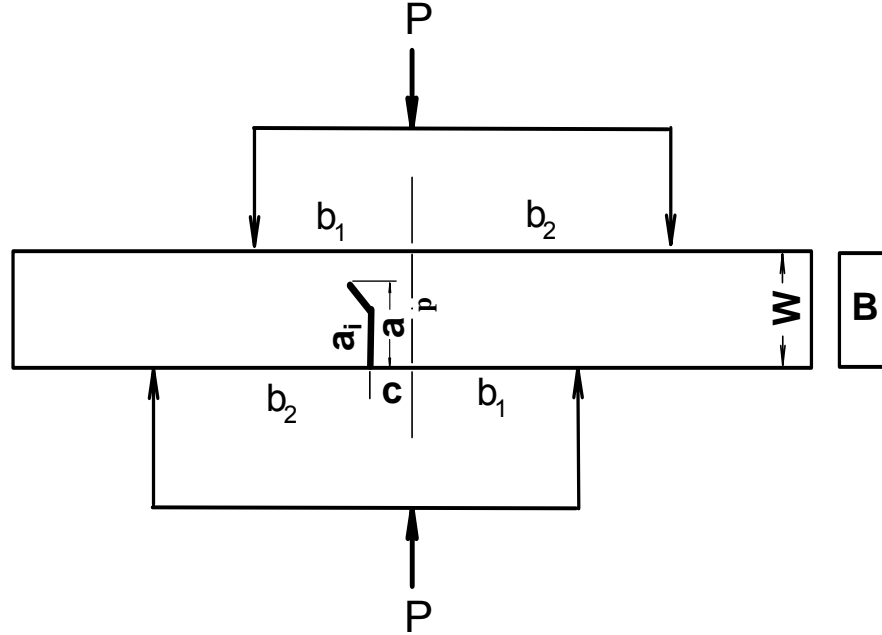where ΔK_I and ΔK_{II} are given in Equations (R3) and (R14).

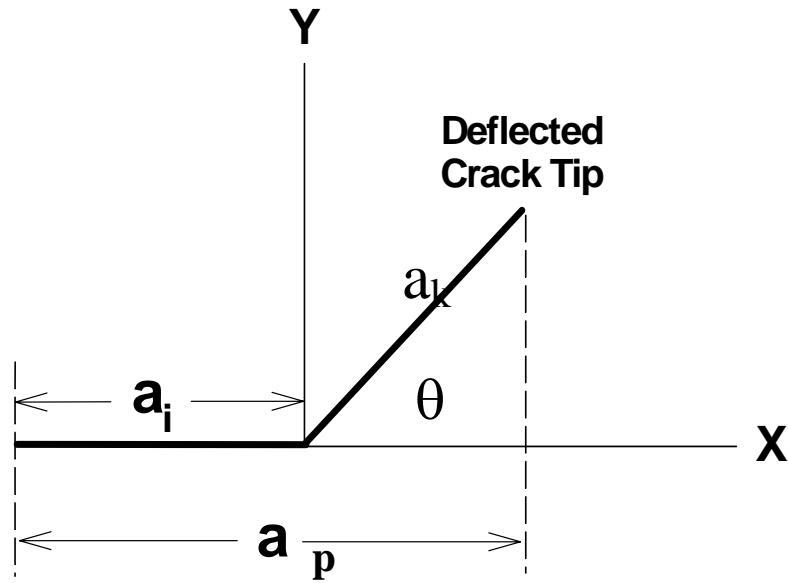Figure R19.   Geometry of the AFPB crack specimen with a deflected crack subjected to mixed-mode loading.

Figure R20.   Nomenclature of a deflected mixed-mode crack with a projected length, a, and a crack angle, θ, measured from the x-axis.

The above methodology is limited to mixed-mode cracks that remain straight and exhibit self-similar crack growth along the existing crack plane ($\theta = 0$). In this situation, the measured crack lengths are the actual crack lengths. The computed stress intensity factor ranges and the fatigue crack growth rates represent the actual crack driving force and the crack growth resistance of the material. However, neither is true when the fatigue crack deflects to propagate on an inclined plane ($\theta > 0$). Under non-self-similar crack growth, the crack length measured by the potential drop technique corresponds only to the projected crack length. The stress intensity factor ranges that were used to compute the projected crack length were not the local values at the crack tip since they did not take into account the deflected crack path. The methodology for computing the stress intensity factors of deflected cracks along the experimentally observed crack path is described in the next section.

R.2.2.2   Deflected or Kinked Cracks

Mixed-mode fatigue cracks in PWA 1484 tested at 1100°F often deflect from the original crack path and do not propagate in a self-similar manner. To better characterize the local crack driving force, the stress intensity factors of individual deflected cracks in PWA 1484 mixed-mode specimens were computed using the finite-element code FRANC2D/L [9]. The computations were first done for a crack path normal to the maximum principal tensile stress, which corresponds to the local Mode I direction. Additional computations were also performed for specimens whose crack paths deviated from the maximum principal tensile stress direction.

Figure R21 shows the FE mesh for computing the K solutions of a mixed-mode crack deflected to propagate normal to the local maximum principal tensile stress. Individual mixed-mode AFPB test specimens were modeled using the experimentally determined crack length and offset distance so that the calculated and measured crack paths could be compared directly. Most of the K computation was performed by Dr. Reji John at the Air Force Research Laboratory (AFRL), while selected cases were computed at Southwest Research Institute™ (SwRI). Figures R22 and R23 show the calculated crack path and the K solutions of the deflected crack for [010]/[001] oriented PWA 1484, respectively. Essentially identical results were obtained by AFRL

and SwRI. Figure R23 indicates that K_{II} is zero shortly after crack deflection along the maximum tensile stress (MTS) direction. The K_I of the deflected crack can generally be expressed as

$$\frac{\Delta K_1}{\left(\dfrac{\Delta P}{BW}\right)\sqrt{\pi a}} = \sum_{n=0}^{n=4} b_n \left(\frac{a}{W}\right)^n \tag{R21}$$

where ΔP is the load range, B is the thickness, W is the width of the specimen, and a is the actual length of the deflected crack. The regression coefficients, b_n, were obtained by fitting the FEM results to an nth order polynomial of a/W, where the number of the terms, n, is 4 in most cases. An example of the regression analysis of the K solutions is shown in Figure R24. Since the cracks deflect at different crack lengths from test-to-test, it was necessary to do an FEM analysis and fit normalized K solutions for each specimen exhibiting deflected cracks.
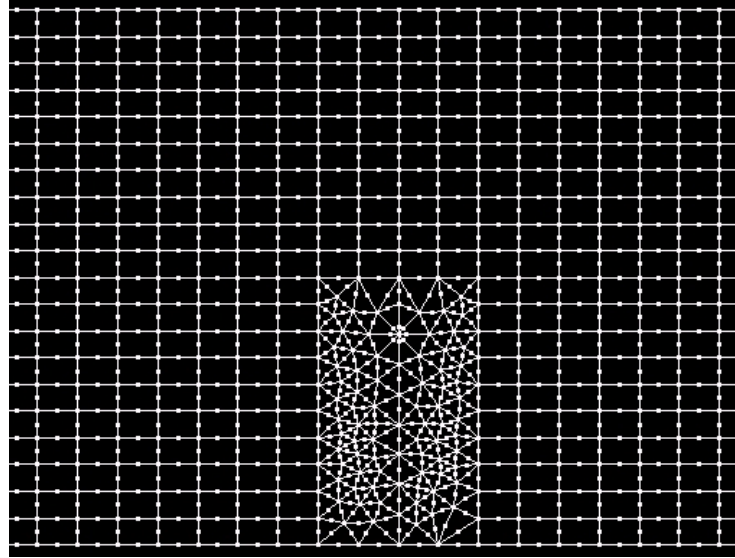
Figure R21.   FEM mesh used to compute the stress intensity factors of a deflected crack using the FRANC2D/L code. Figure shows crack configuration prior to crack deflection.
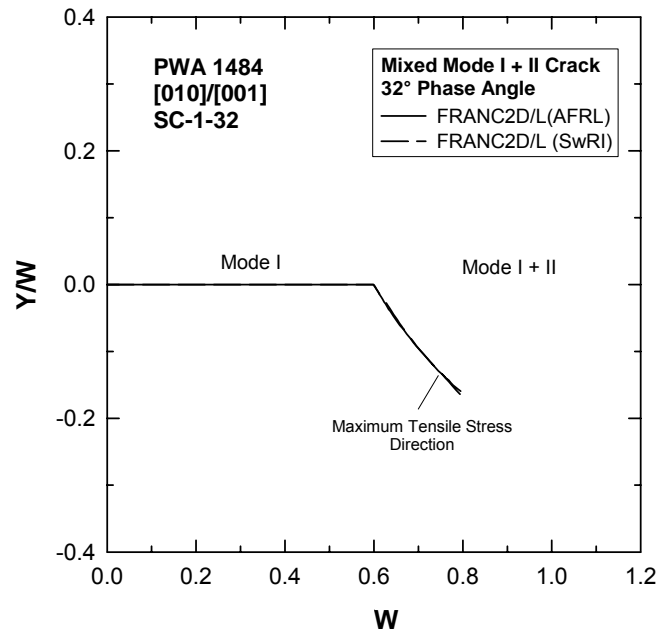
Figure R22.   Calculated crack deflection paths along the direction of maximum tensile stress (MTS) direction via the FRANC2D/L finite-element code for a crack in PWA 1484 subjected to mixed Mode I and II loading at a 32° phase angle.
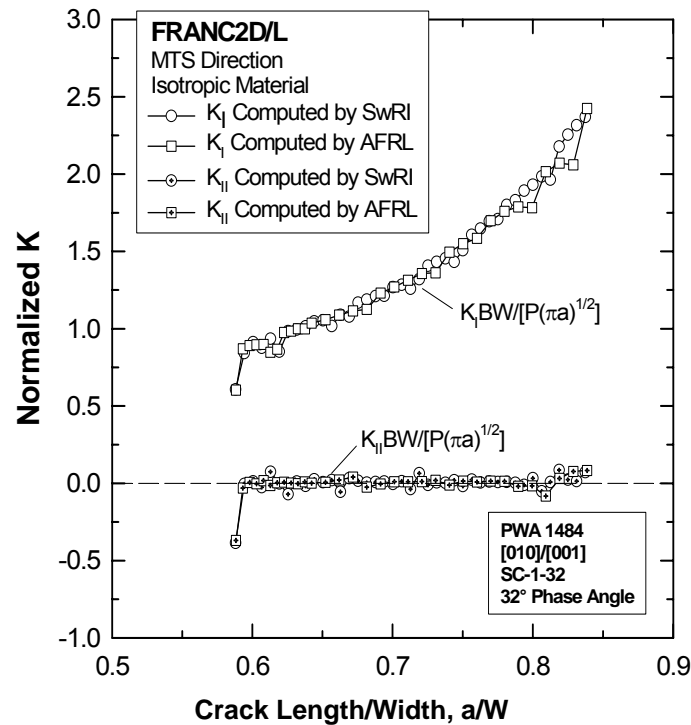

Figure R23.   FRANC2D/L K solutions for a deflected crack along the MTS direction computed by AFRL and SwRI.
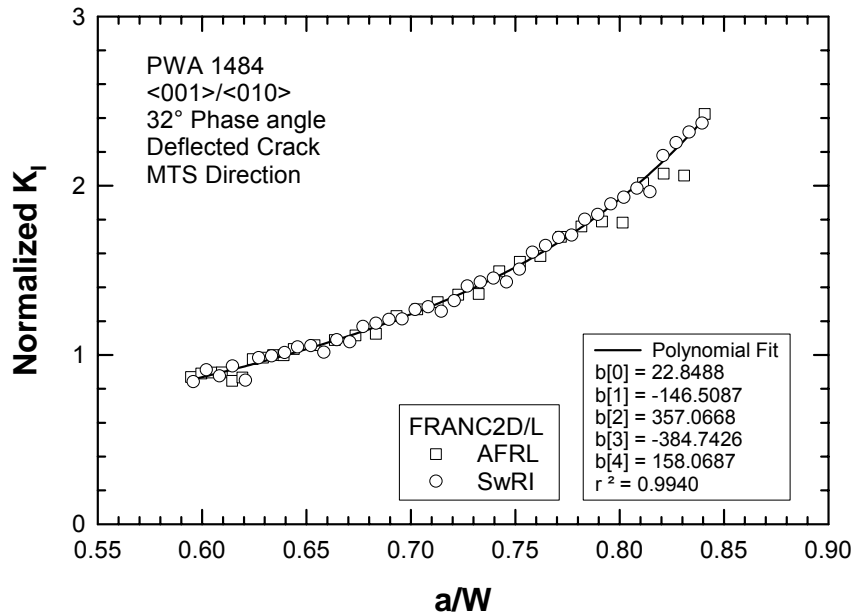
Figure R24.   Regression fit of normalized K_I ($K_I BW/P\sqrt{\pi a}$) results as a function of actual crack length, a, normalized by the width of the specimen, W.

Figure R25 presents the FEM mesh that was used to compute the K solutions for a deflected crack along the experimentally observed crack path. This computation required inputting the experimental crack deflection path manually and computing the K solutions incrementally along the imposed crack trajectory. For this particular case, the K solutions for a deflected crack along the experimentally observed crack path were computed for specimen SC-16-90, which was tested under Mode II and exhibited one of the largest crack deflection angles. The crack deflection angle was 48°, compared to a theoretical angle of 70.5° for pure Mode II based on the MTS criterion. The K solutions for the actual crack path showed predominantly K_I with a small K_{II}. The normalized K_I and K_{II} are plotted as a function of the actual crack length in Figure R26, which also compares the K solutions for the actual path against those for the MTS path. Additional K solutions of the actual crack path in other single crystal specimens are presented in Section R.4.
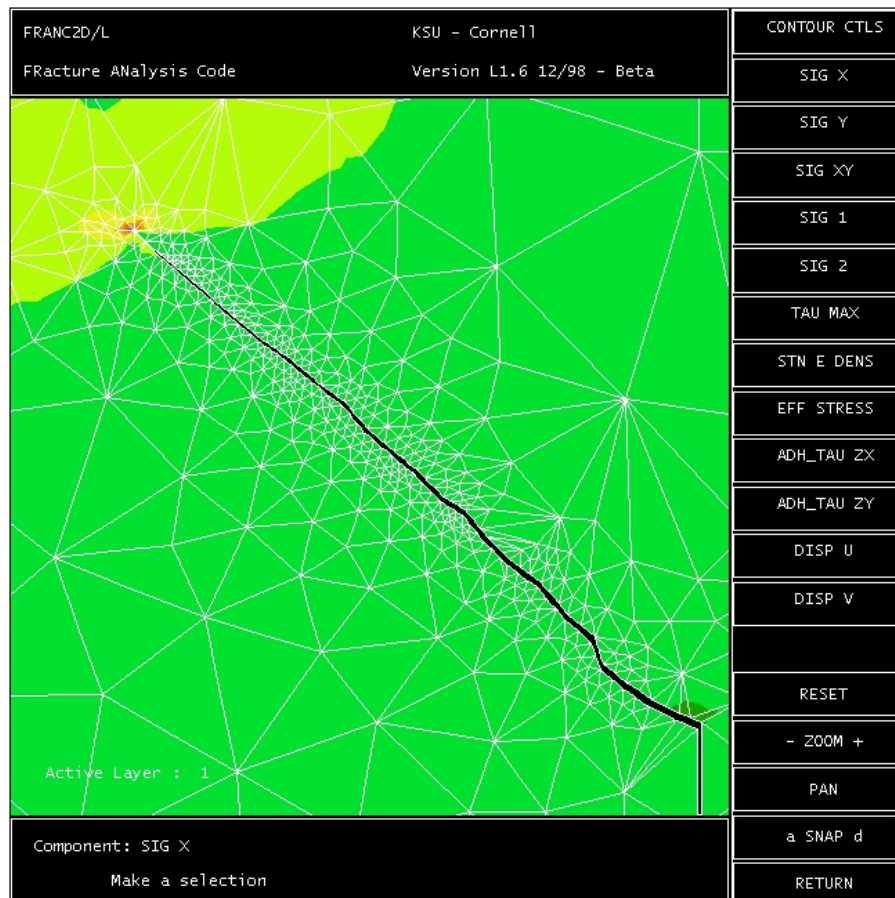
Figure R25.   FEM mesh used to obtain FRANC2D/L K solutions along the actual deflected crack path in specimen SC-16 tested under pure Mode II loading.
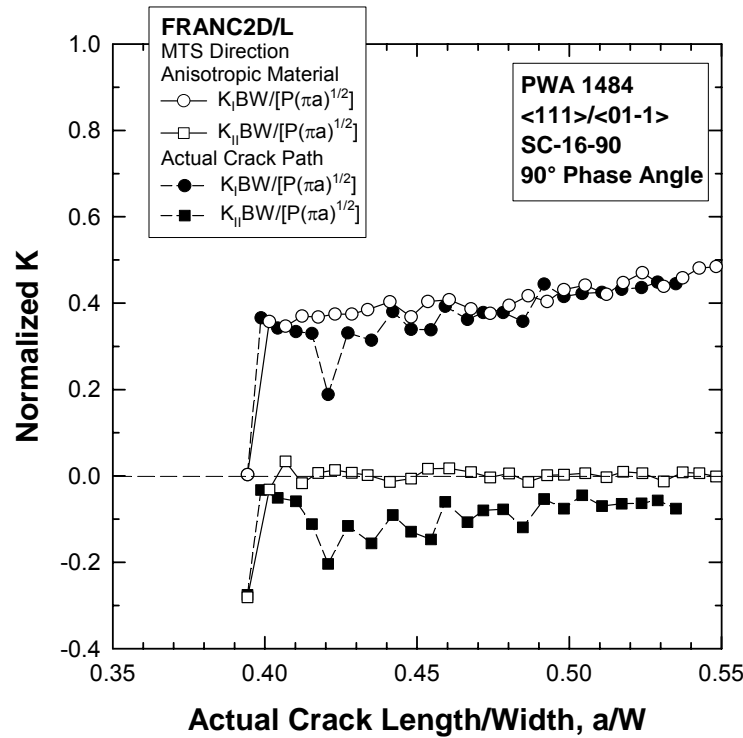
Figure R26.   FRANC2D/L K_I and K_{II} solutions obtained using the actual deflected crack path for specimen SC-16-90 tested under pure Mode II loading.

R.2.3   Experimental Procedure

Fatigue crack growth threshold stress intensity factor values were determined for PWA 1484 at 1100°F, at $R = 0.5$, and at 20 Hz using a shed rate, C, of -20 in^{-1}, where $C = dln\Delta K/da$. Crack length was measured using a potential drop technique. The fatigue crack growth threshold was determined by load shedding starting at an initial ΔK of $\approx$10-12 ksi√in to a crack growth rate of 5×10^{-9} in/cycle or less. Fatigue precracking was performed at the test temperature (1100°F) under Mode I by symmetric four-point-bending. After the Mode I threshold was determined, the specimen was cooled down to ambient temperature. Replicas of the crack tip were taken in order to measure the actual crack path and length. The test fixture was then reconfigured to the AFPB mode by changing the positions of the loading pins and the offset distance, c. The specimen was then heated to the test temperature and FCG testing resumed after the specimen reached and stabilized at the desired temperature. Mixed-mode threshold values were determined by load shedding from an initial equivalent ΔK value of approximately 6 ksi√in to a crack growth rate of 5×10^{-9} in/cycle or less.

R.2.4 Fatigue Crack Growth Results

R.2.4.1 <u>Mode I Fatigue Crack Growth</u>

      A.   <001>/<010> Orientation

Four <001>/<010> specimens (SC-1, SC-2, SC-3, and SC-4) were precracked at 1100°F by the loading shedding technique to determine the Mode I fatigue crack growth thresholds. The fatigue cracks initiated from the notch were not totally straight. The crack path of SC-1 is presented in Figure R27. The fatigue crack that initiated from the notch at a ΔK of $15 \approx$ ksi$\sqrt{\text{in}}$ was initially inclined to the loading axis. It propagated as an inclined crystallographic (111) crack under decreasing ΔK until the ΔK reached about 7.8 ksi$\sqrt{\text{in}}$. Then, the fatigue crack changed growth direction and propagated in a direction normal to the loading axis, i.e., as a predominantly Mode I crack, until crack arrest occurred.
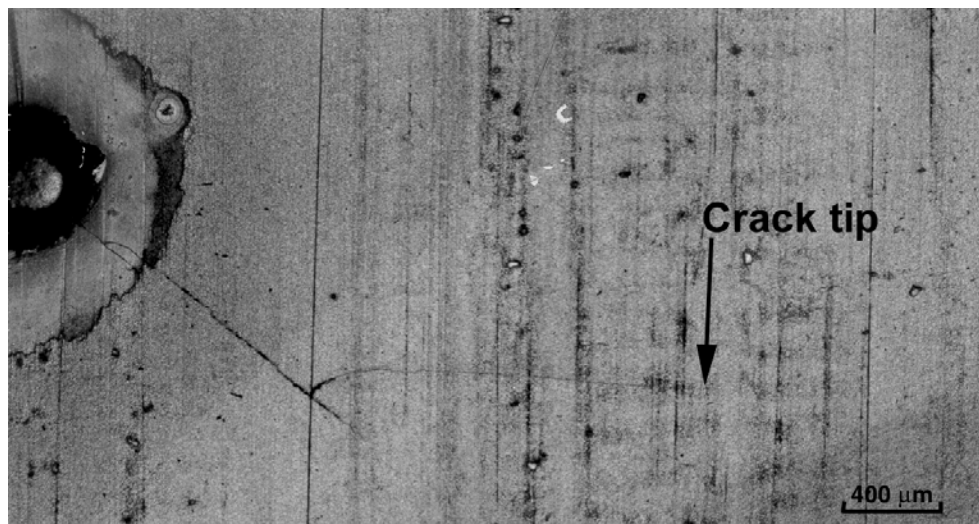
Figure R27.   Fatigue crack growth path of PWA 1484 (Specimen SC-1) during nominal Mode I fatigue precracking by cyclic load shedding at 1100°F. A crystallographic (111) crack initiated from the notch root, but it became a Mode I crack on a TPNC plane when ΔK_I decreased.

A summary of the da/dN data is presented in Figure R28. The Mode I thresholds show some scatter, ranging from 2.83 to 3.66 ksi$\sqrt{\text{in}}$. Figure R28 also shows a comparison of the Mode I threshold data obtained using the four-point-bend test technique against recent results for the same material generated at P&W for this program. The average value of the Mode I threshold for <001> oriented PWA 1484 determined by SwRI is $\approx$ 3.25 ksi$\sqrt{\text{in}}$, which is slightly lower than the value of 3.87 ksi$\sqrt{\text{in}}$ determined by P&W. This discrepancy is believed to be due to a small difference in the crystallographic orientation

between the SwRI and P&W specimens as the SwRI test specimens were about 5° off the <001> axis. It is noted that the crack off-set was ignored in the K_I calculation.
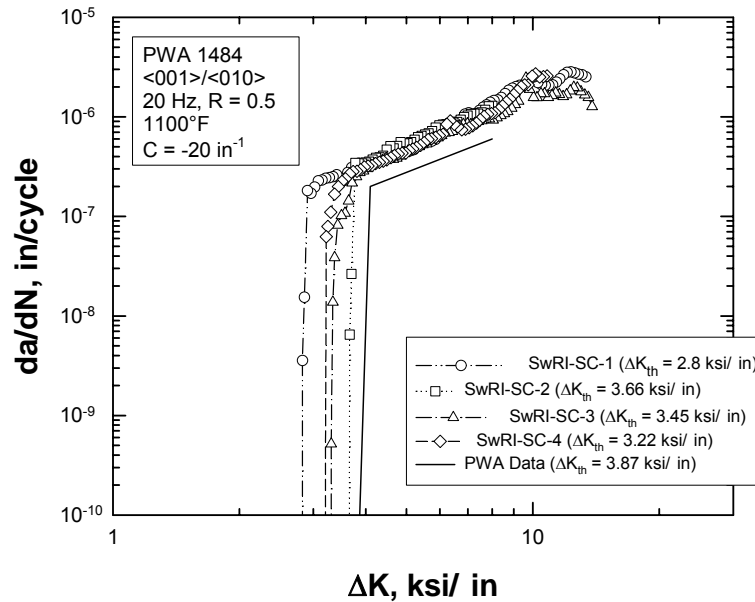

Figure R28.   Comparison of FCG threshold data of PWA 1484 obtained at SwRI using the four-point bend technique against P&W data obtained using the conventional method.

B.   *<001>/<110> Orientation*

Four <001>/<110> single crystal specimens (SC-5, SC-6, SC-7, and SC-8) were precracked under Mode I loading to obtain the thresholds for this crystal orientation at 1100°F. A summary of the Mode I threshold data of these four specimens is presented in Figure R29. The FCG curves of SC-6, SC-7, and SC-8 exhibited a change in the slope at around 7 ksi√in, but such a change did not occur in SC-5. The scatter in the Mode I thresholds is relatively small, ranging from 4.46 to 5.25 ksi√in.

R-29
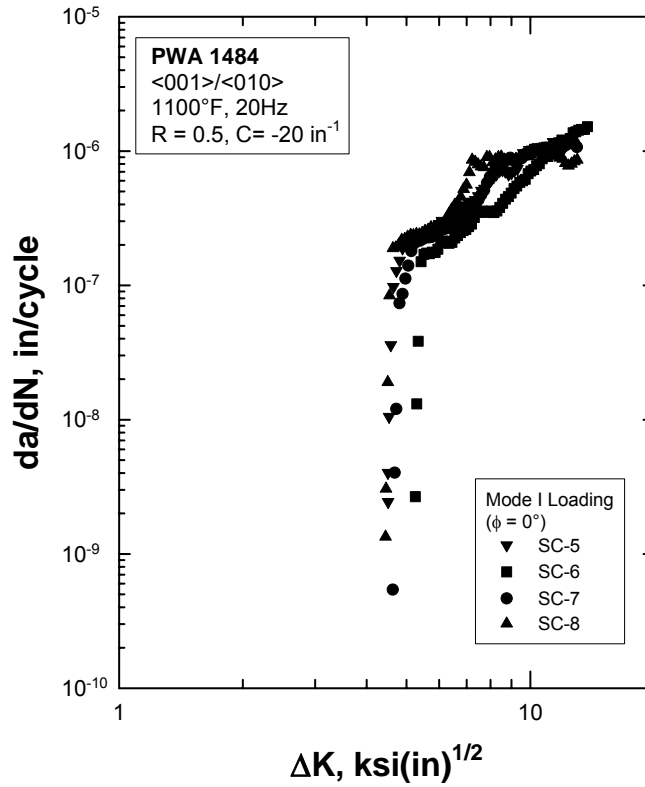
Figure R29.   Summary of Mode I FCG data of <001>/<110> oriented PWA 1484 single
crystals at 1100°F.

C.   *<111>/<11 2̄> Orientation*

Three <111>/<11 2̄> single crystal specimens (SC-9, SC-10, and SC-11) were
precracked under Mode I loading to obtain the thresholds at 1100°F. These precracks were
straight with little deviation from Mode I. A summary of the da/dN data for these specimens
is presented in Figure R30. The scatter in the Mode I thresholds is relatively small, ranging
from 3.40 to 3.63 ksi√in.
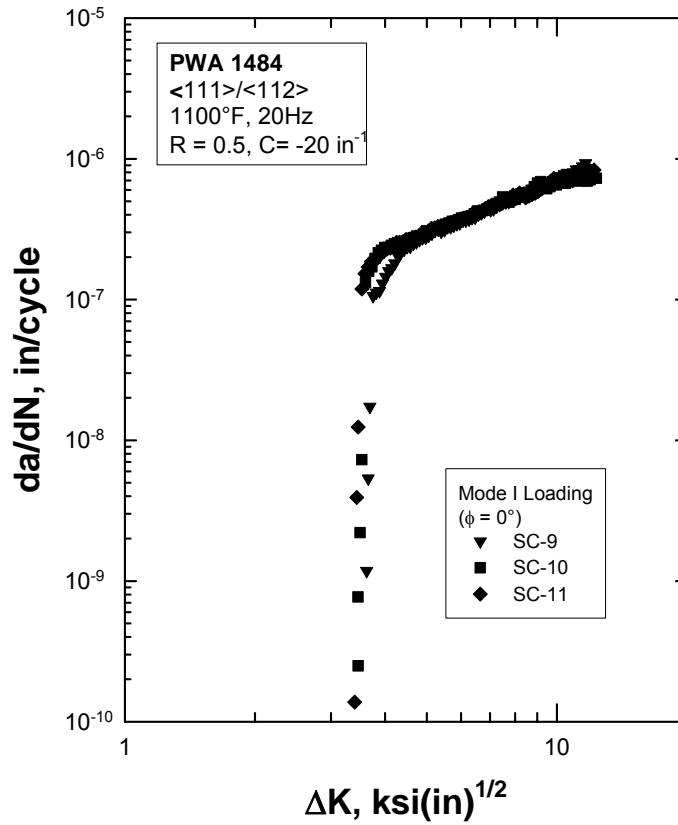
Figure R30.   Summary of Mode I FCG data of <111>/<11$\bar{2}$> oriented PWA 1484 single crystals at 1100°F.

D.   *<111>/<$\bar{1}$ 10> Orientation*

Five <111>/<$\bar{1}$ 10> single crystal specimens (SC-13, SC-14, SC-15, SC-16, and SC-17) were precracked under Mode I loading to obtain the thresholds for this crystal orientation at 1100°F. A summary of the Mode I threshold data of these five specimens is presented in Figure R31. The scatter in the Mode I thresholds is small, ranging from 3.46 to 3.84 ksi√in. SC-15 was overloaded due to an electrical spike after fatigue precracking, consequently, it was not used for subsequent mixed-mode testing.
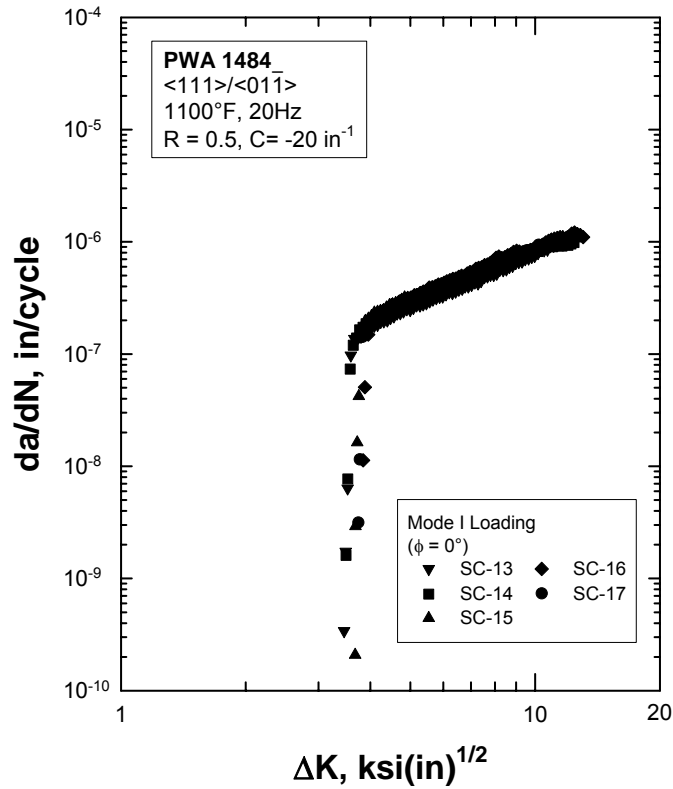
Figure R31.   Summary of Mode I FCG data of $<111>/<01\bar{1}>$ oriented PWA 1484 single crystals at 1100°F.

In all five cases, the Mode I precracks were very straight and aligned normal to the $<111>$ direction. Thus, they should be {111} cracks but they could also be TPNC cracks with an average $<111>$ orientation. Since there are no shear stresses acting on the {111} crack under Mode I loading, it is assumed that the apparent {111} Mode I crack grew by out-of-plane slip as in a TPNC crack, rather than by in-plane slip that is characteristic of slip band cracking.

   E.   *<001>+10°/<110>+10° Orientation*

Two single crystal specimens (SC-19 and SC-20) of this orientation were precracked under Mode I loading to obtain the Mode I thresholds at 1100°F. A summary of the Mode I threshold data of these two specimens is presented in Figure R32.
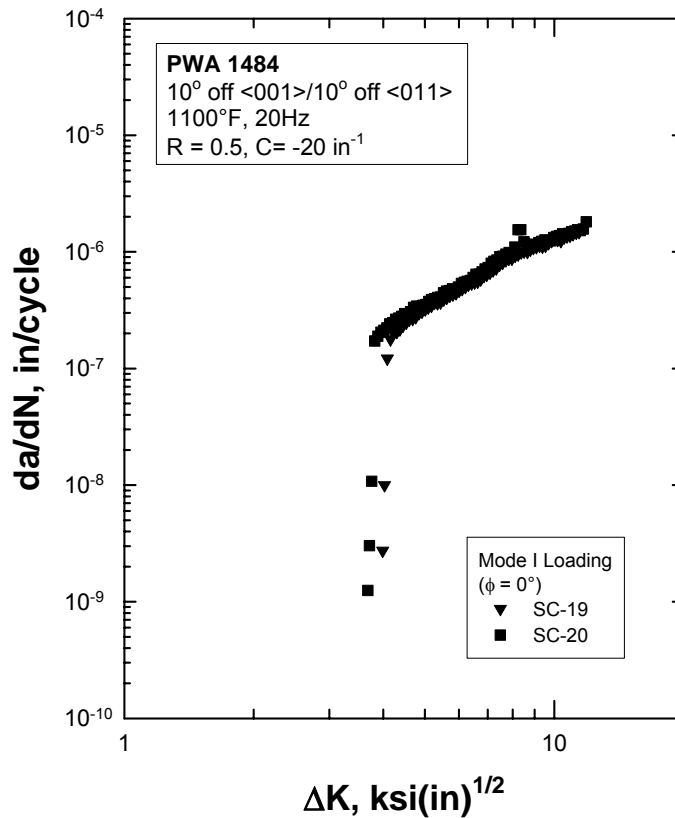
Figure R32.   Summary of Mode I FCG data of <001>+10°/<110>+10°
oriented PWA 1484 single crystals at 1100°F.

R.2.4.2   Mixed-Mode Fatigue Crack Growth

Mixed-mode FCG thresholds were measured for several phase angles (i.e., mode mixity) by loading shedding from an initial ΔK_{eq} of 6 ksi√in until crack arrest. In many cases, crack deflection occurred during threshold testing. As a result, the local stress intensity factors were not correctly described by those calculated based on straight, self-similar crack solutions. Post-test data analyses were performed using the procedures described in Section R.2.2.2 to compute the local stress intensity factors for the deflected cracks. The observed crack path, in general, deviated slightly from the local Mode I condition. K calculations based on FRANC2D/L along the actual crack path, however, indicated that the Mode II component was negligible and could be ignored.   Consequently, the local stress intensity factors of deflected cracks were computed for a crack path normal to the maximum principal stress direction. Details of the FCG results and the corresponding data analyses are described as follows:

Figure R33 illustrates the crack path observed in SC-1, which was tested under a phase angle of 32°. The K solutions from the FRANC2D/L analyses were applied to compute the actual stress intensity factor ranges at the deflected tip of the mixed Mode I and II crack. In particular, the mixed-mode crack was assumed to have deflected in the maximum tensile stress direction along whose path the ΔK_{II} component vanished. The calculated and observed crack trajectories of the mixed-mode crack in <001>/<010> oriented PWA 1484, tested at 32° phase angle, are compared in Figure R34, which shows that the agreement between the calculated and measured crack paths is excellent. Thus, the mixed-mode crack deflected along the MTS direction and was a Mode I crack locally. A comparison of the da/dN data for the Mode I and mixed-mode cracks, both before and after being corrected for crack deflection, is shown in Figure R35. For data represented by open squares, both the da/dN and the ΔK_I values have been corrected for crack deflection, and they are the actual values at the crack tip of the deflected crack. After being corrected for crack path deflection, the threshold of the deflected crack was increased to 3.5 ksi√in, which is slightly higher than the Mode I threshold ($\Delta K_{th} = 2.8$ ksi√in) for PWA 1484.
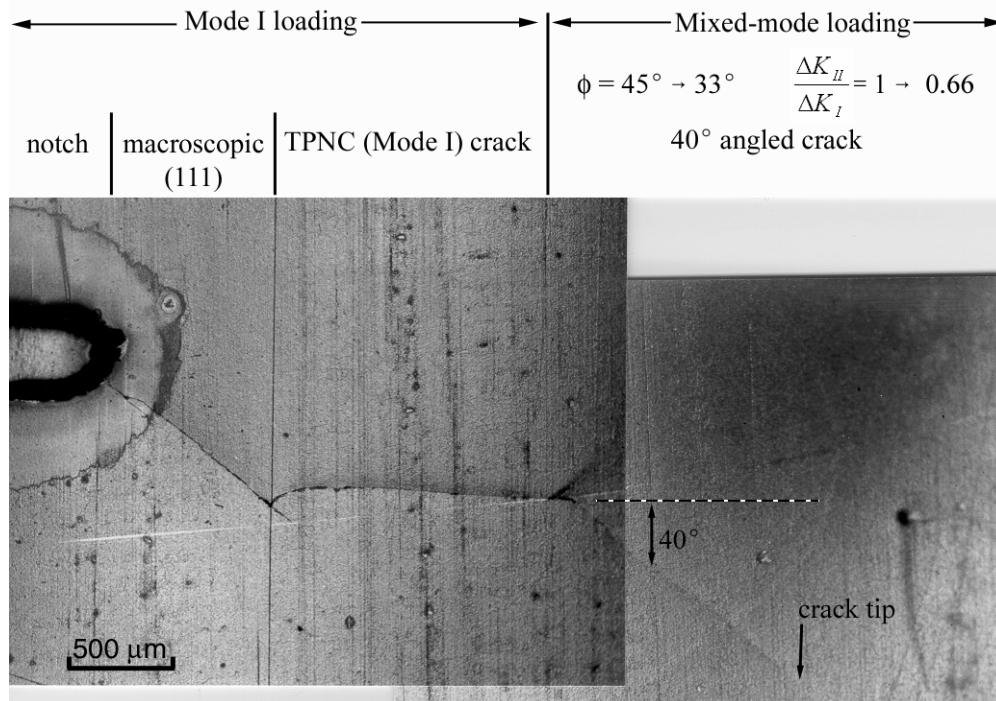

Figure R33.   Fatigue crack path of PWA 1484 (Specimen SWRI-SC-1) during nominal Mode I fatigue loading and mixed-mode fatigue loading at 1100°F.

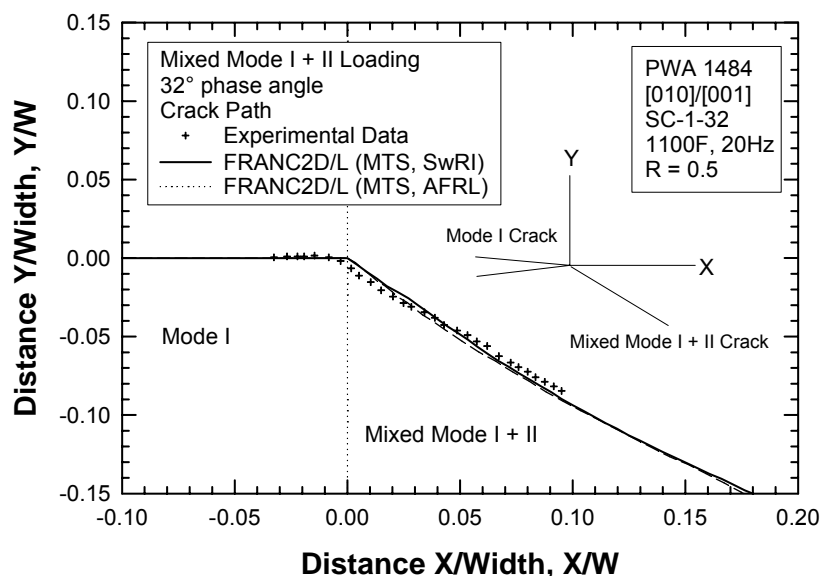Figure R34.   Comparison of calculated and observed crack paths for <001>/<010> oriented PWA 1484 tested under mixed-mode fatigue at a 32° phase angle.
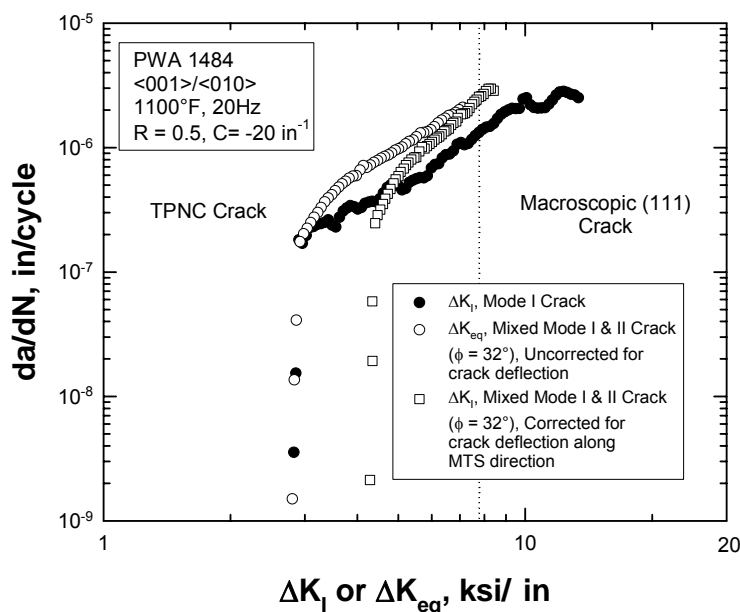
Figure R35.   A comparison of da/dN data vs. ΔK_I or ΔK_{eq} for <001>/<010> oriented PWA 1484 (SC-1) subjected to Mode I or mixed Mode I and II loading at a mode-mixity phase angle (ϕ) of 32°. Correction for crack deflection of the mixed-mode crack, which occurred on a transprecipitate non-crystallographic (TPNC) plane, increased the ΔK_{th} value from 2.8 to 4.2 ksi√in. The mixed-mode FCG threshold is slightly higher than the Mode I FCG threshold.

R-35

FCG curves of mixed-mode cracks in <001>/<010> oriented PWA 1484 are presented in Figures R36 through R38 for phase angles of 34°, 46°, 60°, 80°, and 90°, together with the corresponding FCG curves for Mode I loading. The comparison was based on the ΔK_{eq} parameter (Equation R10), which reduces to ΔK_I for Mode I cracks, as well as the local Mode I stress intensity range, ΔK_I, normal to the maximum tensile stress direction for deflected cracks. For Mode II loading ($\phi = 90°$), the fatigue crack grew very slowly and exhibited a growth threshold (5.9 ksi√in) that is higher than those observed in pure Mode I cracks (2.8 - 3.7 ksi√in), Figure R37. In all cases, the ΔK_{eq} uncorrected for crack deflection are lower than the local ΔK_I corrected for crack deflection. Therefore, the deflected crack path must be taken into account in computing the local stress intensity factors of deflected cracks. A comparison of fatigue thresholds obtained under pure Mode I loading and mixed Mode I & II loading is presented in Figure R39.
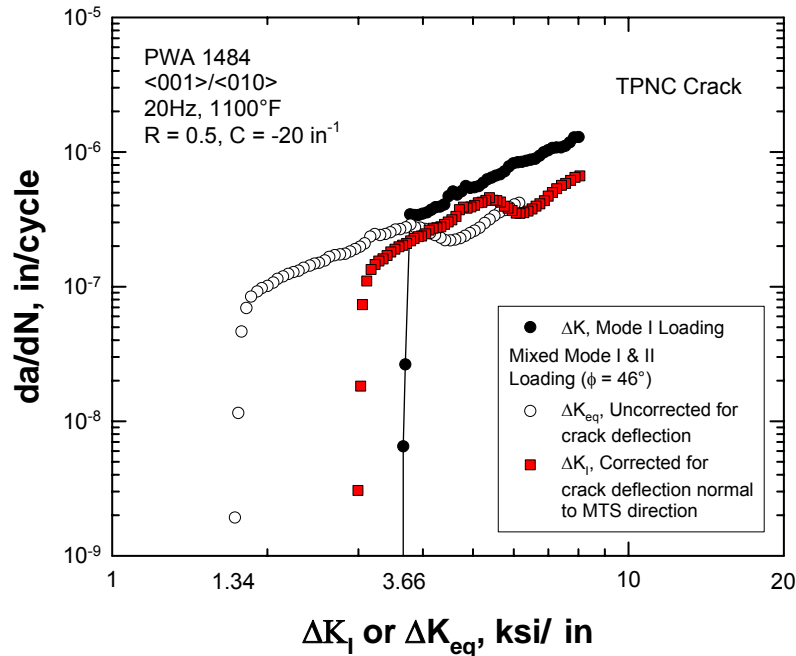

Figure R36.   A comparison of da/dN data vs. ΔK_I or ΔK_{eq} for <001>/<010> oriented PWA 1484 (SC-2) tested under Mode I or mixed Mode I and II loading at a mode-mixity phase angle (ϕ) of 46°.

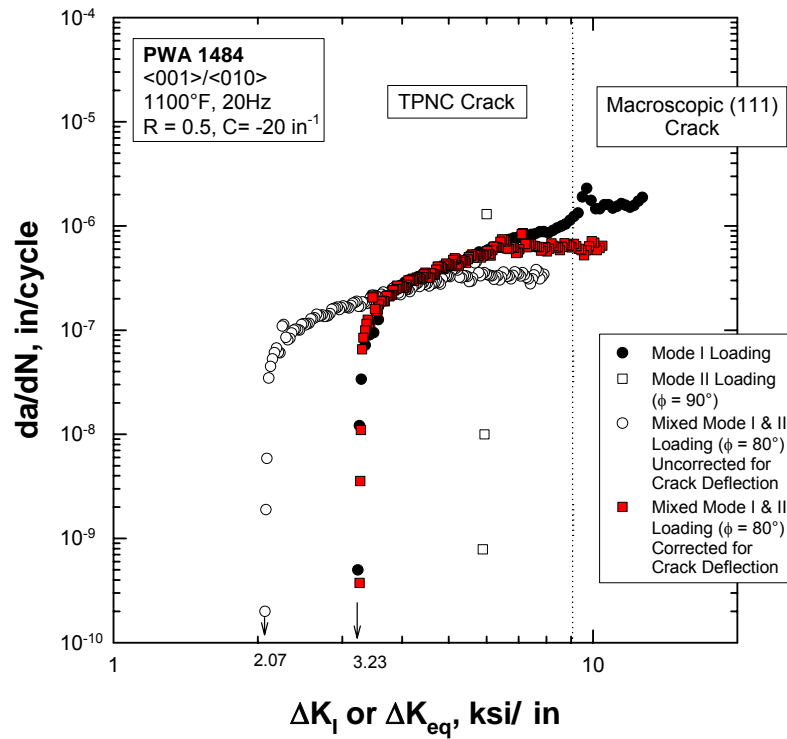Figure R37.   A comparison of da/dN data vs. ΔK_I or ΔK_{eq} for <001>/<010> oriented PWA 1484 tested under Mode I, Mode II, or mixed Mode I and II loading at a mode-mixity phase angle (ϕ) of 80°. The Mode II (ϕ = 90°) crack propagated on a non-crystallographic, self-similar plane, and arrested rapidly.

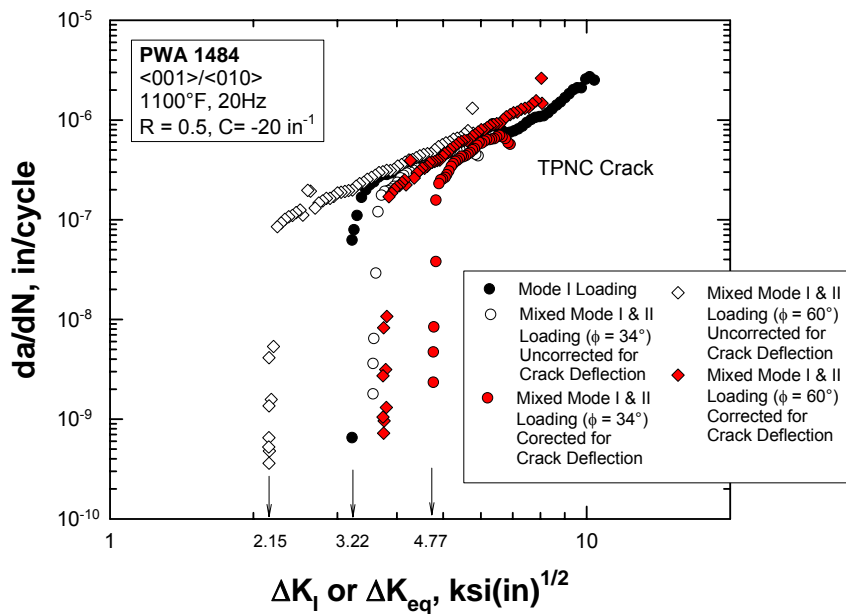Figure R38.   A summary plot of da/dN data vs. ΔK_I or ΔK_{eq} for <001>/<010> oriented PWA 1484 tested under Mode I or mixed Mode I and II loading at ϕ = 34° and 60°.
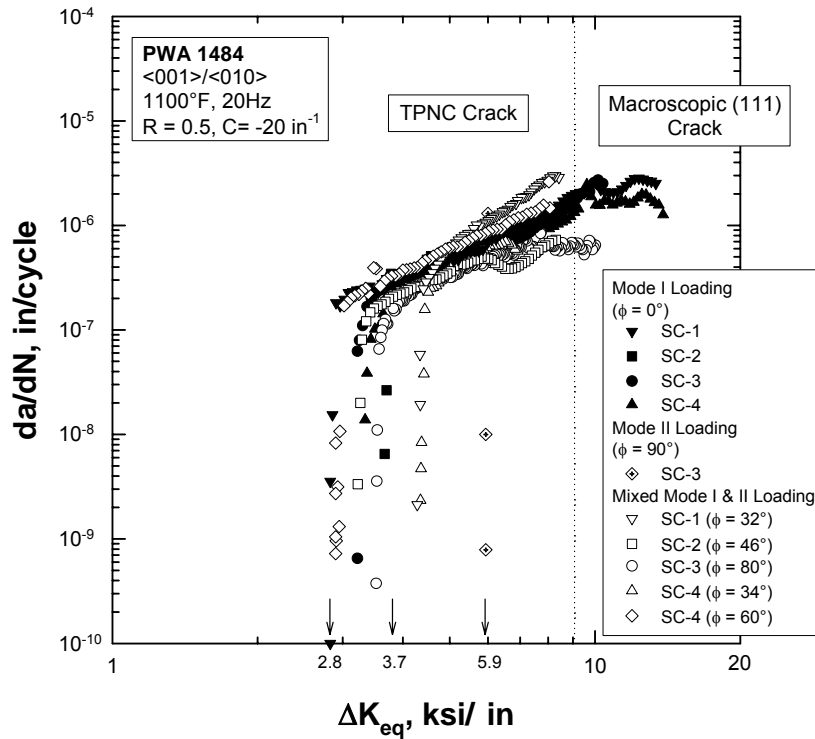
Figure R39.   A summary plot of da/dN data of <001>/<010> oriented PWA 1484 tested at 1100°F under various mixed Mode I and II loading.

B.   *<001>/<011> Orientation*

The crack paths of <001>/<011> oriented PWA 1484 are shown in Figure R40(a)-(d) for mixed-mode loading at phase angles of 45, 48, 60, and 80°, respectively. In all cases, the observed crack paths deviated slightly from the maximum tensile stress direction calculated based on FRAN2D/L.

After Mode I precracking, SC-5 was tested under mixed-mode loading at a 45° phase angle. Figure R41 shows a comparison of the Mode I and the mixed-mode FCG threshold data. Despite correction for the deflected crack path, the local Mode I threshold obtained under mixed-mode loading was lower than that determined under pure Mode I loading, Figure R41. SC-6 was tested at a phase angle of 22.5° but the fatigue precrack did not grow at the mixed-mode loading condition. Instead, another fatigue crack initiated at the notch and propagated under the imposed mixed-mode loading. Post-test measurement of the location of this fatigue crack indicated that FCG occurred at a 48° phase angle. The FCG data was, therefore, analyzed based on this loading condition. For this case, local stress intensity factors were computed for the MTS and actual crack paths using FRANC2D/L. Figure R42 shows a comparison of the Mode I and mixed-mode threshold data for SC-6. The ΔK_{eq} threshold was low when the deflection crack path was not corrected. After crack

path correction, the local $\Delta K_{I,th}$ values were increased both for the MTS and actual crack paths. The difference between the results for the MTS and the actual crack paths are small, as shown in Figure R42. In addition, both threshold values are lower than the Mode I threshold determined under pure Mode I loading.
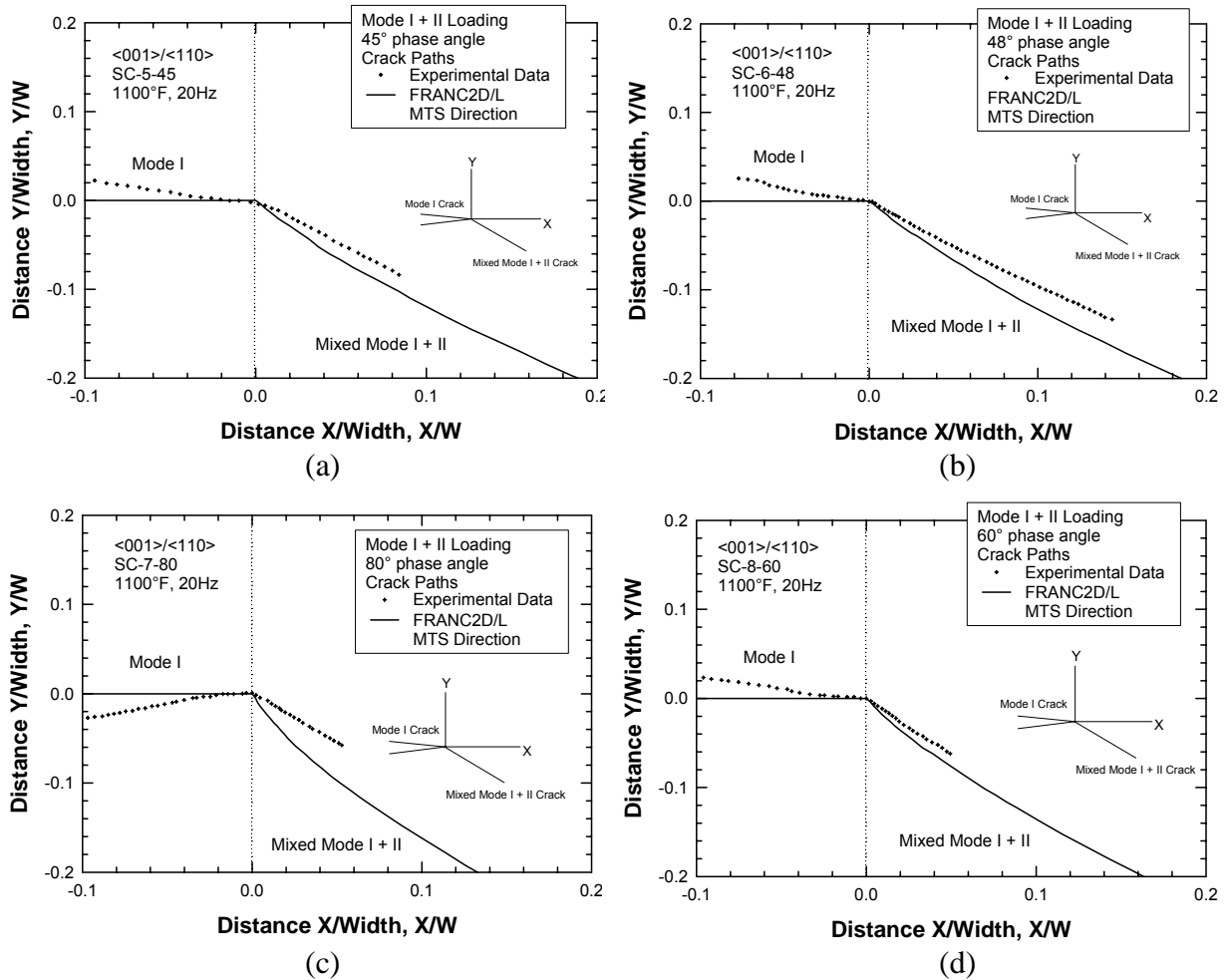

Figure R40.   Measured crack paths compared against calculated crack paths based on the MTS theory: (a) SC-5 ($\phi = 45°$), (b) SC-6 ($\phi = 48°$), (c) SC-7 ($80°$), and (d) SC-8 ($\phi = 60°$).

R-39
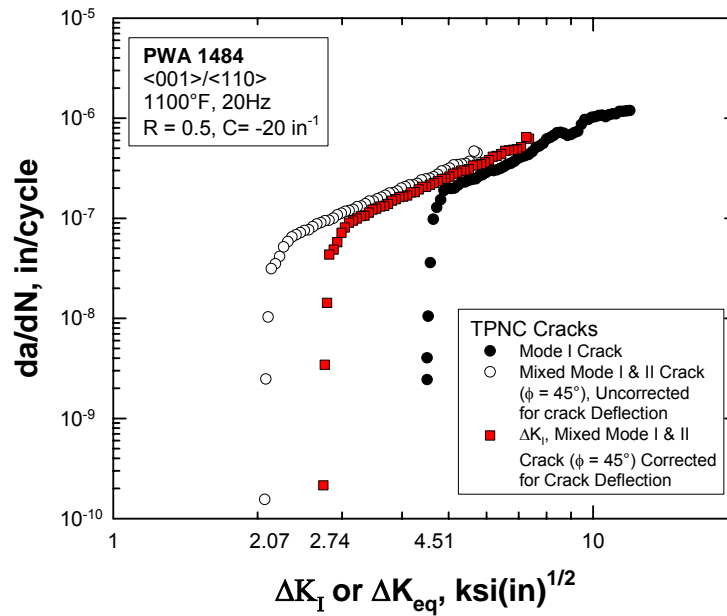
Figure R41. A summary of da/dN data vs. ΔK_I or ΔK_{eq} for <001>/<011> oriented PWA 1484 (SC-5) tested under Mode I or mixed Mode I and II loading at $\phi = 45°$.
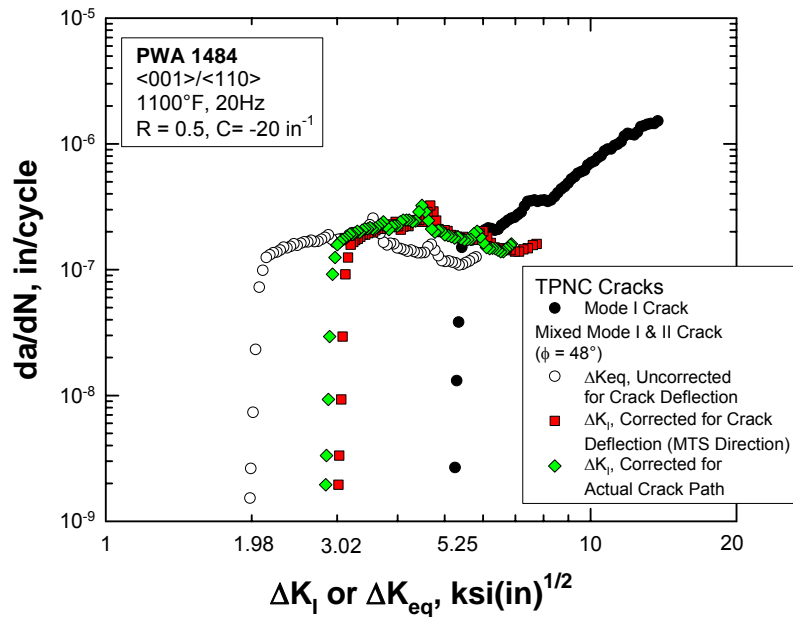
Figure R42. A comparison of da/dN data vs. ΔK_I or ΔK_{eq} for <001>/<011> oriented PWA 1484 (SC-6) tested under Mode I or mixed Mode I and II loading at $\phi = 48°$.

SC-7 was tested under pure Mode II (90° phase angle), but the crack did not propagate at $\Delta K_{II} = 6$ ksi√in. The phase angle was, therefore, lowered to 80° and the fatigue crack propagated under this mixed-mode loading, as shown in Figure R43. The stress intensity factors were corrected for crack deflection to the MTS path and the actual path. Again, the difference in the local $\Delta K_{I,th}$ values between the MTS and actual crack paths is negligible, but both are lower than that measured under pure Mode I loading. SC-8 was tested at a 60° phase and the data is presented in Figure R44. In all four cases, the mixed-mode FCG curves are extensions of FCG curves for Mode I, but the local Mode I FCG thresholds measured under mixed-mode loading occurred at a lower $\Delta K_{I,th}$ value than that measured under pure Mode I. A comparison of the FCG data of all four specimens is presented in Figure R45, which shows that all FCG data for these specimens form one scatter band, but the value of the threshold appears to depend on the phase angle. The latter effect is believed to be due to the dependence of $\Delta K_{I,th}$ on crystallographic orientation as discussed in Section R.2.5.
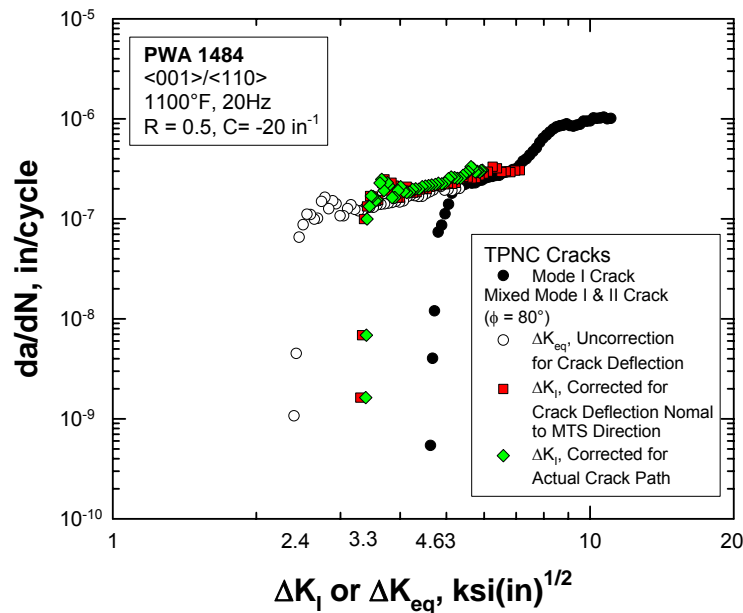

Figure R43. Plot of da/dN data vs. ΔK_I or ΔK_{eq} for <001>/<110> oriented PWA 1484 (SC-7) tested under Mode I or mixed Mode I and II loading at $\phi = 80°$.
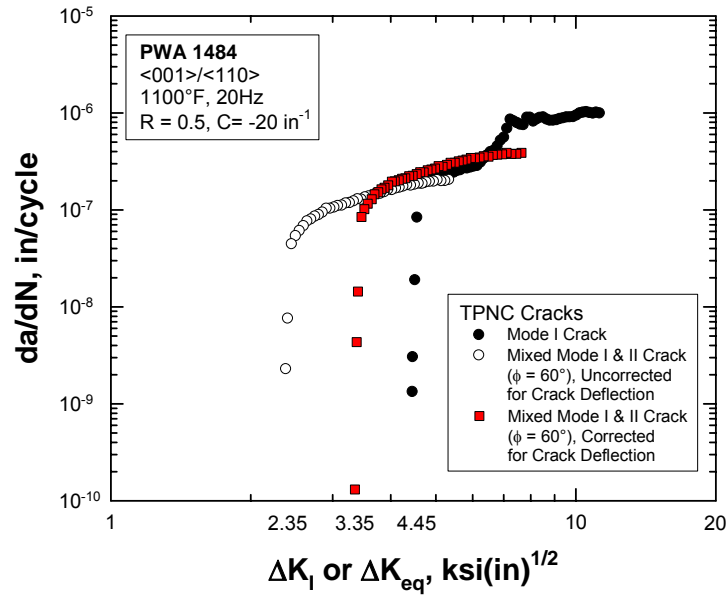
Figure R44.   Plot of da/dN data vs. ΔK_I or ΔK_{eq} for <001>/<110> oriented PWA 1484 (SC-8) tested under Mode I or mixed Mode I and II loading at $\phi = 60°$.
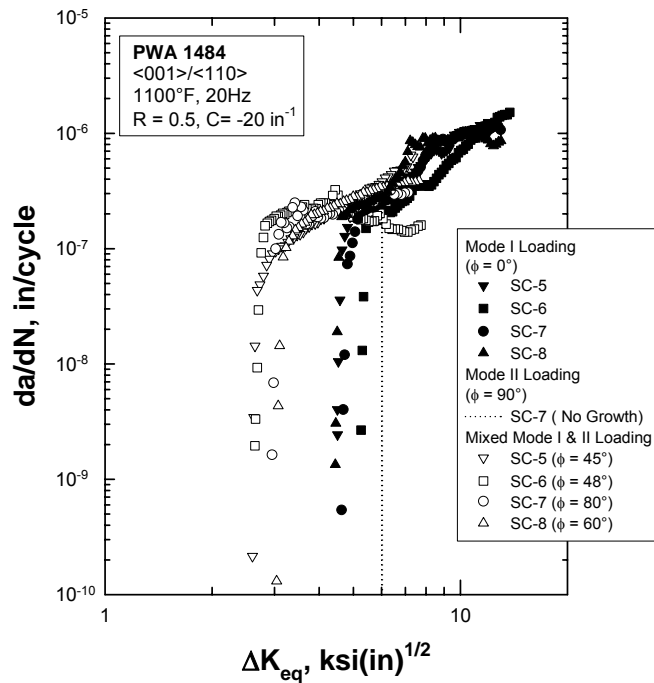
Figure R45.   A summary plot of da/dN data of <001>/<110> oriented PWA 1484 tested at 1100°F under various mixed Mode I and II loading.

C.   *<111>/<01$\overline{1}$> Orientation*

The crack path in this crystal orientation was fairly straight under Mode I fatigue, as shown in Figure R46. Under mixed Mode I and II loading, the originally straight and planar crack propagated crystallographically in a self-similar manner initially, but then kinked and deflected to propagate along a curvilinear path. The self-similar and deflected

crack paths for the mixed-mode fatigue crack at a 45° phase angle are shown in Figure R46. A comparison of calculated and experimental crack paths is presented in Figure R47, which shows that the observed crack path deviated somewhat from the one calculated for the maximum tensile stress. Figure R48 compares the da/dN data of the Mode I and mixed-mode cracks. Under Mode I, the fatigue crack propagated nominally on a (111) plane but this probably did not occur by a crystallographic crack growth mechanism because of the absence of shear stress on the (111) plane in this crystal orientation. The FCG threshold for the Mode I crack was 3.46 ksi√in. Under mixed-mode loading at a 45° phase angle, the fatigue crack propagated crystallographically on the (111) plane at higher growth rates compared to those exhibited by the Mode I crack or the mixed-mode TPNC crack, Figure R48. At ΔK_{eq} = 5.13 ksi√in, the (111) crack arrested and deflected to propagate on a noncrystallographic plane when the ΔK was further reduced. The da/dN results of the deflected crack without correction for crack deflection are shown as open circles in Figure R48. The apparent threshold for this deflected TPNC crack was about 2.42 ksi√in. After correction for the deflected crack path along the MTS direction, the threshold was increased to 4.0 ksi√in (squares and diamonds), in better agreement with the Mode I crack growth threshold (ΔK_{th} = 3.46 ksi√in). The same threshold was obtained using the MTS (squares) and the actual crack paths (diamonds).
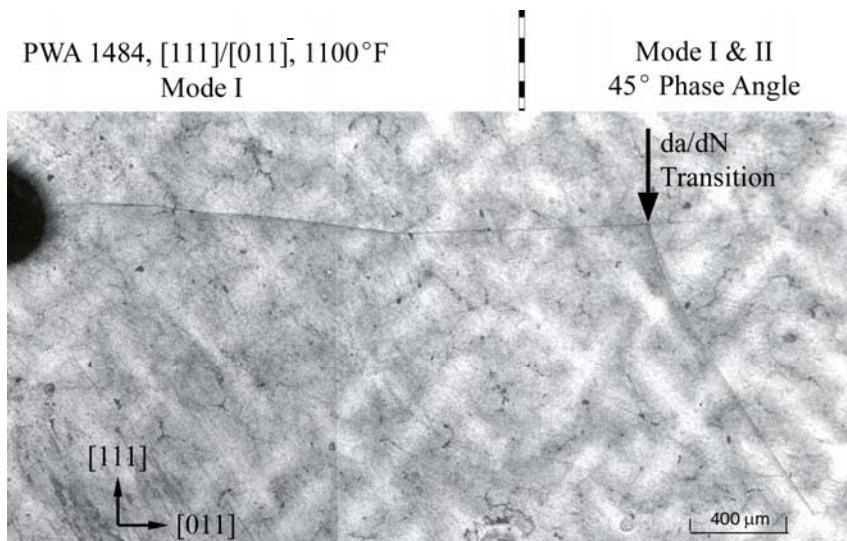

Figure R46. Fatigue crack path of [111]/[01$\overline{1}$] oriented PWA 1484 during Mode I loading and mixed Mode I and II loading at a 45° phase angle. Mode I fatigue occurred on the (111) plane. The mixed-mode crack propagated self-similarly on (111) under mixed Mode I and II initially, but it subsequently deflected on a TPNC plane (Specimen SC-13-45).
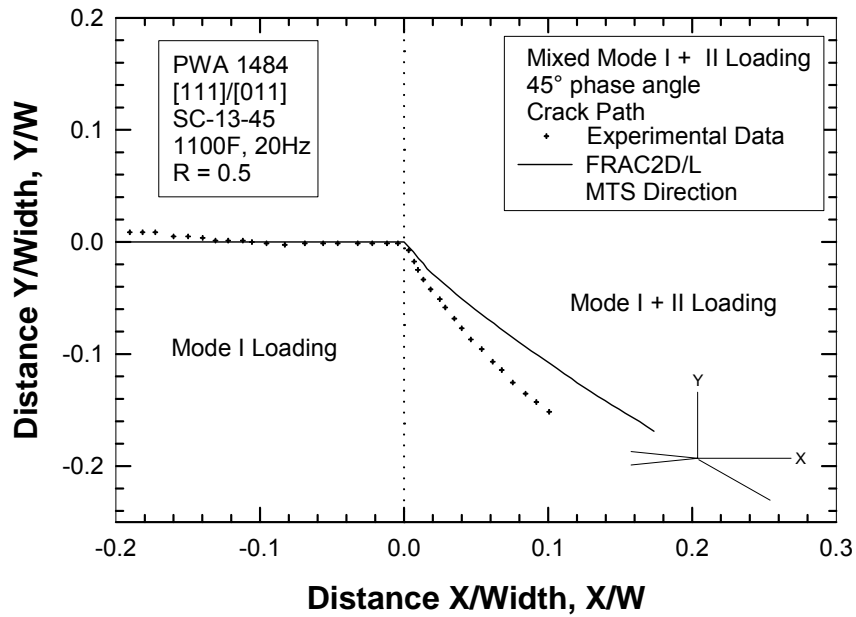
Figure R47. Calculated and observed crack deflection paths for [111]/[01$\bar{1}$]
oriented PWA 1484 subjected to mixed-mode loading at a 45° phase angle.

Figure R48. A comparison of the FCG responses of a self-similar (111) crack and a
transprecipitate noncrystallographic (TPNC) crack as a function of ΔK_I
or ΔK_{eq} for [111]/[01$\bar{1}$] oriented PWA 1484 subjected to mixed-mode
loading at a 45° phase angle. The values of ΔK that are corrected and
uncorrected for crack deflection are both compared against the
Mode I da/dN data (Specimen SC-13-45).

The (111) fatigue crack was able to propagate crystallographically under pure Mode II loading. Figure R49 illustrates the path of a Mode II crack that propagated along a (111) plane. Upon decreasing ΔK_{II}, the Mode II (111) crack eventually arrested, kinked out-of-plane, and deflected to propagate along a TPNC path, as shown in Figure R49. The experimental crack path is compared against that predicted by FRANC2D/L for the maximum tensile stress direction in Figure R50. The calculated crack deflection angle was 70.5°, compared to 48° observed experimentally. A summary of the da/dN data for pure Mode I and pure Mode II is presented in Figure R51. The Mode II (111) crack grew at higher rates than the TPNC Mode I crack at equivalent stress intensity factor ranges. After crack deflection, the (111) crack propagated on a TPNC plane and arrested at a lower FCG threshold. After correction for crack deflection, the FCG threshold of the deflected Mode II crack is 2.38 ksi√in, which is still lower than a threshold of 3.84 ksi√in for the Mode I crack. The same threshold was obtained using the actual and the MTS crack paths, as shown in Figure R51. A comparison of all FCG data of crystals tested in this orientation is presented in Figure R52. A summary of the FCG data of crystallographic (111) cracks is shown in Figure R53.
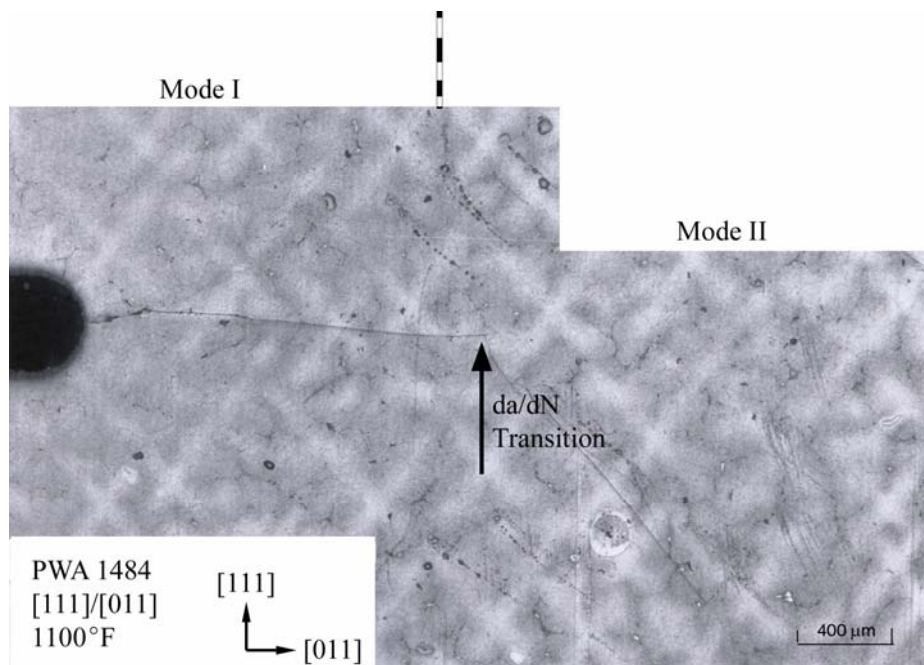
Figure R49. Fatigue crack path of [111]/[01 $\overline{1}$] oriented PWA 1484 during pure Mode I and pure Mode II fatigue. Mode I fatigue crack growth occurred on a (111) plane. Mode II fatigue crack growth occurred on a (111) plane initially and arrested, then deflected to a TPNC plane until it arrested at a lower FCG threshold (Specimen SC-16-90).
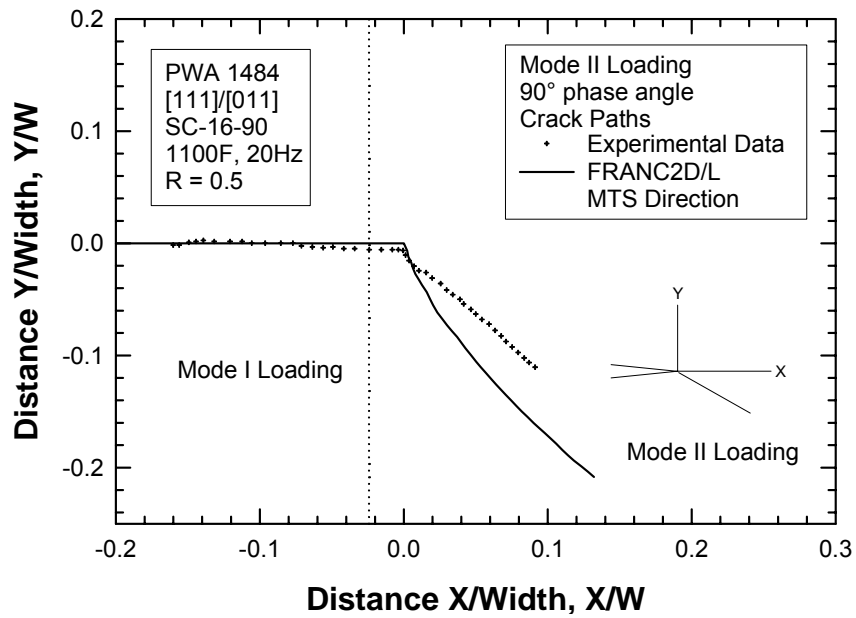
Figure R50. Calculated and observed crack paths for [111]/[01$\overline{1}$] oriented PWA 1484 subjected to pure Mode II loading.
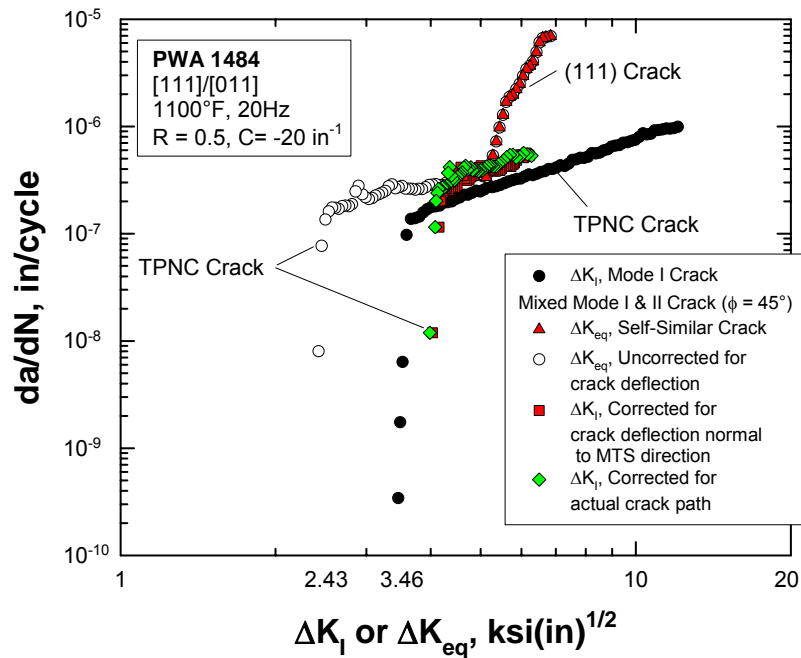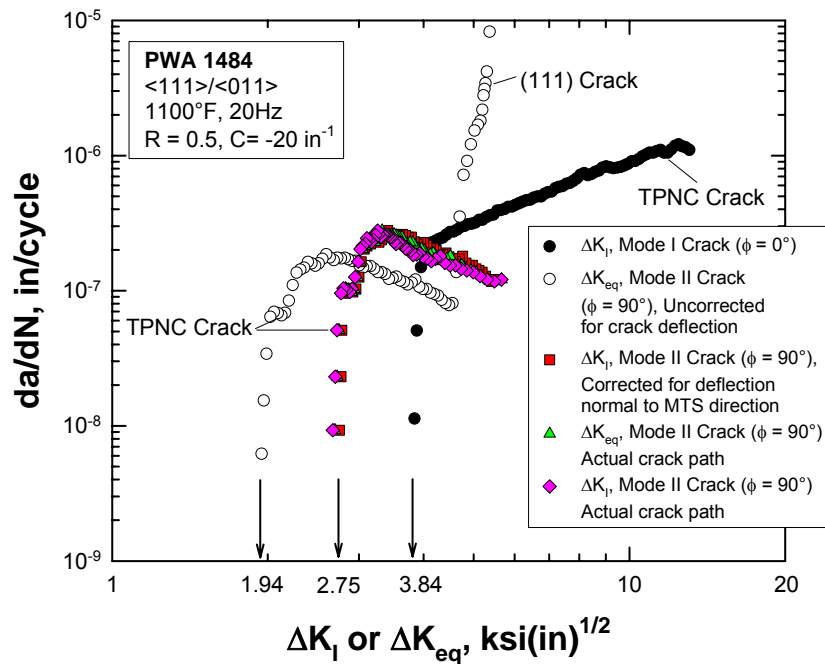

Figure R51. A comparison of the FCG response of self-similar (111) crack and transprecipitate noncrystallographic (TPNC) cracks as a function of ΔK_I or ΔK_{eq} for [111]/[01$\overline{1}$] oriented PWA 1484 subjected to pure Mode II loading. The threshold determined under pure Mode II loading is lower than that determined under pure Mode I loading, even after the corrections for crack deflection have been applied to da/dN and ΔK values (Specimen SC-16-90).

R-46
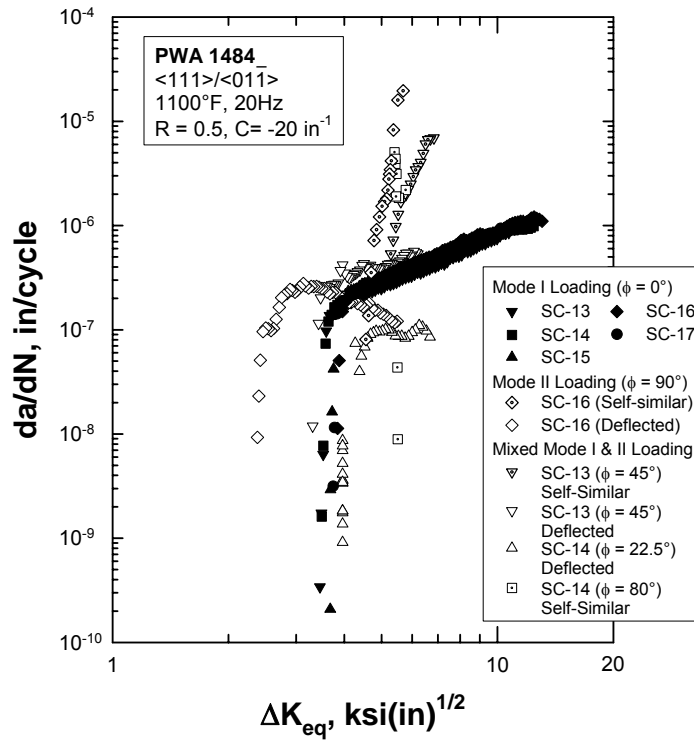
Figure R52.   A summary plot of da/dN data of <111>/<01$\bar{1}$> oriented PWA 1484 tested
at 1100°F various mixed Mode I and II loading. Stress intensity factors
have been corrected for crack deflection.

Figure R53.   A summary plot of da/dN data of crystallographic (111) cracks
in <111>/<01$\bar{1}$> oriented PWA 1484 tested at 1100°F.

D. $<111>/<11\overline{2}>$ Orientation

SC-9 was tested under a 45° mode mixity phase angle. The initial crack path was a self-similar crack on the (111) plane, but it subsequently deflected to a TPNC plane. Figure R54(a) shows a comparison of the mixed-mode FCG data against the Mode I threshold data. In this case, the local Mode I threshold determined under mixed-mode loading agrees with th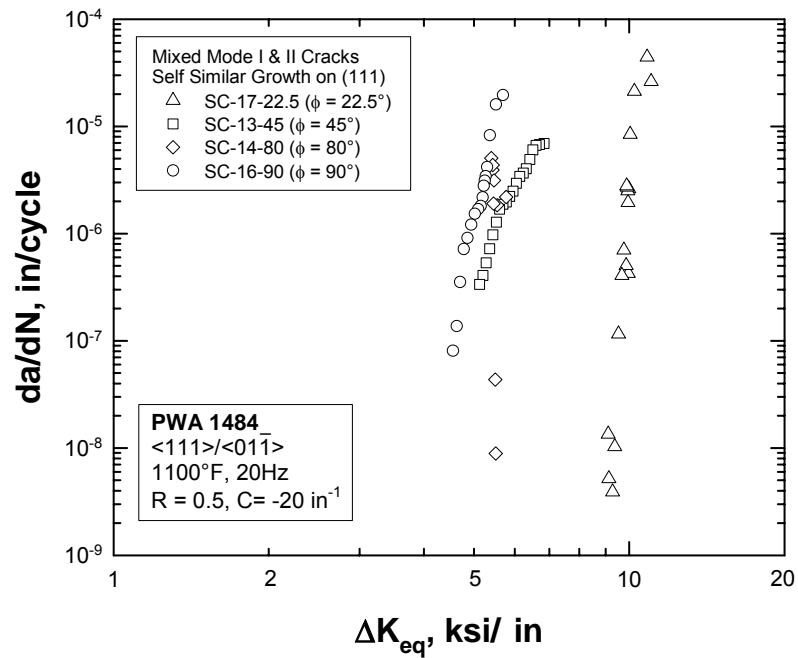at obtained under pure Mode I loading, after the deflected crack path was taken into consideration in computing the local ΔK_I.

SC-10 was tested under a 60° mode mixity phase angle, with load shedding starting from an initial ΔK_{eq} value of 6ksi-√in. The crack propagated as a straight self-similar crack on (111). The crack arrested at a relatively high threshold without deflecting to a TPNC plane. Figure R54(b) shows a comparison of the FCG curve of the mixed-mode crack against that of the pure Mode I crack. In this case, the pure Mode I threshold is substantially lower than the straight self-similar, mixed-mode crack on the (111) plane.

A mode mixity phase angle of 90° was used for SC-11. The fatigue crack growth process was complex as the crack branched into two tips, Figure R55(a). It involved self-similar crack growth on a (111) plane at one tip, and concurrent TPNC growth at the other tip. The corresponding da/dN data for the mixed-mode crystallographic crack and the local Mode I crack are compared in Figure R55(b). The self-similar (111) appeared to exhibit the same threshold as the pure Mode I crack, while the deflected local Mode I crack appeared to show a higher threshold than those of the mixed-mode self-similar (111) crack and the pure Mode I crack. However, possible interactions between the two crack tips were not taken into consideration in the K calculations or the PD method for crack length measurement. Furthermore, the difference between the thresholds of the (111) crack and the TPNC crack is small. A summary of the da/dN data of the $<111>/<11\overline{2}>$ crack orientation is shown in Figure R56.
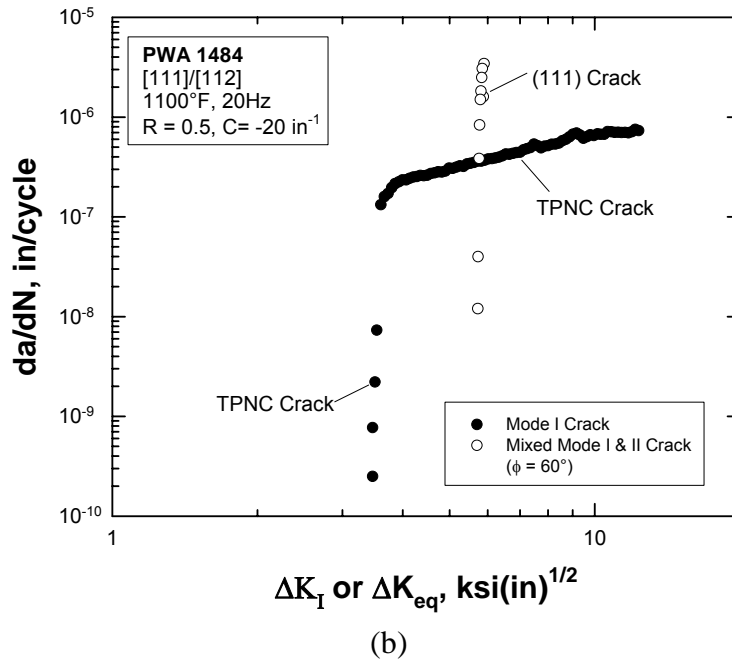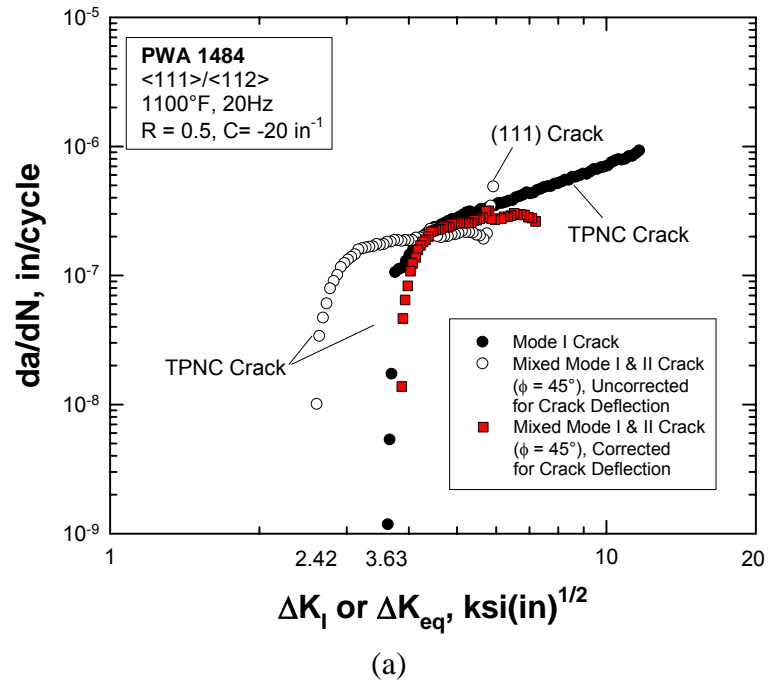
Figure R54.   Plots of da/dN data vs. ΔK_I or ΔK_{eq} for $<111>/<11\bar{2}>$ oriented PWA 1484: (a) SC-9 ($\phi = 45°$), (b) SC-10 ($\phi = 60°$).
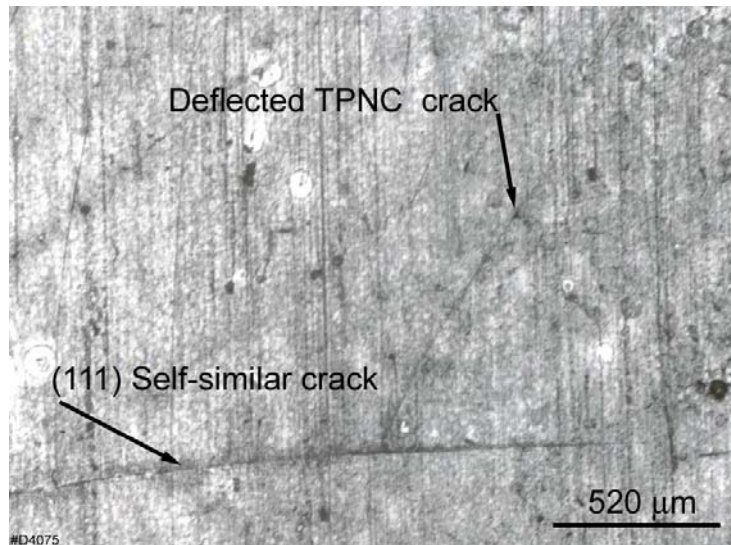
(a)
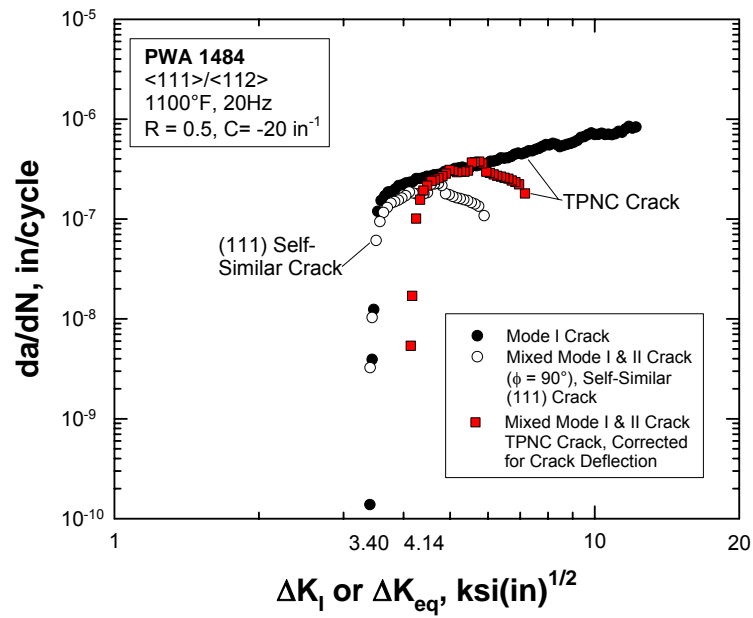
(b)

Figure R55. Concurrent cracking on (111) and TPNC planes observed in SC-11-90 tested under pure Mode II loading; (a) crack paths, and (b) da/dN data vs. ΔK_I or ΔK_{eq} for SC-11 tested under Mode I or Mode II loading.
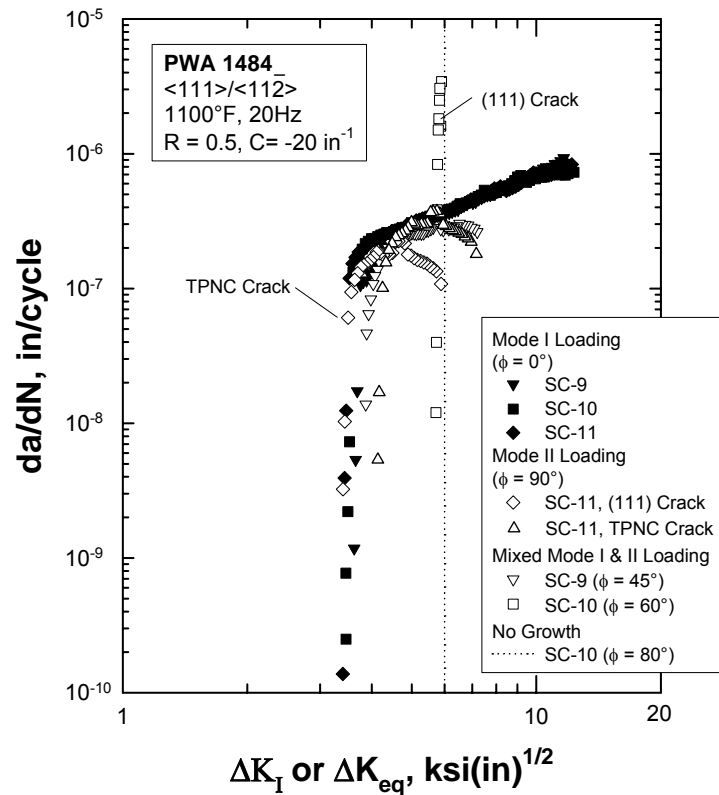
Figure R56.   A summary plot of da/dN data of $<111>/<11\bar{2}>$ oriented PWA 1484 tested
at 1100°F.

E. $<001>+10°/<110>+10°$ Orientation

SC-19 was tested under a mode mixity phase angle of 45°. The Mode I
precrack did not propagate during mixed-mode threshold testing. Instead, another crack
initiated from the notch and propagated to arrest during load shedding. The second crack
was shorter than the original Mode I precrack and was not detected by the potential drop
technique. Consequently, no FCG threshold data was obtained for this test.

A mode mixity phase angle of 60° was used for SC-20. The crack propagated
as a straight self-similar non-crystallographic crack on a TPNC plane without crack
deflection. The crack arrested at an apparent $\Delta K_{eq,th}$ of 5.5 ksi√in, which is higher than a
$\Delta K_{I,th}$ value of 3.69 ksi√in observed in the pure Mode I crack, as shown in Figure R57. Post-
test Laue back-reflection analysis indicated that the specimen was 8° off <001>.
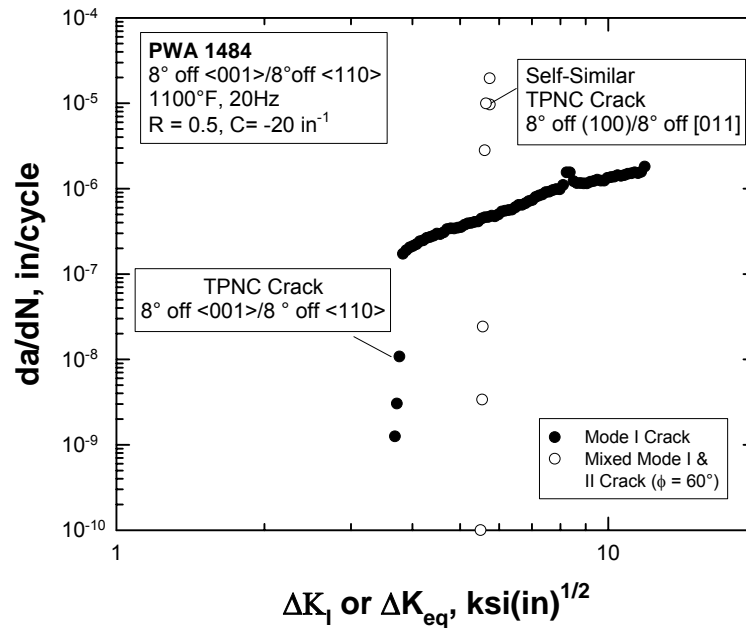
Figure R57.   Plot of da/dN data of <001> + 8°/<110> + 8° oriented PWA 1484 (SC-20) tested under either Mode I or mixed Mode I and II at $\phi = 60°$.

R.2.5.   Crack Deflection Paths and Fracture Planes

R.2.5.1   Experimental Observations

        Two-surface analyses were performed to identify the crystallographic orientation of fatigue crack growth planes for individual PWA 1484 specimens. This technique involved measuring the traces of the fatigue fracture planes on two surfaces and plotting the traces on a stereographic projection containing the crystallographic orientation of the single crystal test specimen. A summary of these results is tabulated in Table R2, which shows the initial orientation of the Mode I crack, Mode I threshold, the mode-mixity phase angle used at the initiation of mixed-mode fatigue, the equivalent ΔK (ΔK_{eq}), ΔK_I, and ΔK_{II} of the deflected crack for the MTS (local Mode I) crack growth criterion, the corresponding crack deflection angle, type of cracks, and fatigue crack growth planes and directions. Two important observations can be made from the results shown in Table R2: (1) the Mode I threshold (Column 3) of PWA 1484 depends on crystallographic orientation, and (2) the Mode I fatigue cracks and deflected mixed-mode cracks propagated on different planes and experienced different crystallographic orientations. Thus, the discrepancy between the Mode I threshold and that obtained under mixed-mode condition is attributed to the change in crystallographic orientation of the deflected crack and the associated dependence of the Mode I threshold on crystallographic orientation.

R-52

Table R2. **A Summary of the Initial Crack Orientation, Thresholds, Crack Deflection Angle, Type of Cracks, and Final Fatigue Crack Plane and Fatigue Crack Growth Directions for PWA 1484 Tested at1100°F, R = 0.5, and 20 Hz**

Specimen	Initial Orientation	Pre-cracking Mode I Threshold ΔK$_{I,th}$, ksi√in	"Mixed Mode" Thresholds Phase Angle, φ°	ΔK$_{eq.the}$ (ksi√in)	ΔK$_{I,th}$ + (ksi√in)	ΔK$_{II,th}$ + (ksi,√in)	Crack Deflection Angle, ° (average)	Remarks	Final Orientation Fatigue Crack Plane	Fatigue Crack Directions
SC-1	<001>/<010>	2.83	32	4.19	4.19	0	40	TPNC crack	5° off ($\bar{1}$10)	5° off [100]
SC-2	<001>/<010>	3.66	46	3.05	3.05	0	40, 62 (51)	TPNC crack	5° off ($\bar{2}$30)	5° off [320]
SC-3	<001>/<010>	3.23	90	5.94	0	5.94	No growth	TPNC crack	—	—
			80	3.26	3.26	0	50, 58 (54)	TPNC crack	($\bar{2}$30)	[320]
SC-4	<001>/<010>	3.22	34	4.77	4.77	0	45	TPNC crack	($\bar{1}$10)	[110]
			60	3.74	3.74	0	60	TPNC crack	3° off ($\bar{1}$20)	3° off [210]
SC-5	<001>/<110>	4.51	45	2.74	2.74	0	44, 36 (40)	TPNC crack	4° off ($\bar{2}$1$\bar{1}$)	4° off [11$\bar{1}$]
SC-6	<001>/<110>	5.25	48	3.02	3.02	0	30, 45 (37.5)	TPNC crack	($\bar{1}$1$\bar{1}$)	[21$\bar{1}$]
SC-7	<001>/<110>	4.63	80	3.30	3.30	0	48, 50	TPNC crack	6° off ($\bar{1}$1$\bar{1}$)	6° off [21$\bar{1}$]
			90	7.6	—	—	—	No growth	—	—
SC-8	<001>/<110>	4.45	60	3.35	3.35	0	58	TPNC crack	5° off ($\bar{1}$1$\bar{1}$)	5° off [21$\bar{1}$]
SC-9	<111>/<11$\bar{2}$>	3.63	45	3.87	3.87	0	43	TPNC crack	6° off (100)	6° off [011]
SC-10	<111>/<11$\bar{2}$>	3.46	60	5.72	2.81	4.99	0	(111) self-similar crack	(111)	[11$\bar{2}$]
SC-11	<111>/<11$\bar{2}$>	3.40	90	3.41	0	3.41	0	(111) self-similar crack	(111)	[11$\bar{2}$]
			90	4.14	4.14	0	53	TPNC crack	(100)	[011]
SC-13	<111>/<$\bar{1}$10>	3.46	45	5.13	3.63	3.63	0	(111) self-similar crack	(111)	[01$\bar{1}$]
			45	4.03	4.03	0	40, 66 (53)	TPNC crack	4° off (1$\bar{2}$0)	7° off [$\bar{1}$02]
SC-14	<111>/<$\bar{1}$10>	3.48	80	5.51	0.96	5.43	0	(111) self-similar crack	(111)	[01$\bar{1}$]
			22.5	4.05	4.05	0	20, 40 (30)	TPNC crack	7° off (23$\bar{1}$)	[$\bar{1}$$\bar{1}$3]
SC-15	<111>/<$\bar{1}$10>	3.68	—	—	—	—	—	Test specimen overloaded during cool-down	—	—
SC-16	<111>/<$\bar{1}$10>	3.84	90	4.55	0	4.55	0	(111) self-similar crack	(111)	[01$\bar{1}$]
			90	2.67	2.67	0	47, 48 (48)	TPNC crack	10° off (1$\bar{2}$0)	[$\bar{1}$02]
SC-17	<111>/<$\bar{1}$10>	3.74	22.5	9.10	8.41	3.48	0	(111) self-similar crack, high starting ΔK$_{eq}$ (11 ksi√in)	(111)	[01$\bar{1}$]
SC-19	10° off <001>/ 10° off <110>	3.99	45	—	—	—	—	Test specimen initiated a second crack	—	—
SC-20	10° off <001>/ 10° off <110>	3.69	60	5.50	2.71	4.79	0	Self-similar crack	8° off (100)	8° off [01$\bar{1}$]

+ Corrected for crack deflection.

Figures R58 through R61 present the Mode I thresholds of PWA 1484 as a function of the angle β between the crack plane normal and a reference crystallographic axis for the initial <001>/<010>, <001>/<011>, <111>/<01$\overline{1}$>, and <111>/<11$\overline{2}$> orientations, respectively. Both the angle β and the reference crystallographic orientation are defined in the inserts in Figures R58 through R61. In these figures, the values of the Mode I threshold, $\Delta K_{I,th}$, at β = 0° correspond to those measured under Mode I conditions, while those for β > 0 were the local $\Delta K_{I,th}$ values determined from deflected cracks during the remote mixed-mode loading. The highest Mode I threshold occurs in the <001>/<011> orientation, Figure R59. Lower values of $\Delta K_{I,th}$ occur in off-axis orientations that are about 40-60° from the <001> in the <001>/<011> system. These orientations are located near the central region of a standard stereographic triangle for cubic materials.

Figure R58.   Mode I threshold as a function of the angle, β, between the crack normal and the <001> axis for the <001>/<010> orientation. Results indicate that $\Delta K_{I,th}$ depends on crystallographic orientation.

Figure R59. Mode I threshold as a function of the angle, β, between the crack normal and the <001> axis for <001>/<110> orientation. Results show anisotropy in ΔK$_{I,th}$.

Figure R60. Mode I threshold as a function of angle β for the <111>/<$\bar{1}$10> orientation.

Figure R61.   Mode I threshold as a function of angle β for the $<111>/<11\overline{2}>$ orientation.

R.2.5.2   Modeling of Crack Deflection Path

Since discrepancies were observed between measured crack paths and those predicted based on the maximum principal tensile stress (MTS) direction (local Mode I criterion [16]), asymptotic solutions for mixed-mode crack growth criteria according to the maximum energy release rate (G_{max}) [17] and minimum strain density (S_{min}) [18] were used to compute the crack deflection angles of a mixed-mode crack. The results are compared against those of FRANC2D/L and experimental data in Figure R62. For a given mode-mixity angle of ϕ, where $\phi = \arctan(\Delta K_{II}/\Delta K_I)$, the predicted crack deflection angles are similar for the MTS, G_{max}, and S_{min} criteria. The FRANC2D/L results are in agreement with those of the MTS criterion since it was the crack growth direction chosen in the computations. About 1/3 of the experimental data agreed with the MTS criterion and the FRANC2D/L criterion results, while the remaining 2/3 showed negative deviation (smaller crack deflection angles) from the MTS criterion. Two conclusions were derived from the results in Figure R62, which are: (1) the G_{max} and S_{min} criteria would not improve the agreement between the computed and measured crack deflection angles, and (2) additional factors other than the crack driving force might have influenced the crack deflection path.

Figure R62. Comparison of the crack deflection angles based on the MTS, G_{max}, and S_{min} crack growth criteria against FRANC2D/L calculations and experimental data.

The influence of an orientation-dependent $\Delta K_{I,th}$ on the deflection of a generalized mixed-mode crack in PWA 1484 was modeled by considering the fatigue crack growth (FCG) response, which can be represented as

$$\frac{da}{dN} = A\left(\Delta K_{eq} - \Delta K_{eq,th}\right)^n \tag{R22}$$

with

$$\Delta K_{eq} = \left[\Delta K_I^2 + \Delta K_{II}^2\right]^{1/2} \tag{R23}$$

where da/dN is the crack growth rate; ΔK_{eq} is the equivalent stress intensity range, and $\Delta K_{eq,th}$ is the corresponding equivalent mixed-mode threshold; A and n are empirical constants. The change of the FCG rate with the crack deflection angle, θ, when a mixed-mode crack kinks is given by

$$\frac{1}{da/dN}\frac{\partial}{\partial\theta}\left[\frac{da}{dN}\right] = \frac{1}{A}\frac{\partial A}{\partial\theta} + \ln\left[\Delta K_{eq} - \Delta K_{eq,th}\right]\frac{\partial n}{\partial\theta} + \frac{1}{\left[\Delta K_{eq} - \Delta K_{eq,th}\right]}\frac{\partial}{\partial\theta}\left[\Delta K_{eq} - \Delta K_{eq,th}\right]$$

$$\tag{R24}$$

R-57

in which both ΔK_{eq} and $\Delta K_{eq,th}$ are taken to be a function of θ. For simplicity, A and n are taken to be independent of the crack deflection angle. It is further assumed that the crack deflects in the direction of the maximum crack growth rate so that

$$\frac{\partial}{\partial \theta}\left[\frac{da}{dN}\right] = 0 \tag{R25}$$

leading to

$$\frac{\partial}{\partial \theta}\left[\Delta K_{eq} - \Delta K_{eq,th}\right] = 0 \tag{R26}$$

for a deflected mixed-mode crack. When crack growth occurs under Mode I conditions, Eq. (2-26) becomes

$$\frac{\partial}{\partial \theta}\left[\Delta K_I - \Delta K_{I,th}\right] = 0 \tag{R27}$$

Equations (R26) and (R27) indicate that crack deflection occurs in the direction where the spread between the crack driving force (ΔK_{eq} or ΔK_I) and the crack resistance ($\Delta K_{eq,th}$ or $\Delta K_{I,th}$) is maximum. For isotropic materials, $\partial \Delta K_{I,th} / \partial \theta = 0$ and Equation (R27) is reduced to the classical MTS criterion. On this basis, Equation (R27) indicates that deviation from the MTS criterion is expected when $\partial \Delta K_{I,th} / \partial \theta \neq 0$. Moreover, the amount of deviation would depend on the threshold anisotropy.

Figure R63 shows the calculated values of ΔK_{eq}, ΔK_I, and ΔK_{II} for a deflected mixed-mode crack as a function of the crack deflection angle, θ, for SC-16 and SC-11 tested under Mode II. Both exhibited self-similar crack growth initially, but deflected to propagate in a direction close to that predicted by the maximum tensile stress criterion (maximum K_I and zero K_{II}). However, there are small deviations such that the crack path did not exactly correspond with Mode I, but contained a small Mode II component. Plots of this type have been generated for all specimens. They show that the region where the maximum K_I occurs is relatively flat so that the critical condition can be attained over the range of crack deflection angle, θ. The actual crack deflection angle was always smaller than the one predicted by the MTS criterion because the deflected crack was able to seek out a direction with a lower $\Delta K_{I,th}$. The probability that a deflected crack is able to find a direction with a lower Mode I threshold depends on the mode mixity. A Mode II crack would have a large

crack deflection angle and, therefore, a high probability to find the direction with a lower crack growth resistance.

Figure R63.   Variation in K_I, K_{II}, and K_{eq} with the crack deflection angle for pure Mode II crack in SC-11-90 and SC-16-90 (90 indicates the phase angle). Note that the K_I values of the deflected cracks are near the local Mode I condition, while the Mode II components are small at the observed crack deflection angles.

For a mixed-mode crack in an isotropic elastic material, Equation (R27) is given by

$$\Delta K \;\sin\theta + \Delta K_{II}\left[3\cos\theta - 1\right] - \frac{\partial \Delta K_{I,th}}{\partial \theta} = 0 \tag{R28}$$

which can be solved only when $\Delta K_{I,th}(\theta)$ is known. Consequently, the dependence of the Mode I threshold on crystallographic orientation must be known since the crystallography encountered by the crack tip changes once the crack deflects from the original path. For simplicity, it is assumed that

$$\frac{\partial \Delta K_{I,th}}{\partial \theta} = \lambda \Delta K_{II} \tag{R29}$$

where λ is an empirical constant. Equation (R29) was motivated by the observation that the deviation from the MTS criterion increased with increasing Mode II. Substituting Equation (R29) into Equation (R28) leads one to

$$\phi = \arctan\left[\frac{\Delta K_{II}}{\Delta K_{I}}\right] = \arctan\left[\frac{-\sin\theta}{\lambda + 1 - 3\cos\theta}\right] \qquad (R30)$$

as the relation between the mode-mixity phase angle (ϕ) and the crack deflection angle (θ). By fitting Equation (R30) to the experimental data, it was determined that $\lambda = 0.8$. Figure R64 shows that the computed crack deflection angles are now in better agreement with the observed values.

Figure R64. Calculated and measured crack deflection angles as a function of 90-ϕ, when ϕ = arctan ($\Delta K_{II}/\Delta K_{I}$) is the mode-mixity phase angle. Deviation of experimental data from the MTS criterion is caused by orientation dependence in the Mode I threshold. Current model, Equation (R30), is fitted to the experiment. The calculation shows how a small threshold anisotropy can cause a relatively large deviation in the crack deflection angle.

The analysis clearly demonstrated that an orientation-dependent Mode I threshold can cause the deflected crack path to deviate substantially from that of the MTS criterion. In addition, the resulting deflected crack path would not be entirely Mode I but would contain a small Mode II component; consequently, the Mode I threshold may also manifest a weak dependence on the Mode II component. This assessment of the crack deflection path was

R-60

confirmed by the FRANC2D/L calculation performed using the actual deflected crack path, which is shown in Figure R51 and in Section R.4.

The above analysis is applicable to the crack deflection of a mixed-mode, transprecipitate noncrystallographic (TPNC) crack in PWA 1484. For this type of crack, $\Delta K_{I,th}$ is dependent on crystallography, but A and n (i.e., da/dN) are independent of mode-mixity or crystallography, as shown in Figure R41. The transition of a mixed-mode crystallographic crack on a (111) plane to a TPNC plane is more complicated because the da/dN curves for these two cracking processes, which are shown in Figure R52, are different with different A, n, and threshold values. Under this circumstance, the dependence of A, n, as well as the FCG threshold on the crack deflection angle (or crystallographic orientation) all need to be taken into consideration. Anisotropy in the A and n values would cause additional changes of the crack deflection path or angle. There is also evidence that self-similar growth on a (111) plane and crack deflection on a TPNC plane could occur concurrently under certain conditions. This is illustrated in Figure R55(a), which shows that both self-similar growth on (111) and deflected crack growth normal to the MTS direction occurred in SC-11 tested under pure Mode II loading.

R.2.6   Assessment of P&W's Anisotropic Mode I Threshold Model

The anisotropic threshold model developed at Pratt & Whitney was used to correlate the Mode I threshold data obtained under remote mixed-mode loading and pure Mode I loading conditions. The model has been formulated on the basis of a function that interpolates the fracture resistance of any arbitrary orientation in terms of the principal values [19]. As illustrated in Figure R65, a crack or a point on an arbitrary crack point is envisioned to propagate in an arbitrary direction defined by

$$a = a_1 i + a_2 j + a_3 k \tag{R31}$$

where i, j, and k are unit vectors corresponding to the principal material axes x_1, x_2, and x_3. The vector a is normal to both the crack front and the unit vector, n,

$$n = n_1 i + n_2 j + n_3 k \tag{R32}$$

which represents the normal of the crack plane at the point along the crack front where a is located. The parameters a_i and n_i denote the directional cosines of the vectors a and n_i, respectively. For cubic single crystals, the principal (x_1, x_2, x_3) axes can be taken to be the

crystallographic (<100>,<010>,<001>) axes. As illustrated in Figure R66, the Mode I thresholds along these principal axes can be denoted as K_{12}, K_{21}, K_{23}, K_{32}, K_{13}, and K_{31}, where the first subscript refers to the principal axis normal to the crack plane and the second subscript identifies the crack growth direction. According to Pettit [19], the fracture resistance, $K_p(n,a)$, at the location (n,a) of the crack front can be obtained by projecting the principal values on the current crack orientation through a transformation process that leads one to

$$K_p(n,a) = \left[\left(\frac{n_1^2}{K_1^2} \right)^n + \left(\frac{n_2^2}{K_2^2} \right)^n + \left(\frac{n_3^2}{K_3^2} \right)^n \right]^{1/2n} \tag{R33}$$

where n is an empirical constant and the K_i are obtained on the basis of the fracture resistance, K_{ij}, along the principal axes through the relations given by

$$K_i(a) = \frac{\sqrt{1-a_i^2}}{\left[\left(\frac{a_j^2}{K_{ij}^2} \right)^m + \left(\frac{a_k^2}{K_{ij}^2} \right)^m \right]^{1/2m}} \tag{R34}$$

where m is another empirical constant.

Figure R65. Geometry of crack orientation at a point on an arbitrary crack front. From Pettit [19].

Figure R66. Principal orthotropic components of crack growth resistance for crack growth parallel to Unit Vector **a**. From Pettit [19].

The P&W model, Equations (R33) and (R34), was applied to treat the Mode I fatigue thresholds of PWA 1484. The empirical constants n and m were evaluated by fitting the model to the Mode I threshold data of <100>/<010> and <100>/<011> oriented single crystal specimens. The former set of data was used to obtain a value of 5 for m, as shown in Figure R67. The latter set of threshold data was used to obtain a n value of 0.6-0.8, as shown in Figure R68. Note that in Figure R67 both the solid line ($n = 0.6$) and the dashed line ($n = 0.8$) lie on top of each other. The same set of n and m values were then used to predict Mode I thresholds of <111>/<01$\overline{1}$> and <111>/<01$\overline{2}$> oriented specimens. A comparison of the computed and measured Mode I thresholds for these two orientations are presented in Figures R69 and R70, respectively.

Figure R67. Fitting of P&W threshold model to FCG threshold data of PWA 1484 for the <001>/<010> orientation. The angle β corresponds to the crack deflection angle or the secondary orientation. Results for n=0.6 and n=0.8 are coincident for this orientation.

Figure R68. Fitting of the P&W threshold model to FCG threshold data of PWA 1484 for the <001>/<110> orientation.

Figure R69. Comparison of predicted and measured FCG threshold data for $<111>/<01\bar{1}>$ oriented PWA 1484.

Figure R70. Comparison of predicted and measured FCG threshold data for $<111>/<11\bar{2}>$ oriented PWA 1484.

R.2.7 Mixed-Mode Fatigue Crack Growth Model Development

R.2.7.1 <u>Continuum Crack Growth Models</u>

Several fatigue crack growth theories exist for mixed-mode continuum crack growth in polycrystalline materials, including the maximum tensile stress (MTS) [16], maximum energy release rate (MG) [17, 18], and cyclic crack tip displacement criteria [20]. Both the maximum tensile stress and maximum energy release rate model predict a deflected crack path and a Mode II threshold ($\Delta K_{II,th}$) that is lower than the Mode I threshold ($\Delta K_{I,th}$). Figures R71(a) and (b) show comparisons of the threshold loci and the crack deflection angles predicted by the MTS and MG criteria against those of a self-similar fatigue crack, while Figure R71(b) shows the corresponding crack deflection angle.

Figure R71. Comparison of mixed-mode fatigue threshold loci and crack deflection angles based on the maximum tensile stress (MTS) [16] and maximum energy release rate (MG) [17] against a self-similar crack without and with crack closure: (a) threshold loci, and (b) crack deflection angle, θ, versus the phase angle, $\phi = \tan^{-1} (\Delta K_{II}/\Delta K_{I})$.

In the MTS theory [16], fracture occurs along a path of maximum tensile stress or zero shear ($\tau_{r\theta} = 0$), while it is on the plane of maximum energy release rate in the MG theory [17]. For fatigue crack growth, the Mode II threshold is often higher than the Mode I threshold, Figure R71(a), because of crack-tip shielding resulting from roughness-induced

crack closure and frictional effects on sliding crack surfaces [15]. Correcting for roughness-induced crack closure often leads to a fatigue crack growth threshold locus given by [15]

$$\Delta K_{eq,th} = \left(\Delta K_{I,th}^2 + \Delta K_{II,th}^2\right)^{1/2} \tag{R35}$$

for a mixed Mode I and II crack. The equivalent growth threshold, $\Delta K_{eq,th}$, can be interpreted in terms of the energy release rate of a self-similar fatigue crack.

In the TPNC failure region, fatigue crack growth in PWA 1484 propagated on planes that lie on or close to the plane of maximum tensile stress, Figure R64. Based on the crack deflection angles, mixed-mode crack growth criteria based on the maximum energy release rate or the minimum strain density do not appear to be applicable for PWA 1484. Deviation of the crack deflection angle from the MTS path is the consequence of the dependence of the Mode I threshold on crystallographic orientation. In addition, the Mode II component along the deflected crack path is negligible. Thus, the maximum tensile stress criterion is applicable for PWA 1484. However, the dependence of the Mode I threshold on crystallography orientation dictates that a modification of the MTS criterion to account for threshold anisotropy must be made before it can be applied to PWA 1484. One possible approach is to use Equations (R33) and (R34) to compute $Kp(\beta)$ as a function of crystallographic orientation, where $Kp(\beta)$ is taken to be the Mode I fatigue threshold. The result can then be used to identify the minimum value of $Kp(\beta)$, and use this minimum value of the Mode I threshold in conjunction with the MTS criterion to compute K_I values in components. An alternate and more rigorous approach is to compute both $\Delta K_I(\beta)$ and $Kp(\beta)$ as a function of crystallographic orientation. The crack growth direction can then be predicted based on the direction that maximizes the function of $\Delta K_I(\beta) – Kp(\beta)$ or equivalently, the $\Delta K_I/(\beta)$ ratio. The latter approach is obviously more complicated.

R.2.7.2 Crystallographic Crack Growth Models

In crystallographic crack growth, a fatigue crack, originally in Mode I, deflects to propagate along one or more (111) slip bands. Instead of a plane of zero shear (maximum tensile stress) or maximum energy release rate, the crack path is often the plane of maximum resolved shear stress where localized (111) slip occurs [20]. The crack deflection angle (θ), which is dependent on the crystal orientation, is often different from those predicted by the MTS and MG theories.

Macroscopic (111) fatigue crack growth has been treated in terms of an equivalent stress intensity range, ΔK_{eq}, given by [21]

$$\Delta K_{eq} = \left(\Delta K_I^2 + \Delta K_{II}^2 + \frac{1}{1-\nu} \Delta K_{III}^2 \right)^{1/2} \tag{R36}$$

which is applicable for a mixed Mode I, II and III crack in an isotropic solid with the Poisson ratio, ν. A similar expression for a mixed-mode crack in an anisotropic solid has also been used [21], but elastic anisotropy is generally small and can be ignored. It should be noted that ΔK_I, $\Delta K_{II,}$ and ΔK_{III} are computed based on the (111) crack.

An alternate equivalent ΔK of the form given by [5, 22] is

$$\Delta K_{eq} = (\Delta K_{rn}^2 + \Delta K_{rss}^2)^{1/2} \tag{R37}$$

where ΔK_{rn} is based on the resolved normal stress on the (111) crack, while ΔK_{rss} is based on the resolved shear stress on the slip plane in the slip direction. It is relatively easy to show that Equations (R36) and (R37) are equivalent since

$$\Delta K_{rn} = \Delta K_I \tag{R38}$$

and

$$\Delta K_{rss}^2 = \Delta K_{II}^2 + \Delta K_{III}^2 \approx \Delta K_{II}^2 + \left(\frac{1}{1-\nu} \right) \Delta K_{III}^2 \tag{R39}$$

based on the argument that the strain energy release rate is an invariant in a transformation of the crack coordinate system.

Correlations of fatigue crack growth threshold data for macroscopic (111) fatigue cracks in terms of Equation (R38) or Equation (R39) are illustrated in Figure R72 for $<111>/<11\overline{2}>$ oriented PWA 1484. These data are taken from specimens SC-9, SC-10 and SC-11. Only straight self-similar cracks under Mode I and mixed Mode I and II loading were used; threshold data pertaining to deflected cracks in SC-9 and SC-11 were not used in this correlation. The mixed-mode cracks in SC-10 and the Mode II crack in SC-11 were crystallographic (111) cracks. It is uncertain whether or not the Mode I cracks, which are nominally perpendicular for the <111> axis, indeed lie on the (111) crystallographic planes. For these straight, self-similar cracks on apparent (111) planes, the fatigue threshold ranges under mixed Mode I and II loading appear to be described by the

equivalent stress intensity range given in Equation (R36), which is shown as a solid line in Figure R72.

Figure R72. Plot of $\Delta K_{II,th}$ vs. $\Delta K_{I,th}$ for self-similar crystallographic (111) cracks in $<111>/<11\overline{2}>$ oriented PWA 1484.

The correlation of Equation (R36) with the fatigue crack growth threshold data for straight, self-similar cracks in $<111>/<011>$ oriented in PWA 1484 is shown in Figures R73 and R74, which plots the results of specimens SC-13, SC-14, SC-15, SC-16, and SC-17. Again, all the crack planes were perpendicular to the $<111>$ direction and appear to lie on a single (111) plane. For this case, Equation (R36) does not correlate well with the FCG threshold data as it under-predicts the $\Delta K_{eq,th}$ for all mixed Mode I and II and pure Mode II cracks. These crystallographic cracks appear to be mostly controlled by ΔK_{II}, rather than by a single (critical) value of ΔK_{eq}. Furthermore, the ΔK_I component varies substantially and exceeds the $\Delta K_{I,th}$ for pure Mode I cracks. This phenomenon is not understood at the present time. In terms of ΔK_{eq}, the FCG thresholds of the mixed-mode crystallographic cracks are higher than the counterparts for pure Mode I cracks. Hence, the data points for the mixed-mode cracks lie outside the threshold locus (solid line) calculated on the basis of Equation (R36). Based on the results shown in Figure R72 through R74, one can conclude that the

FCG thresholds of mixed Mode I and II and pure Mode II (111) cracks in PWA 1480 equal or exceed those of pure Mode I cracks in the same crystallographic orientation.

Figure R73. Comparison of da/dN of mixed-mode self-similar (111) cracks in <111>/<01$\bar{1}$> oriented PWA 1484 against da/dN data of a Mode I crack on an apparent (111) plane.

Figure R74. Plot of $\Delta K_{II,th}$ vs. $\Delta K_{I,th}$ for <111>/<01$\bar{1}$> oriented PWA 1484.

R.2.8   Fatigue Crack Growth Transition Model Development

Fatigue crack growth modes in PWA 1480 and 1484 have been characterized by Cunningham et al., [3, 4] and DeLuca and Annis [6]. They identified five different fatigue crack growth modes in these single crystal alloys, including:

(1) submicroscopic (111),

(2) microscopic (111),

(3) macroscopic (111),

(4) transprecipitate noncrystallographic (TPNC), and

5) ancillary TPNC.

In the submicroscopic and microscopic (111) fatigue crack growth modes, fatigue cracks propagate on (111) planes at submicroscopic (< (' size or < 0.5 μm) or microscopic (≈ (' or 0.5 μm) levels, but the overall microscopic crack path is Mode I. In macroscopic (111), crack growth occurs on (111) as a mixed Mode I, II, and III fatigue crack on a macroscopic scale, forming large (111) fracture facets. The two TPNC fractures are formed by the growth of a dominant Mode I crack on noncrystallographic planes, which may involve decohesion of the γ/γ' interface [6]. The two TPNC modes differ by the absence (TPNC) or the presence (ancillary TPNC) of multiple microcrack planes during fatigue crack growth. The fatigue crack growth mode in PWA 1484 is dependent on temperature, frequency, stress intensity range, and environment [3-6].

The FCG curve for continuum crack growth on the TPNC plane is compared against that for crystallographic crack growth on the (111) plane in Figure R75. For the TPNC crack, the Mode I threshold for the TPNC crack is lower and the slope of the da/dN curve is lower than counterparts for crystallographic growth on the (111) plane. The two da/dN curves intersect at ΔK_t. Above ΔK_t, da/dN is higher for the (111) crack, but the TPNC crack grows faster at a given ΔK_{eq} at $\Delta K < \Delta K_t$. The transition point, ΔK_t, depends on frequency, temperature, and environment and its values can be represented in terms of a map depicting the various fracture morphologies. During load shedding, a crystallographic (111) crack would arrest when ΔK_{eq} drops below the threshold value, $\Delta K_{eq,th}$. Since ΔK_{eq} for the crystallographic (111) crack is still higher than $\Delta K_{I,th}$ for a Mode I crack on a TPNC plane, a driving force exists for the (111) crack to kink and deflect to a TPNC crack plane with a lower Mode I threshold, $\Delta K_{I,th}$.

Figure R75. FCG data of a TPNC crack compared against that of a crystallographic (111) crack in <111>/<01$\bar{1}$> oriented PWA 1484. At $\Delta K_I > \Delta K_t$, the crystallographic (111) crack propagates at a higher FCG rate than a TPNC crack at identical ΔK values. The reverse is true for $\Delta K_I < \Delta K_t$.

The crack transition process is reversed when ΔK is increased. In this case, a Mode I TPNC crack would change to propagate on a (111) plane when ΔK_I exceeds ΔK_t at which the da/dN on the (111) plane is higher than that on the TPNC plane.

Existing data [3, 4, 6, 23] were used to construct a fatigue morphology map for PWA 1484. To aid this effort, a fatigue crack growth mode transition model was developed based on a thermally activated slip process in the crack-tip cyclic plastic zone that correlates fatigue crack growth modes to test parameters such as temperature, frequency, and stress intensity range. Derivation of the model is presented in Section R.5. The model suggested that the transition of macroscopic (111) mixed-mode fracture to TPNC (i.e., TPNC and ancillary TPNC) Mode I fracture can be described by the relation

$$f\Delta K = A' \exp\left(\frac{-Q}{RT}\right) \tag{R40}$$

where *f* is the cyclic frequency, ΔK is the stress intensity factor range, *Q* is the apparent activation energy, *T* is the absolute temperature, *R* is the universal gas constant, and *A'* is a pre-exponent coefficient. Figure R76 shows a log-log plot of *f*ΔK versus 1/*T*, where temperature is in degrees Rankine (°R).
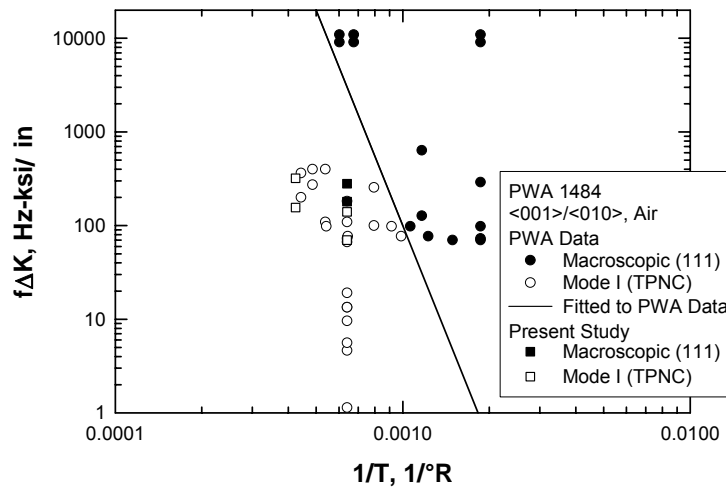

Figure R76. A log-log plot of *f*ΔK vs 1/T shows two fatigue crack growth morphology regimes: (1) mixed-mode macroscopic (111) fracture and (2) Mode I transprecipitate noncrystallographic (TPNC) fracture in PWA 1484. The solid line represents the transition boundary between the two fatigue crack growth modes based on a thermal activation model.

Data for macroscopic (111) mixed-mode fracture are shown as solid circles, while those for TPNC Mode I are shown as open circles. The transition boundary is shown as the solid line that separates the two cracking regimes. The apparent activation energy, *Q*, was determined to be 11.7 kcal/mol and *A*N was 4×10^6 Hz-ksi$\sqrt{}$in. These values were calculated based on the slope and the intercept of the solid line in Figure R76. Equation (R40) provides the basis for the construction of the fatigue crack growth mode map shown in Figure R77, which shows a plot of *f*ΔK versus *T*. The solid line is the macroscopic (111) to TPNC fracture transition boundary predicted by Equation (R40). Macroscopic (111) fracture is prevalent at high *f*ΔK values and low temperature, while TPNC fracture is dominant at lower *f*ΔK values and high temperature. The PWA 1484 data from the literature [3, 4, 6, 23] are divided into two fracture regimes, Macroscopic (111) and TPNC, separated by the calculated transition boundary. Two of the data points generated in this study fall on the wrong side of the transition boundary. This suggests that the transition boundary may be

improved by refitting to the experimental data. A recalibration of the model, however, requires additional experimental data since there are gaps in the fatigue crack growth mode map at high frequency and high temperatures that make a precise determination of the transition boundary uncertain at this time.

Figure R77. A fatigue crack growth morphology map for <001>/<010> PWA 1484 single crystals in air shows two fracture regimes: (1) mixed-mode macroscopic (111) fracture, and (2) Mode I transprecipitate non-crystallographic (TPNC) fracture. The solid line is the fatigue crack growth morphology transition boundary calculated based on the proposed thermal activation model. Experimental data are from Cunningham et al., [3, 4], and Milligan [23], as well as the present study. Mixed-mode macroscopic (111) fracture is favored at high frequency, high ΔK and low temperature, while TPNC fracture is favored at low frequency, low ΔK, and high temperature.

The transition of the fracture morphology appears to be influenced by the deformation shearing and by-pass of the γN precipitates by (111) slip as well as the activation of cube slip. Figure R78 shows the deformation mechanism map based on experimental data in the literature for PWA 1480 [24]. The transition boundaries were calculated on the basis of the experimentally determined activated energies and the appropriate Arrhenius equations for cube cross slip and γN by-pass. For PWA 1480, the activation energies are 12 and 120 kcal/mol [24] for cross slip on the cube plane and γ' by-pass, respectively. The activation

energy for fatigue crack growth mode transition is 11.7 for PWA 1484, which is expected to be similar to that for PWA 1480. This comparison of apparent activation energies suggests that fatigue crack growth mode transition in PWA 1484 may be controlled by the activation of cross slip on the cube plane.

Figure R78.   Deformation mechanism map for PWA 1480 shows three distinct regimes: (1) the formation of faulted dislocation loops in γN, (2) activation of cube slip in γN, and (3) γN by-pass by the Orowan mechanism. Experimental data are from Milligan and Antolovich [24].

R.3   DISCUSSION

This study has demonstrated that the AFPB fatigue fixture is a viable test method for studying fatigue crack growth mode transition and determining the mixed-mode fatigue crack growth thresholds for PWA 1484 single crystals. Experimental data generated herein have clarified the range of ΔK_t conditions where macroscopic (111) crack growth occurs in PWA 1484. The FCG threshold for macroscopic (111) cracks is higher than that for TPNC. At 1100°F, fatigue crack growth in PWA 1484 occurs on TPNC planes in the near-threshold region. Both the threshold and the crack deflection angle can be adequately described using isotropic continuum theories based on the MTS (local ΔK_I) criterion. Deviation of the crack path from the local Mode I condition is caused by the dependence of the Mode I FCG threshold on crystallographic orientation. Figure R79 shows the orientations of the fracture plane normal and crack growth direction of the actual crack in

individual PWA 1484 specimens in a stereographic projection. The lowest Mode I fatigue
threshold (SC-16) is located in the central portion of the standard stereographic triangle.

Figure R79. Fracture plane normal and crack growth direction (measured along the
actual crack path) of fatigue cracks in individual PWA 1484 specimens
plotted in a stereographic projection.

A detailed examination of the initial and final crack orientations shown in Table R2
indicated that the crack orientations for SC-5, SC-6, SC-7, and SC-8 under pure Mode I are
<010>/<110>, which are close to those for the deflected cracks in SC-9 and SC-11. Figure
R80 compares the da/dN curves for <010>/<110> obtained under pure Mode I (SC-5, SC-6,
SC-7, and SC-8) against those of deflected cracks that propagated under local Mode I. There
is good agreement between the da/dN curves for the deflected (local Mode I) cracks and the

pure Mode I cracks. Similarly, the cracks orientation for SC-9, SC-10, and SC-11 are

$<111>/<11\overline{2}>$ under pure Mode I. These crack orientations are comparable to the self-similar crack in SC-11 and to the deflected (local Mode I) cracks observed in SC-5, SC-6, SC-7, and SC-8. A comparison of the da/dN data of these specimens is shown in Figure R81.

The negative slope exhibited by several specimens at ΔK_I = 5-7 ksi√in is believed to be due to the fact that the transition from the initial to final crack planes was gradual, as opposed to the abrupt transition assumed in the FRANC2D/L analysis. Eliminating these data results in a scatter band on rates of 2X to 3X which is typical of most da/dN (ΔK) behavior. Thus, the local analysis of deflected crack growth brings the data into agreement with the self-similar crack growth for a given crystallographic orientation. The corresponding values of ΔK_{th} are also reasonably (within ±17%) consistent for a given crystallographic orientation.
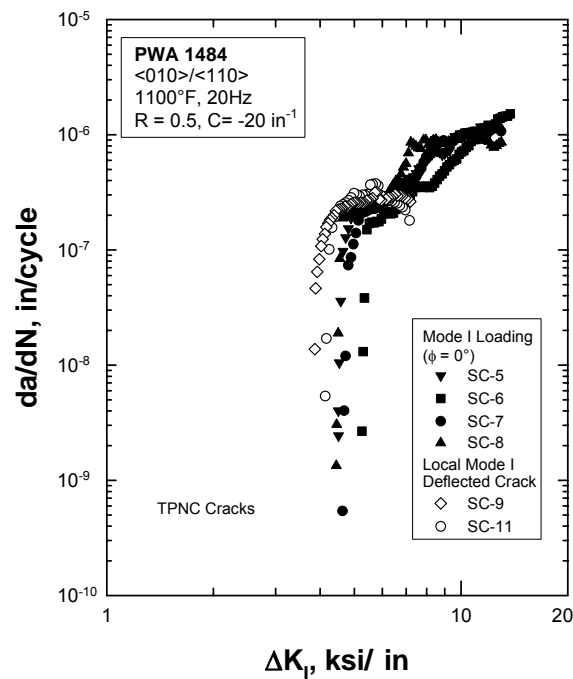

Figure R80. A comparison of da/dN curves for pure Mode I cracks (SC-5, SC-6, SC-7, and SC-8) against local Mode I deflection cracks (SC-9 and SC-11) with the same <010>/<110> crack orientation.
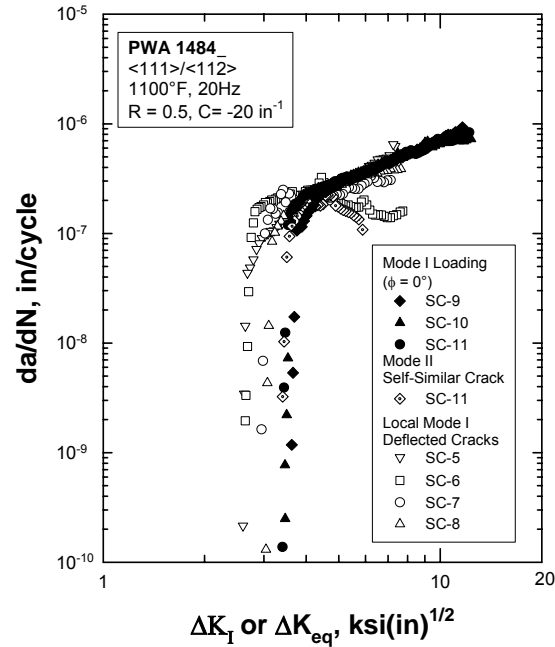
Figure R81.   A comparison of da/dN curves for pure Mode I cracks, a Mode II self-similar
crack, and local Mode I deflected cracks with the approximately same
$<111>/<11\bar{2}>$ crack orientation.

The thresholds of the TPNC cracks are reasonably consistent with the P&W
threshold model described in Section R.2.6. On the other hand, crystallographic (111) cracks
appear to obey a critical $\Delta K_{eq,th}$ criterion, but substantial deviations from this criterion have
also been observed. Crystallographic (111) cracks can propagate under pure Mode II or
mixed Mode I and II loading with a high phase angle (> e.g., $\phi = 80°$). However, these
cracks might not propagate if fracture surface asperities in the crack wake make contact and
cause roughness-induced crack closure. Nonetheless, the lowest FCG threshold is associated
with continuum TPNC Mode I cracks since crystallographic (111) cracks have been observed
to transition to TPNC cracks under decreasing-ΔK conditions for pure Mode I, mixed Mode I
and II, and pure Mode II loading. Alternately, TPNC Mode I cracks can transit to
crystallographic (111) cracks under increasing-ΔK conditions because the FCG curves for
these two crack morphologies are different in both the near-threshold and the Paris regimes.
An accurate prediction of the transition of noncrystallographic and crystallographic (111)
cracks require consideration of the crack driving force, test temperature, frequency, and the
entire FCG curve for individual cracking modes. Because of the above behavior, TPNC
cracks are expected to control the high-cycle fatigue life, while crystallographic (111) cracks

R-78

are expected to dictate the low-cycle fatigue life at 20 Hz. This ranking might vary with frequency since crystallographic cracking is favored at higher frequencies.

Current results suggest that the effects of frequency, temperature, and stress intensity range on fatigue crack growth mode transition in <001>/<010> oriented PWA 1484 subjected to nominal Mode I loading can be treated in terms of a thermal activation model, which is given in Equation (R40). In addition, the effects of mode mixity on the fatigue crack growth thresholds of mixed-mode cracks in PWA 1484 can be described in term of the ΔK_{eq} parameter defined in Equation (R36) or Equation (R37). Replacing ΔK in Equation (R40) by ΔK_{eq} in either Equation (R36) or (R39) leads to

$$f\Delta K_{eq} = A' \exp\left(\frac{-Q}{RT}\right) \tag{R41}$$

which has the potential of incorporating the effects of frequency, temperature, and mode mixity on fatigue crack growth mode transition. Since concurrent TPNC cracking and crystallographic (111) cracking are feasible, the boundaries of two cracking morphologies is likely a scatter band, rather than a distinct boundary. The validity of Equation (R41) and the precise boundary between the various fracture morphologies would benefit from additional data.

R.4   STRESS INTENSITY FACTOR SOLUTIONS FOR DEFLECTED CRACKS CALCULATED USING FRANC2D/L AND THE ACTUAL CRACK PATHS

Additional K solutions of the actual crack path in other single crystal specimens are presented below in Figures R82 through R86. See Section R.2.2.2 for details on other K solutions.

Figure R82. K solutions for SC-2 at ϕ =45°.

Figure R83. K solutions for SC-6 at ϕ = 48°.

Figure R84. K solutions for SC-7 at ϕ =80°.

Figure R85. K solutions for SC-13 at ϕ = 45°.

Figure R86. K solutions for SC-16 at $\phi = 90°$.

R.5   DERIVATION OF FATIGUE CRACK GROWTH MODE TRANSITION MODEL

The transition of fatigue crack growth modes by a thermal activated process is modeled by considering the strain rate at the crack-tip plastic zone boundary. According to linear-elastic fracture mechanics, the strain-range, $\Delta\varepsilon$, of a Mode I crack subjected to a stress intensity range, ΔK, is given by

$$\Delta\varepsilon = \frac{\Delta K \ F(\theta)}{E\sqrt{2\pi r_p}} \tag{R42}$$

when E is the Young's Modulus, r_p is the process zone size, and $f(\theta)$ is a trigometric function. The strain rate at the plastic zone boundary is

$$\dot{\varepsilon} = \frac{\Delta\varepsilon}{\Delta t} = \frac{f\Delta K \ F(\theta)}{E\sqrt{2\pi r_p}} \tag{R43}$$

since the cyclic frequency, $f = 1/\Delta t$. According to thermal activated flow theory,

$$\dot{\varepsilon} = \dot{\varepsilon}_o \left(\frac{\sigma}{\sigma_o} \right)^n \exp\left[-\frac{Q}{RT} \right] \tag{R44}$$

when σ is stress, σ_o is a reference stress, n is the stress exponent, Q is the activation energy, R is the universal gas constant, and T is absolute temperature. Equating Equation (R43) to (R44) leads one to

$$\frac{f \; \Delta K \; F(\theta)}{E\sqrt{2\pi r_p}} = \dot{\varepsilon}_o \left(\frac{\sigma_p}{\sigma_o} \right)^n \exp\left[-\frac{Q}{RT} \right] \tag{R45}$$

where σ_p is the stress at the plastic zone boundary. Rearranging Equation R45) gives

$$f\Delta K = A' \; \exp\left[-\frac{Q}{RT} \right] \tag{R46}$$

when

$$A' = E\sqrt{2\pi r_p} \; \dot{\varepsilon}_o \left(\frac{\sigma_p}{\sigma_o} \right)^n F^{-1}(\theta) \tag{R47}$$

R.6 CONCLUSIONS AND RECOMMENDATIONS

1. Mixed-Mode stress intensity factor solutions from anisotropic and isotropic analyses were similar for the 2-D test specimen geometries analyzed in this program. Since results were indistinguishable over the practical range of crack lengths employed for crack growth testing, isotropic analysis results were used to control the decreasing-K crack growth threshold tests performed herein. These results suggest that for engineering purposes, it may be sufficient to employ isotropic analysis to define the crack driving force when performing fracture mechanics assessments of single crystal nickel components.

2. During mixed-mode decreasing-K crack growth threshold testing, (111) cracks in PWA 1484 initially propagated in a straight, self-similar manner but tended to deflect out of plane as transprecipitate noncrystallographic (TPNC) cracks. In certain instances, the transition occurred immediately on changing the loading from the Mode I precracking to mixed-mode testing.

3. The threshold stress intensities for (111) cracks under mixed Mode I and II and pure Mode II are higher than those for Mode I (111), as well as for TPNC cracks.

Because of this, initially crystallographic (111) cracks can propagate below their threshold stress intensities by deflecting to TPNC cracks. Consequently, it is recommended that Mode I threshold stress intensity factors for TPNC cracks be employed in HCF assessments.

4.   Mode I cracks on (111) or TPNC planes can transition to crystallographic (111) cracks when the ΔK increases beyond a transition limit, ΔK_t. The Paris slope for crystallographic (111) cracks is higher than that for Mode I and TPNC cracks. Consequently, when this fracture morphology occurs, it is recommended that da/dN (ΔK) curves for crystallographic (111) cracks be used for LCF assessments

5.   Following deflection, mixed-mode TPNC cracks in PWA 1484 propagate on or near the maximum principal stress plane where $\Delta K_{II} = 0$. Thus, for engineering purposes, TPNC cracks subjected to mixed-mode loading can be treated as

local Mode I cracks governed by a Mode I threshold. In so doing, crack deflection needs to be accounted for in computing the local stress intensity factors for deflected cracks.

6.   The Mode I threshold in PWA 1484 is a function of crystallographic orientation, and thus depends on the orientation of the crack plane (*n*) and the crack growth direction (*a*). The orientation dependence of $\Delta K_{I,th}$ (*n, a*) can be predicted reasonably well on the basis of the threshold values for the principal (<001>) axes through a transformation procedure using the 3-D model developed by P&W.

7.   Current data indicate that the minimum value of $\Delta K_{I,th}$ at R=0.5 is 2.67 ksi√in and occurs for a local Mode I deflected TPNC crack with a $<1\,\overline{2}\,0> + 10°/<\overline{1}\,02>$ orientation. The use of a minimum $\Delta K_{I,th}$ appears to be a tractable approach for HCF assessments of single crystal material. However, additional testing is warranted to verify that this minimum $\Delta K_{I,th}$(*n, a*) value is valid for all orientations, as well as to define the dependence of the minimum $\Delta K_{I,th}$(*n, a*) on load ratio (R).

8.   Mixed-mode crystallographic (111) cracks may be treated in terms of an equivalent ΔK parameter, ΔK_{eq}, in some cases, but not in all situations. Additional work is required to better understand why this approach does not work for all situations, and to establish a universal crack driving force for this cracking mode/morphology.

9.   Mode I TPNC crack growth and crystallographic (111) crack growth are competing processes that exhibit different da/dN characteristics including different

thresholds and Paris slopes; in some cases these processes can occur concurrently (e.g. in a single test specimen). The dominance of one crack growth morphology over another is dictated by the da/dN response of individual crack morphologies at a given ΔK and the local ΔK when the crack alters its path.

10.   The transition boundary between crystallographic (111) and TPNC fatigue crack growth depends on temperature, cyclic frequency, and applied stress intensity factor. An engineering model to describe this transition has been developed (Equation R40) on the basis of thermal activation of (111) and cube slip in the cyclic plastic zone of the crack tip.

11.   The asymmetric-four-point-bend (AFPB) test technique is a viable technique for studying fatigue crack growth mode transition and determining the mixed-mode fatigue crack growth thresholds of PWA 1484 at elevated temperatures.

R.7   REFERENCES

1.   G. R. Leverant and M. Gell, *Metall. Transactions A*, Vol. 6A, 1975, pp. 367-371.

2.   G. R. Leverant, M. Gell, and S.W. Hopkins, *Mat. Sci. Eng.*, Vol. 8, 1971, pp. 125-133.

3.   S. E. Cunningham, D. P. DeLuca, and F. K. Haake, "Crack Growth and Life Prediction in Single-Crystal Nickel Superalloys," Vol. 1, WL-TR-94-4089, Pratt & Whitney, West Palm Beach, FL, 1996.

4.   S. E. Cunningham, D. P. DeLuca, E. H. Hindle, J. W. Sheldon, and F. K. Haake, "Crack Growth and Life Prediction in Single-Crystal Nickel Superalloys," Vol. 2, WL-TR-96-4048, Pratt & Whitney, West Palm Beach, FL, 1994.

5.   J. Telesman and L. J. Ghosn, "Crack Growth and Life Prediction in Single-Crystal Nickel Superalloys," Vol. 3, WL-TR-94-4090, Pratt & Whitney, West Palm Beach, FL, 1996.

6.   D. P. DeLuca and C. Annis, "Fatigue in Single Crystal Nickel Superalloys," FR23800, Pratt & Whitney, West Palm Beach, FL, 1995.

7.   P. K. Wright, H. Jang, and H. G. Popp, "Fatigue and Fracture of Advanced Blade Materials," AFWAL-TR-84-4166, General Electric, Cincinnati, OH, 1985.

8.   M. D. Snyder and T. A. Cruse, "Crack Tip Stress Intensity Factors in Finite Anisotropic Plates,"AFML-TR-73-209, 1973.

9. D. Swenson and M. James, "FRANC2D/L: A Crack Propagation Simulator for Plane Layered Structures," Kansas State University, Manhattan, Kansas, 1995.

10. N. Hasebe and S. Inohara, "Stress Analysis of a Semi-Infinite Plate with an Oblique Edge Crack," *Ing. Arch.*, 49, pp. 51-62, 1980.

11. M. Isida, "Tension of a Half Plane Containing Array Cracks, Branched Cracks and Cracks Emanating from Sharp Notches," *Trans. Japan Soc. Mech. Engrs.*, Vol. 45, No. 392, pp. 306-317, 1979.

12. C. E. Freese, reported in *Stress Intensity Factors Handbook*, Vol. 2, edited by Y. Murakami, Pergamon Press, pp. 916-920, 1987.

13. W. K. Wilson, Research Report 69-1E7-FMECH-R1, Westinghouse Research Laboratories, Pittsburgh, 1969.

14. M. Y. He and J. W. Hutchinson, "Asymmetric Four-Point Crack Specimen," *J. Appl. Mech.,* Vol. 67, pp. 207-209, 2000.

15. J. P. Campbell and R. O. Ritchie, *Eng. Fract. Mech.*, Vol. 67, 2000, pp. 229-249.

16. F. Erdogan and G. C. Sih, *Journal of Basic Engineering D*, Vol. 85, 1963, pp. 519-527.

17. M. A. Hussain, S. L. Pu and J. Underwood, *ASTM STP* 560, 1974, pp. 2-28.

18. G. C. Sih, "Some Basic Problems in Fracture Mechanics and New Concepts," *Eng. Frat. Mech.*, Vol. 3, 1973, pp. 439-451.

19. R. Pettit, Pratt & Whitney Aircraft, East Hartford, CT, Private communication, December 2001.

20. P. A. S. Reed, X. D. Wu, and I. Sinclair, *Metall. Mat. Transactions A,* Vol. 31A, pp. 109-123, 2000.

21. K. S. Chan, J. E. Hack, and G. R. Leverant, *Metall. Transactions, A*, Vol. 18A, pp. 581-591, 1987.

22. J. Telesman and L. J. Ghosn, "Fatigue Crack Growth Behavior of PWA 1484 Single Crystal Syperalloy at Elevated Temperatures," ASME/IGTI Paper 95-GT-452, International Gas Turbine and Aeroengine Congress & Exposition, June 5-8, 1995, Houston, TX.

23. J. W. W. Milligan, Department of Mat. Sci. & Eng., Michigan Technological University, Houghton, MI, Private Communication, August 2000.

24. W. W. Milligan and S.D. Antolovich, *Metall. Transactions A*, Vol. 18A, 1987, pp. 85-95.

APPENDIX S

HCF BASELINE ENDURANCE LIMIT MODELING

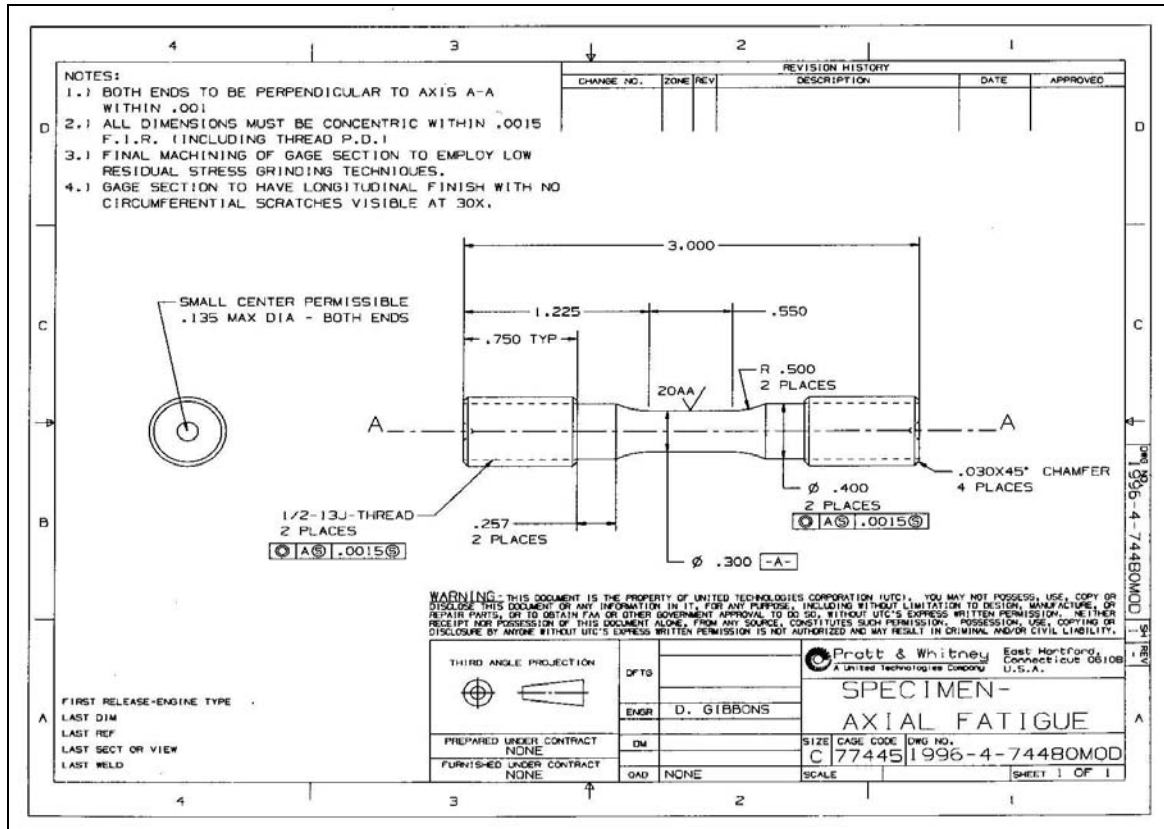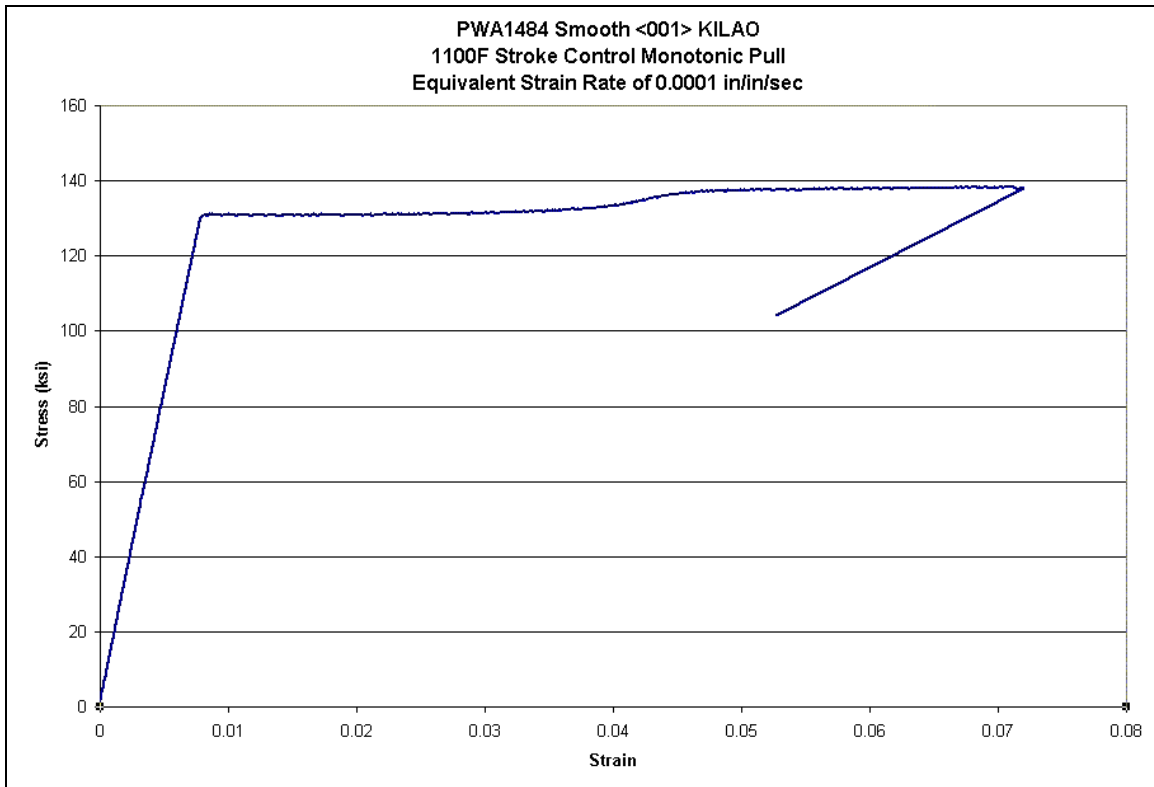Figure S1. Modified MT3-S (short) specimen.
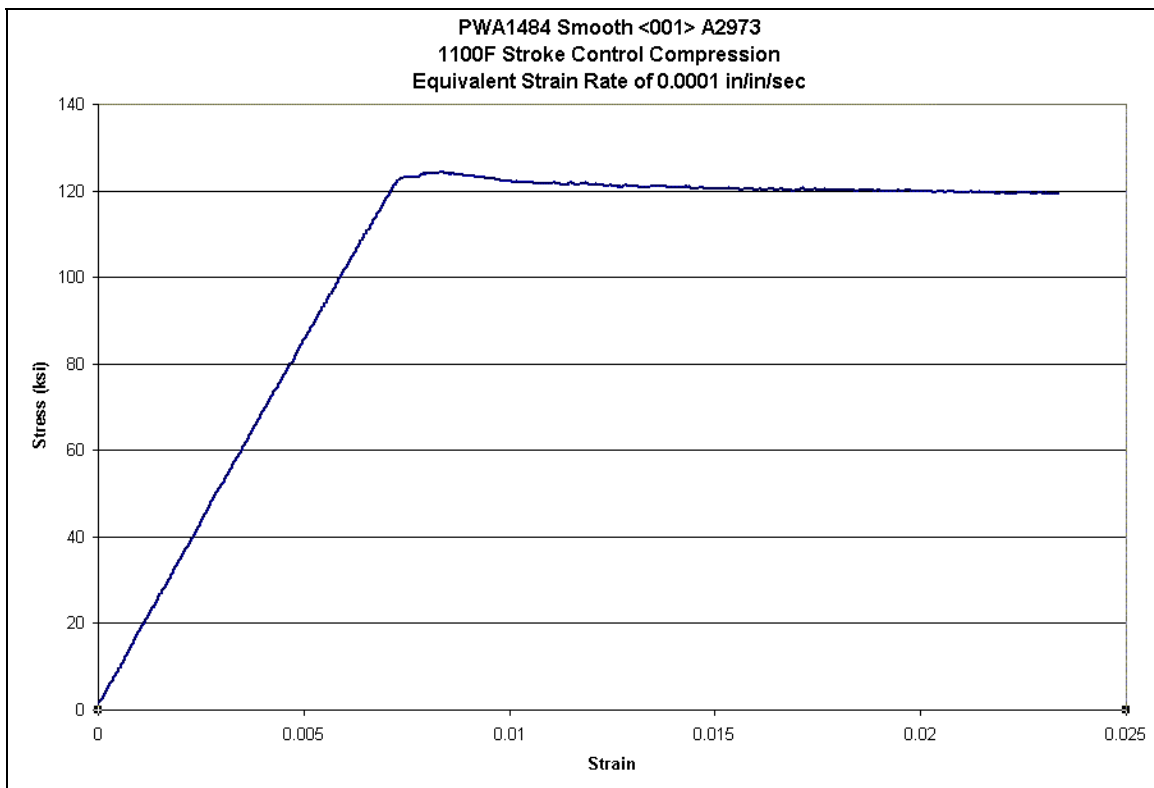
Figure S2. Specimen <001> K1LAO.
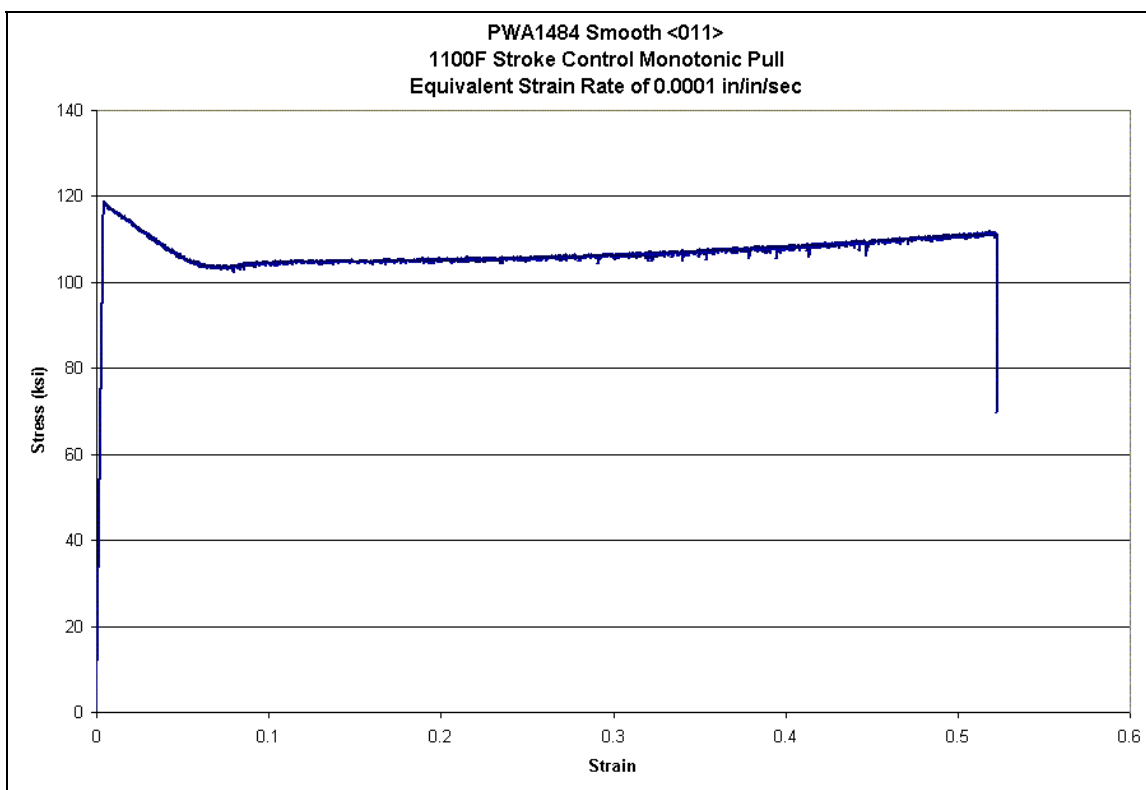

Figure S3. Specimen <001> A2973.

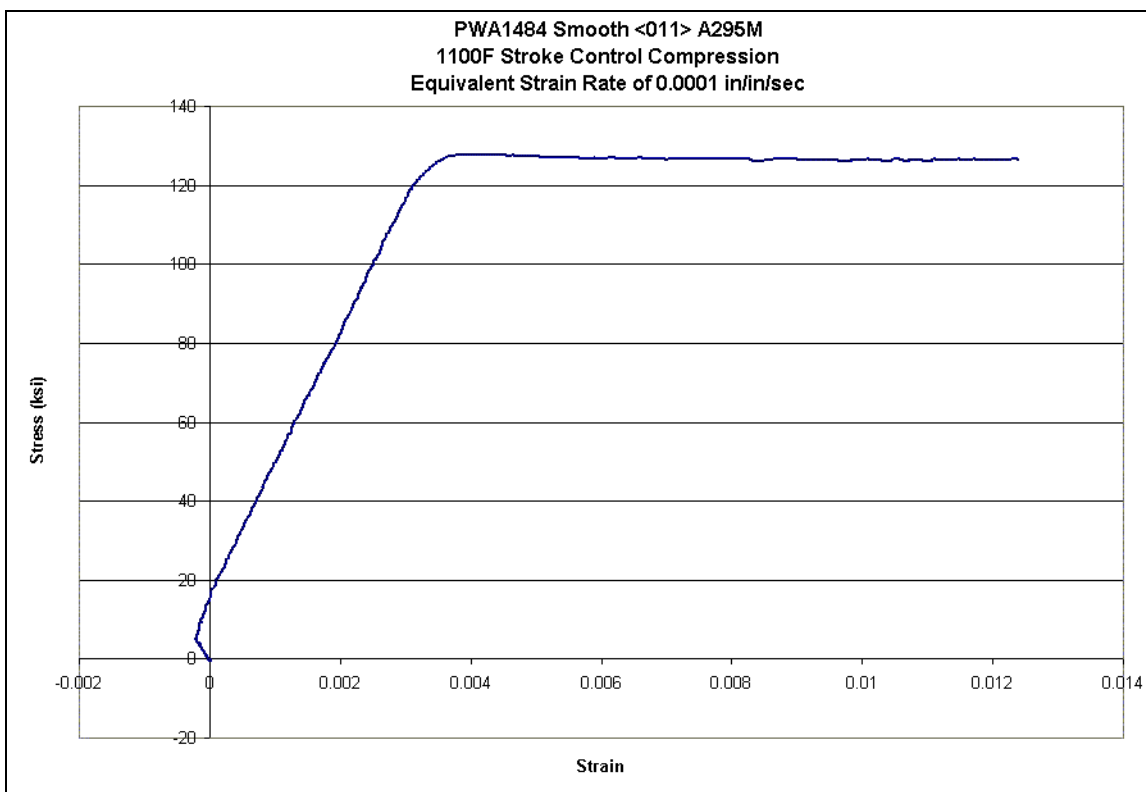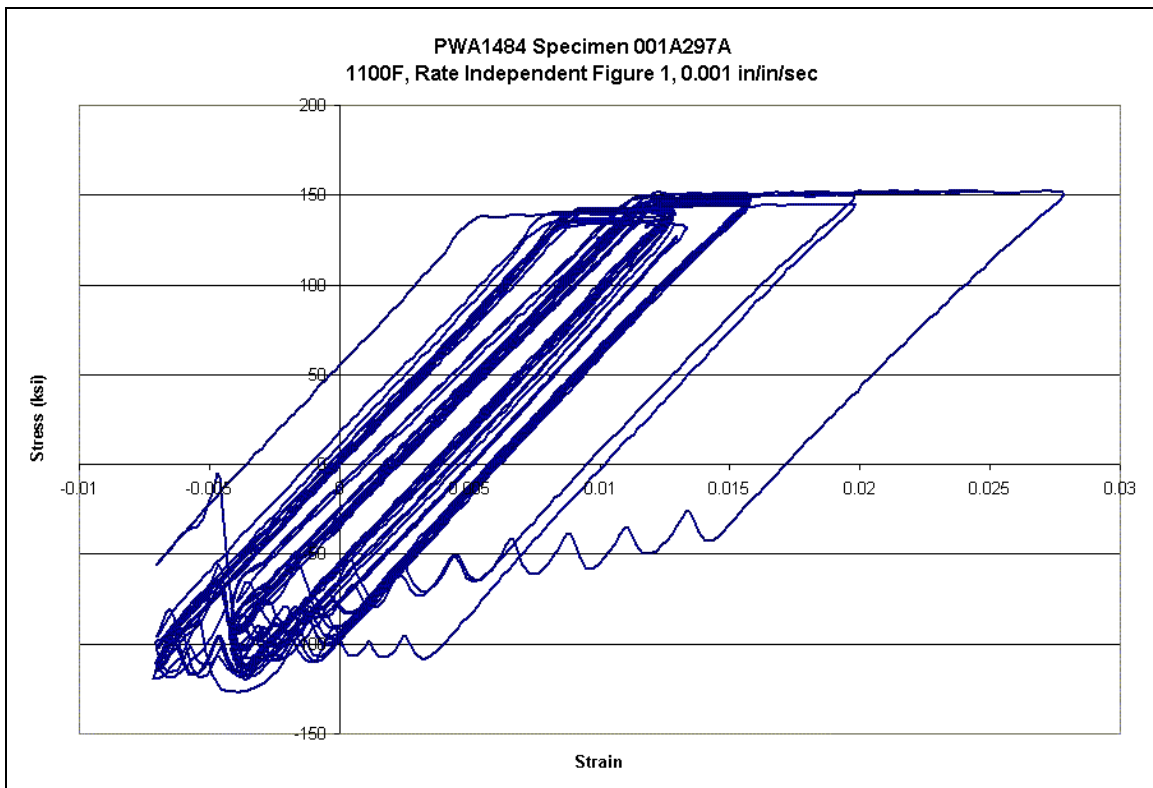Figure S4. Specimen <011> A296F.

Figure S5. Specimen <011> A295M.
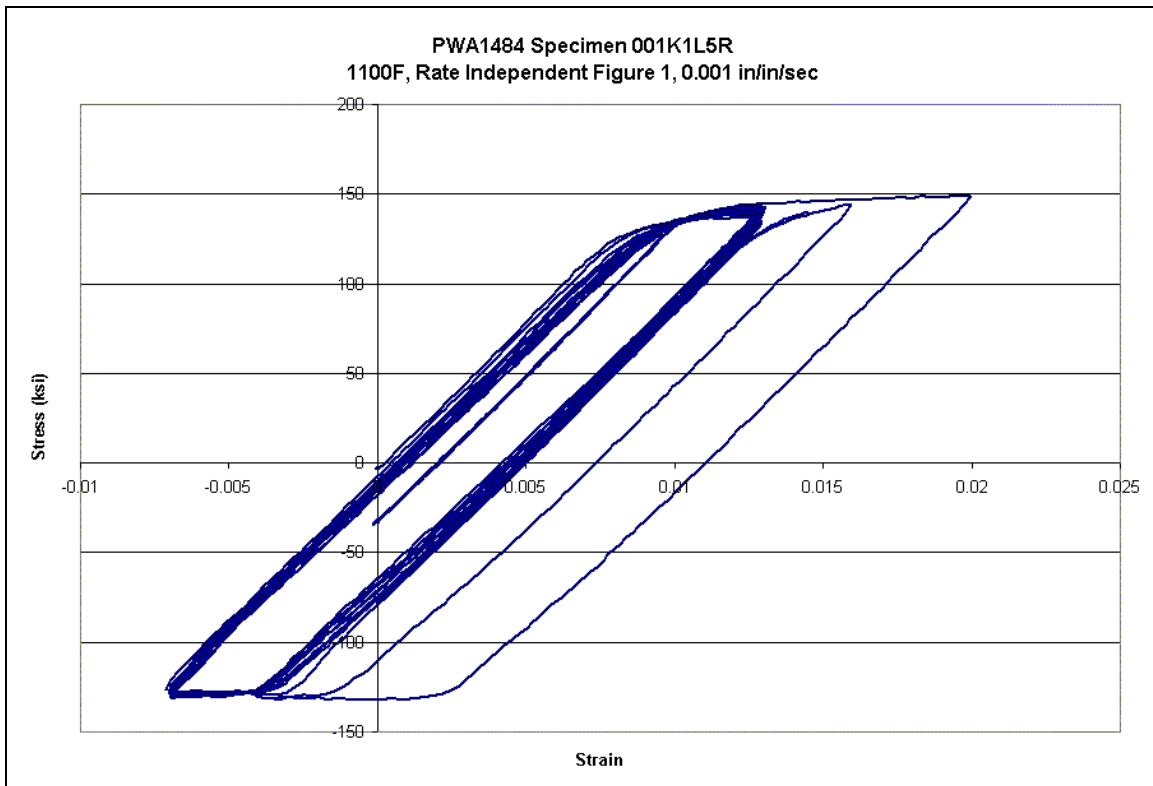
Figure S6. Specimen <001> A297A.

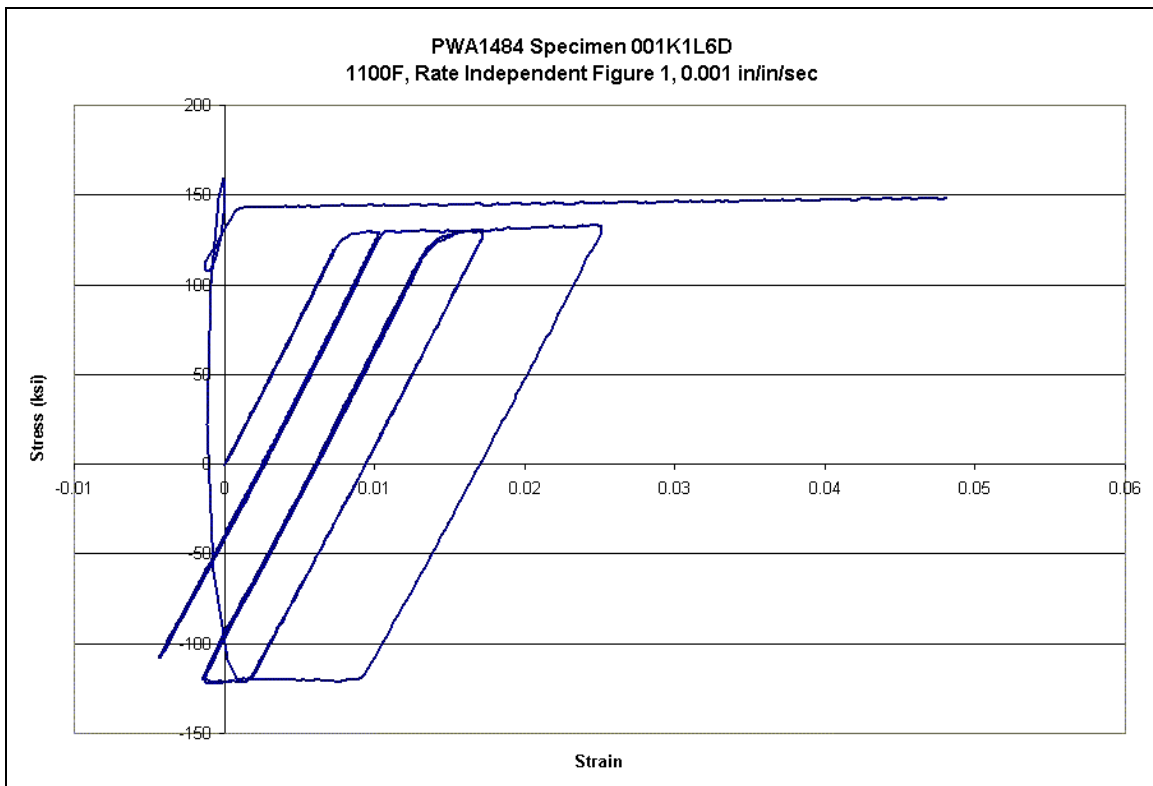Figure S7. Specimen <001> K1L5R.

Figure S8. Specimen <001> K1L6D.

Figure S9. Specimen <001> K1L9C.

Figure S10. Specimen <001> K1L2U.

Figure S11. Specimen <011> A296K.

APPENDIX T

INITIATION FACET LOCATION AND ORIENTATION

A laser location technique was used to locate and orient the initiation facet of each specimen in the vertical direction such that the normal to the facet plane and the specimen axis were in the same vertical (Y-Z) plane (see Figure T1). The specimen X-Y-Z axes were defined with respect to the specimen axis and one end face of the specimen. The specimen Z-axis was drawn along the specimen axis with the positive Z-direction as shown in FigureT1. The specimen Y-axis was defined to be vertically upwards after locating the initiation facet in the vertically upward direction. The specimen X-axis was drawn in the horizontal direction such that the X-Y plane was normal to the specimen Z-axis. Thus, the X-Y plane was along the specimen end face.

Figure T1. Specimen, crystal, and facet orientation and definition of Laue angles.

T.1 LASER FACET LOCATION TECHNIQUE

The laser location technique consisted of projecting a laser beam, aligned at a fixed angle to the specimen axis, on to the initiation facet. The specimen was rotated about its' axis (Z-axis) until the reflection of the laser beam, off the facet, was in the same vertical plane (Y-Z plane) as the specimen axis (see Figure T1). The specimen was fixed in this orientation in a V-block after this laser location procedure. This procedure

fixed the orientation of the initiation facet of each specimen in the Y-Z plane and also provided a fixed reference frame for defining the orientation of the crystallographic axes with respect to the specimen X-Y-Z axes.

T.2   X-RAY DIFFRACTION LAUE ANGLE MEASUREMENT

The orientation of the crystallographic axes was determined using Laue X-ray diffraction techniques. Using the Laue techniques, the orientation of the <001> axis was determined by measuring the orientation angles δ and γ (see Figure T1). The angle δ is defined as the angle between the <001> axis and it's projection on the Y-Z plane. The angle γ is defined as the angle between the projection of the <001> axis on the Y-Z plane and the Z-axis (or specimen axis). The positive direction for both these angles is indicated in Figure T1.

In order to completely define the orientation of the crystallographic axes in three-dimensional (3-D) space, one more angle needs to be measured. The angle β shown in Figure T2 was also measured by observing the pattern of the dendrites on the end of the specimen. As shown in Figure T2, the angle β was defined as the angle between the projection of the <010> axis on the X-Y plane and the Y-axis (β is positive in the clockwise direction from the Y-axis). Based on the measured angles δ, γ, and β, it is possible to derive an expression for the angle ψ (Figures T1, T2) which is the angle between the <010> orientation and the negative Z-axis. These angles were used to completely define the orientation of the crystal axes in 3-D space using direction cosines (described in the next section).

Furthermore, based on the measured angles δ, γ, and β, it was possible to use classical stereographic projection techniques to uniquely identify the octahedral plane on which fatigue initiation occurred. This initiation plane was fixed for each specimen to be in the vertical orientation using the laser location technique before the measurement of the Laue angles. The octahedral planes were identified as, 1, 2, 3, or 4 using the convention shown in Figure T3. The identification number of the octahedral plane on which fatigue initiation occurred was determined using the measured Laue angles and the stereographic projection technique for each specimen and is given in Table 4.29 of Section 4.3.3.4 (Chapter 4 of main report).
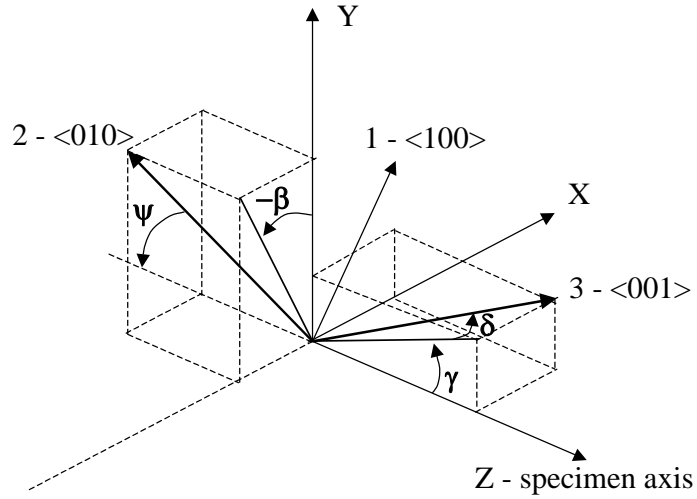
Figure T2.   Orientation angles of the crystal axes (1-2-3) with respect to the specimen axes (X-Y-Z).

Figure T3.   Plan view of octahedral <111> planes and <110> family of slip directions.

APPENDIX U

TRANSFORMATION EQUATIONS

U.1   DIRECTION COSINES

The three Laue angles δ, γ, and β, were used to define the direction cosines between the loading axes (X-Y-Z) and the crystal axes (1-2-3). The direction cosines between the loading coordinate system X-Y-Z with respect to the crystal coordinate system 1-2-3 are given in Table U1. The notation used for the direction cosines was of the form a_{ij}, i = 1, 3, and j = 1, 3. Thus, a_{11} = cosine(angle between the 1-axis and the X-axis), a_{23} = cosine(angle between the 2-axis and the Z-axis), etc. Once the orientations between the two coordinate systems are described, mathematically, in terms of the direction cosines (Table U1), it is possible to proceed with the transformation of the stress and strain tensors between the two axes.

Table U1. Direction Cosines Between the X-Y-Z and the 1-2-3 Axes

	X	Y	Z
1	a_{11}	a_{12}	a_{13}
2	$\sin(\psi)\sin(\beta)$	$\sin(\psi)\cos(\beta)$	$-\cos(\psi)$
3	$\sin(\delta)$	$\cos(\delta)\sin(\gamma)$	$\cos(\delta)\cos(\gamma)$

The angle ψ in Table U.1 is derived in terms of the angles δ, γ, and β, and is given by:

$$\tan(\psi) = \frac{\cos(\delta)\cos(\gamma)}{\sin(\delta)\sin(\beta) + \cos(\beta)\cos(\delta)\sin(\gamma)} \tag{U1}$$

The direction cosines, a_{11}, a_{12}, and a_{13}, can be determined using classical properties and relationships of direction cosines and the known direction cosines in Table U1. Thus, $a_{11} = a_{22}*a_{33} - a_{23}*a_{32}$, $a_{12} = a_{23}*a_{31} - a_{21}*a_{33}$, and $a_{13} = a_{21}*a_{32} - a_{22}*a_{31}$.

U.2 ELASTIC STRESS/STRAIN TRANSFORMATION FROM LOADING AXES TO CRYSTAL AXES

The symmetry in the stress and strain tensors can be exploited to express these tensors in the "contracted" notation, thereby, simplifying the resulting mathematical description of the transformation equations and also making them more suitable for implementation on a computer. The following notation is used for the stress and strain tensors in the two coordinate systems:

$$\{\sigma_{XYZ}\} = \begin{Bmatrix} \sigma_X \\ \sigma_Y \\ \sigma_Z \\ \tau_{XY} \\ \tau_{YZ} \\ \tau_{XZ} \end{Bmatrix} \quad \text{and} \quad \{\sigma_{123}\} = \begin{Bmatrix} \sigma_1 \\ \sigma_2 \\ \sigma_3 \\ \tau_{12} \\ \tau_{23} \\ \tau_{13} \end{Bmatrix} \tag{U2}$$

$$\{\varepsilon_{XYZ}\} = \begin{Bmatrix} \varepsilon_X \\ \varepsilon_Y \\ \varepsilon_Z \\ \gamma_{XY} \\ \gamma_{YZ} \\ \gamma_{XZ} \end{Bmatrix} \quad \text{and} \quad \{\varepsilon_{123}\} = \begin{Bmatrix} \varepsilon_1 \\ \varepsilon_2 \\ \varepsilon_3 \\ \gamma_{12} \\ \gamma_{23} \\ \gamma_{13} \end{Bmatrix} \tag{U3}$$

The transformation of the elastic stresses, $\{\sigma_{XYZ}\}$, in the loading coordinate system to the stresses, $\{\sigma_{123}\}$, in the crystal coordinate system, is given by the following matrix equation:

$$\{\sigma_{123}\} = [P]\{\sigma_{XYZ}\} \tag{U4}$$

where, the stress transformation matrix, [P], is given in terms of the direction cosines as:

$$[P] = \begin{bmatrix} a_{11}^2 & a_{12}^2 & a_{13}^2 & 2a_{11}a_{12} & 2a_{12}a_{13} & 2a_{11}a_{13} \\ a_{21}^2 & a_{22}^2 & a_{23}^2 & 2a_{21}a_{22} & 2a_{22}a_{23} & 2a_{21}a_{23} \\ a_{31}^2 & a_{32}^2 & a_{33}^2 & 2a_{31}a_{32} & 2a_{32}a_{33} & 2a_{31}a_{33} \\ a_{11}a_{21} & a_{12}a_{22} & a_{13}a_{23} & a_{11}a_{22}+a_{12}a_{21} & a_{12}a_{23}+a_{13}a_{22} & a_{13}a_{21}+a_{11}a_{23} \\ a_{21}a_{31} & a_{22}a_{32} & a_{23}a_{33} & a_{22}a_{31}+a_{21}a_{32} & a_{23}a_{32}+a_{22}a_{33} & a_{21}a_{33}+a_{23}a_{31} \\ a_{11}a_{31} & a_{12}a_{32} & a_{13}a_{33} & a_{11}a_{32}+a_{12}a_{31} & a_{12}a_{33}+a_{13}a_{32} & a_{13}a_{31}+a_{11}a_{33} \end{bmatrix} \quad \text{(U5)}$$

The transformation of the elastic strains, $\{\varepsilon_{XYZ}\}$, in the loading coordinate system to the strains, $\{\varepsilon_{123}\}$, in the crystal coordinate system can be described by the following matrix equation:

$$\{\varepsilon_{123}\} = [Q]\{\varepsilon_{XYZ}\} \quad \text{(U6)}$$

where, the strain transformation matrix, [Q], is given in terms of the direction cosines as:

$$[Q] = \begin{bmatrix} a_{11}^2 & a_{12}^2 & a_{13}^2 & a_{11}a_{12} & a_{12}a_{13} & a_{11}a_{13} \\ a_{21}^2 & a_{22}^2 & a_{23}^2 & a_{21}a_{22} & a_{22}a_{23} & a_{21}a_{23} \\ a_{31}^2 & a_{32}^2 & a_{33}^2 & a_{31}a_{32} & a_{32}a_{33} & a_{31}a_{33} \\ 2a_{11}a_{21} & 2a_{12}a_{22} & 2a_{13}a_{23} & a_{11}a_{22}+a_{12}a_{21} & a_{12}a_{23}+a_{13}a_{22} & a_{13}a_{21}+a_{11}a_{23} \\ 2a_{21}a_{31} & 2a_{22}a_{32} & 2a_{23}a_{33} & a_{22}a_{31}+a_{21}a_{32} & a_{23}a_{32}+a_{22}a_{33} & a_{21}a_{33}+a_{23}a_{31} \\ 2a_{11}a_{31} & 2a_{12}a_{32} & 2a_{13}a_{33} & a_{11}a_{32}+a_{12}a_{31} & a_{12}a_{33}+a_{13}a_{32} & a_{13}a_{31}+a_{11}a_{33} \end{bmatrix} \quad \text{(U7)}$$

Equations. (U4) through (U7) are used to transform elastic stresses and strains in the loading axes (X-Y-Z) to stresses and strains in the crystal axes (1-2-3). These equations cannot be used if the applied stresses in the loading axes are high enough to cause yielding of the material. A nonlinear anisotropic elastic-plastic finite element analysis will then be required to compute the stresses, $\{\sigma_{123}\}$, and strains, $\{\varepsilon_{123}\}$, in the crystal coordinate system.

U.3 STRESSES AND STRAINS ON OCTAHEDRAL PLANES AND ALONG SLIP DIRECTIONS

Once the stresses, $\{\sigma_{123}\}$, and strains, $\{\varepsilon_{123}\}$, are determined in the crystal coordinate system (using either the above equations or a finite element analysis), then the stresses, $\{\sigma^{oct}\}$, and strains, $\{\varepsilon^{oct}\}$, normal to the four octahedral planes and the resolved shear stresses, $\{\tau^s\}$, and strains, $\{\gamma^s\}$, along the twelve slip directions (see Figure U3) can be computed. The following notation is used for the stresses and strains normal to the four octahedral planes:

$$\{\sigma^{oct}\} = \begin{Bmatrix} \sigma_1^{oct} \\ \sigma_2^{oct} \\ \sigma_3^{oct} \\ \sigma_4^{oct} \end{Bmatrix} \quad \text{and} \quad \{\varepsilon^{oct}\} = \begin{Bmatrix} \varepsilon_1^{oct} \\ \varepsilon_2^{oct} \\ \varepsilon_3^{oct} \\ \varepsilon_4^{oct} \end{Bmatrix} \tag{U8}$$

where, the subscripts, 1, 2, . . . , 4 refer to the four octahedral planes shown in Figure U3. The following notation is used for the resolved shear stresses and strains along the twelve primary slip directions:

$$\{\tau^s\} = \begin{Bmatrix} \tau_1^s \\ \tau_2^s \\ \tau_3^s \\ \tau_4^s \\ \tau_5^s \\ \tau_6^s \\ \tau_7^s \\ \tau_8^s \\ \tau_9^s \\ \tau_{10}^s \\ \tau_{11}^s \\ \tau_{12}^s \end{Bmatrix} \quad \text{and} \quad \{\gamma^s\} = \begin{Bmatrix} \gamma_1^s \\ \gamma_2^s \\ \gamma_3^s \\ \gamma_4^s \\ \gamma_5^s \\ \gamma_6^s \\ \gamma_7^s \\ \gamma_8^s \\ \gamma_9^s \\ \gamma_{10}^s \\ \gamma_{11}^s \\ \gamma_{12}^s \end{Bmatrix} \tag{U9}$$

where, the subscripts, 1, 2, . . . , 12 refer to the twelve primary slip directions shown in Figure U3.

The octahedral stresses, $\{\sigma^{oct}\}$, can be determined using the known stresses, $\{\sigma_{123}\}$, in the crystal coordinate system, by following matrix equation:

$$\{\sigma^{oct}\} = [R]\{\sigma_{123}\} \qquad\qquad\qquad (U10)$$

where, the stress transformation matrix, [R], is given by:

$$[R] = \frac{1}{3}\begin{bmatrix} 1 & 1 & 1 & 2 & 2 & 2 \\ 1 & 1 & 1 & -2 & 2 & -2 \\ 1 & 1 & 1 & 2 & -2 & -2 \\ 1 & 1 & 1 & -2 & -2 & 2 \end{bmatrix} \qquad\qquad (U11)$$

The octahedral strains, $\{\varepsilon^{oct}\}$, can be determined in a similar fashion using the known strains, $\{\varepsilon_{123}\}$, in the crystal coordinate system, by the following matrix equation:

$$\{\varepsilon^{oct}\} = [S]\{\varepsilon_{123}\} \qquad\qquad\qquad (U12)$$

where, the strain transformation matrix, [S], is given by:

$$[S] = \frac{1}{3}\begin{bmatrix} 1 & 1 & 1 & 1 & 1 & 1 \\ 1 & 1 & 1 & -1 & 1 & -1 \\ 1 & 1 & 1 & 1 & -1 & -1 \\ 1 & 1 & 1 & -1 & -1 & 1 \end{bmatrix} \qquad\qquad (U13)$$

The resolved shear stresses along the primary slip directions, $\{\tau^s\}$, can be determined using the known stresses, $\{\sigma_{123}\}$, in the crystal coordinate system, by the following matrix equation:

$$\{\tau^s\} = [T]\{\sigma_{123}\} \qquad\qquad\qquad (U14)$$

where, the stress transformation matrix, [T], is given by:

$$[T] = \frac{1}{\sqrt{6}} \begin{bmatrix} 1 & 0 & -1 & 1 & -1 & 0 \\ -1 & 1 & 0 & 0 & 1 & -1 \\ 0 & -1 & 1 & -1 & 0 & 1 \\ 0 & 1 & -1 & -1 & 0 & 1 \\ 1 & -1 & 0 & 0 & -1 & -1 \\ -1 & 0 & 1 & 1 & 1 & 0 \\ 1 & 0 & -1 & 1 & 1 & 0 \\ -1 & 1 & 0 & 0 & -1 & 1 \\ 0 & -1 & 1 & -1 & 0 & -1 \\ 0 & 1 & -1 & -1 & 0 & -1 \\ 1 & -1 & 0 & 0 & 1 & 1 \\ -1 & 0 & 1 & 1 & -1 & 0 \end{bmatrix} \tag{U15}$$

The resolved shear strains along the primary slip directions, $\{\gamma^s\}$, can be determined in a similar fashion using the known strains, $\{\varepsilon_{123}\}$, in the crystal coordinate system, by the following matrix equation:

$$\{\gamma^s\} = [U]\{\varepsilon_{123}\} \tag{U16}$$

where, the strain transformation matrix, $[U]$, is given by:

$$[U] = \frac{1}{\sqrt{6}} \begin{bmatrix} 2 & 0 & -2 & 1 & -1 & 0 \\ -2 & 2 & 0 & 0 & 1 & -1 \\ 0 & -2 & 2 & -1 & 0 & 1 \\ 0 & 2 & -2 & -1 & 0 & 1 \\ 2 & -2 & 0 & 0 & -1 & -1 \\ -2 & 0 & 2 & 1 & 1 & 0 \\ 2 & 0 & -2 & 1 & 1 & 0 \\ -2 & 2 & 0 & 0 & -1 & 1 \\ 0 & -2 & 2 & -1 & 0 & -1 \\ 0 & 2 & -2 & -1 & 0 & -1 \\ 2 & -2 & 0 & 0 & 1 & 1 \\ -2 & 0 & 2 & 1 & -1 & 0 \end{bmatrix} \tag{U17}$$

APPENDIX V

CRITICAL PLANE MODELS AND SEARCH ALGORITHMS

Six different critical plane models were evaluated in the present study. These were the Findley (FIN), Walls, Fatemi-Socie-Kurath (FSK), Shear stress range (SSR), Chu-Conle-Bonnen (CCB), and McDiarmid (McD) parameters.

V.1   CRITICAL PLANE MODELS

The FIN parameter was calculated using the maximum shear stress amplitude, τ_a, on a 'critical slip direction' and the maximum normal stress, σ_{max}, on the critical slip plane:

$$FIN = \tau_a + k\sigma_{max} \tag{V1}$$

where k is a fitting parameter. In the present study, k = 1 was used for all the calculations of the FIN parameter.

The FSK parameter was calculated using the maximum shear strain amplitude, γ_a, on a 'critical slip direction' and the maximum normal stress, σ_{max}, on the critical slip plane:

$$FSK = \gamma_a \left(1 + k \left(\frac{\sigma_{max}}{\sigma_{yield}} \right) \right) \tag{V2}$$

where σ_{yield}, is the yield strength and k is a fitting parameter. In the present study, k = 1 was used for all the calculations of the FSK parameter.

The Walls parameter was calculated using the maximum shear strain, γ_{max}, on a 'critical slip direction' and the maximum normal strain, ε_{max}, on the critical slip plane:

$$Walls = 50(\gamma_{max} + \varepsilon_{max}) \left(\frac{\pi}{\arctan(\gamma_{max}/\varepsilon_{max}) + \pi/2} \right)^{0.5} \tag{V3}$$

The SSR parameter was calculated using the maximum shear stress range along a 'critical slip direction' during the fatigue cycle. The CCB parameter was calculated as the sum of

two products: (i) the product of the maximum shear strain amplitude, γ_a, along a 'critical slip direction' and the maximum shear stress, τ_{max}, on the critical slip plane; and (ii) the product of the maximum normal strain amplitude, ε_a, along a 'critical slip direction' and the maximum normal stress, σ_{max}, on the critical slip plane:

$$CCB = 2\gamma_a \tau_{max} + \varepsilon_a \sigma_{max} \qquad (V4)$$

The McD parameter was calculated as the sum of the maximum shear stress amplitude, τ_a, along a 'critical slip direction' and the maximum normal stress, σ_{max}, on the critical slip plane:

$$McD = \tau_a + k\sigma_{max} \qquad (V5)$$

where, k, is a curve-fit parameter. In the present study, k = 0.1 was used for all the calculations of the McD parameter. Although the McD parameter looks similar to the FIN parameter, it differs in the critical plane search algorithm as described in the next section.

V.2   CRITICAL PLANE SEARCH ALGORITHMS

The critical plane was determined by first computing each of the critical plane parameters on each of the 12 slip directions throughout the fatigue cycle. The max normal stresses and strains (computed normal to the octahedral plane associated with the slip direction) and the max shear stress and strain amplitudes, on each slip direction, required to compute the different parameters, were determined by scanning through all the computed stresses and strains at all the time steps of the fatigue cycle. The 'critical slip direction' for the FIN, Walls, FSK, SSR and CCB parameters was determined as the slip direction on which the damage parameter was a maximum during the fatigue cycle. For the McD parameter, the 'critical slip direction' was determined as the slip direction along which the shear stress amplitude, τ_a, was a maximum during the fatigue cycle. The McD parameter (Equation. V5) was then determined along this critical slip direction. In all cases, the critical slip plane was the octahedral plane that contained the critical slip direction.

APPENDIX W

DAMAGE PARAMETER ANALYSIS

All the calculations were performed using the following elastic constants, measured along the primary <001> orientations, for PWA 1484 at 1100^oF: E = 15.69 msi, ν = 0.3995, G = 15.93 msi.

Figures W1 through W5 show plots of the calculated damage parameters versus life for all the specimens using the applied cyclic stresses (from Table 4.28, Section 4.3.3.1) and the measured crystal orientations (Table 4.28, Section 4.3.3.1) for each specimen. These figures also include a curve-fit of the form,

$$\text{Damage parameter} = A\,N^{-b} + C\,N^{-d} \qquad\qquad (W1)$$

where the curve-fit parameters, A, b, C, d, were determined by regression. Each figure also shows the curve-fit correlation coefficient, R^2, which was used as a measure of how well the damage parameter correlated the fatigue data for the different specimen orientations. These values of R^2 for the different damage parameters are also included at the bottom of Table 428 of Section 4.3.3.4.

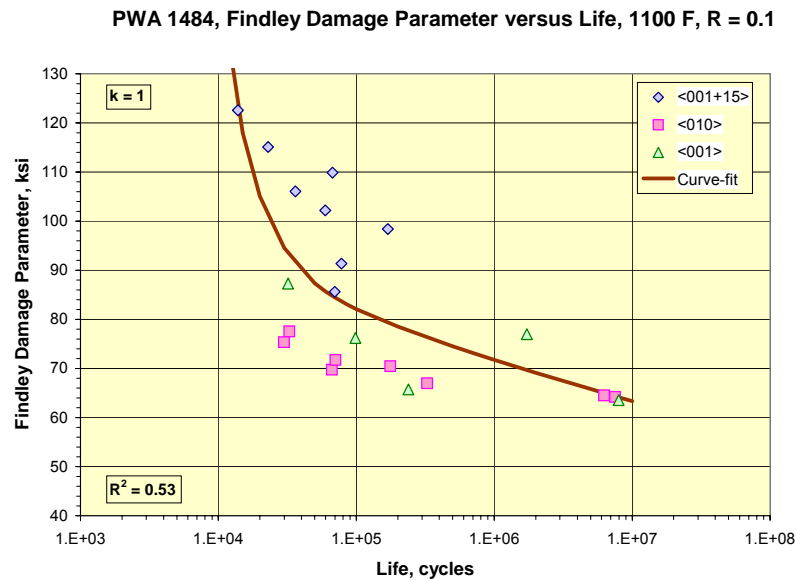

Figure W1. Findley damage parameter versus life for PWA 1484 at 1100^oF and R = 0.1.
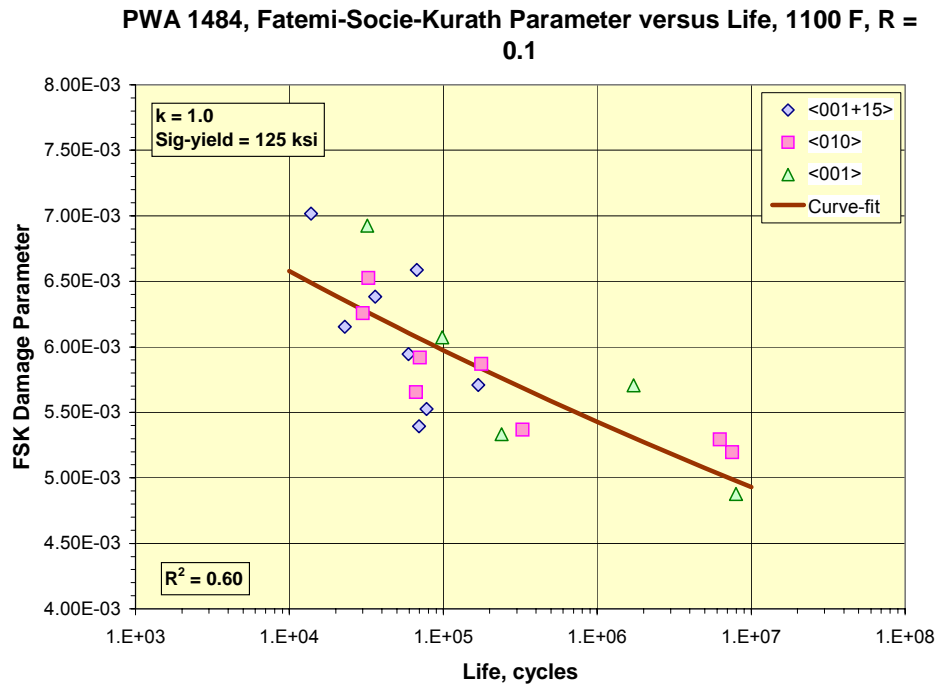
Figure W2. Fatemi-Socie-Kurath parameter versus life, PWA 1484, 1100°F, R = 0.1.
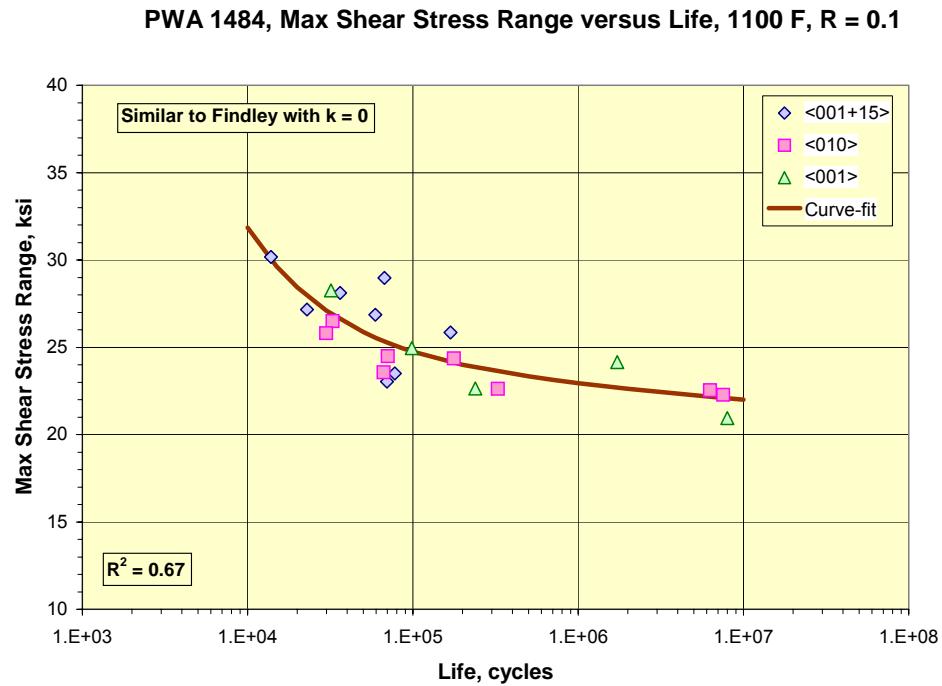

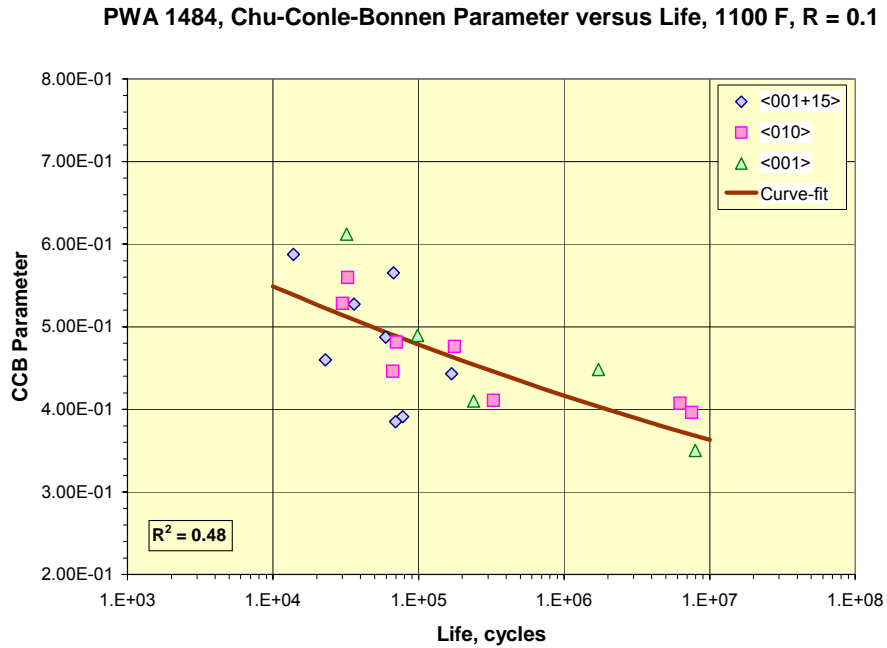Figure W3. Max Shear Stress Range parameter, PWA 1484, 1100°F, R = 0.1.

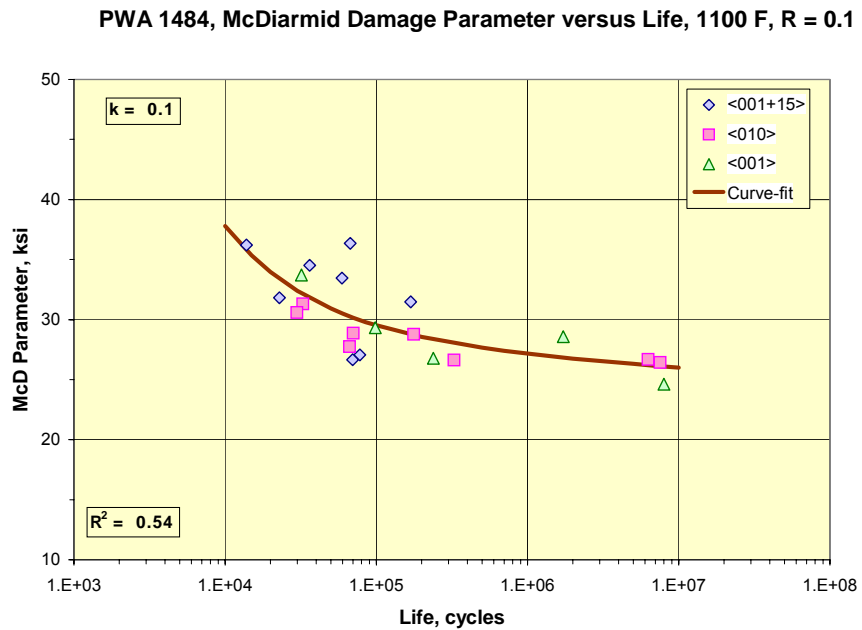Figure W4. Chu-Conle-Bonnen parameter versus life, PWA 1484, 1100°F, R = 0.1.

Figure W5. McDiarmid damage parameter versus life, PWA 1484, 1100°F, R = 0.1.

W-3

From an inspection of the results in Figures W1 through W5, it appears that the SSR, CCB, McD, FSK and the Walls parameters were quite successful in correlating the fatigue data for the different specimen orientations. Considering the variability that is usually associated with single crystal fatigue data, R^2 values around 0.6 are assumed to indicate data correlations that are quite good. The SSR and McD parameters use the shear stress range along the slip directions to determine the critical plane, while the Walls parameter uses the max normal and shear strains together with the mode mixity ratio of the shear and the normal strains on the octahedral planes to determine the critical plane. The FSK damage parameter which uses a combination of the shear strain amplitude (along the slip direction) and the normal stress to the octahedral plane correlated the fatigue data quite well. The CCB damage parameter which uses an energy formulation also performed reasonably well. Both the FIN and McD damage parameters which use a combination of the shear stress amplitude (along the slip direction) and the normal stress to the octahedral plane seemed to be highly dependent on choice of the fitting parameter, k. They were able to correlate the current fatigue data well when $k \cong 0$ was used. In this case these parameters were similar to the SSR parameter.

APPENDIX X

VALIDATION OF THE "ROBUST ATTACHMENT DESIGN INTEGRATING CONTACT AND LIFING" (RADICAL) PROCESS

X.1   INTRODUCTION

This appendix presents an addendum to work performed under the BAA contract, described in the basic report (Section 4.5.1), where efforts were focused upon the development of advanced stress and life prediction techniques for bladed attachments under HCF loading, or combined HCF/LCF loading. The prediction of stress in blade attachment regions centered around an "edge-of-contact" (EOC) approach in which region stresses are known to peak, and are assumed to be a strong driver in certain attachment cracking scenarios. In the initial study, determination of the EOC stress was performed using a code known as CAPRI (for contact between similar materials) and a code known as CAFDEM (for contact between dissimilar materials). As described in Section 4.5.2, P&W evaluated the CAPRI code against laboratory Single Tooth Fir Tree (STFT) data with reasonable success. However, translation of this into an engine environment in which attachment stresses are driven by HCF modal response in the airfoil required the development of an additional analysis process. This process, "Robust Attachment Design Integrating Contact and Lifing" (RADICAL) involves a several step process to translate the effect of airfoil modal excitation into attachment HCF stresses. Under the current effort, the RADICAL process has been exercised against several field and laboratory test cases, for which there is attachment EOC cracking experience. The objective is to understand the robustness of the process as well as to calibrate it. In Section X.2, the steps of the RADICAL process are reviewed. The subsequent sections of this appendix present a description of the hardware on which the calibration/validation is performed, the analysis assumptions and process, and the results of the analyses.

X.2   ANALYSIS METHODOLOGY—RADICAL PROCESS

The RADICAL process consists of 7-steps as illustrated in Figure X.1 and listed below:

Step 1:   Run a 3D steady-state contact analysis with friction (ANSYS)

Step 2:   Identify measured or targeted modes and amplitudes (experimental data)

Step 3:   Perform a pre-stressed 3D modal analysis (ANSYS)

Step 4:   Scale modal vibratory forces based on known experimental data (ANSYS)

Step 5:   Perform a 3D quasi-static vibratory contact analysis with friction (ANSYS)

Step 6:   Extract pressure plane normal loads, tangential loads, and moments (ANSYS)

Step 7:   Run MATLAB based lifing code with loads from step 6 (PW/CAPRI or CAFDEM)

A flowchart that illustrates the ANSYS methodology used to obtain the vibratory loads for the quasi-static vibratory contact analysis is presented as Figure X.2. For a more detailed explanation of each step listed above, see Section X.5.

X.3   DESCRIPTION OF CALIBRATION HARDWARE

X.3.1   Single Crystal

A brief overview of each blade's experience is provided below.

X.3.1.1   Blade A (PWA 1484)

Fir tree edge-of-contact cracking, subsurface initiated.

X.3.1.2   Blade B (PWA 1480)

Experience indicates shallow, fretting induced cracking at edge of contact on the upper serration only (see Figure X.3). However, this cracking does not continue to propagate into the blade. Cracking is due to a low level of vibration, which has been confirmed with strain gage data.

X.3.1.3   Blade C (PWA 1422)

A flight test engine fractured one blade in the attachment area. Loss of the primary blade again resulted in overstress of all remaining blades. Fracture of the initial blade was caused by a crack that initiated just above the bearing surface on the top tooth.

Additional engines fractured one blade below the platform; the remaining blades were all fractured in overstress. HCF initiated cracks propagated by continued operation with elevated dynamic stresses. This resulted in rupture of the primary blades.

X.4   ANALYSIS ASSUMPTIONS

Common assumptions for all three turbine stages are:

1.) ANSYS version 7.0 used for all modal and contact analyses.

2.) A pre-stressed modal analysis is used to obtain vibratory loads for contact analyses.

3.) A cyclic symmetry analysis was not performed since the Stiffwise Bending mode is a blade mode and not a wheel-blade mode at a specific nodal diameter.

4.) Two quasi-static vibratory contact analyses were performed for each turbine stage, with coefficient of friction equal to 0.3 and 0.7 (6-total runs).

5.) Frictionless contact analyses are NOT path dependent and do not require ANSYS FEA loads to be applied in the exact order in which they are applied in actual hardware. Since all analyses detailed in this report contain friction, the non-linear models are path dependent and the order in which loads are applied does matter. However, the exact transient load history for each turbine stage was not available for this RADICAL validation study. Therefore, the static contact analyses performed do not take into account:

   a. Thermal transient gradient differences as a function of engine speed

   b. Gas pressure differences on the Blade as a function of engine speed

c. Frictional variations due to humidity, corrosion, etc as a function of engine speed or cycles

d. Differences in static and dynamic coefficient of friction as a function of engine speed

e. Variations in Disk preload boundary conditions (due to unmodeled adjacent disk segments) as a function of engine speed.

X.4.1   Blade A

1.)   0 RPM engine speed (shaker test)

2.)   Shaker Block and Blade have uniform elevated temperature

3.)   Materials modeled (properties provided in ANSYS database format provided by Pratt & Whitney):

- SHAKER BLOCK—similar to INCO 718 (AMS5663) and assumed to be identical to the Blade's corresponding wheel (not modeled)
- BLADE – PWA1484

4.)   No gas load applied to Blade since none exists in shaker tests

5.)   Three jack screws press against the bottom of the Fir Tree. Each jackscrew provides 400 in-lbf of torque. The normal load provided by each jack screw is:

$N = \tau/Kd = 400$ in-lbf$/ (0.2 \times 0.625$ in$) = 3200$ lbf/jack screw

where: $N =$ jack screw normal load

$\tau =$ jack screw torque

$K =$ torque factor $= 0.2$ for zinc-plated bolts or when condition is unknown[1]

$d =$ major diameter of jack screw

The total jackscrew load (3 screws x 3200 lbf = 9600 lbf) was applied to the bottom-most plane of the Fir Tree as a 10,256 psi pressure (=9600 lbf/0.936 in^2).

6.) The first bending vibratory mode of the blade is excited.

7.) All holes have been removed from the Block for modeling efficiency.

8.) The Load Bar and Push Block were not modeled as shown in the Shaker Block assembly of Pratt & Whitney Detailed Drawing #BB1113.

9.) The Block is constrained as shown in Figure X.4. A strap holds the Block to a Shaker Table.

10.) Friction is not turned on until 10% of the jackscrew pressure is applied.

X.4.2   Blade B (PWA 1480)

1.) 60-blades per stage.

2.) 10204 RPM engine speed (full speed).

3.) Non-uniform temperature distribution used as shown in Figure X.7 provided by Pratt & Whitney.

4.) Materials modeled (properties provided in ANSYS database format provided by Pratt & Whitney):

- BLADE—P1480
- DISK—INCO-718

5.) Gas Pressures are shown in Figure X.8.

6.) Preloads due to adjacent wheel segments are applied as nodal forces and shown in Figure X.9.

7.) The first bending vibratory mode of the blade is excited.

8.) An averaging constraint equation ties the Disk to the Fir Tree in the Axial DOF only. There are two averaging constraint equations as shown in Figures X.9 and X.10. The constraint equations ensure that the FEA nodes of the Disk move by the same average amount as the nodes on the

Fir Tree. These constraints exist due to the presence of unmodeled geometry that locks these planes in place. The Disk and Blade planes constrained are allowed to rotate and deform independently—it's just the average y-displacement that is constrained. The constraint equation works as follows:

$$\overline{U}y_{disk} = \overline{U}y_{blade}$$

$$0 = \overline{U}y_{disk} - \overline{U}y_{blade} = \sum_{i=1}^{i_{max}} \frac{uy_{disk\,i}}{T_{disk}} - \sum_{j=1}^{j_{max}} \frac{uy_{blade\,j}}{T_{blade}}$$

Where, $\overline{U}y$ = Average displacement in y-direction

uy_i = y-displacement for node i

T = total number of nodes

A macro automatically generates these constraint equations. The bending (first flexure) vibratory mode excites the blade.

9.) Friction is not turned on until 25% of full speed is reached when $\mu = 0.3$ or 0.7, respectively. Friction is not turned on sooner due to model stability problem when $\mu = 0.3$ only.

10.) The two symmetry planes of the Disk's solid elements are coupled (Figure X.10) in all 3-DOFs (1 couple per node pair) to ensure the planes behave in the exact same manner from a deflection standpoint. If two adjacent blade segments were modeled, the interface between these two segments would consist of a shared plane (e.g. the pressure side of one Disk is tied to the suction side of the adjacent Disk). Since two Disks are not modeled, the couples serve this purpose of ensuring shared planes behave in the same manner.

11.) Due to the combination of 2D axisymmetric (lower wheel) and 3D solid elements (upper wheel region with slot and blade) in ANSYS, the elastic

modulus, conductivity, density, and pressures of the solid elements are increased by 60X (the blade count). This is because, in ANSYS, loads are applied to axisymmetric models on a per circle basis. Figure X.10 shows how to attach the solid elements to the axisymmetric elements.

X.4.3   Blade C

1.) 8240 RPM engine speed (80% full speed). This is the speed in which resonance occurs.

2.) A Stiffwise Bending vibratory mode excites the blade at 412 Hz.

3.) Non-uniform temperature distribution used as shown in Figure X.11 provided by Pratt & Whitney.

4.) Materials modeled (properties provided in ANSYS database format provided by Pratt & Whitney):

- BLADE—PWA 1422
- DISK—PWA 1074

5.) Gas Pressures are shown in Figure X.12. The real gas pressure gradient was not available, but the gas pressure resultant forces were available in the axial and transverse directions. The blade was divided into two arbitrary sections (an aft and forward half) and the pressures in these two regions were adjusted until the given axial and transverse loads were obtained. This non-real pressure distribution gives the correct gas pressure induced Blade forces, but does not necessarily capture the correct gas pressure induced moments. Gas pressures are not applied until 25% engine speed is obtained (convergence instability arises if pressure is applied sooner).

6.) No preload was applied to the Disk boundaries in contact with adjacent, unmodeled Disk segments. This data was not available during modeling.

7.) An averaging constraint equation ties the Fir Tree hook to the Disk axially. A second averaging constraint equation ties opposite sides of the

Shroud together in the normal direction (where adjacent Shrouds would interface). See assumption #7 for the PW4000 Blade for more details about the averaging constraint equations. Figure X.13 illustrates constraint equation locations.

8.)   Friction is applied from the start (0% engine speed) of the analyses.

9.)   The two symmetry planes of the Disk are coupled.

X.5   ANALYSIS PROCESS

In Section X.2, the Analysis Methodology indicates that there are 7-steps to the RADICAL process. A more detailed explanation of each of these steps follows.

X.5.1   STEP 1: Steady-State Contact Analysis with Friction (ANSYS)

Assumptions, boundary conditions, and loads used for this step are detailed in Section X.4. Non-linear geometry is turned on to allow for large displacements, which may or may not (pending sufficient load) allow the pressure planes of the Fir Tree to conform in a more realistic manner to the broach slot of the Disk.

Node and element count data for each turbine stage and related figures are detailed in Table X.1. To model contact, target elements (TARGE170) were applied to the Disk's pressure planes and contact elements (CONTA173/174) were applied to the Fir Tree's pressure planes. The presence of internal Blade cavities is also indicated in Table X.1.

Table X.1. Mesh, Contact, and Internal Cavity Details

MODEL	NODE COUNT	ELEMENT COUNT	TARGET/CONTACT ELEMENTS	INTERNAL BLADE CAVITIES	MODEL DETAILS
Blade A	140415	100491	TARGE170/CONTA173	yes	Figures X.1-X.3
Blade B	181857	210892	TARGE170/CONTA174*	yes	Figures X.4-X.7
Blade C	110315	77358	TARGE170/CONTA174*	no	Figures X.10-X.12

* CONTA174s are the same as CONTA173 except with midside node capability.

X.5.2   **STEP 2: Identify Experimental Modes and Amplitudes of Interest**

For each turbine stage, Pratt and Whitney has identified modes of interest and their stimuli as shown in Table X.2 and listed in the assumptions of Section X.4. The amplitude of the response and the means used to measure them are also listed in Table X.2.

Table X.2. Stimuli, Excited Modes, and Experimental Amplitudes

MODEL	Stimuli Frequency (hz)	Nodal Diameter	Excited Blade Mode	Strain Gauge, Stress, or NSMS Probe Instrument Data	Instrument Amplitude
Blade A		0	1st Bending	Strain Gauge #6[4]	0.001259 in/in
Blade B		0	1st Bending	Radial Stress	4.0 ksi
Blade C	412[1]	0	Stiffwise Bending (SWB)	NSMS Probe hoop deflection at Blade's TE, 88% span[2]	0.010625[3] in

[1] $f = \omega E/(60\ \text{sec/min})$, where f = stimuli frequency (hz), ω = engine speed (RPM), E = excitation (1/rev)

[2] Page 55 and D1 of reference 2 (NSMS is Non-interference Stress Measurement System)

[3] Page 37 of reference 2

[4] Located 0.82" from top of attachment's platform on PS leading Edge

X.5.3   **STEP 3: Pre-Stressed Modal Analysis (ANSYS)**

A static analysis is performed before the modal analysis to include the thermal load, gas path pressure, and spin loading pre-stressing effects on the stiffness matrix used in the modal analyses. The Block Lanczos equation solver was used to extract the frequencies of interest.

X.5.4   **STEP 4: Scale Vibratory Forces Based on Known Experimental Data (ANSYS)**

Vibratory loads obtained from the modal analysis (step 3) are scaled and applied as nodal forces to the quasi-static contact analysis (step 5) using an ANSYS macro. See Figure X.2 for a graphical illustration of this process.

X.5.5   **STEP 5: 3D Quasi-Static Vibratory Contact Analysis with Friction (ANSYS)**

Loads in the contact analysis are ramped in a saw-tooth manner as shown in Figure X.14. The assembly or idle start condition (1) is ramped to the steady-state condition (2). After steady state is reached, the vibratory load is applied to the blade in one direction (3), and then in the reverse direction (4). Friction loads are then "shaken out" by repeating the forward (5) and reverse (6) application of the vibratory load. Each ramp between these 6 load steps consists of 5 sub-steps (a minimum of 30 sub-steps in total, depending on model stability). Large deflections are allowed if the loads are significant enough.

Six (6) load-steps are used for Blade A and Blade C. 7 load-steps are used for Blade B to assist model stability since axisymmetric elements are used in this model only (i.e. there's more load than in the other blades cases). The extra load step in Blade B is used to get the model to 50% engine speed during the initial ramp up to steady-state.

X.5.6   **STEP 6: Extract Pressure Plane Contact Loads (ANSYS)**

An ANSYS macro extracts normal, tangential, and moment loads from the Fir Tree pressure planes. These loads are used as input into PW/CAPRI or CAFDEM (step 7). The macro radlx.mac converts the 3D loads of ANSYS to 2D loads as used in step 7.

To use the macro radlx.mac, resume from a database that has the contact elements, enter the post1 processor in ANSYS, read in the results (*RST file), and issue the following command for each contact surface separately:

radlx,'diskcm','bladecm',drad,brad,gccs,nsec,tol

'diskcm' =   Disk Contact Side Component Name (in single quotes) or Interface Number

'bladecm' = Blade Side Component Name (in single quotes)

drad =   Radius on Disk Side

brad =   Radius on Blade Side

gccs =   Global cylindrical coordinate system number (0,1: Z=axial, 5:Y=Axial, 6:X=Axial)

nsec =   Number of Sectors (default = 1)

tol =   Tolerance (default = 0.001)

Create a component of blade side (bladecm) and disk side (diskcm) surfaces for each contact face. These components can be nodes, surface elements, or areas. Values for "drad" and "brad" are shown in Figure X.15. The "gccs" value is used to indicate which global cylindrical coordinate system direction in ANSYS is parallel to the engine axial centerline. "Nsec" equals 1 for XTE67 and F100, but equals 60 (blade count) for PW4000 since axisymmetric elements mean all sectors are to be modeled. The macro will generate a file(*.cload) for each contact face (e.g. 4-files created for F100 since it has 2-pressure side contact surfaces and 2-suction side contact surfaces).

X.5.7 STEP 7: Calculate Stress Data from PW/CAPRI or CAFDEM to Determine Life

CAFDEM (Contact Analysis For Dissimilar Elastic Materials) and PW/CAPRI (for similar materials) are Purdue University written MATLAB codes. These codes extract more realistic contact surface stresses and strains than a <u>coarsely</u> meshed ANSYS model could. Even though a <u>finely</u> meshed ANSYS model could perform the same task, the RAM, disk space, and time requirements required of ANSYS make PW/CAPRI and CAFDEM the software of choice for modeling speed.

PW/CAPRI and CAFDEM treat each 2D-slice (see Figure X.16) of the ANSYS model's pressure planes as 2D models with a 1" (per unit width) thickness.

X.6 RESULTS OF ANALYSES

Table X.3 lists the results of the pre-stressed modal analyses. The percent margin to the excitation is also listed in Table X.3.

Table X.3. Natural Frequencies and Margins to Excitations

Model	Excitation Frequency (Hz)	Mode of Interest	Mode of Interest ANSYS Frequency (Hz)	% Margin from Excitation to Mode of Interest
Blade A		1st Bending	601	
Blade B		1st Bending	1033	
Blade C	412	SWB	472	14.6

The contact surface normal stresses are graphed in Section X.11 in the following two ways:

    1.) Normal load/unit depth vs. load step

    2.) Normal load/unit depth vs. location along pressure plane

The term "unit depth" refers to the 2D-slice width (see Figure X.16) in the direction parallel to the pressure planes (and not parallel to the engine centerline or global axial direction).

Data for all pressure planes are not provided for Blade B only. For Blade B, only the upper most pressures planes (2 of 6) are graphed since the stresses are known to be the largest at these planes based on experimental data. Table X.4 summarizes the graphical data shown in Section X.11.

Table X.4. Pressure Plane Normal Load Graphical Data Summary

Model	Coef. of Friction, μ	Pressure Plane Location*	Figure # load vs load step	Figure # load vs location
Blade A	0.3	PS	X.17	X.33
		SS	X.18	X.34
	0.7	PS	X.19	X.35
		SS	X.20	X.36
Blade B	0.3	PS, upper tooth	X.21	X.37
		SS, upper tooth	X.22	X.38
	0.7	PS, upper tooth	X.23	X.39
		SS, upper tooth	X.24	X.40
Blade C	0.3	PS, upper tooth	X.25	X.41
		SS, upper tooth	X.26	X.42
		PS, lower tooth	X.27	X.43
		SS, lower tooth	X.28	X.44
	0.7	PS, upper tooth	X.29	X.45
		SS, upper tooth	X.30	X.46
		PS, lower tooth	X.31	X.47
		SS, lower tooth	X.32	X.48

* PS = Pressure Side, SS = Suction Side

    The lower tooth is closer to the engine centerline than the upper tooth

In several of the load vs. location graphs, the normal stresses drastically drop off at the ends of the pressure planes (e.g. Figure X.41 for Blade C). This is because in

several cases, the Blade attachment's pressure planes extend beyond the axial width of the Disk's pressure planes.

Lifing data based on stress output from CAFDEM is not available since the output files (*.cload) from the ANSYS contact analyses have not been input into the CAFDEM code to date.
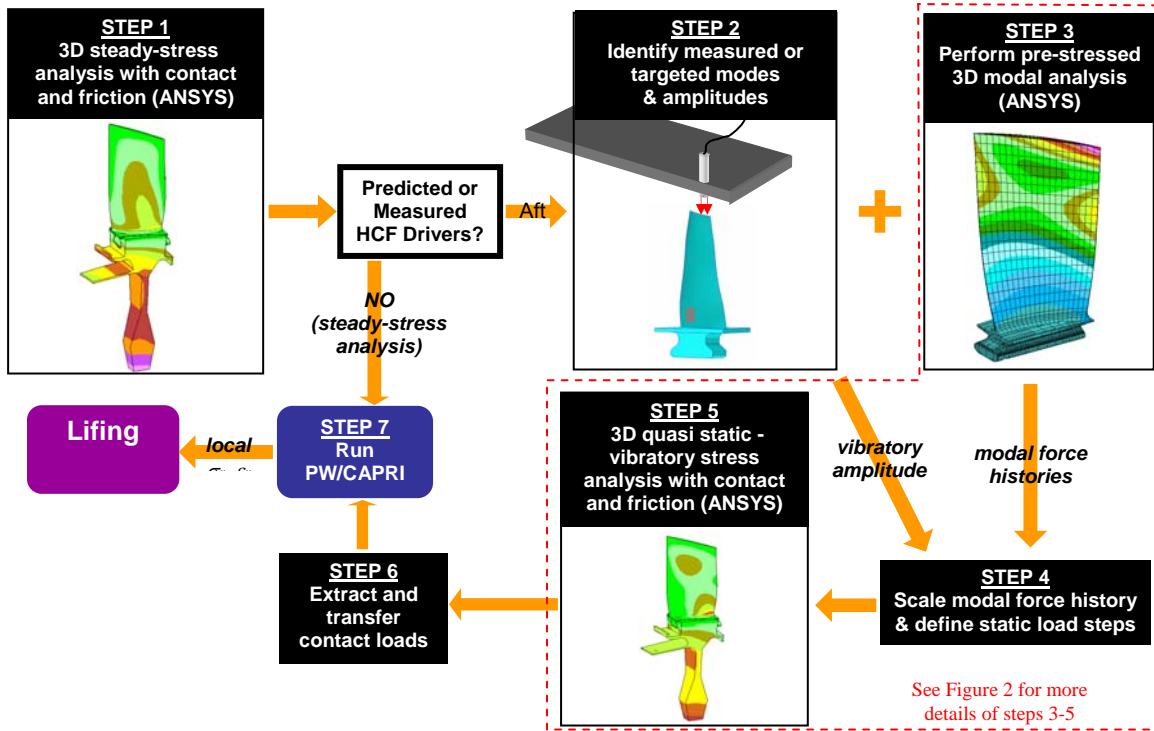
Figure X.1. Robust Attachment Design Integrating Contact And Lifing (RADICAL)
Process.

The following flowchart illustrates the ANSYS methodology used to obtain the vibratory loads
for the quasi-static vibratory contact analysis:
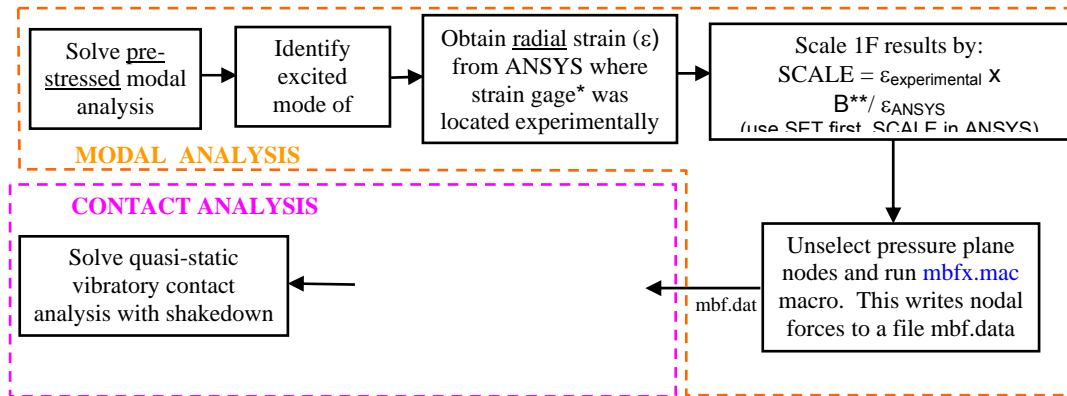
* NSMS probe hoop deflection data or radial stresses were substituted for strain for F100 and PW4000, respectively (see Table 2).
** B = 1 for XTE67 Stage 3 bench test and PW-F100-229 4th Stage Blade
    B = 60 (blade count) for PW4000 Stage 1 since modal analysis was solved with actual material properties, but for the
    contact analysis, axisymmetric elements are used with loads based per unit circle, rather than per unit blade (where the
    blade consists of solid elements).

Figure X.2. Obtaining vibratory loads.
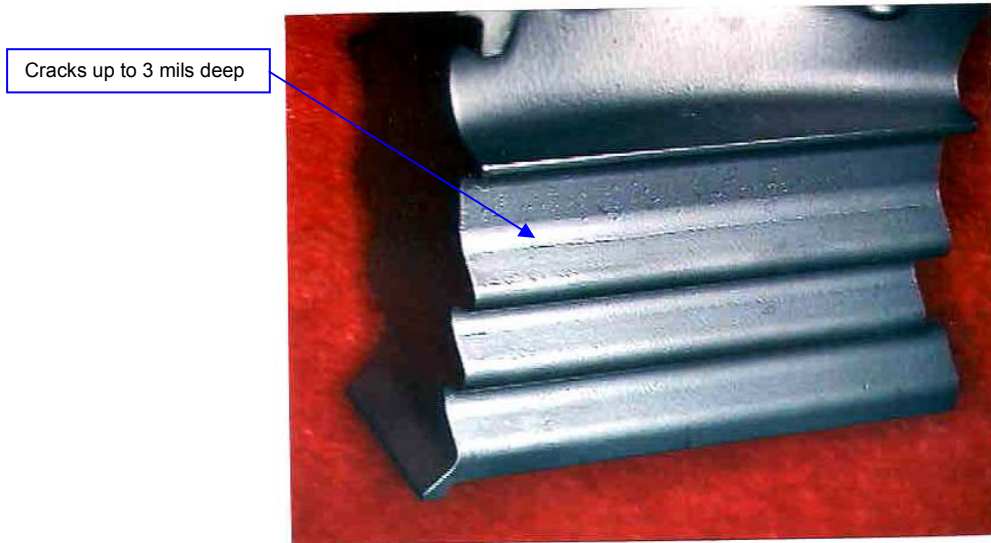
Color photograph of Concave side of blade root
showing pitting along entire length of top serration
and intermittent pitting along middle serration

Figure X.3. Blade B pitting pressure side upper serration.

A strap around the Block holds the Block-Blade assembly firmly to the
Shaker Table. Non-zero strap displacements are applied to this
surface to correspond to the Block's thermal expansion:
$Uz = L\alpha\Delta T = 3.75$ in $(8.8 \times 10^{-6}$ 1/F$)$(Max Temp – 70 F) = 0.05379"$

0.241"
0.482"

Uz=0
(plane)

Shaker
Table

Uy=0
(edge)

Location and width of Strap is not based on actual
measurements (exact dimensions unknown)
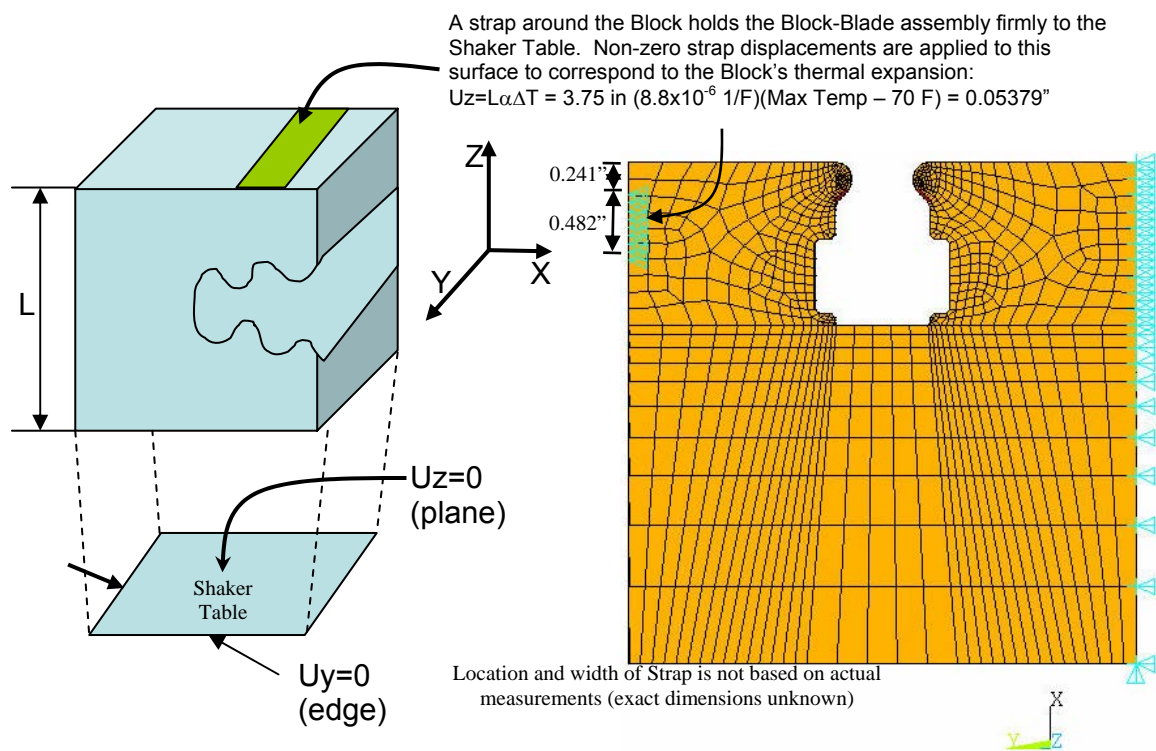
Figure X.4. Blade A block displacement constraints.
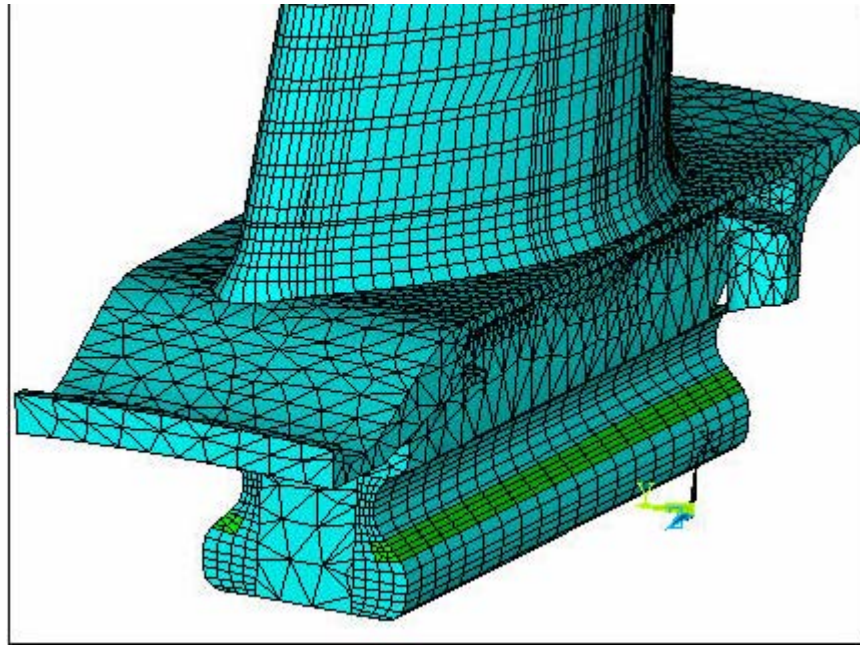
Figure X.5. Blade A mesh.
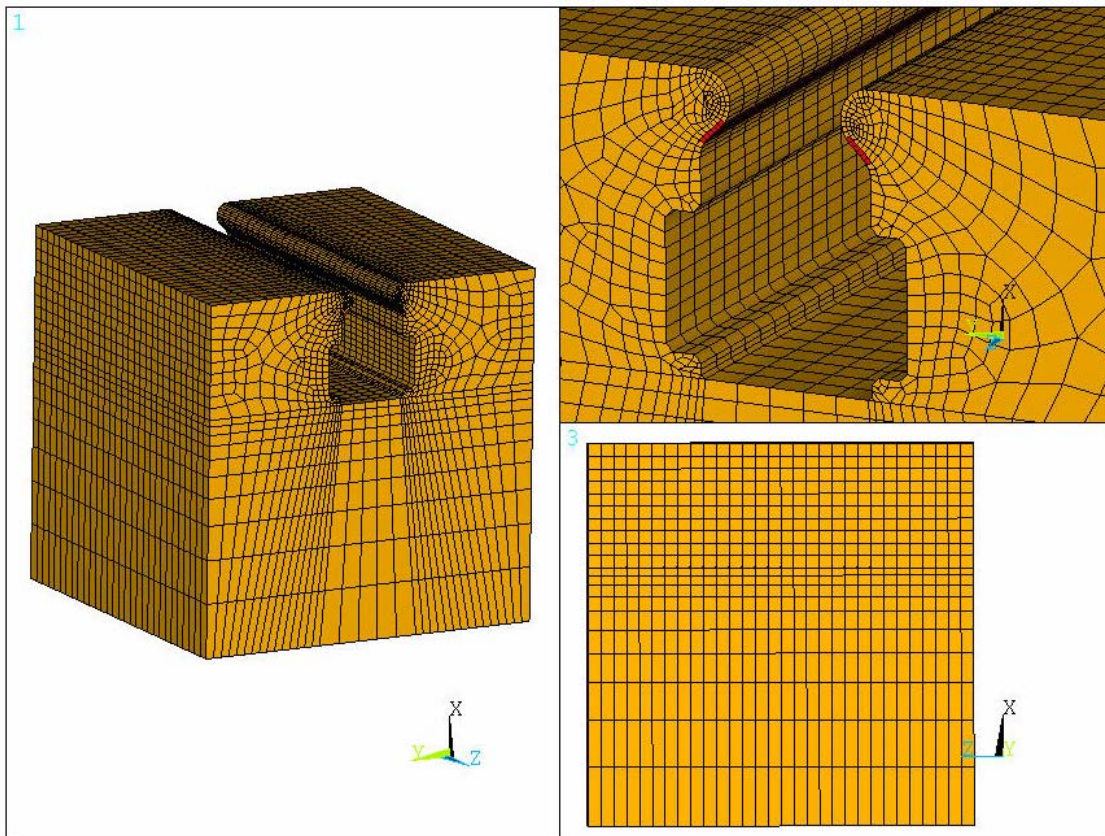
Figure X.6. Blade A shaker block mesh.
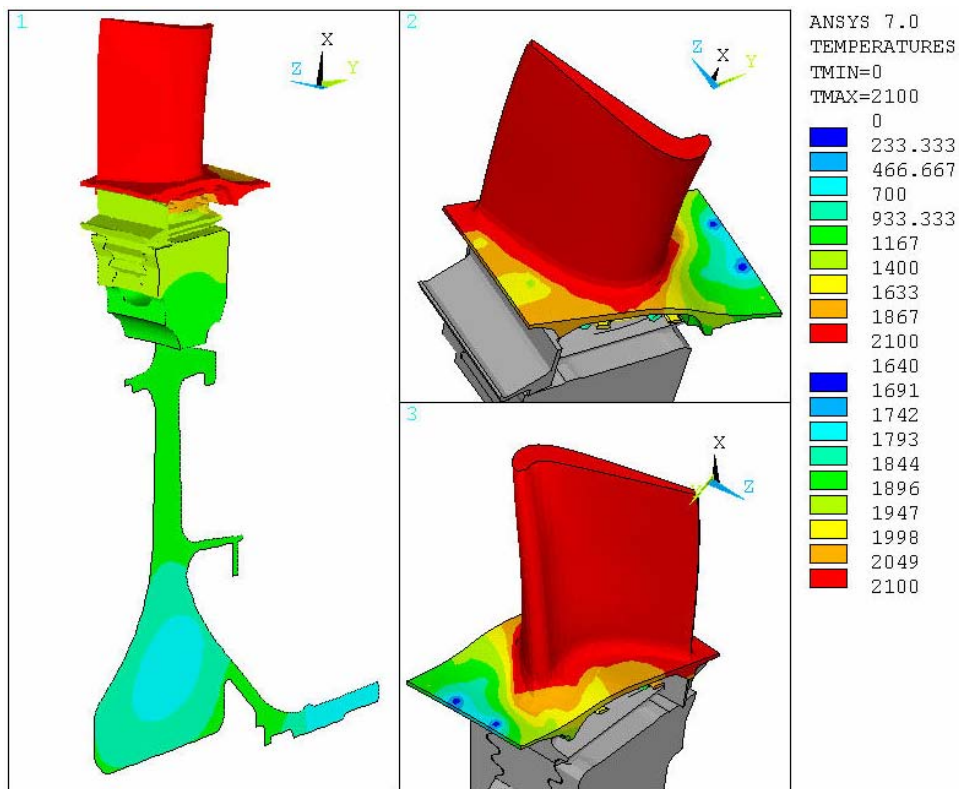
Figure X.7. Blade B temperature distribution.

NOTE: Pressures were not applied to the Disk (not shown)

The pressure magnitudes are so large due to the combination of the axisymmetric 2D elements with the 3D solid elements. The solid elements' density, modulus, and conductivity are scaled by the number of blades. Therefore the pressure loads are also scaled by the same blade count.

Figure X.8. Blade B pressures.

Suction Side:
Total Fx = 52,783 lbf
Total Fy = -44 lbf
Total Fz = 330 lbf

Constraint equations tie dissimilar meshes
together that make up two parts of the Fur

Pressure Side:
Total Fx = 101,744 lbf
Total Fy = 53 lbf
Total Fz = 1,199 lbf

Total Fx =
198,819
lbf

Total Fx = 278,140 lbf
Fy = 12,211 lbf

KEY:
△ Zero-displacement
   constraints
△ Constraint equations
▲ Nodal forces

Two averaging
constraint
equations tie the
Disk to the Fir Tree

Couples (not shown)
tie the two symmetry
planes of the solid
wheel elements
together.

Figure X.9. Blade B constraints and preloads.

Nodes at the 2D-to-3D element
interface are coupled together in
the radial (x-direction) and axial (y-
direction) DOFs only. Hoop DOFs
of the solid elements, that do not
connect directly to the 2D
elements, have zero-displacement
constraints to prevent Solid
element rigid body motion.

Axisymmetric elements
shown in orange, solid
elements shown in blue.

KEY:
△ Zero-displacement
   constraints
△ Constraint equations

pressu
re side

suctio
n side

Axisymmetric elements do not require couples in the

Figure X.10.   Blade B coupling and interfacing of solid elements with axisymmetric
elements.

X-18
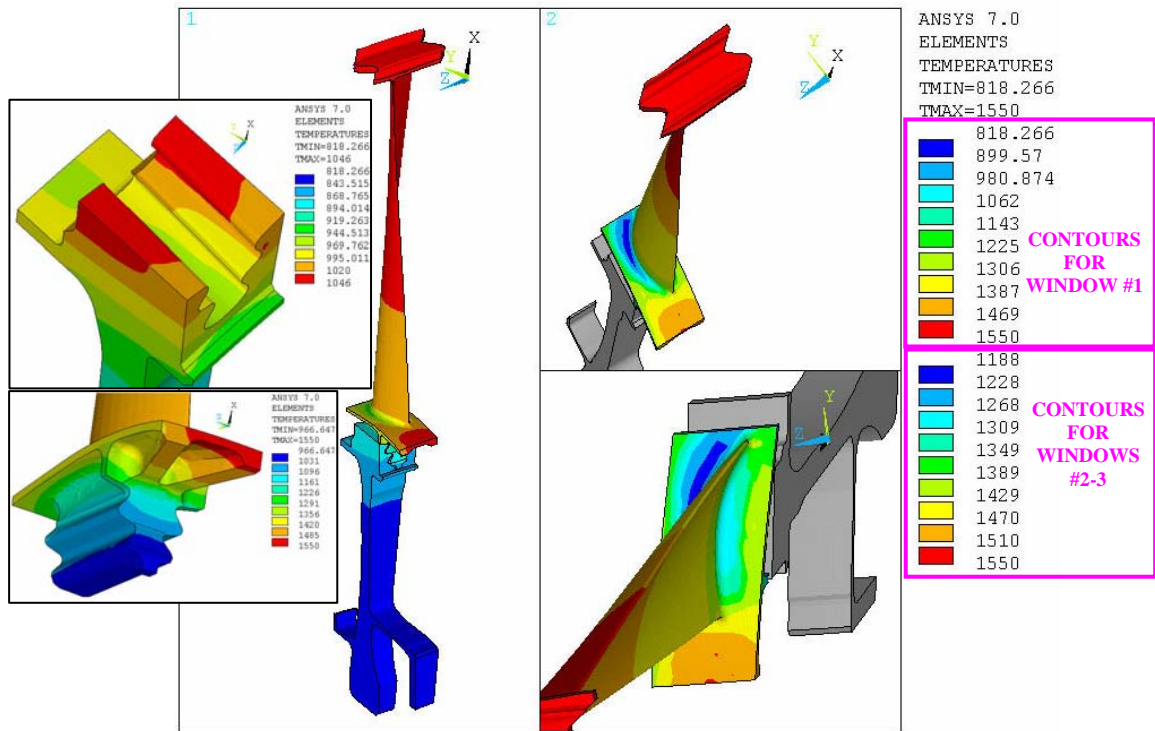
Figure X.11. Blade C temperature distribution.

NOTE: Resultant pressures applied to airfoil only
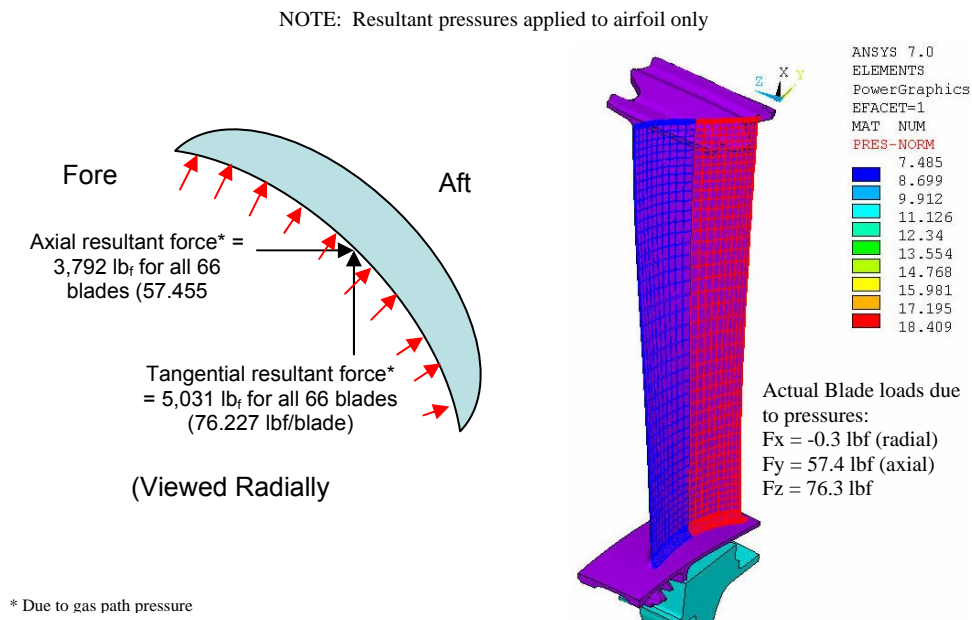
Figure X.12. Blade C pressures.

KEY:
△ Zero-displacement constraints

Preloads on the Disk were not available for modeling and therefore were not included Couples (not shown) tie the two symmetry planes of the solid wheel elements together.

Averaging constraint equation ties mid-sections of Shroud in normal direction. This is the only region where adjacent Shrouds touch.

All nodes constrained axially to simulate interface with adjacent Disk segment and to prevent rotation of the entire model about the global z-axis

Averaging constraint equations ties the Disk to the Fur Tree hook axially

A single line of nodes are constrained tangentially at two locations to prevent rigid body motion (the symmetry plane couples of the Disk do not accomplish this alone).

Figure X.13. Blade C mesh and constraints.

Figure X.14. Quasi-Static contact analysis loading.

X-20

Figure X.15. Fir tree and disk teeth geometry.

Tooth #	Blade Radius, Rb	Disk radius, Rd
1	0.085	0.073
2	0.069	0.063
3	0.063	0.078

- For each slice (shown in red), extract normal (P), tangential (Q), and moment (M) nodal loads at load step(s) of interest using ANSYS macro radlx.mac.

- Determine P, Q and M ("2D" loads/unit depth) over each slice and pass to PW/CAPRI or CAFDEM in a neutral file.

- Conduct analytical contact analysis on each slice to determine near-surface attachment stress field.

Figure X.16.   Pressure plane load conversion from 3D (ANSYS) to 2D (PW/CAPRI or CAFDEM).
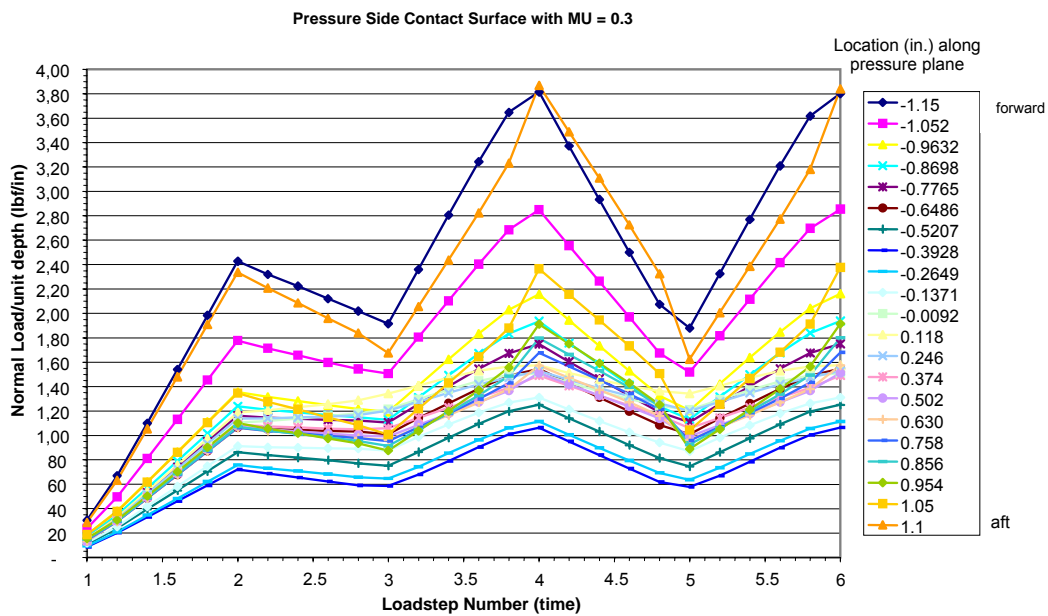
Figure X.17. Blade A, μ = 0.3, pressure side.
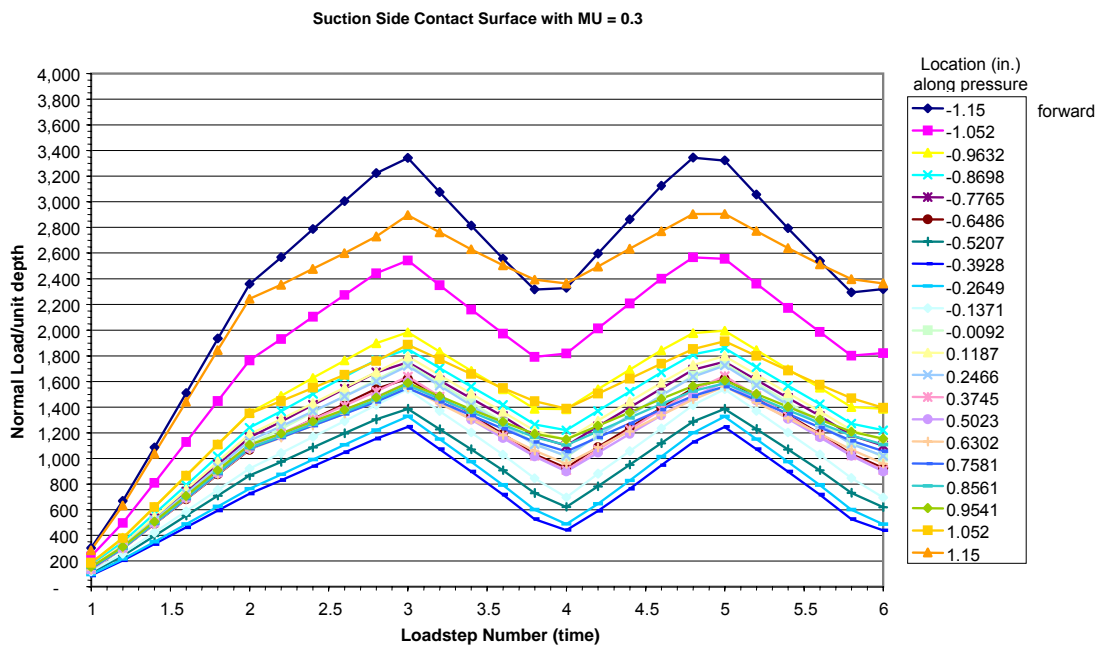
Figure X.18. Blade A, μ = 0.3, suction side.

Pressure Side Contact Surface with MU = 0.7

Figure X.19. Blade A, μ = 0.7, pressure side.

Suction Side Contact Surface with MU = 0.7
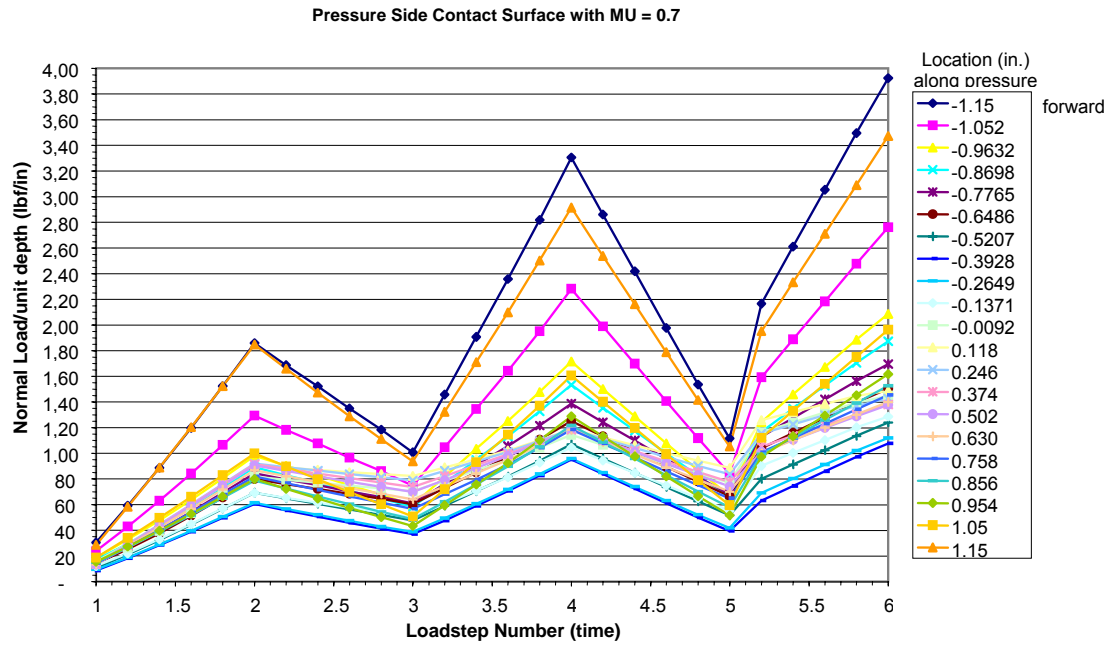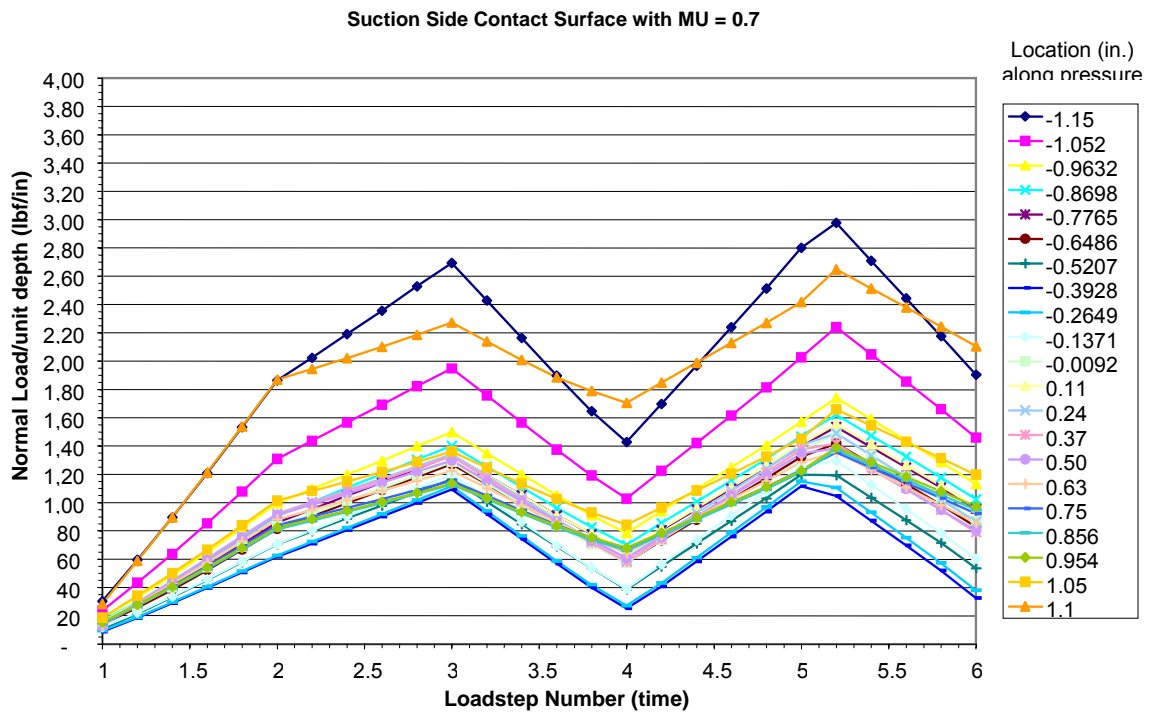
Figure X.20. Blade A, μ = 0.7, suction side.
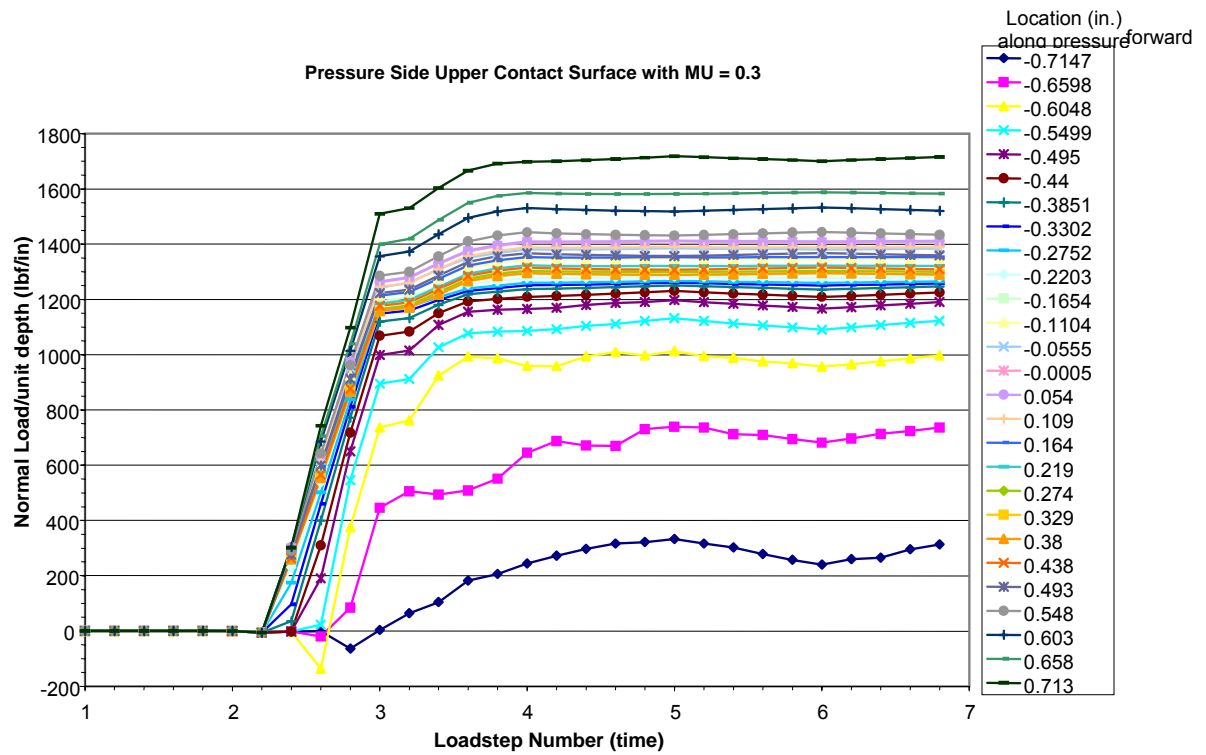
Figure X.21. Blade B, μ = 0.3, pressure side, upper tooth.
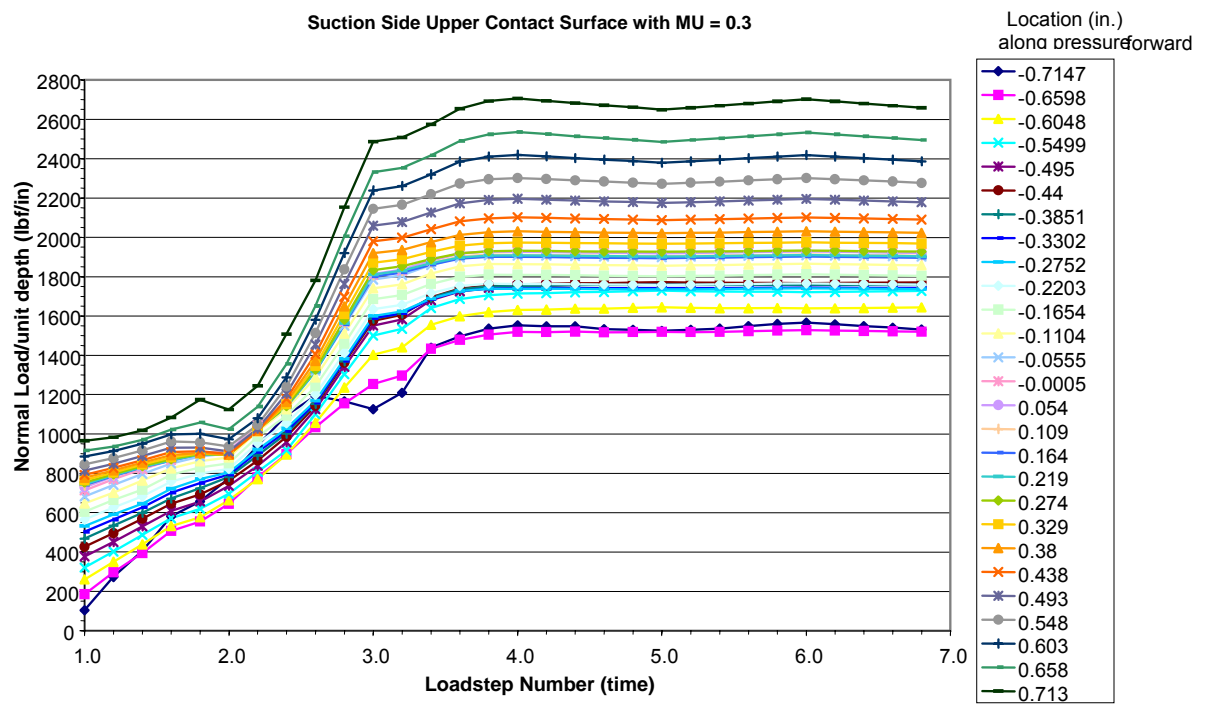
Figure X.22. Blade B, μ = 0.3, suction side, upper tooth.
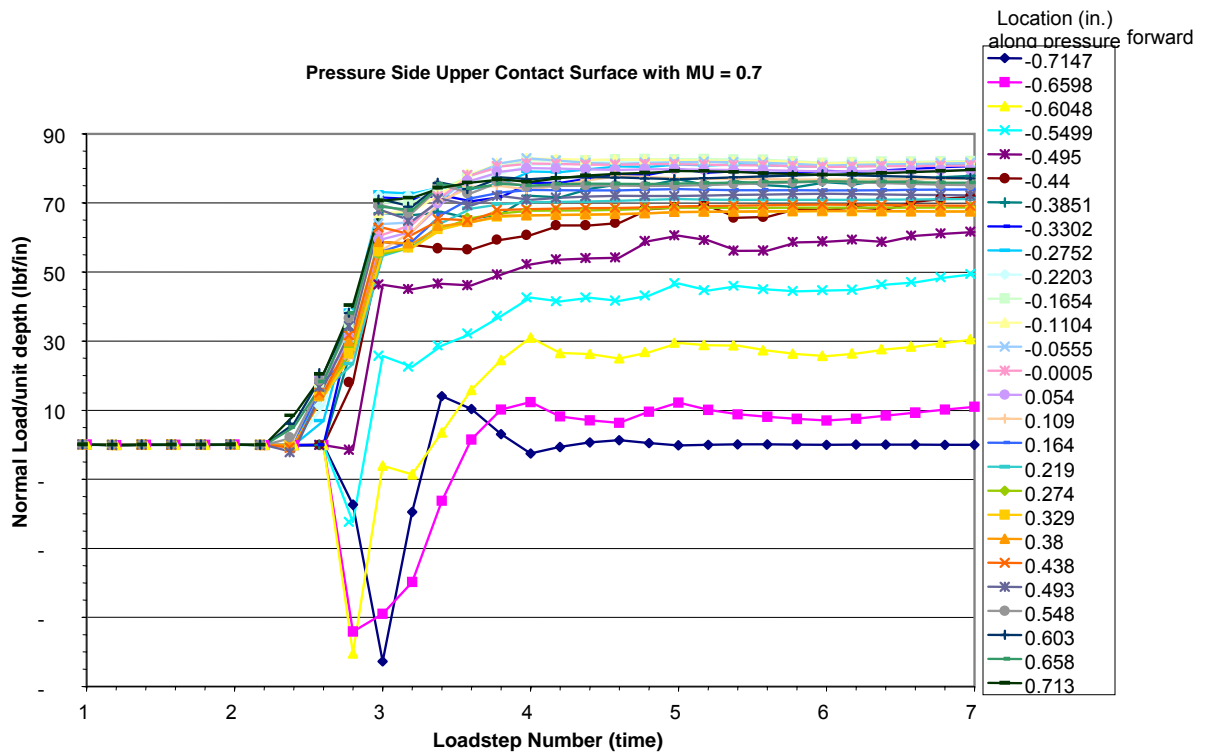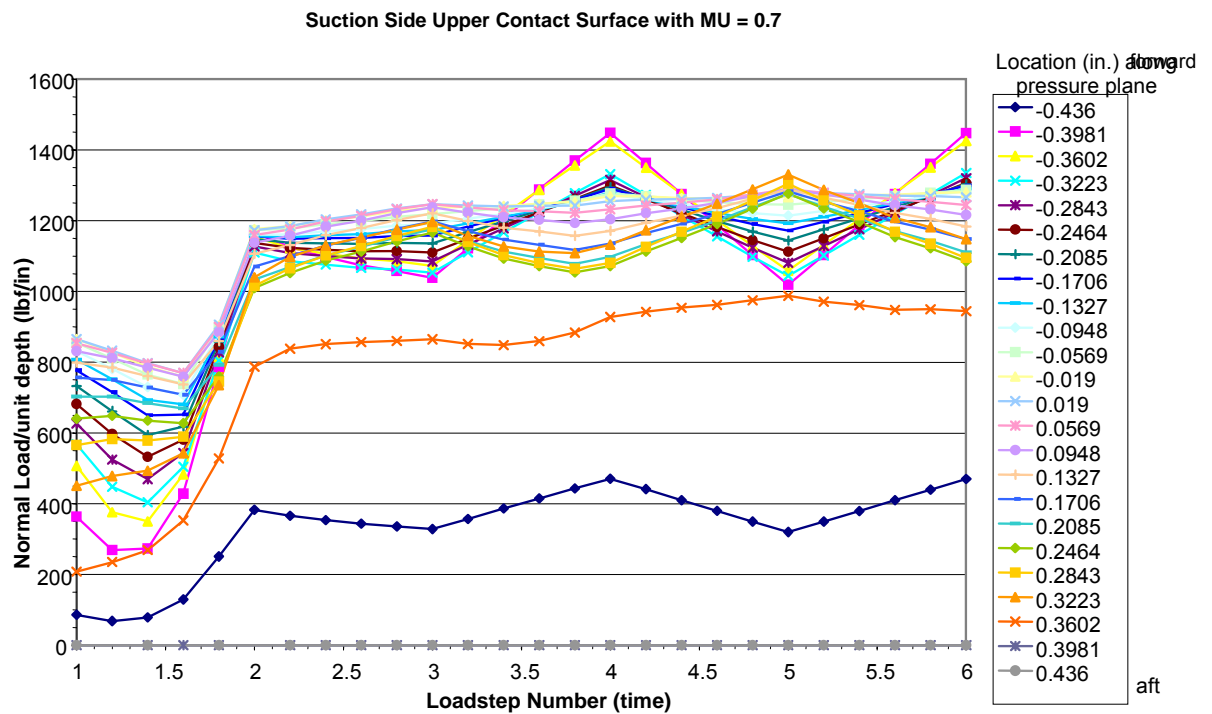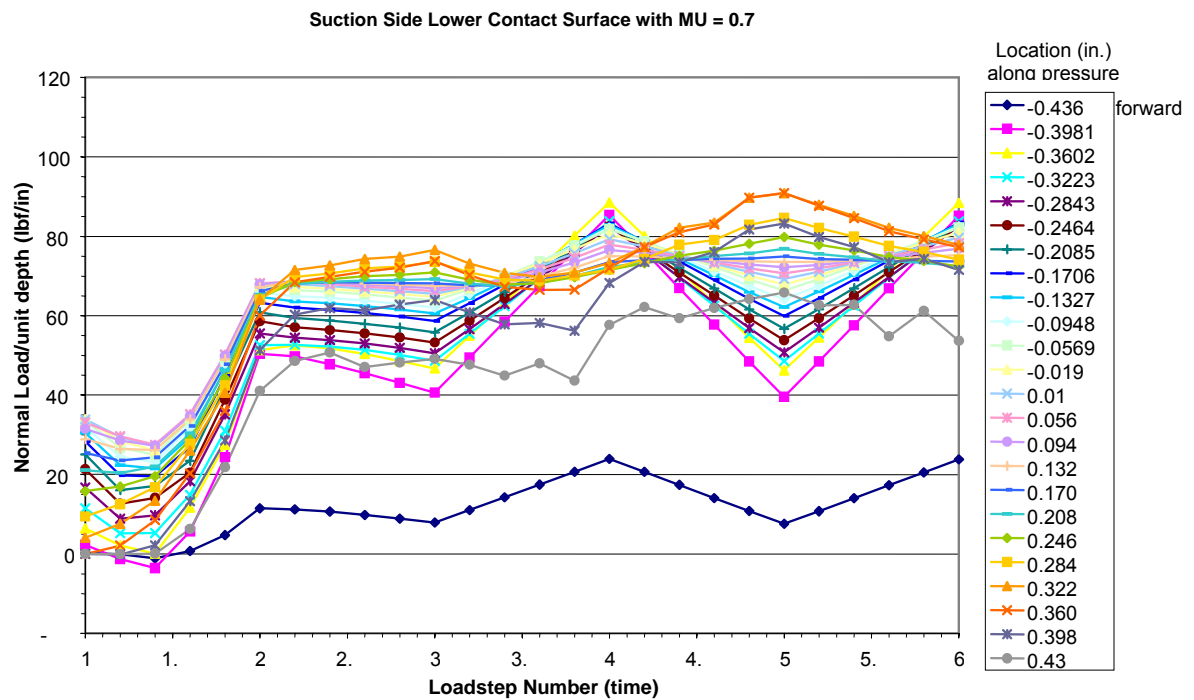
Figure X.23. Blade B, μ = 0.7, pressure side, upper tooth.
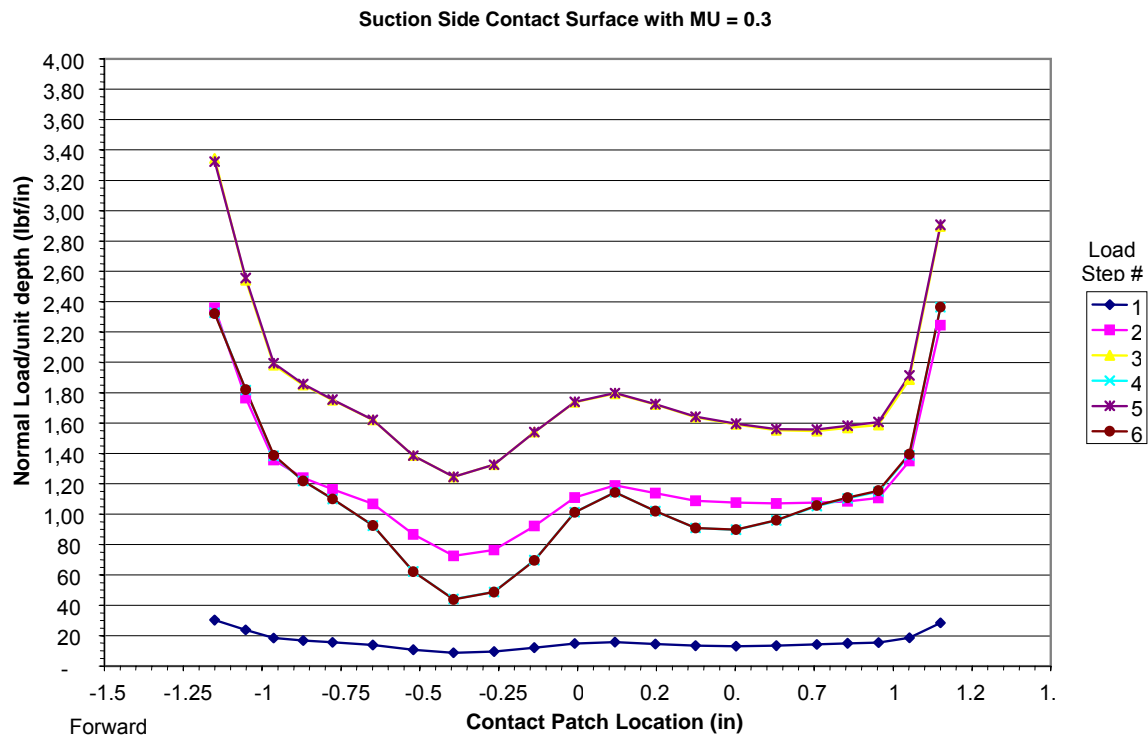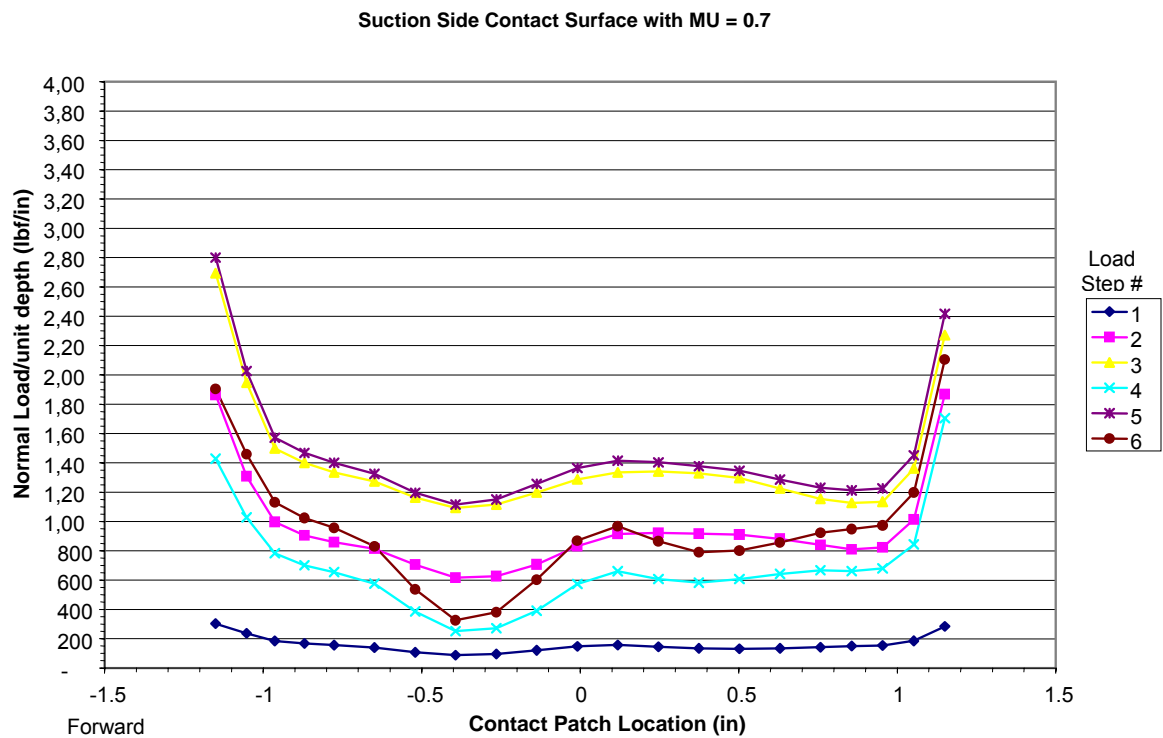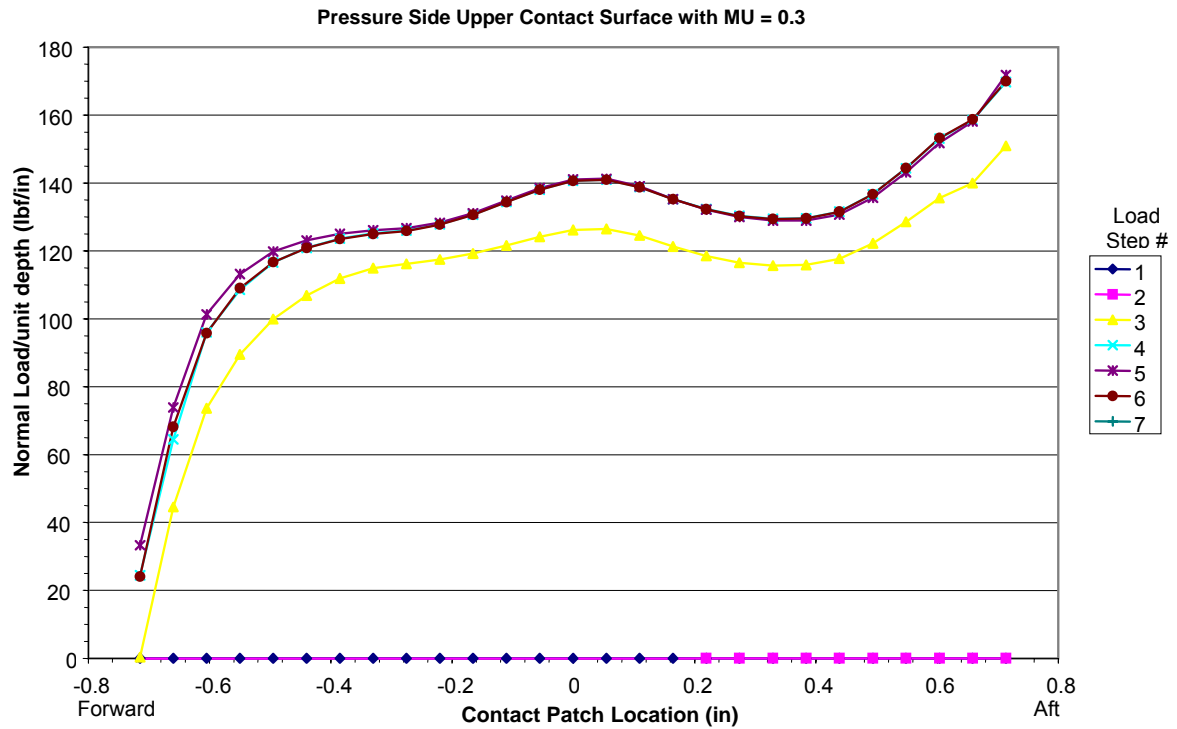

Figure X.24. Blade B, μ = 0.7 suction side, upper tooth.

X-25

Pressure Side Upper Contact Surface with MU = 0.3

Location (in.) along pressure forward

-0.4368
-0.3989
-0.3609
-0.323
-0.2851
-0.2472
-0.2093
-0.1714
-0.1335
-0.0955
-0.0576
-0.0197
0.018
0.056
0.09
0.131
0.169
0.207
0.245
0.283
0.321
0.359
0.397
0.435
0.436
0.437

Blade X.25. Blade C, μ = 0.3, pressure side, upper tooth.

Suction Side Upper Contact Surface with MU = 0.3

Location (in.) along pressure forward

-0.436
-0.3981
-0.3602
-0.3223
-0.2843
-0.2464
-0.2085
-0.1706
-0.1327
-0.0948
-0.0569
-0.019
0.01
0.056
0.094
0.132
0.170
0.208
0.246
0.284
0.322
0.360
0.398
0.43
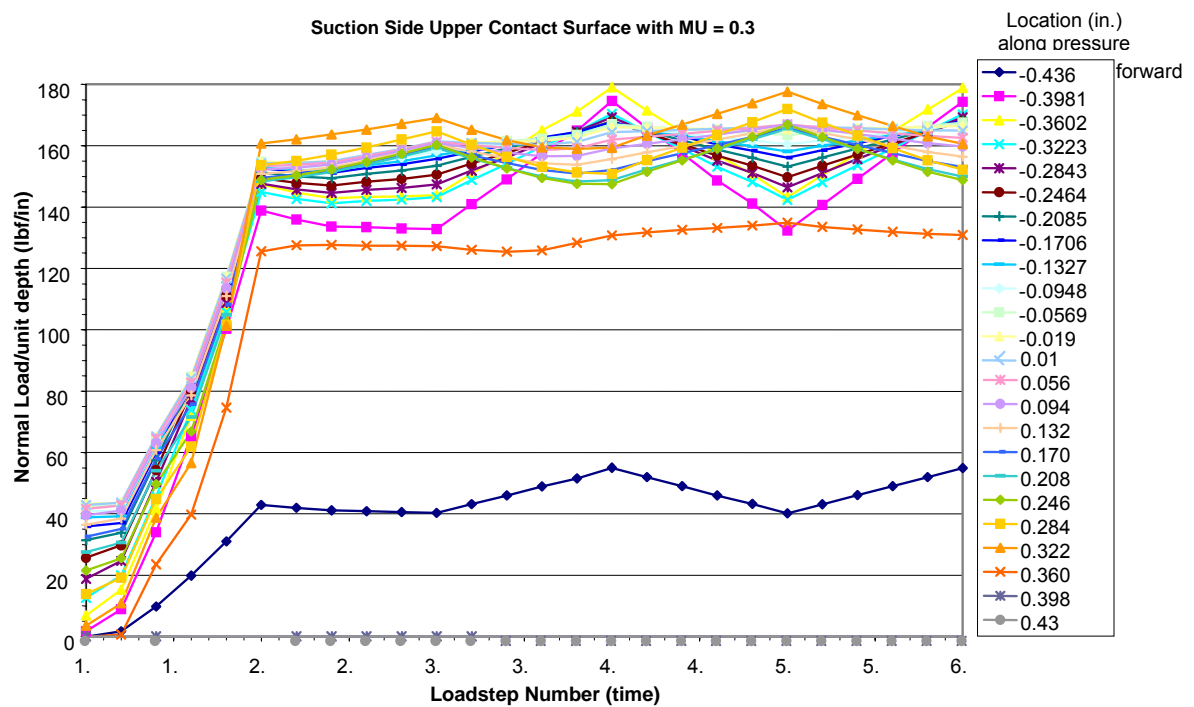
Figure X.26. Blade C, μ = 0.3, suction side, upper tooth.

Figure X.27. Blade C, $\mu = 0.3$, pressure side, lower tooth.
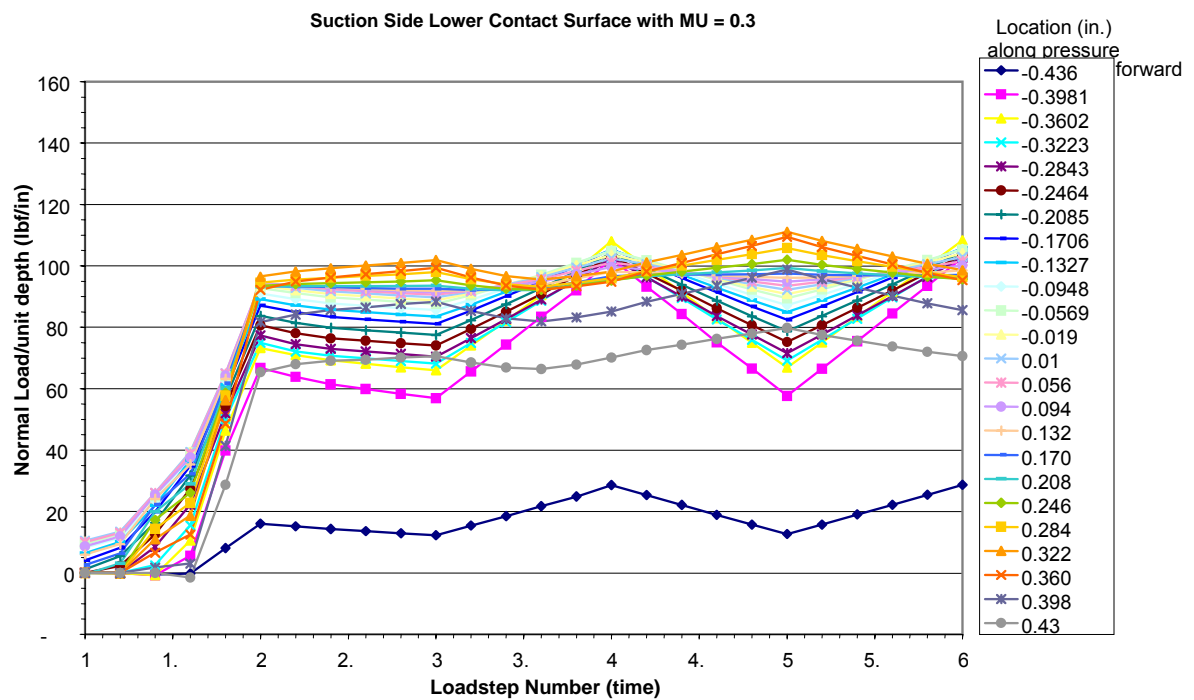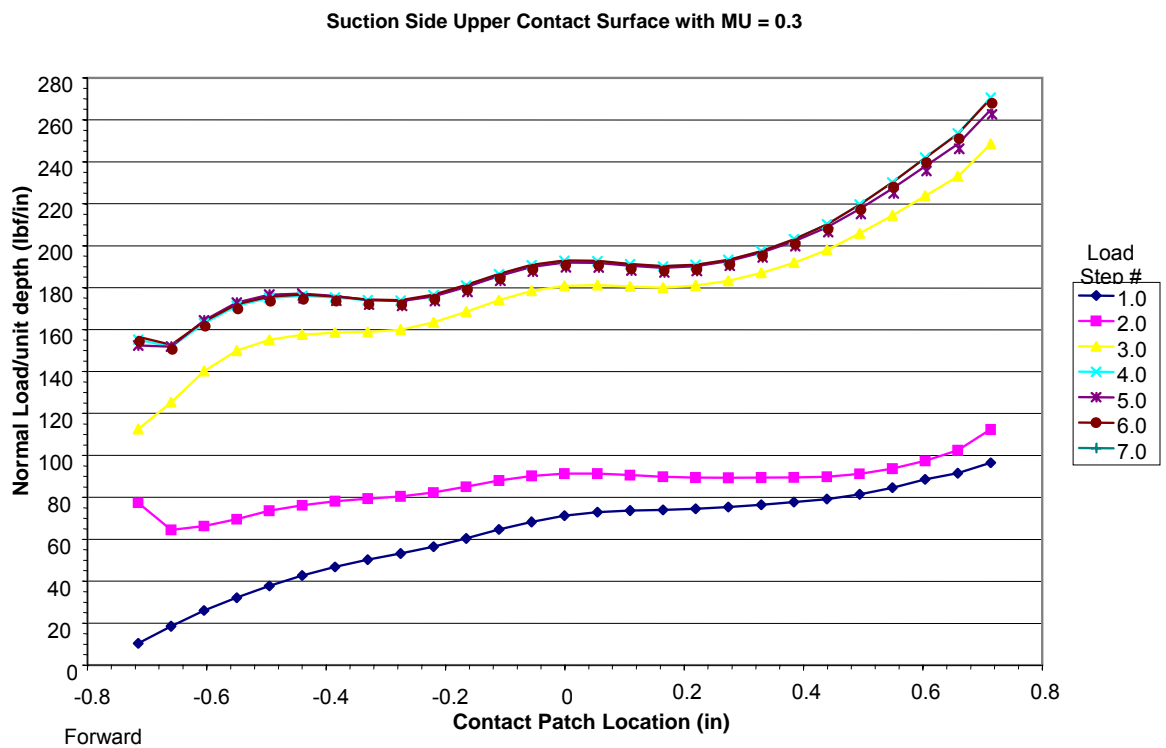

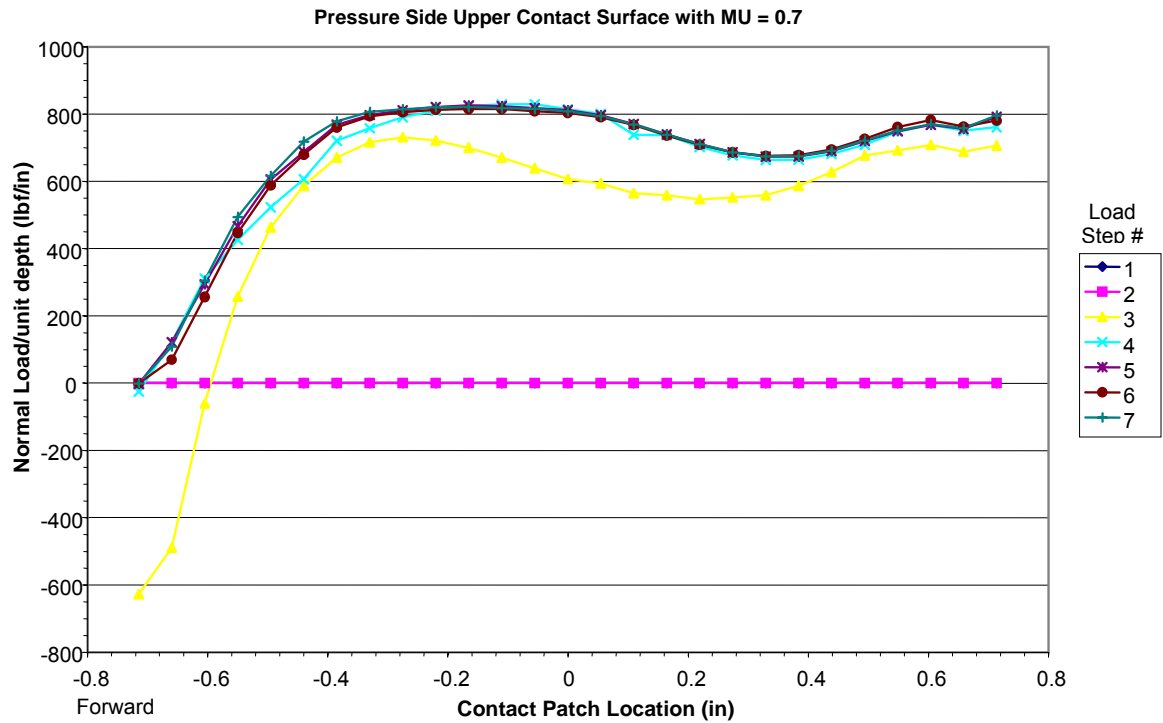
Figure X.28. Blade C, $\mu = 0.3$, suction side, lower tooth.
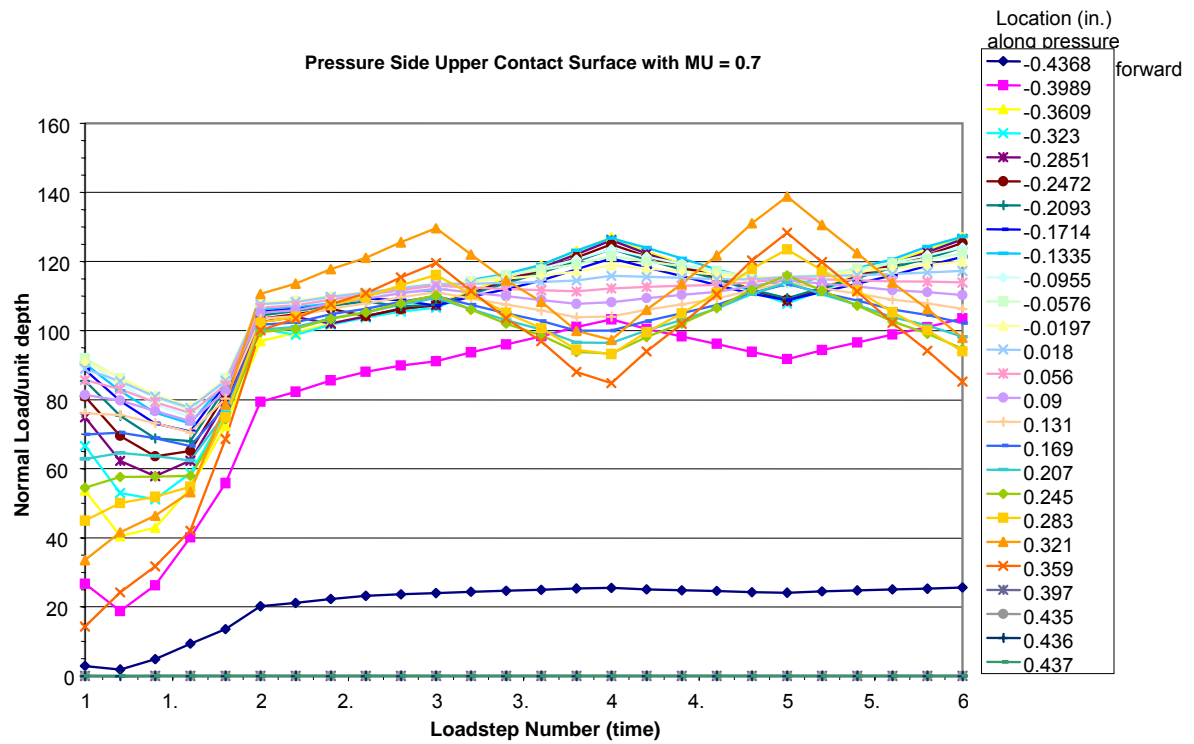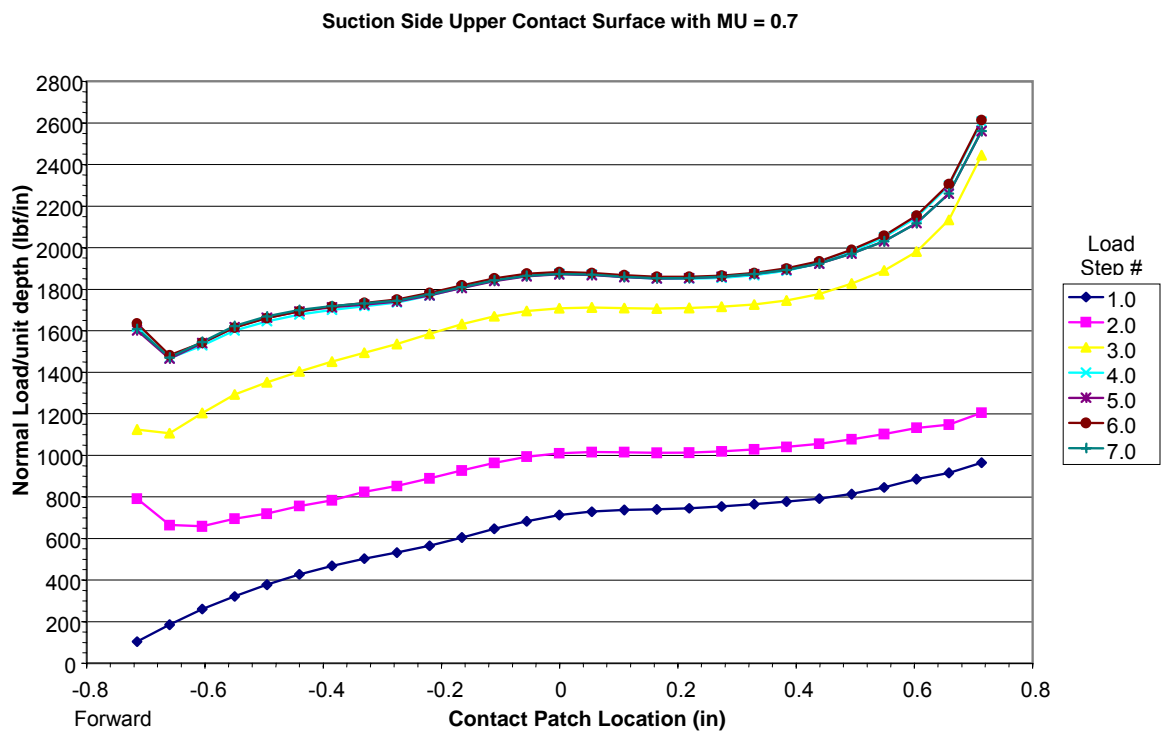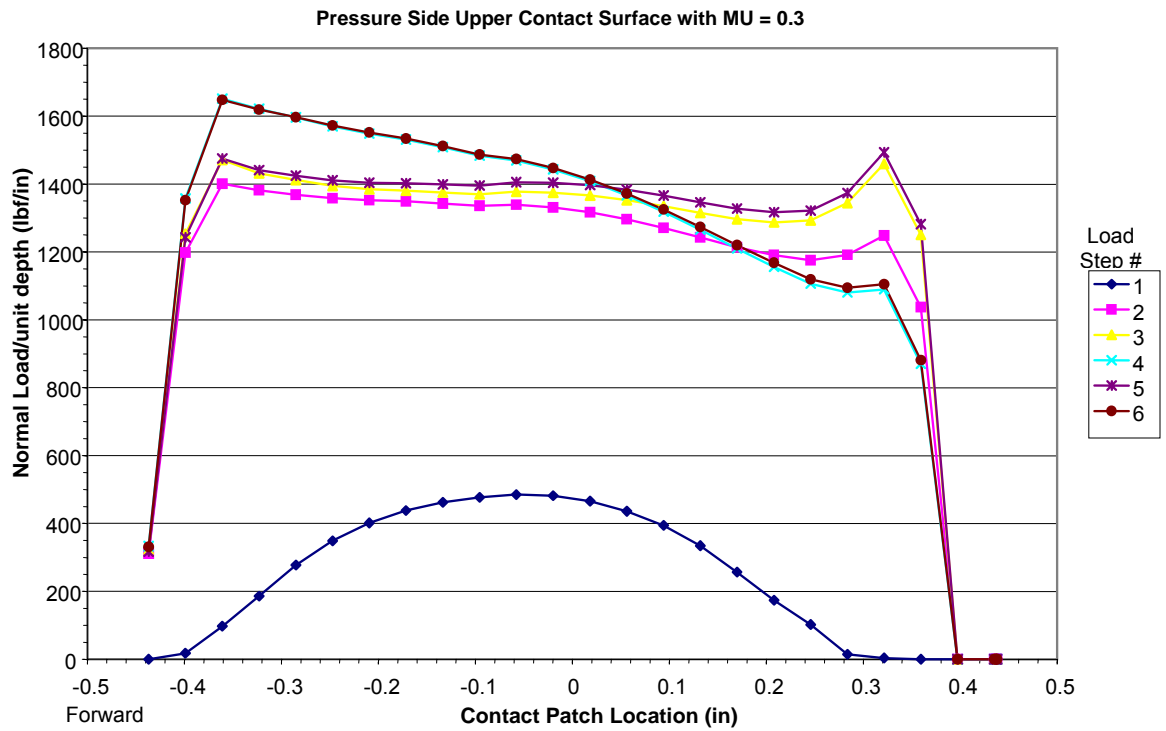
Figure X.29. Blade C, μ = 0.7, pressure side, upper tooth.

Figure X.30. Blade C, μ = 0.7, suction side, upper tooth.
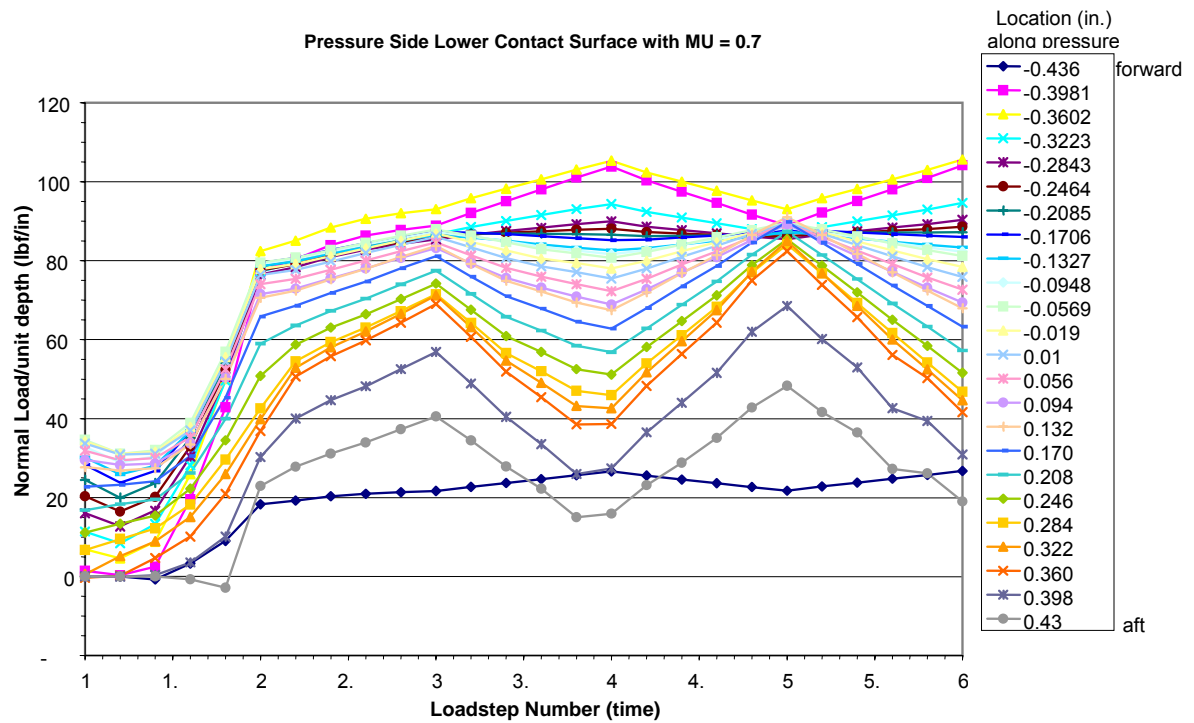
Figure X.31. Blade C, μ = 0.7, pressure side, lower tooth.

Figure X.32. Blade C, μ = 0.7, suction side, lower tooth.
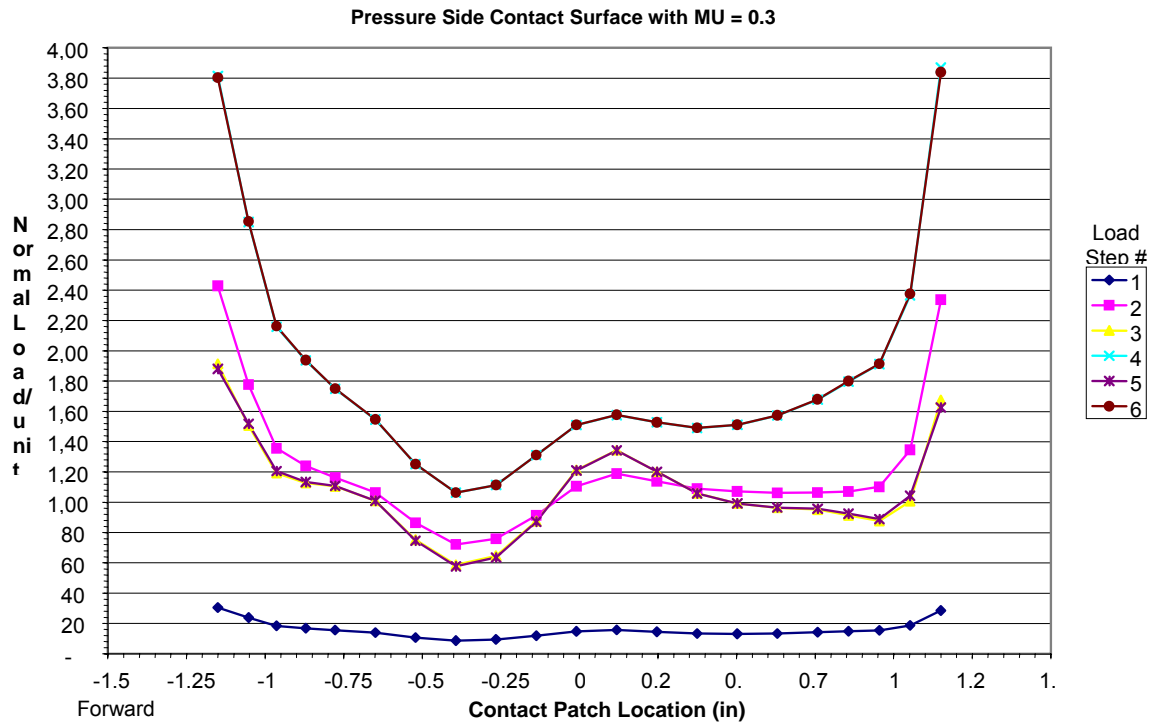
Figure X.33. Blade A, μ = 0.3, pressure side.

Figure X.34. Blade A, μ = 0.3, suction side.
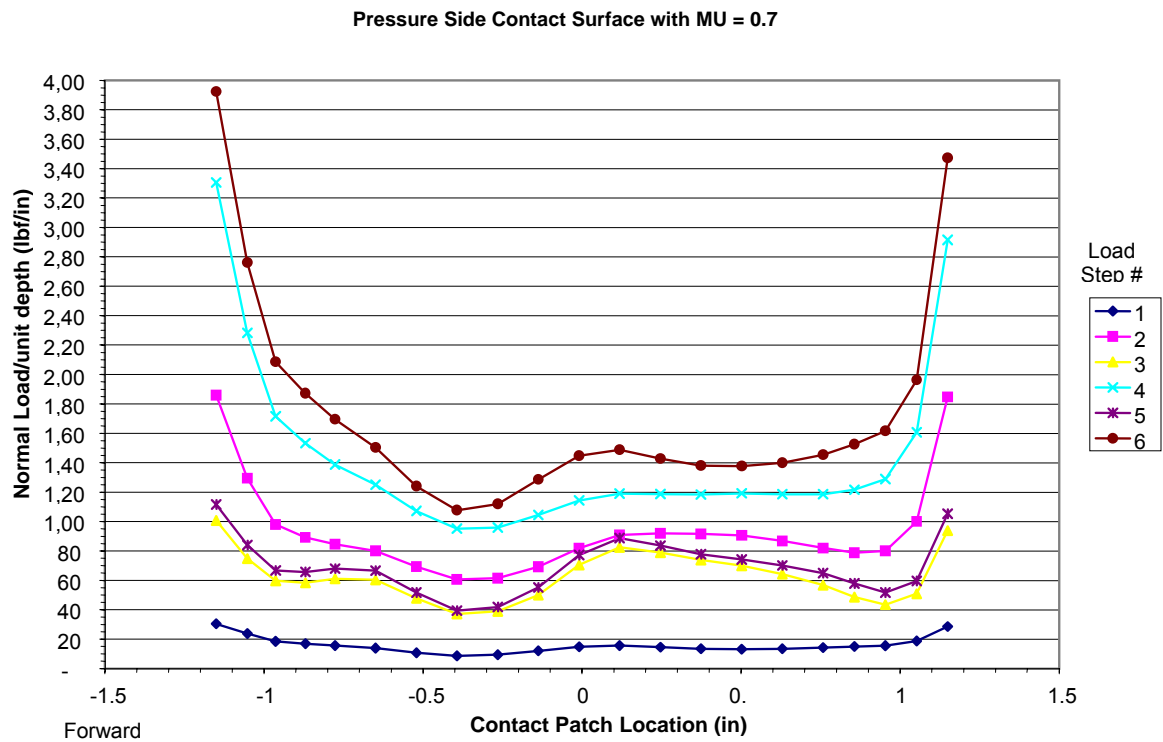
Pressure Side Contact Surface with MU = 0.7

Figure X.35. Blade A, μ = 0.7, pressure side.

Suction Side Contact Surface with MU = 0.7

Figure X.36. Blade A, μ = 0.7, suction side.

X-31

Pressure Side Upper Contact Surface with MU = 0.3

Figure X.37. Blade A, μ = 0.3, pressure side, upper tooth.

Suction Side Upper Contact Surface with MU = 0.3

Figure X.38. Blade B, μ = 0.3, suction side, upper tooth.

Figure X.39. Blade B, μ = 0.7, pressure side, upper tooth.

Figure X.40. Blade B, μ = 0.7, suction side, upper tooth.
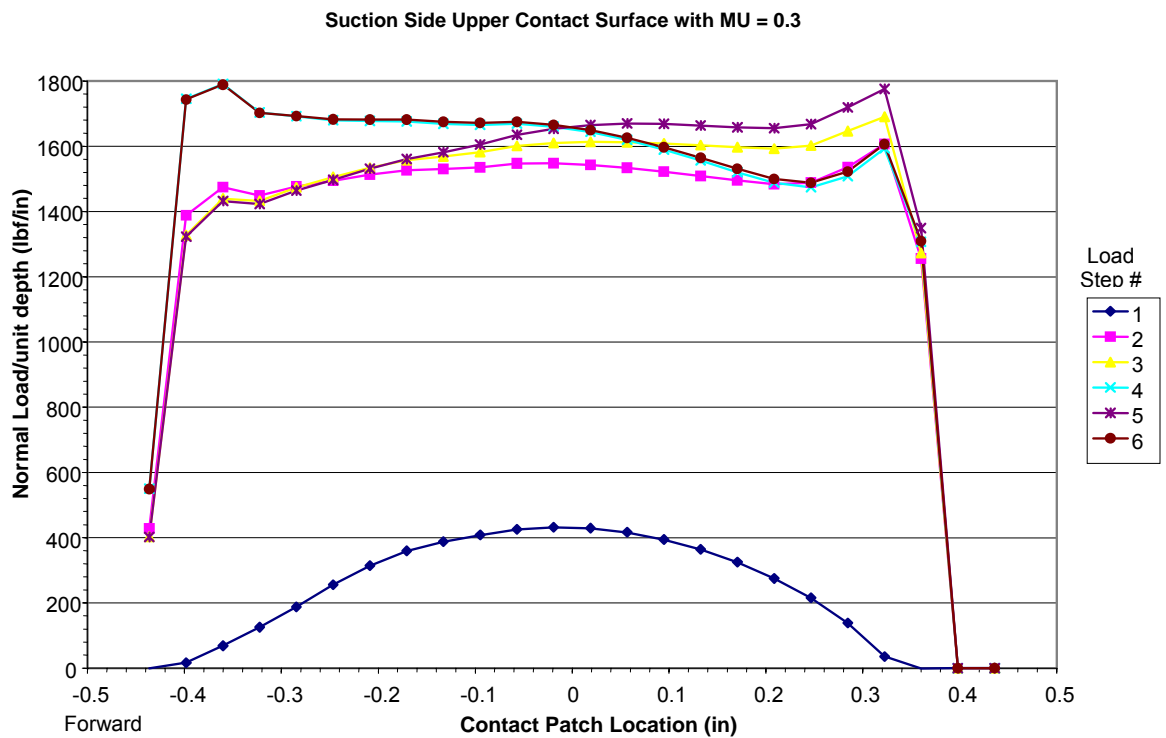
Figure X.41. Blade C, μ = 0.3, pressure side, upper tooth.

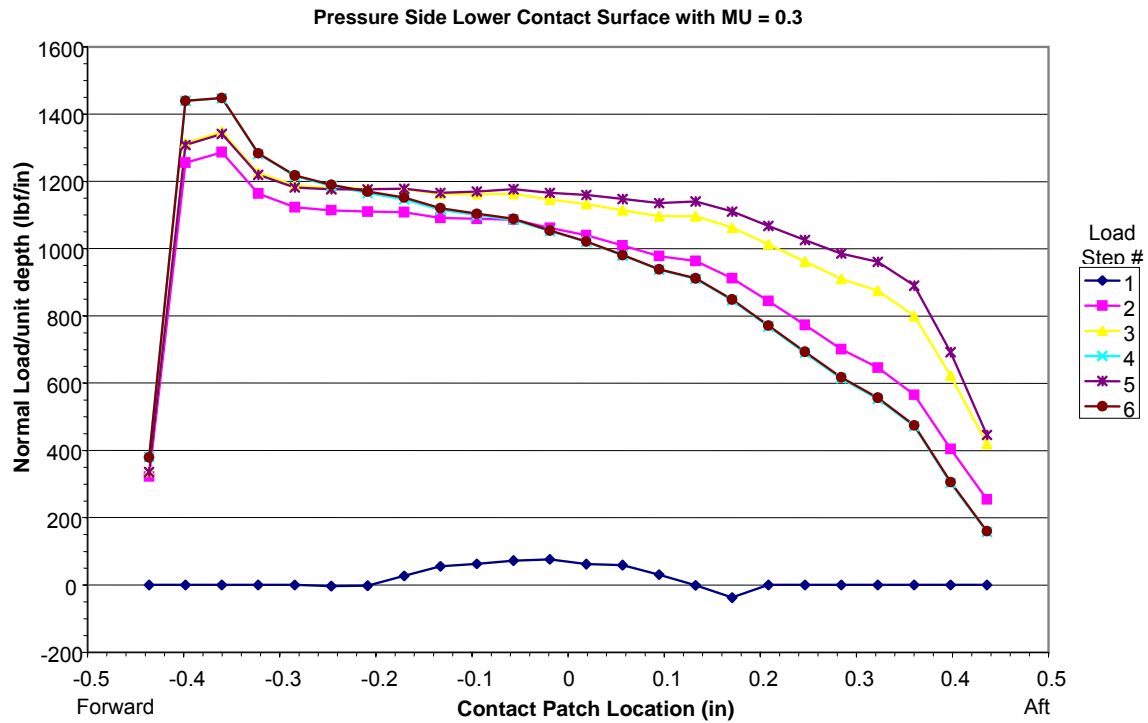

Figure X.42. Blade C, μ = 0.3, suction side, upper tooth.

X-34
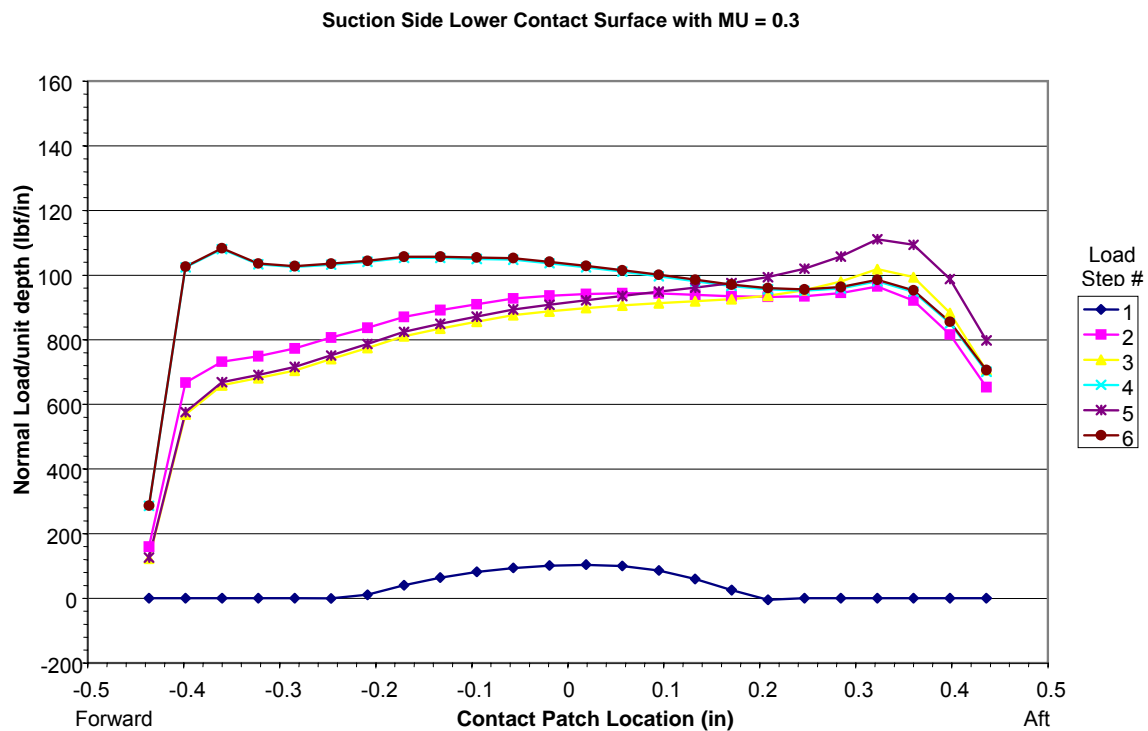
Figure X.43. Blade C, μ = 0.3, pressure side, lower tooth.
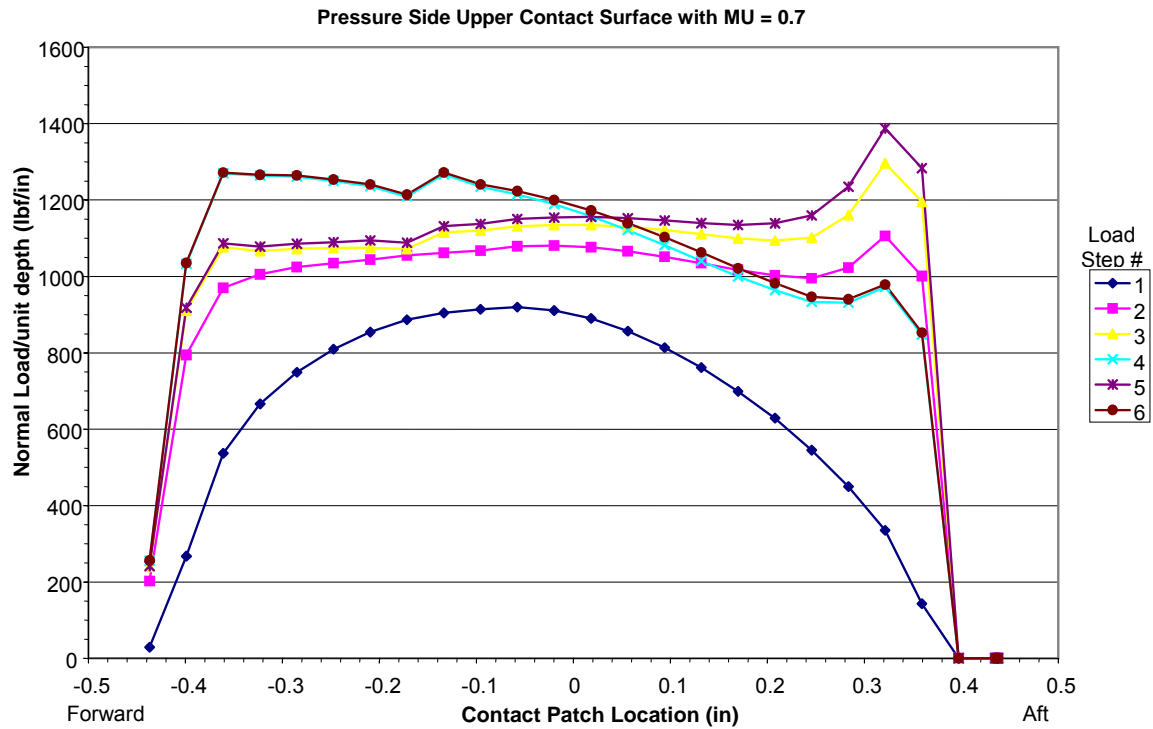

Figure X.44. Blade C, μ = 0.3, suction side, lower tooth.
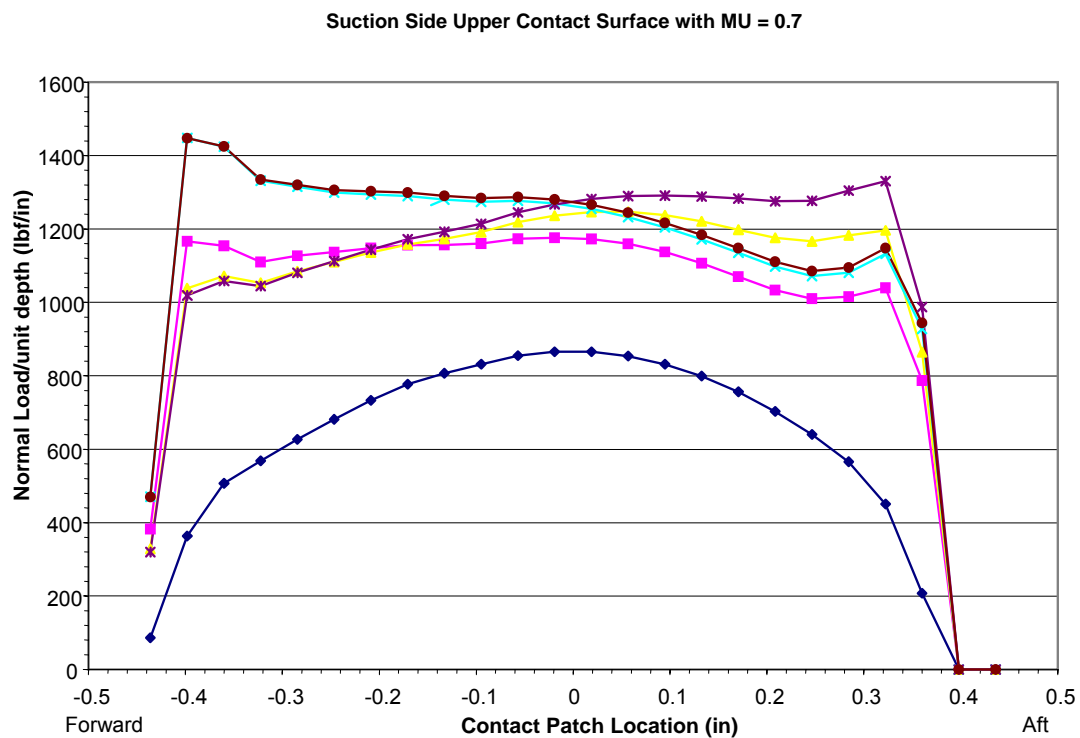
Figure X.45. Blade C, μ = 0.7, pressure side, upper tooth.

Figure X.46. Blade C, μ = 0.7, suction side, upper tooth.

Figure X.47. Blade C, μ = 0.7, pressure side, lower tooth.

Figure X.48. Blade C, μ = 0.7, suction side, lower tooth.